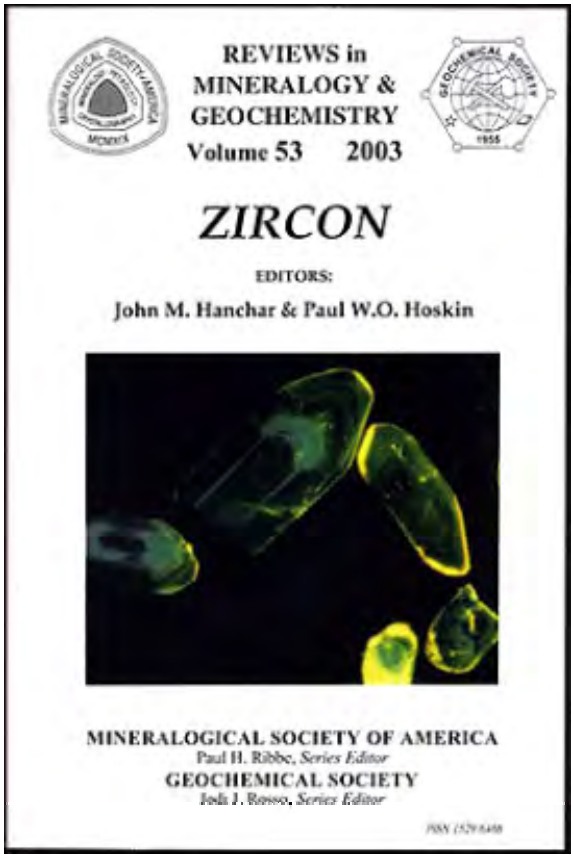


# Volume 53

# Zircon

John M. Hanchar & Paul W.O. Hoskin, editors

(revised 08/18/2004)

---

In the two decades since "Orthosilicates" (Reviews in Mineralogy, Vol. 5), much has been learned about the internal textures, trace-element and isotope geochemistry (both radiogenic and stable) and chemical and mechanical stability of zircon. The application of this knowledge and the use of zircon in geologic studies have become widespread. Today, the study of zircon exists as the pseudo-discipline of "zirconology" that involves materials scientists and geoscientists from across a range of sub-disciplines including stable and radiogenic isotopes, sedimentology, petrology, trace elements and experimental mineralogy. Zirconology has become an important field of research, so much so that coverage of the mineral zircon in a review volume that included zircon as one of many accessory minerals would not meet the needs or interests of the zirconology community in terms of depth or breadth of coverage.

The sixteen chapters in this volume cover the most important aspects of zircon-related research over the past twenty-years and highlight possible future research avenues. Finch and Hanchar (Chapter 1) review the structure of zircon and other mineral (and synthetic) phases with the zircon structure. In most rock types where zircon occurs it is a significant host of the rare-earth elements, Th and U. The abundances of these elements and the form of chondrite-normalized rare-earth element patterns may provide significant information on the processes that generate igneous and metamorphic rocks. The minor and trace element

compositions of igneous, metamorphic and hydrothermal zircons are reviewed by Hoskin and Schaltegger in Chapter 2. The investigation of melt inclusions in zircon is an exciting line of new research. Trapped melt inclusions can provide direct information of the trace element and isotopic composition of the melt from which the crystal formed as a function of time throughout the growth of the crystal. Thomas et al. (Chapter 3) review the study of melt inclusions in zircon. Hanchar and Watson (Chapter 4) review experimental and natural studies of zircon saturation and the use of zircon saturation thermometry for natural rocks. Cation diffusion and oxygen diffusion in zircon is discussed by Cherniak and Watson (Chapter 5). Diffusion studies are essential for providing constraints on the quality of trace element and isotope data and for providing estimates of temperature exposure in geological environments.

Zircon remains the most widely utilized accessory mineral for U-Th-Pb isotope geochronology. Significant instrumental and analytical developments over the past thirty years mean that zircon has an essential role in early Achaean studies, magma genesis, and astrobiology. Four chapters are devoted to different aspects of zircon geochronology. The first of these four, Chapter 6 by Davis et al., reviews the historical development of zircon geochronology from the mid-1950s to the present; the following three chapters focus on particular techniques for zircon geochronology, namely ID-TIMS (Parrish and Noble, Chapter 7), SIMS (Ireland and Williams, Chapter 8) and ICP-MS (Kosler and Sylvester, Chapter 9). The application of zircon chronology in constraining sediment provenance and the calibration of the geologic time-scale are reviewed by Fedo et al. (Chapter 10) and Bowring and Schmitz (Chapter 11), respectively.

Other isotopic systematics are reviewed for zircon by Kinny and Maas (Chapter 12), who discuss the application of Nd¥Sm and Lu¥Hf isotopes in zircon to petrogenetic studies, and by Valley (Chapter 13), who discusses the importance of oxygen isotopic studies in traditional and emerging fields of geologic study.

As a host of U and Th, zircon is subject to radiation damage. Radiation damage is likely responsible for isotopic disturbance and promotes mechanical instability. There is increasing interest in both the effect of radiation damage on the zircon crystal structure and mechanisms of damage and recrystallization, as well as the structure of the damaged phase. These studies contribute to an overall understanding of how zircon may behave as a waste-form for safe disposal of radioactive waste and are discussed by Ewing et al. (Chapter 14). The spectroscopy of zircon, both crystalline and metamict is reviewed by Nadsala et al. (Chapter 15).

The final chapter, by Corfu et al. (Chapter 16), is an atlas of internal textures of zircon. The imaging of internal textures in zircon is essential for directing the acquisition of geochemical data and to the integrity of conclusions reached once data has been collected and interpreted. This chapter¦for the first time¦brings into one place textural images that represent common and notso- common textures reported in the literature, along with brief interpretations of their significance. There is presently no comparable atlas. It is intended that this chapter will become a reference point for future workers to compare and contrast their own images against.

i-xvii and 500 pp. ISBN 093995065-0.

# Contents of Volume 53

*P.D. Kinny and R. Maas*

- Oxygen isotopes in zircon

  *J.W. Valley*

- Radiation effects in zircon

  *R.C. Ewing, A. Meldrum, L. Wang, W.J. Weber, and L.R. Corrales*

- Spectroscopic methods applied to zircon

  *L. Nasdala, M. Zhang, U. Kempe, G. Panczer, M. Gaft, M. Andrut, and M. Plotze*

- Atlas of zircon textures

  *F. Corfu, J.M. Hanchar, P.W.O. Hoskin, and P. Kinny*

---

***ERRATA***

Correction to Reviews in Mineralogy & Geochemistry Vol. 53

--- Zircon ---

**"Preface" by J. M. Hanchar & P. W. O. Hoskin, p. v-vii**

*Last full paragraph at the bottom of page vi should read:*

> The final chapter, by Corfu et al. (Chapter 16), is an atlas of internal textures of zircon. The imaging of internal textures in zircon is essential for directing the acquisition of geochemical data and to the integrity of conclusions reached once data has been collected and interpreted. This chapter, for the first time, brings into one place textural images that represent common and not so common textures reported in the literature, along with brief interpretations of their significance. There is presently no comparable atlas. It is intended that this chapter will become a reference point for future workers to compare and contrast their own images against.

**Chapter 1 "Structure and Chemistry of Zircon and Zircon Group Minerals" by R. J. Finch & J. M. Hanchar, p. 1-25**

*Corrected street address for author Robert J. Finch:*

> 9700 South Cass Avenue

*Page 18, line 10 from top of page:*

> replace "scheelite" with "monazite" such that the line reads:
>
> zircon-type-to-monazite transformations…

**Chapter 2 "The Composition of Zircon and Igneous and Metamorphic Petrogenesis" by P. W. O. Hoskin & U. Schaltegger, p. 27-62**

*Page 29, 9$^{th}$ line from bottom:*

> Reference to Watson and Hanchar (this volume) should be to Hanchar and Watson (this volume).

*Page 36, corrected table 2:*

**Table 2.** Rare-earth element and Y composition of standard zircon 91500 (ppm ± 1σ)*.

| Element | Wiedenbeck[1] | Nesbitt[2] | Hoskin[3] | Belousova[4] | Sano[5] |
|---|---|---|---|---|---|
| *n* | 1–6 | 10 | 17† | 4 | 5–6** |
| Y | | | 160 ± 23 | 147 ± 22 | |
| La | | 0.003 | 0.04 ± 0.03 | | 0.01 ± 0.01 |
| Ce | 2.0 ± 0.1 | 2.14 | 2.5 ± 0.2 | 2.5 ± 0.5 | 2.6 ± 0.4 |
| Pr | | 0.01 | 0.03 ± 0.02 | | 0.04 ± 0.02 |
| Nd | 0.4 | 0.25 | 0.3 ± 0.1 | | 0.30 ± 0.06 |
| Sm | 0.3 | 0.50 | 0.4 ± 0.1 | 0.4 ± 0.2 | 0.28 ± 0.08 |
| Eu | 0.26 ± 0.07 | 0.23 | 0.22 ± 0.01 | 0.4 ± 0.2 | 0.19 ± 0.07 |
| Gd | 1.9 ± 0.1 | 2.38 | 2.0 ±0.4 | 2.1 ± 0.4 | 1.6 ± 0.4 |
| Tb | | 0.83 | 0.86 ± 0.06 | | 0.8 ± 0.2 |
| Dy | 8.0 ± 0.1 | 10.8 | 11.03 ± 0.06 | 12 ± 2 | 12 ± 3 |
| Ho | | 4.4 | 4.8 ± 0.3 | 4.9 ± 0.7 | 5 ± 1 |
| Er | 20.4 ± 0.8 | 24.2 | 25 ± 2 | 26 ± 4 | 29 ± 6 |
| Tm | | 6.4 | 6.6 ± 0.4 | | 8 ± 2 |
| Yb | 57 ± 17 | 69.7 | 65 ± 2 | 66 ± 7 | 77 ± 18 |
| Lu | 12.4 ± 0.9 | 12.6 | 13 ± 2 | 14 ± 2 | 17 ± 4 |
| ΣREE | 103+ | 134 | 132 | 128+ | 154 |

* A blank entry denotes element not analyzed for or below the limit of detection.

** Uncertainty is given as ± 2σ; *n*= the number of analyses contributing to mean REE and Y values.

† Includes SIMS and LA–ICP-MS data.

1. Weidenbeck et al. (1995); 2. Nesbitt et al. (1997); 3. Hoskin (1998); 4. Belousova et al. (2002); 5. Sano et al. (2002).

*Page 39, corrected table 3:*

**Table 3.** Characteristic ratios of chondrite-normalized zircon REE patterns of Figure 4.†

| Ratio** | Vaca Muerta zircon 2 | Simmern | Lunar/ Apollo 14 | Phalaborwa carbonatite | Mud Tank carbonatite | Jwaneng kimberlite |
|---|---|---|---|---|---|---|
| Figure 4 | a | a | b | c | c | c |
| *n* | 1 | 1 | 1 | 1 | 16 | 4 |
| $(Sm/La)_N$ | 1.3 | 0.4 | 4.8 | 164 | 11.3 | 38 |
| $(Lu/Gd)_N$ | 4.6 | 169 | 45 | 15 | 9.3 | 1.4 |
| Ce/Ce* | 0.9 | 1.3 | 0.6 | 49 | 3.7 | 13 |
| Eu/Eu* | 0.2 | 2.1 | 0.1 | 0.4 | 1.0 | 1.0 |

| Ratio** | Blind Gabbro | Mawson ig. charnockite | Syros ophiolite | Manilla plagiogranite | BPZP diorite | BPZP aplite |
|---|---|---|---|---|---|---|
| Figure 4 | d | d | e | e | f | f |
| *n* | 8 | 10 | 8 | 7 | 7 | 4 |
| $(Sm/La)_N$ | 153 | 236 | 547 | 90 | 119 | 57 |
| $(Lu/Gd)_N$ | 16 | 19 | 44 | 44 | 27 | 38 |
| Ce/Ce* | 20 | 79 | 82 | 20 | 39 | 40 |
| Eu/Eu* | 0.2 | 0.2 | 0.3 | 0.9 | 0.2 | 0.3 |

| Ratio** | Torihama dacite | Manaslu granite | Chuquicamata W. porphyry | Los Picos diorite | Elie Ness xenolith | Jack Hills zircon |
|---|---|---|---|---|---|---|
| Figure 4 | g | h | i | j | k | l |
| *n* | 6 | 13 | 10 | 9 | 6 | 8 |
| $(Sm/La)_N$ | 306 | 33 | 145 | 653 | 165 | 18 |
| $(Lu/Gd)_N$ | 74 | – | 47 | 19 | 17 | 35 |
| Ce/Ce* | 132 | – | 230 | 87 | 31 | 8.0 |
| Eu/Eu* | 0.3 | 0.3 | 0.4 | 0.1 | 0.9 | 0.2 |

† Chondrite normalizing values from McDonough and Sun (1995). $Ce_N$ indicates the element has been normalized; $(Sm/La)_N$ indicates that the elements where normalized prior to division.

*n* = the number of analyses contributing to mean.

** Anomalies are calculated in this manner; for example $Ce/Ce^* = Ce_N / (La_N \times Pr_N)^{1/2}$ .

## Chapter 3 "Melt Inclusions in Zircon" by J. B. Thomas, R. J. Bodnar, N. Shimizu and C. A. Chesner, p. 63-87

*Page 71, Figure 5, legend:*

small boxes following "melt inclusions" should be deleted

*Page 73, corrected Table 1:*

**Table 1.** Zircon/melt partition coefficients ($D_{REE}$) calculated using REE abundances of melt inclusions and coexisting zircon crystals from the Quottoon Igneous Complex and from the Toba rhyolite. [Quottoon Igneous Complex data used by permission of Elsevier Science, from Thomas et al. (2002), *Geochimica et Cosmochimica Acta*, Vol. 66, Table 3, p. 2894]

| | $D_{La}$ | $D_{Ce}$ | $D_{Nd}$ | $D_{Sm}$ | $D_{Dy}$ | $D_{Er}$ | $D_{Yb}$ |
|---|---|---|---|---|---|---|---|
| | 0.05 | 2.06 | 1.58 | 11.61 | 72.98 | 72.39 | 51.52 |
| | 0.04 | 0.83 | 0.2 | 2.7 | 20.09 | 29 | 40.63 |
| | 0.07 | 1.46 | 0.5 | 3.56 | 22.45 | 29.35 | 35.88 |
| | 0.22 | 0.99 | 0.53 | 4.14 | 16.79 | 21.09 | 21.9 |
| | 0.03 | 1.4 | 0.77 | 5.02 | 19.41 | 17.89 | 14.04 |
| Quottoon | 0.02 | 0.61 | 0.11 | 2.49 | 36.56 | 58.88 | 66.1 |
| | 0.06 | 0.93 | 0.56 | 4.58 | 12.37 | 13.07 | 13.04 |
| | 0.26 | 1.26 | 0.81 | 3.24 | 51.95 | 74.99 | 76.32 |
| | 0.02 | 0.43 | 0.35 | 0.75 | 19.31 | 52.72 | 82.29 |
| | 0.03 | 1.1 | 0.31 | 11.24 | 52.31 | 60.74 | 35.11 |
| | 0.05 | 0.75 | 0.16 | 1.27 | 26.42 | 70 | 96.72 |
| Median $D_M$ | 0.05 | 0.99 | 0.5 | 3.56 | 22.45 | 52.72 | 40.63 |
| | 0.21 | 0.67 | 0.41 | 4.28 | 11.77 | 20.29 | 16.51 |
| | 0.04 | 0.56 | 0.10 | 0.99 | 14.29 | 20.23 | 17.70 |
| | *0.01 | 0.56 | 0.76 | 4.71 | 84.12 | 220.81 | 242.70 |
| | 0.43 | 1.35 | 0.76 | 5.25 | 41.83 | 38.21 | 32.13 |
| | 0.03 | 0.83 | 0.12 | 2.52 | 29.45 | 33.56 | 39.92 |
| Toba | 0.03 | 0.29 | 0.24 | 1.32 | 90.39 | 19.27 | 29.74 |
| | *0.01 | 0.74 | 0.71 | 2.22 | 68.45 | 187.43 | 460.31 |
| | 0.001 | 0.55 | 0.66 | 3.81 | 49.48 | 63.81 | 86.30 |
| | 0.001 | 0.42 | 0.10 | 1.52 | 22.04 | 45.75 | 85.86 |
| | 0.02 | 0.90 | 0.09 | 2.61 | 23.42 | 29.67 | 37.44 |
| | 0.08 | 0.17 | 0.16 | 0.43 | 14.48 | 27.56 | 36.77 |
| Median $D_M$ | 0.03 | 0.62 | 0.25 | 2.37 | 26.44 | 31.61 | 37.10 |

* hourglass shaped inclusions

*Page 73, corrected Table 2:*

**Table 2.** Zircon/melt partition coefficients ($D_M$) calculated for lowest (top row) and highest (bottom row) La, Sm and Yb abundances in the melt inclusions and zircon hosts. [Used by permission of Elsevier Science, from Thomas et al. (2002), *Geochimica et Cosmochimica Acta*, Vol. 66, Table 4, p. 2896]

| $^{a}La_{MI}$ | $^{b}La_{zircon}$ | $D_{La}$ | $^{a}Sm_{MI}$ | $^{b}Sm_{zircon}$ | $D_{Sm}$ | $^{a}Yb_{MI}$ | $^{b}Yb_{zircon}$ | $D_{Yb}$ |
|---|---|---|---|---|---|---|---|---|
| 13.6 | 0.41 | 0.03 | 0.29 | 3.26 | 11.24 | 1.495 | 144.6 | 96.72 |
| 96.6 | 2.9 | 0.03 | 6.06 | 30.4 | 5.02 | 83.35 | 1170 | 14.04 |

(a) REE abundance in melt inclusion.
(b) REE abundance in zircon.

*Page 80, Figure 10, legend:*

small boxes following "zircon", "matrix glass", "allanite", and "plagioclase" should be deleted

*Page 81, Figure 11, legend*

Small boxes following "zircon", "allanite", and "plagioclase" should be deleted

## Chapter 4 "Zircon Saturation Thermometry" by J. M. Hanchar & E. B. Watson, p. 89-112

*Page 92, corrected Table 1:*

**Table 1.** Calculation of *M* and *FM*.

| Oxide | N-57 rhyolite (Wark 1991) | Oxide wt % / Eq wt[1] | Cation fraction[2] |
|---|---|---|---|
| $SiO_2$ | 69.04 | 1.149 | 0.679 |
| $TiO_2$ | 0.38 | 0.005 | 0.003 |
| $Al_2O_3$ | 13.65 | 0.268 | 0.158 |
| FeO | 0.63 | | |
| $Fe_2O_3$ | 1.26 | | |
| FeO (t) = $Fe_2O_3$*0.8998+FeO | 1.76 | 0.025 | 0.015 |
| MnO | 0.07 | 0.001 | 0.001 |
| MgO | 0.46 | 0.011 | 0.007 |
| CaO | 1.31 | 0.023 | 0.014 |
| $Na_2O$ | 4.61 | 0.149 | 0.088 |
| $K_2O$ | 2.85 | 0.061 | 0.036 |
| $P_2O_5$ | 0.04 | 0.001 | 0.000 |
| $H_2O^-$ | 0.52 | | |
| $H_2O^+$ | 5.07 | | |
| $CO_2$ | 0.00 | | |
| Total | 99.89 | 1.692 | |
| Zr (ppm)[4] | 299 | | |
| [3]M = (Na+K+(2*Ca))/(Al*Si) | | | |
| *M = 1.41* | | | |
| [3]*FM*= (Na+K+(2*Ca+Fe+Mg))/(Al*Si) | | | |
| *FM =1.69* | | | |

*Notes:* Data for bulk sample analysis by X-ray fluorescence spectrometry from Wark (1991).
[1]The values in column 3 are calculated from using the wt. % oxide for each major element in column 2 divided by the equivalent wt. for that oxide.
[2]The values in column 4 are calculated from each value in column 3 divided by the total for column 3.
[3]The values used in the *M* and *FM* calculations are the cation fractions from column 4.
[4]No error was reported for Zr in Wark (1991).

*Page 105, corrected Table 2:*

**Table 2.** Major element comparison between XRF and EMPA for N-57 rhyolite.

| Oxide | XRF (bulksample)[1] | EMPA (*in situ*) |
|---|---|---|
| $SiO_2$ | 69.04 | 69.43 |
| $TiO_2$ | 0.38 | 0.26 |
| $Al_2O_3$ | 13.65 | 12.74 |
| FeO | 0.63 | |
| $Fe_2O_3$ | 1.26 | |
| FeO (t) = $Fe_2O_3$*0.8998+FeO | 1.76 | 1.02 |
| MnO | 0.07 | "fixed value"[1] |
| MgO | 0.46 | 0.15 |
| CaO | 1.31 | 0.53 |
| $Na_2O$ | 4.61 | 4.76[2] |
| $K_2O$ | 2.85 | 2.94 |
| $P_2O_5$ | 0.04 | "fixed value" |
| $H_2O^-$ | 0.52 | |
| $H_2O^+$ | 5.07 | "fixed value" |
| $CO_2$ | 0.00 | n/a |
| Total | 99.89 | n/a |
| Zr (ppm)[4] | 299 | 325 +/- 31[3] |

Notes: [1]Only Si, Ti, Al, Fe, Mg, Ca, Na, and K were analyzed with the EMPA. Fixed values for an average rhyolite composition from Best (1982) were used for other elements in ZAF correction.
[2]$Na_2O$ value in Table 2 corrected to account for Na loss during EMPA analysis (see text).
[3]Error on EMPA Zr concentration value from 1σ absolute standard deviation from counting statistics.

*Page 105, corrected Table 3:*

Table 3. Temperature and $fO_2$ estimates for N-57 rhyolite sample.

| Sample[1] | Fe-Ti oxide thermometry[2] | log $fO_2$ estimate[2] | Two-pyroxene thermometry[2] | Bulk sample (XRF)[2] *M*, Zr, and T | | *In situ* glass analysis (EMPA)[3] *M*, Zr, and T |
|---|---|---|---|---|---|---|
| | | | | | 1.41<br>299 ppm | 1.35<br>325 ± 31 ppm |
| #1 | 903°C | −10.6 | 862°C @ 0.1 GPa | 883°C @ 0.5 GPa | | |
| #2 | 897°C | −10.7 | 836°C | 857°C | | |
| | | | | | 842°C | 855 ± 15°C |

Note: [1]#s 1 and 2 in column 1 refer to two different temperature and fugacity determinations for sample N-57.
[2]Fe-Ti oxide and pyroxene thermometry (Anderson and Lindsley [1985] and Davidson and Lindsley [1988], respectively), $fO_2$ estimate, and XRF bulk sample Zr concentration from Wark (1991).
[3]Error on calculated temperature propagated through from counting statistics uncertainty in Zr determination which is thought to be the largest source of error. Zircon saturation temperatures calculated using Equation 1 in text and data from Tables 1 and 2.

## Chapter 5 "Diffusion in Zircon" by D. J. Cherniak & E. B. Watson, p. 113-143

*Page 137, Figure 17, missing text at end of caption:*

Complete caption should read as follows:

**Figure 17.** Oxygen diffusion center-retention criteria for spherical zircon cores and rims cooling under wet conditions (Watson and Cherniak, 1997). The schematic diagram in (a) shows a radial profile of $\delta^{18}O$ (initially a step distribution) which relaxes toward homogeneity with increasing time at high temperature. There is a critical cooling rate—$(dT/dt)_c$, assumed here to be linear—below which the original $\delta^{18}O$ value at the center of a core or rim will fail to be preserved. If cooling is too slow, $\delta^{18}O$ will detach from the original core or rim value. The thicker lines show the $\delta^{18}O$ profile just prior to detachment at the center of the rim (solid line) and of the core (dashed line). The diagram implies a $\delta^{18}O$ for the surrounding medium equivalent to that of the core but the model results shown in (b) and (c) are independent of the relative $\delta^{18}O$ values of the core, rim and host medium. (b) and (c) Results of numerical simulation of wet oxygen diffusion to determine the critical minimum cooling rate, $(dT/dt)_c$, for retention of the original $\delta^{18}O$ value at the center of a spherical zircon crystal or core (b), or rim (c). The dots represent the actual numerical results; the lines are fits to the numerical data given by Equations (7) and (8). See text for additional discussion.

**Chapter 9 "Present Trends and the Future of Zircon in Geochronology: Laser Ablation ICPMS" by J. Košler & P. J. Sylvester, p. 243-275**

*Page 259, corrected Equations (3a), (3b), and (4b):*

$$R_{1c} = R_{1m} * \left[ \frac{R_{2c}}{R_{2m}} \right]^{\left( \frac{\Delta M_1}{\Delta M_2} \right)} \tag{3a}$$

$$\left( \frac{^{207}Pb}{^{235}U} \right)_c = \left( \frac{^{207}Pb}{^{235}U} \right)_m * \left[ \frac{\left( ^{205}Tl/^{237}Np \right)_c}{\left( ^{205}Tl/^{237}Np \right)_m} \right]^{\left( \frac{M_{235} - M_{207}}{M_{237} - M_{205}} \right)} \tag{3b}$$

$$\left( \frac{^{207}Pb}{^{235}U} \right)_c = \left( \frac{^{207}Pb}{^{235}U} \right)_m * \left[ \frac{\left( ^{205}Tl/^{237}Np \right)_c}{\left( ^{205}Tl/^{237}Np \right)_m} \right]^{\left[ \frac{\ln(M_{235} - M_{207})}{\ln(M_{237} - M_{205})} \right]} \tag{4b}$$

**Chapter 10 "Detrital Zircon Analysis of the Sedimentary Record" by C. M. Fedo, K. N. Sircombe & R. H. Rainbird, p. 277-303**

*Page 293, Figure 4 (missing left edge of figure):*

corrected figure –

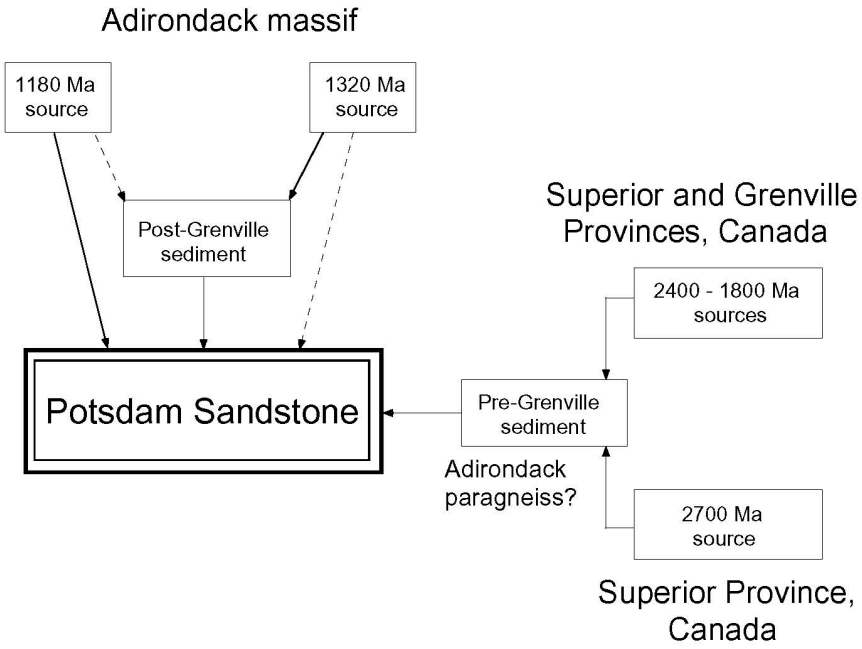

## Chapter 12 “Lu-Hf and Sm-Nd Isotope Systems in Zircon” by P. D. Kinny & R. Maas, p. 327-341

*Page 328, Figure 1, caption:*

Corrected caption should read:

**Figure 1.** Schematic Hf isotope evolution diagram, modified after Patchett et al. (1981), showing how an episode of partial melting in Earth's mantle at time $t_1$ results in divergent Hf isotope evolution paths for the newly generated crust (low Lu/Hf) and the residual mantle (high Lu/Hf). Having extremely low Lu/Hf, any zircons formed within that crust will preserve its initial $^{176}Hf/^{177}Hf$ ratio, and hence over time diverge in composition from the remainder of the host rock. At time $t_2$ a variety of possible sources may contribute to newly formed crust. If wholly derived from depleted mantle the initial $\varepsilon_{Hf}$ will be positive, however mixing with an undepleted or enriched source, for example by crustal contamination, may result in low positive, zero, or negative $\varepsilon_{Hf}$ at the time of crystallization depending on the balance of components. Any inherited zircon cores at $t_2$ would be expected to have lower $\varepsilon_{Hf}$ than the newly-crystallized host rock.

*Page 329, corrected Table 1:*

**Table 1.** Bulk unfractionated silicate Earth reference parameters.

| $(^{176}Hf/^{177}Hf)_{today}$ | $(^{176}Lu/^{177}Hf)_{today}$ | $(^{176}Hf/^{177}Hf)_{init}$ | Parameters for initial Hf | Reference |
|---|---|---|---|---|
| 0.28286 ± 9 | 0.0334 | 0.27978 ± 9 | $t_0$ 4.55 Ga; $\lambda_{Lu}$ 1.94 x $10^{-11}$ | 1 |
| 0.282772 ± 29 | 0.0332 ± 2 | 0.279742 ± 29 | $t_0$ 4.56 Ga; $\lambda_{Lu}$ 1.93 x $10^{-11}$ | 2 |

1. Tatsumoto et al. 1981. 2. Blichert-Toft and Albarède 1997.

**Chapter 13 "Oxygen Isotopes in Zircon" by J. W. Valley, p. 343-385**

*Page 345, Table 1:*

Corrected row 1 (missing subscript and superscripts now included):

| Standard | $\delta^{18}O$ ‰ SMOW | ± 1SD | N | age Ma | U ppm | $HfO_2$ wt% | Refs. | Comments |
|---|---|---|---|---|---|---|---|---|

*Page 348, Table 2:*

Equation (1) in bottom row of table should read:

Eqn 1: 1000 $ln(\alpha_{A-B}) = A_{A-B}(10^6/T^2)$, (T in K). Values should be extrapolated below ~600°C

*Page 357, Figure 13, caption:*

The six occurrences of "$d^{18}O$" in this figure caption should be replaced with "$\delta^{18}O$" (found in lines 1, 3, 5, 10, 14 and 20 of caption)

*Page 359, Figure 15:*

Correct figure is:

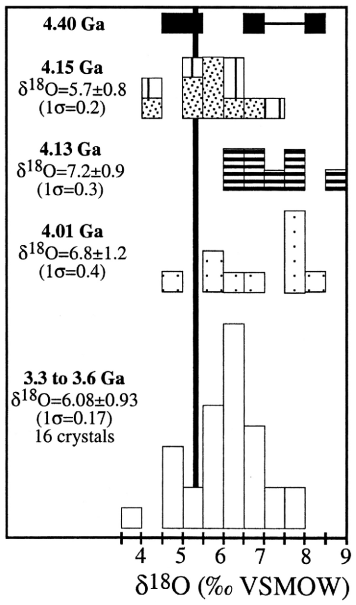

*Page 367, Figure 23:*

Correct figure and figure caption are:

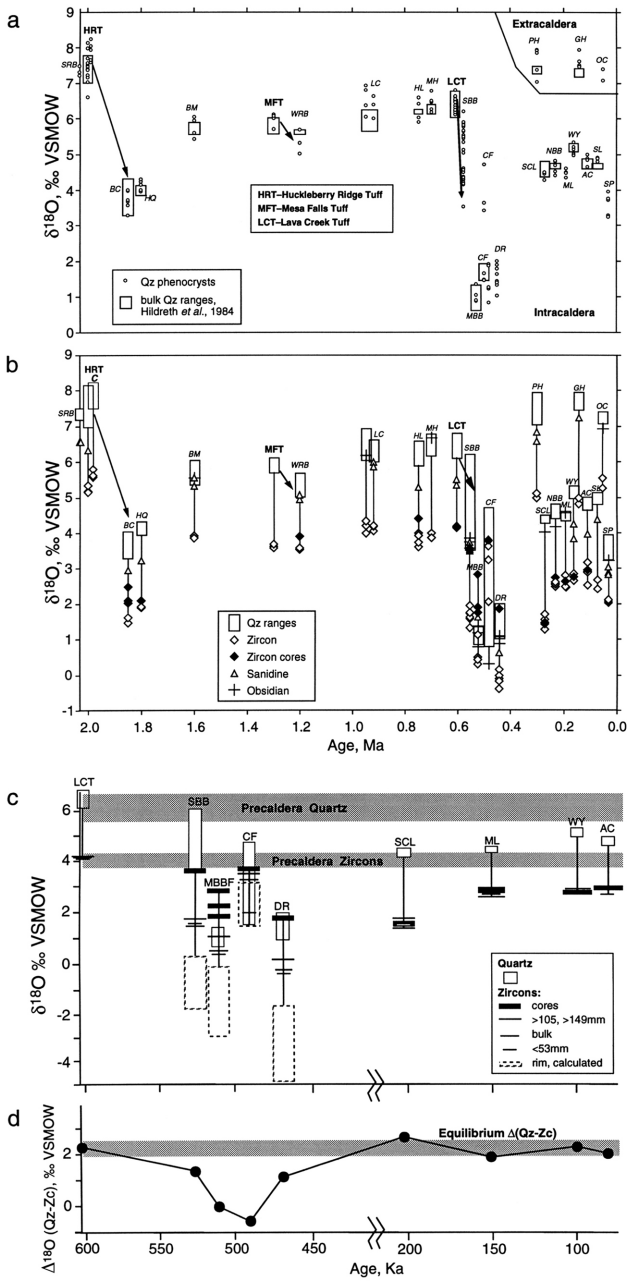


**Figure 23.** Evolution of $\delta^{18}O$ in Yellowstone magmas. Caldera-forming eruptions are Huckleberry Ridge Tuff (HRT), Mesa Falls Tuff (MFT), and Lava Creek Tuff (LCT). (a) Individual quartz phenocrysts and bulk quartz. (b) Zircon, sanidine, and obsidian. Air-abraded zircon cores are filled diamonds. (c) Post LCT intra-caldera lava flows. The range of individual quartz phenocrysts are shown in boxes. Zircons are plotted by crystal size. (d) $\Delta^{18}O$(Qt-Zc) for LCT and post-LCT lavas. The equilibrium value of $\Delta$(Qt-Zc) is 1.9-2.3‰ at 800-900ºC. Note that only low $\delta^{18}O$ rhyolites have quartz and zircon that are not equilibrated (from Bindeman and Valley 2000a, 2001).

*Page 371, Figure 29, caption:*

In line 1 of the caption, "$d^{18}O(Zc)$" should be "$\delta^{18}O(Zc)$".

*Page 383, King et al. (2003b) reference* – remove (in review) from citation

*Page 384, Peck et al. (2003a) reference* – remove (in press) from citation

*Page 385, Valley et al. (2003) reference* – remove (in press) from citation

**Chapter 14 "Radiation Effects in Zircon" by R. C. Ewing, A. Meldrum, LuMin Wang, W. J. Weber and L. R. Corrales, p. 387-425**

*All even pages, running header:*

Should read: Ewing, Meldrum, Wang, Weber, Corrales:

*Page 405, Figure 9, caption:*

Caption should read:

**Figure 9.** Crystalline-to-amorphous transition plotted as functions of equivalent uranium content and age. The lower curve represents the onset of observable damage as measured by electron diffraction, and the upper curve is for "complete" amorphization, at a temperature of 100°C. The open squares represent natural "crystalline" zircon from a variety of locations whose age and equivalent uranium content were measured or calculated. The filled triangles are for "amorphous" natural zircon from different localities. The curves delineate the crystalline-amorphous boundary fairly well, despite the different thermal histories and geologic environments of the different specimens. At higher ambient temperatures, the transitions would be shifted to higher uranium content. [Modified after Meldrum et al. (1999a).]

*Page 414, Figure 12, caption:*

Caption should read:

**Figure 12.** Calculated number of vacancies produced along the path of 4.6 MeV alpha particles in zircon, along with the distribution of alpha particle ranges, using the BCA code SRIM.

**Chapter 15 "Spectroscopic Methods Applied to Zircon" by L. Nasdala, M. Zhang, U. Kempe, G. Panczer, M. Gaft, M. Andrut, & M. Plötze, p. 427-467**

*Page 444, 3rd line from bottom:*

"observed with $\boldsymbol{E} \parallel c$)" should read "observed with $\boldsymbol{E} \perp c$)"

# Structure and Chemistry of Zircon and Zircon-Group Minerals

**Robert J. Finch**

*Argonne National Laboratory*
*9700 South Cass Avenue*
*Argonne, Illinois 60439*

**John M. Hanchar**

*Department of Earth and Environmental Sciences*
*The George Washington University*
*Washington, D.C. 20006*

## INTRODUCTION

Zircon ($ZrSiO_4$) is a common accessory mineral in nature, occurring in a wide variety of sedimentary, igneous, and metamorphic rocks. Known to incorporate an assortment of minor and trace elements, zircon has the ability to retain substantial chemical and isotopic information, leading to its use in a wide range of geochemical investigations, including studies on the evolution of Earth's crust and mantle (e.g., Hanchar et al. 1994, Bowring 1995, Vervoort et al. 1996, Hoskin and Schaltegger, this volume; Valley, this volume) as well as age dating (e.g., Gibson and Ireland 1995, Bowring et al. 1998, Solar et al. 1998, Bowring and Schmitz, this volume; Ireland and Williams, this volume; Parrish et al., this volume). The physical and chemical durability of zircon is a major factor in it being the mineral by which many of Earth's oldest known rocks have been dated (Bowring et al. 1989, Maas et al. 1992, Buick et al. 1995, Bowring and Williams 1999, Wilde et al. 2001) and is also an important factor in zircon being proposed as a candidate waste form for the geologic disposal of excess plutonium from dismantled nuclear weapons (Ewing and Lutze 1997, Ewing 1999, Burakov et al. 2002, Burakov et al. 2003, Ewing et al., this volume).

The chemical and physical properties of zircon and its ability to incorporate and retain trace elements are largely determined by its crystal structure. The zircon structure is adopted by numerous minerals and synthetic compounds with the general formula $ATO_4$, in which high field-strength *T*-site cations occupy isolated tetrahedra, and *A*-site cations occupy larger eight-coordinated structural sites. Zircon-type compounds share many physical properties, as well as displaying variable degrees of solid solution among end members. Because many zircon-group minerals commonly contain radioactive U and Th, natural crystals commonly suffer substantial radiation damage, and most precise structure determinations are based on studies of synthetic analogues (e.g., Taylor and Ewing 1978, Ni et al. 1995, Finch et al. 2001a, Boatner 2002). We rely to a large extent on results from structural studies of synthetic analogues of zircon and zircon-group minerals in this review.

In the sections that follow, we provide an overview of the crystalline structure of zircon, followed by brief discussions of naturally occurring $ATO_4$ compounds that are isostructural with zircon; these are the zircon-group minerals. We also compare the zircon structure with structures of several related compounds, including those of scheelite and monazite, because of the importance that these structures have in understanding phase relationships among zircon-group minerals and their polymorphs. We conclude with a discussion of some effects that changes in pressure, temperature and composition can have on the structure of zircon. Throughout the text, we use the acronym REE (rare-earth elements) to include Sc, Y and the lanthanide elements (La through Lu).

1529-6466/03/0053-0001$05.00

## STRUCTURE OF ZIRCON

Zircon is an orthosilicate in which isolated $SiO_4$ tetrahedra share corners and edges with $ZrO_8$ dodecahedra. The $ZrO_8$ dodecahedra share edges with each other to form chains parallel to <100> (Fig. 1) such that each $ZrO_8$ polyhedron shares edges with four adjacent $ZrO_8$ polyhedra, two in each of the crystallographically equivalent directions [100] and [010]. These <100> chains of $ZrO_8$ polyhedra are cross linked by sharing corners with $SiO_4$ tetrahedra (perpendicular to the page in (Fig. 1). The *Si* and *Zr* polyhedra also form an edge-connected chain of alternating $ZrO_8$ and $SiO_4$ polyhedra parallel to [001] (Fig. 1), between which lie unoccupied channels, also parallel to [001] (Fig. 2). The [001] edge-connected chains of *Zr* and *Si* polyhedra comprise an especially strongly connected feature in the structure, as manifested in many physical properties of zircon, including its prismatic habit, {110} cleavage, high birefringence (Speer 1982a and references therein), anisotropic thermal expansion (Bayer 1972, Subbarao et al. 1990) and compression (Hazen and Finger 1979, Smyth et al. 2000, van Westrenen et al. 2003a).

Zircon is tetragonal and crystallizes in space group $I4_1/amd$. Both cations ($Zr^{4+}$ and $Si^{4+}$) occupy special positions with site symmetry $\bar{4}2m$. The O atom occupies a site with symmetry *m*: the *y* and *z* coordinates of the O atom are the only refineable atomic-site parameters in the zircon structure ($y = 0.066$, $z = 0.195$; Hazen and Finger 1979, Finch et al. 2001a, also see Speer 1982a). Each O atom is bonded to one Si atom at 1.62 Å and two Zr atoms at 2.13 and 2.27 Å, so that each Zr atom is bonded to four O atoms at 2.13 Å and another four at 2.27 Å (Hazen and Finger 1979, Finch et al. 2001a).

### Cation polyhedra

The $SiO_4$ tetrahedron in zircon is a tetragonal disphenoid (symmetry $\bar{4}2m$) elongated parallel to [001]. This distortion of the regular $SiO_4$ tetrahedron has been attributed to repulsion between the $Zr^{4+}$ and $Si^{4+}$ cations, whose polyhedra share a common edge (Speer 1982a). The two O-Si-O angles in the $SiO_4$ group are approximately 97° and 116° (Hazen and Finger 1979, Finch et al. 2001a). The O-O distance along the polyhedral edge shared with the $ZrO_8$ polyhedron is 2.43 Å (opposite the smaller O-Si-O angle) and 2.75 Å along the unshared edge (opposite the larger O-Si-O angle).

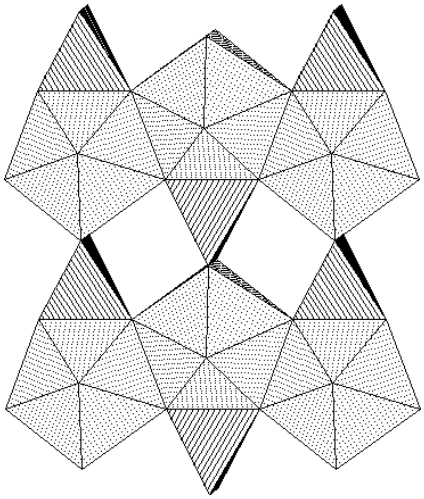

**Figure 1.** Zircon structure projected on (100); *c* axis is vertical, *b* ($a_2$) axis is horizontal. $ZrO_8$ dodecahedra are shaded light gray; $SiO_4$ tetrahedra are striped.

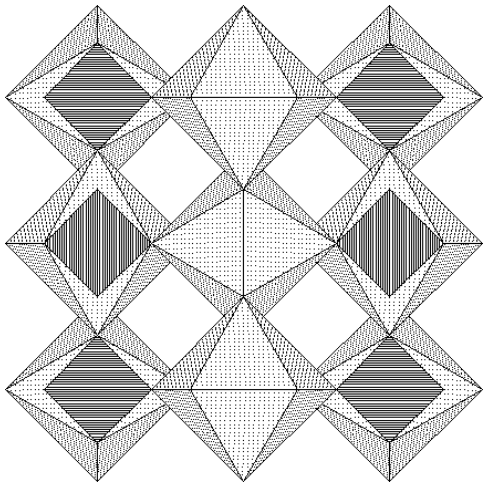

**Figure 2.** Zircon structure projected on (001), showing view down the [001] channels (unshaded). Shading as for Figure 1.

The Zr atom is coordinated by eight O atoms that define a triangular dodecahedron with symmetry $\bar{4}2m$. The $ZrO_8$ dodecahedron in zircon can be described as two interpenetrating $ZrO_4$ tetrahedra (Nyman et al. 1984): one elongated along [001], which we will call $ZrO_4^e$, the other compressed, $ZrO_4^c$ (nomenclature after Ríos et al. 2000) (Fig. 3). (Note that if both tetrahedra were undistorted, the polyhedron that would result from their interpenetration is a cube). As noted above, there are four long and four short Zr-O distances in zircon. The four long Zr-O bond distances are associated with the elongated $ZrO_4^e$ tetrahedron, and the four short Zr-O bond distances are associated with the $ZrO_4^c$ tetrahedron. Using this description, one can visualize the chains of edge-sharing $ZrO_8$ and $SiO_4$ polyhedra as isolated chains of edge-sharing $SiO_4$ and $ZrO_4^e$ tetrahedra, both being tetragonal disphenoids elongated along [001] (Fig. 4). The compressed $ZrO_4^e$ tetrahedra are then seen to share their four corners with $SiO_4$ tetrahedra, forming a tetrahedral array that Nyman et al. (1984) describe as a "C9-type" superstructure (as occurs in "ideal" high cristobalite). In this context, the zircon structure is built of two unconnected interpenetrating C9-type arrays of corner-sharing $SiO_4$ and $ZrO_4^c$ tetrahedra (Fig. 5).

## Interstitial sites

The structure of zircon is relatively open, with small voids between the $SiO_4$ and $ZrO_8$ polyhedra (Fig. 1) and open channels parallel to [001] (Fig. 2). Such structural voids are potential interstitial sites that could incorporate impurities, provided that such sites can accommodate interstitial ions without excessive structural strain. Interstices have been proposed as potential sites for many impurity elements reported from zircon analyses (Speer 1982a). Although most detailed studies of elemental substitution in zircon find that impurity cations can usually be accounted for by substitutions at either the *Zr* or *Si* sites, both natural and synthetic zircon crystals can display non-stoichiometry (e.g., Hinton and Upton 1991, Hoskin et al. 2000, Hanchar et al. 2001a). Finch et al. (2001a) suggested that interstitial sites may incorporate low levels of impurity cations in synthetic zircon crystals. Although present at concentrations below detection by many conventional analytical methods (a few ppm to several tens of ppm), interstitial cations can have a significant impact on charge-balancing heterovalent substitutions on *Zr* and *Si* sites. The possible role of interstitial sites is a potentially fruitful area of research on zircon crystal chemistry.

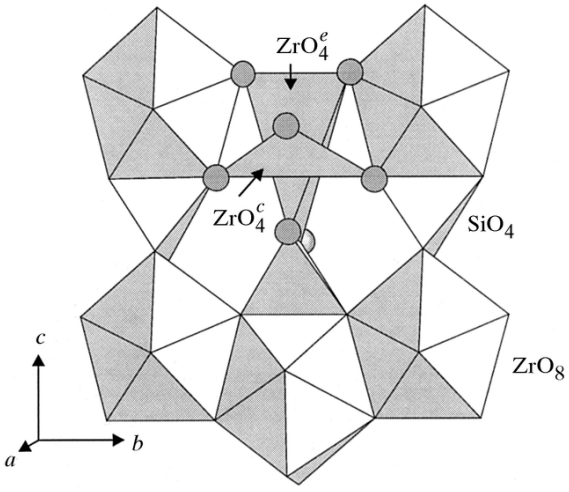


**Figure 3.** View of zircon structure projected on (100) (same orientation as Fig. 1) illustrating extended ($ZrO_4^e$) and compressed ($ZrO_4^c$) tetrahedra (from Ríos et al. 2000).

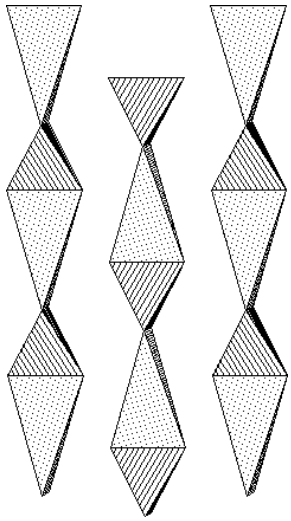

**Figure 4.** Zircon structure projected on (100), illustrating [001] chains of edge-sharing tetrahedra: $ZrO_4^e$ (light gray stippled) and $SiO_4$ (darker gray striped); *c* axis is vertical and *b* axis horizontal.

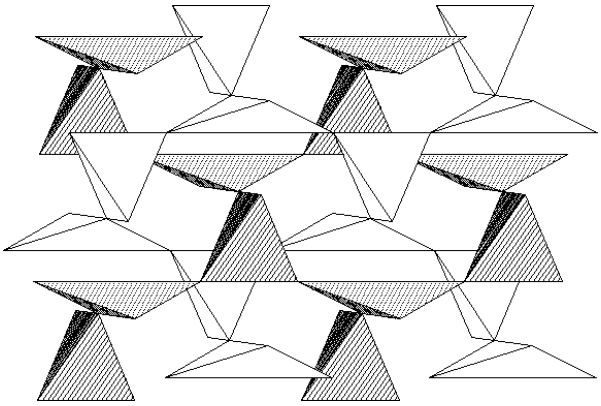

**Figure 5.** Interpenetrating C9-type arrays of $SiO_4$ and $ZrO_4$[c] tetrahedra in zircon. View is approximately down [100], with *c* axis vertical and *b* axis horizontal. Different shadings are to illustrate the two C9-type tetrahedral arrays.

One interstitial site is a distorted octahedron that shares faces with two $ZrO_8$ polyhedra and two $SiO_4$ tetrahedra (Fig. 1) and lies approximately 1.87 Å from two *O* sites and 2.08 Å from four *O* sites. The proximity of two $Si^{4+}$ ions (each at 1.84 Å) across a shared polyhedral face makes this an unlikely site for high field-strength cation impurities. The second interstice is a four-coordinated site that lies within the channels parallel to [001] (Fig. 2). It is adjacent to the distorted octahedral interstice and shares a face with it. This interstice is 1.84 Å from four adjacent *O* sites and shares one face with a neighboring $ZrO_8$ polyhedron (Fig. 6). Low levels of small, high-field-strength ions may be compatible with this site.

Few studies have examined the energetics of impurity substitutions in the zircon structure, including the potential role of interstitial sites. Williford et al. (2000) calculated the energetics of defects in Pu-doped zircons and found that an O vacancy may be stabilized by two $Pu^{3+}$ substitutions at nearby *Zr* sites. Crocombette (1999) calculated the energetics of point defects in zircon (pure $ZrSiO_4$), including Zr, Si and O interstitials and vacancies, and found that interstitial Zr and Si atoms tend to occupy interstices within the open channels along [001], whereas O interstitials tend to occur as one of a dumbbell-shaped pair of O atoms coordinated to a common Si (making a five-coordinated *Si* site). The results of the study by Crocombette (1999) indicate that, with the exception of O interstitials, formation energies for all point defects (interstitials and vacancies) ensure that the equilibrium thermal concentration of point defects in pure zircon is negligible. Furthermore, because the activation energy for O diffusion is less than that required for O-vacancy formation (Williford et al. 1999), O vacancies are unlikely to persist in zircon, especially over geologic time spans.

## ZIRCON-GROUP MINERALS

Several minerals and numerous synthetic $ATO_4$ compounds are isostructural with zircon (Table 1). Classified according to the tetrahedrally coordinated *T*-site cations, zircon-group minerals include silicates, phosphates, vanadates, borates, an arsenate, and a chromate. Dodecahedral *A*-site cations range from low field-strength cations such as $Ca^{2+}$ to high field-strength cations such as $Ta^{5+}$ and $Nb^{5+}$. With the notable exception of $ZrGeO_4$ (with $c/a = 0.936$), compounds having the zircon structure are characterized by axial ratios ($c/a$) between 0.869 (for chromatite, $CaCrO_4$) and 0.908 (for hafnon, $HfSiO_4$), a rather narrow range given the variety of *A*- and *T*-site cations compatible with the zircon structure (Table 1). Axial ratios depend in part on the degree of repulsion between adjacent *A*-site cations and between *A*- and *T*-site cations, due to the fact that the *A* site (*Zr* dodecahedron) shares edges with both *A*- and *T*-site polyhedra (Fig. 1). Strong repulsion

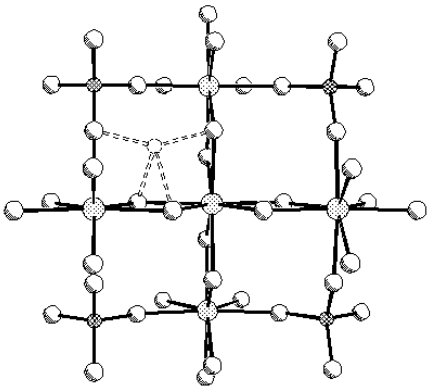

**Figure 6.** Zircon structure viewed approximately down [001] illustrating the four-coordinated interstitial site (same orientation as for Fig. 2).

**Table 1.** Zircon-group minerals and selected synthetic zircon-type compounds*

| Name | Formula | **a** | **c** | V | c/a | density | Ref. |
|---|---|---|---|---|---|---|---|
| Zircon | $ZrSiO_4$ | 6.607 | 5.9835 | 261.2 | 0.906 | 4.66 | [1] |
| Hafnon | $HfSiO_4$ | 6.577 | 5.969 | 258.2 | 0.908 | 6.98 | [2] |
| Thorite | $ThSiO_4$ | 7.1335 | 6.3205 | 321.6 | 0.886 | 6.70 | [3] |
| Coffinite | $USiO_4$ | 6.979 | 6.253 | 304.6 | 0.896 | 6.90 | [4] |
| Xenotime | $YPO_4$ | 6.895 | 6.027 | 286.5 | 0.874 | 4.28 | [5] |
| Xenotime-(Yb) | $YbPO_4$ | 6.438 | 6.400 | 276.5 | 0.874 | 6.44 | [5] |
| Pretulite | $ScPO_4$ | 6.589 | 5.806 | 252.1 | 0.881 | 3.71 | [6] |
| Chromatite | $CaCrO_4$ | 7.242 | 6.290 | 329.9 | 0.869 | 3.14 | [7] |
| Behierite | $(Ta,Nb)BO_4$ | 6.206 | 5.472 | 210.8 | 0.882 | 7.37 | [8] |
| Schiavinatoite | $(Nb,Ta)BO_4$ | 6.219 | 5.487 | 212.2 | 0.882 | 6.57 | [9] |
| Wakefieldite-(Y) | $YVO_4$ | 7.118 | 6.289 | 318.7 | 0.884 | 4.25 | [10,11] |
| Wakefieldite-(Ce) | $(Ce,Pb)VO_4$ | 7.35 | 6.56 | 352.8 | 0.893 | 5.30 | [12] |
| Wakefieldite-(Ce) | $CeVO_4$ | 7.354 | 6.488 | 350.9 | 0.882 | 4.83 | [13] |
| Dreyerite | $BiVO_4$ | 7.303 | 6.458 | 344.4 | 0.884 | 6.25 | [14] |
| | $CeVO_4$ | 7.400 | 6.497 | 355.8 | 0.878 | 4.76 | [11] |
| | $LuVO_4$ | 7.025 | 6.234 | 307.7 | 0.887 | 6.25 | [11] |
| | $ScVO_4$ | 6.780 | 6.135 | 282.0 | 0.905 | 3.76 | [11] |
| Chernovite-(Y) | $YAsO_4$ | 7.044 | 6.248 | 310.0 | 0.887 | 4.85 | [15] |
| | $SmAsO_4$ | 7.20 | 6.40 | 331.8 | 0.890 | 5.77 | [16] |
| | $LuAsO_4$ | 6.949 | 6.227 | 300.7 | 0.896 | 6.94 | [17] |
| | $PrCrO_4$ | 7.344 | 6.428 | 346.7 | 0.875 | 4.92 | [18] |
| | $LuCrO_4$ | 7.027 | 6.200 | 306.1 | 0.882 | 6.31 | [18] |
| | $ThGeO_4$ | 7.230 | 6.539 | 341.8 | 0.904 | 7.16 | [19] |
| | $ZrGeO_4$ | 6.694 | 6.265 | 280.7 | 0.936 | 5.43 | [20] |

* *Notes*: unit-cell parameters (***a***,***c***) in Å; unit-cell volume in $Å^3$; density in g $cm^{-3}$.
*References*: [1] Finch et al. (2001); [2] Speer and Cooper (1982); [3] Taylor and Ewing (1978); [4] Fuchs and Gebert (1958); [5] Ni et al. (1995); [6] Bernard (1998); [7] Weber and Range (1996); [8] Mrose and Rose (1961); [9] Demartin et al. (2001); [10] Miles et al. (1971); [11] Chakoumakos et al. (1994); [12] Deliens and Piret (1977); [13] Baudracco-Gritti et al. (1987); [14] Dreyer and Tillmanns (1981); [15] Goldin et al. (1967); [16] Durif and Forrat (1957); [17] Lomüller et al. (1973); [18] Buisson et al. (1964); [19] Ennaciri et al. (1986); [20] Hirano et al. (2002a).

between *A*- and *T*-site cations tends to increase *c*/*a* (lengthening the *c* axis), whereas strong repulsion between adjacent *A*-site cations tends to decrease *c*/*a* (longer *a*). Although readily identified from their similar X-ray powder diffraction patterns as possessing the zircon structure, complete structural details are still unknown for many zircon-group minerals.

The zircon structure shares structural similarities with the minerals scheelite ($CaWO_4$), monazite ($CePO_4$), rutile ($TiO_2$), garnet ($X_3Y_2T_3O_{12}$), and anhydrite ($CaSO_4$), and some of these similarities are discussed in the section on related structures below. Reidite, the naturally occurring high-pressure $ZrSiO_4$ polymorph (Glass et al. 2002a,b), is isostructural with scheelite; whereas huttonite, the high-pressure and high-temperature polymorph of $ThSiO_4$, is isostructural with monazite. The fact that the high-pressure polymorphs of the isostructural minerals zircon and thorite are not themselves isostructural attests to the importance of *A*- and *T*-site cations in determining polymorphic transitions. At room temperature and pressure, silicates, vanadates, and chromates crystallize with the zircon structure, whereas germanates, molybdates, tungstates,

periodates, and pertechnetates crystallize with the scheelite structure. Phosphates and arsenates crystallize with the zircon structure for middle and heavy lanthanides, Y and Sc, and with the monazite structure for the larger light lanthanides. $LaVO_4$ is the only orthovanadate with the monazite structure; all other REE orthovanadates possess the zircon structure at room temperature and pressure.

Crystal structure is determined primarily by the sizes of ions that make up a crystal (Carron et al. 1958, Fukunaga and Yamaoka 1979). A plot showing the sum of *A* and *T* cation radii versus the ratio of ionic radii $^{[VIII]}A/^{[IV]}T$ for $ATO_4$ compounds known to form zircon-, scheelite-, or monazite-type structures illustrates the importance of *A* and *T* cations in determining $ATO_4$ structure type (Fig. 7: $^{[IV]}T = B^{3+}$, $Si^{4+}$, $Ge^{4+}$, $P^{5+}$, $V^{5+}$, $As^{5+}$, $Cr^{5+}$, $Cr^{6+}$, $Mo^{6+}$, $W^{6+}$, $S^{6+}$, $Tc^{7+}$, $I^{7+}$). Zircon- and monazite-type structures tend to be adopted by $ATO_4$ compounds with *T*-site cations smaller than $Ge^{4+}$ (0.390 Å) or $Tc^{7+}$ (0.37 Å) and larger than $S^{6+}$ (0.12 Å), with the exception of $(Ta,Nb)BO_4$, which is isostructural with zircon (effective ionic radii are from Shannon 1976). There is less apparent dependence on the radius of the *A*-site cation, although the zircon structure is adopted by compounds with the smallest *A*-site cations compatible with a given *T*-site cation. The scheelite structure is adopted by compounds with the largest *T*-site cations ($Ge^{4+}$, $Mo^{6+}$, $W^{6+}$, $Tc^{7+}$, $I^{7+}$) and all but the smallest *A*-site cations (which tend to form $ATO_4$ compounds with the wolframite structure); however, germanates form zircon-type structures at elevated temperatures (Bayer 1972). The monazite structure is adopted by $ATO_4$ compounds with *A*-site cations comparable to, but slightly larger than *A*-site cations in zircon-type structures.

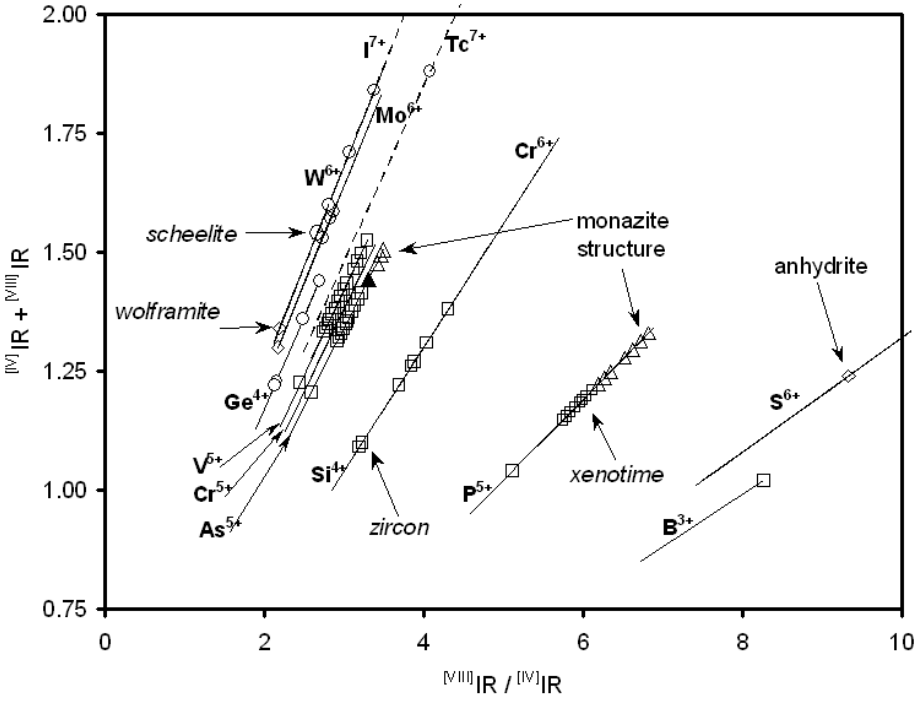


**Figure 7.** Plot showing sums of *A* and *T* cation radii ($^{[VIII]}A + {}^{[IV]}T$) versus their radius ratios ($^{[VIII]}A/^{[IV]}T$) for $ATO_4$ compounds known to adopt structure types discussed in the text. Lines indicate the range of values compatible with each *T*-site cation, and symbols indicate selected known structures. Squares designate zircon-type compounds; triangles are monazite-type compounds; circles correspond to scheelite-type compounds (diamonds are other structures). Structure types are indicated for room-temperature polymorphs where known (shaded circle is $NaIO_4$; filled triangle is $NdAsO_4$). Effective ionic radii from Shannon (1976).

**Silicates**

The structure of hafnon ($HfSiO_4$) is identical to that of zircon in virtually all details except small differences in bond lengths and angles (Speer and Cooper 1982). The ionic radius of $^{[VIII]}Hf^{4+}$ (0.83 Å) is only slightly smaller than that of $^{[VIII]}Zr^{4+}$ (0.84 Å), and the unit-cell dimensions of hafnon are correspondingly similar to those of zircon, with pure $HfSiO_4$ having smaller volume (Table 1). In fact, the similar chemistries of Zr and Hf long delayed discovery of Hf, which was first found in zircon in 1923 by D. Coster and G.C. von Hevesey. The estimated crustal abundance of Zr and Hf corresponds to an atomic ratio Zr:Hf approximately equal to 70:1 (Rudnick and Fountain 1995, Taylor and McLennan 1995, Wedepohl 1995); this is the atomic ratio Zr:Hf in zircon with 1.3 wt % Hf (1.6 wt % $HfO_2$). Zircon crystals typically contain less than about 3 wt % Hf, with concentrations ranging between 0.5 and 7 wt % Hf (Hoskin and Schaltegger, this volume); however, complete solid solution between end-member compositions has been demonstrated (Ramakrishnan et al. 1969, Hoskin and Rodgers 1996).

**Actinide silicates**

There are three naturally occurring $ATO_4$ actinide silicates, two of which are isostructural with zircon: coffinite ($USiO_4$) and thorite ($ThSiO_4$). Thorite is one of two naturally occurring polymorphs of $ThSiO_4$. The structures of thorite and zircon are completely analogous. The $SiO_4$ tetrahedron in thorite is essentially identical to that in zircon, with Si-O distances of 1.63 Å (Taylor and Ewing 1978). The two Th-O distances at 2.37 Å and 2.47 Å, are 11% and 9% longer than the corresponding Zr-O distances in zircon (2.13 and 2.27 Å), reflecting the larger radius of the $Th^{4+}$ ion (1.05 Å). Thorite is the polymorph stable at room temperature and pressure, transforming to huttonite, the denser lower-symmetry polymorph, at elevated pressure and temperature (Dachille and Roy 1964, Finch et al. 1964). Huttonite is monoclinic and isostructural with monazite (Taylor and Ewing 1978), the structure of which is described in more detail in the section on related structures.

Coffinite ($USiO_4$) forms as an alteration product of uraninite ($UO_2$) under reducing conditions and has been identified in many diverse U deposits (Janeczek 1991, Janeczek and Ewing 1992, Fayek and Kyser 1997, Fayek et al. 1997). Coffinite occurs in nature as microscopic intergrowths that are unsuitable for structure determination by conventional X-ray diffraction methods, and hydrothermal syntheses produce only fine-grained powders (Hoekstra and Fuchs 1956). The isostructural relationship between zircon and coffinite was established by a detailed X-ray powder diffraction study of synthetic coffinite (Fuchs and Gebert 1958), and lattice parameters of coffinite and thorite suggest that structural details for those two minerals are similar (Table 1). No single-crystal structure data are available for coffinite, nor are we aware of any reported neutron powder structure refinements of coffinite, although such a study would be valuable.

Although coffinite is isostructural with thorite, the degree of solid solution between the two phases is uncertain, with conflicting reports in the literature. Fuchs and Gebert (1958) reportedly synthesized the complete series $(U,Th)SiO_4$, but Mumpton and Roy (1961) found the limit on U substitution to be about 30 mol % $USiO_4$. Variations in synthesis methods and temperatures may help explain the differences. Natural coffinite may contain substantial amounts of REE and P, suggesting some solid solution with xenotime, $YPO_4$ (Hansley and Fitzpatrick 1989, Janeczek and Ewing 1996), with which coffinite is isostructural.

Essentially all reported analyses of natural coffinite indicate $H_2O$, and the structural role of $H_2O$ has been long been debated (Mumpton and Roy 1961, Speer 1982b, Janeczek 1991). Infrared spectra of hydrothermally synthesized coffinite do not show evidence for OH groups, and no difference in X-ray powder diffraction patterns is observed between anhydrous and hydrous samples (Fuchs and Gebert 1958). $H_2O$ groups in coffinite are believed to occupy open channels along [001] (Fig. 2), and are not believed to be an essential structural constituent (Janeczek 1991).

However, attempts to synthesize coffinite by using anhydrous high-temperature (~1000°C) methods have not been successful (e.g., Lunga 1966, Hanchar 1996).

In addition to U and Th, the tetravalent light actinides, Pa, Np, Pu, and Am also form zircon-type orthosilicates, and like $ThSiO_4$, $PaSiO_4$ is also dimorphous, with a monoclinic huttonite-type polymorph stable at elevated temperature (Speer 1982b). The degree of solid solution among isostructural actinide orthosilicates has not been studied in detail. Complete solid solution cannot be assumed based solely on similarities in ionic radii and valence (e.g., Begg et al. 2000, Burakov et al. 2002).

We should note that thorogummite, $(Th,U)SiO_4 \cdot nH_2O$, is an actinide orthosilicate mineral considered isostructural with zircon. Thorogummite is rather poorly described structurally and chemically (Speer 1982b, Gaines et al. 1997). It probably represents an intermediate in the solid solution between coffinite and thorite, and thorogummite may be superfluous as a mineral name (Finch and Murakami 1999).

**Phosphates**

Three naturally occurring REE phosphates, xenotime ($YPO_4$), xenotime-(Yb) ($YbPO_4$) and pretulite ($ScPO_4$), crystallize with the zircon structure (Boatner 2002), as well as several synthetic heavy-lanthanide orthophosphates (Ni et al. 1995) (Table 1). The structures of xenotime and the other zircon-group orthophosphates are topologically identical to zircon, with $REE^{3+}$ ions occupying Zr-equivalent dodecahedral sites and $P^{5+}$ occupying Si-equivalent tetrahedral sites (Ni et al. 1995). The polyhedral volume of the $PO_4$ tetrahedron in xenotime-type $REEPO_4$ orthophosphates is significantly smaller than the analogous $SiO_4$ tetrahedron in zircon, reflecting the smaller ionic radius of $^{[IV]}P^{5+}$ (0.15 Å) compared with $^{[IV]}Si^{4+}$ (0.26 Å). The polyhedral volume of the $REEO_8$ dodecahedron is correspondingly larger than the analogous $ZrO_8$ dodecahedron in zircon. Boatner (2002) reviews the structures, chemistry and physical properties of zircon-group REE phosphates in more detail.

Due to the lanthanide contraction (ionic radii of light lanthanides are larger than those of heavy lanthanides) orthophosphates of light lanthanides, La through Gd, crystallize with the monoclinic monazite structure (Ni et al. 1995), which is described in the section on related structures. Synthetic $BiPO_4$ possesses the monazite structure at low temperature (Schwarz 1963), as does the trivalent actinide phosphate $PuPO_4$ (Bjorklund 1958).

**Borates**

Two naturally occurring borates are known that possess the zircon structure, both of which share the general formula $(Ta,Nb)BO_4$. Behierite (Nb-rich) and schiavinatoite (Ta-rich) are both exceedingly rare, occurring in B-rich pegmatites (Mrose and Rose 1961, Demartin et al. 2001). Little is known about the stability of these minerals, although Bayer (1972) reported that synthetic $TaBO_4$ decomposes above 900°C to $Ta_2O_5$ with volatilization of $B_2O_3$. We are unaware of any studies on the extent of solid solution between zircon and the borates; however, minor Ta and Nb have been reported in zircon analyses, and $B^{3+}$ is certainly a potential charge-compensating substituent (and one that is notably difficult to detect).

**Vanadates**

Three vanadate minerals possess the zircon structure: wakefieldite-(Y), $YVO_4$, wakefieldite-(Ce), $(Ce,Pb)VO_4$, and dreyerite, $BiVO_4$. The first description of wakefieldite-(Ce) (originally named kusuite) reported that it contained approximately equal proportions of di- and tetravalent Pb, as well as trivalent Ce (Deliens and Piret 1977), although Pb-free wakefieldite-(Ce) was subsequently described by Baudracco-Gritti et al. (1987). Synthetic $ScVO_4$ is isostructural with zircon (Schwarz 1963), and a complete series of lanthanide-bearing vanadates has been synthesized (Ce through Lu), all of which have the zircon structure (Durif 1956, Carron et al. 1958, Lohmüller

et al. 1973). $LaVO_4$ is the only REE orthovanadate with the monazite structure at room temperature and pressure (Stubican and Roy 1963, Schwarz 1963, Rice and Robinson 1976); however it adopts the zircon structure when synthesized hydrothermally (Oka et al. 2000).

Wakefield-(Y) contains 4-6 wt % each of heavy lanthanides (Dy, Yb, Er) and no measurable light lanthanides (Miles et al. 1971). Naturally occurring Pb-free wakefieldite-(Ce) contains several weight percent light lanthanides (up to Sm) and no measurable heavy lanthanides, although it does contain approximately 3 wt % Y (Baudracco-Gritti et al. 1987). Pb-bearing wakefieldite-(Ce) from Zaire reportedly contains no measurable REE other than Ce (Deliens and Piret 1977). Minor substitution by As and P for V is common in naturally occurring zircon-type vanadates, although to our knowledge complete solid solution has not been demonstrated between zircon-group vanadates and the isostructural arsenates or phosphates. Synthetic zircon-type REE vanadates transform to the scheelite structure between about 3.5 and 10 GPa, depending on temperature (Stubican and Roy 1963, Jayaraman et al. 1987, Mazhenov et al. 1988, Duclos et al. 1989, Range and Meister 1990).

Lattice parameters of zircon-type REE orthovanadates depend directly on the radius of the lanthanide ion (Chakoumakos et al. 1994) and can be described with the following polynomials: $a = 2.6809 + 6.3244\ R - 1.9221\ R^2$; $c = 6.2173 - 1.3048\ R + 1.3548\ R^2$, in which $R$ is the effective ionic radius, in Ångströms, from Shannon (1976). The O atomic positional parameters depend linearly on the lanthanide-ion radius (Chakoumakos et al. 1994): $y = 0.4864 - 0.05126R$; $z = 0.1577 + 0.04269R$ (space group $I4_1/amd$, origin at $8c.2/m$). Several zircon-type REE orthovanadates (REE = Pr, Nd, Tb, Ho, Tm, Tb) exhibit anomalous thermal expansion caused by magnetoelastic effects (Kazei et al. 1995, Skanthakumar et al. 1995, Nipko et al. 1997, Bowen 1998). Elastic constants for zircon-type orthovanadates are not so well known; however, elastic constants have been reported for $TbVO_4$ (Melcher 1976), $DyVO_4$ (Sandercock et al. 1972, Melcher 1976), $HoVO_4$ and $ErVO_4$ (Hirano et al. 2002b). Bowden (1998) provides a detailed review of thermal properties of REE vanadates.

Dreyerite ($BiVO_4$) is trimorphous with the minerals pucherite and clinobisvanite. Dreyerite, which is isostructural with zircon, is found in rhyolitic ash-flow tuff (Dreyer and Tillmanns 1981), suggesting a high-temperature and (relatively) low-pressure genesis. Clinobisvanite is monoclinic ($I2/a$); it is not isostructural with monazite but possesses a "distorted scheelite structure" (Mariathasan et al. 1986). Pucherite is orthorhombic and also structurally related to scheelite (Qurashi and Barnes 1953). Clinobisvanite, the $BiVO_4$ polymorph stable at ambient temperature and pressure, transforms to the scheelite structure at elevated temperature or at pressures above 1.4 GPa (Hazen and Mariathasan 1982, Mariathasan et al. 1986). Synthetic clinobisvanite is ferroelastic, whereas the scheelite-type polymorph of $BiVO_4$ is paraelastic. The monoclinic-to-tetragonal transformation in $BiVO_4$ is purely displacive and readily reversible, involving small shifts of Bi and O atoms (Hazen and Mariathasan 1982), which probably explains why the low-pressure polymorph of $BiVO_4$ (clinobisvanite) is known as a mineral, whereas the high-pressure scheelite-type polymorph is not. As for clinobisvanite, the orthorhombic distortion that distinguishes pucherite from the scheelite-type polymorph involves relatively small atomic displacements (Qurashi and Barnes 1952, Mereiter and Preisinger 1986); however, the stability of pucherite relative to other $BiVO_4$ polymorphs is not known.

**Arsenates**

Chernovite ($YAsO_4$) is the only naturally occurring arsenate member of the zircon group (Goldin et al. 1967), although several synthetic zircon-type REE arsenates are also known. $REEAsO_4$ compounds containing heavy lanthanides (Sm through Lu), Y and Sc, crystallize with the zircon structure (Durif and Forrat 1957, Schwarz 1963), whereas the four light lanthanides La, Ce, Pr and Nd form orthoarsenates that are isostructural with monazite (Carron et al. 1958). This is consistent with the trend observed for the REE orthophosphates, except that the "break" between the

xenotime-type (zircon-type) and monazite-type structures occurs between Nd and Sm for REE arsenates, whereas it occurs between Gd and Tb for REE phosphates.

Synthetic $NdAsO_4$ possesses the monazite structure at room temperature and pressure but adopts the scheelite structure at elevated temperature and pressure (Mazhenov et al. 1988, Stubican and Roy 1963). Two naturally occurring orthoarsenates possess the monazite structure: gasparite-(Ce), $CeAsO_4$ (Graeser and Schwander 1987), and rooseveltite, $BiAsO_4$ (Herzenberg 1946, Schwarz 1963). The latter is dimorphous with tetrarooseveltite, which is isostructural with scheelite (Mooney 1948, Sejkora and Rídkošil 1994). Mooney (1948) noted that monoclinic $BiAsO_4$ (monazite structure) precipitates quickly when synthesized hydrothermally, whereas "long digestion periods tend to produce the tetragonal [scheelite-type] form."

Naturally occurring REE arsenates commonly exhibit As-V and As-P solid solution (Cabella et al. 1999), and a complete solid-solution series has been demonstrated between chernovite and xenotime (Graeser et al. 1973). Limited replacement of As by W is also reported. Paranite, $Ca_2Y(AsO_4)(WO_4)_2$, is an ordered derivative of the scheelite structure, with alternating layers of composition $CaWO_4$ and $YAsO_4$ in the ratio 2:1 (Demartin et al. 1992).

**Chromates**

Chromatite ($CaCrO_4$) is a rare chromate isostructural with zircon (Weber and Range 1996). The $CaO_8$ dodecahedron in chromatite is larger than the $ZrO_8$ dodecahedron in zircon, and the $CrO_4$ tetrahedron, which is also slightly larger than the $SiO_4$ tetrahedron in zircon, is less distorted than in zircon. This can be rationalized by there being less repulsion between $Ca^{2+}$ and $Cr^{6+}$ compared to $Zr^{4+}$ and $Si^{4+}$ in zircon.

To our knowledge, no other zircon-type compounds with $Cr^{6+}$ are known, natural or synthetic. However, a full suite of zircon-type REE compounds with the general formula $REECrO_4$ (La through Lu) have been synthesized (Buisson et al. 1964). The three pentavalent cations, $As^{5+}$, $Cr^{5+}$ and $V^{5+}$ possess closely similar ionic radii in tetrahedral coordination (0.335-0.355 Å), so that $REECrO_4$, $REEVO_4$ and $REEAsO_4$ might be expected to form solid-solution series.

**Related structures**

***Reidite*** is the naturally occurring high-pressure polymorph of $ZrSiO_4$. First synthesized in the laboratory (Reid and Ringwood 1969), reidite was discovered recently in zircon-bearing marine sediments in an impact-ejecta layer off the coast of New Jersey (Glass et al. 2002a,b). Reidite is tetragonal, space group $I4_1/m$, and is isostructural with scheelite ($CaWO_4$). Scheelite (and by inference reidite) shares several structural features with zircon. As for zircon, Si atoms in reidite occupy distorted $SiO_4$ tetrahedra and Zr atoms occur within $ZrO_8$ dodecahedra. $ZrO_8$ polyhedra in reidite share edges with adjacent $ZrO_8$ polyhedra, forming zigzag chains along <100>. These chains are crossed linked through $SiO_4$ tetrahedra by sharing corners with them (Fig. 8). Like zircon, there are two Zr-O distances in reidite, and the $ZrO_8$ dodecahedron can be described as two interpenetrating $ZrO_4$ tetrahedra: one elongated, $ZrO_4^e$, the other compressed, $ZrO_4^c$. Thus the reidite structure is composed of two interpenetrating "C-9 type" arrays of corner-sharing tetrahedra, as is zircon. Unlike zircon, however, *Zr* and *Si* polyhedra in reidite do not share edges, and the two C9-type arrays of tetrahedra are composed, not of $SiO_4$ and $ZrO_4^c$ tetrahedra, but of $SiO_4$ and $ZrO_4^e$ tetrahedra (Fig. 9). Also in contrast with zircon, the $ZrO_4^c$ tetrahedra (which also share corners with $SiO_4$ tetrahedra) form layers of corner-sharing tetrahedra parallel to (001) in reidite, and these layers do not share polyhedral constituents with adjacent $ZrO_4^c$ layers (Nyman et al. 1984). These differences in connectivity of the structures of reidite (scheelite) and zircon may explain observed differences in thermal expansion (Bayer 1972) and compressibility (Hazen and Finger 1979, Scott et al. 2002) for the two structure types.

***Monazite*** ($CePO_4$) is the monoclinic form of $REEPO_4$ compounds adopted by light lanthanide orthophosphates (Ni et al. 1995, Boatner 2002). Although $ZrSiO_4$ does not form a poly-

morph with the monazite structure, thorite transforms at high pressure and temperature to huttonite (Dachille and Roy 1964), which is isostructural with monazite (Taylor and Ewing 1978). We discuss the monoclinic monazite/huttonite structure here in order to aid in our discussion of phase transformations in the next section.

Monazite is monoclinic, crystallizing in space group $P2_1/n$. The structure of monazite is similar to that of zircon in several important ways. In monazite, isolated $PO_4$ tetrahedra share corners and edges with $CeO_9$ polyhedra, which superficially resemble $ZrO_8$ dodecahedra in zircon. The *Ce* polyhedra in monazite share edges with each other to form chains parallel to the *a* axis (Fig. 10) that resemble analogous $ZrO_8$ dodecahedral chains in zircon (cf. Fig. 1). The Ce atom in monazite is coordinated by nine O atoms, described by Taylor and Ewing (1978) as four axial O atoms (two each forming the shared edge with two adjacent $PO_4$ tetrahedra) and five equatorial O atoms. The equatorial O atoms are each part of five neighboring $PO_4$ tetrahedra that share their corners with the *Ce* polyhedron. Thus, the Ce polyhedron in monazite shares corners and edges with seven neighboring $PO_4$ tetrahedra, whereas the $ZrO_8$ polyhedron in zircon shares polyhedral elements with six $SiO_4$ tetrahedra. The four axial O atoms define a distorted $CeO_4$ tetrahedron elongated along [001], analogous to the $ZrO_4^e$ tetrahedron in zircon. The edge-sharing *P* and *Ce* polyhedral chains along [001] in monazite (Fig. 11) closely resemble the [001] polyhedral chains in zircon, although the chains in monazite are twisted compared to those in zircon (cf. Fig. 4).

As noted, the zircon structure can be visualized as two interpenetrating arrays of alternating, corner-sharing $SiO_4$ and $ZrO_4^c$ tetrahedra (Fig. 5). Owing to nine O atoms being coordinated to Ce in monazite, the $CeO_9$ polyhedron cannot be adequately described as two interpenetrating tetrahedra. The ninth Ce-O bond in monazite can be seen as arising from a twisting of polyhedra in monazite relative to analogous polyhedra in zircon (compare Figs. 1, 10 and 4, 11), which results in an additional bond between a seventh $PO_4$ group and the $CeO_9$ polyhedron. The two C9-type arrays of $SiO_4$ and $ZrO_4^c$ tetrahedra, which are independent in the zircon structure, are no longer

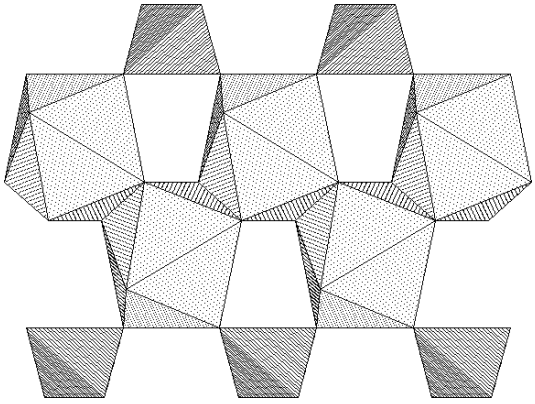

**Figure 8.** Scheelite structure projected on (100) with *c* axis vertical and *b* axis ($a_2$) horizontal. $CaO_8$ dodecahedra ($ZrO_8$ in reidite) are shaded light gray; $WO_4$ tetrahedra ($SiO_4$ in reidite) are striped.

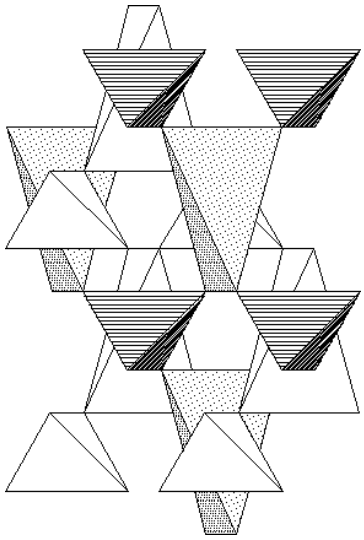

**Figure 9.** C9-type array of tetrahedra in the structure of scheelite: $WO_4$ (dark gray striped) and $CaO_4^e$ (light gray stippled). ($CaO_4^e$ and $WO_4$ tetrahedra in scheelite are equivalent to $ZrO_4^e$ and $SiO_4$ tetrahedra, respectively, in reidite). Projection is approximately on (110) with *c* axis vertical and *b* axis ($a_2$) horizontal.

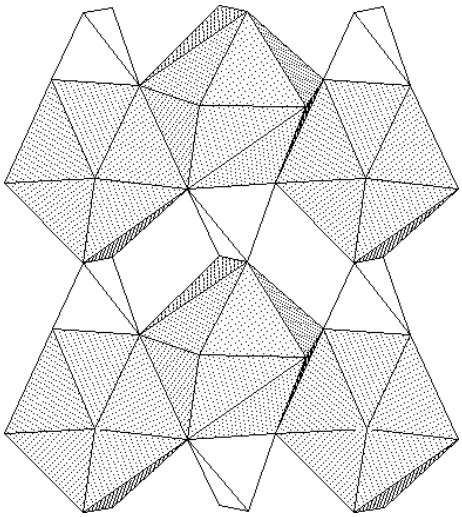

**Figure 10.** Monazite structure projected on (100); *c* axis is vertical, *b* axis is horizontal.

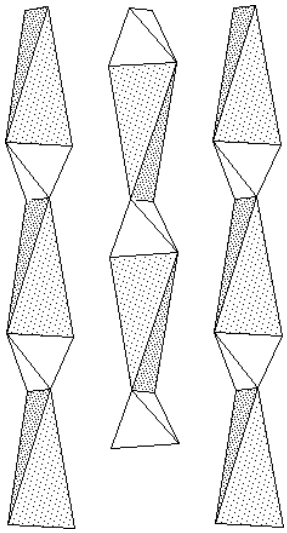

**Figure 11.** Monazite structure projected on (100), illustrating [001] chains of edge-sharing tetrahedra: $CeO_4^e$ (light gray stippled) and $PO_4$ (no shading); *c* axis is vertical, *b* axis is horizontal (cf. Fig. 4).

independent in monazite, due to the ninth Ce-O bond. Thus, monazite has greater overall structural connectivity than does zircon. The structure of monazite is more densely packed and space-filling than zircon, and it lacks the interstitial voids and channels present in the zircon structure.

***Rutile***. Vegard (1916) originally reported that zircon was isostructural with rutile (tetragonal $TiO_2$), although he corrected this later (Vegard 1926). Despite the contention by Bragg and Claringbull (1965) that "there is no relation between the two structures," they can, in fact, be compared in a straightforward manner (Nyman et al. 1984). In zircon, Si and Zr atoms are coordinated by four and eight O atoms, respectively, whereas in rutile, Ti atoms are coordinated by six O atoms. Nyman et al. (1984) point out that each pair of Ti octahedra in rutile can be correlated to a pair of Zr and Si polyhedra in zircon through small displacements of four O atoms. The displacement relates two edge-sharing *Ti* octahedra to an edge-sharing pair of *Zr* and *Si* polyhedra. Thus, the [001] chains of edge-sharing *Zr* and *Si* polyhedra in zircon are analogous to the [001] chains of edge-sharing *Ti* octahedra in rutile.

***Garnet***. Robinson et al. (1971) compared the structures of zircon and garnet ($X_3Y_2T_3O_{12}$). Both structures contain chains of edge-sharing $TO_4$ tetrahedra and $XO_8$ dodecahedra. These chains are oriented along the three crystallographically equivalent [111] directions in garnet, forming cross-linked chains with octahedral interstices. These $YO_6$ octahedra are typically occupied by high field-strength cations, such as $Al^{3+}$, $Fe^{3+}$ and $Cr^{3+}$, whereas the $XO_8$ dodecahedra are occupied by comparatively low field-strength cations such as $Mg^{2+}$, $Ca^{2+}$, $Mn^{2+}$, and $Fe^{2+}$.

***Anhydrite.*** The structure of anhydrite ($CaSO_4$) is similar to that of zircon in several ways. The $Ca^{2+}$ cation in anhydrite occupies a dodecahedron that is closely similar to the $ZrO_8$ dodecahedron in zircon (and the $CaO_8$ dodecahedron chromatite). These $CaO_8$ dodecahedra share edges with $SO_4$ tetrahedra, forming chains along [001] that strongly resemble the [001] chains in zircon. In addition, the $CaO_8$ dodecahedra share edges with adjacent $CaO_8$ dodecahedra along [100], also as seen in zircon. However, unlike the zircon structure, $CaO_8$ dodecahedra in anhydrite share only corners with neighboring $CaO_8$ dodecahedra along [010], thereby breaking the tetragonal symmetry. Anhydrite is orthorhombic, space group *Amma*, with $a$ = 6.993 Å, $b$ = 6.995 Å, $c$ = 6.245 Å

(Hawthorne and Ferguson 1975), and the distortion from tetragonal is seen to be small. Nyman et al. (1984) describe this structural relationship in more detail.

## STRUCTURAL EFFECTS OF TEMPERATURE, PRESSURE AND COMPOSITION

### Temperature

The thermal expansion of zircon is quite low, with an average (bulk) coefficient of thermal expansion ($\beta$) of approximately $4.5 \times 10^{-6}$/°C. As would be expected from the structure, the thermal expansion of zircon is anisotropic, with expansion along [001] greater than along <100> ($\beta_{<100>} = 3.2 \times 10^{-6}$/°C and $\beta_{[001]} = 5.4 \times 10^{-6}$/°C, Bayer 1972). Bayer (1972) examined the thermal behaviors of several synthetic $ATO_4$ compounds with zircon and scheelite structures and found that the thermal expansion of compounds with the zircon structure is generally less than that of scheelite-type compounds, and that thermal expansion tends to increase with decreasing valence of dodecahedral-site cations.

Zircon is stable up to 1690°C (1963 K) at ambient pressure, at which point it decomposes to the constituent oxides. A neutron-diffraction study of zircon up to 1900 K (1627°C) found that zircon undergoes a displacive structural "transition" at approximately 1100 K (827°C), where there is a discontinuity in the thermal expansion of the *a* and *c* lattice parameters (Mursic et al. 1992). The temperature-dependence of lattice parameters *a* and *c* can be described, both above and below the 1100 K transition, by a second-degree polynomial: $A_0 = A_1T + A_2T^2$. Between room temperature and 1100 K, the polynomial coefficients are $A_0 = 6.6003$, $A_1 = 126 \times 10^{-7}$, $A_2 = 82 \times 10^{-10}$ for the *a* axis, and $A_0 = 5.9783$, $A_1 = 29 \times 10^{-6}$, $A_2 = 67 \times 10^{-10}$ for the ***c*** axis; whereas, between approximately 1500 and 1800 K, the polynomial coefficients for the temperature dependence of the *a* axis are $A_0 = 6.65$, $A_1 = -4 \times 10^{-5}$, $A_2 = 24 \times 10^{-9}$, and those for the *c* axis are $A_0 = 6.05$, $A_1 = -5 \times 10^{-5}$, $A_2 = 24 \times 10^{-9}$ (Mursic et al. 1992).

Volume expansion during heating of zircon is due primarily to expansion of the $ZrO_8$ dodecahedron, there being relatively little change in the $SiO_4$ tetrahedral volume below 1100 K. Increased dodecahedral volume correlates with an increase in the longer Zr-O distance, corresponding to the elongated $ZrO_4^e$ tetrahedron, which shares edges with $SiO_4$ tetrahedra. Relatively little change in the shorter Zr-O bonds or the volume of the compressed $ZrO_4^c$ tetrahedron occurs up to the 1100 K transition. Between 1100 and 1200 K, the $SiO_4$ tetrahedron undergoes a sharp increase in volume due to an increase in the Si-O bond length from 1.622 Å to 1.628 Å (Mursic et al. 1992). The corner-sharing tetrahedra ($SiO_4$ and $ZrO_4^c$) respond to these changes in $SiO_4$ volume through rotation, leaving the longer Zr-O distance essentially unchanged through the transition. The edge-sharing $ZrO_4^e$ tetrahedron cannot rotate (independent of the $SiO_4$ tetrahedron), and the longer Zr-O bonds must, therefore, lengthen continuously during and following expansion of the Si-O bond. By approximately 1500°C, the geometry of the $SiO_4$ tetrahedron approaches that of an ideal tetrahedron (O-Si-O angle = 109°). Mursic et al. (1992) explain the decomposition of zircon by the gradual breakdown of the $ZrO_8$ dodecahedral polyhedron due to increasing incompatibility of the two interpenetrating $ZrO_4$ tetrahedra. Thus, the thermal decomposition of $ZrSiO_4$ to (tetragonal) $ZrO_2$ and $SiO_2$ (beta-cristobalite) can be described as a structural rearrangement of the $ZrO_8$ polyhedron, which is no longer compatible with the $SiO_4$ polyhedron. The $SiO_4$ tetrahedra eventually rearrange, crystallizing beta-cristobalite (Mursic et al. 1992, Colombo et al. 1999).

The thermal behavior of zircon contrasts with that of thorite, which transforms to the high-temperature polymorph huttonite before decomposing to $ThO_2$ and $SiO_2$ (Dachille and Roy 1964, Finch et al. 1964). Huttonite, which has the monazite structure, shares some important structural features with thorite (zircon structure); however, Th in huttonite is coordinated by nine O atoms, rather than eight as in thorite, and the $ThO_9$ polyhedron in huttonite shares corners with seven $SiO_4$ tetrahedra, rather than six as in thorite (Taylor and Ewing 1978). The structural change is

accomplished through rotations of $ThO_4^e$ and $SiO_4$ tetrahedra and formation of an additional bond between an O atom of the fifth $SiO_4$ tetrahedron and the *Th* site. The transformation of thorite to huttonite results in a structure with greater overall connectivity than zircon, which, as noted, consists of two independent arrays of *Si* and *Zr* tetrahedra. These arrays both exist in huttonite, but they are not independent, being connected through the additional Th-O-Si linkage. The structure collapses slightly due to the rotation of polyhedra and the additional Th-O bond. The transformation of thorite to huttonite is sluggish, presumably due to formation of an additional Th-O bond. Details of the transformation remain unclear, as no high-temperature structural studies of the thorite-huttonite transformation have, to our knowledge, been reported. The fact that a structural transformation similar to the thorite-huttonite transformation is not observed in zircon before decomposition may be due to the greater tetrahedral rotation required to increase the coordination number around the small $Zr^{4+}$ cation.

Coffinite ($USiO_4$) is isostructural with thorite and zircon (Fuchs and Gebert 1958). The phase stability of coffinite remains largely uncertain. High-temperature synthesis experiments (e.g., Lunga 1966) suggest that coffinite is metastable relative to $UO_2 + SiO_2$. However, coffinite occurs primarily in low-temperature sedimentary rocks (Plant et al. 1999) and formation of coffinite at low temperatures may be kinetically inhibited on laboratory timescales. Considering the similar ionic radii of $^{[VIII]}U^{4+}$ (1.00 Å) and $^{[VIII]}Th^{4+}$ (1.05 Å), a high-temperature polymorph of $USiO_4$ analogous to huttonite might be expected; however, such a phase has never been reported in laboratory experiments or from natural samples. The reason for this apparent disparity between coffinite and thorite is not clear.

**Pressure**

Hazen and Finger (1979) determined the bulk modulus ($K_{0T}$) for natural zircon from crystal-structure refinements up to 4.8 GPa, reporting values of 227 GPa or 234 GPa, depending on the assumed value for the isothermal pressure derivative, $K_{0T}'$ ($K_{0T}' = 6.5$ and 4, for the low and high values, respectively). This makes zircon one of the most incompressible silicate minerals known, with a bulk modulus similar to those of perovskite-type structures and silicates with Si in octahedral coordination (Knittle 1995). Crocombette and Ghaleb (1999) calculated the bulk modulus for pure $ZrSiO_4$, deriving a value of 245 GPa, in excellent agreement with the value reported by Hazen and Finger (1979). Recently, van Westrenen et al. (2003a) measured unit-cell volumes of pure, synthetic zircon up to 27 GPa and report a bulk modulus of 201 GPa (K′ of 4.0), significantly lower than the value reported by Hazen and Finger (1979) for natural zircon.

The bulk modulus of the $SiO_4$ tetrahedron (230 ± 40 GPa) is low compared to other silicates, whereas that of the $ZrO_8$ dodecahedron (280 ± 40 GPa) is anomalously high for a polyhedron with coordination number greater than six (Hazen and Finger 1979). Smyth et al. (2000) suggest that the *Zr* polyhedron largely accounts for the remarkable incompressibility of zircon, attributing this to the high valence and relatively large ionic radius of $Zr^{4+}$ (0.84 Å). As for its thermal expansion, zircon exhibits anisotropic compressibility, being about 70% more compressible along [001] than along <100> (Hazen and Finger 1979). This is explained by the fact that the four short Zr-O bonds (corresponding to the $ZrO_4^c$ tetrahedron), which are sub-parallel to the (001) plane, are less compressible than the longer Zr-O bonds, which are closer to being parallel to [001] (Smyth et al. 2000).

Zircon transforms at high pressure to reidite, which is isostructural with scheelite. The transformation is believed to occur via a martensitic-type transformation (Kusaba et al. 1985, 1986; Leroux et al. 1999). Crystallographically, the structure of reidite can be derived by simultaneously twinning the zircon structure on (200), (020) and (002) (Nyman et al. 1984). Deformation in experimentally shock-metamorphosed zircon crystals is dominated by planar deformation features, interpreted as micro-twins predominantly on (100), (010) and (111), as well as amorphous planar deformation features (Leroux et al. 1999). Experimentally, Kusaba et al. (1986) concluded

that the [110] direction in zircon becomes the [100] direction in reidite during the shock-induced transformation zircon to reidite, a conclusion consistent with a transmission electron microscope study of experimentally shocked zircon crystals, in which the [110] direction of reidite is observed to be parallel to the [100] direction in adjacent zircon (Leroux et al. 1999). The latter study also revealed that the (112) plane in reidite parallels the (100) plane of zircon in shocked crystals. These observations suggest an epitaxial relationship between zircon and reidite.

The transformation of zircon to reidite is sluggish and the equilibrium transition pressure is not well constrained. The transition pressure at 1300 K (1027°C) is reportedly 12 GPa (Liu 1979), and if the Clapyron slope of the zircon-reidite phase boundary is positive, the room-temperature transition pressure must be lower than this. Crocombette and Ghaleb (1998) calculated an equilibrium transition pressure of 5 GPa (at 0 K) by using both empirical potentials and *ab initio* electronic-structure calculations. High-pressure shock and static experiments reveal a rather wide range of observed room-temperature transformation pressures consistently above about 20 GPa (Kusaba et al. 1985, Knittle and Williams 1993, Fiske et al. 1994, Leroux et al. 2001). A recent high-pressure diamond-anvil X-ray powder-diffraction study on the room-temperature compressibility of pure synthetic zircon reports evidence for reidite in powder-diffraction patterns from zircon crystals exposed to just under 20 GPa (van Westrenen et al. 2003a), about 3 GPa lower than the previously reported transition pressure observed for natural zircon (Knittle and Williams 1993). van Westrenen et al. (2003a) suggest that low concentrations of impurities in natural zircon crystals might affect compressibilities and observed transition pressures, a contention that appears to be supported by a recent study of room-temperature compressibility of synthetic zircon crystals doped with approximately 10 wt % REE + P (van Westrenen et al. 2003b). That study reports that the compressibility of REE+P-doped zircon is significantly greater than for pure $ZrSiO_4$, and that evidence for the onset of the zircon-reidite transition is not observed below 22.5 GPa.

As for its temperature dependence, the pressure-dependent behavior of thorite contrasts with that of zircon. The high-pressure polymorph of $ThSiO_4$ is huttonite (which is also the high-temperature $ThSiO_4$ polymorph). The transformation from thorite to huttonite reflects a rotation of tetrahedra such that the coordination number of Th increases from eight in thorite to nine in huttonite, which, as discussed in the section on temperature effects, leads to an increase in structural connectivity in huttonite compared to thorite and a more compact structure.

Huttonite is more dense and has lower symmetry than thorite, which is unusual for a high-temperature polymorph. The Clausius-Clapyron equation relates differences in volumes and entropy across a phase boundary to the slope of the phase boundary in P-T space:

$$dP/dT = (S_i\text{-}S_j)/(V_i\text{-}V_j) = \Delta S/\Delta V \quad (1)$$

Based on their relative densities, molar volumes of the three structure types decrease in the order $V_{Zirc} > V_{Mon} > V_{Sch}$, since, for a given composition, density for each structure type increases in the order $D_{Zirc} < D_{Mon} < D_{Sch}$. Based on the symmetries of these three structure types, molar entropies might be expected to decrease in the order $S_{Zirc} > S_{Sch} > S_{Mon}$, since higher symmetry tends to imply greater entropy. Using these arguments, we can postulate the Clapyron slope for phase boundaries between pairs of structure types zircon-scheelite, zircon-monazite and monazite-scheelite.

The phase boundary between zircon-type structures and scheelite-type structures is characterized by $V_{Sch} < V_{Zirc}$, and $S_{Sch} < S_{Zirc}$, making $\Delta V$ and $\Delta S$ both negative, so that $\Delta V/\ \Delta S$ and, therefore, dP/dT is positive; that is, the Clapyron slope is positive. Although the zircon-to-reidite transition is not well known, the slope of the analogous phase boundary between zircon-type and scheelite-type polymorphs of synthetic $HoVO_4$ is positive (Fig. 12), with the zircon-type polymorph stable at higher temperature and lower pressure than the scheelite-type polymorph (Stubican and Roy 1963), consistent with our expectation.

For the phase boundary between monazite-type and scheelite-type structures we can expect $S_{Sch} > S_{Mon}$ and $V_{Mon} > V_{Sch}$, making $\Delta S$ positive but $\Delta V$ negative, so that dP/dT will be negative for this phase boundary. This, too, is consistent with experiment. The P-T phase boundary between the monazite-type and the scheelite-polymorphs of $NdAsO_4$ has a negative slope (Fig. 13), with the scheelite-type polymorph stable at higher temperature and pressure (Stubican and Roy 1963).

The phase boundary between zircon-type and monazite-type structures has $V_{Zirc} > V_{Mon}$, and symmetry suggests that $S_{Zirc} > S_{Mon}$, making $\Delta V$ and $\Delta S$ both positive and, therefore, dP/dT positive. Of course, a well-known example of this phase boundary is that between thorite and huttonite, which has a *negative* Clapyron slope (Dachille and Roy 1964), contrary to our expectation (Fig. 14). The unit-cell volume of huttonite is less than that of thorite, so it seems clear that $\Delta V$ is negative. The negative Clapyron slope of the huttonite-thorite phase boundary, therefore, requires that the molar entropy of huttonite be greater than that of thorite ($\Delta S > 0$), which is counterintuitive given that huttonite is the lower-symmetry phase. Zircon-type $CeVO_4$ also transforms to the monazite-type structure at elevated temperature and pressure (Fukunaga and Yamaoka 1979); however, the pressure and temperature dependence of this transformation is not known.

It seems notable that the room-temperature polymorph of synthetic $ThGeO_4$ adopts the scheelite structure, transforming to the zircon-type structure above approximately 1100°C (Bayer 1972, Ennaciri et al. 1986). This is consistent with $HoVO_4$ but in apparent contrast with the observed behavior of $ThSiO_4$, which has no known scheelite-type polymorph. Studies of the thorite-huttonite transition have not been reported for pressures above 5 GPa (Dachille and Roy 1964), and whether huttonite might transform to a scheelite-type polymorph at higher pressures (as for $NdAsO_4$) is not known.

Experimental evidence from a variety of $ATO_4$ systems indicates that, for a given temperature, the polymorphic sequence with increasing pressure is *Zircon* → (*Monazite*) → *Scheelite*, where the (*Monazite*) signifies that zircon-type polymorphs of many $ATO_4$ compounds transform directly to the scheelite structure (this is, in fact, the more commonly observed transformation). The polymorphic sequence at fixed pressure and increasing temperature is more ambiguous. The

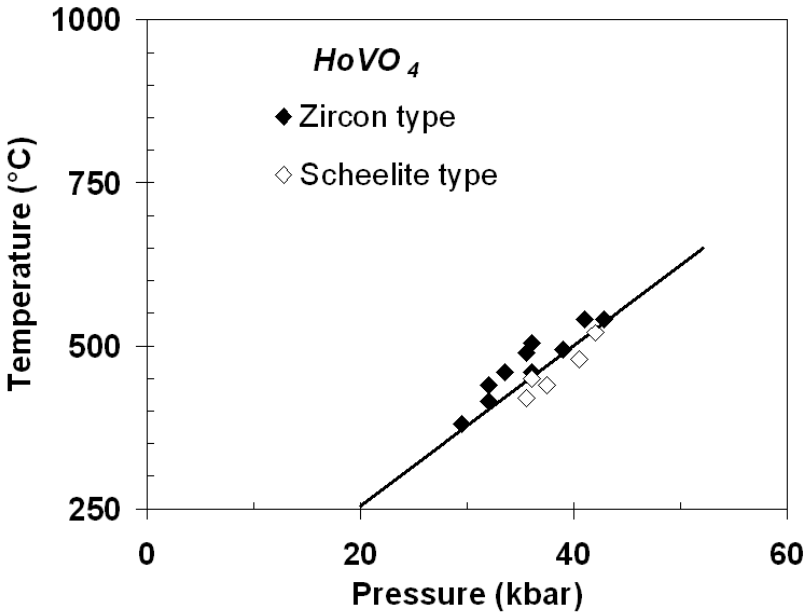


**Figure 12.** Plot of phase boundary between zircon-type and scheelite-type polymorphs of $HoVO_4$ reported by Stubican and Roy (1963). Positive Clapyron slope is consistent with expectation (see text).

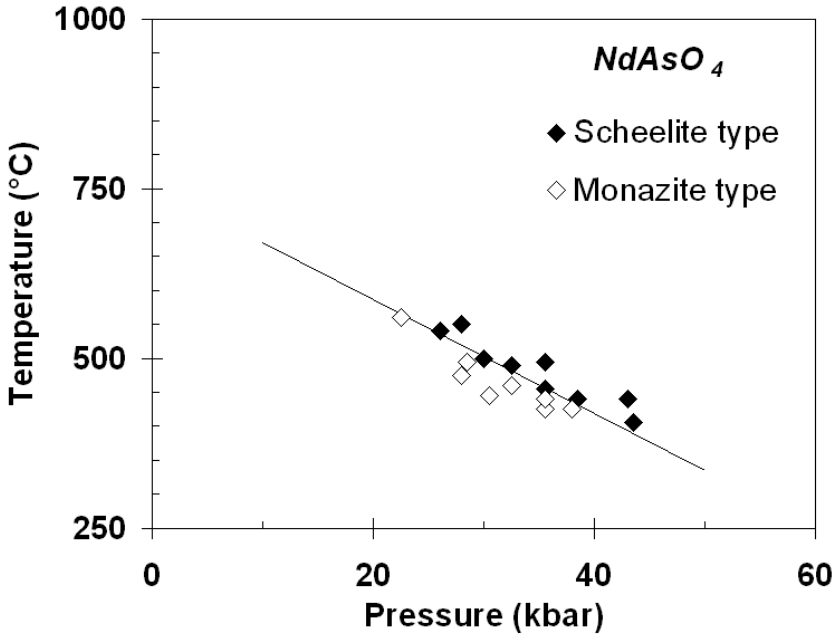


**Figure 13.** Plot of phase boundary between monazite-type and scheelite-type polymorphs of $NdAsO_4$ reported by Stubican and Roy (1963). Negative Clapyron slope is consistent with expectation (see text).

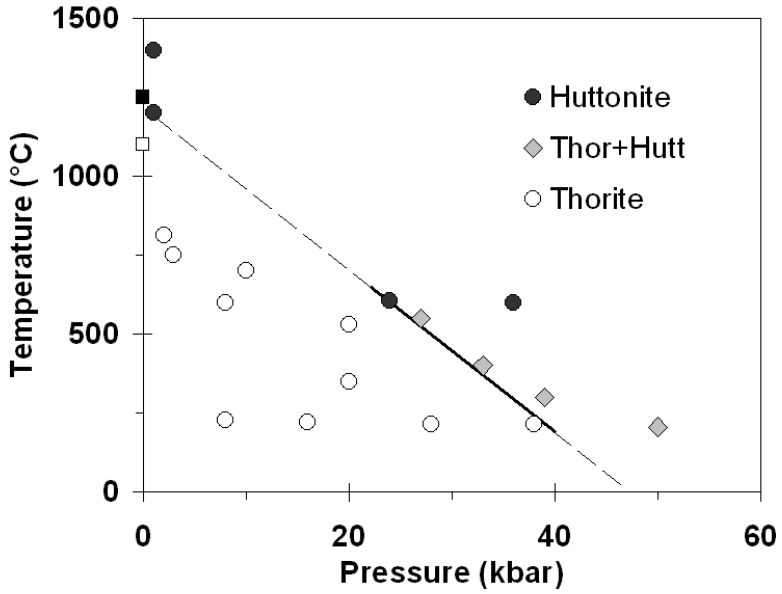


**Figure 14.** Plot of phase boundary between thorite and huttonite from data reported by Dachille and Roy (1964) (circles and diamonds). Squares correspond to synthesis temperatures at 1 bar reported by Taylor and Ewing (1978) for thorite (hollow square 1100°C) and huttonite (filled square 1250°C). Estimated phase boundary is drawn through 1215°C at 1 bar, which is within error of the equilibrium transition temperature reported by Finch et al. (1964): 1225(10)°C. Negative Clapyron slope is contrary to expectation based on changes in density and symmetry (see text).

most likely polymorphic sequence at constant pressure and increasing temperature seems to be *Monazite* → *Scheelite* → *Zircon*, based largely on the study of Stubican and Roy (1963); however, the isobaric transformation *Zircon* → *Monazite* is also known (for $ThSiO_4$, although the thorite-huttonite transformation may be anomalous). Thus, for a given $ATO_4$ composition, the scheelite-type structure is stable at the highest pressures and the zircon-type structure is apparently stable at the lowest pressures. The monazite-type structure is stable at either low temperature and intermediate pressure or at low pressure and intermediate temperature.

This ambiguity in the relative position of the stability field for monazite-type structures, as well as uncertainty about whether the thorite-huttonite phase boundary is representative of other zircon-type-to-monazite-type transformations, present a significant problem when evaluating potential pressure-temperature relationships among the three $ATO_4$ structure types. A schematic P-T phase diagram, based on experimental results from different $ATO_4$ systems, helps to illustrate the problem (Fig. 15). Figure 15 places the stability range of monazite-type structures at low temperatures and intermediate pressures, making zircon-type structures stable at all temperatures for pressures below the triple point. If the thorite-huttonite phase boundary is representative of analogous phase boundaries in other $ATO_4$ systems, phase boundaries between zircon-type structures and their higher-temperature polymorphs form an obtuse angle about the triple point, a violation of thermodynamic principles (the same problem arises if we assume that monazite-type structures are stable at high temperature and low pressure, upper left of diagram in Fig. 15, although this choice is considerably more difficult to rectify with expected Clapyron slopes discussed above). It appears that the thorite-huttonite phase boundary may well be anomalous among $ATO_4$ compounds. Of course, Clapyron slopes for phase boundaries indicated in Figure 15 can change significantly as a function of the $ATO_4$ system under consideration (possibly including whether they are positive or negative), and the degree to which solid solution and impurities might shift phase boundaries is unknown and potentially large. Additional high-pressure and high-temperature studies of $ATO_4$ compounds, especially $ThSiO_4$, $ThGeO_4$ and perhaps $Th(Si,Ge)O_4$ solid solutions, could help clarify P-T relationships among zircon-, scheelite- and monazite-type structures.

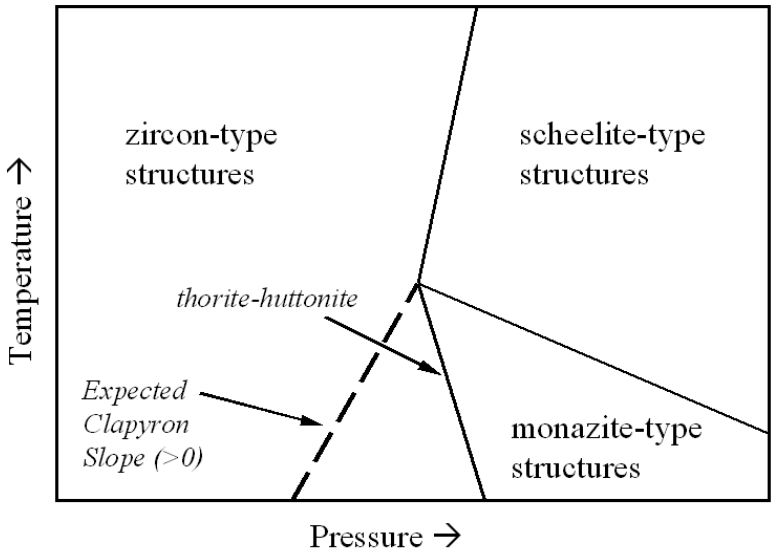


**Figure 15.** Hypothetical schematic phase diagram for $ATO_4$ compounds. Bold lines indicate phase boundaries between selected pairs of zircon-, scheelite-, and monazite-type $ATO_4$ compounds discussed in the text. The experimentally determined thorite-huttonite phase boundary is indicated. Also indicated is the expected positive Clapyron slope of that phase boundary (dashed line) based on changes in density and symmetry (see text).

**Composition**

Analyses of zircon commonly report trace amounts (or more) of P, Y, Hf, U, Th, and lanthanides (Hoskin and Schaltegger, this volume). Substitution of minor constituents into zircon has been studied by several workers (Caruba et al. 1995, Hanchar et al. 2001a), and the potential role of substitutions on the pressure dependence of the zircon structure was mentioned (van Westrenen et al. 2003b). Structural strain imposed by impurities replacing Zr and Si in zircon may affect how trace elements are incorporated into zircon (e.g., Brice 1975). Given the important role that zircon has assumed in geochemical and chronological studies, a clearer understanding of structural changes caused by substitutions may elucidate strain-imposed limits on trace-element substitutions (Hoskin 2000, Finch et al. 2001a, Hanchar et al. 2001b) and may lead to more predictive models for trace-element substitution in zircon and other minerals (Blundy and Wood 1994, Allan et al. 2001, Hanchar et al. 2001c, van Westrenen et al. 2001).

Zircon is commonly enriched in Y and heavy lanthanides relative to light and middle lanthanides (Hinton and Upton 1991, Belousova et al. 1998, Hanchar et al. 2001a, Hoskin and Schaltegger, this volume). REE-bearing zircon crystals commonly contain P, and owing to crystal-chemical similarities between $Y^{3+}$ and heavy $REE^{3+}$, replacement of $Zr^{4+}$ by $REE^{3+}$ in zircon is commonly explained by the coupled xenotime-type substitution, in which $P^{5+}$ replaces $Si^{4+}$, maintaining charge balance. Thus the ideal formula for xenotime-substituted zircon is $REE_xZr_{1-x}P_xSi_{1-x}O_4$, in which $x$ indicates the mole fraction of the xenotime component. Implicit in the xenotime substitution is the assumption that $P^{5+}$ replaces $Si^{4+}$ at the tetrahedral site and REE replace $Zr^{4+}$ at the dodecahedral site.

If xenotime substitution is the only mechanism by which charge balance is maintained in REE-substituted zircon, the atomic ratio REE:P must be unity. However, atomic ratios of REE:P measured in natural and synthetic zircon crystals commonly deviate significantly from one (Hinton and Upton 1991, Maas et al. 1992, Hoskin et al. 2000, Hanchar et al. 2001a), indicating a more complex charge-balance mechanism (or multiple mechanisms). Natural zircon crystals may exhibit charge-preserving substitutions besides, or in addition to, xenotime substitution, including exchange of $OH^-$ groups for $O^{2-}$ ions and coupled substitutions on the *Zr* site (Speer 1982a, Caruba et al. 1985, Hinton et al. 2003). Moreover, some degree of solid solution can be expected between zircon and the large number of isostructural zircon-group compounds discussed here.

A recent study of synthetic zircon crystals doped with REE and P revealed slight excesses of *Zr*-site cations (Zr and REE) that correlate with slight deficits in *Si*-site cations (Si and P) (Hanchar et al. 2001a) suggesting that minor Zr might substitute at the *Si* site (ionic radius of $^{[IV]}Zr$ is 0.59 Å), which is supported qualitatively by single-crystal X-ray diffraction data (Finch et al. 2001a). Examination of these same crystals by EXAFS confirmed that REE occupy the *Zr* site (Finch et al. 2001b). No evidence for interstitial REE was found from either X-ray diffraction data (Finch et al. 2001a) or X-ray absorption spectroscopy (Finch et al. 2001b).

Substitution of REE and P into zircon increases Zr-O bond distances and decreases Si-O bond distances (Finch et al. 2001a), consistent with the expected xenotime substitution. With increasing REE concentration, bond distances in substituted zircon crystals increase most sharply for the short Zr-O bond, whereas the long Zr-O bond distance (Zr-O') increases more gradually (Fig. 16); however, both Zr-O bond distances display maximum strain for Er-doped zircon, despite the fact that REE concentrations in Y and Yb crystals were greater than in Er-doped crystals. This is explained by the decreasing radii of REE, so that heavy lanthanides and Y (HREE) are increasingly compatible in the *Zr* site and, therefore, impart proportionately less strain in REE-substituted crystals than do light lanthanides (Finch et al. 2001a). Because P is incorporated along with REE (maintaining charge balance), the Si-O bond distance decreases monotonically as HREE concentration increases (Fig. 16). Finch et al. (2001a) concluded that strain at the *Si* site, caused by increased P substitution, explains the inability of zircon crystals to incorporate sufficient addi-

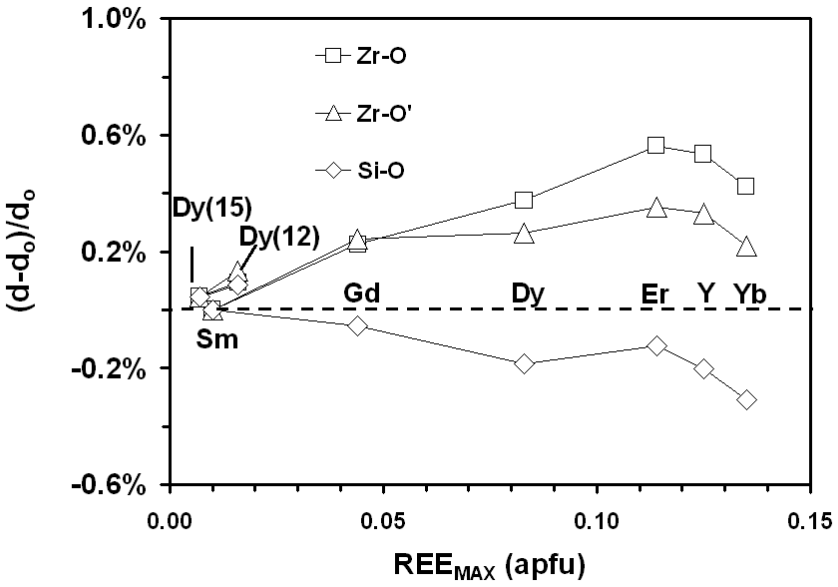


**Figure 16.** Change in cation-oxygen bond lengths (relative to equivalent bond distance in Sm-doped crystal) as a function of increasing REE in synthetic zircon crystals. Zr-O corresponds to the shorter Zr-O bond length; Zr-O' corresponds to the longer Zr-O bond length; "*apfu*" = atoms per formula unit; i.e., the value of $x$ in $REE_xZr_{1-x}P_xSi_{1-x}O_4$ (after Finch et al. 2001a).

tional $P^{5+}$ to charge balance continued incorporation of REE, despite the increased compatibility of HREE in the zircon structure. Strain induced by substitutions at both the *Zr* and *Si* sites in zircon helps explain why complete solid solution between zircon and xenotime has not been observed in synthetic crystals. By comparing analyses of natural zircons in xenotime-saturated rocks with preliminary results from an experimental study, Tomaschek and Ballhaus (2003) estimate that the apparent limit on xenotime substitution in zircon is approximately 10 mol % $YPO_4$.

As noted previously, the only refineable atomic positional parameters in zircon are the fractional coordinates of the *O* site: *y* and *z*. As REE and P increase in synthetic zircon crystals, the *O* site shifts parallel to {100}, approximately along <012>. The *O* site shifts away from the two neighboring *Zr* sites and towards (though not directly towards) the *Si* site, reflecting expansion of the REE-substituted $ZrO_8$ dodecahedron and concomitant contraction of the P-substituted $SiO_4$ tetrahedron. The observed shift in the O position in (REE+P)-doped zircon crystals trends in the direction of *O* positions reported for pure synthetic xenotime-type $REEPO_4$ compounds (Ni et al. 1995) (Fig. 17). It would be instructive to dope xenotime-type REE orthophosphates with Zr and Si (in addition to [REE+P]-doped zircon; e.g., Hanchar et al. 2001a, Tomaschek and Ballhaus 2003) in order to better constrain the extent of miscibility among these isostructural compounds. It seems likely that strain introduced by the substitution $(REE^{3+})_{+1}(P^{5+})_{+1}(Zr^{4+})_{-1}(Si^{4+})_{-1}$ is likely to be the most important factor limiting solid solution between zircon and xenotime.

## ACKNOWLEDGMENTS

We are grateful for helpful reviews by Wim van Westrenen and Paul Hoskin, and for comments on phase transformations by Mats Hillert (KTH). Support to RJF was provided by Argonne National Laboratory under Contract No. W-31-109-ENG-38 with the U.S. Department of Energy, and through a grant from the Department of Energy Environmental Management Science Programs.

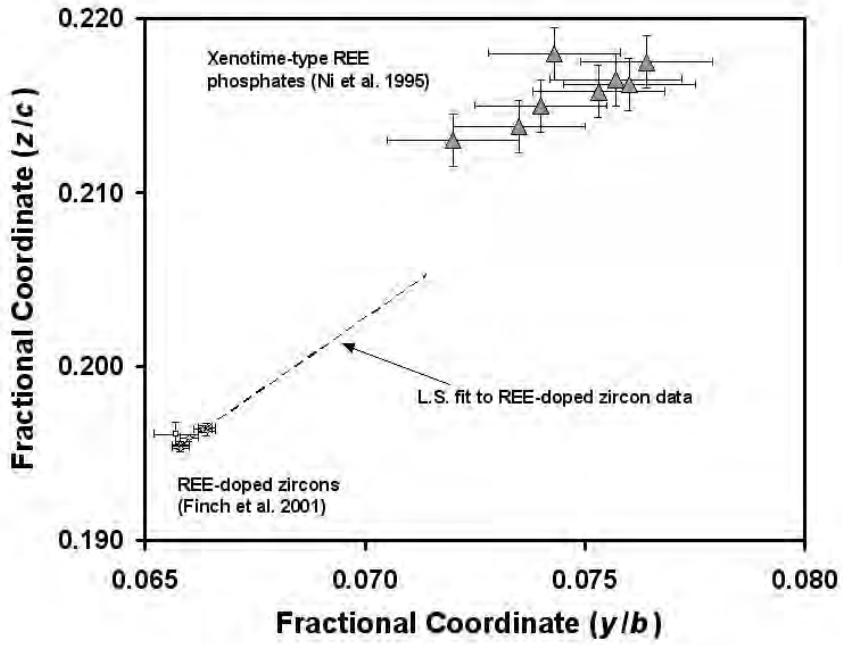


**Figure 17.** Plots of fractional coordinates *y* and *z* in synthetic zircon crystals doped with REE and P (Finch et al. 2001a) and in xenotime-type $REEPO_4$ crystals (Ni et al. 1995).

## REFERENCES

Allan NL, Blundy JD, Purton JA, Lavrentiev My, Wood BJ (2001) Trace element incorporation in minerals and melts. *In* Solid Solutions in Silicate and Oxide Systems. Notes in Mineralogy, Geiger CA (ed) European Mineral Union, Eötvös University Press, 3:251-302

Baudracco-Gritti C, Quartieri S, Vezzalini G, Permingeat F, Pillard F, Rinaldi R (1987) A non plumboan wakefieldite-(Ce): New data on the mineral species corresponding to cerium orthovanadate. Bull Minéral 110:657-663

Bayer G (1972) Thermal expansion of $ABO_4$ compounds with zircon and scheelite structures. J Less Common Metals 26:255-262

Begg BD, Hess NJ, Weber WJ, Conradson SD, Schweiger MJ, Ewing RC (2000) XAS and XRD study of annealed $^{238}Pu$- and $^{239}Pu$-substituted zircons ($Zr_{0.92}Pu_{0.08}SiO_4$). J Nucl Mater 278:212-234

Belousova EA, Griffith WL, Pearson NJ (1998) Trace element composition and cathodoluminescence properties of Southern African kimberlitic zircon. Mineral Mag 62:355-366

Bernard F, Walter F, Ettinger K, Taucher J, Mereiter K (1998) Pretulite, $ScPO_4$, a new scandian mineral from the Styrean and Lower Austrian lazulite occurrences, Austria. Am Mineral 83:625-630

Bjorklund CW (1958) The preparation of $PuP_2O_7$ and $PuPO_4$. J Am Chem Soc 79:6347-6350

Blundy J, Wood B (1994) Prediction of crystal-melt partition coefficients from elastic moduli. Nature 372:452-454

Boatner LA (2002) Synthesis, structure, and properties of monazite, pretulite, and xenotime. Rev Mineral Geochem 48:87-121

Bowden GJ (1998) A review of the low temperature properties of the rare earth vanadates. Austral J Phys 51:201-236

Bowring SA (1995) The Earth's early evolution. Science 269:1535-1540

Bowring SA, Williams IS (1999) Priscoan (4.00-4.03 Ga) orthogneisses from northwestern Canada. Contrib Mineral Petrol 134:3-16

Bowring SA, Erwin DH, Jin YG, Martin MW, Davidek K, Wang W (1998) U/Pb zircon geochronology and tempo of the end-Permian mass extinction. Science 280:1039-1045

Bowring SA, Williams IS, Compston W (1989) 3.96 Ga gneisses from the Slave Province, Northwest Territories, Canada. Geology 17:971-975

Bragg L, Claringbull GF (1965) Crystal Structures of Minerals. Bell, London, p 113

Brice JC (1975) Some thermodynamic aspects of the growth of strained crystals. J Crystal Growth 28:249-253
Buick R, Thornett JR, McNaughton NJ, Smith JB, Barley ME, Savage M (1995) Record of emergent continental crust similar to 3.5 billion years ago in the Pilbara craton of Australia. Nature 375:574-575
Buisson G, Bertaut F, Mareschal J (1964) Étude cristallographique des composés $TCrO_4$ (T = terre rare ou Y). C R Acad Sci Paris 259:411-413
Burakov BE, Hanchar JM, Zamoryanskaya MV, Garbuzov VM, Zirlin VA (2002) Synthesis and investigation of Pu-doped single crystal zircon, $(Zr,Pu)SiO_4$. Radiochim Acta 89:1-3
Burakov BE, Hanchar JM, Zamoryanskaya MV, Anderson EB, Garbuzov VM, Kitsay AA, Krivovichev SV (2003) Investigation of single crystal zircon, $(Zr,Pu)SiO_4$, doped with $^{238}Pu$. Radiochimica Acta (in press)
Cabella R, Lucchetti G, Marescotti P (1999) Occurrence of LREE- and Y-arsenates from a Fe-Mn deposit, Liguruan Briançonnais Domain, maritime Alps, Italy. Can Mineral 37:961-972
Carron MK, Mrose ME, Murata KJ (1958) Relation of ionic radius to structures of rare-earth phosphates, arsenates, and vanadates. Am Mineral 43:985-989
Caruba R, Baumer A, Ganteaume M, Iacconi P (1985) An experimental study of hydroxyl groups and water in synthetic and natural zircons: a model of the metamict state. Am Mineral 70:1224-1231
Caruba R, Baumer A, Ohnenstetter D, Cesbron F, Rouer O, Blanc P (1995) The hydrothermal synthesis of molybdenum, sulfur-doped zircon: a study of charge compensation mechanisms. Neues Jahrb Mineral Mh 1995:241-254
Chakoumakos BC, Abraham MM, Boatner LA (1994) Crystal structure refinements of zircon-type $MVO_4$ (*M* = Sc, Y, Ce, Pr, Nd, Tb, Ho, Er, Tm, Yb, Lu). J Sol State Chem 109:197-202
Colombo M, Chrosch J, Biagini R, Memmi I (1999) An IR analysis of the role of $SiO_4$ tetrahedra in thermally annealed $ZrSiO_4$. Neues Jahrb Mineral Monatsh 1999:113-122
Crocombette J-P (1999) Theoretical study of point defects in crystalline zircon. Phys Chem Minerals 27:138-143
Crocombette J-P, Ghaleb D (1998) Modeling the structure of zircon ($ZrSiO_4$): Empirical potentials, *ab initio* electronic structure. J Nucl Mater 257:282-286
Dachille F, Roy R (1964) Effectiveness of shearing stresses in accelerating solid-phase reactions at low temperature and high pressure. J Geol 72:243-247
Deliens M, Piret P (1977) La kusuite, $(Ce^{3+},Pb^{2+},Pb^{4+})VO_4$, nouveau mineral. Bull Soc Fr Minéral Cristallogr 100:39-41
Demartin F, Gramaccioli CM, Pilati T (1992). Structure of a new natural tungstate arsenate, $[Ca_2Y(AsO_4)(WO_4)_2]$, structurally related to scheelite. Acta Crystallogr C 48:1357-1359
Demartin F, Diella V, Gramaccioli CM, Pezzotta F (2001) Schiavinatoite, $(Nb,Ta)BO_4$, the Nb analogue of behierite. Eur J Mineral 13:159-165
Dreyer G, Tillmanns E (1981) Dreyerite, natural, tetragonal bismuth vanadate from Hirschhorn, Pfalz. Nueus Jahrb Mineral Monatsh 1981:151-154
Duclos SJ, Jayaraman A, Espinosa GP, Cooper AS, Maines RG (1989) Raman and optical absorption studies of the pressure-induced zircon to scheelite structure transformation in $TbVO_4$ and $DyVO_4$. J Phys Chem Solids 50:769-775
Durif A (1956) Structure et valence de $VCeO_4$. Acta Crystallogr 9:471
Durif A, Forrat F (1957) Sur quelques arsénates des terres rares à structure zircon. C R Acad Sci Paris 245:1636-1638
Ennaciri A, Kahn A, Michel D (1986) Crystal structures of $HfGeO_4$ and $ThGeO_4$ germanates. J Less-Common Metals 124:105-109
Ewing RC (1999) Nuclear waste forms for actinides. Proc Nat Acad Sci 967:3432-3439
Ewing RC, Lutze W (1997) Disposing of plutonium. Science 275:737
Fayek M, Janeczek J, Ewing RC (1997) Mineral chemistry and oxygen isotopic analyses of uraninite, pitchblende and uranium alteration minerals from the Cigar Lake deposit, Saskatchewan, Canada. Appl Geochem 12:549-565
Fayek M, Kyser K (1997) Characterization of multiple fluid-flow events and rare-earth-element mobility associated with formation of unconformity-type uranium deposits in the Athabasca basin, Saskatchewan. Can Mineral 35:627-658
Finch RJ, Murakami T (1999) Systematics and paragenesis of uranium minerals. Rev Mineral 38:91-179
Finch CB, Harris LA, Clark GW (1964) The thorite-huttonite phase transformation as determined by growth of synthetic thorite and huttonite single crystals. Am Mineral 49:782-785
Finch RJ, Hanchar JM, Hoskin PWO, Burns PC (2001a) Rare earth elements in synthetic zircon. Part 2. A single-crystal X-ray study of xenotime substitution. Am Mineral 86:681-689
Finch RJ, Kropf AJ, Hanchar JM (2001b) XAFS spectra of rare earth elements in synthetic zircon. Eleventh Annual V.M. Goldschmidt Conference, Abstr # 3791, LPI Contrib No. 1088, Lunar Planet Inst, Houston (CD-ROM)
Fiske PS, Nellis WJ, Sinha AK (1994) Shock-induced phase transition of $ZrSiO_4$, reversion kinetics, and implications for terrestrial impact craters. EOS, Trans Am Geophys Soc 75:416-417
Fuchs LH, Gebert E (1958) X-ray studies of synthetic coffinite, thorite and uranothorites. Am Mineral 43:243-248

Fukunaga O, Yamaoka S (1979) Phase transformations in $ABO_4$ type compounds under high pressure. Phys Chem Minerals 5:167-177

Gaines RV, Skinner HCW, Foord EE, Mason B, Rosenzweig A, King VT, Dowty E (1997) Dana's New Mineralogy. Eighth Edition. Wiley and Sons, New York, 1819 p

Gibson GM, Ireland TR (1995) Granulite formation during continental extension in Fiordland, New Zealand. Nature 375:479-482

Glass BP, Liu L, Leavens PB (2002a) Discovery of high-pressure $ZrSiO_4$ polymorph in naturally occurring shock-metamorphosed zircons. Geology 29:371-373

Glass BP, Liu L, Leavens PB (2002b) Reidite: An impact-produced high-pressure polymorph of zircon found in marine sediments. Am Mineral 87:562-565

Goldin BA, Yushkin NP, Fishman MV (1967) A new yttrium mineral, chernovite. Zap Vses Mineral Obshch 96:699-704

Graeser GP, Schwander H, Stalder HA (1973) A solid solution series between xenotime($YPO_4$) and chernovite ($YAsO_4$). Mineral Mag 39:145-151

Graeser S, Schwander H (1987) Gasparite-(Ce) and monazite-(Nd): two new minerals to the monazite group. Schweiz Mineral Petrogr Mitt 67:103-113

Hanchar JM (1996) A geochemical investigation of zircon. PhD dissertation, Rensselaer Polytechnic Institute, Troy, New York, 210 p

Hanchar JM, Miller CF, Wooden JL, Bennett VC, Staude J-MG (1994) Evidence from xenoliths for a dynamic lower crust, eastern Mojave desert, California. J Petrol 35:1377-1415

Hanchar JM, Finch RJ, Hoskin PWO, Watson EB, Cherniak DJ, Mariano AN (2001a) Rare earth elements in synthetic zircon: Part 1. Synthesis, and rare earth and phosphorous doping. Am Mineral 86:667-680

Hanchar JM, Finch RJ, Hoskin PWO, Watson EB (2001b) Strain-limited rare-earth element incorporation in zircon. Eleventh Annual V.M. Goldschmidt Conference, Abstract # 3712, LPI Contrib No. 1088, Lunar Planet Inst, Houston (CD-ROM)

Hanchar JM, Finch RJ, Watson EB, Hoskin PWO (2001c) Towards a better understanding of rare earth element partition coefficients in zircon. Proc European Union of Geosciences, XI, Strasbourg, France, April 8-12, 2001, p 677

Hansley PL, Fitzpatrick JJ (1989) Compositional and crystallographic data on REE-bearing coffinite from the Grants uranium region, northwestern New Mexico. Am Mineral 74:263-270

Hawthorne FC, Ferguson RB (1975) Anhydrous sulfates. II. Refinement of the crystal structure of anhydrite. Can Mineral 13:289-292

Hazen RM, Finger LW (1979) Crystal structure and compressibility of zircon at high pressure. Am Mineral 64:196-201

Hazen RM, Mariathasan JWE (1982) Bismuth vanadate: A high-pressure, high-temperature crystallographic study of the ferroelastic-paraelastic transition. Science 216:991-993

Herzenberg R (1946) Nuevos minerales de Bolivia. Bol. Técnio No 1, Fac Nac Ingeneria, Univ Técnica Oruro (1946)

Hinton RW, Upton BGJ (1991) The chemistry of zircon: Variations within and between large crystals from syenite and alkali basalt xenoliths. Geochim Cosmochim Acta 55:3287-3302

Hinton RW, MacDonald R, McGarvie DW, Tindle A, Harley SL (2003) The possible role of hydrogen in the substitution of rare earth elements into zircon. Spring AGU-EUG-EGS Joint Assembly, Nice, France, April 6-11, 2003, Geophysical Research Abstracts 5 05968

Hirano M, Morikawa H, Inagaki M, Toyoda M (2002a) Direct synthesis of new zircon-type $ZrGeO_4$ and $Zr(Ge,Si)O_4$ solid solutions. J Am Ceram Soc 85:1915-1920

Hirano Y, Guedes I, Grimsdith M, Loong C-K, Wakabayashi N, Boatner LA (2002b) Brillouin-scattering study of the elastic constants of $ErVO_4$. J Am Ceram Soc 85:1001-1003

Hoekstra HR, Fuchs LH (1956) Synthesis of coffinite-$USiO_4$. Science 123:105

Hoskin PWO (2000) Patterns of chaos: fractal statistics and the oscillatory chemistry of zircon. Geochim Cosmochim Acta 64:1905-1923

Hoskin PWO, Rodgers KA (1996) Raman spectral shift in the isomorphous series $(Zr_{1-x}Hf_x)SiO_4$. Eur J Sol State Inorg Chem 33:1111-1121

Hoskin PWO, Kinny PD, Wyborn D, Chappel BW (2000) Identifying accessory mineral saturation during differentiation in granitoid magmas: an integrated approach. J Petrol 41:1365-1396

Janeczek J (1991) Composition and origin of coffinite from Jachymov, Czechoslovakia. Neues Jahrb Mineral Monatsh 9:385-395

Janeczek J, Ewing RC (1992) Dissolution and alteration of uraninite under reducing conditions. J Nucl Mater 190:157-173

Janeczek J, Ewing RC (1996) Phosphatian coffinite with rare earth elements and Ce-rich françoisite-(Nd) from sandstone beneath a natural fission reactor at Bangombé, Gabon. Mineral Mag 60:665-669

Jayaraman A, Kourouklis GA, Espinoza GP, Cooper SA, Van Uitert LG (1987) A high-pressure Raman study of

yttrium vanadate ($YVO_4$) and the pressure-induced transition from the zircon-type to the scheelite-type structure. J Phys Chem Solids 48:755-759

Kazei ZA, Kolmakova NP (1995) Magnetoelastic anomalies in the thermal expansion of rare-earth vanadates $RVO_4$. Sov Phys Solid State 37:577-582

Knittle E (1995) Static compression measurements of equations of state. *In* Mineral Physics and Crystallography. A Handbook of Physical Constants. AGU Reference Shelf, Ahrens TJ (ed) American Geophysical Union, Washington, DC, 2:8-142

Knittle E, Williams Q (1993) High-pressure Raman spectroscopy of $ZrSiO_4$: Observation of the zircon to scheelite transition at 300 K. Am Mineral 78:245-252

Kusaba K, Syono Y, Kikuchi M, Fukuoka K (1985) Shock behavior of zircon: phase transition to scheelite structure and decomposition. Earth Planet Sci Lett 72:433-439

Kusaba K, Takehiko Y, Masae K, Yasuhiko S (1986) Structural considerations on the mechanism of the shock-induced zircon-scheelite transition in $ZrSiO_4$. J Phys Chem Solids 47:675-679

Leroux H, Reimold WU, Koeberl C, Hornemann U, Doukhan, J-C (1999) Experimental shock deformation in zircon: a transmission electron microscopic study. Earth Planet Sci Lett 169:291-301

Liu L (1979) High-pressure phase transformations in baddeleyite and zircon, with geophysical implications. Earth Planet Sci Lett 44:390-396

Lohmüller G, Schmidt G, Deppisch B, Gramlich V, Scheringer C (1973) Die Kristallstrukturen von Yttrium-Vanadat, Lutetium-Phosphat und Lutetium-Arsenat. Acta Crystallogr B29:141-142

Lunga S (1966) Etude des courbes de liquidus et des proprieties thermodynamiques des systems $SiO_2$-$ThO_2$ et $SiO_2$-$ThO_2$-$UO_2$. J Nucl Mater 19:157-159

Maas R, Kinny PD, Williams IS, Froude DO, Compston W (1992) The Earth's oldest known crust: a geochronological and geochemical study of 3900-4200 Ma old detrital zircons from Mt. Narryer and Jack Hills, Western Australia. Geochim Cosmochim Acta 56:1281-1300

Mariathasan JWE, Hazen RM, Finger LW (1986) Crystal structure of the high-pressure form of $BiVO_4$. Phase Trans 6:165-174

Mazhenov NA, Nurgaliev BZ, Muldakhmetov KZ (1988) Scheelite modification of neodymium arsenate. Izv Akad Nauk SSSR, Neorg Mater 24:1163-1165 (English translation in Inorg Mater 24:991-993)

Melcher RL (1976) The anomalous elastic properties of materials undergoing cooperative Jahn-Teller phase transitions. *In* Physical Acouostics. Mason WP, Thurston RN (eds) Academic Press, New York, p 1-77

Mereiter K, Preisinger A (1986) Kristalstrukturdaten der Wismutminerale Atelestit, Mixit und Pucherit. Anz Oesterr Akad Wiss math-naturwiss Klass 123:79-81

Miles NM, Hogarth DD, Russel DS (1971) Wakefieldite, yttrium vanadate, a new mineral from Quebec. Am Mineral 56:395-410

Mooney RC (1948) Crystal structure of tetragonal bismuth arsenate, $BiAsO_4$. Acta Crystallogr 1:163-165

Mrose ME, Rose JH, Jr (1961) Behierite, $(Ta,Nb)BO_4$, a new mineral from Manajaka, Madagascar. Geol Soc Am Abstracts 1961 Ann Meetings, p 111A; abstracted by Fleischer M (1962) New mineral names. Am Mineral 47:414

Mumpton FA, Roy R (1961) Hydrothermal stability studies of the zircon-thorite group. Geochim Cosmochim Acta 21:217-238

Mursic Z, Vogt T, Frey F (1992) High-temperature neutron powder diffraction study of $ZrSiO_4$ up to 1,900 K. Acta Crystallogr B 48:584-590

Ni Y, Hughes JM, Mariano AN (1995) Crystal chemistry of the monazite and xenotime structures. Am Mineral 80:21-26

Nipko JC, Loong C-K, Kern S, Abraham MM, Boatner LA (1997) Crystal field splitting and anomalous thermal expansion in $YbVO_4$. J Alloys Comp 250:569-572

Nyman H, Hyde BG, Andersson S (1984). Zircon, anhydrite, scheelite and some related structures containing bisdisphenoids. Acta Crystallogr B 40:441-447

Oka Y, Yao T, Yamamoto N (2000) Hydrothermal synthesis and crystal structures of zircon-type $LaVO_4$ and a new compound $LaV_3O_9$. J Solid State Chem 152:486-491

Plant JA, Simpson PR, Smith B, Windley BF (1999) Uranium ore deposits: Products of the radioactive Earth. Rev Mineral 38:255-319

Qurashi MM, Barnes WH (1952) A preliminary structure for pucherite, $BiVO_4$. Am Mineral 37:423-426

Qurashi MM, Barnes WH (1953) The structure of pucherite, $BiVO_4$. Am Mineral 38:489-500

Ramakrishnan SS, Gokhale KVGK, Subarrao EC (1969) Solid solubility in the system zircon-hafnon. Mater Res Bull 4:323-328

Range K-J, Meister H (1990). $ErVO_4$-II, a scheelite-type high-pressure modification of erbium orthovanadate. Acta Crystallogr C 46:1093-1094

Reid AF, Ringwood AE (1969) Newly observed high pressure transformations in $Mn_3O_4$, $CaAl_2O_4$, and $ZrSiO_4$. Earth Planet Sci Lett 6:205-208

Rice CE, Robinson WR (1976) Lanthanum orthovandate. Acta Crystallogr B 32:2232-2233
Ríos S, Malcherek T, Salje EKH, Domeneghetti C (2000) Localized defects in radiation-damaged zircon. Acta Crystallogr B 56:947-952
Robinson K, Gibbs GV, Ribbe PH (1971) The structure of zircon: a comparison with garnet. Am Mineral 56:782-790
Rudnick RL, Fountain DM (1995) Nature and composition of the continental crust: a lower crustal perspective. Rev Geophys 33:267-309
Sandercock JR, Palmer SB, Elliot RJ, Hayes W, Smith SRP, Young AP (1972) Brillouin scattering, ultrasonic and theoretical studies of acoustic anomalies in crystals showing Jahn-Teller phase transitions. J Phys C: Solid State Phys 5:3126-3146
Schwarz VH (1963) Die phosphate, arsenate und vanadate der Seltenen erden. Z Anorg Allg Chemie 323:44-56
Scott HP, Williams Q, Knittle E (2002) Ultralow compressibility silicate without highly coordinated silicon. Phys Rev Lett 88:015506-1-015506-4
Sejkora, Rídkošil (1994) Tetrarooseveltite, ß-Bi($AsO_4$), a new mineral species from Moldava deposit, the Krušné hory Mts., Northwestern Bohemia, Czech Republic. Neues Jahrb Mineral Monatsh 1994:179-184
Shannon RD (1976) Revised effective ionic radii and systematic studies of interatomic distances in halides and chalcogenides. Acta Crystallogr A 32:751-767
Skanthakumar S, Loong C-K, Soderholm L, Nipko J, Richardson JW, Abraham MM, Boatner LA (1995) Anomalous temperature dependence of the lattice parameters in $HoPO_4$ and $HoVO_4$: Rare earth quadrapolar effects. J Alloys Comp 225:595-598
Solar GS, Pressley RA, Brown M, Tucker RD (1998) Granite ascent in convergent orogenic belts: Testing a model. Geology 26:711-714
Speer JA (1982a) Zircon. Rev Mineral 5:67-112
Speer JA (1982b) The actinide orthosilicates. Rev Mineral 5:113-135
Speer JA, Cooper BN (1982) Crystal structure of synthetic hafnon, $HfSiO_4$, comparison with zircon and the actinide orthosilicates. Am Mineral 67:804-808
Stubican V-S, Roy R (1963) High-pressure scheelite-structure polymorphs of rare-earth vanadates and arsenates. Z Kristallogr 119:90-97
Subbarao EC, Agrawal DK, McKinstry HA, Sallese CW, Roy R (1990) Thermal expansion of compounds of zircon structure. J Am Ceram Soc 73:1246-1252
Taylor M, Ewing RC (1978) The crystal structures of the $ThSiO_4$ polymorphs: huttonite and thorite. Acta Crystallogr B 34:1074-1079
Taylor SR, McLennan SM (1995) The geochemical evolution of the continental crust. Rev Geophys 33:241-265
Tomaschek F, Ballhaus C (2003) Zircon-xenotime solid-solubility: An experimental study. Spring AGU-EUG-EGS Joint Assembly, Nice, France, April 6-11, 2003, Geophys Res Abstr 5:13283
van Westrenen W, Wood BJ, Blundy JD (2001) A predictive thermodynamic model of garnet-melt trace element partitioning. Contrib Mineral Petrol 142:219-234
van Westrenen W, Frank MR, Hanchar JM, Fei Y, Finch RJ, Zha C-S (2003a) *In situ* determination of the compressibility of synthetic pure zircon ($ZrSiO_4$) and the onset of the zircon-reidite phase transition. Am Mineral 88 (accepted)
van Westrenen W, Frank MR, Fei Y, Hanchar JM, Finch RJ, Zha C-S (2003b) *In situ* measurements of the compressibility of pure and trace element doped synthetic zircon. Spring AGU-EUG-EGS Joint Assembly, Nice, France, April 6-11, 2003 (abstr)
Vegard L (1916) Results of crystal analysis. Philos Mag Ser 6, 32:65-96
Vegard L (1926) Results of crystal analysis. Philos Mag Ser 7, 1:1151-1193
Vervoort JD, Patchett PJ, Gehrels GE, Nutman AP (1996) Constraints on early Earth differentiation from hafnium and neodymium isotopes. Nature 379:624-627
Weaver BL, Tarney J (1984) Major and trace element composition of the continental lithosphere. *In* Structure and Evolution of the Continental Lithosphere. Physics and Chemistry of the Earth, Pollack HN, Murthy VR (eds) Pergamon Press, Oxford, 15:39-68
Weber G, Range K-J (1996) Die Kristallstruktur von Calziumchromate(VI), $CaCrO_4$. Z Naturforsch 51B:751-753
Wedepohl KH (1995) The composition of the continental crust. Geochim Cosmochim Acta. 59:1217-1232
Wilde SA, Valley JW, Peck WH, Graham CM (2001) Evidence from detrital zircons for the existence of continental crust and oceans on the Earth 4.4 Gyr ago. Nature 409:175-178
Williford RE, Weber WJ, Devanathan R, Cormak AN (1999) Native vacancy migrations in zircon. J Nucl Mater 273:164-170
Williford RE, Begg BD, Weber WJ, Hess NJ (2000) Computer simulation of $Pu^{3+}$ and $Pu^{4+}$ substitutions in zircon. J Nucl Mater 278:207-211

# The Composition of Zircon and Igneous and Metamorphic Petrogenesis

**Paul W. O. Hoskin**

*Institut für Mineralogie, Petrologie und Geochemie, Albert-Ludwigs-Universität Freiburg D-79104 Freiburg, Germany*

**Urs Schaltegger**

*Section des Sciences de la Terre, Départment de Minéralogie, Rue des Maraîchers 13 CH-1211 Genève 4, Switzerland*

## INTRODUCTION

Zircon is the main mineral in the majority of igneous and metamorphic rocks with Zr as an essential structural constituent. It is a host for significant fractions of the whole-rock abundance of U, Th, Hf, and the REE (Sawka 1988, Bea 1996, O'Hara et al. 2001). These elements are important geochemically as process indicators or parent isotopes for age determination. The importance of zircon in crustal evolution studies is underscored by its predominant use in U-Th-Pb geochronology and investigations of the temporal evolution of both the crust and lithospheric mantle. In the past decade an increasing interest in the composition of zircon, trace-elements in particular, has been motivated by the effort to better constrain *in situ* microprobe-acquired isotopic ages. Electron-beam compositional imaging and isotope-ratio measurement by *in situ* beam techniques—and the micrometer-scale spatial resolution that is possible—has revealed in many cases that single zircon crystals contain a record of multiple geologic events. Such events can either be zircon-consuming, alteration, or zircon-forming and may be separated in time by millions or billions of years. In many cases, calculated zircon isotopic ages do not coincide with ages of geologic events determined from other minerals or from whole-rock analysis. To interpret the geologic validity and significance of multiple ages, and ages unsupported by independent analysis of other isotopic systems, has been the impetus for most past investigations of zircon composition. Some recent compositional investigations of zircon have not been directly related to geochronology, but to the ability of zircon to influence or record petrogenetic processes in igneous and metamorphic systems.

Sedimentary rocks may also contain a significant fraction of zircon. Although authigenic zircon has been reported (Saxena 1966, Baruah et al. 1995, Hower et al. 1999), it appears to be very rare and may in fact be related to externally-sourced hydrothermal fluids. Sedimentary zircon is predominantly derived from weathered igneous and metamorphic rocks. Detrital zircon in sedimentary rocks and sediments is highly durable and records age information of crustal units that contributed to the sediment load. In mature sediments where zircon may be one of a few, or the only, remaining heavy-mineral, information on source-rock compositions is largely lost, and may only be attainable through interpretation of zircon composition. The use of zircon trace-element composition as a provenance indicator of detrital zircon—or xenocrystic zircon—will be reviewed in this chapter.

This chapter reviews investigations on the composition of igneous and metamorphic zircon and its role in understanding the petrogenesis of such rocks. Hydrothermal zircon will also be discussed, although there is presently little known about this potentially significant petrogenesis. A growing data-base and understanding of zircon composition is directly related to advances in analytical technology and these are summarized next for where these technologies and techniques have been applied to zircon analysis.

1529-6466/03/0053-0002$05.00

**Analytical techniques**

Analytical techniques where a bulk sample of small crystals, separated from a large volume of rock, are still often used for zircon compositional analysis (Gromet and Silver 1983, Mahood and Hildreth 1983, Murali et al. 1983, Fujimaki 1986, Rupasinghe and Dissanayake 1987, Sawka 1988, Heaman et al. 1990, Wiedenbeck et al. 1995). Such bulk techniques include instrumental neutron activation analysis (INAA), isotope dilution thermal ionization spectrometry (ID-TIMS) and solution inductively coupled plasma mass spectrometry (ICP-MS). Minimum sample size ranges from a few crystals to hundreds-of-milligrams and analyses, therefore, represent an "average" which may include two or more internal structures or mineral and melt inclusions. Often, analyses of zircon by INAA or TIMS have greater abundances of the REE (light REE in particular), Th, U, and possibly Ca, Nb, Ta, and other elements, relative to *in situ* microprobe techniques (Fig. 1). For INAA analyses this may be due to the presence of fission-derived light REE, but for most cases it is likely related to the presence of inclusions which are commonly recorded for zircon (Gorz 1974, Chesner 1998, Thomas et al. 2002). In a study of the composition of a large cm-sized, gem-quality zircon, Jain et al. (2001) attributed increased LREE, Nb, Y, Th, and U abundances relative to *in situ* analyses of fractions of the same crystal to the presence of pyrochlore inclusions. Sano et al. (2002) report anomalously high LREE abundances in their INAA and TIMS analyses due to the presence of 1-5 μm-sized apatite inclusions—their *in situ* microprobe analyses of the same zircon crystals did not have anomalous LREE abundances. This chapter will concentrate on data obtained by *in situ*

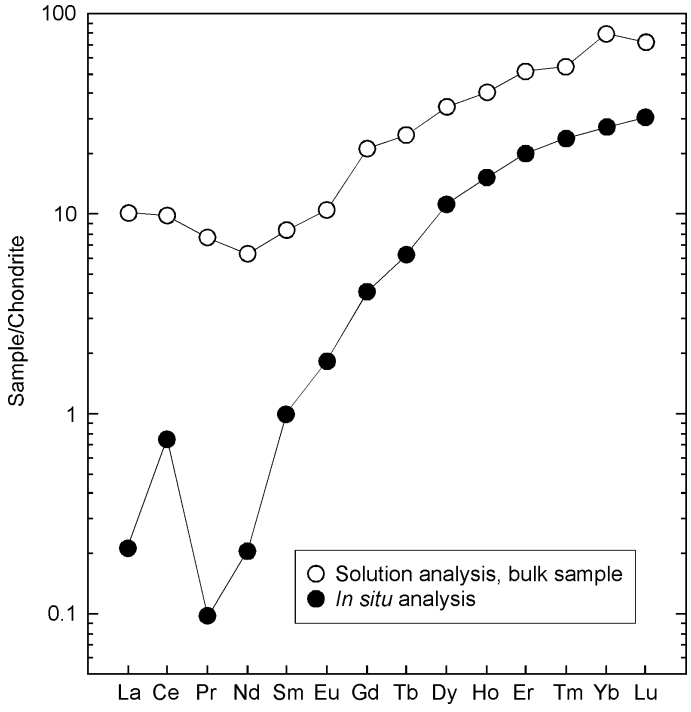


**Figure 1.** Chondrite-normalized plots of average zircon composition determined by *in situ* analysis (laser ablation ICP-MS) and bulk sample solution analysis (ICP-MS). Chips of the same zircon were analyzed. The difference between the two plots is due to unintentional analysis of clear, optically unobserved, mineral inclusions in the solution analysis. This style of pattern (elevated LREE, loss of positive Ce anomaly) is commonly observed for zircon analyses by bulk techniques and is not representative of the zircon composition. Data from Jain et al. (2001).

microprobe techniques where the reported data does not include accidental analysis of inclusions as part of the zircon analysis.

The analysis of zircon in thin-section or grain-mount by a microprobe allows for data acquisition from texturally distinct areas within single crystals. Textural imaging using cathodoluminesence (CL) or back-scattered electrons (BSE) is usually done prior to analysis. The electron microprobe (EMP) remains the most common instrument for compositional analysis, but ion-beam and laser-beam microprobe techniques are preferred above the EMP for trace-element analysis because of better detection limits and analytical precision. Techniques for and accurate and precise trace-element analyses of zircon by secondary ion mass spectrometry (SIMS) were first published in the late 1980s and early 1990s (Zinner and Crozaz 1986, Hinton and Meyer 1991, Hinton and Upton 1991, Ireland and Wlotzka 1992, Maas et al. 1992). This technique requires high mass-resolution or reasonably strong energy-filtering yet retention of high ion transmission. Analysis by SIMS, then, requires a large ion-probe and for nearly two decades these were only accessible in a few laboratories worldwide. Although the number of large ion-probe facilities has increased, the introduction of stable plasma-based analysis has meant that rapid, high-quality isotope and trace-element data can be acquired by a spatially resolved laser-beam microprobe. Early analyses of zircon by inductively coupled plasma mass spectrometry (ICP-MS) with sample introduction by a laser-ablation (LA) microprobe were published in the early and mid-1990s (Perkins et al. 1992, Jackson et al. 1992, Feng et al. 1993, Hirata and Nesbitt 1995, Jeffries et al. 1996). Most of the earliest studies of zircon using LA–ICP-MS focused on geochronology, attempting to develop the technology as an alternative to SIMS analysis. Hoskin (1998) was first to compare SIMS and LA–ICP-MS for zircon trace-element analysis, concluding that the techniques were competitive in terms of accuracy and precision (~5-15%), lower-limits of detection (sub-ppm for most elements), and maximum sample-surface spatial resolution (10-50 μm). Laser-ablation sampling, which excavates a pit tens-of-micrometers into the sample, may encounter inclusions which compromise data quality. SIMS data are much less prone to accidental inclusion analysis. Focused soft (Shnyukov et al. 2002) and hard (Blagojevic et al. 2000, Yusoff 2002) X-ray beams are also utilized for zircon compositional analysis and element-distribution mapping. The advantage of synchrotron radiation in particular, is the high spatial resolution (10 μm) and detection-limits (ppm to sub-ppm) that can be used non-destructively on zircon crystal interiors or surfaces.

## ZIRCON AND IGNEOUS PETROGENESIS

### Saturation, crystallization, occurrences and zoning of igneous zircon

***Saturation and dissolution.*** Many workers refer to the ubiquity of zircon in crustal rocks and indeed its occurrence is widespread. However, zircon is not ubiquitous as it does not occur in every crustal rock; it is most common in igneous rocks of intermediate to Si-saturated composition and least common in less saturated rocks. The relation between zircon saturation, crystallization and melt composition was investigated by Watson (1979) and revisited by Watson and Harrison (1983). The experimental saturation relation is most commonly used for the calculation of zircon saturation temperatures for natural rocks, which are used to assess whether or not zircon was an early or late crystallizing phase. An assessment of the use of saturation temperatures is given by Hanchar and Watson (this volume). Dickinson and Hess (1982) determined from experiment that early zircon saturation (at 1100°C) in lunar granites would require the granites to have a whole-rock Zr abundance of 5000 ppm and late-stage lunar basalts to have 9000 ppm Zr. Given that these lunar rocks have Zr abundances of about 200-1800 ppm, zircon would have saturated at ~1100°C after >99.9% whole-rock crystallization. This precludes zircon crystallization as a significant influence on the trace-element evolution of lunar magmas.

In zircon-undersaturated melts, zircon xenocrysts will dissolve. The kinetics of dissolution have been determined experimentally in "granitic" melts of variable water content (Harrison and

Watson 1983) and in halogen-bearing hydrous "granitic" melts (Keppler 1993, Baker et al. 2002). Watson (1996a) modeled the dissolution of zircon in anatectic melts as a function of melt composition, water content and temperature, and concluded that only the largest crystals (>50-100 μm) would survive crustal fusion and incorporation into a >2 wt % $H_2O$, 750-850°C, zircon-undersaturated melt. A 50-μm diameter zircon would dissolve geologically instantaneously in an undersaturated, water-bearing granite (Harrison and Watson 1983). The presence of halogens up to ~1.5 wt % in the melt appears to have little affect on zircon dissolution kinetics or on Zr diffusion in the melt once zircon is dissolved (Baker et al. 2002). This may relate to the observation that in synthetic glasses Zr–F complexation does not occur (Farges 1996).

For some rock-types, such as intermediate S-type granites, it is common to observe multiple dissolution textures preserved within zircon crystals indicating periods of zircon-undersaturation followed by zircon-saturation in the melt (e.g., Vavra 1994, de la Rosa et al. 2002, Zeck and Williams 2002). Such crystals preserve compositional information for the melt prior to and after dissolution and may, therefore, record a change in composition relatable to an event such as magma-mixing.

***Grain-size and external morphology.*** Typical igneous zircon is between 20 and 250 μm in the longest dimension with subhedral to euhedral face development. Larger mm-sized rare crystals are reported in kimberlites and kimberlite-related rocks (MARID-suite xenoliths); these are usually anhedral but can be subhedral (Kresten et al. 1975, Belousova et al. 1998, Hoskin 1998, Konzett et al. 1998). Large cm-sized colorless "gem-quality" crystals are found in the Mud Tank carbonatite (Hanchar and Hoskin 1998) although brown-colored imperfect crystals up to 30 cm-long from this carbonatite are displayed at the Australian Museum in Sydney. Large, sometimes mm-sized, red-colored zircons are reported from syenitic xenoliths in basalt, often associated with sapphire (Sutherland et al. 1998, 2002; Guo et al. 1996, Upton et al. 1999). In a general sense, form development and grain-size are dependent upon when zircon saturated in the crystallization history of a rock. Small, often acicular crystals, may have formed due to local saturation at the edge of an early-crystallizing phase (Bacon 1989), whereas early zircon-saturated melts tend to produce euhedral, larger crystals with width-to-length ratios of about 1:2-1:4. Late-crystallizing zircon in plutonic rocks tend to be anhedral because they have grown in the interstices between earlier-formed crystals (Scoates and Chamberlain 1995). Rapidly crystallized zircon in volcanic rocks is characterized by large width-to-length ratios (up to about 1:12) producing prismatic to acicular habits. Volcanic zircon, and sometimes plutonic zircon, can contain melt-trails that may be as long as the crystal itself (Chiarenzelli and McLelland 1993, Bussy and Cadoppi 1996).

Zircon has a highly variable external morphology. Often crystals are faceted with combinations of prism ({100} and {110}) and pyramid forms ({211}, {101} and {301}). Since the 1950s there have been attempts to systematically relate zircon morphology to petrogenesis (Poldervaart 1955, 1956; Larsen and Poldervaart 1957, Pupin and Turco 1972a,b,c; Kostov 1973, Hoffmann 1981). A typologic scheme relating the relative development of crystal forms with temperature and host-rock type was published by Pupin (1980) (the principal figure of that paper was reproduced as Fig. 9 in Speer 1982). Although this scheme was initially widely accepted and is still used (e.g., Dabard et al. 1996), three subsequent and ongoing observations have seen it rarely used: (1) zircon from a single rock and single age population can have widely varying morphologies; (2) zircon from widely different rock-types can have similar to identical morphologies with no systematic measurable differences despite claims to the contrary (see Fig. 9a of Wang et al. 2002); and (3) the external morphology of a single crystal can change a number of times during a single growth event (Fig. 2a) as a result of kinetic factors, such as diffusion rates and adsorption, which effect the growth-rates of crystal faces and therefore control the morphology of a growing crystal (Dowty 1980, Vavra 1990, 1993).

***Internal textures.*** A large number of internal textures are now described for igneous zircon as a result of the application of CL and BSE imaging (e.g., Ono 1976, Paterson et al. 1989, 1992; Vavra 1990, Koschek 1993, Hanchar and Miller 1993, Corfu et al., this volume). These techniques are

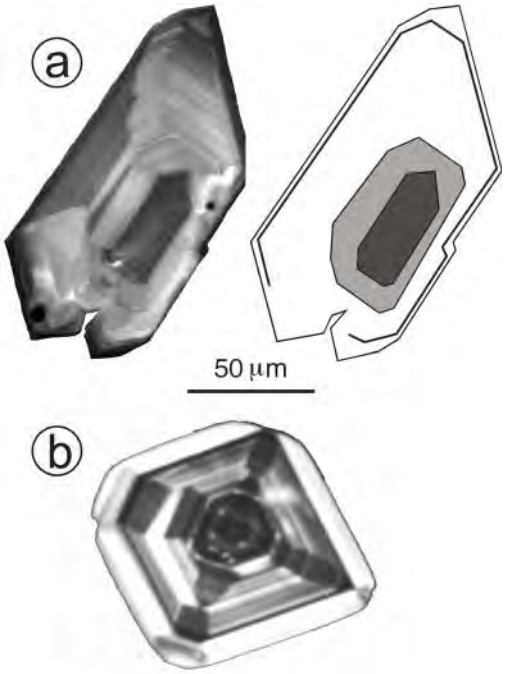


**Figure 2.** (a) *top row:* cathodoluminescence image (left) of zircon from an adamellite revealing changes in the external morphology (represented schematically, right) of the crystal during growth. After Hoskin (2000). (b) *bottom row:* cathodoluminescence image of zircon from an intermediate alkali volcanic rock, northeast Turkey. Both crystals exhibit well developed oscillatory and sector zoning as a result of heterogeneous trace-element distribution.

applicable because of the heterogeneous distribution of elements in most zircon, particularly trace elements. Oscillatory zoning, sometimes called growth zoning, occurs in many minerals (Shore and Fowler 1996) and is the predominant texture of igneous zircon. Early workers considered oscillatory zoning to be evidence that zircon crystallized over a long time period in a cooling magma (e.g., Silver and Deutsch 1963, Köhler 1970), yet saturation calculations and the inability to match zoning profiles (stratigraphy) from crystal to crystal reveals that this is likely to not be true for many zircon populations. Vavra, in the first of three classic studies (1990, 1993, 1994), used CL images of oscillatory zoning patterns (OZPs) of oriented crystal sections and related the OZPs to the relative growth velocities of crystal faces by delineating the boundary between different growth sectors (the delineated sector boundaries were called "Gratbahnen" or *ridge paths* in English). It was concluded that widely spaced OZPs, interrupted by surfaces of dissolution, represent a low degree of zircon-saturation in the melt and narrowly-spaced uninterrupted OZPs represent higher degrees of zircon-saturation (supersaturation). A method to quantify the growth-rate information of OZPs was developed in the second study (Vavra 1993), where the growth-rates of individual crystal faces were normalized to a reference face and plotted as a function of distance from a central point (representing zero time). Application of this quantification method to granitoid zircon indicated that the influence on the growth-rate of different forms can be attributed to either the degree of zircon-saturation or the incorporation of trace-elements (Vavra 1994).

Zircon OZPs have also been quantified by fractal statistics. Quantification in this way uses gray-scale data from CL images although derivation of statistical parameters varies (spectral analysis and Fourier transform, the width method, wavelet analysis). Halden and Hawthorne (1993) calculated the fractal dimension and Hurst exponent ($H$) of the OZP of a carbonatite zircon, finding $H$

to be in the range 0.34-0.42. Mathematically, this characterizes the OZP as "antipersistent," meaning that during crystal growth the growth-surface has a tendency to accept CL-emitting elements (the rare-earth elements, REE; Remond et al. 1992, Hanchar and Rudnick 1995) and then reject them: Halden et al. (1993) showed for the same crystal, that the oscillatory zoning correlated with significant variations in trace-element abundances. Hoskin (2000) and Fowler et al. (2002) also determined antipersistent *H* values; zircon from an I-type pluton in southeast Australia have *H* values averaging 0.44 (Hoskin 2000) and the large (~1.5 cm-long) zircon studied by Fowler et al. (2002) has *H* values ranging 0-0.11. The data of Fowler et al. (2002) fall outside of the *H* value range reported for other mineral species (0.25-0.45; Holten et al. 1997) possibly because the zircon megacryst formed from a brine and not a silicate melt (Fowler et al. 2002, p. 314).

The origin of oscillatory zoning in zircon probably involves a kinetic feedback mechanism operating at the crystal/melt interface. Evidence for processes operating at distance from that interface, even system-wide processes, is provided by large-scale harmonic zones that are broadly correlatable from crystal to crystal (Fowler et al. 2002) and the correlation between the Lyapounov exponent ($\lambda$), a fractal statistic, and NBO/T (Hoskin 2000). This correlation was interpreted by Hoskin (2000) to be due to ordering in the melt by polymerization. A data-constrained model was presented, where the oscillatory distribution of trace elements in zircon is controlled by dynamics at the zircon/melt interface involving cation substitution, diffusion, and melt polymerization and structure generation.

Sector zoning is also a dominant feature of igneous zircon. The texture is typical for volcanic zircon (Fig. 2b), but is also a common feature of plutonic zircon (Vavra 1990, Hanchar and Miller 1993, Benisek and Finger 1993) (Fig. 2a) despite slow growth-rates on the order of $10^{-19}$ to $10^{-15}$ cm/s and the expected attainment of equilibrium partitioning. Watson and Liang (1995) formulate a quantitative model for development of sector zoning in slowly grown crystals such as plutonic zircon (and metamorphic zircon). The model describes the disequilibrium uptake of trace elements as a function of crystal growth-rate and was applied in another study (Watson 1996b) specifically to zircon and surface enrichment of trace-elements during growth. Watson and Liang (1995) show that when surface enrichment occurs, trace-elements are entrapped by a relatively fast growing surface and that re-equilibration with the melt will not be achieved because the growth-rate is much faster than the sluggish intracrystalline elemental diffusivities (3+ cations, Cherniak et al. 1997a; 4+ cations, Cherniak et al. 1997b). These workers suggest that all zircon may be sector zoned and that we fail to detect all occurrences.

**Major-element composition of igneous zircon**

Zircon is zirconium orthosilicate, $ZrSiO_4$, and has a stoichiometric composition of 67.2 wt % $ZrO_2$ and 32.8 wt % $SiO_2$. The structure of zircon, as discussed by Finch and Hanchar (this volume), contains two cation sites; the 4-coordinated Si-site and the distorted 8-coordinated Zr-site. Both Si and Zr are tetravalent and have ionic radii of 0.84 Å and 0.26 Å, respectively. Although other minerals have a zircon-structure (e.g., xenotime, thorite and coffinite) none of these exhibit extensive solid solution with zircon, and only hafnon ($HfSiO_4$) and zircon have complete solid-solution (Ramakrishnan et al. 1969, Hoskin and Rodgers 1996). The extent of this solid solution in natural zircon is typically restricted although variation of the Zr/Hf ratio in zircon away from the chondritic value of ~37 is common. A compilation of published Hf values in zircon up to 1969 by Ahrens and Erlank (1969) showed a range in $HfO_2$ values from ~0.7-8.3 wt % with a mean of 2.0 wt %. Large variation above and below this 1969 mean value has now been reported as shown by the following examples (all values given here are wt % $HfO_2$): meteoritic zircon, 1.08-1.45% (Ireland and Wlotzka 1992); lunar zircon, 1.18% average (Wopenka et al. 1996); carbonatite zircon, Finland, 0.98% (Halden et al. 1993); diorite, China, ~1-3% (Wang et al. 2002) and from Chile, up to 1.65% (Ballard et al. 2002); granodiorite zircon, Chile, as low as 0.15% (Ballard et al. 2002); granite zircon, California, 1.78-3.17% (Wark and Miller 1993) and from the Czech Republic, up to 12.3% (Uher et al. 1998);

rhyolite zircon, Bishop Tuff, 1.04-1.29%; aplitic zircon, California, 5.17% (Wark and Miller 1993); granitic pegmatite zircon, Slovakia, 1-22% (Uher and Cerny 1998) and from Brazil, 0.89-0.95% (Halden et al. 1993); syenite zircon, Canada, 0.74-1.05%. The differentiation of Zr and Hf can be so pronounced as to produce zirconian-hafnon and hafnon (Correria Neves et al. 1974) and Zr/Hf ratios ranging 0.03-0.08.

Hoskin et al. (2000) analyzed zircon from all compositional zones within a zoned I-type pluton. The $HfO_2$ abundance in these zircon range 0.39-3.98 wt % (only 5 of 45 analyses are >3 wt %) and the mean of 2.4 wt % is close to the 2.0 wt % mean of Ahrens and Erlank (1969). These data and those of Hoskin and Ireland (2000) were suggested by Belousova et al. (2002) to be inaccurate on the basis of a comparison with only four other published studies and a selected set of data from Hoskin et al. (2000) and Hoskin and Ireland (2000). It was claimed by Belousova et al. (2002) that these $HfO_2$ values are "…generally much higher than those reported by other studies." (p. 618). This claim is not valid and is unsupported by a survey of the literature and even their own data. For example, Belousova et al. (2002) and Guo et al. (1996) report $HfO_2$ values for nepheline-syenite zircon up to 3.3 wt %, granitoid zircon up to 3.6 wt % and zircon inclusions in corundum up to 3.8 wt %.

Given that the most Hf-enriched zircon occur in evolved rock-types, it appears that the Hf abundance of zircon increases with magmatic differentiation. In a broad sense, this is observed for intrusive rocks from the McMurry Meadow pluton, California (Sawka 1988), the Sweetwater Wash pluton, California (Wark and Miller 1993) (Fig. 3), and the Boggy Plain Zoned Pluton, Australia (Hoskin et al. 2000). The fractionation of Zr and Hf in zircon-crystallizing melts was shown experimentally by Linnen and Keppler (2002) to be related to the Zr/Hf activity coefficient ratio in the melt, such that fractional crystallization of metaluminous and peraluminous granitic melts will decrease the Zr/Hf ratio of the residual melt and increase the abundance of $HfO_2$ in zircon.

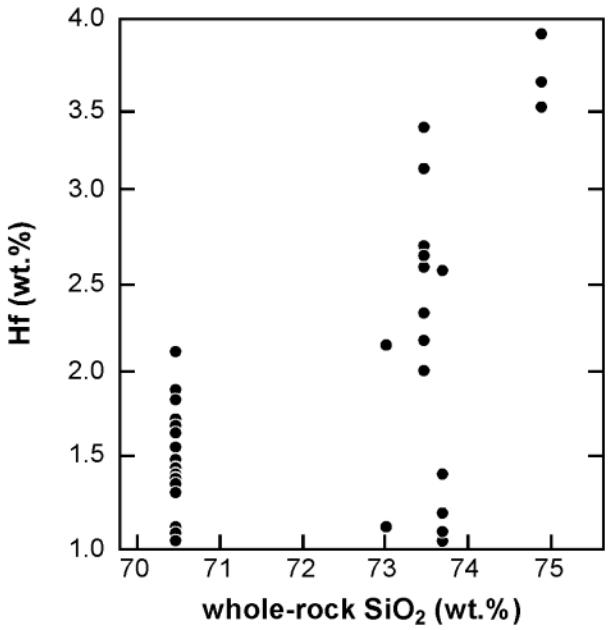


**Figure 3.** Hafnium (wt %) variation in zircon populations from the Sweetwater Wash pluton, southeastern California, U.S.A. Each data point is an analysis of a single crystal, or the mean of multiple analyses on a single crystal. Columns of data points represent the spread of Hf abundance in a single zircon population. Data from Wark and Miller (1993).

**Trace-element composition of igneous zircon**

A large number (~20-25) of trace elements are reported for zircon from *in situ* microprobe analyses (electron, laser, ion and proton beam techniques). In addition to Hf and Y (which for some zircon can be considered a minor-element, $0.1 < Y$ (wt %) $< 1.0$) the elements in greatest abundance are the rare-earth elements (REE), P, U and Th. Elements are substituted into zircon either by simple or coupled substitution mechanisms (general form: element = substituted element, where " = " means *substitutes for*):

Simple substitution mechanisms:

| | | |
|---|---|---|
| $Hf^{4+} = Zr^{4+}$ | | (i) |
| $(U^{4+}, Th^{4+}, Ti^{4+}, Sn^{4+}) = Zr^{4+}$ | | (ii) |
| $(OH)_4 = SiO_4$ | Frondel (1953) | (iii) |

Coupled substitution mechanisms:

(A) *At one site structural site:*

| | | |
|---|---|---|
| $(Y,REE)^{3+} + (Nb,Ta)^{5+} = 2\ Zr^{4+}$ | Es'kova (1959) | (iv) |

(B) *At two structural sites:*

| | | |
|---|---|---|
| $(Y,REE)^{3+} + P^{5+} = Zr^{4+} + Si^{4+}$ | Speer (1982) | (v) |
| $Sc^{3+} + P^{5+} = Zr^{4+} + Si^{4+}$ | Halden et al. (1993) | (vi) |
| $M^{n+} + n(OH)^{-} + (4–n)H_2O = Zr^{4+} + (SiO_4)^{4-}$ | Caruba and Iacconi (1983) | (vii) |

where $M$ is a metal cation and $n$ is an integer.

(C) *At an interstitial site:*

| | | |
|---|---|---|
| $(Mg,Fe)^{2+}_{(int)} + 3\ (Y,REE)^{3+} + P^{5+} = 3\ Zr^{4+} + Si^{4+}$ | Hoskin et al. (2000) | (viii) |
| $(Al,Fe)^{3+}_{(int)} + 4\ (Y,REE)^{3+} + P^{5+} = 4\ Zr^{4+} + Si^{4+}$ | Hoskin et al. (2000) | (ix) |

The dominant mechanism for trace-element substitution in zircon is the "xenotime" substitution mechanism (mechanism v, above). However, the common occurrence of REE (mol %) in excess of P (mol %) in natural zircon, and also synthetic zircon, indicates that other mechanisms also operate (Romans et al. 1975, Speer 1982, Hinton and Upton 1991, Hanchar et al. 2001). Hoskin et al. (2000) argued that interstitial $Mg^{2+}$, $Fe^{2+}$, $Fe^{3+}$, and $Al^{3+}$ in particular, could easily provide charge-balance for REE substitution greater than that allowed for by P substitution. They suggested two "xenotime-type" mechanisms (mechanisms viii and ix, above) and calculated that for their zircon an average abundance of only 380 ppm interstitial Al is required to provide charge-balance. A similar mechanism involving interstitial Li or Mo may have operated to charge-balance the REE-doped synthetic zircon of Hanchar et al. (2001). Other possible mechanisms for REE substitution include coupling with pentavalent Nb and Ta (mechanism iv, above) or by protonation of $O^{2-}$ ions of $(SiO_4)^{4-}$ groups. The incorporation of water and hydroxyl into zircon is possible by mechanism (vii) although hydroxyl groups are probably the only hydrous species incorporated into igneous zircon during crystallization (Nasdala et al. 2001). Electrostatic neutrality could be maintained by $O^{2-}$ vacancies, although static O-site vacancies are energetically unfavorable (Crocombette 1999, Williford et al. 1999) and are unlikely to persist in the zircon structure.

***REE and Y abundance of igneous zircon.*** In the following discussions the REE will be grouped as follows: light REE (LREE), La–Pr; middle REE (MREE), Nd–Gd; and heavy REE (HREE), Tb–Lu. All ionic radii are from Shannon (1976). The 0.84-Å radius of the $^{[8]}Zr^{4+}$ ion is most closely matched by the smaller-radii HREE (e.g., $^{[8]}Lu^{3+}$, 0.977 Å) than the larger LREE (e.g., $^{[8]}La^{3+}$, 1.160 Å) such that the trivalent LREE are generally incompatible in the zircon structure. The absolute abundances of the LREE in igneous zircon are sub-ppm to ppm-level. This generality does not hold

for the element Ce which can be both trivalent and tetravalent; $^{[8]}Ce^{4+}$ has an ionic radius of 0.97 Å, close to Lu, and like the HREE, Ce is abundant in zircon. Hoskin (1998) reported Ce abundances in zircon from MARID xenoliths from South Africa, range 3 to 160 ppm, which almost span the range of Ce abundances reported for all other zircon occurrences (e.g., Hinton and Upton 1991, Barbey et al. 1995, Guo et al. 1996, Hoskin et al. 2000, Poller et al. 2001, Ballard et al. 2002, de la Rosa et al. 2002, Sano et al. 2002). Most analyses of igneous zircon report Ce abundances less than about 50 ppm. Where the abundance is significantly greater there is usually some question as to the provenance of the zircon, e.g., an inherited core (Griffin et al. 2002) or a metamorphic xenocryst (Hidaka et al. 2002). Cerium abundances in lunar and meteoritic zircon are characteristically very low (<1-7 ppm; Hinton and Meyer 1991, Ireland and Wlotzka 1992, Snyder et al. 1993, Wopenka et al. 1996).

In rocks with mantle affinity, zircon has a characteristically low total REE abundance. Belousova et al. (1998) in a study of kimberlitic zircon from southern Africa, documents total REE abundances (ΣREE) of about 5-39 ppm and Y in the range 11-74 ppm (Table 1). Hoskin and Ireland (2000) analyzed zircon megacrysts from the Jwaneng kimberlite which have ΣREE up to 12 ppm and Y up to 23 ppm. MARID suite zircon is relatively more enriched with ΣREE averaging 640 ppm and Y 895 ppm. Carbonatite zircons also have generally low ΣREE and Y abundances (Table 1). Zircon from crustal rocks have highly variable ΣREE abundances that vary from as low as ~250 ppm to as high as 5000 ppm and typically contain an average between 1500 and 2000 ppm. The abundances for zircon from the Syros ophiolite and Blind Gabbro, Australia, are relatively high and may relate to late-stage zircon saturation and growth in interstitial melt-pools that were highly enriched in the REE. Yttrium abundances vary similarly in crustal zircon and range from tens-of-ppm up to ~5000 ppm. Zircon associated with corundum-bearing xenoliths can be very enriched and contain ΣREE + Y up to 1.3 wt % (Guo et al. 1996; Table 1). These represent some of the most enriched, albeit rather uncommon, igneous zircon analyzed by *in situ* techniques. Generally, zircon contain less than 1 wt % ΣREE + Y and analyses containing significantly higher abundances almost certainly represent altered zircon or accidental analysis of inclusions.

A characteristic feature of most zircon is large intra-grain and inter-grain population compositional variation. Inter-grain order-of-magnitude variation of U and Th has long been observed during isotopic analysis of zircon populations (e.g., Black et al. 1986, Chen and Williams 1990) and large variations are also typically observed for the REE and Y. For example, plagiogranite zircon

**Table 1.** Rare-earth element and Y abundances of igneous zircon.

| Lithology, rock name, source | ΣREE (ppm) | Y (ppm) | Reference |
|---|---|---|---|
| Vaca Muerta mesosiderite | 10-719 | - | Ireland & Wlotzka (1992) |
| Lunar, granite | 1724 | - | Hinton & Meyer (1991) |
| Lunar, granite breccia | 735-1105 | - | Snyder et al. (1993) |
| Lunar, monzodiorite breccia | 464-1404 | 776-2660 | Wopenka et al. (1996) |
| Kimberlite | 5-39 | 11-74 | Belousova et al. (1998) |
| | up to12 | up to 23 | Hoskin (1998) |
| MARID suite | 640 av. | 895 av. | Hoskin (1998) |
| Mud Tank carbonatite | 26 av. | 43 av. | Hoskin (1998) |
| Phalaborwa carbonatite | 260 | 1000 | Hoskin & Ireland (2000) |
| Silinjarvi carbonatite | ~11 | - | Halden et al. (1993) |
| Syros ophiolite | 2952 av. | 4437 av. | Hoskin & Ireland (2000) |
| Blind Gabbro | 2780 av. | 5184 av. | Hoskin & Ireland (2000) |
| Mawson igneous charnockite | 986 av. | 1497 av. | Hoskin & Ireland (2000) |
| Chilean diorites-granodiorites | ~1500 | up to ~4000 | Ballard et al. (2002) |
| SE Australian diorite-aplite | 250-3232 | 996-5514 | Hoskin et al. (2000) |
| Torihama dacite | 1180 | - | Sano et al. (2002) |
| Manaslu granite and leucosomes | up to ~4000 | up to ~4000 | Barbey et al. (1995) |
| Carpathian granitoids | 340-4205 | up to ~5000 | Poller et al. (2001) |
| Manila plagiogranite | 1216 av. | 1615 av. | Hoskin & Ireland (2000) |
| Anorthoclase-rich xenolith | up to 1813 | up to 2455 | Hinton & Upton (1991) |
| Corundum-bearing syenite | 3505 | 4194 | Hinton & Upton (1991) |
| Inclusions in corundum | 383-5011 | up to 8456 | Guo et al. (1996) |
| Inclusions in corundum, Laos | 3321-5785 | 3966-6275 | Sutherland et al. (2002) |

av. = mean value of multiple analyses.

from eastern Australia has Y abundances ranging from 399 to 3506 ppm (Hoskin and Ireland 2000) and Himalayan granitic leucosome zircon (sample MB301L) has Yb values ranging from 409 to 2215 ppm (Barbey et al. 1995). Poller et al. (2001) measured Y abundances in granitoid zircon (sample 1053 excluding cores) ranging from 500 to 4534 ppm and also reported near order-of-magnitude variation of REE and Y within an oscillatory zoned region of a single crystal (crystal 1032-8; analysis 1: ΣREE 328 ppm, Y 442 ppm; analysis 2: ΣREE 2830 ppm, Y 3420 ppm).

Inter-laboratory and inter-technique data-quality monitoring has been facilitated by the introduction of an internationally-available zircon REE standard called 91500 (Wiedenbeck et al. 1995). The standard contains about 300 ppm of REE + Y. Pieces of the standard are derived from an originally large megacryst from Ontario, Canada, although its original lithology is uncertain (*op. cit.*, p. 2). Published REE analyses of 91500 chips are few at present, although there is reasonable agreement between analyses from different laboratories using different techniques and data-treatment procedures (Table 2) such that 91500 should continue to be used as a primary or secondary standard.

***REE patterns of igneous zircon.*** Zircon REE abundances are typically normalized to C1-chondrite values (e.g., McDonough and Sun 1995) and plotted on $\log_{10}$ versus element (La–Lu) diagrams (Fig. 4). Relative to chondrite values, lunar and terrestrial zircon are HREE enriched and LREE depleted. The normalized pattern is characterized by a steeply-rising slope from the LREE to the HREE with a positive Ce-anomaly and negative Eu-anomaly (Figs 4d-g, i, j). This style of pattern is characteristic for unaltered igneous zircon. Normalized element ratios are a measure of the steepness of the REE pattern; the greater the $(Sm/La)_N$ ratio, the steeper the LREE portion of the pattern and the greater the $(Lu/Gd)_N$ ratio, the steeper the HREE portion of the pattern (refer Fig. 4 with Table 3). These ratios are limited, however, and do not measure potentially useful petrogenetic information such as the degree of curvature in the HREE pattern of some zircon populations (Fig. 4e; both populations have $(Lu/Gd)_N$ ratios of 44, yet have different HREE concavity).

Compared with chondritic abundances, most zircon have LREE abundances typically less than $10^1\times$ chondrite, La usually much lower, although Ce is characteristically between $10^1$ and $10^2\times$ chondrite. The MREE range from $10^0\times$ to $10^2\times$ chondrite and the HREE typically range between $10^3\times$ and $10^4\times$ chondrite (Fig. 4).

The abundance of Zr in meteorites ranges <4 ppm (chondrites) to 70 ppm (eucrites) and zircon has only been reported for a few occurrences. Ireland and Wlotzka (1992) were first to report *in situ* analyzed REE abundances and patterns of zircon from two meteorites, the Vaca Muerta mesosiderite

**Table 2.** Rare-earth element and Y composition of standard zircon 91500 (ppm ±1σ)*.

| Element | Wiedenbeck[1] | Nesbitt[2] | Hoskin[3] | Belousova[4] | Sano[5] |
|---|---|---|---|---|---|
| *n* | 1-6 | 10 | 17† | 4 | 5-6** |
| Y | | | 160 ± 23 | 147 ± 22 | |
| La | | 0.003 | 0.04 ± 0.03 | | 0.01 ± 0.01 |
| Ce | 2.0 ± 0.1 | 2.14 | 2.5 ± 0.2 | 2.5 ± 0.5 | 2.6 ± 0.4 |
| Pr | | 0.01 | 0.03 ± 0.02 | | 0.04 ± 0.02 |
| Nd | 0.4 | 0.25 | 0.3 ± 0.1 | | 0.30 ± 0.06 |
| Sm | 0.3 | 0.50 | 0.4 ± 0.1 | 0.4 ± 0.2 | 0.28 ± 0.08 |
| Eu | 0.26 ± 0.07 | 0.23 | 0.22 ± 0.01 | 0.4 ± 0.2 | 0.19 ± 0.07 |
| Gd | 1.9 ± 0.1 | 2.38 | 2.0 ± 0.4 | 2.1 ± 0.4 | 1.6 ± 0.4 |
| Tb | | 0.83 | 0.86 ± 0.06 | | 0.8 ± 0.2 |
| Dy | 8.0 ± 0.1 | 10.8 | 11.03 ± 0.06 | 12 ± 2 | 12 ± 3 |
| Ho | | 4.4 | 4.8 ± 0.3 | 4.9 ± 0.7 | 5 ± 1 |
| Er | 20.4 ± 0.8 | 24.2 | 25 ± 2 | 26 ± 4 | 29 ± 6 |
| Tm | | 6.4 | 6.6 ± 0.4 | | 8 ± 2 |
| Yb | 57 ± 17 | 69.7 | 65 ± 2 | 66 ± 7 | 77 ± 18 |
| Lu | 12.4 ± 0.9 | 12.6 | 13 ± 2 | 14 ± 2 | 17 ± 4 |
| ΣREE | 103+ | 134 | 132 | 128+ | 154 |

* A blank entry denotes element not analyzed for or below the limit of detection.
** Uncertainty is given as ± 2σ; *n* = the number of analyses contributing to mean REE and Y values.
† Includes SIMS and LA-ICP-MS data.
1. Weidenbeck et al. (1995); 2. Nesbitt et al. (1997); 3. Hoskin (1998); 4. Belousova et al. (2002); 5. Sano et al. (2002).

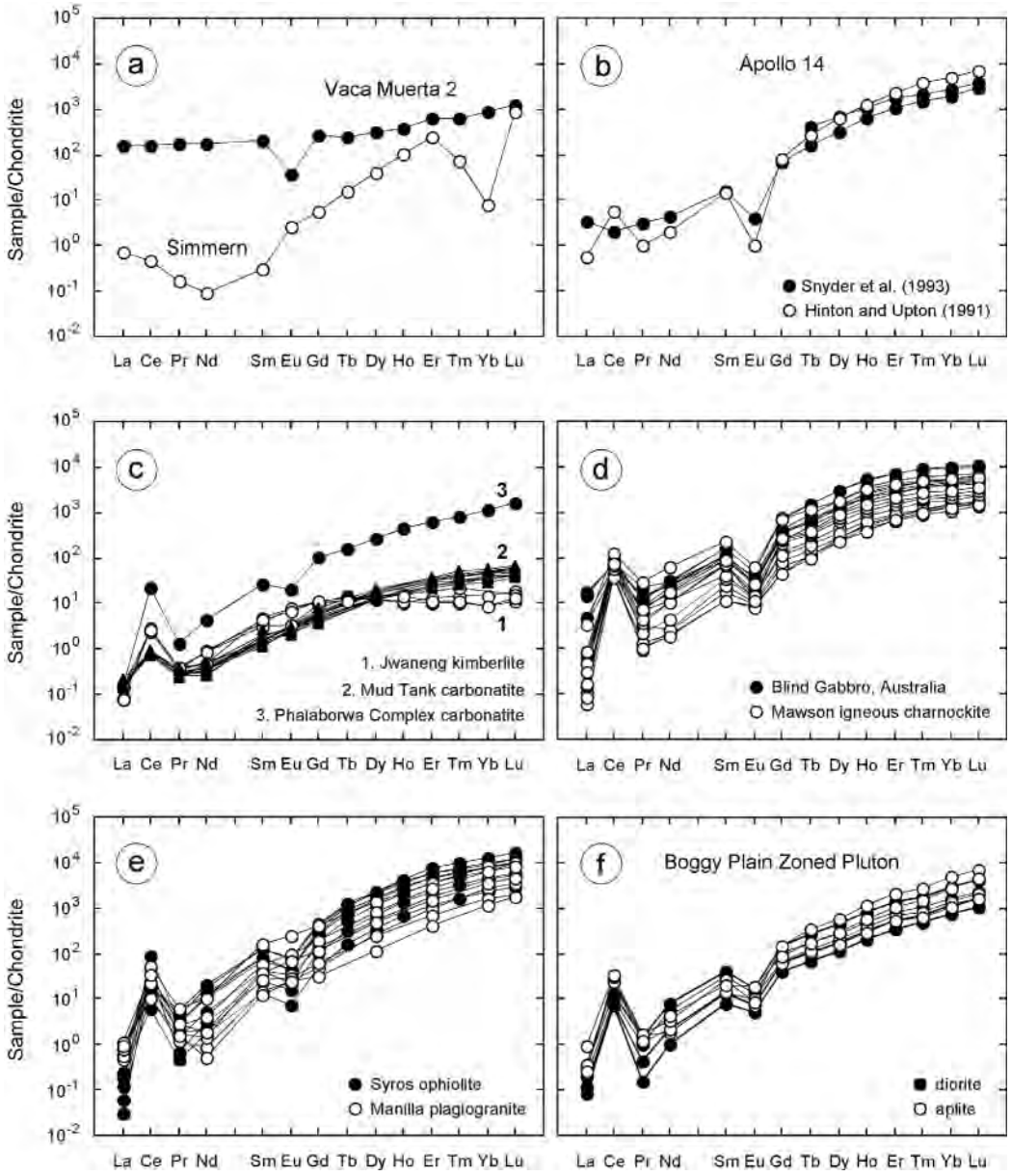


**Figure 4.** Compilation of REE patterns for meteorite, lunar and terrestrial zircon. (a) meteorite zircon from the Vaca Muerta mesosiderite and the H5 chondrite Simmern (Ireland and Wlotzka 1992); (b) lunar zircon from the Apollo 14 landing site (Hinton and Meyer 1991, Snyder et al. 1993); (c) kimberlite and carbonatite zircon (Hoskin and Ireland 2000); (d) zircon from Blind Gabbro, Australia, and Mawson igneous charnockite, Antarctica (Hoskin and Ireland 2000); (e) ophiolite and plagiogranite zircon (Hoskin and Ireland 2000); (f) zircon from two zones, diorite and aplite, of the Boggy Plain Zoned Pluton, BPZP (Hoskin et al. 2000); (g) Torihama dacite pumice, Japan (Sano et al. 2002); (h) zircon from sample NL102 of the Manaslu granite, Tibet (Barbey et al. 1995); (i and j) zircon from the Chuquicamata West porphyry and Los Picos diorite, Chile (Ballard et al. 2002); (k) zircon from corundum-bearing syenitic xenoliths, Elie Ness and Ilmen syentie (Hinton and Upton 1991); (l) Hadean zircon (4.0–4.15 Ga) from Jack Hills metaconglomerate W74, Australia (Peck et al. 2001). All data are replotted from the original source and normalized to the chondrite values of McDonough and Sun (1995).

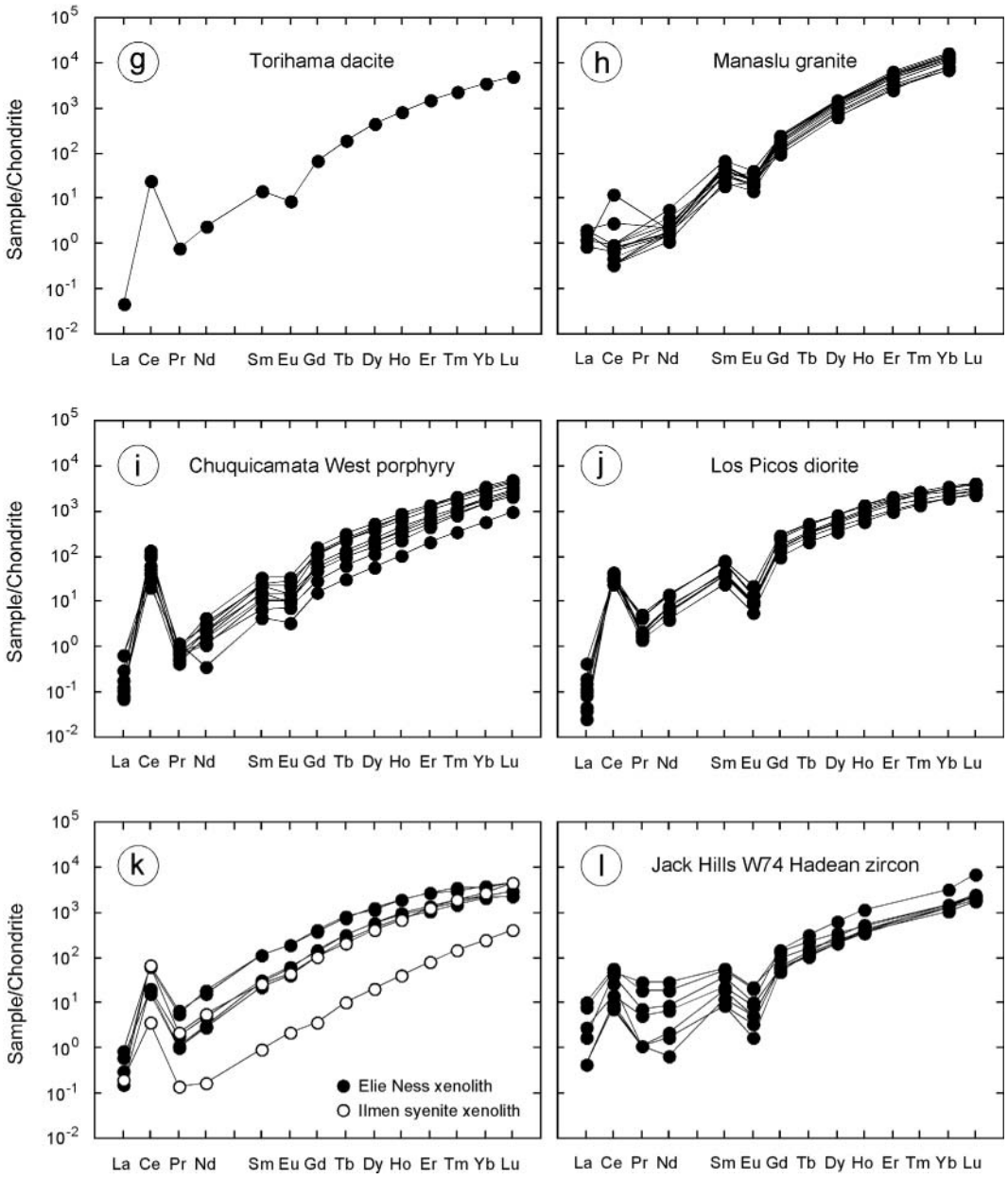


**Figure 4.—Continued.**

and the H5 chondrite Simmern. The REE pattern of zircon from Simmern (Fig. 4a and Vaca Muerta 1, not shown) is HREE enriched like unaltered terrestrial igneous zircon and apart from Tm and Yb, it increases regularly and steeply [$(Lu/Gd)_N$ = 169] from the MREE to the HREE. The similarity of the REE pattern to that of refractory inclusions in the Allende meteorite (Kornacki and Fegley 1986) indicates that the Simmern zircon pattern is an unusual mixture of igneous and volatility-influenced patterns. In contrast, Vaca Muerta zircon 2 formed very early in the evolution of the Solar System (at 4563±15 Ma) from an igneous melt. The REE pattern of this zircon is HREE enriched relative to the LREE, although the LREE are enriched (~$10^3$× chondrite) compared to

**Table 3.** Characteristic ratios of chondrite-normalized zircon REE patterns of Figure 4.†

| Ratio** | Vaca Muerta zircon 2 | Simmern | Lunar/ Apollo 14 | Phalaborwa carbonatite | Mud Tank carbonatite | Jwaneng kimberlite |
|---|---|---|---|---|---|---|
| Figure 4 | a | a | b | c | c | c |
| *n* | 1 | 1 | 1 | 1 | 16 | 4 |
| $(Sm/La)_N$ | 1.3 | 0.4 | 4.8 | 164 | 11.3 | 38 |
| $(Lu/Gd)_N$ | 4.6 | 169 | 45 | 15 | 9.3 | 1.4 |
| Ce/Ce* | 0.9 | 1.3 | 0.6 | 49 | 3.7 | 13 |
| Eu/Eu* | 0.2 | 2.1 | 0.1 | 0.4 | 1.0 | 1.0 |
| Ratio** | Blind Gabbro | Mawson ig. charnockite | Syros ophiolite | Manilla plagiogranite | BPZP diorite | BPZP aplite |
| Figure 4 | d | d | e | e | f | f |
| *n* | 8 | 10 | 8 | 7 | 7 | 4 |
| $(Sm/La)_N$ | 153 | 236 | 547 | 90 | 119 | 57 |
| $(Lu/Gd)_N$ | 16 | 19 | 44 | 44 | 27 | 38 |
| Ce/Ce* | 20 | 79 | 82 | 20 | 39 | 40 |
| Eu/Eu* | 0.2 | 0.2 | 0.3 | 0.9 | 0.2 | 0.3 |
| Ratio** | Torihama dacite | Manaslu granite | Chuquicamata W. porphyry | Los Picos diorite | Elie Ness xenolith | Jack Hills zircon |
| Figure 4 | g | h | i | j | k | l |
| *n* | 6 | 13 | 10 | 9 | 6 | 8 |
| $(Sm/La)_N$ | 306 | 33 | 145 | 653 | 165 | 18 |
| $(Lu/Gd)_N$ | 74 | - | 47 | 19 | 17 | 35 |
| Ce/Ce* | 132 | - | 230 | 87 | 31 | 8.0 |
| Eu/Eu* | 0.3 | 0.3 | 0.4 | 0.1 | 0.9 | 0.2 |

† Chondrite normalizing values from McDonough and Sun (1995). $Ce_N$ indicates the element has been normalized; $(Sm/La)_N$ indicates that the elements where normalized prior to division.
*n* = the number of analyses contributing to mean.

** Anomalies were calculated in this manner; for example $Ce/Ce^* = \frac{Ce_N}{\sqrt{La_N \Delta Pr_N}0}$

unaltered terrestrial igneous zircon.

Lunar zircon have fairly steeply increasing patterns from the LREE ($10^1\times$ chondrite; $(Sm/La)_N = 4.8$) to the HREE ($10^2\times$ to $10^3\times$ chondrite; $(Lu/Gd)_N = 45$) and a pattern that, in general, is similar to terrestrial igneous zircon (Fig. 4b; see also Wopenka et al. 1996). A major difference, however, is that lunar zircon generally do not have a positive Ce-anomaly. The zircon described by Hinton and Meyer (1991) does have a Ce-anomaly but was found in an unusual oxidized granite that contains significant amounts of $Fe_2O_3$ and $WO_3$ (Meyer and Yang 1988).

A number of studies have shown that mantle-affinity zircon have REE patterns distinctively different from crustal-affinity zircon (Heaman et al. 1990, Belousova et al. 1998, Hoskin 1998, Hoskin and Ireland 2000). Zircon from kimberlite, MARID suite xenoliths (Hoskin 1998, Konzett et al. 1998) and the Mud Tank carbonatite (Currie et al. 1992, Hanchar and Hoskin 1998) (Fig. 4c) have HREE enriched patterns ($10^1\times$ to $10^2\times$ chondrite) with no significant Eu-anomaly ($Eu/Eu^* = 1.0$, i.e., no anomaly on average, Table 3) and relatively flat HREE patterns ($(Lu/Gd)_N \approx 1\text{-}10$). The exception to this is zircon from the Phalaborwa Complex carbonatite although its provenance may be silicic selvedges within the carbonatite (Hoskin and Ireland 2000, p. 629).

The REE patterns for continental crustal zircon populations from rock-types ranging igneous charnockite, gabbro, diorite, dacite, granite and aplite are given in Figures 4d-j. The patterns are generally similar with HREE abundances increasing from ~$10^2$ (Tb) to $10^4$ (Lu) times chondrite, $(Sm/La)_N$ ranging 57-547 and $(Lu/Gd)_N$ ranging 16-74. The low $(Sm/La)_N$ value of 33 for Manaslu granite zircon is likely to be an artifact of analytical error because the patterns generally lack a positive-Ce anomaly which is observed for all other terrestrial zircon. Similarly, the very high $(Sm/La)_N$ value of 653 (Table 3) for Los Picos diorite zircon may be a result of underestimated La abundances.

Zircon from the Elie Ness and Ilmen syenite xenoliths are similar to other reported occurrences of corundum-associated zircon (Sutherland et al. 2002) in that they lack a negative Eu-anomaly, yet differ in this respect to other occurrences (Guo et al. 1996, Sutherland et al. 1998, 2002). Corundum-associated zircon tends to be more enriched than typical crustal zircon although the overall REE pattern (Fig. 4k) and normalized element ratios (Table 3) are not unusual.

Figure 4l is a series of REE patterns from early Archean (Hadean 4.0-4.15 Ga) zircon from Jack Hills metaconglomerate W74, Australia. These crystals are interpreted to have crystallized from an evolved granitic magma (Peck et al. 2001). Nearly identical REE patterns from the oldest recognized terrestrial mineral, zircon grain W74-2/36, also from Jack Hills, are likewise suggested to be of primary igneous origin, inherited from a silica-saturated granitic magma. These zircon crystals have been proposed to preserve evidence for a differentiated crust and liquid oceans on the very early Earth (Wilde et al. 2001, Valley et al. 2002). Zircon from W74 has a $(Lu/Gd)_N$ value (35) that falls within the range observed for zircon from continental crust rock-types (Table 3) although the $(Sm/La)_N$ value of 18 and Ce/Ce* value of 8.0 are most similar to mantle-affinity zircon ($(Sm/La)_N$ = 11.3-38, Ce/Ce* = 3.7-13). The Hadean zircons are LREE enriched. Abundances range from ~$10^{-1}\times$ to >$10^{1}\times$ chondrite. Peck et al. (2001) noted that these abundances are "…unusually high compared to REE concentrations…" (p. 4225) in typical crustal zircon, but noted that they "…are similar to LREE enrichment seen in late zircons from ~400-Ma aplitic rocks…" (p. 4225) from the Boggy Plain Zoned Pluton. Indeed this observation is correct, yet Wyborn (1983), Hoskin et al. (1998) and Hoskin (1999) demonstrated with textural, isotopic and trace-element data that those "late zircons" are most likely of a hydrothermal origin and did not crystallize from a magma. The observation of LREE enrichment in early Archean zircon cannot be used as evidence in support of a Hadean differentiated crust.

***Ce and Eu anomalies of igneous zircon.*** Anomalous abundances of Ce or Eu, usually both, are a feature of all igneous zircon. Accurate and precise *in situ* data reveal that where anomalous abundances occur, the sense of the anomaly is always the same; Ce is always in greater abundance and Eu is depleted. Most zircons have both a positive Ce-anomaly and negative Eu-anomaly, but not all (e.g., Jwaneng kimberlite and Mud Tank carbonatite zircon, Fig. 4c; MARID suite zircon, Hoskin (1998), Fig. 5 therein). The magnitude of the anomalies are expressed as Ce/Ce* and Eu/Eu* ratios where Ce* and Eu* are the expected values for a smooth normalized pattern. These ratios are calculated according to the expression given in Table 3. Values of Ce/Ce* vary upward from 1.0 (lower values represent analytical artifacts or are in agreement with a value of 1.0 within analytical uncertainty) and Eu/Eu* varies between 1.0 (no anomaly) and zero.

Murali et al. (1983) first documented positive Ce-anomalies in zircon from Indian beach sands and a syenite and attributed it to the presence of $Ce^{4+}$ in the crystallizing magma. Schreiber et al. (1980) suggested on the basis of $Ce^{4+}/Ce^{3+}$, $Eu^{3+}/Eu^{2+}$ and $Fe^{3+}/Fe^{2+}$ vs. $fO_2$ relations that $Ce^{4+}$ cannot exist in magmas as it is reduced by $Fe^{3+}$, yet a small fraction of the Ce present can be tetravalent and on the basis of ionic charge and radius is compatible in zircon (Hinton and Upton 1991). Assuming equilibrium partitioning, the magnitude of the Ce-anomaly will be governed by the abundance of $Ce^{4+}$ in the melt and this is related to the $Ce^{4+}/Ce^{3+}$ ratio which is a function of oxygen fugacity. The small to non-existent Ce-anomalies in meteorite, lunar and mantle-affinity zircon (Fig. 4; Table 3) is consistent with their formation under reducing conditions and the "universal" and sometimes very large Ce-anomaly in crustal zircon is consistent with crystallization under variable yet relatively oxidized conditions.

Europium may exist in magmas as both a divalent and trivalent cation. The magnitude of the Eu-anomaly, like the Ce-anomaly, may be redox sensitive. If under oxidizing magma conditions all Eu is trivalent, the resulting normalized zircon REE pattern should not have a Eu-anomaly. However, under $fO_2$ conditions where $Eu^{2+}$ is stable, a negative Eu-anomaly is expected because of the relative incompatibility of the large $^{[8]}Eu^{2+}$ ion (1.25 Å) relative to $^{[8]}Zr^{4+}$ (0.84 Å). Because all Eu should be trivalent under all conditions where $Ce^{4+}$ is stable (Robie et al. 1979, Hanchar et al. 2001), a negative Eu-anomaly is not expected for crustal zircon. This consideration results in a paradox where the presence of a positive Ce-anomaly indicates oxidized magma conditions and a co-existing negative Eu-anomaly indicates reducing conditions. Previous discussion of this paradox lead Maas et al. (1992) to conclude that $fO_2$ is not the only factor controlling $Ce^{4+}/Ce^{3+}$ and $Eu^{3+}/Eu^{2+}$ in magmas.

This paradox may be explained by plagioclase fractionation which depletes Eu from the magma

prior to or during zircon crystallization (Snyder et al. 1993, Hoskin 1998, Hoskin et al. 2000). The Eu-anomaly in zircon, then, is both inherited from the Eu-depleted melt as well as being influenced by $fO_2$. This explanation may prove to only be one part of the paradox explanation and it may be that under some $fO_2$ and compositional conditions $Eu^{2+}$ and $Ce^{4+}$ can co-exist, or that redox reactions at the zircon/melt interface influence the oxidation state of Ce.

A systematic relation between zircon Ce and Eu-anomalies, the oxidation-state of a suite of host rocks and their age has been demonstrated for the first time by Ballard et al. (2002). In this study of zircon from barren and Cu-mineralized intrusive rocks from Chile, the $Ce^{4+}/Ce^{3+}$ ratio was calculated using a lattice-strain model for zircon/melt partitioning of $Ce^{3+}$ and $Ce^{4+}$. These workers found that $Ce^{4+}/Ce^{3+}$ and Eu/Eu* ratios varied systematically in time and with compositional evolution of the intrusive suite. The greater variation was found for the $Ce^{4+}/Ce^{3+}$ ratio (Fig. 5). In general, $Ce^{4+}/Ce^{3+}$ and Eu/Eu* in the Chilean zircon—and by inference, magmatic oxidation-states—increased from older mafic host rocks to younger felsic rocks. For this suite of rocks, Cu-mineralization is associated with zircon populations having average $Ce^{4+}/Ce^{3+}$ ratios >300 (i.e., Ce/Ce* >70) and Eu/Eu* >0.4 (e.g., the Chuquicamata West porphyry, Table 3). A similar temporal relation with Ce/Ce* and Eu/Eu* was observed for igneous zircon populations preserved in Palaeoproterozoic paragneisses in Japan, although the trend is opposite from that found by Ballard et al. (2002) and Ce/Ce* and Eu/Eu* ratios decrease over time (Hidaka et al. 2002). The authors do not offer an explanation for this apparent trend which becomes simple scatter when the anomalies are recalculated in the manner of those in Table 3.

***Other trace-element occurrences in igneous zircon.*** The most studied trace elements in zircon are U, Th and Pb produced by radioactive decay (e.g., Ahrens 1965, Ahrens et al. 1967, Poller et al. 2001, hundreds of U-Th-Pb geochronology studies). While non-radiogenic Pb ($^{[8]}Pb^{2+}$ 1.29 Å) is largely excluded from a crystallizing zircon (Watson et al. 1997), Th and U are somewhat compatible (ionic radii: $^{[8]}Th^{4+}$ 1.05 Å, $^{[8]}U^{4+}$ 1.00 Å) and occur in crustal zircon with abundances typically ranging tens- to thousands-of-ppm. The lowest abundance of U and Th yet reported for zircon is for Vaca Muerta meteorite crystal 1 where U is 0.58 ppm and Th is 0.051 ppm (Ireland and Wlotzka 1992). The intracrystalline distribution of Th and U in igneous zircon is heterogeneous and even varies about 35% (2σ) in the 91500 zircon standard (Belousova et al. 2002). Despite such variation on a ~30-50 µm scale, the Th/U ratio varies much less as pointed out by Ahrens (1965) and confirmed many times since. Generally, the Th/U ratio of igneous zircon is ≥0.5. Clear exceptions to this are zircon from less common rock-types such as kimberlite and MARID suite xenoliths

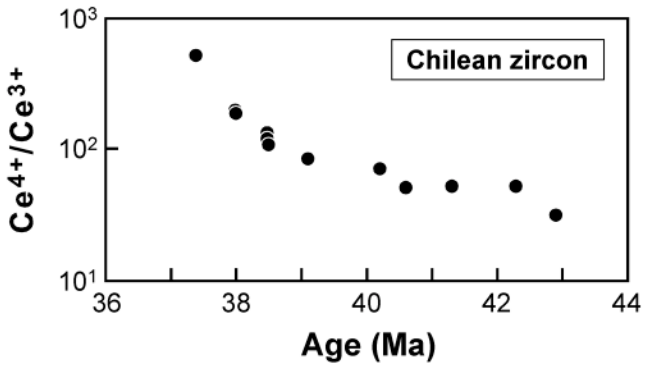


**Figure 5.** Average $Ce^{4+}/Ce^{3+}$ ratios versus U-Pb age of zircon from the Los Picos-Fortuna/Pajonal-El Abra igneous complex and the El Abra mine porphyry, Chile. The $Ce^{4+}/Ce^{3+}$ ratios increase systematically from the oldest, most mafic rocks, to the youngest, most felsic rocks, which are also Cu-mineralized. This relation is inferred to reflect a systematic oxidation increase of the magmas producing these rocks. Data from Ballard et al. (2003).

where Th/U values range ~0.2-1.0 (Konzett et al. 1998) and zircon from carbonatites from the Kola Peninsula, Russia, where Th/U ratios vary up to 9000 (Amelin and Zaitsev 2002).

Unaltered igneous zircon has very low concentrations of all other *in situ* measured elements. These elements include Li, Be, B, F, Na, Mg, Al, P, Ca, Sc, Ti, V, Cr, Mn, Fe, Sr, Nb, Ba and Ta. With the exception of P, the combined abundance of these elements in a single crystal is likely to be much less than a few hundred ppm and they are most often below the limit of detection. Values for these elements as given below (except P) should be considered as indicative of the upper ppm limits of abundance. Phosphorous values for zircon from the calc-alkaline intrusive suite of Ballard et al. (2002) range 49-388 ppm and for diorites through aplites of the Boggy Plain Zoned Pluton, zircon P values range 281-1379 ppm (Hoskin et al. 2000). For most of the crystals analyzed in these two studies, the mol % of P is not sufficient to charge-balance the mol % of REE indicating that the "xenotime" substitution mechanism must be only one of the operating REE substitution mechanisms. Niobium varies up to 62 ppm, Ta is <3, Li <3, Be <0.01, B <0.1, F <10, Na up to 28, Sc up to 250, Ti up to 75, V <5, Cr <0.5, Mn <40, Sr up to 6 and Ba <2 ppm (Hinton and Upton 1991, Maas et al. 1992, Halden et al. 1993, Hoskin et al. 2000, Ballard et al. 2002). The abundances of Mg, Al and Fe are highly variable and can be present at the hundreds-of-ppm level or below detection limits. Wopenka et al. (1996) reported an average $Al_2O_3$ value of 0.02 wt % and FeO of 0.10 wt % for lunar zircon, whereas Dickinson and Hess (1982) report up to 1.3 wt % $Al_2O_3$ in a lunar zircon. Guo et al. (1996) measured up to 0.54 wt % $Al_2O_3$ and 0.32 wt % $Fe_2O_3$ in corundum-associated zircon. Magnesium is less abundant (MgO <0.2 wt %; Dickinson and Hess 1982, Guo et al. 1996, Sutherland et al. 2002).

A number of trace-elements in zircon including the REE, where analyzed by Belousova et al. (2002), including Ti, Mn, Fe, Ga and Sn. However, their data-base includes analyses of supposed zircon containing MnO abundances up to 0.4 wt %, 0.5 wt % $Nb_2O_5$, 1.4 wt % $UO_2$, 2.9 wt % $P_2O_5$, 4.1 wt % $TiO_2$, and 6.0 wt % $Fe_2O_3$. These data cannot represent primary igneous zircon and reflect analysis of altered zircon or zircon + inclusions. Non-primary abundances of $Fe_2O_3$ like those of Belousova et al. (2002), as well as other oxides including elevated MnO, $Al_2O_3$ and CaO are reported for metamict and fluid-altered zircon (e.g., Kopchenova et al. 1974, Geisler and Schleicher 2000, Geisler et al. 2003).

Given the very low abundances of elements that may have a role in REE-coupled substitutions in addition to P (e.g., Nb, Ta), it seems that interstitial cations, $Al^{3+}$ in particular (Hoskin et al. 2000), and perhaps hydrous species, play an essential role in REE and Y substitution.

## Zircon composition and investigations of igneous processes

***Zircon saturation, fractionation and melt composition.*** Due to the HREE enriched character of igneous zircon, saturation and fractionation of this phase during magmatic differentiation might cause significant depletion of the magma in the HREE. For this to be the case, however, relatively large amounts of zircon may be required. In a study of the distribution of REE among minerals in "Route 111" granodiorite from California, Gromet and Silver (1983) found that along with zircon, titanite, allanite and apatite were the main HREE phases. However, on the basis of compositional and modal analysis, the fractional contribution of zircon to the total whole-rock HREE abundance is almost insignificant. In the Route 111 granodiorite, most of the REE are hosted in titanite (MREE and HREE), allanite (LREE) and hornblende. In this case, during magma evolution, zircon could not have been expected to have exerted a noticeable influence on the HREE. This is also the case for granitoid samples from the Saganaga tonalite, Minnesota–Ontario, where despite the presence of zircon, apatite and titanite, the REE characteristics of the magmas seem to have been governed by petrogenetic processes operating prior to the saturation of these REE-bearing phases (Evans and Hanson 1993). Sawka (1988) also concluded that zircon did not influence the REE characteristics of magmas forming the McMurry Meadows Pluton, California, because zircon may have crystallized from the bulk (homogeneous) magma prior to differentiation.

Zircon fractionation has, however, been demonstrated for other igneous systems to be an important fractionator of the HREE, Y and Hf. Tertiary lavas ranging from basaltic andesite to high-silica rhyolite from the Batopilas area of Mexico were examined by Evans and Hanson (1993). The variation of Zr abundance in the Batopilas lavas strongly suggests zircon was an early-liquidus saturation phase in the high-silica rhyolite lavas. The inclusion of zircon in a model fractionating assemblage, improved an earlier modeling attempt (Cameron and Hanson 1982) to relate the high-silica rhyolites to less felsic dacites by bringing the REE modeling results into better agreement with the major-element modeling results. Because zircon is HREE enriched, only 0.06 wt % of zircon was required in the model assemblage to produce a better agreement. Another demonstration of the role of zircon during differentiation was given for granitoid rocks of a small I-type pluton in southeast Australia. The Boggy Plain Zoned Pluton (BPZP) contains a range of REE-bearing accessory phases including apatite, titanite, allanite, monazite and zircon. Hoskin et al. (2000) demonstrate an integrated approach to identifying the point at which these minerals saturate in the evolution of the magmatic system. Once a mineral saturation point is identified, and assuming fractionation, that mineral can be included in the model assemblage for numerical modeling of differentiation processes. Erroneous modeling results will occur if a mineral is included in the model assemblage prior to its saturation point and fractionation. Hoskin et al. (2000) modeled compositional variation within the adamellite zone of the BPZP by 90% fractional crystallization of an assemblage containing 22 wt % calcic-amphibole, 19 wt % alkali-feldspar, 37 wt % plagioclase, 17 wt % biotite, 4 wt % clinopyroxene, 0.13 wt % apatite, 0.1 wt % allanite and 0.19 wt % zircon. The difference between measured whole-rock REE abundances and modeled abundances is between 1 and 15% and the model reproduces the measured normalized REE pattern (Hoskin et al. 2000, Fig. 16 therein).

***Melt-composition calculations.*** A number of studies have attempted to determine trace-element zircon/melt partition coefficients either by experiment or analytically (Nagasawa 1970, Watson 1980, Mahood and Hildreth 1983, Murali et al. 1983, Fujimaki 1986, Bea et al. 1994, Sano et al. 2002, Thomas et al. 2002, Thomas et al., this volume) or partly by theoretical considerations (Hinton and Upton 1991, Guo et al. 1996). These have been used in attempts to determine the composition of melts from which zircon has crystallized. Success of the application of partition coefficients, $^{\text{zircon/melt}}D_{\text{element}}$, for the back-calculation of melt composition is dependent upon high-quality trace-element data for zircon and well known $D_{\text{element}}$ values, as well as the assumption that zircon crystallized early from the melt. If this last assumption is not justified, neither is the use of $D_{\text{element}}$ values because the best of these values have been determined from known melt compositions and generally, the composition of a later-stage zircon-crystallizing melt is unconstrained, and $D_{\text{element}}$ values vary strongly as a function of melt composition. It is likely that this is one reason why many workers have not been able to back-calculate melt compositions that look reasonably similar to any common melt or rock-type on Earth or the Moon (e.g., Hinton and Upton 1991, Snyder et al. 1993, Guo et al. 1996). Perhaps more important is the further assumption one must make when using $D_{\text{element}}$ values, which is that equilibrium trace-element partitioning governs the abundance of trace-elements in zircon. It is suspected however, that disequilibrium partitioning is normal for zircon (Watson and Liang 1995, Barbey et al. 1995, Watson 1996b). Moreover, the partitioning of REE, Y and P into zircon appears to be limited not so much by melt composition or cation diffusion, but by intracrystalline strain imposed by cation substitution (Finch et al. 2001). Despite these real difficulties, the determination of $D_{\text{element}}$ values by Sano et al. (2002) and Thomas et al. (2002) appear to be more realistic and able to reproduce known melt compositions (Sano et al. 2002, p. 227-228).

**Provenance-indicator studies using igneous zircon composition**

The chemical and mechanical durability of zircon means that it can persist on and within Earth's crust for billions of years. As well as preserving textural information and age data, a record of the source-rock composition of detrital or xenocrystic zircon may be preserved by trace-element abundances and patterns. It would be of immense interest in crustal evolution studies to be able to

"finger-print" source-rock lithology and age from detrital and xenocrystic zircon. The dual approach of assessing zircon isotope and trace-element composition would have potential in determining sediment provenance and its applications to studies of, for example, uplift, erosion and tectonics.

For the composition of *ex situ* zircon to be used to identify source lithology, it must be demonstrated that zircon composition can be systematically related to lithology. Such a demonstration could be via the use of partition coefficients, or by identifying compositional features of zircon that can be systematically related to lithology. The latter approach seems most promising and studies taking this approach are discussed here. Early studies relating zircon composition and isotopic age to source lithology were limited by the inability to measure or accurately determine REE, Y and other trace elements in zircon (Köppel and Grünenfelder 1971, Köppel and Sommerauer 1974, Murali et al. 1983). Using multi-grain INAA analysis of seventeen zircon populations, Heaman et al. (1990) proposed that zircon from kimberlite, carbonatite and nepheline syenite, mafic and ultramafic samples, felsic samples, and basalts could be distinguished from each other on the basis of plots of Lu, Sc, Th/U and Lu/Sm versus Hf. However, on the basis of Lu, Sc, Th/U and Lu/Sm alone, there is no clear discrimination, and only partial discrimination based on the reported Hf abundances. Nonetheless, this important paper indicated the potential for zircon composition as a provenance and petrogenetic indicator.

The first *in situ* measurements of zircon composition from a variety of rock-types, including meteorites, lunar rocks, metamorphic zircon and two granitoid zircons, were made by Ireland and Wlotzka (1991). Their nine REE analyses showed that despite the diverse geologic settings in which the terrestrial, lunar and meteoritic zircon formed, their REE patterns are remarkably similar. Interestingly, there is greater difference between the REE patterns of two zircons from a single meteorite than there is for all terrestrial zircon measured in their investigation. A much larger data set of REE, Y, P and $HfO_2$ was collected by Hoskin and Ireland (2000) for zircon from a wide-range of mantle-affinity and crustal rock-types. This study concluded that the REE abundances and patterns of zircon from rocks with a mantle-affinity are distinctive from crustal zircons and have much flatter patterns and lower abundances. This conclusion is supported by Belousova et al. (1998). Despite this difference in REE characteristics, no systematic difference between zircon from disparate crustal rock-types was observed.

To evaluate the actual variation in detrital zircon REE composition in a real sediment, zircon from a sandstone sample from the North Sea were analysed by Hoskin and Ireland (2000). The sandstone is from the Statfjord Formation (Zone A) and was sampled at 9877.5 ft (3.01 km) downhole of Brent Field well 211/29-6 located on the sea floor between Scotland and Norway. Evidence from Sm–Nd isotopes, palaeocurrent data, heavy mineral assemblages, detrital garnet composition, and detrital zircon U-Pb isotope spectra, indicate that the source region of this sample comprised high-grade metasediments and a range of Caledonian intrusive rocks. The REE abundances for zircon from this sandstone reveal that despite different crustal elements in the source region and a U-Pb zircon age range of 2.82 billion years, the zircon REE patterns are essentially identical. This result cannot be attributed to a homogeneous source region or derivation of detritus from a single source, but was considered by Hoskin and Ireland (2000) to confirm the apparent monotony of REE patterns and abundances in zircon derived from a range of common crustal rock-types.

Belousova et al. (2002) measured a large range of trace-elements in zircon from a variety of rock-types, but dominantly kimberlite, lamproite and carbonatite. This study and that of Hoskin and Ireland (2000) and Heaman et al. (1990) are summarized in Table 4. The value of the study by Belousova et al. (2002) is reduced because their data-base includes analyses of "metamict zircons…" that have compositions that have been affected by "…secondary alteration" (p. 609). Moreover, their supposed basalt zircon actually derive from xenoliths within the basalt, while other zircon are detrital and derived from a "palaeochannel" (p. 604) and the original source-rock(s) is unknown. Data from these zircon occurrences are included in statistical classification and regression trees

**Table 4.** Characteristics of zircon trace-element and provenance studies.

**Heaman, Bowins and Crocket (1990) Geochim Cosmochim Acta 54:1597-1607**

Strengths
• first analyses of zircon from a variety of widely sourced rock-types.
• demonstrated a degree of discrimination for zircon provenance on the basis of Hf (wt %).

Limitations
• very small data set of multi-grain analyses (INAA)

**Hoskin and Ireland (2000) Geology 28:627-630**

Strengths
• first high-quality *in situ* analyses of zircon from a variety of widely sourced rock-types.
• REE and Y data for well-constrained whole-rock samples, texture imaged and U-Pb isotope analyzed zircon from those whole-rock samples.
• provided a "real-life" test of zircon provenance identification on a well studied sandstone from the Statfjord Formation, North Sea.

Limitations
• limited data set

**Belousova, Griffin, O'Reilly and Fisher (2002) Contrib Mineral Petrol 143:602-622**

Strengths
• zircon analyses from a variety of widely sourced rock-types.
• data set of elements includes REE, Y and other trace-elements.

Limitations
• no documentation of intra-sample compositional variation or "representativeness".
• data set of rock-types includes some of uncertain origin or identification.
• data set of zircon compositions include analyses of altered zircon or zircon + inclusions.
• statistical determination of zircon source rock-type is based on the flawed data sets above.
• statistical treatment (CART tree) is a description of original data set and should not be used predictively.

(CART tree) that are intended to be used to identify the source rock-type of a detrital or xenocrystic igneous zircon. The CART trees are a "description" of the specific data set from which they are constructed such that the "description" is only as good as the data-base.

At this point in time, delineation and recognition of systematic relations between igneous zircon composition and source rock-type are only slowly emerging. Studies of metamorphic zircon, however, reveal that the composition provides a great deal of information about the processes that form metamorphic zircon and metamorphic rocks.

## ZIRCON AND METAMORPHIC PETROGENESIS

### Textural characterization of metamorphic zircon

Metamorphic zircon is characterized by a number of features that differ from igneous zircon and these are considered separately below. A more detailed review of metamorphic zircon textures is given by Corfu et al. (this volume).

***External morphology of metamorphic zircon***. Zircons in low-grade metamorphic rocks are usually inherited from the protolith and may show signs of resorption or metamorphic overgrowth. High-grade rocks such as granulites may contain zircon that grew during metamorphism in the presence or absence of an anatectic melt (Fraser et al. 1997, Roberts and Finger 1997). Typical morphologies are rounded or ovoid shapes (Fig. 6a) which are interpreted to be formed by resorption by a zircon-undersaturated intergranular fluid (Hoskin and Black 2000) which may also produce surface etching and pitting (Wayne and Sinha 1988, Hanchar and Miller 1993). Ovoid morphologies were also documented by Degeling et al. (2001) who proposed that new zircon formed during the decompression reaction of garnet + sillimanite + quartz to produce zircon-bearing cordierite. Rounded and ovoid zircons are often accompanied by "soccer-ball" shaped zircon (e.g., Vavra et al. 1996, Schaltegger et al. 1999; Fig. 6b). Soccer-ball zircon represents the S22-type in the Pupin (1980) morphology classification scheme, with subordinate development of prism faces. Hoskin

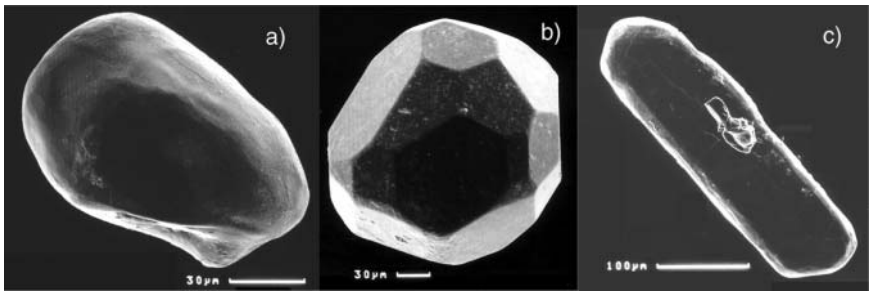


**Figure 6.** Zircon in granulite-grade rocks, Vosges Mountains, eastern France: (a) rounded-ovoid grain; (b) "soccer-ball" zircon; (c) prismatic zircon from the same granulite as the grain in (a), but occurring on the grain-boundaries of rock-forming minerals. Figure after Schaltegger et al. (1999).

and Black (2000) found that within their high-grade rocks, zircon included within different rock-forming minerals and those from grain-boundaries did not differ morphologically. However, it was reported by Schaltegger et al. (1999) that soccer-ball zircon included in ternary feldspars are coeval with prismatic grains that occur on grain-boundaries (Fig. 6c).

***Internal textures of metamorphic zircon***. Internal textures are observed by CL and BSE imaging (Hanchar and Rudnick 1995, Rubatto and Gebauer 2000, Kempe et al. 2000, Corfu et al., this volume). These images allow for visual distinction between metamorphic growth zones, preserved igneous cores, recrystallized domains and domains showing other types of structural reorganization. Zircon that grew in high-grade metamorphic rocks often shows a distinct sequence of internal structures: an initial low-luminescence growth zone (sometimes overgrowing an inherited core) sequentially overgrown by sector zoned domains. These textures are commonly followed by oscillatory zoned domains (Vavra et al. 1996, 1999; Schaltegger et al. 1999; Fig. 7). This succession of zones has yet to be adequately explained and has not yet been the subject of specific research attention.

Metamorphic zircon can preserve a wide variety of textures, largely because it can grow under a wide variety of *P-T-x*-stress conditions that may collectively be termed as metamorphic. Zircon-forming events may occur prior to, after, or at peak *P-T* conditions. The geologic significance of an isotopic age determined from a metamorphic zircon depends upon when in the petrogenesis of the rock the zircon (or a specific growth zone) formed, whether or not it formed in the solid-state, by precipitation from a fluid (carbonic, aqueous, or melt), or by recrystallization of protolith zircon. Given the complexity of zircon textures and the ambiguity associated with interpreting isotopic age determinations, trace-element analysis is becoming widely applied as another line of evidence for more confident petrogenetic interpretation.

## The growth of new zircon during metamorphism and its composition

The crystallization of new zircon during metamorphism has been recorded for a wide range of temperatures and pressures during prograde (Liati and Gebauer 1999, Bingen et al. 2001), retrograde (Pan 1997, Roberts and Finger 1997, Degeling et al. 2001, Whitehouse and Platt 2003) and peak (Bea and Montero 1999, Hoskin and Black 2000, Möller et al. 2002) metamorphic conditions. At *P-T* conditions lower than upper-amphibolite and granulite-grade, new zircon is rare and recrystallization of protolith zircon is responsible for producing "metamorphic" zircon. At granulite-grade conditions, new zircon can form at sub-solidus conditions and also during anatexis (Schaltegger et al. 1999, Rubatto et al. 2001). The volume of new zircon formed is dependent upon temperature and the volume and composition of melt (Watson and Harrison 1983, Watson 1996a). There are examples, however, where the volume of new zircon exceeds-by-far that expected from calculated

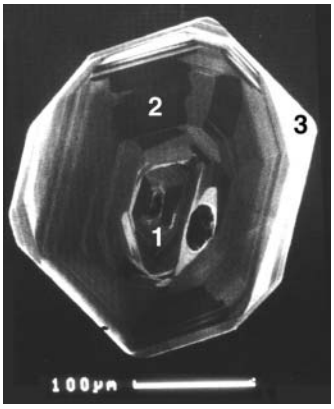


**Figure 7.** A metamorphic zircon illustrating the commonly observed sequence of growth structures: (1) low-luminescence center; (2) sector zoned domain; (3) oscillatory zoned outer part. The bright-CL area to the right of domain 1 is an area of localized recrystallization around a 40-µm mineral inclusion. Figure after Schaltegger et al. (1999).

saturation limits. Vavra et al. (1996, 1999) report that zircon in metasediments from the Ivrea Zone, southern European Alps, are comprised of 5 vol % of inherited zircon overgrown by large volumes of new zircon. They also describe voluminous overgrowths in associated melanosomes, which according to compositional criteria should not have been favorable to high Zr solubility and subsequent zircon growth. Other factors that determine whether new zircon will form or not include the grain-size of zircon and the crystal size-distribution of rock-forming minerals (Nemchin et al. 2001), the location of protolith zircon on grain-boundaries or as inclusions (Watson et al. 1989, Watt and Harley 1993), diffusion of Zr in a melt phase and the Zr abundance and stability of rock-forming minerals.

The Zr abundances of major metamorphic minerals in four different granulite-grade rocks from Rundvågshetta, east Antarctica, were determined by Fraser et al. (1997). Both garnet and hornblende contain tens of ppm of Zr, enough to produce new zircon by Zr release if these minerals partake in breakdown reactions such as garnet + sillimanite + quartz → cordierite + zircon. Vavra et al. (1996) had proposed that biotite was a source of Zr for new zircon growth during anatexis in the Ivrea Zone. Pan (1997) proposed zircon, titanite and rutile formation by breakdown of zirconolite, and zircon formation after allanite breakdown in upper-amphibolite grade gneisses. Ilmenite was proposed as a source of Zr for metamorphic zircon by Bingen et al. (2001). The formation of new zircon by these net-transfer reactions is, however, dependant upon the solubility of Zr in product phases. At Rogaland in southwest Norway, zircon formed in high-grade rocks by the reaction garnet + sillimanite + quartz → cordierite + zircon, but did not form during the reaction garnet + sillimanite + quartz + biotite → osumilite + orthopyroxene + spinel + magnetite, because of the higher solubility of Zr in osumilite and orthopyroxene at higher grades than in cordierite at lower grades (Degeling et al. 2001). Unfortunately, compositional data for zircon formed by net-transfer reactions are scarce, largely due to very small grain-sizes (typically <20 µm).

In a study of trace-element partitioning between co-existing zircon and garnet, Rubatto (2002) demonstrates that among the REE, Ce has by-far the highest preference for zircon ($^{Ce}D_{zir/gt}$ = 69-90; next largest is $^{Lu}D_{zir/gt}$ = 12-24) thus producing extremely large positive Ce anomalies in zircon that even exceed the chondrite-normalized Yb and Lu values (Fig. 8). The REE patterns of zircons that formed by net-transfer reactions in the high-grade rocks of Rubatto (2002) are additionally characterized by relatively depleted HREE abundances due to partitioning competition with garnet and very small (Eu/Eu* = 0.24-0.63) negative Eu anomalies which are believed to be "inherited" from the whole-rock composition as well as indicate formation in the absence of plagioclase. Nearly identical REE patterns were reported by Whitehouse and Platt (2003) for zircon rims on protolith cores included in metamorphic garnet, although these workers suggest that Ca-rich garnet rims and zircon rims grew from melt produced during decompressional melting. In addition to *P-T* indicator minerals that can be included in metamorphic zircon (e.g., Hermann et al. 2001, Katayama et al.

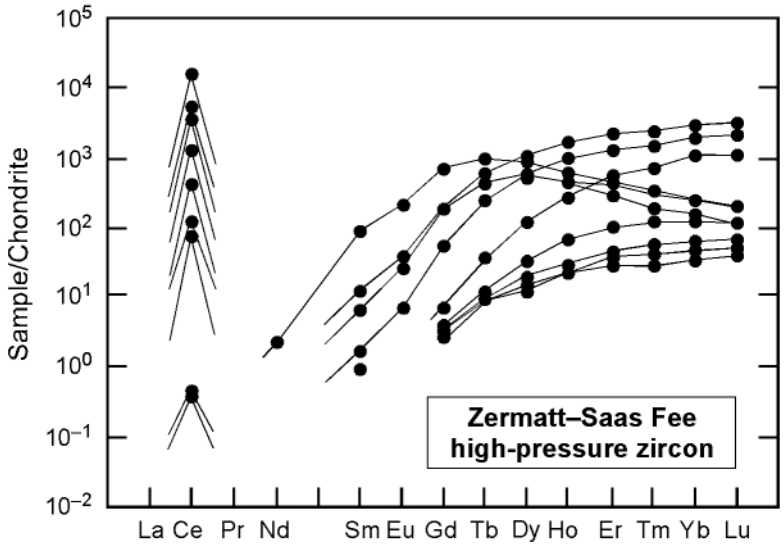


**Figure 8.** Chondrite-normalized REE patterns for metamorphic zircon from Lago di Cignana (Zermatt–Saas Fee, European Alps) eclogitic-grade metasediments. The zircons grew in equilibrium with garnet and have extremely large positive Ce anomalies and relatively depressed HREE patterns. Figure after Rubatto (2002).

2001, 2002; Liu et al. 2002), the work of Schaltegger et al. (1999) and Rubatto (2002) relating the REE composition of new net-transfer/metamorphic zircon to specific stages of metamorphic petrogenesis means that zircon U–Pb isotopic ages can be linked with specific *P-T* conditions thus allowing direct assessment of the rate of tectonic and metamorphic processes.

The composition of metamorphic zircon in equilibrium with an anatectic melt does not differ greatly from igneous zircon. The zircons are enriched in trace-elements with ionic radii close to that of Zr (i.e., Hf, Y, U, P) and have steep REE patterns increasing from La to Lu with positive Ce and negative Eu anomalies (Fig. 9a). Such patterns are clearly distinguishable from REE patterns produced by sub-solidus growth with garnet (Figs. 8 and 9b). The metamorphic-melt zircons described by Rubatto et al. (2001) and Rubatto (2002) have relatively depleted MREE abundances that are attributed to similarly depleted abundances in the precipitating melt and not to co-crystallization with a REE-rich phase such as monazite. The only apparent systematic distinction between igneous zircon and metamorphic-melt zircon is the Th/U ratio, which is very low for the latter (<0.07, Rubatto 2002).

## Solid-state recrystallization and dissolution-reprecpitation of protolith zircon and compositional changes

Metamorphic zircon may be produced by intra-grain "reworking" of protolith igneous or detrital zircon or previously formed metamorphic zircon. The processes of reworking are solid-state recrystallization and local dissolution-reprecipitation. These processes appear not to be significant at low metamorphic grades were non-metamict protolith zircon tends to survive, although it can be mechanically fractured (Wayne and Sinha 1992). At higher grades these processes create a variety of internal textures. These secondary textures have been described by Vavra et al. (1996, 1999), Schaltegger et al. (1999), Hoskin and Black (2000), Möller et al. (2002) and Rubatto (2002) and include the following:

***Blurred primary zoning***. Primary igneous oscillatory zoning may be blurred (or "faded") as a first indication of metamorphic disturbance of the structure.

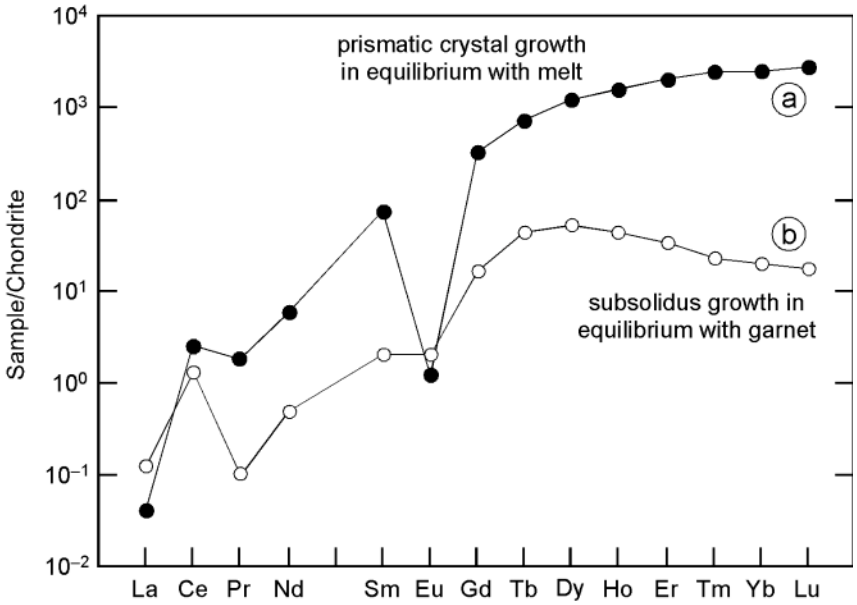


**Figure 9.** Chondrite-normalized representative REE patterns for metamorphic zircon equilibrated with a melt phase (a) and zircon equilibrated with garnet (b) under subsolidus conditions. Figure after Schaltegger et al. (1999).

***Convoluted zoning***. External parts of metamorphic zircon may show non-planar zoning formed by a series of low-CL and high-CL sinuous zones that may appear to be folded. This texture was called "flow zones" by Vavra et al. (1999) and Schaltegger et al. (1999). Individual zones can become discontinuous and truncated. The texture is considered to be the result of further convolution of blurred primary zoning (Hoskin and Black 2000).

***Transgressive recrystallization***. Local recrystallization of zircon under non-metamorphic conditions was described by Pidgeon (1992), Nemchin and Pidgeon (1997) and Pidgeon et al. (1998). The secondary texture produced is internally featureless, has sinuous and lobate edges, and cuts across other primary and secondary textures. Analogous textures in zircon from high-grade metamorphic rocks were described from Mount Sones, Antarctica (Black et al. 1986), Northwest Territories, Canada (van Breemen et al. 1987), Seve Nappes, Scandinavia (Williams and Claesson 1987), Vosges Mountains, France (Schaltegger et al. 1999) and the Georgetown Region, Australia (Hoskin and Black 2000). Although areas of transgressive recrystallization are generally internally featureless, they may preserve relics ("ghosts") of primary textures including oscillatory zoning. Transgressive recrystallized areas are separated from other structures by a grey-CL featureless recrystallization front (see Fig. 2 of Hoskin and Black 2000). In most examples, the recrystallization front appears to migrate from crystal pyramidal-terminations towards the interior of grains, although recrystallization may occur at locations away from crystal terminations, at domain boundaries or around inclusions (Figs. 7 and 10a).

The end result of transgressive recrystallization is complete recrystallization. Some zircon from high-grade rocks have no internal textures and are considered to have been fully recrystallized, for example the ~570 Ma gem-quality zircons in the Sri Lanka gem-gravels. Recrystallization has been proposed to occur in the solid-state without an essential role for a fluid-phase (Hoskin and Black 2000), although Tomaschek et al. (2003) provide strong evidence for an essential fluid-phase. Möller et al. (2002) argue for both fluid-present and fluid-absent zircon recrystallization in ultra-high-temperature granulites from southwest Norway. Evidence for solid-state, isochemical (on a

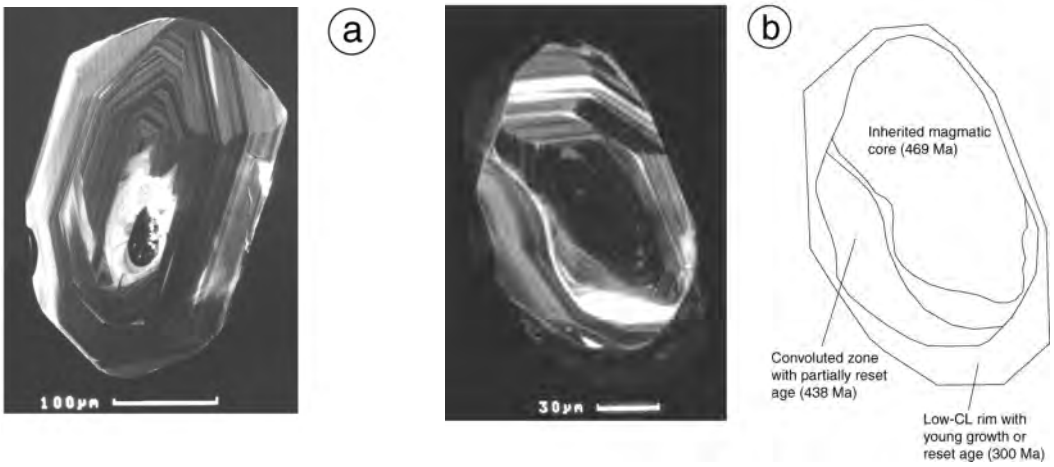


**Figure 10.** Zircon recrystallization textures: (a) *top row:* recrystallization around a mineral inclusion. The area of recrystallization is delineated by bright-CL as in Figure 7; (b) *bottom row:* various recrystallization features in a granulite-grade zircon with a large inherited core (469 Ma): convoluted zone with partially reset U–Pb age (438 Ma); low-CL rim with reset U–Pb age (300 Ma). Figure after Schaltegger et al. (1999).

crystal-scale) recrystallization, is the preservation of primary textures, in particular ghost textures, and the "mixed" isotopic ages (Figs. 10b and 11a) and trace-element compositions measured from these.

Recrystallization of protolith zircon has the effect of purging non-essential structural constituent cations (ESCs; Zr, Hf, Si) from the recrystallized structure. Cations with ionic radii significantly different from Zr (and Hf) and Si are purged from the structure. This was documented by Hoskin and Black (2000) for zircon from a meta-granitoid gneiss (Fig. 11). Eightfold coordinated $Th^{4+}$ has a larger ionic radius than $U^{4+}$ and appears to be preferentially purged with a consequent decrease in the Th/U ratio. This decrease correlates with a decrease in the $^{207}Pb/^{206}Pb$ age of the zircon; the youngest cluster of ages with Th/U <0.1 (solid circles, Fig. 11a) represent completely recrystallized zircon. Within a single crystal, trace elements are partitioned between recrystallized areas and the recrystallization front described above, enriching the front and depleting the recrystallized areas (see Er vs. P, U vs. Th and P vs. U plots, Fig. 11b). An exception to this trend is observed for Hf (see U vs. Hf plot, Fig. 11b). Hafnium enrichment is a feature of recrystallized zircons described by Pan (1997), where protolith zircon is recrystallized to trace-element-depleted–Hf-enriched zircon and xenotime according to the reaction $(Zr,Hf,Y,REE)(Si,P)O_4 \rightarrow (Zr,Hf)SiO_4 + (Y,REE)PO_4$. This reaction mechanism, with the addition of U-Th-silicates as a product, is advocated by Tomaschek et al. (2003) (Fig. 12). Normalized REE patterns for co-existing recrystallized zircon and recrystallization fronts in a single zircon (Fig. 11c) reveal the recrystallized zircon to be relatively depleted in the LREE and MREE with no measurable difference for Tm, Yb or Lu. As for Th and U, this is interpreted to be a consequence of cation size difference to Zr, which is greatest for the LREE and least for the HREE.

Differential trace-element purging as a function of cation ionic radii provides an explanation for U–Pb isotopic resetting and preservation of the Lu–Hf isotopic system. The ~570 Ma Sri Lanka zircons which on the basis of internal textures and likely source lithology are believed to be recrystallized, have a young U–Pb age (~570 Ma) and a Hf isotope model age of ~1.5 Ga (Kinny et al. 1991).

The mechanism or driving-force for recrystallization proposed by Hoskin and Black (2000) is thermoactivated grain-boundary and defect migration and the reduction of structural strain imposed by substituted trace elements. It is an observation that recrystallization is typically initiated at crystal terminations where trace elements are typically enriched above abundances at prism faces. Ghost

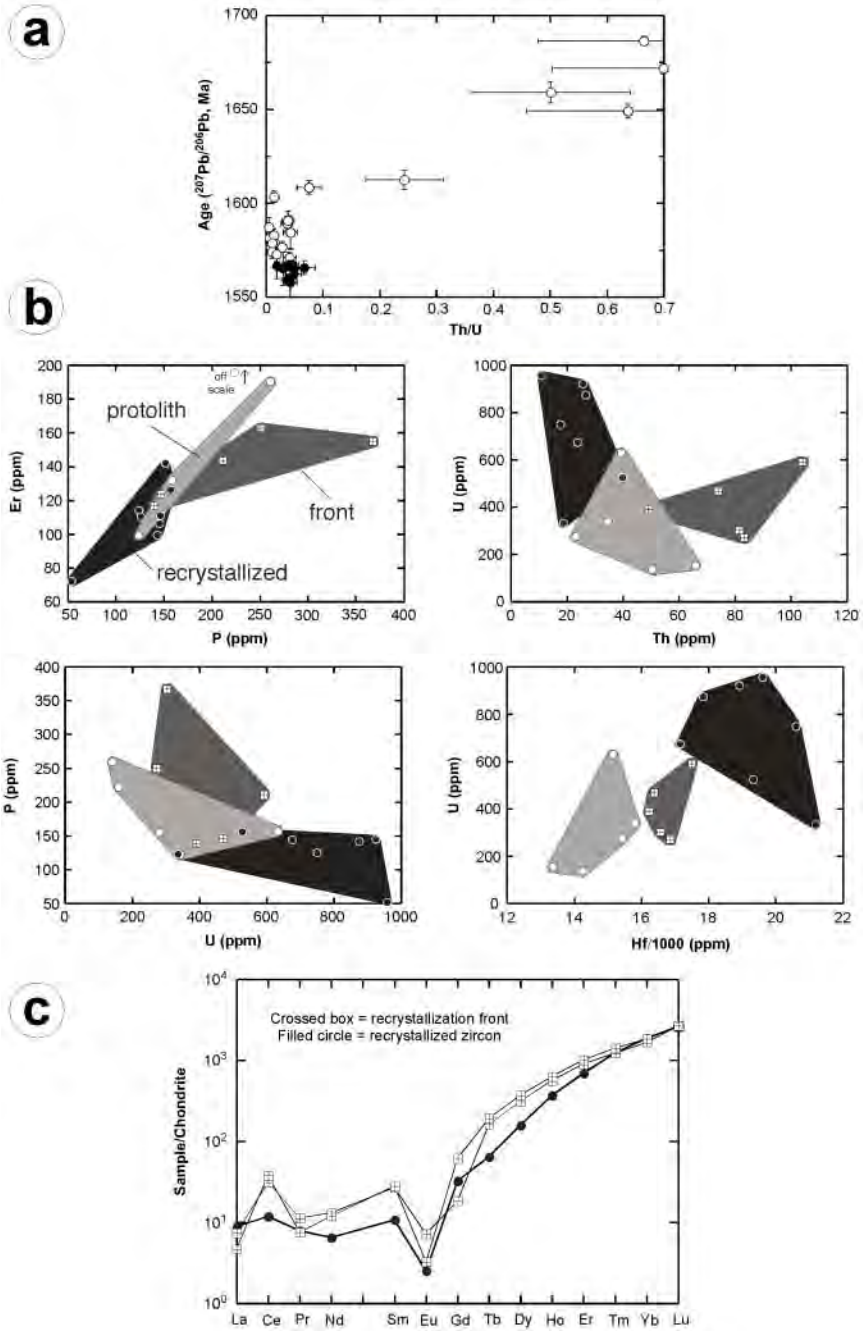


**Figure 11.** Isotope and trace-element characteristics of zircon from a meta-granitoid gneiss, northern Queensland, Australia. The zircon are partially to fully recrystallized. Internal textures observed in most crystals include primary igneous (protolith) zircon, recrystallized areas, and between these two, a recrystallization front: (a) $^{207}$Pb/$^{206}$Pb age versus Th/U plot indicating the decrease in both age and Th/U ratio as recrystallization proceeds from partial (open symbols) to complete (solid symbols). Error bars are 1σ; (b) element–element plots for internal structures; (c) chondrite-normalized REE plots for recrystallized zircon and recrystallization front in a single crystal. Figure after Hoskin and Black (2000).

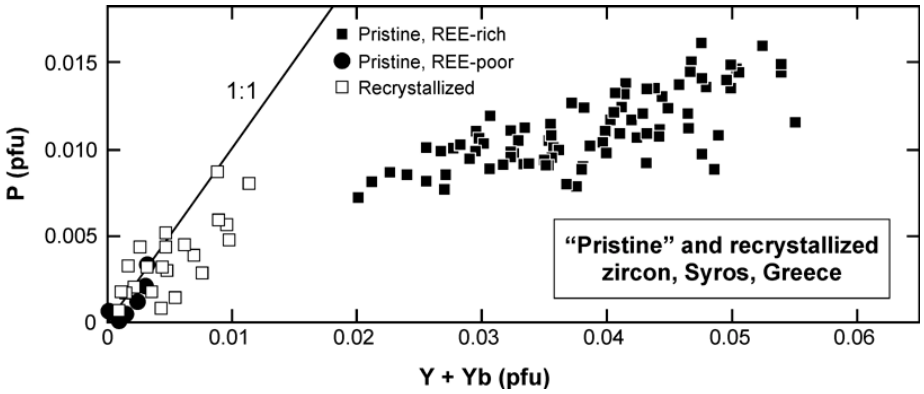


**Figure 12.** Phosphorus (per formula unit, pfu) versus Y + Yb (pfu) composition of zircon from a felsic meta-tuff, Syros, Greece. Pristine zircon with Y + Yb greater than 0.02 pfu (solid square symbols) have experienced partial to complete recrystallization with consequent reduction of P, Y and Yb (open square symbols). Pristine zircon that is relatively REE-poor has not recrystallized (solid circle symbols). The solid line joins points of equal P (pfu) and Y + Yb (pfu). Figure after Tomaschek et al. (2003).

textures—the preservation of primary textures, albeit altered—do not favor a mechanism of local dissolution-reprecipitation. This is, however, the mechanism proposed by Tomaschek et al. (2003) (see also Putnis 2002, p. 694), whose recrystallized zircon do not preserve ghost textures, but have ~10 vol % porosity and remnant fluid-inclusion voids, both of which are not observed in unaltered ("pristine") crystals. The fluid responsible for dissolution in this case, must also have been responsible for the dissolution of the numerous apatite and silicate inclusions in those crystals.

The role of metamictization in recrystallization by dissolution-reprecipitation and compositional change has been evaluated experimentally and analytically by Geisler et al. (2001, 2002, 2003). Metamict zircon is more susceptible to dissolution-reprecipitation because of the occurrence of amorphous zones and metamictization-induced fractures which allow fluid infiltration and exchange (Valley et al. 1994). Geisler et al. (2001), in hydrothermal experiments at 450°C, 1.3 kbar and 2 M $CaCl_2$ solution, recrystallized metamict rims on Sri Lanka zircon. The reaction rims are partially to fully structurally recovered (i.e., crystalline, not metamict) and have sharp, curved and transgressive boundaries with unreacted zircon (Putnis 2002, Fig. 5 therein) similar to the secondary transgressive textures produced geologically. Compositionally, the rims have lost radiogenic Pb, Zr, Si and have a reduced Th/U ratio, and have been enriched relative to unreacted zircon in Ca, Al (Geisler et al. 2002) and an undefined "water species". Metamict areas in zircon from the eastern Desert, Egypt, have exchanged with a low-temperature (120-200°C) aqueous fluid and are heavily enriched in Ca, Al, Fe, Mn, LREE and a water species, and have lost Zr, Si and radiogenic Pb (Geisler et al. 2003). Although these data indicate that fluid-induced recrystallization and isotopic resetting or discordance might be important in nature, the applicability of the results to higher-grade metamorphic zircon is unclear especially because many of the experimentally produced secondary textures are not commonly observed naturally, if at all. This may be because fluid-present recrystallization can also occur for non-metamict zircon, producing different secondary textures but similar compositional change including lowering of Th/U ratios and U–Pb isotope resetting (e.g., Liati and Gebauer 1999, Rubatto et al. 1999, Schaltegger et al. 1999).

## HYDROTHERMAL ZIRCON

Zircon formation is not commonly associated with hydrothermal activity. In fact, it has been documented to be replaced by the hydrothermal deposition of zirconolite, $(Ca,REE)ZrTi_2O_7$, and a series of REE-phosphates, carbonates and oxides-hydroxides (Gieré 1996). Consequently, early

reports of hydrothermal zircon were met with skepticism (Claoué-Long et al. 1990, Corfu and Davis 1991, Claoué-Long et al. 1992). Since the early 1990s there have been an increasing number of reports of hydrothermal zircon. Williams et al. (1996) documented an extended episode of fluid-flow during high-grade metamorphism by dating hydrothermal zircon from metamorphic quartz veins. Most reports of hydrothermal zircon, however, are from relatively low- to medium-temperature and low-pressure events associated with economic deposition of Au and other metals and these occurrences are considered below.

Hydrothermal zircon has been reported from Archean massive sulfide deposits (Yeats et al. 1996), vein-type Archean gold deposits in Canada, China and Australia (Claoué-Long et al. 1990, Kerrich and King 1993, Li et al. 1997, Yeats et al. 1996), and a variety of shear and terrane suture zones (Wyoming Province, Mueller et al. 1996; Kaapvaal Craton, Flowers 2000; Newfoundland Appalachians, Ramezani et al. 2000). Despite these studies no consistent picture of hydrothermal zircon textures and composition has been forthcoming; anhedral and faceted morphologies and zoned and unzoned crystals have been described as hydrothermal, as have low common-Pb and high common-Pb zircon. The hydrothermal zircon of Yeats et al. (1996) fall into two distinct sub-populations on the basis of REE composition (P.W.O. Hoskin, unpublished data) even though there is no distinction between them on the basis of morphology or internal textures and they form a single U–Pb age population. The igneous-style normalized REE patterns and the absence of fluid-inclusions brings into question the interpretation of these zircons as being hydrothermal. In fact, the occurrence of zircon in hydrothermal veins, or even as inclusions in hydrothermal minerals, is not evidence enough that the zircon is likewise hydrothermal. For example, Hack et al. (1998) separated zircon from near-monomineralic hydrothermal quartz veins (with accessory Au-Bi alloys and zircon) and on the basis of U–Pb isotope ages concluded that the zircon was xenocrystic from the host meta-sediment. Zircon from the assimilated host-rock was the only mineral phase not to completely dissolve into the quartz-depositing hydrothermal fluid.

No such doubt of origin exists in the case of zircons described by Kerrich and King (1993) which contain inclusions of Au and fluid, or for fluid-inclusion-rich and "stringer" zircon from the Sierra Blanca Peaks, Texas (Rubin et al. 1989). Other criteria for identifying zircon as hydrothermal may include: "spongy texture" due to a high frequency of fluid-inclusions (Hoskin et al. 1998); high common-Pb abundance (Watson et al. 1997); and elevated abundances of F, LREE, Nb, Ta and other incompatible elements (Rubin et al. 1989, Hoskin et al. 1998) as expected from the type of fluids that mobilize Zr (Taylor et al. 1980, Rubin et al. 1993, Campbell 1998).

Trace-element characteristics of hydrothermal zircon have been described in two independent studies both of granitoids in eastern Australia (Boggy Plain Zoned Pluton, Hoskin et al. (1998) and Hoskin (1999); Mole Granite, Pettke et al. (2001) and Schaltegger et al. (2001)). Both granitoids are W-mineralized by fluids derived by magmatic differentiation (the Mole Granite is also Sn-mineralized). Despite similar geographical and geological contexts, the zircon compositional characteristics are contradictory (Fig. 13). Hydrothermal zircon from the Boggy Plain Zoned Pluton is enriched in the REE relative to igneous zircon which has a typical igneous-style normalized REE pattern. In particular, the LREE are enriched by about two orders of magnitude, although the Ce-anomaly is decreased from Ce/Ce* = 32-77 for igneous zircon to Ce/Ce* = 0.06-4.2 for hydrothermal zircon. Enrichment in the LREE is accompanied by enrichment in F, Y, Sc, Nb, Ta, Hf, Th and U (with fluid-inclusion hosted Mo, W and Au detected in some analyses). In contrast, REE abundances of hydrothermal zircon from the Mole Granite are depleted by 1 to 3 orders of magnitude relative to igneous zircon and have an increased Ce-anomaly. The significance of these contradictory data is presently unknown, but may reflect different hydrothermal mineral assemblages: in the Boggy Plain Zoned Pluton, hydrothermal zircon is precipitated with scheelite, ilmenite, rutile and yttrobetafite, whilst in the Mole Granite, hydrothermal zircon precipitated with monazite, thorite and xenotime. Differences in fluid origins, composition and $fO_2$ are also likely to be important.

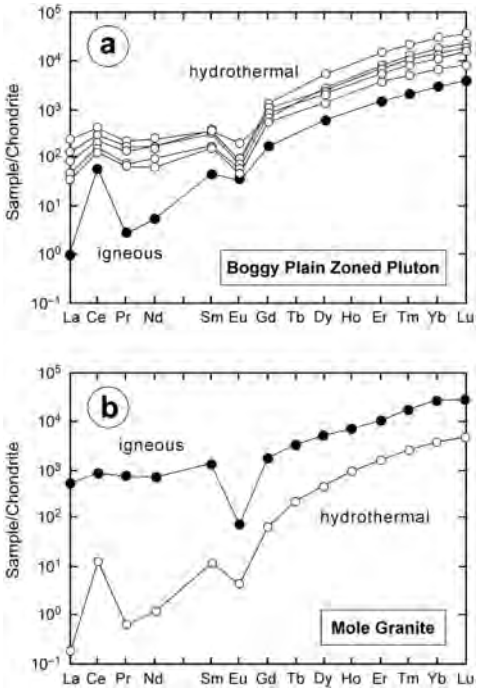


**Figure 13.** Chondrite-normalized REE patterns of hydrothermal zircon. The zircon crystallized under conditions of high aqueous-fluid activity at the end of magmatic crystallization. Both examples are from mineralized intrusions in southeast Australia: (a) Boggy Plain Zoned Pluton (Hoskin et al. 1998); (b) Mole Granite (Pettke et al., unpublished data).

## CONCLUSIONS AND OUTLOOK

Zircon is a host of geochemically important elements that are used for isotopic age determination and for petrogenetic process investigation. Unaltered igneous zircon generally contains less that 1 wt % of the REE and Y. Chondrite normalized abundance patterns are HREE enriched relative to the LREE and rise steeply from La to Lu. If zircon saturates early in the differentiation of a magma and fractionates, it tends to deplete the residual melt in the HREE. The normalized REE pattern varies little and zircon from very different source-rocks have very similar REE patterns. There appears to be no systematic compositional differences between zircon from different parageneses. The implications of this are that back-calculation of melt compositions from zircon trace-element abundances and partition coefficients, as well as provenance investigations and source-rock "finger-printing," can lead to spurious results. Although zircon with a mantle-affinity has distinct REE characteristics, it is not clear why crustal zircons are so similar. This is an obvious area for future research that must include experimental and high-quality analytical studies of trace-element substitution mechanisms. It seems reasonable to predict that $H^+$ and OH, as well as interstitial Al, play a significant, yet currently under-recognized role in charge-balancing Y and REE in zircon. An important feature of the normalized igneous zircon REE pattern is the occurrence of Ce and Eu-anomalies, both of which are probably fully or partly controlled by oxygen fugacity. Experimental investigations of these anomalies should improve current understanding of why the anomalies exist and what they can tell us about magma genesis.

Metamorphic zircon appears to better retain a record of petrogenesis. A few studies have demonstrated that cogenetic zircon and garnet growth produces a normalized HREE pattern where the HREE in zircon dramatically drop away from expected values due to competition from co-crystallizing garnet. More dramatic patterns may be observed for zircon that has grown in the presence of metamorphic xenotime, monazite or an epidote-group mineral. Surprisingly, there is no clear understanding of why the Th/U ratio of metamorphic zircon is often ~0.01 or lower, when apparently igneous zircon has a value of >0.5. It may be that this is due to the presence of a fluid during metamorphic crystallization and in some cases due to differential expulsion of cations from zircon

during recrystallization. The phenomenon of sector zoning has received theoretical treatment from Watson and Liang (1995) and its occurrence is fairly well understood. The occurrence of sector zoning due to intersectoral trace-element partitioning may be temperature sensitive and could be calibrated as a thermometer.

## ACKNOWLEDGMENTS

Discussions with John Hanchar, Ian Williams, Trevor Ireland, Hugh O'Neill, Richard Armstrong, Rodney Grapes, Richard Wysoczanski, Wayne Taylor, Thorsten Geisler, Chris Ballhaus, Michael Palin and Robert Linnen helped clarify various aspects of this contribution. We thank Paul Ribbe for his professional assistance.

## REFERENCES

Ahrens LH (1965) Some observations on the uranium and thorium distributions in accessory zircon from granitic rocks. Geochim Cosmochim Acta 29:711-716

Ahrens LH, Cherry RD, Erlank AJ (1967) Observations on the Th-U relationship in zircons from granite rocks and from kimberlites. Geochim Cosmochim Acta 31:2379-2387

Ahrens LH, Erlank AJ (1969) Hafnium. *In* Handbook of Geochemistry. Vol 2, part 5, sections B-O. Wedepohl KH (ed) Springer-Verlag, Berlin–Heidelberg–New York

Amelin Y, Zaitsev AN (2002) Precise geochronology of phoscorites and carbonatites: the critical role of U-series disequilibrium in age interpretations. Geochim Cosmochim Acta 66:2399-2419

Bacon CR (1989) Crystallization of accessory phases in magmas by local saturation adjacent to phenocrysts. Geochim Cosmochim Acta 53:1055-1066

Baker DR, Conte AM, Freda C, Ottolini L (2002) The effect of halogens on Zr diffusion and zircon dissolution in hydrous metaluminous granitic melts. Contrib Mineral Petrol 142:666-678

Ballard JR, Palin JM, Campbell IH (2002) Relative oxidation states of magmas inferred from Ce(IV)/Ce(III) in zircon: application to porphyry copper deposits of northern Chile. Contrib Mineral Petrol 144:347-364

Barbey P, Allé P, Brouand M, Albarède F (1995) Rare-earth patterns in zircons from the Manaslu granite and Tibetan Slab migmatites (Himalaya): insights in the origin and evolution of a crustally-derived granite magma. Chem Geol 125:1-17

Baruah J, Kotoky P, Sarma JN (1995) Zircons in Jhanji river sediments. Bull Pure Appl Sci, Section F: Geol Sci 14F:35-40

Bea F (1996) Residence of REE, Y, Th and U in granites and crustal protoliths; implications for the chemistry of crustal melts. J Petrol 37:521-552

Bea F, Montero P (1999) Behaviour of accessory phases and redistribution of Zr, REE, Y, Th and U during metamorphism and partial melting of metapelites in the lower crust: an example from the Kinzigite Formation of Ivrea-Verbano, NW Italy. Geochim Cosmochim Acta 63:1133-1153

Bea F, Pereira MD, Stroh A (1994) Mineral/leucosome trace-element partitioning in a peraluminous migmatite (a laser ablation-ICP-MS study). Chem Geol 117:291-312

Belousova EA, Griffin WL, Pearson NJ (1998) Trace element composition and cathodoluminescence properties of southern African kimberlitic zircons. Mineral Mag 62:355-366

Belousova EA, Griffin WL, O'Reilly SY, Fisher NJ (2002) Igneous zircon: trace element composition as an indicator of source rock type. Contrib Mineral Petrol 143:602-622

Benisek A, Finger F (1993) Factors controlling the development of prism faces in granite zircons: A microprobe study. Contrib Mineral Petrol 114:441-451

Bingen B, Austrheim H, Whitehouse M (2001) Ilmenite as a source for zirconium during high-grade metamorphism? Textural evidence from the Caledonides of W. Norway and implications for zircon geochronology. J Petrol 42:355-375

Black LP, Williams IS, Compston W (1986) Four zircon ages from one rock: the history of a 3930 Ma-old granulite from Mount Sones, Enderby Land, Antarctica. Contrib Mineral Petrol 94:427-437

Blagojevic N, Garrett RF, Stampfl APJ, Cai Z, Lai B, Legnini DG, Rodrigues W (2000) Synchrotron X-ray microprobe analysis of radioactive trace elements in zircon and ilmenite. *In* Speciation, Techniques and Facilities for Radioactive Materials at Synchrotron Light Sources. NEA Workshop Proc, Grenoble, France, p 199-206

Bussy F, Cadoppi P (1996) U-Pb zircon dating of granitoids from the Dora-Maira massif (western Italian Alps). Schweiz Mineral Petrogr Mitt 76:217-233

Cameron KL, Hanson GN (1982) Rare earth element evidence concerning the origin of voluminous mid-Tertiary rhyolitic ignimbrites and related volcanic rocks, Sierra Madre Occidental, Chihuahua, Mexico. Geochim Cosmochim Acta 46:1489-1503

Campbell LS (1998) Zircon-fluid interaction in the Bayan Obo REE-Nb-Fe ore deposit, Inner Mongolia, China. *In*

Water-Rock Interaction, WRI-9. Arehart GB, Hulston JR (eds) AA Balkema, Rotterdam, p 521-523
Caruba R, Iacconi P (1983) Les zircons des pegmatites de Narssârssuk (Groëland)—l'eau et les groupments OH dans les zircons meamictes. Chem Geol 38:75-92
Chen YD, Williams IS (1990) Zircon inheritance in mafic inclusions from Bega Batholith granites, southeastern Australia: an ion microprobe study. J Geophys Res 95:17,787-17,796
Cherniak DJ, Hanchar JM, Watson EB (1997a) Rare-earth diffusion in zircon. Chem Geol 134:289-301
Cherniak DJ, Hanchar JM, Watson EB (1997b) Diffusion of tetravalent cations in zircon. Contrib Mineral Petrol 127:383-390
Chesner CA (1998) Petrogenesis of the Toba Tuffs, Sumatra, Indonesia. J Petrol 39:397-438
Chen YD, Williams IS (1990) Zircon inheritance in mafic inclusions from Bega Batholith granites, southeastern Australia: an ion microprobe study. J Geophys Res 95:17,787-17,796
Chiarenzelli JR, McLelland JM (1993) Granulite facies metamorphism, palaeo-isotherms and disturbance of the U-Pb systematics of zircon in anorogenic plutonic rocks from the Adirondack Highlands. J Metamor Geol 11:59-70
Claoué-Long JC, King RW, Kerrich R (1990) Archaean hydrothermal zircon in the Abitibi greenstone belt: constraints on the timing of gold mineralisation. Earth Planet Sci Lett 98:109-128
Claoué-Long JC, King RW, Kerrich R (1992) Reply to comment by F. Corfu and D.W. Davis on "Archaean hydrothermal zircon in the Abitibi greenstone belt: constraints on the timing of gold mineralisation". Earth Planet Sci Lett 109:601-609
Corfu F, Davis DW (1991) Comment on "Archean hydrothermal zircon in the Abitibi greenstone belt: constraints on the timing of gold mineralization" by J.C. Claoué-Long, R.W. King and R. Kerrich. Earth Planet Sci Lett 104:545-552
Correia Neves JM, Lopes Nunes JE, Sahama ThG (1974) High hafnium members of the zircon-hafnon series from the granite pegmatites of Zambézia, Mozambique. Contrib Mineral Petrol 48:73-80
Crocombette JP (1999) Theoretical study of point defects in crystalline zircon. Phys Chem Minerals 27:138-143
Currie KL, Knutson J, Temby PA (1992) The Mud Tank carbonatite complex, central Australia—an example of metasomatism at mid-crustal levels. Contrib Mineral Petrol 109:326-339
Dabard MP, Loi A, Peucat JJ (1996) Zircon typology combined with Sm-Nd whole-rock isotope analysis to study Brioverian sediments from the Armorican Massif. Sed Geol 101:243-260
de la Rosa JD, Jenner GA, Castro A (2002) A study of inherited zircons in granitoid rocks from the South Portuguese and Ossa-Morena Zones, Iberian Massif: support for the exotic origin of the South Portuguese Zone. Tectonophysics 352:245-256
Degeling H, Eggins S, Ellis DJ (2001) Zr budgets for metamorphic reactions, and the formation of zircon from garnet breakdown. Mineral Mag 65:749-758
Dickinson JE Jr, Hess PC (1982) Zircon saturation in lunar basalts and granites. Earth Planet Sci Lett 57:336-344
Dowty E (1980) Crystal growth and nucleation theory and the numerical simulation of igneous crystallization. *In* Physics of Magmatic Processes. Hargraves RB (ed) Princeton University Press, Princeton, New Jersey, p 419-485
Es'kova EM (1959) Geochemistry of Nb and Ta in the nepheline syenite massifs of the Vishnevyie Mountains. Geokhimiya 2:130-139 (in Russian)
Evans OC, Hanson GN (1993) Accessory-mineral fractionation of rare-earth element (REE) abundances in granitoid rocks. Chem Geol 110:69-93
Farges F (1996) Does Zr-F "complexation" occur in magmas? Chem Geol 127:253-268
Feng R, Machado N, Ludden J (1993) Lead geochronology of zircon by laser probe inductively coupled plasma mass spectrometry (LP-ICP-MS). Geochim Cosmochim Acta 57:3479-3486
Finch RJ, Hanchar JM, Hoskin PWO, Burns PC (2001) Rare-earth elements in synthetic zircon: Part 2. A single-crystal X-ray study of xenotime substitution. Am Mineral 86:681-689
Flowers RM (2000) Structural and geochronological investigation of the Archean basement along the projection of the Vredefort discontinuity, Vredefort impact structure, Kaapvaal Craton, South Africa. MS thesis, University of Utah, Provo, Utah
Fowler A, Prokoph A, Stern R, Dupuis C (2002) Organization of oscillatory zoning in zircon: Analysis, scaling, geochemistry, and model of a zircon from Kipawa, Quebec, Canada. Geochim Cosmochim Acta 66:311-328
Fraser G, Ellis D, Eggins S (1997) Zirconium abundance in granulite-facies minerals, with implications for zircon geochronology in high-grade rocks. Geology 25:607-610
Frondel C (1953) Hydroxyl substitution in thorite and zircon. Am Mineral 38:1007-1018
Fujimaki H (1986) Partition coefficients of Hf, Zr, and REE between zircon, apatite, and liquid. Contrib Mineral Petrol 94:42-45
Geisler T, Pidgeon RT, van Bronswijk W, Kurtz R (2002) Transport of uranium, thorium, and lead in metamict zircon under low-temperature hydrothermal conditions. Chem Geol 191:141-154
Geisler T, Rashwan AEA, Rahn MKW, Poller U, Zwingmann H, Pidgeon RT, Schleicher H, Tomaschek F (2003) Low-temperature hydrothermal alteration of natural metamict zircons from the Eastern Desert, Egypt. Mineral Mag (in press)

Geisler T, Schleicher H (2000) Improved U-Th-total Pb dating of zircons by electron microprobe using a simple new background modeling procedure and Ca as a chemical criterion of fluid-induced U-Th-Pb discordance in zircon. Chem Geol 163:269-285

Geisler T, Ulonska M, Schleicher H, Pidgeon RT, van Bronswijk W (2001) Leaching and differential recrystallization of metamict zircon under experimental hydrothermal conditions. Contrib Mineral Petrol 141:53-65

Gieré R (1996) Formation of rare earth minerals in hydrothermal systems. *In* Rare earth minerals: chemistry, origin and ore deposits. Jones AP, Wall F, Williams CT (eds) Chapman Hall, p 105-150

Gorz H (1974) Microprobe studies of inclusions and compilation of minor and trace elements in zircons from the literature. Chemie der Erde 33:326-357

Griffin WL, Wang X, Jackson SE, Pearson NJ, O'Reilly SY, Xu X, Zhou X (2002) Zircon chemistry and magma mixing, SE China: *in situ* analysis of Hf isotopes, Tonglu and Pingtan igneous complexes. Lithos 61:237-269

Gromet LP, Silver LT (1983) Rare earth element distributions among minerals in a granodiorite and their petrogenetic implications. Geochim Cosmochim Acta 47:925-939

Guo J, O'Reilly SY, Griffin WL (1996) Zircon inclusions in corundum megacrysts: I. Trace element geochemistry and clues to the origin of corundum megacrysts in alkali basalts. Geochim Cosmochim Acta 60:2347-2363

Hack AC, Mavrogenes JA, Hoskin PWO, Scott RJ (1998) A turbidite-hosted gold(-bismuth) quartz vein deposit, Union Hill Mine, Maldon, central Victoria. Geol Soc Austral (abstr) 49:194

Halden NM, Hawthorne FC (1993) The fractal geometry of oscillatory zoning in crystals: application to zircon. Am Mineral 78:1113-1116

Halden NM, Hawthorne FC, Campbell JL, Teesdale WJ, Maxwell JA, Higuchi D (1993) Chemical characterization of oscillatory zoning and overgrowths in zircon using 3 MeV μ-PIXE. Can Mineral 31:637-647

Hanchar JM, Finch RJ, Hoskin PWO, Watson EB, Cherniak DJ, Mariano AN (2001) Rare earth elements in synthetic zircon: Part I. Synthesis, and rare-earth element and phosphorous doping of zircon. Am Mineral 86:667-680

Hanchar JM, Hoskin PWO (1998) Mud Tank Carbonatite, Australia, zircon. Soc Lum Micros Spec News 10:2-3

Hanchar JM, Miller CF (1993) Zircon zonation patterns as revealed by cathodoluminescence and backscattered electron images: implications for interpretation of complex crustal histories. Chem Geol 110:1-13

Hanchar JM, Rudnick RL (1995) Revealing hidden structures: the application of cathodoluminescence and backscattered electron imaging to dating zircon from lower crustal xenoliths. Lithos 36:289-303

Harrison TM, Watson EB (1983) Kinetics of zircon dissolution and zirconium diffusion in granitic melts of variable water content. Contrib Mineral Petrol 84:66-72

Heaman LM, Bowins R, Crocket J (1990) The chemical composition of igneous zircon suites: implications for geochemical tracer studies. Geochim Cosmochim Acta 54:1597-1607

Hermann J, Rubatto D, Korsakov A, Shatsky VS (2001) Multiple zircon growth during fast exhumation of diamondiferous, deeply subducted continental crust (Kokchetav massif, Kazachstan). Contrib Mineral Petrol 141:66-82

Hidaka H, Shimizu H, Adachi M (2002) U-Pb geochronology and REE geochemistry of zircons from Palaeoproterozoic paragneiss clasts in the Mesozoic Kamiaso conglomerate, central Japan: evidence for an Archean provenance. Chem Geol 187:279-293

Hinton RW, Meyer C (1991) Ion probe analysis of zircon and yttrobetafite in a lunar granite. Lunar Planet Sci 22:575-576

Hinton RW, Upton BGJ (1991) The chemistry of zircon: variations within and between large crystals from syenite and alkali basalt xenoliths. Geochim Cosmochim Acta 55:3287-3302

Hirata T, Nesbitt RW (1995) U-Pb isotope geochronology of zircon: evaluation of the laser probe inductively coupled plasma mass spectrometry technique. Geochim Cosmochim Acta 59:2491-2500

Hoffmann C (1981) Chi-square testing of zircon populations from an Archean granite-greenstone terrain, Minas Gerais, Brazil. Neues Jahrb Mineral Abh 140:202-220

Holten T, Jamtveit B, Meakin P, Cortini M, Blundy J, Austrheim H (1997) Statistical characteristics and origin of oscillatory zoning in crystals. Am Mineral 82:596-606

Hoskin PWO (1998) Minor and trace element analysis of natural zircon ($ZrSiO_4$) by SIMS and laser ablation ICPMS: a consideration and comparison of two broadly competitive techniques. J Trace Microprobe Tech 16:301-326

Hoskin PWO (1999) SIMS determination of μg $g^{-1}$-level fluorine in geological samples and its concentration in NIST SRM 610. Geostand News: J Geostand Geoanal 23:69-76

Hoskin PWO (2000) Patterns of chaos: Fractal statistics and the oscillatory chemistry of zircon. Geochim Cosmochim Acta 64:1905-1923

Hoskin PWO, Black LP (2000) Metamorphic zircon formation by solid-state recrystallization of protolith igneous zircon. J Metamor Geol 18:423-439

Hoskin PWO, Ireland TR (2000) Rare earth element chemistry of zircon and its use as a provenance indicator. Geology 28:627-630

Hoskin PWO, Kinny PD, Wyborn D (1998) Chemistry of hydrothermal zircon: investigating timing and nature of water-rock interaction. *In* Water-Rock Interaction, WRI-9. Arehart GB, Hulston JR (eds) AA Balkema, Rotterdam, p 545-548

Hoskin PWO, Kinny PD, Wyborn D, Chappell BW (2000) Identifying accessory mineral saturation during differentiation in granitoid magmas: an integrated approach. J Petrol 41:1365-1396

Hoskin PWO, Rodgers KA (1996) Raman spectral shift in the isomorphous series $(Zr_{1-x}Hf_x)SiO_4$. Eur J Solid State Inorg Chem 33:1111-1121

Hower JC, Ruppert LF, Eble CF (1999) Lanthanide, yttrium, and zirconium anomalies in the Fire Clay coal bed, Eastern Kentucky. Intl J Coal Geol 39:141-153

Ireland TR, Wlotzka F (1992) The oldest zircons in the solar system. Earth Planet Sci Lett 109:1-10

Jackson SE, Longerich HP, Dunning GR, Freyer BJ (1992) The application of laser-ablation microprobe; inductively coupled plasma-mass spectrometry (LAM-ICP-MS) to in situ trace-element determinations in minerals. Can Mineral 30:1049-1064

Jain JC, Neal CR, Hanchar JM (2001) Problems associated with the determination of rare earth elements of a "gem" quality zircon by inductively coupled plasma-mass spectrometry. Geostand News: J Geostand Geoanal 25:229-237

Jeffries TE, Pearce NJG, Perkins WT, Raith A (1996) Chemical fractionation during infrared and ultraviolet laser ablation inductively coupled plasma mass spectrometry; implications for mineral microanalysis. Anal Comm 33:35-39

Katayama I, Masahito O, Yoshihide O (2002) Mineral inclusions in zircon from diamond-bearing marble in the Kokchetav Massif, northern Kazakhstan. Eur J Mineral 14:1103-1108

Katayama I, Maruyama S, Parkinson C, Terada K, Sano Y (2001) Ion micro-probe U-Pb zircon geochronology of peak and retrograde stages of ultrahigh-pressure metamorphic rocks from the Kokchetav massif, northern Kazachstan. Earth Planet Sci Lett 188:185-198

Kempe U, Gruner T, Nasdala L, Wolf D (2000) Relevance of cathodoluminescence for the interpretation of U-Pb zircon ages, with example of an application to a study of zircons from the Saxonian Granulite Complex, Norway. *In* Cathodoluminescence in Geosciences. Pagel M, Barbin V, Blanc P, Ohnenstetter D (eds) Springer, Berlin, p 415-455

Keppler H (1993) Influence of fluorine on the enrichment of high field strength trace elements in granitic rocks. Contrib Mineral Petrol 114:479-488

Kerrich R, King R (1993) Hydrothermal zircon and baddeleyite in Val d'Or Archean meothermal gold deposits: characteristics, compositions, and fluid-inclusion properties, with implications for timing of primary gold mineralization. Can J Earth Sci 30:2334-2352

Kinny PD, Compston W, Williams IS (1991) A reconnaissance ion-probe study of hafnium isotopes in zircons. Geochim Cosmochim Acta 55:849-859

Köhler H (1970) Die änderung der Zirkonmorphologie mit dem differentiationsgrad eines Granits. Neues Jahrb Mineral Mh 9:405-420

Konzett J, Armstrong RA, Sweeny RJ, Compston W (1998) The timing of MARID metasomatism in the Kaapvaal mantle: an ion probe study of zircons from MARID xenoliths. Earth Planet Sci Lett 160:133-145

Kopchenova YV, Mineyeva IG, Mineyev DA (1974) Calcium and sodium cyrtolite from albitite bodies in the Ukraine. Doklady Trans USSR Acad Sci Earth Sci 217:116-119

Köppel V, Grünenfelder M (1971) A study of inherited and newly formed zircons from paragneisses and granitised sediments of the Strona-Ceneri-zone (Southern Alps). Schweiz Mineral Petrogr Mitt 51:385-409

Köppel V, Sommerauer J (1974) Trace elements and the behaviour of the U—Pb system in inherited and newly formed zircons. Contrib Mineral Petrol 43:71-82

Kornacki AS, Fegley B Jr (1986) The abundance and relative volatility of refractory trace elements in Allende Ca, Al-rich inclusions: implications for chemical and physical processes in the sola nebula. Earth Planet Sci Lett 79:217-234

Koschek G (1993) Origin and significance of the SEM cathodoluminescence from zircon. J Micros 171:223-232

Kostov I (1973) Zircon morphology as a crystallogenetic indicator. Kristal Tech 8:11-19.

Kresten P, Fels P, Berggren G (1975) Kimberlitic zircons—a possible aid in prospecting for kimberlites. Mineral Dep 10:47-56

Larsen LH, Poldervaart A (1957) Measurement and distribution of zircons in some granitic rocks of magmatic origin. Mineral Mag 31:544-564

Li J, Shen B, Mao D, Li S, Zhou H, Cheng Y (1997) Mineralization ages of the Jiapigou gold deposits, Jilin. Acta Geologica Sinica 71:180-188

Liati A, Gebauer D (1999) Constraining the prograde and retrograde *P-T-t* path of Eocene HP rocks by SHRIMP dating of different zircon domains: inferred rates of heating, burial, cooling and exhumation for central Rhodope, northern Greece. Contrib Mineral Petrol 135:340-354

Linnen RL, Keppler H (2002) Melt composition control of Zr/Hf fractionation in magmatic processes. Geochim Cosmochim Acta 66:3293-3301

Liu F, Xu Z, Liou JG, Katayama I, Masago H, Maruyama S, Yang J (2002) Ultrahigh-pressure mineral inclusions in zircons from gneissic core samples of the Chinese Continental Scientific Drilling Site in eastern China. Eur J Mineral 14:499-512

Maas R, Kinny PD, Williams IS, Froude DO, Compston W (1992) The Earth's oldest known crust: a geochronological and geochemical study of 3900-4200 Ma old detrital zircons from Mt. Narryer and Jack Hills, Western

Australia. Geochim Cosmochim Acta 56:1281-1300
Mahood G, Hildreth W (1983) Large partition coefficients for trace elements in high-silica rhyolites. Geochim Cosmochim Acta 47:11-30
McDonough WF, Sun S-S (1995) The composition of the Earth. Chem Geol 120:223-253
Meyer C, Yang SV (1988) Tungsten-bearing yttrobetafite in lunar granophyre. Am Mineral 73:1420-1425
Möller A, O'Brien PJ, Kennedy A, Kröner A (2002) Polyphase zircon in ultrahigh-temperature granulites (Rogaland, SW Norway): constraints for Pb diffusion in zircon. J Metamor Geol 20:727-740
Mueller PA, Wooden JL, Mogk DW, Nutman AP, Williams IS (1996) Extended history of a 3.5 Ga trondhjemitic gneiss, Wyoming Province, USA: evidence from U-Pb systematics in zircon. Precambrian Res 78:41-52
Murali AV, Parthasarathy R, Mahadevan TM, Sankar Das M (1983) Trace element characteristics, REE patterns and partition coefficients of zircons from different geological environments—A case study on Indian zircons. Geochim Cosmochim Acta 47:2047-2052
Nagasawa H (1970) Rare earth concentrations in zircon and their host dacites and granites. Earth Planet Sci Lett 9:359-364
Nasdala L, Beran A, Libowitzky E, Wolf D (2001) The incorporation of hydroxyl groups and molecular water in natural zircon ($ZrSiO_4$). Am J Sci 301:831-857
Nemchin AA, Pidgeon RT (1997) Evolution of the Darling Range Batholith, Yilgarn Craton, Western Australia: a SHRIMP zircon study. J Petrol 38:625-649
Nesbitt RW, Hirata T, Butler IB, Milton JA (1997) UV laser ablation ICP-MS: some applications in the Earth Sciences. Geostand News: J Geostand Geoanal 20:231-243
O'Hara MJ, Fry N, Prichard HM (2001) Minor phases as carriers of trace elements in non-modal crystal-liquid separation processes II: illustrations and bearing on behaviour of REE, U, Th and the PGE in igneous processes. J Petrol 42:1887-1910
Ono A (1976) Chemistry and zoning of zircon from some Japanese granitic rocks. J Japan Assoc Mineral Petrol Econ Geol 71:6-17
Pan Y (1997) Zircon- and monazite-forming metamorphic reactions at Manitouwadge, Ontario. Can Mineral 35:105-118
Paterson BA, Stephens WE, Herd DA (1989) Zoning in granitoid accessory minerals as revealed by backscattered electron imagery. Mineral Mag 53:55-62
Paterson BA, Stephens WE, Rogers G, Williams IS, Hinton RW, Herd DA (1992) The nature of zircon inheritance in two granite plutons. Trans Roy Soc Edinburgh: Earth Sci 83:459-471
Peck WH, Valley JW, Wilde SA, Graham CM (2001) Oxygen isotope ratios and rare earth elements in 3.3 to 4.4 Ga zircons: ion microprobe evidence for high $\delta 18O$ continental crust and oceans in the Early Archean. Geochim Cosmochim Acta 65:4215-4229
Perkins WT, Pearce NJG, Fuge R (1992) Analysis of zircon by laser ablation and solution inductively coupled plasma mass spectrometry. J Anal Atomic Spec 7:611-616
Pettke T, Audétat A, Schaltegger U, Heinrich CA (2001) Zircon trace element chemistry by LA-ICP-MS: a monitor for the magmatic-to-hydrothermal evolution of a crystallizing pluton? J Conf Abstr 6:680
Pidgeon RT (1992) Recrystallisation of oscillatory zoned zircon: some geochronological and petrological implications. Contrib Mineral Petrol 110:463-472
Pidgeon RT, Nemchin AA, Hitchen GJ (1998) Internal structures of zircons from Archaean granites from the Darling Range batholith: implications for zircon stability and the interpretation of zircon U-Pb ages. Contrib Mineral Petrol 132:288-299
Poldervaart A (1955) Zircons in rocks, 1. Sedimentary rocks. Am J Sci 253:433-461
Poldervaart A (1956) Zircons in rocks, 2. Igneous rocks. Am J Sci 254:521-554
Poller U, Huth J, Hoppe P, Williams IS (2001) REE, U, Th, and Hf distribution in zircon from western Carpathian Variscan granitoids: a combined cathodoluminescence and ion microprobe study. Am J Sci 301:858-876
Pupin JP (1980) Zircon and granite petrology. Contrib Mineral Petrol 73:207-220
Pupin JP, Turco G (1972a) Une typologie originale du zircon accessoire. Bull Soc Fr Minéral Cristallogr 95:348-359
Pupin JP, Turco G (1972b) Application des données morphologiques du zircon accessoire en pétrologie endogène. C R Acad Sci Paris 275D:799-802
Pupin JP, Turco G (1972c) Le zircon accessoire en géothermométrie. C R Acad Sci Paris 274D:2121-2124
Putnis A (2002) Mineral replacement reactions: from macroscopic observations to microscopic mechanisms. Mineral Mag 66:689-708
Ramakrishnan SS, Gokhale KVGK, Subbarao EC (1969) Solid solubility in the system zircon-hafnon. Mater Res Bull 4:323-328
Ramezani J, Dunning GR, Wilson MR (2000) Geologic setting, geochemistry of alteration, and U-Pb age of hydrothermal zircon from the Silurian Stog'er Tight gold prospect, Newfoundland Appalachians, Canada. Explor Mining Geol 9:171-188
Remond G, Cesbron F, Chapoulie R, Ohnenstetter D, Rosques-Carmes C, Schoverer M (1992) Cathodoluminescence applied to the microcharacterization of mineral materials: a present status in experimentation and interpretation.

Scanning Micros 6:23-68
Roberts MP, Finger F (1997) Do U-Pb zircon ages from granulites reflect peak metamorphic conditions? Geology 25:319-322
Robie RA, Hemingway BS, Fisher JR (1979) Thermodynamic properties of minerals and related substances at 298.15 K and 1 bar ($10^5$ Pascals) pressure and at higher temperatures (reprinted with corrections). U S Geol Surv Bull
Romans PA, Brown LL, White JC (1975) An electron microprobe study of yttrium, rare earth and phosphorous distribution in zoned and ordinary zircon. Am Mineral 60:475-480
Rubatto D (2002) Zircon trace element geochemistry: partitioning with garnet and the link between U-Pb ages and metamorphism. Chem Geol 184:123-138
Rubatto D, Gebauer D (2000) Use of cathodoluminescence for U-Pb zircon dating by ion microprobe: some examples from the Western Alps. *In* Cathodoluminescence in Geosciences. Pagel M, Barbin V, Blanc P, Ohnenstetter D (eds) Springer, Berlin, p 373-400
Rubatto D, Gebauer D, Compagnoni R (1999) Dating of eclogite-facies zircons: the age of Alpine metamorphism in the Sesia-Lanzo zone (Western Alps). Earth Planet Sci Lett 167:141-158
Rubatto D, Williams IS, Buick IS (2001) Zircon and monazite response to prograde metamorphism in the Reynolds Range, central Australia. Contrib Mineral Petrol 140:458-468
Rubin JN, Henry CD, Price JG (1989) Hydrothermal zircons and zircon overgrowths, Sierra Blanca Peaks, Texas. Am Mineral 74:865-869
Rubin JN, Henry CD, Price JG (1993) The mobility of zirconium and other "immobile" elements during hydrothermal alteration. Chem Geol 110:29-47
Rupasinghe MS, Dissanayake CB (1987) The geochemistry and mineralogy of zircons from Sri Lanka. Bull Geol Soc Finland 59:3-19
Sano Y, Terada K, Fukuoka T (2002) High mass resolution ion microprobe analysis of rare earth elements in silicate glass, apatite and zircon: lack of matrix dependency. Chem Geol 184:217-230
Sawka WN (1988) REE and trace element variation in accessory minerals and hornblende from the strongly zoned McMurry Meadows Pluton, California. Trans Roy Soc Edinburgh: Earth Sci 79:157-168
Saxena SK (1966) Evolution of zircons in sedimentary and metamorphic rocks. Sedimentology 6:1-33
Schaltegger U, Audétat A, Pettke T, Heinrich CA (2001) Dating of magmatic and hydrothermal stages in a Sn-W-granite. J Conf Abstr 6:681
Schaltegger U, Fanning CM, Günther D, Maurin JC, Schulmann K, Gebauer D (1999) Growth, annealing and recrystallization of zircon and preservation of monazite in high-grade metamorphism: conventional and in-situ U-Pb isotope, cathodoluminescence and microchemical evidence. Contrib Mineral Petrol 134:186-201
Schreiber HD, Lauer HV, Thanyasir T (1980) The redox state of cerium in basaltic magmas: an experimental study of iron-cerium interactions in silicate melts. Geochim Cosmochim Acta 44:1599-1612
Scoates JS, Chamberlain KR (1995) Baddeleyite ($ZrO_2$) and zircon ($ZrSiO_4$) from anorthositic rocks of the Laramie anorthosite complex, Wyoming: petrologic consequences and U-Pb ages. Am Mineral 80:1317-1327
Shannon RD (1976) Revised effective ionic radii and systematic studies of inter-atomic distances in halides and chalcogenides. Acta Crystallogr A32:751-767
Shore M, Fowler AD (1996) Oscillatory zoning in minerals: a common phenomenon. Can Mineral 34:1111-1126
Shnyukov SE, Andreev AV, Savenok SP (2002) Monitoring of region-scale geological/metallogenic events on a basis of single-grain trace element geochemistry of zircon, monazite and apatite large detrital populations: Ukrainian Shield and some other regions as an example. Intl Symp Metallogeny Precam Shields, Kiev, Ukraine (abstr)
Shnyukov SE, Andreev AV, Belousova EA, Savenok SP (2002) X-ray fluorescence milliprobe analysis in geochemistry of accessory minerals: research potential in comparison with high spatial resolution analytical methods. Mineral Zh (Ukraine) 24:80-95 (in Russian)
Silver LT, Deutsch S (1963) Uranium-lead isotopic variations in zircons: a case study. J Geol 71:721-758
Snyder GA, Taylor LA, Crozaz G (1993) Rare earth element selenochemistry of immiscible liquids and zircon at Apollo 14: an ion probe study of evolved rocks on the Moon. Geochim Cosmochim Acta 57:1143-1149
Speer JA (1982) Zircon. Rev Mineral 5($2^{nd}$ edn):67-112
Sutherland FL, Bosshart G, Fanning CM, Hoskin PWO, Coenraads RR (2002) Sapphire crystallization, age and origin, Ban Huai Sai, Laos: age based on zircon inclusions. J Asian Earth Sci 20:841-849
Sutherland FL, Hoskin PWO, Fanning CM, Coenraads RR (1998) Models of corundum origin from alkali basalt terrains: a reappraisal. Contrib Mineral Petrol 133:356-372
Taylor RP, Strong DF, Kean BF (1980) The Topsoils igneous complex: Silurian-Devonian peralkaline magmatism in western Newfoundland. Can J Earth Sci 17:425-439
Thomas JB, Bodnar RJ, Shimizu N, Sinha AK (2002) Determination of zircon/melt trace element partition coefficients from SIMS analysis of melt inclusions in zircon. Geochim Cosmochim Acta 66:2887-2901
Tomaschek F, Kennedy A, Villa I, Lagos M, Ballhaus C (2003) Zircons from Syros, Cyclades, Greece—recrystallisation and mobilization of zircon during high pressure metamorphism. J Petrol (in press)
Uher P, Breiter K, Kleèka M, Pivec E (1998) Zircon in highly evolved Hercynian Homolka Granite, Moldanubian

Zone, Czech Republic: indicator of magma source and petrogenesis. Geologica Carpathica 49:151-160
Uher P, Cerny P (1998) Zircon in Hercynian granitic pegmatites of the western Carpathians, Slovakia. Geologica Carpathica 49:261-270
Upton BGJ, Hinton RW, Aspen P, Finch A, Valley JW (1999) Megacrysts and associated xenoliths: evidence for migration of geochemically enriched melts in the upper mantle beneath Scotland. J Petrol 40:935-956
Valley JW, Chiarenzelli JR, McLelland JM (1994) Oxygen isotope geochemistry of zircon. Earth Planet Sci Lett 126:187-206
Valley JW, Peck WH, King EM, Wilde SA (2002) A cool early Earth. Geology 30:351-354
van Breemen O, Henderson JB, Loveridge WD, Thompson PH (1987) U-Pb zircon and monazite geochronology and zircon morphology of granulites and granite from the Thelon Tectonic Zone, Healey Lake and Artillery Lake map areas, NWT. Current Research Part A, Geol Survey Canada Paper 87-1A:783-801
Vavra G (1990) On the kinematics of zircon growth and its petrogenetic significance: a cathodoluminescence study. Contrib Mineral Petrol 106:90-99
Vavra G (1993) A guide to quantitative morphology of accessory zircon. Chem Geol 110:15-28
Vavra G (1994) Systematics of internal zircon morphology in major Variscan granitoid types. Contrib Mineral Petrol 117:331-334
Vavra G, Gebauer D, Schmid R, Compston W (1996) Multiple zircon growth and recrystallisation during polyphase Late Carboniferous to Triassic metamorphism in granulites of the Ivrea Zone (Southern Alps): an ion microprobe (SHRIMP) study. Contrib Mineral Petrol 122:337-358
Vavra G, Schmid R, Gebauer D (1999) Internal morphology, habit and U-Th-Pb microanalysis of amphibolite-to-granulite facies zircons: geochronology of the Ivrea zone (Southern Alps). Contrib Mineral Petrol 134:380-404
Wark DA, Miller CF (1993) Accessory mineral behavior during differentiation of a granite suite: monazite, xenotime and zircon in the Sweetwater Wash pluton, southeastern California, U.S.A. Chem Geol 110:49-67
Wang X, Griffin WL, O'Reilly SY, Zhou XM, Xu XS, Jackson SE, Pearson NJ (2002) Morphology and geochemistry of zircons from late Mesozoic igneous complexes in coastal SE China: implicaitions for petrogenesis. Mineral Mag 66:235-251
Watson EB (1979) Zircon saturation in felsic liquids: experimental results and applications to trace element geochemistry. Contrib Mineral Petrol 70:407-419
Watson EB (1980) Some experimentally determined zircon/liquid partition coefficients for the rare earth elements. Geochim Cosmochim Acta 44:895-897
Watson EB (1996a) Dissolution, growth and survival of zircons during crustal fusion: Kinetic principles, geological models and implications for isotopic inheritance. Trans Roy Soc Edinburgh: Earth Sci 87:43-56. Also: Geol Soc Am Spec Paper 315:43-56
Watson EB (1996b) Surface enrichment and trace-element uptake during crystal growth. Geochim Cosmochim Acta 60:5013-5020
Watson EB, Cherniak DJ, Hanchar JM, HarrisonTM, Wark DA (1997) The incorporation of Pb into zircon. Chem Geol 141:19-31
Watson EB, Harrison TM (1983) Zircon saturation revisited: temperature and composition effects in a variety of crustal magma types. Earth Planet Sci Lett 64:295-304
Watson EB, Liang Y (1995) A simple model for sector zoning in slowly grown crystals: implications for growth rate and lattice diffusion, with emphasis on accessory minerals in crustal rocks. Am Mineral 80:1179-1187
Watson EB, Vicenzi EP, Rapp RP (1989) Inclusion/host relations involving accessory minerals in high-grade metamorphic and anatectic rocks. Contrib Mineral Petrol 101:220-231
Watt GR, Harley SL (1993) Accessory phase controls on the geochemistry of crustal melts and restites produced during water-undersaturated partial melting. Contrib Mineral Petrol 114:550-556
Wayne DM, Sinha AK (1988) Physical and chemical response of zircons to deformation. Contrib Mineral Petrol 98:109-121
Wayne DM, Sinha AK (1992) Stability of zircon U-Pb systematics in a greenschist-grade mylonite: an example from the Rockfish Valley Fault Zone, Central Virginia, USA. J Geol 100:593-603
Whitehouse MJ, Platt JP (2003) Dating high-grade metamorphism—constraints from rare-earth elements in zircon and garnet. Contrib Mineral Petrol (in press)
Wiedenbeck M, Allé P, Corfu F, Griffin WL, Meier M, Oberli F, von Quadt A, Roddick JC, Spiegel W (1995) Three natural zircon standards for U-Th-Pb, Lu-Hf, trace element and REE analyses. Geostand Newslett 19:1-23
Wilde SA, Valley JW, Peck WH, Graham CM (2001) Evidence from detrital zircons for the existence of continental crust and oceans on the Earth 4.4 Gyr ago. Nature 409:175-178
Williams IS, Buick IS, Cartwright I (1996) An extended episode of early Mesoproterozoic fluid flow in the Reynolds Range, central Australia. J Metamor Geol 14:29-47
Williams IS, Claesson S (1987) Isotopic evidence for the Precambrian provenance and Caledonian metamorphism of high grade paragneisses from the Seve Nappes, Scandinavian Caledonides II. Ion microprobe zircon U-Th-Pb. Contrib Mineral Petrol 97:205-217

Williford RE, Weber WJ, Devanathan R, Cormak AN (1999) Native vacancy migrations in zircon. J Nuc Mater 273:164-170

Wopenka B, Jolliff BL, Zinner E, Kremser DT (1996) Trace element zoning and incipient metamictization in a lunar zircon: application of three microprobe techniques. Am Mineral 81:902-912

Wyborn D (1983) Fractionation processes in the Boggy Plain zoned pluton. PhD dissertation, Australian National University, Canberra

Yeats CJ, McNaughton NJ, Groves DI (1996) SHRIMP U-Pb geochronological constraints on Archean volcanic-hosted massive sulfide and lode gold mineralisation at Mount Gibson, Yilgarn Craton, Western Australia. Econ Geol 91:1354-1371

Yusoff M (2002) EDXRF as an important tool in the selective leaching of uranium and thorium from contaminated zircon. 51st Ann Denver X-ray Conf, Colorado (abstr)

Zeck HP, Williams IS (2002) Inherited and magmatic zircon from Neogene Hoyazo cordierite dacite, SE Spain—anatectic source rock provenance and magmatic evolution. J Petrol 43:1089-1104

Zinner E, Crozaz G (1986) A method for the quantitative measurement of rare earth elements in the ion microprobe. Intl J Mass Spect Ion Proc 69:17-38

# Melt Inclusions in Zircon

**J. B. Thomas[1], R. J. Bodnar[1], N. Shimizu[2] and C. A. Chesner[3]**

[1]*Department of Geological Sciences, Virginia Tech, Blacksburg, Virginia 24061*

*E-mail: bubbles@vt.edu*

[2]*Department of Geology and Geophysics, Woods Hole Oceanographic Institution, Woods Hole, Massachusetts 02543*

[3]*Department of Geology and Geography, Eastern Illinois University, Charleston, Illinois 61920*

## INTRODUCTION

Silicate melt inclusions (MI) are small samples of melt that are trapped during crystal growth at magmatic pressures and temperatures. The MI represent a sample of the melt that was isolated from the bulk melt during host crystallization. Thus, MI preserve the composition of the melt that was present during crystal growth and record the P-T growth conditions. As such, MI provide a valuable tool for constraining the magmatic history of igneous systems. Melt inclusions may be composed of a single-phase glass or they may contain multiple phases (vapor bubbles ± crystals) that nucleated from the melt within the inclusion during cooling, or were produced by devitrification of the glass following trapping. Heating and homogenization techniques applied to multiphase MI produce a glass suitable for microanalysis, and may also provide information regarding the temperature of MI and crystal formation (Roedder 1984).

Many workers have used MI in major rock-forming minerals to constrain igneous processes, such as crystal fractionation and magma degassing (e.g., Anderson et al. 1989, Hervig and Dunbar 1992, Sobolev and Shimizu 1993, Sobolev and Danyushevsky 1994, Lu 1991), but there have been far fewer studies of MI in accessory minerals (e.g., Chupin et al. 1998, Spandler et al. 2000, Sokolov 2002, Thomas et al. 2002). Melt inclusions in zircons of igneous origin are common, and have been identified in a wide range of igneous rock types, including quartz diorite and rhyolite, and in detrital zircon grains from heavy mineral sands (Fig. 1).

The same properties that make zircon an excellent geochronometer also make zircon an ideal host for MI. Zircon is stable in most geologic environments (Watson 1996) and trace element diffusivities through the zircon crystal structure (Cherniak et al. 1997, Cherniak and Watson, this volume) are sufficiently slow to prevent exchange of components between the MI and the surrounding zircon host and/or melt, so long as the zircon crystal remains crystalline. Zircon has been of interest to petrologists for many years because it is one of the minerals that controls the rare earth element (REE) budget of crustal magmas (Nagasawa 1970, Bea 1996, O'Hara et al. 2001). The compositions of melts from which accessory minerals crystallize generally have not been well constrained, especially in plutonic rocks. As such, inverse modeling using zircon mineral chemistry and partition coefficients has been employed to back-calculate melt compositions (Hinton and Upton 1991, Guo et al. 1996, Hoskin et al. 2000, Wilde et al. 2001). Some workers have used the bulk rock as an approximation of the melt composition (e.g., Hoskin et al. 2000); however, it is difficult to unequivocally establish that a bulk rock composition represents the melt composition at any given time, especially in coarse-grained plutonic rocks. Other workers have used zircon morphology as an indicator of melt composition, magma temperature and crystallization rates (Poldervaart 1955, 1956; Pupin and Turco 1972, Vavra 1990). However, zircon morphology commonly varies considerably within any given rock, and the various chemical and physical parameters that may affect zircon morphology are poorly understood.

Melt inclusions provide an unambiguous method to directly determine compositions of melts from which zircon crystallized, provided that the MI have not leaked or re-equilibrated following

1529-6466/03/0053-0003$05.00

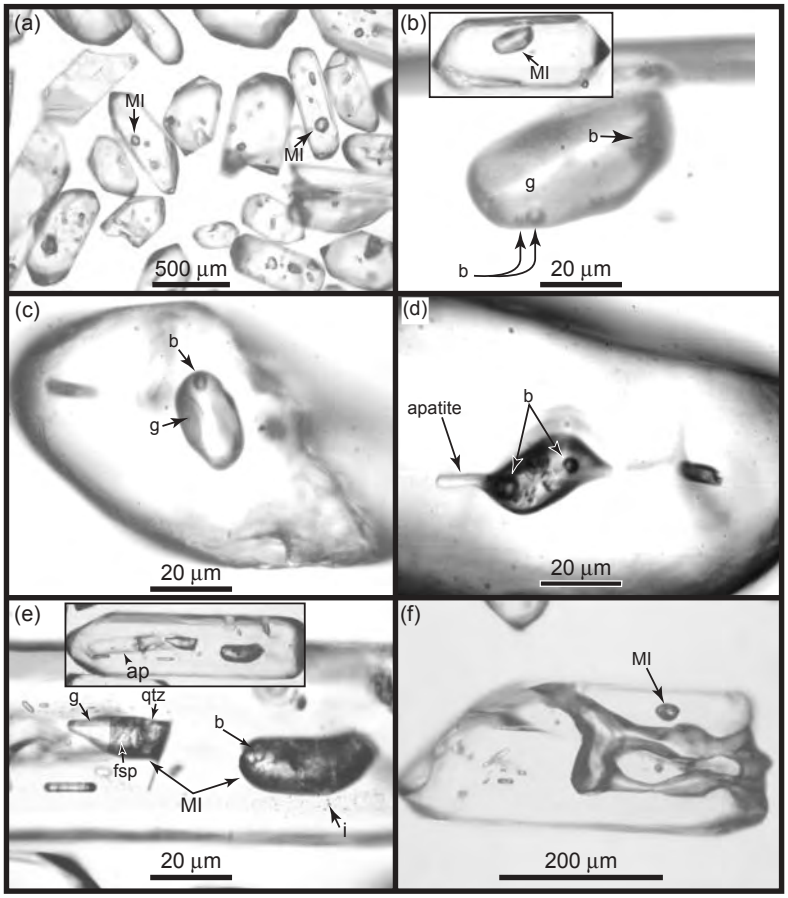


**Figure 1.** Transmitted light photographs of crystalline and glass melt inclusions (MI) in zircons. The zircons commonly contain solid inclusions of apatite (labeled "ap"), feldspar (labeled "fsp") and less commonly, oxide minerals. The zircons in the photographs are from: the 56 Ma quartz dioritic Quottoon Igneous Complex in British Columbia, Canada (shown in a, e and f), a rhyolitic member of the 74 ka youngest Toba Tuff of Sumatra, Indonesia (shown in b), and a heavy mineral sand deposit from north Stradbroke Island, Queensland, Australia (shown in c and d). (a) Crystalline melt inclusions in zircons extracted from the Quottoon quartz diorite. Most zircons contain dark-colored, ovoid inclusions that are crystalline melt inclusions. (b) The inset shows a low magnification photograph of a zircon from the Toba rhyolite containing an ovoid-shaped glass inclusion that is shown below the inset at higher magnification. The melt inclusion is comprised of crystal-free glass (labeled "g") and three bubbles (labeled "b"). (c) A glass melt inclusion is preserved in a rounded and broken fragment of a detrital zircon. The melt inclusion is comprised of glass and a bubble. (d) A partially crystalline melt inclusion hosted by a detrital zircon contains a crystal of apatite that was trapped along with the inclusion-forming melt. The partially crystalline melt inclusion also contains two bubbles, several transparent daughter crystals and feathery masses of dark-colored daughter crystals. (e) The inset shows a zircon from the Quottoon quartz diorite that contains a solid inclusion of apatite (labeled "ap") and two large crystalline melt inclusions that are shown below the inset at higher magnification. The large melt inclusion on the left contains a large transparent phase (glass? or quartz?), many transparent lath-shaped daughter crystals (feldspar?), a large anhedral daughter crystal (quartz? labeled "qtz"), and interstitial dark-colored daughter crystals. The large melt inclusion on the right contains a bubble that is partially obscured by daughter crystals. A decrepitation halo of small inclusions (labeled "i") occurs around the large melt inclusion on the right. (f) Zircon from the Quottoon quartz diorite containing a crystalline melt inclusion and an elongated tube-shaped inclusion that parallels the c-axis of the zircon host. The tube-shaped inclusions are commonly composed mostly of glass, however, some tube-shaped inclusions were found to be empty after the tubes were exposed at the surface.

entrapment (e.g., Qin et al. 1992, Gaetani and Watson 2000, Danyushevsky et al. 2002). As such, coupled petrographic examination (before, during and after heating) and geochemical analyses of MI and host zircons can reveal information about crystal/melt processes in igneous systems that are difficult (or impossible) to assess through conventional methods. In the first section of this chapter we summarize some of the previous studies of MI in zircon. The second section describes some general methods for preparing MI in zircons for geochemical analyses. In section three we describe the use of trace element analyses of MI and the immediately adjacent zircon to determine zircon/melt partition coefficients. Next, we discuss the significance of boundary layer development adjacent to growing crystals and compare the trace element compositions of MI in zircon with those from MI in minerals that have significantly different trace element mineral/melt partitioning behavior. The chapter concludes with some remarks regarding potential avenues for future research using MI in zircon.

## PREVIOUS INVESTIGATIONS

There have been surprisingly few reports of MI in zircon. Li (1994), Chesner (1998), Chupin et al. (1998), Hoskin and Black (2000) and Frezzotti (2001) describe MI in zircon. Only two of these studies (Li 1994, Chupin et al. 1998) conducted microthermometric and/or geochemical analyses of the MI. Li (1994) focused primarily on the phase changes observed during heating of crystalline MI in zircons from southwestern and northwestern China to obtain homogenization temperatures. The crystalline melt inclusions were step-heated using one-atmosphere furnaces and heating stages. Li (1994) documented the sequence of phase changes during heating and reported homogenization temperatures ranging from 950-1100°C. Several electron microprobe analyses of MI in zircons were also reported. However, the $ZrO_2$ contents of these MI were very high (0.94-5.02 wt % Zr), suggesting that the analytical volume included not only melt but also zircon. Perhaps most importantly, the Li (1994) investigation demonstrated that MI occur in zircons from many different igneous environments spanning the wide compositional range from diorite to alkali syenite.

Chupin et al. (1998) performed detailed geochemical analyses of MI in zircon crystals from an Archean age greenschist facies quartzite (Witwatersrand Supergroup), a granulite facies quartzite (Beit Bridge Group) and from a granulite facies S-type granitic orthogneiss in South Africa. Zircon crystals from the Beit Bridge quartzites contained igneous cores with abundant MI, but zircon overgrowths were free of MI. These petrographic relationships were interpreted to indicate that the overgrowths were metamorphic in origin. In addition to determining the ages of detrital zircons containing MI, Chupin et al. (1998) pioneered the use of MI as a provenance tool to constrain source terranes that supplied sediments to basins in South Africa. Other studies of detrital zircon provenance have relied only upon U-Pb ages, zircon geochemistry and/or isotopic data from zircons to infer the compositions of magmas that comprised source region terranes (e.g., Wilde et al. 2001).

The MI investigated by Chupin et al. (1998) were crystalline and, therefore, required heating to dissolve daughter crystals that precipitated from the melt during cooling. The daughter crystals were optically identified as quartz, feldspar and an unidentified opaque mineral. The MI were heated using a one atmosphere heating stage mounted on a microscope. During heating, vapor bubbles were recognized as daughter crystals dissolved to form a melt. The daughter crystals melted between 750°C and 900°C. The vapor bubbles never homogenized into the melt, even when heated to 1250°C and held at that temperature for ten hours. After daughter crystals were melted, the MI were quenched to a glass containing a vapor bubble(s). Chupin et al. (1998) reported that some MI decrepitated during heating experiments, most likely due to elevated internal pressures generated in the MI during heating.

After heating and homogenization experiments, the MI were analyzed for major elements and Cl by electron microprobe. Melt inclusions in zircons from the Witswatersrand Supergroup quartzite were chemically classified as granite, trondhjemite and tonalite (Barker 1979). Melt inclusions

from the Beit Bridge Group quartzite were classified as granite and trondhjemite. Melt inclusions from the S-type orthogneiss had granitic and granodioritic compositions. Analyses of incompletely homogenized MI yielded exceptionally high concentrations of either $SiO_2$ (>87 wt %) or $Al_2O_3$ (22 wt %) or $TiO_2$ (2 wt %) or FeO (>3.8 wt %). Chupin et al. (1998) suggested that the unmelted crystals were trapped along with silicate melt during MI formation, because the crystals did not melt when heated to temperatures as high as 1250°C.

Based on MI compositions from detrital zircons, Chupin et al. (1998) were able to suggest several different source terranes for the sediments. The zircons in both quartzites formed in magmas of tonalitic-trondhjemitic to granitic composition that were emplaced into the sediment source regions at ~3.26 Ga. Zircons from both quartzites also had similarly rounded and pitted shapes and the crystals were interpreted as having traveled similar distances from source regions. Based on the similarity of external morphologies of the detrital zircons containing MI with tonalitic-trondhjemitic compositions with those having granitic compositions, Chupin et al. (1998) further suggested that the two sources were proximal to one another. The MI in these detrital zircons document the earliest granitoid magmatism in South Africa. The Chupin et al. (1998) study illustrates that MI compositions from detrital zircons provide important compositional information (in addition to zircon ages, geochemical/isotopic composition) that may be useful to fingerprint sediment sources.

## METHODOLOGY

Melt inclusions in zircons are common but many are not suitable for geochemical analysis. Most often, the MI are rejected because they show obvious cracks intersecting the inclusion walls. In many cases only a very small proportion (~10%) of all the zircons in the rock are suitable for microthermometric and geochemical analysis. Because a given thin section may only contain a few tens (or fewer) of zircon crystals, petrographic observation of thin sections is not the most efficient means of identifying and selecting zircons for MI studies. Mineral separates are usually more suitable than thin sections for selection of zircon crystals for study. Conventional rock crushing, heavy liquid and magnetic separation are used to concentrate zircons into a mineral separate. Immersion of individual zircon crystals in refractive index oil makes it easier to observe internal features in crystals, especially if crystals have a rough surface and/or if matrix glass is attached to the crystal surfaces. Zircons containing suitable inclusions are handpicked from mineral separates under a binocular microscope using an Irwin loop. Crystalline MI are typically dark colored and polymineralic, sometimes containing a visible vapor phase. The vapor phase can be difficult to identify within crystalline MI because it commonly occurs as distorted bubbles and/or as films on daughter crystals.

Crystalline MI may be distinguished from solid mineral inclusions during careful petrographic observation using strongly collimated light, owing to the fine-grained texture of the polymineralic aggregates that formed during slow cooling. In contrast, glass inclusions are commonly clear to light brown in color and may contain one (or more) discernible vapor bubbles.

The methods used to prepare both crystalline and glass MI contained in zircons for analysis are discussed below. Melt inclusions and zircons used to illustrate these techniques are from a 56 Ma quartz diorite from the Quottoon Igneous Complex (British Columbia, Canada) and from a 74 ka rhyolite unit of the youngest Toba Tuff (Sumatra, Indonesia). Field relations, sample locations, bulk rock chemistry and petrogenesis are described in detail in Thomas and Sinha (1999; sample 2093) for the quartz diorite and in Chesner (1998) for the rhyolite. Zircons from both localities are typically clear and euhedral, and contain MI as well as solid inclusions of apatite, feldspar, and less commonly, oxide minerals. The MI from the quartz diorite were crystalline and, therefore, required heating to produce a homogeneous glass suitable for microanalysis. Techniques described for MI in the Quottoon MI would be applicable to any inclusions that crystallized or devitrified during cooling, whereas, the techniques described for the Toba MI would be applicable to glassy MI.

**Petrography of melt inclusions hosted in zircon**

Melt inclusions discussed in this chapter may be subdivided into two general types, glassy inclusions (Fig. 1b,c) and crystalline inclusions (Figs. 1a,d-f; see Figs. 2 and 3 below). Glass and crystalline MI are end-member types reflecting differences in the cooling rate, size and composition (including volatile content) of the trapped melt (Roedder 1979). A continuous spectrum of MI textures between the end-member types occurs depending on the geologic setting in which the zircon formed. Melt inclusions in zircon crystals from volcanic rocks are usually glassy (± vapor bubbles) due to rapid cooling of the entrapped melt after eruption (Fig. 1b). Glass MI have also been observed in detrital zircons (Fig. 1c) indicating that glass inclusions can be preserved in zircons that have undergone weathering, erosion and transport. In contrast, MI in zircons from plutonic rocks are normally crystallized to polymineralic aggregates (Figs. 1d,e). In this chapter glassy MI will be referred to as glass inclusions to distinguish them from crystalline MI. Glass MI that are the result of laboratory heating are referred to as homogenized MI.

In rapidly cooled rocks, such as plinian pumices, the entrapped melt may be quenched to a single-phase glass if cooling is sufficiently rapid, or one (or more) vapor bubbles may form with slower cooling (Fig. 1b). Some small amount of the host mineral may precipitate onto the inclusion walls during slow cooling. The amount of zircon that crystallizes onto the MI walls is generally small, compared to MI in host minerals such as quartz or feldspar. The amount of zircon that can crystallize from the melt within the inclusion is limited by the Zr content of the melt. For most felsic melts, this amount of zircon is very small because Zr concentrations are generally less than about 300 ppm (e.g., Taylor and McLennan 1981). Owing to the large amount of quartz that typically precipitates on the walls of quartz hosted MI, the size of the inclusion after heating is usually noticeably larger compared to before heating. Zircon hosted MI, however, show no discernible difference in size before and after heating.

In plutonic rocks (and in some volcanic rocks) the host phase and entrapped melt cool slowly allowing vapor bubbles and daughter crystals to nucleate and grow from the melt (Figs. 1d,e). However, some small MI remain glassy while larger MI in the same zircon crystal have crystallized to fine-grained aggregates. Crystalline MI may be composed of some mixture of glass and daughter crystals or may be entirely fine-grained aggregates of daughter crystals. Daughter crystals range from lath-shaped to anhedral feathery masses of both transparent and dark-colored minerals. The refraction of light by daughter crystal aggregates causes MI to appear dark. Petrographic observation and electron microprobe analyses of polished crystalline MI indicate that the daughter crystals in the zircon hosted MI from the Quottoon quartz diorite are mostly quartz and feldspar (Figs. 1d,e). Apatite occasionally (and feldspar rarely) occurs as a solid phase trapped with the melt that formed the MI (Fig. 1d) and as solid mineral inclusions in zircon crystals (Fig. 1e). In crystalline MI it may be difficult to distinguish between daughter crystals and trapped crystals. Trapped crystals may sometimes be identified if they extend far beyond the MI wall into the zircon host, are exceptionally large, or do not melt at temperatures similar to the homogenization temperatures recorded for other MI in the same group (Roedder 1984, Chupin et al. 1998).

Morphologies of MI in zircon range from ovoid (Figs. 1a-d) to irregularly-shaped (Fig. 2) to negative-crystal-shaped (Fig. 3a). Melt inclusions range from <1 μm to several tens or hundreds of microns in maximum dimension. The maximum dimension is limited only by the size of the host crystal. Zircons in most rocks are typically <1 mm long and, therefore, most MI in zircon are <100 μm in their longest dimension. Halos of small inclusions occur around some crystalline MI, suggesting that the MI decrepitated and expelled some of its contents into the surrounding zircon (Fig. 1e). Decrepitation halos have not been observed around glass MI in zircons, suggesting that the halos most likely form by over-pressurization of the inclusion due to volatile exsolution during crystallization of the melt within the inclusion (Roedder 1984, Student and Bodnar 1996).

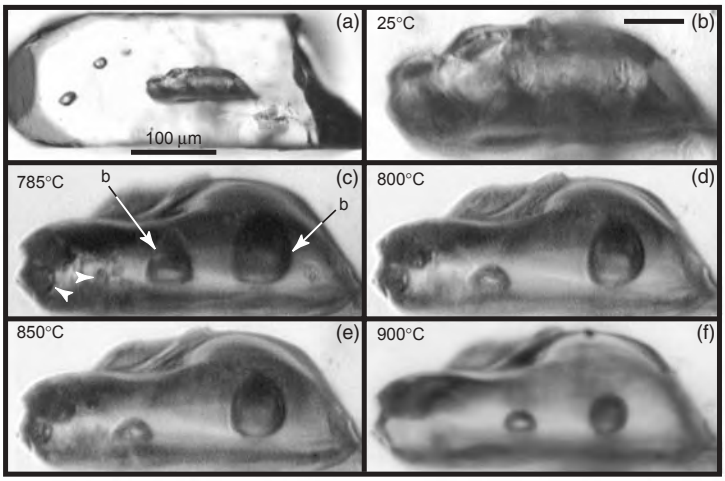


**Figure 2.** Transmitted light photographs of a heating sequence (~12 hours for each heating step). Zircon is from the Quottoon quartz diorite. (a) A large crystalline melt inclusion occurs near the center of the zircon and two smaller inclusions occur near the unbroken crystal termination. (b) A higher magnification photograph, taken before heating, of the large crystalline melt inclusion located near the center of the crystal. No distinct outlines of daughter crystals or bubbles are visible in the melt inclusion due to its fine-grained texture. The bar in the upper right of the photograph is 25 µm long. (c) After the first heating step at 785°C, two distinct vapor bubbles formed and several small daughter crystals (feldspar? and/or quartz?, denoted by white arrowheads) surrounded by glass were visible in the left side of the melt inclusion. (d-e) Daughter crystals and bubbles continually decreased in size during each successive heating step. (f) At 900°C the daughter crystals completely dissolved into the melt and quenching formed a glass containing two vapor bubbles. Note the increased clarity of the inclusion as the daughter crystals dissolved into the melt.

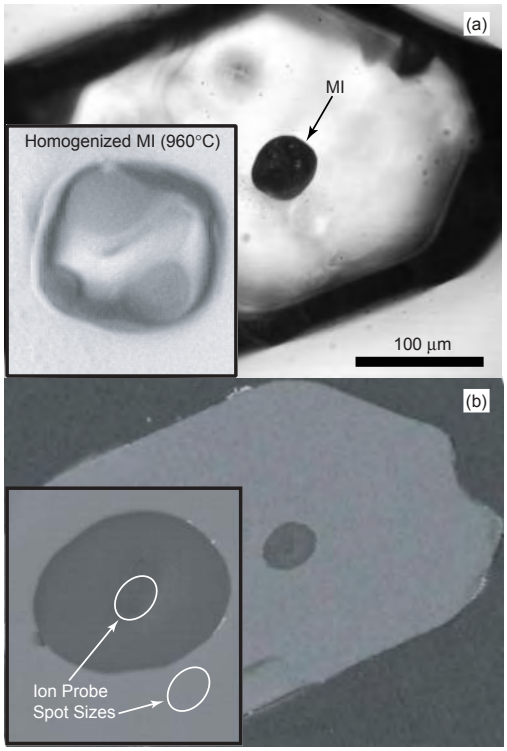


**Figure 3.** Melt inclusion in a zircon crystal from the Quottoon quartz diorite. (a) Transmitted light photograph of a zircon containing a crystalline melt inclusion. The inset shows an enlargement of the same inclusion after homogenization at 960°C. (b) A back-scattered electron image of the same zircon containing the homogenized melt inclusion exposed at the surface by grinding-polishing. The inset shows an enlargement of the inclusion along with representative ion probe spot sizes. [Used by permission of Elsevier Science, from Thomas et al. (2002) *Geochimica et Cosmochimica Acta*, Vol. 66, Fig. 1, p. 2889]

**Heating and homogenization of crystalline melt inclusions in zircon**

The applications of crystalline and glassy inclusions in igneous petrology are similar; however, a major difference is related to sample preparation for microanalysis. Glass MI do not require heating to produce a homogeneous glass for analysis, therefore, preparation simply requires exposure of the inclusion on the surface for microbeam analysis. In contrast, crystalline MI are heterogeneous aggregates of daughter crystals. Therefore, spot analyses (e.g., electron or ion microprobe) of crystalline MI would yield a mixed composition of the phases within the analytical volume of the microbeam, and not the composition of the melt originally trapped. Laboratory heating of crystalline MI is necessary to produce a homogeneous glass for analysis. Inclusions open to the surface and/or intersected by cracks should not be selected for homogenization experiments because they may not have remained closed systems after entrapment in the host crystal. Alternatively, crystalline MI may be analyzed by laser ablation inductively coupled plasma mass spectrometry (LA-ICP-MS) without the need to homogenize the inclusion. In general, a crystalline MI is positioned beneath a laser beam so that the hole drilled during ablation passes through any host crystal surrounding the inclusion and includes the entire volume of the MI into the analytical volume (Halter et al. 2002). The proportions of MI and host phase included in the analytical volume are calculated based on ratios of certain elements in the bulk rock (Halter et al. 2002).

Crystalline MI in many minerals (e.g., quartz, feldspar, pyroxene, olivine, etc.) are routinely homogenized using microscope heating stages and one-atmosphere furnaces (e.g., Sobolev and Kostyuk 1975, Roedder 1984, Kamenetsky et al. 1997, Nielsen et al. 1997). It is preferable to homogenize crystalline MI using a heating stage mounted on a microscope so that phase changes can be observed during heating. Alternatively, crystalline MI may be step-heated in a furnace and phase changes can be observed after each heating step. However, it has been our experience that heating crystalline MI at one atmosphere generates high internal pressure that commonly causes decrepitation. Decrepitation of MI and loss of volatiles results in incomplete melting of the daughter crystals that precipitated from the melt. Other workers have experienced similar problems (Chupin et al. 1998; C. Czabo 2002, pers. comm.) when attempting to homogenize crystalline MI in zircon at one atmosphere. We have successfully homogenized crystalline MI by heating them under pressure (1200-1600 bars in argon) in TZM (titanium-zirconium-molybdenum alloy) vessels, followed by rapid quenching to produce a homogeneous glass (Figs. 2 and 3). Other workers (Thomas 1994, Schmidt et al. 1998) have shown that heating inclusions under pressure minimizes decrepitation, compared to heating at one atmosphere.

To prevent losing the small crystals during heating, zircons containing crystalline MI are folded into Pt foil and inserted into unwelded Pt capsules before loading into the TZM vessel. To determine the sequence of phase changes during heating, zircons containing crystalline MI were step-heated in approximately 20°C increments, typically starting at 750°C, and held at temperature for ~12 hours. After each increment of heating, the inclusions were quenched and examined to determine the degree of homogeneity. If an inclusion had not completely homogenized, the crystals were placed back into the TZM vessel and heated to a temperature ~15-20 degrees higher than the previous step. This process was repeated until all daughter crystals were completely melted as illustrated in Figure 2. The first signs of melting typically occurred after the 750°C heating step (Fig. 2c), evidenced by increased clarity of the inclusions and recognition of vapor bubbles. Daughter crystals and bubbles progressively decrease in size during each heating step as more melt forms (Figs. 2b-f). Following homogenization and quenching, the MI contain a crystal-free glass (± vapor bubbles). The crystalline MI in zircons from the quartz diorite homogenized between 875°C and 1000°C.

**Major and trace element compositions of melt inclusions in zircon**

Melt inclusion compositions have been determined using a variety of microanalytical techniques. For example, major and minor element concentrations have been determined by electron

microprobe (Morgan and London 1996), trace element and isotopic abundances have been determined by SIMS, secondary ion mass spectrometry (Shimizu and Hart 1982, Hervig et al. 1989, Sisson and Layne 1993, Webster and Duffield 1991, Shimizu et al. 1997, Shimizu 1998), LA-ICP-MS (Halter et al. 2002), and volatile contents have been determined by FTIR or Raman spectroscopy (Anderson et al. 1989, Ihinger et al. 1994, Lowenstern 1994, Thomas 2000). When developing an analytical protocol, nondestructive techniques, such as electron microprobe and Raman spectroscopy, should be employed first, followed by destructive techniques such as SIMS and LA-ICP-MS. Here we describe an analytical protocol involving electron microprobe and SIMS analyses, designed to determine major element and REE and other trace element abundances in MI. We first conduct major and minor element analyses of the MI and host zircons using an electron microprobe followed by trace element analyses using SIMS. With this analytical protocol, zircons containing glass MI were cast in epoxy and ground-polished to expose the inclusion at the surface. Thomas and Bodnar (2002) describe a method for mounting individual zircon crystals so that each zircon can be ground and polished to expose a pre-selected MI at the crystal surface.

Major and minor element compositions of the melt inclusions were determined at Virginia Tech with a Caméca® SX-50 electron microprobe equipped with four wavelength-dispersive spectrometers enabling four elements to be measured simultaneously. For glass (melt inclusion) analyses, an accelerating voltage of 15 kV was used with a beam current of 2-5 nA, and a beam diameter <5 μm. Na and K were measured in the first 30 s to minimize the effect of volatilization. For electron microprobe analyses of zircon the beam current was increased to 100 nA with a beam diameter of ~1 μm. Analytical schemes for melt inclusions and zircons used 20-40 s counting times (peak and background) for major elements; for minor and trace elements the counting times were 60-600 s. Initial standardization was performed with a combination of minerals and glasses similar in composition to the melt inclusions and the host zircons. The accuracy of major element data is better than ±2% relative, and the accuracy of minor element analyses varies from 2-10% relative.

Trace element abundances were measured with a Caméca® IMS 3f ion microprobe at Woods Hole Oceanographic Institution using previously described procedures (e.g., Shimizu and Hart 1982, Shimizu et al. 1997, Shimizu 1998). Gold-coated polished sections were analyzed using a primary $O^-$ beam with a primary beam current of ~1 nA. A beam diameter of ~12-15 μm was used for REE analyses. Molecular ion interferences were suppressed by offsetting the secondary-ion accelerating voltage by 60 V for REE with an energy window of ±10 V using an energy-filtering technique (Shimizu and Hart 1982). Element abundances were determined by converting secondary-ion intensity (ratioed against silicon), using empirical relationships between intensity and concentration based on analyses of rhyolite glass standards. Analytical uncertainties are mainly due to counting statistics (5-15% for the REE).

Some typical analytical results obtained from homogenized crystalline MI from the Quottoon quartz diorite and from glass MI from the Toba rhyolite are described below. Petrographic observations (Figs. 1, 2 and 3a), back-scattered electron imagery (Fig. 3b), electron microprobe major element traverses and electron microprobe/SIMS trace element traverses confirmed the chemical homogeneity of individual MI (including homogenized crystalline inclusions) and the host zircon crystals. $SiO_2$ contents range from 68.9 to 74.9 wt % for MI in zircons from the quartz diorite and from 74.9 to 78.8 wt % for MI in zircons from the rhyolite (Fig. 4). The major element concentrations show little correlation with $SiO_2$ content (Fig. 4). Other than $SiO_2$, no systematic differences are observed between major element concentrations of MI in zircon grains from the quartz diorite and those from the rhyolite. In both cases, melts that precipitated zircon are calc-alkaline, peraluminous and chemically classified as granite (or rhyolite; Barker 1979, Cox et al. 1979).

Chondrite-normalized (Nakamura 1974) REE abundances of MI and the immediately adjacent zircon host are shown in Figure 5. Melt inclusions display smooth U-shaped chondrite-normalized REE patterns (Figs. 5a,b) that differ significantly from the host zircons (Figs. 5c,d). $La_N/Yb_N$ ratios (where the subscript N refers to the chondrite normalized concentration) for MI from the

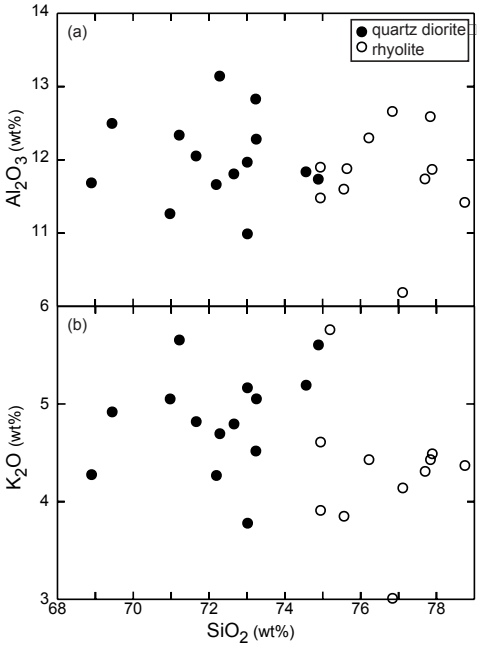


**Figure 4.** Major element variation diagrams for $SiO_2$ vs. (a) $Al_2O_3$ and (b) $K_2O$ for melt inclusions in zircon from the Quottoon quartz diorite and from the Toba rhyolite.

quartz diorite range from 0.63 to 7.51 (average = 2.6) and from 0.42-8.33 (average = 2.14) for MI from the rhyolite, indicating that light REE are not strongly fractionated from heavy REE (Figs. 5a,b). The highest $La_N/Yb_N$ ratios correspond to inclusions with the lowest Yb abundances. While the light REE are not strongly fractionated from the heavy REE in MI, light REE are somewhat fractionated from the middle REE (Figs. 5a,b) as shown by the U-shaped chondrite-normalized REE patterns. With the exception of two analyses of MI from the quartz diorite, the REE abundances of the MI and zircons from the quartz diorite and from the rhyolite are similar.

The zircon crystals analyzed are enriched in heavy REE, but depleted in the light REE, relative to the melt inclusions (Figs. 5c,d). With the exception of Ce, concentrations of REE in zircon increase smoothly from La to Yb. Zircon crystals

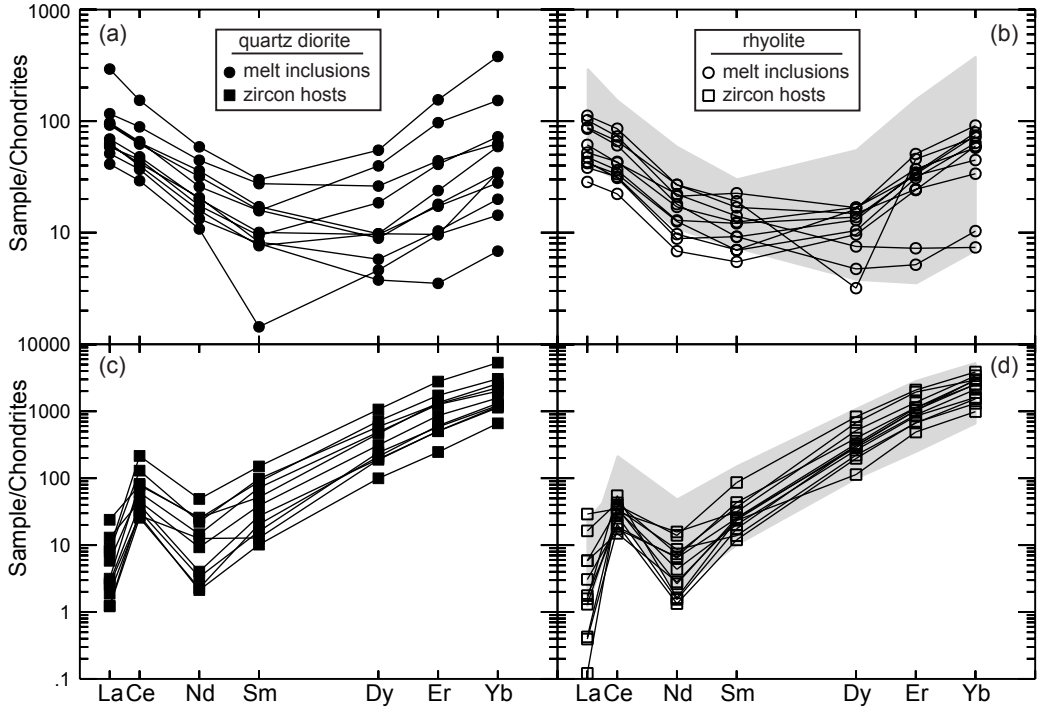


**Figure 5.** Chondrite-normalized rare earth element abundances of melt inclusions and zircon hosts from the Quottoon quartz diorite and the Toba rhyolite. The gray-shaded overlays in (b) and (d) outline the rare earth element patterns of the melt inclusions and zircons from the quartz diorite.

display large positive Ce anomalies ($Ce/Ce^* = Ce_N/\sqrt{[La_N \times Nd_N]}$) ranging from 3.16 to 15.8 (average = 9.4) for zircon crystals from the quartz diorite and from 2.34 to 36.4 (average = 13.76) in zircon crystals from the rhyolite. The $La_N/Yb_N$ ratios of the zircons from the quartz diorite range from 0.00093 to 0.00927 (average = 0.00333) and the $La_N/Yb_N$ for zircons from the rhyolite range from <0.001 to 0.019 (average = 0.004). Total REE of the zircon crystals (for the seven REE analyzed in the zircon crystals) from the quartz diorite range from 263 to 2411 ppm (average = 910 ppm) and from 388 to 1662 ppm (average = 930 ppm) for zircon crystals from the rhyolite. This range is consistent with abundances for these same REE measured in zircon crystals from other felsic igneous rocks (Hoskin et al. 2000).

## DETERMINING ZIRCON/MELT TRACE ELEMENT PARTITION COEFFICIENTS USING MELT INCLUSIONS IN ZIRCON

In this section we describe the application of trace element analyses of MI and host zircon to determine zircon/melt (= zc/melt) partition coefficients ($^{zc/melt}D_M$, where the subscript M refers to the trace element of interest). The melt inclusion-mineral (MIM) technique was used to calculate partition coefficients for the REE (La, Ce, Nd, Sm, Dy, Er and Yb) and Ba, Rb, B, Sr, Ti, Y and Nb, based on analyses of natural MI contained in zircon crystals. The MIM technique combines many of the advantages of conventional techniques used previously to determine $^{zc/melt}D_M$, while at the same time minimizing or eliminating many of the drawbacks of those techniques (e.g., accidentally including small crystals in the glass separate). Most previous partitioning studies used bulk analyses of zircon and either coexisting glass or whole rock separates to represent the melt composition (Nagasawa 1970, Mahood and Hildreth 1983, Murali et al. 1983, Fujimaki 1986, Bea et al. 1994). Watson (1980) determined $^{zc/melt}D_M$ for La, Sm, Ho, and Lu using synthetic zircon crystals grown from peralkaline melts (with no additional element(s) added for charge compensation, e.g., $P^{5+}$ to utilize the xenotime substitution).

With the MIM technique, trace element concentrations in MI and in the immediately adjacent host mineral are measured by SIMS and used to calculate *in situ* mineral/melt partition coefficients. Lu et al. (1992) and Sobolev et al. (1996) pioneered this technique to determine partition coefficients in mineral/melt systems. The technique has been extended to determine zircon/melt partition coefficients for REE and other trace elements in felsic systems (granitic and rhyolitic), using crystalline MI in zircon extracted from a quartz diorite of the Quottoon Igneous Complex in British Columbia, Canada (Thomas et al. 2002) and from a rhyolite of the Toba Tuffs in Sumatra, Indonesia (Chesner 1998). The partition coefficients obtained from analyses of homogenized MI and zircon hosts from the quartz diorite are comparable to those obtained from analyses of unheated glass MI and zircon hosts from the Toba rhyolite.

### Trace element partitioning data and interpretations

***Rare earth element partitioning.*** Zircon/melt partition coefficients for each zircon/MI pair are listed in Table 1 and shown on Figure 6a. Zircon/melt REE partition coefficients increase with increasing atomic number—the trend is similar to that determined by other workers (Nagasawa 1970, Hinton and Upton 1991, Watson 1980, Fujimaki 1986, Guo et al. 1996, and others; see also the compilation at the GERM website at: http://earthref.org/GERM/ ). While the concentrations of individual trace elements vary by more than one order of magnitude from one MI to the next (Fig. 5a) and from one zircon crystal to the next (Fig. 5c), the calculated partition coefficients for individual REE generally vary by less than one order of magnitude (Table 1), reflecting the fact that MI with the highest REE abundances are generally associated with zircon crystals with the highest REE abundances. For example, the La concentration in the MI from the Quottoon Igneous Complex zircon crystals varies from about 14 to 97 ppm, and the La concentration in host zircon ranges from 0.4 to 7.89 ppm. Assuming that the La concentrations in MI and zircon host vary randomly, one could expect a range in calculated $^{zc/melt}D_{La}$ of greater than two orders of magnitude (from 0.0041 to

**Table 1.** Zircon/melt partition coefficients ($D_{REE}$) calculated using REE abundances of melt inclusions and coexisting zircon crystals from the Quottoon Igneous Complex and from the Toba rhyolite. [Quottoon Igneous Complex data used by permission of Elsevier Science, from Thomas et al. (2002) *Geochimica et Cosmochimica Acta*, Vol. 66, Table 3, p. 2894]

| | $D_{La}$ | $D_{Ce}$ | $D_{Nd}$ | $D_{Sm}$ | $D_{Dy}$ | $D_{Er}$ | $D_{Yb}$ |
|---|---|---|---|---|---|---|---|
| | 0.05 | 2.06 | 1.58 | 11.61 | 72.98 | 72.39 | 51.52 |
| | 0.04 | 0.83 | 0.2 | 2.7 | 20.09 | 29 | 40.63 |
| | 0.07 | 1.46 | 0.5 | 3.56 | 22.45 | 29.35 | 35.88 |
| | 0.22 | 0.99 | 0.53 | 4.14 | 16.79 | 21.09 | 21.9 |
| | 0.03 | 1.4 | 0.77 | 5.02 | 19.41 | 17.89 | 14.04 |
| Quottoon | 0.02 | 0.61 | 0.11 | 2.49 | 36.56 | 58.88 | 66.1 |
| | 0.06 | 0.93 | 0.56 | 4.58 | 12.37 | 13.07 | 13.04 |
| | 0.26 | 1.26 | 0.81 | 3.24 | 51.95 | 74.99 | 76.32 |
| | 0.02 | 0.43 | 0.35 | 0.75 | 19.31 | 52.72 | 82.29 |
| | 0.03 | 1.1 | 0.31 | 11.24 | 52.31 | 60.74 | 35.11 |
| | 0.05 | 0.75 | 0.16 | 1.27 | 26.42 | 70 | 96.72 |
| Median $D_M$ | 0.05 | 0.99 | 0.5 | 3.56 | 22.45 | 52.72 | 40.63 |
| | 0.21 | 0.67 | 0.41 | 4.28 | 11.77 | 20.29 | 16.51 |
| | 0.04 | 0.56 | 0.10 | 0.99 | 14.29 | 20.23 | 17.70 |
| | *0.01 | 0.56 | 0.76 | 4.71 | 84.12 | 220.81 | 242.70 |
| | 0.43 | 1.35 | 0.76 | 5.25 | 41.83 | 38.21 | 32.13 |
| | 0.03 | 0.83 | 0.12 | 2.52 | 29.45 | 33.56 | 39.92 |
| Toba | 0.03 | 0.29 | 0.24 | 1.32 | 90.39 | 19.27 | 29.74 |
| | *0.01 | 0.74 | 0.71 | 2.22 | 68.45 | 187.43 | 460.31 |
| | 0.001 | 0.55 | 0.66 | 3.81 | 49.48 | 63.81 | 86.30 |
| | 0.001 | 0.42 | 0.10 | 1.52 | 22.04 | 45.75 | 85.86 |
| | 0.02 | 0.90 | 0.09 | 2.61 | 23.42 | 29.67 | 37.44 |
| | 0.08 | 0.17 | 0.16 | 0.43 | 14.48 | 27.56 | 36.77 |
| Median $D_M$ | 0.03 | 0.62 | 0.25 | 2.37 | 26.44 | 31.61 | 37.10 |

*hourglass shaped inclusions

**Table 2.** Zircon/melt partition coefficients ($D_M$) calculated for lowest (top row) and highest (bottom row) La, Sm and Yb abundances in the melt inclusions and zircon hosts. [Used by permission of Elsevier Science, from Thomas et al. (2002) *Geochimica et Cosmochimica Acta*, Vol. 66, Table 4, p. 2896]

| $^{a}La_{MI}$ | $^{b}La_{zircon}$ | $D_{La}$ | $^{a}Sm_{MI}$ | $^{b}Sm_{zircon}$ | $D_{Sm}$ | $^{a}Yb_{MI}$ | $^{b}Yb_{zircon}$ | $D_{Yb}$ |
|---|---|---|---|---|---|---|---|---|
| 13.6 | 0.41 | 0.03 | 0.29 | 3.26 | 11.24 | 1.495 | 144.6 | 96.72 |
| 96.6 | 2.9 | 0.03 | 6.06 | 30.4 | 5.02 | 83.35 | 1170 | 14.04 |

(a) REE abundance in melt inclusion.
(b) REE abundance in zircon.

0.563). However, partition coefficients calculated for the two end-member melt concentrations reported above are identical at 0.03 (Table 2), and the total range in $^{zc/melt}D_{La}$ is only about one order of magnitude (from 0.02 to 0.26; Table 1). The variations in partition coefficients determined using the MIM technique are consistent with those determined in both experimental studies (Watson 1980) and from analyses of natural samples (Mahood and Hildreth 1983). Watson (1980) reports a range in $^{zc/melt}D_{Lu}$ from less than 20 to greater than 100 based on experimental data, and Mahood and Hildreth (1983) report a range in $^{zc/melt}D_{La}$ from 7.2 to 26.6 based on analyses of zircon and rhyolitic glass from the Bishop Tuff of the Long Valley caldera in California, U.S.A.

In a dynamic crystallizing igneous system, major and trace element abundances vary as crystallization proceeds. The range in REE contents of MI and zircon shown in Figures 5a-d reflects this natural variation in REE abundances in igneous systems. Based on the occurrence of zircon in early crystallizing plagioclase and also in later crystallizing biotite and quartz, zircon is believed to have formed over a significant portion of the crystallization history. As such, the REE budgets of the melt and the zircons precipitating from that melt would be expected to vary with time as the melts evolve during crystallization of zircon and other minerals. The variation of $^{zc/melt}D_M$ observed at the individual single zircon host/MI scale determined using the MIM technique is similar to the variation observed at the zircon separate/bulk rock (or glass) scale in other studies (e.g., Mahood and Hildreth 1983).

The mechanism by which REE substitute into the zircon structure is fairly well understood. The zircon structure contains two sites for cation substitution, a tetragonal Si and a larger triangular dodecahedral $Zr^{4+}$ *site* (Speer 1982, Finch and Hanchar, this volume). Heavy REE enrichment is due to substitution into the site containing $Zr^{4+}$ (Speer 1982). Xenotime-type substitution (whereby

a $REE^{3+}$ ion and $P^{5+}$—or some other pentavalent cation—substitute for $Zr^{4+}$ and $Si^{4+}$) has been reported in zircon (e.g., Speer 1982, Hinton and Upton 1991, Hoskin et al. 2000, Hanchar et al. 2001, Finch et al. 2001). However, this substitution mechanism is minimal in zircons described here, presumably because of low concentrations of P in the melts (Thomas et al. 2002), so some other element(s) must assist in charge-balancing the trivalent REEs and Y.

The compatibility of $REE^{3+}$ in zircon is controlled mostly by $REE^{3+}$ radii (Hinton and Upton 1991, Guo et al. 1996). As such, $^{zc/melt}D_{REE}$ increase from La through Yb as the ionic radii decrease from 1.16 Å to 0.985 Å, and approach the ionic radius of $Zr^{4+}$ (0.84 Å; ionic radii in VIII-coordination are from Shannon 1976). Due to differences in the ionic radius of $Zr^{4+}$ compared to radii of the $REE^{3+}$, substitution of $REE^{3+}$ for $Zr^{4+}$ in the zircon structure results in lattice strain. Blundy and Wood (1994) and Wood and Blundy (1997) describe a method based on a lattice strain model developed by Brice (1975) to predict partitioning behavior in mineral/melt systems. According to this model, partition coefficients should display a parabolic form when log $^{mineral/melt}D_M$ is plotted versus ionic radii for a group of isovalent cations. The maximum on the parabola defines the optimum cation size that fits into the site involved in the partitioning (Onuma et al. 1968), and it is generally close to the size of the major cation that is being replaced. For zircon, the maximum on the parabola should be at approximately 0.84 Å, which corresponds to the ionic radius of $Zr^{4+}$ in the zircon structure (Speer 1982, Shannon 1976). However, it should be noted that several investigations have shown that the optimal size of the cation that fits into the site onto which partitioning occurs increases as the trace element charge decreases (Van Westrenen et al. 2000, Hill et al. 2000). Therefore, the maximum on the parabola may in fact be somewhat greater than 0.84 Å for the partitioning of $REE^{3+}$ cations into the $Zr^{4+}$ site.

The $^{zc/melt}D_{REE}$ values predicted from the Brice (1975) equation are compared to values calculated from MI and zircon analyses on Figure 6. The predicted $^{zc/melt}D_{REE}$ were obtained using 0.84 Å as the optimum cation radius ($r_o$) of the Zr site onto which partitioning occurs, a Young's modulus for the Zr site (E) of 2003 kbar, and the homogenization temperatures obtained from each MI (Thomas et al. 2002). The Young's modulus was derived by fitting partitioning data to Equation (10) of Wood and Blundy (1997) and then using the relationship between Young's modulus and bulk modulus described by Hazen and Finger (1979) and shown in Blundy and Wood (1994; their Fig. 3). The Brice (1975) model requires that the partition coefficient for one cation of the isovalent group be known in order to calculate partition coefficients for other elements of the isovalent group. In the model calculations shown on Figure 6, the value $^{zc/melt}D_{Sm}$ from each zircon/MI pair was used to represent the "known" ($D_a$) value for that inclusion. The predicted values shown on Figure 6b define only one limb of the parabola because the radius of the Zr site (0.84 Å) is smaller than the radius of the smallest REE (Yb) measured. The maximum on the parabola is at a radius of 0.84 Å and lies off of the diagram to the left. The partition coefficients predicted by the Brice (1975) equation lie within the range of $^{zc/melt}D_{REE}$ for all of the REE measured using the MIM technique, and the predicted values vary by less than one order of magnitude from the median $^{zc/melt}D_{REE}$ values reported in Table 1 (except for Ce, which is discussed in more detail below).

Partition coefficients predicted by the Brice equation from the MI data are compared to published values on Figure 6c. All studies, including data obtained using the MIM technique (Thomas et al. 2002), show an increase in compatibility with decreasing ionic radius. However, in contrast to most previously published results (with the exception of the data of Murali et al. 1983), the MIM data indicate that La and Nd are not partitioned into zircon in felsic melts (i.e., $^{zc/melt}D_M < 1$). Petrogenetic implications of this difference are considered later. Most previous studies show flat partitioning patterns for the light through middle REE (i.e., no change in the partition coefficient with ionic radius), whereas MIM results indicate continuously decreasing compatibility from Yb through La as predicted by the Brice equation. Watson (1980) shows the same general pattern as determined by the MIM technique (Fig. 5c), although the absolute values for $^{zc/melt}D_M$ between the two studies differ by more than one order of magnitude for La (and less for the other REE). These differences

may be related to differences in melt compositions between these two studies (i.e., peralkaline versus granitic, respectively). Note that the $^{zc/melt}D_{LREE}$ trends from previously published studies are opposite of that predicted by the Brice (1975) model. Hinton and Upton (1991) noted that many published $^{zc/melt}D_{LREE}$ are significantly higher than would be expected if REE substitution is exclusively a function of ionic radius, and that the high partition coefficients from these studies may be affected by impurities contained in zircon separates.

Differences in calculated $^{zc/melt}D_M$ described above also reflect the different experimental and analytical techniques employed in these various studies. Hinton and Upton (1991), Maas et al. (1992) and Guo et al. (1996) suggested that many of the reported $^{zc/melt}D_M$ values may have large errors associated with them owing to bulk analysis of zircons containing solid inclusions or altered zircons, and other workers have documented the significant effects of small amounts of contaminants during analysis (Michael 1988, Beattie 1994). Our calculations indicate that including less than 0.01 to 0.001% of an accessory mineral that strongly partitions the LREE (e.g., allanite or mona-

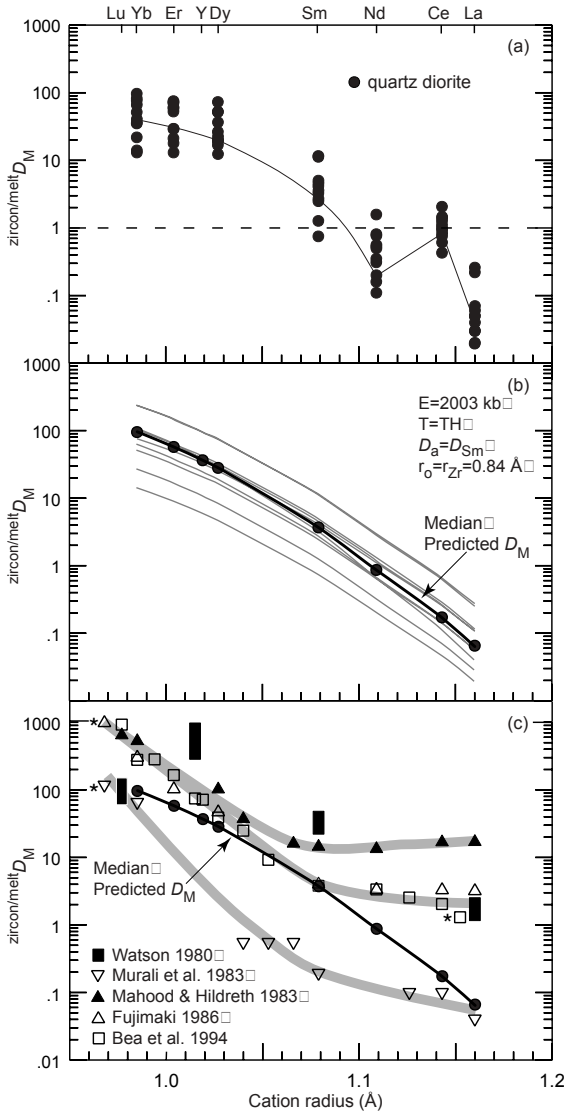


**Figure 6.** Zircon/melt partition coefficients ($^{zc/melt}D_{REE}$) vs. cation radii of the rare earth elements (cation radii in VIII-coordination are from Shannon 1976). The homogenized melt inclusions in zircons used to determine partition coefficients are from the Quottoon quartz diorite. (a) $^{Zc/melt}D_{REE}$ calculated from secondary ion mass spectrometric analyses of host zircon/MI pairs. The calculated values are listed in Table 1. The line connects values determined from one zircon/MI pair and shows the expected parabolic trend (see Fig. 6b) as well as the significant Ce anomaly. Similar trends are exhibited by the other ten inclusions, but are not shown because the overlap in data makes it difficult to identify lines connecting individual inclusions. The dashed line separates the elements that are compatible in the zircon crystal structure (i.e., $^{zc/melt}D_{REE}$ >1) from elements that are incompatible in the zircon crystal structure. (b) $^{Zc/melt}D_{REE+Y}$ predicted by the Brice (1975) calculated using the measured homogenization temperature for each melt inclusions (see text for details). The heavy solid line defines the median predicted partition coefficient ($D_M$). (c) Comparison of median predicted $D_M$ to previously published results. The upper shaded line shows the trend for the data of Mahood and Hildreth (1983), the middle shaded line approximates the trends for the data of Fujimaki (1986) and Bea et al. (1994), and the lower shaded line shows the trend for the data of Murali et al. (1983). Five of the data points (denoted by asterisks) from previous studies have been offset to the along the cation radius axis to avoid overlapping of the symbols. [Used by permission of Elsevier Science, from Thomas et al. (2002) *Geochimica et Cosmochimica Acta*, Vol. 66, Fig. 7, p. 2895]

zite) within the bulk sample could produce the observed flat $^{zc/melt}D_{LREE}$ pattern reported by other workers (Fig. 6c). We suggest that the good agreement between model results predicted by the Brice equation and those obtained using the MIM technique, indicate that $^{zc/melt}D_{REE}$ obtained using the MIM technique may have smaller errors compared to those obtained from bulk analyses of mineral separates because "pure" zircon and/or glass separates may be impossible to obtain.

***Positive Ce anomalies in zircon.*** Terrestrial zircon commonly shows a positive Ce anomaly (Murali et al. 1983, Hinton and Upton 1991, Ireland and Wlotzka 1992), which has been interpreted to indicate the incorporation of $Ce^{4+}$ into zircon. Because $Ce^{4+}$ has the same charge and a similar ionic radius ($Ce^{4+}$ = 0.97; $Zr^{4+}$ = 0.84 Å) as the $Zr^{4+}$ it replaces, it is incorporated into the zircon structure much more readily than the larger $Ce^{3+}$ ($Ce^{3+}$ = 1.143 Å). Thus, the calculated partition coefficient for Ce (Fig. 6a) represents an apparent partition coefficient that includes both $Ce^{3+}$ and $Ce^{4+}$ (Hinton and Upton 1991). The strong positive Ce anomalies in zircon (e.g., Murali et al. 1983, Hinton and Upton 1991, Maas et al. 1992, Guo et al. 1996, Hoskin et al. 2000, Ireland and Wlotzka 1992) indicate that Ce occurs in melts as both $Ce^{4+}$ and $Ce^{3+}$, although $Ce^{3+}$ dominates in terrestrial melts (Schreibber et al. 1980). Ce anomalies are absent in most lunar zircons (Hinton and Myer 1991, Wopenka et al. 1996) that formed under reducing conditions.

The expected partition coefficient assuming 100% $Ce^{3+}$ was calculated using the Brice (1975) equation described earlier. Using the same values for the input parameters as described above for the other $REE^{3+}$ gives $^{zc/melt}D_{Ce^{3+}}$ = 0.14 (Fig. 6b). The median value for the apparent partition coefficient for Ce determined from the MIM technique is 0.99 (Table 1). The partition coefficient for $Ce^{4+}$ in zircon was predicted using the ionic radius for $Ce^{4+}$ (0.97 Å), a Young's modulus (E) for the site of 4226 kbar (based on the relationship between cation charge/site volume ratio ($Z/d^3$) and bulk modulus, after Hazen and Finger (1979) and using $^{zc/melt}D_{Zr^{4+}}$ = 1700 (based on the average Zr concentration in the MI and host zircon). Using these values, the median value predicted by the Brice (1975) equation is $^{zc/melt}D_{Ce^{4+}}$ = 102.6.

The $Ce^{4+}/Ce^{3+}$ ratio in the MI was estimated using the calculated $^{zc/melt}D_{Ce^{4+}}$ and $^{zc/melt}D_{Ce^{3+}}$ values, the apparent $^{zc/melt}D_{Ce}$ values from Table 1, and equation 2 from Hinton and Upton (1991). The calculated $Ce^{4+}/Ce^{3+}$ ratios range from 0.0029 to 0.0188, and (except for one value) show a systematic increase in Ce concentration in zircon with increasing $Ce^{4+}/Ce^{3+}$ ratio in the melt, suggesting that zircons with the highest Ce content crystallized from melts with the highest $Ce^{4+}/Ce^{3+}$ ratios. The wide range in Ce concentration in zircon is likely the result of variable Ce and evolving $Ce^{4+}/Ce^{3+}$ ratio in the melt during crystallization. It should be noted, however, that zircons with positive Ce anomalies (reflecting an elevated concentration of $Ce^{4+}$ in the zircon) can be produced from melts with relatively low $Ce^{4+}/Ce^{3+}$ (Hinton and Upton 1991).

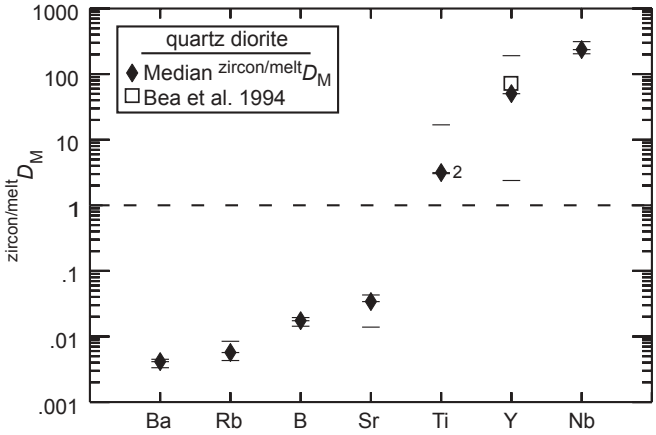


**Figure 7.** Trace element $^{zc/melt}D_M$ determined from zircon/melt inclusion pairs from homogenized melt inclusions in zircon from the Quottoon quartz diorite. The elements are plotted in terms of increasing compatibility in zircon. Tic marks indicate individual values, and the "2" adjacent to the tic mark for Ti indicates two data points with overlapping values. Also shown for comparison is a single value for $^{zc/melt}D_Y$ from the literature (Bea et al. 1994). The dashed line is the same as in Figure 6a. [Used by permission of Elsevier Science, from Thomas et al. (2002) *Geochimica et Cosmochimica Acta*, Vol. 66, Fig. 8, p. 2897]

**Table 3.** Zircon/melt partition coefficients ($D_M$) calculated from the trace element concentrations of three melt inclusions and their coexisting zircon hosts. [Used by permission of Elsevier Science, from Thomas et al. (2002) *Geochimica et Cosmo-chimica Acta*, Vol. 66, Table 5, p. 2897]

| | $D_{Ba}$ | $D_{Rb}$ | $D_B$ | $D_{Sr}$ | $D_{Ti}$ | $D_Y$ | $D_{Nb}$ |
|---|---|---|---|---|---|---|---|
| | 0.003 | 0.008 | 0.019 | 0.034 | 3.30 | 50.2 | 312 |
| | 0.005 | 0.006 | 0.014 | 0.043 | 16.8 | 191 | 236 |
| | 0.004 | 0.004 | 0.017 | 0.014 | 3.15 | 2.39 | 204 |
| Median $D_M$ | 0.004 | 0.006 | 0.017 | 0.034 | 3.30 | 50.2 | 236 |

***Other trace elements.*** In addition to REE, the MIM technique may be used to determine partitioning behavior of a wide range of other trace elements. For example, zircon/melt partition coefficients for Ba, Rb, B, Sr, Ti, Y and Nb were obtained using the MIM technique (Table 3). Zircon/melt partition coefficients for these elements were calculated as described above for the REE, and are plotted on Figure 7 in terms of increasing compatibility. $^{Zc/melt}D_M$ values are listed in Table 1. As expected based on charge/size ratios, Ba, Rb, B and Sr behave incompatibly, whereas Y and Nb are highly compatible, with Ti showing moderate compatibility. These values are consistent with elevated Nb and Y concentrations often reported for zircon (cf. Hoskin et al. 2000), and with the single value for $^{zc/melt}D_Y$ from Bea et al. (1994).

## Petrogenetic implications

Partition coefficients are required for quantitative modeling of petrogenetic processes and relatively small errors in partition coefficients can significantly affect model predictions. To illustrate this, we have modeled batch partial melting (Shaw 1970) and fractional crystallization (Greenland 1970) using the $^{zc/melt}D_{La}$ and $^{zc/melt}D_{Yb}$ determined using the MIM technique and compared these results to those predicted using the partition coefficients of Fujimaki (1986). We se-

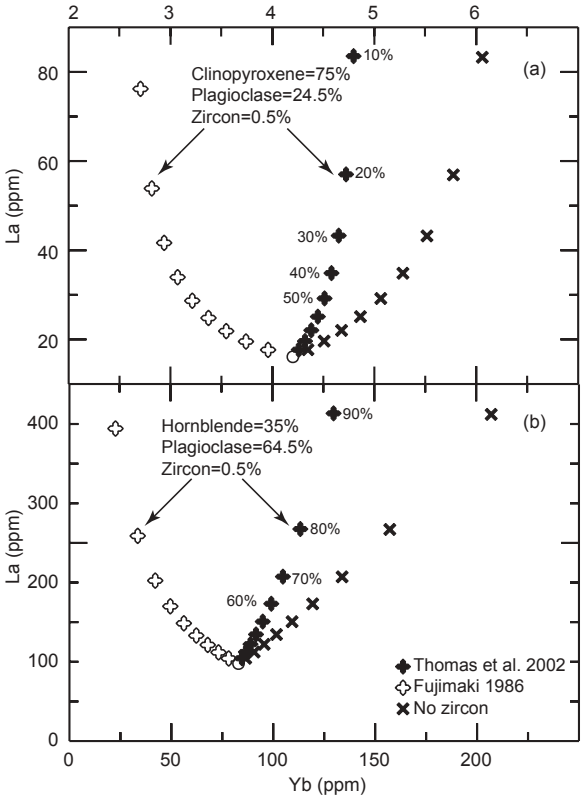


**Figure 8.** Petrogenetic models for (a) batch partial melting (Shaw 1970) and (b) fractional crystallization (Greenland 1970) showing the effect of variation in $^{zc/melt}D_{La}$ and $^{zc/melt}D_{Yb}$ on melt evolution, using values determined by the melt inclusion-mineral technique and from Fujimaki (1986). Also shown for comparison are model results without zircon in the residual assemblage for batch partial melting (a) and in the fractionation assemblage for fractional crystallization (b). The numbers next to the model values indicate the mass percent melt generated for partial melting and the mass percent crystallization for fractional crystallization. The La (16.1 ppm) and Yb (4.2 ppm) concentrations of the starting composition for the partial melting model are from a mafic (amphibolite) protolith (Thomas and Sinha 1999). The fractional crystallization model uses 96.6 ppm La and 4.38 ppm Yb (MI #4 from Thomas et al. 2002) as the starting concentrations. The partition coefficients for clinopyroxene and plagioclase are from Klein et al. (2000), Schnetzler and Philpotts (1970) and Fujimaki et al. (1984). [Used by permission of Elsevier Science, from Thomas et al. (2002) *Geochimica et Cosmochimica Acta*, Vol. 66, Fig. 9, p. 2898]

lected La and Yb for these calculations because published partition coefficients for these elements show the largest departure from results obtained using the MIM technique described above. Results using the MIM technique are compared to those of Fujimaki (1986) because those values are widely used in published petrogenetic models.

The La concentrations modeled by batch partial melting are not significantly different between the zircon-free and zircon-bearing models, or using the Fujimaki (1986) data or data obtained from the MIM technique. As shown on Figure 8a, Yb is most incompatible in the residue for the model with 0% zircon in the residual assemblage, as well as in the model including 0.5% zircon and using $^{zc/melt}D_{Yb}$ obtained from the MIM technique. However, using $^{zc/melt}D_{Yb}$ from Fujimaki (1986) results in Yb depletion in the melt for the zircon-bearing case. During fractional crystallization, Yb is conserved in the melt for the model with 0% zircon in the fractionated assemblage, as well as in the model including 0.5% zircon and using $^{zc/melt}D_{REE}$ obtained from the MIM technique (Fig. 8b). However, using $^{zc/melt}D_{REE}$ of Fujimaki (1986) results in strongly Yb-depleted melt for the zircon-bearing case. These calculations illustrate the significant differences that may result using different values for REE partition coefficients in petrogenetic models and highlight the need for accurate partitioning data for use in modeling.

**Summary of trace element partitioning by the MIM technique**

It is important to emphasize that partition coefficients in natural systems vary as a function of many parameters, including ionic potential, temperature, pressure, oxygen fugacity, crystal chemistry, and melt composition, including water content (Onuma et al. 1968, Drake and Weill 1975, Watson 1977, Matsui et al. 1977, Philpotts 1978, Hart and Davis 1978, Lindstrom and Weill 1978, Ryerson and Hess 1978, Green and Pearson 1983, 1986; Dunn 1987, Blundy and Wood 1991, Hill et al. 2000). For example, the volatile content of a melt may significantly affect partitioning behavior of trace elements between the melt and crystallizing phases. Wood and Blundy (2002) note that water has the effect of lowering $^{cpx/melt}D_{REE}$ but that water has no effect on $^{garnet/melt}D_{REE}$. Blundy (pers. comm. 2002) further notes that zircon may behave more like garnet. A great advantage of the MIM technique is that many of the parameters that may affect trace element partitioning can be measured directly by analysis of the MI. For instance, Thomas et al. (2002) estimated water contents as high as 8 to 9 wt % in zircon hosted MI, and some of the differences in partitioning behavior that they observed (compared to other published results) may be due to these high water contents.

Median zircon/melt $D_{REE}$ determined from 11 zircon/MI pairs from the Toba rhyolite and from

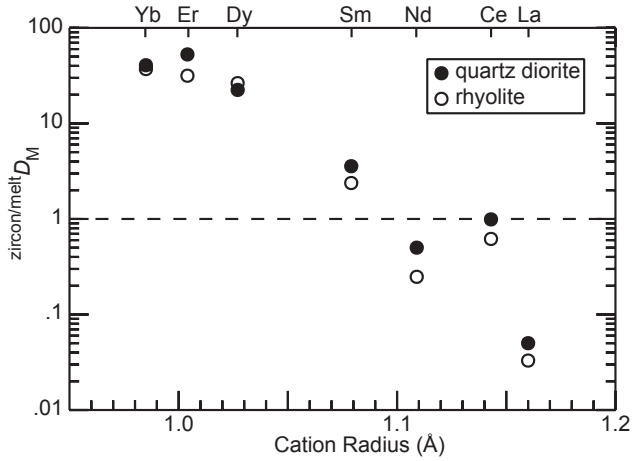


**Figure 9.** Comparison of $^{zc/melt}D_M$ determined from homogenized melt inclusions in zircons from the Quottoon quartz diorite and glass inclusions in zircons from the Toba rhyolite. Note that similar partition coefficients were obtained using both homogenized and glass melt inclusions in zircons. The dashed line is the same as in Figure 6a.

11 zircon/MI pairs from the Quottoon quartz diorite are shown on Figure 9. The median partition coefficients are remarkably similar even though the zircons were extracted from rocks with significantly different bulk rock compositions (62 wt % $SiO_2$ for the quartz diorite and 76 wt % $SiO_2$ for the rhyolite). Although the bulk rock compositions are very different, compositions of MI in zircon from these two rocks show much smaller differences. The similarity of the partition coefficients determined from zircon/MI pairs extracted from two different bulk rocks, from different types of MI (homogenized versus glass MI) provides strong evidence for the validity of the MIM technique for determining partition coefficients. The differences between the bulk rock composition and the melt inclusion compositions, perhaps, illustrate the dangers of using the bulk rock as a measure of the melt for determination of partitioning behavior. It is also important to note that the MI in zircons from the rhyolite were not heated, yet the partition coefficients determined using the MIM technique yielded essentially the same results as those obtained from the homogenized MI in zircons from the quartz diorite. The similarity of the partition coefficients from these two rocks indicates that the REE abundances of the homogenized MI were not changed during heating and homogenization experiments.

The MIM technique described above to determine trace element partition coefficients is valid for the mineral zircon. The validity of the technique is based on the fact that diffusion rates for REE in zircon are extremely slow (Cherniak et al. 1997, Cherniak and Watson, this volume). Thus, the REE concentrations of MI and host zircon are unlikely to change as a result of diffusion following trapping. However, similar behavior is not expected for all minerals from all environments. While Sobolev et al. (1996) were able to determine trace element partitioning behavior between basaltic melt and clinopyroxene based on MI in clinopyroxene from the Upper lavas of the Troodos Massif, Cyprus, it is not clear that the approach would have worked for clinopyroxene (or other minerals) that cooled more slowly in a deep-seated environment.

## ARE MI COMPOSITIONS REPRESENTATIVE OF THE BULK MELT?

To use MI to better understand geologic processes, it must be assumed that the MI compositions are representative of the bulk melt. Below we consider several mechanisms that could produce MI with compositions different from that of the bulk melt at the time of trapping. First we address the possibility that MI compositions are not representative of the bulk melt due to boundary layer processes. Next, we consider if the MI remained a closed system since the time of formation and whether compositions of MI have changed by diffusive exchange with melt (or other fluids) outside the host crystal. Finally, we discuss potential analytical errors (homogenization of crystalline MI, and electron microprobe and SIMS analyses).

### Boundary layer effects

A primary concern of MI studies is whether MI compositions are representative of the bulk melt (e.g., Watson et al. 1982, Bacon 1989). During crystal growth, compatible elements are depleted from the melt near the crystal-melt interface, and incompatible elements accumulate in the boundary layer because they are excluded from the growing crystal. The width of the boundary layer is governed by the crystal growth rate, the rate at which compatible elements diffuse towards a growing crystal and the rate at which incompatible elements diffuse away from the boundary layer. If a significant proportion of the MI is composed of melt from a chemically differentiated boundary layer, the MI composition may not be representative of the bulk melt. The scale of the boundary layer and its role in affecting MI trace element chemistry is poorly understood. If boundary layers have dimensions similar to melt inclusion sizes (i.e., tens of microns), then systematic variations between MI size and trace element concentration should be observed. Additionally, the extent of enrichment and depletion for different elements should vary from one host mineral to the next. Several studies addressed the significance of boundary layer development, and concluded that its effect on MI compositions is small for most inclusions greater than ~25 μm (Anderson 1974,

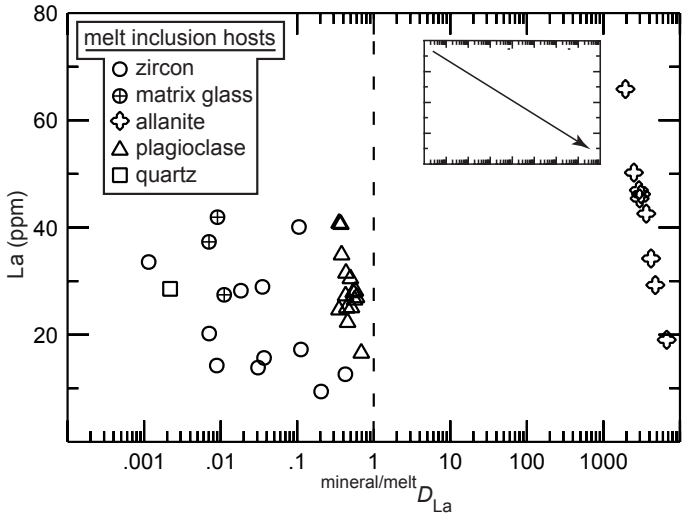


**Figure 10.** $^{Mineral/melt}D_{La}$ versus La contents of melt inclusions hosted by zircon, allanite, plagioclase and quartz from the Toba rhyolite. The arrow in the inset schematically shows the trend that would be expected if melt inclusion scale boundary layers had affected the trace element compositions of the inclusions. The mineral/melt partition coefficients were determined using the melt inclusion-mineral technique (see text). The dashed line is the same as in Figure 6a.

Lowenstern 1995) and can be ignored for inclusions >50 μm in diameter (Lu et al. 1995). Webster and Rebbert (2001) found no boundary layer effects in MI smaller than 70 μm in quartz from Ascension Island.

To better understand the role of boundary layers during MI formation, the trace element chemistry (La, Ce, Nd, Sm, Dy, Er, Yb and Sr) of MI in zircon, allanite, plagioclase and quartz from the Toba rhyolite was examined. Matrix glass adhering to zircon crystals was also analyzed. Based on petrographic evidence and major element chemistry, zircon, allanite, plagioclase and quartz co-crystallized from the same rhyolitic melt. Solid inclusions of each mineral occur in all the other minerals. For example, solid inclusions of zircon occur in allanite, plagioclase and quartz indicating that zircon was precipitating at the same time (and perhaps earlier) as the last mineral to crystallize from the melt. Major element concentrations of the MI in the different minerals overlap suggesting co-crystallization.

If boundary layers on the order of tens of microns developed adjacent to growing crystals, then MI in zircon should be enriched in the incompatible elements La, Nd and Sr compared to the bulk melt. Conversely, the heavy REE are compatible in zircon and should be depleted in the MI compared to the average melt. Melt inclusions in allanite crystals should be depleted in all REE (especially La), because the REE are highly compatible in the allanite crystal structure. $REE^{3+}$ are incompatible in plagioclase, whereas, Sr is compatible in plagioclase. Therefore, all REE should be enriched in MI in plagioclase crystals compared to the bulk melt. REE and Sr are incompatible in quartz; thus, MI in quartz should contain higher concentrations of the trace elements than the bulk melt.

Results of SIMS analyses show that MI hosted by allanite are not depleted in La compared to MI hosted by zircon, plagioclase, or quartz (Fig. 10) as would be expected if a La-depleted boundary layer had affected MI compositions. Likewise, MI hosted by plagioclase are not depleted in Sr compared to MI in zircon, allanite or quartz as would be expected if a Sr-depleted boundary layer had affected MI compositions. The MI contained in quartz have lower concentrations of REE and Sr than MI hosted by zircon, allanite and plagioclase. Furthermore, there are no systematic variations in trace element concentrations as a function of MI size (Fig. 11) as would be expected if the compositions of MI were modified by boundary layer processes. Also, the La concentration of

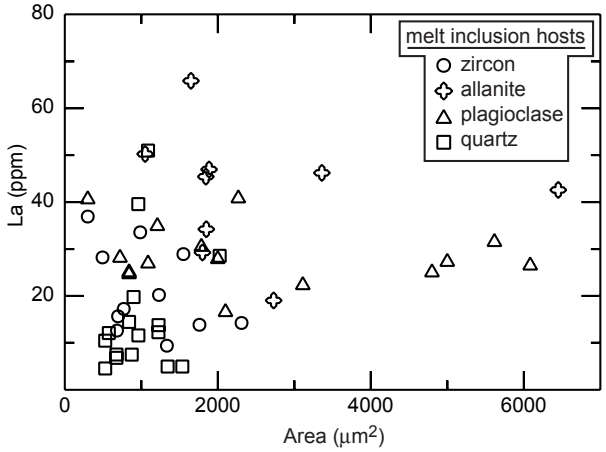


**Figure 11.** The La abundances of melt inclusions hosted in zircon, allanite, plagioclase and quartz crystals from the Toba rhyolite are not correlated with melt inclusion size, as would be expected if melt inclusion scale boundary layers had affected the trace element compositions of the inclusions. Melt inclusion cross-sectional area was calculated using the maximum dimensions of the melt inclusions.

matrix glass adhering to zircon is similar to MI hosted by zircons. We note that the inclusions described here range from 20 to 100 μm and do not preclude the possibility that boundary layer processes affect the compositions of smaller MI. Based on our studies of MI contained in minerals with significantly different partitioning behavior, we conclude that boundary layer processes did not affect the compositions of the MI contained in these crystals, and are probably insignificant in most MI studies.

**Re-equilibration of melt inclusions**

An additional assumption involved in the use of MI is that they remain closed systems after trapping. However, under some conditions and in some host minerals (e.g., olivine), melt trapped in an inclusion may continue to equilibrate with the bulk melt surrounding the host mineral as a result of diffusive exchange of components. For example, it is well known that water (Sobolev et al. 1990, Lowenstern and Mahood 1991, Lu 1991, Vityk et al. 2000) and some major elements (Gaetani and Watson 2000, Danyushevsky et al. 2000, 2002) in MI may continue to exchange with the host phase or surrounding melt, either during slow cooling in nature or during prolonged heating experiments in the laboratory. Qin et al. (1992) modeled the diffusive re-equilibration of chemical species in inclusions with the surrounding melt. For a host crystal 1 mm in diameter containing a 10 μm MI, it would take approximately $3 \times 10^{14}$ years for Lu in a zircon hosted inclusion to reach 10% re-equilibration with the melt surrounding the crystal (based on the diffusion coefficient for Lu from Cherniak et al. 1997, Cherniak and Watson, this volume). The time required to reach a given degree of re-equilibration increases as the diffusion coefficient decreases. According to Cherniak et al. (1997), the diffusion coefficients for the REE in zircon decrease with decreasing atomic number; thus, the time required for all other REE will be longer than that calculated above for Lu. Thus, the theoretical model of Qin et al. (1992) indicates that the probability of changing the REE concentration of MI in zircon as a result of diffusion is essentially nil, even if the MI had been maintained at the formation temperature for hundreds of millions of years. Of course, rates of diffusion will be faster in most host phases other than zircon, and may significantly affect the MI composition. We also note that the diffusion coefficients for other trace elements (such as Ba, Rb, B, Sr, Ti Y and Nb described above) are not as well constrained as those for REE in zircon, and could have been modified by later processes.

The closure temperature for REE diffusion in zircon is higher than that for most other min-

erals, such as diopside, titanite, garnet and apatite (Dahl 1997, Cherniak et al. 1997), suggesting that inclusions in these minerals would continue to exchange REE with the melt surrounding the crystal to a lower temperature compared to zircon (Qin et al. 1992). Thus, the MIM technique should only be used to determine partition coefficients for trace elements in minerals with high closure temperatures for those elements, and/or from environments in which post-entrapment cooling was rapid.

**Potential errors during homogenization and analysis**

As discussed above, compositions of MI in zircons were unlikely to have been affected by boundary layer processes or diffusion-related re-equilibration following entrapment. This allows us to focus on errors resulting from homogenizing the inclusions, and analytical errors. During the course of heating inclusions to produce a homogeneous glass for microanalysis, it is assumed that any zircon that precipitated onto the MI walls following entrapment would have been incorporated back into the melt during the homogenization experiments. The amount of zircon precipitated during cooling (or dissolved during later reheating) is controlled by zircon solubility in the melt as a function of temperature (and melt composition). Good agreement between measured homogenization temperatures and temperatures predicted from the zircon saturation equation of Watson and Harrison (1983) (using the measured Zr concentrations in the MI), suggests that MI equilibrated with the zircon host during the homogenization process, i.e., all zircon precipitated during cooling was subsequently dissolved during heating to homogenize the MI.

To assess potential errors associated with dissolving too much or too little zircon host during homogenization, Thomas et al. (2002) compared MI homogenization temperatures to zircon saturation temperatures (Watson and Harrison 1983) calculated from compositions of inclusions. For example, one inclusion in zircon from the quartz diorite had 649 ppm Zr, an M-value of 1.26 (where M is the cation ratio [Na+K+2Ca]/Si·Al), and yielded a temperature (937°C) that is in excellent agreement with the measured homogenization temperature (950°C). If it is assumed that during cooling and crystallization all of the Zr in the original melt was incorporated into zircon crystallizing on the walls, and if only 10% (65 ppm) of the Zr that precipitated was re-incorporated into the melt during homogenization, then the calculated zircon saturation temperature would be 721°C. Similarly, overheating the inclusion and adding 1% excess zircon (containing ~500,000 ppm Zr) to the MI would change the Zr concentration in the melt from 649 to 5573 ppm. The zircon saturation temperature predicted from this Zr concentration is 1242°C. Note that dissolving excess zircon during homogenization is analogous to placing the ion beam partially on the MI and partially on the host zircon during SIMS analysis. Incorporation of excess zircon in the inclusion, either from overheating or incorrect beam placement, would result in a zircon saturation temperature significantly different from those calculated for the MI (and significantly different from the measured homogenization temperatures), and is not supported by the measured Zr concentrations of the MI.

## FUTURE DIRECTIONS

Melt inclusions hold great promise as a tool to better understand geologic processes. As demonstrated by Chupin et al. (1998), MI hosted in detrital zircons may be a valuable tool (in addition to zircon ages and geochemical-isotopic data from the zircon crystal itself) to fingerprint sediment sources and help constrain tectonic reconstruction models. Melt inclusions should become a widely used tool in provenance studies to directly measure the compositions of zircon-precipitating melts. Wilde et al. (2001) used oxygen isotopic and trace element data from detrital zircons from western Australia to infer the existence of granitoid magmatism in Earth's early history at 4.404 Ga. As such, MI in old zircons may preserve compositions of ancient crust forming melts, providing direct measurement of melt chemistry and possibly revealing an unprecedented understanding of the Earth's early history.

In many cases it is difficult to infer the geologic environment in which a particular zircon

crystal grew, especially in rocks with polygenetic histories (e.g., growth from a melt versus hydrothermal growth; see Hoskin and Black (2000) for details regarding modes of zircon growth). It is important to note that inherited zircon cores are common in igneous zircons (but not in peralkaline rocks) (Vavra 1990) and have been identified through detailed microscopy (e.g., petrography, cathodoluminescence, back-scattered electron imaging) and/or differences in composition and age between core and overgrowth (Hanchar and Rudnick 1995). As discussed above, Chupin et al. (1998) documented that MI in 3.4 Ga zircons survived episodes of metamorphism that reached granulite facies in some rocks.

Assuming that a significant portion of all zircon that crystallized from a melt contain MI, the presence or absence of MI in zircon would not only verify (or refute) that the enclosing zircon precipitated from a melt, but would also yield the composition of the melt from which the zircon crystallized. Ideally, both an inherited zircon core and the overgrowth would contain MI if both crystallized from a melt. The MI in the core would yield the composition of the melt that crystallized to form the source region protolith that was later partially melted to form a new batch of magma. Melt inclusions in the zircon overgrowth would represent the zircon-precipitating melt that formed during (or after) partial melting of the source protolith. To date there have been no measurements of isotopic compositions of MI in zircon. An obvious application would be to use the isotopic compositions of MI in zircons to constrain melt source regions, models of magma mixing and assimilation/crystallization.

The position in the crystallization sequence represented by a particular MI is usually inferred by its $SiO_2$ content or some other fractionation index. To more accurately constrain the petrogenetic history of magmatic systems, it would be useful to combine geochemical/isotopic information from MI with the absolute ages of the host zircon using $^{238}U$-$^{230}Th$ disequilibrium ages. Such information would provide a method to assess melt compositional variations on an absolute time scale. Acquiring U-Th disequilibrium ages of MI host phases is most likely possible for U- and Th-rich accessory minerals like zircon (Reid et al. 1997, Lowenstern et al. 2000, Vasquez and Reid 2001) from rocks ranging in age from ~1 ka to ~1 Ma. As analytical techniques continue to become more miniaturized and as lower detection limits are achieved in mass spectrometry, zircon hosted MI investigations will allow us to answer many currently unresolved questions.

## ACKNOWLEDGMENTS

The authors thank L. Fedele, J.J. Student, G. Benedix and R.J. Tracy for advice and assistance concerning electron microprobe analyses of glass inclusions. J.J. Student provided valuable advice on techniques for homogenizing crystalline melt inclusions. Constructive reviews by J.M. Hanchar and W. Van Westrenen greatly improved an earlier version of this manuscript. Funding was provided by grant EAR-0001168 from the National Science Foundation to R.J. Bodnar and A.K. Sinha.

## REFERENCES

Anderson AT (1974) Evidence for a picritic, volatile-rich magma beneath Mt. Shasta, California. J Petrol 15:243-267

Anderson AT, Newman S, Williams SN, Druitt TH, Skirius C, Stolper E (1989) $H_2O$, $CO_2$, Cl and gas in Plinian and ash-flow Bishop rhyolitic tuff. Am Mineral 76:221-225

Bacon CR (1989) Crystallization of accessory phases in magmas by local saturation adjacent to phenocrysts. Geochim Cosmochim Acta 53:1055-1066

Barker F (1979) Trondhjemites: Definition, Environment and Hypothesis of Origin. *In* Barker F (ed) Trondhjemites, Dacites and Related Rocks. Elsevier, Amsterdam, p 1-12

Bea F (1996) Residence of REE, Y, Th and U in granites and crustal protoliths: implications for the chemistry of crustal melts. J Petrol 37:521-552

Bea F, Pereira MD, Stroh A (1994) Mineral/leucosome trace-element partitioning in a peraluminous migmatite (a laser ablation-ICP-MS study). Chem Geol 117:291-312

Beattie P (1994) Systematics and energetics of trace-element partitioning between olivine and silicate melts: Implications for the nature of mineral/melt partitioning. Chem Geol 117:57-71

Blundy JD, Wood BJ (1991) Crystal-chemical controls on the partitioning of Sr and Ba between plagioclase feldspars, silicate melts and hydrothermal solutions. Geochim Cosmochim Acta 55:193-209
Blundy JD, Wood BJ (1994) Prediction of crystal-melt partition coefficients from elastic moduli. Nature 372:452-454
Brice JC (1975) Some thermodynamic aspects of the growth of strained crystals. J Cryst Growth 28:249-253
Cherniak DJ, Hanchar JM, Watson EB (1997) Rare-earth diffusion in zircon. Chem Geol 134:289-301
Chesner CA (1998) Petrogenesis of the Toba Tuffs, Sumatra, Indonesia. J Petrol 39:397-438
Chupin SV, Chupin VP, Barton JM, Barton ES (1998) Archean melt inclusions in zircon from quartzite and granitic orthogneiss from South Africa: magma compositions and probable sources of protoliths. Eur J Mineral 10:1241-1251
Cox KG, Bell JD, Pankhurst RJ (1979) The Interpretation of Igneous Rocks. George, Allen and Unwin, London
Dahl PS (1997) A crystal-chemical basis for Pb retention and fission-track annealing systematics in U-bearing minerals, with implications for geochronology. Earth Planet Sci Lett 150:277-290
Danyushevsky LV, Della-Pasqua FN, Sokolov S (2000) Re-equilibration of melt inclusions trapped by magnesian olivine phenocrysts from subduction-related magmas: petrological implications. Contrib Mineral Petrol 138:68-83
Danyushevsky LV, McNeill AW, Sobolev AV (2002) Experimental and petrological studies of melt inclusions in phenocrysts from mantle-derived magmas: an overview of techniques, advantages and complications. Chem Geol 183:5-24
Drake MJ, Weill DF (1975) Partition of Sr, Ba, Ca, Y, $Eu^{2+}$, $Eu^{3+}$, and other REE between plagioclase feldspar and magmatic liquid: an experimental study. Geochim Cosmochim Acta 39:689-712
Dunn T (1987) Partitioning of Hf, Lu, Ti, and Mn between olivine, clinopyroxene and basaltic liquid. Contrib Mineral Petrol 96:476-484
Finch RJ, Hanchar JM, Hoskin PWO, Burns PC (2001) Rare earth elements in synthetic zircon: Part 2. A single-crystal X-ray study of xenotime substitution. Am Mineral 86:681-689
Frezzotti ML (2001) Silicate-melt inclusions in magmatic rocks: applications to petrology. Lithos 55:273-299
Fujimaki H (1986) Partition coefficients of Hf, Zr, and REE between zircon, apatite, and liquid. Contrib Mineral Petrol 94:42-45
Fujimaki H, Tatsumoto M, Aoki K (1984) Partition coefficients of Hf, Zr and REE between phenocrysts and groundmass. J Geophys Res 89:B662-B672.
Gaetani GA, Watson EB (2000) Open system behavior of olivine-hosted melt inclusions. Earth Planet Sci Lett 183:27-41
Green TH, Pearson NJ (1983) Effect of pressure on rare earth element partition coefficients in common magmas. Nature 305:414-416
Green TH, Pearson NJ (1986) Rare-earth element partitioning between sphene and coexisting silicate liquid at high pressure and temperature. Chem Geol 55:105-119
Greenland LP (1970) An equation for trace element distribution during magmatic crystallization. Am Mineral 55:455-465
Guo J, O'Reilly SY, Griffin WL (1996) Zircon inclusions in corundum megacrysts: I. Trace element geochemistry and clues to the origin of corundum megacrysts in alkali basalts. Geochim Cosmochim Acta 60:2347-2363
Halter WE, Pettke T, Heinrich CA, Rothen-Rutishauser B (2002) Major to trace element analysis of melt inclusions by laser-ablation ICP-MS: methods of quantification. Chem Geol 183:63-86
Hanchar JM, Rudnick RL (1995) Revealing hidden structures: the application of cathodoluminescence and back-scattered electron imaging to dating zircons from lower crustal xenoliths. Lithos 36:289-303
Hanchar JM, Finch RJ, Hoskin PWO, Watson EB, Cherniak DJ, Mariano AN (2001) Rare earth elements in synthetic zircon: Part 1. Synthesis, and rare earth element and phosphorous doping. Am Mineral 86:667-680
Hart SR, Davis KE (1978) Nickel partitioning between olivine and silicate melt. Earth Planet Sci Lett 40:203-219
Hazen RM, Finger LW (1979) Bulk modulus-volume relationship for cation-anion polyhedra. J Geophys Res 84:6723-6728
Hervig RL, Dunbar NW (1992) Causes of chemical zoning in the Bishop (California) and Bandelier (New Mexico) magma chambers. Earth Planet Sci Lett 111:97-108
Hervig RL, Dunbar NW, Westrich HR, Kyle P (1989) Pre-eruptive water content of rhyolitic magmas as determined by ion microprobe analyses of melt inclusions in phenocrysts. J Volc Geotherm Res 36:293-302
Hill E, Wood BJ, Blundy JD (2000) The effect of Ca-Tschermaks component on trace element partitioning between clinopyroxene and silicate melt. Lithos 53:203-215
Hinton RW, Myer C (1991) Ion probe analysis of zircon and yttrobetafite in a lunar granite. Lunar Planet Sci XXII:575-576
Hinton RW, Upton BGJ (1991) The chemistry of zircon: Variations within and between large crystals from syenite and alkali basalt xenoliths. Geochim Cosmochim Acta 55:3287-3302
Hoskin PWO, Black LP (2000) Metamorphic zircon formation by solid-state recrystallization of protolith igneous zircon. J Metamor Geol 18:423-439
Hoskin PWO, Kinny PD, Wyborn D, Chappell BW (2000) Identifying accessory mineral saturation during differen-

tiation in granitoid magmas: an integrated approach. J Petrol 41:1365-1396
Ihinger PD, Hervig RL, McMillan PF (1994) Analytical methods for volatiles in glasses. Rev Mineral 30:67-121
Ireland TR, Wlotzka F (1992) The oldest zircons in the solar system. Earth Planet Sci Lett 109:1-10
Kamenetsky VS, Crawford AJ, Eggins SM, Muehe R (1997) Phenocryst and melt inclusion chemistry of near-axis seamounts, Valu Fa Ridge, Lau Basin: insight into mantle wedge melting and the addition of subduction components. Earth Planet Sci Lett 151:205-223
Klein M, Stosch H-G, Seck HA, Shimizu N (2000) Experimental partitioning of high field strength and rare earth elements between clinopyroxene and garnet in andesitic andtonalitic systems. Geochim Cosmochim Acta 64:99-115.
Li Z (1994) The silicate melt inclusions in igneous rocks. *In* De Vivo B, Frezzotti ML (eds) Fluid Inclusions in Minerals: Methods and Applications. Virginia Tech, Blacksburg, Virginia, p 73-94
Lindstrom DJ, Weill DF (1978) Partitioning of transition metals between diopside and coexisting silicate liquids: I. Nickel, cobalt, and manganese. Geochim Cosmochim Acta 42:817-832
Lowenstern JB (1994) Dissolved volatile concentrations in an ore-forming magma. Geology 22:893-896
Lowenstern JB (1995) Applications of silicate-melt inclusions to the study of magmatic volatiles. *In* Thompson FH (ed) Magma, Fluids, and Ore Deposits. Mineral Assoc Canada, Short Course Ser 23:71-99
Lowenstern JB, Mahood G (1991) New data on magmatic $H_2O$ contents of pantellerites, with implications for petrogenesis and eruptive dynamics at Pantelleria. Bull Volcanol 54:78-83
Lowenstern JB, Persing HM, Wooden JL, Lanphere M, Donnely-Nolan J, Grove TL (2000) U-Th dating of single zircons from young granitoid xenoliths: new tools for understanding volcanic processes. Earth Planet Sci Lett 183:291-302
Lu F (1991) The Bishop Tuff: Origin of the high-silica rhyolite and its thermal and compositional zonations. PhD dissertation, University of Chicago, Chicago, Illinois
Lu F, Anderson AT, Davis AM (1992) New and larger sanidine/melt partition coefficients for Ba and Sr as determined by ion microprobe analyses of melt inclusions and their sanidine host crystals. Geol Soc Am Abstr Progr 24:A44
Lu F, Anderson AT, Davis AM (1995) Diffusional gradients at the crystal/melt interface and their effect on the compositions of melt inclusions. J Geol 103:591-597
Maas R, Kinny PD, Williams IS, Froude DO, Compston W (1992) The Earth's oldest known crust: A geochronological and geochemical study of 3900 Ma detrital zircons from Mt. Narryer and Jack Hills, western Australia. Geochim Cosmochim Acta 56:1281-1300
Mahood G, Hildreth W (1983) Large partition coefficients for trace elements in high-silica rhyolites. Geochim Cosmochim Acta 47:11-30
Matsui Y, Onuma N, Nagasawa H, Higuchi H, Banno S (1977) Crystal structure control in trace element partition between crystal and magma. Bull Soc Fr Minéral Cristallogr 100:315-324
Michael PJ (1988) Partition coefficients for rare earth elements in mafic minerals of high silica rhyolites: The importance of accessory mineral inclusions. Geochim Cosmochim Acta 52:275-282
Morgan GB, London D (1996) Optimizing the electron microprobe analysis of hydrous alkali aluminosilicate glasses. Am Mineral 81:1176-1185
Murali AV, Parthasarathy R, Mahadevan TM, Sankar D (1983) Trace element characteristics, REE patterns and partition coefficients of zircons from different geological environments-A case study on Indian zircons. Geochim Cosmochim Acta 47: 2047-2052
Nagasawa, H (1970) Rare earth concentrations in zircon and their host dacites and granites. Earth Planet Sci Lett 9:359-364
Nakamura N (1974) Determination of REE, Ba, Fe, Mg, Na, and K in carbonaceous and ordinary chondrites. Geochim Cosmochim Acta 38:757-775
Nielsen TFD, Solovova IP, Veksler IV (1997) Parental melts of melilitolite and origin of alkaline carbonatite: evidence from crystallized melt inclusions, Gardiner Complex. Contrib Mineral Petrol 126:331-344
O'Hara MJ, Fry N, Prichard HM (2001) Minor phases as carriers of trace elements in non-modal crystal-liquid separation processes II: illustrations and bearing on behaviour of REE, U, Th and the PGE in igneous processes. J Petrol 42:1887-1910
Onuma N, Higuchi H, Wakita H, Nagasawa H (1968) Trace element partitioning between two pyroxenes and the host lava. Earth Planet Sci Lett 5:47-51
Philpotts JA (1978) The law of constant rejection. Geochim Cosmochim Acta 42:909-920
Poldervaart A (1955) Zircon in rocks: 1, sedimentary rocks. Am J Sci 253:433-461
Poldervaart A (1956) Zircon in rocks: 2, igneous rocks. Am J Sci 254:521-554
Pupin JP, Turco G (1972) Une typologie originale du zircon accessoire. Bull Soc Fr Minéral Cristallogr 95:348-359
Qin Z, Fangqiong F, Anderson AT (1992) Diffusive reequilibration of melt and fluid inclusions. Am Mineral 77:565-576
Reid MR, Coath CD, Harrison TM, McKeegan KD (1997) Prolonged residence times for the youngest rhyolites associated with Long Valley Caldera: $^{230}$Th-$^{238}$U ion microprobe dating of young zircons. Earth Planet Sci Lett 150:27-39

Roedder E (1979) Origin and significance of magmatic inclusions. Bull Minéral 102:487-510
Roedder E (1984) Fluid Inclusions. Rev Mineral, Vol 12, 644 p
Ryerson FJ, Hess PC (1978) Implications of liquid-liquid distribution coefficients to mineral-liquid partitioning. Geochim Cosmochim Acta 42:921-932
Schmidt C, Chou I-M, Bodnar RJ, Basset WA (1998) Microthermal analysis of synthetic fluid inclusions in the hydrothermal diamond anvil cell. Am Mineral 83:995-1007
Schnetzler CC, Philpotts JA (1970) Partition coefficients of rare earth elements between igneous matrix material and rock-forming mineral phenocrysts-II. Geochim Cosmochim Acta 34:331-340.
Schreibber HD, Lauer HV, Thanyasir T (1980) The redox state of cerium in basaltic magmas: An experimental study of iron-cerium interactions in melts. Geochim Cosmochim Acta 44:1599-1612
Shannon RD (1976) Revised effective ionic radii and systematic studies of interatomic distances in halides and chalcogenides. Acta Crystallogr A32:751-767
Shaw DM (1970) Trace element fractionation during anatexis. Geochim Cosmochim Acta 34:237-243
Shimizu N (1998) The geochemistry of olivine-hosted melt inclusions in a FAMOUS basalt ALV519-4-1. Phys Earth Planet Inter 107:183-201
Shimizu N, Hart S (1982) Applications of the ion microprobe to geochemistry and cosmochemistry. Ann Rev Earth Planet Sci 10:483-526
Shimizu N, Sobolev NV, Yefimova ES (1997) Chemical heterogeneities of inclusions in garnet and juvenile character of peridotitic diamonds from Siberia. Russ Geol Geophys 38:356-372
Sisson TW, Layne GD (1993) $H_2O$ in basalt and basaltic andesite glass inclusions from four subduction-related volcanoes. Earth Planet Sci Lett 117:619-635
Sobolev AV (1996) Melt inclusions in minerals as a source of principle petrologic information. Petrology 4:209-220
Sobolev AV, Danyushevsky LV (1994) Petrology and geochemistry of boninites from the north termination of the Tonga Trench: constraints on the generation conditions of high-Ca boninite magmas. J Petrol 35:1183-1211
Sobolev AV, Shimizu N (1993) Ultra-depleted primary melt included in an olivine from the Mid-Atlantic Ridge. Nature 363:151-154
Sobolev AV, Kamenetsky VS, Metrich N, Clochiatti R, Konokova NN, Devirts AL, Ustinov VI (1990) Volatile regime and crystallization conditions in Etna Hawaiite lavas. Geochem Intl 990:53-65
Sobolev AV, Migdisov AA, Portnyagin MV (1996) Incompatible element partitioning between clinopyroxene and basaltic liquid revealed by study of melt inclusions in minerals from Troodos Lavas, Cyprus. Petrology 4:307-317
Sobolev VS, Kostyuk VP (1975) Magmatic crystallization based on a study of melt inclusions. Fluid Inclusion Res 9:182-253 (translated from original publication in Russian)
Sokolov S (2002) Melt inclusions as indicators of the magmatic origin of carbonatite rare metal and rare earth minerals. Chem Geol 183:373-378
Spandler CJ, Eggins SM, Arculus RJ, Mavrogenes JA (2000) Using melt inclusions to determine parent-magma compositions of layered intrusions: application to the Greenhills Complex (New Zealand), a platinum group minerals-bearing, island-arc intrusion. Geology 28:991-994
Speer JA (1982) Zircon. *In* Ribbe PH (ed) Orthosilicates. Rev Mineral 5:67-112
Student JJ, Bodnar RJ (1996) Melt inclusion microthermometry: petrologic constraints from the $H_2O$-saturated haplogranite system. Petrology 4:310-325
Taylor SR, McLennan SM (1981) The composition and evolution of the continental crust: rare earth element evidence from sedimentary rocks. Phil Tran R Soc A301:381-399
Thomas JB, Bodnar RJ (2002) A technique for mounting and polishing melt inclusions in small (<1 mm) crystals. Am Mineral 87:1505-1508
Thomas JB, Sinha AK (1999) Field, geochemical, and isotopic evidence for magma mixing and AFC processes in the Quottoon Igneous Complex, northwestern British Columbia and southeastern Alaska. Can J Earth Sci 36:819-831
Thomas JB, Bodnar RJ, Shimizu N, Sinha AK (2002) Determination of zircon/melt trace element partition coefficients from SIMS analysis of melt inclusions in zircon. Geochim Cosmochim Acta 66:2887-2901
Thomas R (1994) Estimation of viscosity and water content of silicate melts from melt inclusion data. Eur J Mineral 6:511-535
Thomas R (2000) Determination of water contents of granite melt inclusions by confocal laser Raman microprobe spectroscopy. Am Mineral 85:868-872
Van Westrenen W, Allan NL, Blundy JD, Purton JA, Wood BJ (2000) Atomistic simulation of trace element incorporation into garnets: comparison with experimental garnet-melt partitioning data Geochim Cosmochim Acta 64:1629-1639
Vasquez JA, Reid MR (2001) Timescales of magmatic evolution by coupling core-to-rim $^{238}U$-$^{230}Th$ ages and chemical compositions of mineral zoning in allanite from the Youngest Toba Tuff. EOS Trans, Am Geophys Union 82:F1019
Vavra G (1990) On the kinematics of zircon growth and its petrogenetic significance: a cathodoluminescence study.

Contrib Mineral Petrol 106:90-99
Vityk MO, Bodnar RJ, Doukhan JC (2000) Synthetic fluid inclusions XV. TEM investigation of plastic flow associated with reequilibration of fluid inclusions in natural quartz. Contrib Mineral Petrol 56:119-134
Watson EB (1977) Partitioning of Mn between forsterite and silicate liquid. Geochim Cosmochim Acta 41:1363-1374
Watson EB (1980) Some experimentally determined zircon/liquid partition coefficients for the rare earth elements. Geochim Cosmochim Acta 44:895-897
Watson EB (1996) Dissolution, growth and survival of zircons during crustal fusion: Kinetic principles, geologic models and implications for isotopic inheritance. Proc Roy Soc Edinburgh 8:43-56
Watson EB, Harrison TM (1983) Zircon saturation revisited: temperature and composition effects in a variety of crustal magma types. Earth Planet Sci Lett 64:295-304
Watson EB, Sneeringer MA, Ross A (1982) Diffusion of dissolved carbonate in magmas: experimental results and applications. Earth Planet Sci Lett 61:346-358
Webster JD, Duffield WA (1991) Volatiles and lithophile elements in Taylor Creek Rhyolite: Constraints from glass inclusion analysis. Am Mineral 76:1628-1645
Webster JD, Rebbert CR (2001) The geochemical signature of fluid-saturated magma determined from silicate melt inclusions in Ascension Island granite xenoliths. Geochim Cosmochim Acta 65:123-136
Wilde SA, Valley JW, Peck WH, Graham CM (2001) Evidence from detrital zircons for the existence of continental crust and oceans on the Earth 4.4 Gyr ago. Nature 409:175-178
Wood BJ, Blundy JD (1997) A predictive model for rare earth element partitioning between clinopyroxene and anhydrous silicate melt. Contrib Mineral Petrol 129:166-181
Wood BJ, Blundy JD (2002) The effect of $H_2O$ on crystal-melt partitioning of trace elements. Geochim Cosmochim Acta 66:3647-3656
Wopenka B, Jolliff BL, Zinner E, Kremser D (1996) Trace element zoning and incipient metamictization in a lunar zircon: application of three microprobe techniques. Am Mineral 81:902-912

# Zircon Saturation Thermometry

**John M. Hanchar**

*Department of Earth and Environmental Sciences*
*The George Washington University*
*Washington, DC 20006*

**E. Bruce Watson**

*Department of Earth and Environmental Science*
*Rensselaer Polytechnic Institute*
*Troy, New York 12180*

## INTRODUCTION

The ability of crystalline zircon ($ZrSiO_4$) to incorporate and retain trace element and isotopic information, due to sluggish diffusion, makes it an indispensable tool for geochemists and geochronologists (Valley, this volume; Cherniak and Watson, this volume) in deciphering the Earth's geologic history. The stability of crystalline zircon over long periods of geologic time led researchers to prefer this mineral for geochronology (Heaman and Parrish 1991, Dickin 1995, Davis et al., this volume; Parrish and Noble, this volume). In fact, much of what is known about the timing of major geologic events has been accomplished through geochronology using U/Pb isotopic analyses of zircon (Froude et al. 1983, Bowring and Housch 1995, Buick et al. 1995, Bowring et al. 1998, Amelin et al. 1998, Amelin et al. 1999, Bowring and Williams 1999, Amelin et al. 2000, Mojzsis et al. 2001, Wilde et al. 2001, Peck et al. 2001, Bowring and Schmitz, this volume). Because of its durability, zircon has also been proposed as a potential storage material for weapons-grade plutonium from dismantled nuclear weapons (Ewing et al. 1995, Ewing 1999, Ewing et al., this volume).

In addressing the petrogenesis of granitoid rocks, a thorough understanding of the role of accessory minerals is crucial for constraining the distribution of trace elements and isotopes that are hosted mainly by those minerals. In particular, in granitoid rocks that were derived from melting of preexisting crustal sediments or rocks, it is often desirable to understand the role of Zr (and Hf), which is primarily concentrated in zircon. This includes determining whether the zircon crystals are single generation growth having crystallized in the magma in which they were most recently found. Or, if preexisting zircon was entrained (i.e., did not dissolve) in the magma, what volume of the zircon was inherited from the source material and what volume was grown over the preexisting zircon. Other isotopic systems in zircon, such as Lu-Hf and Sm-Nd and O, are also important in crustal evolution studies (Vervoort et al. 1996, Kinny and Maas, this volume; Valley, this volume).

Experimental studies have demonstrated that zircon, when crystalline, has low solubility in crustal melts and fluids (e.g., Watson 1979, Ewing et al. 1982, Watson and Harrison 1983, Tole 1985, Ayers and Watson 1991). Experimental studies such as these help constrain the temperature at which zircon crystallized and the amount of zirconium required to saturate and crystallize zircon in the rock from which the zircon was extracted, to better understand the nature (e.g., the physical properties and chemical composition) of inherited zircon in natural systems, or to determine the nature of zircon dissolving in zircon-undersaturated silicate melts.

The goal of this review paper is to discuss the role of zircon saturation thermometry in illuminating crustal melting processes. This includes a review of the literature on the historical development of zircon crystallization and dissolution, and zircon saturation thermometry studies over the past four decades; some selected examples of applications of using zircon saturation

1529-6466/03/0053-0004$05.00

thermometry in solving petrologic problems involving igneous and metamorphic rocks; and finally a worked example of how zircon saturation temperature is calculated, including a brief discussion of the different analytical problems that may be encountered.

## ZIRCON SATURATION THERMOMETRY

### Historical development

***Natural samples***. In a classic early study by Poldervaart (1955, 1956), petrographic evidence was presented for the occurrence and distribution of zircon in igneous rocks from basaltic to granitic composition. Due to the limited analytical techniques available to that author at the time (e.g., binocular and petrographic microscopes), the observations about the nature and occurrence of zircon were qualitative to semi-quantitative at best. With that said, Poldervaart nevertheless was able to observe that zircon crystals from different rocks types looked different and within a given rock sample there were differences among the separated zircon crystals. This study led the way for later investigations of the distribution and occurrence accessory minerals in granitoid rocks. The study by Poldervaart does not directly discuss zircon saturation thermometry, but it is included here because it does discuss the occurrence of zircon in different rocks types, which is related to zircon saturation in magmas. Murthy (1958) discussed zircon crystallization in granitic magmas using crystal chemistry constraints and determined that for the samples investigated, zircon crystallized early and for a brief duration. Siedner (1965) proposed that the high solubility of zircon in strongly alkaline magmas may result in late stage and relatively minor crystallization of zircon in rocks of that composition (see also Wager and Mitchell 1951, Goldschmidt 1954, Chao and Fleischer 1960).

Bowden (1965), in a study of the Younger granites from Northern Nigeria, proposed that zircon solubility increases with increasing alkalinity of the magma as determined by the alkali/aluminum ratio, (called agapaitic coefficient in Bowden [1965] [(Na+K)/Al expressed as the atomic ratio of these elements from whole-rock analyses]). The Younger granite samples with the highest Zr content also contained riebeckite with a paucity of zircon crystals indicating that Zr was incorporated in other phase(s) in those rocks.

In the past 30 years or so, there have been numerous studies that discuss the occurrence, or lack thereof, of zircon in crustal rocks, and the number of papers that discuss the petrogenesis of accessory minerals in on the increase. In part, this can be attributed to the use of imaging techniques, such as cathodoluminescence (CL) and back-scattered electrons (BSE) (see Corfu et al., this volume and Nasdala et al., this volume), and to the development of high-resolution *in situ* analytical techniques such as secondary ion mass spectrometry (SIMS) (see Davis et al., this volume; Ireland and Williams, this volume), laser ablation inductively coupled plasma mass spectroscopy (LA-ICPMS) (see Kosler and Sylvester, this volume), and improvements in isotope dilution thermal ionization mass spectrometry techniques (ID-TIMS) (Davis et al., this volume; Parrish et al., this volume; Bowring and Schmitz, this volume).

Speer (1982) discussed many studies of the chemistry of zircon that were published up to that time, and provides a good overview of several aspects of zircon chemistry. It should be noted, however, that many of the early studies reported in Speer (1982) were whole zircon analyses, and for this reason the reported analyses should be viewed with particular scrutiny. This is due to the limitations of the imaging and analytical techniques used at the time, and the difficulty of excluding small mineral inclusions of REE- and other trace element-rich minerals that would bias the analysis. Many of those older analyses were done without the aid of any imaging techniques (except for binocular or petrographic microscopy and possibly secondary electrons in a scanning electron microscope) so it is difficult to determine exactly what was analyzed and the significance of the published analyses. Hoskin and Schaltegger (this volume) discuss the geochemistry of zircon in igneous and metamorphic rocks with a current review of the literature.

***Experimental studies.*** Prior to the 1960s there were few experimental studies on the stability of zircon. One exception is a study by Maurice (1949), in which the synthesis and stability of zirconium compounds in a wide range of acidic and alkaline aqueous solutions at 400°C and 0.09 GPa were investigated. Maurice determined that zircon has a very limited stability field in alkaline solutions, and that the maximum stability at which zircon and quartz can coexist is a 0.07 N solution of $Na_2O$. Studies involving the synthesis and/or stability of zircon (and other zircon-group minerals, thorite and huttonite) were reviewed by Frondel and Colette (1957) and Mumpton and Roy (1961) (see also Finch and Hanchar [this volume] for a further discussion of zircon-group minerals and a review of the literature on that subject).

The first experimental study of zircon solubility using materials of direct petrologic relevance was by Dietrich (1965) in which synthetic rock compositions of Q-Or-Ab (quartz-orthoclase-albite) and with the addition of either $Na_2SiO_5$ of NaF, at 650-900°C and 0.1 GPa water pressure, were used to constrain the conditions required for crystallization of zircon. Dietrich determined that in agreement with petrographic evidence of natural samples, more Zr could be dissolved in peralkaline liquids, with the addition of $Na_2SiO_5$ or NaF, than in pure Q-Or-Ab liquids. This study determined quantitatively the effects of temperature and composition on the solubility of zircon in simple, but geologically relevant, melts. In a later study, Larsen (1973) used a water-saturated haplogranite (n.b., haplo in this context means Fe-free synthetic granite) composition ($Q_{45}Ab_{15}Or_{40}$) at 830°C and 0.2 GPa water pressure. Larsen reported that for the liquid composition and conditions he used, only 57 ppm Zr was required to saturate the melt and crystallize zircon.

The next experimental study involving zircon saturation was by Watson (1979), in which hydrothermal experiments were done in cold-seal pressure vessels at 0.2 GPa water pressure and 700-800°C, in the system $SiO_2$-$Al_2O_3$-$Na_2O$-$K_2O$. Watson determined that the saturation level required for zircon to crystallize strongly depends upon the molar proportions of $(Na_2O+K_2O)/Al_2O_3$ of the melt with surprisingly little sensitivity to temperature, $SiO_2$ content, or $Na_2O/K_2O$. For peraluminous melts, and melts lying in the Q-Or-Ab composition plane, Watson determined that less than 100 ppm Zr is required to saturate the melt and crystallize zircon. In contrast to those findings, Watson also reported that for peralkaline melts, zircon saturation shows a nearly linear dependence on the $(Na_2O+K_2O)/Al_2O_3$ content of the melt with the amount of Zr that can be dissolved up to 3.9 wt % el. for a $(Na_2O+K_2O)/Al_2O_3$ ratio equal to 2.0 without crystallizing zircon. Watson concluded that in nature, any felsic, non-peralkaline magma is likely to contain inherited zircon crystals due to the low solubility of Zr in such melts, and the sluggish dissolution kinetics of zircon, in those rock compositions under crustal conditions. Zircon saturation in felsic melts appears to be controlled by the formation of alkali-zircono-silicate complexes with a simple (e.g., 2:1) alkali oxide:$ZrO_2$ stoichiometry.

Dickinson and Hess (1982) determined the zircon saturation surface for synthetic late-stage lunar basalts and granites in experiments done anhydrous at ambient pressure in the temperature range 1070 to 1400°C. The zircon saturation surface for basaltic composition melts shows a strong temperature dependence from 1200 to 1400°C, whereas below 1200°C, the surface turns downward sharply with little temperature dependence. The saturation surface for granitic compositions is similar to basaltic compositions; however, less Zr is required for saturation. At 1100°C, lunar granites would require a whole rock Zr concentration of 5000 ppm, and late-stage lunar basalts would require 9000 ppm Zr, to saturate and hence crystallize zircon. For a magma with a chondritic Zr content (e.g., 3.97 ppm [Anders and Grevesse 1989], 3.82 ppm [McDonough and Sun 1995]), zircon saturation would not be reached until 99.92-99.96% crystallization of the magma. These results suggest that crystallization of zircon has a minor influence on the trace-element evolution of lunar magmas.

In a subsequent study, Watson and Harrison (1983) revisited zircon saturation thermometry and investigated the relation between zircon crystallization and melt composition which is given

by the solubility model:

$$\ln D_{Zr}^{zircon/melt} = (-3.80 - [0.85(M - 1)]) + 12900/T \quad (1)$$

where $D_{Zr}^{zircon/melt}$ is the concentration ratio of Zr in zircon to Zr in the melt, $M$ is the cation ratio (Na + K + 2*Ca)/(Al*Si) (see worked example in Table 1 and discussion below), and $T$ is temperature (Kelvin). The experiments were done using either a piston cylinder apparatus or cold-seal pressure vessel with variable water contents over the temperature range 750-1020°C. The results defined the saturation behavior of zircon in crustal anatectic melt compositions as a function of both composition and temperature. For an $M$ = 1.3, an average peraluminous granite, the experimental results of Watson and Harrison (1983) suggest zircon has relatively low solubilities ranging from ~100 ppm of dissolved Zr at 750°C to 1300 ppm Zr at 1020°C (Figs. 1 and 2). These experimental results predict that in natural systems, granitic composition rocks should show a range in their geochemical behavior with respect to zircon saturation due to their wide range in bulk-rock chemistries (i.e., $M$ value), Zr concentrations, and temperature of crystallization. Anatectic melts lacking sufficient Zr for saturation most likely would have consumed any residual zircon in the source region. In contrast to this, the results of Watson and Harrison (1983) suggest that in zircon-saturated melts, any zircon in the source region will most likely be entrained in the melt and will not completely dissolve, producing what will eventually be nucleation sites for subsequent zircon growth (e.g., inherited cores with magmatic overgrowths). An important implication of the findings from this study is that for certain melt compositions geochemical information (e.g., trace and minor element concentrations of Hf, Y, REE, U, Th, and Pb and radiogenetic and stable isotopic information) from the source region will be transported in the anatectic melt in entrained zircon crystals that would retain the information due to the sluggish diffusion (Cherniak and Watson, this volume).

**Table 1.** Calculation of *M* and *FM*.

| Oxide | N-57 rhyolite (Wark 1991) | Oxide wt % / Eq wt [1] | Cation fraction[2] |
|---|---|---|---|
| $SiO_2$ | 69.04 | 1.149 | 0.679 |
| $TiO_2$ | 0.38 | 0.005 | 0.003 |
| $Al_2O_3$ | 13.65 | 0.268 | 0.158 |
| FeO | 0.63 | | |
| $Fe_2O_3$ | 1.26 | | |
| FeO (t) = $Fe_2O_3$*0.8998+FeO | 1.76 | 0.025 | 0.015 |
| MnO | 0.07 | 0.001 | 0.001 |
| MgO | 0.46 | 0.011 | 0.007 |
| CaO | 1.31 | 0.023 | 0.014 |
| $Na_2O$ | 4.61 | 0.149 | 0.088 |
| $K_2O$ | 2.85 | 0.061 | 0.036 |
| $P_2O_5$ | 0.04 | 0.001 | 0.000 |
| $H_2O^-$ | 0.52 | | |
| $H_2O^+$ | 5.07 | | |
| $CO_2$ | 0.00 | | |
| Total | 99.89 | 1.692 | |
| Zr (ppm)[4] | 299 | | |
| [3]M = (Na+K+(2*Ca))/(Al*Si) | | | |
| *M* = 1.41 | | | |
| [3]*FM* = (Na+K+(2*Ca+Fe+Mg))/(Al*Si) | | | |
| *FM* =1.69 | | | |

*Notes:* Data for bulk sample analysis by X-ray fluorescence spectrometry from Wark (1991).
[1]The values in column 3 are calculated from using the wt % oxide for each major element in column 2 divided by the equivalent wt. for that oxide.
[2]The values in column 4 are calculated from each value in column 3 divided by the total for column 3.
[3]The values used in the *M* and *FM* calculations are the cation fractions from column 4.
[4]No error was reported for Zr in Wark (1991).

In a subsequent study of the kinetics of zircon dissolution and Zr diffusion in granitic melts of variable water content, Harrison and Watson (1983) investigated the dissolution kinetics of zircon at high pressure in a piston cylinder apparatus at 0.8 GPa over the range 1020° to 1500°C. These experiments are effectively reversal saturation experiments in which the apparent concentration of Zr at the dissolving crystal/melt interface (e.g., $C_o$ in Fig. 2a of Harrison and Watson 1983) is the maximum amount of dissolved Zr that can be contained in the melt at the temperature of the experiment (i.e., the saturation value). The results from the experiments in Harrison and Watson (1983) and Watson and Harrison (1983) for similar melt composition with an $M$ value of 1.3, and water contents greater than ~2%, agree well within experimental error. These data suggest that the solubility model presented in

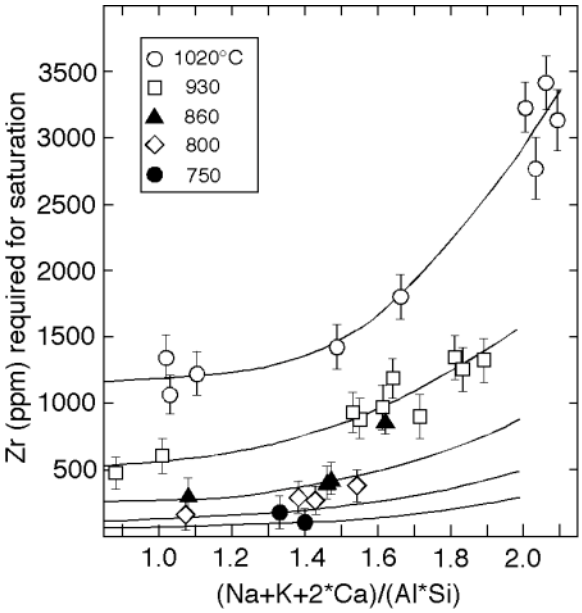


**Figure 1.** Results of hydrothermal zircon saturation/solubility experiments at temperatures of 1020°, 930°, 860°, and 750°C. The residual Zr concentration in the glass following zircon crystallization is plotted against the *M* value (see text and Table 1). The error bars indicate the 2σ confidence level. After Watson and Harrison (1983).

Watson and Harrison (1983) is valid for melts that contain greater than ~2% water and that are within the *M* values of their experiments.

The results in Harrison and Watson (1983) indicate that a 50 µm diameter zircon crystal would dissolve in a 3 to 6% water-bearing melt at 750°C in approximately 100 years; however, it could take as long as 200 Ma to dissolve the same crystal in an equivalent composition anhydrous system. An implication of these results is that zircon dissolution in an undersaturated water-bearing granitic melt occurs instantaneously on geologic timescales with little possibility that such preexisting zircon would survive a crustal melting event.

Ryerson and Watson (1987) introduced a modification of the *M* parameter called *FM* for constraining rutile solubility in magmas, in which the role of Mg and total Fe (but not the $Fe^{3+}/Fe^{2+}$) are taken into account. In many cases, the *M* parameter works well to determine the zircon saturation temperature; however, as pointed out by Baker et al. (2002), the *M* parameter fails to consistently predict zircon saturation in Fe-free melts at 800°C in that the solubility in such Fe-free systems falls below the correlation line between zircon saturation values in the melt and *M*. If the results from several studies involving Fe-bearing (Harrison and Watson 1983) and Fe-free (Larson 1973, Watson 1979, Keppler 1983) melts from the literature are plotted on Zr vs. *M* and *FM* plots, as pointed out by Baker et al. (2002), a stronger correlation can be drawn using *FM* vs. Zr content rather than *M* vs. Zr (Fig. 3). Additionally, as noted by Baker et al. (2002), although the *FM* parameter works better to describe the composition effects that control zircon saturation, it does not address the $Fe^{3+}/Fe^{2+}$, and considers all Fe in the melt to behave as a network modifier which may not necessarily be correct. The results of Baker et al. (2002) suggest that a new *M*-type parameter should be derived that takes into account major elements, $Fe^{3+}/Fe^{2+}$, water, and as discussed below, halogens.

Keppler (1993) investigated the effects of fluorine on the solubility of zircon and other accessory minerals (e.g., rutile, manganocolumbite [$MnTaO_6$], and rare earth phosphates [$LaPO_4$, $GdPO_4$, and $YbPO_4$]) in water-saturated haplogranitic melts. The experiments contained between 0 to 6 wt % el. F, and were done at 800°C and 0.2 GPa in cold-seal pressure vessels. The compositions used for those experiments differ only in the F contents with identical proportions of Na, K, Al, and Si in all experiments. Keppler determined that, unlike rutile, zircon solubility shows a strong nonlinear dependence on the F content in the melt with a quadratic functional relationship and that F suppresses zircon crystallization (i.e., at high F contents, more Zr is needed for zircon to crystallize) (Fig. 4). Keppler suggested that a complexing mechanism in which non-bridging oxygens (NBO) are expelled from coordination with Al through a reaction in which F complexes with Zr in a NBO:Zr of 2:1 which suppresses zircon saturation. Keppler also proposed that direct complexing by F cannot be ruled out as a possible mechanism, although this is in contradiction

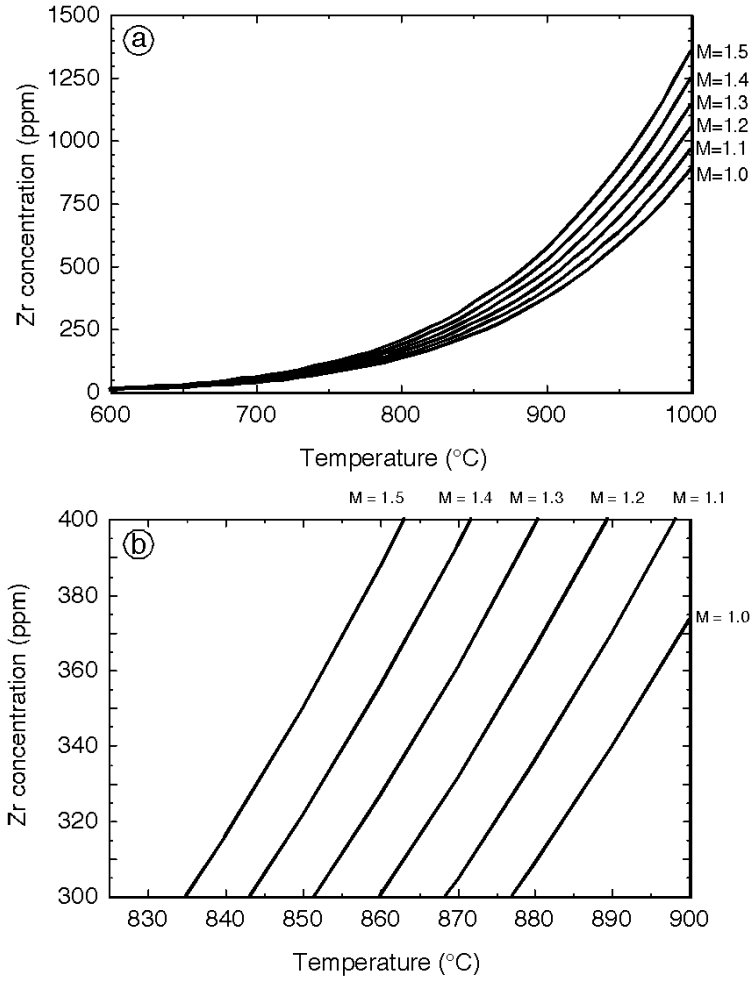


**Figure 2.** Zircon solubility in melts of granitic composition according to the model of Watson and Harrison (1983). (a) Zr concentration required for zircon saturation plotted against temperature. The curves are for the different *M* composition values determined experimentally by Watson and Harrison (1983). (b) Expanded region of (a) showing the temperature dependence on Zr required for saturation to crystallize zircon as a function of *M* (see text and Table 1). See Figure 1 for the actual experimental data upon which the model is based.

with the results discussed in Farges (1996). Geologic implications of the results discussed in Keppler (1993) suggest that in F-rich systems high field strength elements (HFSE) will be enriched in the residual melt with HFSE becoming more incompatible as a function of the F content.

Baker et al. (2002) determined the effects of halogens on Zr diffusion and zircon dissolution in hydrous metaluminous granitic melts. The experiments were done with 4.5 wt % water and contained either 0.35 wt % Cl, 1.2 wt % F, or halogen-free, at 1.0 GPa, over a temperature range of 1050 to 1400°C in a piston cylinder apparatus. The halogen contents used by Baker et al. are typical of natural peraluminous felsic rocks. Baker et al. (2002) found that, for the melt compositions studied, the addition of halogens has a small effect on the solubility of zircon at all water concentrations and temperatures investigated. This is especially true at temperatures greater than 800°C. As noted above, Baker et al. (2002) discussed that in many cases there is a discrepancy between the experimental results of Watson and Harrison (1983) and what is observed in natural

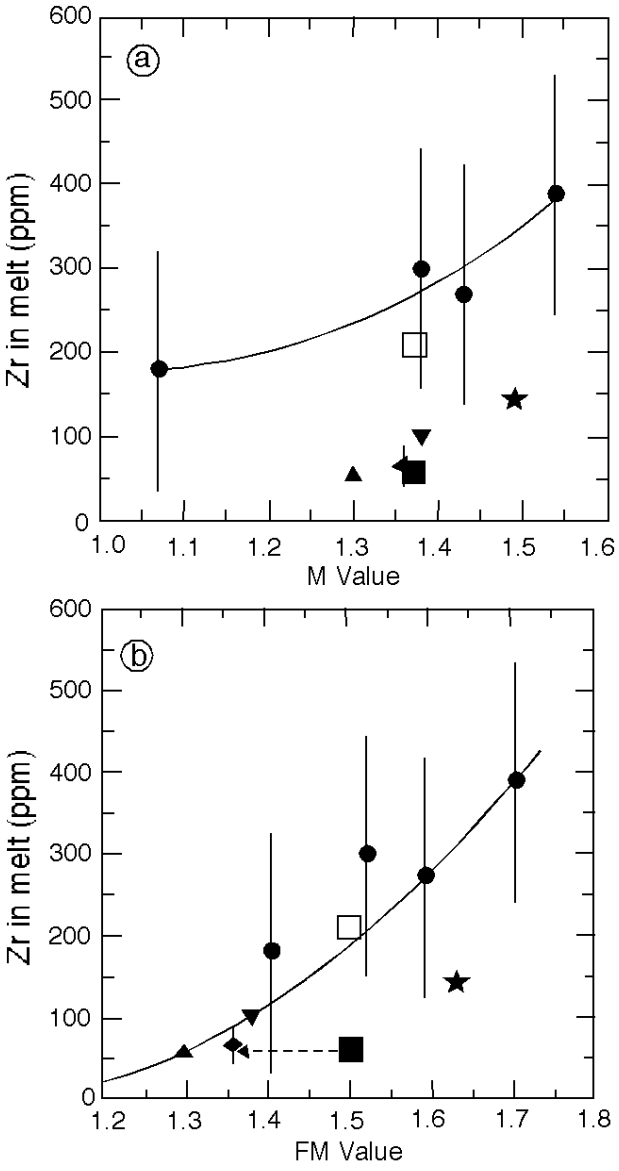


**Figure 3.** Zirconium concentration in melts saturated at 800°C and 0.2 GPa and greater than 66 wt % $SiO_2$ plotted as a function of (a) the *M* value, and (b) the FM value. Filled circles are measurements from Watson and Harrison (1983), diamond is from Keppler (1993) at 800°C, upward pointing triangle is from Larsen (1973) at 800°C, downward pointing triangle is the maximum value determined by Watson (1979) at 800°C, the star is the high-temperature end member of the Bishop Tuff with an iron-oxide temperature of 790°C (Hildreth 1981), the filled square is extrapolated from high-temperature measurements of zircon saturation using lake County, Oregon, obsidian (LCO) (Baker et al. 2002), and the open square is extrapolated from similar measurements in the same composition by Harrison and Watson (1983). The curve in (a) is fit only to the data of Watson and Harrison (1983), whereas in (b) the curve is fit to experimental solubility measurements at 800°C, but not to the extrapolation of LCO measurements. The dashed line with the arrow in (b) shows the effect on the *FM* value treating all Fe in the LCO as a network former and adding it to the value for Al in the denominator in the *FM* equation. After Baker et al. (2002)

samples. Additionally, the results in Baker et al. (2002) suggest that the solubilities determined at 700 and 800°C are well below the Zr contents of natural granitic and rhyolitic composition rocks that are known to have no inheritance in the zircon crystals and only trace amounts of zircon crystals. Baker et al. (2002) attribute this difference between experiments and natural samples to the effects of Fe and oxygen fugacity on the solubility determination.

Linnen and Keppler (2002) determined zircon and hafnon ($HfSiO_4$) solubilities in water-saturated granitic melts, as a function of melt composition, at 800°C and 1035°C at a pressure of 200 MPa. These experiments used either cold-seal pressure vessels in some experiments and titanium-zirconium-molybdenum (TZM) alloy bombs with Ar as the pressure medium. Linnen and Keppler determined that the solubilities of both minerals are orders of magnitude lower in peraluminous and metaluminous melts than in strongly peralkaline melts, a result first determined experimentally by Watson (1979) (Fig. 5) and discussed above. In peralkaline melts, Linnen and Keppler determined that the solubilities, on a molar basis, of zircon and hafnon are nearly identical; however, the solubility of zircon in peraluminous melts, on a molar basis, is nearly five times

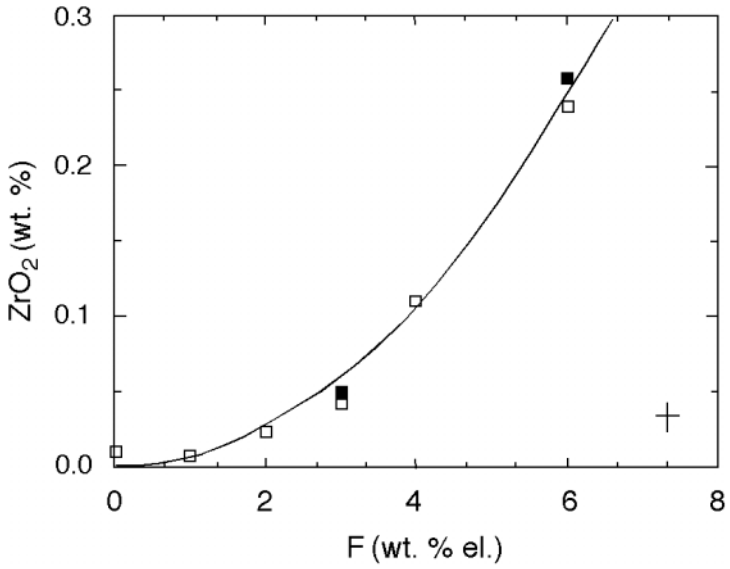


**Figure 4.** Solubility of zircon in water-saturated haplogranite melt at 0.2 GPa and 800°C Open symbols are dissolution experiments and filled symbols are precipitation experiments. The F contents are quoted form the dry base compositions. The curve is a quadratic regression curve fit to the data. The cross in the bottom right is estimated error in F and the maximum error for Zr. After Keppler (1993).

greater than hafnon, which is somewhat unexpected because Hf and Zr have such similar chemical properties. Related to these results, Linnen and Keppler determined that the partition coefficients for Zr and Hf between zircon and melt are nearly equal for peralkaline melts, but for metaluminous and peraluminous melts, $D_{Hf}/D_{Zr}$ range from 0.5 to 0.2, respectively. A significant implication of these findings is that zircon fractionation will decrease the Zr/Hf ratio in some granites, whereas zircon fractionation in peralkaline or similarly de-polymerized melts will have little effect on the Zr/Hf ratio.

In a theoretical study using finite difference numerical simulations, Watson (1996), using both one- and three-dimensional models, calculated the rates of diffusion-controlled dissolution and growth of zircon in anatectic melts as a function of melt composition, water content, and temperature. These numerical simulations utilized known solubility and Zr diffusivity relationships for granitic composition melts under geologically reasonable conditions and containing 3 wt % dissolved $H_2O$. The results from this study indicate that the likelihood of a zircon surviving a crustal melting event depends on several factors, the most important of which are the initial radius of the zircon, the intensity and duration of the melting event, and the volume of local melt reservoirs with which the zircon interacts. Watson concluded that only the largest zircon crystals (>50–100 μm) would survive crustal fusion and incorporation in a zircon-under saturated melt containing >2 wt % $H_2O$ and over the temperature range 750–850°C.

## APPLICATIONS OF ZIRCON SATURATION THERMOMETRY

### Background

In the original study by Watson (1979), and later Watson and Harrison (1983) and Harrison and Watson (1983), the experiments were done with the expectation that the results would be applied mainly to natural samples in which the composition of the magmatic liquid could be accurately assessed and lay within the calibration range (i.e., *M* range, see below) of their experiments. The ideal sample is a volcanic rock consisting of regions of unaltered volcanic glass con-

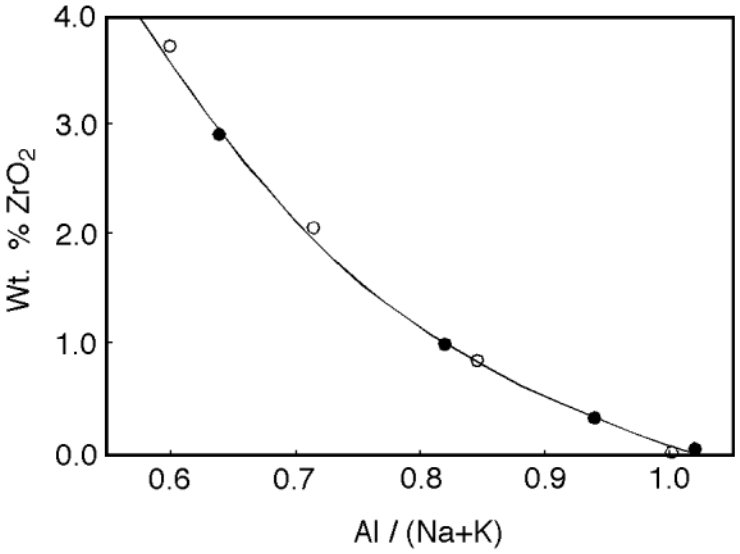


**Figure 5.** Comparison of the results of zircon solubility in granitic melts at 800°C and 0.2 GPa from Linnen and Keppler (filled circles) and Watson (1979) closed circles. The glass compositions are expressed as molar Al/(Na+K) ratios.

taining magmatic zircon crystals, and with few phenocrysts of rock-forming minerals (e.g., <5-10% by volume) to ensure that the bulk rock composition is as close as possible to the glass composition that was in equilibrium with the zircon when it crystallized. In doing a search on zircon saturation thermometry in the GeoRef database, however, nearly all the "hits" (close to 200 including articles, abstracts, and book chapters) that came up for the keywords, "zircon-saturation-thermometry" are for plutonic igneous or metamorphic rocks, but virtually none for volcanic rocks (see Barrie 1995, below). The most likely reason for this is that in felsic volcanic rocks zircon is either absent, or nearly so, inheritance may not be as great as in plutonic rocks (see Miller et al. 2003, below) and usually the zircon crystals are small (<100 μm), making zircon difficult to identify in such rocks. A few examples selected by the authors that discuss different applications of zircon saturation thermometry are presented below. Most studies of zircon saturation thermometry in the literature address one of the following: (1) using the bulk rock composition, whether the corresponding melts reached zircon saturation within the temperature range constrained by the liquidus and solidus temperatures; and (2) whether inherited zircon components from the source region could have survived under the conditions of melting. As discussed below, in some cases rocks that should have been undersaturated, in fact contain inherited zircon, and suggests that either dissolution kinetics for zircon may be limited by kinetic barriers, or that the Watson and Harrison (1983) zircon saturation model may not be applicable for those rocks, or a combination of those two factors.

**Selected examples of studies that used zircon saturation thermometry**

To our knowledge, the first study in which the zircon saturation experimental results of Harrison and Watson (1983) were used in a petrologic investigation was by Harrison et al. (1987) in which the nature of zircon inheritance in two Concord-type plutons from near Sunapee and Long Mountain (near Dixville Notch), New Hampshire was investigated. The *M* values for the bulk sample analyses of the two samples investigated by Harrison et al. (1987) are within the experimental calibration range of Watson and Harrison (1983) (e.g., 1.3 and 1.2), although as

pointed by Harrison et al., the actual *M* values may be slightly lower due to restitic plagioclase and biotite, and that the $SiO_2$ content of the Long Mountain sample was slightly lower than expected due to a minor degree of fractionation.

Using an estimated temperature of crystallization of 650-730°C, Harrison et al. determined for that temperature of crystallization and *M* values, the Long Mountain and Sunapee plutons would have required 50 $^{+24}/_{-16}$, and 46 $^{+22}/_{-15}$ ppm Zr, respectively, to be saturated for zircon to crystallize. Harrison et al. (1987) determined that the Sunapee pluton contained only slightly more Zr than was needed to saturate the melt with zircon at the peak temperature of crystallization and that relatively minor amount of inherited zircon in this sample occur as small, largely resorbed grains. The Long Mountain pluton, in contrast, contains approximately 240% more Zr than is required to be saturated with zircon, which suggests that over half the Zr in the Long Mount pluton is contained in inherited zircon crystals. Harrison et al. attributed that these differences in zircon inheritance are directly related to variations in the melt chemistries of the two plutons.

Copeland et al. (1987) in an attempt to identify the nature of inherited radiogenic Pb in monazite from a Tertiary two-mica, tourmaline-bearing, weakly unfoliated granite from the Himalayas, used zircon saturation thermometry to calculate the peak temperatures that were encountered when this sample melted. The zircon samples that were dated using multi grain U/Pb geochronology are bounded by two discordia with a lower intercept of 19.5±0.4 Ma and upper intercepts of ~500 Ma and ~2300 Ma, respectively. Copeland et al. (1987) proposed, based on a comparison to other Himalayan Tertiary leucogranites, that this particular sample did not experience significant fractionation and that the whole rock chemistry reflects the melt composition.

These authors suggest that even if "significant" crystals were present in the melt at peak melting temperature conditions that *M* would not vary greatly for their purposes. Hence the Zr content of 66 ppm, and the calculated M of 1.2, corresponds to a melting temperature of ~730°C. Copeland et al., however, point out that this temperature is probably an overestimate because of inherited zircon that contributed to the bulk sample Zr content. For this reason, Copeland et al. (1987) applied a correction factor to the bulk sample Zr content of 50-80% which lowered the melting temperature to between 680 and 710°C. Copeland et al. used similar arguments for the monazite saturation temperature, also taking into account a correction for an inherited component and reported a temperature of melting of ~710-720°C. Finally, Copeland et al. (1987) used these calculated melt temperatures to infer a closure temperature for Pb in monazite of 720-750°C for a cooling rate of 20°C per Myr and a crystal dimension of 10-100 μm.

In a study aimed at understanding isotopic zonations in silica magma chambers, Johnson (1989) used zircon dissolution (and inferred crystallization) rates from Harrison and Watson (1983) to explain the lack of inherited Proterozoic zircon cores from deep in the magma chamber in the Amalia Tuff from the Questa caldera of northern New Mexico. Johnson noted that the zircon crystals from deep in the magma chamber contained early-formed magmatic zircon exclusively of Tertiary age that suggested that the magma in that level of the magma chamber was saturated with zircon. The lack of Proterozoic zircon cores according to Johnson (1989) cannot simply be explained by complete dissolution of inherited zircon prior to crystallization of the Tertiary magmatic zircon crystals based on the dissolution kinetics results of Harrison and Watson (1983). Johnson (1989) reported that the Amalia tuff samples from the roof of the magma chamber, in contrast, contained a greater number of zircon crystals with inherited Proterozoic cores which is also reflected in the amount of assimilated material and the corresponding isotopic zonation in rocks from that level of the magma chamber.

Brouand et al. (1990) in a study of the behavior of zircon during crustal anatexis in Tibetan Slab *in situ* and injected migmatites (low-Zr and high-Zr samples), found that the morphology and internal structures of zircon crystals from these rock samples were distinctly different depending on the rock type from which the zircon crystals were extracted. In the mesosomes and melanosomes, the zircon crystals were primarily inherited with rounded morphologies, low aspect ratios,

and thin overgrowths, suggesting a detrital or metamorphic origin.

The zircon crystals from the leucosomes exhibited distinctive features. Brouand et al. (1990) reported that in the low-Zr tonalitic leucosomes the zircon crystals were characterized by rounded morphologies, low aspect ratios, and thin overgrowths, suggesting a detrital or metamorphic origin, similar to the mesosome and melanosome zircon crystals, indicating little transformation during migmatization. In contrast, Brouand et al. (1990) found that the high-Zr-tonalitic leucosomes contained euhedral zircon crystals, with morphologies and internal zoning typical of magmatic zircon similar to what are found in peraluminous granites. The internal zoning of those zircon crystals suggests a complex geologic history involving dissolution and reprecipitation. Brouand et al. (1990) also found that the injected granitic leucosome samples contained typical magmatic zircon crystals.

Brouand et al. determined for the low-Zr leucosome samples (e.g., ~35 ppm), at an estimated temperature of migmatization of 730°C, the low-Zr leucosomes are slightly undersaturated in Zr for zircon to crystallize. In the high-Zr leucosome samples (e.g., ~270 ppm), the Zr data indicate that zircon should have been a saturated phase in those rocks at the estimated temperatures of migmatization (< 750°C).

The observations by Brouand et al. (1990) do not agree well with the experimental results using the Watson and Harrison (1983) zircon saturation model for rocks of their *M* range (e.g., high-Zr leucosome sample MB374L $M = 1.26$). In particular, Brouand et al. (1990) interpret the zircon from the low-Zr leucosomes, which are similar to the mesosome and melanosome zircon crystals to be primarily inherited whereas the results using the Watson and Harrison (1983) zircon saturation model indicate a rock of that composition should be slightly undersaturated. Also, Brouand et al. (1990) suggest that the zircon crystals from the high-Zr leucosome, albeit with typical magmatic morphologies, are too abundant to have entirely crystallized from a melt and should have a significant inherited component. An assumed maximum temperature of 750°C for migmatization of the Tibetan slab would indicate for the high-Zr leucosome an excess of 175 ppm Zr in the melt based on the Watson and Harrison (1983) zircon saturation model. Brouand et al. (1990) suggest that either the inherited zircon component was not identified in their zircon crystals, or that the solubility of Zr is melts of their high-Zr leucosome composition is higher than the Watson and Harrison (1983) experiments indicate. Back-scattered electron images of zircon crystals from the high-Zr leucosomes in Brouand et al. (1990) are complex (e.g., patchy internal zoning, evidence for partial dissolution and reprecipitation, etc.) and do not lend to a simple interpretation of the nature of the inheritance, or lack thereof.

The authors of this review paper suggest this study might be an excellent example of "misusing" the Watson and Harrison (1983) zircon saturation model on plutonic or metamorphic rocks. To no fault of those authors, Brouand et al. (1990), tried to explain their results in the context of an experimental model, and the natural sample and experiments did not agree. In that the melt composition and temperature at the time zircon are not precisely known, one would have to do a significant amount of work, both experimental and using natural samples, to be able to fully understand the implications of applying the Watson and Harrison (1983) saturation to high-grade metamorphic and igneous rocks such as these Himalayan samples.

In a study of a suite of igneous rocks (ranging from gabbro to granitic composition) from the Adamello batholith, in the Italian Alps, Hansmann and Oberli (1991) used the Watson and Harrison (1983) zircon saturation thermometry model to explain the complex nature of U/Pb isotope systematics, including the nature of inherited radiogenic Pb in zircon, in the samples studied. Inheritance is most prominent in rocks with crustal $\varepsilon_{Nd}$ and $\varepsilon_{Sr}$ isotopic values. The extent of inheritance was shown to vary with differentiation and reaches a maximum for intermediate to acidic composition (e.g., granodiorite, tonalite, trondhjemite). These same samples also show the highest zircon saturation temperatures of all the samples investigated. Quartz diorite and leucotonalite samples do not exhibit this same trend, and the $\varepsilon_{Nd}$ data suggest that their magmas from which these rocks crystallized contained less crustal material than the intermediate to acidic composition rocks.

Hansmann and Oberli (1991) assumed that their rocks were within the ≥2% $H_2O$ water calibration range of Watson and Harrison model. The Watson and Harrison (1983) *M* range from the original experiments is from 0.9 and 1.7 and covers most of the more acidic composition rocks studied by these workers. Hansmann and Oberli (1991) suggest that zircon should not have been a stable phase in most of the Adamello samples they investigated yet all the samples they studied contained some inherited component. If the dioritic to tonalitic composition melts were the result of bulk anatexis, in a crustal environment undergoing regional metamorphism, being a relatively slow process, any preexisting zircon should have dissolved. Had the Adamello melts been the result of partial melting, Hansmann and Oberli suggest that some zircon would have remained in the restite material with the preservation of xenocrystic zircon enhanced by the crystallization of plagioclase and amphibole. Hansmann and Oberli extrapolated the *M* calibration range of Watson and Harrsion (1983) (e.g., $>M = 1.9$) to mineral/melt mixtures of tonalitic bulk composition the results from which suggested that the zircon solubility in the residual melt fraction is significantly reduced by crystallization of plagioclase and amphibole, and that the survival of xenocrystic zircon grains may be explained by sluggish dissolution kinetics.

In an isotopic and trace element study of accessory minerals from a tonalite and granodiorite from Tertiary Alpine Bergell intrusion of southern Switzerland-northern Italy, von Blankenburg (1992) used the Watson and Harrison (1983) zircon saturation thermometer to explain the nature of inheritance in zircon from the Bergell samples. Similar to Hansmann and Oberli (1991), von Blankenburg also extrapolated the experimental calibration range of Watson and Harrison (1983) to >1.9 (e.g., $M = 2.1$) in order to apply this model to rocks of tonalitic composition. Von Blankenburg reported that the granodiorite sample yielded a higher zircon saturation temperature than the tonalite, and suggested that could be attributed to inherited zircon in the original melt. According to the zircon saturation temperature for tonalite calculated by von Blankenburg (1992), the largest portion of the tonalite melting interval is in the temperature region where zircon should dissolve. Von Blankenburg attributed the presence of a significant portion of inherited cores in the tonalitic composition rocks to either problems extrapolating the calibration range of Watson and Harrison (1983) zircon saturation model, or by the fractional crystallization model suggested by Hansmann and Oberli (1991). Both of these studies illustrate potential problems with extrapolation beyond the original experimental calibration of Watson and Harrison (1983). As noted above, in the tonalite samples discussed by Hansmann and Oberli (1991) and von Blankenburg (1992) any residual zircon should have dissolved, yet both samples contain inherited zircon.

Mojzsis and Harrison (2000) and Mojzsis and Harrison (2002) in studies a quartz dioritic composition dike from the Itsaq Gneiss complex on Akilia Island from southern West Greenland, suggested that due to the relatively low Zr contents and high zircon saturation crystallization temperatures of the granodioritic-tonalitic composition protoliths, that any residual zircon would dissolve in such zircon undersaturated melts. Mojzsiz and Harrison (2002) suggest that one sample from Akilia Island that contains 144 ppm, has a bulk rock composition similar to the melt composition from which the zircon crystallized. Therefore, for a calculated $M = 1.54$ that rock would have had a zircon saturation temperature of ~950°C, and required ~900 ppm of Zr to be saturated with zircon as a crystallizing phase. Any uncertainties regarding the assumptions about the bulk rock composition reflecting the magma composition (and hence the *M* value used), and the temperature of ~950°C, could greatly affect the Zr content required to saturate and crystallize zircon (a ~50% uncertainty in the Zr content, results in a zircon saturation temperature uncertainty of ~±35°C, and an uncertainty in *M* over the complete range of 1.3 to 1.9 results in a zircon saturation temperature introduces and uncertainty of ±25°C with the Watson and Harrison [1983] zircon saturation model). Other authors have reported inheritance of zircon from these Greenland samples (see discussion in Mojzsis and Harrison 2002). If correct, most likely the main uncertainties in the assumptions made by Mojzsis and Harrison (2002) are either that the present day bulk-rock composition is not similar to the original magma, or the assumed temperature of crystallization is too high

(by as much as 100-150°C). In that Zr and M play a relative minor role in errors in zircon saturation temperature determinations, it seems likely that the temperature estimate of ~950°C is too high.

Paterson et al. (1992) investigated the nature of inheritance of Sm-Nd isotopes in zircon from Strontian granitoid rocks from northwest Scotland. Patterson et al. used the Watson and Harrison (1983) zircon saturation model to constrain the extent of refractory zircon in the granitic rocks they studied, and to estimate the zircon saturation temperature. Using BSE images, Paterson et al. estimated the amount of refractory zircon in the Loch Stuart granodiorite to be less than 5%. This amount of refractory zircon suggests that the bulk rock Zr content is close to the amount of Zr that was dissolved in the original melt. Paterson et al. (1992) calculated a zircon saturation temperature for the Loch Stuart granodiorite of 774±30°C, taking into the 5% inheritance, this lowers the zircon saturation temperature by 4°C. For the Glenn Sanda granodiorite, the inherited zircon component is approximately 50% and when corrected for the 50% inheritance yields a temperature of 703±30°C. Paterson et al. suggested that these corrected temperatures reflect the magma temperature when zircon was a crystallizing phase. Paterson et al. also suggested that the presence of inherited Sm-Nd isotopes in the refractory zircon suggest that the inherited isotopes remained a closed system with regard to diffusion of the REEs and that the Sm-Nd isotopic composition of inherited zircon will be significantly different from the host rocks in which the zircons were extracted.

Barrie (1995) used the Watson and Harrison (1983) model to constrain the zircon saturation temperature of metamorphosed high-silica rhyolites from the Archean Abitibi subprovence of northeastern Ontario, Canada. Similar to other greenstone-granitoid trerranes, these Abitibi voilcanic rocks are metamorphosed to prehenite-pumpellyite to mid-greenschist facies (and in some places higher grade) metamorphism. These samples are usually hydrated, precluding the use of mineral-pair, or mineral-liquid, geothermometers. Unlike the problems with rocks that are outside of the experimental calibration range of Watson and Harrison (1983) such as the tonalite samples mention above, there rhyolite composition samples are well suited for such an investigation. These samples contain zircon as a saturated phase, and based on previous isotopic studies, the zircon is interpreted to not contain a residual zircon component.

Barrie (1995) suggests that the calculated zircon saturation temperatures reflect the temperature of the melt that produced the ryholites at the time of extraction from the restite, and may be considered as the emplacement temperature of the magma so long as there is not significant cooling as the magma rises to the surface. Barrie also discussed the role of $H_2O$ in the original Watson and Harrison (1983) experiments and how $H_2O$ may affect the zircon saturation temperature on primarily anhydrous anatectic melts. Barrie proposed that more meaningful temperature estimates will be obtained if phenocryst-rich and unaltered samples are avoided whereby the bulk rock rhyolite composition will more closely reflect the original melt composition.

Based on the results obtained for his samples, Barrie (1995) suggests from a comparison in the literature for other average composition Cenozoic rhyolites using zircon saturation thermometry and conventional mineral pair geothermometers, that the Watson and Harrison (1983) zircon saturation model provides geologically reasonable results for nonalkaline rhyolites so long as the above conditions are met. The zircon saturation temperatures calculated by Barrie (1995) for the Abitibi rhyolites are in the range of 840-940°C.

In a slightly different application of zircon saturation thermometry, Chappell et al. (1998) used zircon saturation thermometry (Watson and Harrison 1983) to explain the nature of zircon inheritance in I-type granites from the Lachlan Fold Belt in southeastern Australia. Chappell et al. found that for the most mafic granites from the Cobargo Suite, and the three most mafic rocks from the Inlet pluton, have zircon saturation temperatures in the interval from 740 to 762°C. Chappell et al. interpret those temperatures to represent the maximum temperatures at which zircon could have been present in melts under those conditions, and suggest that the differences they observe in the chemical trends between the Cobargo and Inlet rocks and the more felsic Towgon Grange and Boggy Plain rocks are due to differences in the crystallization temperature of

the respective magmas. Chappell et al. suggest that the Towgon Grange and Boggy Plain crystallized at high temperature from molten or mostly molten magmas in which zircon was a soluble phase. In contrast, the Cobargo and Inlet rocks are interpreted to have been derived from partially molten magmas, and considerably lower temperatures, in which the crystallizing melt contained crystals of zircon and other restitic minerals.

Miller et al. (2003) discussed their results in using the Watson and Harrison (1983) zircon saturation thermometry to understand zircon saturation temperatures and preservation of inheritance in 54 plutons they investigated. In the samples studied, there is a clear division in the zircon saturation temperatures for the inheritance-rich (mean zircon saturation temperature = 766°C) and the inheritance-poor (mean zircon saturation temperature = 837°C) granites. Miller et al. suggest that the inheritance-rich granitoids were probably undersaturated with respect to zircon at the source, and therefore the calcualted zircon saturation temperature is most likely an underestimation of the actual temperature of crystallization. The zircon saturation temperatures and zircon inheritance comprise two distinct classes of granites: Cold, inheritance-rich granitoids rocks with zircon saturation temperatures < 800°C; and hot, inheritance-poor granitoid rocks with zircon saturation temperatures > 800°C.

Miller et al. suggest that the calculated zircon saturation temperatures provide good melt temperature estimates for granitoid rocks with crystal poor, zircon saturated magmas, and relatively useful approximations of melt temperatures for granitoid rocks rich in inheritance. Some implications of this study include that these different types of granites have fundamentally different mechanisms for magma generation, transport, and emplacement. Miller et al. also suggest that cold granites are relatively unlikely to erupt, and hot granites formed under drier conditions, contain fewer crystals, and are more likely to erupt. These results may partially explain why felsic volcanic rocks may have relatively high Zr contents, high zircon saturation temperatures and yet have a small amount of zircon inheritance.

## CALCULATION OF ZIRCON SATURATION TEMPERATURES

### Considerations for using zircon saturation thermometry with plutonic rocks

In using the zircon saturation thermometry model of Watson and Harrison (1983) on plutonic rocks one needs to address the problem of the bulk-rock composition (and the resulting *M* and Zr values) and how that relates to the chemical composition of the magmatic melt at the time when zircon crystallized in that rock. Was zircon an early or late crystallizing phase? In which rock-forming mineral(s) does zircon occur? Are the zircon crystals primarily at grain boundaries or do they primarily occur within other minerals? This last question is vitally important, because any consideration of zircon saturation behavior implicitly assumes that the zircons "see" the melt. This is clearly not always the case, inasmuch as zircon inclusions in major phases are common in some rock types. Watson et al. (1989) showed that in metamorphic and anatectic rocks most of the mass of accessory minerals appears to reside in grains located at grain boundaries. These grains are likely to be accessible to melt and therefore involved in any chemical equilibration processes. In holocrystalline igneous rocks formed by cooling of largely-liquid bodies, zircons may be more commonly included in major rock-forming minerals due to growth occlusion. Clearly, detailed petrography is necessary so that the textural relations between zircon and the other rock-forming minerals are considered along with the changing composition of the rock as the magma evolved. Caution is warranted even in the use of inclusion-host relationships to deduce order of crystallization (see Means and Park 1994).

Also, the inheritance of pre-existing zircon that may have been entrained in the magma in which the resulting zircon crystals were extracted (i.e., the volume of inherited zircon—and thus the ppm Zr) must be accounted for and subtracted from the whole rock Zr content before determining the zircon saturation temperature (which is a function of both *M* and the Zr content).

One way this can be addressed is by using BSE or CL images of selected zircon crystals from a sample, and a digital image-processing program, such as NIH Image, to estimate the volume of zircon that was inherited from the source region and the volume of zircon that grew as magmatic overgrowths on the inherited grains. Then an average amount of Zr can be subtracted from the bulk-rock Zr content to correct for the inherited zircon component. This may also be done using the discordance caused by mixing two different age components from a U/Pb isotopic measurement on a U/Pb isotope Concordia diagram (Parrish and Noble, this volume) using the lever rule. This latter approach would have to take into account the U content of each end member. For example, if a thin (e.g., 5 μm) rim contained 100 times the U as a much larger (by volume) inherited core, the discordance would be pulled towards the high U end member yielding an overestimation of for the amount of Zr to be subtracted from the bulk rock Zr.

One may also ask how precise an answer is needed, which often depends on the nature of the geologic question being asked. In other words, does the temperature at which zircon saturation occurred need to be known to within 10°C or will 100°C suffice? If the latter, then the role of the bulk rock composition, or the presence of inherited zircon, on the calculated temperature will be minimal and may only contribute to an error in the temperature calculation of ±~50°C. Any related errors that are generated in the original measurements (e.g., EMPA, XRF, etc.) used in the zircon saturation temperature calculation must be propagated through, and include the estimation of the volume of inherited and magmatic zircon discussed above.

**Bulk sample or *in situ* analyses?**

Whether to do a bulk sample analysis of a plutonic or volcanic rock or an *in situ* analysis of volcanic glass is an important issue that needs to be considered in any study that involves zircon saturation thermometry. In a bulk sample analysis of a plutonic rock, the chemical analysis is an average of the whole rock including all the minerals in that rock. In a volcanic rock, a bulk sample analysis includes glass, crystals of rock-forming minerals, and accessory minerals, some of all of which may contain some Zr. If the amount of phenocrysts in a volcanic rock is small (e.g., less than 10-15%), the bulk rock composition and the *in situ* glass major element compositions are generally quite close based on a survey of the relevant literature.

For *in situ* analyses of volcanic rocks, it is anticipated that the analyst will analyze regions of the glass that are unaltered and far from any phenocrysts or other accessory minerals (Fig. 6) (e.g., 40 μm from adjacent phenocrysts is a good estimate for the EMPA based on secondary fluorescence considerations) and guided by BSE and/or CL photomicrographs. Apart from purely analytical problems, it is important to recognize that phenocrysts of both major and accessory phases in volcanic rocks could be surrounded by diffusive boundary layers in the melt resulting from relatively rapid late-stage growth.

The EMPA, SIMS, or LA-ICPMS, may be used for determining the Zr content in volcanic glasses. In most felsic volcanic rocks, the Zr content is less than 500 ppm (and in some cases much lower, e.g., tens of ppm level). The main limitation in using the EMPA is that in some samples the Zr content may be below the minimum detection limits for that technique (<40-50 parts per million) for the conditions used to analyze trace elements (e.g., 150 nA beam current, 15 kV accelerating voltage, and 600-720 seconds count time on both peak and background).

In the example in the last section of this paper, we used *in situ* EMPA (JM Hanchar and EB Watson unpublished results) for major elements and Zr. We could also have used SIMS or LA-ICPMS for Zr and achieved better analytical precision; however, that would be at the expense of poorer spatial resolution in the case of the LA-ICPMS. Depending on the sample, that might be a problem, or if spatial resolution is not an issue, LA-ICPMS would provide a more precise determination of the Zr content of the sample.

For SIMS or LA-ICPMS analyses, one would also have to determine the major element composition using another complementary technique, such as the EMPA, and use a suitable ele-

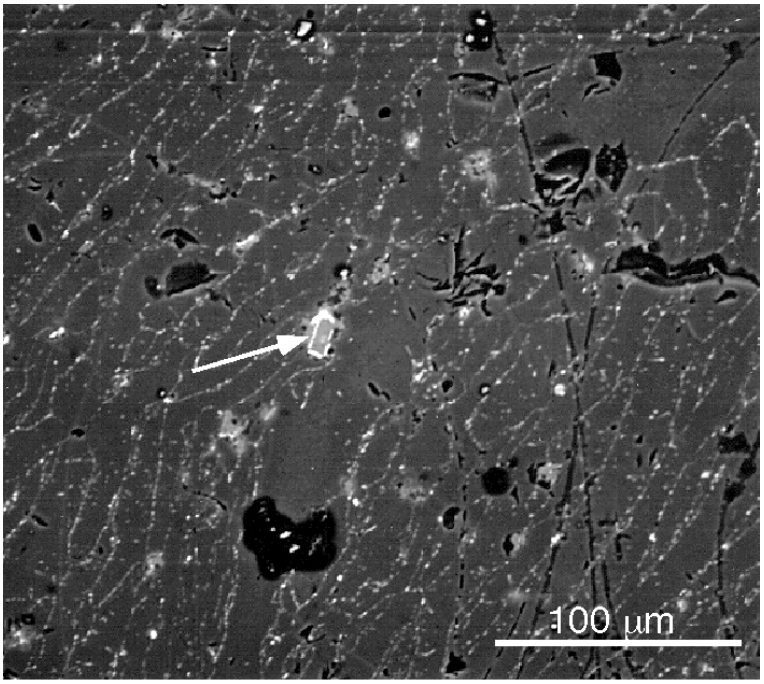


**Figure 6.** Back-scattered electron photomicrograph of thin section of rhyolite sample N-57 from Wark (1991). Arrow points to small zircon crystal in glass.

ment as an internal standard (e.g., Ca) to normalize the LA-ICPMS or SIMS results. This would also require obtaining a primary standard for Zr and well characterized secondary standards to constrain the accuracy of the analyses. The difficulty of obtaining these standards presents the largest uncertainty for such *in situ* measurements.

### Calculation of *M* for geologic samples

In order to calculate the zircon saturation temperature for a natural rock sample, a chemical analysis (bulk sample or *in situ*) for major elements must be done, from which the cation ratios are calculated and then *M* (or *FM*) determined (see discussion of Eqn. 1 at the bottom of Table 1 and calculated *M* and *FM* values therein). Next, the Zr content must be determined (bulk sample or *in situ*). For the rhyolite example discussed below, XRF (from Wark 1991) and EMPA (JM Hanchar and EB Watson unpublished results) analyses were both used to calculate *M* (and *FM*) and to determine the Zr content and the zircon saturation temperature, for that sample (Tables 2 and 3, Fig. 9).

Once an *M* value is calculated, one must determine if the sample falls within or outside of the calibration range of the Watson and Harrison (1983) experiments (Figs. 1 and 2). If the calculated *M* value lies within the experimental range of Watson and Harrison (1983), then the user may feel relatively confident that the calculated *M* can provide useful zircon saturation and temperature information. If the sample falls outside of the original calibration range (e.g., carbonatite, kimberlite, etc.) the *M* value may not be an accurate gauge of melt structure and the resulting apparent saturation temperature may have no geologic relevance. In addition to the major elements that are used to calculate *M* that may be outside the calibration range, the role of elements such as F, Cl, or Fe as noted above (Keppler 1993, Baker et al. 2002, Linnen and Keppler 2002) needs to be further addressed experimentally over a range of rock compositions to determine their role in the calculated zircon saturation temperature. Elements such as Li and B, for which no experimental data exist with regard to zircon saturation, may enhance or suppress zircon satura-

**Table 2.** Major element comparison between XRF and EMPA for N-57 rhyolite.

| Oxide | XRF (bulk sample)[1] | EMPA (*in situ*) |
|---|---|---|
| $SiO_2$ | 69.04 | 69.43 |
| $TiO_2$ | 0.38 | 0.26 |
| $Al_2O_3$ | 13.65 | 12.74 |
| FeO | 0.63 | |
| $Fe_2O_3$ | 1.26 | |
| FeO (t) = $Fe_2O_3$*0.8998+FeO | 1.76 | 1.02 |
| MnO | 0.07 | "fixed value"[1] |
| MgO | 0.46 | 0.15 |
| CaO | 1.31 | 0.53 |
| $Na_2O$ | 4.61 | 4.76[2] |
| $K_2O$ | 2.85 | 2.94 |
| $P_2O_5$ | 0.04 | "fixed value" |
| $H_2O^-$ | 0.52 | |
| $H_2O^+$ | 5.07 | "fixed value" |
| $CO_2$ | 0.00 | n/a |
| Total | 99.89 | n/a |
| Zr (ppm) | 299 | 325 +/- 31[3] |

[1]Only Si, Ti, Al, Fe, Mg, Ca, Na, and K were analyzed with the EMPA. Fixed values for an average rhyolite composition from Best (1982) were used for other elements in ZAF correction.
[2]$Na_2O$ value in Table 2 corrected to account for Na loss during EMPA analysis (see text).
[3]Error on EMPA Zr concentration value from 1σ absolute standard deviation from counting statistics.

tion. In the case of the Macusani volcanic glasses from southeast Peru (Pichavent et al. 1987), for example, some of the samples contain up to 0.8 wt % $Li_2O$, and 1.35 wt % F (with a calculated *M* or 1.02 and FM of 1.4 for sample JV-1 in Pichavant et al. 1987) with very low Zr (< 50 ppm) and contain zircon (albeit in low abundance) as a saturated phase.

The sample chosen for zircon saturation assessment should contain enough Zr so that an analytical precision appropriate for the question being addressed (e.g., generally ~15-20% relative standard deviation for the EMPA) may be achieved. It should be noted that the uncertainty in measuring Zr with XRF is significantly smaller (e.g., less than 5% relative standard deviation for elements such as Rb, Sr, and Zr at the 100 to 500 ppm range) than with the EMPA and as such in some cases the tradeoffs involved for bulk sample vs. *in situ* analyses is balanced by the increase in analytical precision.

In using the EMPA, appropriate analytical procedures should be used in order to optimize the precision and accuracy of the analyses (see below). If these conditions are satisfied, then the M value calculated and the Zr content may be used to calculate a zircon saturation temperature by rearranging Equation 1 and solving for temperature. With the recent advances of SIMS and LA-ICPMS technologies, there are likely to be many more studies forthcoming involving the determination of zircon saturation temperatures in geologic materials; however, it cannot be stressed enough that the accuracy of any such analyses are only as good as the standards that are used and one should be not confuse the higher precision that can be achieved by SIMS and LA-ICPMS with the accuracy of the resulting analyses. It is a nontrivial exercise obtaining high quality primary and secondary standards for this type of work and clearly more standards need to be developed for the geologic community.

## Worked example to determine *M* and Zr content and zircon saturation temperature

In the following example, the major element composition and values for *M* and *FM* and the Zr concentration that are presented in Table 1 and will be used below to calculate a zircon saturation temperature for that sample. The sample chosen is a rhyolitic ash-flow tuff (sample N-57) from the northern Sierra Madre Occidental in Chihuahua, Mexico (Wark 1991). The petrogenesis of this sample is discussed in Wark (1991). This sample consists of ~85% glass, ~15% plagioclase

**Table 3.** Temperature and $fO_2$ estimates for N-57 rhyolite sample.

| Sample[1] | Fe-Ti oxide thermometry[2] | log $fO_2$ estimate[2] | Two-pyroxene thermometry[2] | | Bulk sample (XRF)[2] *M*, Zr, and T | *In situ* glass analysis (EMPA)[3] *M*, Zr, and T |
|---|---|---|---|---|---|---|
| | | | | | 1.41 | 1.35 |
| | | | @ 0.1 GPa | @ 0.5 GPa | 299 ppm | 325±31 ppm |
| #1 | 903°C | -10.6 | 862°C | 883°C | | |
| #2 | 897°C | -10.7 | 836°C | 857°C | | |
| | | | | | 842°C | 855±15°C |

[1]#1 and #2 in column 1 refer to two different temperature and fugacity determinations for sample N-57.
[2]Fe-Ti oxide and pyroxene thermometry (Anderson and Lindsley [1985] and Davidson and Lindsley [1988], respectively), $fO_2$ estimate, and XRF bulk sample Zr concentration from Wark (1991).
[3]Error on calculated temperature propagated through from counting statistics uncertainty in Zr determination which is thought to be the largest source of error. Zircon saturation temperatures calculated using Equation 1 in text and data from Tables 1 and 2.

phenocrysts, ~1% pyroxene, < 1% Fe-Ti oxides, and trace amounts of zircon. The chemical composition, and the calculated *M* and *FM* parameters in Table 1 were determined from a bulk sample analysis using XRF spectrometry as reported in Wark (1991). The protocol for calculating *M* and *FM* are discussed in the note at the bottom of Table 1.

In thin section, the zircon crystals in sample N-57 are small euhedral grains, typical of zircon in rhyolitic composition volcanic rocks (Fig. 6). The zircon shown in the BSE image in Figure 6 is typical of zircon in this sample. The zircon grains are not abundant, but when they are observed they are usually in the glass and do not occur as inclusion in other minerals (e.g., it is common in felsic rocks to find zircon and other accessory minerals as inclusions in opaque minerals such as ilmenite or magnetite or in ferromagnesian minerals).

***EMPA glass analyses for major elements and Zr.*** One advantage in using the EMPA for major elements and selected trace elements such as Zr is that these elements can all be measured *in situ* in the glass at the same location in the sample. Also, the EMPA offers excellent spatial resolution (~10 μm) and the availability and convenience of EMPA instruments is greater than other options. As long as the Zr content in the rock is above the minimum detection limits for the analytical conditions used, it is the analytical method preferred by the authors for such studies.

The EMPA analyses for sample N-57 were done on a polished thin section using a JEOL 733 Superprobe at Rensselaer Polytechnic Institute following a modification of the procedures discussed in Nielsen and Sigurdsson (1981), Rutherford et al. (1985), Jercinovic and Keil (1988), Devine et al. (1995), Morgan and London (1995), and especially Hanson et al. (1996). This electron microprobe is equipped with five spectrometers and employs on-line ZAF matrix correction procedures. After some preliminary analyses to determine how well the glass would behave under the electron beam, the locations of ten areas where fresh glass could be found guided by BSE images were recorded.

Each of the ten analysis locations on the thin section was analyzed three times using three separate element packages. The first two analyses were for major elements and were done sequentially at each location (i.e., each of the ten analyses were done for the first package, and then each of the analyses were repeated for the second package). The third analyses, for Zr, were done after all of the major element analyses were completed, because of the different EMPA conditions required for those analyses. In the first set of analyses, a beam diameter to beam current ratio of 2 was maintained to minimize Na and K loss in the glass. It should be noted that the analytical conditions described below are somewhat sample dependent and while these conditions should be used as starting points, a future investigator should be prepared to optimize these conditions through trial and error for a particular sample.

Package 1: Si, Na, Al, K, and Fe (five analyses for each element for each of the analysis locations, 15 kV accelerating voltage, 15 nA beam current, 30 micron beam diameter, and 20 second count time on each peak). Twenty-second background acquisitions on each side of each major element peak position were collected from one random point on the glass prior to the actual analyses. This allowed the spectrometers to remain in fixed positions during the actual analyses. The background values were stored and subsequently used for processing the ten glass analyses. Sodium and K were monitored for loss during the analyses (e.g., five analyses for each element at 20 seconds each during each analysis in Package 1. Potassium was found not to decrease significantly during the analyses of this sample (Fig. 7). Sodium, however, showed a significant decrease over the initial 125-second duration of the analyses (Fig. 8a), so those data had to be corrected using the procedure outlined in Nielsen and Sigurdsson (1981), Jercinovic and Kiel (1988), and Hanson et al. (1996) (Fig 8b). The reader is referred to those papers for a more thorough explanation of the methodology used to correct for this problem. Briefly, the corrected Na content is determined by taking the natural logarithm of the wt % $Na_2O$ and fitting a straight line through the data (Fig. 8a and b). The y-intercept is interpreted to be the true Na content of the glasses. Values for Ti, Mg, Mn, Ca, and $H_2O$ were "fixed" for the analyses using an average rhyolite composition

from Best (1982).

Package 2: Mg, Ca, Al, Ti, and Fe (one analysis per each of the ten locations, 180 seconds per analysis on the peak with backgrounds determined similar to Package 1, 15 kV accelerating voltage, 45 nA beam current, and a 30 μm beam diameter). Aluminum and Fe were analyzed in each Package and used to normalize the values for Ca, Mg, and Ti in Package 2 due to Na loss from the initial analyses. For the Package 2 analyses, the EMPA was recalibrated and new background values were obtained and stored as mentioned above, prior to the Package 1 analyses. One must also watch for dead time from the Al $K_\alpha$ peak, and if a problem, apply an appropriate correction. For the ZAF matrix corrections, "fixed" values for Si, Na, K, Mn, and $H_2O$ for an average rhyolite from Best (1982) were used.

Package 3: For the Zr concentrations, one analysis was done for each of the ten predefined analysis locations. The Zr value in Table 2 is an average of the ten analyses. The analytical conditions used were 15 kV accelerating voltage, 200 nA beam current, and 30 μm beam diameter. Under these conditions, for a Zr concentration of ~325 ppm Zr, this will produce a 1σ uncertainty from the counting statistics of ~9% relative standard deviation. This corresponds to a temperature uncertainty of ±15°C (Table 3). For the matrix corrections, "fixed" values for all major elements and $H_2O$ for an average rhyolite from Best (1982).

In the course of this investigation, the authors experimented with different average rhyolite compositions for the major element and Zr ZAF corrections. It was determined that the "fixed" composition used for the matrix corrections played a minor role in the major element compositions and hence the calculated M value, and the Zr content. It should be noted, however, that if no ZAF correction was applied to the Zr analyses, the Zr concentration could be off by as much as 10-15% relative standard deviation from the ZAF-corrected value. It is also worth mentioning that for samples with Zr contents approaching the minimum detection limit for the EMPA (e.g., 40-50 ppm for the conditions used), the error from the measurement will approach 100%.

***Determination of T.*** In Table 2 the results from bulk sample XRF (Wark 1991) and *in situ* EMPA analyses (this study) of sample N-57 are presented. In general there is quite good agreement between the two techniques. One would expect that any elements contained in phenocrysts (e.g., Fe, Ca, Na, K, Mg) in the sample would be lower in the *in situ* analyses than the bulk sample analyses and that is indeed the case. The *M* value calculated from the bulk sample is slightly higher than the *in situ* value (e.g., 1.41 vs. 1.35, respectively), and the Zr contents agree within the

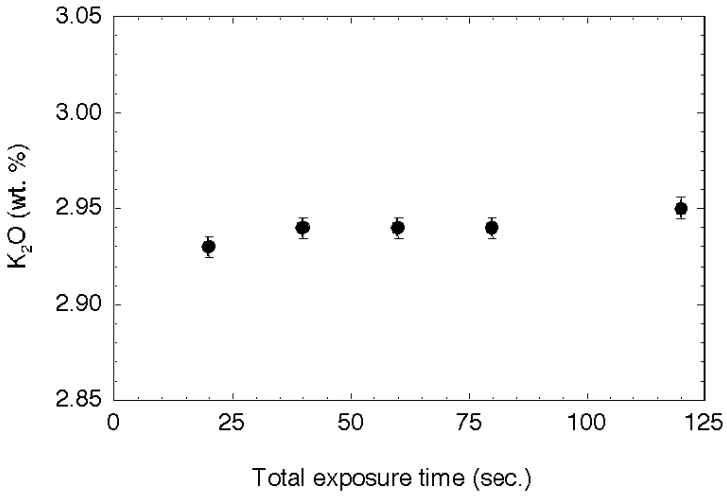


**Figure 7.** Plot of K vs. time for *in situ* EMPA analyses (average of 10 analyses) of sample N-57. Note the small change in K over time. Error bars are 1σ errors from counting statistics.

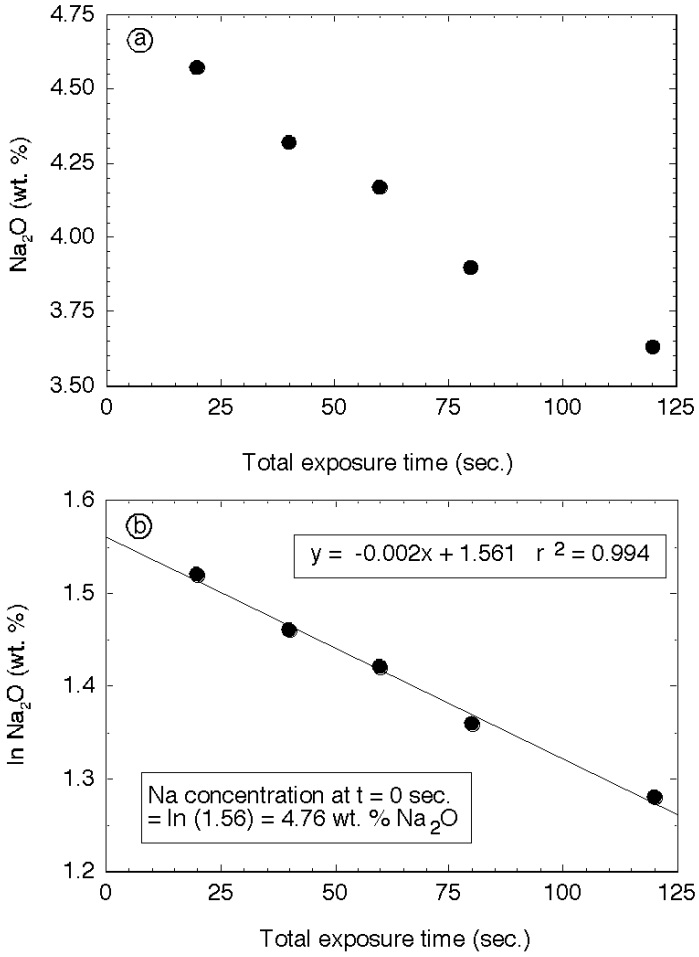


**Figure 8.** Plot of Na vs. time for *in situ* EMPA analyses (average of 10 analyses) of sample N-57. (a) Note the marked decrease in $Na_2O$ over 125 seconds. (b) Plot of natural logarithm vs time used to calculate the actual $Na_2O$ content at t = 0. The equation in (b) is a linear fit to the data.

1σ error for the EMPA analyses (Table 3).

In order to calculate the zircon saturation temperature, one must rearrange Equation (1) to solve for T. Once this is done, the value for $D_{Zr}^{zircon/melt}$, where $D_{Zr}^{zircon/melt}$ is the concentration ratio of Zr in zircon (e.g., assume a stoichiometric Zr concentration for zircon of 497,646 ppm Zr) to the Zr content measured in the melt and the M value obtained using the equation at the bottom of Table 1 are inserted into Equation (1).

The temperature calculated for sample N-57 using the *in situ* glass analyses, 855±15°C, (Table 3) agrees within the 1σ error for the bulk sample XRF analysis zircon saturation temperature, 842°C (with no error reported in Wark 1991). The error bars on Figure 9 reflect the uncertainties in the Zr concentration and calculated temperature for that sample at the 1σ confidence level. The XRF and EMPA zircon saturation temperatures that were calculated are lower than the Fe-Ti oxide temperatures reported by Wark (1991) for sample N-57. As discussed in Davidson and Lindsley (1985) their two-pyroxene geothermometer yielded temperatures ~25°C higher than other pyroxene geothermometers published up to that time, and the error associated with their experimental calibration may be as high as 40-80°C. The two-pyroxene thermometry values reported in Wark (1991) for his sample #1 at 0.1 GPa, and sample #2 at 0.5 GPa are within error of

the zircon saturation temperatures calculated using the EMPA values; however, the other two two-pyroxene temperatures yielded temperatures outside of the uncertainty of the EMPA analyses. The uncertainty in the Davidson and Lindsley (1985) experimental calibration is ~±50°C.

For sample N-57, the bulk sample XRF and *in situ* EMPA major element and Zr analyses agree well within error and the temperatures agree reasonably well with two other independent geothermometers discussed in Wark (1991). Therefore, for this sample, either bulk sample XRF or *in situ* EMPA analyses would work to determine the major element and Zr compositions, and would have produced geologically reasonable zircon saturation temperature estimates. As the percentage of phenocrysts increases, one would expect to find greater deviations from the bulk sample and *in situ* analyses for *M* and Zr and the calculated zircon saturation temperature.

## SUMMARY

There have been several studies over the past few decades that discussed zircon saturation in geologic systems. These studies involved either natural samples or high-temperature experiments. The most widely cited series of experimental papers were written with the intention that the results be used to constrain the temperature of zircon saturation in magmatic liquids whose compositions fall within the experimental calibration range. Most studies published subsequently use zircon saturation systematics as a way to understand or interpret zircon inheritance (or the temperature at which zircon crystallized) and were done on intrusive rocks using analyses of bulk, holocrystalline samples to determine the *M* and Zr values. In some cases, useful results were obtained. In other cases, when the rock samples analyzed are either outside the *M* calibration range, or assumptions have to be made about magma composition or crystallization temperature, or both, uncertainties arise because the results may not agree with the results of the Watson and Harrison (1983) experimental results.

The worked example showed that for that particular sample the bulk sample XRF analysis and the *in situ* glass analyses both provided geologically reasonable zircon saturation temperatures that generally agree with other independent mineral-pair geothermometers.

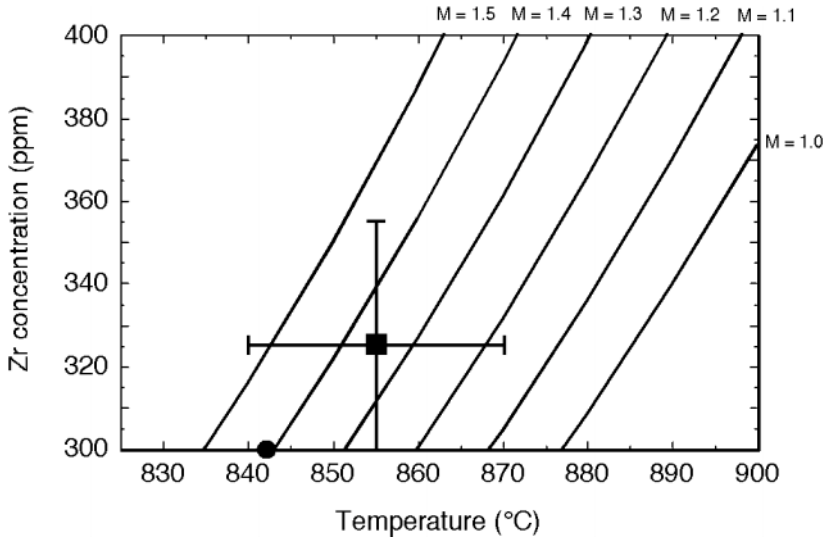


**Figure 9.** Same plot as Figure 2b, but with EMPA result for Zr (filled box) (average of ten analyses) plotted again the calculated temperature. The error bars for Zr are 1σ errors from the EMPA counting statistics and were carried through to the temperature estimation. Filled circle symbol is temperature estimate using 299 ppm Zr and a calculated *M* = 1.41 using the bulk sample XRF analysis reported in Wark (1991).

## ACKNOWLEDGMENTS

This research was supported in part by NSF grants EAR-8904177, EAR-9205793, EAR-9220095, EAR-9527014 and EAR-0073752 to E.B. Watson, and EAR-9909383 to J.M. Hanchar. We thank Calvin Miller, Dave Wark, Don Baker and Mark Harrison for fruitful discussions on zircon saturation, Ben Hanson for assistance with the N-57 glass analyses, and to Paul Ribbe for his editorial assistance.

## REFERENCES

Amelin Y (1998) Geochronology of the Jack Hills detrital zircons by precise U-Pb isotope dilution analysis of crystal fragments. Chem Geol 146:25-38

Amelin Y, Lee D-C, Halliday AN, Pidgeon RT (1999) Nature of the Earth's earliest crust from hafnium isotopes in single detrital zircons. Nature 399:252-255

Amelin Y, Lee D-C, Halliday AN (2000) Early-middle Archean crustal evolution deduced from Lu-Hf and U-Pb isotopic studies of single zircons. Geochim Cosmochim Acta 64:4205-4225

Anders E, Grevesse N (1989) Abundances of the elements: meteoric and solar. Geochim Cosmochim Acta 53:197-214

Anderson DJ, Lindsley DH (1988) Internally consistent solution models for Fe-Mg-Mn-Ti oxides: Fe-Ti oxides. Am Mineral 73:714-726

Ayers JC, Watson EB (1991) Solubility of apatite, monazite, zircon, and rutile in supercritical aqueous fluids with implications for subduction zone geochemistry. Phil Trans R Soc London A335:365-375.

Baker DR, Conte AM, Freda C, Ottolini L (2002) The effect of halogens on Zr diffusion and zircon dissolution in hydrous metaluminous granitic melts. Contrib Mineral Petrol 142:666–678

Barrie CT (1995) Zircon thermometry of high-temperature rhyolites near volcanic-associated massive sulfide deposits Abitibi subprovince, Canada. Geology 23:169-172

Best MG (1982) Igneous and Metamorphic Petrology. San Francisco, WH Freeman and Company, 630 p

Bowden P (1966) Zirconium in Younger Granites of Northern Nigeria. Geochim Cosmochim Acta 30:985-993

Bowring SA, Housh T (1995) The Earth's early evolution. Science 269:1535-1540

Bowring SA, Erwin DH, Jin YG, Martin MW, Davidek K, Wang W (1998) U/Pb zircon geochronology and tempo of the end-Permian mass extinction. Science 280:1039-1045

Bowring SA, Williams IS (1999) Priscoan (4.00-4.03 Ga) orthogneisses from northwestern Canada. Contrib Mineral Petrol 134:3-16

Brouand M, Ganzet G, Barbey P (1990) Zircon behavior during crustal anatexix. Evidence from the Tibetan Slab migmatites (Nepal). J Volcan Geotherm Res 100:19-40

Buick R, Thornett JR, McNaughton NJ, Smith JB, Barley ME, Savage M (1995) Record of emergent continental crust differs from 3.5 billion years ago in the Pilbara Craton of Australia. Nature 375:574-577

Chao ECT, Fleischer M (1960) Abundance of zirconium in igneous rocks. Rept 21st Intl Geol Congr Copenhagen, Part 1:106-131

Chappell BW, Bryant CJ, Wyborn D, White AJR, Williams IS (1998) High- and low-temperature I-type granites. Res Geol 48:225-235

Copeland P, Parrish RR, Harrison TM (1988) Identification of inherited radiogenic Pb in monazite and its implications for U-Pb systematics. Nature 333:760-763

Davidson PM, Lindsley, DH (1985) Thermodynamic analysis of quadrilateral pyroxenes Part II: Model calibration from experiments and applications to geothermometry. Contrib Mineral Petrol 91:390-404

Devine, JD, Gardner JE, Brack HP, Layne GD, Rutherford MJ (1995) Comparison of microanalytical methods for estimating $H_2O$ contents of silicic volcanic glasses. Am Mineral 80:319-328

Dickin AP (1995) Radiogenic Isotope Geology. Cambridge University Press, New York, 490 p

Dickinson JE Jr, Hess PC (1982) Zircon saturation in lunar basalts and granites. Earth Planet Sci Lett 57:336–344

Dietrich RV (1968) Behavior of zirconium in certain artificial magmas under diverse P-T coniditons. Lithos 1:20-29

Ewing RC, Haaker RF, Lutze W (1982) Leachability of zircon as a function of alpha dose. *In* Scientific Basis for Radioactive Waste Management V. Lutze W (ed) Elsevier, Amsterdam, p 389-397

Ewing RC, Lutze W, Weber WJ (1995) Zircon: a host-phase for the disposal of weapons plutonium. J Mater Res 10:243-246

Ewing RC (1999) Nuclear waste forms for actinides. Proc Nat Acad Sci 96:3432-3439

Farges F (1996) Does Zr–F "complexation" occur in magmas? Chem Geol 127:253–268

Frondel C, Colllette, RL (1957) Hydrothermal synthesis of zircon, thorite and huttonite. Am Mineral 42:759-765

Froude DO, Ireland TR, Kinny PD, Williams IS, Compston W, Williams IR, Myers JS (1983) Ion microprobe identification of 4,100 - 4,200 Myr-old terrestrial zircons. Nature 304:616-618

Goldschmidt VM (1954) Geochemistry. Clarendon Press, Oxford, 730 p

Harrison TM, Aleinikoff JN, Compston W (1987) Observations and controls on the occurrence of inherited zircon in Concord-type granitoids, New Hampshire. Geochim Cosmochim Acta 51:2549-2558

Harrison TM, Watson EB (1983) Kinetics of zircon dissolution and zirconium diffusion in granitic melts of variable water content. Contrib Mineral Petrol 84:66–72

Hansmann W, Oberli F (1991) Zircon inheritance in an igneous rock suite from the southern Adamello batholith (Italian Alps). Contrib Mineral Petrol 107:501-518

Hanson BJ, Delano, JW, Lindstrom DJ (1996) High-precision analysis of hydrous rhyolite glass inclusions in quartz phenocrysts using the electron microprobe and INAA. Am Mineral 81:1249-1262

Heaman L, Parrish RR (1991) U-Pb geochronology of accessory minerals. *In* Heaman L, Ludden J (eds) Applications of Radiogenic Isotope Systems to Problems in Geology. Mineral Assoc Can Short-Course Handbook 19:59-102

Hildreth W (1981) Gradients in silicic magma chambers: implications for lithospheric magmatism. J Geophys Res 89:8339-8369

Jercinovic MJ, Keil K (1988) Electron microprobe analyses of basaltic glasses and associated alteration products. Micro Anal 23:495-497

Johnson CM (1989) Isotopic zonations in silicic magma chambers. Geology 17:1136-1139

Keppler H. (1993) Influence of fluorine on the enrichment of high field strength trace elements in granitic rocks. Contrib Mineral Petrol 114:479-488.

Larsen L (1973) Measurement of solubility of zircon ($ZrSiO_4$) in synthetic granitic melts. EOS, Trans Am Geophys Union 54:479

Linnen RL, Keppler H (2002) Melt composition control of Zr/Hf fractionation in magmatic processes. Geochim Cosmochim Acta 66:3293–3301

McDonough WF, Sun S-S (1995) Composition of the Earth. Chem Geol 120:223-253

Maurice OD (1949) Transport and deposition of the non-sulphide vein minerals. V. Zirconium minerals. Econ Geol 44:721-731

Means WD, Park Y (1994) New experimental approach to understanding igneous texture. Geology 22:323-326

Miller CF, McDowell SM, Mapes RW (2003) Hot and cold granites? Implications of zircon saturation temperatures and preservation of inheritance. Geology 31:529-532

Morgan GB, London D (1996) Optimizing the electron microprobe analysis of hydrous alkali aluminosilicate glasses. Am Mineral 81:1176-1185

Mojzsis SM, Harrison TM (2000) Vestiges of a beginning: clues to the emergent bioshpere recorded in the oldest known sedimentary rocks. GSA Today 10:1-5

Mojzsis SM, Harrison TM (2002) Establishment of a 3.83-Ga magmatic age for the Alilia tonalite (southern West Greenland). Earth Planet Sci Lett 202:563-576

Mojzsis SM, Harrison TM, Pidgeon RT (2001) Oxygen-isotope evidence from ancient zircons for liquid water at the Earth's surface 4,300 Myr ago. Nature 409:178-181

Mumpton FA, Roy R (1961) Hydrothermal stability studies of the zircon-thorite group. Geochim Cosmochim Acta 21:217-238

Murthy MVN (1958) On the crystallization of accessory zircon in granitic rocks of magmatic origin. Can Mineral 6:260-263

Nielsen CH, Sigurdsson H (1981) Quantitative methods for electron microprobe analysis of sodium in natural and synthetic glasses. Am Mineral 66:547-552

Paterson BA, Rogers G, Stephens WE (1992) Evidence for inherited Sm-Nd isotopes in granitoid zircons. Contrib Mineral Petrol 111:378-390

Peck WH, Valley JW, Wilde SA, Graham CG (2001) Oxygen isotope ratios and rare earth elements in 3.3 to 4.4 Ga zircons: ion microprobe evidence for high $d^{18}O$ continental crust and oceans in the Early Archean. Geochim Cosmochim Acta 65:4215-4229

Pichavant M, Herrera JV, Boulmier S, Briqueu L, Joron J-L, Juteau M, Marin L, Michard A, Shepparrd SMF, Treuil M, Vernet M (1987) The Macusani glasses, SE Peru: evidence of chemical fractionation in peraluminous magmas. *In* Magmatic Processes: Physicochemical Principles. BO Mysen (ed) The Geochemical Society, Spec Publ No 1, University Park, Pennsylvania, p 359-373

Peck WH, Valley JW, Wilde SA, Graham CM (2001) Oxygen isotope ratios and rare earth elements in 3.3 to 4.4 Ga zircons: ion microprobe evidence for high ?$^{18}O$ continental crust and oceans in the Early Archean. Geochim Cosmochim Acta 65:4215–4229

Poldervaart, A. (1955) Zircon in rocks. 1, Sedimentary rocks. Am J Sci 253:433-461.

Poldervaart A (1956) Zircon in rocks. 2, Igneous rocks. Am J Sci 254:521-554

Rutherford MJ, Sigurdsson H, Carey S, Davis A (1985) The May 18, 1980 eruption of Mount St. Helens: 1. melt composition and experimental phase equilibria. J Geophys Res 90:2929-2947

Ryerson FJ, Watson EB (1987) Rutile saturation in magmas: implications for Ti-Nb-Ta depletion in island-arc basalts. Earth Planet Sci Lett 86:225-239

Siedner G (1965) Geochemical features of a strongly fractionated alkali igneous suite. Geochim Cosmochim Acta 29:113-137

Speer JA (1982) Zircon. Rev Mineral 5:67-112

Tole MP (1985) The kinetics of dissolution of zircon ($ZrSiO_4$). Geochim Cosmochim Acta 49:453-458

Vervoort JD, Patchett PJ, Gehrels GE, Nutman AP (1996) Constraints on early Earth differentiation from hafnium and neodymium isotopes. Nature 379:624-627

Von Blankenburg, F (1992) Combined high-precision chronometry and geochemical tracing using accessory minerals: applied to the Central-Alpine Bergell intrusion (central Europe). Chem Geol 100:1940

Wager LR, Mitchell RL (1951) The distribution of trace elements during strong fractionation of basic magma - a further study of the Skaergaard intrusion, East Greenland. Geochim Cosmochim Acta 1:129-208.

Wark DA (1991) Oligocene ash flow volcanism, northern Sierra Madre Occidental: Role of mafic and intermediate-composition magmas in rhyolite genesis. J Geophys Res 96, B8:13,389-13,411

Watson EB (1979) Zircon saturation in felsic liquids: experimental results and applications to trace element geochemistry. Contrib Mineral Petrol 70:407–419

Watson EB (1996) Dissolution, growth and survival of zircons during crustal fusion: Kinetic principles, geological models and implications for isotopic inheritance. Trans Roy Soc Edinburgh: Earth Sci 87:43–56 (also published as Geol Soc Am Spec Paper 315:43–56)

Watson EB, Harrison TM (1983) Zircon saturation revisited: temperature and composition effects in a variety of crustal magma types. Earth Planet Sci Lett 64:295–304

Watson EB, Vicenzi EP, Rapp RP (1989) Inclusion/host relations involving accessory minerals in high-grade metamorphic and anatectic rocks. Contrib Mineral Petrol 101:220-231

Wilde SA, Valley JW, Peck WH, Graham CM (2001) Evidence from detrital zircons for the existence of continental crust and oceans on Earth 4.4 Gyr ago. Nature 409:175-178

# Diffusion in Zircon

**Daniele J. Cherniak and E. Bruce Watson**

*Department of Earth and Environmental Sciences*
*Rensselaer Polytechnic Institute*
*Troy, New York 12180*

## INTRODUCTION

Despite its low abundance in most rocks, zircon is extraordinarily useful in interpreting crustal histories. The importance of U-Th-Pb isotopic dating of zircon is well and long established (Davis et al., this volume; Parrish et al., this volume). Zircon also tends to incorporate trace elements useful as geochemical tracers, such as the REE, Y, and Hf. A number of characteristics of zircon encourage the preservation of internal isotopic and chemical variations, often on extremely fine scale, which provide valuable insight into thermal histories and past geochemical environments. The relative insolubility of zircon in crustal melts and fluids, as well as its general resistance to chemical and physical breakdown, often result in the existence of several generations of geochemical information in a single zircon grain. The fact that this information is so frequently retained (as evidenced through backscattered electron or cathodo-luminescence imaging that often reveal fine-scale zoning down to the sub-micron scale) has long suggested that diffusion of most elements is quite sluggish in zircon.

In this chapter, we present an overview of the findings to date from laboratory measurements of diffusion of cations and oxygen in zircon. Because of its importance as a geochronometer, attempts have been made to measure diffusion (especially of Pb) for over 30 years. But only in the last decade or so have profiling techniques with adequate depth resolution been employed in these studies, resulting in a plethora of new diffusion data. These findings have important implications for isotopic dating, interpretation of stable-isotope ratios, closure temperatures, and formation and preservation of primary chemical composition and zoning in zircon.

## HISTORY—A BRIEF REVIEW OF BULK-RELEASE AND EARLY LOWER-RESOLUTION DIFFUSION MEASUREMENTS

Efforts have been made for some time to quantify and characterize diffusion in zircon, most notably of Pb, in deference to its significance in interpreting Pb isotopic signatures and refining understanding of thermal histories. As is evident from the summary of data plotted in Figure 1, there has historically been relatively little agreement between determinations of Pb diffusion rates, and values span a remarkably broad range (more than 10 orders of magnitude) in measured $D$. Many of these Pb diffusion studies have been considered in detail by Lee (1993); only brief discussion and summary are offered here.

The experiments of Shestakov (1969, 1972) and Magomedov (1970) relied upon bulk release methods, with the zircon crystals heated and the amount of Pb released recorded as a function of time. Such measurements are plagued by several difficulties, among them the presence of cracks, cleavage surfaces, dislocations and other features that might provide shortcut pathways for Pb transport through mineral grains. In addition, real mineral surfaces depart from model assumptions of ideal smooth surfaces, which would increase available surface area for exchange and affect calculated diffusivities. In these studies, Pb release did not obey a typical volume diffusion relationship, indicating the possibility of grain-boundary diffusion, and suggesting that surface volatilization as well as Pb migration might be a factor influencing Pb release patterns.

Sommerauer (1976) heated both crystalline and metamict zircons with PbO powder, and obtained an upper-limit estimate of Pb diffusion in the crystalline zircon based on an electron microprobe profile (or lack thereof, as Pb penetration was found to be <1 μm for an anneal of 2 days at

1529-6466/03/0053-0005$05.00

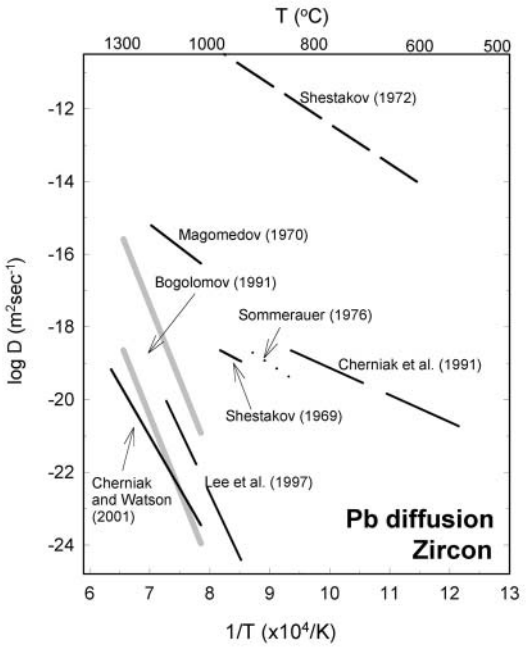


**Figure 1.** Summary of measurements of Pb diffusion in zircon. Sources for data are noted on the graph. Measurements gathered over more than three decades show relatively little agreement, and values span a remarkably broad range (more than 10 orders of magnitude) of diffusivities.

840°C). It is not surprising that an appreciable profile was not detected, since penetration distances would be <1 Å for these time-temperature conditions given values for diffusion parameters measured in recent work (Cherniak and Watson 2001).

The thermal evaporation experiments of Bogolomov (1991), which yield quite high activation energies (790-1180 kJ $mol^{-1}$) likely involved decomposition of zircon to $ZrO_2$ + $SiO_2$ during heating, as suggested by the work of Chapman and Roddick (1994). Pb loss in this case is not governed by simple volume diffusion but is instead controlled by the decomposition process and movement of the reaction front which would greatly enhance the mobility of Pb.

Measurements have also been made of the diffusion of noble gases, some of which are intermediate products in U-Pb decay sequences. Rn diffusion has been investigated in powdered zircon aliquots by measuring alpha activity of released $^{222}Rn$ (Gasparini et al. 1984). In that study, an activation energy for diffusion of 3.8 kJ $mol^{-1}$ and pre-exponential factor of $6.4\times10^{-18}$ $m^2sec^{-1}$ were obtained over the temperature range 50 - 400°C. This extremely small activation energy may indicate that Rn diffusion was facilitated by alpha recoil damage to the zircon structure; the influence of radiation damage on diffusion is considered in more detail in subsequent sections.

Reiners et al. (2002) investigated He diffusion in zircon through a series of step-heating experiments. They obtained activation energies ranging from 145 to 185 kJ $mol^{-1}$ (35 to 44 kcal $mol^{-1}$). However, they argue that temperature-dependent He release from the zircon crystals investigated is not consistent with thermally activated diffusion from a single diffusion domain, and that release patterns may reflect radiation damage to the zircon structure or the presence of distinct intracrystalline domains.

The studies outlined in this section point out some of the difficulties inherent in determining diffusivities from bulk release experiments, namely that factors other than volume diffusion contribute to and complicate interpretation of observed data. Measuring diffusion profiles directly removes some of this ambiguity, as it can be determined whether the profiles conform to appropriate solutions to the diffusion equation given the boundary conditions imposed by the experiment, or whether other non-diffusional processes are also taking place. One problem with diffusion measurements in zircon is that diffusion of most atomic species is extremely sluggish, so techniques of modest spatial resolution (e.g., EMPA) are of limited use, as was shown in Sommerauer's (1976) study. However, the development of SIMS, and the application of ion-beam techniques such as Rutherford Backscattering Spectrometry (RBS) and Nuclear Reaction Analysis (NRA) to geological studies, has permitted depth-profiling with depth resolution up to three orders of magnitude better than EMPA and thus made measurements of diffusivities of numerous elements in zircon possible.

## CATIONS

In this section, we consider the diffusion of cations in zircon. Most of the experimental work on cation diffusion has involved the measurement of chemical diffusion. In chemical diffusion there

is a chemical potential gradient, and there will be a change in the total concentration of the diffusing element in the material and substitution of the diffusing species for another element in the mineral structure. In contrast, the oxygen diffusion experiments described in the next section represent self-diffusion, with simple exchange of oxygen atoms for other oxygen atoms in the material (with $^{18}O$ used as a tracer isotope to indicate the extent of exchange) producing no change in total oxygen concentration, only a change in the oxygen isotopic composition.

**Pb**

As noted previously, efforts to measure Pb diffusion in zircon extend back well over three decades. There are relatively few studies, and those only in the past decade or so, of Pb diffusion in zircon in which analytical techniques with superior depth resolution have been employed. The first of these was by Cherniak et al. (1991), in which RBS was used to characterize Pb profiles. This analytical method, although somewhat limited in sensitivity (to ~100 ppm for heavy elements) and isotope selectivity (except for lighter elements), is in many ways an excellent technique for measuring the diffusion of heavy elements in minerals such as zircon. Its superior depth resolution (to ~10 nm near-surface) permits the measurement of short diffusion profiles and quantification of the sluggish kinetics characteristic of cations in zircon.

In the Cherniak et al. (1991) study, Pb ions were implanted in natural zircon (from the Mud Tank carbonatite), and implanted samples were annealed under a range of time-temperature conditions, with resultant profiles measured by Rutherford Backscattering Spectroscopy. The process of ion implantation, however, produced significant amounts of damage to the zircon crystal, leading to apparently elevated diffusion rates for Pb, and a comparatively low activation energy for diffusion (142 kJ $mol^{-1}$). Interestingly, implantation of Pb at energies in the range of those used by Cherniak et al. (1991) creates damage comparable to that produced by alpha-recoil events in the decay of U to Pb in natural zircon (e.g., Ewing et al., this volume; Headley et al. 1982, Petit et al. 1987), so these results, as the authors then noted, provide a determination of Pb diffusion in zircons that have experienced significant radiation damage.

Lee et al. (1997) measured out-diffusion of Pb (as well as U and Th, to be discussed below) in a natural zircon from Sri Lanka. Experiments were run by immersing polished fragments of the zircon in a reservoir of molten NaCl to act as a "sink" for Pb, with ground zircon added to the salt in attempts to discourage zircon dissolution. Depth profiles were measured with SIMS, a technique that has been employed in diffusion studies in the geological sciences for a few decades (e.g., Giletti et al. 1978). They obtained an activation energy of 675 kJ $mol^{-1}$ and pre-exponential factor of $3.9\times10^{5}$ $m^2sec^{-1}$ over the temperature range 900-1100°C.

More recently, Cherniak and Watson (2001) reported a thorough study of Pb diffusion in zircon, with diffusion experiments encompassing a broad range of experimental conditions and zircon compositions. The majority of the experiments were run on synthetic zircons (grown in a $Li_2CO_3$:$MoO_3$ flux) with a diffusant source consisting of a mixture of $PbSO_4$ and finely ground zircon. The zircon and this source were sealed under vacuum in silica glass capsules. Prepared capsules were then annealed in vertical 1-atmosphere tube furnaces at temperatures ranging from 1000 to 1300°C and times ranging from a few hours to several months. Profiles were measured with RBS. These are "in-diffusion" experiments, because a sample with a low initial concentration of the diffusing species (in this case, Pb) is annealed with a source enriched in the diffusant, resulting in a net increase in concentration of the diffusing species in the material. Example profiles are shown in Figure 2. A fit to the data from these diffusion experiments yielded the following Arrhenius relation:

$$D_{Pb} = 1.1\times10^{-1}\, exp(-550 \pm 30 \text{ kJ mol}^{-1}/RT) \text{ m}^2\text{sec}^{-1}$$

Experiments run with natural zircons crystals from the Mud Tank, Australia, carbonatite yielded diffusivities similar to those for the synthetic zircon crystals, suggesting that differences in trace-

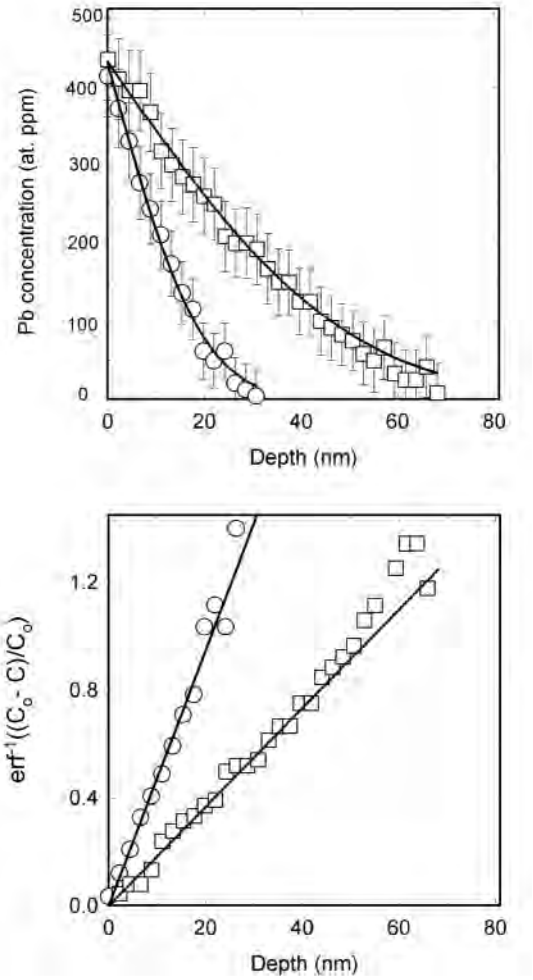


**Figure 2.** Typical diffusion profiles for Pb in-diffusion experiments measured by RBS. (a) The diffusion data are plotted with complementary error function curves. (b) The data are inverted through the error function. Slopes of lines are equal to $(4Dt)^{-1/2}$, where D is the diffusion coefficient and t is the duration of the experiment.

element compositions or defect concentrations have little influence on Pb diffusion in zircon. Similar diffusivities were obtained for zircon crystals oriented parallel and perpendicular to the *c*-axis, indicating little anisotropy in Pb diffusion (Fig. 3). In addition, measured diffusivities at a constant temperature (1200°C) agreed within experimental uncertainty for diffusion anneal times ranging over nearly an order of magnitude, providing evidence that what is being measured is volume diffusion of Pb (Fig. 3).

To investigate the effects of pressure on Pb diffusion, Cherniak and Watson (2001) ran experiments at 1.0 GPa in a piston-cylinder apparatus using pressure-sealing Pt liners inserted into holes in oxidized Ni cylinders (see Watson and Lupulescu 1993). The Pb sulfate/zircon source employed in the one-atmosphere experiments was also used in these high-pressure experiments. For "wet" high-pressure experiments, designed to investigate the effect of hydrous species on Pb diffusion in zircon, the $PbSO_4$/zircon source was mixed with finely ground zirconia and hydroxyapatite. Experiments were run at temperatures from 1100 to 1200°C, with both the "wet" and "dry" high-pressure experiments showing Pb diffusion rates similar to those for the one-atmosphere experiments (Fig. 3).

To further enhance the robustness of the data set, Cherniak and Watson (2001) performed a few types of "out-diffusion" experiments in addition to the "in-diffusion" experiments described above. "Out diffusion" experiments begin with a comparatively high concentration of the diffusing species in the sample material. Samples are annealed in a medium with lower concentration of the diffusant, which acts as a "sink;" net concentration of diffusant in the sample decreases as some of the diffusing species migrates out of the sample into the sink. For one of these experiments, a synthetic zircon was annealed with the $PbSO_4$ source in a silica glass capsule for 60 h at 1300°C, as in the "in-diffusion" experiments. The sample was removed from the source, cleaned, and the Pb uptake profile measured with RBS. It was then annealed in a Pt capsule surrounded by ground synthetic (Pb-free) zircon, which served as a sink for the Pb. The Pb distribution was again profiled with RBS, and a diffusion coefficient extracted from the Pb profile "relaxed" from its initial form by the second anneal. This experiment produced a diffusion coefficient that agreed within uncertainty with that of the in-diffusion experiments run at 1250°C (Fig. 3).

A second type of out-diffusion experiment was done with a natural zircon from Sri Lanka with relatively high Pb content (similar to the zircon sample used by Lee et al. 1997). Fragments of

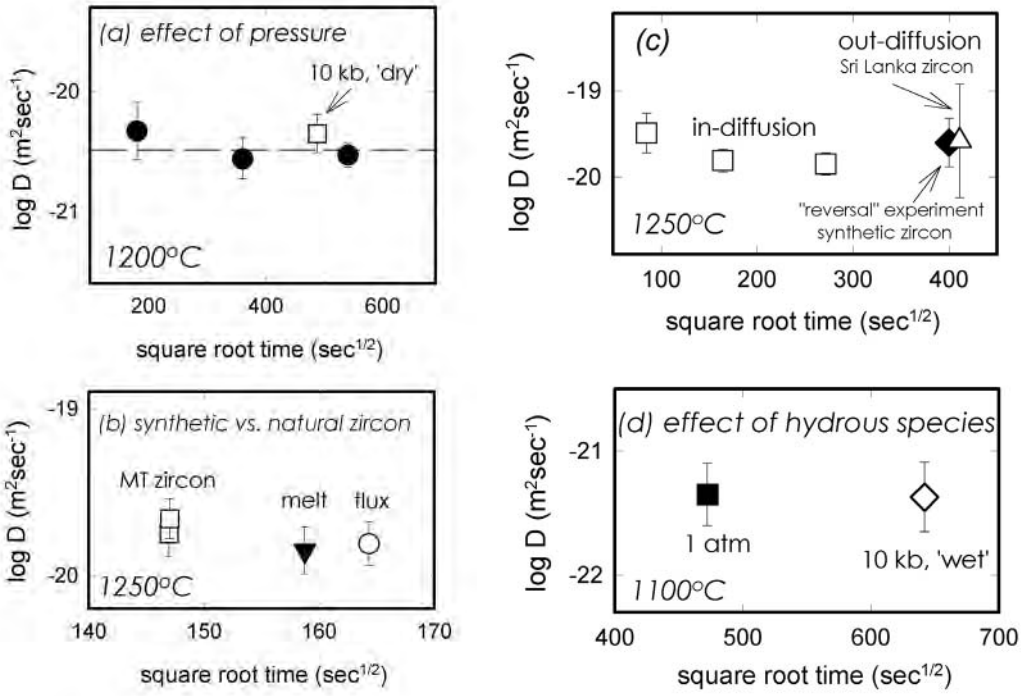


**Figure 3.** Time series for Pb diffusion anneals, and consideration of the influences of various factors on Pb diffusion in zircon from the study of Cherniak and Watson (2001). (a) Time series at 1200°C. diffusivities at constant temperature are generally quite similar for anneal times differing by a factor of 9. In addition, diffusion coefficients for experiments run at one atmosphere agree within uncertainty with that for an experiment run at 10 kbar, suggesting little influence of pressure on Pb diffusion in zircon. (b) Comparison of Pb diffusion for synthetic zircons grown in lithium carbonate/molybdenum oxide flux and in Pb silicate melt, and a natural zircon from the Mud Tank Carbonatite (MT). Zircons, regardless of origin or means of synthesis, have similar Pb diffusion rates. Further, measurements on the MT zircon indicate little anisotropy of Pb diffusion. (c) In-diffusion vs. out-diffusion. Diffusion coefficients for in-diffusion in synthetic zircon are comparable to that for Pb out-diffusion from a natural (Sri Lanka) zircon, and a "reversal" experiment (described in text) on a synthetic zircon. (d) Wet vs. dry diffusion. Diffusion rates at 1100°C for experiments at 1 atmosphere and at 10 kbar in the presence of water agree within experimental uncertainty, and indicate that the presence of hydrous species has little influence on Pb diffusion in zircon.

the zircon were polished to 0.05 μm using gamma alumina, and annealed overnight at 900°C in air in an open Pt capsule order to repair surface damage that might be a consequence of the polishing process. The specimens were then annealed at higher temperatures (one at 1250°C, another at 1470°C) in Pt capsules surrounded by finely powdered synthetic zircon as a sink for Pb. A third type of out-diffusion experiment was run using Pb (and P) doped zircons grown in a $PbO$-$SiO_2$-$ZrO_2$-$P_2O_5$ melt (Watson et al. 1997). The zircon grains were annealed in Pt capsules at 1500°C, again surrounded by finely ground synthetic (undoped) zircon. For the latter two types of out-diffusion experiments, Pb profiles of the highest-temperature experiments (i.e., 1470 and 1500°C) were measured with an electron microprobe; that for the lower temperature experiment was measured with RBS. The latter out-diffusion experiment on the natural zircon from Sri Lanka yielded a diffusivity entirely consistent with the other measurements of Pb diffusion made at the same temperature in this study (Fig. 3), and, even with the large uncertainty taken into account (due to the relatively small number of counts in the RBS spectra produced by Pb and the limited depth range over which the Pb signal could be followed due to the presence of Hf), was still found to be significantly smaller than the diffusivities measured by Lee et al. (1997), in which a similar experimental protocol (i.e., out-

diffusion of Pb from a natural zircon into a Pb-poor medium) was employed.

The 1470°C experiment on the Sri Lanka zircon, and the out-diffusion experiment on the Pb doped synthetic zircon (at 1500°C), were also consistent with the lower-temperature results from this study, as they lie on an up-temperature extrapolation of the Arrhenius line determined from the out-diffusion data gathered at temperatures 1000-1300°C (Fig. 4). A "global" fit to all the Cherniak and Watson (2001) data yields an activation energy of 545 ± 25 kJ $mol^{-1}$ and pre-exponential factor of $7.8\times10^{-2}$ $m^2sec^{-1}$ (log $D_o$ = -1.11 ± 0.88), for temperatures spanning 500°C and diffusivities ranging over 6 orders of magnitude (Fig. 3).

The differences in Pb diffusion parameters (Fig. 1) determined in the most recent depth profiling studies (Lee et al. 1997, Cherniak and Watson 2001) warrant a brief discussion. The Lee et al. (1997) Arrhenius equation for a Sri Lanka zircon is based on only a few data points (7 points, at only three temperatures) acquired in experiments involving a Pb sink (molten NaCl) known to be reactive with zircon. Their study included a modest time series (i.e., experiments of differing duration at a single temperature), one of the standard tests to confirm diffusion-controlled transport. However, the experiment durations in their time series vary by a factor of only 1.8, leading to a small difference in expected diffusive transport distance (~1.3, as diffusion distance *x* scales with the square root of time), which is not definitive. Judging from the diffusivities and durations reported for experiments at 900°C, the SIMS depth profiles at this temperature were only a few nanometers long, which challenges the spatial resolution of the SIMS method and would lead to uncertainties in diffusivities inconsistent with the values reported. The Cherniak and Watson (2001) study, in contrast, included a rigorous time series (9-fold variation in experimental duration, Fig. 2), experiments involving both in- and out-diffusion of Pb, three different zircons (both synthetic and natural, including one out-diffusion experiment on a Sri Lanka zircon), and two different analytical methods (RBS and EPMA).

**Substitutional processes involving Pb**

An important consideration in Pb diffusion is the role of coupled substitution in Pb exchange, and whether the type of exchange process involved affects diffusivities. Such dependence of D on the substitutional process has been noted for REE diffusion in apatite, for example, where diffusion with coupled substitutions involving highly charged cations (e.g., $REE^{+3}$ +$Si^{+4}$ → $Ca^{+2}$ + $P^{+5}$) proceeds much more slowly than simple $REE^{+3}$→ $REE^{+3}$ exchange (Cherniak 2000). Since Pb cations will most commonly be found in nature in the +2 valence state (e.g., Otto 1966,

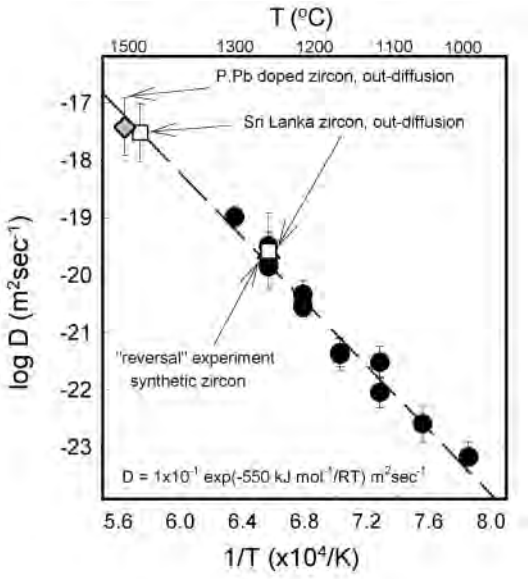


**Figure 4.** Arrhenius plot of Pb diffusion in zircon, from the study of Cherniak and Watson (2001). Plotted are in-diffusion experiments on synthetic and natural (Mud Tank) zircon, and out-diffusion and "reversal" experiments. The line is a least-squares fit to the data from 1000-1300°C; Arrhenius parameters extracted from the fit are: activation energy 550 kJ $mol^{-1}$, and pre-exponential factor $1.1\times10^{-1}$ $m^2sec^{-1}$. Also plotted are diffusivities from high-temperature out-diffusion experiments on natural (Sri Lanka) zircon and zircon grown from Pb silicate melt doped with phosphorus. These data lie on an up-temperature extrapolation from the lower-temperature measurements, illustrating the consistency between these data sets.

Watson et al. 1997), other cations (or defects such as oxygen vacancies) must provide charge balance. This is also a matter of concern when applying results from the laboratory to Pb diffusion in nature, since most Pb in natural zircon is a result of radioactive decay. Although radiogenic Pb may initially occupy locations other than "normal" structure sites due to displacement as consequence of the multistage decay process, as soon as Pb atoms become mobile (and over a very short length scale) they will occupy sites in a manner comparable to common Pb, and therefore should diffuse in a similar way. However, there is the possibility that Pb diffusion rates may differ if there are other species involved in a coupled exchange, and if the other species are rate-limiting in the diffusion process.

Because there is relatively little latitude in zircon for a broad range of substituent cation species on either the *Zr* or *Si* sites, we consider the possibility of either $S^{+6}$ or $P^{+5}$ on the *Si* site to charge-balance Pb on the *Zr* site (e.g., $Pb^{+2} + 2P^{+5} \rightarrow Zr^{+4} + 2Si^{+4}$; $Pb^{+2} + S^{+6} \rightarrow Zr^{+4} + Si^{+4}$). The study of Watson et al. (1997) has shown that significant amounts of Pb can be incorporated into zircon crystals grown from a melt when P is present. Zircon crystals grown from $PbO$-$SiO_2$-$ZrO_2$ melts incorporate little Pb (<1 ppm; Watson et al. 1997). However, when phosphorus (~several wt % $P_2O_5$) is included in the melt, Pb concentrations in the resulting zircons are orders of magnitude higher (~1000 ppm; Watson et al. 1997). This finding is also consistent with the observation in natural zircon crystals that high levels of common Pb are often associated with the presence of P (e.g., Watson et al. 1997).

The other candidate is sulfur in the hexavalent state. While sulfur has been reported in chemical analyses of zircon (e.g., Speer 1982), it may be due to inclusions of other minerals such as galena. It is less clear that it is ubiquitous in zircon itself, or whether it might be present in sufficient quantity to play some charge-compensating role. Conceivably, Pb could be charge compensated in substituting for Zr through a substitution of S (in the hexavalent state) for Si. In the interest of thoroughness, Cherniak and Watson (2001) explored this possibility by measuring S on a number of their zircon samples from experiments using the $PbSO_4$ diffusant source, with NRA using the 6.90 MeV resonance of the $^{32}S(\alpha,p)^{35}Cl$ reaction (Soltani-Farshi et al. 1996). These analyses showed no evidence of sulfur above detection limits of about 50 ppm (atomic), indicating that sulfur played no significant role in the exchange process for Pb diffusion, even where abundant S was available in the environment.

In the experiments of Cherniak and Watson (2001), Pb diffusivities at a given temperature were found to be quite similar for the different types of experiments in which diffusion via different mechanisms might be possible (i.e., Pb in-diffusion using a $PbSO_4$ source, out diffusion from synthetic P- and Pb-doped zircon, out-diffusion from natural Pb-bearing Sri Lanka zircon). This suggests that several factors that might have been heretofore suspected of affecting Pb diffusion in zircon seem to exert little significant influence. If either $P^{+5}$ or $S^{+6}$ played a compensating role, it would be most likely the case that Pb diffusion would be rate limited by the diffusion of these highly charged cations, so Pb diffusivities would differ depending on the substitutional process involved. Given the apparent similarities of Pb diffusion rates over this range of conditions, it seems likely that divalent Pb is charge compensated in another way, possibly by oxygen vacancies ($O^{-2}$ centers), as may be the case for the REEs in zircon (Cherniak et al. 1997a, and discussion in the next section). Diffusion of oxygen, even under dry conditions (Watson and Cherniak 1997), is also faster than diffusion of Pb in zircon (see Fig. 10 below), so movement of Pb would then be expected to be the rate-limiting factor in Pb diffusion.

**Diffusion systematics of trivalent cations**

Diffusion measurements on the trivalent cations have concentrated on the rare earth elements because of their importance as indicators of geochemical processes. Cherniak et al. (1997a) measured diffusion rates of Sm, Dy and Yb in synthetic zircon, and natural zircon from the Mud Tank carbonatite. Experiments were run at 1-atm with rare-earth phosphate powder sources, over temperatures ranging from 1150 to 1650°C; profiles were analyzed with RBS and electron microprobe.

Little evidence of anisotropy was noted for experiments run on zircons cut parallel and perpendicular to *c*-axis (as was also observed in the case of Pb), and Dy diffusivities in natural and synthetic zircons were quite similar. Over the temperature range 1150-1400°C (1150-1650°C for Yb) the following Arrhenius relations were obtained:

$D_{Sm} = 2.9\times10^{8} exp(-841 \pm 57\ kJmol^{-1}/RT)\ m^2sec^{-1}$
$D_{Dy} = 2.3\times10^{5} exp(-734 \pm 35\ kJmol^{-1}/RT)\ m^2sec^{-1}$
$D_{Yb} = 3.8\times10^{4} exp(-691 \pm 47\ kJmol^{-1}/RT)\ m^2sec^{-1}$

It is evident from these expressions that diffusion rates vary among the rare earth elements (REEs) in a systematic manner: Diffusion rates of the heavy rare earths (with smaller ionic radii) are faster than the larger lighter REE (Fig. 5). In addition, activation energies for diffusion increase when going from the smaller heavy REE to the light REE. To attempt to quantify this observed behavior, we plot ionic rare-earth ionic radius (8-fold coordination; Shannon 1976) against the activation energy (Fig. 6a) and the log of the pre-exponential factor $D_o$ (Fig. 6b). Both activation energy and log of the pre-exponential factor fall along second-order polynomial curves, so the data permit us to predict diffusivities for the other REEs at a given temperature as a function of ionic radius. Curves generated with the derived expression for various temperatures are plotted in Figure 7. At 1200°C, there is a difference of about 2 orders of magnitude in diffusivities of Lu and La. At lower temperatures, because of predicted differences in activation energies, the disparity between diffusivities of the light and heavy REEs becomes more pronounced.

Since there are only three points to constrain the lines, it cannot be assured that the REEs as a group define the simple relationship discussed above and there may not necessarily be any physical significance attached to it. It might be argued that activation energies are a function not only of site energy but also porosity of the structure (e.g., Dowty 1980) and that the larger REEs would therefore have greater difficulty in moving through the relatively compact and stiff zircon structure.

Van Orman et al. (2001) developed a simple elastic model for diffusion to qualitatively describe observed dependencies of diffusion of like-charged cations (such as the REE) on ionic radii. This model, adapted from the work of Mullen (1966) and Zener (1952) assumes that the motion energy of diffusing ions is due to elastic strain, and considers the difference in motion energy that results from the difference between the size of an impurity ion and the ideal site radius. This quantity, expressed as a size factor $\delta$, where $\delta = (r_{imp} - r_{site})/r_o$ with $r_{imp}$ the impurity ion radius, $r_{site}$ the ideal site radius, and $r_o$ the average cation-anion distance. Activation

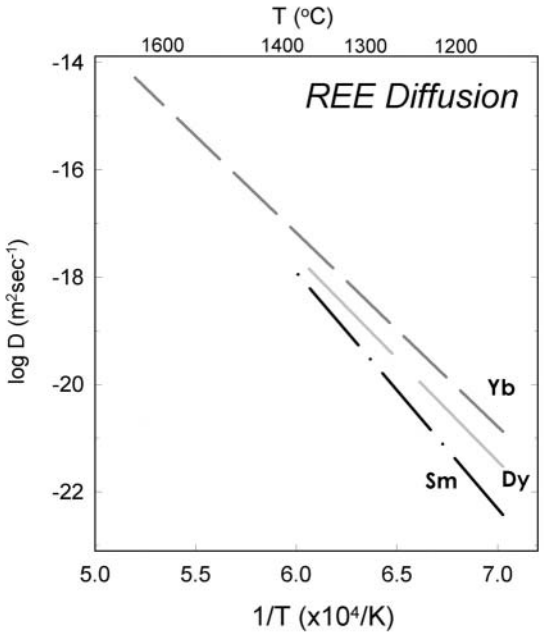


**Figure 5.** Summary of REE diffusion data for zircon, from the study by Cherniak et al. (1997a). REE diffusivities display a consistent trend of increasing diffusivity and decreasing activation energy for diffusion when going from the light to heavy rare earths (and larger to smaller ionic radii). Arrhenius parameters for the REE are: Sm - $E_a = 841\pm57$ kJ mol$^{-1}$, $D_o = 2.9\times10^{8}$ m$^2$sec$^{-1}$; Dy - $E_a = 734\pm35$ kJ mol$^{-1}$, $D_o = 2.3\times10^{5}$ m$^2$sec$^{-1}$; Yb - $E_a = 691\pm47$ kJ mol$^{-1}$, $D_o = 3.8\times10^{4}$ m$^2$sec$^{-1}$.

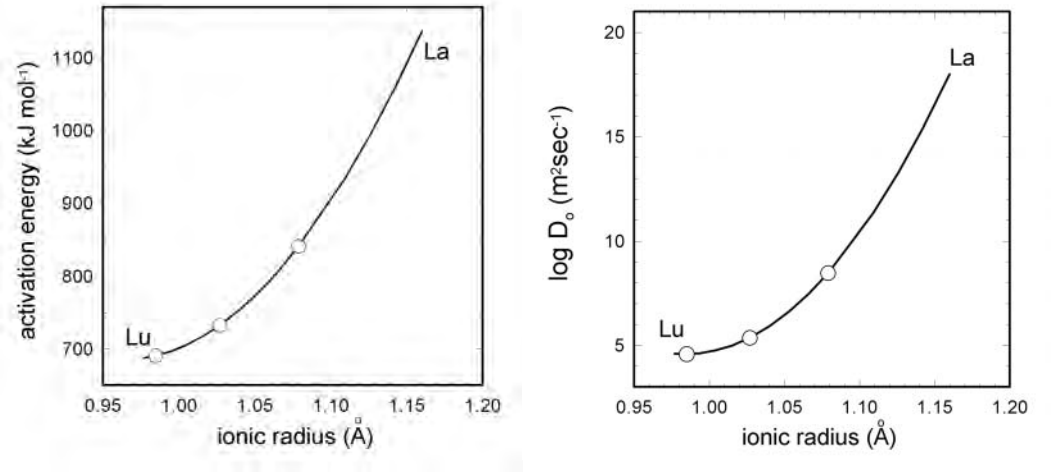


**Figure 6.** Correlation of activation energy and pre-exponential factor with ionic radius for the rare earth elements, from the study of Cherniak et al. (1997a). Lines in (a) and (b) are second-order polynomial curves passing through the data (symbols) extended over the full range of the rare earths. (a) Activation energy. The relationship between ionic radius (r, in Å) and activation energy ($E_a$, in kJ $mol^{-1}$) expressed by the curve is: $E_a = 1.15\times10^4 - 2.25\times10^4 r + 1.17\times10^4 r^2$. (b) Pre-exponential factor. The relationship between ionic radius (r, in Å) and log of the pre-exponential factor ($D_o$, in $m^2sec^{-1}$) expressed by the curve is: $\log D_o = 4.28\times10^2 - 8.60\times10^2 r + 4.37\times10^2 r^2$.

energies for diffusion may be larger for cations larger than the ideal size. A relationship relating the activation energy to ion size can be derived if one assumes that a large proportion of the energy expended in an atomic jump is due to lattice strain, so cation size can then be related to the motion energy of a cation (i.e., $E_m$) as follows:

$$E_m = E_m^o\{1 + 2[\delta(1 - 1/\sqrt{2})^{-1} - \delta^2(1 - 1/\sqrt{2})^{-2}]\} \quad (1)$$

Here, $E_m^o$ refers to the motion energy for an ion with an ideal radius. This equation describes a parabola, with a minimum value when $\delta = 0.146$. In the expression above, the minimum motion energy for zircon will occur for an ionic radius of 0.116 nm, which corresponds to the ionic radius of $La^{+3}$ in 8-fold coordination (Shannon 1976). However, it is counterintuitive to assume that motion energies will increase with increasing ionic radius beyond this minimum; the data presented here explore only the region where $\delta < \delta_{min}$ so we can offer no comment on the diffusional behavior of cations beyond this size limit (and La is of course the largest of the REE).

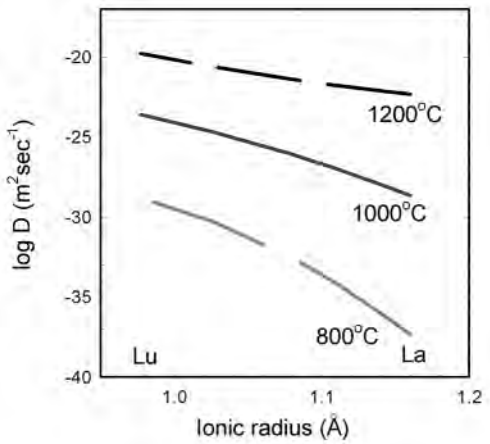


**Figure 7.** Plot of REE diffusivities at various temperatures as a function of ionic radius. Diffusivities are calculated using the expressions discussed in the text and presented in Figure 6. Because of the differences in predicted activation energies, differences between diffusivities of the light and heavy rare earths grow increasingly larger with decreasing temperature.

If we assume diffusion via an intrinsic vacancy mechanism, the activation energy for diffusion will consist of energies for vacancy formation and migration. Energies for vacancy formation will be independent of ionic radii, so the dependence on ionic radii will be present in the migration

energy. If we use the theoretical Zr vacancy formation energy (~600 kJ $mol^{-1}$; Williford et al. 1999) and take $E_m^o$ in the above expression as equal to the Zr vacancy migration energy (~110-130 kJ $mol^{-1}$; Williford et al. 1999), ignoring for the moment any charge dependence of migration energy. If we use the latter value in Equation (1) above to estimate migration energies for the rare earths, and sum with the vacancy formation energy to estimate activation energy, we obtain values ranging from 790 kJ $mol^{-1}$ (for Sm) to 695 kJ $mol^{-1}$ (for Yb), compared with the experimental results of 841 to 691 kJ $mol^{-1}$, indicating reasonable agreement of experimental and theoretical findings.

Because the pre-exponential factor depends on the temperature derivative of the material's bulk modulus (e.g., Zener 1952, Van Orman et al. 2001) as well as the ionic radius, it is expected that variations in diffusivities with ionic radius in zircon will be greater than for less rigid mineral structures. This appears to be the case under some circumstances, as REE diffusion in clinopyroxene (Van Orman et al. 2001) displays a much less pronounced dependence on ionic radii than zircon. In other minerals, including plagioclase (Cherniak 2002), apatite (Cherniak 2000), fluorite (Cherniak et al. 2001) and calcite (Cherniak 1998b) there is little evidence of dependence of REE diffusivities on ionic radii. However, some minerals with comparatively stiff structures, such as aluminosilicate (Van Orman et al. 2002) and aluminate garnets (Cherniak 1998a), show little variation of REE diffusivities with ionic radii, indicating that the simple elastic model cannot provide broad quantitative predictions of diffusivities for a range of minerals. And although this model can describe qualitative trends for diffusion of the REE in zircon (and clinopyroxene) it predicts larger variances among REE diffusivities than the experimental data indicate.

**Substitutional processes for trivalent cations**

The xenotime-type substitution (i.e., $REE^{+3} + P^{+5} \rightarrow Zr^{+4} + Si^{+4}$) is commonly reported in natural zircon crystals (e.g., Speer 1982, Hinton and Upton 1991), and may be a means for charge compensation during REE diffusion. The substitutional processes involved in REE exchange were investigated by Cherniak et al. (1997a) through complementary NRA and RBS measurements of phosphorus and the rare earths, respectively, with phosphorus measured using the 3.048 and 3.640 MeV resonances of the $^{31}P(\alpha,p)^{34}S$ nuclear reaction (McIntyre et al. 1988). Measurements of P on several of the zircon samples show that there is no phosphorus above detection limits (~600 atomic ppm).

The finding that phosphorus has at most a minor involvement in REE diffusion is consistent with the observed trend of increasing REE diffusivity with decreasing ionic radius. If coupled REE + P diffusion were occurring, diffusion would likely be rate-limited by pentavalent P rather than the trivalent REEs, so major differences in REE diffusivities would be unlikely. Oxygen, on the other hand, diffuses much more rapidly than the REEs (e.g., at 900°C, oxygen diffuses about 3 orders of magnitude faster than Yb; Watson and Cherniak 1997), so, as in the case of Pb diffusion, oxygen defects are a potential candidate for charge compensation of the REE in zircon. The formation of oxygen vacancies ($O^{-2}$ centers) is possible at high concentrations of REE when there is a high probability of two REEs in adjacent *Zr* sites. In addition, the calculated energy for oxygen vacancy migration (0.99-1.16 eV; Williford et al. 1999) is considerably less than that for oxygen vacancy formation (5.6 eV, Crocombette 1999), so while significant numbers of static *oxygen* site vacancies are unlikely to persist in the zircon structure (e.g., Hanchar et al. 2001), they may be present (and mobile) in sufficient quantity to facilitate exchange not charge-balanced by P. Because of the difficulty in measuring relatively small changes in oxygen concentration, however, it is not possible to directly determine whether the REEs are predominantly compensated by oxygen defects.

Other possibilities do exist. Zircons that contain up to 0.8 mol % rare earth elements have been synthesized in the absence of phosphorus (Hanchar et al. 2001), a concentration on order of the maximum REE uptake measured in the Cherniak et al. (1997a) diffusion experiments (REE surface contents ranging from 1 to 0.05 mol %). In these cases, it has been determined that some charge compensation of the REE occurs via inclusion of $Li^{+1}$ and $Mo^{+6}$ (both species are present in the flux used to grow the zircons) interstitially. Watson (1980) also synthesized zircon crystals with high

REE contents in felsic peralkaline melts with no phosphorus present, a system more closely resembling that found in nature than the lithium metasilicate-molybdenum oxide flux used by Hanchar et al. (2001). In some natural zircon crystals, it has also been found that at least 50% (on an atomic basis) of REE-Zr substitutions are not compensated by phosphorus or pentavalent cations (Hinton and Upton 1991). Under hydrous conditions, REE can be compensated by substitution of hydroxyl groups $(OH)^-$ for $(SiO_4)^{4-}$ (e.g., Caruba et al. 1974, Medenbach 1976, Robinson 1979), with the formula $(Zr_{1-y}REE_y)(SiO_4)_{1-x}(OH)_{4x-y}$, or by protonation of the $O^{2-}$ ions of the $(SiO_4)^{4-}$ groups (i.e, $SiO_{4-x}(OH)_x)_{x-4}$, or simply by the presence of interstitial $H^+$ (see Hanchar et al. 2001 for a discussion of possible substitution mechanisms). It remains unclear whether other species in natural zircons might provide charge balance.

**Tetravalent cations**

Diffusion of tetravalent cations (Hf, Th and U) was characterized by Cherniak et al. (1997b). Experiments were done by annealing synthetic zircon in Pt capsules with a source material. For Hf diffusion, the source consisted of a mixture of $HfO_2$ and $SiO_2$ powders in proportions of stoichiometric hafnon ($HfSiO_4$). The source for Th experiments was a mixture of ground synthetic thorite and zircon, while for U diffusion experiments it consisted of a mixture of $UO_2$, $SiO_2$, and ground synthetic zircon. Diffusion profiles were measured with RBS. Over the temperature range 1400-1650°C, the following Arrhenius relations were obtained (Fig. 8):

$D_{Th} = 9.6\times10^{1} exp(-792 \pm 34 \text{ kJ mol}^{-1}/RT) \text{ m}^2\text{sec}^{-1}$
$D_{U} = 1.6 exp(-726 \pm 83 \text{ kJ mol}^{-1}/RT) \text{ m}^2\text{sec}^{-1}$
$D_{Hf} = 8.6\times10^{2} exp(-812 \pm 54 \text{ kJ mol}^{-1}/RT) \text{ m}^2\text{sec}^{-1}$

The results for Hf diffusion are consistent with the "upper limit" value of $10^{-19}$ $m^2sec^{-1}$ at 1600°C, determined by Suzuki et al. (1992) using electron microprobe analysis of synthesized zircon-hafnon couples annealed at high temperatures. Lee et al. (1997) measured apparent out-diffusion of U and Th from a natural zircon from Sri Lanka containing ~240 ppm U and 20 ppm Th, with Pb profiles measured as well (as discussed above). These experiments were run by immersing zircons in a reservoir of molten NaCl containing ground zircon in attempts to minimize dissolution, with diffusive-loss profiles measured by SIMS. They ob-

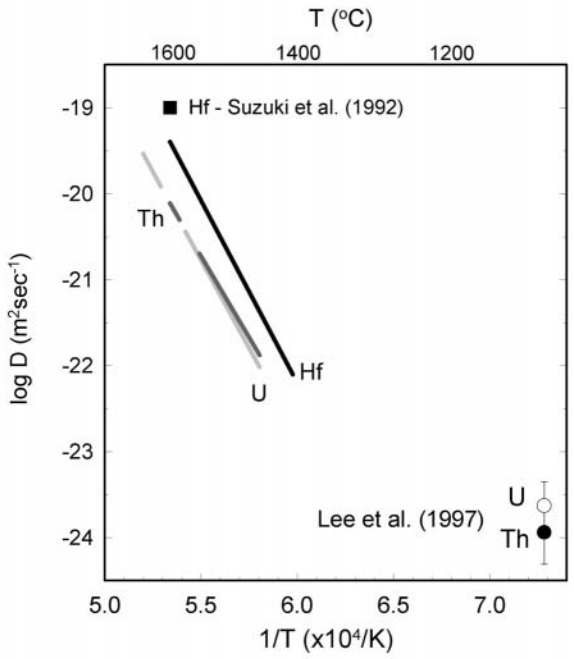


**Figure 8.** Arrhenius plot of U, Th and Hf diffusion in zircon from the study of Cherniak et al. (1997b). Measurements are for diffusion perpendicular to c. The lines are least-squares fits to the data. Arrhenius parameters for these fits: Hf - activation energy 812 kJ $mol^{-1}$, pre-exponential factor $1.6\times10^3$ $m^2sec^{-1}$. U - activation energy 726 kJ $mol^{-1}$, pre-exponential factor 1.6 $m^2sec^{-1}$. Th - activation energy 792 kJ $mol^{-1}$, pre-exponential factor $8.6\times10^2$ $m^2sec^{-1}$. Also plotted is the upper-limit estimate for Hf diffusion at 1600°C from the study of Suzuki et al. (1992), and the data reported by Lee et al. (1997) for U and Th diffusion at 1100°C.

tained diffusivities of $1.16\times10^{-24}$ $m^2sec^{-1}$ (log D = -23.94 ± 0.37) for Th, and $2.34\times10^{-24}$ $m^2sec^{-1}$ (log D = -23.63 ± 0.28) for U at 1100°C. However, given the diffusion times and calculated diffusivities reported in their study, the lengths of the resulting diffusion profiles would be on the order of only a few tens of angstroms, and so may not be easily quantified with the SIMS instrument used in their measurements.

Although Cherniak et al. (1997b) could not measure diffusivities at 1100°C, down-temperature extrapolation using their Arrhenius relations yield $6.8\times10^{-29}$ $m^2sec^{-1}$ for Th and $3.1\times10^{-28}$ $m^2sec^{-1}$ for U, or about 4 orders of magnitude slower than the Lee et al. (1997) results. A possible reason for this discrepancy may be that the molten salt medium used for a "sink" for the diffusant in the Lee et al. (1997) experiments caused incongruent dissolution and recrystallization of the zircon surface despite the presence of ground zircon in the melt. Thus, concentration gradients may have been produced by a reaction rather than simple volume diffusional exchange.

As in the case of the REE, Cherniak et al. (1997b) find a systematic variation of diffusion rates for the tetravalent cations with ionic radius, where diffusivities increase with decreasing ionic radius. Efforts to quantify this observed trend were first made by Cherniak et al. (1997b), where they "normalized" pre-exponential factor for the U, Th, and Hf diffusion data by assuming a constant activation energy (795 kJ $mol^{-1}$ [190 kcal $mol^{-1}$]) for all three cations. This was considered a reasonable approach since, in contrast to the REE, no clear systematic dependence of activation energy for diffusion on ionic radii could be determined. However, it is likely that there is some dependence does exist, but the limited range in 1/T that could be sampled in these measurements does not allow for strong constraints. We instead take into consideration variations in both $D_o$ and activation energy by plotting log of the diffusivities themselves (calculated at a temperature included in the range over which diffusivities were measured) against ionic radii of the tetravalent cations. These data can be fit (albeit somewhat arbitrarily) to a second-order polynomial (Fig. 9). The data may then be used to predict diffusivities for other tetravalent cations as a function of ionic radius. Other functional forms can be plotted against the data, but predicted pre-exponential factors in such cases differ little (up to [and in most cases much less than] 0.1 log unit) over a reasonable range of ionic radii. Further, the parabolic function form is consistent with a simple elastic model, which can be used to qualitatively describe diffusional behavior as a function of cationic radius.

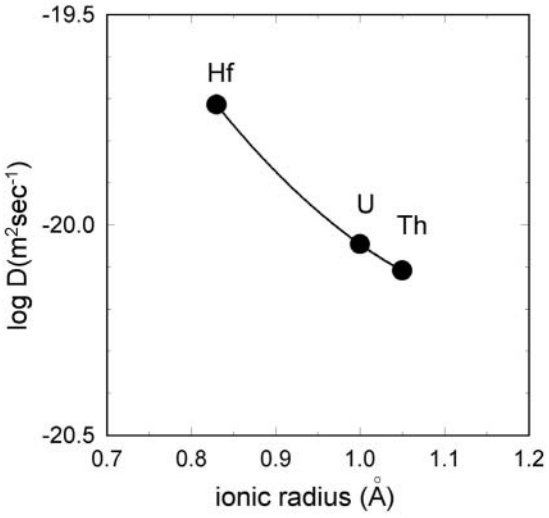


**Figure 9.** Correlation of diffusivities (at 1600°C) with ionic radius for the tetravalent cations U, Th and Hf in zircon. The data fall along a second-order polynomial curve representing the following relationship between ionic radius (r, in Å) and log of the diffusivity ($D_o$, in $m^2sec^{-1}$): log D = -15.47 – 7.74 r + 3.16$r^2$.

The differences in diffusivities among these tetravalent cations are less pronounced than among the trivalent REEs. A stronger dependence on ionic radius of both the pre-exponential factor and activation energy (Cherniak et al. 1997a) is evident in the latter case. The reason for this is not yet clear. It is possible that the larger deviation of the LREE from the size of the Zr ionic radius may contribute to this stronger dependence. Trivalent REEs from La to Gd all have ionic radii (8-fold coordination, +3 valence) larger than the largest tetravalent cation (Th) investigated.

While dependence of diffusivities on ionic radii among tetravalent cations is much less significant than for the REE, the tetravalent cations do exhibit slower overall diffusivities than the trivalent REE. The

REEs diffuse 3-5 orders of magnitude faster than the tetravalent cations. Such pronounced variations in diffusivities with cation charge have been noted in other mineral systems. For example, K diffusion in orthoclase (Foland 1974) is more than three orders of magnitude faster than Sr and Pb diffusion (Cherniak and Watson 1992, Cherniak 1995). In plagioclase, univalent cations (Na and K) diffuse 3-6 orders of magnitude faster (Giletti and Shanahan 1997) than divalent cations Sr (Cherniak 1996, Cherniak and Watson 1994, Giletti and Casserly 1994), Pb (Cherniak 1995), and Ba (Cherniak 2002a) for feldspars of a given compositional range, which in turn diffuse 1-4 orders of magnitude faster than the trivalent REE (Cherniak 2002b).

**Cation diffusion in zircon—a general summary**

***A consideration of some trends.*** As outlined above, there now exists a body of data for diffusion of various cations and anions in zircon (Fig. 10). Certain systematic behaviors have been observed among trivalent and tetravalent cations. For cations of a given charge, diffusivities increase with decreasing ionic radius. The REE, for example, exhibit marked variation in diffusion rates from the light to heavy REE, with diffusion coefficients of Lu and La expected to differ by roughly two orders of magnitude. Among tetravalent cations, Hf diffuses more rapidly than U or Th, but these differences are not as pronounced as those found among trivalent cations. The influence of cation charge is also great; the (trivalent) REEs diffuse 3-5 orders of magnitude faster than tetravalent cations in zircon. Pb likely exists in the divalent state in these diffusion studies, and in zircons in nature as well, since Pb is stable in the +4 valence state at elevated temperatures only under conditions of very high $f_{O2}$ (e.g., Otto 1966, Watson et al. 1997). At the same time, the ionic radius of $Pb^{+2}$ is quite large (1.29 Å in 8-fold coordination; Shannon 1976). It appears in the case of Pb that these two factors, i.e., lower charge tending to increase diffusion rates and larger ionic radius tending to reduce them, provide competing influences.

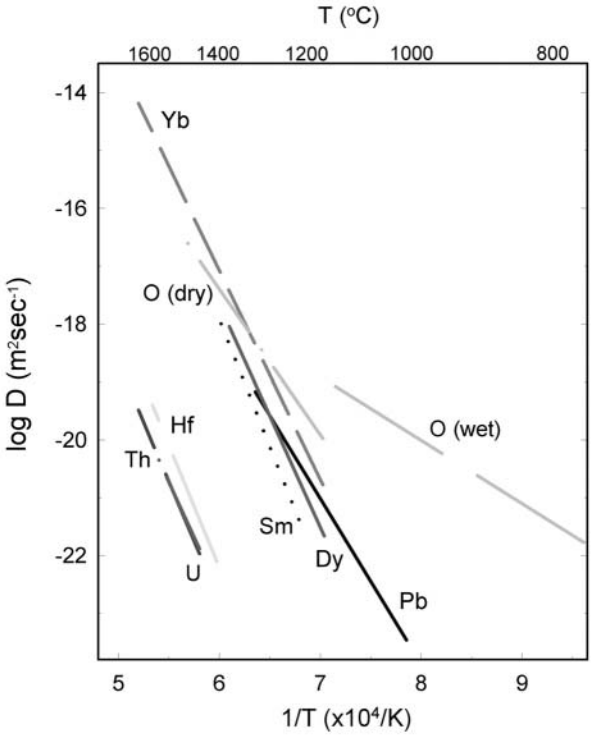


**Figure 10.** Summary of diffusion data for various cations and anions in zircon. Sources for data: Yb, Dy, Sm - Cherniak et al. (1997a); Hf, U, Th - Cherniak et al. (1997b); oxygen - Watson and Cherniak (1997); Pb - Cherniak and Watson (2001).

***Possible mechanisms for diffusion***. The results from these experimental studies of cation diffusion, as well as recent theoretical determinations of energies of formation and migration of various defects in zircon (Williford et al. 1999, Crocombette 1999, Meis and Gale 1998), permit us to speculate on possible mechanisms for diffusion. For a few reasons it appears most likely that cations diffuse via an intrinsic vacancy mechanism. Diffusivities for both synthetic and natural zircon crystals with varying concentrations of aliovalent impurities are quite similar, which suggests that extrinsic cation vacancies are an unlikely mechanism, because the concentrations of these defects

would be proportional to the concentration of the dominant aliovalent impurity (e.g., $P^{+5}$). Further, theoretically-determined Zr vacancy migration energies (Williford et al. 1999) range from 1.16-1.38 eV (110-130 kJ $mol^{-1}$), considerably smaller than the activation energies for cation diffusion. However, energies for creation of Zr vacancies by Schottky defect formation are 6.2 eV/defect (600 kJ $mol^{-1}$) and 12.28 eV/defect (1190 kJ $mol^{-1}$) for Frenkel defect formation (Williford et al. 1999, He and Cormack 1999), so the experimental activation energies are consistent with an intrinsic regime reflecting energies of both formation and migration of Zr vacancies. Zr intersitials can be reasonably ruled out as unfavorable because of their very high estimated energy of formation (18.0 eV [1740 kJ $mol^{-1}$]; Crocombette 1999). Calculations by Meis and Gale (1998) using empirical potentials for zircon and applying static transition state theory, estimate an activation energy for diffusion of $U^{+4}$ (via a vacancy mechanism) in zircon of 5.9-9.4 eV (570-900 kJ $mol^{-1}$), consistent with experimentally determined activation energies for diffusion of tetravalent cations (e.g., 726-812 kJ $mol^{-1}$).

## OXYGEN DIFFUSION

### Experimental results

Oxygen diffusion in zircon was first measured by Muehlenbachs and Kushiro (1975), using a bulk-diffusion method with zircon heated in the presence of $^{18}O$-enriched gas. At 1300°C, they obtained a diffusivity of ~$10^{-19}$ $m^2sec^{-1}$.

More recently, oxygen diffusion has been measured under both dry and hydrothermal conditions, using $^{18}O$ enriched sources (Watson and Cherniak 1997) and direct characterization of $^{18}O$ diffusional uptake profiles with NRA using the $^{18}O(p,\alpha)^{15}N$ reaction. The dry diffusion experiments were run by sealing $^{18}O$-enriched quartz powder with a polished zircon specimen in Pt capsules, with a small amount of Zr metal powder added to scavenge atmospheric $N_2$ and $O_2$ sealed in the Pt capsule upon welding, which might cause capsule rupture.

Hydrothermal experiments were run in both cold-seal pressure vessels and solid-media piston-cylinder apparatus, using a source consisting of both the $^{18}O$ enriched quartz and $^{18}O$ enriched water, to simulate near-surface and lower-crustal conditions, respectively. Cold-seal runs covered the pressure range ~7-83 MPa and temperature range 767-1003°C, with piston-cylinder runs at pressures from 0.4 to 1.0 GPa and temperatures ranging from 925 to 1160°C.

For the dry experiments, the following Arrhenius relation was obtained (Fig. 11):

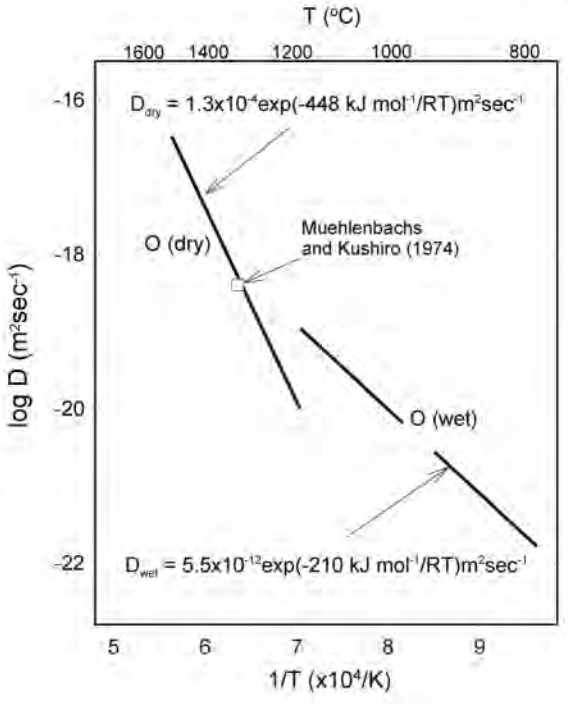


**Figure 11.** Comparison of dry and wet diffusion results from the work of Watson and Cherniak (1997). Also on the plot is the datum for oxygen diffusion under dry conditions measured by Muehlenbachs and Kushiro (1974). Diffusion of oxygen under dry conditions is slower and has a higher activation energy for diffusion than oxygen diffusion under wet conditions (448 vs. 210 kJ $mol^{-1}$), a finding consistent with that observed for other silicates.

$D_{oxygen,\ \text{“dry”}} = 1.3\times10^{-4} exp(-448\ \text{kJ mol}^{-1}/RT)$

Little anisotropy was noted in dry diffusion, as diffusion rates parallel and perpendicular to *c* were found to be quite similar. The diffusivities defined by this Arrhenius relation are consistent with the diffusivity at 1300°C obtained by Muehlenbachs and Kushiro (1975).

While most of the dry experiments conformed well to a complementary error function, which is the solution to the diffusion equation for the initial and boundary conditions imposed by the experiments, profiles from some of these dry experiments showed evidence of "tails," i.e., somewhat elevated (above natural abundance) $^{18}O$ concentrations extending to depths in the zircons up to twice the length of the error-function portion of the profile. The presence of the tails did not affect diffusivities calculated from the steep portion of the profile, since diffusivities from samples with and without tails yielded similar results when fitting this portion of the spectrum. The tails are most likely attributed to the presence of localized regions containing either fluid inclusions (which had not decrepitated in the 1300°C pretreatment of zircons before diffusion anneals) or oxygen defects.

Oxygen diffusion under "wet" conditions in significantly faster than "dry" diffusion, although D is insensitive to $P_{H_2O}$ at values ≥7 MPa. The hydrothermal experiments run in the piston-cylinder show no indication of a dependence of oxygen diffusion on $P_{H_2O}$ over the pressure range 0.4-1.0 GPa. Further, in experiments run with a 50:50 (molar) $H_2O$:$CO_2$ mix, so that $P_{H_2O} < P_{total}$, diffusivities obtained were indistinguishable statistically from cases where $P_{H_2O} = P_{total}$. The cold seal runs at lower pressures (7-70 MPa) have a mean value of log D about half a log unit lower than the mean value of log D for the higher-pressure experiments (Fig. 12). Although there is no systematic variation in D with pressure among the cold-seal runs, a slight dependence of $D_{wet}$ on $P_{H_2O}$ between ~70 and 400 MPa cannot be ruled out. While the possible weak dependence of $D_{wet}$ on $P_{H_2O}$ may introduce minor complication to Arrhenian behavior, the data for the wet experiments can nonetheless be considered generally consistent over the entire range of T and P, and therefore it is not wholly unreasonable to plot these data and fit to a single Arrhenius relation, which yields (Fig. 11):

$D_{oxygen,\ \text{“wet”}} = 5.5\times10^{-12} exp(-210\ \text{kJ mol}^{-1}/RT)$

The "wet" and "dry" Arrhenius relations indicate that oxygen diffusion in zircon is significantly enhanced by the presence of water in the system, in contrast to the behavior of Pb in zircon, for which diffusivities appear unaffected by the presence of hydrous species. Further, since the activation energy for diffusion of oxygen is much smaller under wet conditions than under dry (i.e., 210 vs. 448 kJ $mol^{-1}$), the difference between dry and wet diffusivities will increase with decreasing T (the variance will be, for example, about 6 orders of magnitude at 700°C). This sort of behavior, i.e., faster diffusivities and lower activation energies for oxygen diffusion under hydrothermal versus dry conditions, is common in silicates, including diopside (Ryerson and McKeegan 1994, Farver 1989), anorthite (Ryerson and McKeegan 1994, Giletti et al. 1978), sanidine (Freer et al. 1997, Derdau et al. 1998), and quartz (Dennis 1984, Giletti and Yund 1984). It is commonly argued (e.g., Farver and Yund 1990, 1991; Zhang et al. 1991, Doremus 1996) that molecular water is the dominant species transporting oxygen under hydrothermal conditions, and that the uncharged $H_2O$ molecule moves move readily than highly-charged oxygen anions.

The weak (to nonexistent) dependence on $f_{H_2O}$ for oxygen diffusion in zircon under hydrothermal conditions contrasts with trends observed for other minerals. Quartz (Farver and Yund 1991), calcite (Farver 1994) and alkali feldspar (Farver and Yund 1990) all exhibit increasing oxygen diffusivities with increasing $f_{H_2O}$. Assuming that fast-diffusing oxygens are carried by neutral water molecules (e.g., Zhang et al. 1991), it is perhaps the case that the closely-packed zircon structure becomes 'saturated' with water molecules at comparatively low water pressures, while the more open lattices of the other minerals can carry increasing amounts of water when water fugacities are increased.

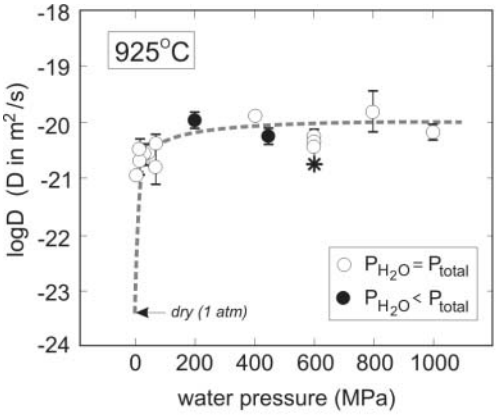


**Figure 12.** Oxygen diffusion as a function of water pressure at ~925°C. The cluster of points at $P_{H_2O} < 100$ MPa represents experiments made in cold-seal pressure vessels (two actually run at 917°C); all other symbols are for data obtained in piston-cylinder runs. The filled symbols show diffusivities resulting from experiments in which the fluid surrounding the zircon was a 50:50 (molar) $H_2O$:$CO_2$ mix; for these experiments, $P_{total}$ is 400 and 800 MPa, respectively. The asterisk symbol represents a duplicate analysis, by ion microprobe (all others were done with nuclear reaction analysis), of one of the 600 MPa experiments. From the study of Watson and Cherniak (1997).

**Diffusion mechanisms**

As in the case of cations, we can look at theoretical calculations of energies of formation and migration of defects in zircon to explore possible mechanisms for oxygen diffusion. Williford et al. (1999) obtain oxygen vacancy migration energies ranging between 0.99-1.16 eV (95-110 kJ $mol^{-1}$), considerably smaller than activation energies for oxygen diffusion. Formation energies for oxygen vacancies are much higher: He and Cormack (1998) predict 3.31-6.52 eV/defect (320-630 kJ $mol^{-1}$). The experimentally determined activation energy for oxygen diffusion in zircon under dry conditions (448 kJ $mol^{-1}$; Watson and Cherniak 1997) falls within the range bracketed by the summed value of energies of formation and migration of oxygen vacancies. Crocombette (1999) estimates a value of 5.6 eV (540 kJ $mol^{-1}$) for formation energies of oxygen vacancies, but a much smaller value, 1.7 eV, for formation of oxygen interstitials. Migration energies for oxygen interstitials were not determined, but may be considerably higher than those for oxygen vacancies. Because of this uncertainty, an interstitial mechanism cannot be ruled out.

The presence of "tails" on some of the oxygen diffusion profiles measured by Watson and Cherniak (1997) (see also the section above) points to the possibility of two distinct diffusion mechanisms under some circumstances. It should be noted, however, that these features only appeared for a small number of the zircon specimens analyzed, and are not a dominant contributor to oxygen diffusion under dry conditions. Williford et al. (1999) and Watson and Cherniak (1997) argue that the tails may be a consequence of the presence of pre-existing oxygen vacancies in the zircon permitting a fast diffusion pathway with lower activation energy, those zircons more "vacancy deficient" would require a significant contribution to the activation energy from vacancy formation. However, this explanation would require that the fast diffusion pathway communicate poorly with the bulk structure. Otherwise, since individual atoms cannot distinguish between intrinsic and extrinsic vacancies, the profile would appear as a simple single error function rather than a "normal" diffusion profile superposed on an extended tail region akin to that observed for grain-boundary diffusion. A possible way around this dilemma is to invoke the presence of a localized region containing oxygen vacancies that is much smaller than the ~1$mm^2$ area of the proton beam used for $^{18}O$ analysis in NRA, but of significant extent in the direction of diffusion. The existence of such regions is not unreasonable given the complex internal chemical structure of the Mud Tank zircon as revealed, for example, by cathodoluminescence imaging. This model would also explain the sporadic occurrence of the tails in the oxygen diffusion profiles. An alternative explanation is that the fast oxygen transport path can be attributed to the presence of fluid inclusions (which had not decrepitated in the 1300°C pretreatment of zircons before diffusion anneals). Oxygen can likely migrate interstitially as a component of molecular $H_2O$, with transport facilitated by the fluid inclusions, and, as noted above, oxygen diffusion in the presence of water is considerably faster than under dry conditions.

## IMPLICATIONS AND APPLICATIONS OF DIFFUSION FINDINGS

### Diffusive fractionation

We now consider some potential consequences of differences in diffusion rates among the REEs and other cations. Could there be, for example, diffusional fractionation effects over geologically relevant time-temperature conditions? We first consider the Sm-Nd system. Using the expression above for variation of diffusion coefficients with REE ionic radii, diffusivities of Sm and Nd may differ by a factor of about 8 at 1000°C. This translates to diffusion distances differing by a factor of about 2.8 (i.e., diffusion distance $x \sim (Dt)^{1/2}$) for a given time at this elevated temperature. At 800°C, the difference in diffusivities would be over 2 orders of magnitude, but diffusivities are so small (i.e., $10^{-30}$ $m^2sec^{-1}$) as to be geologically irrelevant. Diffusion for a billion years at 800°C would result in diffusion distances on order of several nanometers at most. Even at 1000°C, diffusion distances would only amount to a few tens of microns over the same duration.

Diffusional fractionation does seem a more likely possibility for the Lu-Hf system. Hf diffuses 4-5 orders of magnitude more slowly than the REEs. A difference in diffusion rates of 4 orders of magnitude would lead to diffusion distances differing by a factor of ~100; at 1000°C this is equivalent to about 150 μm for Lu vs. < 2 μm for Hf over a billion years.

### Closure temperatures

We can use experimentally-determined diffusion parameters to directly calculate closure temperatures ($T_c$) for various species in zircon as a function of effective diffusion radius and cooling rate, and these values can be compared with field based estimates for the closure temperatures for Pb. The closure temperature equation (Dodson 1973) is:

$$E/(RT_c) = \ln((ART_c^2D_o/a^2)/(EdT/dt)) \quad (2)$$

where $E$ and $D_o$ are the activation energy and pre-exponential factors for diffusion of the relevant species, $dT/dt$ is the cooling rate, $a$ is the effective diffusion radius, and $A$ is a geometric factor. The derivation of the above expression rests on several assumptions (Dodson 1973, 1986); among these is the condition that at peak temperature $T_o$, the mineral grain is not retentive of the daughter product over short timescales. This assumption, which makes $T_c$ independent of $T_o$, is, as Ganguly et al. (1998) note, not satisfied for slowly diffusing species. Given that cation diffusion in zircon appears to be exceedingly slow under crustal conditions, this condition is not satisfied nor can it even be assumed that homogeneity is achieved at peak metamorphic temperatures.

When the dependence of $T_c$ on $T_o$ is taken into account in calculating closure temperatures, the deviations of $T_c$ from conventional closure temperatures calculated using Equation (2) are smaller with increasing peak temperature ($T_o$) and slower cooling rate (Ganguly et al. 1998). The geometric factor, $A$, in Dodson's expression of mean closure temperature above, is equal to $\exp(G)$, where $G$ is the value of the closure function, $G(x)$, spatially averaged over the crystal. In deriving the expression for $G(x)$, and ultimately $A$, the dimensionless parameter $M$ [where $M$ is defined as $D(T_o)RT^2/(Ea^2dT/dt)$], is much greater than 1 (Dodson 1986). For smaller values of $M$, $G$ will decrease, thus $A$ will be smaller than the value of 55 [i.e., exp(4.0066)] one obtains when the condition of $M >> 1$ is met. As the factor $A$ decreases, mean closure temperatures will be increased.

As noted above, closure temperatures calculated using Equation (2) are mean values, as closure temperature varies with distance from the crystal surface. However, except for a very narrow outermost layer, closure temperatures will not differ from the mean by more than a few tens of degrees for cooling rates between 1-10°C/Ma and grain sizes up to a few mm. For example, for 100-μm radius grains, mean $T_c$ for Pb in zircon is about 10°C higher than that for a point 10 μm from the surface; $T_c$ for the grain center will be about 40°C higher than the mean value. A point 1 μm from the surface, however, will have a $T_c$ 80-90°C lower than the mean.

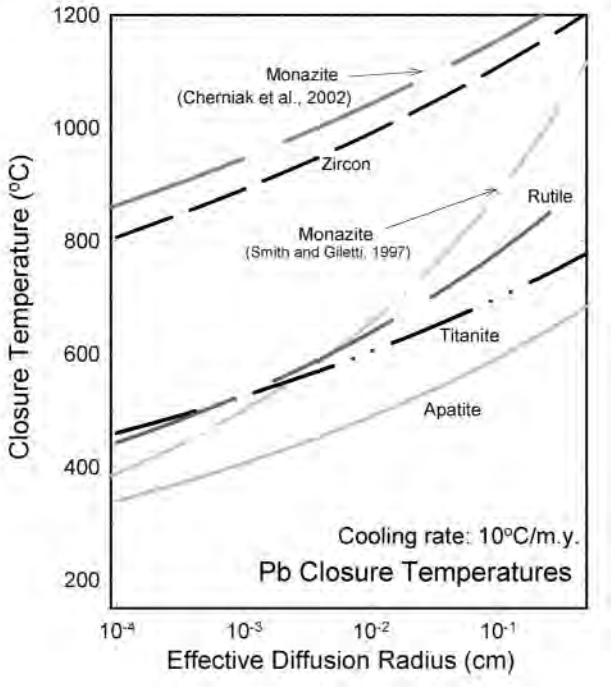


**Figure 13.** Closure temperatures for Pb in accessory minerals as function of effective diffusion radius for a cooling rate of 10°C per million years. Calculations were made employing the standard expression of Dodson (Eqn. 2). Sources for data: apatite - Cherniak et al. (1991); monazite - Smith and Giletti (1997); Cherniak et al. (2002); rutile - Cherniak (1998b); titanite - Cherniak (1993); zircon - Cherniak and Watson (2001). Closure temperatures Pb in zircon are quite high, considerably in excess of those for other accessory minerals except for monazite.

It should be clear from the above discussion that $T_c$ is dependent on many factors. Nonetheless, we can use the simplified expression above to make broad comparisons of closure of Pb in various accessory minerals, and to consider closure temperature values calculated from the diffusion parameters presented earlier in this chapter in light of field-based estimates of closure temperatures for Pb in zircon.

In Figure 13 we plot closure temperature of Pb for various accessory minerals as function of effective diffusion radius, using the "traditional" Dodson equation (Eqn. 2). We plot curves calculated using the geometric factor for spherical geometry (i.e., $A = 55$). Closure temperatures for Pb in zircon are quite high, considerably in excess of those for other accessory minerals, with the exception of monazite (Cherniak et al. 2002). For example, the closure temperature for Pb in a zircon of 100 μm effective diffusion radius for a cooling rate of 10°C/Ma is 991°C. Evidence in field based studies of the high closure temperature (in excess of 950-1000°C) for Pb in zircon has long been noted (e.g., Black et al. 1986, Claoué-Long et al. 1991, Williams 1992). Higher closure temperatures for zircon in comparison to most other accessory minerals are evidenced by various studies (e.g., McLelland et al. 1988, Mezger et al. 1991, Chiarenzelli and McLelland 1993, Hölzl et al. 1994) that have observed, for example, that titanite from high grade metamorphic terranes yield U-Pb ages younger than zircons from the same samples, or other samples experiencing the same geologic history. Given the same cooling rate and effective diffusion radii (i.e., 10°C/Ma and 100 μm), calculated closure temperatures for titanite are 385°C lower than that of zircon. Both apatite and rutile have even lower closure temperatures, with only monazite displaying closure temperatures comparable to zircon.

**The preservation of zoning in zircon**

Sharp compositional zoning in zircon is often observed, as the slow diffusivities characteristic of most elements in zircon can influence both the likelihood of formation of such zoning (e.g., Watson and Liang 1995) and its preservation under a broad range of geologic conditions (Watson and Cherniak 1997, Cherniak et al. 1997a,b). Both sector zoning and igneous growth or "oscillatory" zoning have been reported in various zircon populations, with zoning down to micron and sub-micron scales (e.g., Hanchar and Miller 1993, Halden et al. 1992, Wayne et al. 1992, Corfu et al., this volume). Species for which zoning is most commonly noted are the high-Z elements incorporated into zircon in relatively high abundance (Hf, and to lesser extent, U), with zoning observ-

able in back-scattered electron (BSE) images, and the REE (most notably Dy), whose emissions often dominate the visible in cathodoluminescence (CL) spectra (e.g., Marfunin 1979, Mariano 1989).

While zoning in Pb generally cannot be observed by these means because of its low abundance and the fact that its electronic structure militates against its being a CL activator in zircon, marked variations in Pb isotopes across individual grains, representing different stages (and ages) of zircon growth, have been detected in ion probe analyses (e.g., Hanchar and Rudnick 1995, Ireland and Williams, this volume), and discordance in many cases has been attributed to "mixing" as consequence of combining isotope information from distinct regions into a single analysis.

Given the slow diffusion rates of Pb, REE, and the tetravalent cations in crystalline zircon under most geologic conditions, distinct zones, even on relatively fine scales, will quite often be preserved. This can be illustrated by a simple model. Zones in a zircon are modeled as plane sheets of thickness $l$; adjacent planes have different concentrations of diffusant. Only diffusion normal to the planar interface is considered. Two different (and somewhat arbitrary) criteria for alteration of zones are evaluated: (i) "blurring" of zones, defined by a compositional change of 10% one-tenth of the way into the zone; and (ii) "disappearance" of zones, defined by a compositional change of 10% in the zone's center. The dimensionless parameter $Dt/l^2$ is equal to $1.8\times10^{-3}$ for condition (i), and $3.3\times10^{-2}$ for condition (ii). Figure 14 shows curves constraining the time-temperature conditions

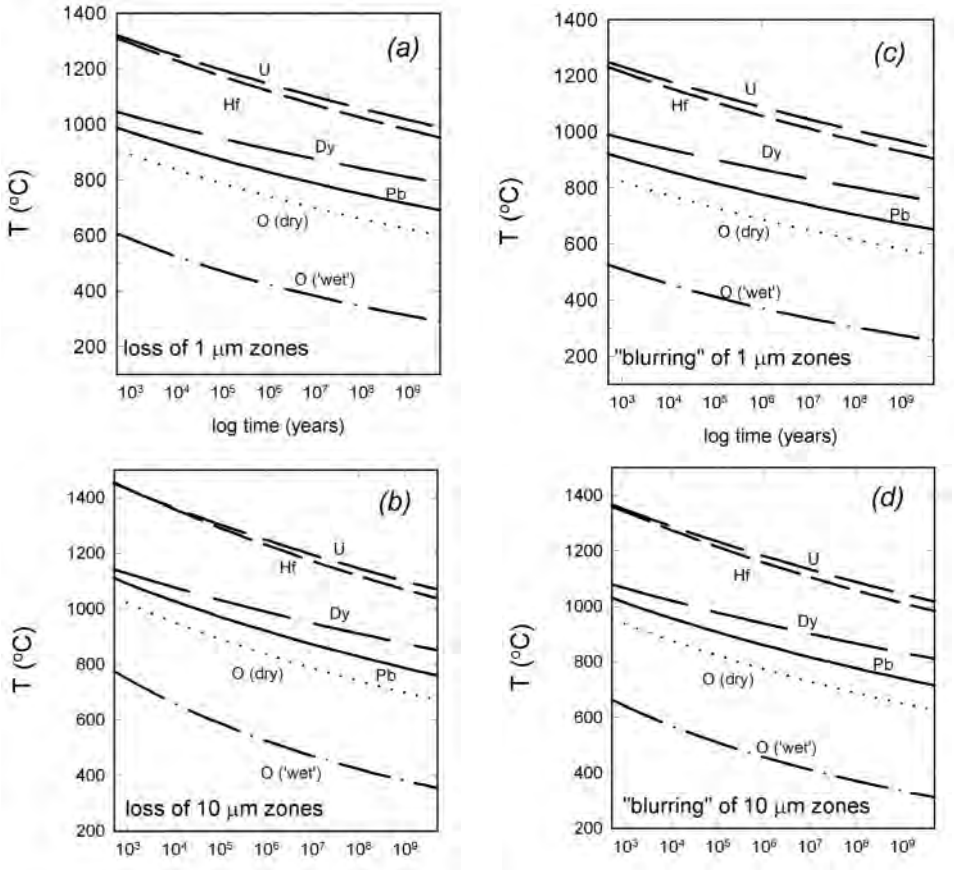


**Figure 14.** Preservation of cation and oxygen zoning in zircon. Curves represent maximum time-temperature conditions under which 1 and 10 μm zoning of U, Th, Dy, Pb and O (under dry and wet conditions) will be preserved in zircon. For conditions above the curves in a and b, well-defined zoning will be lost. For conditions above the curves in c and d, edges of zones will be "blurred" but still retain initial composition in zone centers.

under which Pb, REE, U, and Hf zoning of various dimensions will be retained given the above criteria. For example, 10-μm scale zones would resist obliteration at 750°C over times greater than the age of the Earth; even at 900°C, zones of this dimension would endure for a few million years.

Although the diffusion rates of Pb in zircon do not differ greatly from those of the REE over the investigated temperature range (Fig. 10), the differences in activation energy for diffusion (550 kJ $mol^{-1}$ for Pb vs. 690-840 kJ $mol^{-1}$ for the REE) result in significant differences in diffusion rates at most temperatures of geologic interest. For example, at 800°C, diffusion rates of Dy and Pb will differ by more than 2 orders of magnitude, with diffusion distances (which scale as the square root of $D$) differing by a factor of ~20. Differences become even more pronounced with decreasing temperature. Hence, the preservation of REE zoning observable with CL spectroscopy does not guarantee preservation of Pb isotope signatures on the same scale, as can be seen from the set of curves for Dy zoning also plotted in Figure 14. Preservation of BSE-observable zoning in Hf or U offers even less evidence for simultaneous preservation of Pb zoning, as diffusion of the tetravalent cations is considerably slower than that of the REE (Cherniak et al. 1997b).

Similarly, the preservation of Pb isotope ratios in no way guarantees that oxygen isotopes from the same region of zircon are preserved, given the large differences in Pb and oxygen diffusivities, even under dry conditions (Fig. 10). For example, zoning on the 10 μm scale would be preserved for Pb over nearly 100 Ma at 900°C; for oxygen these time would be 100,000 years and only a few decades for dry and wet conditions, respectively (Fig. 14).

It should be made clear, however, that these diffusion data apply strictly to crystalline zircon. Diffusion may be significantly enhanced in severely radiation-damaged zircon (e.g., Cherniak et al. 1991), thus permitting the obliteration of zoning under much less extreme thermal conditions. Further discussion of the influence of radiation damage, and other factors, on Pb transport will be taken up in the next section.

**Pb loss**

Discordant U-Pb ages are on occasion attributed, generically, to "Pb loss" (Parrish et al., this volume; Davis et al., this volume). Laboratory diffusion measurements indicate that Pb diffusion in crystalline zircon is remarkably slow, thus it is highly unlikely that significant amounts of Pb will be lost from crystalline zircon at geologically reasonable temperatures due to volume diffusion. Figure 15 illustrates this point. The curves represent the percent of Pb loss for zircons of 10- and 100-μm radii when subjected to various time-temperature conditions. Zircon crystals of 10-μm radius would lose only about 1% of their Pb if residing at 750°C for times on order of the age of the Earth. Zircons exposed to upper mantle temperatures for extended periods of time would, however, experience significant Pb loss through diffusion, although not always complete resetting, as suggested by studies of kimberlitic zircons (Scharer et al. 1992, Mezger and Krogstad 1997).

Pb loss due to diffusion is more likely in metamict zircons, since Pb diffusion has been found to be much more rapid in zircon that has been severely radiation-damaged (Cherniak et al. 1991). Radiation damage, however, takes significant amounts of time to accumulate because of the natural annealing that occurs on geologic timescales (e.g., Lumpkin and Ewing 1988, Meldrum et al. 1998). The annealing process is such that zircons residing at temperatures above a "critical amorphization temperature" will not become metamict. The critical amorphization temperature is a weak function of activity, i.e., zircon U content and age (Meldrum et al. 1998). The critical amorphization temperature for zircons with 1000 ppm U is about 360°C, and only about 20°C higher for zircons with as much as 10,000 ppm (i.e., 1%) uranium; it varies as a function of zircon age by less than a degree per billion years for a given U content. Zircon crystals exposed to temperatures below the critical amorphization temperature can accumulate damage, but only over long time scales.

Using the expressions derived by Meldrum et al. (1998), curves can be generated defining the range of time-temperature conditions that radiation damage in zircon will accumulate to sufficient degree that the zircon becomes metamict. This curve is plotted in Figure 15. It can be readily noted

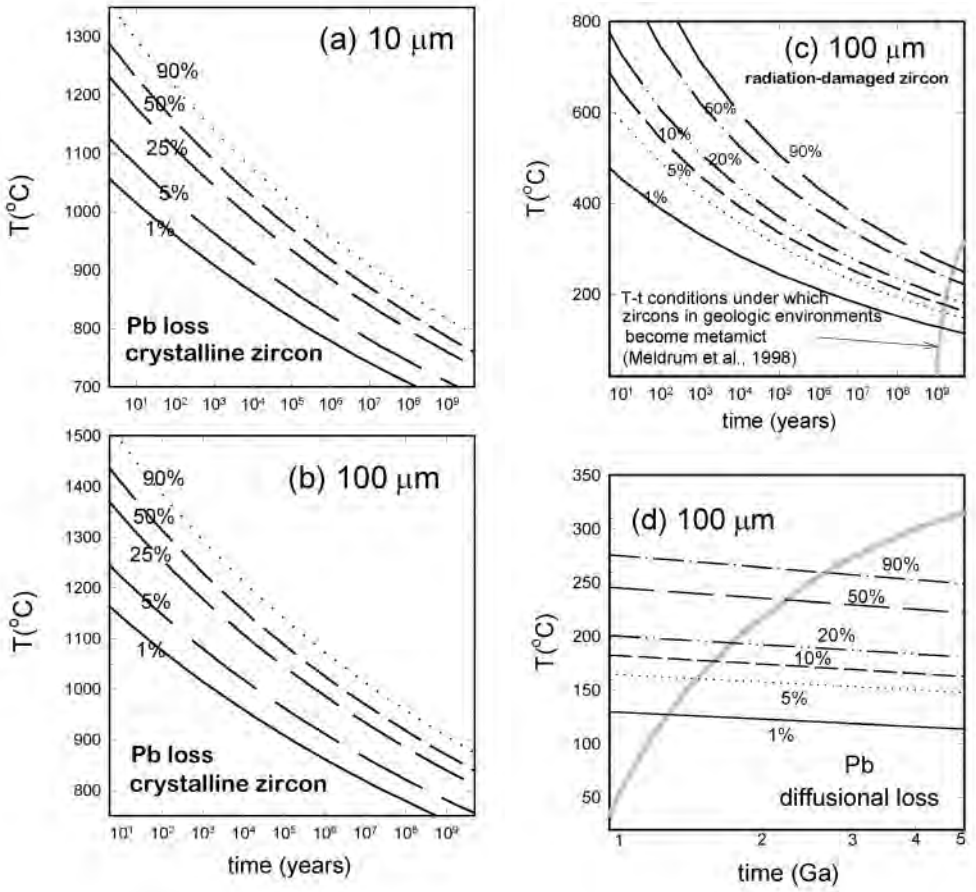


**Figure 15.** (a) and (b) Conditions for diffusional Pb loss in crystalline zircon for zircons of effective radii of 10 and 100 μm. Curves represent time-temperature conditions under which zircon will lose the indicated fraction of total Pb, calculated using the diffusion parameters from Cherniak and Watson (2001). (c) and (d) Conditions for diffusional Pb loss in metamict zircon. Curves represent time-temperature conditions under which a zircon of 100 μm radius will lose the indicated fraction of Pb. These are generated using the diffusion data of Cherniak et al. (1991) for radiation-damaged zircon. Also plotted is a curve indicating time-temperature conditions under zircon with 100 ppm U will become metamict, calculated from the expressions in Meldrum et al. (1998). Times in excess of a billion years, even at near-surface temperatures, are necessary in order for the zircon to accumulate sufficient radiation damage to become metamict. Significant Pb loss will be likely only in the region below this curve.

that times upward of a billion years at low temperatures are required to induce amorphization, and, as noted above, damage sufficient to cause amorphization will fail to accumulate at elevated temperatures. Also plotted against this curve are curves indicating the degree of diffusional Pb loss for metamict zircon. The diffusion data of Cherniak et al. (1991) are used here, since the zircons are considered severely radiation-damaged under these circumstances. Added complexities, such as the possibility that Pb transport rates may change with differing degrees of radiation damage, and the two-stage annealing kinetics of zircon (e.g., Weber et al. 1994, Meldrum et al. 1998) were not considered in this simple model. In severely radiation-damaged zircon, in contrast to crystalline zircon, significant amounts of diffusional Pb loss are possible, even at relatively low temperatures given the enhanced transport rates in the damaged material. Complete resetting of Pb isotopes through volume diffusion could also occur if zircon possessing significant amounts of radiation damage (in residing at low temperatures) were rapidly heated, since the zircon structure is slow to recover

crystallinity after experiencing radiation damage beyond certain levels (e.g., Weber et al. 1994, Murakami et al. 1991, Weber 1990), and Pb diffusion would remain relatively rapid.

It has long been argued (e.g., Silver and Deutsch 1963) that there exists a correlation between U content and discordance, although there are cases (e.g., Schärer and Allègre 1982) where this relationship does not seem to apply. Recent work (Sanborn et al. 1998, Stern et al. 1998), however, continues to point to the complexity of the phenomenon of "Pb loss" in natural zircon. While some correlation between U content and degree of discordance in mildly discordant (<10%) zircons studied has been found, suggesting a possible role of enhanced volume diffusion in radiation damaged zircon, there is often no such correlation in severely discordant zircon, indicating possible influence of other (non-diffusional) processes, such as recrystallization and various fluid-assisted processes, including physical deformation (e.g., Pidgeon et al. 1998, Sinha et al. 1992), that could significantly alter Pb isotope ratios and zircon U contents. The zircon composition itself can be an important factor influencing the probability of recrystallization. Pidgeon et al. (1998) argue that recrystallization (and consequent exclusion of trace elements from the zircon structure) is more likely in zircon (or regions of zircon) with high trace element concentrations, as the zircon crystal, experiencing strain due to the significant substitution of these other elements, can become metastable upon cooling from magmatic temperatures.

**Preservation of oxygen isotope signatures**

It is now possible to measure oxygen isotopic ratios in minerals *in situ* (e.g., Valley et al. 1994, 1998; Sharp 1992, Elsenheimer and Valley 1993, Reeder et al. 1997, Wiechert et al. 2002, Valley, this volume), and it is likely that techniques will continue to be refined and find broader application. The capability of measuring isotopic profiles within single mineral grains may, in conjunction with experimentally acquired data on oxygen diffusion and isotopic fractionation among minerals, permit the extraction of information on the thermal history of host rocks.

Time-temperature information can be obtained from measured diffusion profiles in a mineral by applying analytical or numerical solutions to the non-steady state diffusion equation, given relatively simple grain geometries and constrained initial conditions (e.g., Crank 1975). A small complication arises in applying these solutions in isotope geochemistry. 'Standard' diffusion equations describe changes in time and space of absolute concentrations of a diffusant, However, the quantities measured in natural samples are isotope ratios, but what are actually moving through the mineral structure are the atoms of $^{18}O$ and $^{16}O$ themselves, not the isotopic ratio. A simple case illustrates this point. Consider a one-dimensional, isothermal diffusive exchange between the near-surface region of a zircon and an infinite reservoir in which concentrations of both $^{18}O$ and $^{16}O$ are constant for the time interval concerned (e.g., a case with a contacting metamorphic fluid). The concentration of $^{18}O$ in the zircon as a function of time ($t$) and distance ($x$) is described by:

$$C_{18} = C_{18,i} + (C_{18,o} - C_{18,i})\ erfc(x/(4Dt)^{1/2}) \quad (3)$$

and similarly, the concentration of $^{16}O$ by:

$$C_{16} = C_{16,i} + (C_{16,o} - C_{16,i})\ erfc(x/(4Dt)^{1/2}) \quad (4)$$

where $C_{18}$ and $C_{16}$ are the concentrations of the isotopes at a distance $x$ from the zircon-reservoir interface, and the subscripts $i$ and $o$ refer to the initial and surface concentrations of the isotopes in the zircon. It is assumed that both isotopes share the same diffusivity ($D$). Because the total amount of oxygen in the zircon is fixed by stoichiometry, there is the additional constraint in this case:

$$C_{18} + C_{16} = C_{18,o} + C_{16,o} = C_{tot} \quad (5)$$

where $C_{tot}$ is a constant. [This last constraint would not apply to most isotope systems. For example, the total amount of Sr in a plagioclase feldspar need not be fixed at a constant value, as Sr could exchange for Ca, so $^{87}Sr$ and $^{86}Sr$ could vary.] Equations (3) and (4) make it clear that the quantity actually profiled in a mineral grain (i.e., $C_{18}/C_{16}$) would vary with depth in a sample not as a simple error function but as the ratio of two quantities described by two distinct error function relationships (e.g., Zhang et al. 1991). However, given the relative abundances of $^{18}O$ and $^{16}O$ found in nature (~0.2% and ~99.8%), the value of $^{18}O/^{16}O$ as a function of $t$ and $x$ does in fact closely conform to an error function because the numerator is effectively constant. Consequently, $^{18}O/^{16}O$ can be thought of as the diffusant, and measured gradients in the isotope ratio can be accurately modeled using standard solutions to the diffusion equation.

Some controversy exists concerning whether the Arrhenius relations for 'dry' or 'wet' oxygen diffusion should be applied to particular systems (e.g., Kohn 1999, Valley et al. 2002, Peck et al. 1999, 2001; Wilde and Valley 2001). Most applications of the zircon data will likely be to igneous and metamorphic events in the Earth's crust. Since the transition from 'dry' to 'wet' diffusion behavior appears to be essentially complete at $P_{H_2O} \approx 6.9$ MPa, the 'wet' Arrhenius relation is probably appropriate for most crustal processes. Oxygen diffusion in zircons participating in crustal igneous events is likely to be 'wet' merely because melting in the crust is generally predicated upon the presence of water. Oxygen diffusion in zircons from metamorphic systems containing a fluid phase and/or hydrous minerals is also probably well described by the 'wet' diffusivites. Kohn (1999) notes that most metamorphic rocks have mineral assemblages that can buffer $f_{H_2O}$ during cooling, and that although a rock may be 'dry' in the sense of lacking a fluid phase it may still be 'wet' in the thermodynamic sense that $f_{H_2O}$ is much greater than 1 bar. The only natural zircons, then, to which the 'dry' diffusion results appear applicable would be those from granulite facies rocks, from dry regions of the mantle, or from extraterrestrial samples. This conclusion seems inevitable provided that $H_2O$ fugacity (with fluid absent) has the same effect on oxygen diffusion as does $H_2O$ pressure (with fluid present). This proviso seems thermodynamically reasonable, but has not been confirmed by experiment.

### $^{18}O/^{16}O$ retention in zircon cores and rims

*In situ* determination of oxygen isotope ratios in natural materials can now be carried out on ~20-μm spots with an accuracy of ~0.5 $\delta^{18}O$ units (e.g., Valley et al. 1997), making it possible to investigate the internal oxygen isotope structure of minerals with the aim of deciphering complex crystallization and/or thermal histories. It is therefore useful to explore the systematics of retention of oxygen isotopic ratios in local regions of individual grains.

It is well known that zircon crystals often contain a record of multiple crystallization events that may be revealed by CL or BSE imaging (e.g., Hanchar and Miller 1993, Hanchar and Rudnick 1995, Vavra et al. 1996, Corfu et al., this volume). In the simplest case, complex histories are manifested by an 'old' core mantled by a 'young' rim. Given the typically small size of crustal zircons (~50-200 μm) it may not be possible to characterize intra-grain $^{18}O/^{16}O$ gradients in detail, but measurements of isotope ratios in the central regions of grain cores and rims—where the original isotopic signatures of these features are most likely to be preserved—is an attainable goal. The question when approaching analyses of these features concerns what time-temperature conditions will preserve the original $^{18}O/^{16}O$ signature in the central region of the feature of interest. The average (bulk) $\delta^{18}O$ value of a core or rim may be modified considerably by diffusion, but as long as the center of a specific feature is unaffected by diffusive exchange, key information related to the environment of crystallization may be retained.

For cases of isothermal annealing, calculation of time-temperature conditions for "center preservation" is straightforward because the diffusivity is independent of time, allowing the use of standard solutions to the non-steady state diffusion equation. For diffusion in a sphere, which could represent either a spherical zircon grain or a core within a larger zircon, the center will retain the

original $^{18}O/^{16}O$ for values of $Dt/a^2$ of up to 0.03, assuming that the oxygen isotope ratio remains constant at the sphere surface over the annealing interval (Crank 1975, p. 92). For a rim or mantle, the maximum time for center preservation differs from that of a sphere of the same radius because diffusion occurs radially both inward and outward. Given constant $^{18}O/^{16}O$ ratios at both the internal and external bounding surfaces, the analytical solution for a "hollow sphere" can be employed (Crank 1975, p. 98). The constant- surface condition is not strictly met at the inner boundary (due to radial diffusion effects), but it nearly holds for the range of core/rim dimensions of interest, so the solution of Crank (1975) can be used with more than adequate accuracy. [This was confirmed by detailed numerical of core-rim interdiffusion modeling in which the concentration at the internal bounding surface was allowed to vary (Watson and Cherniak 1997).] The maximum time for preservation of the original $^{18}O/^{16}O$ at the center of an overgrowth zircon rim is given by $Dt/x^2 \approx 0.012$, where $x$ is the thickness of the rim.

Figure 16 illustrates the conditions of annealing time and temperature corresponding to the center-retention criteria stated above for $^{18}O/^{16}O$ in zircon cores ($Dt/a^2 = 0.03$) and rims ($Dt/x^2 = 0.012$). Calculations in Figure 16a are shown for 'wet' systems only, because they are thought to be most applicable to the Earth's crust. At an extreme lower crustal temperature of 900°C, center isotope retention is brief; only 160 or 5700 years, respectively, for cores of 20 and 120 μm. For overgrowth rims, time frames are even shorter: 16 to 570 years for rim thicknesses of 10 and 60 μm. In contrast, at a mid-crustal metamorphic temperature of 500°C, center retention times become geologically significant: $10^7$ to $4\times10^8$ years for 20- to 120-μm cores, and $10^6$ to $4\times10^7$ years for 10- to 60-μm rims. The conditions shown in Figure 16 should serve as a useful guide for evaluation of $^{18}O/^{16}O$ spot analyses made in the central regions of zircon cores and rims revealed by CL or BSE

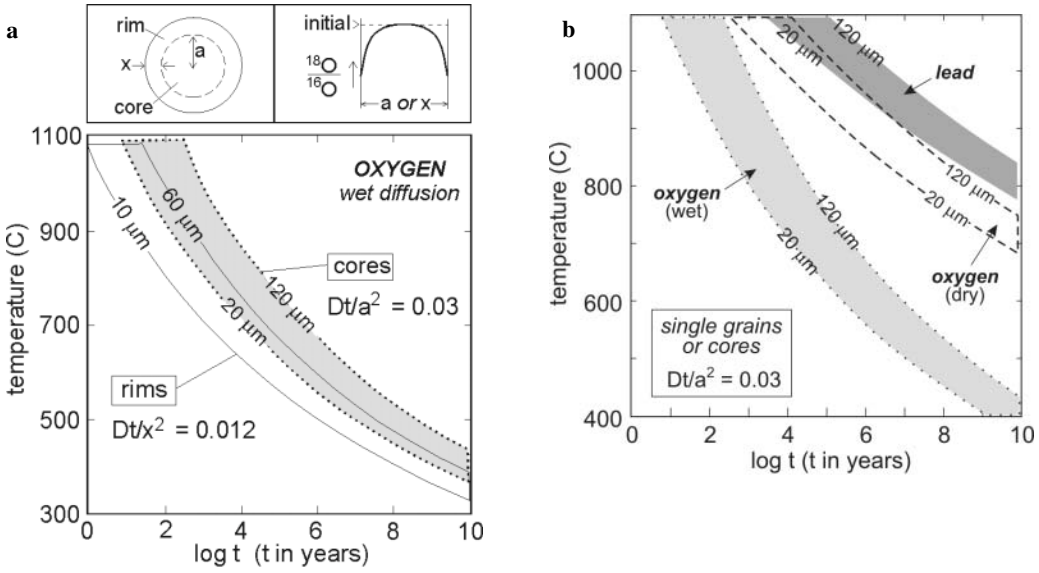


**Figure 16.** (a) Oxygen isotope center-retention criteria for isothermal annealing of zircon cores and rims under wet conditions, using the diffusion data from Watson and Cherniak (1997). The curves define the maximum annealing duration that a spherical core of rim can experience at a particular temperature and still retain the original $\delta^{18}O$ at its center (see diagram at upper right). These maximum times are defined by critical values for $Dt/a^2$ or $Dt/x^2$ (where $a$ is core radius and $x$ is rim thickness) of 0.03 and 0.012, respectively. (b) Curves comparing center-retention criteria for oxygen under wet and dry conditions (Watson and Cherniak 1997), and Pb (Cherniak and Watson 2001). In this figure, only curves for retention in cores (or single grains) of 20 and 120 μm are plotted. Zircon is significantly more retentive of Pb than oxygen isotopes, even for oxygen diffusion under dry conditions.

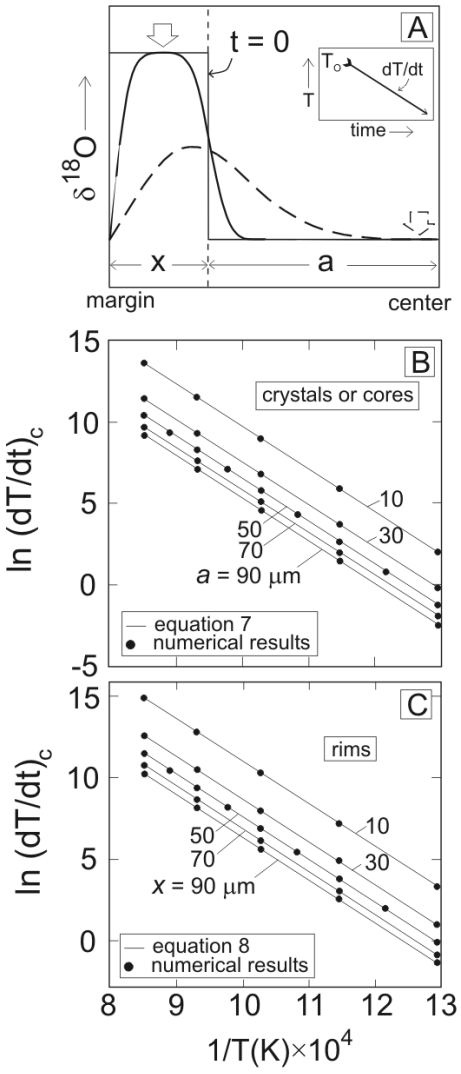


**Figure 17.** Oxygen diffusion center-retention criteria for spherical zircon cores and rims cooling under wet conditions (Watson and Cherniak 1997). The schematic diagram in (a) shows a radial profile of $\delta^{18}O$ (initially a step distribution) which relaxes toward homogeneity with increasing time at high temperature. There is a critical cooling rate - $(dT/dt)_C$, assumed here to be linear—below which the original $\delta^{18}O$ value at the center of a core or rim will fail to be preserved. If cooling is too slow, $\delta^{18}O$ will detach from the original core or rim value. The thicker lines show the $\delta^{18}O$ profile just prior to detachment at the center of the rim (solid line) and of the core (dashed line). The diagram implies a $\delta^{18}O$ for the surrounding medium equivalent to that of the core but the model results shown in (b) and (c) are independent of the relative $\delta^{18}O$ values of the core, rim and host medium. (b) and (c) Results of numerical simulation of wet oxygen diffusion to determine the critical minimum cooling rate, $(dT/dt)_C$, for retention of the original $\delta^{18}O$ value at the center of a spherical zircon crystal or core (b), or rim (c). The dots represent the actual numerical results; the lines are fits to the numberical data given by Eqs. (7) and (8). See text for additional discussion.

imaging. However, it should be stressed that diffusivities of the middle REE (the predominant activators of CL in zircon) and especially the tetravalent cations Hf and U (elements often responsible for zoning visible in BSE imaging) are considerably slower than diffusion rates for oxygen, so the zoning in these elements may be preserved well after distinct oxygen isotope signatures are lost through diffusional exchange. Also important to consider when interpreting oxygen isotope signatures from zircons for which U/Pb isotope ages are also obtained is the relative retentivity of Pb vs. oxygen isotopes in zircon. Curves for Pb, using the same center-retention criteria above, are plotted in Figure 16b along with those for oxygen. It is clear that zircons will be much less retentive of oxygen isotope signatures than Pb, so great care must be taken when attempting to correlate oxygen isotope ratios with U/Pb ages.

At present, the principal limitation to the usefulness of such analyses may well be the lack of information on oxygen isotope fractionation between zircon and other phases. The main shortcoming of the results shown in Figure 16 is that (for lack of a better choice) we assumed an initial 'step' distribution in $^{18}O/^{16}O$; that is, an abrupt discontinuity at the core/rim boundary. In many instances, zircon growth is likely to be slow in relation to oxygen diffusion, so an isotopic discontinuity, if preserved at all, may be 'blurred' substantially by diffusion during growth of the rim. This disclaimer may be especially important for igneous overgrowth situations, where the temperatures are high (thus promoting oxygen isotopic equilibration), and growth is slow because it is limited by Zr diffusion in the melt.

**Retention at rim and core centers during cooling**

Having treated bulk $^{18}O/^{16}O$ in a cooling regime, as well as local retention during isothermal annealing, we turn now to the question of retention in central regions of zircon cores and rims during cooling. The problem was addressed from a somewhat different angle by Dodson (1986), who provided the mathematical basis for calculating closure profiles (i.e., closure temperature vs. radial position) within mineral grains. Oxygen isotopes do not provide information on mineral age, so we posed the closure question in a different way: How fast must a zircon cool in order to preserve at its center the $^{18}O/^{16}O$ ratio acquired at the time of its growth? This question seems important if $\delta^{18}O$ values are to be used to deduce zircon provenance.

For the sake of completeness, we consider as before a hypothetical "mantled" zircon. At some initial temperature ($T_o$), the core and rim and isotopically distinct, with $^{18}O/^{16}O$ changing abruptly at the interface (Fig. 17). If cooling from $T_o$ is slow, the oxygen isotopes will interdiffuse, possibly obliterating the original core and rim signatures. On the other hand, if cooling is fast, memory of the original ratios may be retained in the central region of the core and/or rim. As previously noted, the assumption of an initially abrupt discontinuity in $^{18}O/^{16}O$ at the core/rim interface (Fig. 17) is unrealistic for many circumstances, especially if $T_o$ is of lower crust magnitude. There may be few cases where $^{18}O/^{16}O$ retention in rim features is relevant to cooling scenarios such as those considered. The core retention results, however, do have general relevance because the conclusions apply to any crystal or region of a crystal having a broadly spherical shape.

The initial step distribution shown in Figure 17 was used as a starting point to model $^{18}O/^{16}O$ interdiffusion during cooling from initial temperatures ranging between 400°C and 900°C. Both intracrystalline exchange (i.e., core-rim interdiffusion) and exchange with the zircon host medium are assumed to occur. A standard explicit finite-difference approach was adapted to a spherical geometry as described by Crank (1975, Chapter 8), using mass-centered volume elements. Additional details of the procedure are outlined in Watson and Cherniak (1997).

The most salient aspect of the numerical simulation is that the minimum (critical) cooling rate $(dT/dt)_c$ needed to preserve $^{18}O/^{16}O$ at the center of a spherical crystal or core is perfectly log-linear in $T_o^{-1}$ (where $T_o$ is the initial temperature in Kelvin):

$$\ln (dT/dt)_c = -27076/T_o + \text{const} \quad (6)$$

The same form of relationship applies to preservation of the initial ratio at the centers of overgrowth rims, and in both cases the constant is a simple function of the core radius ($a$) or rim thickness ($x$). Accordingly, the numerical results lead to simple equations that accurately describe the minimum cooling rates need to just preserve $^{18}O/^{16}O$ values inherited at high temperature:

$$\ln (dT/dt)_c = -27076/T_o - 2.041 \ln a + 41.9 \quad \text{(for crystals or cores)} \quad (7)$$

$$\ln (dT/dt)_c = -27076/T_o - 2.12 \ln x + 43.2 \quad \text{(for rims)} \quad (8)$$

where $a$ and $x$ are in microns, and $dT/dt$ is expressed as °C/Ma. The relationships defined by Equations (7) and (8) are illustrated in Figure 17, which shows the near-perfect agreement between the actual numerical simulations (dots) and these generalized equations. An example calculation: Assume that a zircon in the lower crust (at, say, 650°C) has just grown a new 30-µm rim on a preexisting 70-µm core, and that the rim and core are characterized by distinct oxygen isotopic ratios. Equations (7) and (8) reveal that the zircon would have to cool at a rate of at least 49°C/Ma to preserve the $\delta^{18}O$ value at the center of the core, and at least 776°C/Ma to preserve $\delta^{18}O$ at the center of the rim.

At first glance, the above calculation would appear to call into question the conclusions (e.g., Valley et al. 1994, Peck et al. 1999) concerning the high $\delta^{18}O$ retentivity of Adirondack zircons. It is

important to bear in mind, however, that the diffusivity of oxygen must drop dramatically at $f_{H2O}$ somewhat below 7 MPa. Because $f_{H_2O}$ during retrograde metamorphism of high-grade rocks is poorly constrained (and may even vary locally within a given rock unit) it is not unreasonable to expect variability in isotopic closure of individual zircon crystals—caused, perhaps, by 'dry' diffusion behavior in some grains. However, as earlier noted, a rock may be 'dry' in the sense of lacking a fluid phase but may still be 'wet' in the thermodynamic sense that $f_{H_2O}$ is much greater than 1 bar, and it remains unclear exactly at what values of $f_{H_2O}$ the transition between 'wet' and 'dry' diffusion regimes occurs.

## FUTURE DIRECTIONS

A large body of diffusion data exists for zircon, as this chapter has shown, but there are many directions for future research. One area of interest is diffusion of the noble gases, most notably He given its potential in low temperature thermochronometry (e.g., Reiners et al. 2002).

Also of interest are diffusion rates of other highly charged cations, including Nb and Ta, whose abundance and relative proportions have potential use in distinguishing zircons from various sources (e.g., Belousova et al. 2002), and which may also play a role in coupled substitutions involving other geochemically significant cation species (e.g., $(Nb, Ta)^{+5} + REE^{+3} \rightarrow 2\ Zr^{+4}$).

As mentioned in the previous section, there remains the issue of exploring fluid-absent but still thermodynamically 'wet' systems (i.e., with $f_{H_2O} > 1$ bar but less than 7 MPa) such as those with hydrous mineral phases present but no free water. This will permit a better understanding of the transition between 'wet' and 'dry' diffusion behaviors for oxygen diffusion in zircon, which may be of considerable importance in interpreting oxygen isotope measurements in natural systems.

The effects of radiation damage on diffusion are still to be systematically investigated. For Pb diffusion, there exist measurements of the "end member" cases: severely radiation-damaged zircon (Cherniak et al. 1991) and fully crystalline zircon (Cherniak and Watson 2001). It is not clear how intermediate amounts of radiation damage in the zircon structure would affect diffusivities. However, the fact that there are two simultaneously occurring kinetic processes (i.e., atomic diffusion and repair of the damaged zircon lattice) with potentially quite different activation energies and rates, complicates characterization of diffusivities (not to mention degree of radiation damage) under these circumstances.

## ACKNOWLEDGMENTS

We thank Jim Van Orman and Rick Ryerson for their thorough reviews of the manuscript. Thanks also to John Hanchar for his editorial efforts, and to him and Paul Hoskin for their work on this volume and in organizing the short course from which it resulted. This work was supported by grants EAR-9527014 and EAR-0073752 from the National Science Foundation (to E.B. Watson).

## REFERENCES

Belousova EA, Griffin WL, O'Reilly SY, Fisher NI (2002) Igneous zircon: trace element composition as an indicator of source rock type. Contrib Mineral Petrol 143:602-622

Black LP, Williams IS, Compston W (1986) Four zircon ages from one rock: the history of a 3939 Ma-old granulite from Mt. Sones, Enderby Land, Antarctica. Contrib Mineral Petrol 94:427-437

Bogolomov YS (1991) Migration of lead in non-metamict zircon. Earth Planet Sci Lett 107:625-633

Caruba R, Turco G, Iacconi P, Keller P (1974) Solution solide d'elements de transition trivalents dans le zircon et l'oxyde de zirconium, etude par thermoluminescence artificelle. Bull Soc Fr Minéral Cristallogr 97:278-283

Chapman HJ, Roddick JC (1994) Kinetics of Pb release during the zircon evaporation technique. Earth Planet Sci Lett 121:601-611

Cherniak DJ (2002a) Ba diffusion in feldspar. Geochim Cosmochim Acta 66:1641-1650

Cherniak DJ (2002b) REE diffusion in feldspar. Chem Geol 193:25-41

Cherniak DJ (2000) Rare earth element diffusion in apatite. Geochim Cosmochim Acta 64:3871-3885

Cherniak DJ (1998a) Rare earth element and gallium diffusion in yttrium aluminum garnet. Phys Chem Minerals 26:156-163

Cherniak DJ (1998b) REE Diffusion in calcite. Earth Planet Sci Lett 160:273-287

Cherniak DJ (1996) Strontium diffusion in sanidine and albite, and general comments on Sr diffusion in alkali feldspars. Geochim Cosmochim Acta 60:5037-5043
Cherniak DJ (1995) Diffusion of lead in plagioclase and K-feldspar: an investigation using Rutherford Backscattering and resonant nuclear reaction analysis. Contrib Mineral Petrol 120:358-371
Cherniak DJ (1993) Lead diffusion in titanite and preliminary results of the effects of radiation damage on Pb transport. Chem Geol 110:177-194
Cherniak DJ, Watson EB (2001) Pb Diffusion in zircon. Chem Geol 172:5-24
Cherniak DJ, Watson EB (1994) A study of strontium diffusion in plagioclase using Rutherford Backscattering Spectroscopy. Geochim Cosmochim Acta 58:5179-5190
Cherniak DJ, Watson EB (1992) A study of strontium diffusion in K-feldspar, Na-K feldspar and anorthite using Rutherford Backscattering Spectroscopy. Earth Planet Sci Lett 113:411-425
Cherniak DJ, Zhang XY, Wayne NK, Watson EB (2001) Sr, Y and REE diffusion in fluorite. Chem Geol 181:99-111
Cherniak DJ, Hanchar JM, Watson EB (1997a) Rare-Earth diffusion in zircon. Chem Geol 134:289-301
Cherniak DJ, Hanchar JM, Watson EB (1997b) Diffusion of tetravalent cations in zircon. Contrib Mineral Petrol 127:383-390
Cherniak DJ, Lanford WA, Ryerson FJ (1991) Lead diffusion in apatite and zircon using ion implantation and Rutherford Backscattering techniques. Geochim Cosmochim Acta 55:1663-1673
Cherniak DJ, Watson EB, Harrison TM, Grove M (2002) Pb diffusion in monazite. Geol Soc Am Ann Mtg, paper #138-5
Chiarenzelli JR, McLelland JM (1993) Granulite facies metamorphism, paleoisotherms and disturbance of the U-Pb systematics of zircon in anorogenic plutonic rocks from the Adirondack highlands. J Metamor Geol 11:59-70
Claoué-Long JC, Sobolev NN, Shatsky VS, Sobolev AV (1991) Zircon response to diamond-pressure metamorphism in the Kokchetav Massif, USSR. Geology 95:87-105
Crank J (1975) The Mathematics of Diffusion (2nd edn). Oxford Univ Press, Oxford, UK, 414 p
Crocombette JP (1999) Theoretical study of point defects in crystalline zircon. Phys Chem Minerals 27:138-143
Dennis PF (1984) Oxygen self-diffusion in quartz under hydrothermal conditions. J Geophys Res B 89:4047-4057
Derdau D, Freer R, Wright K (1998) Oxygen diffusion in anhydrous sanidine feldspar. Contrib Mineral Petrol 133:199-204
Dodson MH (1973) Closure temperature in cooling geochronological and petrological systems. Contrib Mineral Petrol 40:259-274
Dodson MH (1986) Closure profiles in cooling systems. Mater Sci Forum 7:145-154
Doremus RH (1996) Diffusion of oxygen in silica glass. J Electrochem Soc 143:1992-1995.
Dowty E (1980) Crystal-chemical factors affecting the mobility of ions in minerals. Am Mineral 65:174-182
Elsenheimer D, Valley JW (1993) Submillimeter scale zonation of $\delta^{18}O$ in quartz and feldspar, Isle of Skye, Scotland. Geochim Cosmochim Acta 57:3669-3676
Farver JR (1994) Oxygen self-diffusion in calcite: dependence on temperature and water fugacity. Earth Planet Sci Lett 121:575-587
Farver JR (1989) Oxygen self-diffusion in diopside with application to cooling rate determinations. Earth Planet Sci Lett 92:386-396
Farver JR, Yund RA (1991) Oxygen diffusion in quartz: dependence on temperature and water fugacity. Chem Geol 90:55-70
Farver JR, Yund RA (1990) The effect of hydrogen, oxygen, and water fugacity on oxygen diffusion in alkali feldspar. Geochim Cosmochim Acta 54:2953-2964
Foland KA (1974) Alkali diffusion in orthoclase. *In* Geochemical Transport and Kinetics. Hofmann AW, Giletti BJ, Yoder Jr HS, Yund RA, (eds) Carnegie Institution of Washington, Washington,DC, p 77-98
Fortier SM, Giletti BJ (1989) An empirical model for predicting diffusion coefficients in silicate minerals. Science 245:1481-1484
Freer R, Wright K, Kroll H, Göttlicher J (1997) Oxygen diffusion in sanidine feldspars and a critical appraisal of oxygen-isotope mass-effect measurements in non-cubic materials. Philos Mag A 75:485-503
Ganguly J, Tirone M, Hervig RL (1998) Diffusion kinetics of samarium and neodymium in garnet, and a method for determining cooling rates of rocks. Science 281 805-807
Gasparini P, Mantovani MSM, Ribiero FB (1984) Temperature dependence of radon diffusion from some rocks and minerals. Bollettino di Geofisica Teorica ed Applicata XXVI:135-141
Giletti BJ, Shanahan TM (1997) Alkali diffusion in plagioclase feldspar. Chem Geol 139:3-20
Giletti BJ, Casserly JED (1994) Strontium diffusion kinetics in plagioclase feldspars. Geochim Cosmochim Acta 58:3785-3793
Giletti BJ, Yund RA (1984) Oxygen diffusion in quartz. Chemical effects of water on the strength and deformation of crustal rocks. J Geophys Res B 89: 4039-4046
Giletti BJ, Semet MP, Yund RA (1978) Studies in diffusion: III, Oxygen and feldspars, an ion microprobe determination. Geochim Cosmochim Acta 42:45-57
Halden NM, Hawthorne FC, Campbell JL, Teesdale WJ, Maxwell JA, Higuchi D (1993) Chemical characterization

of oscillatory zoning and overgrowths in zircon using 3 MeV μm-PIXE. Can Mineral 31:637-647
Hanchar J M, Rudnick RL (1995) Revealing hidden structures: the application of cathodoluminescence and backscattered electron imaging to dating zircons from lower crustal xenoliths. Lithos 36:289-303
Hanchar JM, Miller CF (1993) Zircon zonation patterns as revealed by cathodoluminescence and backscattered electron images: Implications for interpretation of complex crustal histories. Chem Geol 110:1-14
Hanchar JM, Finch RJ, Hoskin PWO, Watson EB, Cherniak DJ, Mariano AN (2001) Rare earth elements in synthetic zircon: Part 1. Synthesis, and rare earth element and phosphorus doping. Am Mineral 86:667-680
He Y, Cormack AN (1999) Atomistic simulation study of defect structure of zircon as a high-level nuclear waste host form. J China Univ Geosci 10:309-313
Headley TJ, Arnold GW, Northrup CJM (1982) Dose-dependence of Pb-ion implantation damage in zirconolite, hollandite and zircon. *In* Scientific Basis for Radioactive Waste Management V. Lutze W (ed) Elsevier, p 379-388
Hinton RW, Upton BGJ (1991) The chemistry of zircon: Variations within and between large crystals from syenite and alkali basalt xenoliths. Geochim Cosmochim Acta 55: 3287-3302
Hölzl S, Hofmann AW, Todt W, Kohler H (1994) U-Pb geochronology of the Sri Lankan basement. Precambrian Res 66:23-149
Kohn MJ (1999) Why most "dry" rocks should cool "wet." Am Mineral 84:570-580
Lee JKW (1993) Problems and progress in the elucidation of U and Pb transport mechanisms in zircon. *In* Defects and Processes in the Solid State: Geocscience Applications: The McLaren Volume. Boland JN, FitzGerald JD (eds) Elsevier, p 423-446.
Lee JKW, Williams IS, Ellis DJ (1997) Pb, U and Th diffusion in natural zircon. Nature 390:159-162
Lumpkin GL, Ewing RC (1988) Alpha-decay damage in minerals of the pyrochlore group. Phys Chem Minerals 16:2-20
Magomedov SA (1970) Migration of radiogenic products in zircon (in Russian). Geokhimiya 2:263-267
Marfunin AS (1979) Spectroscopy, Luminscence, and Radiation Centers in Minerals. Springer-Verlag, Berlin, 352 p
Mariano AN (1989) Cathodoluminescence emission spectra of rare earth element activators in minerals. Rev Mineral 21:339-348
McIntyre LC Jr, Leavitt JA,Dezfouly-Arjomandy B, Oder J (1988) Depth profiling of phosphorus using resonances in the $^{31}P(\alpha,p)^{34}S$ reaction. Nucl Instr Meth B35:446-450
McLelland JM, Chiarenzelli J, Whitney P, Isachsen Y (1988) U-Pb zircon geochronology of the Adirondack Mountains and implications for their tectonic evolution. Geology 16:920-924
Medenbach O (1976) Geochemic der elemente in Zirkon und ihre Rung-Eine Untersuchung mit der elektronenstrahlmikrosonde. PhD dissertation, Ruprecht Karl Universität, 58 p
Meis C, Gale JD (1998) Computational study of tetravalent uranium and plutonium lattice diffusion in zircon. Mater Sci Engin B57:52-61
Meldrum A, Boatner LA, Weber WJ, Ewing RC (1998) Radiation damage in zircon and monazite. Geochim Cosmochim Acta 62:2509-2520
Mezger K, Krogstad EJ (1997) Interpretation of discordant U-Pb zircon ages: An evaluation. J Metamor Geol 15:127-140
Mezger K, Rawnsley C, Bohlen S, Hanson G (1991) U-Pb garnet, sphene, monazite and rutile ages: implications for the duration of high-grade metamorphism and cooling histories, Adirondack Mountains, New York. J Geol 99:415-428
Muehlenbachs K, Kushiro I (1975) Measurements of oxygen diffusion in silicates EOS Trans, Am Geophys Union 56:459
Mullen JG (1966) Theory of diffusion in ionic crystals. Phys Rev 143:658-662
Murakami T, Chakoumakos BC, Ewing RC, Lumpkin GR, Weber WJ (1991) Alpha-decay event damage in zircon. Am Mineral 76:1510-1532
Otto EM (1966) Equilibrium pressures of oxygen over oxides of lead at various temperatures. J Electrochem Soc 113:525-527
Peck WH, Valley JW, Wilde SA, Graham CM (2001) Oxygen isotope ratios and rare earth elements in 3.3 to 4.4 Ga zircons: ion microprobe evidence for high $\delta^{18}O$ continental crust and oceans in the early Archean. Geochim Cosmochim Acta 65:4215-4229
Peck WH, Valley JW, McClelland J (1999) Slow oxygen diffusion in zircon during cooling of Adirondack orthogneiss. Geol Soc Am 1999 Ann Mtg Abstr Progr 31:103
Petit JC, Dran JC, Della Mea G (1987) Effects of ion implantation on the dissolution of minerals. Part II: Selective dissolution. Bull Fr Minéral Cristallogr 110:25-42
Pidgeon RT, Nemchin AA, Hitchen GJ (1998) Internal structures of zircons from Archean granites from the Darling Range batholith: implications for zircon stability and the interpretation of zircon U-Pb ages. Contrib Mineral Petrol 132:288-299
Reeder RJ, Valley JW, Graham CM, Eiler JE (1997) Ion microprobe study of oxygen isotopic compositions of structurally nonequivalent growth surfaces on synthetic calcite. Geochim Cosmochim Acta 61:5057-5063

Reiners PW, Farley KA, Hickes HJ (2002) He diffusion and (U-Th)/He thermochronometry of zircon: initial results from Fish Canyon Tuff and Gold Butte. Tectonophysics 349:297-308
Robinson GW (1979) The occurrence of rare earth elements in zircon. PhD dissertation, Queen's University, London, Ontario, 155 p
Ryerson FJ, McKeegan KD (1994) Determination of oxygen self-diffusion in akermanite, anorthite, diopside, and spinel: implications for oxygen isotopic anomalies and the thermal histories of Ca-Al-rich inclusions. Geochim Cosmochim Acta 58:3713-3734
Sanborn N, Stern RA, Carr SD (1998) Discordance and Pb-loss mechanisms in 3.35 Ga zircon from the Acasta Gneiss complex, N.W.T., Canada: A SHRIMP ion microprobe study. Geol Soc Am Abstr Progr 30:A-240
Schärer U, Allègre CJ (1982) Uranium-lead system in fragments of a sinlge zircon grain. Nature 295:585-587
Scharer U, Corfu F, Demaiff D (1992) Heterogeneity of the subcontinental mantle: U-Pb and Lu-Hf isotopes in megacrysts of baddeleyite and zircon for the Mbuji-Mayi kimberlite. EOS Trans, Am Geophys Union Spring Mtg Suppl, p 339
Shannon RD (1976) Revised effective ionic radii and systematic studies of interatomic distances in halides and chalcogenides. Acta Crystallogr A32:751-767
Sharp ZD(1992) *In situ* laser microprobe techniques for stable isotope analysis Chem Geol 101:3-19
Shestakov GI (1969) On diffusional loss of lead from a radioactive mineral. Geochem Intl 6:888-896
Shestakov GI (1972) Diffusion of lead in monazite, zircon, sphene, and apatite. Geochem Intl 9:801-807
Shewmon P (1989) Diffusion in Solids. Minerals, Materials, and Metals Society, Warrendale, Pennsylvania
Silver LT, Deutsch S (1963) Uranium-lead isotopic variations in zircons—A case study. J Geol 71:721-758
Sinha AK, Wayne DM, Hewitt DA (1992) The hydrothermal stability of zircon: preliminary experimental and isotopic studies. Geochim Cosmochim Acta 56: 3551-3560
Smith HA, Giletti BJ (1997) Lead diffusion in monazite. Geochim Cosmochim Acta 61:1047-1055
Soltani-Farshi M, Meyer JD, Misaelides P, Bethge K (1996) Cross section of the $^{32}S(\alpha,p)^{35}Cl$ nuclear reaction for sulphur determination. Nucl Instr Meth B113: 399-402
Sommerauer J (1976) Die chemisch-physikalische Stabilität natürlicher Zirkone und ihr U-(Th)-Pb System. Doctoral dissertation, Eidgenoessischen Tech Hochschule, Zürich, Switzerland, 151 p
Speer JA (1982) Zircon. *In* Orthosilicates (2nd edn). Ribbe PH (ed) Mineral Soc Am, Rev Mineral 5:67-112
Stern RA, Sanborn N, Bleeker W (1998) Exploiting the high spatial sensitivity of the ion micoprobe in studying Pb-loss mechanisms and U-Pb ages of metamict and altered zircon. EOS Trans, Am Geophys Union, Fall Mtg Suppl, p F951
Suzuki K, Kouta H, Nagasawa H (1992) Hf-Zr interdiffusion in single crystal zircon. Geochem J 26:99-104
Valley JW, Peck WH, King EM, Wilde SA (2002) A cool early Earth. Geology 30:351-354
Valley JW, Chiarenzelli JR, McClelland JM (1994) Oxygen isotope geochemistry of zircon. Earth Planet Sci Lett 126:187-206
Valley JW, Graham CM, Harte B, Eiler JM, Kinny PD (1998) Ion microprobe analysis of oxygen, carbon, and hydrogen isotope ratios. *In* Applications of microanalytical techniques to understanding mineralizing processes. Rev Econ Geol 7:73-98
Van Orman JA, Grove TL, Shimizu N (2001) Rare earth element diffusion in diopside: Influence of temperature, pressure and ionic radius, and an elastic model for diffusion in silicates. Contrib Mineral Petrol 141:687-703
Van Orman JA, Grove TL, Shimizu N, Layne GD (2002) Rare-earth element diffusion in a natural pyrope single crystal at 2.8 GPa. Contrib Mineral Petrol 142:416-424
Vavra G, Gebauer D, Schmid R, Compston W (1996) Multiple zircon growth and recrystallization during polyphase Late Carboniferous to Triassic metamorphism in granulites of the Ivrea Zone (Southern Alps): an ion microprobe (SHRIMP) study. Contrib Mineral Petrol 122:337-358
Wang LM, Ewing RC (1992) Detailed in-situ study of ion-beam induced amorphization of zircon. Nucl Instr Meth B65:324-329
Watson EB (1980) Some experimentally determined zircon/liquid partition coefficients for the rare earth elements. Geochim Cosmochim Acta 44:895-896
Watson EB, Cherniak DJ (1997) Oxygen diffusion in zircon. Earth Planet Sci Lett 148:527-544
Watson EB, Liang Y(1995) A simple model for sector zoning in slowly grown crystals: Implications for growth rate and lattice diffusion, with emphasis on accessory minerals in crustal rocks. Am Mineral 80:1179-1187
Watson EB, Lupulescu A (1993) Aqueous fluid connectivity and chemical transport in clinopyroxene-rich rocks. Earth Planet Sci Lett 117:279-294
Watson EB, Cherniak DJ, Hanchar JM, Harrison TM, Wark DA (1997) The incorporation of Pb into zircon. Chem Geol 141:19-31
Wayne DM, Sinha AK, Hewitt DA (1992) Differential response of zircon U-Pb isotope systematics to metamorphism across a lithologic boundary: an example from the Hope Valley Shear Zone, southeastern Massachusetts, USA. Contrib Mineral Petrol 109:408-420
Weber WJ, Ewing RC, Wang LM (1994) The radiation-induced crystalline-to-amorphous transition in zircon. J

Mater Res 9:688-698
Weber WJ (1990) Radiation-induced defects and amorphization in zircon. J Mater Res 5:2687-2697
Wiechert U, Fiebig J, Przybilla R, Xiao Y, Hoefs J (2002) Excimer laser isotope-ratio-monitoring mass spectrometry for *in situ* oxygen isotope analysis Chem Geol 182:179-194
Wilde SA, Valley JW (2001) Evidence from detrital zircons for the existence of continental crust and oceans on the Earth 4.4 Gyr ago. Nature 409:175-178
Williams IS (1992) Some observations on the use of zircon U-Pb geochronology on the study of granitic rocks. Trans Royal Soc Edinburgh: Earth Sci 83:447-458
Williford RE, Weber WJ, Devanthan R, Cormak AN (1999) Native vacancy migrations in zircon. J Nucl Mater 273:164-170
Zener C (1952) Theory of diffusion. *In* Imperfections in Nearly Perfect Crystals. Shockley W, Hollomon JH, Maure R, Seitz F (eds) Wiley, New York, p 289-314
Zhang Y, Stolper EM, Wasserburg GJ (1991) Diffusion of a multi-species component and its role in oxygen and water transport in silicates. Earth Planet Sci Lett 103:228-240

# 6 Historical Development of Zircon Geochronology

**Donald W. Davis[1], Ian S. Williams[2] and Thomas E. Krogh[1]**

*[1]Earth Sciences Department, Royal Ontario Museum*
*100 Queen's Park, Toronto, Ontario, Canada M5S 2C6*

dond@rom.on.ca tomk@rom.on.ca

*[2]Research School of Earth Sciences*
*The Australian National University*
*Canberra, ACT, Australia*

ian.williams@anu.edu.au

*Profit comes from what is there; usefulness, from what is not there. - Lao Tzu*

## INTRODUCTION

An exact knowledge of rock formation ages is perhaps the single most important tool needed for assembling the geologic record into a coherent history. Moreover, the age of Earth and the time scale of pre-human events are central to a civilization's sense of origin and purpose. Therefore, the quest for precise and reliable geochronometers has had a scientific and a cultural importance that few other enterprises can match.

Since the beginning of the last century it has been recognized that long-lived radioactive decay systems provide the only valid means of quantifying geologic time. The uranium-lead decay system has always played a central role for several reasons. Minerals that contain very high U concentrations, although rare, are well known and easily obtained. The half lives of the natural U isotopes $^{238}U$ and $^{235}U$ are long enough to span all of Earth's history but short enough that both parent and radiogenic daughter elements could be measured in such minerals even with the methods of a century ago. After the discovery that the U decay system is paired

$$^{238}U \rightarrow {}^{206}Pb + 8\ \alpha + 6\ \beta^- \ (T_{1/2} = 4468\ Myr)$$

$$^{235}U \rightarrow {}^{207}Pb + 7\ \alpha + 4\ \beta^- \ (T_{1/2} = 704\ Myr)$$

it was realized that two age determinations could be made on the same sample using the same two elements. If the system has been closed to mobility of parent or daughter these two ages should agree, thus furnishing an internal test on the accuracy of the age. Further, the chemical coupling of the decays allows the age of the radiogenic daughter to be determined solely from its isotopic composition without knowing the parent-daughter ratio, a more difficult and less reliable parameter to measure. The wide utilization of the U-Pb geochronometer would not have been possible without the mineral zircon ($ZrSiO_4$). Zircon normally contains U in concentrations well above its host rock average but discriminates strongly against the daughter element Pb during crystallization. Also, in many cases it is sufficiently robust to preserve its original U and accumulated radiogenic Pb contents even through remelting events. Although several other minerals have similar properties, zircon is the most widespread, being a common trace component of felsic rocks. Progress in U-Pb geochronology over the last 50 years has essentially involved the development of techniques for accurate determination of the U and Pb isotopic compositions of smaller and smaller quantities of zircon, culminating in our current ability to select and analyze those parts of single zircon grains that are concordant and record single or successive growth events. This chapter recounts the history of this development and reviews its impact on our understanding of Earth's past.

1529-6466/03/0053-0006$05.00

## PRELUDE

Geology began as a scientific discipline near the end of the 1700s, yet for the century following there was no reliable way to measure absolute geologic time. A detailed relative time scale was constructed based on the fossil record, but only for the Phanerozoic eon. Many geologists were content with the notion of an indefinitely long time span for Earth history, in accord with the uniformitarian concept put forth by Lyell in 1830. The need for more quantitative age estimates became acute, however, after the publication of Darwin's Origin of Species in 1859. Darwin proposed that evolution by natural selection required at least hundreds of millions of years and argued that the geological record of erosion furnished evidence of such time spans.

William Thompson (Lord Kelvin) was the first to try to set quantitative limits on geologic time. He used various physical approaches including estimating tidal deceleration of the Earth's rotation, the energy consumption required to keep the Sun burning and the cooling rate of the Earth. In 1862 he announced that the Earth could be no older than about 500 Myr. He subsequently reduced this estimate to 20-40 Myr based on new information on the melting temperatures and heat transport properties of rocks (Thompson 1899). No one knew of any process that could generate heat within the Earth, so for 40 years Kelvin's arguments posed a significant problem for Darwin's theory, as well as for the lengthy time estimates of geologists. The debate pitted scientific authority against geological observation in a similar way to the later debate between physicists and geologists over continental drift. Ironically, three years before Kelvin published his final paper on the subject, his arguments had already been invalidated by Becquerel's discovery of radioactivity. Nuclear processes furnished an energy source to keep the Earth warm and the Sun burning over a time span much longer than previously thought possible (Rutherford 1905a). It was quickly recognized that long-lived radioactive decay systems also have the potential to date geologic events.

Uranium was the first radioactive element to be discovered and to be exploited for geochronology (a term coined by Williams in 1893). The discovery of radium by the Curies in 1898, along with the work of Rutherford and Soddy (1902) and others, led to the realization that U disintegration produces a chain of shorter lived radioactive daughter elements including a 'radium' and an 'actinium' series. Rutherford and Soddy (1903) published the law of radioactive decay and Ramsay and Soddy (1903) demonstrated that helium was accumulating in substances that decay by $\alpha$ emission. Rutherford (1905b) was probably the first to suggest that this accumulation could be used to determine the formation age of rock.

Before the discovery of radioactivity, Hillebrand (1890) had analyzed uraninites at the U.S. Geological Survey and pointed out that they contain an excess of a non-reactive gas that he called nitrogen but which was actually He. His analyses also showed that uraninites consistently contain Pb. Following a suggestion by Rutherford, Boltwood (1907) used Hillebrand's analyses to support his contention that Pb is the stable end member of the U disintegration series. He showed that the Pb/U ratios in U-rich minerals are roughly constant in unaltered samples from the same area but higher in samples from areas that were thought to be older. When he failed to find excess Pb in analyses of thorite, however, he mistakenly concluded that the Th decay series produced no Pb. Boltwood calculated the decay constant of U using the estimated decay constant of Ra, its proportion relative to U in pitchblende and the assumption of secular equilibrium. His figure of $10^{-10}$/year compares reasonably well with the actual value of $1.5\times10^{-10}$/year. He was thus able to determine approximate ages for his samples, which ranged from 410 Ma to 2200 Ma. These were the first radiometric age determinations on minerals. They conclusively resolved the debate about the terrestrial time scale in favor of Darwin. Thus, even at its most primitive stage, U-Pb geochronology was able to provide evidence essential to the acceptance of natural selection, arguably the single most important scientific discovery.

Rutherford's suggestions inspired John Strutt (Lord Rayleigh) to measure He in uraniferous substances (including shark's teeth and bones) to assess their dating potential. He was the first to attempt dating zircon (Strutt 1909). After experimenting with various methods of decomposition,

he settled on fusing zircon with borax in a platinum crucible, the same method adopted 50 years later for early U-Pb isotopic studies. His oldest sample, based on the measured Th, U and He, was a Grenville-aged zircon from Renfrew County in southern Ontario, for which he calculated an age of about 600 Ma. The real age of the specimen was probably about 1100 Ma, but Strutt realized that, because of He loss, his ages were likely to be minimum estimates. He discussed the possibility of zircon in some rocks being inherited, but pointed out that such grains would have outgassed pre-existing He at magmatic temperatures. Strutt remarked that zircon showed excellent potential for dating because of its chemical inertness. The U-He method was tried for several more decades but He leakage made it unreliable.

Attempts were made to date zircon using pleochroic haloes (Joly 1907), spheres of radiation damage that are visible in thin section around radioactive mineral inclusions in biotite. Without knowing the U content of the inclusions, however, it was impossible to arrive at better than order of magnitude age estimates. Arthur Holmes, a graduate student of Strutt at Imperial College, argued that the most reliable way to determine ages would be to measure Pb accumulation in high-U minerals (Holmes 1911). In this, the first real geochronology paper, Holmes listed the necessary criteria for an effective geochronometer. He re-evaluated Boltwood's data and presented new analyses of various minerals including zircon, which he again recommended because of its stability. Using the limited data available, Holmes constructed a Paleozoic to Precambrian time scale. Remarkably, considering the large errors in decay constants and isotopic compositions, the ages mostly fell within the presently accepted period boundaries. A few years later, Barrell (1917) presented a review of geochronology that included the earliest U-Pb dates.

Because normal zircon contains U in trace concentrations and occurs only in trace amounts in rocks, attempts to date it chemically were not pursued further for forty years. Instead, efforts concentrated on more radioactive minerals such as uraninite, thorite and monazite. Holmes remained a tireless promoter of the U-Pb method of dating. Largely through his efforts, by the late 1920s the Phanerozoic time scale was broadly delineated with absolute ages for the era boundaries accurate to within 20% or better (Holmes and Lawson 1927).

For fifty years, U-Pb ages were determined by chemical analyses of total U and Pb contents. The fact that elements can have different isotopes (different numbers of neutrons in their nuclei) was postulated independently by Soddy and Fajans in 1913. J.J. Thompson separated the isotopes of neon in an electric field the same year. The first thermal ionization magnetic mass spectrometer was constructed by Dempster (1918) who used an electrometer detector to observe $^{23}$Na and $^{39}$K ion beams. Aston (1929) used a photo-plate detector to make the first measurement of an isotopic ratio from radiogenic Pb. The sample had been extracted from a Norwegian broggerite (thorian-uraninite) specimen, converted to liquid lead tetramethyl at the Carnegie Institution of Washington (CIW), and shipped to Aston at Cambridge University. The experiment was in fact delayed a year because the first sample tube broke in transit. After analyzing a second sample, Aston noted that the relative proportions of the exposure lines for masses 206, 207 and 208 respectively were about 100 : 10.7±3 : 4.5±2. As he had previously determined that the dominant isotope in Pb ores is $^{208}$Pb, he suggested that the $^{207}$Pb from broggerite must contain a radiogenic component. Therefore $^{207}$Pb must be the end product of decay of the 'actinium' series. In a companion paper, Rutherford (1929) deduced from Aston's data that the parent of this decay series must be $^{235}$U. Using the Pb isotopic composition and a guess of about 1 Ga for the age of the broggerite, he estimated a value for the $^{235}$U decay constant. Considering also the relative activities of the 'radium' ($^{238}$U) and 'actinium' ($^{235}$U) series he was able to calculate an isotopic abundance for $^{235}$U, obtaining a value that was in error by only about a factor of 2. From this he suggested an upper limit on the Earth's age of 3.4 Ga, based on the assumptions that U production ceased when Earth separated from the Sun and that $^{235}$U, with an odd number atomic weight, was unlikely to have been produced in greater abundance than the even numbered $^{238}$U. No closer estimate of the Earth's age would be forthcoming until the mid-1950s. Although luck was a large factor in the accuracy of Rutherford's result, deduc-

ing the age of the Earth from such a thin shred of evidence stands as a brilliant feat of scientific imagination.

Aston's broggerite data were interpreted by Fenner and Piggot (1929), who had prepared the original Pb sample, to indicate an age of 900 Ma. Aston continued to analyze radiogenic Pb and the implications of his data for determining geologic ages were discussed by Grosse (1932), who furnished new estimates of the U isotopic composition and the $^{235}U$ decay constant, although these were still substantially in error. The $^{235}U$ isotope was finally detected by Dempster (1935). However the photographic method used was not sensitive enough to measure its relative abundance. Rose and Stranathan (1936) measured Pb isotopic compositions in various uraninites by intensity readings of hyper-fine structure lines from Pb optical emission, although this novel method was of limited usefulness since it required about 4 g of Pb. These authors were perhaps the first to suggest that, because the $^{207}Pb/^{206}Pb$ ratio is relatively insensitive to parent-daughter mobility, it could be used as a more robust age indicator than Pb/U.

The modern era of geochronology began in 1938 with Nier's development of quantitative mass spectrometry. He used a 180° instrument as had Dempster and Aston but with an electrometer vacuum tube detector, which was much more suitable for quantitative measurements than the photographic plate or older electrometer designs (Nier 1981). Nier was the first to determine the precise isotopic abundance of $^{235}U$ as well as that of $^{234}U$ (Nier 1939a). His initial values of 139±1% for $^{238}U/^{235}U$ and 17,000±10% for $^{238}U/^{234}U$ are within error of present day estimates. He used these data to calculate the first accurate decay constants for $^{235}U$ and $^{234}U$. Nier also performed the first precise measurements of isotopic compositions of radiogenic Pb (Nier 1939b, 1941) and of common Pb (Nier 1938; Nier et al. 1941). The samples were converted into PbI vapor and ionized by electron bombardment. Analyses took "less than two days and less than six mg of lead are consumed in the process" (Nier 1939b, p. 155). Precisions on isotopic ratios were about 1% or better (Nier 1939a,b). A wide range of uraninites were investigated, as well as thorite and a cyrtolite (metamict zircon). Nier discussed the problem of correcting for common Pb and showed again how the most accurate ages could be calculated from the radiogenic $^{207}Pb/^{206}Pb$ ratio. He pointed out that his oldest $^{207}Pb/^{206}Pb$ age, 2200 Ma from a uraninite in Manitoba, was older than the then accepted age of the Earth. Nier's subsequent development of the 60° sector mass spectrometer, with lighter and cheaper magnets, made mass spectrometry accessible to many more laboratories and greatly aided the development of all forms of isotope work.

At the time of Nier's initial investigations, the oldest mineral considered to have been reliably dated gave 1750 Ma (Holmes 1937). Subsequently, by solving the growth curve equation for various Pb compositions, which Nier had measured on Pb ore deposits of different ages, Gerling (1942), Holmes (1946) and Houtermans (1946) independently calculated ages for the Earth in the range 3000-4000 Ma. As late as 1954, the oldest known mineral ages (from monazite) were only about 2600 Ma. The true breadth of the planetary time scale was finally established by Patterson (1956) from Pb isotopic analyses of meteorites. His measurement of 4550±70 Ma remains in agreement with current more precise estimates (Amelin et al. 2002).

## ISOTOPIC DATING OF ZIRCON – 1955 TO 1973

After the outstanding success of Nier's initial studies World War II intervened. Work on uranium became focused on nuclear energy and there was little further activity in U-Pb geochronology for the next 15 years. A review of the U-Pb method by Kulp et al. (1954) listed only 28 published isotopic dates, most of which were from Nier's original papers. Only seven of these were considered to be accurate to within 5 per cent. The authors concluded optimistically, however, that "it would be wrong to conclude that the ultimate has been achieved" (Kulp et al. 1954, p. 364). They predicted that Pb measurements should approach the "phenomenal accuracy" of 2 percent in the near future.

Interest in dating zircon by the chemical Pb method was awakened by Larsen et al. (1952)

working at the United States Geological Survey. Larsen recommended zircon as a geochronometer because of its high (although trace) U content, resistance to alteration and the large difference in ionic radii between $Zr^{+4}$ (0.84 Å) and $Pb^{+2}$ (1.32 Å) in 8-fold coordination with O, which meant that zircon would probably contain no primary Pb. Because mass spectrometer methods required at least several milligrams of Pb for an analysis, isotopic dating of typical zircon would need to use on the order of 100 g from about a ton of rock. Larsen therefore preferred measuring the total Pb by atomic emission and the U by $\alpha$ counting (Pb-$\alpha$ method), which required much less than a gram of zircon. Detailed equations for calculating chemical Pb ages according to the proportion of U to Th had been worked out by Keevil (1939) and the U decay constants were more precisely measured by Fleming et al. (1952). The oldest sample dated by Larsen et al. was from Renfrew County, Ontario. This gave an age of 900 Ma, an improvement over the helium dating of zircon from the same area by Strutt (1908). The Pb-$\alpha$ method was popular during the 1950s and produced some important results (e.g., Webber et al. 1956). However, the zircon ages had a precision of only about 10%. Such results demonstrated that zircon might prove much more useful if methods could be found to precisely measure the parent and daughter isotopes on smaller amounts of sample.

Larsen's work attracted the interest of a group at the University of Chicago where graduate students Clair Patterson and George Tilton (Fig. 1) were determining U and Pb concentrations in meteorites under Harrison Brown. They had developed methods for measuring microgram and sub-microgram amounts of those elements by isotope dilution (ID). This involves mixing the sample with a known quantity of what is ideally a single non-radiogenic isotope of the element to be measured. This is called a spike and is usually prepared in a large isotope separator. Once sample and spike are mixed, the sample weight can be determined by measuring the ratio of its isotopes relative to the spike isotope, after subtracting off the proportion of spike isotope in the sample (Hayden et al. 1949). This work was possible because Brown's group had access to the advanced thermal ionization mass spectrometer (TIMS) laboratory of Mark Inghram in the physics department. The ID-TIMS method was especially important for Pb because it permitted accurate isotope analyses on microgram-size samples instead of the milligram amounts required in the PbI vapor method previously used by Nier.

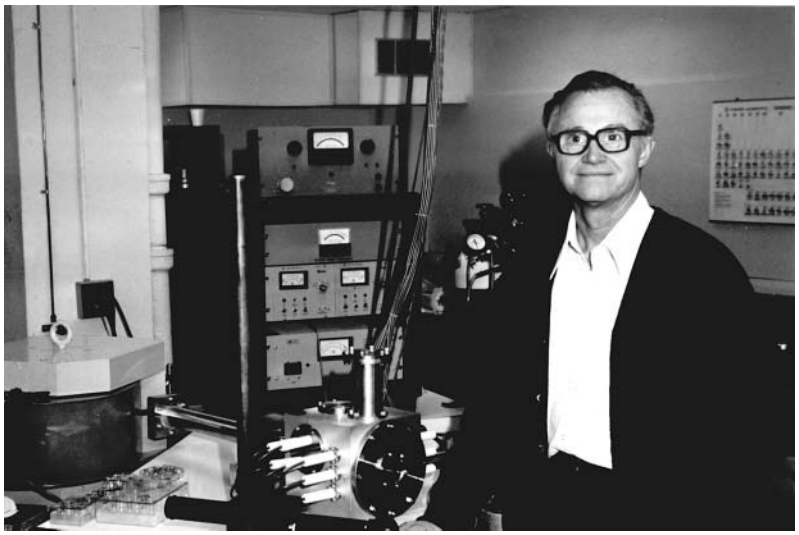

**Figure 1.** George Tilton in 1979 during a sabbatical return to the Carnegie Department of Terrestrial Magnetism.

On a trip to Washington, Brown met Larsen and recognized immediately that the methods already developed at Chicago would be a vast improvement over the alpha-lead method that Larsen had initiated. As a result, a group was formed with Larsen, Brown, Patterson, Tilton, and Inghram to measure a zircon age with corrections for the Pb isotope composition. Larsen provided the Chicago group with mineral separates from a granite in the Grenville province of southern Ontario. They analyzed a variety of minerals, but zircon and sphene (titanite) were the only ones in which Pb was sufficiently radiogenic to calculate a reliable age (Tilton et al. 1955). The two U-Pb ages for zircon (1030 Ma and 1060 Ma) were only slightly younger than the $^{207}Pb/^{206}Pb$ age of 1090 Ma, indicating that there had been little parent/daughter disturbance. These results agreed closely with previously measured $^{207}Pb/^{206}Pb$ ages (Nier 1939b, Nier et al. 1941) and chemical Pb ages (Ellsworth 1931) on uraninite samples from the area.

After graduating from Chicago, Tilton left to join the isotope group at the CIW, established by Thomas Aldrich and Gordon Davis. George Wetherill (another Chicago graduate) then arrived, followed by Stan Hart, Al Hofmann and Tom Krogh. The group set out to test the validity of age determinations by cross-comparing the systems U-Pb, Th-Pb, Rb-Sr and K-Ar. The work included extensive measurements on zircon of different ages from different areas (Tilton et al. 1957). Some of this work was used to determine better decay constants for $^{87}Rb$ (Aldrich et al. 1956) and $^{40}K$ (Wetherill et al. 1956), but the 1957 paper was also seminal for subsequent developments in the field of zircon geochronology. The authors pointed out that zircon often shows evidence of discordance (disagreement between the $^{206}Pb/^{238}U$ and $^{207}Pb/^{235}U$ ages), and discussed its possible causes. They noted that discordance tended to be greater in older samples and was associated with increased amounts of common Pb. They associated it with accumulated radiation damage, although an annealing experiment on metamict zircon showed that little Pb was lost during recrystallization. They concluded that zircon discordance was probably due to Pb loss caused by some post-crystallization geologic event. They also remarked on the presence of cores in zircons, which could potentially contribute an older inherited age component. Trying to understand and interpret discordance in zircon was to preoccupy U-Pb geochronologists over the next quarter century.

U-Pb isotopic data from zircon and other minerals became easier to assess following Wetherill's (1956a) introduction of the concordia diagram, in which the two daughter/parent isotope ratios ($^{206}Pb/^{238}U$ and $^{207}Pb/^{235}U$) are plotted against each other. The concordia is the locus of compositions for which the two U-Pb decay systems give the same age. This followed efforts to understand discordant but linearly correlated U-Pb data on monazites and uraninites from Canada and Africa (Ahrens 1955a,b; Wetherill 1956b). Assuming a simple two-stage history, the upper concordia intersection of a best-fit line through a data array should give the crystallization age of the zircon while the lower intersection should give the age of isotopic disturbance (Fig. 2). A variant of this diagram in which radiogenic $^{207}Pb/^{206}Pb$ is plotted versus $^{238}U/^{206}Pb$ was introduced by Tera and Wasserburg (1972). It has the advantage that the two variables are only weakly correlated.

Tilton (1960) noted that analyses of late Archean zircon from several different continents loosely defined a Pb loss line with a lower concordia intercept age of about 600 Ma, although there was little or no evidence for a geologic event of this age having affected the samples. He proposed that radiogenic Pb slowly diffuses out of zircon crystals over their entire history. Building on work by Wasserburg (1954) and Nicolaysen (1957), Tilton presented a mathematical model for this process where Pb loss was considered to result from intrinsic properties of zircon rather than environmental influences. Wasserburg (1963) and Wetherill (1963) derived more elaborate models in which the diffusion constant increases with the amount of radiation damage but these produced curves that were broadly similar to Tilton's. Since continuous diffusion produces a discordia that differs from a straight line only when Pb loss exceeds about 80% (Fig. 2), this mechanism of Pb loss was difficult to confirm, although as Tilton (1960) pointed out, the model predicted a unique Pb loss trajectory for a given age and could not apply in cases where the lower concordia age differed from that predicted by the model. Nevertheless, the continuous diffusion idea was very influential and de-

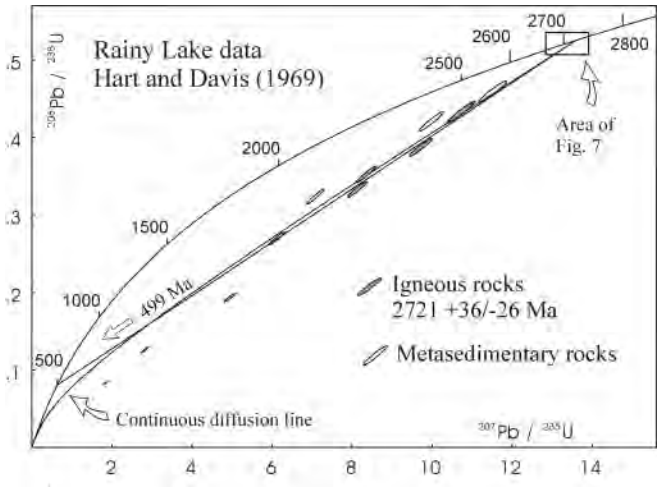


**Figure 2.** U-Pb concordia diagram showing episodic and continuous diffusion (Tilton 1960) Pb loss models fitted to moderately discordant zircon data from igneous rocks in the Rainy Lake area (Hart and Davis 1969). The concordia age is calculated using presently accepted U decay constants.

bates about the general validity of episodic versus continuous Pb loss models continued for over twenty years following Tilton's paper.

There were some cases in which discordance appeared clearly related to episodic Pb loss. Zircon data from gneisses in Minnesota defined a line with an upper concordia intercept age of about 3550 Ma, the oldest terrestrial age determined at that time, and a lower intercept age of 1850 Ma, which agreed with Rb-Sr and K-Ar biotite ages for metamorphism in the area (Catanzaro 1963). However, other studies of metamorphic resetting gave ambiguous results. Effects of contact metamorphism were tested by Gastil et al. (1967) using the Pb-$\alpha$ method and by Davis et al. (1968) with isotopic dating. In both cases significant Pb losses were observed, although the age of Pb loss could not be determined in the Pb-$\alpha$ study, and in the isotopic study resetting was accompanied by morphological changes in zircon, suggesting that the observed discordance may have resulted from mixing metamorphic overgrowths with older zircon. Aldrich et al. (1965) found no measurable effect on zircon that had been through amphibolite facies metamorphism, while Kuovo and Tilton (1966) found only minor thermal resetting of zircon from a xenolith in a granitoid pluton. Catanzaro and Kulp (1964) argued that discordance in zircon from the Beartooth, Little Belt and Santa Catalina Mountains was due to Pb loss caused, in some cases by metamorphism, in others by groundwater leaching. By analyzing zircon from weathered parts of the Archean gneiss dated by Catanzaro (1963), Stern et al. (1966) demonstrated that zircon could lose 50-85% of its radiogenic Pb even at ambient temperature. Such open system characteristics were evidently related to the metamict state of the zircon. For example, Pidgeon et al. (1966) showed that up to 85% of radiogenic Pb could be leached from metamict zircon in a hydrothermal salt solution with only minor loss of U whereas annealing greatly reduced Pb loss (Pidgeon et al. 1973). Shukolyukov (1964) suggested another radiation-related episodic Pb loss model in which Pb atoms are displaced into micro-fractures by alpha recoil, from which they can be leached. Goldich and Mudrey (1972) used this mechanism to explain how radiogenic Pb might be lost due to pressure release during regional uplift, possibly the cryptic event recorded by lower intercept ages.

The successes and frustrations in trying to date a variety of igneous and metasedimentary rocks using early methods were summarized by Hart et al. (1963). Despite uncertainty about the Pb loss mechanism it seemed clear that for many igneous rocks upper concordia intercept ages approximated crystallization ages. Silver and Deutsch (1963) carried out a detailed study of zircon from a Mesoproterozoic granite, demonstrating that U and Th concentrations varied considerably

within and between grains from a single rock sample and that greater discordance correlated with higher radioactivity. They concluded that the primary cause of discordance was Pb loss, not U gain and that whether the loss was episodic or by continuous diffusion (although Silver was a strong advocate for episodic loss), it was promoted by radiation damage. Most importantly, they noted that cogenetic zircon fractions of different grain size and magnetic susceptibility can have variably discordant compositions which broadly define a discordance line. This paper was extremely influential over the next two decades because it provided a method for determining primary ages by generating arrays of variably discordant data that could be extrapolated to concordia. The accuracy of these ages was limited by the degree of concordance achieved, scatter about the discordance line and uncertainty about whether linear extrapolation was valid in many cases. Such considerations often produced errors of tens of million years for zircon crystallization even when it was possible to determine $^{207}Pb/^{206}Pb$ ages with precisions of a few million years.

Another problem with zircon dating is inheritance, although in favorable circumstances inheritance can also provide important age information on protoliths. Zircon is usually dated to determine the age of its host rock, but it is a leap of faith to assume that both are the same. If ages measured on concordant zircon fractions of different morphologies agree, this is normally taken as sufficient evidence that the zircon does date the rock. Producing a discordia with little or no scatter outside of experimental error is a less reliable indicator. Zircon fractions from some igneous rocks, however, yield scattered ages that are clearly older than the rock itself. This inheritance arises because zircon grains can survive episodes of partial melting with little or no effect on their U-Pb systems. The physical persistence of zircon through crustal melting events was demonstrated by Poldervaart and Eckelmann (1955) who documented core-overgrowth relationships in zircon crystals from anatectic granite. Some of the earliest accounts of inherited zircon ages are by Pasteels (1964) from a xenolith-bearing granite in the Swiss Alps and by Stern et al. (1965) who reported anomalously old zircon xenocrysts in a quartz diorite from the La Sal Mountains, Utah. Small amounts of inheritance were also noted by Grauert and Arnold (1968) in zircon from orthogneisses in the Swiss Alps. Older zircon cores were identified by Köppel and Grünenfelder (1971) and Gulson and Krogh (1973) in rocks from the Swiss Alps and by Pidgeon and Johnson (1974) and Pankhurst and Pidgeon (1976) in Scottish granites. In most of these cases the inherited component was fairly minor or it showed a roughly uniform average age that was much older than the age of igneous emplacement. Assuming a single age of inheritance and negligible post-igneous Pb loss, an emplacement age can be determined from the lower concordia intersection of the best fit line to the array of data, the upper intersection giving the age of the inherited component (Fig. 3). The linearity of these data from multigrain zircon fractions was taken as evidence that this simple model is valid. However, later single-grain dating on some of these samples showed that the averaging effect of large zircon fractions can preserve linearity even if there are diverse ages of inheritance, and concordia intersections may not be meaningful (Williams 1992).

Early researchers considered inheritance to be less of a problem than discordance, although Coppens et al. (1965) pointed out that analytical methods of the time, which required analysis of fractions containing $10^4$-$10^6$ grains, would make inheritance difficult to avoid. This paper presented age results from single zircons using a method developed by Durand (1962) and Kosztolanyi (1965) for enhancing Pb ionization from zircon fixed to a filament with hydrofluoric and phosphoric acid. Coppens et al. (1965) observed that $^{207}Pb/^{206}Pb$ ages increased to a plateau and $^{204}Pb$ dropped to low levels as the temperature was increased, suggesting that Pb contaminants evaporated at lower temperature than radiogenic Pb in the crystal. This was a forerunner to the Kober evaporation method introduced two decades later (see below). At the time it was never strongly pursued, perhaps because the limited sensitivity of mass spectrometers made it difficult to determine Pb isotopic ratios to better than about 10%.

Interpreting ages of detrital zircon in sedimentary rocks was a problem of still greater complexity. In one of the earliest studies, bulk zircon fractions from North American beach sands (LeDent

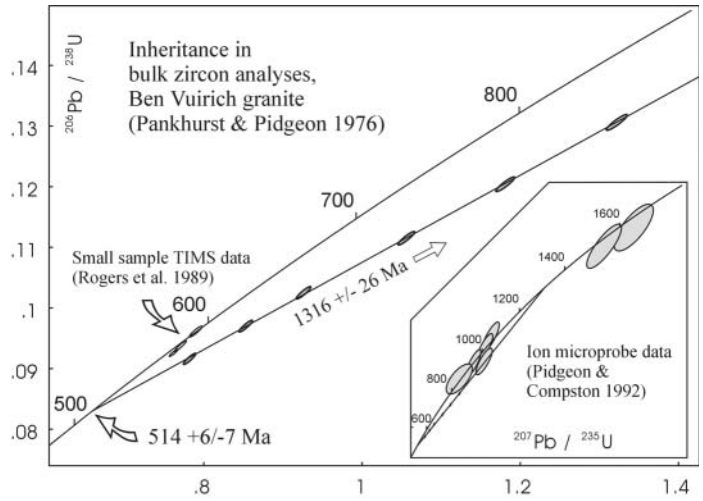


**Figure 3.** Inheritance mixing line based on data of Pankhurst and Pidgeon (1976) from the Ben Vuirich granite in Scotland. In a later ion microprobe study on single zircon grains (inset) these data were found to result from mixing concordant zircon xenocrysts, with ages ranging from 950 Ma to 1700 Ma, with 590±2 Ma zircon from the pluton (Rogers et al. 1989).

et al. 1964) and a Cambrian sandstone (Tatsumoto and Patterson 1964) were analyzed with the aim of determining the average age of rocks in the drainage basins and relating this to the growth rate of North American crust. There were few measurements and considerable uncertainties about the degree and time of Pb loss, but the authors found the data to be consistent with primary formation of the bulk of the North American continent between 3.0 Ga and 1.0 Ga. Pidgeon (1969), working at the Scottish Universities Reactor Centre, analyzed zircon from schist and quartzite from the Dalradian sequence in Ireland. This gave a quasi-linear array of discordant data with lower concordia intercepts of 400-500 Ma, which was the same age range that he found for granites in the region. Upper intercepts gave 1.3-1.6 Ga but Pidgeon pointed out the problem in distinguishing whether the linear array had been generated by partial Pb loss from a uniform aged source or was an artifact of mixing zircon populations with different ages.

The Swiss Federal Institute of Technology in Zürich (ETH) became an early center for zircon geochronology. Consequently, much work in the 1960s and 1970s was focused on some of the most complex rocks: polymetamorphosed gneisses from the Alpine fold belt. The survival of Precambrian zircon U-Pb ages through a later high-grade thermal event was first reported in early studies of paragneisses from the Swiss Alps (Pasteels 1964, Grünenfelder et al. 1964). More detailed work was carried out by Grauert and Arnold (1968), Pidgeon et al. (1970) and Köppel and Grünenfelder (1971) all of whom noted that highly discordant zircon data from different paragneisses formed distinct quasi-linear arrays with upper intercept ages in the range 1500-2500 Ma but similar lower intercept ages of about 440-500 Ma (Caledonian). This pattern was generally interpreted as due to severe Pb loss imposed upon a zircon population of roughly uniform age during metamorphism. However, Grauert et al. (1973) found that zircon from low-grade metasedimentary rocks in the Alps also give a quasi-linear array of data with similar intercept ages to the paragneisses, although with less discordance and more scatter. Allègre et al. (1974) attempted to interpret these data patterns with a generalized model involving multi-episodic and diffusive Pb loss. They pointed out that complex Pb loss histories could produce data arrays similar to those from the Alps but with meaningless concordia intercept ages. By assuming a cogenetic population with a 4-stage history and known ages of 30 Ma (Alpine) and 300 Ma (Hercynian) for the last two stages, they concluded that the original age of the Alpine zircon was late Archean or Paleoproterozoic and the major time of

disturbance was 520-580 Ma (Cadomian rather than Caledonian). As emphasized by both Grauert and Pidgeon, data interpretation on bulk fractions would always be unclear because of uncertainty over the effects of averaging heterogeneous populations. This could only be resolved by improving analytical methods to the point where it was possible to date individual grains or parts of grains that represent single-growth episodes.

Zircon analysis during this period was extremely laborious, limiting the amount of age data that could be acquired. The basic procedures for sample extraction and purification had been worked out by Tilton and Patterson in the 1950s. Because of its chemical inertness, zircon was fused with borax in a Pt crucible, then dissolved with HCl. The solution was split into two aliquots. One was spiked with $^{208}Pb$ and $^{235}U$ for concentration determinations while the other was analyzed for Pb isotopic composition. This was necessary because zircon contains a substantial amount of radiogenic $^{208}Pb$ from the decay of $^{232}Th$, which had to be subtracted from the composition of the spiked sample. Pb was separated from each aliquot either by multiple liquid-liquid extraction using dithizone (plus potassium cyanide and other chemicals) or with ion exchange columns. Pb-sulfide was precipitated by bubbling $H_2S$ into the solution while U (and Th) bearing solutions were purified with ion exchange columns. The large amount of manipulation and the relatively primitive clean-lab conditions resulted in Pb blanks of about a microgram.

The method of loading Pb for TIMS as the oxide or sulfide developed by the Chicago group (Tilton et al. 1955) was the most important factor in making isotopic studies of zircon possible. However, such loads still required hundreds of milligrams of zircon so that only zircon-rich rocks could be dated and fractions normally had to contain thousands of grains. A more sensitive loading method was devised by Akishin et al. (1957) who used a mixture of silica and zirconium gel with phosphoric acid, but this was not used widely outside the USSR. The single-zircon method described by Coppens et al. (1965) and Kosztolanyi (1965), mentioned above, represented another early use of ionization activators. Cameron et al. (1969) found that by loading Pb with pure silica gel and phosphoric acid, stable signals could be produced with ion yields a thousand fold greater than by using PbS. Apparently, they electron probed mass spectrometer loads that produced unusually strong Pb signals, finding silica that had probably come from the quartz rod used to scratch the inside of the $H_2S$ reaction vessel to promote PbS precipitation. This astute observation led to precise analysis of nanogram-size Pb samples with available mass spectrometers; this was an essential precursor to further improvements in U-Pb analytical methods. It also simplified the chemical extraction procedure, because Pb no longer had to be precipitated as a sulfide. Following its introduction, the high blanks of the dissolution and extraction procedures became the major barrier to reducing sample sizes. Overcoming this became the main focus of the next phase of development.

## ADVANCES IN TECHNIQUE — 1973 TO 1982

The 1960s and early 1970s saw a paradigm shift in geologic thinking: the widespread acceptance of plate tectonics as a unifying theory of Earth history. K-Ar dating was used extensively to test and elaborate the theory, especially by tying the paleomagnetic record to an absolute time scale. Zircon had not yet achieved its potential as a precise geochronometer because of analytical difficulties and a lack of understanding of how to deal with discordance. However, major developments were imminent. The work of Tom Krogh (Fig. 4), who arrived at the CIW in 1965 just as George Tilton was leaving, would be pivotal.

Significant advances usually come about because of a pressing need to solve a particular geologic problem. Krogh had been attempting to resolve a closely spaced succession of magmatic and metamorphic events in the Grenville province of southern Ontario, an historical testing ground for U-Pb geochronology. Rb-Sr whole rock data had given inadequate precision and Rb-rich minerals were susceptible to metamorphic resetting. Zircon had the potential to record both precise primary and metamorphic ages precisely but multiple testing and experimentation would have involved a prohibitive amount of work. While on a visit to the CIW from South Africa, Tony Erlank intro-

duced Krogh to a Teflon dissolution capsule for rock powders. Krogh refined the design and produced a capsule that could support the 220°C temperature needed to dissolve zircon in HF (Krogh 1973). He also introduced a method for separation of U and Pb in small anion exchange columns, based on his experience with Rb-Sr geochronology. Together, these techniques reduced Pb blanks by three orders of magnitude and made the dissolution and separation process much easier. Another important advance in blank reduction was the perfection of the two-bottle sub-boiling still by Jim Mattinson (1971), a concept explored earlier by Krogh. This furnished a cheap and effective method for producing reagents with picogram blanks.

Krogh's synthesis of $^{205}$Pb spike using a cyclotron at Oak Ridge National Laboratories was another major step forward (Krogh and Davis 1975a). $^{205}$Pb does not occur in nature because it has a half-life of only 30 Myr. Use of $^{205}$Pb as a spike therefore allows isotopic compositions and concentrations to be determined on the same solution. Proton bombardment of a $^{206}$Pb target produces $^{205}$Bi and a minor amount of $^{206}$Bi. $^{205}$Bi, with a 15-day half-life, is intensely radioactive but can be chemically separated from Pb in a hot cell. However, the purification would have to occur in an environment surrounded by lead bricks and in a stream of unfiltered air, raising the possibility of contaminating the spike with common Pb. Even though the prospect of success was uncertain, Phil Abelson committed $5,000 to purchase the accelerator time. The irradiated $^{206}$Pb-enriched target was dissolved and an initial separation of Bi was carried out by liquid-liquid extraction. Remaining Pb was then stripped from the Bi on an ion exchange column and the $^{205}$Bi left to decay to $^{205}$Pb (plus a few percent of $^{206}$Pb from $^{206}$Bi). A concern was whether the radiation would destroy the function of the ion exchange resin, which might also contaminate the spike. Fortunately, this was not the case (although the Teflon column became extremely brittle). $^{205}$Pb is also produced when $^{204}$Pb absorbs neutrons in a reactor. This process was exploited by Tatsumoto who had the product purified in an isotope separator, although it could not be made as free of common Pb as Krogh's spike without prohibitive $^{205}$Pb loss.

More precise determinations of the $^{238}$U and $^{235}$U decay constants, carried out by Jaffey et al. (1971), were essential for exploiting the potential precision of the U-Pb method. Their values are still considered to be by far the most accurately determined geochronological decay constants.

The advances in dissolution and purification methods at CIW made low blank analyses available to many more laboratories. Ten samples could be chemically processed with a few hours of bench time, whereas each sample took a full day by the old method. This probably accounts for the

**Figure 4.** Tom Krogh in 1973 at the Carnegie Institution in Washington.

increase in the average output of zircon U-Pb geochronology papers from less than 10 per year in the decade before 1972 to over 50 per year in the decade after (Fig. 5). By the early 1980s the zircon U-Pb method had been used to determine primary ages for major periods of igneous activity in many areas. This growing database had an important impact on the Precambrian time scale and on the interpretation of results from other geochronometers. Many zircon ages from the Canadian shield, for example, were found to be older than ages obtained by the K-Ar and Rb-Sr methods (Stockwell 1982). Like the U-Pb system in zircon, K-Ar can produce precise ages because the Ar in K-bearing minerals is generally highly radiogenic. However, it was realized that Ar can be lost from minerals by subsolidus heating events. In these cases it records the time when the minerals passed through their blocking temperatures, which in metamorphosed terranes can be substantially later than when they crystallized. Use of the $^{40}$Ar-$^{39}$Ar step heating method (Merrihue and Turner 1966), while revealing important information about the thermal history, only in part overcomes this resetting problem. The advantage of zircon ages is that they usually record primary igneous crystallization events.

A more subtle discrepancy was found between Rb-Sr whole rock and U-Pb zircon ages. It was recognized that Rb-Sr dating of minerals was subject to metamorphic resetting, but it was commonly assumed that whole rocks would remain closed systems. This seemed to be the case for granulites. Rb-Sr whole rock ages on the Amitsoq gneisses in West Greenland (3700-3750 Ma; Moorbath et al. 1972) approximately agreed with U-Pb zircon ages (3650±50 Ma; Baadsgaard 1973) and established the area as the oldest known segment of crust. However, Rb-Sr ages in rocks of lower metamorphic grade sometimes gave younger ages than zircon. As shown later, whole rocks can be open to fluid transport of Rb and Sr along micro-fractures, although they may remain closed in 'dry' metamorphic systems such as granulites (Heaman et al. 1986). During the 1970s the whole rock Rb-Sr method remained the most popular method for dating Precambrian rocks. As multi-collector mass spectrometers were introduced in the early 1980s, whole rock Sm-Nd dating, which probably does act as a closed system in most cases, also became popular. Because the radio-

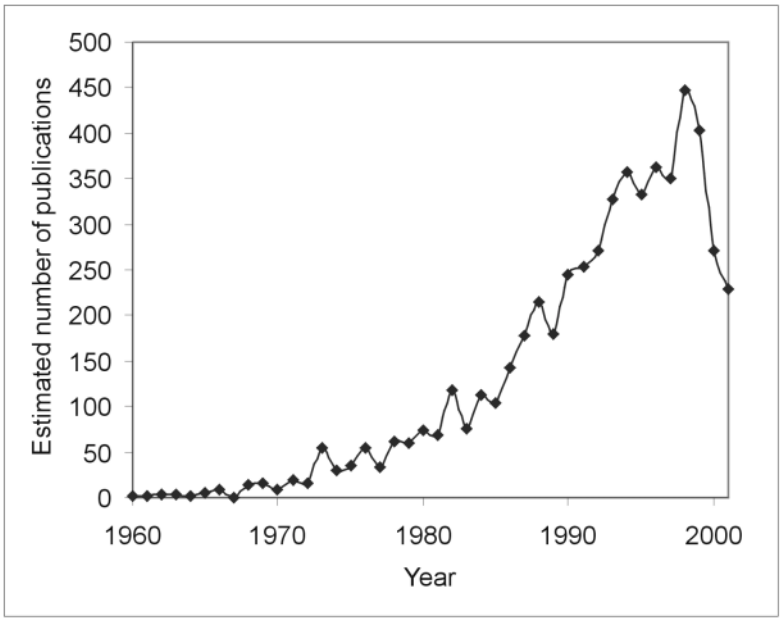


**Figure 5.** Publication rate of works with keywords "zircon" and "U-Pb" as recorded in the GEOREF database.

genic component is usually only a small proportion of the total Sr and Nd in rocks, however, determining an age requires construction of an isochron from analyses of several rocks with varying degrees of radiogenic enrichment. The result is commonly imprecise. Further, the differentiated sample suite necessary to generate an isochron might not be comagmatic, leading to ages that are not even accurate. This became evident in several studies after much debate (e.g., Claoué-Long et al. 1988; Cattell et al. 1984) and signaled the end of widespread use of isochron methods for dating metamorphosed rocks. Rb-Sr and Sm-Nd were supplanted as primary geochronometers by zircon U-Pb, although both decay systems are still very useful as petrogenetic tracers.

Attempts to use the full resolving power of the U-Pb system were frustrated by the limits that discordance imposed on precision and accuracy. Further, methods of data interpretation lacked rigor. Discordant arrays were often fitted by eye or using standard least-squares methods and concordia intercept errors were quoted without regard to whether the data actually defined a line. To regress isochron data, York (1969) had extended least-squares fitting to include error correlation. Ludwig (1980) adapted this method to U-Pb concordia data, while Davis (1982) incorporated Bayesian statistics in an even more sophisticated approach. To evaluate errors properly it was important to calculate a goodness-of-fit parameter such as the mean-square of weighted deviations (MSWD) or probability of fit. A poor fit usually indicates that the assumption of a simple two-stage model is invalid, either because of inheritance or multi-stage Pb loss. Also, as pointed out by Allègre et al. (1974), complex multi-stage episodes of Pb loss could result in quasi-linear data arrays with meaningless concordia intercept ages, but these would likely scatter outside of error in natural systems. Ludwig (1980) suggested dealing with the problem of poor fit by expanding the errors using Student's t, assuming a simple one-stage Pb loss model in which the excess dispersion about the line is random, such as might be caused by underestimating analytical errors. Davis (1982), on the other hand, expanded errors in proportion to discordance, assuming a random distribution of ages of Pb loss events. Both approaches are model-dependent and almost certainly over-simplistic when applied to natural zircons. A paradox in using the simple discordia model is that the apparent precision of intercept ages can be increased by analyzing the most altered samples. Such data increase the spread of discordance but are most likely to deviate from the linear model. The best, but more difficult, approach was to strive for concordance by analyzing pristine material.

The reduction in sample sizes allowed by the new analytical techniques permitted greater discrimination among zircon grains. The most cracked and altered grains could be eliminated to produce more concordant data. For many samples, however, especially from the Precambrian, it was still difficult to achieve data that were less than a few percent discordant, so much debate concerning age interpretation continued to revolve around Pb loss mechanisms. Grünenfelder (1963), working on a Hercynian granite, noted that some zircon had milky-white alteration zones with a cracked mosaic structure. Hand-picked concentrates of milky zircon contained higher U and water contents (measured by IR absorption) than associated clear zircon and gave a younger age. He suggested that the alteration was due to recrystallization of metamict zircon during the Alpine orogeny, which partially reset their U-Pb system. Gebauer and Grünenfelder (1976) elaborated on this interpretation in a study of zircon in metasedimentary rocks from southern France. Their samples ranged from chlorite to sillimanite metamorphic grade, but all of them gave quasi-linear data arrays with about the same degree of discordance. Rather than recording the age of Hercynean peak metamorphism (ca. 300 Ma), however, the lower intercepts were Caledonian (400-440 Ma). They proposed a model in which metamict crystal domains recrystallized and lost Pb during the low grade Caledonian metamorphism, then became annealed and resistant to further Pb loss during the later higher grade Hercynean event.

Grünenfelder's original observation supported a multi-phase mixing model for discordance that was later proposed by Steiger and Wasserburg (1966). These authors showed that zircon data from some Precambrian rocks, when plotted on a $^{208}Pb/^{232}Th$ versus $^{207}Pb/^{235}U$ diagram, formed linear arrays with negative lower intercept ages, but defined a normal discordia on a $^{206}Pb/^{238}U$

versus $^{207}Pb/^{235}U$ diagram. This was interpreted to result from mixing between a highly discordant phase with relatively high Th/U and a near-concordant phase. They reached a similar conclusion based on data from late Archean rocks with similar ages but different metamorphic histories (Steiger and Wasserburg 1969). They observed that discordant zircon data from many rocks seemed to reflect a mixing of non-metamict near-concordant phases and metamict phases that had lost much of their Pb by continuous diffusion or during low-grade events such as regional uplift.

Although high-uranium, radiation-damaged zircon was commonly found to be the most discordant, there were also cases of metamict zircon with slight or negligible discordance. Single-grain etching studies by Krogh and Davis (1974, 1975b) showed that polyphase radiation damaged zircon was susceptible to reaction with HF vapor, but undamaged zircon was not. This etching technique revealed amorphous altered domains that turned powdery-white and replaced damaged, high-U zones (Fig. 6). The altered zones contain several percent of Ca, Fe, Al (measured by electron microprobe) as well as $H_2O$. Krogh suggested that radiogenic Pb loss and gain of common Pb occurred when such radiation-damaged areas became altered. In his view, radiation damage does not itself cause Pb loss, although severely damaged areas can be leached, as was shown by Pidgeon et al. (1966). The main effect of radiation damage is to prepare the crystal for later alteration, which can occur by interaction with fluid at ambient temperature. The lower concordia intercepts might then represent an average age of multiple Pb loss events that affected individual zones as they accumulated sufficient damage to react with external fluid. Zircon in granitoid rocks often shows oscillatory zoning with inter-zone differences in U content of at least an order of magnitude (Fig. 6A). Holland and Gottfried (1955) documented the lattice expansion that accompanies radiation damage in high-U zones. This work grew out of attempts during the 1950s to date zircon by measuring its accumulated radiation damage (e.g., Kulp et al. 1952, Hurley and Fairbairn 1953). Differential expansion produces internal stress that often pervasively cracks the crystal (Fig. 6B) and provides access to aqueous fluid that can alter the damaged domains as documented by Krogh and Davis (1974, 1975b). Some later discussions of radiation damage in zircon are given in Ewing et al. (1987), Chakoumakos et al. (1987) and Lee and Tromp (1995).

The dependence of zircon-Pb loss characteristics on local conditions is shown by examples where discordia lines with a wide range of lower intercept ages are found from coeval rocks in the same area (e.g., Davis et al. 1985). Such observations suggest that Pb loss is not an inevitable property of zircon and potentially can be eliminating altogether. If portions of zircon grains that have escaped alteration or leaching can be identified and separated, they should produce concor-

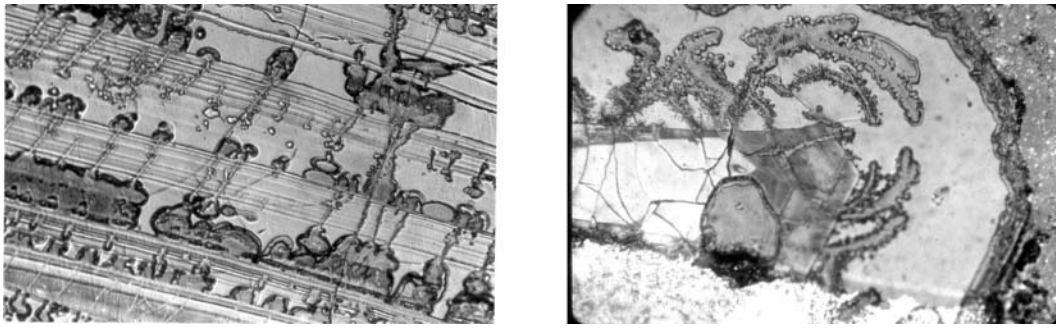

**Figure 6.** Optical images of alteration in zircon revealed by HF vapour etching of polished grains. (A, left) Oscillatory zoned zircon in which alteration appears to have developed preferentially in high-U zones. Alteration is localized where micro-fractures that cross the high-U zones provided access for fluid. (B, right) High-U zircon with a low-U core. Note how altered domains in the metamict outer zone are rooted at fluid-access cracks in the low-U central zone, which may have ruptured due to expansion of the damaged zone.

dant U-Pb data. In many cases careful visual observation can effectively identify altered crystals while etching with HF or NaOH makes alteration highly visible (Krogh 1994). Because most Precambrian zircon populations are highly damaged, however, dating the rare primary concordant phase usually requires the ability to analyze a few grains (or less) of zircon.

During this period, the isotope group at the Université de Paris under Claude Allègre began dating zircon at the single-grain level. The first such study was by Lancelot et al. (1976) on a charnockite paragneiss from West Africa. Bulk zircon fractions gave an age of ca. 2.05 Ga in agreement with regional metamorphism but in conflict with the Rb-Sr whole rock age of ca. 3.1 Ga. Single clear zircon crystals gave a roughly consistent age of 2.04 Ga while single brown grains gave a scattered array pointing toward ca. 3.0 Ga. Analyses of single grains were thus able to reveal an older age component that was not evident in the bulk analyses. A subsequent paper by Michard-Vitrac et al. (1977) applied single-grain analysis to early Precambrian rocks. Zircon from clasts in a metaconglomerate at Isua, Greenland, pushed the oldest terrestrial age back to 3769±11 Ma. The single-grain approach was first applied to detrital zircon by Gaudette et al. (1981) who sampled a Cambrian sandstone in the eastern United States. Only 5 single zircon grains were analyzed, however, the main aim of the study being to resolve age differences by identifying distinct detrital populations based on color and morphology then dating them in bulk. The single-grain analyses fell within the cluster of bulk fraction compositions, which scattered along distinct mixing lines although most of the analyses may have been significantly affected by secondary Pb loss as well as mixing from multiple sources. Single detrital zircon dating was applied more successfully to metaturbidites of the Archean Slave and Superior provinces by Schärer and Allègre (1982a) and Gariépy et al. (1984), respectively. As shown by later studies, their data roughly but correctly reflected the age distribution of probable source rocks.

Early single-grain studies unfortunately suffered from secondary Pb loss as well as analytical blanks that were too high to permit precise age determinations. Such problems generally limited errors to about ±30 Ma in the above Archean studies. The data were useful, however, for distinguishing widely spread age components and the studies demonstrated the utility of analyzing zircon from complex rocks at the single-grain level. This approach was carried a step further with the analysis of fragments of a single zircon, albeit a large one (500 μg), by Schärer and Allègre (1982b). The zircon, from a syenite in the Pikes Peak batholith, was broken into 11 fragments that were dated individually and the results compared to those from smaller single grains. The main importance of this study was in showing that the zircon fragments produced a much broader spread of data than the whole grains. In particular, some fragments were concordant or near-concordant, whereas all the single whole-grain analyses were quite discordant. As stated by the authors: "These results suggest that the discordancy phenomenon should be discussed in terms of domains within a single grain and not in terms of grain dimensions or volume diffusion relative to grain size" (Schärer and Allègre 1982b, p. 587). This conclusion, the same as that of Steiger and Wasserburg fifteen years earlier, aptly summarized the approach necessary to solve the discordance problem. At the same time, two quite different solutions to the problem were being pursued.

## RESOLUTION OF THE PB LOSS PROBLEM — 1982 TO THE PRESENT

### Further advances in ID-TIMS methods

In the mid-1970s John Wood and Ken Card at the Ontario Geological Survey (OGS) along with Syd Lumbers at the Royal Ontario Museum arranged funding for a U-Pb geochronology lab at the museum under the directorship of Tom Krogh. It was a natural decision, although not without controversy, to exploit the new methods of precise geochronology developed at the CIW in order to resolve complex geologic problems that had arisen as a result of the Survey's mapping programs. The Jack Satterly Geochronology Laboratory (JSGL), named for a pioneering Ontario geologist, opened in 1977. Paul Nunes was hired to help set up the laboratory and function as the OGS geo-

chronologist. Don Davis joined as a post-doctoral fellow in 1978 to apply the method in the western Wabigoon greenstone belt of the Superior province. Fernando Corfu arrived in 1980 and eventually carried on the program of OGS dating.

Pb blanks at the time were about 50 pg and zircon sample sizes about 1 mg. Even picking the most pristine-looking grains from low-U zircon populations would usually produce data that were several percent discordant. Although some greenstone belts were found to have developed over hundreds of million years (Nunes and Thurston 1980), results from others, such as the western Wabigoon belt, suggested time spans of less than 50 Myr. Locally, volcanic and plutonic sequences might record much shorter periods but these could not be resolved with discordant data. While mass spectrometer data from large zircon fractions were very precise, and upper intercept ages gave precisions of a few million years, in some cases these ages were shown to be inaccurate, such as plutons appearing older than their host rocks. Failing to solve such geological problems despite so much work created considerable frustration. There was ongoing discussion in the lab on how to best interpret data and a great deal of time was spent experimenting with a variety of new sample preparation and analytical techniques.

The paramagnetic response of discordant zircon, which had first been exploited by Silver and Deutsch (1963) to increase the spread of discordance using the Frantz separator, could be enhanced using the high-gradient magnetic field around a pointed soft iron wire connected to a hand-held bar magnet (Krogh 1982a). The least magnetic fraction from the Frantz thereby could be split further by testing individual grains. Low-U unaltered grains were repelled from the wire tip due to the natural diamagnetism of zircon, while grains in which only one end was altered showed a much stronger paramagnetic attraction from that end. It was observed however, that paramagnetism sometimes correlated not only with degree of alteration, but also with high-U content (a desirable feature for small samples), so concordant high-U zircon grains could not be effectively separated.

The most important advance was a method for removing the outer layer of zircon crystals by air abrasion (Krogh, 1982b). For the first time, this allowed concordant, precise data to be extracted from a wide variety of samples. Combined with careful selection, it made redundant the question of how secondary (low-temperature) discordance should be interpreted because it eliminated such discordant domains from the analyzed sample.

Krogh used fission track maps and etched grain mounts to show that many zircon crystals are surrounded by a thin high-U layer. Damage to this layer, even if it is not unusually U-rich, could easily result in alteration and Pb loss because it is directly accessible to the outside environment. Removing the primary crystal surfaces therefore seemed a promising approach for achieving concordance. The air abrasion method was inspired by a technique developed in India to prepare single crystals for X-ray diffraction. In the Krogh design, zircon is placed in a steel chamber in a circulating stream of air that exits through a fine nylon sieve. After several hours, the grains become rounded through collisions with the chamber walls. Analyses of abraded zircon from early experiments were more concordant than those of the starting material but abrasion alone often failed to eliminate all Pb loss. To achieve concordant data it was essential to choose abraded zircon grains with no visible cracks or internal alteration. The clearest, crack-free crystals with primary magmatic morphology were picked, abraded, and then carefully re-picked. Davis et al. (1982) found that the presence of pyrite during the abrasion process polished the surface of the grains, making it much easier to examine their interiors for any alteration, inclusions or fractures.

Some of the first abrasion experiments used zircon from noritic phases of the Sudbury mafic complex, which Krogh and others had attempted to date using discordant zircons. Analyses of carefully picked abraded samples are mostly concordant and show that all phases of the mafic complex are precisely coeval at 1850±1 Ma (Krogh et al. 1984). The complex is now thought to be a total crustal melt that resulted from a large meteorite impact. Application of abrasion to samples from Superior province greenstone belts resulted in a marked improvement in concordance and, for inheritance-free samples, produced more accurate ages that accord with geological relationships

(e.g., Davis et al. 1982, Corfu and Ayres 1984).

When the main objective of zircon geochronology had been to define discordia, large magnetic and size fractions were often analyzed to give maximum precision. The uncertainty in the age arose mainly from having to extrapolate discordant data. After the introduction of abrasion it became clear that discordance is not an unavoidable property of zircon. It also became clear that achieving a concordant but less precise datum was better than attaining greater analytical precision with a larger sample, but one of lower quality, and be left with having to interpret discordant results. Discordance was thus eliminated as an acceptable option. However, only a minute amount of totally undamaged zircon could be separated from many rocks, especially Precambrian ones. Therefore there was an ongoing need to reduce sample sizes, which created the need for ever-lower blanks. For ID-TIMS, abrasion ended the period of acceptance of milligram-size samples. It created another cycle of innovation that led to routine precise analysis of single grains and parts of grains. This greatly reduced the problem of secondary Pb loss and enabled samples with polyphase zircon and multiple age populations to be studied more effectively.

High blanks and limited sensitivity on conventional mass spectrometers such as the Micromass 30 initially continued to limit sample selection. This situation improved dramatically during the early 1980s. The JSGL achieved a reduction in Pb blank to several picograms by including a high-temperature 6N HCl wash in the Teflon bomb cleaning procedure and by reducing bomb and column sizes. The introduction of extended geometry mass spectrometers with improved source design such as the VG54/354 and MAT260 increased ion transmission by a factor of five. For silica gel loads, ionization efficiency increases as the sample size is reduced, a virtue of many TIMS loading methods. This method therefore is even more effective for the analysis of picogram-sized samples. The Daly collector used on the VG354 proved to have exceptionally stable linearity and mass fractionation relative to electron multipliers so it began to be used routinely for all isotopic ratios, instead of the less sensitive Faraday collector.

Throughout the 1980s the JSGL hosted a large number of students and visitors who applied the new method to a wide range of geologic problems. Many of these individuals, such as Larry Heaman, Greg Dunning, Bob Tucker, Nuno Machado, Urs Shärer and later Urs Schaltegger and Fernando Corfu went on to lead geochronology labs elsewhere. The new techniques were adopted at other labs such as the Geological Survey of Canada, where Otto van Breeman assembled a team of geochronologists including Randy Parrish, Chris Roddick and Jim Mortensen, later followed by Bill Davis, who added their own innovations. Parrish (1987) introduced a design for Teflon microdissolution capsules that allowed many parallel dissolutions to be carried out inside one larger capsule. This approach was inspired by the earlier efforts of Krogh (1978) to build capsules in which zircon could be dissolved by HF vapor. Another variant was introduced later by Wendt (1991). Methods for zircon U-Pb isotopic analysis by multicollection (Roddick et al. 1987) and efficient data reduction software (Roddick 1987) were developed at the GSC. Parrish and Krogh (1987) synthesized a new batch of $^{205}$Pb using the accelerator at the University of British Columbia and aliquots were sold to numerous laboratories. Automated data-reduction software and automated zircon analytical software developed by Ludwig were in routine use at the USGS by the early to mid 1980s. Fully automated U/Pb TIMS analyses for even single Phanerozoic zircons, using both commercial (VG Sector54) and custom (Ludwig, USGS) software became routine at some laboratories thus improving the time efficiency of the mass spectrometry. The database of precise zircon ages grew rapidly after 1982 and U-Pb zircon geochronology became recognized as an essential tool for understanding the record of ancient orogenies (e.g., Corfu 1993). From this time onward, progress in ID-TIMS methods would be a matter of incremental refinements in technique and improvements in understanding the zircon U-Pb system.

An outstanding example of precise U-Pb dating using abrasion is the work on the Duluth layered mafic complex, part of the Midcontinent Rift structure in Minnesota, by Paces and Miller (1993) at the U.S. Geological Survey. Multiple zircon fractions from four anorthositic and troctolitic

rocks gave concordant data with ages that range from 1099.3±0.3 Ma to 1098.6±0.5 Ma. $^{208}$Pb-$^{232}$Th isotopes were also measured and agree at the 1% level but give more discordant, scattered ages.

The Th-Pb system has never proved to be as useful as U-Pb in zircon, although attempts have been made to apply it since the earliest papers. Modeling of the U-Th-Pb system was discussed by Steiger and Wasserburg (1966). Tilton et al. (1955) noted early on that Th-Pb ages on zircon and titanite were much younger than U-Pb ages. They suggested that Th and U might be concentrated in different parts of the crystal and $^{208}$Pb preferentially lost from the Th-rich phase. As seen with the Duluth data, Th-Pb discordance persists at a reduced level even for unaltered zircon where the U-Pb system is concordant. This might be due to differential loss of U (as well as Pb) relative to Th, or to the difficulty of keeping Th in solution during sample processing, which could result in poor equilibration between sample and spike. Further, the $^{232}$Th decay constant is not as well determined as the U decay constants.

For mid to early Precambrian samples, by combining abrasion with reasonably careful sample selection, it was possible in most cases where the zircon population is cogenetic and has experienced only low temperature Pb loss to achieve data showing less than 1-2% discordance. An added bonus was that common Pb levels in near-concordant fractions fell to the point where they were indistinguishable from laboratory blank, showing that excess common Pb in discordant zircon is probably added at the time of radiogenic Pb loss. It was often difficult to eliminate all discordance so a common procedure in the early 1990s was to analyze two or more fractions of abraded zircon and one of unabraded grains, which would produce a more discordant datum. It was thought that this allowed correction for the small amount of residual Pb loss that affected the abraded fractions. Extensive later experience has shown, however, that near-concordant data from abraded fractions tend to agree in their radiogenic $^{207}$Pb/$^{206}$Pb and give the correct age. The reasons for the small amount of relatively recent (<100 Ma) Pb loss are still not clearly understood. Regression with data from unabraded fractions which lie on an older Pb-loss line can in fact produce an intercept age that is spuriously high (examples are discussed in Davis and Krogh 2000). The difference is small if the best data are nearly concordant, but it can exceed the inferred error.

An alternative approach to achieving concordance in a single age population is to avoid or dissolve out altered domains by chemical attack. Krogh and Davis (1974, 1975b) and Krogh (1994) observed that a few minutes of attack by 5% HF turned otherwise invisible zircon alteration chalky-white so it could be easily avoided during picking. Mattinson (1994) used hot HF to dissolve discordant domains in Mesozoic zircons, extracting a small amount of concordant residue after a series of leaches that lasted several days. Krogh (1994) and Krogh et al. (2002) used a variation of this method on Precambrian zircon in which the extent of radiation damage was revealed by a 2-hour leach in NaOH or HF at 200°C. The few grains that show no sign of attack, once abraded, typically have U values up to ten times lower than selected high-quality untreated grains from the same population. They give data that are more concordant and that are collinear with data from grains that were abraded but untreated with acid. This result is consistent with the findings of Mattinson (1994) but is in conflict with leach results of Davis and Krogh (2000) and Corfu (2000). These authors leached non-magnetic unabraded Archean zircon in warm HF. Data from analyses of the residues are 5-10% discordant but give $^{207}$Pb/$^{206}$Pb ages older than those of concordant analyses from unleached abraded zircons. This implies that the Pb that accumulated during the early part of the sample history is less susceptible to leaching. One explanation could be that the zircon suffered early annealing during metamorphism. Apparently zircon that remains inert to chemical attack was not affected by this process and also remained as a closed system over geologic time.

Mattinson (1987) pointed out that many zircon geochronology papers were still using inadequate error analysis. He discussed the factors limiting U-Pb age precision and emphasized the effect of uncertainty in the U decay constants. Optimal statistical methods for dealing with concordant data were devised by Ludwig (1998a, 2001). Ludwig's refinements of data analysis and reduction software, especially the ISOPLOT program (Ludwig 1998b), have been a major ongoing

contribution to zircon geochronology and to a wide range of other isotopic studies.

The increased activity stimulated by the new methods opened up new environments and minerals to precise U-Pb geochronology. Zircon was found to be common in plagiogranites, providing a means to date oceanic crust in ophiolites (Dunning and Krogh 1985). Van Schmus and Bickford used zircon ages from drill cores to map the sub-surface Precambrian basement of North America (later summarized in Van Schmus et al. 1996). Metamorphic zircon, often distinguishable by low Th/U (Krogh and Davis 1973), was found to be common in high-grade mafic rocks (Percival and Krogh 1983). Other minerals besides titanite and rare earth phosphates were found to contain radiogenic Pb, for example perovskite (Heaman 1989), rutile (Richards et al. 1988) and opal (Ludwig et al. 1980). The most important of these is baddeleyite ($ZrO_2$), which typically has several hundred ppm U, virtually no common Pb and is not as easily altered as zircon, so it usually produces near-concordant data without abrasion. Baddeleyite was one of several U-rich minerals from lunar rocks on which $^{207}Pb/^{206}Pb$ ages were measured with an early ion probe by Andersen and Hinthorne (1972). It was first utilized for precise dating in ID-TIMS studies by Krogh et al. (1984, 1987). The mineral is relatively rare in terrestrial rocks but is sometimes found in mafic dikes, which often cannot be precisely dated in any other way (Krogh et al. 1987, Heaman and LeCheminant 1993). Swarms of mafic dikes are important markers in the geological record since they probably record the impacts of ancient mantle plumes and sometimes accompany continental breakup (LeCheminant and Heaman 1989, Kamo et al. 1989).

By the late 1980s, Pb blanks at the JSGL had fallen to the 1-2 pg range and single zircon dating began. This, combined with abrasion, finally allowed precise ages to be measured on single detrital zircon grains in sedimentary rocks. The first such study was carried out on Archean sandstones from the Rainy Lake area of the western Superior province. Historically this has been considered a type area for Archean geology. It was first mapped by Andrew C. Lawson in the mid-1880s, and the geologic relationships have been debated ever since. Zircons from the area, including bulk fractions from metasandstones, had been dated by Hart and Davis (1969). These early data scattered around a discordia with an upper intercept age of about 2720 Ma (Fig. 2) so individual igneous events could not be resolved. The new concordant data (Davis et al. 1989) revealed a clear pattern of discrete events over a 2728-2685 Ma age range (Fig. 7A). In the classic stratigraphy of Lawson, the oldest units were turbiditic sandstones because they appeared to be at the base of the section. However, precise concordant ages from single detrital zircon grains showed that the sandstones were some of the youngest supracrustal units (Fig. 7B). They were probably over-thrust by older rocks and structural evidence indicated that the section had been overturned. Data from else-

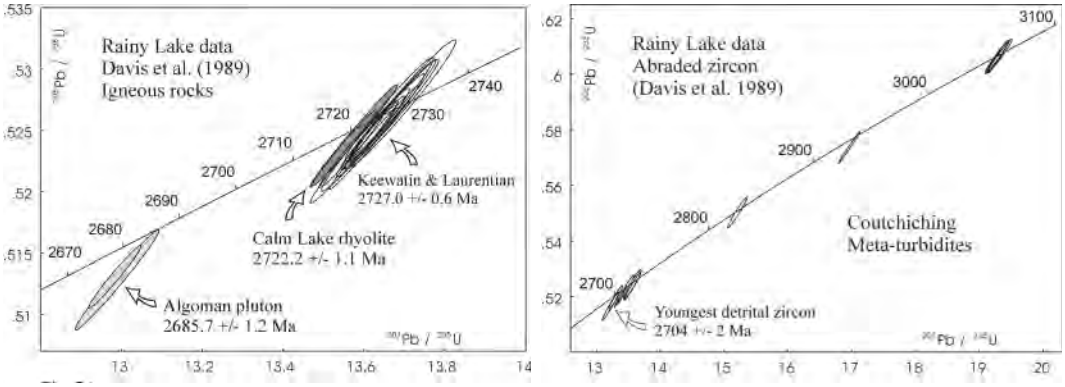


**Figure 7.** (A) U-Pb data on abraded zircon from igneous rocks in the Rainy Lake area, NW Ontario, Canada by Davis et al (1989). Compare to Hart and Davis (1969) data on the same units in Fig 2. (B) U-Pb data on single detrital zircon grains from Archean metasandstone in the Rainy Lake area.

where in the Superior province revealed that some other stratigraphic packages were out of sequence and supported models of thrust deformation similar to that at modern collisional boundaries (Davis et al. 1988, Corfu and Ayres 1991). Such studies helped initiate a conceptual change from regarding Archean tectonic processes as unique to the early Earth to explaining them in terms of actualistic models.

Krogh (1993) further extended the single grain method by dating single zircon cores and metamorphic overgrowths that he broke off average-size grains from the Kapuskasing structural zone of Ontario, an upthrust section within the Superior province that exposes deep levels of the Archean crust. Precise dating of such tiny fragments was only possible because of the low procedural blanks. Corfu (1987) had previously found that metamorphic zircon growth became younger at deeper paleo-levels of the crust. Krogh (1993) showed that metamorphic overgrowths surrounding metamorphic cores in zircon from amphibolites corresponded in age to metamorphic zircon cores in mafic granulites at deeper crustal paleo-levels. The data can be explained if the deep continental crust in this area had been built up progressive underthusting and dehydration of oceanic crust. Fluids released during granulite metamorphism apparently re-hydrated higher-level thrust sheets that had been emplaced and metamorphosed earlier, growing a new generation of metamorphic zircon. The most compelling evidence came from igneous zircon ages in granitoid clasts from a deep-level metaconglomerate. These gave ages younger than the youngest Archean supracrustal rocks in adjacent structurally overlying greenstone belts, implying that they must have been emplaced by late underthrusting rather than by burial.

A novel application was the use of zircon in meteorite ejecta layers to identify the impact site. Shock metamorphism associated with meteorite impacts produces characteristic planar deformation features in zircon. Such features were documented in zircon from Archean rocks adjacent to the Sudbury structure (Krogh et al. 1984, 1996) and from the thin world-wide ejecta layer associated with the K-T (end-Cretaceous) impact (Bohor et al. 1994). Single-grain dating of shocked zircon from this layer in several locations showed a predominant pattern of Pb loss at 65 Myr from a primary age of about 550 Ma, identical to that found in the basement to the Chicxulub crater in Mexico. This implicated Chicxulub as the impact site (Krogh et al. 1993, Kamo and Krogh 1995).

Routine sub-picogram blanks were achieved at some labs in the mid-1990s. Single zircon dating had become the norm for most samples by that time. Column separation of U and Pb from small zircon samples was shown to be unnecessary long before (Ludwig and Stuckless 1978) making low blanks easier to maintain. Pb blanks are now routinely in the range 0.2-0.8 pg at JSGL. This represents a drop of six orders of magnitude since the 1960s largely because of improvements in technique but also likely due to a progressive reduction in environmental Pb pollution over the past three decades. The factor of ten drop since the mid-1980s is difficult to explain in any other way since analytical procedures changed only in minor ways over that period to make the process more efficient. Blank levels at the JSGL are all the more remarkable since, unlike most clean labs, workers do not use any special clothing and the actual clean environment is restricted to small filtered air boxes that were constructed at the lab's inception. Such basic equipment is sufficient to produce the cleanest analyses, along with skill and concentration on the part of the analyst.

**The Sensitive High-Resolution Ion Micro-Probe (SHRIMP)**

Despite the improvements introduced at CIW, zircon dating in the 1970s was still limited by complex chemical procedures and high laboratory blanks. Single-grain analyses were imprecise and bulk fraction analyses risked being inaccurate because of discordance and inheritance. Efforts began to overcome these limitations by analyzing zircon directly at the intra-grain level using secondary ion mass spectrometry (SIMS).

SIMS instruments (ion probes) designed for geoscience use a focused beam of high-energy ions to sputter (ablate) a small area (usually ~20 μm diameter) on the polished surface of a sectioned target crystal, producing secondary ions from the crystal which are analyzed for their isoto-

pic composition in a double-focusing mass spectrometer. The process is almost non-destructive, about 3 ng of sample being consumed per analysis. The small sample size limits the analytical precision, however, so the most appropriate use of ion probes is in analyzing mineral samples that are scarce, complexly structured or of composite age.

The potential of SIMS for U-Pb geochronology was first demonstrated by Andersen and Hinthorne (1972) who used an ARL ion microprobe at the Hasler Research Center in California to measure $^{207}Pb/^{206}Pb$ ages in zircon and other U-bearing minerals from lunar samples. The ages compared favorably with those measured on the host rocks by other techniques, but the sensitivity of their probe was too low to detect $^{204}Pb$, so no corrections were made for common Pb. Also Pb/U was not measured so there was no test for concordance. Both these shortcomings were addressed by Hinthorne et al. (1979). Using a prediction from the work of Andersen and Hinthorne (1973) that the secondary ion ratios $Pb^+/U^+$ and $UO^+/U^+$ should co-vary for any target of uniform Pb/U, they analyzed zircon grains from Proterozoic pegmatite from Ontario and Archean gneiss from the Stillwater complex against silicate and glass standards with known Pb and U contents. Because the ARL probe had low mass resolution it was necessary to make large corrections for molecular interferences. Further, $^{204}Pb$ was still below detection limits, so common Pb was corrected using the measured $^{208}Pb/^{206}Pb$ and Th/U. Nevertheless, the analyses agreed reasonably well with bulk zircon data from the two samples (Tilton et al. 1957), and one grain from the Stillwater gneiss gave a near-concordant composition 300 Ma older than the others, supporting the suggestion of Nunes and Tilton (1971) that the gneiss contained inheritance from an older terrane.

Hinton and Long (1979) reduced the effects of molecular interferences by operating their AEI ion microprobe at higher mass resolution (3200). They succeeded in measuring $^{204}Pb$, but the loss in sensitivity was such that each analysis took several hours. One of their samples, a gneiss from Lac Seul, Ontario, had previously been dated by Krogh et al. (1976) at 3040±40 Ma. The ion probe analyses showed the central regions of the zircons, some of which had visible discrete cores, to have higher average $^{207}Pb/^{206}Pb$ than the rims. The difference was interpreted to reflect the effects of metamorphism at ~2.7 Ga, the original age of the zircon being at least 3.3±0.1 Ga. Although later ID-TIMS dating of another sample by Corfu et al. (1995) yielded 3040±3 Ma, confirming the Krogh et al. (1976) result, the Hinton and Long (1979) analyses were the first direct evidence that an isotopic record of two stages of zircon growth could be preserved within individual crystals.

The need to achieve sufficient mass resolution to resolve molecular interferences (about 5000) without a major loss of sensitivity drove subsequent advances in ion microprobe design. The approach adopted by a group led by Bill Compston at the Australian National University was to use a larger analyzer magnet (1 m radius), which provided high mass resolution without the need to narrow the analyzer slits and cut secondary ion transmission. Commercial ion probe manufacturers followed the same course several years later. The project to build a Sensitive High-Resolution Ion Micro-Probe (SHRIMP) was initiated in 1974. Designed by Steve Clement, Gordon Newstead and Compston using a low-aberration ion optic configuration devised by Matsuda (1974), the first SHRIMP became operational in 1981. SHRIMP proved to be much more successful than its predecessors, a typical analysis taking about 20 minutes, and opened up a new chapter in zircon geochronology (Compston 1996, Williams 1998). It was a major contributor to the notable increase in the publication rate of U-Pb zircon papers after 1982 (Fig. 5).

Some of the first SHRIMP U-Pb analyses (Williams et al. 1983) were carried out on the same zircon crystals from Antarctic orthogneisses on which the low resolution ARL probe had measured ages of 1600-3500 Ma (Lovering et al. 1981), much older than those determined by Rb-Sr (950-1400 Ma). The SHRIMP results were consistent with the Rb-Sr data, validating concerns that the $^{207}Pb/^{206}Pb$ measurements by the ARL probe had been under-corrected for isobaric interferences and common Pb. Another early application was to date rare lunar zircon grains discovered in sawdust and thin sections from breccias (Compston et al. 1984). Of particular value were those zircon grains contained within minute lithic fragments, from which the source lithologies could be in-

ferred. Zircon as old as 4.37 Ga provided evidence for early solidification of the lunar magma ocean, a wide range of ages from 4.32 to 3.88 Ga in granopyhres recorded a protracted but episodic history of differentiated magmatism, and some cases of extreme discordance reflected late isotopic disturbance by large impactors (Meyer et al. 1996). Zircon from the Vaca Muerta mesosiderite, also dated in thin section, gave an age for meteorite formation near the beginning of the solar system, 4563±15 Ma (Ireland and Wlotzka 1992).

The high productivity of SHRIMP is ideally suited to studies of sediment provenance, in which it is necessary to date large numbers of grains individually (a minimum of 60 to have a 95% chance of sampling every component present at above 5% abundance). Searching for evidence of the oldest terrestrial crust, Froude analyzed hundreds of zircon grains from numerous early Archean quartz-rich metasedimentary rocks in the Murchison district of Western Australia, finding one quartzite at Mt. Narryer in which ~2.5% of the zircon had ages of 4.1-4.2 Ga (Froude et al. 1983), at the time more than 300 Myr older than the oldest-known terrestrial mineral. Given the checkered history of ion probe analysis the result was received with skepticism by some of the geoscience community (Moorbath, 1983), especially when single grain ID-TIMS analyses of zircon from the same rock failed to find any grains older than 3.5 Ga (Schärer and Allègre 1985). Further old grains were soon unearthed, however, in metasedimentary rocks at nearby Jack Hills (Compston and Pidgeon 1986 and Fig. 8), and the SHRIMP ages were confirmed by the zircon evaporation method (Kober et al 1989, method described below) and by ID-TIMS (Fanning and McCulloch 1990, Amelin 1998). The Murchison region remains the only place where such ancient remnants of the early Earth are known.

SHRIMP microsampling was also instrumental in the discovery of the oldest-known terrestrial rocks, the Acasta gneiss from the western Slave Province in the Northwest Territories, Canada. ID-TIMS analyses by Bowring et al. (1989a) of small zircon fractions and single grains from one Acasta sample yielded discordant analyses with a range of $^{207}Pb/^{206}Pb$ ages up to 3.83 Ga, clearly indicating the antiquity of the rock but only loosely defining its actual age. SHRIMP analyses showed the zircon grains to be a mixture of cores and rims, and zoned, structureless and altered domains, only a small portion of which recorded the primary crystallization age of 3962±3 Ma (Bowring et al. 1989b). Further ion probe work in the area (Stern and Bleeker 1998, Bowring and Williams 1999) has since located gneiss with ages up to 4031±3 Ma, but the complexity of the zircons is such that these ages have yet to be resolved by ID-TIMS.

A decade of development of SHRIMP I was followed by the introduction of SHRIMP II in

**Figure 8.** Bill Compston and Bob Pidgeon with a sample of Jack Hills conglomerate, taken at Curtin University in 1986.

1992. Improvements in the ion extraction optics gave the new instrument four times the sensitivity of its predecessor, Köhler focusing produced a more sharply defined, uniform primary ion beam, increasing the accuracy of the measurements of Pb/U, and better magnet design reduced analysis times. SHRIMP II was also a more versatile instrument, being designed to accept a Cs ion source for stable isotope analysis and a multiple collector. At about the same time, high-resolution ion microprobes manufactured by VG (Isolab 120) and Cameca (Cameca 1270) also became available. In 1998 a SHRIMP with even higher mass resolution, the SHRIMP RG, was brought on line, further expanding the scope for analyses free of isobaric interferences. The Cameca Nanosims 50 introduced in 2000 reduced the scale of isotopic analysis to sub-micron, but its accuracy and precision for geochronology at this scale have yet to be thoroughly evaluated.

High-resolution ion probes are now distributed in isotope laboratories throughout the world, but they are limited by their high price to major research institutions. Most are operated by consortia, many of which have strong links to government. The high productivity of the instruments is particularly attractive to government geological surveys, ion probe geochronology now being an integral part of regional geological mapping programs in several countries (e.g., Stern 1997). The body of ion microprobe data is now comparable to, or greater than, that of ID-TIMS.

High-resolution ion probes expanded the scope of U-Pb geochronology. Not only did the higher speed of analysis make it practical to date more samples and many more grains per sample, but the high spatial resolution made it possible to study individual grains containing several generations of growth. Studies of sediments, poly-metamorphosed rocks and polychronic inheritance flourished. For example, Pell et al. (1997) used the composite detrital zircon populations in desert dune sands from throughout Australia to determine the geographic regions from which the sands were derived, demonstrating unexpectedly that the principal sediment transport mechanism was water, not wind. Armstrong et al. (1990) showed that, contrary to earlier interpretations, the Barberton Greenstone Belt was not a simple stratigraphic succession, but part of an allochthonous sequence with major tectonic and stratigraphic breaks and inversions evolved in a tectonically active convergent environment. Taking the large scale approach, Kalsbeek and Nutman (1996) revealed the general history of an entire Greenland orogen in one week analyzing a few zircon grains from each of 90 samples, sketching out the principal tectonic units, their ages and metamorphic histories. Williams (1992) showed that inherited zircon in Paleozoic S-type granites from Australia was composite in age, the ages and relative abundances of the inherited components accurately matching those of detrital zircon populations in the host metasedimentary rocks.

Analysis of $^{207}Pb/^{206}Pb$ by ion probe is straightforward but measuring Pb/U isotopic ratios is more difficult because Pb and U have different secondary ionization efficiencies which change during each analysis. The efficiencies are also matrix dependent, so Pb/U and Pb/Th are measured relative to concordant reference minerals, a procedure currently reliable to about 1%. These reference standards must be dated independently by ID-TIMS. Early zircon work in the ANU lab was referenced to a U-rich Sri Lankan zircon megacryst, SL3. As techniques improved, this metamict crystal was replaced by another megacryst with lower U and more uniform composition, SL13 (Williams et al. 1988, Claoué-Long et al. 1995). This also proved heterogeneous on the microscale, however (Compston 1999), and has been abandoned except as a U concentration reference. As ion probe geochronology has expanded, so have attempts to identify minerals suitable for international standards, but reference minerals still remain largely laboratory specific. Fragments of zircon megacryst 91500 from a syenite complex near Kuehl Lake, Ontario (Wiedenbeck et al. 1995) have been widely distributed, but they are heterogeneous. The Australian geological survey (Geoscience Australia) and ANU now use zircon from a Paleozoic diorite (Temora; Black et al., submitted). ANU also uses zircon from the Duluth complex (Paces and Miller 1993), a standard also adopted in Stanford and at NIPR, Tokyo. SHRIMP and ID-TIMS groups continue to work together to intercompare and evaluate zircon standards (Roddick and van Breemen 1994, Black et al., submitted).

One of the most demanding applications of U-Pb geochronology is precise calibration of

fossil-based stratigraphic boundaries, the Paleozoic time scale. Questions about standardization as well as small-scale cryptic Pb loss and inheritance from zircons analyzed by SHRIMP versus ID-TIMS have been sources of argument between groups using each method (e.g., Compston and Williams 1992, Tucker and McKerrow 1995). Valid points have been raised on both sides. SHRIMP does have difficulty achieving better than 1% accuracy in Pb/U measurements, but it has demonstrated that zircon grains in volcanic rocks commonly are the product of igneous episodes of subtly different ages, an observation that is supported by ID-TIMS (Mundil et al. 2001, Oberli et al. 2002). Of further concern for accurate zircon dating of young volcanism, ion probe U-series disequilibrium studies of zircon from very young eruptive sequences show that magma chambers persist for hundreds of thousands of years, the zircon age of volcanic rocks recording not crystallization after eruption but an earlier time when the magma chamber became saturated in Zr (Reid et al. 1997).

The ion microprobe has advanced U-Pb geochronology, not only through instrumental improvements but also through a better understanding of zircon itself. It has been difficult to determine the closure temperature of zircon, mainly because Pb, U and Th diffuse so slowly in well-crystallized zircon that the rates are very difficult to measure (Cherniak et al. 1997). Operating SHRIMP II in depth profiling mode, Lee et al. (1997) were able to measure Pb, U and Th diffusion profiles only a few nanometers deep produced in chips of SL13 by laboratory heating experiments up to 1100°C. The volume diffusion closure temperature for a 100 μm diameter grain, determined mainly by the diffusivity of Pb, was calculated to be ~900°C, about 100°C less than diffusion closure temperatures later measured on natural and synthetic zircon by Cherniak and Watson (2000) using Rutherford backscattering. These results are in agreement with numerous observations that zircon is highly resistant to isotopic resetting at high-grade metamorphic and even magmatic temperatures. For example, Williams (2001) found the U-Pb ages of detrital zircon in a regionally metamorphosed turbidite sequence at Cooma, Australia, to be unaffected by metamorphism, even where that zircon survived only as cores in an anatectic granite (Fig. 9). There is evidence that in some situations the U-Pb closure temperature of zircon might be even higher. Kinny et al. (1989), for example, found Archean mantle zircons in Cretaceous kimberlites. Although the thermal history of the grains was not known, they inferred that the zircon had remained closed to diffusion of Pb and U at a temperature greater than 1100°C over billions of years. More convincing is the work of Möller and others (2002), who documented preservation of U-Pb ages in zircon subjected to dry contact metamorphism up to 950°C lasting at least 1 Myr, implying a diffusion closure temperature >1000°C.

The need for accurate targeting of SHRIMP analyses stimulated the development and application of methods for imaging chemical and structural zonation in zircon such as cathodoluminescence (CL) and backscattered electron (BSE). Such images reveal features such as cores, magmatic and metamorphic overgrowths and areas of recrystallization (Fig. 10). They also show up alteration, fractures and inclusions. Zoning patterns provide clues to the U content of each domain and the environment in which it formed. Sampling complex grains can pose a significant challenge to the ID-TIMS method but is a strength of the ion microprobe. In two early studies, Williams et al. (1984) and Black et al. (1986) showed that within the zircon from one sample of early Archean orthogneiss from the Napier complex, Antarctica, there were three distinct generations of zircon growth recording at least four thermal events that spanned 2 Gyr. Some zircon domains contained unsupported radiogenic Pb characterized by $^{207}Pb/^{206}Pb$ 'ages' older than the grains, probably resulting from intra-grain redistribution of radiogenic Pb during high-grade metamorphism. Gebauer et al. (1988) used CL imaging combined with SHRIMP dating to resolve ages of primary magmatic phases from older xenocrysts and younger metamorphic overgrowths in an eclogite. SHRIMP dating of cores and metamorphic overgrowths in single detrital zircons from Hercynian paragneisses produced concordant data with ages ranging from 3.84 Ga to 0.32 Ga (Gebauer et al. 1989). Bulk zircon dating on these rocks during the 1970s had produced quasi-linear arrays of discordant data similar to those measured on paragneisses from the Swiss Alps. The SHRIMP results resolved earlier debates over the interpretation of these arrays by showing that they resulted from mixtures of diverse

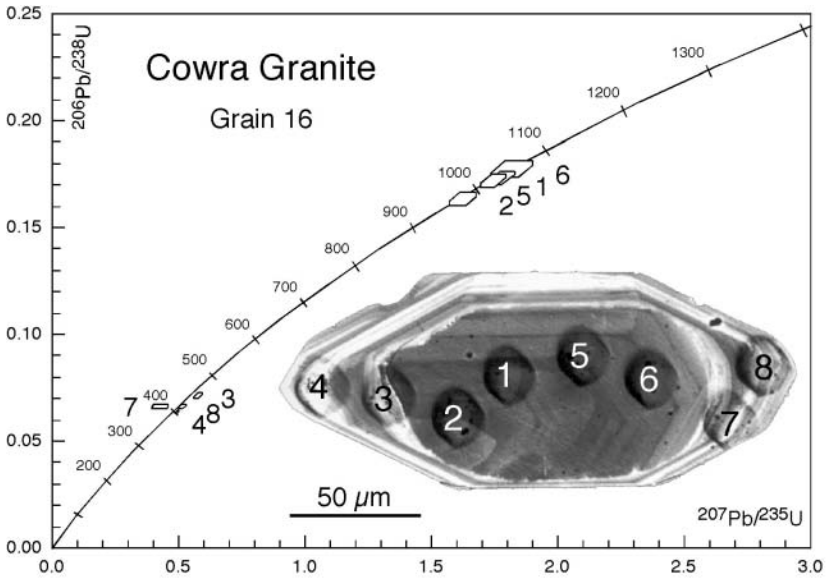


**Figure 9.** CL image of polyphase zircon from the Cowra granite, Australia, showing pits produced by the SHRIMP primary ion beam. Concordia data show that the overgrowth is about 600 Myr younger than the core.


**Figure 10.** Images of zircon from Archean gneisses in the Winnipeg River belt, NW Ontario, Canada. (A) BSE image of a grain with a core from a ca. 2700 Ma gneiss. BSE is sensitive to the average atomic number so trace element enriched areas are brighter. (B) CL image of the grain in A. CL is sensitive to both elemental composition and structural state. Emission is suppressed by radiation damage so areas that are bright in BSE are often dark in CL. (C) BSE image of a zircon from a 2880 Ma old gneiss with 3060 Ma inheritance. The overgrowth has been cracked by differential expansion of the higher U core. The core is altered (dark regions) and contains bright inclusions that are probably REE phosphate. (D) BSE image of zircon from the older gneiss with four phases of growth. Lower-U phases are preferentially cracked.

concordant ages rather than metamorphically induced Pb loss. Similarly, SHRIMP dating of individual zircon cores and overgrowths in granites intruding the Dalradian of Scotland (Pidgeon and Compston 1992) showed that the data arrays generated by earlier analyses of bulk zircon fractions (e.g., Pankhurst and Pidgeon 1976) were the result of mixing magmatic zircon with inherited cores that showed little evidence of Pb loss despite having been heated to magmatic temperatures (Fig. 3 inset).

Serious application of imaging really began in the early 1990s with the study by Vavra (1990), who produced high quality CL images of complex zircon structures and used these to interpret magmatic growth histories. This was an extension of earlier work by Pupin (1980) who had classified zircon morphologies and attempted to relate them to the temperature and composition of the host magma. High-quality BSE images of inherited cores in zircons that had been dated by SHRIMP were published by Paterson et al. (1992). Hanchar and Miller (1993) discussed the potential of BSE and CL imaging combined with SHRIMP as a tool for investigating complex growth histories due either to changes within the crystallization sequence or to episodic growth events that were sufficiently different in age to be dated separately. High-quality imaging was combined with SHRIMP dating to help define metamorphic P-T-t paths in the Swiss Alps by Gebauer (1996) and by Vavra et al. (1996). Schaltegger et al. (1999) studied metamorphic and igneous zircon in the Variscan belt of France using SHRIMP and ID-TIMS combined with CL imaging and intra-grain trace element studies. They found that zircon grew under granulite facies conditions at 335 Ma but was apparently reset during amphibolite facies overprinting about 10 Myr later by a process of annealing or recrystallization. This occurred at about 700°C, substantially below the normal closure temperature for volume diffusion of Pb. Unexpectedly, coexisting monazite, which was thought to have a lower closure temperature, was not reset. How and why zircon recrystallizes and is reset under some low temperature metamorphic conditions is not yet understood. Recrystallization fronts due to metamorphism and/or magmatic cooling have been documented by Hoskin and Black (2000) and by Pidgeon et al. (1998). Without the spatial resolution of the SHRIMP, such intra-grain structures would be difficult or impossible to date and there would be much less incentive to understand them.

The accuracy of SHRIMP microanalyses is achieved at the expense of precision, a consequence of the small number of ions available from the sampled volume. Age precisions from SHRIMP are normally 5 to 10 times worse per spot than they are from analyzing a whole grain by ID-TIMS. Uncertainty can be reduced by pooling analyses from different spots but the fact that the error varies inversely with the square-root of the number of analyses makes for a law of diminishing returns. Also, large individual uncertainties make it difficult to detect small amounts of secondary Pb loss or inheritance, either of which can bias the mean beyond its measured precision. On the other hand, the ion microprobe approach excels for complex zircons and/or where very high age-precision is not essential. For example, sufficient data can be acquired from detrital zircon populations to define statistically robust age populations, allowing the application of sophisticated numerical methods to study provenance (e.g., Sircombe 2000). Also, zircons for which a more precise age determination would be valuable (usually the youngest) can be removed from the mount and dated by ID-TIMS. The strengths of SHRIMP are largely complementary to those of ID-TIMS. Unfortunately, until recently a degree of competitiveness tended to prevail between their practitioners and the two techniques were largely developed and applied independently of each other. Early publications from the SHRIMP group often claimed a superiority over ‘conventional’ zircon dating. This was true by comparison with traditional bulk zircon methods. However early SHRIMP results often showed considerable discordance, because of difficulty in seeing alteration, and gave imprecise U/Pb ratios, because of difficulty with standardization, while advances in ID-TIMS methods had largely eliminated secondary discordance as a serious problem. Discordance ceased to be a problem with SHRIMP analyses as well once sampling became guided by high quality imaging of the grains. Competition between the two methods produced some interesting debates (e.g., Schärer and Allègre 1985, Corfu and Davis 1991) but was ultimately of little value to the progress of geochronology. The most effective strategy for dating complex terranes is to utilize the strengths of both.

### The zircon evaporation method

Kober (1986, 1987) developed a method for selective evaporation of Pb from single zircons at progressively higher temperature. Evaporation of Pb from single zircons had been experimented with earlier by Buchs et al. (1970) and Coppens et al. (1965) using a single filament. In the Kober method, Pb evaporated from zircon on a side filament is deposited on a blank center filament from which it can be re-evaporated. The effectiveness of this technique relies on the fact that zircon converts to $ZrO_2$ (baddeleyite) when it is heated (Chapman and Roddick 1994) releasing $SiO_2$, which acts as an ionization activator, as well as Pb. A wide rhenium side filament is wrapped partly around the sample grain and heated step-wise in the mass spectrometer. Evaporated silica and Pb are deposited on a cooler center filament which can then be re-heated to measure the Pb isotopic composition. The double filament approach gives greater stability of emission and more control of the evaporation process.

Like SHRIMP, this method dispenses with the necessity of chemical extraction but, most importantly, Pb in undamaged parts of the zircon evaporates at a higher temperature than Pb in altered or damaged domains. In partly altered zircons, the $^{207}Pb/^{206}Pb$ age can be seen to increase with temperature and the $^{204}Pb$ to decrease until a plateau is reached where $^{204}Pb$ is negligible. This should represent the age of the pure radiogenic component from undamaged domains and therefore the primary age of the zircon. Because the Pb is extracted at the atomic scale, even pervasively cracked zircons where unaltered domains would be too small for analysis by ID-TIMS or SHRIMP can theoretically be dated. A disadvantage of the method is that Pb/U information is lost. However, this may not be a severe problem for rocks having simple zircon populations. Demonstrating reproducibility of $^{207}Pb/^{206}Pb$ ages from different grains is probably a reliable test that the age is meaningful. Another disadvantage is that the small ion beams and the necessity for stepped analyses require large amounts of mass spectrometer time, sometimes as much as one day per sample. Results from the evaporation method may be unreliable if good measurement protocols are not followed in order to ensure that the labile Pb component is completely removed. Correctly applied, the method has produced reliable and moderately precise zircon ages from many rocks (e.g., Kröner et al. 1991, 1993).

### Other developments

Fission track dating of zircon will not be covered here except to say that it has been very useful for constraining thermal and uplift histories (Gleadow and Brooks 1979). It was developed over the same period as isotopic analysis and has produced a voluminous literature that would require a review on its own. Zircon also shows significant promise for thermoluminescence (TL) and optically stimulated luminescence (OSL) dating (Smith 1988), which are useful over archeological time scales.

Over the past two decades a number of other methods have been developed for drawing geological information from zircon. Dating by laser ablation – inductively coupled mass spectrometry (LA-ICPMS), where zircon is volatilized and U and Pb isotopes ionized in an inductively coupled plasma source followed by mass analysis in a quadrupole or multi-collector mass spectrometer, is still in a state of active development. This, along with studies of Hf and O isotopes, trace element compositions, and melt inclusions in zircon are reviewed elsewhere in this volume.

## THE LEGACY OF ZIRCON DATING

The first half-century of U-Pb geochronology was a time of fundamental discovery when the problem of dating was tied to broader questions about the nature of matter. At that time, the true breadth of geologic time was poorly understood. Isotopic dating of zircon subsequently began as an arcane and difficult art developed in large measure by physicists and chemists with an interest in geology. There followed an extended period of technical advances that vastly increased its capabilities. Smaller samples, more efficient ID-TIMS analytical protocols and the development of the SHRIMP broadened the range of rock samples that could be dated and made the method much more accessible. Dating zircons is still demanding but much less so than in the early days. Today most zircon geochronologists

are geologists by training who have adopted the method to help them with field-based studies.

The history of zircon geochronology illustrates some of the factors that drive, and in some cases retard, scientific progress. The general pattern of development is stepped rather than smooth: extended periods of application and refinement are interspersed by relatively brief periods of revolutionary advance. The early Pb-α method (1950-1957), was quickly replaced by isotope dilution (Tilton et al. 1955) but the next major advances required nearly 15 years until the silica gel ionization activator was widely adopted (Cameron et al. 1969) quickly followed by bomb dissolution, miniaturized column chemistry, and $^{205}$Pb spike (Krogh 1973). Subsequently, after about a decade of applications but few major advances in technique, zircon abrasion was introduced (Krogh 1982) at almost the same time as effective SIMS dating using the SHRIMP (Compston et al 1982). SIMS opened up a new approach to zircon dating and was followed by zircon evaporation (Kober 1986), a new branch of TIMS dating. Again, an extended period of applications followed accompanied by gradual refinements such as blank reduction in ID-TIMS and improvements in SIMS instrumentation. At present, LA-ICPMS has begun to emerge as a new technology that may eventually challenge earlier methods. Overcoming technical problems in mass spectrometer design was an obvious limiting factor in the progress of methods such as SIMS and LA-ICPMS, which have shown a measured and continuous advance in capabilities. Progress in ID-TIMS is less easily explained in this way since much of the technology necessary to eliminate secondary Pb loss and perform precise single grain analysis was available long before it was actually used. For example ionization activators (Akishin et al. 1957), the use of high-pressure Teflon dissolution capsule for dissolving minerals (Ito 1961) and picogram blank chemistry (Tera and Wasserburg 1975) were experimented with many years before they came to be perfected and widely adopted for zircon geochronology. With ID-TIMS the rate of progress seems to have depended more on psychological and philosophical factors and it is here that the 'revolutionary' pattern of progress shows most strongly.

An important factor in innovation was having the right research environment, a critical mass of researchers focused on zircon dating who were in a position to experiment, as well as the existence of personalities with the imagination to conceive new ways of doing things and the determination to perfect them. The perception of an impasse that existing methods could not overcome was perhaps the most important trigger for major advances. The Pb-α method had shown the potential of zircons for dating but workers must have been frustrated by the limitation in precision. This was greatly improved by the introduction of isotope dilution by the Chicago group, made possible by the availability of enriched isotopes from the nuclear program. There followed a long period of applications during which U-Pb geochronology started to be used, for the first time, as a practical method of detailed geologic investigation. The complications presented by discordance in zircon became obvious and understanding these occupied much of the subsequent research effort. The Caltech lab of Silver was active at this time and was particularly influential as Silver introduced mineralogy into the interpretation of zircon U-Pb ages, which laid the groundwork of present-day research on complex zircons. Despite the enormous amount of work involved in performing zircon analyses, there does not seem to have been a general ongoing effort to further improve techniques until the early 1970s at CIW. The CIW innovations greatly increased the number of zircon dates by making the analytical process more efficient in terms of time and sample consumption. There followed again a period of intense application but groups like ETH ran into problems of inheritance in Alpine zircons while others still found that accuracy of ages was limited by secondary Pb loss. Insightful studies by Steiger and Wasserburg (1966, 1969) and Grünenfelder (1964) suggested early on that zircon consists of a mixture of concordant and discordant phases. The logical conclusion is that one can eliminate discordance by identifying and isolating concordant phases. A wider appreciation of these observations might have provided an early impetus to isolate concordant phases and strive for the low blanks necessary to do precise single zircon work. Instead, for a long time efforts were more focused on debates over the nature and meaning of Pb loss and the most appropriate methods of data treatment. Ultimately, it was the failure of theory to produce consistent reliable

ages that created the impasse leading to developments such as abrasion, ultra-low blanks and SHRIMP. Perhaps the key lesson from this is that the urge to push measurements into new regions of sensitivity and precision is the most important force driving scientific progress.

The cumulative legacy of zircon dating is the precise calibration of most of geologic time. This is a great achievement resulting from the perseverance of many dedicated individuals. Its scientific value lies in the power to test geologic models and resolve controversies that commonly arise due to the incompleteness of the geologic record. Perhaps the best example is the impact of zircon dating on understanding the history and pace of evolution. Precise dating of volcanic ash beds by Tucker et al. (1990), Compston and Williams (1992) and others served to establish an absolute time scale for the paleontological record. By dating units that closely bracket era boundaries, Bowring has shown that the pace of evolution was explosive following major extinctions such as at the base of the Cambrian (Bowring et al. 1993). The greatest known mass extinction, the Permo-Triassic boundary, can now be correlated at the sub-million year level with the Siberian Traps, the largest known flood volcanic province (Bowring et al. 1998, this volume; Kamo et al. 1996, submitted). Unlike the earlier debate with Lord Kelvin, results from this work have gone against uniformitarianism. They have favored episodic evolutionary events associated with global catastrophes as the driving force for major evolutionary change. Thus, U-Pb dating continues to influence and modify Darwin's theory.

The rich chronological record revealed by zircons does not quite end at 4.0 Ga, the age of the oldest rocks. The Hadean eon remains almost hidden from direct observation, except for a single area in western Australia where zircons older than 4.0 Ga are preserved as detrital grains and xenocrysts. The oldest is now dated at 4404 Ma (Valley et al. 2002), only about 100 Myr younger than the massive collision that formed the Earth-Moon system. These zircons are our only window into the first 500 Myr of Earth's history. Their ages have been precisely established by U-Pb dating. The pre-history of crust-mantle differentiation reflected in their magmatic reservoirs has been studied using Hf isotopes (Amelin et al. 1999). Their O isotopes give tantalizing indications of an early hydrosphere (Mojzsis et al. 2001, Wilde et al. 2001), while mineral inclusions show that they were derived from granitoid rocks, a major component of continental crust (Maas et al. 1992). What a rich trove of information to be mined from such tiny specks of matter. Without zircon, the details of our planet's history would be mostly lost. We are indeed fortunate to have such a wonderful mineral.

## ACKNOWLEDGMENTS

The authors thank Fernando Corfu, George Tilton, Sandra Kamo and John Ketchum for comments on earlier versions of the manuscript. The reviewers Ken Ludwig, John Hanchar, and especially Bob Pidgeon are thanked for many helpful comments and suggestions. Important sources of information and inspiration for the present work were the historical introductions by Faure (1986) and Dickin (1995), reviews by Armstrong (1991), Heaman and Parrish (1991), and Gebauer and Grünenfelder (1979) as well as the compilation of historic papers with insightful comments by Harper (1973). The authors apologize for the emphasis on developments at JSGL and ANU, resulting from the fact that we are most familiar with these parts of the story. We have tried to cover the most influential advances in technique but the history of zircon geochronology is full of many other interesting developments and outstanding applied studies that, regretfully, we have not been able to include. We apologize for any other oversights and omissions resulting from our limited knowledge.

## REFERENCES

Ahrens, LH (1955a) The convergent lead ages of the oldest monazites and uraninites (Rhodesia, Manitoba, Madagascar, and Transvaal). Geochim Cosmochim Acta 7:294-300

Ahrens, LH (1955b) Implications of the Rhodesian age pattern. Geochim Cosmochim Acta 8:1-15

Akishin PA, Nikitin OT, Panchenkov GM (1957) A new effective ionic emitter for the isotopic analysis of lead. Geochemistry 5:500-505

Aldrich LT, Wetherill GW, Tilton GR, Davis GL (1956) Half-life of Rb-87. Phys Rev 103:1045-1047

Aldrich LT, Davis GL, James HL (1965) Ages of minerals from metamorphic and intrusive rocks near Iron Mountain, Michigan. J Petrol 6:445-472

Allègre CJ, Albarède F, Grünenfelder M, Köppel V (1974) $^{238}U/^{206}Pb$-$^{235}U/^{207}Pb$-$^{232}Th/^{208}Pb$ zircon geochronology in alpine and non-alpine environment. Contrib Mineral Petrol 43:163-194

Amelin Y (1998) Geochronology of the Jack Hills detrital zircons by precise U-Pb isotope dilution analysis of crystal fragments. Chem Geol 146:25-38

Amelin Y, Krot AN, Hutcheon ID, Ulyanov AA (2002) Pb isotopic ages of chondrules and Ca-Al rich inclusions. Science 297:1678-1683

Amelin Y, Lee D-C, Halliday AN, Pidgeon RT (1999) Nature of the Earth's earliest crust from hafnium isotopes in single detrital zircons. Nature 399:252-255

Andersen CA, Hinthorne JR (1972) U, Th, Pb and REE abundances and $^{207}Pb/^{206}Pb$ ages of individual minerals in returned lunar material by ion microprobe mass analysis. Earth Planet Sci Lett 14:195-200

Andersen CA, Hinthorne JR (1973) Thermodynamic approach to the quantitative interpretation of sputtered ion mass spectra. Anal Chem 45:1421-1438

Armstrong RA, Compston W, de Wit MJ, Williams IS (1990) The stratigraphy of the 3.5-3.2 Ga Barberton Greenstone Belt revisited: a single zircon ion microprobe study. Earth Planet Sci Lett 101:90-106

Armstrong RL (1991) A brief history of geochronometry and radiogenic isotopic studies. *In* Applications of radiogenic isotope systems to problems in geology. Heaman L, Ludden JN (eds) Mineral Assoc Can 19:1-26

Aston, FW (1929) The mass spectrum of uranium lead and the atomic weight of protactinium. Nature 123:313

Baadsgaard H (1973) U-Th-Pb dates on zircons from the early Precambrian Amitsoq gneisses, Godthaab district, West Greenland. Earth Planet Sci Lett 19:22-28

Barrell J (1917) Rhythms and the measurement of geologic time. Bull Geol Soc Am 28:745-904

Black LP, Kamo SL, Williams IS, Mundil R, Davis DW, Foudoulis C, Korsch RJ The application of SHRIMP to Phanerozoic geochronology; a critical appraisal of four zircon standards. In press Chem Geol

Black LP, Williams IS, Compston W (1986) Four zircon ages from one rock: the history of a 3,930 Ma-old granulite from Mount Scones, Enderby Land, Antarctica. Contrib Mineral Petrol 94:427-437.

Bohor BF, Betterton WJ, Krogh TE (1994) Impact-shocked zircons: discovery of shock-induced textures reflecting increasing degrees of shock metamorphism. Earth Planet Sci Lett 119:419-424

Boltwood BB (1907) On the ultimate disintegration products of the radioactive elements. Part II. The disintegration products of uranium. Am J Sci 23:77-88

Bowring SA, Erwin DH, Jin YG, Martin MW, Davidek K, Wang W (1998) U/Pb zircon geochronology and tempo of the End-Permian mass extinction. Science 280:1039-1045

Bowring SA, Grotzinger JP, Isachsen CE, Knoll AH, Pelechaty SM, Kolosov P (1993) Calibrating rates of Early Cambrian evolution. Science 261:1293-1298

Bowring SA, King JE, Housh TB, Isachsen CE, Podosek FA (1989a) Neodymium and lead isotope evidence for enriched early Archaean crust in North America. Nature 340:222-225

Bowring SA, Williams IS (1999) Priscoan (4.00-4.03 Ga) orthogneisses from northwestern Canada. Contrib Mineral Petrol 134:3-16

Bowring SA, Williams IS, Compston W (1989b) 3.96 Ga gneisses from the Slave province, Northwest Territories, Canada. Geology 17:971-975

Buchs A, Chessex R, Delaloye M, Landry J-C, Bertrand M, Vuagnat M (1970) U-Pb and Pb-Pb age determinations on zircons – Results obtained with a direct ionization method for the isotopic analysis of lead. Schweiz Mineral Petrogr Mitt 50:509-518

Cameron AE, Smith DE, Walker RL (1969) Mass spectrometry of nanogram size samples of lead. Anal Chem 41:525-526

Catanzaro EJ (1963) Zircon ages in southwestern Minnesota. J Geophys Res 68:2045-2048

Catanzaro EJ, Kulp JL (1964) Discordant zircons from the Little Belt (Montana), Beartooth (Montana) and Santa Catalina (Arizona) Mountains. Geochim Cosmochim Acta 28:87-124

Cattell A, Krogh TE, Arndt NT (1984) Conflicting Sm-Nd whole rock and U-Pb zircon ages for Archean lavas from Newton Township, Abitibi Belt, Ontario. Earth Planet Sci Lett 70:280-290

Chapman HJ, Roddick JC (1994) Kinetics of Pb release during the zircon evaporation technique. Earth Planet Sci Lett 121:601-611

Chakoumakos BC, Murakami T, Lumpkin GR, Ewing RC (1987) Alpha decay-induced fracturing in zircon: the transition from the crystalline to the metamict state. Science 236:1556-1559

Cherniak DJ, Watson EB (2000) Pb diffusion in zircon. Chem Geol 172:5-24

Cherniak DJ, Hanchar JM, Watson EB (1997) Diffusion of tetravalent cations in zircon. Contrib Mineral Petrol 127:383-390

Claoué-Long JC, Compston W, Cowden A (1988) The age of Kambalda greenstone resolved by ion microprobe: implication for Archean dating methods. Earth Planet Sci Lett 89:239-259

Claoué-Long JC, Compston W, Robersts J, Fanning CM (1995) Two Carboniferous ages: A comparison of SHRIMP

zircon dating with conventional zircon ages and $^{40}Ar/^{39}Ar$ analysis. *In* Geochronology, Time Scales and Global Stratigraphic Correlation. Benninghoven A, Evans CA, McKeegan KD, Storms HA, Werner HW (eds) Soc Sediment Geol Spec Publ 4:3-21
Compston W (1996) SHRIMP: origins, impact and continuing evolution. J Roy Soc West Austr 79:109-117
Compston W (1999) Geological age by instrumental analysis: the 29th Hallimond Lecture. Mineral Mag 63:297-311
Compston W, Pidgeon RT (1986) Jack Hills, evidence of more very old detrital zircons in Western Australia. Nature 321:766-769
Compston W, Williams IS (1992) Ion probe ages for the British Ordovician and Silurian stratotypes. *In* Global Perspectives on Ordovician Geology. Webby BD, Laurie JR (eds) Balkema, Rotterdam, p 59-67
Compston W, Williams, IS, Clement, SW (1982) U-Pb ages within single zircons using a sensitive high-resolution ion microprobe. Am Soc Mass Spectros 30th Conf, Honolulu, p 593-595
Compston W, Williams IS, Meyer C (1984) U-Pb geochronology of zircons from lunar breccia 73217 using a sensitive high mass-resolution ion microprobe. J Geophys Res 89 Supp, p B525-B534
Coppens R, Durand G, Roubault M (1965) Etude de l'age des zircons par le rapport des plombs 207 et 206. Sciences de la Terre 10:293-304
Corfu F (1989) Inverse age stratification in the Archean crust of the Superior Province: evidence for infra- and subcrustal accretion from high-resolution U-Pb zircon and monazite ages. Precambrian Res 36:259-275
Corfu F (1993) The evolution of the southern Abitibi greenstone belt in light of precise U-Pb geochronology. Econ Geol 88:1323-1340
Corfu F (2000) Extraction of Pb with artificially too-old ages during stepwise dissolution experiments on Archean zircon. Lithos 53:279-291
Corfu F, Ayres LD (1984) U-Pb ages and genetic significance of heterogeneous zircon populations in rocks from the Favourable Lake area, northwestern Ontario. Contrib Mineral Petrol 88:86-101
Corfu F, Ayres LD (1991) Unscrambling the stratigraphy of an Archean greenstone belt: a U-Pb geochronological study of the Favourable Lake Belt, northwestern Ontario, Canada. Precambrian Res 50:201-220
Corfu F, Davis DW (1991) Comment on the paper Archean hydrothermal zircon in the Abitibi greenstone belt: constraints on the timing of gold mineralization. Earth Planet Sci Lett 104:545-552
Corfu F, Stott GM, Breaks FW (1995) U-Pb geochronology and evolution of the English River Subprovince, an Archean low P-high T metasedimentary belt of the Superior Province. Tectonics 14:1220-1233
Davis DW (1982) Optimum linear regression and error estimation applied to U-Pb data. Can J Earth Sci 19:2141-2149
Davis DW, Blackburn CE, Krogh TE (1982) Zircon U-Pb ages from the Wabigoon-Manitou Lakes region, Wabigoon Subprovince, northwest Ontario. Can J Earth Sci 19:254-266
Davis DW, Krogh TE (2000) Preferential dissolution of $^{234}U$ and radiogenic Pb from α-recoil-damaged lattice sites in zircon: implications for thermal histories and Pb isotopic fractionation in the near surface environment. Chem Geol 172:41-58
Davis DW, Krogh TE, Hinzer J, Nakamura E (1985) Zircon dating of polycyclic volcanism at Sturgeon Lake and implications for base metal mineralization. Econ Geol 80:1942-1952
Davis DW, Poulsen KH, Kamo SL (1989) New insights into Archean crustal development from geochronology in the Rainy Lake area, Superior Province, Canada. J Geol 97:379-398
Davis DW, Sutcliffe RH, Trowell NF (1988) Geochronological constraints on the tectonic evolution of a late Archean greenstone belt, Wabigoon Subprovince, northwest Ontario, Canada. Precambrian Res 39:171-191
Davis GL, Hart SR, Tilton GR (1968) Some effects of contact metamorphism on zircon ages. Earth Planet Sci Lett 5:27-34
Dempster AJ (1918) A new method of positive ray analysis. Phys. Rev 11:316-325
Dempster AJ (1935) Isotopic composition of uranium. Nature 136:180
Dickin AP (1995) Radiogenic Isotope Geology. Cambridge University Press, Cambridge, UK, 490 p
Dunning GR, Krogh TE (1985) Geochronology of ophiolites of the Newfoundland Appalachians. Can J Earth Sci 22:1659-1670
Durand G (1962) Méthode permettant de mesurer directement au spectrmètre de masse leas rapports isotopiques du plomb contenu dans les traces de pechblende sans traitemnt chimique préalable. C R Acad Sci 254:1032-34
Ellsworth HV (1931) Uraninite from Henvey Township, Parry Sound district, Ontario. Am Mineral 16:576-579
Ewing RC, Chakoumakos BC, Lumpkin GR, Murakami T (1987) The metamict state. Mater Res Soc Bull 12:58-66
Fajans K (1913) Radioactive transformations and the periodic system of the elements. (in German) Berichte der Deutschen Chemischen Gesellschaft 46:422-439
Fanning CM, McCulloch MT (1990) A comparison of U-Pb isotopic systematics in early Archaean zircons using isotope dilution thermal ionization mass spectrometry and the ion-microprobe. *In* Glover JE, Ho SE (eds) Third Intl Archaean Symp, Extended Abstr, Perth, p 15-17
Faure G (1986) Principals of Isotope Geology, 2nd edn. J Wiley & Sons, New York, 589 p
Fenner CN, Piggot CS (1929) The mass-spectrum of lead from broggerite. Nature 123:793-794
Fleming EH, Ghiorso A, Cunningham BB (1952) The specific activities and half-lives of $U^{234}$, $U^{235}$, $U^{236}$. Phys Rev 88:642-652

Froude DO, Ireland TR, Kinny PD, Williams IS, Compston W, Williams IR, Myers JS (1983) Ion microprobe identification of 4,100-4,200 Myr-old terrestrial zircons. Nature 304:616-618

Gariépy C, Allègre CJ, Lajoie J (1984) U-Pb systematics in single zircons from the Pontiac metasediments, Abitibi greenstone belt. Can. J. Earth Sci 21:1296-1304

Gastil RG, De Lisle M, Morgan JR (1967) Some effects of progressive metamorphism on zircons. Geol Soc Am Bull 78:879-905

Gaudette HE, Vitrac-Michard A, Allègre CJ (1981) North American Precambrian history recorded in a single sample: high-resolution U-Pb systematics of the Potsdam sandstone detrital zircons, New York State. Earth Planet Sci Lett 54:248-260

Gebauer D (1996) a P-T-t path for an (ultra?-) high-pressure ultramafic/mafic rock-association and its felsic country-rocks based on SHRIMP dating of magmatic and metamorphic zircon domains. Example: Alpe Arami (central Swiss Alps). *In* Earth Processes: Reading the Isotopic Code. Basu A, Hart S (eds) American Geophysical Union Geophys Monogr 95:307-329

Gebauer D, Grünenfelder M (1976) U-Pb zircon and Rb-Sr whole rock dating of low-grade metasediments. Example: Montagne Noire (southern France). Contrib Mineral Petrol 59:13-32

Gebauer D, Grünenfelder M (1979) U-Th-Pb dating of minerals. *In* Lectures in Isotope Geology. Jäger E, Hunziker JC (eds) Springer-Verlag, Berlin, p 105-131

Gebauer D, Quadt A, Compston W, Williams IS, Grünenfelder M (1988) Archean zircons in a retrograded, Caledonian eclogite of the Gotthard Massif (Central Alps, Switzerland). Schweiz Mineral Petrogr Mitt 68:485-490

Gebauer D, Williams IS, Compston W, Grünenfelder M (1989) The development of the central European continental crust since the Early Archean based on conevntional and ion-microprobe dating of up to 3.84 b.yr. old detrital zircons. Tectonophysics 157:81-96

Gerling EK (1942) Age of the Earth according to radioactivity data. Doklady (Proc Russian Acad Sci) 34:259-261

Gleadow AJW, Brooks CK (1979) Fission track dating, thermal histories and tectonics of igneous intrusions in East Greenland. Contrib Mineral Petrol 71:45-60

Goldich SS, Mudrey MG (1972) Dilatancy model for discordant U-Pb ages. *In* Contributions to Recent Geochemistry and Analytical Chemistry. Tugarinov AI (ed) Nauka Publ Office, Moscow, p 415-418

Grauert B, Arnold A (1968) Deutung diskordanter Zirkonalter der Silrettadecke und des Gotthardsmassivs (Schweizer Alpen). Contrib Mineral Petrol 20:34-56

Grauert B, Hanny R, Soptrajanova G (1973) Age and origin of detrital zircons from the pre-Permian basements of the Bohemian Massif and the Alps. Contrib Mineral Petrol 40:105-130

Grosse Av (1932) On the origin of the actinium series of radioactive elements. Phys Rev 42:565-570

Grünenfelder M (1963) Heterogenität akzessorischer Zirkone und die petrographische Deutung ihrer Uran/Blei-Zerfallsalter I. Der Zirkon des Granodioritgneises vanAcquacalda (Lukmanierpass). Schweiz Mineral Petrogr Mitt 43:235-257

Grünenfelder M, Hofmanner F, Grogler N (1964) Heterogenität akzessorischer Zirkone und die petrographische Deutung ihrer Uran/Blei-Zerfallsalter II. Präkambrische Zirconbildung im Gotthardmassiv. Schweiz Mineral Petrogr Mitt 44:543-558

Gulsen BL, Krogh TE (1973) Old lead components in the young Bergell Massif, south-east Swiss alps. Contrib Mineral Petrol 40:239-252

Hanchar JM, Miller CF (1993) Zircon zonation patterns as revealed by cathodoluminescence and backscattered electron images: implications for interpretation of complex crustal histories. Chem Geol 110:1-13.

Harper CT (1973) Geochronology: radiometric dating of rocks and minerals. Harper CT (ed) Benchmark Papers in Geology Series, Dowden, Hutchinson and Ross Inc., Stroudsburg, Pa., 469 p.

Hart SR, Aldrich LT, Davis GL, Tilton GR, Baadsgaard H, Kuovo O, Steiger RH (1963) Geochronology and isotope geology. Carnegie Inst Washington Yrbk 62:264-280

Hart SR, Davis GL (1969) Zircon U-Pb and whole rock Rb-Sr ages and early crustal development near Rainy Lake, Ontario. Bull Geol Soc Am 80:595-616

Hayden RJ, Reynolds JH, Inghram MG (1949) Reactions induced by slow neutron irradiation of europium. Phys Rev 75:1500-1507

Heaman LM 1989 The nature of the subcontinental mantle from Sr-Nd-Pb isotopic studies on kimberlitic perovskite Earth Planet Sci Lett 92:323-334

Heaman LM, LeCheminant AN (1993) Paragenesis and U-Pb systematics of baddeleyite ($ZrO_2$). Chem Geol 110:95-126

Heaman LM, McNutt RH, Krogh TE (1986) Geological significance of U-Pb and Rb-Sr ages for two pre-tectonic granites from the Central Metasedimentary Belt, Ontario. *In* The Grenville Province. Moore JM, Davidson A, Baer AJ (eds) Geol Assoc Canada Spec Paper 31:209-221

Heaman L, Parrish R (1991) U-Pb geochronology of accessory minerals. *In* Applications of radiogenic isotope systems to problems in geology. Heaman L, Ludden JN (eds) Mineral Assoc Can Short Course Handbook 19:59-102

Hillebrand WF (1890) On the occurance of nitrogen in uraninite and on the composition of uraninite in general. Am J Sci 140:384-394

Hinthorne JR, Andersen CA, Conrad RL, Lovering JF (1979) Single-grain $^{207}Pb/^{206}Pb$ and U/Pb age determinations with a 10-μm spatial resolution using the ion microprobe mass analyzer (IMMA). Chem Geol 25:271-303
Hinton RW, Long JVP (1979) High-resolution ion microprobe measurement of lead isotopes: variations within single zircons from Lac Seul, northwestern Ontario. Earth Planet Sci Lett 45:309-325
Holland HD, Gottfried D (1955) The effect of nuclear radiation on the structure of zircon. Acta Crystallogr 8:291-300
Holmes A (1911) The association of lead with uranium in rock-minerals, and its application to the measurement of geologic time. Proc Roy Soc (London) 85A:248-256
Holmes A (1937) The origin of primary lead ores. Econ Geol 32:763-782.
Holmes A (1946) An estimate of the age of the Earth. Nature 157:680-684
Holmes A, Lawson RW (1927) Factors involved in the calculation of the ages of radioactive minerals. Am J Sci 13:327-344
Hoskin PWO, Black LP. (2000) Metamorphic zircon formation by solid-state recystallization of protolith igneous zircon. J Metamor Geol 18:423-439
Houtermans FG (1946) Die Isotopenhaufigkeiten im Naturlichen Bloi und das Alter des Urans. Naturwissenschaften 33:185-186
Hurley PM, Fairbairn HW (1953) Radiation damage in zircon. Geol Soc Am Bull 64:659-674
Ireland TR, Wlotzka F (1992) The oldest zircons in the solar system. Earth Planet Sci Lett 109:1-10
Ito J (1961) A new method of decomposition for refractory minerals and its application for the determination of ferrous iron and alkalies. Scientific papers of the College of General Education, University of Tokyo 11:47-68
Jaffey AH, Flynn KF, Glendenin LE, Bentley WC, Essling AM (1971) Precision measurement of half-lives and specific activities of $^{235}U$ and $^{238}U$. Phys Rev C4:1889-1906
Joly J (1909) Radioactivity and Geology. Archibald Constable & Co, London
Kalsbeek F, Nutman AP (1996) Anatomy of the Early Proterozoic Nagssugtoqidian orogen, West Greenland, explored by reconnaissance SHRIMP U-Pb zircon dating. Geology 24:515-518
Kamo SL, Czamanske GK, Amelin Y, Fedorenko VA, Davis DW, Trofimov VR Rapid eruption of Siberian flood-volcanic rocks, coincident with the Permian-Triassic boundary and mass extinction at 251 Ma. Earth Planet Sci Lett (submitted)
Kamo SL, Czamanske GK, Krogh TE (1996) A minimum U-Pb age for Siberian flood-basalt volcanism. Geochim Cosmochim Acta 60:3505-3511
Kamo SL, Gower CF, Krogh TE (1989) A birthdate for the lapetus Ocean? A precise U-Pb zircon and baddeleyite age for the Long Range dikes, southeast Labrador. Geology 17:602-605
Kamo SL, Krogh TE (1995) Chicxulub crater source for shocked zircon crystals from the Cretaceous-Tertiary boundary layer, Saskatchewan: evidence from new U-Pb data. Geology 23:281-284
Keevil NB (1939) The calculation of geologic age. Am J Sci 237:195-214
Kinny PD, Compston W, Bristow JW, Williams IS (1989) Archean mantle xenocrysts in a Permian kimberlite: two generations of kimberlitic zircon in Jwaneng DK2, southern Botswana. *In* Kimberlites and Related Rocks. Ross J (ed) Geol Soc Austral Spec Publ 14:833-842
Kober B (1986) Whole-grain evaporation for $^{207}Pb/^{206}Pb$ age investigations on single zircons using a double-filament thermal ion source. Contrib Mineral Petrol 93:482-490
Kober B (1987) Single-grain evaporation combined with $Pb^+$ emitter bedding for $^{207}Pb/^{206}Pb$ age investigations using thermal ion mass spectrometry, and implications to zirconology. Contrib Mineral Petrol 96:63-71
Kober B, Pidgeon RT, Lippolt HJ (1989) Single zircon dating by stepwise Pb-evaporation constrains the Archean history of detrital zircons from Jack Hills, Western Australia. Earth Planet Sci Lett 91:286-296
Köppel V, Grünenfelder M (1971) A study of inherited and newly formed zircons from paragneisses and granitized sediments of the Strona-Cerneri-Zone (Southern Alps). Schweiz Mineral Petrogr Mitt 51:385-409
Kosztolanyi C (1965) Nouvelle méthode d'analyse isotopique des zircons à l'état. C R Acad Sci 260:5849-5851
Krogh TE (1973) A low contamination method for hydrothermal decomposition of zircon and extraction of U and Pb for isotopic age determinations. Geochim Cosmochim Acta 37:485-494
Krogh TE (1978) Vapour transfer for the dissolution of zircons in a multi-sample capsule, at high pressure. *In* Short Papers, Fourth Intl Conf Geochron Cosmochron Iso Geol, U S Geol Surv Open-File Rep 78-701:233-234
Krogh TE (1982a) Improved accuracy of U-Pb ages by selection of more concordant fractions using a high-gradient magnetic separation technique. Geochim Cosmochim Acta 46:631-635
Krogh TE (1982b) Improved accuracy of U-Pb ages by the creation of more concordant systems using an air abrasion technique. Geochim Cosmochim Acta 46:637-649
Krogh TE (1993) High-precision U-Pb ages for granulite metamorphism and deformation in the Archean Kapuskasing Structural Zone, Ontario: Implications for structure and development of the lower crust. Earth Planet Sci Lett 119:1-18
Krogh TE (1994) Identification of concordant zircons using etch techniques. Abstr Eighth Intl Conf Geochron Cosmochron Iso Geol, US Geol Surv Circular 1107:180
Krogh TE, Corfu F, Davis DW, Dunning GR, Kamo SL, Greenough J, Nakamura E (1987) Precise U-Pb isotopic ages of diabase dykes and gabbros using trace baddeleyite. *In* Mafic Dyke Swarms. Halls HC, Fahrig WH (eds) Geol Assoc Canada Spec Paper 33:147-152

Krogh TE, Davis GL (1973) The effect of regional metamorphism on U-Pb systems in zircon and a comparison with Rb-Sr systems in the same whole rock and its constituent minerals. Carnegie Inst Washington Yrbk 72:601-605
Krogh TE, Davis GL (1974) Alteration in zircons with discordant U-Pb ages. Carnegie Inst Washington Yrbk 73:560-567
Krogh TE, Davis GL (1975a) The production and preparation of 205Pb for use as a tracer for isotope dilution analyses. Carnegie Inst Washington Yrbk 74:416-417
Krogh TE, Davis GL (1975b) Alteration in zircons and differential dissolution of altered and metamict zircon. Carnegie Inst Washington Yrbk 74:619-623
Krogh TE, Davis DW, Corfu F (1984) Precise U-Pb zircon and baddeleyite ages for the Sudbury area. *In* The Geology and Ore Deposits of the Sudbury Structure. Pye EG, Naldrett AJ, Giblin, PE (eds) Ontario Geol Surv Spec Vol 1:431-446
Krogh TE, Harris NBW, Davis GL (1976) Archean rocks from the eastern Lac Seul region of the English River gneiss belt, northwestern Ontario: Part 2. Geochronology. Can J Earth Sci 13:1212-1215
Krogh TE, Kamo SL, Bohor BF (1993) Fingerprinting the K/T impact site and determining the time of impact by U-Pb dating of single shocked zircons from distal ejecta. Earth Planet Sci Lett 119:425-429
Krogh TE, Kamo SL, Bohor B (1996) Shock metamorphosed zircons with correlated U-Pb discordance and melt rocks with concordant protolith ages indicate an impact origin for the Sudbury Structure. *In* Earth Processes: Reading the Isotopic Code. Basu A, Hart S (eds) Am Geophys Union Geophys Monogr 95:343-353
Krogh TE, Kamo SL, Kwok YY (2002) An isotope dilution etch-abrasion solution to the Akilia Island U-Pb age controversy. Abstr 12th annual V.M. Goldschmidt Conf, Davos, Switzerland, Aug 18-23, Geochim Cosmochim Acta Spec Suppl, p A419
Kröner A, Byerly GR, Lowe DR (1991) Chronology of early Archean granite-greenstone evolution in the Barberton Mountain Land, South Africa, based on precise dating by single zircon evaporation. Earth Planet Sci Lett 103:41-54
Kröner A, Zwand GW, Sun Y (1993) Granulites in the Tongbai area, Qinling belt, China: geochemistry, petrology, single zircon geochronology, and implications for the tectonic evolution of eastern Asia. Tectonics 12:245-255
Kulp JL, Bate GL, Broecker WS (1954) Present status of the lead method of age determination. Am J Sci 252:345-365
Kulp JL, Volchock HL, Holland HD (1952) Age from metamict minerals. Am Mineral 37:709-718
Kuovo O, Tilton GR (1966) Mineral ages from the Finnish Precambrian. J Geol 74:421-442
Lancelot J, Vitrac A, Allegre, CJ (1976) Uranium and lead isotopic dating with grain-by-grain isotopic analysis. Earth Planet Sci Lett 29:357-366
Larsen ES, Keevil NB, Harrison HC (1952) Method for determining the age of igneous rocks using the accessory minerals. Geol Soc Am Bull 63:1045-1052
LeCheminant AN, Heaman LM (1989) Mackenzie igneous events, Canada: Middle Proterozoic hotspot magmatism associated with ocean opening. Earth Planet Sci Lett 96:38-48
LeDent D, Patterson C, Tilton GR (1964) Ages of zircon and feldspar concentrates from North American beach and river sands. J Geol 72:112-122
Lee JKW, Tromp J (1995) Self-induced fracture generation in zircon. J.Geophys Res B 100:17753-17770
Lee JKW, Williams IS, Ellis DJ (1997) Pb, U and Th diffusion in natural zircon. Nature 390:159-162
Lovering JF, Travis GA, Comaford DJ, Kelly PR (1981) Evolution of the Gondwana Archaean shield: Zircon dating by ion microprobe, and relationships between Australia and Wilkes Land, Antarctica. *In* Glover JE, Groves DI (eds) Archaean Geology. Geol Soc Austral Spec Pub 7:193-203
Ludwig KR (1980) Calculation of uncertainties of U-Pb isotopic data. Earth Planet Sci Lett 46:212-220
Ludwig KR (1998a) On the treatment of concordant uranium-lead ages. Geochim Cosmochim Acta 62:665-676
Ludwig KR (1998b) Using the ISOPLOT/Ex version 1.00b—a geochronological toolkit for Microsoft Excel. Berkeley Geochronology Center Spec Publ 1, 43 p.
Ludwig KR (2001) Eliminating mass-fractionation effects on U-Pb isochron ages without double spiking. Geochim Cosmochim Acta 65:3139-3145
Ludwig KR, Lindsley DA, Zielinski RA, Simmons KR (1980) U-Pb ages of uraniferous opal and implication for the history of beryllium, fluorine and uranium mineralization at Spor Mountain, Utah. Earth Planet. Sci. Lett. 46:221-232
Ludwig KR, Stuckless JS (1978) Uranium-Lead isotope systematics and apparent ages of zircons and other minerals in Precambrian granitic rocks, Granite Mountains, Wyoming. Contrib Mineral Petrol 65:243-254
Maas R, Kinney PD, Williams IS, Froude DO, Compston W (1992) The Earth's oldest known crust: A geochronological and geochemical study of 3900-4200 Ma old detrital zircons from Mt. Narryer and Jack Hills, Western Australia. Geochim Cosmochim Acta 56:1281-1300
Mattinson JM (1971) Preparation of ultra-pure HF, HCl, and $HNO_3$. Carnegie Inst Washington Yrbk 70:266-268
Mattinson JM (1987) U-Pb ages of zircons: a basic examination of error propagation. Chem Geol 66:151-162
Mattinson JM (1994) A study of complex discordance in zircons using step-wise dissolution techniques. Contrib Mineral Petrol 116:117-129
Matsuda H (1974) Double focusing mass spectrometers of second order. Intl J Mass Spectrom Ion Phys 14:219-233
Merrihue C, Turner G (1966) Potassium-argon dating by activation with fast neutrons. J Geophys Res 71:2852-2857

Meyer C, Williams IS, Compston W (1996) U-Pb ages for lunar zircons: evidence for a prolonged period of granophyre formation from 4.32 to 3.88 Ga. Meteor Planet Sci 31:370-387
Michard-Vitrac M, Lancelot J, Allègre CJ (1977) U-Pb ages on single zircons from the early Precambrian rocks of west Greenland and the Minnesota River Valley. Earth Planet Sci Lett 35:449-453
Mojzsis SJ, Harrison TM, Pidgeon RT (2001) Oxygen-isotope evidence from ancient zircons for liquid water at the Earth's surface 4,300 Myr age. Nature 409:178-181
Möller A, O'Brien PJ, Kennedy A, Kröner A (2002) Polyphase zircon in ultrahigh-temperature granulites (Rogaland, SW Norway): constraints for Pb diffusion in zircon. J Metamor Geol 20:727-740
Moorbath S (1983) The most ancient rocks? Nature 304:585-586
Moorbath S, O'Nions RK, Pankhurst RJ, Gale NH, McGregor, VR (1972) Further rubidium-strontium age determinations on the very early Precambrian rocks of the Godthaab district, West Greenland. Nature Phys Sci 240:78-82
Mundil R, Metcalfe I, Kudwig KR, Renne PR, Oberli F, Nicoll RS (2001) Timing of the Permian-Triassic biotic crisis: implications from new zircon U/Pb age data (and their limitations). Earth Planet Sci Lett 187:131-145
Nicolaysen LO (1957) Solid diffusion in radioactive minerals and the measurement of absolute age. Geochim Cosmochim Acta 11:41-59
Nier AO (1938) Variations in the relative abundances of the isotopes of common lead from various sources. J Am Chem Soc 60:1571-1576
Nier AO (1939a) The isotopic composition of uranium and the half-lives of the uranium isotopes. I. Phys Rev 60:150-153
Nier AO (1939b) The isotopic constitution of radiogenic leads and the measurement of geologic time. II. Phys Rev 55:153-163
Nier AO (1981) Some reminiscences of isotopes, geochronology and mass spectrometry. Ann Rev Earth Planet Sci 9:1-17
Nier AO, Thompson RW, Murphy BF (1941) The isotopic constitution of lead and the measurement of geologic time. III. Phys Rev 55:112-116
Nunes PD, Thurston PC (1980) Two hundred and twenty million years of Archean evolution: a zircon U-Pb age stratigraphic study of the Uchi-Confederation Lakes greenstone belt, northwestern Ontario. Can J Earth Sci 17:710-721
Nunes PD, Tilton GR (1971) Uranium-lead ages of minerals from the Stillwater Igneous Complex and associated rocks, Montana. Bull Geol Soc Am 82:2231-2250
Oberli F, Bachmann O, Meier M, Dungan MA (2002) The Fish Canyon tuff: Ar-Ar versus U-Pb age discrepancy reassessed. Abstr 12$^{th}$ annual V.M. Goldschmidt Conf, Davos, Switzerland, Aug 18-23, Geochim Cosmochim Acta Spec Suppl, p A565
Paces JB, Miller JD (1993) Precise U-Pb ages of Duluth complex and related mafic intrusions, northeastern Minnesota: geochronological insights into physical, petrogenetic, paleomagnetic and tectonomagmatic processes associated with the 1.1 Ga Midcontinent Rift system. J. Geophys Res 98B:13997-14013
Pankhurst RJ, Pidgeon RT (1976) Inherited isotope systems and the source region pre-history of early Caledonian granites in the Dalradian series of Scotland. Earth Planet Sci Lett 31:35-68
Parrish RR (1987) An improved micro-capsule for zircon dissolution in U-Pb geochronology. Chem Geol 66:99-102
Parrish RR, Krogh TE (1987) Synthesis and purification of $^{205}$Pb for U-Pb geochronology. Chem Geol 66:103-110
Pasteels P (1964) Mesures d'ages sur les zircons de quelques roches des Alpes. Schweiz Mineral Petrogr Mitt 44:519-541
Paterson BA, Stephens WE, Rogers G, Williams IS, Hinton RW, Herd DA (1992) The nature of zircon inheritance in two granite plutons. Trans Roy Soc Edinburgh: Earth Sci 83:459-471
Patterson C (1956) Age of meteorites and the Earth. Geochim Cosmochim Acta 10:230-237
Pell SD, Williams IS, Chivas AR (1997) The use of protolith zircon-age fingerprints in determining the protosource areas for some Australian dune sands. Sed Geol 109:233-260
Percival JA, Krogh TE (1983) U-Pb zircon geochronology of the Kapuskasing Structural Zone and vicinity in the Chapleau-Foleyet area, Ontario. Can J Earth Sci 20:830-843
Pidgeon RT (1969) Zircon U-Pb ages from the Galway granite and the Dalradian, Connemara, Ireland. Scott J Geol 5:375-392
Pidgeon RT, Compston W (1992) A SHRIMP ion microprobe study of inherited and magmatic zircons from four Scottish Caledonian granites. Trans Roy Soc Edinburgh: Earth Sci 83:473-483
Pidgeon RT, Johnson MRW (1974) A comparison of zircon U-Pb and whole rock Rb-Sr systems in three phases of the Carn Chuinneag granite, northern Scotland. Earth Planet Sci Lett 24:105-112
Pidgeon RT, Köppel V, Grünenfelder M (1970) U-Pb isotopic relationships in zircon suites from a para- and orthogneiss from the Ceneri zone, southern Switzerland. Contrib Mineral Petrol 26:1-11
Pidgeon RT, Nemchin AA, Hitchen GJ (1998) Internal structures of zircons from Archean granites from the Darling Range batholith: implications for zircon stability and the interpretation of zircon U-Pb ages. Contrib Mineral Petrol 132:288-299
Pidgeon RT, O'Neil JR, Silver LT (1966) Uranium and lead isotopic stability in a metamict zircon under experimen-

tal hydrothermal conditions. Science 154:1538-1540
Pidgeon RT, O'Neil JR, Silver LT (1973) Observations on the crystallinity and the U-Pb isotopic system of a metamict Ceylon zircon under experimental hydrothermal conditions. Fortschr Mineral 50:118
Poldervaart A, Eckelmann FD (1955) Growth phenomena in zircon of autochthonous granites. Geol Soc Am Bull 66:947-948
Pupin JP (1980) Zircon and granite petrology. Contrib Mineral Petrol 73:207-220
Ramsay W, Soddy F (1903) Experiments in radioactivity and the production of helium from radium. Proc Roy Soc 72:204-207
Reid MR, Coath CD, Harrison TM, McKeegan KD (1997) Prolonged residence times for the youngest rhyolites associated with Long Valley Caldera: $^{230}$Th-$^{238}$U ion microprobe dating of young zircons. Earth Planet Sci Lett 150:27-39
Richards JP, Krogh TE, Spooner ETC (1988) Fluid inclusion characteristics and U-Pb rutile age of late hydrothermal alteration at the Musoshi stratiform copper deposit, Central African copper belt, Zaire. Econ Geol 83:118-139
Roddick JC (1987) Generalized numerical error analysis with applications to geochronology and thermodynamics. Geochim Cosmochim Acta 51:2129-2135
Roddick JC, Loveridge WD, Parrish RR (1987) Precise U-Pb dating of zircon at the sub-nanogram level. Chem Geol 66:111-121
Roddick JC, van Breemen O (1994) U-Pb zircon dating: A comparison of ion probe and single grain conventional analyses. *In* Radiogenic Age and Isotopic Studies, Report 8. Geol Surv Canada Current Res 1994-F, p 1-9
Rogers G, Dempster TJ, Bluck BJ, Tanner PWG (1989) A high-precision U-Pb age for the Ben Vuirich granite: implications for the evolution of the Scottish Dalradian supergroup. J Geol Soc London 146:789-798
Rose JL, Stranathan RK (1936) Geologic time and isotopic composition of radiogenic lead. Phys Rev 50:792-796.
Rutherford E (1905a) Radium—the cause of the Earth's heat. Harper's Mag 6:390
Rutherford E (1905b) Present problems in radioactivity. Popular Sci Monthly 57:1-34.
Rutherford E (1929) Origin of actinium and the age of the Earth. Nature 123:313-314
Rutherford E, Soddy F (1902) The cause and nature of radioactivity. Phil Mag 4:370-396
Rutherford E, Soddy F (1903) Radioactive change. Phil Mag 5:576-591
Schaltegger U, Fanning CM, Gunther D, Maurin JC, Schulmann K, Gebauer D (1999) Growth, annealing and recrystallization of zircon and preservation of monazite in high-grade metamorphism: conventional and *in situ* U-Pb isotope, cathodoluminescence and microchemical evidence. Contrib Mineral Petrol 134:186-201
Schärer U, Allègre CJ (1982a) Investigation of the Archean crust by single-grain dating of detrital zircon: a greywacke of the Slave Province, Canada. Can J Earth Sci 19:1910-1918
Schärer U, Allègre CJ (1982b) Uranium-lead system in fragments of a single zircon grain. Nature 295:585-587
Schärer U, Allègre CJ (1985) Determination of the age of the Australian continent by single grain analysis of Mt. Narryer metaquartzite. Nature 315:52-55
Shukolyukov YuA (1964) Interpretation of discordant ages calculated from the isotopic ratios: $Pb^{206}/U^{238}$ and $Pb^{207}/U^{235}$. Geochem Intl 1:843-852
Silver LT, Deutsch S (1963) Uranium-lead isotopic variations in zircons: a case study. J Geol 71:721-758.
Sircombe KN (2000) Quantitative comparison of large data sets of geochronological data using multivariate analysis: A provenance study example from Australia. Geochim Cosmochim Acta 64:1593-1616
Smith BW (1988) Zircon from sediments: a combined OSL and TL autoregenerative dating technique. Q Sci Rev 7:401-406
Soddy F (1913) Intra-atomic charge. Nature 92:399-400
Steiger RH, Wasserburg GJ (1966) Systematics in the $Pb^{208}$-$Th^{238}$, $Pb^{207}$-$U^{235}$, and $Pb^{206}$-$U^{238}$ systems. J Geophys Res 71:6065-6090
Steiger RH, Wasserburg GJ (1969) Comparative U-Th-Pb systematics in $2.7\times10^9$ yr plutons of different geologic histories. Geochim Cosmochim Acta 33:1213-1232
Stern RA (1997) The GSC sensitive high-resolution ion microprobe (SHRIMP): analytical techniques of zircon U-Th-Pb age determinations and performance evaluation. Geol Surv Canada–Current Res, p 1-31.
Stern RA, Bleeker W (1998) Age of the world's oldest rocks refined using Canada's SHRIMP: The Acasta gneiss complex, Northwest Territories, Canada. Geosci Can 25:27-31
Stern TW, Goldich SS, Newell MF (1966) Effects of weathering on the U-Pb ages of zircon from the Morton gneiss, Minnesota. Earth Planet Sci Lett 1:369-371
Stern TW, Newell MF, Kistler RW (1965) Zircon uranium-lead and thorium-lead ages and mineral potassium-argon ages from the La Sal Mountains rocks, Utah. J Geophys Res 70:1503-1507.
Stockwell CH (1982) Proposals for time classification and correlation of Precambrian rocks and events in Canada and adjacent parts of the Canadian Shield. Part 1: A time classification of Precambrian rocks and events. Geol Surv Canada Paper 80-19, 135 p
Strutt RJ (1909) The accumulation of helium in geologic time III. Proc Roy Soc 83A:298-301.
Tatsumoto M, Patterson P (1964) Age studies of zircon and feldspar concentrates from the Franconia sandstone. J

Geol 72:232-242.
Tera F, Wasserburg GJ (1972) U-Th-Pb systematics in three Apollo 14 basalts and the problem of initial Pb in lunar rocks. Earth Planet Sci Lett 14:281-304
Tera F, Wasserburg GJ (1975) Precise isotopic analysis of lead in picomole and subpicomole quantities. Anal Chem 47:2214-2220
Thompson W (1899) The age of the Earth as an abode fitted for life. Phil Mag 47:66-90
Tilton GR (1960) Volume diffusion as a mechanism for discordant lead ages. J Geophys Res 65:2933-2945
Tilton GR, Davis GL, Wetherill GW, Aldrich LT (1957) Isotopic ages of zircon from granites and pegmatites. Trans Am Geophys Union 38:360-371
Tilton GR, Patterson C, Brown H, Inghram M, Hayden R, Hess D, Larsen E (1955) Isotopic composition and distribution of lead, uranium and thorium in a Precambrian granite. Geol Soc Am Bull 66:1131-1148
Tucker RD, Krogh TE, Ross RJ, Williams SH (1990) Time-scale calibration by high-precision U-Pb zircon dating of interstratified volcanic ashes in the Ordovician and Lower Silurian stratotypes of Britain. Earth Planet Sci Lett 100:51-58
Tucker RD, McKerrow WS (1995) Early Paleozoic chronology: a review in light of new U-Pb zircon ages from Newfoundland and Britain. Can J Earth Sci 32:368-379.
Valley JW, Cavosie AJ, Graham CM, King EM, Peck WH, Wilde SA (2002) Zircon evidence of the earliest Archean crust: 4.0-4.4 Ga. Abstr 12th annual V.M. Goldschmidt Conf, Davos, Switzerland, Aug 18-23, Geochim Cosmochim Acta Special Supplement, p A794
Van Schmus WR, Bickford ME, Turek A (1996) The Proterozoic geology of the east-central Miidcontinent basement. *In* Basement and Basins of Eastern North America. van der Pluijm BA, Catacosinos PA (eds) Geol Soc Am Spec Paper 308:7-32
Vavra G (1990) On the kinematics of zircon growth and its petrogenetic significance: a cathoodoluminescence study. Contrib Mineral Petrol 106:90-99
Vavra G, Gebauer D, Schmid R, Compston W (1996) Multiple zircon growth and recrystallization during polyphase Late Carboniferous to Triassic metamorphism in granulites of the Ivrea zone (Southern Alps): an ion microprobe (SHRIMP) study. Contrib Mineral Petrol 122:337-358
Wasserburg GJ (1954) Argon$^{40}$/potassium$^{40}$ dating. *In* Nuclear Geology. Faul H (ed) Wiley & Sons, New York, p 341-349
Wasserburg GJ (1963) Diffusion processes in lead-uranium systems. J Geophys Res 68:4823-4846
Webber GR, Hurley PM, Fairbairn HW (1956) Relative ages of eastern Massachusetts granites by total lead ratios in zircon. Am J Sci 254:574-583
Wendt JI, Todt W (1991) A vapour digestion method for dating single zircons by direct measurement of U and Pb without chemical separation. Terra Abstr 3:507-508
Wetherhill GW (1956a) Discordant uranium-lead ages, I. Trans Am Geophys Union 37:320-326
Wetherhill GW (1956b) An interpretation of the Rhodesia and Witwatersrand age patterns. Geochim Cosmochim Acta 9:290-292
Wetherill GW (1963) Discordant uranium-lead ages—Part 2: Discordant ages resulting from diffusion of lead and uranium. J Geophys Res 68:2957-2965
Wetherill GW, Wasserburg GJ, Aldrich LT, Tilton GR, Hayden RJ (1956) Decay constants of K-40 as determined by the radiogenic argon content of potassium minerals. Phys Rev 103:1045-1047
Wiedenbeck M, Allé P, Corfu F, Griffin WL, Meier M, Oberli F, von Quadt A, Roddicj JC, Spiegel W (1995) Three natural zircon standards for U-Th-Pb, Lu-Hf, trace element and REE analyses. Geostandards Newsletter 19:1-23
Wilde SA, Valley JW, Peck WH, Graham CM (2001) Evidence from detrital zircons for the existence of continental crust and oceans on the Earth 4.4 Gyr ago. Nature 409:175-178.
Williams HS (1893) The elements of the geological time scale. J Geol 1:283-295
Williams IS (1992) Some observations on the use of zircon U-Pb geochronology in the study of granitic rocks. Trans Roy Soc Edinburgh 83:447-458
Williams IS (1998) U-Th-Pb geochronology by ion microprobe. Rev Econ Geol 7:1-35
Williams IS (2001) Response of detrital zircon and monazite, and their U-Pb isotopic systems, to regional metamorphism and host rock partial melting, Cooma Complex, southeastern Australia. Austral J Earth Sci 48:557-580
Williams IS, Compston W, Black LP, Ireland TR, Foster JJ (1984) Unsupported radiogenic Pb in zircon: A case of anomalously high Pb-Pb, U-Pb and Th-Pb ages. Contrib Mineral Petrol 88:322-327
Williams IS, Compston W, Collerson KD, Arriens PA (1983) A reassessment of the age of the Windmill metamorphics, Casey area. *In* Oliver RL, James PR, Jago JB (eds) Antarctic Earth Science. Austral Acad Sci, Canberra, p 73-76
Williams IS, Compston W, Foster JJ, Page RW, McColloch MT (1988) The comparison of conventional and SHRIMP ion probe ages. Abstr, First Australian Conference on Geochronology, Canberra, p 1
York D (1969) Least-squares fitting of a straight line with correlated errors. Earth Planet Sci Lett 5:320-324

# Zircon U-Th-Pb Geochronology by Isotope Dilution — Thermal Ionization Mass Spectrometry (ID-TIMS)

**Randall R. Parrish[1,2] and Stephen R. Noble[2]**

[1] *Department of Geology, University of Leicester*
[2] *NERC Isotope Geosciences Laboratories Keyworth, Notts., NG12 5GG, United Kingdom*
r.parrish@nigl.nerc.ac.uk

## INTRODUCTION

ID-TIMS is the acronym for Isotope Dilution Thermal Ionization Mass Spectrometry. This refers to the addition of an isotope tracer to a dissolved sample to make a homogeneous isotopic mixture, and the measurement of isotopic composition of the mixture using a thermal ionization mass spectrometer. The method is one of the most accurate and precise methods of isotopic techniques because it is relatively insensitive to chemical yields or mass spectrometric sensitivity. It is a method very widely applied both in earth and many other areas of science involving the measurement of element or isotope concentrations and isotopic ratios.

The ID-TIMS technique was first applied to the U-Th-Pb dating of zircon in the 1950s (Tilton et al. 1955, Wetherill 1956, Tilton et al. 1957), exploiting the general availability to academia of enriched uranium isotopes developed in the 1940s and 1950s related to nuclear energy research. ID-TIMS has remained the main foundation to zircon geochronology ever since, in spite of the proliferation of other analytical methodologies. In the past 50 years, many improvements have been made and they have contributed to the maturity and reliability of the method. As a method, it was effectively unchallenged until the 1980s when secondary ionization mass spectrometry (Anderson and Hinthorne 1972) was further developed and applied to zircon geochronology by W. Compston and colleagues at the Australian National University (Compston et al. 1984). The instrument developed by the ANU group (SHRIMP, or Sensitive High Resolution Ion Microprobe) and the associated measurement protocols facilitated measurement of Pb/U isotopic ratios within a small region of a single zircon grain, and it proved to be a powerful tool to address complex age structure of multi-component zircons. In the 1990s, laser ablation quadrupole ICP-MS methods came on stream and offered an alternate way to make intra-grain U-Th-Pb isotopic measurements. The advent of double-focusing ICP-MS instruments has offered much better measurement precision compared to quadrupole machines, and while still developing, they have yet to make quite the same impact, though many current laboratories are working to close the gap with SIMS methods.

There has been an unfortunate tendency for advocates of TIMS on the one hand and SIMS on the other to unfairly criticize each other's methodology, or at least the ways those methodologies have been applied to zircon geochronology. While this trend has decreased in recent years it is reflected in some of the literature and can give a biased impression of the *complementary* capabilities of both methods, often ignoring the strengths and weaknesses of the alternative. It is imperative that students of zircon geochronology become more aware of the capabilities of all useful methods, so that when confronted with a problem to solve, they know how to design their measurement experiment. The lack of a comprehensive textbook means we must rely on individual research and review papers and our own abilities at synthesis to gain a reasonable understanding of the field. As an alternative, short courses can be very effective at bringing the views of experts together, as this and other volumes (Heaman and Parrish 1991) attempt to do.

1529-6466/03/0053-0007$05.00

A great range of geochronological problems can be addressed effectively with either ID-TIMS or intra-grain microbeam techniques (SIMS or LA-ICP-MS). While this is the case for many applications, some problems are best-solved using ID-TIMS methods and vice-versa. This chapter describes TIMS methods and it comments on the strengths and weaknesses of method variations, using examples of zircon dating mainly from the literature. Naturally it will pay special attention to those applications where ID-TIMS analysis is preferred, if not essential, and it will portray the field of U-Th-Pb geochronology using ID-TIMS as having a very bright future in modern earth science.

## METHODS AND DATA PRESENTATION

### Background

Zircon is a refractory mineral, being very difficult to destroy both in nature where it can survive many cycles of sedimentation, metamorphism and melting, and in the laboratory where it is one of the most difficult of all minerals to dissolve for analysis.

The crystal structure favors the incorporation of uranium and thorium in typically modest amounts (10-1000 ppm U, 1-100 ppm Th), and it virtually excludes Pb from its structure during crystallization and many other elements (Speer 1982). Its U/Pb ratio upon formation is therefore extremely high.

By the particularly useful quirk of nature, two long-lived radioactive uranium isotopes, $^{238}$U and $^{235}$U, decay to different isotopes of Pb ($^{206}$Pb and $^{207}$Pb, respectively), while $^{232}$Th decays to $^{208}$Pb. A fourth Pb isotope, $^{204}$Pb has no radioactive parent and its abundance in the earth has effectively not changed with time except for addition from bolide impacts. This isotope system provides the framework for U-Th-Pb geochronology using U- and Th-bearing accessory minerals, with zircon being the most frequently used due to its widespread occurrence in rocks of the continental crust.

The ID-TIMS U-Pb zircon method relies upon measurement of the isotopic composition of U and Pb. Even decades ago using less sophisticated mass spectrometers than are available today, it was possible to make these isotopic measurements to a precision better than 0.1%. Given the nature of the U-Pb isotopic system with its two uranium isotopes of differing rate of decay, this means that it is theoretically possible to measure the age of a zircon to better than ca. ±1-2 Ma throughout all of geological time, which makes the system unique to all isotopic chronometers. Thus, the method of zircon dating has long been applied to geological problems to study the rates of detailed processes, and it has been especially pivotal to the unraveling of the history of the earth in the Precambrian because of the lack of biostratigraphic control.

### Evolution of analytical methods

The first methods of U-Th-Pb isotopic analysis using ID-TIMS on zircon were conducted in the 1950s (Tilton et al. 1955, 1957; Wetherill 1956) and involved the flux-assisted decomposition of zircon, the use of tracers enriched in $^{208}$Pb, $^{230}$Th, and $^{235}$U, and analysis on custom-built mass spectrometers without computer control. The paper by Tilton et al. (1955) is seminal and includes methodology, the first isotopic ages, and additional analyses of sphene and other minerals. In the 1960s and 1970s, improvements to vacuum systems, computer-controlled data acquisition, the very limited availability of $^{205}$Pb tracer (Krogh and Davis 1975), the use of sub-boiling Teflon® stills for acid distillation (Mattinson 1972) and high temperature decomposition of zircon (Krogh 1973) allowed several laboratories to make important progress in methodology. These improvements resulted in significant decrease in contamination levels and sample size.

A period of major expansion took place in the 1980s when commercially-available mass spectrometers, new synthesis of $^{205}$Pb (Parrish and Krogh 1987), and other laboratory improvements including air abrasion (Krogh 1982) and multiple ion collection using mixed detector arrays (Roddick et al. 1987) came on stream. Together, these improvements allowed the routine analysis of single zircons containing sub-nanogram quantities of Pb, leading to better data quality, greater

concordance of zircon U-Pb data, and improved interpretations. Other minerals became part of the mainstream (monazite, allanite, baddeleyite, titanite) and served further to improve the understanding of U-Th-Pb systematics (Heaman and Parrish 1991). Important milestones in these methods will be discussed below.

***Sample selection and preparation.*** There are two important aspects about zircon that set this mineral apart from all other accessory phases. The first was alluded to earlier and is its refractory nature and the resultant difficulty with which it is fully recycled by dissolution in magmatic or metamorphic systems. The enduring aspect of the mineral has led to the frequent preservation of older components within magmatic or metamorphic grains and the formation and preservation of composite zircon grains with multiple age components, reflected in the Concordia diagram as discordant analyses. Examples of the complexity of zircon are abundant in the literature (e.g., Ashwal et al. 1999, Connelly 2000). The second distinguishing aspect of zircon is the paradoxical ease with which it is capable of losing Pb at relatively low temperatures, a non-diffusive process that is related broadly to accumulated radiation damage (Geisler et al. 2002). It can be shown that there are physicochemical differences between different zircon crystals, and even between different domains within a single zircon, that result in variable degrees of Pb-loss.

In some scientific investigations it is desirable to make measurements on materials without any pre-selection of samples, i.e., rigorously avoiding biasing what is analyzed. Conversely, it turns out that being able to bias what one analyzes by ID-TIMS is extremely important in obtaining high-precision and high-accuracy ages because one does not seek to determine the average age and its standard deviation. Clearly, one does not have to be a rocket scientist to realize that the isotopic imprint of the physical complexity of some zircons is likely to be equally complex, and therefore complex zircons require cautious, and often complex interpretation of the U-Pb systematics. The spectrum of differing degrees of Pb loss is

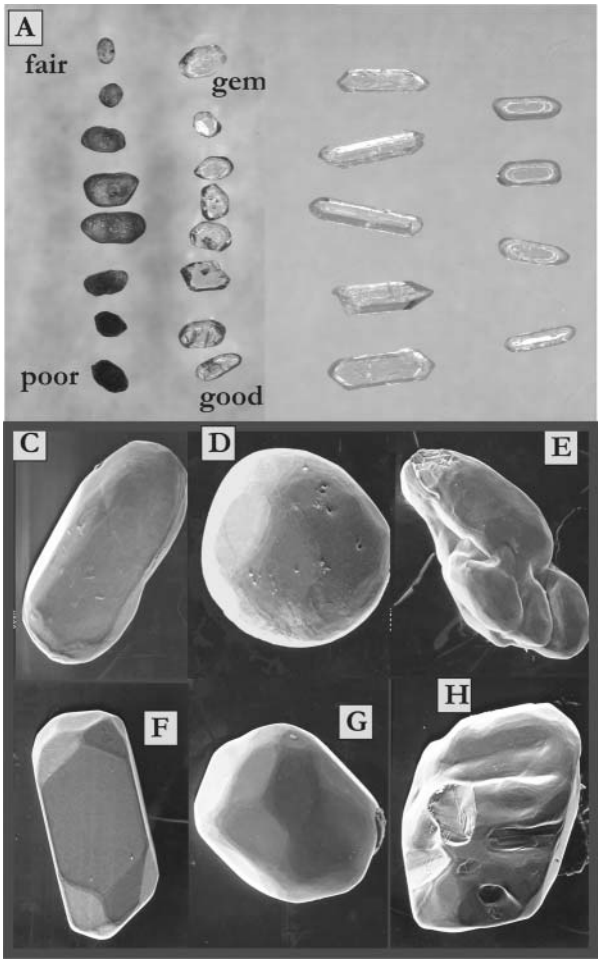


**Figure 1.** Collage of zircon photomicrographs. (A) Two columns of zircons illustrating ranges of quality of crystals, from poor to gem quality; these crystals were from beach sand adjacent garnet-rich granulite facies paragneiss and orthogneiss. (B) Two columns of Mesozoic igneous zircons showing a comparison of original euhedral shapes with those following a moderately air abrasion treatment. (C) Secondary electron (SE) image of resorbed igneous zircon. (D) Very round metamorphic zircon from paragneiss. (E) Composite zircon grain formed by the welding together of several smaller grains by a metamorphic overgrowth. (F) Euhedral zircon morphology from a migmatitic leucosome. (G) Metamorphic zircon from paragneiss showing traces of crystal facets. (H) Annedral metamorphic zircon from sillimanite-grade paragneiss showing 'casts' of minerals around which zircon has grown.

not surprising when one considers the wide range of crystal quality (Fig. 1a).

Since the first U-Th-Pb zircon measurements of Tilton et al. (1955), it was clear that the two U-Pb decay systems do not always reveal the same age—that is, they are discordant. Furthermore, in many early studies the Th-Pb system appeared to often be somewhat decoupled from the U-Pb system and more difficult to interpret. The simplest explanation was that Pb loss had taken place at some time in the past, and this phenomenon was thought to be associated with the accumulation of radiation damage within the crystal structure. Silver and Deutsch (1963) realized that magnetic susceptibility could be used in some cases to distinguish between relatively high- and low-U zircons. Relatively low-U zircons have less radiogenic Pb, but are better suited for analysis because there is less radiation damage and generally less Pb-loss. This latter attribute outweighs the greater difficulty in analyzing low levels of U and Pb on a mass spectrometer and is effective in improving the concordance of analyses, but not eliminating it. Following Silver and Deutsch's study it was generally accepted that pre-selection of the best crystals from a large population was a necessary component of ID-TIMS work.

While the two coupled U-Pb decay systems allowed one to work out the original age of crystallization from discordant zircon analyses (Wetherill 1956), the Th-Pb system often failed to provide additional insight. For these reasons as well as the difficulty of Th mass spectrometry relative to U arising from poorer thermal ionization, the $^{232}$Th-$^{208}$Pb system was rarely measured.

In 1982 Krogh (1982) made another major improvement in ID-TIMS geochronology whereby a method of air abrasion designed to remove the outer portion of grains was presented. The notion was that the Pb loss was likely to be more abundant in the outer portions of grains exposed over eons to fluids. Krogh showed in this and later papers how to reduce or eliminate discordance (arising mainly from low temperature Pb loss) with air abrasion of high quality, crack-free, visually clear zircons. Figure 1b shows examples of un-abraded and abraded crystals, the latter giving results consistent with closed system behavior.

This abrasion technique has been available now for 20 years, having become standard procedure in nearly all ID-TIMS zircon geochronology laboratories, and the improvement in results is undeniably impressive. This is one of if not *the* most important technique development in zircon geochronology, in spite of the improvements in computer and mass spectrometer wizardry. The attention to detail of the sample characteristics—the quality of grains and the quality of the abrasion—made a huge difference to results.

While the presence of internal multi-age complexity can be daunting to sort out, the careful preparation of high quality abraded grains for analysis allows their complex compositions to be established, notwithstanding subsequent Pb loss. Air abrasion has been a key procedure in allowing ID-TIMS to address the dating of complex crystals, a task that is clearly well suited to alternative micro-beam techniques that can sample single components within grains.

A further development in sample preparation took place by Mattinson (1994) whereby zircon was subjected to an aggressive HF–$HNO_3$ acid-leaching procedure to partially dissolve relatively soluble portions of grains. The enhanced solubility was thought to be related to radiation damage and other crystal imperfections, and has a relationship to uranium and thorium concentration and of course age. Experiments clearly showed in many cases that the first stages of leachate contained evidence of more soluble radiogenic Pb, and that if further steps were performed, the residue was likely to be more concordant than the original crystal. Several recent detailed studies showed that the procedure could in certain cases produce artifacts (Corfu 2000, Davis and Krogh 2000, Chen et al. 2002). Sample-tracer equilibration has been shown to be a problem in the dissolution of fluorides from the leachate, and in some samples $^{206}$Pb appears to be more soluble than $^{207}$Pb, potentially linked to the variable energies of decay for each radioactive parent isotope. The HF leaching procedure is a less mature alternate preparation technique than air abrasion; it has been only occasionally adopted (Mundil et al. 2000). An example of this will be mentioned below.

Finally, an example of a thoughtful, but common sense approach has again come from Krogh

(1998) in an application to the very old rocks of West Greenland that have seen so much attention from isotope geochemists and geochronologists (e.g., Whitehouse et al. 1999, 2001; Nutman et al. 2000, 2001). In this procedure, he first used etching (NaOH; HF can also be used) to induce partial dissolution in order to 'screen' grains for their relative damage from radiation accumulation. The least affected grains were then selected and air abraded to fully remove the leached portions. These abraded grains then yielded mainly concordant data that fell into several age clusters, rather than the more diffuse and discordant pattern of ages of many previous studies. This appears to be a particularly useful approach that should be widely applicable to studies of older rocks.

The study of zircon grains using optical and/or scanning electron (back-scattered, secondary, and cathodoluminescence) microscopy is paramount to a correct interpretation of U-Pb analyses (Vavra 1990, Paterson et al. 1992, Hanchar and Miller 1995). Many studies have highlighted the variable internal and external morphological characteristics produced during geological process. These include magmatic growth and resorption, metamorphic growth and resorption in the solid state, occlusion of grains within other crystals, reaction textures and intergrowths with other phases, and the partial dissolution of external surfaces. Magmatic morphologies in themselves are quite varied and in part indicative of geological environments, residence time, and temperature of crystallization. This subject is beyond the scope of this chapter, but Figure 1 provides the reader with a sampling of the variety of textures. Needless to say, the geological setting of the sample (state of deformation and metamorphism, for example) is equally vital to linking the isotopic measurements to a sensible interpretation.

## Mass spectrometry

Thermal ionization mass spectrometers have been used for making Pb and U isotope measurements for over 50 years. The long-lived viability of this analytical technique is the product of a number of key attributes. These are: reasonable ionization efficiency, a simple mass spectrum, excellent signal to noise characteristics, relatively small-order mass fractionation, negligible Pb and U contamination of samples by the instrument, and the lack of reliance on mineral standards in the calibration process. Remarkably, modern instruments are all founded upon the design principles of Alfred Nier's early mass spectrometers (e.g., Nier 1940). Nevertheless, significant advances have been necessary in achieving the current state-of-the-art performance. A crucial advance for U-Pb geochronology has been the use of silica gel and phosphoric acid as an exceptionally efficient and stable Pb+ (and $UO_2^+$) ion emitter (Cameron et al. 1968). The silica gel method has only evolved modestly over the past 35 years with most of the improvements relating to lowering of U and Pb contents in the gel and increasing ionization efficiency by up to an order of magnitude (Gerstenberger and Hasse 1996). Emission stability is crucial because it facilitated the easy use of peak-switching of U and Pb isotopes on single collector mass spectrometers, a practice still widely applied. The advent of commercially available mass spectrometers with multiple arrays of faraday detectors in ca. 1981-82, usually supplemented by an axial electron multiplier detector, permitted the more rapid acquisition of isotopic ratios of increased precision, with a more efficient duty cycle (Roddick et al. 1987). Some laboratories also routinely used simultaneous collection of isotopes using both faraday and electron multiplier detectors, allowing large increases in data production. For several laboratories these improvements, in conjunction with miniaturization of chemistry and using a mixed $^{205}Pb$-$^{235}U$±$^{233}U$ tracer resulted in an increase of productivity by up to 5-10 fold within a few years. The differences between the measurement state of the art now and that in 1985-90 are relatively unimportant, mainly being a reduction in Pb blank levels from 5-20 picograms to less than 1 picogram in the chemical procedure.

## Advances in chemical procedures and tracers

***Of Teflon and tracers.*** The modern era of U-Pb zircon dating was ushered in by developments of T. Krogh and J. Mattinson at the Carnegie Institute of Washington. Mattinson adapted FEP and TFE Teflon©-ware to the distillation and production of ultra-pure acids that resulted in a large de-

crease in levels of Pb contamination (Mattinson 1972). Krogh made two advances during this era. First he used Teflon capsules in a steel pressure vessel at ca. 210°C to decompose zircon with low contamination, and followed this with a simple HCl-based chromatographic separation (Krogh 1973), this being a much cleaner procedure than flux decomposition. Second, along with workers at Carnegie and the U.S. Oak Ridge National Laboratory, he synthesized $^{205}$Pb via the cyclotron-produced (p,2n) reaction on $^{206}$Pb via short-lived $^{205}$Bi for use in a routine mixed tracer with $^{235}$U (Krogh and Davis 1975). While not the first instance of production of $^{205}$Pb (the other being by neutron capture on $^{204}$Pb followed by calutron isotope separation, this tracer was widely and routinely applied and set a standard to which others aspired.

In 1987 Parrish and Krogh (1987) repeated the experiment to synthesize $^{205}$Pb using the Canadian cyclotron facilities of the TRIUMF physics consortium, but on a larger scale. Figure 2c shows the silver cyclotron target containing plated enriched $^{206}$Pb, subsequently bombarded with ca. 27 MeV protons to produce $^{205}$Bi, that subsequently decayed to $^{205}$Pb with a 14-day half-life. Figure 2d

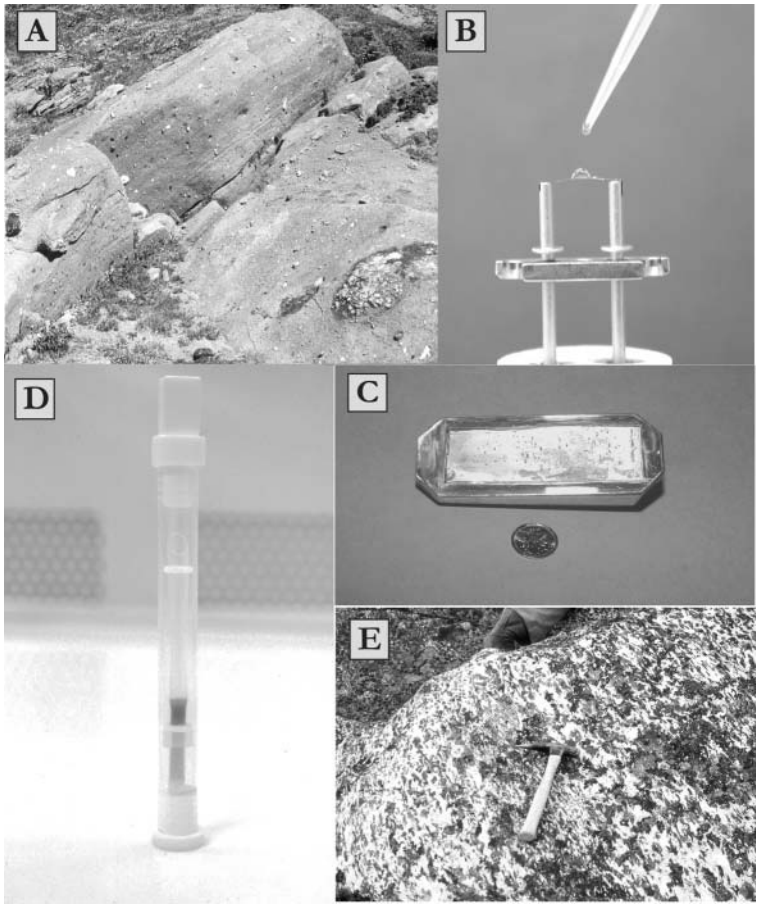


**Figure 2.** Montage of images relevant to this chapter. (A) Photograph of crystalline carbonate rock representing a metamorphosed pyroclastic carbonatite from which metamorphic zircons were extracted. (B) Outgassed Re filament upon which a drop of sample dissolved in phosphoric acid and a silica gel suspension is loaded, prior to drying down. (C) The silver cyclotron target with ~2g of enriched $^{206}$Pb prior to proton irradiation in the TRIUMF 30MeV cyclotron. (D) The Teflon© holder containing an ion exchange column with ~50 micrograms of $^{205}$Pb from the 1986 synthesis at the Geological Survey of Canada; note the strong discolouration stemming from intense radiation damage to anion exchange resin. (E) Photograph of the ca. 2.0 Ga anorthositic gabbro forming a main constituent of the Purtuniq ophiolite of Northern Quebec.

illustrates the ion exchange column containing the then world's supply of purified $^{205}$Pb after decay from $^{205}$Bi. This material was made available to about 50 laboratories, and this development allowed many laboratories around the world to approach the state of the art, and it was partly responsible for the rapid increase in zircon dating in the 1980s and 1990s.

The use of a $^{233}$U-$^{235}$U double spike mixed with $^{205}$Pb was developed by a few laboratories to allow higher precision uranium isotope measurements (Roddick et al. 1987) by reducing the uncertainty in uranium fractionation. Due to the extreme scarcity of $^{202}$Pb (a by-product of medical production of $^{201}$Tl), the only examples of the use of $^{202}$Pb-$^{205}$Pb double spiking for Pb isotope measurements addressed highly specialized measurements on standards (Todt et al. 1996) and the assessment of Pb fractionation for zircon dating studies (Roddick et al. 1987).

***How not to dissolve a zircon***. One of the authors (RRP) recalls early in his 'zircon' career trying to date a 1mm zircon of suspected Mesozoic age and low uranium content from a metamorphosed carbonatite in British Columbia. Using TFE dissolution vessels and the standard mixture of HF and HNO3, attempts were made to secure complete dissolution at 220°C. After five 1-week cycles, each involving evaporation and addition of fresh acid, the crystal was only approximately 50% reduced in size. From this it was concluded that it is difficult to assume that the 220°C temperature for even a week is sufficient to dissolve all types of zircons. The difficulty of achieving higher dissolution temperatures was due to thermal expansion-driven flowage of Teflon capsules, when they are subjected to heating within a steel confining jacket, a nuisance that seriously deformed capsules, shortening their useful life. Even today, many laboratories use this arrangement, and have to live with this limitation to ca. 220°C as the maximum temperature. Given this, it is imperative to determine whether a sample is fully dissolved.

Parrish (1987) published a subsequent innovation that avoids this limitation. That study used multiple miniature Teflon© capsules for sample dissolution, all residing within a larger Teflon© container that was itself confined by a steel jacket. This arrangement of plastic and steel allowed the temperature of dissolution to be increased to 250°C, without any deformation of sample capsules, thereby ensuring an indefinite useful life. Tests were conducted using low-U, young, large zircons and it was shown that at 245°C all zircons (even ~2 mg in single crystal size) could be dissolved within 36 hours, and that there was no cross-contamination between samples. This innovation allowed the procedure to be scaled up in quantity, with a lowering of cost, while achieving more reliable dissolution.

Many laboratories have more faith than evidence in their ability to dissolve zircons, and only occasionally do laboratories provide any procedural evidence of complete dissolution. Due to the difficulty of observing a small un-dissolved fragment of zircon within a white or light-colored Teflon© dissolution vessel, the *only* way to test for complete dissolution is to transfer the HF-$HNO_3$ solution from the dissolution capsule to a clear non-wetting pre-cleaned plastic container such as poly-methyl-pentane (PMP) under brilliant fiber-optic illumination. Without such a procedure, complete dissolution is really a matter of faith. For example, having checked more than a thousand zircon samples using this procedure at ~240°C for 30-48 hours, the number of not-entirely-dissolved samples was less than 5, and they tended to be very large low-U crystals.

The consequences of failing to fully dissolve zircons are (1) there is a significant likelihood that there will be differential release of U and Pb which means that (2) the tracer would fail to equilibrate with 100% of the sample isotopes, potentially resulting in Pb/U fractionation related to laboratory procedures. These types of artifacts have been documented in careful studies of sequential leaching of zircon (Mattinson 1994, McClelland and Mattinson 1996, Corfu 2000, Davis and Krogh 2000, Chen et al. 2002). Several of these authors have shown that it is possible both to preferentially dissolve Pb isotopes and produce $^{207}$Pb/$^{206}$Pb ages that are too old and to produce Pb/U ratios of the leachates that differ from the true composition of the total crystal. The failure to dissolve fully a zircon could result in the analysis of a solution that may not be representative of the total crystal. Unless the effect was dramatic, it would be nearly impossible to recognize that this had happened.

**Standards, reproducibility, corrections, errors, and presentation**

In spite of better U-Th-Pb analyses in the last 15-20 years, rigorous assessment of errors and reproducibility and the consistency of presentation of data still leave room for improvement. Several excellent seminal papers dealing with error analysis have been published (Roddick 1987, Mattinson 1987) that present methods to assess measurement and related errors, but there is no comprehensive data reduction software package for U-Th-Pb dating in common use. A number of crucial aspects are reviewed below.

***Standards and external reproducibility***. It is unusual for a zircon population to be sufficiently homogeneous that multiple analyses constitute replicates of an identical 'sample.' Although it is possible to propagate all sources of measurement error to arrive at the uncertainty in the Pb*/U ratio of an individual measurement (Roddick 1987), this alone does not necessarily reflect the external reproducibility of analyses (Mattinson 1987). This is partly because individual analyses may have vastly different amounts of Pb analyzed (related to sample size, age and uranium content) that may translate into variable quality of measurements and different magnitudes of corrections (Roddick et al. 1987).

The best way to estimate how close calculated errors for individual measurements approach the external reproducibility is to repeatedly measure a mineral standard along with unknowns, and to do so with amounts of Pb in the measurements that are comparable to unknowns. The ideal material for this purpose is an unspiked *dissolved* standard that is certain to have a homogeneous composition. The use of solid mineral standards (such as the commonly used 91500 zircon of Weidenbeck et al. 1995) is useful but inferior to a liquid. This is clear even from the interlaboratory study of Weidenbeck (1995) where excess scatter in analyses is present both within and amongst laboratories, in contrast to measurements on the 'Haliburton zircon solution'. The reasons for this are not entirely clear, but they could be a combination of heterogeneity in the mineral standard (fairly likely) and/or lack of complete equilibration between sample and tracer during mineral dissolution (not probable for the Weidenbeck study, but of real concern generally). A project for the near future could be the provision of a dissolved U-Th-Pb mineral solution to worldwide laboratories for analysis to assess a laboratory's external reproducibility, to check the calibration of its tracer(s), and to allow better inter-laboratory comparability.

***Blanks and corrections***. The analysis of sub-nanogram quantities of Pb* in zircon analyses is commonplace amongst published data, but additional awareness of corrections and problems endemic to the analysis of picogram amounts of Pb* is necessary. As described by Mattinson (1987) it is very important to measure the small 204 mass signal accurately, and to make any necessary corrections for organic molecules or $BaPO_4$ that may interfere with $^{204}Pb$. In order to minimize the common Pb correction in zircon analyses, low blanks are pivotal.

Realistic uncertainties need to be assigned to the amount and isotopic composition of the Pb blank, the common Pb isotopic composition (including correlation between $^{207}Pb/^{204}Pb$ and $^{206}Pb/^{204}Pb$), and to the mass fractionation for Pb and U (unless using a U double spike). These uncertainties must be weighted and propagated to accurately define the final uncertainty in Pb*/U.

Provided that individually calculated errors of analyses of a dissolved zircon standard solution are distributed about the mean value and fit a Gaussian distribution (i.e., 95% of $2\sigma$ error ellipses on analyses overlapping the mean) it is likely that the individual contributions to the final error are being estimated correctly. Only by repeated analyses on quite variable amounts of such a standard mineral solution (i.e., 20-2000 picograms of radiogenic Pb) can the degree to which individual calculated ages reflect external reproducibility be properly tested. Such analyses should of course be in addition to analyses of U and Pb isotopic standards that are used to assess the performance of the mass spectrometer alone.

***Systematic errors: tracer and decay constants***. There is always uncertainty in the Pb/U ratio of a mixed tracer (i.e., $^{205}Pb$-$^{233}U$-$^{235}U$-$^{230}Th$), even when carefully calibrated against a primary

mixed metal reference solution. Such uncertainty may be as small as 0.05% or much larger, depending on the quality of the calibration. When assessing the relative age difference between analyses using the same tracer, this uncertainty is not relevant. However, when making comparisons to U-Pb data from other laboratories or especially to inter-comparisons to other methods of dating (i.e., $^{40}Ar/^{39}Ar$), it must be taken into account (i.e., Schmitz and Bowring 2001). Because all laboratories should be using the internationally agreed values for the decay constants of U and Th (Steiger and Jäger 1977), the uncertainty in the decay constants Jaffey et al. 1971) is only relevant when comparing U-Th-Pb data with dates using other decay schemes.

***Presentation***. Tables of data vary in their format and presentation. It is desirable to present details that clearly state the number of grains analyzed, their morphological characteristics, the weight of the grain(s), the uranium concentration and the Th/U ratio (calculated from the radiogenic $^{208}Pb^*/^{206}Pb^*$ or as measured if Th measurements are made). These are in addition to the radiogenic Pb content, the relative proportion of common Pb in the analysis (i.e., measured $^{206}Pb/^{204}Pb$ or $^{207}Pb/^{204}Pb$) and the relevant isotopic ratios, individual uncertainties, and error correlations. The weight of grain(s), uranium content and Th/U form part of the information needed to make the best interpretation of the data.

## OTHER METHODS OF ID OR TIMS

### Pb evaporation (TIMS but no ID)

Kober (1986) developed a method by which the Pb isotopic signature of a zircon could be recovered without any chemical pre-treatment or dissolution. This method involved wrapping a crystal of zircon (or other mineral, monazite will also work) almost completely within a shaped ribbon of Re that formed part of a double filament assembly within a thermal ionization mass spectrometer. Alternations of heating of the evaporation and ionization filaments allowed the deposition of evaporated components (Pb, Si, Zr, etc.) onto the opposite filament, followed by thermal ionization and analysis of those components for Pb isotopes. High precision measurements have proved possible if the quality of the crystal is high, and in many cases where rigorous tests have been applied, the results appear consistent with ID-TIMS analysis. However, Chapman and Roddick (1994) showed that the procedure can produce a complex evaporation signature and lead to mixing of components within zircon that may have different compositions, some being more affected by Pb loss than others. Because there is no measurement of uranium content in the crystals, it is impossible to quantify the extent of discordance of grains, and therefore the interpretation of the data have to be treated with caution in many cases. However, the method has been applied in recent years mainly by A. Kroner and associates (Universität Mainz) to elucidate patterns of ages within Precambrian crystalline terrains on a reconnaissance basis (e.g., Kroner et al. 2000, 2001). It should be emphasized that for the most part, the method is mainly applicable to Precambrian geochronology.

### ID-PIMMS (ID but no TIMS)

In spite of the historical close association of isotope dilution analysis of zircon with thermal ionization mass spectrometry, other mass spectrometers can be used. It is possible to make the Pb and U isotopic measurements on spiked, chemically separated samples using plasma ionization multicollector mass spectrometers (PIMMS or MC-ICP-MS). These new instruments offer the ability to correct for Pb and U mass fractionation using Tl (or Pb) and uranium double spiking that theoretically could produce higher precision measurements than achievable with TIMS. Such measurements of U and Pb could be done more or less simultaneously using the same solution, and considerably more rapidly. The main drawback is higher common Pb and Hg contained in the carrier gas, complicating the precise measurement $^{204}Pb$ due to $^{204}Hg$ interference, and of course the difficulty of measuring signals so small as to require ion counting detection. This application

has only just been attempted in our laboratory.

In the measurements, the U and Pb (and Th if desired) are chemically separated from the dissolved spiked zircon and dissolved in ca. 2% $HNO_3$. The multicollector ICP-MS is tuned using Pb or U reference solutions and the cup array configured to measure the masses 203-208, 230, 232, 233, 235, and 238, with 204 being on an ion counting multiplier. An assessment of the mass bias is made by analyzing separate Pb, U and Th reference solutions that bracket samples. The gain of the multiplier can also be measured using reference solutions (or using a suitable ratio in a sample solution with peak switching). Once a sample solution is introduced, minor $^{205}Tl$ corrections are made using the 203 mass (using the multiplier with a peak jump), and the remaining Pb isotopes are measured using a mixture of faraday cups and the electron multiplier. The masses 203-208 can be measured statically, and with one or two peak jumps, the U and Th peaks can be measured using faraday cups. The method offers considerable promise for the future in certain types of applications where a small compromise in analytical precision on the common Pb correction could be tolerated without affecting the geological interpretation.

## THE MAPPING OF U-TH-PB DATA ONTO DIAGRAMS

### Age equations

The age equation for any of the $^{238}U$-$^{206}Pb$*, $^{235}U$-$^{207}Pb$*, and $^{232}Th$-$^{208}Pb$* decay systems (* refers to radiogenic lead) takes the form

$$T = (1/\lambda) * \ln (1 + D/P) \quad (1)$$

where T is the age, $\lambda$ the decay constant for either $^{238}U$, $^{235}U$ or $^{232}Th$, and D/P the daughter-parent atomic ratio of the respective parent: $^{206}Pb/^{238}U$, $^{207}Pb/^{235}U$, or $^{208}Pb/^{232}Th$. The D/P ratio for any given T can be calculated by

$$D/P = e\lambda^{T} - 1 \quad (2)$$

By taking Equation (2) for each of the two U-Pb systems and dividing, one can write the following equation which can be iteratively solved iteratively for T if the $^{207}Pb*/^{206}Pb*$ is measured, noting that the present day $^{238}U/^{235}U$ is 137.88,

$$\frac{^{207}Pb*/^{235}U}{^{206}Pb*/^{238}U} = \frac{e^{\varsigma^{235}T} - 1}{e^{\varsigma^{238}T} - 1} \quad or \quad \frac{^{207}Pb*}{^{206}Pb*} = \frac{1}{137.880} \cdot \frac{e^{\varsigma^{235}T} - 1}{e^{\varsigma^{238}T} - 1} \quad (3)$$

Equation (3) shows that $^{207}Pb*/^{206}Pb*$ is a function of age and is termed the so-called 'lead-lead' age. The decay constants for $^{238}U$, $^{235}U$, and $^{232}Th$ as determined by Jaffey et al. (1971) and Le Roux and Glendenin (1963) are $1.55125e^{-10}$, $9.8485e^{-10}$, and $4.9475e^{-11}$. These equations form the basis for all U-Th-Pb age calculations and the construction of all relevant diagrams, as outlined below.

### Wetherill Concordia diagram

Once common Pb and blank U and Pb corrections have been made to sample data, the daughter-parent ratios $^{206}Pb*/^{238}U$, $^{207}Pb*/^{235}U$, and $^{208}Pb*/^{232}Th$ (if measured) can be determined (Pb* referring to the radiogenic component only). Wetherill (1956) invented the Concordia diagram and defined the meaning of concordant and discordant points. A concordant point is that in which the two Pb*/U ratios correspond to a given age. A discordant point is one that has different calculated ages for the two Pb*/U measured ratios. If one plots out all concordant points for all times in the

past, the result is a curve termed the Concordia (Fig. 3). Due to the uncertainties in the decay constants for the parent isotopes (fortunately they are quite small; Jaffey et al. 1971), the concordia curve is actually a band with finite width.

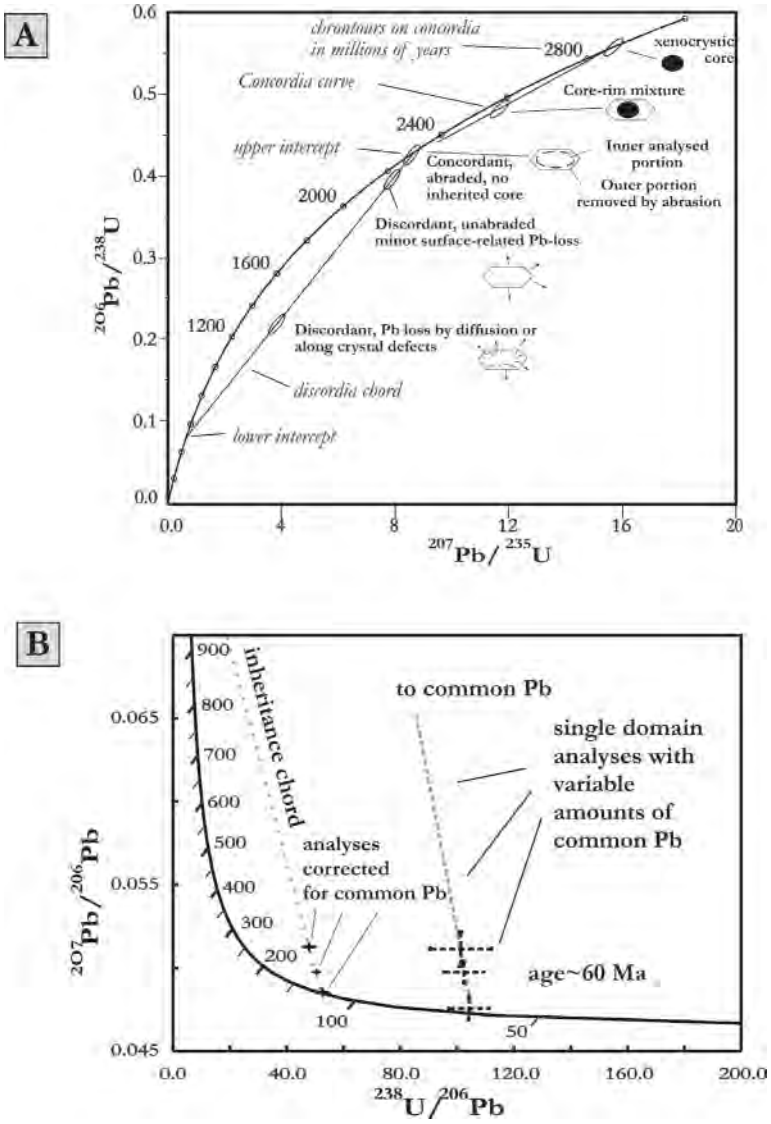


**Figure 3**. Wetherill and Tera-Wasserburg concordia diagrams with annotations. The Wetherill Concordia (A) illustrates situations commonly encountered including inherited grains, mixed-age crystals that may define a chord, concordant data on single-domain crystals, and discordant analyses on crystals with surface-correlated Pb loss due to radiation damage. The Tera-Wasserburg diagram (B) shows two examples of data; on the left are more precise common Pb-corrected analyses (i.e., the $^{238}U/^{206}Pb^*$ and $^{207}Pb^*/^{206}Pb^*$ ratios are plotted) that define a chord that might be caused by a mixture of inherited and magmatic grains. On the right side are less precise analyses (for example, very low-U crystals with poorer analytical precision and/or larger common Pb corrections) that are not corrected for common Pb; here, the upper intercept defines the $^{207}Pb/^{206}Pb$ of the common Pb and the lower intercept defines the $^{238}U/^{206}Pb^*$ of the crystals which might be the interpreted age. Data points are diagrammatic only.

Isotopic compositions of zircon, if undisturbed, should generally lie on this curve, but if a series of crystals of a single age are differentially affected by either a disturbance involving Pb loss or are mixed with a second component, then a linear array can result. Such analyses that fall below the Concordia curve are termed 'normally' discordant, whereas analyses that plot above or to the left of the Concordia curve are 'reversely' discordant. The affect of careful air abrasion of zircons can reduce or in some cases eliminate Pb loss effects, allowing the reconstruction of either a precise single age component or a more complex array of data demonstrating mixing of components. Zircon analyses that comprise more than two age components obviously make for non-linearity and increased complexity of interpretation.

Another useful diagram can be employed if Pb*/Th isotopic data is available, plotting either of the Pb*/U systems against the $^{208}Pb^*/^{232}Th$ system. Such a diagram is helpful to show the degree of agreement between the Pb*/U and Pb*/Th systems and to identify Th/U fractionation in systems, which could have a mineralogical control. This latter variation is rarely used however, because few laboratories produce Th isotopic data, especially on zircon. The U-Pb Concordia diagram is the most common method of displaying U-Pb zircon data.

**Tera-Wasserburg diagram**

An alternate way of plotting U-Pb data was developed by Tera and Wasserburg (1972) that makes few assumptions about the composition of the common Pb in zircons (Fig. 3b). In can be used in two ways.

By plotting the measured $^{207}Pb/^{206}Pb$ against the $^{238}U/^{206}Pb$ (the Pb including common Pb contained in the analysis), data on single component zircons with variable amounts of common Pb will form an array with upper intercept corresponding to the $^{207}Pb/^{206}Pb$ of the common Pb, and the lower intercept being the $^{238}U/^{206}Pb^*$ ratio. If additional processes such as mixed ages or Pb loss are present, in addition to variable amounts of common Pb, there may be little or no linearity to the array, with a complex interpretation resulting. This diagram is particularly useful when it has been difficult to measure the common Pb in a sample, i.e., the small $^{204}Pb$ signal, or when the common Pb isotopic composition is poorly known or difficult to estimate. Ion microprobe U-Pb data are generally displayed using either this diagram or the Concordia diagram, depending on the convention of the author or laboratory.

Alternatively, one can plot blank- and common-Pb-corrected $^{207}Pb^*/^{206}Pb^*$ against the $^{238}U/^{206}Pb^*$ in a manner analogous to the Concordia diagram. This diagram has the advantage of lack of strong X-Y correlation of data and can in some cases permit a more rigorous assessment of linearity to an array of points. The arrangement of points in terms of discordance, inheritance, Pb loss, etc. are analogous to the Concordia diagram when the radiogenic Pb is used.

**Isochron diagram**

The simplest plot in the U-Th-Pb system is the isochron diagram for a single radioactive parent, the parent and daughter isotopes being normalized by the $^{204}Pb$ in the sample. This diagram is rarely used for any type of zircon analysis because of the relative insensitivity of the final age to the common Pb isotopic composition. It is more commonly used for analyses of other minerals (titanite, apatite, rutile, etc.) that have low proportions of radiogenic to common Pb. In favorable circumstances a measurement of common Pb (usually with potassium feldspar) can be made to constrain the correction for common Pb incorporated into the mineral. This approach is much more robust than simply making an assumption of the common Pb composition using a model like that of Stacey and Kramers (1975).

**The interpreted age of crystallization**

Many students of U-Pb dating will realize that it is common practice when evaluating Precambrian zircon age data to use regression or data evaluation schemes that emphasize the more

precisely determined $^{207}Pb^*/^{206}Pb^*$ ratio in preference to Pb/U ratios to arrive at a final age. In contrast, much younger zircons (Palaeozoic–Cenozoic) may have measured $^{207}Pb^*/^{206}Pb^*$ ratios that are less precise (mainly due to less Pb in the measured sample), and in many cases it is the mutual agreement of Pb/U ratios that may be emphasized in a final age determination. A cynical view might be that authors wish to portray their data as precisely as possible, but there is a sound basis for this, though assumptions are implicit in either assessment. Some of this reasoning has been formalized in the very useful discussion of error analysis in U-Pb dating by Ludwig (1998) who refers to the latter method of age assessment as a *Concordia* age.

As compared with the Precambrian, the more recent portion of the Concordia curve has a greater amount of elapsed time for a given change in measured $^{207}Pb^*/^{206}Pb^*$ value. Therefore, if one can produce concordant or at least highly consistent and mutually overlapping errors on analyses of zircon and be assured of the elimination of Pb loss, then one should probably use Concordia ages (in the sense of Ludwig 1998), which are effectively the mutual overlap of multiple analyses on the Concordia curve. In contrast, the elimination of Pb loss using air abrasion in Precambrian zircons is more difficult to achieve due to the long history of accumulation of radiation damage and potential complexity of subsequent events. In these types of crystals, the single stage Pb loss pattern is often documented, and it is then reasonable to extrapolate the discordant array to the upper intercept and calculate its statistical intersection accordingly (using standard York I (1966) or York II (1969) regressions, modified for additional scatter), if possible emphasizing the more concordant points (Davis 1982). One must be aware in young zircons of the probability of intermediate daughter isotope fractionation effects, some of which are described below; these may have a bearing on the final age interpretation.

## ZIRCON DATING APPLICATIONS AND U-TH-PB SYSTEMATICS

ID-TIMS dating of zircon is a very powerful technique that has contributed enormously to the understanding of earth evolution, both ancient to recent. These contributions are amazingly diverse, ranging from time scale calibration, precise chronostratigraphy, residence time in magmatic processes, calibration of rates of tectonic processes, provenance characteristics of sedimentary successions, petrological aspects of zircon growth in metamorphic rocks, and dating of metamorphism, to name some. Many of these applications are best addressed using ID-TIMS methods, though many benefit from (and some require) a combined approach using micro-beam intra-grain analysis. This section of the chapter will present examples that illustrate the power of the ID-TIMS method and its advantageous application to particular problems.

### High precision dating of igneous zircon across the scope of geological time

***Fish Canyon Tuff: a well-studied eruption.*** The Fish Canyon tuff is a large ash-flow deposit in the western United States, several minerals of which have been adopted as 'standards' for inter-laboratory comparison. Sanidine is used as a $^{40}Ar/^{39}Ar$ dating standard, and the apatite and zircon are used as a standard for fission track dating. The commonly accepted age using the $^{40}Ar/^{39}Ar$ method for the sanidine is regarded as just over 28.0 Ma with minor variations according to laboratory (Renne et al. 1998). Schmitz and Bowring (2001) exhaustively analyzed both zircon and titanite from the deposit using U-Pb ID-TIMS methods and derived an age of 28.50±0.045 Ma (including quadratically added tracer and decay constant errors) based on the agreement of both minerals. These data are redrawn in Figure 4 to show the level of mutual agreement of analyses when air abrasion and rigorous assessment of analytical parameters and tracer calibration is employed. The data illustrate many interesting points. First, data for nearly thirty analyses are consistent with the conclusion that the zircons are behaving as a closed undisturbed system, with scatter amongst analyses being the result of measurement uncertainty alone. Second, the mean of the analyses forms a region that does not clearly fall on the Concordia diagram, even when the latter's uncertainty is taken into account. This latter point requires an explanation. Following the

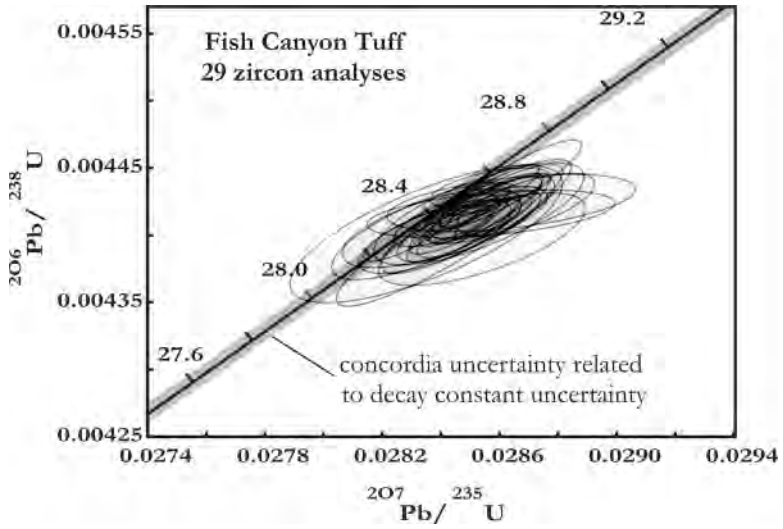


**Figure 4**. Concordia plot of 29 analyses of zircon from the Fish Canyon Tuff showing excellent mutual agreement but a slight degree of discordance, redrawn from Schmitz and Bowring (2001). The uncertainty in the position of the Concordia curve arising from uncertainty in the decay constants is shown in light gray shading.

early seminal paper of Mattinson (1973), the authors asserted that due to the fact that zircon chemically fractionates Th and U relative to the magma from which it crystallizes, it would exclude a significant proportion of the $^{230}$Th present in the magma, and after decay, this would lead to a deficiency in $^{206}$Pb. This is a real effect, leading to zircons often plotting slightly below the Concordia curve (by up to ca.100,000 years), and has been documented in numerous previous examples, some of which are illustrated later in the chapter. A correction for this effect can be made by knowing the Th/U of the magma and the Th/U of the zircons, employing equations outlined by Schärer (1984). The correction serves to move the points upward on the Concordia diagram and become concordant. Finally, this example emphasizes that zircons are likely to be slightly normally discordant with $^{207}$Pb*/$^{206}$Pb* ages being slightly too high. Only high precision measurements are capable of documenting this effect.

***Rates of ammonite evolution and time scale calibration.*** Palfy and others (in press) dated successive ash layers within several biostratigraphic substages of the Middle Triassic Ladinian succession in Hungary to determine the rate of ammonite evolution and provide additional constraints on the geological time scale. Figure 5 shows U-Pb zircon data of a subset of analyses used to assign final ages to these ash layers, with analyses with much older inheritance not considered. These data show that, in a manner similar to the Fish Canyon Tuff study, it is possible to produce data with very good mutual agreement that overlap the Concordia curve (only one analysis shown having apparent Pb loss). The age estimates of these four stratigraphically ordered ash beds, all from the Reitzi ammonite zone, range from 241.1±0.5 for the lowest to 240.4±0.4 for the highest, with all of the ages being stratigraphically consistent. The precision on these layers is similar to that of the Fish Canyon Tuff data of Schmitz and Bowring (2001), approximately 0.2% of the absolute age at the 95% confidence level. Thus in spite of the additional likelihood of Pb loss in these older samples, a similar precision on the age has been determined. This would have been difficult or impossible to achieve with any method other than ID-TIMS. Similar studies of time calibration using air abrasion are addressed in Bowring (this volume).

Some other studies that address time scale issues in the Palaeozoic have used the HF leaching method (rather than the air abrasion) in the sample preparation procedure. The study of Mundil et al. (2000) dated several layers of ash bracketing the Permo-Triassic boundary beds in China. That study used only single grain dating, and therefore had individual analytical errors larger than in the

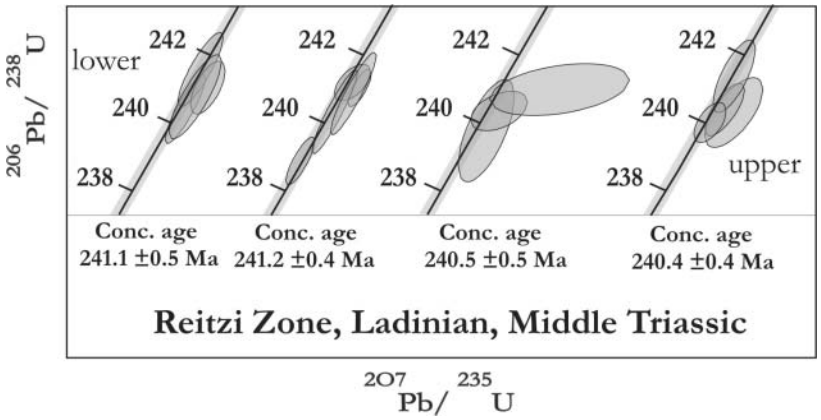


**Figure 5.** Concordia diagram showing concordant zircon analyses from four ahs beds within the Reitzi ammonite zone of the Ladinian, Middle Triassic, redrawn from Palfy et al. (in press). Both biostratatigraphic and local stratigraphic order increase from left (older) to right (younger). The youngest analysis in the second plot may have had a small degree of residual Pb loss. The uncertainty in the position of the Concordia curve arising from uncertainty in the decay constants is shown in light gray shading.

above study. The results for several of the ash beds showed a degree of scatter that exceeded that expected if the population of zircon was assumed to be homogeneous. From this observation the authors concluded that invisible xenocrystic zircons were present that caused the scatter. They advocated that studies should therefore only use single grain analysis so as not to produce mixed ages. However, the scatter may also be explained by being an artifact of the HF leaching process, with potential problems with dissolution and/or tracer-sample equilibration, both of which can cause dispersion in Pb/U ratio. It is likely that this method does indeed offer a way forward, but the detailed leaching procedure could differ from sample to sample. This implication here is that careful tests would have to show that analytical artifacts were not produced by the pre-treatment. Improvements in the method are currently being made by a number of workers (e.g., Mattinson 2000).

***Chronostratigraphy in the Archean.*** Many studies have applied U-Pb ID-TIMS dating to the Archaean and demonstrated the ability to produce high precision robust concordant to near concordant ages with a minimum of analytical data (3-5 analyses per sample). To illustrate how the method was applied to chronostratigraphy, selected analyses are redrawn in Figure 6 from the study of Bleeker et al. (1999) on the Kidd Creek massive sulfide deposit of Ontario and its surrounding rocks. In that study, about 30 samples were dated. Zircons weighing around 1 microgram were routinely used and these were strongly air abraded, with half or more of the ca. 100 analyses being concordant within their analytical errors (approximately 0.5% at the 95% confidence level). Figure 6 shows zircon analyses from two rhyolite samples from the vicinity of the massive sulfide deposit. The two samples yield concordant and self-consistent analyses, all falling within the Concordia envelope constrained by the uncertainty in the $^{238}U$ and $^{235}U$ decay constants. The ages of the zircons from the two samples are 2714.2±0.5 Ma and 2716.0±0.5 Ma, respectively on the basis of the weighted mean of the $^{207}Pb^*/^{206}Pb^*$ ages. The uncertainty in the $^{206}Pb^*/^{238}U$ ages was only 0.2% at the 95% confidence level, effectively the limit of the measurement precision on the basis of tracer uncertainty and uncertainty in mass fractionation. The study showed that an enormous range of magmatic, sedimentological, and tectonic history was packed into a short period of time, less than 10 Ma, with felsic volcanism responsible for formation of the ore-bodies lasting but ~4 Ma. They also showed that it was possible to estimate the rates of production of massive sulfide generation on the sea floor as between 10 and 100 metric tones/year, an average rate of production comparable to that observed on some currently forming mid-ocean ridge sulfide deposits. This study illustrates that there are few limitations to the detail that can potentially be temporally resolved in the Precambrian using ID-TIMS zircon dating.

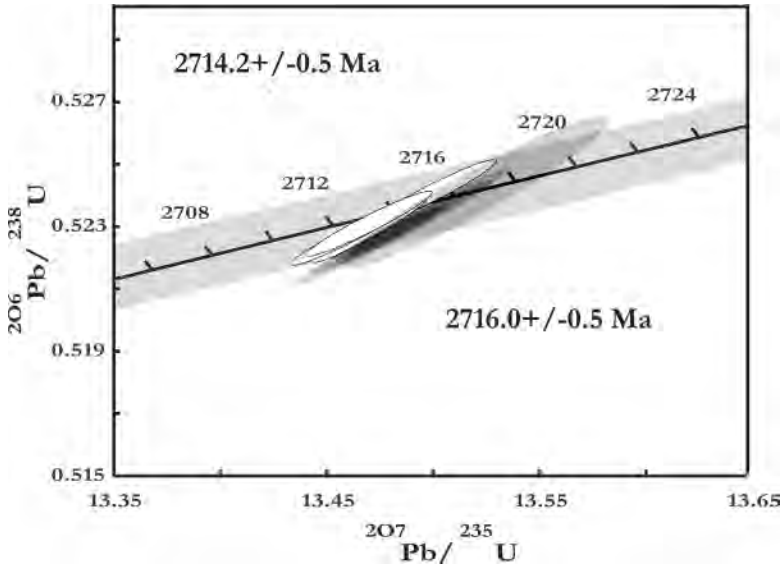


**Figure 6.** Concordant zircon analyses from two rhyolite samples in the vicinity of the Kidd Creek volcanogenic massive sulfide orebody of Ontario, Canada, modified from Bleeker et al. (1999). The data show that the two samples (illustrated as unshaded and shaded ellipses) are clearly separable at the 95% confidence, even though less than two million years different in age. The uncertainty in the position of the Concordia curve arising from uncertainty in the decay constants is shown in light gray shading.

***The dating of mafic rocks using zircon.*** In spite of the virtual absence of zircon in basaltic rocks, zircon and baddeleyite ($ZrO_2$) can occur in similar compositions of broadly gabbroic composition. Such Zr-bearing minerals are more likely to form larger datable crystals if extracted from coarser-grained portions of the mafic protolith. An example from a gabbroic anorthosite of the Purtuniq ophiolite, Cape Smith Belt (Northern Quebec) is shown in Figure 2e. Zircons from this rock were irregular in form, relatively large, and low in uranium content. The morphology could be explained by the late crystallization of zircon in an igneous rock that was nearly crystalline by the time the residual melt became saturated in zircon. In Figure 7a, zircons from this rock provide an age of ~1997±1 Ma (Parrish 1989).

The Norilsk mafic intrusion of Russia was dated by Kamo et al. (1996) and the data are redrawn in Figure 7b. Like the Fish Canyon Tuff, clustered analyses fall slightly off Concordia, probably reflecting the effect of partitioning of intermediate daughter isotopes, but the age was inferred to provide a minimum age of 251.2±0.3 Ma while not entirely explaining the slight discordance of the mean of the analyses. Another example is given in Figure 7c of zircons from an olivine-bearing mafic syenite of the zoned Tulameen ultramafic Complex of British Columbia (from Rublee 1994). These abraded zircon analyses lie near 204 Ma ($^{206}Pb^*/^{238}U$ ages are ~204.0±0.5 Ma) while $^{207}Pb^*/^{206}Pb^*$ ages were 209±2 Ma. The likely age of the zircons is ~204 Ma with the older $^{207}Pb^*/^{206}Pb^*$ ages being explained by an excess of $^{207}Pb^*$, as explained in a later section. Readers will note that it is possible to produce multiple analyses that are consistent with complete lack of Pb loss, and that it is not uncommon to find that they are slightly discordant due to intermediate daughter effects.

***The dating of granitic rocks using zircon.*** Provided that granitic rocks contain zircon devoid of older components, it is possible to produce precise U-Pb dates using air-abraded zircon in a completely analogous fashion to mafic zircons cited above, or to the Fish Canyon Tuff zircons as shown in Figure 4. Several examples of U-Pb dates from plutonic zircon from hornblende-bearing granodioritic to quartz dioritic rocks are shown in Figure 7e-7f. Again, when high quality zircon is air abraded and have been analyzed precisely, a high degree of mutual consistency often results, and the zircons often remain slightly discordant, for the same reasons cited above.

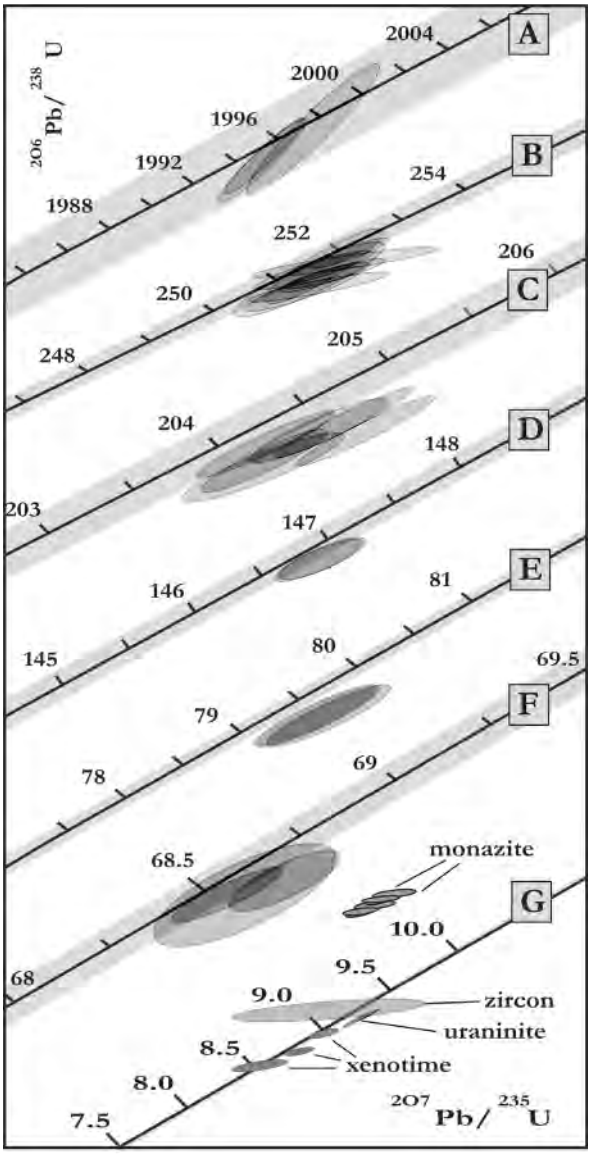


**Figure 7.** Composite segments of the Concordia plot showing U-Pb analyses. (A) Zircons from the anorthositic gabbro of the Purtuniq ophiolite shown in Figure 2e. (B) Zircons from the Norilsk intrusion, Russia, redrawn from Kamo et al. (1996). (C) Zircons from olivine syenite of the Tulameen zoned ultramafic complex, British Columbia from Rublee (1994). (D-F) Zircons from three samples of hornblende-bearing granitic rock in the Coast Plutonic Complex of British Columbia illustrating the slight discordance characteristic of young zircons. (G) Zircon, uraninite, xenotime and monazite analyses from the 9.3 Ma old Sumiyar granite, Pakistan (redrawn from Fraser et al. 2001) showing the obvious effects of excess $^{206}Pb^*$ in Th-rich monazite as compared to $^{206}Pb^*$ deficiency in Th-poor xenotime and uraninite, along with a relatively imprecise analysis of zircon. The uncertainty in the position of the Concordia curve arising from uncertainty in the decay constants is shown in light gray shading on all diagrams, though in (G) it is about the same width as the Concordia line.

## Difficulties with igneous U-Pb zircon geochronology

While the above examples illustrate the power of the technique, they are admittedly based on situations where the zircons are simple and composed of but one age component, and where the effect of Pb loss has been effectively eliminated by application of air abrasion techniques. There are other situations where the U-Pb systematics are much more complicated.

***Zircon inheritance.*** The incorporation of older xenocrystic zircon into a younger magma to produce either xenocrystic single component grains or magmatic grains containing an older xenocrystic core is termed *inheritance* (Gulson and Krogh 1973, Williams 1992*)*.In crustally derived granitic or volcanic rocks of felsic composition, inheritance is moderately common, and can often be observed under examination with a binocular microscope. It can be revealed more clearly by cathodoluminescence (CL) or back-scattered electron (BSE) imaging in a polished section or grain mount of zircon in an electron microscope. When the age of the xenocrystic component is

variable, the pattern of analyses will be a field mainly constrained by a region on the Concordia diagram given by the magmatic component, and the youngest and oldest inherited components (Fig. 3a). Knowing the age of the magmatic event it is possible to analyze abraded single grains with cores and accurately estimate the age of the xenocrystic component, as they will lie on a mixing line between the magmatic and inherited age (Fig. 3a), once Pb loss is minimized or eliminated.

***High uranium grains of low quality.*** Many granitic rocks are highly fractionated, and in particular enriched in uranium while their zirconium content may be relatively low, for example leucogranite. Zircons in such lithologies, if of significant age (Palaeozoic–Precambrian), will have poor quality zircons with significant metamictization, abundant cracks and cloudy zones, and potentially older cores (see zircons in Fig. 1a). These types of crystals present a real challenge for zircon dating by ID-TIMS because little of the crystal will be of sufficient quality so as to have retained quantitatively the radiogenic Pb. Such regions can potentially be isolated by breaking crystals and abrading the clearer portions of the grains, or by HF leaching pre-treatment to remove the soluble damaged portions. The most tractable approach is to date alternative minerals like monazite or xenotime that often provide excellent age determinations in such rocks.

## Dating of metamorphic zircon

Metamorphism can give rise to mineral reactions that either destabilize a Zr-bearing phase (i.e., baddeleyite, $ZrO_2$) or release Zr that was contained in a reacting phase as a minor or trace element (e.g., clinopyroxene, Jones and Peckett 1980; ilmenite, Bingen et al. 2001). If the $SiO_2$ activity is sufficiently high, as is generally the case, zircon will form. Morphologies of metamorphic zircon differ from igneous zircon. Round grains and grains with smooth external surfaces are common (Figs. 1d, 1g, 1h). Metamorphic processes can weld together formerly separate zircon grains by the formation of a communal overgrowth (Fig. 1e), and metamorphism can also corrode or resorb grains to produce a smooth external surface (Fig. 1c) modification of an originally igneous crystal (Fig. 1f). In Figure 1h, the external surface of a zircon reveals 'casts' of other grains, in part sillimanite needles that were evidently stable during zircon growth, and this can help to ascertain P-T conditions of zircon formation. Notwithstanding this latter example, it is usually very difficult to ascertain the exact zircon-producing mineral reaction, and therefore the P-T significance of any age determination on metamorphic zircon. However, ID-TIMS as well as micro-beam ion microprobe dating has been widely applied to produce insights into the metamorphic history of orogenic belts. Examples of ID-TIMS applications to such rocks are given below.

## Baddeleyite-zircon reactions in coronitic gabbro

In a seminal study, Davidson and van Breemen (1988) studied the accessory mineral textures within coronitic gabbroic rocks of the Grenville Province of Eastern Canada and showed that igneous baddeleyite ($ZrO_2$) was replaced by neoblastic zircon during the conversion of diabase to coronitic gabbro during metamorphism at moderately high pressure. Overgrowths of zircon variably replaced baddeleyite (Fig. 8), and these were physically separated by breaking off the composite zircon overgrowths from the residual baddeleyite for U-Pb dating of the 'end-member' mineral phases. Following air abrasion pre-treatment, the results produced a near perfect mixing line between the 1170 Ma age of the dykes (i.e., the baddeleyite end-member) and the 1045 Ma age of metamorphism forming the coronitic textures in zircons, as shown in Figure 8. This data illustrates the ability of ID-TIMS to resolve the relatively precise ages of both events by the dating of the two mineralogical phases. This study would have been more difficult to conduct with ion probe techniques because of the need to measure different minerals, and the relatively small sub-grains of zircon.

## Growth of zircon in granulites and upper amphibolite facies rocks

During granulite facies metamorphic conditions, it is quite common to find widespread growth of metamorphic zircon, especially evident by relatively round equant metamorphic grains and dis-

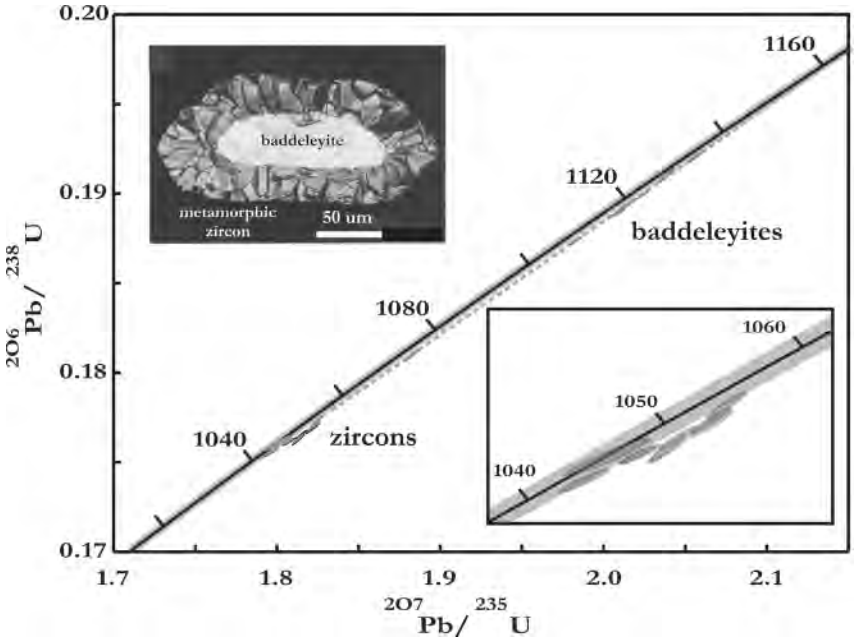


**Figure 8.** Concordia diagram of baddeleyite and zircon analyses from coronitic mafic rocks of the Grenville Province, Ontario, and a BSE image of a composite baddeleyite-zircon crystal, redrawn from Davidson and van Breemen (1988). The uncertainty in the position of the Concordia curve arising from uncertainty in the decay constants is shown in light gray shading.

tinctive intra-grain textures revealed by CL or BSE microscopy (Fig. 1). Both ID-TIMS and ion microprobe dating have been extensively applied to these situations in the Precambrian, including samples in Greenland, Canada, and elsewhere of Earth's oldest rocks (Bowring et al. 1989, Amelin et al. 1999, Nutman et al. 2000, Krogh 1998). Usually, the dry conditions of granulites appear associated with lower degrees of later Pb loss, in spite of quite high uranium contents in metamorphic grains, a particularly good example being the study of granulites in the Torngat Mountains of Labrador (Bertrand et al. 1993). The exact reason for this is unclear, but it is a reasonable rule of thumb. Such studies, regardless of analytical method, have resolved igneous and metamorphic events in a detailed time framework with a high degree of precision.

**Metamorphic growth of zircon in amphibolite facies**

Amphibolite facies metamorphism commonly provokes the growth of zircon in a wide range of rock types, including mafic amphibolite, pelite, and other less common lithologies. Release of zirconium from mineral phases that become unstable is a reasonable explanation. The study of Parrish and Scammell (1988) and Parrish (1995) provide examples of the growth of very low-U zircon in metamorphosed nepheline syenite and carbonatite where the host rock Zr content was very high, and silica activity relatively low, with both rocks lacking free quartz.

***Metamorphosed nepheline syenite.*** Figure 9 shows U-Pb data of zircon from nepheline syenite gneiss that form a distinctive array of data between ca. 60 Ma and 740 Ma (array not shown on diagram). Zircons had clearly visible cloudy cores with extremely clear overgrowths, with many grains being composed only of the clear variety. The zircons all had a relatively equant, but euhedral to subhedral complex crystal shape, with facets consistent with growth in the solid state. The composite grains define the array of points with an upper intercept of ca. 740 Ma, and this was interpreted as the age of the original igneous zircon within the nepheline syenite. The clear grains plot on Concordia, have less than 15ppm uranium, and provide a precise age of 59±1 Ma for the metamor-

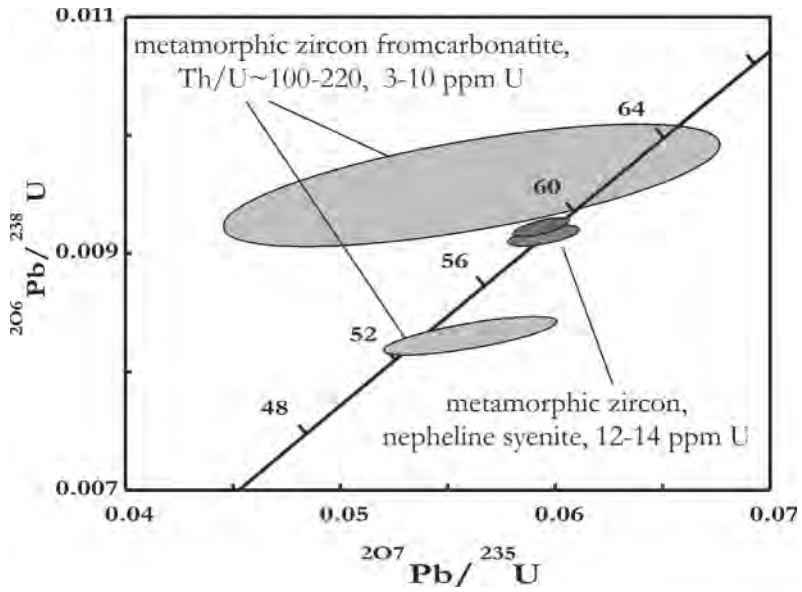


**Figure 9.** Concordia diagram of analyses of metamorphic zircon from nepheline syenite and carbonatite, the latter being very unusually high in its Th/U ratio, with resultant excess $^{206}$Pb*, both being very poor in U, less than 15ppm. The uncertainty in the position of the Concordia curve arising from uncertainty in the decay constants is shown in light gray shading.

phic zircon. This age accords with the age of metamorphism of many other rocks within this metamorphic complex, on the basis of both zircon and monazite U-Pb data, and was period of significant release of hot fluid resulting from the crystallization of pegmatites and leucogranitic melts. These fluids may have helped catalyse the formation of metamorphic zircon.

Metamorphosed carbonatites. From the same general area as cited immediately above, metamorphosed carbonatite with relict pyroclastic texture occurs within metasedimentary rocks in a deformed stratigraphic succession as shown in Figure 2a. Zircon recovered from this rock was abundant, generally quite large in size and extremely low in uranium, ranging from 0.5-10 ppm. Most unusually, these zircons had very high Th/U ratios, all between 60 and 220. This is an extremely unusual situation and can only be explained by the sequestering of U in other mineral phases that were stable during the metamorphic episode. Dating these crystals using U-Pb proved difficult because of the very low U and Pb contents and because the Th/U fractionation led to a potentially large amount of excess $^{206}$Pb from $^{230}$Th incorporation during metamorphic crystallization. The mass spectrometric measurement may also have been complicated by tailing of $^{208}$Pb due to the very high measured $^{208}$Pb/$^{207}$Pb ratio (up to 1400). Of the two analyses (Fig. 9) that appeared to be free of any older component (which could have arisen from a tiny detrital zircon incorporated into the pyroclastic deposit as it mixed with underlying sediments), one appeared reversely discordant in a manner analogous to monazite or allanite U-Pb systematics (Parrish 1995). Tailing as mentioned above could explain the discrepancy of the two analyses, both of which should have plotted reversely discordant. The $^{206}$Pb/$^{238}$U ages were 53-61 Ma, slightly older than the 50-54 Ma ages of peak temperatures for this portion of the metamorphic complex (Crowley and Parrish 1999). The older $^{206}$Pb/$^{238}$U ages can be explained by a variable but significant (~10%) amount of excess $^{206}$Pb in these zircons arising from incorporation of $^{230}$Th. In spite of the relative imprecision of these analyses on zircons with radiogenic $^{206}$Pb content <0.1 ppm, this example illustrates how zircons can be Th-rich and very U-poor in certain environments, but still be datable. The analysis of

these zircons would, ironically, have been more tractable using Th-Pb ID-TIMS. To have used intra-grain micro-beam U-Pb methods would have resulted in unusable data due to the extremely low radiogenic Pb contents.

**The dating of zircon in eclogite and other UHP rocks**

In spite of considerable published work on eclogites, there is a general perception by many geologists that it is not feasible to use zircon dating in eclogites, presumably because of the belief that zircon does not occur in mafic rocks. While the latter is generally the case for basaltic rocks (with very rare exceptions in extremely thick, in part differentiated flows) once such compositions are subjected to metamorphism at amphibolite or higher pressure eclogite facies, zircon will generally become a stable phase. Not uncommonly, its abundance is low, with the recovery of trace amounts of zircon from such rocks. It is also not uncommon for the uranium content to be relatively low in such zircons, sometimes below 10 ppm, making measurements by TIMS the only efficient method to date such grains.

A recent study of the eclogites in the Glenelg area of the Scottish Highlands (Brewer et al. in press) recovered small amounts of zircon from variably retrogressed basaltic eclogitic rocks with a MORB geochemical signature. In that study, the zircon was noted to occur both as tiny grains apparently stable in eclogitic phases (garnet, omphacite) but more abundantly as grains within the plagioclase and hornblende-bearing hydration zones that formed during exhumation. Rutile and titanite replacement overgrowths on rutile were also dated, with all minerals being characterized by extremely low uranium contents not exceeding 10 ppm. While not being what would be classed as high precision data, the zircon data, shown in Figure 10, illustrate the relative concordance and precision obtained on such extremely low-U crystals, with analyses consisting of as little as 20 picograms of radiogenic Pb.

In a recent study, Kaneko et al. (2001) dated by repeated measurement using the SHRIMP ion microprobe thin metamorphic zircon rims containing tiny inclusions of coesite from granitic gneiss and obtained ages of 46 Ma. Gough (2003) used ID-TIMS on zircon, allanite and titanite from the

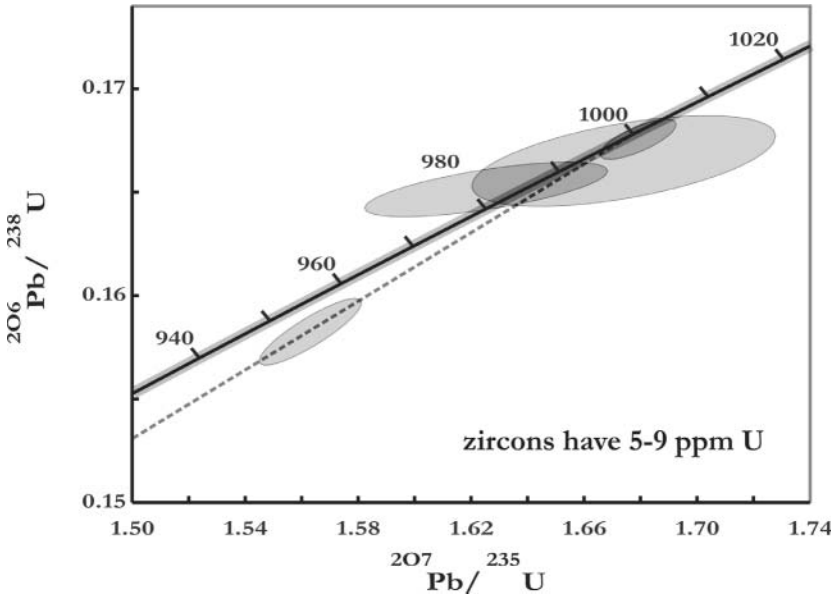


**Figure 10.** Concordia plot of four analyses of very low-U (<10 ppm) zircon from eclogite, Glenelg, Scotland. The uncertainty in the position of the Concordia curve arising from uncertainty in the decay constants is shown in light gray shading.

same granitic gneiss and zircon and rutile from the adjacent coesite-bearing eclogite. This latter data showed that 46 Ma zircons with high U and low Th/U were growing in the eclogite during the UHP event, and that older lower U and higher Th/U zircon were present in both the eclogite and granitic gneiss that relate to the age of the Palaeozoic protolith in both rocks. Zircon in both rocks was inferred to have grown during the UHP event, in part by its association with coesite micro-inclusions. The 46 Ma concordant zircon date produced by ID-TIMS was on a single distinctive grain from the coesite eclogite and provided an age of UHP metamorphism directly from eclogite. This suggests that although rare, such zircons are more common than is thought, suggesting that zircon dating of eclogite is an underutilized technique, especially when combined with U-Th-Pb dating of other accessory minerals (allanite, rutile, titanite) and other isotopic systems (Lu-Hf, Sm-Nd).

Recent intra-grain U-Pb zircon dating using ion microprobe methods on eclogitic rocks of the Alps (Rubatto et al. 1999) provided ages of ca. 60-75 Ma for high pressure metamorphism. The results resolve clearly that the high-pressure metamorphic event was of a pre-collisional nature within the Alps. These dates were on complex zircons of low uranium content, and the relatively large errors of both individual measurements and of pooled measurements (to increase the analytical precision) reflects the difficulties of precise dating on such young and low-U zircons using these methods. It might be worth noting that provided that the zircons were relatively simple in origin, ID-TIMS would deliver more precise dates for eclogitic zircons in high-pressure metamorphic environments. The precision issue comes into focus when one realizes that high pressure metamorphism and exhumation can be extremely rapid, requiring high age resolution to shed light on the detailed tectonics processes.

## Th and Pa chemical partitioning in zircon and its implications

***Th-U partitioning and its effects*.** Because the U and Th decay series are complex and include multiple intermediate daughters of variable half-life, it is possible to have significant concentrations of $^{230}$Th and $^{231}$Pa, the two longest-lived non-U daughters, within magma. It is well known that minerals that preferentially partition Th relative to U into their structures (i.e., monazite, thorite, allanite) can and do incorporate $^{230}$Th which subsequently decays to $^{206}$Pb without the uranium parent being present (Schärer 1984, Barth et al. 1989, Parrish 1990). This produces an excess of $^{206}$Pb and causes U-Pb analyses to lie above Concordia shortly after crystallization. In young rocks this can lead to $^{207}$Pb*/$^{206}$Pb* ages being measurably lower than the crystallization age, even being negative (future ages). This is extremely rare in zircon because it favors U over Th in the overwhelming majority of situations. The example of a Th-rich zircon from the metamorphosed carbonatite, described above and shown in Figure 9, is a rare example of this effect within zircon, leading to $^{206}$Pb*/$^{238}$U ages that are too old.

The complementary effect occurs when minerals of high U/Th ratio, like zircon, exclude the $^{230}$Th present in the magma, a feature that leads to a deficiency in $^{206}$Pb* and results in zircons plotting slightly below Concordia, a feature that is resolvable in young zircons with high precision analyses. Figure 7 illustrates several high precision zircon analyses redrawn from the published literature that show that given excellent quality analyses, this effect can be routinely measured in young samples. Figure 7g shows data from a particularly young (9.3 Ma) leucogranite (Fraser et al. 2001) containing uraninite, monazite and xenotime in addition to zircon, with all accessory minerals (except the relatively imprecise zircon) showing the effects of excess (monazite) or deficiency (Th-poor xenotime and uraninite) of $^{206}$Pb*. If it is present in young samples it is highly probably that it would be widespread in older zircons. This has implications for the interpretation of $^{207}$Pb*/$^{206}$Pb* ages for zircons.

Regardless of whether there is an excess or a deficiency of $^{206}$Pb*, a correction can be made if one assumes (or measures) a value for the Th/U of the magma or reservoir from which the mineral crystallized. A caveat to this assumption is that this may not be valid if the Th/U of the magmatic liquid is unrepresentative of the liquid + crystal volume due to sequestration of U or Th in other mineral phases

(i.e., inherited zircon, allanite, etc.). This correction takes the form (modified from Schärer 1984),

$$^{206}Pb^*/^{238}U_{corrected} = ^{206}Pb^*/^{238}U_{measured} - [(f\text{-}1)(\lambda_{238}/\lambda_{230})] \quad (4)$$

where $f = [^{232}Th/^{238}U_{mineral}]/[^{232}Th/^{238}U_{reservoir}]$ and $\lambda_{238}$ and $\lambda_{230}$ refer to the decay constants for $^{238}U$ and $^{230}Th$ ($1.55125 \times 10^{-10}$/yr and $9.158 \times 10^{-6}$/yr, respectively; Jaffey et al. 1971, Cheng et al. 2000). The corrected $^{207}Pb^*/^{206}Pb^*$ can be calculated by the following,

$$^{207}Pb^*/^{206}Pb^* = (^{207}Pb^*/^{235}U_{measured})/(^{206}Pb^*/^{238}U_{corrected})/137.88 \quad (5)$$

where 137.88 is the natural atomic $^{238}U/^{235}U$ abundance ratio. The maximum deficiency of $^{206}Pb^*$ in this situation can be calculated and is ~108,000 years (Schärer 1984, Parrish 1990). Notwithstanding this correction, readers need to be aware that it is virtually impossible to apply this correction to the growth of metamorphic zircon because of the difficulty of estimating the Th/U of the fluid reservoir from which the zircon grew, due to U and Th sequestration in other minerals.

One can turn this 'problem' around and use it to calculate the Th/U evolution of a magma if the age of dated crystals is known (from Th/Pb dating for example) and if the Th/U ratio of crystals is accurately measured. Equation (4) can be used therefore to estimate the fractionation factor, from which the $^{232}Th/^{238}U_{reservoir}$ can be calculated. A very elegant recent study of the evolving Th/U ratio of the Bergell granite of the southern Alps by Oberli et al. (in press) using U-Th-Pb dating of allanite illustrates this approach.

***Protactinium (Pa) partitioning and its effects.*** A second effect, and apparently more unusual in occurrence, has been inferred in two samples of igneous zircon. Protactinium-231 is the most long-lived intermediate isotope in the $^{235}U$ decay series, with a half-life of approximately 32,500 years and there are no other stable or long-lived isotopes of Pa. As a consequence of the latter point, very little is known about the potential partition coefficients of Pa in the numerous accessory minerals. If $^{231}Pa$ isotope effects are present in accessory minerals, this can be inferred only by the measurement of the decay products of $^{231}Pa$, not to the measurement of $^{231}Pa$ directly. Thus explanations invoking $^{231}Pa$-excesses are really inferences and cannot necessarily be regarded as proof that $^{231}Pa$ was responsible.

The first discovery of zircons with a potential $^{231}Pa$ effect was reported by Mortensen et al. (1992) from a pegmatite in the Yukon Territory of Canada. The second example was very similar and is from Anczkiewicz et al. (2001). Both are characterized by a horizontal array of zircon analyses on a concordia diagram, with consistent $^{206}Pb^*/^{238}U$ ages, but highly variable $^{207}Pb^*/^{235}U$ ages. The example of Mortensen is shown in Figure 11a and is particularly instructive in that there is an inverse correlation between uranium content and $^{207}Pb^*/^{235}U$ age, and because the zircons themselves contain relatively low but highly variable uranium contents. This inverse correlation is born out by a plot of U concentration against $^{207}Pb^*/^{206}Pb^*$ (Fig. 11b). This was explained by the dilution of a relatively constant amount of excess unsupported $^{207}Pb^*$ in each grain by variable amount of $^{207}Pb^*$ produced in situ by the parent $^{235}U$ isotope. A calculation based on reasonable contents of U and Zr in the magma suggested that this explanation was broadly plausible, but such an explanation would require that virtually all of the $^{231}Pa$ be sequestered into zircon, rather than other phases.

There are other examples where $^{231}Pa$ could be affecting U-Pb systematics, but where the effect is less dramatic due to higher degree of dilution of the excess $^{207}Pb^*$ signal. Examples from the work of Kamo et al. (1996) and Rublee (1994) are illustrated in Figures 7b and 7c. In other examples of Figure 7 where the cluster of analyses lie more than ~100,000 years from Concordia, this could be a partial explanation, regardless of whether the rocks are mafic or felsic. In these cases, what one has is very consistent air abraded, somewhat discordant data with a clearly older $^{207}Pb^*/^{206}Pb^*$ age than the $^{206}Pb^*/^{238}U$ age. Additionally, the effect is larger than merely the deficiency in $^{206}Pb^*$ arising from $^{230}Th$ exclusion, for example Figures 7c and 7e. Clearly in trying to

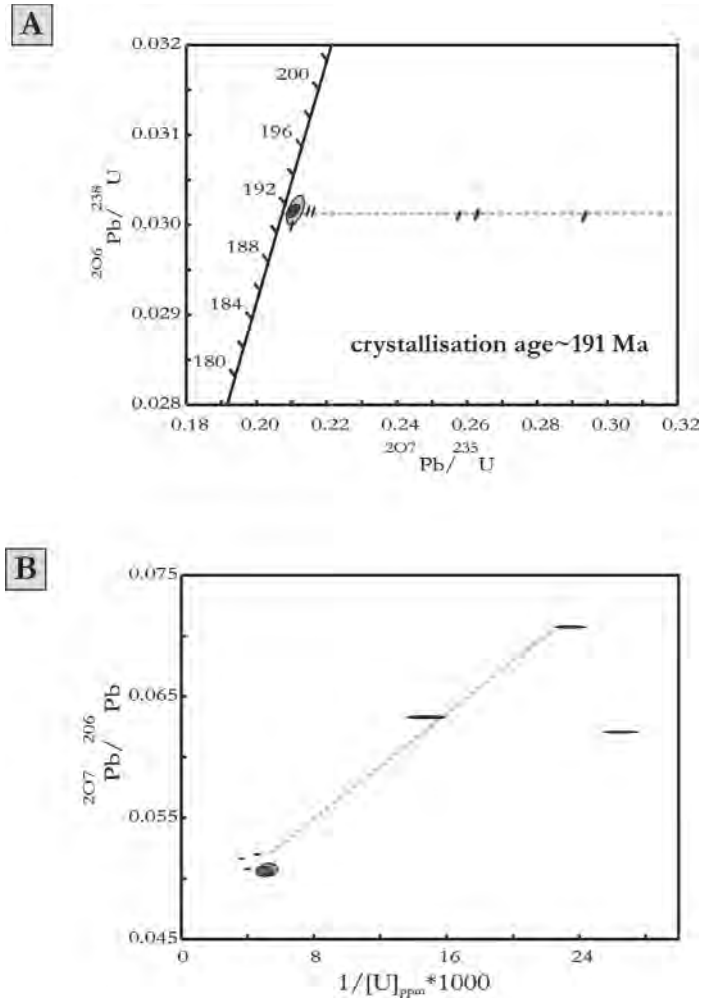


**Figure 11.** (A) Concordia plot of 8 zircons from pegmatite showing marked excess of $^{207}Pb^*$. (B) Plot of $^{207}Pb^*/^{206}Pb^*$ vs. 1/[U] for the same zircons, demonstrating a strong inverse correlation between excess $^{207}Pb^*$ content and uranium concentration. Data courtesy of J.K. Mortensen and Mortensen et al. (1992).

resolve such small effects, the uncertainty in the decay constants must be continually kept in mind.

These are particularly interesting examples because they tell us much about the detailed interpretation of U-Pb systematics, even in very 'simple' zircons, and provide sobering evidence that there are difficulties lurking in the interpretation to even straightforward samples. These effects are entirely masked by the imprecision of micro-beam U-Th-Pb techniques and their much higher errors, and can only be revealed by ID-TIMS analysis.

***4.4 Ga oceans could be dried up.*** Lest we think that these annoying details of U-Pb systematics only concern young samples, consider the recent paper by Wilde et al. (2001) in *Nature* that made ion microprobe U-Pb, trace element, and oxygen isotope measurements on the purported oldest zircon from Earth, a detrital grain from the Jack Hills meta-conglomerate of western Australia. That study made U-Pb measurements of spots within a single grain of zircon and produced both discordant and nearly concordant ages with one spot analysis being 4404±4 Ma. Zones from this crystal with similar appearance and REE pattern revealed age variations of up to 60 Ma (Fig. 12). This variation was discounted as the result of ancient Pb loss and the age of the grain was inter-

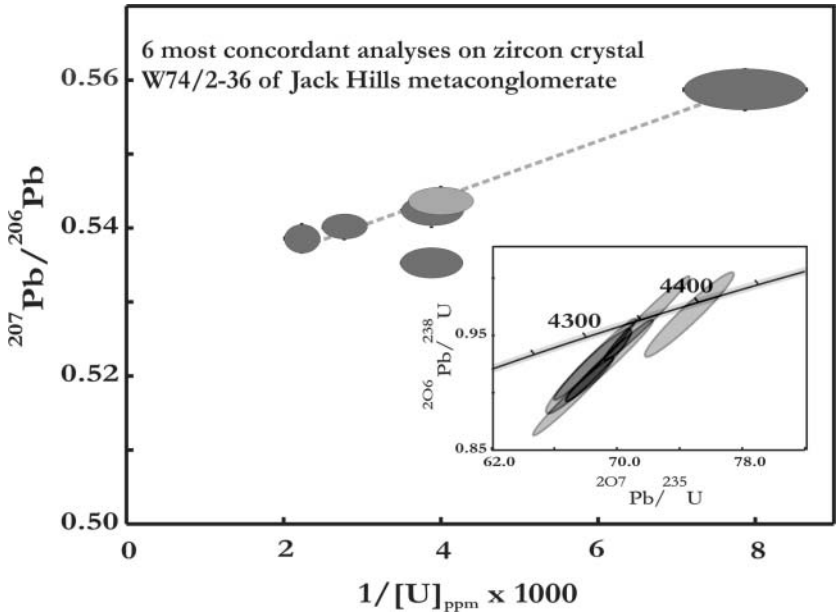


**Figure 12.** Data from 6 zircon ion microprobe analyses of regions within a single crystal of zircon from the Jack Hills meta-conglomerate, illustrating the same type of correlation as in Figure 11, drawn using data of Wilde et al. (2001). The inset shows a concordia plot of the six analyses, with the uncertainty in the position of the Concordia curve arising from uncertainty in the decay constants shown in light gray shading.

preted as 4.4 Ga on the basis of this one spot. Oxygen isotope measurements on one of two measured spots in the crystal not coincident with the 4404±4 Ma spot revealed a signature indicative to the authors of interaction with the hydrosphere, from which they deduced that an early earth ocean existed 4.4 Ga ago.

Contrary to the assertion of Wilde et al. (2001), there is an excellent correlation between $^{207}Pb^*/^{206}Pb^*$ or $^{207}Pb^*/^{235}Pb^*$ of the most concordant 7 or 8 points and uranium concentration or 1/[U] (Fig. 12), similar in form to the example of Mortensen et al. (1992) described above and shown in Figure 11. This suggests, but of course does not prove, that this variation in $^{207}Pb^*/^{206}Pb^*$ and $^{207}Pb^*/^{235}U^*$ is the result of variable amounts of excess $^{231}Pa$-derived $^{207}Pb^*$, and that the $^{207}Pb^*/^{206}Pb^*$ ages are too old, with ca. 4.3 Ga being more likely to be a *maximum* age. Readers should note the fact that in early earth history, $^{235}U$ and $^{231}Pa$ would have been much more abundant than at present, so that there is no reason to suspect that these effects are more likely to be observed only in younger zircons. The implications of this different interpretation to the U-Pb systematics to early earth evolution are therefore potentially profound, and this underlines why the study of these 'small' effects is quite important.

## Other examples where ID-TIMS data has proved effective

There are other geological applications of ID-TIMS dating that we will describe that involve provenance studies of single zircons, and a case study on resolving rapid tectonic events in the Precambrian. Both of these are very successfully accomplished with ID-TIMS methods where the advantages of ID-TIMS analysis are clear.

***Provenance studies of sedimentary rocks.*** Amelin et al. (1999) revisited the old zircons of the Jack Hills meta-conglomerate in western Australia and determined the U-Pb ages of single grains by ID-TIMS methods, and subsequently analyzed the Lu and Hf isotope ratios *of the same grains* by a combination of ID-TIMS (for Lu) and multicollector ICP-MS (for Hf). This type of

approach is analogous to the U-Pb and Sm-Nd isotope study of single grains of detrital monazite, both by ID-TIMS, of Ross et al. (1991, 1992) whereby precise U-Pb ages and $\varepsilon_{Nd}$ (monazite) were measured for each grain at their crystallization age to estimate crustal residence pre-history. Both studies provide elegant examples of the combined use of a geochronometer and a natural radiogenic tracer isotope to reveal much more information on the source characteristics of the detritus than would be apparent from U-Pb dating alone. The ID-TIMS approach used in these studies allows the tracer isotopes to be spiked, separated and purified for high precision tracer isotope analysis in a manner than would not be possible with micro-beam techniques. The disadvantage of this approach is that fewer U-Pb ID-TIMS analyses can be produced in a given time as compared to micro-beam methods, and that a potential bias towards higher quality grains might result. As previously mentioned the use of isotope dilution methods with a multicollector ICP-MS for both U-Pb and Lu-Hf (or Sm-Nd) analysis would provide a major advantage with regards to analysis time, and this represents one way forward that will be increasingly used in future years in provenance studies.

***Resolving rapid tectonic events.*** We next present a portion of a major study of the tectonic history of the northern Ungava peninsula (Canada), a continent-continent collision zone formed when a series of arcs and older continental crust collided with the Archaean Superior Province about 1.8 Ga ago. The example is instructive because it documents a case of extremely rapid geological evolution culminating in granulite facies metamorphism during the climax of continental collision/terrane accretion. For further information on the tectonic setting of the region readers are referred to a summary paper of St-Onge et al. (2001).

The rocks and area mentioned here form part of the accretion zone that juxtaposes the Ungava terrane (mainly Palaeoproterozoic crustal elements) with the Archaean Superior Craton to the south and beneath it. In the vicinity of Sugluk Inlet on the north coast of the Ungava Peninsula at latitude ca. 75°45'W longitude, a series of deformed igneous and metasedimentary rocks occur in a sheared tectonic assemblage at granulite facies conditions, with peak pressures of ca. 7-8 kbar at >800°C (St-Onge et al. 2000). Contained within this succession is a relatively coarse-grained quartzite, which is intruded by leucogranitic igneous sheets, both being equilibrated at granulite facies conditions. Nearby a few kilometers to the west along the coast are banded quartzo-feldspathic orthopyroxene-bearing biotite gneisses that appear to resemble metamorphosed and strained quartzose turbitidic sedimentary rocks. Locally, these rocks have melted to produce undeformed irregular leucosomes that truncate the banding within the metasedimentary rocks. The structural basement upon which the metasedimentary rocks were deposited could be the 1.83-1.86 Ga calc-alkaline meta-plutonic rocks of the Narsajuaq arc, but the actual contact is now of a tectonic origin. Together the following sequential geological events can be inferred:

- formation of the Narsajuaq arc,
- deposition of the quartzite and turbiditic sedimentary rocks
- intrusion of leucogranitic rocks during metamorphism
- metamorphism to granulite facies, accompanied by strong deformation
- partial melting of quartzo-feldspathic lithologies at granulite facies

A U-Pb Concordia diagram with selected ID-TIMS data relevant to each of these events is shown in Figure 13. All of the zircon analyses were air abraded, and most analyses represent single grains.

The youngest precisely dated rock of the Narsajuaq arc is 1836±1 Ma (two concordant zircons), providing evidence for the arc remaining active to at least this age. Other dates on related arc rocks are older, up to 1.86 Ga.

Single detrital zircons from the quartzite (4 analyses shown) contain concordant or near-concordant zircons as young as 1832-1834 Ma, and other detrital grains are 1.84-1.86 and >2.0 Ga. From this it is possible to infer that the erosion of a source containing zircons that may have been derived from

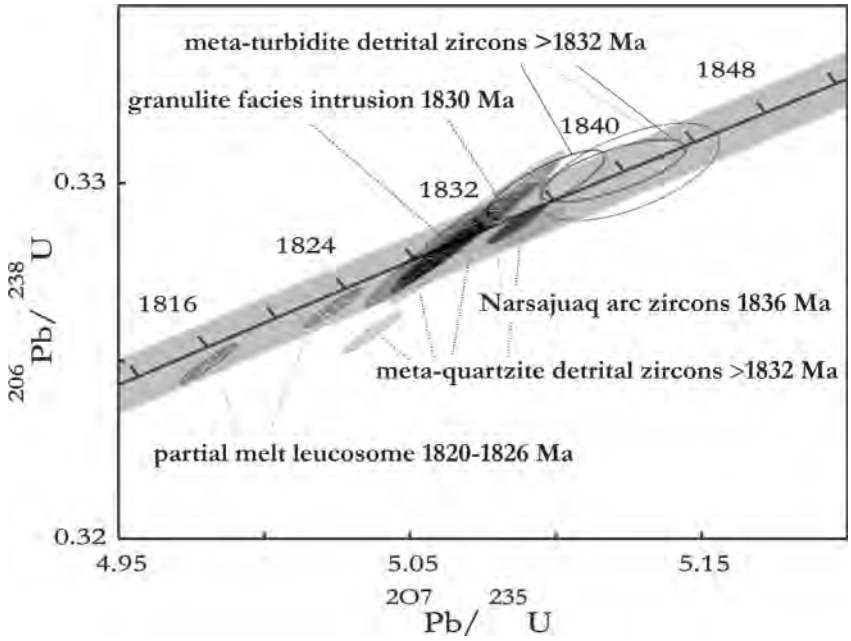


**Figure 13.** Concordia plot of zircons from five samples constraining tectonic and sedimentation events within the northern Ungava orogen, northernmost Quebec, unpublished data of Parrish as summarized in Parrish (1989). See text for description of the samples and data interpretation. The uncertainty in the position of the Concordia curve arising from uncertainty in the decay constants is shown in light gray shading.

the Narsajuaq arc, and deposition of the quartzitic sediment took place after about 1833 Ma.

The turbiditic metasedimentary rocks have a similar assemblage of detrital zircons ranging in age from 1833-1840 Ma, but including other grains >2.1 Ga. These too may have been derived from the arc, but were deposited no earlier than 1833 Ma. Three concordant analyses of these grains are illustrated in Figure 13.

Intrusion of leucogranitic igneous rocks into the metasedimentary assemblage took place after the deposition of the sedimentary rocks, and a date on a granulite facies leucocratic metagranitoid sheet is 1830±2 Ma (3 concordant analyses). Other intrusive igneous rocks are 1832±2 Ma, but contain some inherited slightly older grains. Deformation and granulite facies metamorphism probably accompanied the intrusion of some of these samples, but in any case, they were brought to granulite facies conditions prior to the thermal peak.

Partial melting of the turbiditic lithology produced an undeformed cross-cutting leucosome. Zircons from this sample include detrital grains inevitably entrained in the local partial melt, but also highly irregular, low-U grains that likely crystallized from the leucosome. These latter analyses (two shown in the figure, slightly discordant) provide ages in the range of 1820-1826 Ma.

The assumption made in the construction of the chronology of these samples is that concordant zircon dates on air-abraded zircons provide ages of crystallization and are unaffected by either Pb loss (recent or ancient) or mixing with other age components. These assumptions are hard to prove in a definitive sense, but the consistency of the data, supported by numerous samples, and the strong air abrasion combined with selection of distinct morphological types of zircons, argues that these assumptions are reasonable. The precision on single analyses varies but is generally ±1-4 Ma.

This example shows how samples collected with a view to ascertaining a tectonic chronology, when combined with detailed ID-TIMS U-Pb dating, can document with very detailed resolution the complex and extremely rapid geological events contained within the cores of orogens.

ID-TIMS methods on zircon inherently have the potential to resolve these events in this kind of detail, and the advantages of the method in this and previous cases are plain to see.

## SUMMARY

ID-TIMS zircon U-Pb geochronology is an extremely powerful technique in resolving the chronology of geological events in the Earth, and the U-Pb system alone retains the ability to potentially resolve events on the sub-million year scale throughout all of Earth's 4.5 Ga history. ID-TIMS analysis has a long and mature history of development, throughout which important analytical breakthroughs have taken place. The bedding-in process of the most important analytical developments have been thoroughly tested, but the attention to detail in their application by laboratories to sample analysis needs to be retained, and it is essential to retain the historical perspective of the crucial advances.

This chapter has presented a discussion of many useful applications of the method to earth science, and has emphasized the importance of learning about the implications of complex interpretations of U-Pb systematics, but also the implications of variations on the analytical methodology. The method has stood the test of time and emerged as extremely versatile and robust, when appropriately applied to the wide variety of applications. There is little doubt of the importance of complementary U-Pb methods of micro-beam analysis, especially ion microprobe in solving complex problems, but with the proliferation of methodologies and the pressures of time and cost for U-Pb analysis, there is a real danger that more rapid micro-beam methods of U-Pb analysis may be seen as supplanting ID-TIMS and making it seem redundant as a methodology. This chapter hopes to have convinced readers of the *complementarity* of ID-TIMS with other micro-beam methods in the application of U-Th-Pb dating to earth science.

## ACKNOWLEDGMENTS

The authors thank staff of the NERC Isotope Geosciences Laboratories for assistance in the production of this manuscript and colleagues in our previous posts at the Geological Survey of Canada and the Royal Ontario Museum for discussions and assistance in data production in past years. This work was supported by a block grant to the NERC Isotope Geosciences Laboratories from the Natural Environment Research Council and from NERC grant GR3/13006 to the senior author. RP thanks J Kramers for discussion of excess $^{207}$Pb* in the context of the Wilde et al. (2001) paper, and we thank Jim Mortensen for permission to include in Figure 11 some of his zircon data acquired at the Geological Survey of Canada. The authors thank Bill Davis, George Gehrels, James Mattinson and John Hanchar for detailed and thoughtful reviews that substantially improved the paper.

## REFERENCES

Amelin Y, Lee D-C, Halliday AN, Pidgeon RT (1999) Nature of the Earth's earliest crust from Hafnium isotopes in single detrital zircons. Nature 399:252-255

Anczkiewicz R, Oberli F, Burg JP, Villa IM, Gunther D, Meier M (2001) Timing of normal faulting along the Indus Suture in Pakistan Himalaya and a case of major Pa-231/U-235 initial disequilibrium in zircon. Earth Planet Sci Lett 191:101-114

Anderson CA, Hinthorne JR (1972) U, Th, Pb, and REE abundances and 207Pb/206Pb ages of individual minerals in returned lunar material by ion microprobe mass analysis. Earth Planet Sci Lett 14:195-200

Ashwal LD, Tucker RD, Zinner EK (1999) Slow cooling of deep crustal granulites and Pb-loss in zircon. Geochim Cosmochim Acta 63:2839-2851

Barth S, Oberli F, Meier M (1989) U-Th-Pb systematics of morphologically characterized zircon and allanite: A high-resolution isotopic study of the Alpine Rensen Pluton (northern Italy). Earth Planet Sci Lett 95:235-254

Bertrand J-M, Roddick JC, Van Kranendonk MJ, Ermanovics I (1993) U-Pb geochronology of deformation and metamorphism across a central transect of the Early Proterozoic Torngat Orogen, North River map-area, Labrador. Can J Earth Sci 30:1470-1489

Bleeker W, Parrish RR, Kinsman A (1999) High-precision U-Pb geochronology of the Late Archean Kidd Creek deposit and surrounding Kidd volcanic complex. Econ Geol Monogr 10:43-70

Bingen B, Austrheim H, Whitehouse M (2001) Ilmenite as a source for zirconium during high-grade metamorphism? Textural evidence from the Caledonides of Western Norway and implications for zircon geochronology. J Petrol 42:355-375

Bowring SA, Williams IS, Compston W (1989) 3.96 Ga gneisses from the Slave Province, Northwest Territories, Canada. Geology 17:971-975

Brewer TS, Storey CD, Parrish RR, Temperley S, Windley BF (in press) Grenvillian age exhumation of eclogites in the Glenelg-Attadale inlier, NW Scotland. J Geol Soc

Cameron AE, Smith DE, Walker RL (1969) Mass spectrometry of nanogram size samples of lead. Analyt Chem 41:525-526

Chapman HJ, Roddick JC (1994) Kinetics of Pb release during the zircon evaporation technique. Earth Planet Sci Lett 121:601-611

Chen F, Siebel W, Satir M (2002) Zircon U-Pb and Pb-isotope fractionation during stepwise HF acid leaching and geochronological implications. Chem Geol 191:155-164.

Cheng H, Edwards RL, Hoff J, Gallup CD, Richards DA, Asmerom Y (2000) The half-lives of uranium-234 and thorium-230. Chem Geol 169:17-33

Compston W, Williams IS, and Meyer C (1984) U-Pb geochronology of zircons from lunar breccia 73217 using a sensitive high mass resolution ion microprobe. J Geophys Res 89B:525-534

Connelly JN (2000) Degree of preservation of igneous zonation in zircon as a signpost for concordancy in U/Pb geochronology. Chem Geol 172:25-39

Corfu F (2000) Extraction of Pb with artificially too-old ages during stepwise dissolution experiments on Archean zircon. Lithos 53:279-291

Corfu F, Noble SR (1992) Genesis of the southern Abitibi greenstone belt, Superior Province, Canada: Evidence from zircon Hf-isotope analyses using a single filament technique. Geochim Cosmochim Acta 56:2081-2097

Crowley JL, Parrish RR (1999) U-Pb isotopic constraints on diachronous metamorphism in the northern Monashee complex, southern Canadian Cordillera. J Metamor Geol 17:483-502

Davidson A, van Breemen O (1988) Baddeleyite-zircon relationships in coronitic metagabbro, Grenville Province, Ontario: Implications for geochronology. Contrib Mineral Petrol 100:291-299

Davis, DW (1982) Optimum linear regression and error estimation applied to U-Pb data. Can J Earth Sci 19:2141-2149

Davis DW, Krogh TE (2000) Preferential dissolution of $^{234}U$ and radiogenic Pb from alpha-recoil damaged sites in zircon: Implications for thermal histories and Pb isotopic fractionation in the near surface environment. Chem Geol 172:41-58

Fraser JE, Searle MP, Parrish RR, Noble SR (2001) Chronology of deformation, metamorphism, and magmatism in the southern Karakoram Mountains. Geol Soc Am Bull 113:1443-1455

Geisler T, Pidgeon RT, van Bronswijk W, Kurtz R (2002) Transport of uranium, thorium, and lead in metamict zircon under low-temperature hydrothermal conditions. Chem Geol 191:141-154

Gerstenberger H, Haase G (1997) A highly effective emitter substance for mass spectrometric Pb isotope ratio determinations. Chem Geol 136:309-312

Gough S (2003) Subduction-related metamorphism, structure and tectonic evolution of the Kohistan Arc and Main Mantle Thrust zone, Pakistan Himalaya. D.Phil. dissertation, University of Oxford, Oxford

Gulson B, Krogh TE 1973 Old lead component in the young Bergell Massif, south-central Swiss Alps. Contrib Mineral Petrol 40:239-252

Hanchar JM, Miller CF (1993) Zircon zonation patterns as revealed by cathodoluminescence and backscattered electron images—implication for interpretation of complex crustal histories. Chem Geol 110:1-13

Heaman L, Parrish RR (1991) U-Pb geochronology of accessory minerals. *In* Applications of radiogenic isotope systems to problems in geology. Short Course Handbook 19. Heaman L, Ludden JN (eds) Mineralogical Association of Canada, p 59-102

Jaffey AH, Flynn KF, Glendenin LE, Bentley WC, Essling AM (1971) Precision measurements of half-lives and specific activities of $^{235}U$ and $^{238}U$. Phys Rev C4:1889-1906

Jones AP, Peckett A (1980) Zirconium-bearing aegirines from Motzfeldt, South Greenland. Contrib Mineral Petrol 75:251-255

Kamo SL, Czamanske GK, Krogh TE (1996) A minimum U-Pb age for Siberian flood-basalt volcanism. Geochim Cosmochim Acta 60:3505-3511

Kaneko Y, Yamamoto H, Katayama I, Misawa K, Ishikawa M, Hafees RU, Shiraishi K (2001) Coesite inclusions and prograde compositional zonation of zircons in Himalayan gneisses, NW Himlaya, Pakistan: Evidence from SHRIMP-dating of coesite-bearing zircon. Abstracts, Workshop on Ultra High Pressure Metamorphism, Tokyo

Kober B (1986) Whole-grain evaporation for $^{207}Pb/^{206}Pb$-age-investigations on single zircons using a double-filament thermal ion source. Contrib Minera Petrol 93:482-490

Krogh TE (1973) A low contamination method for the hydrothermal decomposition of zircon and extraction of U and Pb for isotopic age determinations. Geochim Cosmochim Acta 37:485-494

Krogh TE (1982) Improved accuracy of U-Pb zircon ages by the creation of more concordant systems using an air

abrasion technique. Geochim Cosmochim Acta 46:637-649
Krogh TE (1998) Etch selection and abrasion techniques applied to complex populations and revealed spurious ion probe ages. Goldschmidt Conf Abstr Vol, Part 2. Mineral Mag A62:816-817
Krogh TE, Davis GL (1975) The production and preparation of $^{205}$Pb for use as a tracer for isotope dilution analyses. Carnegie Institution of Washington Yrbk 1974:416-417
Kroner A, Hegner E, Collins AS, Brewer TS, Razakamanana T, Pidgeon RT (2000) Age and magmatic history of the Antananarivo Block, central Madagascar, as derived from zircon geochronology and Nd isotopic systematics. Am J Sci 300:251-288
Kroner A, Willner AP, Hegner E, Jaeckel P, Nemchin A (2001) Single zircon ages, PT evolution and Nd isotopic systematics of high-grade gneisses in southern Malawi and their bearing on the evolution of the Mozambique belt in southeastern Africa. Precambrian Res 109:257-291
Le Roux LJ, Glendenin LE 1963 Half-life of $^{232}$Th. *In* Proc National Meeting on Nuclear Energy, Pretoria, South Africa, p 83-94
Ludwig KR (1998) On the treatment of concordant uranium-lead ages. Geochim Cosmochim Acta 62: 665-676
Mattinson JM (1972) Preparation of hydrofluoric, hydrochloric, and nitric acids at ultra-low lead levels. Analyt Chem 44:1715-1716
Mattinson JM (1973) Anomalous isotopic composition of Pb in young zircons. Carnegie Institute of Washington Yrbk, 72:613-616
Mattinson JM (1987) U-Pb ages of zircons: A basic examination of error propagation. Chem Geol (Isotope Geosci Section) 66:151-162
Mattinson JM (1994) A study of complex discordance in zircons using step-wise dissolution techniques. Contrib Mineral Petrol 116:117-129
Mattinson JM (2000) U-Pb analysis by 'chemical abrasion': Combined high-temperature annealing and partial dissolution analysis. EOS Trans, Am Geophys Union 81 n.19 GS32A-02
McClelland WC, Mattinson JM (1996) Resolving high precision U-Pb ages from Tertiary plutons with complex zircon systematics. Geochim Cosmochim Acta 60:3955-3965
Mortensen JK, Roddick JC, Parrish RR (1992) Evidence for high levels of unsupported radiogenic $^{207}$Pb in zircon from a granitic pegmatite: Implications for interpretation of discordant U-Pb data. EOS Trans, Am Geophys Union 73:370
Mundil R, Metcalfe I, Ludwig KR, Renne PR, Oberli F, Nicoll RS (2000) Timing of the Permian-Triassic biotic crisis: Implications from new zircon U/Pb age data (and their limitations). Earth Planet Sci Lett 187:131-145
Nier A (1940) A mass spectrometer for routine isotope abundance measurements. Rev Sci Instrument 11:212-216
Nutman AP, Bennett VC, Friend CRL, McGregor VR (2000). The early Archaean Itsaq Gneiss Complex of southern West Greenland: The importance of field observations in interpreting age and isotopic constraints for early terrestrial evolution. Geochim Cosmochim Acta 64:3035-3060
Nutman AP, McGregor VR, Bennett VC, Friend CRL (2001) Age significance of U-Th-Pb zircon data from early Archaean rocks of west Greenland—A reassessment based on combined ion-microprobe and imaging studies: Comment. Chem Geol 175:191-199
Oberli F, Meier M, Berger A, Rosenberg C, Giere R (in press) U-Th-Pb and $^{230}$Th/$^{238}$U disequilibrium isotope systematics: Precise accessory mineral chronology and melt evolution tracing in the Alpine Bergell intrusion. Geochimica Cosmochimica Acta.
Pálfy J, Parrish RR, David K, Vörös A (in press) Middle Triassic integrated U-Pb geochronology and ammonoid biochronology from the Balaton Highland (Hungary) and their bearing on problems of time scale, evolution, and sedimentation. J Geol Soc
Parrish RR (1987) An improved micro-capsule for zircon dissolution in U-Pb geochronology. Chem Geol (Isotope Geosci Section) 66:99-102
Parrish RR (1989) U-Pb geochronology of the Cape Smith Belt and Sugluk block, northern Quebec. Geosci Canada 16:126-130
Parrish RR (1990) U-Pb dating of monazite and its application to geological problems. Can J Earth Sci 27:1431-1450
Parrish RR (1995) Thermal and tectonic evolution of the southeastern Canadian Cordillera. Can J Earth Sci 32:1618-1642
Parrish RR, Krogh TE (1987) Synthesis and purification of $^{205}$Pb for U-Pb for geochronology. Chem Geol (Isotope Geosci Section) 66:103-110
Parrish RR, Scammell RJ (1988) The age of the Mount Copeland syenite gneiss and its metamorphic zircons, Monashee complex, southeastern British Columbia. *In* Radiogenic Age and Isotopic Studies. Report 2. Geol Surv Canada Paper 88-2:21-22
Patterson BA, Stephens WE, Rogers G, Williams IS, Hinton RW, Herd DA (1992) The nature of zircon inheritance in 2 granite plutons. Trans Royal Soc Edinburgh-Earth Sci 83:459-471
Renne PR, Swisher CC, Deino AL, Karner DB, Owens T, DePaolo DJ 1998. Intercalibration of standards, absolute ages and uncertainties in 40Ar/39Ar dating. Chem Geol (Isotope Geosci Section) 145:117-152

Roddick JC (1987) Generalized numerical analysis with applications to geochronology and thermo-dynamics. Geochim Cosmochim Acta 51:2129-2135

Roddick JC, Loveridge WD, Parrish RR (1987) Precise U/Pb dating of zircon of the sub-nanogram Pb Level. Chem Geol (Isotope Geosci Section) 66:111-121

Ross GM, Parrish RR, Dudas FO (1991) Provenance of the Bonner Formation (Belt Supergroup), Montana: Insights from U-Pb and Sm-Nd analyses of detrital minerals. Geology 19:340-343

Ross GM, Parrish RR, Winston D (1992) Provenance and U-Pb geochronology of the Middle Proterozoic Belt Supergroup (northwestern United States): Implications for age of deposition and pre-Panthalassa plate reconstructions. Earth Planet Sci Lett 113:57-76

Rubatto D, Gebauer D, Compagnioni R (1999) Dating of eclogite facies zircons: The age of Alpine metamorphism in the Sesia-Lanzo Zone (Western Alps). Earth Planet Sci Lett 167:141-158

Rublee J (1994) Chemical petrology, mineralogy and structure of the Tulameen Complex, Princeton area, British Columbia. MSc thesis, University of Ottawa, Ottawa

Schärer U (1984) The effect of initial $^{230}$Th disequilibrium on young U-Pb ages: The Makalu case, Himilaya. Earth Planet Sci Lett 67:191-204

Schmitz MD, Bowring SA (2001) U-Pb zircon and titanite systematics of the Fish Canyon Tuff: An assessment of high-precision U-Pb geochronology and its application to young volcanic rocks. Geochim Cosmochim Acta 65:2571-2587

Silver LT, Deutsch S (1963) Uranium-lead isotopic variations in zircons: A case study. J Geol 71:721-758

Speer JA (1982) Zircon. Rev Mineral 5 (2$^{nd}$ edn):67-112

Stacey JS, Kramers JD (1975) Approximation of terrestrial lead isotope evolutionby a two-stage model. Earth Planet Sci Lett 26:207-221

Steiger RH, Jäger E (1977) Subcommission on Geochronology: Convention on the use of decay constants in geo- and cosmochronology. Earth Planet Sci Lett 36:359-362

St-Onge MR, Wodicka N, Lucas SB (2000) Granulite- and amphibolite-facies metamorphism in a convergent-plate-margin setting: Synthesis of the Quebec-Baffin segment of the Trans-Hudson Orogen. Can Mineral 38:379-398

St-Onge MR, Scott DJ, Wodicka N (2001) Terrane boundaries within Trans-Hudson Orogen (Quebec-Baffin segment), Canada: Changing structural and metamorphic character from foreland to hinterland. Precambrian Res 107:75-91

Tera F, Wasserburg GJ (1972) U-Th-Pb systematics in three Apollo 14 basalts and the problem of initial Pb in lunar rocks. Earth Planet Sci Lett 17:281-304

Tilton GR, Patterson C, Brown H, Inghram M, Hayden R, Hess D, Larsen Jr E (1955) Isotopic composition and distribution of lead, uranium, and thorium in a Precambrian granite. Geol Soc Am Bull 66: 1131-1148

Tilton GR, Davis GL, Wetherill GW, Aldrich LT (1957) Isotopic ages of zircon from granites and pegmatites. EOS Trans, Am Geophys Union 38:360-371

Todt W, Cliff RA, Hanser A, Hofmann AW (1996) Evaluation of a $^{202}$Pb-$^{205}$Pb double spike for high-precision lead isotope analysis. *In* Earth Processes: Reading the Isotopic Code. Geophys Monogr 95. Basu A, Hart S (ed) Am Geophys Union, Washington, DC, p 429-437

Vavra G (1990) On the kinematics of zircon growth and its petrogenetic significance—A cathodoluminescence study. Contrib Mineral Petrolo 106:90-99

Weidenbeck M, Allé P, Corfu F, Griffin WL, Meier M, Oberli F, von Quadt A, Roddick JC, Spiegel W (1995) Three natural zircon standards for U-Th-Pb, Lu-Hf, trace element and REE analyses. Geostandards Newslett 19:1-23

Wetherill GW (1956) Discordant Uranium-Lead Ages, I. Trans Am Geophys Union 37:320-326

Wilde SA, Valley JW, Peck WH, Graham CM (2001) Evidence from detrital zircons for the existence of continental crust and oceans on the Earth 4.4 Ga ago. Nature 409:175-178

Whitehouse MJ, Kamber BS, Moorbath S (1999) Age significance of U-Th-Pb zircon data from early Archaean rocks of west Greenland—A reassessment based on combined ion-microprobe and imaging studies. Chem Geol 160:201-224.

Whitehouse MJ, Kamber BS, Moorbath S (2001) Age significance of U-Th-Pb zircon data from early Archaean rocks of west Greenland—A reassessment based on combined ion-microprobe and imaging studies. Reply. Chem Geol 175:201-208.

Williams IS (1992) Some observations on the use of zircon U-Pb geochronology in the study of granitic rocks. Trans Royal Soc Edinburgh-Earth Sci 83:447-458

# 8 Considerations in Zircon Geochronology by SIMS

**Trevor R. Ireland and Ian S. Williams**

*Research School of Earth Sciences*
*The Australian National University*
*Canberra ACT 0200, Australia*

trevor.ireland@anu.edu.au

## INTRODUCTION

Secondary ion mass spectrometry (SIMS) is a versatile technique for measuring the chemical and isotopic composition of solid materials on a scale of a few microns. A beam of high-energy primary ions is focused onto the polished target surface, sputtering (ablating) atoms and molecules, and in the process ionizing a small fraction. These secondary ions, which reflect the target composition, are analyzed by mass spectrometry. The SIMS instrument most common in geoscience is the ion microprobe, which uses a focused primary ion beam in either static or scanning mode to sample target areas usually 10- to 50-μm diameter. Total sampling depth is typically less than 5 μm and the sampled mass only a few nanograms, making the analysis for most samples effectively non-destructive. Coupled with surface imaging techniques such as backscattered electron (BSE) and cathodoluminescence (CL), SIMS enables finely targeted chemical and isotopic analysis of specific domains exposed on a crystal surface.

Zircon is particularly suitable for SIMS U–Th–Pb geochronology. It is a physically and chemically robust mineral that crystallizes under a range of geological conditions, incorporating trace U and Th, but little or no Pb. Zircon grains are commonly composite, having survived and grown during several geological events. This growth record is sometimes visible under an optical microscope, but is best revealed by CL and BSE imaging of polished sectioned grains (Fig. 1). The U–Th–Pb closure temperature of unaltered zircon is very high (>900°C), and the growth domains commonly can preserve an isotopic record of thermal events spanning tens to thousands of millions of years. This record of provenance, and igneous and metamorphic history, is accessible only to microanalytical techniques such as SIMS.

The first ion microprobe constructed specifically for isotopic analysis of geological materials, the SHRIMP (Sensitive High Resolution Ion MicroProbe), was designed with zircon in mind. Earlier U–Pb dating of lunar minerals using the ARL ion microprobe (Andersen and Hinthorne 1972) had demonstrated the feasibility of the technique, but also revealed a major limitation—the measured Pb isotopic compositions required large corrections for molecular isobaric interferences. These interferences arose because sputtering produces a complex array of molecular secondary ions, some of which have masses very similar to the Pb isotopes. The problem could be overcome by tuning the ion probe mass analyser to high mass resolution (>3000), but with a grievous loss of signal and precision (Hinton and Long 1979). The SHRIMP design philosophy was to achieve high mass resolution without loss of sensitivity by using the widest possible object slit, and therefore the largest practicable double focusing mass spectrometer (magnet turning radius 1 m). The concept proved extremely effective and was later adopted in the design of other ion probes, the Cameca 1270 and VG Isolab 120.

The application of SHRIMP to zircon geochronology rapidly revealed the rich and complex record of geologic history preserved within individual zircon grains. Although at first received with some skepticism (e.g., Moorbath 1983), SIMS has now become the benchmark for the dating of polychronic zircon populations. SIMS analysis does not, and probably never will, achieve the precision attainable by isotope dilution thermal ionization mass spectrometry (ID–TIMS) because of

1529-6466/03/0053-0008$05.00

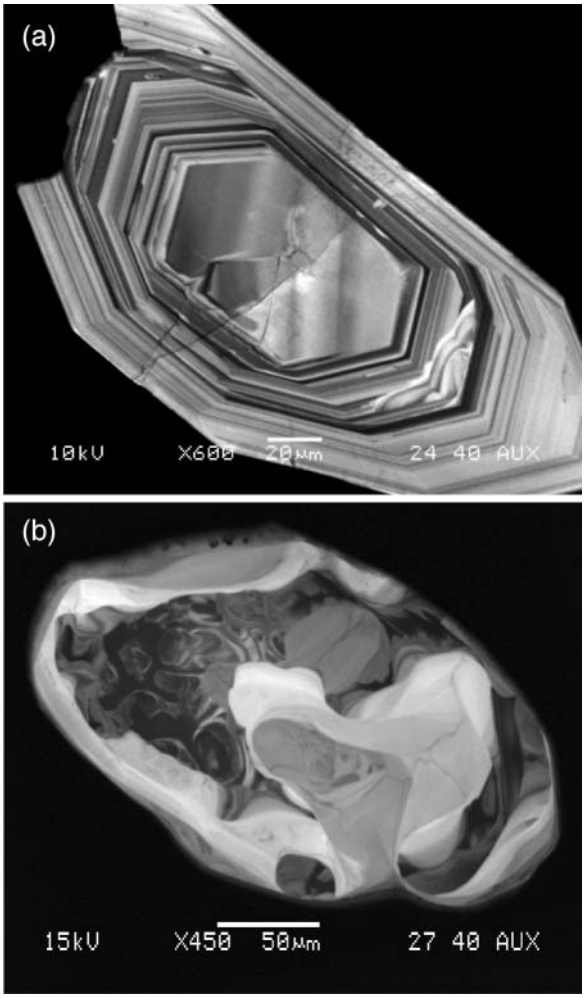


**Figure 1.** Both zircon crystals appear homogeneous in transmitted light but cathodoluminescence images show the true growth structures: (a) an igneous zircon with simple euhedral oscillatory zoning, and (b) a complex metamorphic zircon with chaotic internal structures. Such images are essential if specific growth domains are to be precisely targeted.

the small volume of material sampled, but it remains unrivaled for its precision and accuracy in U–Th–Pb dating at an intra-crystalline scale (Fig. 2).

In this paper we review the current state of SIMS geochronology and consider its possible future. This work is not intended to be a comprehensive review of all aspects of SIMS geochronology but rather an outline of the procedures involved so as to allow a reference frame for discussion of the current analytical status and potential developments for the future. A more comprehensive discussion of analytical and instrumental parameters can be found in Ireland (1995) and Williams (1998).

## SELECTED APPLICATIONS

SIMS-based zircon geochronology has been applied to virtually the whole age range of rocks from Earth and the solar system. SIMS has the particular advantage over other analytical techniques that the tiny sample size required (~2 ng per analysis) makes it possible to analyze very small grains or domains within zoned grains and thereby to deconvolute the products of complex thermal histories. The benefits inherent in SIMS analysis have been exploited in a wide diversity of applications, examples of which are given below. This list is far from exhaustive. Some further examples have been discussed in more detail by Williams (1998).

### Oldest zircon in the solar system

The sensitivity and selectivity afforded by ion probe analysis are well illustrated in the dating of 4.56 Ga zircons from the Vaca Muerta and Simmern meteorites (Ireland and Wlotzka 1992). Meteoritic zircon is quite rare, and it normally occurs as small, sometimes interstitial, grains about 10-µm, and occasionally up to 30-µm, diameter. Making analysis even more difficult, the U content of the zircon can be very low (<1 ppm). Ireland and Wlotzka (1992) analyzed three zircon grains <20-µm diameter in thin section, and therefore in a known petrographic context, first for U-Th-Pb to measure their ages, then for rare earth and other trace elements to determine their genesis, still leaving enough sample for subsequent Hf-W isotopic analyses to measure the abundance of extinct $^{182}$Hf (Ireland 1991). Even after all this work, most of the zircon still remains for future study.

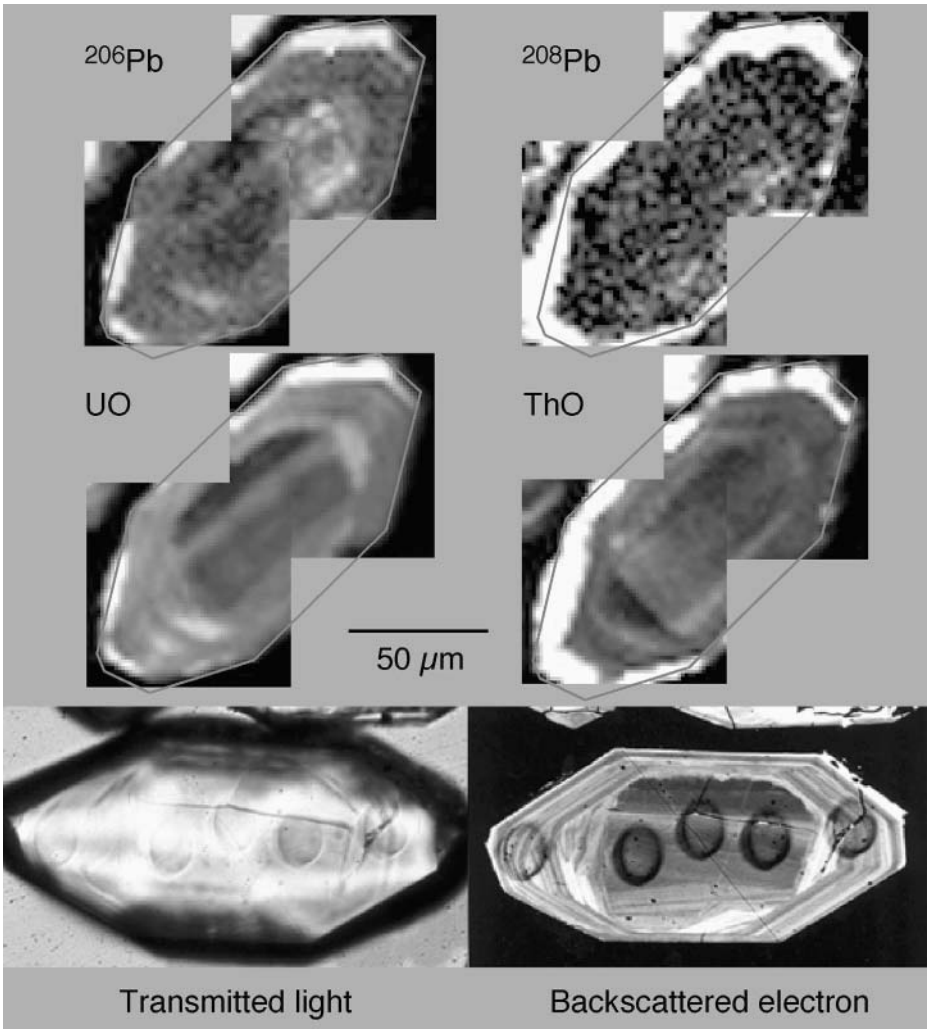


**Figure 2.** Rastered ion images of $^{206}Pb$, $^{208}Pb$, UO and ThO distributions in a zircon from the Paleozoic Cowra granodiorite showing the broad correlation between U and uranogenic Pb, Th and thorogenic Pb, and lack of correlation between Th and U. Core of the zircon as seen in BSE image is Paleoproterozoic and rim is 410 Ma. The core shows an extreme range of discordance but in detail, the $^{206}Pb$ is seen to be graded along the length of the core rather than varying as a function of the U zoning. Note that the core is barely visible in the transmitted light image.

**Development of fractionated lunar crust**

Large numbers of zircon grains were recovered from the sawdust produced by the processing of rocks returned from the Moon. Although these could be dated relatively easily by ID-TIMS, the great majority of the rocks were breccias, so the measured ages had no petrographic context. After exhaustive searches of lunar breccia thin sections, however, numerous single zircons, and rare zircon clusters, were found. Many were isolated grains, but in rare cases the zircon was clearly part of a lithic fragment, the mineralogy of which indicated the composition of the source rock. Dating lunar zircon was one of the earliest applications of the SHRIMP (Compston et al. 1984) and provided much of the impetus to achieve the highest possible accuracy in the measurement of Pb/U. A subsequent more comprehensive study of lunar zircon in lithic fragments made it possible to trace

the extended history of the evolution of the lunar crust (Myer et al. 1996). It demonstrated that the earliest zircon-bearing rocks (~4.37 Ga) were the most mafic, but they were soon followed (at ~4.32 Ga) by highly evolved rocks (granophyres). Production of both rock types continued for more than 300 million years, ceasing abruptly at ~3.9 Ga, the proposed time of the terminal lunar cataclysm. As in the case of the meteoritic zircon, the SIMS analyses consumed so little material that these rare, invaluable samples remain intact for future study.

**The oldest-known terrestrial rocks**

SIMS is not only useful for studying complexity, but also for measuring accurate ages in spite of it. The Acasta gneiss complex from the Northwest Territories, Canada, contains the oldest-known terrestrial rocks, and the only rocks presently available from the Priscoan eon (Stern and Bleeker 1998, Bowring and Williams 1999). The gneiss has had an extremely complex history, including at least four major thermal events, each involving the production of partial melts. The rocks therefore contain multiple generations of zircon, commonly co-existing within individual grains. Making the age measurements even more difficult, most of the zircon crystals are extensively altered and or recrystallized. Using relict euhedral oscillatory zoning as a guide, Bowring and Williams (1999) analyzed remnants of original igneous zircon. Even though such zircon had a single primary age, the patterns of discordance were complex because different domains had responded in different ways to the later thermal events. Instead if defining a quasi-linear discordance array, as is common in the zircon from most high-grade rocks, the data were widely dispersed towards a range of lower concordia intercepts. Only from their consistent convergence towards the same upper intercept, and a few concordant analyses at that intercept, was it possible to infer that the zircon first crystallized at 4.03 Ga.

**Detrital-zircon age spectra**

The high speed of ion-probe analysis opened up a range of new applications in which the dating of large numbers of grains was more important than achieving high precision on individual measurements. A dramatic early success was the discovery of rare >4.1 Ga zircon grains in early Archean sediments from Western Australia (Froude et al. 1983), the first direct evidence for evolved terrestrial crust prior to 4.0 Ga and the first samples of crust known to have survived the massive meteorite bombardment of Earth at 3.9 Ga, the time of the terminal lunar cataclysm. An intensive search is currently under way to identify enough pre-4.0 Ga zircon to be used for a range of further geochemical studies of the composition of the Priscoan crust. Surveying the requisite many thousands of detrital zircons can only be done by ion probe because other techniques for measuring the radiogenic Pb isotopic composition, including laser ICP-MS, are too destructive. Use of multiple collection has reduced the time per reconnaissance analysis to about 20 seconds (Mojzsis et al. 2002). The more common use of ion probes in the study of sediments and sedimentary rocks is to define the complete detrital zircon (or monazite, rutile etc.) age spectra. The relative abundances of grains of different ages are a fingerprint from which it is possible to infer the provenance of a sediment and to make very reliable correlations with other sedimentary units. Changes in that fingerprint through time can be a very sensitive record of changes in erosion patterns and the continental scale tectonics that have caused those changes. Notable examples are the studies by Ireland et al. (1998) and Goodge et al. (2002) of the early Paleozoic sediment sequences in eastern Australia which record the tectonic development of the Pacific margin of Gondwana. These signatures also pervade the southern Australian beach sands with little influence from the adjacent craton (Sircombe 1999). The detrital zircon in desert dune sands has provided important new insights into more recent sediment transport patterns in Australia, identifying water, not wind, as the principal transport mechanism (Pell et al. 1997). Wind played a major role, however, in the formation of bauxite deposits in Western Australia, the zircon in the bauxite showing the contribution to the ore from the underlying basement rocks to be relatively minor (Brimhall et al. 1992).

**Analysis of thin rims and near-surface concentration gradients (depth profiles)**

A major application of SIMS instruments, particularly in the semiconductor industry, is for the measurement of near-surface concentration profiles. The finest depth resolution (less than a nanometer) is achieved when the primary beam is rastered over the sample surface and the measurements are made only at the centre of the rastered area. This eliminates edge effects and guarantees a very uniform penetration rate. Depth profiling of small geological samples is usually done with a static primary beam, however, relying on the relatively uniform beam density produced by Kohler illumination to achieve uniform penetration. An early application of the technique was the dating of very thin Miocene metamorphic overgrowths on Precambrian zircons from Himalayan paragneisses (Zeitler et al. 1989). The zircon was prepared for the experiment with minimal polishing, but nevertheless even the 2-μm deep analysis pit in some cases penetrated through the overgrowth and into the core. Within the resolution of the method, no evidence was found for diffusion of core Pb into the overgrowth during the granulite grade metamorphic event. Measuring the rates of Pb, U and Th diffusion in natural zircon has proved extremely difficult, not least because the rates are so slow and zircon with even moderate U and Th contents is prone to radiation damage. Using ion probe depth profiling, Lee et al. (1997) were able to measure all three rates directly by analyzing the concentration gradients produced when low-U, gem-quality zircon was heat treated at temperatures of up to 1100°C for up to three months. Even for the highest temperatures and longest times, the depths of Th and U diffusion were less than 20 nm. The closure temperature for Pb diffusion, measured on only 19 ppm $^{206}$Pb, was calculated to be •940°C, consistent with the value later measured by Cherniak and Watson (2000) using Rutherford Backscattering Spectrometry.

**The youngest zircons**

The blanks for SIMS U-Pb geochronology are intrinsically very low, depending only on how well the mount is cleaned after polishing and the Pb content of the Au coat. They are reduced even further if the primary beam is used to ion etch the surface of the target prior to analysis. It is therefore possible to measure radiogenic Pb contents down to a few ppb and thereby to measure the Pb/U age of zircon as young as a few hundred thousand years. At this age, the principal limitation on precision is counting statistics, not uncertainty in the Pb/U calibration. Those statistics can be improved by longer counting times and targeting zircon grains or zones that are U-rich. Care must be taken, however, not to take the latter to excess as SIMS determinations of Pb/U become increasingly biased with increasing U once U levels exceed about 3000 ppm (Williams and Hergt 2000). Even lower ages can be measured using $^{234}$U-$^{230}$Th disequilibria (Reid et al. 1997, Bacon et al. 2000). In some cases, isochrons can be constructed for individual zircons (Lowenstern et al. 2000).

**Timescale**

Nothing tests the limits of a dating technique more than measurements of absolute age to calibrate the geological time scale. Not only does this require the greatest precision and accuracy, but there is a very large pre-existing data set with which any new measurements must be reconciled. Discrepancies quickly become evident and reasons for them, either geological or analytical, have to be found. The low precision of SIMS geochronology limits its usefulness for time scale calibration, particularly when the question arises of which, if any, of the analyses are concordant. There is also concern about the possibility of analytical bias at about the 1% level, particularly since the standard used for much of the SIMS time scale work has been shown to be heterogeneous (Compston 1999). The uncertainty in SIMS measurements of $^{207}$Pb/$^{206}$Pb on Phanerozoic zircon is such that the concordance of individual analyses cannot be tested. SIMS does have the advantage, however, that independently of standardisation, quite subtle differences in age between the grains in ostensibly homogeneous zircon populations can be detected as excess scatter in the Pb/U measurements. Such differences were missed in much of the early TIMS work on multigrain samples of volcanic zircon

populations, but having been pointed out (e.g., Compston and Williams 1992), are now also being found by TIMS single grain analyses (e.g., Mundil et al. 2001). Compston (1999, 2000a,b) continues to be a strong advocate for the application of SIMS to time-scale work, but the highest precision will always be achieved when analyzing larger samples by TIMS. Ideally the two techniques should be employed in tandem, SIMS for testing large numbers of grains for age uniformity, and TIMS for precise, accurate analyses of a chosen few. Only if the results of both techniques are internally consistent can the measured age be considered reliable. That leaves only the question of geological significance, which given the long residence time of zircon in magmatic systems and the propensity of volcanism to resample the products of previous eruptions, does not necessarily have a simple answer.

## INSTRUMENTAL AND ANALYTICAL APPROACHES

To prepare zircon for SIMS analysis, it is mounted in epoxy with reference zircon of known age, polished to expose the centres of the grains, documented by a range of imaging techniques (reflected and transmitted light microscopy, CL, BSE), and gold coated to prevent charging during sputtering. The primary ion beam is usually focused to 10- to 30-μm diameter. Narrower beams are possible, but for a given primary beam density, secondary ion yield falls in proportion to spot area. If, for example, the spot diameter is halved, analysis time must be increased by a factor of four to maintain precision. To some extent, loss of secondary ion yield can be compensated by increasing the primary beam density, but this is ultimately limited by increasing inter-element fractionation. As a general rule, up to a beam diameter of ~40 μm, the best data are obtained using moderate primary beam densities and the largest diameter permitted by the scale of the growth domains to be analyzed.

The main isobaric interferences potentially affecting the analysis of Pb in zircon are molecules of Zr, Hf, Si, rare earth element (REE), O and H (Fig. 3). Complex molecules, such as $Zr_2O$, are readily separated at a resolution of ~1200. To resolve HfSi requires ~3750, REE and Hf dioxides require ~5100 and Pb hydrides about 30000. Given a practical upper limit of ~1 m for the turning radius of the mass analyzer magnet, both the SHRIMP and Cameca 1270 have been designed for a mass resolving power of ~10000, which translates to a routine high transmission operating resolution of ~5000, sufficient to resolve all interferences except hydrides, which are minimized by the use of cryogenic pumping. In other respects, however, the two instruments differ, the Cameca 1270

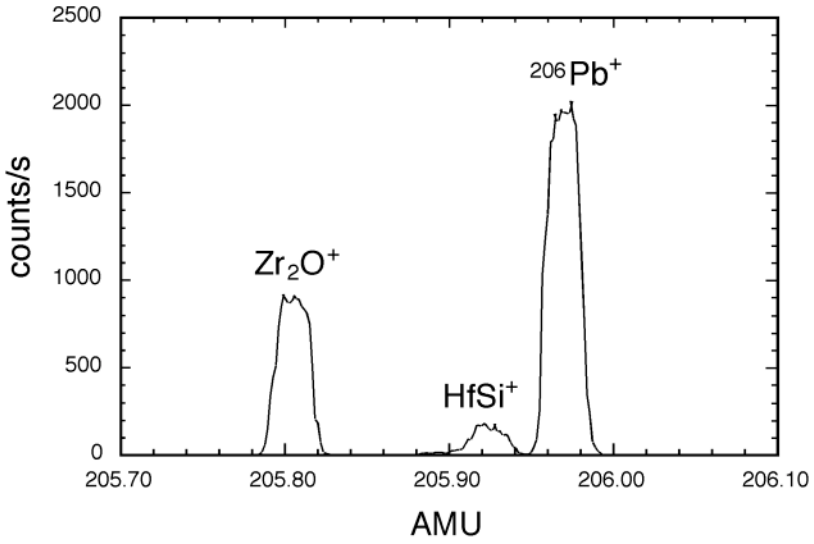


**Figure 3.** Mass spectrum of $^{206}Pb$ showing separation of isobaric interferences in zircon. Mass resolution is 6,000 R (10% peak height), a standard operating condition for high mass resolution SIMS instruments. Ineffective separation of these interferences caused inaccuracies in data from lower resolution ion probes.

being a derivative of the secondary ion microscope designed by Castaing and Slodzian (1962), and the SHRIMP a derivative of the ion probe mass analyzer of Liebl (1967). The main difference is in the secondary ion focusing—whereas the Cameca 1270 is designed primarily to provide ion images of the target, the SHRIMP transforms the secondary ions to a line image which accurately matches the acceptance of the mass analyzer in dimension and divergence but does not transfer a direct image of the target. The two instruments have been compared in detail by Ireland (1995), so will be discussed only briefly here.

**SHRIMP**

SHRIMP I was built in the late 1970s based on one of a series of theoretical ion optic designs devised by Matsuda (1974) to correct for image aberrations up to second order in double-focusing mass spectrometers. SHRIMP II, an improved version of the instrument built in the late 1980s and now also produced commercially by Australian Scientific Instruments, is similar in basic concept and operation.

Oxygen is the preferred primary ion beam for U–Pb analysis. It is highly electronegative, thereby chemically enhancing secondary ion production, and it is an easy gas to handle, causing much less damage to ion optical components than other electronegative gases such as Cl and F. The oxygen ions are produced in a cold-cathode duoplasmatron then passed through a Wein mass filter to select the required primary ion species, $O_2^-$ in most cases. The primary column is held at +10 kV relative to ground, and the duoplasmatron at approximately -10 kV relative to the column, namely close to real-ground potential. Sharp focus and uniform primary beam density at the target surface are achieved using Kohler illumination, in which the image of an intermediate aperture, not the primary ion source, is projected onto the target. A Schwarzchild optic system provides a high quality reflected or transmitted light image of the sample surface.

Secondary ions are extracted at -10 kV relative to the sample, which is biased about 750 V above column potential to minimize secondary ion fractionation. The ions are focused onto the object slit of the secondary mass analyzer by a quadrupole lens triplet adjusted to match the emittance at the slit to the acceptance of the analyzer. In doing so they are sampled by a beam monitor, the signal from which can be used to normalize out secondary beam noise. The forward geometry mass analyzer consists of three main elements, an 85° electrostatic sector, a static quadrupole and a 72.5° magnetic sector. The purpose of the electrostatic sector is to cancel the energy component of the momentum dispersion in the magnet, essential because of the large energy spread (~150 V) in the secondary ions, producing pure mass dispersion at the collector slit. For zircon analysis the ions are normally counted by a single electron multiplier. Analysis combining multiple collection of the Pb isotopes with single collection of the Zr, U and Th species is also possible.

**Cameca 1270**

The Cameca 1270 is a high-resolution derivative of the successful Cameca ims 3f–6f product line. These instruments were developed as ion microscopes and as such the main secondary lens system is stigmatic, designed to project ion images of the target or slits onto a channel plate detector at the exit to the mass spectrometer. The source of negative primary ions again is a duoplasmatron, the required primary ion species being selected using a sector magnet. Typically, Cameca ion probes use atomic $^{16}O^-$ rather than molecular $O_2^-$ for zircon analysis, the higher flux of $^{16}O^-$ more than compensating for the lower secondary ion yield per primary ion. The electrical configuration is similar to that of SHRIMP, although the primary ion energies are commonly higher, up to 20 kV. The secondary ion beam is focused onto the object slit of the mass spectrometer by cylindrical einzel lenses. Apertures can be used to constrain the beam such that only ions from the centre of the analyzed area pass into the mass spectrometer. Unlike SHRIMP, an energy window is commonly used to restrict the range of secondary ion energies transferred to the main analyzer magnet in order to optimize mass resolution. An alternative astigmatic secondary lens system provides enhanced

transmission for secondary ion analysis. Zircon is normally analyzed using a single electron multiplier, but multiple collection of the Pb isotopes also is an option.

### Operational comparison

Although in general terms the operation of the two instruments for zircon U–Pb isotopic analysis is quite similar, there are some significant differences in detail.

The main difference apparent to operators of the two instruments is the sole use of photon imaging (reflected light) to select targets on the SHRIMP and the additional availability of ion imaging on the Cameca 1270, both for spot verification and for tuning. The Schwarzchild optics on SHRIMP allow high-magnification images to be viewed continuously and the quality of the normal reflected light imaging on SHRIMP is sufficient to permit precise targeting guided by reflected light and CL photomicrographs of the grain mount. Reflected-light images are available on the Cameca but the lighting is oblique and at lower magnification, and accurate spot positioning is more difficult. Spot placement can be confirmed by ion imaging although zircon grains are generally of sufficient size that within grain placement is not difficult. For heterogeneous zircons, ion imaging on the Cameca 1270 allows targeting based on the sample composition, as well as the potential to mask out of unwanted areas within the analyzed spot.

The availability or not of secondary ion imaging also governs the way the ion optics of the two instruments are tuned. On the Cameca 1270, an ion image of the primary beam on the target is used to tune the primary beam for size, shape, sharpness and uniformity, an ion image of the source slit is used to maximize secondary ion transmission, and an ion image of the collector slit is used to maximize mass resolution. On the SHRIMP, the shape and sharpness of the primary beam is tuned using the reflected light image of the target, the transmission is maximized using a secondary beam monitor between the electrostatic analyzer and magnet, and the resolution is maximized using scans of the secondary beam across the collector slit.

Raising the partial pressure of oxygen in the vicinity of the target has been found to increase the secondary ion yield of the Cameca 1270 by a factor of 2 to 3 (Schuhmacher et al. 1993, Quidelleur et al. 1997). For SHRIMP, the $Pb^+$ ion yield increases by only about 20% under the same O-flooding conditions. The Cameca 1270 is therefore operated with an oxygen bleed to the source chamber, whereas the SHRIMP is not. Under these conditions, both instruments have a similar sensitivity for Pb, about 25 cps per ppm Pb per nA of primary beam. Primary beam fluxes for both instruments typically are limited to ~10 nA to minimize charging and depth effects on inter-element discrimination, making the normal maximum sensitivity for zircon analysis about 200 cps/ppm. Analytical precisions are therefore similar. Stronger primary beams can be used to increase the sensitivity and precision for common-Pb analyses.

For both instruments, good initial tuning and consistency in retuning between analyses are of paramount importance in achieving the stable analytical conditions required for accurate, precise measurement of U–Pb ratios.

## ZIRCON ANALYSIS

The procedures for SIMS U-Th-Pb isotopic analysis and instrumental factors to be taken into account have been discussed in detail by Ireland (1995) and Williams (1998). The single-collector analysis cycle for zircon U-Th-Pb typically consists of a Zr molecular species (e.g., $Zr_2O$), the Pb isotopes $^{204}Pb$, $^{206}Pb$, $^{207}Pb$, and $^{208}Pb$, two of the U and U oxide species (U, UO, and/or $UO_2$) and a Th species, normally ThO. Measurement of the Zr molecule serves two main purposes, as a major element reference for the calculation of Pb, U, and Th concentrations, and as a mass reference for location of the $^{204}Pb$ peak. The four Pb isotopes are used to calculate both the size of the common Pb correction and the radiogenic Pb isotopic composition. At least two U species must be measured in order to calculate the true target Pb/U, because the basis for the Pb/U calibration is an empirical observation that the secondary ion ratio $Pb^+/U^+$ changes in sympathy with the ratios of the U oxide

ions. The Th species is measured for the calculation of Pb/Th age, to provide a measure of Th/U (sometimes a chemical diagnostic of the conditions under which zircon crystallized), and in special cases to allow calculation of the expected radiogenic $^{208}Pb/^{206}Pb$ for common Pb corrections.

**Pb isotopes**

The Pb isotope composition of zircon is generally taken as measured. Several attempts have been made to estimate the mass-dependent mass fractionation of the Pb isotopes but the low Pb concentrations in zircon and the difficulty of resolving any PbH isobars (M/ΔM = 33000; Fig. 4) make an accurate measurement of fractionation very difficult. Currently it is considered unlikely that the fractionation exceeds about 0.2%/amu, that measured on common Pb from feldspar. The good agreement between SHRIMP and conventional ID-TIMS Pb isotope analyses of a number of zircon samples has been used to suggest that the mass fractionation is minimal (as is the hydride component) and therefore that no correction need be applied (Compston et al. 1986). Hydrides and fractionation have opposite effects, however, raising and lowering the $^{207}Pb/^{206}Pb$ respectively. The apparent lack of Pb fractionation might in part be due to mutual cancellation of the two contributions.

The mass resolution required for the isotopic analysis of Pb in zircon, >5000, is determined mainly by the need to resolve the Pb isotopes from $HfO_2^+$ and $HfSi^+$ isobaric interferences. $^{204}Pb$ is also theoretically subject to interferences from complex REE hydroxides, $Hg^+$ and $WO^+$, although in practice these effects are usually extremely small. Such interference might account, however, for rare cases where excess 204 counts are detected that cannot be explained in other ways (e.g., wrong corrections for background or scattered ions). Isobaric interferences are also present in the vicinity of the $U^+$, $UO^+$ and $UO_2^+$ peaks, but they are small and easily resolved (M/ΔM < 1500).

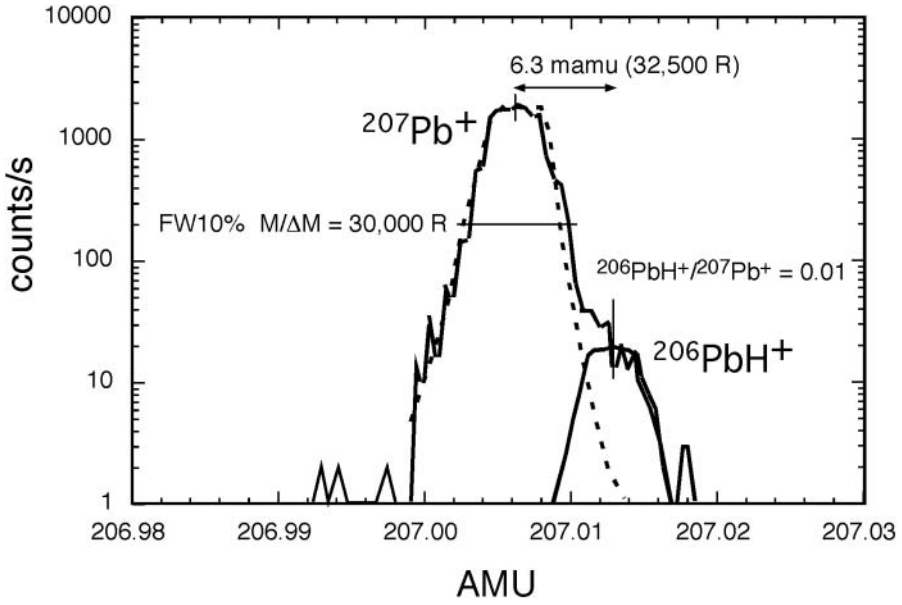


**Figure 4.** Mass spectrum of mass 207 from a uraninite grain showing presence of $PbH^+$ adjacent to $^{207}Pb^+$. The spectrum was obtained on SHRIMP RG at ANU operating with a mass resolution of ca. 30,000 R (10% peak height). The Pb hydride appears on the high mass side of $^{206}Pb^+$ at a mass separation of 6.3 mamu (equivalent to 32,500 R). The hydride appears only partially resolved because of the relative peak heights. The shape of the Pb hydride is estimated from the $^{207}Pb$ peak and the $^{207}Pb$ tail is estimated from the shape of the $^{206}Pb^+$ peak.

**Correction for common Pb**

Although most zircon incorporates vanishingly small amounts of Pb at the time of crystallization, the presence of common Pb in zircon analyses cannot be ignored if an accurate age is to be calculated. This is particularly so for analyses of zircon poor in radiogenic Pb, for example low-U or young zircon. Common Pb in a zircon analysis can originate from several sources: sub-microscopic mineral inclusions, Pb added to the zircon during or after alteration, Pb physically trapped in microfractures, laboratory Pb from polishing compounds, aerosols, and coating materials. Each is of a different composition, and the measured common Pb will be a mixture. In practice, low levels of common Pb are assumed to be laboratory-derived, and higher levels to be a mixture of laboratory Pb and rock Pb. Only in very rare cases, such as lunar zircons in which the common Pb is unusually radiogenic, is the measured age very sensitive to the choice of common Pb composition.

Common or initial Pb content can be estimated in several different ways. The most direct method is by measuring $^{204}$Pb, the only Pb isotope unique to common Pb. Knowing the initial Pb isotopic composition, the other Pb isotopes can be subtracted from the analysis. If $f$ is defined as the fraction of total $^{206}$Pb in an analysis that is initial $^{206}$Pb, i.e.,

$$f = {}^{206}Pb_{init}/{}^{206}Pb_{tot}$$

then $f$ can be calculated from the measured $^{204}$Pb/$^{206}$Pb as,

$$f = \frac{\left({}^{204}Pb/{}^{206}Pb\right)_{tot}}{\left({}^{204}Pb/{}^{206}Pb\right)_{init}}$$

The isotopic composition of initial rock Pb can be measured on cogenetic common Pb-rich minerals such as feldspar, or estimated from common Pb growth curves, knowing the approximate age of the zircon. The composition of laboratory-derived Pb, in continental Australia at least, is that of late Proterozoic massive Pb sulfide ore. If a cogenetic suite of zircons has a wide range of common Pb contents, the composition of the common Pb can be estimated with reasonable reliability by plotting a set of Pb isotope and U/Pb mixing lines and extrapolating to zero U.

Although $^{204}$Pb provides the most direct measure of common Pb, the low relative abundance of $^{204}$Pb makes the correction imprecise, particularly for analyses of young or low-U zircons with low $^{207}$Pb/$^{204}$Pb. A more precise estimate of common Pb can sometimes be made from $^{208}$Pb/$^{206}$Pb and the measured Th/U, $f$ being calculated as:

$$f = \frac{\left({}^{208}Pb/{}^{206}Pb\right)_{tot} - \left({}^{208}Pb/{}^{206}Pb\right)_{rad}}{\left({}^{208}Pb/{}^{206}Pb\right)_{init} - \left({}^{208}Pb/{}^{206}Pb\right)_{rad}}$$

To calculate the expected radiogenic $^{208}$Pb/$^{206}$Pb from Th/U relies on the assumptions that neither Th/U nor radiogenic $^{208}$Pb/$^{206}$Pb has changed throughout the zircon's history, except by radioactive decay, and that the zircon's age is known. The last is not critical, as the factor relating radiogenic $^{208}$Pb/$^{206}$Pb to Th/U ranges only from 0.25 to 0.32 over the full range of geological time. This method of correction normally works very well for zircon with low Th/U (<0.1), but becomes less precise for Th-rich zircon (Th/U > 1) as radiogenic $^{208}$Pb/$^{206}$Pb approaches the $^{208}$Pb/$^{206}$Pb of common Pb. It is also prone to error, because altered zircon tends to lose $^{208}$Pb more readily than $^{206}$Pb, resulting in an underestimate of the common Pb content. A variant of this procedure devised by Andersen (2002) takes better account of Pb loss, but requires the additional assumption that the time of the loss is known.

If it is assumed that the zircon analyses are concordant, a very precise correction for common

Pb can be made using the measured $^{207}Pb/^{206}Pb$. The correction is iterative, a calculation of $f$ from

$$f = \frac{\left(^{207}Pb/^{206}Pb\right)_{tot} - \left(^{207}Pb/^{206}Pb\right)_{rad}}{\left(^{207}Pb/^{206}Pb\right)_{init} - \left(^{207}Pb/^{206}Pb\right)_{rad}}$$

giving a corrected $^{206}Pb/^{238}U$ age, from which a revised $f$ and age is derived. The method is applicable only to zircon so young (Phanerozoic) that the discordance of individual analyses cannot be detected within the limits of analytical uncertainty. It produces a suite of radiogenic $^{206}Pb/^{238}U$ estimates that can be assessed for equivalence free of correlated errors propagated from the common Pb corrections. Any discordance and/or inheritance is evident as excess scatter in the corrected $^{206}Pb/^{238}U$ values.

**U/Pb calibration**

Determination of accurate interelement ratios such as Pb/U and Pb/Th is more difficult by SIMS than by isotope dilution. Using isotope dilution, Pb, U and Th concentrations are measured directly with high precision and accuracy, and interelement ratios are calculated from them. Measurement of these concentrations by SIMS is indirect, involving estimation of abundances from secondary ion ratios between trace and major element species (e.g., $^{206}Pb^+/^{196}(Zr_2O)^+$) relative to a reference material of known trace element content. This procedure is subject to inaccuracies of several percent or more, so interelement isotope ratios are best determined directly from the secondary ion ratios of those isotopes. A complication is that different elements have different secondary ionization efficiencies and different propensities to form multiple oxides, so not only do the measured secondary ion ratios differ substantially from the isotope ratios in the target, but those ion ratios also change during a SIMS analysis, even if the target is chemically homogeneous. The calibration procedures used to correct for these effects, and their accuracy, are one of the most contentious issues in SIMS U–Pb geochronology.

The Local Thermodynamic Equilibrium (LTE) Model of Andersen and Hinthorne (1973) has been one of the most successful in calculating target compositions from secondary ion yields. The model is based on the premise that a plasma in thermodynamic equilibrium is present at the sputter site, and predicts the secondary ion yields of atoms and oxide molecules based on the electron density and "temperature" of that plasma. Although such a plasma is unlikely to exist, because the sputtering process is so fast that the energy injected by each primary ion is dissipated before the next arrives (Williams 1979), the model is capable of providing elemental concentration estimates, usually accurate within a factor of two, for a wide range of target materials. While this accuracy is insufficient for U–Pb geochronology, a prediction from the LTE model that the secondary ion ratios $Pb^+/U^+$ and $UO^+/U^+$ will co-vary for a target of constant Pb/U (Hinthorne et al. 1979) has become the basis for subsequent SIMS U–Pb calibration procedures (Fig. 5).

Hinthorne et al. (1979) first calculated zircon Pb/U based on an exponential relationship between $^{206}Pb^+/^{238}U^+$ and $UO^+/U^+$. When calculating Pb/U in lunar zircon, Compston et al. (1984) assumed the correlation to be linear, but subsequent more extensive data sets indicated that a quadratic relationship was more appropriate (Williams and Claesson 1987). This was later simplified to a power law (Claoué-Long et al. 1995) with an exponent of 2.0, although debate continues over whether the exponent can be regarded as a constant or a variable (e.g., Claoué-Long et al. 1995, Black et al., submitted). The question applies particularly to small or clustered data sets for which the form of the calibration curve is poorly defined. In reality the answer is of little consequence unless there is a wide dispersion in UO/U, which in itself is a warning that there was unusually large variation in target bulk composition and/or sputtering conditions during a run. Normal practice is to assume an exponent of 2 unless there is a compelling reason for a particular data set to do otherwise. Based on this assumption, and given a homogeneous reference zircon, Pb/U isotope ratios can be measured in zircon samples with an accuracy of about 1%. Multiple analyses are necessary to

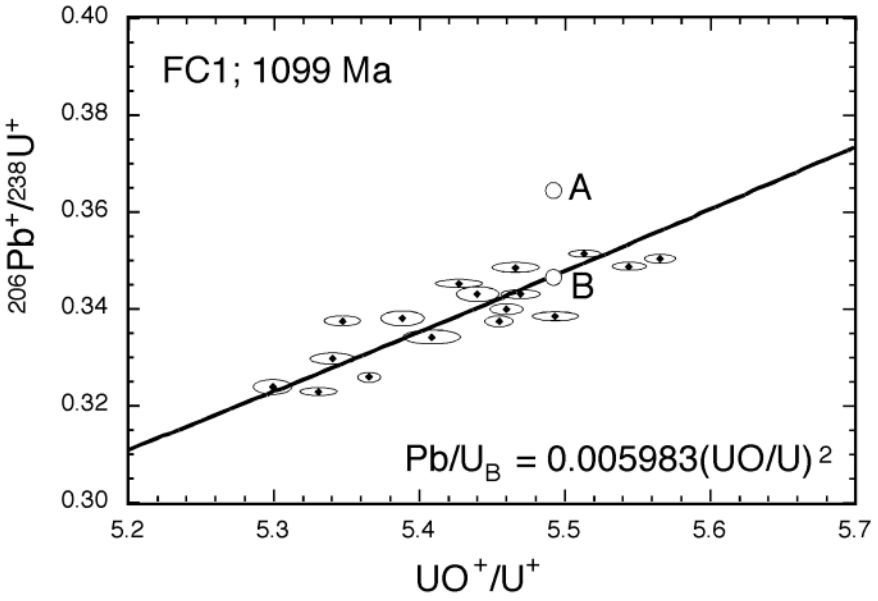


**Figure 5.** The $Pb^+/U^+$ vs. $UO^+/U^+$ has been the cornerstone of SIMS Pb/U calibration. Pb/U covaries with UO/U for different analyses allowing a calibration curve for a specific age to be determined. Data for unknowns, with their own measured Pb/U and UO/U can then be referenced to this curve and an age determined. Data for 17 analyses of 1099 Ma FC1 are shown. In this case the age of the unknown A would be given by $Age_A = 1099^* (Pb/U)_A/(Pb/U)_B$, where $(Pb/U)_B$ represents the Pb/U of the 1099 Ma standard at the UO/U of the unknown A. Errors are 1σ (relative standard deviation).

achieve comparable precision.

Zircon calibrations also have been developed based on other combinations of $U^+$ and U oxide molecular-ion species. In examining the energy distributions of $Pb^+$, U, and U oxide ions, Schumacher et al. (1993) noted the closer similarity of $Pb^+$ to the molecular U oxide species, with the $UO_2^+$ and $Pb^+$ in particular having very similar distributions. Schumacher et al. (1993) therefore noted the potential for better calibration based on the $Pb^+/UO^+$ and $Pb^+/UO_2^+$ species. Whitehouse et al. (1997) have used the $UO_2^+/U^+$ as the discriminant. Stern (2000) has evaluated the $Pb^+/UO_2^+$ system and found it to be substantially less affected by sputtering conditions, that is, $Pb^+/UO_2^+$ is fairly constant during the course of an analytical session. These observations suggest that secondary ion energy is an important parameter in calibrating U/Pb ratios. However, the basis of the calibration and the species used to monitor the fractionation are not as important as the robustness of the calibrated ratios they produce. The reproducibility of ratios from known materials (standards) should be the sole discriminator between the available procedures. Stern and Amelin (in press) indicate that residual artifacts limit SIMS U/Pb data to ca. 1% independent of the calibration procedure.

A calibration procedure must be used to calculate Pb/Th and Th/U from $Pb^+/Th^+$ and $Th^+/U^+$ respectively. Because of the difficulty of obtaining reference materials with known and constant Th/U, the latter is normally calculated as a correction factor to $ThO^+/UO^+$ based on the difference between the measured and expected slope of the $^{208}Pb/^{206}Pb - {}^{232}Th/^{238}U$ isochron. For zircon, the correction factor correlates weakly with measured $UO^+/U^+$.

Concentrations of Pb, U, and Th are not used for any geochronological calculations but are obtained for information regarding zircon chemistry and possible petrogenetic relationships. The U concentration is calibrated from the measured $Zr_2O^+/U^+$ and the U concentration in a standard. The Pb and Th concentrations are then derived from the calibrated Pb/.U and Th/U ratios respectively. The concentration standard and the Pb/U standard need not be based on the same reference material.

## OTHER MINERALS

This discussion is concerned primarily with zircon, but the same analytical approach, with some modifications, is applicable to a range of other U-bearing minerals that can be used for U–Pb geochronology.

### Monazite

Monazite is a light REE phosphate common in sediments, metasediments, and peraluminous igneous rocks. Th substitution for the light REE can reach several weight percent, so the Pb/Th age of monazite can be measured with greater analytical precision than the Pb/U age (e.g., Harrison et al. 1995, Ireland and Gibson 1998). The Pb/Th age also is likely to be the more accurate because of uncertainties in the amount of $^{206}Pb$ produced by the decay of initial $^{230}Th$. The mass spectrum of monazite in the vicinity of the Pb isotopes contains unresolvable complex molecular isobaric interferences. This is particularly apparent at $^{204}Pb$, which if used as a measure of common Pb leads to major over-corrections. The interference under $^{204}Pb$, identified as $(^{232}Th^{144}Nd^{16}O_2)^{++}$ (Ireland et al. 1999), can be monitored at mass 143.5 ($^{232}Th^{143}Nd^{16}O_2{}^{++}$) and the $^{204}Pb$ corrected by peak-stripping. Alternatively, moderate levels of energy filtering will remove the interference from the mass spectrum. Monazite U/Pb and Th/Pb calibrations have utilized a variety of element / element oxide ratios (UO/U, $UO/UO_2$, etc., and similarly for Th and its oxides). The extent to which each of these is sensitive to changes in the monazite composition, for example to the substitution of huttonite ($ThSiO_4$)—the high-temperature monoclinic polymorph of thorite—for $CePO_4$, has yet to be explored in detail. The variable Th and Ce concentrations due to this substitution compromise the use of Ce as an internal concentration reference (cf. Zr in zircon).

### Xenotime

Xenotime is a HREE phosphate with a high degree of substitution of other elements, including U and Th. It has a low common Pb content and can retain radiogenic Pb better than zircon of similar U content, but it is much less common than zircon and monazite, occurring in highly fractionated granites and in association with monazite in high-grade metamorphic rocks (Pyle et al. 2001), so has been little used for geochronology. Xenotime is isostructural with zircon, and can occur as a component in zircon in solid solution. It also forms a solid solution with monazite, the miscibility gap between the two providing a sensitive geothermobarometer (Gratz and Heinrich 1997). SIMS U–Pb analysis of diagenetic xenotime nucleated on detrital zircon provides one of the few direct ways to date the deposition of Precambrian sediments (McNaughton et al. 1999). Calibration of SIMS determinations of xenotime Pb/U using element/element-oxide ratios has proved problematic because of variable matrix effects, but greater success has been reported with a calibration based on $UO^+/YPO^+$ (Stern and Rainbird 2001). Interferences from $(ThNdO_2)^{++}$ isobars, are likely to be present at low levels but have not been reported, even at $^{204}Pb$.

### Apatite (+whitlockite)

The Ca phosphates contain only low levels of U and relatively high initial Pb, and also have relatively low U–Pb closure temperatures, so have not been widely used for geochronology. They were, however, amongst the group of minerals first analyzed by SIMS to date lunar rocks by Pb–Pb (Andersen and Hinthorne 1972, 1973). More recent work on apatite has included measurement of Pb/U using calibrations based on UO/U (Sano et al. 1999). Because of the high initial Pb contents, however, apatite ages are better calculated using the U/Pb–Pb/Pb isochron approach than from the conventional concordia diagram. For apatite with high OH contents, it is also necessary to monitor and correct for PbH. The potential of apatite dating in the study of thermal histories has yet to be realized. It also is one of the few available techniques for the direct U–Pb dating of biological materials (e.g., Sano and Terada 1999).

### Titanite

Titanite (sphene) is one of the few minerals suitable for U–Pb dating that has a well-understood paragenesis in metamorphic rocks (Aleinikoff et al. 2002, Castelli and Rubatto 2002). It also occurs in some metaluminous igneous rocks. Calibration procedures are similar to those for zircon, and work well with either $UO_2$/UO or UO/U as the reference parameter. Although there is some variability in titanite chemistry (especially Fe substitution) no matrix effects on the calibration have yet been reported. There are no obvious interferences on the Pb isotopes. Most titanite contains less U and more common Pb than zircon, so common Pb corrections can be very large, compromising the precision of the Pb/U age. Accuracy also can be compromised unless the isotopic composition of the common Pb is well known. Best practice is to analyze a range of titanite grains from a single sample, defining a mixing line on a Tera-Wasserburg diagram from which both the radiogenic $^{238}U/^{206}Pb$ and initial $^{207}Pb/^{206}Pb$ can be inferred. This procedure only works if the titanite radiogenic U–Pb system is concordant.

### Baddeleyite

Baddeleyite ($ZrO_2$) is the principal Zr trace mineral in igneous rocks that are silica undersaturated or marginally saturated. Even in suitable lithologies it usually occurs in very low abundance and the mineral separation process is difficult, usually involving digesting the host rock in HF. Nevertheless, baddeleyite remains the most widely used mineral for ID–TIMS U–Pb dating of mafic dikes (LeCheminant and Heaman 1989). Early SHRIMP work on baddeleyite used a logarithmic $UO_2$/UO-based calibration, but this was later replaced by a power law UO/U calibration with an exponent close to 2. This calibration is compromised, however, by being sensitive to the orientation of each baddeleyite grain relative to the direction of the incoming primary ion beam (Wingate and Compston 2000), a sensitivity sought, but never found, in zircon. No simple solution has been found, so the precision and accuracy of baddeleyite U–Pb ages remains limited to several percent. Pb–Pb ages are unaffected, however, so SIMS baddeleyite dating has been applied most widely to rocks of Precambrian age.

### Rutile

Rutile ($TiO_2$) occurs as an accessory mineral in mafic igneous and high grade metamorphic rocks and, because of its chemical and physical stability, is a common component in sedimentary rocks. It has not been used widely for SHRIMP geochronology, however, because of its relatively low U and high initial Pb contents. It also has a relatively low Pb–U closure temperature, ~400°C (Mezger et al. 1989). Pb/U calibrations based on both UO/U and $UO_2$/UO have proved equally effective for rutile (Sircombe 1997, Clark et al. 2000). Th contents are commonly extremely low, meaning that all $^{208}Pb$ measured can be attributed to common Pb, giving a much more accurate common Pb correction than can be obtained using $^{204}Pb$. To improve precision, rutile is commonly analyzed with very large primary beams of $O^-$.

### Perovskite

Perovskite ($CaTiO_3$) occurs as a trace mineral in some peridotites, norites, nephelinites and kimberlites. It is also a minor constituent of the refractory inclusions in some meteorites. The propensity of perovskite to contain fine grained inclusions of other minerals makes it difficult to date well by ID–TIMS, so for work on kimberlites in particular, SIMS is often the technique of choice. The preferred calibration curve for perovskite is a quadratic equation based on $UO_2$/UO (Ireland et al. 1990).

### Allanite

Allanite is an epidote group mineral with high levels of REE and quite variable chemistry that occurs in metaluminous and alkaline igneous rocks, metasediments, some pegmatites and skarns. A $ThO_2$ content of about 1% makes it amenable to Pb–Th dating. The Pb/Th calibration for allanite is

very matrix sensitive, however, and calibration relative to $ThO_2^+/Th^+$ alone, as is sometimes used for monazite, can lead to large systematic errors. Accuracy is greatly improved by introducing a calibration parameter that reflects the allanite Fe content ($FeO^+/SiO^+$), thereby defining a calibration plane (Catlos et al. 2000). In this way, allanite Pb/Th ages can be measured to ±10%, quite useful for young allanites, although having only restricted application for samples that are older than late Mesozoic.

## DATA ANALYSIS

Unlike ID–TIMS, SIMS data acquisition and reduction procedures must be designed with the expectation that the measured isotopic ratios are changing with time in different ways. The changes can be large (several percent), caused not only by small-scale heterogeneity in the composition of the target, but also by a falling contribution from surface contaminants and by sputtering-related changes in the secondary ion emissions of the various elements and oxides. It is common, for example, that during an analysis the $Pb^+$ signals fall, the $U^+$ and $Zr_2O^+$ rise, and the $ThO^+$ and $UO^+$ remain relatively constant. Some of these changes are correlated and accommodated by the Pb/U calibration procedures, but the problems remain of how to make an unbiased measurement of the ratios and in particular, how to estimate the analytical uncertainties.

Most TIMS instruments measure isotope ratios in pairs or in a cycle of several isotopes repeated many times over. The latter is more appropriate if the isotopic composition is changing, but has the drawback that the repeat measurements of each isotope are separated by relatively long periods of time, necessitating corrections for time-dependent changes in signal strength. This correction normally takes the form of a linear interpolation of the denominator isotope count rate to the times at which each other isotope was measured. More sophisticated approaches include interpolation by fitting a polynomial or cubic spline curve to the denominator measurements, or the double interpolation of both numerator and denominator counts (Dodson 1978). The end product is always the same, multiple estimates of each isotope ratio that are averaged to obtain a best estimate of each and their associated precisions.

This procedure is largely unsuitable for SIMS geochronology where the objective is rapid analysis of a composite secondary ion beam of changing composition. There is time for only a few cycles through the isotopes of interest, and simply averaging the changing ratios yields inflates analytical uncertainties. A preferred solution developed for SHRIMP (in the PRAWN data reduction program) is to fit lines to the time-variant count rates for each isotope, and from these to obtain a best estimate of the count rates at the mid time of the analysis, the uncertainties in the estimates being a simple function of the counting statistics and quality of the fit (Mendenhall and Sincich 1995). If the fit is poor, the data set can be tested for outliers. One value for each isotope ratio is calculated from the mid-time estimates, and the uncertainties are determined by error propagation. The uncertainties are lowest when the changes in ion yields are systematic and correlated, such as result from the sputtering process, but become higher in targets where the scale of compositional heterogeneity is small compared to the depth of sampling (~2 μm).

Changes in target composition during analysis in most cases result in non-linear changes in count rate with time, but the changes nevertheless will be systematic. Changes in common Pb content will cause correlated changes in the count rates for all four Pb isotopes. If there is no Pb loss, changes in U content will be tracked by changes in $^{206}Pb$ and $^{207}Pb$, and changes in Th content will be tracked by changes in $^{208}Pb$. Such data are best reduced by treating each scan through the isotopes as a separate analysis. A cubic spline (as used in PRAWN) or other functional curve can be fitted to the isotope measurements, isotope ratios are calculated for each scan, each set of ratios is corrected for interelement fractionation and common Pb, then all values are combined to yield mean isotope ratios independent of the fluctuations in parent element abundance. This is also the basis for the program SQUID (Ludwig 2001), an Excel program for processing SHRIMP U–Th–Pb geochronology data in conjunction with the widely used IsoPlot (Ludwig 1999).

## Analytical uncertainties

Accurate determination of the target isotopic composition is of prime importance, but it is also important to make an accurate estimate of the analytical uncertainties. Knowing the uncertainties makes it possible to discriminate between more and less reliable measurements, to assess a set of measurements for evidence of significant variations in target composition, and to ensure that measurements are correctly weighted in the calculation of their mean. Underestimation of uncertainties leads to the identification of age differences that in fact are not significant, and the unjustified rejection of measurements as outliers. Overestimation leads to real age differences and outliers being overlooked. Both can result in the final age determination being inaccurate. The desire to measure with an accuracy limited only by counting statistics is the driving force behind the progressive refinement of SIMS analytical procedures.

### $^{207}Pb/^{206}Pb$ ratio

Because $^{238}U$ and $^{235}U$ decay at different rates, producing $^{206}Pb$ and $^{207}Pb$, respectively, the isotope ratio $^{207}Pb/^{206}Pb$ provides a measure of age that is independent of Pb/U, and therefore of the uncertainties associated with Pb/U calibrations. Given the relatively low precision of SIMS analyses, however, age measurements using $^{207}Pb/^{206}Pb$ are usually feasible only for Precambrian zircons. There are several reasons. Because $^{235}U$ ($T_{1/2}$ = 704 Ma) now comprises less than 1% of natural U, relatively little $^{207}Pb$ has been produced in the Phanerozoic. Not only are most Phanerozoic zircon radiogenic $^{207}Pb$ contents low (<2.5 ppm) and therefore difficult to measure with high precision, but also the change in radiogenic $^{207}Pb/^{206}Pb$ for zircon between 500 and 0 Ma old is small (0.057–0.046). The measurements are very sensitive to the common Pb correction and error magnifications are high, for example a 1% error in measuring radiogenic $^{207}Pb/^{206}Pb$ in a 100 Ma old grain results in a 23% error in the calculated age. The situation becomes much more favorable as the zircon becomes older. An average 3.0 Ga zircon, for example, will contain ~65 ppm of $^{207}Pb$, have a $^{207}Pb/^{206}Pb$ of 0.22, and a 1% error in measuring that $^{207}Pb/^{206}Pb$ will result in only a 0.5% error in the age.

To some extent the precision of $^{207}Pb/^{206}Pb$ measurements can be improved by increasing the count time on $^{207}Pb$, but there are practical limits. For count times over about 1 minute the cycle time becomes too long and there is an increased risk of partial signal loss due to instrumental drift. The optimal allocation of time to $^{207}Pb$ and $^{206}Pb$, or in fact to any isotope ratio, is to set the ratio of the count times to the inverse of the square root of the count rates. If $^{207}Pb/^{206}Pb$ = 0.06, for example, $^{207}Pb$ is best counted for four times as long as $^{206}Pb$. Even if this is done, counting errors remain so large that SIMS cannot measure radiogenic $^{207}Pb/^{206}Pb$ on average composition Phanerozoic zircon well enough to detect the discordance due to Pb loss. This is only possible by checking for excess dispersion in the radiogenic $^{206}Pb/^{238}U$.

### U–Pb ratio

The detection of discordance and inheritance within ostensibly cogenetic zircon populations has become a contentious issue in the interpretation of zircon ages measured by SIMS, particularly those measured on volcanic rocks to calibrate the Phanerozoic time scale (Tucker and McKerrow 1995, Mundil et al. 2001). Much of the argument hinges on questions of precision and accuracy. ID–TIMS analyses are demonstrably more precise than SIMS analyses, but are they also more accurate? In part the question reduces to one of whether the imprecision of SIMS analyses masks dispersion in radiogenic $^{206}Pb/^{238}U$. The answer depends upon the correct assessment of uncertainties in the $^{206}Pb/^{238}U$ measurements.

As discussed above, SIMS determinations of Pb/U are based on calibrations against reference minerals that are assumed to have uniform radiogenic $^{206}Pb/^{238}U$. If this assumption is valid, then any apparent variation in $^{206}Pb/^{238}U$ measured on the reference material is due either to a failure of the calibration procedure or underestimation of the analytical uncertainties. Early SIMS analysts at the ANU assumed the former, adding to every sample analysis a component of uncertainty calcu-

lated from the scatter in the analyses of the reference material. As a consequence, little dispersion in radiogenic $^{206}Pb/^{238}U$ was detected in most samples, but the mean ages were relatively imprecise. As calibration procedures improved, it became evident that the principal zircon reference standard, SL13, was in fact heterogeneous; many zircon samples were found to have more reproducible radiogenic $^{206}Pb/^{238}U$ than SL13. Thus any error propagation based on reproducibility of the standard was flawed and dispersion in $^{206}Pb/^{238}U$ was assessed on counting statistics alone. The precision of the age measurements therefore improved (except for very young samples, where the counting errors far outweighed the calibration errors) and Pb loss and inheritance were detected more often. However, attributing deviations to inheritance and Pb loss has consequences in geological interpretation. Furthermore, the accuracy of the measurement remained in doubt because the composition of the standard remained poorly defined. The problem could only be solved by locating reference material in which radiogenic $^{206}Pb/^{238}U$ was more uniform.

**Standards**

Reference material for SIMS U–Pb geochronology ideally should be, on a sub-micron scale, uniform in Pb, U and Th content, uniform in radiogenic $^{206}Pb/^{238}U$, $^{207}Pb/^{235}U$ and $^{208}Pb/^{232}Th$, free of initial Pb, isotopically concordant, sufficiently rich in radiogenic Pb that the Pb isotope ratios can be measured precisely, but not so old or U- and Th-rich that there has been a significant accumulation of radiation damage. No known natural zircon fulfills these requirements perfectly, but some are good enough to be a viable standard. Synthetic standards have been considered, but at present are not favored. Glasses are not suitable because it is not yet possible to correct for the differences in secondary ion emission between glass and different crystalline matrices with the 1% accuracy required (Stern and Amelin, in press). The standard for zircon would need to be synthetic zircon, and for monazite, synthetic monazite etc. Zircon with a suitable Pb/U (~0.1) has not yet been synthesized that matches the quality of the best natural zircon, namely is uniform in Pb/U to better than 1% on a sub-micron scale.

The first standards used for SHRIMP analysis were Neoproterozoic zircon megacrysts from stream gravels in Sri Lanka. Some of these relatively large grains ( 1 g) are quite uniform in trace element content (most importantly U), with no obvious growth zoning. Following a series of γ-counting experiments two grains were selected for ID–TIMS characterization, SL3 (U = 3540 ppm) and SL13 (U = 238 ppm). SL3 was used as a standard first because of its higher, and therefore more easily measured, radiogenic Pb content. However analytical inconsistencies began to emerge, with samples of known age yielding Pb/U ratios about 4% lower than expected. The problem was twofold. Transmission electron microscope examination of SL3 showed that it was badly radiation damaged, being about 60% structureless zirconium oxide and silica glass (McLaren et al. 1994). Analysis of this mixture with an unfiltered primary ion beam consisting of approximately equal amounts of $O^-$ and $O_2^-$ was introducing matrix effects for which the calibration procedure was not compensating. SL3 was therefore superseded by SL13.

TIMS analyses of 19 fragments of SL13 by five analysts from three laboratories showed it to be very uniform in U and Pb/U on a microgram scale. However, as it was used as a SIMS standard and as analytical procedures improved, significant heterogeneity in Pb/U became evident. The heterogeneity was on two scales, ~5% range in Pb/U on a scale of microns, possibly reflecting the presence of zircon of two different ages, and sub-micron regions with radiogenic Pb contents up to an order of magnitude greater than that attributable to *in situ* U and Th decay (Compston 1999). The latter have yet to be satisfactorily explained. Both effects precluded the use of SL13 as anything other than a U concentration standard, and as soon as alternatives became available most analysts abandoned it. The SIMS zircon standard used at Curtin University, CZ3, is also a Sri Lankan megacryst. It has a higher U content than SL13 (500 ppm) but no similar heterogeneity in Pb/U has been reported.

Reservations remain about the suitability of megacrysts as reference materials. Apart from the

fact that the supply of individual crystals is limited, these crystals have geological attributes that are of potential analytical consequence. The megacrysts appear to be metamorphic as suggested by geological association as well as lack of trace element zoning and low Th/U. Possibly, the megacrysts were extant prior to metamorphism, as indicated by old initial Hf isotopes (Kinny et al. 1991). These grains are different in trace element content from the igneous zircon that most commonly is dated. They also sputter somewhat differently, under some circumstances giving different secondary ion yields and $UO^+/U^+$ from igneous zircon. In part this might be due to the way the zircon grains are mounted, igneous zircon normally being oriented with the *c*-axis parallel to the mount surface, chips of standard being oriented at random. Although the differences might be of no consequence, in the quest to optimize Pb/U to higher levels, such potential matrix effects need to be considered.

Identifying zircon suitable for use as an international SIMS isotope standard has proved difficult. Harvard University zircon sample 91500, distributed through Geostandards (Weidenbeck et al. 1995), is the best currently available for a variety of elemental abundances and isotopic compositions. It has been analyzed for U–Pb isotopes by several ID–TIMS laboratories, and also for trace elements and Hf and O isotopes. Being a megacryst, however, its supply is limited. Further, as a SIMS geochronology standard it is too low in U (81 ppm) and radiogenic Pb (15 ppm) for use in monitoring $^{207}Pb/^{206}Pb$ fractionation. The low radiogenic Pb also makes it difficult to measure Pb/U with high precision, and there is evidence that suggests 91500 is not uniform in Pb/U at the 1% level.

SIMS laboratories still mostly rely on in-house standards for each of the minerals they are dating. SHRIMP analysts at ANU have tried a succession of potential zircon standards, retaining SL13 as a concentration reference but searching for zircon more uniform in Pb/U for interelement calibrations. First choice was AS3, zircon from a 1.1 Ga anorthositic syenite from the Duluth Complex, Minnesota, from which Paces and Miller (1993) obtained consistently concordant ID–TIMS analyses. AS3 also proved quite uniform in Pb/U when analyzed by SIMS, however, good quality zircon was scarce (Schmitz et al. in press), with most grains being skeletal, finely fractured and stained by iron oxides. Attempts to collect better material from the original sample site were unsuccessful, so a site at Forest Centre, 250 km NW of Duluth (FC1: Paces and Miller 1993), was chosen from which abundant good quality zircon was obtained. FC1 is now widely used as a Pb/U standard in the ANU lab, and also in the National Institute of Polar Research laboratory in Tokyo.

Geoscience Australia (formerly AGSO, and before that the BMR) initially referenced their SHRIMP analyses to sample QGNG, zircon from a 1.85 Ga gabbro from the Cape Donnington Suite, South Australia. This zircon has the advantage that it contains sufficient $^{207}Pb$ for $^{207}Pb/^{206}Pb$ fractionation to be monitored, but both ID–TIMS and SIMS analyses have shown it to be heterogeneous in Pb/U. Further, cross calibration against other zircon of known age showed that even the most concordant of the QGNG SIMS analyses must be about 0.6% discordant. Although this could be accommodated in calibration calculations, it reduced QGNG's value as a Pb/U standard. The standard now used by Geoscience Australia and ANU analysts working particularly on Phanerozoic zircon is Temora, zircon collected from the 417 Ma Middledale quartz diorite. More than two dozen ID–TIMS analyses show this zircon to be extremely unifom in Pb/U on a microgram scale, and similar uniformity on a nanogram scale has been demonstrated by SIMS (Black et al., submitted). A weakness of the Temora standard is that radiogenic Pb is generally low (<20 ppm), limiting the precision of the SIMS Pb/U measurements, and too low to monitor the fractionation of $^{207}Pb/^{206}Pb$. Temora has been widely distributed and is available from Geoscience Australia on request.

Use of several zircon standards creates the problem of relating analyses based on one standard to analyses based on another. To address this, Black and others (submitted) undertook a major interstandard comparison, including SL13, QGNG, AS3, two Temora samples (Temora 1 and 2), and R33, a proposed standard from the Braintree complex, Vermont. The study showed, with the notable exception of SL13, that when the best quality material was selected and analytical conditions

were stable, most Pb/U measurements on each standard were equal within counting statistics error. There were small but consistent discrepancies in the calibrated mean ages, however. Relative to Temora, QGNG and AS3 yielded a lower Pb/U than expected from their ID–TIMS ages, and SL13 yielded a higher Pb/U. Relative to ages measured against Temora, therefore, ages referenced to SL13 would be low and those referenced to QGNG or AS3 high. The differences are of the order 1%. The reasons for these differences have yet to be determined, but must be resolved if SIMS Pb/U calibrations are to achieve better than ~1% accuracy.

Stern and Amelin (in press) have also assessed error propagation in SIMS U-Pb analysis based on measurements of a suitable natural zircon (z6266) and NIST SRM 610 glass. Their findings are similar to those described above in that reproducibility of U-Pb analysis exceeds that expected from the measurement errors with an unaccounted error of ca. ±1% (1$\sigma$) error per analysis.

**Data assessment**

The literature now contains a large amount of SIMS geochronology data that are available for comparison and assessment. Comparisons can be made between, for example, different sessions from one laboratory, different analysts from one laboratory, different SIMS laboratories, and SIMS and other techniques. Such comparisons invariably lead to attempts at reconciliation even when results differ within the cited levels of uncertainty. While the scrutiny of comparison is a necessary part of the scientific process, the caveats inherent in the data analysis must be appreciated before sound conclusions can be reached.

A basic premise of comparison is that all data are equal. They are not. There is no canonical data reduction procedure common to all SIMS labs, and even if there were it would not necessarily help. SIMS data are measurements of isotope ratios, but the scientific questions addressed even by different analysts of the same sample may be quite different and hence the sampling strategy and statistical treatment quite different as well. Even when two practitioners ask the same question, most commonly, "How old is that rock?", the ways of getting to that endpoint may be quite different.

Propagation of errors is of particular importance both in assessing the data within an analytical session and in arriving at a final answer. SIMS analyses are not absolute determinations, but measurements relative to a standard of independently known age. The statistics governing this procedure are reasonably straightforward but as is often the case with scientific analysis, the distinction between random and systematic errors must be addressed at several levels of, and propagated through, the calculations. Unfortunately the approach of many analysts is to minimize uncertainties rather than to produce a statistically robust data set.

The statistics governing the estimation and combination of measurement errors are critical in assessing geological data. In the case of SIMS U–Pb analysis, there are two virtually independent sets of measurements, each of which needs to be pooled—estimates of $^{207}Pb/^{206}Pb$ and estimates of $^{206}Pb/^{238}U$ (or the ages calculated from them). Pooling $^{207}Pb/^{206}Pb$ data is straightforward; a weighted mean is calculated, the weighting of each estimate being inversely proportional to its variance. The weighted mean has an associated statistical parameter, the reduced $\chi\nu^2$ or mean-square of weighted deviates (MSWD), by which scatter beyond that expected from the analytical uncertainties can be detected and possible outliers identified. The uncertainty in most SIMS $^{207}Pb/^{206}Pb$ data is dominated by counting errors in the measurement and common Pb correction, and the age resolution is poor compared to TIMS analyses over most of geological time.

It is in combining $^{206}Pb/^{238}U$ data that there is the greatest variation in statistical approach. From the time of the earliest SHRIMP analyses, it was noted that measurements of Pb/U in ostensibly cogenetic zircon populations commonly were more dispersed than could be accounted for by measurement errors alone. Either the samples were heterogeneous or there was a source of analytical error that was not being taken into account. In addition, there was an error in measuring the $^{206}Pb/^{238}U$ of the zircon standard that must somehow be propagated into error in measuring the $^{206}Pb/^{238}U$ of the unknowns. The question was how best to do it.

No matter how errors are assessed, the $^{206}Pb/^{238}U$ age of a sample cannot be known better than the relative error in measuring $^{206}Pb/^{238}U$ in the calibration standard. In statistical terms, the coefficient of variation of the standards should be summed in quadrature with that of the sample. This is no different from the summing of errors when forming a ratio. The error in measuring the standards is treated as a systematic analytical error and represents a minimum error for the calibration.

When assessing replicate analyses of standards and samples, however, it is common to find more scatter than expected from counting error alone. It then becomes a question of determining the relative contributions of analytical and geological affects. One approach is to assert that the standard is isotopically homogeneous and that all the error observed is analytical. The reproducibility of the standard thereby represents the external reproducibility of all analyses. The relative standard deviation of the $^{206}Pb/^{238}U$ measurements of the standards is therefore added in quadrature to the uncertainty for each $^{206}Pb/^{238}U$ measurement of the sample. If the number of standard and sample analyses is the same, this has the same effect on the uncertainty in the final age measurement as summing the standard error of the standards in quadrature with the standard error of the unknowns. If many more samples than standards are analyzed, however, then the error in the mean age may be underestimated because the calibration error should have been treated as being systematic, rather than random.

Summing the error in this way takes no account of possible heterogeneity in the standard and risks obscuring heterogeneity in the sample. This became evident in early analyses relative to SL13 where the standard deviation of the samples commonly was smaller than that of the standards. Inflating individual analytical uncertainties masks the statistical distribution of the sample data, making it more difficult to detect true variation due to isotopic disturbance, inheritance, or mixed populations of slightly different age (Fig. 6). The procedure reduces the MSWD, however, allowing more analyses to be combined before scatter is detected, adding credibility to the end result.

On the other hand, reliance on counting errors alone at this stage of the calculation can result in some analyses receiving undue weight. Analyses of high-U zircons, for example, commonly have very small counting errors due to the high count rates, but because of radiation damage are often subject to (low-temperature?) Pb loss. Such analyses rarely reproduce within analytical error yet dominate the weighted mean and inflate the MSWD. Knowing this, is it appropriate that they receive more weight than less precise analyses of lower-U zircon that are more likely to represent the undisturbed isotopic composition?

One possible solution is to use a minimum error for each analysis that equates to the long-term average standard deviation of U–Pb analyses of well-behaved samples, whether they be standards or unknowns. Such an error component is essentially a calibration error and will be a function of the specific technique used for analysis. Our long-term experience at ANU is that the minimum calibration error is typically 0.5%. Using this minimum error for each analysis still requires that the final error in the Pb/U calibration be summed in quadrature with the final error in measuring the unknown.

## COMPARISON OF DIFFERENT ANALYTICAL SESSIONS

Assessment of systematic error between analytical sessions, particularly if different standards are used, is the most difficult error assessment of all. SIMS access is so restricted and costly that rarely is a sample run more than once. Exceptions are the cross-calibrations between standards, and analyses of some Paleozoic samples where very fine time resolution is required (e.g., Black et al., submitted). Usually the mean Pb/U ages for different sessions on the same sample agree within the assigned uncertainties, but sometimes apparently well-calibrated measurements differ by up to 2%, far more than can be explained by any random error.

Comparisons are even more difficult when assessing analyses against different standards, because systematic biases in the analyses and assumed compositions of those standards must be taken into account. There is much difference of opinion, however, over what those biases might be, especially given the different approaches to data reduction. Early comparisons of analyses against SL3

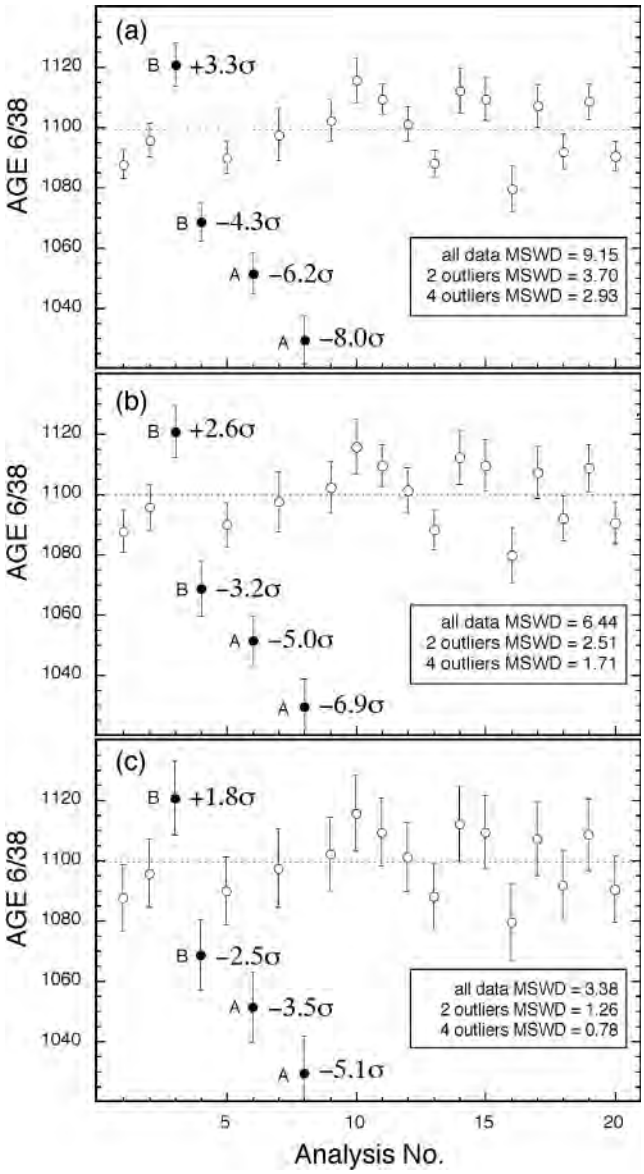


**Figure 6.** The choice of statistical treatment affects the assessment of possible outliers as well as potentially biasing data when outliers are dominantly on one side of the mean. This data set consisting of 20 $^{206}Pb/^{238}U$-age analyses of AS3 illustrates the effects of choosing three different error treatments. Outliers are rejected in two groups (A,B). Group A is two points of very low age suggesting Pb loss. Group B is two points that are closer to the mean, one high and one low. It is difficult to assess whether data like these are due to analytical effects or geological, but in this case the high point is almost certainly analytical because of no documented inheritance in AS3. (a) Errors shown are internal measurement errors alone; a high initial MSWD indicates excess scatter. After rejecting outliers A and B, the scatter remains excessive suggesting there is an additional error component. (b) Errors are augmented by 0.5% (summed in quadrature). After rejection of outliers A, the MSWD is still marginally excessive but the outliers B are only marginally deviant from the mean. (c) Errors are augmented by 1%. The MSWD of all points is excessive but after rejecting outliers A, the MSWD is consistent with a single population. In SIMS zircon geochronology, the variance of the standard is commonly added to the unknowns that can mask outliers. If minimum errors are used, excess scatter can be used to misidentify marginally deviant points as due to geological effects (Pb loss, inheritance).

and SL13 showed a systematic bias between the two of about 4% that required the age of SL3 to be assigned as 570 Ma, not 552 Ma as measured by ID–TIMS. This was eventually identified as a matrix effect exacerbated by high-U, radiation damage, and the use of a mixed species primary ion beam. Possible biases between other standards are more subtle. Analyses of several Paleozoic time scale samples by SIMS and ID–TIMS showed the SIMS ages referenced to SL13 to be consistently ≤1% less than the TIMS ages, the difference attributed to inheritance by the SIMS analysts and to calibration error by the TIMS analysts (Tucker and McKerrow 1995). Subsequent single grain ID–TIMS analyses and SIMS comparisons of standards suggest that both are probably correct at some level. The question remains, however, whether simple correction factors can be applied in comparing data referenced to different standards. The comprehensive comparisons of standards by Black et al. (submitted) provide a huge data set on which to make a more educated decision. They show that although the sense of difference between the standards is consistent, the magnitude of the differences varies from session to session, such that any correction factors applied are only approximations. Furthermore, it should be noted that a correction factor must necessarily have an uncertainty associated with it and it is likely that the propagation of that uncertainty will further reduce age resolution such that the correction factor would be irrelevant in terms of the augmented errors.

The question of accuracy remains because for the best standards there is no compelling reason to prefer one over another, yet they yield slightly different calibrations. The possibility of systematic biases between standards remains an extremely important matter to be resolved and will impose a fundamental limitation on the accuracy of analyses by current methods if it is not. Nevertheless, the use of at least two known standards in the course of analysis would offer an assessment of reliability for any given analytical session. One of the standards can be reported as an unknown allowing an independent criterion for assessing the veracity of the unknown sample. This of course requires an added time commitment but when accuracy is paramount such a method may be worthwhile.

The bottom line is, if the result is critical, take all necessary means to replicate the analyses and justify the error conditions. If seeking maximum resolution of the age difference between two or three samples, run them on the same mount at the same time against the same standards so that the differences are measured independently of the absolute Pb/U calibration. $^{206}Pb/^{238}U$ is measured most accurately when the standard is measured as frequently as the sample. Measure two or more standards in the session. Ultimately, check the result by running a duplicate session.

## FUTURE DEVELOPMENTS

It is now twenty years since the first publications of SHRIMP U–Pb data (Compston et al. 1982, Froude et al. 1983, Williams et al. 1983). Although over that time there has been a growing appreciation of the measurement technique and especially the uncertainties involved, there has been no fundamental change in the method. This is a testament to the original choice of approach to the analysis of zircon and other minerals, and to the utility of SIMS geochronology in solving often complex geological problems. However it also reflects analytical conservatism. It is widely recognized that ID–TIMS provides much higher precision than SIMS, although for complex zircon the accuracy of the answer can be difficult to assess without reference to microanalyses of individual components. A concerted effort is now required if the accuracy of SIMS is to be improved.

Replicate SIMS analyses of well-characterized reference materials suggest that with present Pb/U calibration techniques, the accuracy of SIMS determinations of $^{206}Pb/^{238}U$ and $^{208}Pb/^{232}Th$ appears limited to about 1%. For samples less than 100-Ma old this equates to an uncertainty of less than 1 Myr, an acceptable age resolution, but for early Paleozoic samples the same uncertainty amounts to as much as 5 Myr, of little value for defining the numerical time scale or dating rapid faunal changes. The principal limitation on accuracy is not counting error, which for average composition zircon becomes significant at the 1% level only for ages less than about 15 Ma, but the Pb/U calibration procedure. Theoretically, with perfect standards and calibration, with existing SIMS instruments it should be possible to analyse the $^{206}Pb/^{238}U$ of an average 400 Ma zircon with a

precision, reproducibility and accuracy of about 0.4% (95% confidence limits). Pooling 16 such analyses potentially could define the age with an accuracy of about 0.1%, comparable to the precision achieved by ID–TIMS.

Improvement will come only with improved calibration procedures. There are clearly some factors affecting relative secondary ion emissions that are not accounted for by present calibration methods. First, it is observed that analyses of apparently homogeneous standard zircons sometimes scatter about the UO/U- or $UO_2$/UO-referenced calibration lines, or Pb/$UO_2$, more than predicted from counting errors, that scatter in the standards is commonly accompanied by similar scatter in the sample analyses, and that the amount of scatter varies from session to session (See also Stern and Amelin, in press). Secondly, there are the small but consistent differences between the ages expected and measured in the interstandard comparisons. It is known that for other minerals (e.g., xenotime and baddeleyite) there are matrix effects not accommodated by simple uranium oxide-based calibrations, so the same is possibly true of zircon. Black et al. (submitted) suggest that one factor needing to be taken into account is the zircon REE content. Substitution of $YPO_4$ for $ZrSiO_4$ might also be important. Wingate and Compston (2000) suggest that for baddeleyite, the composition of the secondary ion beam is affected by the orientation of the crystal relative to the incoming primary ions.

When zircon Pb/U calibration procedures were first being developed for SHRIMP, several different element/element-oxide combinations of Zr and U were explored as possible reference parameters. Pb/U–UO/U was chosen because it showed the best correlation, even though Pb/UO varied over a much smaller range. To improve calibrations further, it will be necessary either to change the procedure entirely, or to introduce another reference parameter that correlates with the deviation of analyses from perfect Pb/U–UO/U correlation. One possibility, but as yet untried procedure, is calibration against a reference plane defined by U/UO, $UO_2$/UO and a ratio of Pb against one of these three species. The logic is that there are virtually no Pb oxides in the secondary ion spectrum, so the ratio of $Pb^+$ to a U ion species will change primarily as a function of the U-oxide speciation. A disadvantage of this procedure is that it takes no direct account of changes in the bulk zircon composition. If the calibration scatter is matrix sensitive, it would perhaps be more beneficial to include P, Y, Hf, and REE species, as proxies for total trace element substitution, which is reasonable for most zircon crystals, as calibration parameters. The calibration correction based on U concentration proposed by Williams and Hergt (2000) is a crude way of doing this. There is another indication that introducing an extra parameter can help—before SHRIMP II at ANU, was correctly tuned, scatter of several percent about the Pb/U–UO/U line was found to be closely correlated with the $Zr_2O_3^+$ count rate.

Even if an improved calibration procedure is found, the accuracy of calibrations will still ultimately be limited by the sub-micron scale heterogeneity of Pb/U in the reference material. It has been argued that in any natural zircon of heterogeneous U content, small scale Pb/U heterogeneity is inevitable because of the micro-redistribution of Pb due to $\alpha$-recoil. Also, even though the volume diffusion rate of Pb in zircon is extremely slow below about 1000°C (Cherniak and Watson, this volume), grain boundary diffusion of Pb along micro or macro defects in the crystal structure, particularly under hydrous conditions, occurs at much lower temperatures.

An alternative to a natural zircon would be an artificial standard. Synthetic zircon of suitable composition and uniformity is unlikely to become available in the near future. First, it is extremely difficult to synthesize zircon doped with trace elements of isotopic interest, that are homogeneous to within 1% due to zoning that is inherent to synthetic zircon grown under laboratory conditions (Hanchar et al. 2001). Second, due to the sluggish volume diffusivities of those elements in zircon (Cherniak and Watson, this volume), it is not practical to attempt to homogenize doped synthetic zircon crystals in the laboratory, due to temperature and time constraints (e.g., months to years, and temperatures as high as 1600°C would be required). It might be possible to produce a glass with sufficiently uniform levels of Zr, U, Th, and Pb to be measured by SIMS at high precision. Such a

material would not necessarily be the primary calibration standard for age determinations, but rather could serve as a monitor of those instrumental conditions that cause fluctuations in the secondary ion ratios. Instrumental factors contributing to scatter could thereby be quantified independently and used to refine the analyses of both zircon standards and unknowns.

Collectors equipped with multiple ion counters, now available on the Cameca 1270 and SHRIMP II ion probes, offer scope for substantial improvement in the precision of the Pb isotope measurements, which is limited by counting statistics, but not in the measurements of Pb/U. The improvement comes at a price, however. The tiny electron multipliers required in constructing multiple collectors, even for high-dispersion instruments such as SHRIMP II, change their gain as a function of total ions counted much more rapidly than do the physically larger multipliers used for single collection. These changes must be closely monitored if analyses are to be accurate, incurring a substantial additional overhead in gain calibrations or the measurement of isotope standards. The gain drift is also a function of count rate, restricting multiple collectors to the analysis of minerals with relatively low U and Th concentrations. Until electron multiplier technology improves, multiple collectors are likely to be used more for the analysis of rare, valuable, heterogeneous or very-low-level samples than for routine geochronology.

The main strength of SIMS analysis is its spatial selectivity. For most applications, the internal variations in target composition that are the objective of the analysis are very much larger than the precision and accuracy of individual measurements. It is principally in resolving small age differences in the early Phanerozoic, as is required in defining the geologic time scale, that the limitations of SIMS geochronology become apparent. Even then, however, it was SIMS work that first picked up the subtle range in the ages of zircons in tuffs (Compston 2000) that subsequently has been confirmed by high precision ID-TIMS (Mundil et al. 2001). As with many new isotopic techniques, SIMS has not proved to be the universal panacea that some early proponents claimed. Nor has it made ID-TIMS redundant. The ultimate resolution of the most demanding geochronological problems, particularly time scale, is going to require the combined approach of mineral characterization by imaging techniques such as BSE and CL, testing by SIMS for age homogeneity and single-grain sample selection, and analysis by ID-TIMS for maximum precision and accuracy. For work on complex, polychronic zircons, however, SIMS remains the technique of choice. The thrill of instant gratification as the ion probe turns out a new age measurement every few minutes is one few geochronologists can now resist.

## ACKNOWLEDGMENTS

We are grateful to our colleagues, particularly at the Research School of Earth Sciences, for sharing unpublished data and their experiences in the analysis of zircon. Comments by J. Hanchar, J. Wooden and R. Stern are greatly appreciated.

## REFERENCES

Aleinikoff JN, Wintsch RP, Fanning CM, Dorais MJ (2002) U-Pb geochronology of zircon and polygenetic titanite from the Glastonbury Complex, Connecticut, USA: an integrated SEM, EMPA, TIMS, and SHRIMP study. Chem Geol 188:125-147

Andersen T (2002) Correction of common lead in U–Pb analyses that do not report $^{204}$Pb. Chem Geol 192:59-79

Andersen CA, Hinthorne JR (1972) U, Th, Pb and REE abundances and $^{207}$Pb/$^{206}$Pb ages of individual minerals in returned lunar material by ion microprobe mass analysis. Earth Planet Sci Lett 14:195-200

Andersen CA, Hinthorne JR (1973) Thermodynamic approach to the quantitative interpretation of sputtered ion in mass spectra. Analyt Chem 45:1421-1438

Bacon CR, Persing HL, Wooden JL, Ireland TR (2000) Late Pleistocene granodiorite beneath Crater Lake caldera, Oregon, dated by ion microprobe. Geology 28:467-470

Black LP, Kame SL, Allen CM, Davis DW, Aleinikoff JN, Valley JW, Mundil R, Campbell IH, Korsch RJ, Williams IS, Foudoulis C (submitted) Towards more reliable Pb/U micro-probe geochronology: SHRIMP, ID-TIMS, ELA-ICP-MS and oxygen isotope documentation for a series of zircon standards. Chem Geol

Bowring SA, Williams IS (1999) Priscoan (4.00–4.03 Ga) orthogneisses from northwestern Canada. Contrib Mineral Petrol 134:3-16

Brimhall GH, Chadwick OA, Lewis CJ, Compston W, Williams IS, Danti KJ, Dietrich WE, Power ME, Hendricks D, Bratt J (1992) Deformational mass transport and invasive processes in soil evolution. Science 255:695-702.
Castaing R, Slodzian G (1962) Microanalyse par émission ionique secondaire. J Micros 1:395-410
Castelli D, Rubatto D (2002) Stability of Al- and F-rich titanite in metacarbonate: petrologic and isotopic constraints from a polymetamorphic eclogitic marble of the internal Sesia Zone (Western Alps). Contrib Mineral Petrol 142:627-639.
Catalos EJ, Sorensen SS, Harrison TM (2000) Th–Pb ion-microprobe dating of Allanite. Am Mineral 85:633-648
Cherniak DJ, Watson EB (2000) Pb diffusion in zircon. Chem Geol 172:5-24
Claoué-Long JC, Compston W, Roberts J, Fanning CM (1995) Two Carboniferous ages: A comparison of SHRIMP zircon dating with conventional zircon ages and $^{40}Ar/^{39}Ar$ analysis. *In* Geochronology, Time Scales and Global Stratigraphic Correlation. Berggren WA, Kent DV, Aubrey M-P, Hardenbol J (eds) SEPM (Soc Sedimentary Geology) Spec Publ 4:3-21
Clark DJ, Hensen BJ, Kinny PD (2000) Geochronological constraints for a two-stage history of the Albany–Fraser Orogen, Western Australia. Precambrian Res 102:155-183
Compston W (1999) Geological age by instrumental analysis: the 29th Hallimond Lecture. Mineral Mag 63:297-311
Compston W (2000a) Interpretations of SHRIMP and isotope dilution zircon ages for the geological time-scale: I. The early Ordovician and late Cambrian. Mineral Mag 64:43-57
Compston W (2000b) Interpretation of SHRIMP and isotope dilution zircon ages for the Palaeozoic time-scale: II. Silurian to Devonian. Mineral Mag 64:1127-1146
Compston W, Williams IS (1992) Ion probe ages for the British Ordovician and Siluriam stratotypes. *In* Global Perspectives on Ordovician Geology. Webby BD, Laurie JR (eds) Proc 6th Intl Symp on the Ordovician System, Sydney, p 59-67
Compston W, Williams IS, Clement SW (1982) U–Pb ages within single zircons using a sensitive high mass-resolution ion microprobe. 30th Am Soc Mass Spectrometry Conf, Honolulu, p 593-595
Compston W, Williams IS, Meyer C (1984) U–Pb geochronology of zircons from lunar breccia 73217 using a sensitive high mass-resolution ion microprobe. J Geophys Res Suppl 89:B525-B534
Compston W, Kinny PD, Williams IS, Foster JJ (1986) The age and Pb loss behaviour of zircons from the Isua Supracrustal Belt as determined by ion microprobe. Earth Planet Sci Lett 80:71-81
Dodson MH (1978) A linear method for second-degree interpolation in cyclical data collection. J Phys E: Sci Instru 11:296
Froude DO, Ireland TR, Kinny PD, Williams IS, Compston W, Williams IR, Myers JS (1983) Ion microprobe identification of 4,100–4,200 Myr-old terrestrial zircons. Nature 304:616-618
Gratz R, Heinrich W (1997) Monazite-xenotime thermobarometry: experimental calibration of the miscibility gap in the binary system $CePO_4$–$YPO_4$. Am Mineral 82:772-780
Goodge JW, Myrow P, Williams IS, Bowring SA (2002) Age and provenance of the Beardmore Group, Antarctica: Constraints on Rodinia supercontinent breakup. J Geol 110:393-406
Hanchar JM, Finch, RJ, Hoskin PWO, Watson EB, Cherniak DJ, Mariano AN (2001) Rare Earth Elements in Synthetic Zircon. 1. Synthesis and Rare Earth Element and Phosphorus Doping. Am Mineral 86:667-680
Harrison TM, McKeegan KD, LeFort P (1995) Detection of inherited monazite in the Manaslu leucogranite by $^{208}Pb/^{232}Th$ ion microprobe dating: Crystallization age and tectonic implications. Earth Planet Sci Lett 133:271-282
Hinthorne JR, Andersen CA, Conrad RL, Lovering JF (1979) Single-grain $^{207}Pb/^{206}Pb$ and U/Pb age determinations with a 10 μm spatial resolution using the ion microprobe mass analyser (IMMA). Chem Geol 25:271-303
Hinton RW, Long JVP (1979) High-resolution ion-microprobe measurement of lead isotopes: variations within single zircons from Lac Seul, northwest Ontario. Earth Planet Sci Lett 45:309-325
Ireland TR (1991) The abundance of $^{182}Hf$ in the early solar system. Lunar Planet Sci XXII:609-610
Ireland TR (1995) Ion microprobe mass spectrometry: Techniques and applications in cosmochemistry, geochemistry, and geochronology. *In* Advances in Analytical Geochemistry. Hyman M, Rowe M (eds) JAI Press 2:1-118
Ireland TR, Wlotzka F (1992) The oldest zircons in the solar system. Earth Planet Sci Lett 109:1-10
Ireland TR, Gibson GM (1998) SHRIMP monazite and zircon geochronology of high-grade metamorphism in New Zealand. J Metamorph Geol 16:149-167
Ireland TR, Compston W, Williams IS, Wendt I (1990) U–Th–Pb systematics of individual perovskite grains from the Allende and Murchison carbonaceous chondrites. Earth Planet Sci Lett 101:379-387
Ireland TR, Flöttmann T, Fanning CM, Gibson GM, Preiss WV (1998) Development of the lower-Paleozoic Pacific margin of Gondwana from zircon-age structure across the Delamerian orogen. Geology 26:243-246
Ireland TR, Wooden JL, Persing H, Ito B (1999) Geological applications and analytical development of the SHRIMP-RG. EOS Trans, Am Geophys Union 80:F1117
Kinny PD, Compston W, Williams IS (1991) A reconnaissance ion-probe study of hafnium isotopes in zircon. Geochim Cosmochim Acta 55:849-859.
LeCheminant AN, Heaman LM (1989) Mackenzie igneous events, Canada: Middle Proterozoic hotspot magmatism associated with ocean opening. Earth Planet Sci Lett 96:38-48

Lee JKW, Williams IS, Ellis DJ (1997) Pb, U and Th diffusion in natural zircon. Nature 390:159-162
Liebl H (1967) Ion microprobe mass analyser. J Appl Phys 38:5277-5283
Lowenstern JB, Persing HM, Wooden JL, Lanphere M, Donnelly-Nolan J, Grove TL (2000) U-Th dating of single zircons from young granitoid xenoliths: new tools for understanding volcanic processes. Earth Planet Sci Lett 183:291-302
Ludwig KR (1999) IsoplotEx v. 2.6. Berkeley Geochronology Center Spec Publ 1a, 47 p
Ludwig KR (2001) SQUID 1.00, a users manual. Berkeley Geochronology Center Spec Publ 2, 17 p
McLaren AC, Fitz Gerald JD, Williams IS (1994) The microstructure of zircon and its influence on the age determination from Pb/U isotopic ratios measured by ion microprobe. Geochim Cosmochim Acta 58:993-1005
McNaughton NJ, Rasmussen B, Fletcher IR (1999) SHRIMP uranium–lead dating of diagenetic xenotime in siliciclastic sedimentary rocks. Science 285:78-80
Matsuda H (1974) Double focusing mass spectrometers of second order. Intl J Mass Spec Ion Phys 14: 219-233
Mendenhall W, Sincich T (1995) Statistics for Engineering and the Sciences. Prentice-Hall, Englewood Cliffs, New Jersey
Meyer C, Williams IS, Compston W (1996) Uranium-lead ages for lunar zircons: Evidence for a prolonged period of granophyre formation from 4.32 to 3.88 Ga. Meteor Planet Sci 31:370-387
Mezger K, Hanson GN, Bohlen SR (1989) High precision U–Pb ages of metamorphic rutile: application to the cooling history of high grade terranes. Earth Planet Sci Lett 96:106-118
Mojzsis SJ, Harrison TM, McKeegan KD (2001) Oxygen isotope evidence from ancient zircons for liquid water at the Earth's surface 4,300 Myr ago. Nature 409:178-181
Moorbath S (1983) The most ancient rocks? Nature 304:585-586
Mundil R, Metcalfe I, Ludwig KR, Renne PR, Oberli F, Nicoll RS (2001) Timing of the Permian–Triassic biotic crisis: implications from new zircon U/Pb age data (and their limitations). Earth Planet Sci Lett 187:131-145
Paces JB, Miller Jr JD (1993) Precise U–Pb ages of Duluth complex and related mafic intrusions, northeastern Minnesota: geochronological insights into physical, petrogenetic, paleomagnetic, and tectonomagmatic processes associated with the 1.1 Ga mid-continental rift system. J Geophys Res 98:13997-14013
Pell SD, Williams IS, Chivas AR (1997) The use of protolith zircon-age fingerprints in determining the protosource areas for some Australian dune sands. Sed Geol 109:233-260
Pyle JM, Spear FS, Rudnick RL, Mcdonough WF (2001) Monazite-xenotime-garnet equilibrium in metapelites and a new monazite-garnet thermometer. J Petrol 42:2083-2107
Quidelleur X, Grove M, Lovera OM, Harrison TM, Yin A, Ryerson FJ (1997) The thermal evolution an slip history of the Renbu Zedong Thrust, southeastern Tibet. J Geophys Res102:2659-2679
Reid MR, Coath CD, Harrison TM, McKeegan KD (1997) Ion microprobe dating of young zircons reveals prolonged residence times for the youngest rhyolites associated with Long Valley caldera. Earth Planet Sci Lett 150:27-35
Sano Y, Terada K (1999) Direct ion microprobe U–Pb dating of fossil tooth of a Permian shark. Earth Planet Sci Lett 174:75-80
Sano Y, Takayuki O, Terada K, Hidaka H (1999) Ion microprobe U-Pb dating of apatite. Chem Geol 153:249-258
Schuhmacher M, de Chambost E, McKeegan KD, Harrison TM, Migeon HN (1993) *In situ* U/Pb dating of zircon with the CAMECA ims 1270. *In* Secondary Ion Mass Spectrometry SIMS IX. Benninghoven A, Nihei Y, Shimizu R, Werner HW (eds) John Wiley, Chichester, UK, p 919-922
Sircombe KN (1997) Detrital mineral SHRIMP geochronology and provenance analysis of sediments in Eastern Australia. Unpubl PhD dissertation, Australian National University, Canberra
Sircombe KN (1999) Tracing provenance through the isotope ages of littoral and sedimentary detrital zircon, eastern Australia. Sed Geol 124:47-67
Stern RA (2000) The significance of secondary ion energy profiles for understanding inter-element calibration curves in SIMS analyses of zircon and monazite. *In* Beyond 2000: New Frontiers in Isotope Geoscience. Woodhead JD, Hergt JM, Noble WP (eds) Lorne, Abstr Proc, p 167-170
Stern RA, Bleeker W (1998) Age of the world's oldest rocks refined using Canada's SHRIMP: The Acasta Gneiss Complex, Northwest Territories, Canada. Geosci Canada 25:27-31
Stern RA, Rainbird RH (2001) Advancements in xenotime U–Pb geochronology by ion microprobe. *In* Eleventh Ann V.M. Goldschmidt Conf Abstr #3872. LPI Contrib #1088, Lunar and Planetary Institute, Houston (CD-ROM)
Stern RA, Amelin Y (in press) Assessment of errors in SIMS zircon U–Pb geochronology using a natural zircon standard and NIST SRM 610 glass. Chem Geol
Tucker RD, McKerrow WS (1995) Early Paleozoic chronology: a review in light of new U–Pb zircon ages from Newfoundland and Britain. Can J Earth Sci 32:368-379
Whitehouse MJ, Claesson S, Sunde T, Vestin J (1997) Ion microprobe U–Pb zircon geochronology and correlation of Archaean gneisses from the Lewisian Complex of Gruinard Bay, northwestern Scotland. Geochim Cosmochim Acta 61:4429-4438
Wiedenbeck M, Allé P, Corfu F, Griffin WL, Meier M, Oberli F, von Quadt A, Roddick JC, Spiegel W (1995) Three

natural zircon standards for U–Th–Pb, Lu–Hf, trace element and REE analyses. Geostandard Newslett 19:1-23

Williams IS (1998) U-Th-Pb geochronology by ion microprobe. *In* Applications of Microanalytical Techniques to Understanding Mineralizing Processes. McKibben MA, Shanks III WC, Ridley WI (eds) Rev Econ Geol 7:1-35

Williams IS, Claesson S (1987) Isotopic evidence for the Precambrian provenance and Caledonian metamorphism of high-grade paragneisses from the Seve Nappes, Scandinavian Caledonides II. Ion microprobe zircon U–Th–Pb. Contrib Mineral Petrol 97:205-217

Williams IS, Hergt JM (2000) U–Pb dating of Tasmanian dolerites: a cautionary tale of SHRIMP analysis of high-U zircon. *In* Beyond 2000: New Frontiers in Isotope Geoscience. Woodhead JD, Hergt JM, Noble WP (eds) Lorne, Abstr Proc, p 185-188

Williams IS, Compston W, Collerson KD, Arriens PA, Lovering JF (1983) A reassessment of the age of the Windmill metamorphics, Casey area. *In* Antarctic Earth Science. Oliver RL, James PR, Jago JB (eds) Australian Academy of Science, Canberra, p 73-76

Williams P (1979) The sputtering process and sputtered ion emission. Surf Sci 90:588-634

Wingate MTD, Compston W (2000) Crystal orientation effects during ion microprobe U–Pb analysis of baddeleyite. Chem Geol 168:75-97

Zeitler PK, Sutter JF, Williams IS, Zartman R, Tahirkheli RAK (1989) Geochronology and temperature history of the Nanga Parbat-Haramosh Massif, Pakistan. Geol Soc Am Spec Paper 232:1-22

# 9 Present Trends and the Future of Zircon in Geochronology: Laser Ablation ICPMS

**Jan Košler**

*Department of Geochemistry*
*Charles University*
*Prague, CZ 12843, Czech Republic*

**Paul J. Sylvester**

*Department of Earth Sciences*
*Memorial University of Newfoundland*
*St John's, Newfoundland A1B 3X5, Canada*

## INTRODUCTION

*In situ* U-Th-Pb geochronology was born some two decades ago with the introduction and development of high-resolution secondary ion mass spectrometry (SIMS or SHRIMP [Sensitive High Mass Resolution Ion MicroProbe]; Compston et al. 1984, Williams 1998, Compston 1999, Davis et al.; this volume, Ireland and Williams, this volume). This technique clearly demonstrated the existence of age heterogeneities within the single crystals of zircon and other accessory phases and therefore the need for high-spatial resolution (tens to hundreds of cubic micrometers) geochronological data. *In situ* dating by ion probe is capable of achieving an analytical precision that is only an order of magnitude worse than the conventional isotope dilution-thermal ionization mass spectrometry (ID-TIMS) dating technique. It has the advantage, however, of more readily identifying concordant portions of grains, does not require chemical treatment of samples prior to the analysis, is essentially nondestructive, and can achieve greater sample throughputs. A major obstacle to the wider use of ion probe dating has always been the high cost of instrumentation and hence relative scarcity of suitably equipped geologic laboratories.

Laser ablation inductively coupled plasma mass spectrometry (LA-ICPMS) emerged in 1985 and rapidly became an important analytical tool for trace element determinations in geological samples (Jackson et al. 1992). It was soon realized that the large variations in radiogenic Pb and Pb/U isotopic ratios found in nature could be resolved by ICPMS techniques and, when coupled to a laser, ICPMS could be used as a dating tool similar to the ion probe. The pioneering work of Feng et al. (1993), Fryer et al. (1993), Hirata and Nesbitt (1995) and Jackson et al. (1996) illustrated the potential usefulness of laser sampling for *in situ* dating by ICPMS particularly well. However, these studies and others that followed also revealed the major difficulties with the method, namely large and variable discrimination of isotopes (mass bias) due to space-charge effects in the instrument interface region and electrostatic lens stack of the ICPMS, well known from earlier solution-based work (Tanner 1992); elemental fractionation of U and Pb at the ablation site (Hirata and Nesbitt 1995, Jeffries et al. 1996, Hirata 1997, Horn et al. 2000, Russo et al. 2000, Košler et al. 2002a) and in the ICP source (Guillong and Günther 2002) due to volatility differences, and limited availability of suitable mineral standards required to correct for mass bias and elemental fractionation. Some of these problems have been overcome by a better understanding of the fundamentals of the laser ablation process and advancements in laser and ICPMS technologies, but others remain, and some more subtle problems have emerged with improved precision and accuracy of our measurements. The purpose of this paper is to describe the remarkable progress made in laser ablation ICPMS U-Th-Pb dating of zircon and other U-Th-bearing accessory minerals, point out its present problems and their potential solutions, and reflect on the future of this new and rapidly evolving geochronologic technique.

1529-6466/03/0053-0009$05.00

# LASER ABLATION

## Laser principles

A laser (light amplification by stimulated emission of radiation) is a device capable of producing a narrow, directed and intense beam of radiation that has a uniform wavelength, phase and polarization. Laser sampling for ICPMS is based on interactions of high intensity photons—laser radiation—with solid material, resulting in vaporization and ablation, which involves ejection of atoms, ions, molecules, melt and solid particles (Darke and Tyson 1993, Durrant 1999). The most commonly used lasers for laser ablation sampling are based on light amplification in gaseous or solid-state media. The principle of light amplification in a solid-state laser is shown in Figure 1. Briefly, the population of atoms in the lasing medium can change their energy state by absorption of photons that excite the electrons to higher energy levels. The excited electrons would normally decay back to their ground states by spontaneous emission but the higher energy state (inverse population of atoms) is maintained by external pumping of light. If a photon with energy that is equal to the difference between the excited and ground state interacts with an excited electron, it triggers its decay and emission of another photon with the same energy and direction. This process is called stimulated emission and it results in the amplification of light. The active medium of the most widely used solid-state laser is yttrium-aluminum garnet ($Y_3Al_5O_{12}$) doped with ca. 1% $Nd^{3+}$ (Nd:YAG). It is usually a rod with two end-mirrors, one of them is only partially reflective. The light pumping is achieved by light pulses from a high-intensity flash-lamp and the emitted photons oscillate between the two mirrors, passing through the active medium and triggering further photon emissions until an inverted population is formed. A cascade of photons released from the inverted population passes through the semi-reflective mirror as a laser pulse. Laser pulses normally occur whenever the energy of emitted photons exceeds the energy losses by absorption in the rod (i.e.,

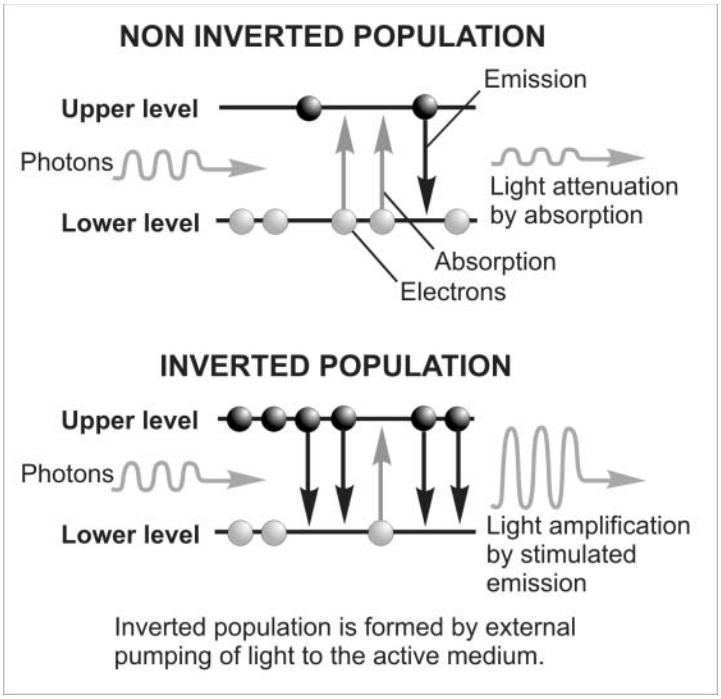


**Figure 1.** Principles of solid-state laser operation. Modified from Silfvast (1991).

several times during the light pumping), resulting in a series of low-amplitude pulses, the so-called "free-running" mode of the laser. For a better coupling of laser radiation with solid samples, most of the Nd:YAG lasers used for ablation are operated in the Q-switched mode which produces high-amplitude short laser pulses (5-10 ns). This is achieved by employing a rotating mirror or Pockels cell that acts as a shutter and allows a larger inverse population to build-up by limiting the spontaneous emission in the active medium. The fundamental wavelength of Nd:YAG lasers is 1064 nm (IR) which is not suitable for sampling of most geological materials, which absorb much better in the ultraviolet (e.g., Jeffries et al. 1996). The conversion to shorter UV wavelengths is achieved by passing the laser light through harmonic generators (optically non-linear crystals) that can be combined in series to produce output wavelengths of 532, 355, 266 and 213 nm. Nd:YAG systems employing wavelengths of 266 nm and, increasingly, 213 nm have been used most widely for geologic applications (e.g., Jackson 2001).

Excimer (excited dimer gas molecule) is the most frequently used gas laser in LA-ICPMS (Loucks et al. 1995, Günther et al. 1997, Horn et al. 2000). Its operation is based on electronic transitions in diatomic molecules of noble gases and halides where the component atoms of gas are bound in the excited state, but not in the ground state. By creating a large number of excited dimers by electric discharge in the gas, the lasing effect can occur between the excited energy state and the ground state of the molecules. The pumping mechanisms are complex and the reactions include not only the atoms that form the dimer, but also atoms of an additional rare gas whose presence in a small quantity is required for conservation of energy and momentum. The important dimer molecules and their fundamental wavelengths are Xe-F (351 nm), Xe-Cl (308 nm), Kr-F (248 nm), Ar-F (193 nm) and F-F (157 nm); however, only the Ar-F excimer laser has been widely used for laser ablation ICPMS of geological samples (e.g., Sylvester and Ghaderi 1997, Horn et al. 2000).

**Laser ablation system**

A laser ablation system or Laser Ablation Microprobe (LAM) is a device that combines the laser with beam delivery optics that steers the laser beam on to the surface of a sample placed in an ablation cell. Most commercially available systems are computer driven, allowing the operator to precisely control and monitor the performance of the laser, the motorized stage that carries the ablation cell, and the flow rate of the sample carrier gas. The schematics of a typical Nd:YAG laser ablation system is given in Figure 2. The laser beam is passed through the second and fourth harmonic generator that convert its wavelength from the fundamental (1064 nm) to the quadrupled 266 nm. Alternatively, a quintupled 213-nm wavelength can be obtained by combination of 1$^{st}$ and 4$^{th}$ (Jeffries et al. 1998) or 2$^{nd}$ and 3$^{rd}$ harmonics. The output 266- or 213-nm laser wavelength is then cleaned in a series of dielectric mirrors or a Pellin Broca prism before passing the beam through the optical attenuator that controls the laser beam energy. The attenuator consists of a rotating silica prism or a combination of half-wave plate with a prism polarizer.

Some laser ablation systems control the laser beam diameter by a series of apertures, others employ a combination of apertures with an adjustable beam expander. For reproducible ablation of samples, it is essential to detect and monitor the laser power, so a power meter is usually included. The final part of the optics is a viewing system that incorporates a camera, often mounted on a modified petrographic microscope, allowing spot selection by conventional microscopic examination. Many Nd:YAG ablation systems employ a "focused beam," wherein laser radiation passes through the objective lens of the microscope and onto the sample. In such systems it is possible to control the laser spot size and energy density on the sample surface and position of the laser focal plane by changing the working distance of the lens. Other Nd:YAG ablation systems and excimer laser microprobes employ the "imaged beam" technology where the spot size is controlled by apertures and beam expanders. The advantage of the latter is that the laser beam does not have to pass through the objective lens (e.g., Loucks et al. 1995, Horn et al. 2000), in which case a less expensive viewing optics can be used. The imaged beam technology also provides a constant laser energy

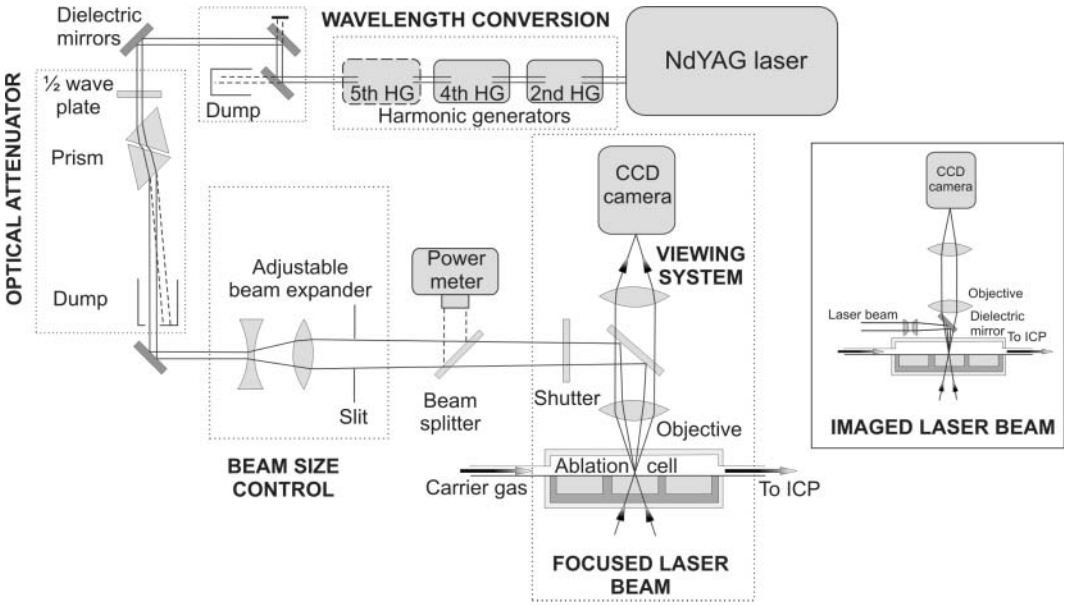


**Figure 2.** Schematics of a typical laser ablation system. Modified from Jackson (2001).

density, regardless of the spot size (e.g., Günther et al. 1997).

An important part of the laser microprobe is the ablation cell that is mounted on the motorized stage. The design of the cell must allow the laser beam to interact with the sample; this is usually through an anti-reflection-coated UV-transparent window. Good viewing of the sample and efficient transport of the ablated material in the carrier gas to the ICP source of the mass spectrometer are both important parameters of the ablation cell. Different cell designs suit different applications but the general conclusion from numerous tests with cells of different sizes and shapes (Jackson et al. 1996, Eggins et al. 1998, Bleiner and Günther 2001) is that a good ablation cell is a compromise between the size of sample that needs to be accommodated and the efficiency of flushing the cell with carrier gas. Ablation cells of low volume minimize the amount of dispersion of aerosol ablated from the sample; this leads to higher signal-to-noise ratios for analytes but shorter counting times for each analyte signal if the sample is of limited mass. The flush time needed to return to the background intensities of each signal is also reduced for small-volume cells (Moenke-Blackenburg et al. 1989). Bleiner and Günther (2001) demonstrated that the transport efficiency of laser-induced aerosol is independent of the geometry of the transport system for optimized operating conditions. Precision of measurements, however, tends to decrease in large ablation cells (>50 $cm^3$) for different sampling positions within the cell while in very small cells (~1-2 $cm^3$), the reactions between aerosol and the cell wall can limit the aerosol transportation efficiency. Hence a simple cylindrical and small-medium size cell design (~10 $cm^3$) is generally well suited to the U-Th-Pb dating of accessory minerals by LA-ICPMS. Precise positioning of the sample relative to the stationary laser beam requires a high-quality motorized stage. Commercially available systems often include computer-driven motors with micrometer reproducibility over several centimeters of traveling distance. For effective control of laser ablation measurements, it is best if the resolution of the viewing system matches the precision of the stage positioning.

## Interaction of laser radiation with solid samples

Laser–solid interaction is a complex process that includes reflection of part of the laser beam; absorption of incoming photons and formation of photoelectrons; emission of electrons, ions, at-

oms, molecular species and particles; conversion of the incoming energy to heat; melting, boiling and/or vaporization of the sample; and shock wave formation (Darke and Tyson 1993, Durrant 1999 and the references therein). Initially, the electrons in the solid become excited and some electrons may be emitted from the sample surface. The excited electrons then transfer their energies to the structure and the sample melts and/or vaporizes. Ions released during this process form a plasma plume above the sample surface. The expanding high-pressure plasma triggers further melting and/or vaporization of the solid and emission of particulates, forming an aerosol.

Variations in laser energy density across the laser beam can result in the formation of a strong temperature gradient at the ablation site, especially near the periphery of the laser pit. Because different elements have different melting and boiling temperatures and different rates of vaporization, the existence of these thermal gradients can lead to non-representative sampling of the solid during the laser ablation. Also, as the pit deepens, refractory elements such as U preferentially condense on the growing crater walls compared to more volatile elements such as Pb. This effect leads to increasing Pb/U ratios measured by the ICP with increasing pit depth and directly impacts on the quality of U/Pb isotope data. It is especially pronounced for craters with small aspect (diameter/depth) ratios (Eggins et al. 1998, Mank and Mason 1999).

The significance of different processes that occur during interaction of the laser with the solid sample depends on a number of inter-related laser ablation parameters, some of which are discussed below.

**Choice of laser ablation parameters**

There are several parameters that can affect the precision and accuracy of data obtained from laser ablation ICPMS. They include laser wavelength and pulse duration, laser beam profile, laser repetition rate, focusing conditions of the laser, laser energy density and energy per pulse, spot size and composition of ambient gas. Some of the parameters are fixed for a given laser system, others are adjustable.

***Laser wavelength.*** It has been demonstrated that shorter (ultraviolet) laser wavelengths are often better absorbed by minerals and silicate glasses, particularly transparent ones, than are longer (infrared) wavelengths (Jeffries et al. 1998, Horn et al. 2001, Jackson 2001). This leads to better laser-sample coupling, less melting, a more constant production rate of particles with a narrower size distribution and hence more stable analyte signals. Günther and Hattendorf (2001) and Guillong and Günther (2002) reported that, within the deep UV, 193-nm ablation produces a larger proportion of small particles (<0.5 μm) in silicate glass than does 266-nm ablation. Horn and Günther (2003) reported that 193-nm ablation produces large amounts of vapor that subsequently condense to form aggregate particles. How differences in the particle size distribution of ablated aerosols may affect the quality of U-Th-Pb isotope data, for instance in the degree of Pb/U fractionation, is not yet known. However, no significant differences were found in Pb/U fractionation during the ablation of silicate glasses using 266-, 213- and 193-nm lasers in the studies of Liu et al. (2000) and Gonzales et al. (2002). Thus there is no consensus on whether one short UV wavelength is clearly more suitable for U-Pb dating than another. It has been difficult to make a precise comparison of different UV laser wavelengths because the effects of other differences between most Nd:YAG and excimer laser systems such as focused beam vs. aperture imaging delivery, and different pulse durations, are difficult to quantify beforehand. However, with development of a solid-state (Nd:YAG) 193-nm laser (Horn et al. 2003), more precise comparisons between wavelengths may be possible in the near future. It is important to note that the laser wavelength is usually fixed for most commercial laser systems, and the choice of the wavelength used for U-Pb geochronology must be made in the context of other ongoing laser applications in a particular laboratory.

***Laser pulse duration.*** Most Nd:YAG lasers that are used with ICPMS operate in the pulse Q-switched mode with pulse duration of 5 to 10 nanoseconds. The ArF excimers used for ICPMS have slightly longer pulse widths (~20 ns). During the nanosecond laser pulse there is sufficient time for

photons to dissipate in the solids as heat. This may lead to catastrophic ablation and/or sample melting during ablation. Ablation differences using 5 and 20 ns pulse widths have not been well documented. However, Russo et al. (2002) reported that lasers with a pulse duration of only a few hundred femtoseconds minimize heating of the sample, which reduces melting at the ablation site. This could potentially result in a more homogeneous particle size distribution and more stable signals. Initial experiments with silicate glasses have shown that infrared femtosecond lasers may suppress Pb/U fractionation, suggesting their potential use for Pb/U dating of accessory mineral phases (Russo et al. 2002). The limiting factor will be their high capital cost.

***Laser beam profile.*** The energy distribution across the laser beam is an important factor that affects the ablation process (Horn et al. 2001). A Gaussian beam profile provides higher energy at the center of the beam than at the margins. Interaction of a Gaussian laser beam with a solid sample can thus produce greater ablation yields and enhanced melting and vaporization at the center of the ablation pit compared to at the margins. It should be noted that a greater ablation yield (more ablated material) does not necessarily lead to an increase in the analyte signal as this will also depend on the proportions of particles of different sizes that can be effectively ionized in the ICP (Horn et al. 2001, Guillong and Günther 2002). Non-representative sampling of the target material may be the result of uneven energy distribution across the laser beam. Also, a Gaussian beam produces pits that rapidly narrow downward, reducing ablation yields and hence analyte sensitivity, and exacerbating depth-dependent volatile/refractory element fractionation along the pit walls. In contrast, a "flat-top" laser beam with a homogeneous energy profile produces pits that, other factors (such as the numerical aperture of an objective used) being equal, narrow downward more slowly during ablation. This is less likely to lead to differential sample melting and vaporization between the center and margin of the pit (Horn et al. 2001). Excimer lasers possess flat-top beam profiles intrinsically, whereas Nd:YAG lasers will have Gaussian profiles unless modified by homogenization arrays (Guillong et al. 2002).

***Laser energy density, energy per pulse and spot size.*** The amount of laser radiation that interacts with the sample during ablation is quantified by the energy density ($J/cm^2$), which is related to the energy per laser pulse (mJ/pulse) and the diameter of the laser beam where it intersects the sample surface (laser spot size). All three parameters are adjustable. The laser spot size is difficult to measure accurately because the resulting ablation pit is usually larger than the beam diameter due to thermal effects near its margins. The spot size will also depend on the divergence of the laser beam, its diameter, energy distribution and diffraction (Günther and Mermet 2000). The spot size (or size of the resulting laser pit) is often incorrectly given as the spatial resolution of laser ablation analysis. It is important to note that the laser pit is a three dimensional cavity and spatial resolution is a function of the volume of the pit and mass of ablated material. The minimum mass of ablated material needed for a single analysis depends on the concentration of analytes and precision required. For a typical laser ablation analysis of zircon for U-Pb dating, between 20 to 60 thousand $\mu m^3$ is analyzed.

***Laser repetition rate.*** For a given spot size and laser energy density, the repetition rate (number of laser pulses fired per second) will control the amount of ablated material and, to some extent, also the stability of the signal measured by ICPMS. The repetition rate on most laser systems is adjustable and typically varies between 1 and 20 Hz. There are trade-offs to consider in choosing repetition rates. Higher rates usually produce large and hence more stable signals but drill down into the sample more rapidly, producing pits with small aspect (diameter/depth) ratios and thus increasing the extent of depth-dependent element fractionation. For many applications, including U-Pb dating, a repetition rate of 5 to 20 Hz is commonly employed depending on the sensitivity of the ICPMS, the concentration of the analyte in the target material and the spatial resolution required.

***Focus of laser beam.*** For laser systems in which the beam passes through the objective lens of a microscope, the operator can choose between focused and defocused laser beams. By moving the laser focal point up from the surface of the sample (Jackson et al. 1996, Jackson 2001), a larger

"defocused" beam with a lower energy density on the sample surface is generated. This minimizes the relative change in focus as the laser beam drills into the sample and leads to a more stable signal. Laser beam defocus also produces pits with larger aspect (diameter/depth) ratios and, with a lower laser energy density, effectively reduces depth-dependent Pb/U fractionation.

***Ambient gas.*** The composition and flow rate of ambient gas into the sample cell and in tubing leading from the cell to the ICP, referred to as the carrier gas, affect the properties and transport efficiency of the aerosols generated at the ablation site. Helium is typically used as the carrier gas and is combined with the argon feed to the ICP, commonly some distance "downstream" from the sample cell (Günther and Heinrich 1999) or within the cell itself (Loucks et al. 1995, Eggins et al. 1998). Relative to ablation in Ar, less ablated material is left around the crater with ablation in He, and more sample is delivered to the ICP, which produces a more stable signal with a higher intensity (Günther and Heinrich 1999). The factor of improvement in signal intensity varies between 1 and 3 for individual laser systems. Guillong and Günther (2002) and Horn and Günther (2003) showed that the signal enhancement is greater for 193-nm systems than for 266-nm systems, suggesting that helium preferentially increases the transport efficiency of the large numbers of small particles generated by the 193-nm beam. Low concentrations of gas impurities in the ambient gas, such as nitrogen (Durrant 1994, Hirata and Nesbitt 1995) or oxygen (Košler et al. 2002a), may also have both positive and negative effects on the properties and transport efficiency of the ablated aerosols. Understanding and utilizing the effects of gas impurities to maximize the quality of ICPMS data for U-Pb geochronology is likely to be a rich area of research in coming years.

## INDUCTIVELY COUPLED PLASMA MASS SPECTROMETRY

Inductively Coupled Plasmas (ICPs) were introduced as ion sources on commercially available mass spectrometers in 1983-1984. Since then, ICPMS technology has made large advances and plasma source instruments now dominate the inorganic field of mass spectrometry in the Earth sciences. Mass spectrometers in general have four main parts: ion source, mass filter, detector and vacuum system. The three types of instruments that are now used in the Earth Science community—quadrupole ICPMS, magnetic sector ICPMS and time-of-flight ICPMS—differ in the type of mass filter employed. ICP mass spectrometers come as single-detector (single-collector) and multiple-detector (multi-collector) instruments that are capable of sequential and simultaneous detection of ions, respectively. The design of a mass spectrometer, especially the type of mass filter and the detection system used are important for the analytical precision of isotopic measurements that can be achieved and hence determine the range of geological applications that can be addressed by measurements on a particular type of instrument.

### Inductively coupled plasma as ion source

An inductively coupled plasma (a hot, luminous and partially ionized gas) is an excellent source of ions. It is generated in argon (or another inert gas) that flows through three concentric glass tubes—the torch (Fig. 3). The innermost tube carries the sample gas, which, for laser ablation ICPMS, is usually Ar or Ar-He mixture. A copper coil surrounds the end of the torch. It is connected to a radio-frequency power generator that creates an oscillating RF magnetic field within the Ar gas. The plasma is generated by seeding the argon with few electrons that oscillate and collide in the RF field created by the coil. As more collisions between free electrons and Ar atoms occur, the argon gets increasingly more ionized. The ions oscillate in the magnetic field while the atoms do not, which results in heating of the Ar gas, further ionization and formation of the plasma. The argon plasma reaches temperatures of 8000-10000 K and thus can easily ionize elements that have lower ionization energies than argon (15.76 eV). The ionization efficiency of most lithophile and siderophile elements is close to 100%, while ionization of chalcophile elements is only somewhat lower (Houk 1986).

The technical problem that for a long time prevented the use of plasma as an ion source for mass spectrometry, was how to effectively transfer ions from atmospheric pressure to the vacuum

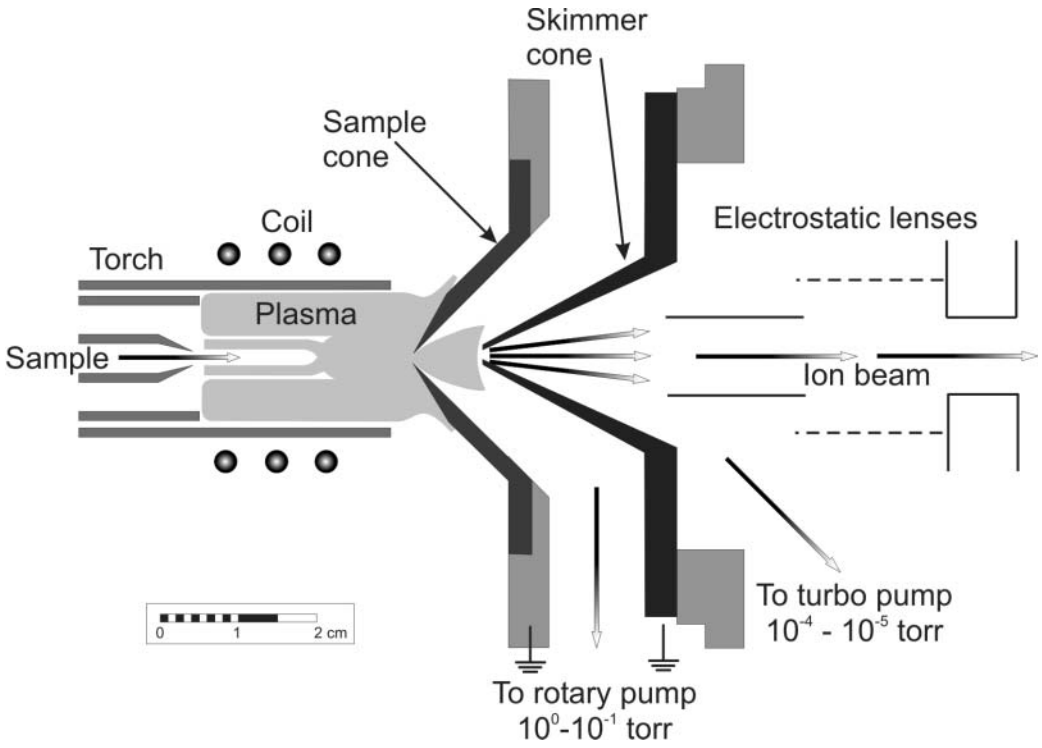


**Figure 3.** Schematic cross-section of plasma torch and ICPMS interface (after Houk 1986).

inside the instrument. This was solved in the early 1980s by designing an interface that has two steps of differential pressure between the atmospheric plasma and the vacuum inside the instrument ($10^{-4}$-$10^{-6}$ torr, Fig. 3, Houk et al. 1980, Date and Gray 1981, Houk et al. 1981). The ions in the plasma enter the instrument at high speed through a hole in the tip of a sampler cone (made of Ni, Cu, Pt or Al) in the water-cooled interface of the ICPMS. A further fraction of the plasma is skimmed off by another cone (skimmer cone) so that approximately only 1% of the sample finally reaches the mass spectrometer (Longerich and Diegor 2001). The ion beam is then shaped by a system of electrostatic lenses and accelerated to the mass analyzer. The operation and design of the ICP source is similar for quadrupole, magnetic sector, and time-of-flight instruments.

In contrast to thermal ionization sources, where some elements are difficult to ionize and only one element can be efficiently converted to ions at a time, the high ionization efficiency of the ICP allows for simultaneous ionization and isotopic measurements of a number of elements, including those with high ionization potentials (e.g., Fe, Cu, W, Re, Os, Hf). This has enabled the determination of isotopic ratios of Pb, U and Th during a single ICPMS measurement, which makes *in situ* dating of accessory minerals possible by this method. Other exciting new applications for ICPs have also emerged in recent years; precise measurements of isotopic fractionations in metals such as copper, tungsten and hafnium by multi-collector magnetic sector ICPMS being perhaps the most significant (e.g., Jackson et al. 2001).

## Quadrupole ICPMS

The schematic of a quadrupole ICPMS instrument is given in Figure 4. The mass analyzer consists of four parallel metal rods of elliptical shape in a square arrangement. Each two opposite rods are connected and have applied AC and DC potential. By varying the AC/DC between the two pairs of rods, ions traveling down the flight path oscillate between the four rods. For a given quadru-

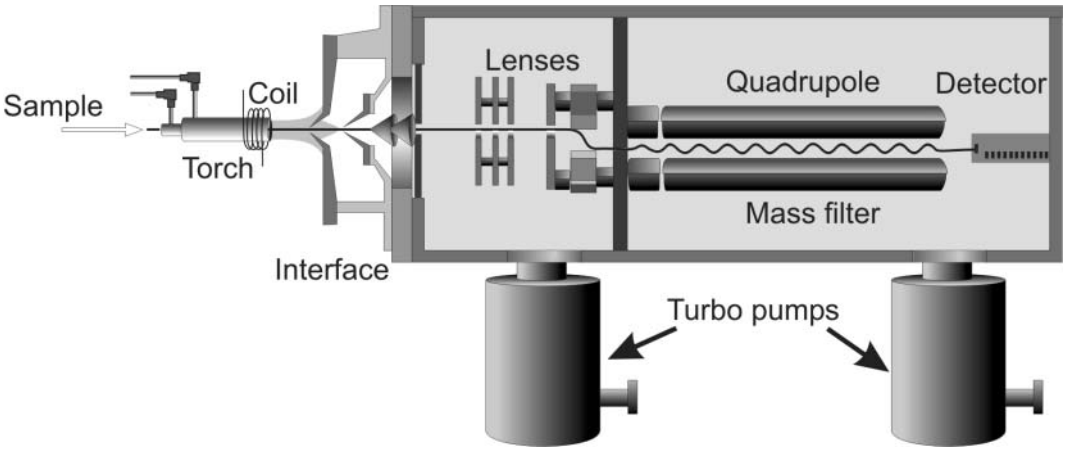


**Figure 4.** Schematic cross-section of a quadrupole ICPMS. Modified from Agilent Technologies.

pole setting it is possible to transmit only ions within a very small mass/charge (m/z) ratio, other ions collide with the rods and are pumped away from the mass analyzer region. A quadrupole is a fast-switching sequential analyzer and therefore quadrupole ICPMS instruments are only equipped with a single detector, usually an electron multiplier or a Faraday cup. The measurements of isotopic ratios or scans of the mass spectrum are obtained by measuring intensities of the ions passing through the quadrupole filter as the voltages on the rods are varied. In order to achieve a useful precision on transient signals like that from laser ablation, the monitored mass peaks have to be scanned as fast as possible to eliminate the effect of signal fluctuations on the measured elemental or isotopic ratios. This is achieved by minimizing the time spent on each mass peak. Laser ablation signals are collected in peak jumping mode with one point measured per mass peak (atomic mass unit, amu).

**Magnetic sector ICPMS**

The principle of mass filtering in the magnetic sector is that ions that move through the magnetic field created by an electromagnet are deflected from their straight trajectories. If the ions have identical kinetic energies, the amount of deflection is proportional to the intensity of the magnetic field and the mass of the ions. Magnetic sector ICPMS (Fig. 5) commonly combines magnet and ion acceleration mass filtering to extract the required isotopes from the ICP source to the detector. Magnetic sector ICPMS instruments come in single and double focusing configurations: the latter employs a magnet together with an electrostatic filter—a device that separates ions according their kinetic energies. Instruments with normal and reverse geometry have the electrostatic filter placed either before or after the magnetic sector, respectively. Similar to quadrupole instruments, the single detector magnetic sector ICPMS is a sequential instrument and fast scanning of the monitored peaks is essential to reduce signal fluctuations with time. On the other hand, multi-collector magnetic sector instruments are capable of simultaneous detection of several isotopes which effectively eliminates problems with temporal variations of signal intensity during the measurement. Faraday cups and electron multipliers can be used for simultaneous detection, some magnetic sector instruments are equipped with an additional Daly detector.

An important difference between quadrupole and magnetic sector instruments is in the shape of the ion beam and energy spread of ions that reach the detector—the two factors that affect the shape of mass peaks. While quadrupole instruments would typically have “Gaussian” mass peaks, flat-topped mass peaks are usually obtained in magnetic sector mass spectrometers, where the ion beam is energy-filtered. The measured signal intensity on flat-topped mass peaks is not affected by taking the on-peak measurement slightly off-center on the peak. This results in 1-2 orders of magni-

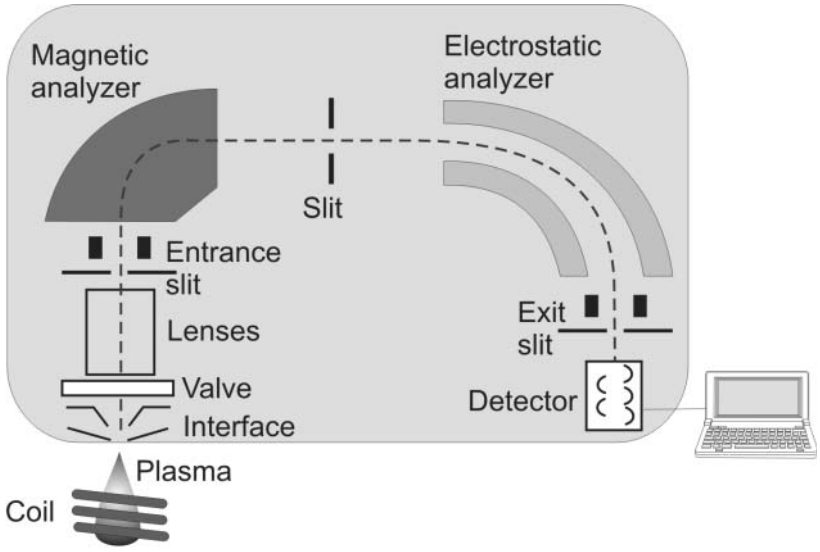


**Figure 5.** Schematics of a double focusing, reverse-geometry, single-collector magnetic sector ICPMS.

tude better precision for magnetic sector ICPMS measurements compared to quadrupole ICPMS measurements. Precision of measurements by single-detector (both magnetic sector and quadrupole) ICPMS instruments is also limited by the plasma flicker noise which can be overcome by simultaneous detection of ions in multiple-collector magnetic sector ICPMS or simultaneous ion sampling in time-of-flight ICPMS.

**Time-of-flight ICPMS**

Mass separation in time-of-flight (TOF) ICPMS is based on the principle that if all ions are given the same kinetic energy, the lighter ions travel faster in the flight tube of the mass spectrometer and reach the detector before the heavier ions. Although the differences in arrival times of the light and heavy ions to the detector are small (in nanoseconds for ca. 1 m flight tube), they are resolvable by fast sequential detectors. In TOF-ICPMS (Fig. 6) the ions are collected from the ICP in a contained volume for a period of few microseconds and then accelerated and released to the flight tube. The effective length of the flight tube is doubled by forcing the ions to travel the distance twice as they are repelled backwards by the reflector placed at the opposite end of the flight tube. The ions are detected in large area detectors such as the micro-channel plates and the whole mass spectrum can be acquired on the time-scale of a few microseconds. Similar to the quadrupole ICPMS, detection of ions in TOF-ICPMS is sequential, however, sampling of the plasma is "simultaneous" on the time-scale of few micro-seconds. Despite the great potential of TOF-ICPMS for measuring short-lived transient signals, it has not been widely used with the laser ablation sampling. The major obstacle to using TOF-ICPMS for U-Th-Pb dating by laser ablation is its low sensitivity which, for commercially available TOF instruments, is, at the time of writing this review, at least an order of magnitude less than for quadrupole ICPMS.

**Mass discrimination (bias) and fractionation of isotopes and elements**

The raw isotopic and elemental ratios as measured by ICPMS are almost never in agreement with the "true" values. There are three fundamentally different processes that cause this discrepancy. *Instrument mass discrimination* (bias) is an offset of the measured values relative to the true values which is constant at least over the period of time of a single analysis. It results from differen-

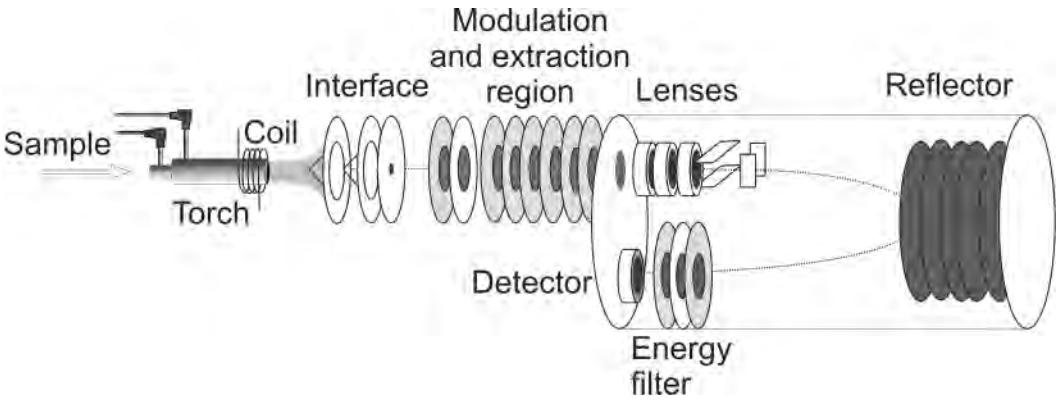


**Figure 6.** Schematics of an axial time-of-flight ICPMS (after Ray and Hieftje 2001).

tial transmission of ions of different masses from the ICPMS interface to the detector. Different processes are thought to contribute to mass discrimination, including matrix and space-charge effects (Douglas and Tanner 1998) and differential ion transmission related to particular instrument settings. Differences in the ionization potentials of elements contribute to different responses of ICPMS and can also bias the measured elemental ratios. The other two processes causing differences between measured and "true" elemental and isotopic ratios may be referred to as *fractionation* and defined as a continuous change of isotopic or elemental ratios with time during the measurement, as is well known in TIMS analysis. We have already described *laser-induced depth-dependent fractionation*, which affects volatile/refractory element pairs such as Pb/U ratios as the laser beam drills progressively into the target material (Eggins et al. 1998, Mank and Mason 1999). It has been suggested that a second kind of *plasma-induced fractionation* also occurs during LA-ICPMS (e.g., Guillong and Günther 2002). This is thought to result from non-representative sampling of the ablated aerosols supplied to the plasma, particularly incomplete atomization and ionization of the larger particles.

The size distribution of particles produced during laser ablation is considered to be an important parameter affecting elemental fractionation as well as the stability of the signal measured by ICPMS (Guillong and Günther 2002). It is affected by the fluence (laser energy per sample area) and wavelength of laser radiation, laser pit diameter/depth ratio, composition of sample carrier gas (Eggins et al. 1998, Mank and Mason 1999) and size-dependent transport efficiency (Brockman 2001) of ablated particles. Nanometer-sized particles are transported with the highest efficiency and are thus mostly atomized and ionized in the plasma (Guillong and Günther 2002), whereas coarse particles (>1.0 μm) are more effectively trapped in the sample carrier tube, on ablation cell interior surfaces, or form a thin deposit (ejecta blanket) on the sample surface. Research carried out the time of writing this review (Koch et al. 2002, Kuhn and Günther 2003, Košler et al. submitted) should help to establish whether the nature and composition of ablated particles vary with their size.

The combination of mass discrimination and elemental fractionation and difficulties in separating the two processes represent a serious challenge for U-Th-Pb dating of accessory minerals by laser ablation ICPMS. In order to derive precise and accurate age data, appropriate corrections must be applied to the raw isotopic and elemental ratios. The correction procedures that are applicable to laser ablation zircon dating will be discussed in the following section.

## DATING OF ZIRCON BY LASER ABLATION ICPMS

Principles of U-Th-Pb zircon geochronology are discussed in a more detail elsewhere (see Parrish et al. this volume, Davis et al. this volume, and Ireland and Williams this volume) and will not be reviewed here. This section will focus on technical aspects of U-Th-Pb zircon dating by LA-

ICPMS. Briefly discussed will be the history of the technique, elemental fractionation, zircon sampling strategies and spatial resolution of laser ablation, instrument mass bias, correction for initial common-Pb, precision and accuracy of laser ablation age dating and strategies for data acquisition and reduction. The examples will be largely from quadrupole ICPMS measurements as this is still the most widely used technique, with references made to the procedures used in the authors' home laboratories. However, magnetic sector ICPMS dating as well dating techniques used elsewhere will also be discussed.

## Past studies of U-Pb zircon dating by laser ablation ICPMS

The first attempts to date zircon crystals with a laser probe coupled to an ICPMS (Feng et al. 1993, Fryer et al. 1993) illustrated the potential of this technique but also pointed out some difficulties. These included mass discrimination of isotopes (mass bias; Horn et al. 2000) due to space-charge effects in the instrument interface region and electrostatic lens stack of the ICPMS, elemental fractionation of Pb and U during ablation due to volatility differences between the two elements and lack of suitable mineral standards appropriate for mass bias and elemental fractionation corrections. Because of the problems with corrections for elemental fractionation of Pb and U, most of the early work concentrated on $^{207}Pb/^{206}Pb$ dating. Mass bias and decoupling of Pb and U during laser ablation have since been the subject of numerous studies (Hirata and Nesbitt 1995, Jackson et al. 1996, Jeffries et al. 1996, Hirata 1997, Parrish et al. 1999, Horn et al. 2000, Liu et al. 2000, Russo et al. 2000, Li et al. 2001, Gonzales et al. 2002, Guillong and Günther 2002, Košler et al. 2002a, Russo et al. 2002). Several techniques have been employed solely to reduce Pb/U fractionation during laser sampling. At the same time, two different procedures, so-called external and internal corrections, have been used to correct for the combination of instrument mass bias and laser-induced Pb/U fractionation. The effect of plasma-induced fractionation on Pb/U ratios is not well understood and remains an area of future investigation.

Most of the early work on laser ablation zircon dating was done with quadrupole ICPMS instruments but recently there have been several successful attempts to date zircons and other accessory minerals by single- and multi-collector magnetic sector ICPMS (Machado and Simonetti 2001, Willigers 2002, Foster et al. 2002, Tiepolo et al. in press). These clearly demonstrated the potential of magnetic sector instruments to obtain more precise data. However, as the precision and accuracy of U-Pb dating by laser ablation is mostly controlled by elemental fractionation of Pb and U, the precision of final age data from magnetic sector ICPMS is still comparable to that of quadrupole ICPMS.

## Elemental fractionation of Pb and U and methods of correction

Elemental fractionation is an important source of error in U-Pb dating of zircon by LA-ICPMS. This problem is clearly demonstrated in Figure 7, which shows the measured Pb/U ratios over 180 s of single-spot ablation of a 1065 Ma old zircon standard 91500 (Wiedenbeck et al. 1995). During this analysis, the measured $^{207}Pb/^{235}U$ ratio changed from ca. 2 at the start of ablation to almost 6 at the end of data acquisition. Translated to the isotopic age, the shift in measured $^{207}Pb/^{235}U$ ratios corresponds to a time difference of almost $10^9$ years, i.e., approximately 100% of the age of the sample. This might give the impression that laser ablation could hardly be used for U-Pb age dating of zircons by ICPMS.

There are, however, several techniques that have been successfully used to suppress this fractionation or to correct for it. One correction approach is to use an external standard of zircon of known age to derive an empirical correction factor that could be applied to the unknown sample (Jackson et al. 1996, Ketchum et al. 2001, Knudsen et al. 2001). Pb/U ratios are measured in the standard before and after the analysis of the unknown zircon sample and the correction factor is calculated as a ratio of known ($R(std)_{true}$) and averaged measured ($R(std)_{meas}$) values for the standard. The corrected Pb/U ratios for the sample ($R(sam)_{true}$) can then be derived from the measured sample ratios ($R(sam)_{meas}$) as

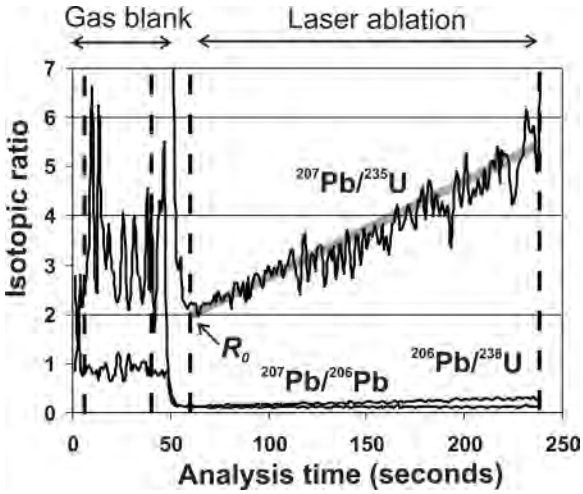


**Figure 7.** Time-resolved signal collected from single spot ablation of zircon reference material 91500. $R_0$ is the intercept value calculated from regression of the fractionating $^{207}Pb/^{235}U$ data.

$$R(sam)_{true} = R(sam)_{meas} * [R(std)_{true}/R(std)_{meas}] \quad (1)$$

It is important to note that the data have to be corrected for instrument drift (change in sensitivity with time) prior to the correction for elemental fractionation. This method can produce accurate ages only if instrument and data acquisition parameters remain constant for the standard and the unknown sample and if there are no significant matrix effects on the measured Pb/U and Pb isotopic ratios between the standard and the sample. External correction following Equation (1) simultaneously corrects for instrument mass bias and Pb/U fractionation.

Elemental fractionation of Pb and U can also be corrected for mathematically by using empirical equations that describe the fractionation (Horn et al. 2000, Tiepolo et al. in press). The rationale behind this method is that for a given laser spot size and laser energy density, there is a linear relationship between the depth of the laser pit (number of laser pulses applied) and the measured Pb/U ratio. It is therefore possible to derive an external fractionation correction that is based on empirical equations that quantify the fractionation slope for different spot sizes. Horn et al. (2000) suggested that this correction is constant for a given laser ablation system and, using the 193-nm wavelength, constant between some matrices (e.g., zircon and silicate glass). Tiepolo et al. (in press) confirmed that the calibration curve between slope of the fractionation line and laser spot size varies for different laser ablation systems.

Another approach to correct for Pb/U elemental fractionation was used by Košler et al. (2002b). This method, like Horn et al. (2000), assumes that Pb/U ratios measured at the start of ablation are biased only by the mass discrimination (bias) of the ICPMS instrument. Fractionation-corrected Pb/U isotopic ratios are calculated as zero ablation time intercepts of least-squares linear regression lines fitted to the time-resolved isotopic ratio data (Fig. 7). The regression line has a form of $R = R_0 + ST$, where $R$ is the isotopic ratio, $R_0$ is the isotopic ratio (intercept) at the start of laser ablation, $S$ is the slope of the line and $T$ is laser ablation time which is proportional to the number of laser pulses applied. The fractionation-corrected isotopic ratio $R_0$ is calculated as

$$R_0 = \frac{\sum r_i \sum t_i^2 - \sum t_i \sum t_i r_i}{n \sum t_i^2 - (\sum t_i)^2} \quad (2)$$

where $n$ is the total number of isotopic ratio measurements; $t_i$ and $r_i$ are individual time and isotopic ratio values that are each summed over the period of sample signal acquisition. Unlike the correction procedure of Horn et al. (2000), this correction eliminates the potential calibration problems that could result from matrix differences between external standards and unknown samples because the intercept is calculated from the data for each individual sample. Horn et al. (2000) found, for instance, that there was little evidence for differences in Pb/U fractionation between zircon and silicate glass using their 193-nm laser ablation system but Košler et al. (2002) found that this is not the case for their 266-nm ablation system.

Both the Horn et al. (2000) and Košler et al. (2002) methods rest on the premise of Sylvester and Ghaderi (1997) that laser-induced, volatile/refractory element fractionation is a linear function of time and can be corrected by extrapolating the measured ratios back to the start of ablation. Both methods assume that the analyzed volume of zircon has a homogenous Pb/U ratio, and thus require the analyst to identify any analyses that may include mixed age populations before carrying out the correction procedure. The analytical uncertainty due to the correction for elemental fractionation will increase with the size of the correction. It is therefore important to reduce the fractionation as much as possible. As mentioned above, various laser parameters can be used to suppress the size of the fractionation. Reduction of fractionation can also be achieved through a range of techniques that utilize particular sampling strategies.

**Sampling strategies**

For focused beam systems, it has been demonstrated that the position of the focal plane of the laser relative to the sample surface is an important factor that affects the amount of elemental fractionation. Hirata and Nesbitt (1995) have shown that the laser-induced fractionation increases as the laser drills deep into the sample and the beam becomes progressively defocused. They suggested that by raising the stage of the microscope at the same rate at which the laser penetrates into the sample, the laser beam remains focused at the bottom of the laser pit (so called "active focus"). This procedure effectively keeps the laser fluence constant over the time of the analysis. Successful application of this technique requires the laser drilling rate to be known precisely for each sample matrix, so it is not widely employed.

Jackson et al. (1996) used a different approach and focused the laser beam above the sample surface, which minimized the relative degree of defocusing of the laser with drilling depth (cf. Fig. 3.14 in Jackson 2001). As a consequence, the aspect ratio (diameter/depth) of the ablation pit is increased (compared to when focused on the sample surface) which results in a more stable signal and less Pb/U fractionation.

Laser-induced fractionation may also be limited by moving the stage beneath the stationary laser beam, so-called "rastering." This produces a square laser pit or linear traverse in the sample (Parrish et al. 1999, Li et al. 2001, Košler et al. 2002b). In this case, the effect is similar to drilling a large shallow laser pit, which produces only limited Pb/U fractionation (Eggins et al. 1998, Mank and Mason 1999). Hirata (1997) suggested that Pb/U elemental fractionation can be significantly reduced by maintaining a constant signal of Pb and U. This can be achieved by a slow increase of incident laser energy, so-called "soft ablation." The slow increase of laser power throughout the ablation probably reduces the number of large particles and fragments of sample released in the early stages of ablation. As the large particles are the main source of signal instability, the technique effectively improves the precision of measurement and, by doing so, it also improves the spatial resolution by limiting the amount of ablated material that is necessary to obtain that precision.

Efficient removal of ablated particles from the ablation cell has also been achieved by directing the carrier gas flow directly onto the ablation site through a "jet cell" designed by Sterling Shaw at Macquarie University (cf. Fig. 3.5 in Jackson 2001). Finally, differences in the volatility of Pb and U during ablation have been reduced by converting U to the more volatile uranium fluoride by adding a small amount of freon ($CH_2FCF_3$) to the He carrier gas. This technique is referred to as

"chemically assisted laser ablation" (Hirata 2002).

In conclusion, there are a number of methods that can be combined to suppress Pb/U fractionation to trivial levels. This is demonstrated in Figure 8 by almost constant measured Pb/U ratios during ablation of the 1065 Ma 91500 zircon reference material of Wiedenbeck et al. (1995). During this analysis the use of He in the ablation cell was combined with defocus and rastering of the laser beam.

**Spatial resolution**

Spatial resolution in laser ablation ICPMS dating is effectively limited by the amount of the least abundant analyte, often $^{207}$Pb. The general rule of thumb is that the younger the zircon, the more material has to be ablated in order to achieve a useful precision. It follows that there is no difference in spatial resolution between two single laser spots with small and large diameter, provided that the volume (mass) of ablated material is identical. The same holds for laser rasters. Comparison of the spatial resolution for typical laser ablation ICPMS and SIMS analyses of zircon is given in Figure 9. An important consideration is the geometry of the laser pit. It is more practical

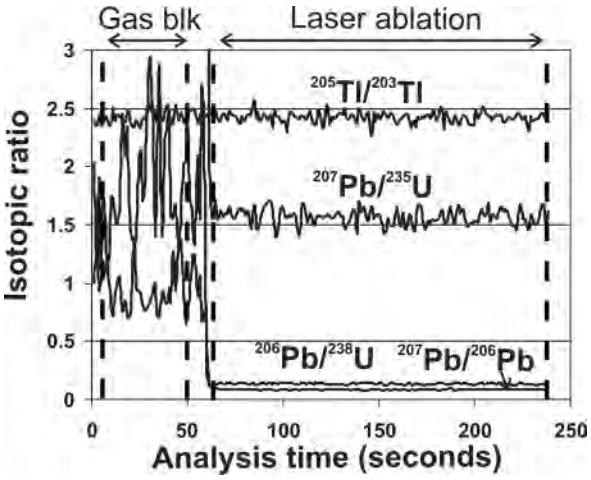


**Figure 8.** Non-fractionating, time-resolved signal collected from laser raster ablation of zircon reference material 91500 with simultaneous nebulization of tracer solution containing $^{203}$Tl and $^{205}$Tl.

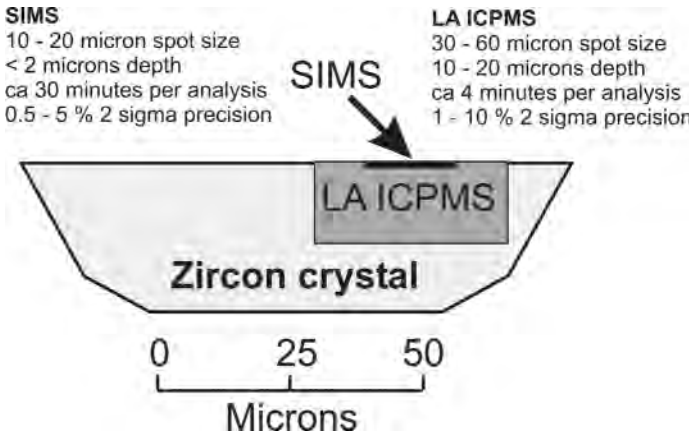


**Figure 9.** Spatial resolution of a typical zircon analysis by SIMS and LA-ICPMS on a schematic cross-section of a mounted and polished sample. Estimated external uncertainties are for $^{206}$Pb/$^{238}$U ages obtained from quadrupole ICPMS measurements of ca. 300 Ma zircon containing 50 ppm U.

to ablate the sample close to the surface not only because a large diameter/depth ratio is more favorable for suppression of the elemental fractionation, but also because major and minor element variations in the sample surface, analyzed by electron microprobe, can be related directly to age data from the ablation pits (Foster et al. 2002). This would not be possible for single laser spots that have only a small diameter but reach deep into the sample (Fig. 10).

**Correction for instrument mass bias (standardization)**

After correction for time-dependent fractionation, Pb/U isotopic ratios are still biased relative to the "true" values due to mass discrimination in the ICPMS. Instrument mass bias also affects Pb/Pb isotopic ratios. There are two fundamentally different approaches for the mass bias correction, which is, in essence, a form of standardization. The external correction method utilizes a measurement of an external standard of known isotopic composition to correct for mass bias on measured isotopic ratios in the unknown samples. This correction requires matrix-matched external standards for most laser ablation systems and it follows the calculation procedure described in Equation (1). For U-Pb zircon dating, labs employing external corrections commonly use a well-dated reference zircon such as 91500 (Weidenbeck et al. 1995) or UQ-Z (Machado and Gauthier 1996) as the standard. The degree to which matrix matching of standards and unknowns is necessary, particularly for accessory phases other than zircon, has not been well documented.

The internal correction method is matrix-independent as it utilizes measurements of known isotopic ratios in the unknown sample to correct the measured unknown isotopic ratios in the same sample. Formulations for internal mass bias corrections used in ICPMS have largely been adopted from thermal ionization mass spectrometry. Internal corrections in TIMS can only be used for elements that have at least one pair of isotopes with known (non-radiogenic) isotopic composition (e.g., Sr or Nd). This is not necessarily the requirement in ICPMS where the known isotopic composition of one element can be used to correct for mass bias on the isotopic ratio of another element. A classical example of this approach is given by Longerich et al. (1987) who used the known $^{205}Tl/^{203}Tl$ ratio of 2.3871 (Dunstan et al. 1980) to correct for mass bias on measured Pb isotopic ratios (masses 204, 206, 207 and 208).

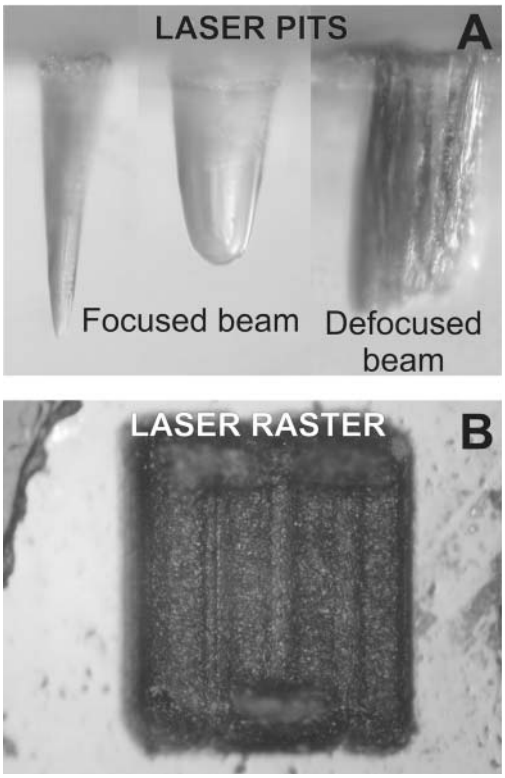


**Figure 10.** (A) Side view photo micrograph of laser ablation pits in zircon, diameter of the pits is 30 and 60 μm. (B) Bottom part of a 200×200 μm laser raster in zircon 91500.

For laser ablation ICPMS analysis of zircon some laboratories utilize a variant of the internal mass bias correction method in which a tracer solution of known isotopic composition is nebulized to the plasma during the laser ablation (Chenery and Cook 1993, Parrish et al. 1999, Horn et al. 2000, Košler et al. 2002b). The aspirated solution is used only to correct for instrument mass bias of Pb/U and Pb/Pb ratios. Laser-induced fractionation of Pb and U must be corrected separately (cf. previous section). The tracer solution must contain isotopes that are not present in the analyzed sample so that the isotopic ratio of interest in the tracer is not disturbed by contributions from the sample. Horn et al. (2000) aspirated a natural

Tl-enriched $^{235}U$ solution for calibration of U-Pb zircon analyses by laser ablation ICPMS. They anticipated that the corrections would be more precise if artificial $^{233}U$ was used instead of $^{235}U$, thereby avoiding the need to account for natural $^{235}U$ present in zircon. The improvements in accuracy and precision gained from using $^{233}U$ was demonstrated by Košler et al. (2002b) for U-Pb zircon dating, and by Košler et al. (2001a) for U-Pb monazite dating. The composition of the somewhat more complex tracer solution currently used for U-Pb dating at Memorial and Charles universities is shown in Table 1.

Isotopic ratios of interest in the tracer solution should have a mean isotopic mass similar to that of the isotopic ratios being corrected in the analyzed sample (Hirata 1996, cf. Table 1). When isotopes of two elements are used to correct for mass bias of a third element (e.g., when the $^{209}Bi/^{205}Tl$ ratio is used to correct for the mass bias of the $^{207}Pb/^{206}Pb$ ratio), the tracer isotopes should also have ionization potentials and rates of oxide formation in the ICP that are similar to the isotopes of interest in the sample.

There are three fractionation laws commonly used for mass bias corrections in mass spectrometry—linear, power and exponential. The linear law is scarcely used in ICPMS and it will not be discussed further. Mathematical formulas for the power and exponential fractionation laws are given below with examples that illustrate their application to measurement of Pb/U isotopic ratios in zircon.

***Power law*:**

$$R_{1c} = R_{1m} * \left[ \frac{R_{2c}}{R_{2m}} \right]^{\left( \frac{\Delta M_1}{\Delta M_2} \right)}, \tag{3a}$$

$$\left( \frac{^{207}Pb}{^{235}U} \right)_c = \left( \frac{^{207}Pb}{^{235}U} \right)_m * \left[ \frac{\left( ^{205}Tl/^{237}Np \right)_c}{\left( ^{205}Tl/^{237}Np \right)_m} \right]^{\left( \frac{M_{235} - M_{207}}{M_{237} - M_{205}} \right)} \tag{3b}$$

***Exponential law*:**

$$R_{1c} = R_{1m} * \left[ \frac{R_{2c}}{R_{2m}} \right]^{\left( \frac{\ln \iota M_1}{\ln \iota M_2} \right)} \tag{4a}$$

$$\left( \frac{^{207}Pb}{^{235}U} \right)_c = \left( \frac{^{207}Pb}{^{235}U} \right)_m * \left[ \frac{\left( ^{205}Tl/^{237}Np \right)_c}{\left( ^{205}Tl/^{237}Np \right)_m} \right]^{\left( \frac{\ln(M_{235}/M_{207})}{\ln(M_{237}/M_{205})} \right)} \tag{4b}$$

In the above equations, $R_1$ and $R_2$ are isotopic ratios (e.g., $^{207}Pb/^{235}U$ and $^{205}Tl/^{237}Np$), subscripts *m* and *c* refer to measured and mass bias corrected or known values, respectively, $\delta M$ and $\Delta M$ are the isotopic mass ratio and difference between isotopes in ratios $R_1$ and $R_2$, respectively.

Either of the laws given by Equations (3) and (4) can be used to correct data obtained from

**Table 1.** Isotopic ratios used for mass bias correction.

| Ratios used for mass bias correction | | Ratios to be corrected for mass bias | |
|---|---|---|---|
| *Ratio in tracer solution ($R_2$)* | *Mean mass of ($R_2$)* | *Mean mass of ($R_1$)* | *Measured ratio in zircon ($R_1$)* |
| $^{209}Bi/^{205}Tl$ | 207 | 206.5 | $^{207}Pb/^{206}Pb$ |
| $^{205}Tl/^{237}Np$ | 221 | 221 | $^{207}Pb/^{235}U$ |
| $^{205}Tl/^{237}Np$ | 221 | 222 | $^{206}Pb/^{238}U$ |
| $^{209}Bi/^{233}U$ | 221 | 220 | $^{208}Pb/^{232}Th$ |
| $^{233}U/^{237}Np$ | 235 | 235 | $^{232}Th/^{238}U$ |

laser ablation with quadrupole ICPMS measurements, although most analysts favor the exponential law in which the extent of mass bias increases with decreasing mass. However, the assumption that mass discriminations observed for $R_1$ and $R_2$ are equal is often not correct and the differences become significant when more precise isotopic measurements from magnetic sector multi-collector ICPMS are to be corrected for mass bias (Hirata 1996, Maréchal et al. 1999). Empirical cross-calibration of mass discrimination factors for $R_1$ and $R_2$ is often required if accurate mass bias corrections of high-precision data are being made (Rehkämper and Mezger 2000, White et al. 2000, Thirlwall 2002).

**Correction for initial common-Pb**

Laser ablation ICPMS dating of zircon does not usually require large common (i.e., non-radiogenic) Pb corrections. Experiments conducted in the laboratories at Memorial and Charles University between 1999 and 2002 have shown that most zircons from a wide range of rock types contained so little common-Pb that the correction was always insignificant. Common-Pb corrections may, however, be important for some zircons and for other accessory phases (e.g., monazite, titanite, allanite, rutile, apatite, xenotime) and thus appropriate protocols should be developed for LA-ICPMS measurements. The source of common-Pb that contributes to the isotopic signal of the three radiogenic Pb isotopes varies for different analytical techniques and sample preparation procedures. Most of the common-Pb in a typical laser ablation ICPMS analysis originates from the sample and its isotopic composition can therefore be accurately estimated using models of Pb isotopic evolution (e.g., Stacey and Kramers 1975) or it can be derived from analyses of Pb isotopes in minerals (e.g., feldspars) co-genetic with the zircons.

There are three frequently used methods for common-Pb corrections (Williams 1998). The "204 method" is based on measurement of the very low abundance non-radiogenic $^{204}$Pb isotope. Measured Pb isotopic signals are corrected using the assumed $^{206}$Pb/$^{204}$Pb, $^{207}$Pb/$^{204}$Pb and $^{208}$Pb/$^{204}$Pb ratios of the common-Pb to extract the net signal intensities of the radiogenic daughter $^{206}$Pb$^*$, $^{207}$Pb$^*$ and $^{208}$Pb$^*$ isotopes. If $C$ is the contribution of common-Pb to the daughter ($D^*$) radiogenic Pb signal, the correction equation has the form:

$$D^* = (1\text{-}f) * (D^*+C) \tag{5a}$$

which for $^{206}$Pb becomes

$$^{206}\text{Pb}^* = (1\text{-}f) * (^{206}\text{Pb})_{\text{total}} \tag{5b}$$

The proportion ($f$) of common-Pb is calculated as

$$f = [C/^{204}\text{Pb}]_{\text{common}} / [(D^*+C)/^{204}\text{Pb}]_{\text{measured}} \tag{6a}$$

and the corresponding equation for $^{206}$Pb is

$$f = [^{206}\text{Pb}/^{204}\text{Pb}]_{\text{common}} / [^{206}\text{Pb}/^{204}\text{Pb}]_{\text{measured}} \tag{6b}$$

The "208 method" is based on the assumption that the ratio of $^{232}$Th to the parent U isotope in the analyzed sample has not been disturbed following the closure of U-Pb and Th-Pb isotopic systems and that any excess $^{208}$Pb (i.e., $^{208}$Pb-$^{208}$Pb$^*$) can be attributed to the common-Pb component. The proportion of common-Pb in this case can be calculated as

$$f = [^{208}\text{Pb}/(D^*+C)_{\text{measured}} - {}^{208}\text{Pb}^*/D^*] / [^{208}\text{Pb}/C_{\text{common}} - {}^{208}\text{Pb}^*/D^*] \tag{7a}$$

Equation (7a) for $^{206}Pb$ becomes

$$f = [^{208}Pb/^{206}Pb_{measured} - ^{208}Pb^*/^{206}Pb^*] / [^{208}Pb/^{206}Pb_{common} - ^{208}Pb^*/^{206}Pb^*] \quad (7b)$$

This approach requires the assumption of a concordant composition in the U-Th-Pb system. The "207 method" utilizes the measured $^{207}Pb/^{206}Pb$ ratios to calculate the proportion of common $^{206}Pb$ as

$$f = [^{207}Pb/^{206}Pb_{measured} - ^{207}Pb^*/^{206}Pb^*] / [^{207}Pb/^{206}Pb_{common} - ^{207}Pb^*/^{206}Pb^*] \quad (8)$$

Similarly to the 208 method, this correction also assumes that U-Pb composition is concordant.

The major problem with the 204 method in laser ablation ICPMS is that it requires precise measurement of the miniscule $^{204}Pb$. For samples with very little common-Pb, such as zircon, the 204 isotopic signal is overwhelmingly dominated by isobaric interference of $^{204}Hg$. Mercury is often present in trace amounts in the Ar gas, in metal parts of the gas piping and probably also in the interface and electrostatic lens stack of the ICPMS instrument, and it contributes to the 204 signal intensity. In theory, one could calculate and subtract the appropriate amount of $^{204}Hg$ contributed to the 204 signal by measuring another Hg isotope and knowing the natural Hg isotopic composition. However, there is a large (several percent) uncertainty in the natural composition of Hg (cf. Rosman and Taylor 1999, Evans et al. 2001) and the correction for highly radiogenic samples, such as zircon, can easily exceed 99%. For instance, a typical signal intensity of $^{204}Hg$ during laser ablation analysis of zircon using a 266-nm Nd:YAG laser and quadrupole ICPMS at Memorial University is 400-800 cps while the calculated count rate due to $^{204}Pb$ is only 10 cps or less. As a result, uncertainties associated with the common-Pb correction would be too high to give a useful precision on the resulting isotopic ages. In samples with high common/radiogenic Pb, the use of 204 method is a viable option, especially if the $^{204}Pb$ can be precisely and accurately determined (e.g., using a multicollector ICPMS; Foster et al. 2002) and the $^{204}Hg$ isotopic signal can be suppressed. The necessity of the correction is then judged on whether the corrected $^{207}Pb/^{206}Pb$ lies outside of the internal errors of the measured ratio.

The 208 method is potentially useful for laser ablation ICPMS as it, unlike the 204 method, does not suffer from isobaric interferences. This method is suitable for a wide range of isotopic compositions except for samples with high Th/U ratio (e.g., monazite) and samples with radiogenic $^{208}Pb^*/D^*$ ratio close to 7 which sets the value of $f$ in the Equation (7a) close to infinity. Finally, the 207 method is most appropriate for young samples that have a concordant U-Pb composition. Due to their low $^{207}Pb$ contents, the $^{207}Pb/^{206}Pb$ and $^{207}Pb/^{235}U$ ages of such samples would not yield a geologically useful precision and therefore their $^{206}Pb/^{238}U$ ages are usually preferred. It should be noted that the assumption of concordancy in the 208 and 207 methods may not be valid for some young monazites and zircons that contain unsupported $^{207}Pb$ and $^{206}Pb$ due to the incorporation of $^{231}Pa$ and $^{230}Th$, respectively, during the crystallization (Schärer 1984, Parrish 1990).

**Precision and accuracy**

Precision of U-Pb ages obtained by *in situ* laser ablation ICPMS analysis is a function of the stability of the analyte signals, number of detected ions and uncertainties on corrections applied to the measured signals. It follows that precision of individual analyses varies subject to qualities of the analyzed sample, especially the amount of radiogenic Pb in the ablated mass of the zircon. Different methods of data reduction and the corresponding propagation of errors adopted by different LA-ICPMS laboratories make inter-laboratory comparisons difficult. However, the precision of data recently obtained by magnetic sector instruments (Machado and Simonetti 2001, Foster et al. 2002, Tiepolo et al. in press) suggests that uncertainties on Pb-U ages will be further improved. Presently, ages that are precise to ca. 0.5% ($1\sigma$) can be obtained on typical size zircons containing tens of ppm Pb, provided that the laser-induced fractionation can be suppressed below a significant level.

Accuracy and reproducibility of U-Pb zircon analyses is in most laboratories monitored by periodic measurements of natural zircon standards of known U-Pb age, such as the 1065 Ma zircon reference material 91500 (Wiedenbeck et al. 1995). Large numbers of ion probe analyses by SIMS (Whitehouse and Sunde, 2000) and laser ablation ICPMS measurements at Memorial University suggest that zircon 91500 is homogeneous for U-Pb age dating within the error of the measurements. The concordia age calculated for 52 analyses of this standard collected at Charles University over the period 2001-2002 using a 266-nm Nd:YAG laser and a quadrupole ICPMS is 1060±9 Ma (concordia age ±2σ; Fig. 11). Within analytical error, the results are consistent with the weighted mean of $^{238}U$-$^{206}Pb$ and $^{235}U$-$^{207}Pb$ TIMS ages for this material (1065.4±0.6 Ma and 1062.4±0.8 Ma, respectively; all errors are 2σ). Similar results were reported using an ArF excimer laser coupled to a quadrupole ICPMS (Horn et al. 2000) and Nd:YAG laser and single-collector magnetic sector ICPMS (Tiepolo et al., in press).

**Strategies for data acquisition and reduction**

Analytical strategies vary for different laser systems and ICPMS instruments but there are several general rules that should be followed in order to obtain precise and accurate age data as well as to maintain good spatial resolution. The samples must be prepared as polished grain mounts or polished rock slabs or sections (similar to samples for electron microprobe analysis) with clean surfaces for analysis. It is important to image using cathodoluminescence or back-scattered electron imaging, or HF etching, or X-ray mapping the samples prior to analysis (see Corfu et al., this volume, Cox, in press). Zircon crystals commonly contain cores and overgrowths that have different ages or domains of Pb-loss or unsupported radiogenic Pb. Such heterogeneities must be identified and located to avoid their boundaries during the laser sampling.

There are no "best" laser parameters for U-Pb dating of zircon except that the laser beam should be kept within the homogeneous domains of the analyzed grain to avoid mixed analyses. Subject to the content of radiogenic Pb and required spatial resolution, the aspect ratio (diameter/depth) of the laser pit should be maintained as large as possible and, as discussed above, a combination of several techniques that limit the elemental fractionation of Pb and U is preferred.

Data should be acquired in time-resolved analysis mode, i.e., a number of isotopic ratios (typically between 300 and 1500) should be collected during a single analysis. Obtaining the data in time slices allows monitoring the homogeneity of composition as the laser penetrates into the zircon sample. Real-time data acquisition is also useful as it allows signal intensities to be observed while the sample is being ablated. The analytical protocol should be designed to measure the "gas blank" (signal without the laser on) for ca. 60 s followed by data acquisition with the laser firing. For single detector instruments, measurements should be carried out in peak jumping mode, keeping the number of monitored isotopes to a minimum, using as few points per spectral peak as practical. Short quadrupole or magnet settling times and variable dwell times (time spent measuring the intensities of spectral peaks) should be used in order to maximize the acquisition efficiency (duty cycle).

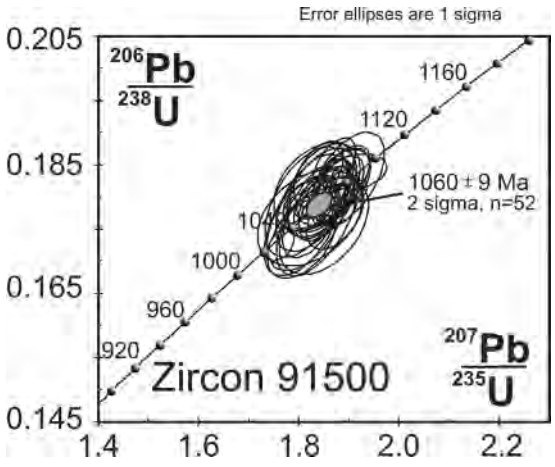


**Figure 11.** Reproducibility of U-Pb data for zircon 91500. Shaded ellipse corresponds to the concordia age (Ludwig 1998).

Two examples of acquisition parameters for zircon dating by laser ablation

ICPMS are given in Table 2, one using a magnetic sector instrument, the other using a quadrupole ICPMS. A 266-nm Nd:YAG laser was used in each experiment but different calibration and correction strategies were applied to the measurements. For the magnetic sector data, external calibration with a zircon standard was performed. For quadrupole ICPMS data, an empirical mathematical correction for Pb/U fractionation and an internal correction for instrument mass bias were used.

The complex nature of the laser ablation signals acquired for each zircon analysis requires sophisticated data reduction software that can handle the large amount of data generated during time-resolved acquisitions. The software should allow the user to view the signal intensity (or ratio) vs. time plots and select the intervals for gas blank and laser ablation signals, handle all necessary corrections, calculate ages together with the propagated errors and finally plot the data in histograms, concordia plots or other types of projections. At the time of writing this review, there were three software packages available for reduction of U-Pb laser ablation ICPMS data.

The automated, macro-driven spreadsheet LAMTRACE was written in Lotus 123 for Microsoft Windows (Jackson et al. 1996). It is capable of importing raw data in ASCII format. After manual or automatic selection of intervals for gas blank and laser signal, the program calculates ages and errors as well as plots the data on a concordia diagram. GLITTER is an interactive compiled program written in IDL language that is compatible with Microsoft Windows, MacOS and Unix (van Achterbergh et al. 2001). It is capable of on-line data reduction, manual or automatic selection of signal intervals and it calculates ages, their errors and exports the data to the concordia plot. Both LAMTRACE and GLITTER are written for calibration with an external zircon standard and assume no initial common Pb. LAMDATE is a macro-driven spreadsheet written in MS Excel that runs on Microsoft Windows and MacOS platforms (Košler et al. 2002b). It imports count rate data in ASCII format and, after manual selection of signal intervals, does a complete error propagation and calculation of ages. The data are corrected mathematically for laser-induced Pb/U fractionation and an internal correction for instrument mass bias is used. The software is also capable of correcting data for common Pb. Concordia and other plots can be generated from LAMDATE using the IsoplotEx add-in (Ludwig 1999) in MS Excel.

**Table 2.** Instrument acquisition parameters used for laser ablation zircon dating.

| *Monitoredelement* | *Mass* | *Settling time (ms)* | *Dwell time (ms)* | *Points per peak* |
|---|---|---|---|---|
| Single-col. mag. sector ICPMS (Tiepolo et al. in press) | | | | |
| Hg | 201 | 40 | 1.5 | 12 |
| Pb | 204 | 6 | 1.5 | 12 |
| Pb | 206 | 5 | 1.5 | 12 |
| Pb | 207 | 2 | 1.5 | 12 |
| Pb | 208 | 2 | 1.5 | 12 |
| Th | 232 | 25 | 3.5 | 6 |
| U | 235 | 6 | 1.5 | 12 |
| U | 238 | 6 | 3.5 | 6 |
| Quadrupole ICPMS (Europe, e.g., Charles University)(1) | | | | |
| Hg | 202 | 1 | 5.1 | 1 |
| Tl | 203 | 1 | 10.2 | 1 |
| Tl | 205 | 1 | 10.2 | 1 |
| Pb | 206 | 1 | 10.2 | 1 |
| Pb | 207 | 1 | 30.7 | 1 |
| Bi | 209 | 1 | 10.2 | 1 |
| U | 233 | 1 | 10.2 | 1 |
| Np | 237 | 1 | 10.2 | 1 |
| U | 238 | 1 | 10.2 | 1 |
| UO | 249 | 1 | 10.2 | 1 |
| NpO | 253 | 1 | 10.2 | 1 |
| UO | 254 | 1 | 10.2 | 1 |

(1) Corresponding dwell time used in North America (e.g., Memorial University) would be somewhat different due to differences in the mains frequencies (Longerich et al. 1996).

## LASER ABLATION ICPMS DATING IN PRACTICE

There are numerous geochronological applications that can be tackled by laser ablation ICPMS. The main strength of dating by laser ablation, in contrast to TIMS and SIMS techniques, is shorter analysis times, less expensive, and wider availability in the geological community. In some cases where higher precision is needed, LA-ICPMS can be used to define different age populations that later can be dated more precisely by SIMS, or ID-TIMS. Here we review those applications where the qualities of laser ablation ICPMS dating are equal or superior to the more traditional geochronological techniques. Such applications include zircon dating for sediment provenance studies, magmatic events and fission track studies. Although this review is primarily dedicated to zircon, we briefly comment on the use of laser ablation ICPMS for *in situ* dating of other accessory minerals, especially monazite.

### Laser ablation ICPMS dating of zircon for sedimentary provenance studies

Analysis of the heavy mineral fraction of clastic sediments and particularly age dating of clastic zircon have proven to be useful tools for stratigraphic correlations, identification of sediment sources and, or, transport and depositional histories. Previous studies of sedimentary provenance that utilized U-Pb dating of detrital zircon grains (Morton et al. 1996, Whitehouse et al. 1997, Fernández-Suárez et al. 2000) have shown that precise and accurate U-Pb and Pb-Pb isotopic ages of 80-100 zircon grains in each sample are typically needed to be confident that all major sedimentary source components have been identified (Dodson et al. 1988). It is difficult to obtain such a large number of U-Pb isotopic dates by conventional isotope dilution TIMS techniques on a timely and cost-effective basis. SIMS spot analysis (Morton et al. 1996, Whitehouse et al. 1997) can often resolve age differences between sedimentary source components and, at the same time, provide sufficient confidence that the revealed age pattern includes all major sedimentary sources.

Laser ablation ICPMS has been successfully used to resolve the provenance of sediments in a variety of terrains worldwide. In early studies, sedimentary provenance was based only on Pb-Pb zircon ages. For instance, Machado and Gauthier (1996) reported Pb-Pb ages from detrital sediments in the Ribiera Belt of southeastern Brazil. Their results were in agreement with previous U-Pb geochronology in the region. However, Pb-Pb ages of detrital zircons may severely underestimate the true ages if the grains have suffered Pb loss and thus are discordant on a U-Pb concordia diagram. Thus, a more rigorous approach adopted in most recent laser ablation ICPMS and SIMS studies is to report the U-Pb ages to demonstrate the concordance of zircon composition and to use the more precise Pb-Pb ages to better resolve the age differences in the sedimentary sources (Whitehouse et al. 1997, Fernández-Suárez et al. 2000, Ketchum et al. 2001, Knudsen et al. 2001, Fernández-Suárez et al. 2002, Košler et al. 2002b, Fonneland et al. 2002). The Pb-Pb ages are usually considered reliable for sedimentary provenance if they are within 5-10% of concordancy and such data are presented as cumulative probability plots of $^{207}Pb/^{206}Pb$ ages (Sircombe 2000). It should be noted, however, that the degree of discordance beyond which the data are considered unreliable for sedimentary provenance is highly subjective and so far there has been no agreement as for which cut-off value of discordance should be used for data rejection.

Comparison of results from dating the same samples of detrital zircons by SIMS and LA-ICPMS (Košler et al. 2002b) has demonstrated that both techniques are equally accurate and suitable for U-Pb dating of zircon for provenance studies (Fig. 12). The advantages of SIMS are slightly more precise ages, less damage to samples and better spatial resolution, especially in depth profiling (Grove and Harrison 1999). LA-ICPMS is the more cost-effective technique with the potential to analyze 3-5 times as many samples in a given time compared to SIMS. Laser ablation ICPMS therefore represents a method of choice for sediment provenance studies where large numbers of analyses are often required to identify all the major sources of sediments.

In order to provide more detailed information about the sources of detrital zircons, age data may be combined with other compositional data from the grains. Recently, Knudsen et al. (2001) and Machado and Simonetti (2001) reported U-Pb ages and Hf isotopic data obtained by laser

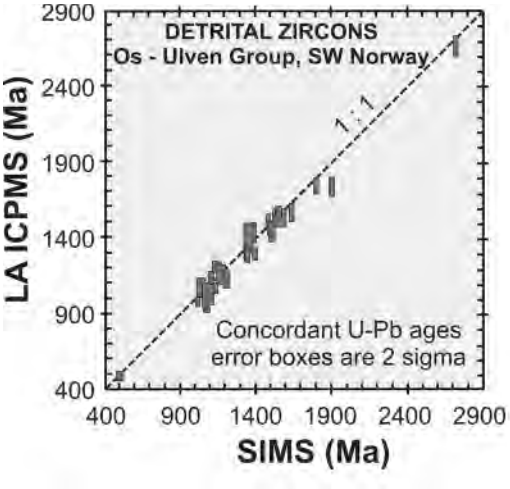


**Figure 12.** Comparison of concordant ages measured on detrital zircons from the Os Group, SW Norway using laser ablation ICPMS and SIMS techniques. Error bars are 2s. Modified from Košler et al. (2002b).

ablation from the same zircon grains. Zircon often contains percent to several percent level concentrations of Hf (which substitutes for Zr) and because of the high Hf content, its isotopic composition is usually not significantly affected by *in situ* decay of the much less abundant $^{176}$Lu. Direct measurement of $^{176}$Hf/$^{177}$Hf ratios by laser ablation magnetic sector ICPMS in detrital zircon grains can thus yield useful information on the origin of their source rocks. Combined U-Pb dating and rare earth element analysis of detrital zircons has been carried out using SHRIMP (e.g., Wilde et al. 2001) and a similar approach is available using laser ablation ICPMS (Belousova et al. 2001).

## Dating magmatic events by laser ablation ICPMS

In contrast to SHRIMP, which has a long record of successful age dating of plutonic and volcanic rocks (Williams 1998 and references therein; Ireland and Williams, this volume), laser ablation ICPMS has not been widely used for dating magmatic zircons. It can be anticipated that, similar to SHRIMP, laser ablation ICPMS will not be capable of resolving short time intervals between individual magmatic intrusions in complex batholiths except for particularly large and, or, U-rich or ancient zircons. This task will remain the niche of high-precision TIMS. However, laser ablation ICPMS can, in conjunction with suitable imaging techniques, resolve the age of inherited (xenocrystic) cores and late overgrowths in magmatic zircons. There are few published studies that can serve as good examples.

Rawlings-Hinchey et al. (in press) have studied zircon grains from a suite of metaplutonic rocks in a calc-alkaline batholith in northern Labrador. Sr and Nd isotopic compositions of the whole rocks reflect crustal contamination of mantle-derived magmas. They used laser ablation ICPMS in an attempt to identify and date crustal inheritance in zircons and to constrain the nature of the contaminant. They found that heterogeneities in zircons observed by back-scattered electron imaging corresponded to xenocrystic cores, demonstrating the spatial resolution of the technique (Fig. 13). With these results, it was possible to constrain the age of the lower crust that interacted with the parent magmas to early Proterozoic and not Archean age, as previously suspected.

Another example is the identification of two age populations of zircons from the Mesozoic Timber Creek kimberlite in Northern Territories, Australia (Belousova et al. 2001). The two populations of zircons have laser ablation ICPMS U-Pb ages of 1483±15 (2σ, weighted mean of 25 $^{207}$Pb/$^{206}$Pb ages) and 179±2 Ma (2σ, weighted mean of 14 $^{206}$Pb/$^{238}$U ages; Fig. 14) and differ in their trace element compositions and isotopic compositions of Hf (Fig. 15; Griffin et al. 2000). The data suggest that the two phases of zircon were derived from different magma sources at different times. The age of the Proterozoic population is in a good agreement with previously obtained U-Pb ages by SHRIMP. The Jurassic age of the younger population provides a good constraint on the maximum emplacement age of the kimberlite.

Finally, in an example of high-precision U-Pb zircon dating, Ballard et al. (2001) determined the ages of three ore-bearing felsic porphyries from the Chuquicamata porphyry copper-molybdenum deposit, northern Chile, by excimer laser ablation ICPMS. They identified two discrete igneous events, one with a $^{206}$Pb/$^{238}$U age of 34.6±0.2 Ma, and another with ages of 33.3±0.3 Ma and 33.5±0.2 Ma. U-Pb ages were determined by SHRIMP on the same samples. Although the SHRIMP

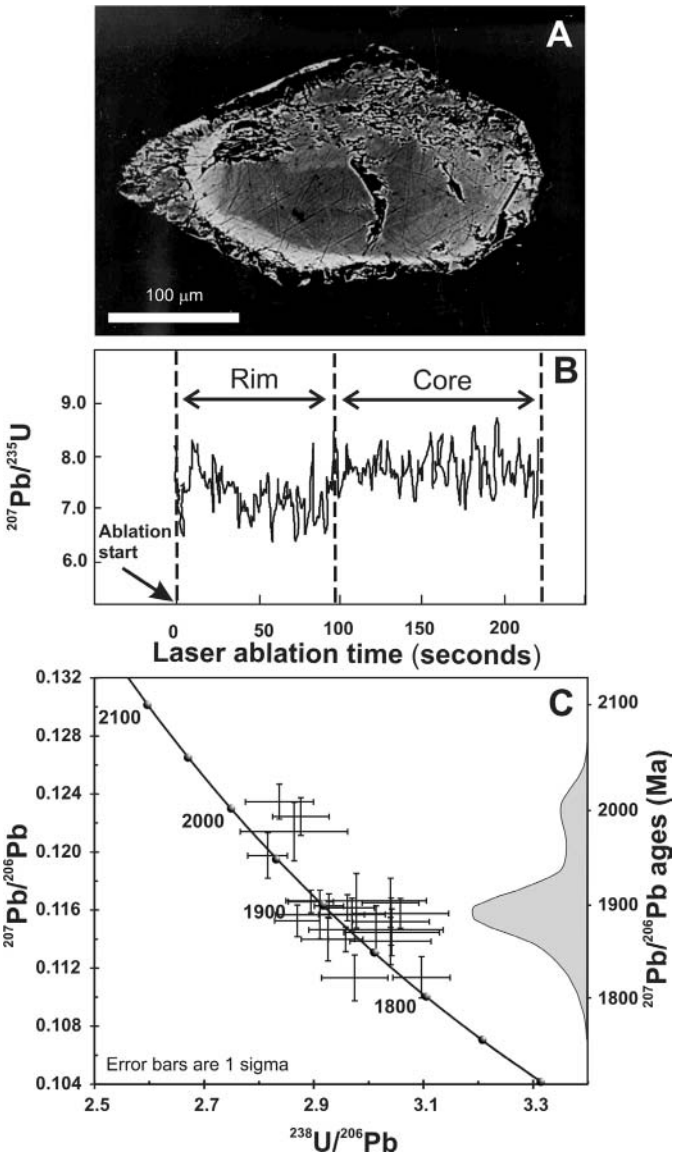


**Figure 13.** (A) Backscattered electron image of zircon grain containing older core from the Torngat Orogen, Labrador. (B) $^{207}Pb/^{235}U$ time resolved signal of zircon core and rim. (C) Tera-Wasserburg concordia diagram for two age populations of zircons, same sample as (A). Modified from Rawlings-Hinchey et al. (in press).

ages were 1.5 to 2.5% older than the LA-ICPMS ages for each of the three porphyries, the relative age differences between the rocks identified by the two techniques were similar. The authors ascribed the differences in absolute ages to a combination of the analytical biases and procedural differences specific to each instrument.

### Application of laser ablation ICPMS to fission track dating of zircon

Fission-track (FT) dating of accessory minerals such as zircon, titanite and apatite is a useful tool for determining ages of a variety of geological processes including exhumation and cooling of metamorphic and igneous rocks, and for sedimentary provenance studies (Galagher et al. 1998 and

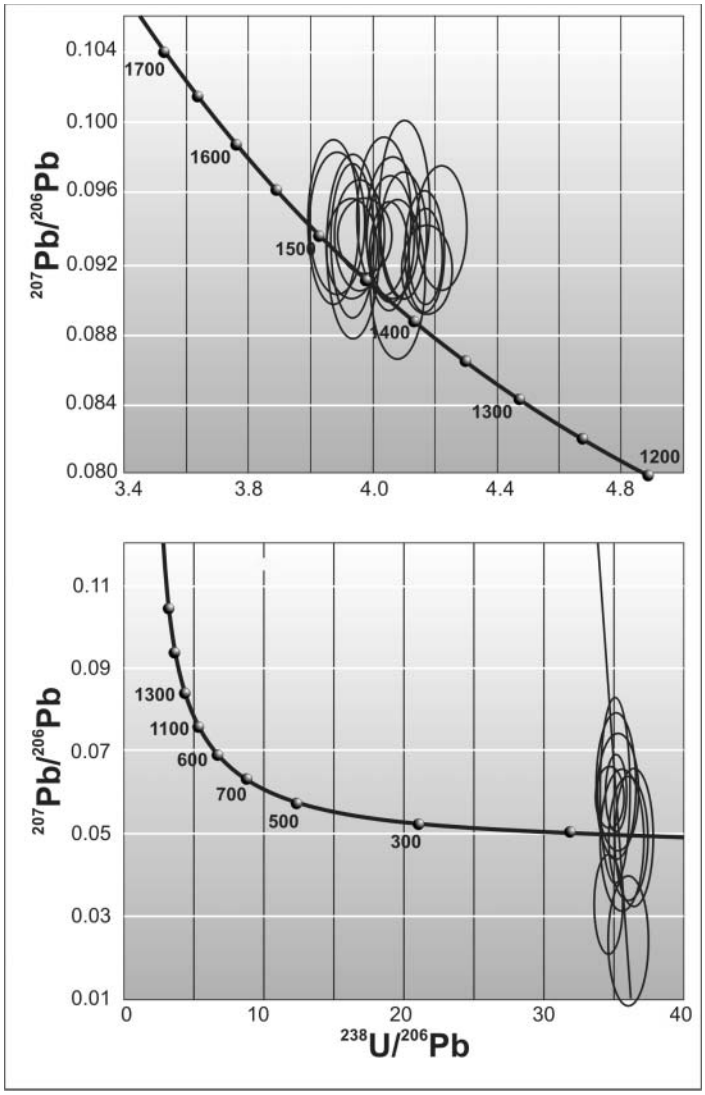


**Figure 14.** Tera-Wasserburg concordia diagrams for two zircon age populations from Timber Creek kimberlite in Northern Territories, Australia (modified from Belousova et al. 2001). Scatter of data along regression line in the lower diagram is likely due to the variable content of common Pb in the analyzed zircons.

references therein). Combined with information on the annealing of the tracks, the age data provide valuable constraints on the cooling models of crustal rocks.

FT ages are derived from the counted number of spontaneous fission tracks present in the zircon structure, the known decay constant for the spontaneous fission and from the measured concentration of $^{238}U$. Conventionally, the concentration of uranium is obtained by irradiation of samples with thermal neutrons and counting the proportion of tracks induced by the fission of $^{235}U$. This step represents a serious hurdle as the samples must be shipped to a nuclear reactor facility and then treated as radioactive material. In addition, the number of suitable nuclear reactors has dropped over the last decade due to closures on environmental and safety grounds, limiting the options for

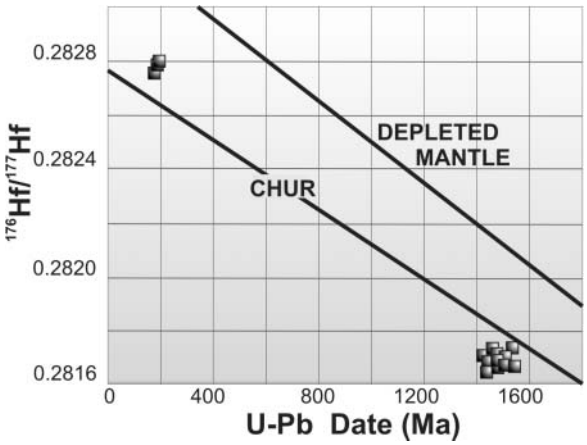


**Figure 15.** Age and Hf isotopic composition of two zircon age populations from Timber Creek kimberlite in Northern Territories, Australia (modified from Belousova et al. 2001).

FT dating in the future. Laser ablation ICPMS may be used for measurement of U concentrations in apatite as an alternative to the conventional irradiation method (Cox et al. 2000). This approach has been recently successfully applied to fission track dating of zircon (Svojtka and Košler 2002). The results obtained by laser ablation ICPMS FT dating were in good agreement with the previously determined conventional FT ages (Fig. 16).

The spatial resolution of laser ablation ICPMS is well-suited for the purpose of fission track dating. The preferred procedure is to produce a shallow laser pit by rastering the laser beam across the area where the spontaneous tracks were previously counted. The method used to convert the measured U concentration to the number of U atoms per analyzed volume of zircon includes measurement of U concentration and track density in an external zircon standard and calculation of the ratio of the number of tracks to the number of $^{238}U$ atoms in the analyzed volume (Cox et al. 2000). This technique offers the advantage of a higher sample throughput and hence lower cost of the analysis. Laser ablation ICPMS can measure U concentrations in accessory minerals directly, using external standardization, with an analytical uncertainty of only 2-5%. This procedure also eliminates the uncertainties associated with the conventional method, i.e., errors in counting the induced tracks and measuring the neutron flux in the reactor. Hence more precise age data is provided. However, the laser method is still limited by low track densities in young and U-poor samples and track overlaps in old and U-rich zircons.

**In situ dating of accessory minerals by laser ablation ICPMS**

At present, LA-ICPMS is almost exclusively used for U-Pb and Pb-Pb dating of zircons, while other geochronologically important minerals such as monazite, allanite, titanite, apatite, xenotime, or rutile are dated rarely, and then often using only the $^{207}Pb/^{206}Pb$ method (e.g., Machado and Gauthier 1996, Willigers et al. 2002). Monazite is probably the most useful accessory mineral for constraining the timing of metamorphic events in amphibolite and higher-grade facies rocks. Monazite ages can potentially be related to the crystallization of other rock-forming minerals and hence to the pressure and temperature conditions of metamorphism (Foster et al. 2000, Catlos et al. 2002 and references therein). Like zircon, monazite can also be used to constrain the ages of magmatic rocks. Laser ablation ICPMS U-Th-Pb dating of monazite was pioneered by Parrish et al. (1999) who first demonstrated that precise and accurate monazite ages may be obtained using a multi-collector magnetic sector instrument. Subsequently, a method that yields U-Th-Pb age data with comparable precision and accuracy was developed for laser ablation with quadrupole ICPMS (Košler et al. 2001a). The major obstacle to measuring the U-Th-Pb ages on a single-collector ICPMS is the detection range of secondary electron multipliers used in most single-collector ICPMS instruments. The very high concentrations of parent isotopes, especially $^{238}U$ and $^{232}Th$ in monazite, combined with the often low $^{207}Pb$ content of young crystals, do not permit simultaneous collection of all isotopes required to calculate monazite concordia ages. On the other hand, it is often practical to measure only one isotopic pair with high abundances (e.g., $^{232}Th$-$^{208}Pb$) in that little material has to be ablated to achieve the required precision. By using a small spot and low laser power, a high

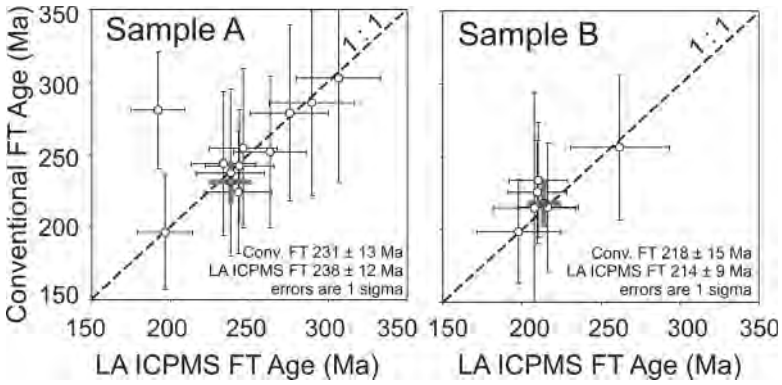


**Figure 16.** Comparison of conventional and LA-ICPMS fission track ages for two zircon samples from the Bohemian Massif. Each data point corresponds to a zircon grain, bold symbols are weighted means of individual ages from each sample. Modified from Svojtka and Košler (2002).

spatial resolution geochronological work can be carried out on monazites even in a polished petrographic thin section.

This technique has been successfully used for U-Th-Pb dating of ca. 100-μm monazite grains in standard electron probe thin sections (30 μm thick) of a garnet-biotite-sillimanite paragneiss from eastern Nepal. The analytical uncertainty on ca. 30 Ma monazite is less than 10% (1σ) for each analysis (Fig. 17; Košler et al. 2001b). Foster et al. (2002) used a similar approach to date monazite from the Canadian Cordillera and Pakistan Himalaya. They successfully dated, to 2-3% (2 σ uncertainty on $^{206}Pb/^{238}U$ ages) ca. 57 Ma monazite grains as polished mineral separates using a multi-collector magnetic sector ICPMS, Nd:YAG laser system and 50×45×10 μm laser raster patterns. They also used laser ablation to identify age heterogeneities in the monazites which they attributed to incorporation of an older monazite component in the crystals.

Laser ablation ICPMS has been applied to U-Th-Pb dating of baddeleyite (Horn et al. 2000, Hirata 2001), allanite (Cox et al., submitted) and titanite and rutile (Tubrett et al. 2001). Accurate ages for allanite and titanite could only be obtained after the data were corrected for the presence of initial common-Pb using the 208 method of correction (see above). The examples discussed here clearly demonstrate that U-Th-Pb dating by laser ablation ICPMS is not limited to zircon and there are numerous possibilities for other applications.

## FUTURE PROSPECTS OF LASER ABLATION ICPMS DATING

There are probably very few disciplines in the Earth Sciences that have evolved as fast as the ICPMS-based isotope and trace element geochemistry. At the same time, the isotope geochemistry has been the driving force behind the technical advancement of ICPMS since its very beginning. It is still an ongoing process, and in few years from now we can anticipate improvements in the stability of the ICPs and better sensitivity of the plasma source spectrometers, especially with respect to TOF-ICPMS. There will be even faster mass scanning for single-collector instruments, and the addition of multiple ion counting—the use of several electron multipliers at a time—will become a routine technique. On the laser side, the major problem in U-Th-Pb dating and other laser applications still lies in the elemental (and isotopic) fractionation caused during ablation. Shorter laser wavelengths (157 nm) and short laser pulse widths (pico- to femtoseconds; Russo et al. 2002), in conjunction with ongoing development of sampling strategies, will probably help to suppress the fractionation even further, possibly below levels significant for most geologic applications. An interesting combination is that of laser ablation with collision and reaction cell ICPMS (not discussed in this review) which has only become available in the last four years (cf. Mason 2001). The collision and reaction cell can improve the sensitivity and promote the formation of polyatomic ions.

Such reactions can help to resolve some isobaric interferences that are an obstacle to isotopic dating by laser ablation ICPMS (Moens et al. 2001). These anticipated technical advancements will improve the precision and accuracy of U-Th-Pb dating and, within a few years, we can credibly predict that the number of laser ablation age dating publications will be on a par with that of SIMS.

**Quadrupole vs. magnetic sector and single- vs. multi-collector comparisons**

***Precision and elemental fractionation.*** Magnetic sector ICPMS is capable of measuring isotopic ratios to a precision of hundreds to tens of ppm, i.e., two orders of magnitude more precise than the present day quadrupole instruments. However, the uncertainty on the isotopic ages derived from laser ablation ICPMS is to a large extent controlled by laser-induced elemental fractionation. The full advantage of the higher precision of the magnetic sector instrument will only become apparent when better control and significant reduction of the Pb/U fractionation is achieved but some improvements are already apparent. The superior precision of multi-collector magnetic sector instruments allows data to be acquired for shorter times than with quadrupole instruments (typically less than 60 s and 120 s, respectively) with the same level of precision. As the extent of elemental

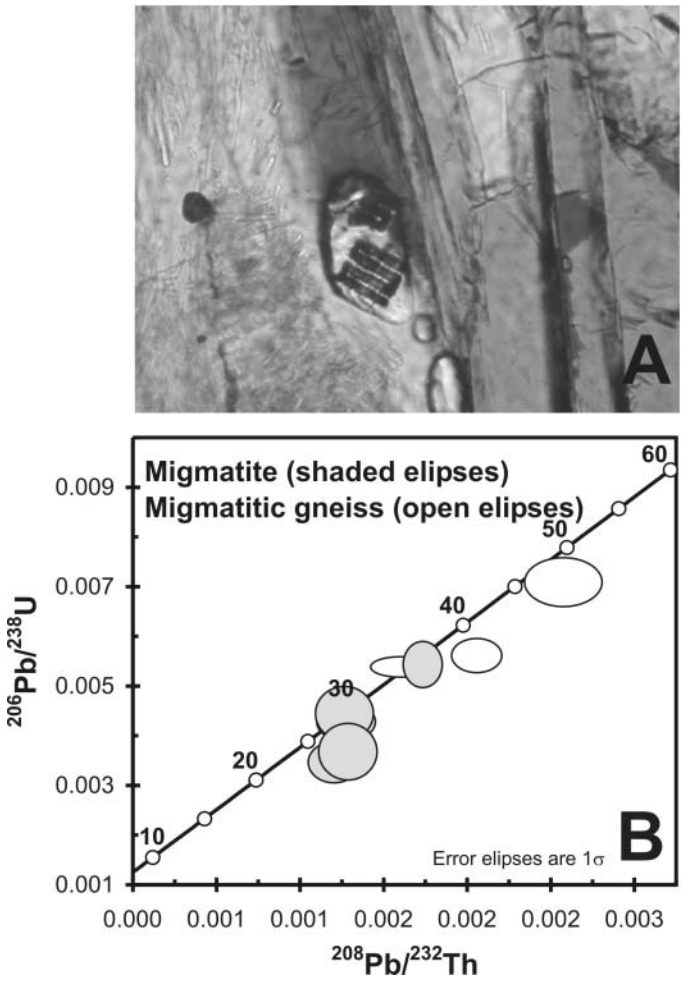


**Figure 17.** (A) Photomicrograph of a petrographic thin-section showing 100×100 μm laser raster in a monazite grain in a migmatite from the Makalu region, eastern Nepal. (B) U-Th-Pb concordia plot for monazites, same locality as (A). After Košler et al. (2001b).

fractionation during the laser ablation is related to the aspect ratio of the laser pit, shorter ablation times will generally result in less fractionation. In fact, Foster et al. (2002) reported that elemental fractionation can often be suppressed below a significant level using the short analysis time and multi-collector magnetic sector ICPMS. Increased instrument sensitivity of ICPMS systems is another avenue to reducing analysis times and thus reducing fractionation.

***Sensitivity and spatial resolution.*** The spatial resolution of successful laser ablation dating is related to the amount of analyte needed to achieve the required precision. Higher sensitivity thus means a better spatial resolution for a given level of precision. Present day quadrupole mass spectrometers and single-collector magnetic sector ICPMS instruments tend to be more sensitive than the multi-collector instruments due to different detection systems used (electron multiplier vs. Faraday cup). It can be anticipated that with the application of multiple ion counting to laser ablation U-Th-Pb dating (Schwieters et al. 2003), multi-collector instruments will be at least as sensitive as the quadrupole ICPMS. The major obstacle to a wider implementation of multiple ion counters in ICPMS has been the stability and linearity of the electron multipliers and problems associated with their cross-calibration. A single-collector magnetic sector instrument coupled to a laser ablation system already has a better sensitivity compared to a quadrupole ICPMS (Latkoczy and Günther 2002, Tiepolo et al., in press).

### New applications in laser ablation ICPMS dating of zircon

The application of laser ablation ICPMS to fission track dating of zircon (and indeed other U-bearing accessory phases) is still under development and has a great potential in terms of reduction of analytical uncertainties, sample throughput and substantial reduction of analytical cost. Another dating method where laser ablation will probably play a key role in the near future is zircon (U-Th)/He thermochronology. This very old dating method (Strutt 1908) has recently been revived and successfully applied for studies of thermal development of sedimentary basins with important implications for the oil industry. It was originally used for apatite dating (Farley 2000) but recently also to other phases, including zircon (Reiners et al. 2002). The dating method is based on accumulation of radiogenic $^{4}He$ in U and Th rich accessory minerals. The subsequent diffusive loss of He from the mineral structure due to heating can be calibrated against time and temperature and the data can be used for thermal modeling in sedimentary basins and calculation of erosion rates.

Similar to fission track dating, the method requires precise and accurate measurements of U and Th concentrations, which can be achieved easily by laser ablation ICPMS. Presently zircon samples are analyzed for U and Th concentrations only through bulk dissolution methods such as solution ICPMS. However, He could be released from spots in the zircon crystals by laser fusion and analyzed by mass spectrometry, and the same spots could be later analyzed for U and Th by laser ablation ICPMS, providing spatial information about the thermal history of grains.

## ACKNOWLEDGMENTS

This paper benefited from numerous discussions with colleagues at Memorial and Charles Universities and from interactions with the users of our labs who contributed to development of the laser ablation dating technique. Comments by Ingo Horn and an anonymous reviewer are gratefully acknowledged. The ICPMS facility at Memorial University is supported by NSERC.

## REFERENCES

Ballard JR, Palin JM, Williams IS, Campbell IH, Faunes A (2001) Two ages of porphyry intrusion resolved for the super-giant Chuquicamata copper deposit of northern Chile by ELA-ICP-MS and SHRIMP. Geology 29:383-386

Belousova EA, Griffin WL, Shee SR, Jackson SE, O'Reilly SY (2001) Two age populations of zircons from the Timber Creek kimberlites, Northern Territory, as determined by laser-ablation ICP-MS analysis. Austral J Earth Sci 48:757-765

Bleiner D, Günther D (2001) Theoretical description and experimental observation of aerosol transport processes in

laser ablation inductively coupled plasma mass spectrometry. J Anal Atom Spectrom 16:449-456
Brockman J (2001) Sampling and Transport of Aerosols. *In* Aerosol Measurement, Principles Techniques and Applications. Baron PA, Willeke K (eds) J Wiley & Sons, New York, p 143-196
Bruguier O, Télouk P, Cocherie A, Fouillac AM, Albarède F (2001) Evaluation of Pb-Pb and U-Pb laser ablation ICP-MS zircon dating using matrix-matched calibration samples with a frequency quadrupled (266 nm) Nd-YAG laser. Geostandard Newslett 25:361-373
Catlos EJ, Gilley LD, Harrison TM (2002) Interpretation of monazite ages obtained via *in situ* analysis. Chem Geol 188:193-216
Chenery S, Cook JM (1993) Determination of rare earth elements in single mineral grains by laser ablation microprobe-inductively coupled plasma-mass spectrometry—preliminary study. J Anal Atom Spectrom 8:299-303
Compston W (1999) Geological age by instrumental analysis: The 29th Hallimond lecture. Mineral Mag 63:297-311
Compston W, Williams IS, Meyer C (1984) U-Pb geochronology of zircons from Lunar breccia 73217 using a sensitive high mass-resolution ion microprobe. J. Geophys Res 89B:525-534
Cox R, Košler J, Sylvester P, Hodych J (2000) Apatite fission-track (FT) dating by LAM-ICP-MS analysis. J Conf Abstr 5:322
Cox RA (in press) Morphological, chemical, and geochronological techniques for characterizing detrital zircon. *In* Geochemistry of sediments and sedimentary rocks: Evolutionary considerations to mineral deposit-forming environments. Lents DR (ed) Geological Association of Canada, Geotext 4
Cox RE, Wilton D, Košler J (submitted) Laser ablation U-Th-Pb dating of zircon and allanite: an example of *in situ* dating from October Harbour granite, central coastal Labrador. Can Mineral
Cromwell EF, Arrowsmith P (1995) Fractionation effects in laser ablation inductively coupled plasma mass spectrometry. Appl Spectros 49:1652-1660
Darke SA, Tyson JF (1993) Interaction of laser radiation with solid materials and its significance to analytical spectrometry. J Anal Atom Spectrom 8:145-209
Date AR, Gray AL (1981) Plasma source mass spectrometry using an inductively coupled plasma and a high resolution quadrupole mass filter. Analyst 106:1255-1267
Dodson MH, Compston W, Williams IS, Wilson JF (1988) A search for ancient detrital zircons from Zimbabwean sediments. J Geol Soc London 145:977-983
Douglas DJ, Tanner SD (1998) Fundamental considerations in ICPMS. *In* Inductively coupled plasma mass spectrometry. Montaser A (ed) Wiley-VCH, New York, p 615-681
Dunstan LP, Gramch JW, Barnes IL, Purdy WC (1980) The absolute abundance and the atomic weight of a reference sample of thallium. J Res Natl Bur Stand 85:1-10
Durrant SF (1994) Feasibility of improvement in analytical performance in laser-ablation inductively-coupled plasma-mass spectrometry (LA-ICP-MS) by addition of nitrogen to the argon plasma. Fresen J Anal Chem 349:768-771
Durrant SF (1999) Laser ablation inductively coupled plasma mass spectrometry: achievements, problems, prospects. J Anal Atom Spetrom 14:1385-1403
Eggins SM, Kinsley LPJ, Shelley JMM (1998) Deposition and element fractionation processes during atmospheric pressure laser sampling for analysis by ICPMS. Appl Surf Sci 129:278-286
Evans RD, Hintelmann H, Dillon PJ (2001) Measurement of high precision isotope ratios for mercury from coals using transient signals. J Anal Atom Spectrom 16:1064-1069
Farley KA (2000) Helium diffusion from apatite: general behavior as illustrated by Durango fluorapatite. J Geophys Res 105:2903-2914
Feng R, Machado N, Ludden J (1993) Lead geochronology of zircon by LaserProbe-Inductively coupled plasma mass spectrometry (LP-ICPMS). Geochim Cosmochim Acta 57:3479-3486
Fernández-Suárez J, Alfonso GG, Cox R, Jenner GA (2002) Assembly of the Armorica microplate: a strike-slip terrane delivery? Evidence from U-Pb ages of detrital zircons. J Geol 110:619-626
Fernandez-Suárez J, Guttiérez-Alfonso G, Jenner GA, Tubrett MN (2000) New ideas on the Proterozoic-Early Palaeozoic evolution of NW Iberia: insights from U-Pb detrital zircon ages. Precambrian Res 102:85-206
Fonneland HC, Lienb T, Martinsen OJ, Pedersen RB, Košler J (2002) Onshore and offshore provenance studies: A key to understanding the deposition of deep marine sandstones in the Norwegian Sea. *In* Radiogenic isotope systematics of clastic sedimentary rocks on detrital zircon geochronology. Fonneland HC, PhD dissertation, University of Bergen, Paper 4
Foster G, Gibson HD, Parrish RR, Horstwood M, Fraser J, Tindle A (2002) Textural, chemical and isotopic insights into the nature and behaviour of metamorphic monazite. Chem Geol 191:183-207
Foster G, Kinny P, Vance D, Prince C, Harris N (2000) The significance of monazite U-Th-Pb age data in metamorphic assemblages: a combined study of monazite and garnet chronometry. Earth Planet Sci Lett 181:327-340
Fryer BJ, Jackson SE, Longerich HP (1993) The application of laser ablation microprobe-inductively coupled plasma mass spectrometry (LAM-ICPMS) to *in situ* (U)-Pb geochronology. Chem Geol 109:1-8
Gallagher K, Brown R, Johnson C (1998) Fission track analysis and its applications to geological problems. Ann Rev Earth Planet Sci 26:519-72

Gonzales J, Mao XL, Roy J, Mao SS, Russo RE (2002) Comparison of 193-, 213- and 266-nm laser ablation ICPMS. J Anal Atom Spectrom 17:1108-1113

Griffin WL, Pearson NJ, Belousova EA, Jackson SE, van Achterbergh E, O'Reilly SY, Shee SR (2000) The Hf isotopic composition of cratonic mantle: LAM-MS-ICPMS analysis of zircon megacrysts in kimberlites. Geochim Cosmochim Acta 64:133-147

Grove M, Harrison MT (1999) Monazite Th-Pb depth profiling. Geology 27:487-490

Guillong M, Günther D (2002) Effect of particle size distribution on ICP-induced elemental fractionation in laser ablation-inductively coupled plasma-mass spectrometry. J Anal Atom Spectrom 8:831-837

Guillong M, Horn I, Günther D (2002) Capabilities of a homogenized 266-nm Nd:YAG laser ablation system for LA-ICP-MS. J Anal Atom Spectrom 17:8-14

Günther D, Frischknecht R, Heinrich CA, and Kahlert HJ (1997) Capabilities of an argon fluoride 193-nm excimer laser for laser ablation inductively coupled plasma mass spectrometry microanalysis of geological materials. J Anal Atom Spectrom 12: 939-944

Günther D, Hattendorf B. (2001) Elemental fractionation in LA-ICP-MS. *In* Laser Ablation-ICPMS in the Earth Sciences. Sylvester P (ed) Mineral Assoc Can Short Course Handbook 29:83-91

Günther D, Heinrich C (1999) Enhanced sensitivity in laser ablation-ICP mass spectrometry using helium-argon mixtures as aerosol carrier. J Anal Atom Spectrom 14:1363-1368

Günther D, Mermet JM (2000) Laser ablation for inductively coupled plasma-mass spectrometry. *In* Comprehensive Analytical Chemistry 34: Discrete sample introduction techniques for inductively coupled plasma mass spectrometry. Barceló D (ed) Elsevier, Amsterdam, p 445-501

Hirata T (1996) Lead isotopic analyses of NIST standard reference materials using multiple collector inductively coupled plasma mass spectrometry coupled with a modified external correction method for mass discrimination effect. Analyst 121:1407-1411

Hirata T (1997) Soft ablation technique for laser ablation-inductively coupled plasma-mass spectrometry. J Anal Atom Spectrom 12:1337-1342

Hirata T (2001) Determinations of Zr isotopic composition and U-Pb ages for terrestrial and extraterrestrial Zr-bearing minerals using laser ablation-inductively coupled plasma mass spectrometry: implications for Nb-Zr isotopic systematics. Chem Geol 176:323-342

Hirata T (2002) Chemically assisted-laser ablation-ICP-mass spectrometry. Geochim Cosmochim Acta 66:A331

Hirata T, Nesbitt RW (1995) U-Pb isotope geochronology of zircon: Evaluation of the laser probe-inductively coupled plasma mass spectrometry technique. Geochim Cosmochim Acta 59:2491-2500

Horn I, Rudnick RL, McDonough WF (2000) Precise elemental and isotope ratio measurement by simultaneous solution nebulisation and laser ablation-ICP-MS: Application to U-Pb geochronology. Chem Geol 164:281-301

Horn I, Guillong M, Günther D (2001) Wavelength dependant ablation rates for metals and silicate glasses using homogenized laser beam profiles—implications for LA-ICP-MS. Appl Surf Sci 182:91-102

Horn I, Günther D (2003) A solid state 193-nm Nd:YAG for LA-ICP-MS. 2003 European Winter Conf on Plasma Spectrochemistry Abstr P-LA-005:376

Horn I, Günther D (2003) The influence of ablation carrier gasses Ar, He and Ne on the particle size distribution and transport efficiencies of laser ablation-induced aerosols: implications for LA–ICP–MS. Appl Surface Sci (in press)

Houk RS (1986) Mass spectrometry of inductively coupled plasmas. Analyt Chem 58:97A-105A

Houk RS, Fassel VA, Flesch GD, Svec HJ, Gray AL, Taylor CE (1980) Inductively coupled argon plasma as an ion source for mass spectrometric determination of trace elements. Analyt Chem 52:2283-2289

Houk RS, Fassel VA, Svec HJ (1981) Inductively coupled plasma mass spectrometry: sample introduction, ionization, ion extraction and analytical results. Dyn Mass Spectrom 6:234-251

Jackson SE (2001) The application of Nd:YAG lasers in LA-ICP-MS. *In* Laser Ablation-ICPMS in the Earth Sciences. Sylvester P (ed) Mineral Assoc Can Short Course Handbook 29:29-46

Jackson SE, Pearson NJ, Griffin WL (2001) *In situ* isotope ratio determination using laser-ablation (LA)-magnetic sector-ICP-MS. *In* Laser Ablation-ICPMS in the Earth Sciences. Sylvester P (ed) Mineral Assoc Can Short Course Handbook 29:105-119

Jackson SE, Longerich HP, Dunning R, Fryer BJ (1992) The application of laser-ablation microprobe-inductively coupled plasma mass spectrometry LAM-ICP-MS to *in situ* trace element determinations in minerals. Can Mineral 30:1049–1064

Jackson SE, Longerich HP, Horn I, Dunning R (1996) The application of laser ablation microprobe (LAM)-ICP-MS to *in situ* U-Pb zircon geochronology. J Conf Abstr 1:283

Jeffries TE, Jackson SE, Longerich HP (1998) Application of a frequency quintupled Nd:YAG source (= 213 nm) for laser ablation ICP-MS analysis of minerals. J Anal Atom Spectrom 13:935-940.

Jeffries TE, Pearce NJG, Perkins WT, Raith A (1996) Chemical fractionation during infrared and ultraviolet laser ablation inductively coupled plasma mass spectrometry—implications for mineral microanalysis. Anal Com 33:35-39

Ketchum JWF, Jackson SE, Culshaw NG, Barr SM (2001) Depositional and tectonic setting of the Paleoproterozoic Lower Aillik Geoup, Makkovik Province, Canada: evolution of a passive margin-foredeep sequence based on petrochemistry and U-Pb (TIMS and LAM-ICP-MS) geochronology. Precambrian Res 105:331-356

Koch J, Feldmann I, Jakubowski N, Niemax K (2002) Elemental composition of laser ablation aerosol particles deposited in the transport tube to an ICP. Spectrochim Acta B57:975-985

Košler J, Tubrett M, Sylvester P (2001a) Application of laser ablation ICPMS to U-Th-Pb dating of monazite. Geostandards Newslett 25:375-386

Košler J, Buriánková K, Tubrett M, Sylvester P (2001b) Timing of metamorphism in the central High Himalaya (Makalu region) constrained by *in situ* Th-U-Pb dating of monazite by laser ablation ICPMS. J Conf Abstr 6:600-601

Košler J, Longerich HP, Tubrett M (2002a) Effect of oxygen on laser-induced elemental fractionation in LA-ICP-MS analysis. Anal Bioanal Chem 374:251-254

Košler J, Fonneland H, Sylvester P, Tubrett M, Pedersen RB (2002b) U-Pb dating of detrital zircons for sediment provenance studies—a comparison of laser ablation ICPMS and SIMS techniques. Chem Geol 182:605-618

Košler J, Wiedenbeck M, Hovorka J, Tubrett M, Sylvester P, Míková J (submitted) Size and composition of particles produced by laser ablation—effects on elemental fractionation during ICPMS analysis. Geoanalysis 2003 Abstracts, Rovaniemi, Finland.

Knudsen TL, Griffin WL, Hartz EH, Andresen A, Jackson SE (2001) *In situ* hafnium and lead isotope analyses of detrital zircons from the Devonian sedimentary basin of NE Greenland: a record of repeated crustal reworking. Contrib Mineral Petrol 141: 83-94

Kuhn HR, Günther D (2003) Elemental fractionation studies on laser induced brass aerosols. 2003 European Winter Conf on Plasma Spectrochemistry Abstr P-LA-004:375

Latkoczy C, Günther D (2002) Enhanced sensitivity in inductively coupled plasma sector field mass spectrometry for direct solid analysis using laser ablation (LA-ICP-SFMS). J Anal Atom Spectrom 17:1264-1270

Li X, Liang X, Sun M, Guan H, Malpas JG (2001) Precise $^{206}Pb/^{238}U$ age determination on zircons by laser ablation microprobe-inductively coupled plasma-mass spectrometry using continuous linear ablation. Chem Geol 175:209-219

Liu H, Borisov OV, Mao X, Shuttleworth S, Russo RE (2000) Pb/U fractionation during Nd:YAG 213-nm and 266-nm laser ablation sampling with inductively coupled plasma mass spectrometry. Appl Spectros 54:1435-1442

Longerich HP, Fryer BJ, Strong DF (1987) Determination of lead isotope ratios by inductively coupled plasma-mass spectrometry (ICP-MS). Spectrochim Acta 42B:39-48

Longerich HP, Jackson SE, Günther D (1996) Laser ablation inductively coupled plasma mass spectrometric transient signal data acquisition and analyte concentration calculation. J Anal Atom Spectrom 11:899-904

Longerich HP, Diegor W (2001) Introduction to mass spectrometry. *In* Laser Ablation-ICPMS in the Earth Sciences. Sylvester P (ed) Mineral Assoc Can Short Course Handbook 29:1-19

Loucks RR, Eggins SM, Shelley LMG, Kinsley LPJ, Ware NG (1995) Development of the inductively-coupled-plasma mass spectrometry ultraviolet laser trace-element micro-analyzer (ICPMS-ULTEMA), Research School of Earth Sciences—Annual Report 1995, p 138-140

Ludwig KR (1998) On the treatment of concordant uranium-lead ages. Geochim Cosmochim Acta 62: 665-676

Ludwig KR (1999) IsoplotEx v. 2.6. Berkeley Geochronological Center Spec Publ no. 1a.

Machado N, Gauthier G (1996) Determination of $^{207}Pb/^{206}Pb$ ages on zircon and monazite by laser ablation ICPMS and application to a study of sedimentary provenance and metamorphism in southeastern Brazil. Geochim Cosmochim Acta 60:5063-5073

Machado N, Simonetti A (2001) U-Pb dating and Hf isotopic composition of zircon by laser-ablation-MC-ICP-MS. *In* Laser Ablation-ICPMS in the Earth Sciences. Sylvester P (ed) Mineral Assoc Can Short Course Handbook 29:121-146

Mank AJG, Mason PRD (1999) A critical assessment of laser ablation ICP-MS as an analytical tool for depth analysis in silica-based samples. J Anal Atom Spectrom 14:1143-1153

Maréchal CN, Télouk P, Albarède F (1999) Precise analysis of copper and zinc isotopic compositions by plasma-source mass spectrometry. Chem Geol 156:251-273

Mason PRD (2001) Expanding the capabilities of laser-ablation ICP-MS with collision and reaction cells. *In* Laser Ablation-ICPMS in the Earth Sciences. Sylvester P (ed) Mineral Assoc Can Short Course Handbook 29:63-81

Moenke-Blackenburg L, Gäckle M, Günther D, Kammel J (1989) Processes of laser ablation and vapour transport to the ICP. R Soc Chem Spec Publ 85:117

Moens L, Vanhaecke F, Bandura DR, Baranov VI, Tanner SD (2001) Elimination of isobaric interferences in ICP-MS, using ion-molecule reaction chemistry: Rb/Sr age determination of magmatic rocks: a case study. J Anal Atom Spectrom 16:991-994

Morton AC, Claoué-Long JC, Berge C (1996) SHRIMP constraints on sediment provenance and transport history in the Mesozoic Statfjord Formation, North Sea. J Geol Soc London 153:915-929

Parrish RR, Nowell G, Noble SR, Horstwood M, Timmerman H, Shaw P, Bowen IJ (1999) LA-PIMMS: A new

method of U-Th-Pb geochronology using micro-sampling techniques. J Conf Abstr 4:799
Parrish RR (1990) U-Pb dating of monazite and its application to geological problems. Can J Earth Sci 27:1431-1450
Rawlings-Hinchey AM, Sylvester PJ, Myers JS, Dunning GR, Košler J (in press) Paleoproterozoic crustal genesis: Calc-alkaline magmatism of the Torngat Orogen, Voisey's Bay area, Labrador. Precambrian Res
Ray SJ, Hieftje GM (2001) Mass analyzers for inductively coupled plasma time-of-flight mass spectrometry. J Anal Atom Spectrom 16:1206-1216
Rehkämper M, Mezger K (2000) Investigation of matrix effects for Pb isotope ratio measurements by multiple collector ICP-MS: verification and application of optimized analytical protocols. J Anal Atom Spectrom 15:1451-1460
Reiners PW, Farley AK, Hickles HJ (2002) He diffusion and (U-Th)/He thermochronometry of zircon: initial results from Fish Canyon Tuff and Gold Butte, Nevada. Tectonophysics 349:297-308
Rosman KJR, Taylor PDP (1999) Isotopic composition of the elements 1997. J Anal Atom Spectrom 14:5N-24N
Russo RE, Mao X, Gonzales JJ, Mao S (2002) Femtosecond laser ablation ICP-MS. J Anal Atom Spectrom 17: 1072-1075
Russo RE, Mao XL, Borisov OV, Liu H (2000) Influence of wavelength on fractionation in laser ablation ICP-MS. J Anal Atom Spectrom 15:1115-1120
Schärer U (1984) The effect of initial $^{230}$Th disequilibrium on young U-Pb ages: The Makalu case, Himalaya. Earth Planet Sci Lett 67:191-204
Schwieters JB, Bouman C, Tuttas D (2003) Laser ablation multi-ion-counting-ICPMS. 2003 European Winter Conf on Plasma Spectrochemistry Abstr P-Is-005:333
Silfvast WT (1991) Lasers. *In* Encyclopedia of Lasers and Optical Technology. Meyers RA (ed) Academic Press, San Diego, p 209-226
Sircombe K (2000) The usefulness and limitations of binned frequency histograms and probability density distributions for displaying absolute age data. Geol Soc Can Current Res 2000-F2, Radiogenic age and isotope studies Report 13:1-11
Stacey JS, Kramers JD (1975) Approximate of terrestrial lead isotope variation by a two-stage model. Earth Planet Sci Lett 26:207-221
Strutt RJ (1908) On the accumulation of helium in geological time. Proc R Soc A81:272-277
Svojtka M, Košler J (2002) Fission-track dating of zircon by laser ablation ICPMS. Geochim Cosmochim Acta 66:A756
Sylvester PJ, Ghaderi M (1997) Trace element analysis of scheelite by excimer laser ablation inductively coupled plasma mass spectrometry (ELA-ICP-MS) using a synthetic silicate glass standard. Chem Geol 141:49-65.
Tanner SD (1992) Space-charge in ICP-MS—calculation and implications. Spectrochim Acta B47:809-823
Thirlwall MF (2002) Multicollector ICP-MS analysis of Pb isotopes using a $^{207}$Pb-$^{204}$Pb double spike demonstrates up to 400 ppm/amu systematic errors in Tl-normalization. Chem Geol 184:255-279
Tiepolo M, Botazzi P, Palenzona M, Vanucci R (2002) A laser probe coupled with ICP-double focusing sector field mass spectrometer for *in situ* analysis of trace elements in geological samples and U-Pb dating of zircons. Can Mineral (in press)
Tubrett M, Košler J, Sylvester P (2001) Applying a common Pb correction in dating of accessory minerals by laser ablation—ICP-MS. Geol Assoc Can / Mineral Assoc Can Ann Mtg Abstr 26:151-152
van Achterbergh E, Ryan C, Jackson S, Griffin W (2001) Data reduction software for LA-ICP-MS. *In* Laser Ablation-ICPMS in the Earth Sciences. Sylvester P (ed) Mineral Assoc Can Short Course Handbook 29:239-243
White MW, Albarède F, Télouk P (2000) High-precision analysis of Pb isotope ratios by multi-collector ICP-MS. Chem Geol 167:257-270
Whitehouse MJ, Claesson S, Sunde T, Vestin J (1997) Ion microprobe U-Pb zircon geochronology and correlation of Archaean gneisses from the Lewisian Complex of Gruinard Bay, northwestern Scotland. Geochim Cosmochim Acta 61:4429-4438
Whitehouse MJ, Sunde T (2000) Reference materials for SIMS U-Pb analyses: observations and recommendations from >3000 analyses of Geostandards zircon 91500. Geoanalysis 2000 abstracts, CNRS-CRPG Nancy, p 28-29
Wiedenbeck M, Alle P, Corfu F, Griffin WL, Meier M, Oberli F, von Quadt A, Roddick JC, Spiegel W (1995) Three natural zircon standards for U-Th-Pb, Lu-Hf, trace element and REE analyses. Geostandards Newslett 19:1-23
Wilde SA, Valley JW, Peck WH, Graham CM (2001) Evidence from detrital zircons for the existence of continental crust and oceans on the Earth 4.4 Gyr ago. Nature 409:175-178
Williams I (1998) U-Th-Pb geochronology by ion microprobe. *In* Applications of microanalytical techniques to understanding mineralizing processes. McKibben MA, Shanks III WC, Ridley WI (eds), Rev Econ Geol 7:1-35
Williger BJA, Baker JA, Krogstad EJ, Peate DW (2002) Precise and accurate *in situ* Pb-Pb dating of apatite, monazite, and sphene by laser ablation multiple-collector ICP-MS. Geochim Cosmochim Acta 66:1051-1066

# 10 Detrital Zircon Analysis of the Sedimentary Record

**Christopher M. Fedo**

*Department of Earth and Environmental Sciences*
*The George Washington University*
*Washington, DC 20052*

**Keith N. Sircombe**

*Tectonics Special Research Centre*
*School of Earth and Geographical Sciences*
*University of Western Australia, M.004*
*35 Stirling Highway*
*Crawley, WA 6009 Australia*

**Robert H. Rainbird**

*Geological Survey of Canada*
*601 Booth Street*
*Ottawa, Ontario K1A 0E8 Canada*

## INTRODUCTION

The composition of "heavy," or accessory, detrital minerals in sediments and sedimentary rocks has been a topic of quantitative study for at least the last seventy years, beginning with the first issue of the *Journal of Sedimentary Petrology* in May 1931 (Tyler 1931, Pentland 1931). Zircon has since played a prominent and complex role in interpreting the composition and history of modern and ancient sediments. Because zircon is highly refractory at Earth's surface, it occurs in virtually all sedimentary deposits and so provides a critical link in understanding the source history of a deposit. Twenhofel (1941), in a pioneering paper on the frontiers of sedimentary mineralogy and petrology, noted that the simple presence of detrital zircon would be of little value in determining its source: "Zircons from a half dozen sources with as many different properties may be present in a sediment and merely be identified as zircon. *Parent rocks cannot be positively identified on such data*. The variety or varieties must be identified and their optical properties determined." From very early on, then, it was recognized that detrital zircon would be a powerful tool in understanding provenance, and thus, sedimentary dispersal systems.

Interpretive goals matured considerably in the subsequent decades, especially with major advances in microscopy, mineral chemistry, isotope tracer geochemistry, and geochronology, each addressing different aspects of provenance, sedimentation, and Earth history. The hundreds of published studies utilizing detrital zircon in the last 20 years indicate the increasing success in assessing provenance, paleogeography, and tectonic reconstructions. Selected studies are highlighted in this review to illustrate ways in which detrital zircon can be used for interpreting the stratigraphic record, and thus, the past surface conditions of Earth. In it we will outline the quantitative techniques involved in the sampling protocol and interpretation of data and then illustrate the application of detrital zircon studies to: (1) determine maximum age of stratigraphic successions and to help recognize time gaps in the geologic record, (2) determine provenance characteristics such as age and composition, (3) test regional paleogeographic reconstructions via provenance analysis, and (4) unravel facets of Earth history locked in the mineral chemistry of detrital zircon.

1529-6466/03/0053-0010$05.00

## STATISTICS AND METHODOLOGY OF SAMPLING

Detrital zircon analysis uses the interpreted provenance of the zircon to develop a geological history of sedimentary basins and their surrounding source regions. Ideally, the analyzed sample would completely represent geological history by including evidence of all the possible provenances and their relationships to each other. However, natural complexity and artificial bias preclude such a situation.

The aim of any research is to unravel complexity in order to gain insight into natural processes, but this is a formidable task with detrital zircon. The complexity begins with the source rocks themselves, as detrital zircon is not necessarily representative of the entire set of detritus in a sedimentary unit. Rocks with low zircon abundance will be under-represented in a sedimentary sample focusing on detrital zircon. For instance, zircon is not typically found in ultramafic/mafic igneous rocks and any detrital zircon record will underestimate the contribution of such rocks to a sedimentary deposit. Even if zircon is present, then the rock type will determine the amount of zircon present, and, as discussed below, the size of those grains. Beyond the source rock, all detrital minerals are subject to processes during weathering, erosion, transportation, deposition and diagenesis capable of further modifying mineral proportions and compositions. Because zircon has a higher density and hardness than coeval minerals, such as quartz and feldspar that may form the bulk of a sedimentary rock, they will have a different path through these sedimentary processes. There is also general consensus that abrasion may eliminate older, higher-U grains, or regions in such grains, that are more likely to be metamict. Although detrital zircon analysis is a powerful tool, it should always be remembered that evaluating natural complexity in sedimentary systems requires more than one analytical method.

The various processes involved in conducting an analysis can introduce artificial bias and occur from field sampling to the presentation of results. These sources of bias and potential steps for mitigation are discussed below.

### Sampling

The potential for bias begins with selecting samples in the field. The nature of the research project dictates the type of sample taken and there are no strict guidelines for sample selection in detrital zircon studies. However, some studies have shown that sedimentary rock type and depositional setting can be a significant factor in the results obtained.

A systematic study of the Methow Basin in northern Washington and southern British Columbia targeted samples at different stratigraphic levels from the same formation (DeGraaff-Surpless et al. 2000). This approach revealed that the age distributions of detrital zircons from the turbiditic Harts Pass Formation were relatively homogeneous throughout the vertical section. In contrast, the fluvial Winthrop Formation revealed great variation in detrital zircon age distributions, commonly within a small spatial distance.

The link between sedimentary maturity and detrital zircon ages is also seen in the Roberts Mountains allochthon, Nevada (Smith and Gehrels 1994). The mature quartz arenite Valmy Formation contains well-rounded detrital zircons revealing a range of U-Pb ages indicative of multiple sedimentary cycles. In contrast, the Harmony Formation contains euhedral zircons generally yielding younger and more homogenous ages.

Linking sedimentological maturity with homogeneity in detrital zircon age distributions cannot be assumed. For instance, in the Slave Province a highly mature metaquartzite was analyzed as part of a regional study. The basal quartzite unit of the Central Slave Cover Group is a distinctive regional marker horizon on the basis of distinct lithostratigraphic correlation (Sircombe et al. 2001). Sensitive high-resolution ion microprobe (SHRIMP) dating revealed a range of Archean modes from five samples. Although there were a number of common components, there also were significant differences among samples. These differences indicate that, despite lithostratigraphic correlation and maturity, the detrital zircons in some samples have a localized provenance and there was

only limited mixing between sources.

These cases illustrate the need for careful consideration of sampling strategies. Any detrital zircon study requires thorough knowledge of the depositional environments of the sedimentary units being sampled, assessment of paleocurrent indicators, and the need for regional-scale studies to detect provenance localization.

## Sample preparation

The physical preparation of samples for geochronological analysis (cleaning, chipping, crushing and milling) is largely standardized and simple precautions (e.g., sample splitters) are considered to preclude biasing. Little regard is given to the extent of zircon breakage during crushing and milling. Larsen and Poldervaart (1957) conducted tests to compare the zircon yield between separates obtained by acid and crushing and found a significant number of apparently broken zircons in the acid separate. They concluded that the damaged zircons were predominantly a result of imperfect crystallization and that crushing did not significantly contribute to the breakage. This is clearly an area for further investigation. There is little suggestion of Wilfley table and heavy liquid separation causing bias, although detailed investigation is required to confirm this.

***Size grading.*** A major source of bias in laboratory preparation is size grading. Some milling procedures include sieving milled material at 250 μm (60-mesh) or similar, thus excluding larger zircons. Minimum analytical quantities and simple physical limitations on handling exclude smaller zircons. For thermal ionization mass spectrometry (TIMS) analysis, the minimum analyzable grain depends on the expected age and U concentrations (and thus quantity of Pb) and may typically vary between ~45 μm for Precambrian grains to ~100 μm for Mesozoic grains (Gehrels 2000). For secondary ion mass spectrometry (SIMS) analysis, the minimum spot size is typically ~15 μm, although in the near future NanoSIMS technology may reduce this another order of magnitude. In both analytical methods, the physical difficulty of micro-manipulating grains <~30 μm often excludes their use in analysis unless such small grains have been deliberately sought (e.g., aeolian-deposited zircon in soils, Gatehouse et al. 2001). Analyzing grains >100 μm is considered to bias provenance interpretations toward coarse-grained granitoids (Gehrels 2000).

Also considering grain size as a potential provenance indicator and citing standards used in heavy mineral analysis, Morton et al. (1996) advise analysis of the 63-125 μm (very fine sand) fraction in detrital zircon studies. Using such a common size standard is considered crucial in provenance assessment using detrital zircon to avoid the hydrodynamic fractionation in samples of differing grain sizes (Morton and Hallsworth 1994). The increasing use of digital imaging for zircon sample documentation also provides a relatively simple way to quantify grain sizes using image analysis software. Measured grain-sizes can be reported alongside isotopic data to test for any size biases (Sircombe et al. 2001, Sircombe and Stern 2002).

***Magnetic separation.*** Use of a Frantz magnetic barrier separator is a ubiquitous process of both TIMS and SIMS sample preparation, stemming from the long-noted positive correlation between Pb-loss/discordance, U content and magnetic susceptibility (Silver 1963). Heaman and Parrish (1991) speculated that selection of grains from the least-magnetic fraction could cause an artificial bias in the measured zircon age distribution. Sircombe and Stern (2002) confirmed the potential for such a bias in a sample from Dwyer Lake in the Slave Province with a bimodal age distribution. In that study, one age mode had grains with higher α-dosage [as determined following the method of Gottfried and Holland (1955) which was later modified by Murakami et al. (1991)] and thus correspondingly higher magnetic susceptibility. The implicit assumption in such α-dose calculations, however, is that there has not been any thermal perturbation to the zircon crystals since the last geologic event preserved in the crystals, which represents an assumption that cannot always be adequately assessed. The relative proportions of the mode changed with different magnetic fractions and it may have been missed entirely in an extremely non-magnetic fraction. Sampling a relatively broad range of magnetic susceptibilities is recommended for detrital samples and this has

been a standard procedure in many laboratories (e.g., Gehrels 2000). Calculating and reporting α-dosage based on isotopic data is a straightforward test for any bias due to magnetic separation.

## Analysis

There are two strategies in detrital zircon analysis. The analyst needs to be aware of which strategy they are pursuing because the interpretations based on each strategy are not necessarily identical.

***Qualitative analysis.*** The first approach is a qualitative strategy where ages representing each source component within the population are sought. Gehrels and Dickinson (1995, p. 23) adopted a typical qualitative method where "grains from all color and morphology groups were analyzed irrespective of their abundance among the available grains." This method has an advantage of including potential age components that a purely random selection may miss (Gehrels 2000). Most TIMS and some SIMS detrital zircon analyses follow this strategy. For example, the examination of detrital zircon from the Mount Roberts Formation in the Quesnellia terrane in northern Washington (Roback and Walker 1995) was based on grain morphology and revealed that well-rounded grains were generally Proterozoic and Archean, in contrast to euhedral Devonian zircons. The qualitative approach has been used to establish a reference for a particular unit or region that indicates all possible contributing provenances (e.g., western North America; Gehrels 2000, Gehrels et al. 1995).

The optical classification of zircon grains and their relationship with age components is useful, but as pointed out by Roddick and Bevier (1995), it is not totally reliable. Although initially used as tools for aiding the identification of inherited zircon cores in granitic rocks (e.g., Williams 1992, Hanchar and Miller 1993), back-scattered electron (BSE) and/or cathodoluminescence (CL) imaging of zircon prior to analysis has become routine for detrital studies. As well as aiding the location of ion probe spots to avoid potential defects or zonal overlap, cathodoluminescence can also be used to classify detrital zircon components prior to analysis, as illustrated by Åhäll et al. (1998) in a study of Proterozoic supracrustal units in southern Scandinavia.

***Quantitative analysis.*** The aim of the second approach to detrital zircon analysis, a quantitative strategy, is for the analyzed sample to be as representative of the overall detrital zircon population as possible (i.e., an age component comprising *x*% of the analyses represents *x*% of the total zircon in the sample). Minimizing handling can enhance the randomness of selection during handpicking. Detrital zircon grains are often scooped en-mass from the slide or petri-dish. During SIMS analysis, an array of mounted zircons is systematically analyzed, and the only operator input is avoiding any obvious imperfections, such as inclusions and metamict zones, and avoiding analysis across zircon domain boundaries (e.g., between core and rim).

Ensuring that an analyzed sample is representative of the population invokes the concept of statistical adequacy. The number of analyses required for a given level of confidence is given by Dodson et al. (1988), which assesses the probability of missing a provenance component comprising a certain proportion that component within the total sample, and the number of grains analyzed. The typical case is a provenance component comprising 1 in 20 in the total sample. Using the expression in Dodson et al. (1988), at least 59 randomly selected grains need to be measured to reduce the probability of missing this component to 5% (Fig. 1).

Achieving such large numbers of analyses for a single sample is prohibitively expensive in TIMS analysis, thus quantitative analysis is generally the domain of SIMS and laser ablation–inductively coupled plasma mass spectrometry (LA-ICPMS) techniques, where relatively rapid *in situ* analyses can be achieved. The quantitative approach has an advantage of providing meaningful comparisons between the proportions of age components. This is powerfully illustrated in the Perth Basin where detrital zircon samples from various stratigraphic levels within the rift sedimentary sequence have been examined (Cawood and Nemchin 2000). The results revealed a complex pattern of evolving source contributions that challenges simplistic models of a half-graben filling with cratonic debris. Similar cases of sequence evolution have been demonstrated in the Pennine Basin (Hallsworth et al. 2000) and the Great Valley Group (DeGraaff-Surpless et al. 2002). The quantita-

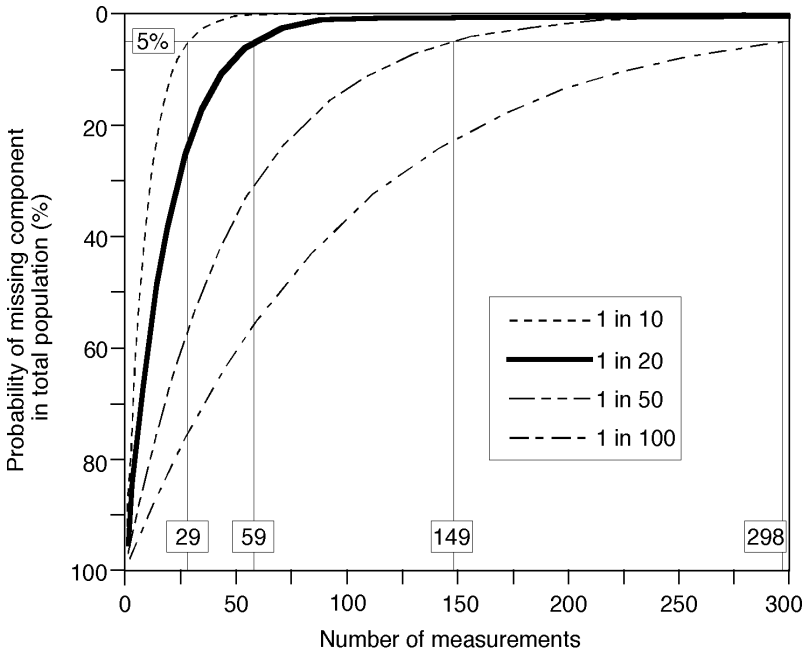


**Figure 1.** Graphical representation of the Dodson et al. (1988) equation illustrating the probability of missing a provenance component based on number of measurements. Bold line shows the typical case of a provenance component comprising 1 in 20 in the total sample, where analysis of 59 grains reduces the possibility of missing a component to 5%. Other curves show the 5% cut-off for different proportions in the total sample.

tive approach has also been used in modern systems to explore provenance evolution in longshore drift (eastern Australia, Sircombe 1999) and deserts (central Australia, Pell et al. 1999).

***Qualitative vs. quantitative.*** The qualitative and quantitative approaches are complementary, but interpretations are not necessarily the same. For instance, a qualitative regime may reveal significant provenances, but attempting to compare the proportions of age-components among samples (and references) may be meaningless because the selected analyzed grains do not represent the true proportions in the sample. Conversely, a quantitative regime will allow meaningful comparison of proportions, but geologically significant provenances may have been missed. In both cases, care must be taken not to over-interpret the data, given the serious constraints imposed by natural complexity during the formation of a sedimentary unit.

The technique will decide the analytical approach in any detrital zircon project. Without an extraordinary amount of resources, TIMS methods will be restricted to a qualitative regime. Although SIMS is capable of being utilized for both approaches, ensuring statistical adequacy in a quantitative regime remains time consuming and often precludes a complementary qualitative approach. LA-ICPMS is emerging as a technique that may allow for quantitative analysis within a reasonable time frame and cost. TIMS analysis will remain useful to provide precise ages on grains that were first dated by SIMS or LA-ICPMS as being of considerable interest (i.e., the youngest grains in the sample or ones that perhaps match exactly in age with known rocks in a possible source region).

## Data display

U-Pb isotopic data are typically displayed using concordia diagrams to convey information about the analytical process such as sample size, accuracy and precision. However, as sample size increases, as is typical of detrital zircon analysis, these concordia diagrams can become visually cluttered. Thus detrital zircon data are commonly displayed in univariate diagrams such as histograms or probability density distributions.

Because the ability to display accuracy in terms of concordance is lost, the first stage of producing a univariate diagram is to filter the isotopic data. For instance, in SIMS studies, this is typically based on an arbitrary constraint on concordance such as between 95% and 105%. Although excluded from further provenance interpretation, it may be beneficial to display both concordant-only and combined concordant-discordant results in diagrams (e.g., Roback and Walker 1995, Morton et al. 1996).

Binned frequency diagrams (Fig. 2) are common method for displaying age data where modes, ranges and proportions may relate to the timing, duration and relative significance of geologic events. While these diagrams are well understood and easily communicate salient information about the data, there are two critical limitations. Firstly, the histograms are based only on the age measurement and the inherent errors in the ages are discarded. Thus a measurement with a ±100 Myr standard error could appear in the same bin as one with a ±1 Myr standard error even though the two measurements are strictly not comparable. Secondly, the size of the bins themselves is arbitrary with values in the literature including 5 Myr (Davis et al. 1994, their Fig. 8B), 20 Myr (Gehrels and Dickinson 1995, their Fig. 6), 33.3 Myr (Scott and Gauthier 1996, their Fig. 4), and 100 Myr (Roback and Walker 1995, their Fig. 8). Morton et al. (1996) suggest a standard bin width for SHRIMP data of 25 Myr. There are a number of mathematical approaches to optimizing bin width (Sircombe 2000a), but these are based on assumptions about the data distribution that are often invalid for detrital suites.

In an attempt to circumvent these two limitations to histograms use of probability density distributions (Fig. 3) has become widespread. These diagrams incorporate the errors in the age data and produce a probability distribution of the entire sample based on Gaussian kernels that vary with each individual age. The mathematical basis for this approach is typically attributed to Silverman (1986), with first application to detrital zircon being Dodson et al. (1988) using a program called "Noveau Stats" developed by Dr. P. Zeitler, then at the Research School of Earth Sciences of the Australian National University (I.S. Williams, written comment). The approach had also been demonstrated earlier for $^{40}Ar$-$^{39}Ar$ data (Jessberger et al. 1980).

The disadvantage of this approach is that it is the area beneath the curve that conveys frequency and proportion information rather than the height as in a histogram. Therefore, the number of measurements in each mode can be difficult to communicate and many recent univariate diagrams combine both probability density distributions and histograms (Figs. 4 and 5; e.g., Nutman 2001, their Fig. 4; Sircombe and Stern 2002, their Fig. 2; DeGraaff-Surpless et al. 2002, their Fig. 5).

## Interpretation

In igneous and metamorphic systems, geochronological analyses can often be considered as samples from a single, usually normal, distribution. This means that the analyses are amenable to straightforward statistical comparisons of similarity. Many detrital zircon distributions contain multiple modes so that such statistical comparisons are invalid. Early detrital zircon studies generally used visual methods to assess and interpret these distributions both in their relationship to other samples and potential provenances. While such interpretations are often reasonable and valid, a number of quantitative, and objective, methods have evolved to aid interpretation.

***Mixture modeling.*** The first issue in detrital zircon interpretation is identifying, or deconvolving, the inevitable mixture of age modes seen in the distribution. If age modes are relatively close, then resolution may be compromised by the inherent errors in the measurements and it will be difficult to objectively identify the age modes. This is notable with lower precision SIMS analyses. Building on the experience in similar situations with fission-track dating (Galbraith and Green 1990), Sambridge and Compston (1994) developed a mixture modeling method that estimates the most likely ages, proportions and number of components in a set of zircon data, based on a maximum likelihood approach. This method has been used widely in zircon analyses, particularly detrital studies, although it emphasized that the results obtained are models of the age distribution and thus

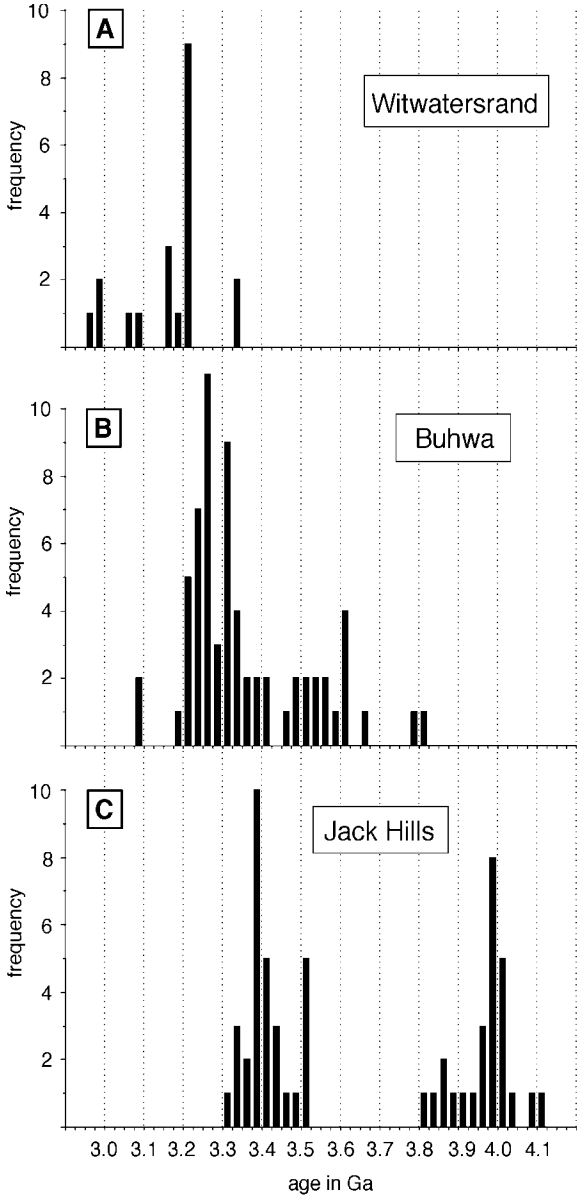


**Figure 2.** Frequency histograms for detrital zircons from three quartzites deposited at ~3.0 Ga. Bin width for histograms is 25 Myr. (A) Grains analyzed using SHRIMP from the Orange Grove Quartzite Formation, Witwatersrand Supergroup, South Africa (data from Barton et al. 1989). (B) Grains analyzed using SHRIMP from Buhwa quartzite, Zimbabwe (data from Dodson et al. 1988). (C) Grains analyzed by TIMS from meta-conglomerate, Jack Hills, Western Australia (data from Amelin 1998). Nelson (2001) reported a single grain at ~3.1 Ga and Wilde et al. (2001) reported grains up to 4.404 Ga from different samples from the Jack Hills. These are not shown on this frequency histogram.

need to be treated with caution when correlating with known references.

***Comparisons.*** A fundamental aspect of detrital zircon geochronology is the comparison of data with other detrital data or with known provenances to interpret origins of the zircon. This requires a priori knowledge of the age distributions of potential provenances. A number of cases have illustrated the need to look widely for sources (e.g., Rainbird et al. 1997).

There have been a number of attempts at moving beyond simplistic visual comparisons of age distributions. Gehrels (2000) introduced the concept of overlap and similarity between new samples and established western North American references. Both values vary from 0.0 to 1.0 and use the calculated probability distributions of the analyses incorporating the inherent errors (as above). Overlap is defined as the presence of an age in both age distributions being compared (Gehrels et al. 2002). Similarity is calculated by summing the square root of the product of each pair of probabilities. While quantifying visual comparison, neither can be considered an objective statistical test when using a qualitative analysis.

In order to compare potential provenance similarities between Tasmania and North America, Berry et al. (2001) used Kolmogorov-Smirnov (K-S) goodness-of-fit tests. This provides a statistical basis for hypothesis testing that the samples are similar, but the standard method is potentially insensitive to dispersed data (Press et al. 1986) and does not account for age errors.

Multivariate statistical analysis has also been applied to large sets of detrital zircon data in eastern Australia (Sircombe 2000b). Based on the age probability distributions this approach proved useful in quantifying the effect of longshore drift on the detrital zircon age distributions without

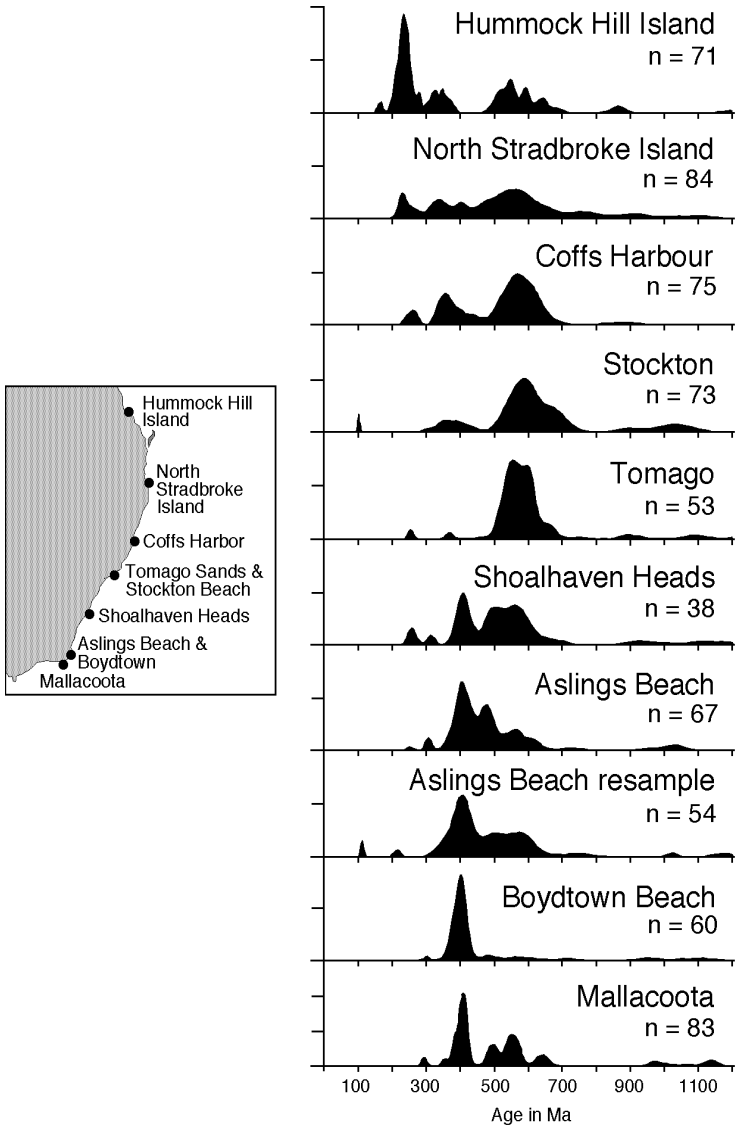


**Figure 3.** Probability distribution diagrams of zircon ages for modern sediments on the eastern coast of Australia. n is the number of grains analyzed. Modified from Sircombe (1999).

direct comparison with external references. However, the method is cumbersome and only beneficial for comparison of ten or more samples (unless a statistical software package like JMP, Systat, or MVSP is used).

## AGE OF STRATIGRAPHIC SUCCESSIONS

### Maximum age and age bracketing

One of the common goals in a detrital zircon study is to place constraints on the ages of siliciclastic stratigraphic successions. The premise, based on the principal of inclusions, is simply that age of deposition must be younger than the age of the youngest detrital zircon (typically U-Pb dating), with the proviso of no disturbance in the U-Pb isotopic system. The results are typically crude in the sense that only the maximum age of deposition is generally revealed. Detrital zircon studies where this has been done include Barton et al. (1989) and Robb et al. (1990) for the Archean

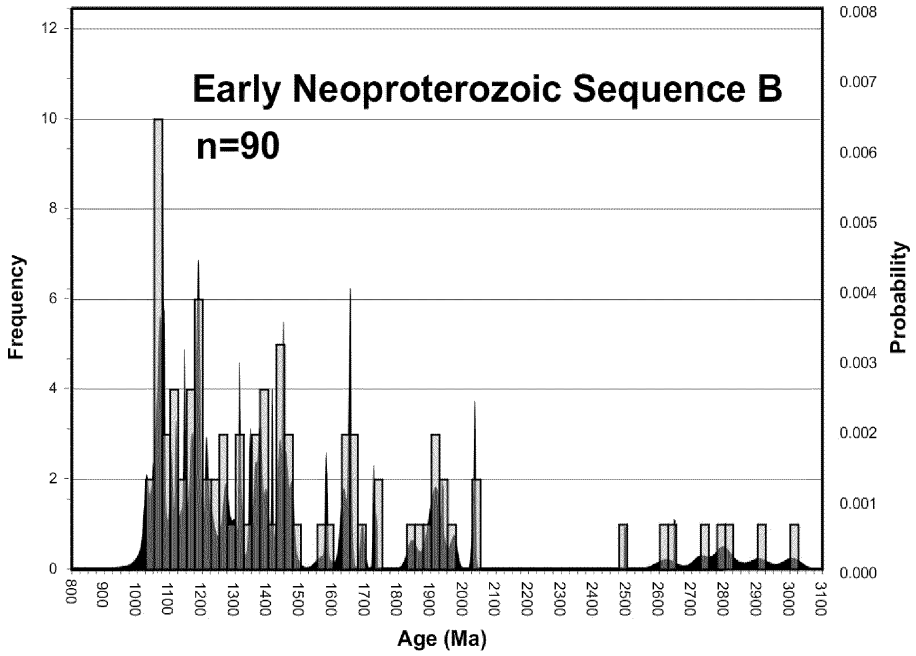


**Figure 4.** Probability density distribution-histogram plot of $^{207}Pb/^{206}Pb$ ages of detrital zircons from early Neoproterozoic quartzarenites from northwestern Canada, including the Shaler Supergroup, Mackenzie Mountains Supergroup and Hematite Creek Group (ID-TIMS data from Rainbird et al. 1997).

Witwatersrand Supergroup (Fig. 1A), Sircombe et al. (2001) for quartzites in the Archean Slave Province, Canada, and in the case of the Stirling Range Formation, Western Australia which brackets the age of the currently oldest known metazoans (Rasmussen et al. 2002). However, when detrital zircon geochronology is linked with geochronology of crosscutting younger igneous rocks or metamorphic mineral ages (e.g., Schiøtte et al. 1988), then both a maximum and minimum age bracket for deposition can be determined. Because of the crude age constraints provided by this approach, it is most widely applied to Precambrian successions where biostratigraphy cannot be used.

This approach yielded surprising results in the supracrustal rocks of the Zimbabwe Archean craton. Dodson et al. (1988) determined the age of several tens of detrital zircon grains using the SHRIMP from a thick (~1 km) orthoquartzite from the Buhwa (Mweza) greenstone belt in a search for very ancient grains, perhaps comparable in age to those discovered in the Jack Hills, Australia (Froude et al. 1983). Although the search for >4 Ga grains was unsuccessful (cf. Fig. 2B and C), the detrital zircon population in the orthoquartzite yielded a polymodal age distribution with modes at ~3250 Ma, ~3600 Ma, and a small mode at ~3800 Ma, with the youngest grain at 3.09±0.08 Ga. Realization of the importance of the detrital zircon age spectra for Buhwa did not come until much later. The distribution of zircon ages, and thus, basement ages is consistent with the sedimentary package at Buhwa being related to either of the two major episodes of craton-wide supracrustal greenstone deposition known as the Lower (~2.9 Ga) and Upper (~2.7 Ga) Bulawayan groups (Wilson et al. 1978). However, recognition that the tonalites that intruded the quartzite succession correlated with the nearby ~2.9 Ga Chingezi tonalite suite required that the succession at Buhwa represent an entirely unknown cycle of sedimentation in the Zimbabwe Archean craton, deposited between ~2900 and 3100 Ma (Fedo et al. 1996). The presence of similar aged orthoquartzite and shale deposits in the Kaapvaal craton and intervening granulite-facies Limpopo Belt south of the Zimbabwe craton suggests that the Zimbabwe craton was an integral part of the Archean crust in southern Africa by this time.

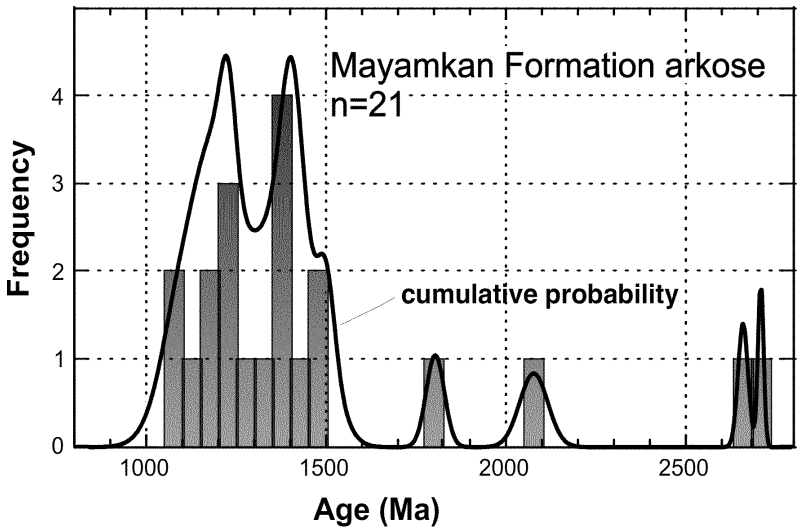


**Figure 5.** Probability density distribution-histogram plot of $^{207}Pb/^{206}Pb$ ages of detrital zircons from an arkose collected from the upper Uy Group, an early Neoproterozoic sequence from southeastern Siberia (SHRIMP data from Rainbird et al. 1998). Note the comparative similarity of the data from northwestern Canada shown in Figure 7.

## Direct depositional ages

The most reliable means of directly determining depositional sedimentary ages is through the dating of interstratified volcanic rocks, such as those near the Precambrian–Cambrian boundary (e.g., Bowring et al. 1993, Bowring and Schmitz, this volume), or with the newly emerging possibilities of dating time-of-deposition authigenic xenotime overgrowths on detrital zircon grains (e.g., McNaughton et al. 1999).

Because of their "passive" subsidence mechanisms, many cratonic and continental margin successions lack abundant volcanic units for direct dating. In Precambrian, or pre-Devonian terrestrial, successions the problem is compounded by the absence of a biologic record. Although the global volume of Precambrian strata is small relative to that of the Phanerozoic due to recycling, Precambrian deposits exist on all the continents and the Precambrian accounts for nearly 90% of Earth history. Consequently, extracting depositional ages for much of the stratigraphic record is fraught with uncertainty.

Under certain circumstances, the age of the youngest detrital zircon in a population can approach the age of deposition (Nelson 2001). This method, which has utilized SHRIMP analyses, depends on three major conditions and the premise that by tightening the age constraints of the youngest detrital zircon by pooling analyses on a few grains, a single grain, or even a single analysis, an accurate interpretation can be made (Nelson 2001). The first condition is that the studied samples should be at a low metamorphic grade in order to exclude contaminants such as veins and melt patches formed after deposition. Secondly, because the youngest detrital age may come from a single grain, great care needs to be exercised to avoid field and laboratory contamination. Lastly, only the least weathered or altered samples should be collected in order to avoid problems associated with isotopically disturbed samples (Nelson 2001).

This method of determining depositional age was applied by Nelson (2001) to three Precambrian basins in Australia, including a quartzite from the Jack Hills in the Archean Yilgarn Province. Metaconglomerate and quartzite from this region are renowned for hosting very ancient (up to 4404 Ma) detrital zircons (Fig. 2C; Froude et al. 1983, Wilde et al. 2001), yet its depositional age is considerably younger than the oldest detrital grains. The sample analyzed by Nelson (2001) con-

tains five major detrital zircon age populations, three of which (~3360 Ma, ~3400 Ma, and ~3480 Ma) can be assigned to various gneiss sources in the adjacent Narryer Complex, and a population of >4 Ga grains derived from a different composite gneiss terrane. Five analyses of a single grain define the fifth group at 3064 Ma. Kinny et al. (1990) suggested a maximum age of deposition of the metasedimentary protoliths at 3100 Ma by association with other metasedimentary sequences, while Maas and McCulloch (1991) interpreted detrital zircon ages and Nd isotopes to indicate a depositional age between 3.0 and 3.1 Ga. Consequently, the youngest detrital zircon group identified by Nelson (2001), Maas and McCulloch (1991), and Compston and Pidgeon (1986) at slightly greater than 3.0 Ga closely approximates the inferred time of deposition.

A key part of the success of this approach, according to Nelson (2001), is that highly mature sedimentary successions be sampled to ensure a broad spectrum of zircon source ages. However, there are some obvious limitations to the technique, and the extent of these limitations cannot be known in advance. For example, the youngest detrital zircon grains in some Holocene beach sands in eastern Australia are Permian (Sircombe 1999), some 250 Myr older than the age of deposition. Also, although Nelson (2001) does not favor sampling texturally and mineralogically immature sediments such as those found in tectonically active basins, the study by Kimbrough et al. (2001) indicates that Turonian forearc sediments in southern and Baja California received detrital zircons of essentially the same age from a rapidly crystallizing, uplifting, and eroding Peninsular Ranges batholith. Lastly Nelson (2001) recognizes that because of low temperature Pb loss, a detrital zircon could yield an age younger than the time of deposition. Despite these limitations, the near ubiquitous presence of zircon in sedimentary deposits makes them an ideal target for precise U-Pb age dating and at the very least establishing the maximum age of deposition.

**Disconformity recognition**

Disconformities, which are relatively easy to identify in fossiliferous sedimentary successions, commonly provide critical information about the subsidence mechanisms of sedimentary basins because they reveal information about coeval tectonics/uplift and sea-level fluctuations. In the absence of fossils to identify gaps in the geologic record, Precambrian basins are prone to major misunderstandings in properly identifying stratigraphic packaging, even on the continental scale of Sloss Sequences (e.g., Sloss 1988a). In many circumstances, km-thick sedimentary packages contain few, if any, interlayered volcanic rocks for direct dating, so that detrital zircon grains and sedimentary-reworked ash deposits provide the only critical age constraints for assembling time-stratigraphic packages and making interbasinal stratigraphic correlations.

The kilometers-thick Paleoproterozoic Hurwitz Group in the western Churchill Province of northern Canada provides an excellent example where detrital zircon ages, together with bulk rock isotopic analyses have revealed a time gap of approximately 200 Myr across a cryptic internal unconformity within the succession (Aspler et al. 2001; Fig. 6). Hurwitz Group strata, which crop out over an area of approximately 140,000 km$^2$, are divided into four major sequences, with basal deposits resting unconformably on a varied assemblage of Archean (2.6-2.7 Ga) granite-greenstone rocks and locally developed siliciclastic rocks of the Montgomery Group (Aspler et al. 2001). The rocks are exposed as a north-east trending series of infolded erosional remnants and are inferred to have been deposited in an intracratonic basin (Aspler et al. 2001), though they may form part of a much larger depositional basin that accumulated near the margins of Late Archean proto-continents (Young et al. 2001).

Sequences 1 and 2 were derived from predominantly Archean sources, with detrital zircons in sequence 1 ranging from 2750 to 2650 Ma (Patterson and Heaman 1990, Davis et al. 2000); gabbro sills that yield 2111±1 Ma U-Pb baddeleyite ages (Heaman and LeCheminant 1993) are scattered through sequence 2 and provide a minimum age of deposition for the lower two sequences, which were deposited in response to continental stretching and break-up processes (Aspler et al. 2001). Sequences 3 and 4, by contrast, contain abundant Proterozoic detrital zircons (2.50-1.91 Ga) as

well as Archean grains, suggesting a significant change in provenance between sequences 2 and 3 (Davis et al. 2000, Aspler et al. 2001) and a depositional age younger than the youngest detrital grain at 1.91 Ga. Stratigraphic relations for sequences 3 and 4 are consistent with deposition in response to crustal shortening. Consequently, the contact separating sequences 2 and 3 represents a disconformity spanning 200 Myr, but a hiatus of this magnitude was not predicted from stratigraphy alone, and the duration, spanning half the time of a Wilson cycle, was critical in linking regional tectonic events with stratigraphic sequences that formed in their response. This example illustrates the critical need for detrital zircon geochronology in poorly or non-fossiliferous successions.

## PROVENANCE ANALYSIS

### Petrographic and petrologic

"Heavy," or accessory, mineral suites, including zircon, have been used extensively as markers of petrologic identity and provenance in sediments and sedimentary rocks. In most circumstances, the accessory mineral assemblage was used to identify provenance composition on a grand scale, such as in the example of Carroll (1941), who recognized that the "heavy residues" from Cretaceous sediments in Western Australia could have been derived from spatially related "pre-Cambrian" shield rocks. Becker (1931) examined the heavy mineral assemblage, including zircon, of Precambrian and Paleozoic quartzites of the Baraboo Range, Wisconsin and recognized that it was similar to underlying bedrocks and suggested them as potential source, but he recognized that even accessory minerals do not necessarily fingerprint a specific source when the assemblage contains nothing unique. By contrast, the Paleozoic quartzite contains tourmaline and garnet. These minerals were not found in the underlying quartzites and suggested a distant provenance for some of the detritus.

Hubert (1962) defined a ZTR (zircon-tourmaline-rutile) index as a measure of mineralogic maturity of a sedimentary deposit and noted the importance of heavy mineral assemblages in determining provenance and paleogeographic reconstructions, a technique still widely applied today (e.g., Dill 1995, Garzanti et al. 2001). Morton and Hallsworth (1994) recognized that the final accessory mineral assemblage in a deposit was varyingly affected during weathering, transport, deposition, and diagenesis, so that it should be unlike that of the source. They proposed that certain mineral ratios, such as $TiO_2$-minerals:zircon, monazite:zircon, and Cr-spinel:zircon, in sediments should reflect source values because of their similar hydrodynamic properties and diagenetic behavior. Hallsworth et al. (2000) expanded this approach by adding U-Pb dating of detrital zircons. Schäfer and Dörr (1997) and Loi and Dabard (1997) have applied the zircon typology characteristics recognized by Pupin (1980) to identify provenance in Paleozoic sandstones in Germany and Italy, respectively, and Dunkl et al. (2001) combined typology with the study of zircon fission tracks, although the general utility of zircon typology is debatable (Vavre 1993), especially in sedimentary deposits where original crystal faces may be abraded through transport.

Most of the papers discussed to this point emphasize the traditional sedimentary petrology approach to provenance analysis based on thin section microscopy of accessory minerals that include zircon, and show that microscopy is still a widely applied approach. Adherence to this traditional approach also underscores the historically divergent routes of sedimentary versus igneous and metamorphic petrology, which have focused not only on petrography, but also on bulk geochemistry, mineral chemistry, and isotope geochemistry.

### Geochemistry

Zircon chemistry has been considered a potential provenance indicator functioning on the notion that its chemistry is sufficiently variable in different source rocks to enable their identification. Owen (1987) analyzed the hafnium concentration in detrital zircons from the Pennsylvanian Jackfork Sandstone and Parkwood Formation in the south-central United States. Based on a "statistically insignificant" difference in Hf concentration in the detrital zircons, he suggested that these

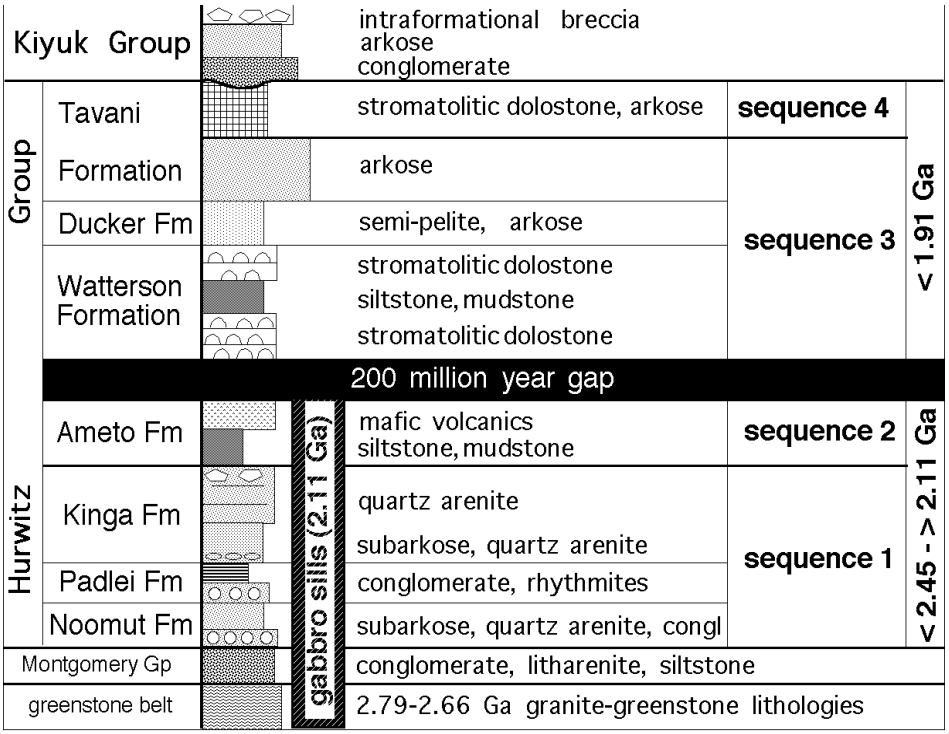


**Figure 6.** Stratigraphic context of the Hurwitz Group, Canada, showing a 200 Myr disconformity within the stratigraphic section, revealed in part by detrital zircon geochronology. Modified from Aspler et al. (2001).

sandstones were derived from a similar proximal source, distinct from that of other stratigraphic units. Hoskin and Ireland (2000) tested the hypothesis that there might be enough variation in rare earth element (REE) concentrations in zircon to differentiate their origin. Unlike the findings of Owen (1987), however, the investigation of zircon REE compositions showed that they are generally not sufficiently varied to provide a sensitive provenance indicator (Fig. 7), except perhaps in extreme compositions such as kimberlites (Griffin et al. 2000).

**Fission track (FT)**

Detrital zircon fission track (FT) analysis has been used successfully to identify provenance characteristics that differ from those derived by U-Pb geochronology (see below) because fission tracks yield data on low temperature (200-320°C) processes, such as source terrane thermo-tectonic evolution (Garver and Brandon 1994, Carter and Moss 1999, Liu et al. 2001, Bernet et al. 2001). Consequently, detrital zircon FT ages do not represent unambiguous provenance ages, except in circumstances where this can be confirmed with single crystal U-Pb geochronology (Carter 1999), a promising direction for zircon FT analysis (Carter and Moss 1999). The strength in zircon FT analysis is that it can document low-grade metamorphic events characteristic of a specific terrane. Such events would be otherwise missed because U-Pb dates are reset at higher temperatures. Detrital zircon FT is most applicable in provenance reconstructions for evaluating source denudation rates and providing depositional age constraints in unfossiliferous successions (Carter 1999).

**Geochronology**

U-Pb geochronology is by far the most powerful and common technique for extracting source information from detrital zircon grains. It has been in use for about forty years (e.g., Ledent et al.

1964, Tatsumoto and Patterson 1964). This approach has been revolutionized with the development and use of SIMS (Ireland and Williams, this volume) and LA-ICPMS (Kosler and Sylvester, this volume), which permit rapid analysis of many grains (Kosler et al. 2002), so that large data sets useful in provenance analysis can be evaluated. Dating of individual grains potentially permits the identification of specific source rocks. However, because zircon is so refractory, a problem that may be encountered is that of recycling, such that the U-Pb age provides information about the initial source, and not about a younger recycled sedimentary source (e.g., McLennan et al. 2001). This problem can be addressed in some measure by evaluating bulk rock Zr/Sc, which becomes increasingly elevated as more zircon (the primary host for Zr) is sequestered at the expense of Sc-bearing phases lost to multiple episodes of weathering and deposition (McLennan et al. 1993). The following examples, illustrating the use of detrital zircon geochronology as a provenance indicator, are grouped by age of deposition.

***Archean.*** The geologically significant Archean Witwatersrand Supergroup in South Africa is a kilometers-thick siliciclastic package that hosts the largest known gold and uranium deposits in the world. Barton et al. (1989) determined the provenance ages for two units of the Witwatersrand and showed that the dominant source had zircon ages between 3100 and 3200 Ma (Fig. 2A). These results suggested a granitoid source NW of the basin and determined a maximum depositional age for the units at just under 3000 Ma, not unlike the results of broadly correlative quartzites in Zimbabwe (Dodson et al. 1988, Fedo and Eriksson 1996). These studies followed on the heels of a pioneering study of detrital zircons on Mount Narryer (Yilgarn Province) by Froude et al. (1983), who identified >4 Ga grains in a quartzite deposited at about 3.0 Ga (Nelson 2001). Recent work on a metaconglomerate from the nearby Jack Hills has identified a detrital grain as old as 4.404 Ga (Wilde et al. 2001), extending the terrestrial record nearly to the age of the Earth. This unit will be discussed in more detail below.

The Archean Slave Province in Canada represents a composite granite-greenstone terrane that forms part of the Canadian Shield. Sircombe et al. (2001) examined the age spectra for detrital zircons from five quartzite units that form part of the Central Slave Cover Group, which sits unconformably on ~4.0-2.9 Ga basement. Examined samples do not share a single age mode, however, significant overlap in some modes supports a shared provenance. A distinct age population in one sample suggests that it may be some 30 Myr older than the other samples despite a strong basis for lithostratigraphic correlation. Tectonic processes controlling deposition may also have been diachronous. In either case, without geochronology, the problem would not have been recognized.

In a parallel study of detrital and magmatic zircon grains from nearby granitoids from the Yangtze craton, China, Qiu et al. (2000) highlighted the complexities of interpreting zircon geochronology in geologically complex terranes that have been intruded and metamorphosed. Trondhjemite plutons yield populations of zircons at 2.95 and 2.90 Ga and younger populations at 2.75 and ~1.9 Ga. The older dates are considered to be the intrusive age and the younger ones are metamorphic ages. Detrital zircons from adjacent metapelites have abundant 2.95 Ga grains indicating that the trondhjemites were the dominant provenance. The youngest detrital zircon is 2.87 Ga, and because both the pelites and trondhjemites were metamorphosed at upper amphibolite facies at 2.75 Ga, the age of deposition can be bracketed. The metapelites also contain detrital grains >3.2 Ga providing evidence of an older Archean sialic provenance in the Yangtze craton, which had been previously thought to be Proterozoic (Qiu et al. 2000).

***Proterozoic.*** Paleoproterozoic rocks of the Nagssugtoqidian orogen in West Greenland consist dominantly of Archean gneiss protoliths reworked at upper amphibolite and granulite facies conditions (Nutman et al. 1999). The foreland to the orogen has been intruded by a set of mafic dykes dated at ~2040 Ma in advance of the main TTG plutonism and tectonism at ~1920-1800 Ma. Detrital zircon ages from two samples of allochthonous meta-pelites in the foreland sequence have ages between 2100 and 1950 Ma. Such ages suggest the presence of a presently unknown igneous provenance that coincided with intrusion of the mafic dykes (Nutman et al. 1999). Samples of quartzite

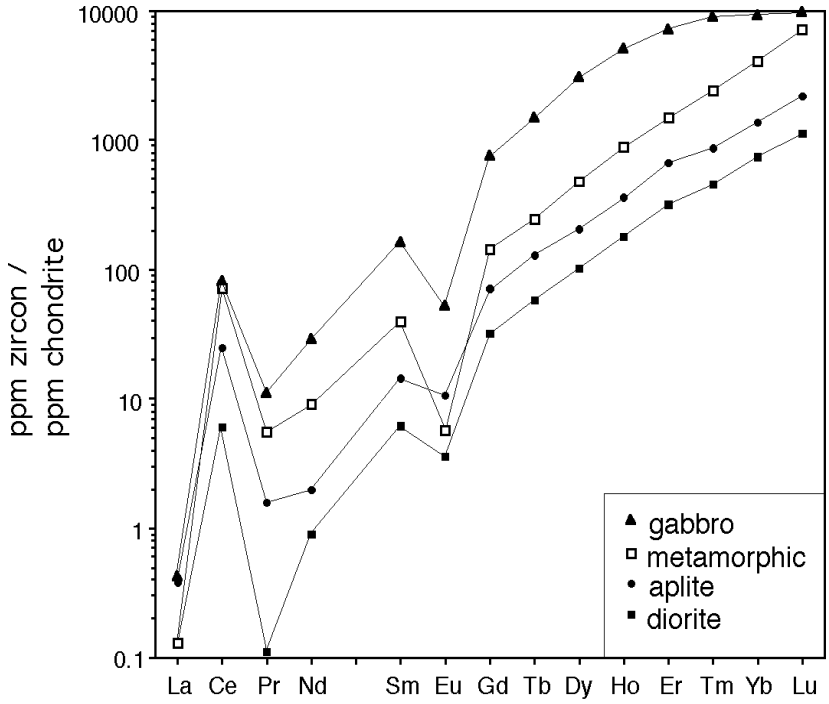


**Figure 7.** REE plots for zircons derived from compositionally disparate sources. The plots show that zircon composition is not dramatically different regardless of composition. Consequently, REE typically cannot fingerprint provenance. Note particularly the similarity of patterns for aplite, diorite, and high-grade gneiss from Sri Lanka. Such lithologies dominate the major composition of the continental crust and so are likely to represent a large fraction of detrital grains in continental sedimentary deposits. Data from Hoskin and Ireland (2000).

yielded detrital zircons with ages that include modes at 3300-3400 and ~2400 Ma, neither of which can be linked to potential sources in Greenland, which suggests derivation from a distal provenance.

Studies of detrital zircons in the Mesoproterozoic Belt Supergroup in the northwestern United States and southern Canada have implications for pre-Rodinia continental assembly. Ross et al. (1991) and Ross et al. (1992) identified detrital zircon ages from different units in Belt rocks that were westerly derived to test whether the sediment had come from known North American sources. They reported populations of detrital zircon populations of 1070-1244, 1590-1600, and 1670-1859 Ma. In particular, there are no known probable sources in western North America that could provide ~1.6 Ga detritus, and the 1070 Ma grains hint that the top of the Belt Supergroup is some 200 Myr younger than previously thought or that this represents discovery of a unit younger than the Belt. In combination with Nd isotopic data, the detrital zircon ages suggest that basement terranes of south-central Australia were joined to western Laurentia during the Mesoproterozic, and provide a template for understanding the Neoproterozoic fragmentation history of Rodinia.

***Paleozoic.*** One of the earliest papers to evaluate provenance by examining U-Pb ages of detrital zircons is that of Gaudette et al. (1981). They took a sample of Cambrian Potsdam Sandstone from the eastern flank of the Adirondack Dome, New York State, and separated four populations of zircon crystals based on color, crystal habit, and morphology and analyzed, for the first time, *single zircon grains* and small groups from the same population to extract defined provenance ages. Prior to this work, multi-crystal dissolutions yielded average provenance ages. Gaudette et al. (1981) identified provenance ages of 1180, 1320, 2100, and 2700 Ma (Fig. 8). These ages could be linked to known sources in the Superior and Southern Provinces of the Canadian Shield (2100, 2700 Ma),

Grenville Province of the Adirondacks (1180 Ma), and pre-Grenville rocks presumably from the Adirondacks (1320 Ma). A broadly similar conclusion was drawn by Johnson and Winter (1999) for lower Paleozoic quartzites from the mid-continent of North America. Besides showing the importance of imaging to define distinct zircon populations, Gaudette et al. (1981) demonstrated that sedimentary processes may sample large tracts of exposed bedrock, such that important geologic events spanning more than a billion years could be preserved and detected in a single sample of sandstone.

Fault-bounded Lower Paleozoic sedimentary rocks from Alaska examined by Gehrels et al. (1999) reveal partly overlapping and partly contrasting provenance characteristics for Cambrian and Devonian sandstones. A sample of Cambrian Adams Argillite has three main age modes, two of which indicate provenance from the Canadian Shield (1801-1868, and 2564-2687 Ma) and a third (1047-1094 Ma) may indicate derivation from the Grenville orogen in eastern Laurentia (thousands of km distant), a terrane in the Canadian Arctic, or some presently unexposed provenance. The Devonian Nation River Formation has detrital zircon populations that are Archean and Paleoproterozoic as well, and is also thought to have been derived from the Canadian Shield. It also has a population between 424-434 Ma that could have been derived from Cordilleran terranes such as the Alexander, or rocks of the Caledonian orogen, or perhaps the high Canadian Arctic (Gehrels et al. 1999).

Later Paleozoic units stretching from Ireland to Poland form part of a kilometers-thick package of sediments whose sources are critical in unraveling Carboniferous paleogeography in the region (Drewery et al. 1987). U-Pb dates from detrital zircons from fluvial sandstones collected in the United Kingdom indicate active erosion of Archean provenances, perhaps located in western Greenland or Fennoscandia and grains recycled through the Caledonian. Drewery et al. (1987) recognized that the provenance ages seemed to require a "huge" continental-scale drainage system, a conclusion that foreshadowed understanding of the massive sedimentary dispersal systems covering Rodinia and Laurentia during the Neoproterozoic and Cambrian (discussed below).

***Mesozoic and Cenozoic.*** Cawood et al. (1999) examined the U-Pb geochronology of several hundred detrital zircons from late Mesozoic arc-trench complexes in New Zealand. Most of the grains are Permian or Mesozoic in age, but sources with zircon ages extending from the Paleozoic through the Archean indicates input from a composite provenance. Cathodoluminescence (CL) imaging (Vavra 1990, Hanchar and Miller 1993, Götze et al. 1999) of grains suggests an exclusively igneous origin for the Permian and younger zircons, whereas the older grains preserve a more complex history. As with the Peninsular Ranges example (Kimbrough et al. 2001), the youngest grains approximate the time of deposition, which argues for coeval igneous activity. Cawood et al. (1999) interpreted the age spectra to mean that the zircons were derived from an Andean-type magmatic arc on the Gondwana margin in preference to exotic terranes accreted to the margin. Paleozoic and older grains represent recycled, older, Gondwanan sedimentary rocks or input from the original provenance.

The inherent complexity of provenance analysis is highlighted by studying recent sediments where sediment-transport pathways can be more easily reconstructed. Sircombe (1999) illustrated the importance of intermediate repositories by describing the presence of Neoproterozoic zircon in modern beach sand on the east Australian coastline (Fig. 3). This age component is regarded as exotic to southeastern Australia and its presence is greatest near the Mesozoic Sydney Basin. Neoproterozoic ages were also found in the Middle Triassic Hawkesbury Sandstone presently forming prominent coastal outcrops. The original source of these exotic grains remains uncertain, but an Antarctic source is strongly suspected (Sircombe 1999, Veevers 2000).

The ability of intermediate repositories to overwhelm local provenance is further illustrated by an example from modern beach sands in Western Australia (Sircombe and Freeman 1999). Despite close proximity to the extensive Archean Yilgarn craton, modern beach-sand samples were dominated by Neoproterozoic and Mesoproterozoic grains presumably derived from orogens marginal to the Yilgarn and poorly exposed at present. The paucity of Archean detritus is also seen as far back as the Ordovician in the Perth Basin (Cawood and Nemchin 2000), thereby providing important clues about the evolution of the rift margin along west Australia.

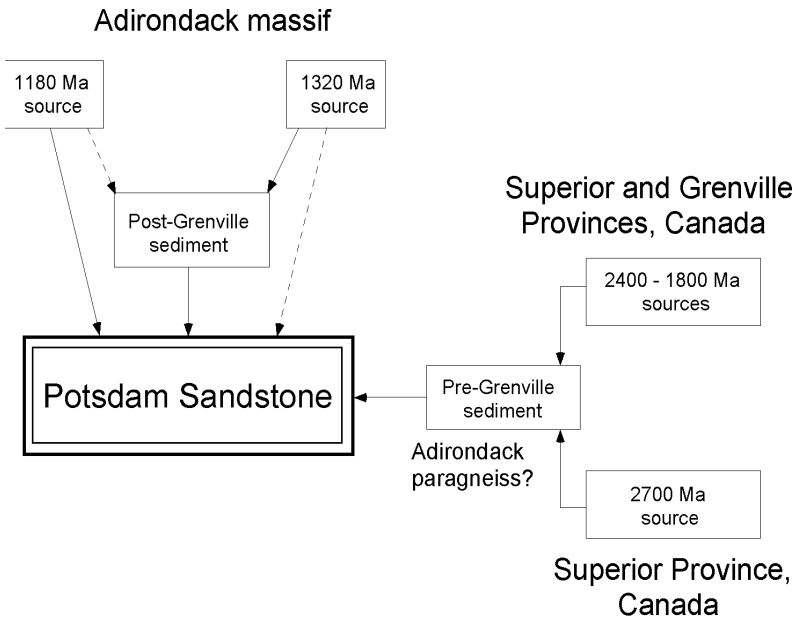


**Figure 8.** Flow diagram illustrating the different zircon provenance ages and the possible delivery pathways into the Potsdam Sandstone. The geochronology results portrayed in this diagram demonstrated for the first time the power of isolating zircon populations in provenance reconstructions. Modified from Gaudette et al. (1981).

## PALEOGEOGRAPHIC AND TECTONIC RECONSTRUCTIONS

### Introduction

Detrital zircon geochronology is a powerful tool for provenance analysis, particularly for helping to constrain paleogeography, tectonic reconstructions, and crustal evolution (e.g., Ross and Bowring 1990, Ireland 1992, Gehrels and Dickinson 1995, Gehrels et al. 1995, Knudsen et al. 1997, Gehrels and Ross 1998, Holm et al. 1998, Mahoney et al. 1999, Wallin et al. 2000, Cawood and Nemchin 2001, Gehrels et al. 2002). One example where detrital zircon geochronology has been critical in building paleogeographic and tectonic reconstructions is in the fragmentation history of the Neoproterozoic supercontinent Rodinia and the establishment of Laurentia. This topic has received considerable attention in the past decade, although there is increasingly divergent opinion concerning its configuration and timing of its break-up (e.g., Dalziel 1991, Hoffman 1991, Moores 1991, Ross et al. 1992, Brookfield 1993, Karlstrom et al. 1999, Burrett and Berry 2000, Wingate et al. 2002). Rodinia's assembly was accompanied by global collisional orogenesis that is preserved today as an extensive belt of moderate to high-grade metamorphic rocks, such as the Grenville orogeny of Laurentia and Baltica. This belt likely is preserved on other continents (e.g., Australia, Africa, China), and its presence has been used to constrain some of the reconstructions. The occurrence of high-grade metamorphic rocks at the Earth's surface today indicates uplift and erosion of tens of kilometers of crust. Erosion and denudation has continued ever since the completion of the bulk of mountain building at ~1.0 Ga. The record of this uplift and erosion should be preserved in the vestiges of a pan-Rodinian drainage system that would have delivered huge volumes of detritus to adjacent basins, located across the interior of Rodinia (and Laurentia).

**Initial studies—Shaler Supergroup**

U-Pb TIMS dating of detrital zircons was applied to assess the provenance of fluvial sandstones of the Shaler Supergroup, an early Neoproterozoic (~1.0-0.75 Ga) intracratonic basin succession preserved on the northwestern (present coordinates) margin of the North American craton (Laurentia) in the Canadian Arctic. These and correlative sandstones exhibit consistent northwesterly paleocurrents (Young and Long 1977, Miall 1976, Rainbird 1992). Following the ideas of Potter (1978) concerning "big river" systems, Young (1978) suggested that the source for these sediments may have lain in the Grenville province on the opposite side of the continent (Fig. 9). Subsequent detrital zircon geochronology supported this assertion with a significant proportion of the ages matching that of the adjacent Archean Slave province and its marginal Paleoproterozoic orogenic belts. However, the majority of the detrital zircons from the Shaler Supergroup yielded late Mesoproterozoic ages, unlike any known proximal source terrain, but quite similar to the ages of extensive synorogenic plutons in the Grenville province of southeastern Laurentia (Fig. 4). The observation confirmed the hypothesis (Young 1978) that detritus was transported approximately 3000 km northwestward from the rising Grenvillian orogeny by a pan-continental fluvial system (Rainbird et al. 1992).

Goodge et al. (2002) drew analogies to results of detrital zircon dating in the Shaler Supergroup in their analysis of Neoproterozoic and Cambrian quartzites in the Transantarctic Mountains in Antarctica. Detrital zircon populations of ~1.4 and 1.6-1.8 Ga from the Beardmore Group closely match with episodes of crust formation in Laurentia reinforcing a possible tie between East Antarctica and Laurentia in one of the original Rodinia reconstructions (e.g., SWEAT hypothesis of Moores 1991). Eastward paleocurrents in the Transantarctic Mountains preclude transport of these grains from Laurentia because this part of Antarctica had separated from Laurentia long before, according to most reconstructions (e.g., Dalziel 1997), which led to the conclusion that a 1.4 Ga source lies buried under the ice (Goodge et al. 2002).

**Regional studies—northern Cordillera**

The big-river hypothesis was tested by comparing the detrital zircon geochronology of the Shaler Supergroup with that of potentially correlative strata from the Ogilvie and Mackenzie platforms in the northern Canadian Cordillera (Rainbird et al. 1996, Rainbird et al. 1997). U-Pb TIMS analysis of 54 detrital zircons, separated from five regionally correlative samples from the Mackenzie Mountains Supergroup and the Pinguicula Group, revealed that 85% are Mesoproterozoic with a high proportion of these clustering in a range between 1.25 and 1.0 Ga (Fig. 4). Sm-Nd isotopic data from intercalated mudrocks indicated a source with relatively juvenile model ages ($T_{DM}$ = 1.74-1.54 Ga), consistent with the provenance indicated by detrital zircon geochronology. These results strongly supported the big-river model and suggested that the fluvial system was laterally extensive and may have formed a broad cratonic sheet originating from multiple sources along the length of the Grenvillian mountain front.

**Regional studies—central Cordillera**

Detrital zircon geochronology of Neoproterozoic and lowermost Cambrian rocks from sedimentary basins located along the western margin of Laurentia, and now exposed mainly in the central Cordillera of California and Nevada, yielded detrital zircons with characteristic "Grenvillian" ages (e.g., Stewart et al. 2001, Fedo and Farmer 2001). Although Stewart et al. (2001) attribute some of these ages to provenance from local volcanic centers, much of the material is considered to have derived via west-flowing rivers from the Grenville orogen, elements of which extend into west Texas and northern Mexico (Stewart et al. 2001) and beyond into the present Appalachian Mountains. These data provide further support for the big-river hypothesis and for the presence of a craton-scale fluvial blanket in Neoproterozoic and Early Cambrian times and illustrate the successful integration of sedimentological information, such as paleocurrent analysis, with U-Pb geochronology.

**Siberia**

A tectonic connection between Laurentia and Siberia was proposed by Sears and Price (1978) and Condie and Rosen (1994) and the similarities between the northern Cordillera and fold-belts along the eastern margin of Siberia have long been recognized (Khudoley and Guriev 1990). Subsequent models have been proposed but the position of Siberia remains an enigmatic component of the Rodinia supercontinent (e.g., Rainbird et al. 1998, Sears and Price 2000). Neoproterozoic (upper Riphean) sandstones of the Siberian platform share first-order stratigraphic similarities with contemporaneous sequences in Laurentia and it is possible that they were part of the same intracratonic basin before separation occurred with the break-up of Rodinia (Rainbird et al. 1996, Khudoley et al. 2001). To test this hypothesis and the "Laurentia-Siberia" connection, detrital zircons were analyzed from sandstones at three stratigraphic levels from the Riphean section (see Khudoley at al. 2001). The detrital zircon U-Pb SHRIMP age profile of the Mayamkan Formation, a fluvial arkose from the southern Sette-Daban fold belt, is almost identical to that of early Neoproterozoic fluvial sandstones of the Shaler and Mackenzie Mountains supergroups in northwestern Canada and includes a high proportion (~85%) of Mesoproterozoic zircons (Fig. 5; Rainbird et al. 1998). There is no known source region for detritus of such age in Siberia and isopachs and facies relations suggest provenance from an exotic terrane to the east. These data indicated that provenance of the late Riphean sandstones was mainly from rocks of Grenvillian age that were perhaps adjacent to an unidentified continent (Laurentia or Baltica?).

**Scotland**

Provenance of the late Mesoproterozoic to early Neoproterozoic Torridonian succession in northwest Scotland is relevant to the nature and timing of the formation and break-up of Rodinia. Previous provenance studies based on the sedimentology, geochemistry and mineralogy of these

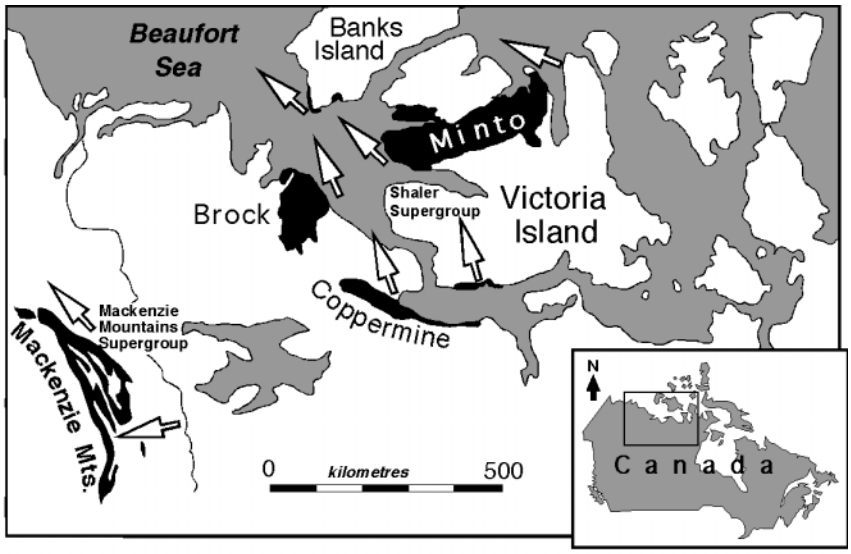


**Figure 9.** Northwestern Canada showing location of inliers containing fluvial quartz-arenites of early Neoproterozoic (1.0-0.75 Ga) age, considered to be remnants of an extensive river system originating from the Grenville orogen, some 3000 km to the southeast. Arrows represent generalized paleocurrents based on measurements of cross-bedding (minimum of 20 readings for each arrow). Modified from Rainbird et al. (1992).

relatively immature coarse clastic rocks argued for a possible influence from Laurentia, from which Scotland is now separated. Recent SHRIMP detrital zircon geochronology indicated that the lower part of the Torridonian (Stoer Group) is composed mainly of sediment weathered from proximal, late Archean (Lewisian) sources in the Hebridean block, a piece of the North Atlantic craton of Laurentia, orphaned during the opening of Iapetus (Rainbird et al. 2001). The upper part of the Torridonian (Torridon Group) exhibits more varied provenance with distinctive detrital zircon age modes at ~1.80 Ga, 1.65 Ga and 1.10 Ga. The latter two modes are considered to be characteristic of the Grenville Province in eastern Laurentia. These data, together with paleocurrents, suggest that the Torridon Group could have been deposited by a late-post Grenvillian foreland trunk river system. This is significant because the foreland basin part of the big-river system should be preserved somewhere along the great length of the Grenville thrust front.

**A cryptic Grenvillian foreland basin in the U.S. mid-continent**

Proximal parts of the big-river system may be present in a westward-tapering wedge of coarse, immature clastic red-beds of interpreted Neoproterozoic age from the subsurface of western Ohio (Shrake et al. 1991). These rocks, known as the Middle Run Formation, have been cored and imaged in subsurface seismic profiles, which reveal a wide, well-defined zone of east-dipping reflectors inferred to represent thrust structures of the Grenville front tectonic zone (COCORP Line OH-1, Hauser 1993). In the subsurface to the west is a shallow, east-dipping sequence of sedimentary strata, similar to Middle Run Formation elsewhere. Together these rocks were interpreted as the molasse phase of a previously unrecognized foreland basin to the Grenville orogen (Hauser 1993). This paleogeographic model is supported by the detrital zircon geochronology of the Middle Run Formation, which reveals that at very high percentage of the basin fill was derived from erosion of the adjacent Grenville Province (Santos et al. 2002).

A potential correlative to the Middle Run Formation is the Jacobsville sandstone, a >900-m thick succession of subarkosic to sublithic arenites, conglomerates and siltstones, which are exposed in the Keweenaw Peninsula on the south shore of Lake Superior. Tectonic uplift and provenance from the south is indicated by petrology and paleocurrent analysis (Kalliokoski 1982). Paleocurrents from fluvial units in the main part of the basin suggest axial (NE and SW) transport, perhaps related to development of a fluvial trunk system, as is commonly found in foreland basins.

**Rodinian paleogeography**

The development of Rodinia appears to have involved significant clastic sedimentation arising from tectonism and mountain building. A better-preserved analogue of the proposed Rodinian paleogeographic model comes from the supercontinent Pangea, which amalgamated during the Appalachian-Hercynian orogeny in the Carboniferous-Triassic. The paleogeography of the Laurasia block of Pangea was dominated by a series of coalescing, alluvial-deltaic wedges and axial braided rivers that filled foreland basins formed by flexural loading along the Alleghenian-Appalachian thrust front (Absaroka Sequence, Sloss 1988b). The Central Appalachian Basin is an example whose infill has been interpreted to represent an Amazon-scale drainage system (Archer and Greb 1995). As the foreland basins filled, excess detritus was transported westward, across the craton, by fluvial and eolian processes. In a similar fashion, the foreland basin to the Grenville orogen was probably overfilled with excess detritus spilling westward across Rodinia and Laurentia into basins in the interior of the supercontinent. Some of this material reached the (present-day) western margin of Laurentia in the Early Cambrian (Stewart et al. 2001, Fedo and Farmer 2001) suggesting that the pan-continental fluvial system persisted for at least 400 Myr. The rare preservation of the proximal parts of this system is in part due to Phanerozoic cover, but may also be related to subdued flexural loading, a consequence of climate-controlled erosional unroofing of the mountain front (Rainbird et al. 1997). The model predicts that correlative early Neoproterozoic cratonic sandstones on other putative pieces of the Rodinia supercontinent (e.g., Australia, Amazonia) should preserve evidence of this vast drainage system.

## IMPLICATIONS FOR EARLIEST EARTH HISTORY

Ever since their discovery by Froude et al. (1983), the >4 Ga detrital zircon grains from metasedimentary units in the Narryer Gneiss Complex, Western Australia have been the subject of speculations regarding the earliest history of Earth. As the only "direct evidence" of Earth's first 500 Myr, the mineral chemistry and isotope geochemistry of the detrital zircons in these metaconglomerates and quartzites (particularly well known from the Jack Hills) may provide a window into determining processes in the earliest Archean (Hadean), a time in which almost nothing is known.

A number of studies subsequent to Froude et al. (1983) have confirmed the presence of a small but persistent population of grains up to ~4200 Ma (Compston and Pidgeon 1986, Kober et al. 1989, Maas and McCulloch 1991, Maas et al. 1992, Amelin 1998, Fig. 1C), with a recent discovery of part of a zircon as old as 4404 Ma, with other grains >4300 Ma (Wilde et al. 2001). There is no positively identified provenance for these ancient grains, although Nelson et al. (2000) reported the discovery of >4.0 Ga xenocrysts from 2.6-2.7 Ga granitic gneisses in the adjacent Narryer and Murchison terranes and interpreted the xenocrysts to have crystallized in a granitic melt. Based principally on the notion that zircons with a Th/U > 1 crystallize in mafic melts, Amelin (1998) suggested the contribution of a mafic source component for some grains, an idea first postulated by Froude et al. (1983) because of low U concentrations in some zircons. Consequently, the source of the >4.0 Ga grains is likely to have been compositionally heterogeneous.

Wilde et al. (2001) attempted to prove an evolved granitic origin for the 4404 Ma zircon based on REE compositions, and calculated partition coefficients suggestive of LREE enrichment. Furthermore, this particular zircon has inclusions of quartz, which are also said to support a felsic origin. The implication of such a conclusion is that evolved continental crust had appeared in the Hadean (Peck et al. 2001), only about 150 Myr after the Moon-forming impact, which suggests the operation of modern-style subduction processes involving hydrated rocks (Wilde et al. 2001). Oxygen isotope analyses from very old parts of some zircons yield a $\delta^{18}O$ compositions >6.5‰, which suggests crystallization from melts that have interacted with hydrated supracrustal rocks (Wilde et al. 2001, Valley et al. 2002, Peck et al. 2001, Valley, this volume), leading to the conclusion of a cool, liquid-water covered Hadean Earth (Valley et al. 2002) that is speculated to potentially host a biosphere (Mojzsis et al. 2001). Other interpretations of the REE in zircon, in particular that of Whitehouse and Kamber (2002), indicate that application of zircon/melt partition coefficients cannot be used to unambiguously constrain melt compositions. Such a conclusion directly questions that the source magmas of the ~4.4 Ga grains were derived from subduction-derived melting of hydrated ocean crust. Furthermore, the REE patterns from the >4.0 Ga detrital zircons of the Jack Hills and Mt. Narryer metasedimentary rocks share many characteristics with lunar highland zircons, which did not form from modern subduction-like processes (Whitehouse and Kamber 2002).

Amelin et al. (1999, 2000) combined U-Pb geochronology and Hf isotopic compositions from the same Jack Hills zircon grains in order to address the earliest history of crust formation on Earth. Previous application of Sm-Nd isotopic studies to Early Archean rocks in Greenland and Canada pointed to their derivation from a depleted mantle source, but the possibility of subsequent metamorphic re-equilibration raised certain concerns (Amelin et al. 1999). In contrast, examination of Hf isotopes from Jack Hills detrital zircons up to 4.14 Ga old reveals that they did not originate from depleted mantle. Instead many grains have an Hf isotopic composition showing that they came from a source that is similar in composition to chondritic meteorites and that some had formed from anatexis of older crust (Amelin et al. 1999).

## SUMMARY

Detrital zircon analysis has grown from early varietal studies to the application of isotopic and compositional techniques, which have become powerful tools for provenance study and understanding of geological history. The age of detrital zircon, principally via U-Pb isotopic analysis, has

become particularly significant. Such ages provide vital constraints on the stratigraphy of sedimentary units. The youngest grains analyzed can, with suitable caution, provide a maximum age of deposition. Age distributions can also illuminate significant disconformities or diachroneities in stratigraphic sections that may not have been previously recognized with conventional techniques.

Assuming that the ages of detrital zircon are a suitable proxy for sedimentary provenance, detrital zircon geochronology has been applied to a wide variety of issues over a wide range of geologic time. Detrital zircon grains from Archean sedimentary units has been notably topical with the discovery of >4000 Ma zircons providing a unique opportunity to glean information about the very early Earth. Proterozoic sedimentary units have yielded zircon data of great relevance to tectonic reconstructions notably in various Laurentia and Rodinia models.

Detrital zircon data from sedimentary units from the Proterozoic to the present is often accompanied by more detailed geological history and this has served to highlight the complexities involved in provenance analysis. The importance of considering distal provenances, potentially thousands of kilometers from the site of deposition, has been strongly illustrated. The ability of a distal provenance to overwhelm representation of a local source either directly or via intermediate repositories is also a constant concern when interpreting detrital zircon data.

Complexities in natural processes are further compounded by sources of artificial bias during the research cycle from field sampling, through mineral separation, to data interpretation and display. As the application of detrital zircon analysis grows, developing procedures to mitigate potential biasing will become increasingly important and steps have been taken in this direction.

The future of detrital zircon analysis is promising. Advances in technology mean that the rate of data acquisition is increasing allowing more detailed and thorough analytical programs to be applied to a range of geologic problems. Interest in the history of the earliest Earth and continental reconstructions will provide steady demand, while the potential for integrating other sedimentological and geochemical techniques with isotopic age determination offers future dimensions for detrital zircon analysis.

## ACKNOWLEDGMENTS

We thank L. Aspler, J. Goodge, and M. Whitehouse for helpful discussions and for commenting on early versions of the paper. L. Aspler generously provided help with the production of Figure 2. Our thanks also go to J. Crowley, J.M. Hanchar, and G. Young who provided thorough and constructive comments on the manuscript. CMF acknowledges support from NSF grant EAR 99-09308. KNS acknowledges support from ARC grant DP0208797. Tectonics Special Research Centre publication #216.

## REFERENCES

Åhäll KI, Cornell DH, Armstrong R (1998) Ion probe zircon dating of metasedimentary units across the Skagerrak: new constraints for early Mesoproterozoic growth of the Baltic Shield. Precambrian Res 87:117-134

Amelin Y (1998) Geochronology of the Jack Hills detrital zircons by precise U-Pb isotope dilution analysis of crystal fragments. Chem Geol 146:25-38

Amelin Y, Lee D-C, Halliday AN, Pidgeon RT (1999) Nature of the Earth's earliest crust from hafnium isotopes in single detrital zircons. Nature 399:252-255

Amelin Y, Lee D-C, Halliday AN (2000) Early-middle Archean crustal evolution deduced from Lu-Hf and U-Pb isotopic studies of single zircons. Geochim Cosmochim Acta 64:4205-4225

Archer AW, Greb SF (1995) An Amazon-scale drainage system in the early Pennsylvanian of central North America. J Geol 103:611-628

Aspler LB, et al. (2001) Paleoproterozoic intracratonic basin processes, from breakup of Kenorland to assembly of Laurentia: Hurwitz basin, Nunavut, Canada. Sed Geol 141-142:287-318

Barton ES, et al. (1989) Provenance ages for the Witwatersrand Supergroup and the Ventersdorp contact reef: constraints from ion microprobe U-Pb ages of detrital zircons. Econ Geol 84:2012-2019

Becker H (1931) A study of heavy minerals of the Pre-Cambrian and Paleozoic rocks of the Baraboo Range, Wisconsin. J Sed Pet 1:91-95

Bernet M, Zattin M, Garver JI, Brandon MT, Vance JA (2001) Steady-state exhumation of the European Alps.

Geology 29:35-38
Berry RF, Jenner GA, Meffre S, Tubrett MN (2001) A North American provenance for Neoproterozoic to Cambrian sandstones in Tasmania. Earth Planet Sci Lett 192:207-222
Bowring SA, Grotzinger JP, Isachsen CE, Knoll AH, Pelechaty SM, Kolosov P (1993) Calibrating rates of Early Cambrian evolution. Science 261:1293-1298
Brookfield ME (1993) Neoproterozoic Laurentia-Australia fit. Geology 21:683-686
Burrett C, Berry R (2000) Proterozoic Australia-Western United States (AUSWUS) fit between Laurentia and Australia. Geology 28:103-106
Carroll D (1941) Heavy residues from some Upper Cretaceous sediments at Gingin, Western Australia. J Sed Pet 11:85-91
Carter A (1999) Present status and future source region discrimination and characterization using fission track analysis. Sed Geol 124:31-45
Carter A, Moss SJ (1999) Combined detrital-zircon fission-track and U-Pb dating: a new approach to understanding hinterland evolution. Geology 27:235-238
Cawood PA, Nemchin AA (2000) Provenance record of a rift basin: U/Pb ages of detrital zircons from the Perth Basin, Western Australia. Sed Geol 134:209-234
Cawood PA, Nemchin AA (2001) Paleogeographic development of the east Laurentian margin: constraints from U-Pb dating of detrital zircons in the Newfoundland Appalachians. Geol Soc Am Bull 113:1234-1246
Cawood PA, Nemchin AA, Leverenz A, Saeed A, Balance PF (1999) U/Pb dating of detrital zircons: implications for the provenance record of Gondwana margin terranes. Geol Soc Am Bull 111:1107-1119
Compston W, Pidgeon RT (1986) Jack Hills, evidence of more very old detrital zircons in Western Australia. Nature 321:766-769
Condie KC, Rosen MO (1994) Laurentia-Siberia revisited. Geology 22:168-170
Dalziel IWD (1991) Pacific margins of Laurentia and East Antarctica-Australia as a conjugate rift pair: evidence and implications for an Eocambrian supercontinent. Geology 19:598-601
Davis DW, Hirdes W, Schaltegger U, Nunoo EA (1994) U-Pb age constraints on deposition and provenance of Birmian and gold-bearing Tarkwaian sediments in Ghana, West Africa. Precambrian Res 67:89-107
Davis WJ, Aspler LB, Rainbird RH, Chiarenzelli JR (2000) Detrital zircon geochronology of the Proterozoic Hurwitz and Kiyuk Groups: a revised post 1.92 Ga age for deposition of the upper Hurwitz Group. GeoCanada 2000 Conf CD, Iron Leaf Communications
DeGraaff-Surpless K, Graham SA, Wooden JL, McWilliams MO (2002) Detrital zircon provenance analysis of the Great Valley Group, California: Evolution of an arc-forearc system. Geol Soc Am Bull 114:1564-1580
DeGraaff-Surpless K, McWilliams MO, Wooden JL, Ireland TR (2000) Limitations of detrital zircon data for provenance analysis: an example from the Methow Basin, Washington and British Columbia. Geol Soc Am Abstr Progr 32:9
Dill HG (1995) Heavy mineral response to the progradation of an alluvial fan: implications concerning unroofing of source area, chemical weathering and palaeo-relief (Upper Cretaceous Parkstein fan complex, SE Germany). Sed Geol 95:39-56
Dodson MH, Compston W, Williams IS, Wilson JF (1988) A search for ancient detrital zircons in Zimbabwean sediments. J Geol Soc London 145:977-983
Drewery S, Cliff RA, Leeder MR (1987) Provenance of Carboniferous sandstones from U-Pb dating of detrital zircons. Nature 325:50-53
Dunkl I, Di Giulio A, Kuhlemann J (2001) Combination of single-grain fission-track chronology and morphological analysis of detrital zircon crystals in provenance studies—sources of the Macigno Formation (Apennines, Italy). J Sed Res 71:515-525
Fedo CM, Eriksson KA (1996) Stratigraphic framework of the ~3.0 Ga Buhwa greenstone belt: a unique stable-shelf succession in the Zimbabwe Archean craton. Precambrian Res 77:161-178
Fedo CM, Farmer GL (2001) Constraints on the evolution of the Cordilleran margin from detrital zircon analyses in the middle member Wood Canyon Formation, Marble Mountains, southeastern California. Geol Soc Am Abstr Progr 33:A-223
Froude DO, Ireland TR, Kinny PD, Williams IS, Compston W, Williams IR, Myers JS (1983) Ion microprobe identification of 4,100–4,200 Myr-old terrestrial zircons. Nature 304:616-618
Galbraith RF, Green PF (1990) Estimating the component ages in a finite mixture. Nuclear Tracks Rad Measure 17:197-206
Garzanti E, Vezzoli G, Andò S, Castiglioni G (2001) Petrology of rifted-margin sand (Red Sea and Gulf of Aden, Yemen). J Geol 109:277-297
Garver JI, Brandon MT (1994) Fission-track ages of detrital zircons from Cretaceous strata, southern British columbia: implications for the Baja BC hypothesis. Tectonics 13:401-420
Gatehouse RD, Williams IS, Pillans BJ (2001) Finger-printing windblown dust in southeastern Australia soils by uranium-lead dating of detrital zircon. Austral J Soil Res 39:7-12

Gaudette HE, Vitrac-Michard A, Allègre CJ (1981) North American Precambrian history recorded in a single sample: high-resolution U-Pb systematics of the Potsdam Sandstone detrital zircons, New York State. Earth Planet Sci Lett 54:248-260

Gehrels GE (2000) Introduction to detrital zircon studies of Paleozoic and Triassic strata in western Nevada and northern California. Geol Soc Am Spec Paper 347:1-17

Gehrels GE, Dickinson WR (1995) Detrital zircon provenance of Cambrian to Triassic miogeoclinal and eugeoclinal strata in Nevada. Am J Sci 295:18-48

Gehrels GE, Ross GM (1998) Detrital zircon geochronology of Neoproterozoic to Permian miogeoclinal strata in British Columbia and Alberta. Can J Earth Sci 35:1380-1401

Gehrels GE, Dickinson WR, Ross GM, Stewart JH, Howell DG (1995) Detrital zircon reference for Cambrian to Triassic miogeoclinal strata of western North America. Geology 23:831-834

Gehrels GE, Johnsson MJ, Howell DG (1999) Detrital zircon geochronology of the Adams Argillite and Nation River Formation, east-central Alaska, USA. J Sed Res 69:135-144

Gehrels GE, Stewart JH, Ketner KB (2002) Cordilleran-margin quartzites in Baja California—implications for tectonic transport. Earth Planet Sci Lett 199:201-210

Goodge JW, Myrow P, Williams IS, Bowring SA (2002) Age and provenance of the Beardmore Group, Antarctica: constraints on Rodinia supercontinent breakup. J Geol 110:393-406

Götze J, Kempe U, Habermann D, Nasdala L, Neuser RD, Richter DK (1999) High-resolution cathodoluminescence combined with SHRIMP ion probe measurements of detrital zircons. Mineral Mag 62:179-187

Griffin WL, et al. (2000) The Hf isotope composition of cratonic mantle: LAM-MC-ICPMS analysis of zircon megacrysts in kimberlites. Geochim Cosmochim Acta 64:133-147

Hallsworth CR, Morton AC, Claoué-Long J, Fanning CM (2000) Carboniferous sand provenance in the Pennine Basin, UK: constraints from heavy mineral and detrital zircon age data. Sed Geol 137:147-185

Hanchar JM, Miller CF (1993) Zircon zonation patterns as revealed by cathodoluminescence and backscattered electron images: implications for interpretation of complex crustal histories. Chem Geol 110:1-13

Hauser EC (1993) Grenville foreland thrust belt hidden beneath the U.S. midcontinent. Geology 21:61-64

Heaman LM, LeCheminant AN (1993) Paragenesis and U-Pb systematics of baddeleyite ($ZrO_2$). Chem Geol 110:95-126

Heaman L, Parrish RR (1991) U-Pb geochronology of accessory minerals. *In* Heaman L, Ludden J (eds) Applications of Radiogenic Isotope Systems to Problems in Geology. Mineral Assoc Can Short Course Handbook 19:59-102

Hoffman PF (1991) Did the breakout of Laurentia turn Gondwanaland inside-out? Science 252:1409-1412

Holland HD, Gottfried D (1955) The effect of nuclear radiation on the structure of zircon. Acta Crystallogr 8:291-300

Holm D, Schneider D, Coath CD (1998) Age and deformation of Early Proterozoic quartzites in the southern Lake Superior region: implications for extent of foreland deformation during final assembly of Laurentia. Geology 26:907-910

Hoskin PWO, Ireland TR (2000) Rare earth element chemistry of zircon and its use as a provenance indicator. Geology 28:627-630

Hubert JF (1962) A zircon-tourmaline-rutile maturity index and the interdependence of the composition of heavy mineral assemblages with the gross composition and texture of sandstones. J Sed Pet 32:440-450

Ireland TR (1992) Crustal evolution of New Zealand: evidence form age distributions of detrital zircons in Western Province paragneisses and Torlesse greywacke. Geochim Cosmochim Acta 56:911-920

Jessberger EK, Dominik B, Staudacher T, Herzog GF (1980) $^{40}$Ar-$^{39}$Ar ages of Allende. Icarus 42:380-405

Johnson CM, Winter BL (1999) Provenance analysis of lower Paleozoic cratonic quartz arenites of the North American mid-continent region: U-Pb and Sm-Nd isotope geochemistry. Geol Soc Am Bull 111:1723-1738

Kalliokoski J (1982) Jacobsville sandstone. *In* Geology and Tectonics of the Lake superior Basin. Wold RJ, Hinze WJ (eds) Geol Soc Am Memoir 156:147-155

Karlstrom KE, Harlan SS, Williams ML, McLelland J, Geissman JW, Åhäll K-I (1999) Refining Rodinia: Geologic evidence for the Australia-Western U.S. connection in the Proterozoic. Geol Soc Am Today 9:1-7

Khudoley AK, Guriev GA (1990) South Verkhoyansk and Cordillera—a comparative analysis. Soviet Geol N6:67-76 (in Russian)

Kimbrough DL, et al. (2001) Forearc-basin sedimentary response to rapid Late Cretaceous batholith emplacement in the Peninsular Ranges of southern and Baja California. Geology 29:491-494

Kinny PD, Wijbrans JR, Froude DO, Williams IS, Compston W (1990) Age constraints on the geological evolution of the Narryer Gneiss Complex, Western Australia. Austral J Earth Sci 37:51-69

Kober B, Pidgeon RT, Lippolt HJ (1989) Single-zircon dating by stepwise Pb-evaporation constrains the Archean history of detrital zircons from the Jack Hills, Western Australia. Earth Planet Sci Lett 91:286-296

Kosler J, Fonneland H, Sylvester P, Turbrett M, Pedersen R-B (2002) U-Pb dating of detrital zircons for sediment provenance studies—a comparison of laser ablation ICPMS and SIMS techniques. Chem Geol 182:605-618

Knudsen T-L, Andersen T, Whitehouse MJ, Vestin J (1997) Detrital zircon ages from southern Norway—implications for the Proterozoic evolution of the southwestern Baltic Shield. Contrib Mineral Petrol 130:47-58

Larsen LH, Poldervaart A (1957) Measurement and distribution of zircons in some granitic rocks of magmatic origin. Mineral Mag 31:544-564
Ledent D, Patterson C, Tilton GR (1964) Ages of zircon and feldspar concentrates from North American beach and river sands. J Geol 72:112-122
Loi A, Dabard MP (1997) Zircon typology and geochemistry in the paleogeographic reconstruction of the Late Ordovician of Sardinia (Italy). Sed Geol 112:263-279
Liu T-K, Hsieh S, Chen Y-G, Chen W-S (2001) Thermo-kinetic evolution of the Taiwan oblique-collision mountain as revealed by zircon fission-track dating. Earth Planet Sci Lett 186:45-56
Maas R, McCulloch MT (1991) the provenance of Archean metasediments ion the Narryer Gneiss Complex, Western Australia: trace element geochemistry, Nd isotopes, and U-Pb ages for detrital zircons. Geochim Cosmochim Acta 55:1915-1932
Maas R, Kinny PD, Williams IS, Froude DO, Compston W (1992) The Earth's oldest known crust: a geochronological and geochemical study of 3900-4200 Ma old detrital zircons from Mt. Narryer and Jack Hills, Western Australia. Geochim Cosmochim Acta 56:1281-1300
Mahoney JB, Mustard PS, Haggart JW, Friedman RM, Fanning CM, McNicoll VJ (1999) Archean zircons in Cretaceous strata of the western Canadian Cordillera: the "Baja B.C." hypothesis fails a crucial test. Geology 27:195-198
McLennan SM, Hemming S, McDaniel DK, Hanson GN (1993) Geochemical approaches to sedimentation, provenance, and tectonics. Geol Soc Am Spec Paper 284:21-40
McLennan SM, Bock B, Compston W, Hemming SR, McDaniel DK (2001) Detrital zircon geochronology of Taconian and Acadian foreland sedimentary rocks in New England. J Sed Res 71:305-317
McNaughton NJ, Rasmussen B, Fletcher IR (1999) SHRIMP uranium-lead dating of diagenetic xenotime in siliciclastic sedimentary rocks. Science 285:78-80
Miall AD (1976) Proterozoic and Paleozoic geology of Banks Island, Arctic Canada. Geol Surv Can Bull 258:77
Mojzsis SM, Harrison TM, Pidgeon RT (2001) Oxygen-isotope evidence from ancient zircons for liquid water at the Earth's surface 4,300 Myr ago. Nature 409:178-181
Moores EM (1991) Southwest U.S.–East Antarctic (SWEAT) connection: An hypothesis. Geology 19:425-428
Morton A, Clauoé-Long JC, Berge C (1996) SHRIMP constraints on sediment provenance and transport history in the Mesozoic Statfjord Formation, North Sea. J Geol Soc London 153:915-929
Morton AC, Hallsworth CR (1994) Identifying provenance-specific features of detrital heavy mineral assemblages in sandstones. Sed Geol 90:241-256
Murakami T, Chakoumakos BC, Ewing RC, Lumpkin GR, Weber WJ (1991) Alpha-decay event damage in zircon. Am Mineral 76:1510-1532
Nelson DR (2001) An assessment of the determination of depositional ages for Precambrian clastic sedimentary rocks by U-Pb dating of detrital zircon. Sed Geol 141-142:37-60
Nelson DR, Robinson BW, Myers JS (2000) Complex geological histories extending for •4.0 Ga deciphered from xenocryst zircon microstructures. Earth Planet Sci Lett 181:89-102
Nutman AP (2001) On the scarcity of >3900 Ma detrital zircons in •3500 Ma metasediments. Precambrian Res 105:93-114
Nutman AP, Kalsbeek F, Marker M, van Gool JAM, Bridgwater D (1999) U-Pb zircon ages of Kangâmiut dykes and detrital zircons in metasediments in the Paleoproterozoic Nagssugtoqidian Orogen (West Greenland) clues to the pre-collisional history of the orogen. Precambrian Res 93:87-104
Owen MR (1987) Hafnium content of detrital zircons: a new tool for provenance study. J Sed Pet 57:824-830
Patterson JG, Heaman LM (1990) Geochronological constraints on the depositional age of the Hurwitz Group, NWT. Geol Assoc Can Abstr 5:A102
Peck WH, Valley JW, Wilde SA, Graham CG (2001) Oxygen isotope ratios and rare earth elements in 3.3 to 4.4 Ga zircons: ion microprobe evidence for high d18O continental crust and oceans in the Early Archean. Geochim Cosmochim Acta 65:4215-4229
Pell SD, Chivas AR, Williams IS (1999) Great Victoria Desert: development and sand provenance. Austral J Earth Sci 46:289-299
Pentland A (1931) The heavy minerals of the Franconia and Mazomanie Sandstones, Wisconsin. J Sed Pet 1:23-26
Potter PE (1978) Significance and origin of big rivers. J Geol 86:13-33
Press WH, Flannery BP, Teukolsky SA Vetterling WT (1986) Numerical Recipes: The Art of Scientific Computing. Cambridge University Press, Cambridge, UK, 818 p
Pupin JP (1980) Zircon and granite petrology. Contrib Mineral Petrol 73:207-220
Qiu YM, Gao S, McNaughton NJ, Groves DI, Ling W (2000) First evidence of >3.2 Ga continental crust in the Yangtze craton of south China and its implications for Archean crustal evolution and Phanerozoic tectonics. Geology 28:11-14
Rainbird RH (1992) Analysis of a large scale braid-plain quartz-arenite from the Neoproterozoic Shaler Group, Victoria Island, Northwest Territories, Canada. Can J Earth Sci 29:2537-2554

Rainbird RH, Heaman LM, Young GM (1992) Sampling Laurentia: Detrital zircon geochronology offers evidence for an extensive Neoproterozoic river system originating from Grenville orogen. Geology 20:351-354
Rainbird RH, Jefferson CW, Young GM (1996) The early Neoproterozoic sedimentary Succession B of northwest Laurentia: correlations and paleogeographic significance. Geol Soc Am Bull 108:454-470
Rainbird RH, et al. (1997) Pan-continental River System Draining Grenville Orogen Recorded by U-Pb and Sm-Nd Geochronology of Neoproterozoic Quartz-arenites and Mudrocks, Northwestern Canada. J Geol 105:1-18
Rainbird RH, et al. (1998) U-Pb geochronology of Riphean sandstone and gabbro from southeast Siberia and its bearing on the Laurentia-Siberia connection. Earth Planet Sci Lett 164:409-420
Rainbird RH, Hamilton MA, Young GM (2001) Detrital zircon geochronology and provenance of the Torridonian, NW Scotland. J Geol Soc London 158:15-27
Rassmussen B, Bengston S, Fletcher IR, McNaughton NJ (2002) Discoidal impressions and trace-like fossils more than 1200 million years old. Science 296:1112-1115
Roback RC, Walker NW (1995) Provenance, detrital zircon U-Pb geochronometry, and tectonic significance of Permian to Lower Triassic sandstone in southeastern Quesnellia, British Columbia and Washington. Geol Soc Am Bull 107:665–675
Robb LJ, Davis DW, Kamo SL (1990) U-Pb ages on single detrital zircon grains from the Witwatersrand basin, South Africa: constraints on the age of sedimentation and on the evolution of granites adjacent to the basin. J Geol 98:311-328
Roddick JC, Bevier ML (1995) U-Pb dating of granites with inherited zircon: conventional and ion microprobe results from two Paleozoic plutons, Canadian Appalachians. Chem Geol 119:307-329
Ross GM, Bowring SA (1990) Detrital zircon geochronology of the Windermere Supergroup and the tectonic assembly of the southern Canadian Cordillera. J Geol 98:879-893
Ross GM, Parrish RR, Dudàs FÖ (1991) Provenance of the Bonner formation (Belt Supergroup), Montana: insights from U-Pb and Sm-Nd analyses of detrital minerals. Geology 19:340-343
Ross GM, Parrish RR, Winston D (1992) Provenance and U-Pb geochronology of the Mesoproterozoic Belt Supergroup (northwestern United States): implications for the age of deposition and pre-Panthalassa plate reconstructions. Earth Planet Sci Lett 113:57-76
Sambridge MS, Compston W (1994) Mixture modelling of multi-component data sets with application to ion-probe zircon ages. Earth Planet Sci Lett 128:373-390
Santos JOS, Hartmann LA, McNaughton NJ, Easton RM, Rea RG, Potter PE (2002) Sensitive high resolution ion microprobe (SHRIMP) detrital zircon geochronology provides new evidence for a hidden Neoproterozoic foreland basin to the Grenville Orogen in the eastern Midwest U.S. Can J Earth Sci 39:1505-1515
Schäfer J, Dörr W (1997) Heavy-mineral analysis of detrital zircons: a new approach to provenance study (Saxothuringian flysch, Germany). J Sed Res 67:451-461
Schiøtte L, Compston W, Bridgwater D (1988) Late Archean ages for the deposition of clastic sediments belonging to the Malene supracrustals, southern West Greenland: evidence from an ion probe U-Pb zircon study. Earth Planet Sci Lett 87:45-58
Scott DJ, Gauthier G (1996) Comparison of TIMS (U-Pb) and laser ablation microprobe ICP-MS (Pb) techniques for age determination of detrital zircons from Paleoproterozoic metasedimentary rocks from northeastern Laurentia, Canada, with tectonic implications. Chem Geol 131:127-142
Sears JW, Price RA (1978) The Siberian connection: a case for Precambrian separation of the North American and Siberian cratons. Geology 6:267-270
Sears JW, Price RA (2000) New look at the Siberian connection: no SWEAT. Geology 28:423-426
Shrake DL, Carlton RW, Wickstron LH, Potter PE, Richard BH, Wolfe PJ, Sitler GM (1991). Pre-Mount Simon basin under the Cincinnati Arch. Geology 19:139-142
Silver L (1963) The relation between radioactivity and discordance in zircons. National Academy of Sciences–National Research Council Publ 1075:34-52
Silverman (1986) Density Estimation for Statistics and Data Analysis. Chapman and Hall, London, 175 p
Sircombe KN (1999) Tracing provenance through the isotope ages of littoral and sedimentary detrital zircon, eastern Australia. Sed Geol 124:47-67
Sircombe KN (2000a) The utility and limitations of binned frequency histograms and probability density distributions for displaying absolute age data. Geol Survey Can–Current Res 2000:11
Sircombe KN (2000b) Quantitative comparison of large sets of geochronological data using multivariate analysis: a provenance study example from Australia. Geochim Cosmochim Acta 64:1593-1616
Sircombe KN, Freeman MJ (1999) Provenance of detrital zircons on the Western Australian coastline: implications for the geologic history of the Perth basin and denudation of the Yilgan craton. Geology 27:879-882
Sircombe KN, Bleeker W, Stern RA (2001) Detrital zircon geochronology and grain-size analysis of a ~2800 Ma Mesoarchean proto-cratonic cover succession, Slave Province, Canada. Earth Planet Sci Lett 189:207-220
Sircombe KN, Stern RA (2002) An investigation of artificial biasing in detrital zircon U-Pb geochronology due to magnetic separation in sample preparation. Geochim Cosmochim Acta 66:2379-2397

Sloss LL (1988a) Forty years of sequence stratigraphy. Geol Soc Am Bull 100:1661-1665
Sloss LL (1988b) Tectonic evolution of the craton in Phanerozoic time. *In* Sedimentary Cover—North American Craton. Sloss LL (ed) Geol Soc Am, Boulder, Colorado, D-2
Smith M, Gehrels GE (1994) Detrital zircon geochronology and the provenance of the Harmony and Valmy Formations, Roberts Mountains allochthon, Nevada. Geol Soc Am Bull 106:968-979
Stewart JH, Gehrels GE, Barth AP, Link PK, Christie-Blick N, Wrucke CT (2001) Detrital zircon provenance of Meosproterozoic to Cambrian arenites in the western United States and northwestern Mexico: Geol Soc Am Bull 113:1343-1356
Tatsumoto M, Patterson C (1964) Age studies of zircon and feldspar concentrates from the Franconia Sandstone. J Geol 2:232-242
Twenhofel WH (1941) The frontiers of sedimentary mineralogy and petrology. J Sed Pet 11:53-63
Tyler SA (1931) The petrography of some bottom samples from the North Pacific Ocean. J Sed Pet 1:12-22
Valley JW, Peck WH, King EM, Wilde SA (2002) A cool early Earth. Geology 30:351-354
Vavra G (1990) On the kinematics of zircon growth and its petrogenetic significance: a cathodoluminescence study. Contrib Mineral Petrol 106:90-99
Vavra G (1993) A guide to quantitative morphology of accessory zircon. Chem Geol 110:15-28
Veevers JJ (2000) Billion-year Earth History of Australia and Neighbours in Gondwana. GEMOC Press, Sydney, 388 p
Wallin ET, Noto RC, Gehrels GE (2000) Provenance of the Antelope Mountain Quartzite, Yreka terrane, California: evidence for large-scale late Paleozoic sinistral displacement along the North American Cordilleran margin and implications for the mid-Paleozoic fringing-arc model. Geol Soc Am Spec Paper 347:119-132
Whitehouse MJ, Kamber BS (2002) On the overabundance of light rare earth elements in terrestrial zircons and its implications for Earth's earliest magmatic differentiation. Earth Planet Sci Lett 204:333-346
Wilde SA, Valley JW, Peck WH, Graham CM (2001) Evidence from detrital zircons for the existence of continental crust and oceans on Earth 4.4 Gyr ago. Nature 409:175-178
Williams IS (1992) Some observations on the use of zircon U-Pb geochronology in the study of granitic rock. Trans Royal Soc Edinburgh 83:447-458
Wilson JF, Bickle MJ, Hawkesworth CJ, Martin A, Nisbet E, Orpen JL (1978) Granite-greenstone terranes of the Rhodesian Archean craton. Nature 271:23-27
Wingate MTD, Pisarevsky SA, Evans DAD (2002) Rodinia connections between Australia and Laurentia: no SWEAT, no AUSWUS? Terra Nova 14:121-128
Young GM (1978) Proterozoic (<1.7 b.y.) stratigraphy, paleocurrents and orogeny in North America. Egyptian J Geol 22:45-64
Young GM, Long DGF (1977) A tide-influenced delta complex in the upper Proterozoic Shaler Group, Victoria Island, Canada. Can J Earth Sci 14:2246-2261
Young GM, Long DGF, Fedo CM, Nesbitt HW (2001) Paleoproterozoic Huronian basin: product of a Wilson cycle punctuated by glaciations and a meteorite impact. Sed Geol 141/142:233-254

# 11 High-Precision U-Pb Zircon Geochronology and the Stratigraphic Record

**Samuel A. Bowring**

*Department of Earth, Atmospheric and Planetary Sciences,*
*Massachusetts Institute of Technology 54-1126*
*Cambridge, Massachusetts 02139*

**Mark D. Schmitz**

*Department of Terrestrial Magnetism,*
*Carnegie Institution of Washington*
*Washington, D.C. 20015*

## INTRODUCTION

The rock stratigraphic record exists as a rich, albeit complex and incomplete repository of Earth history, tracing the processes of biological evolution, climate change, oceanic and atmospheric chemistry, sea-level fluctuations, mountain-building and erosion, and basin subsidence. Without a detailed and precise temporal framework, however, the richness of the record, including global stratigraphic correlations, evaluation of cyclicity and rates of regional and global change, major sedimentary depositional hiatuses, and biological extinctions cannot be fully exploited.

In the past two decades major advances in U-Pb zircon geochronology have allowed us to evaluate the distribution of time in the rock record and rates of geological processes with unprecedented precision (see Parrish et al., this volume; Davis et al., this volume). While much work has focused on major transitions in Earth history, there is considerable promise for a highly calibrated time scale from the Neoproterozoic to Holocene that will permit increasingly more sophisticated questions to be addressed using the rock record. It has been long appreciated that there are dramatic events in the diversification and extinction of life such as the Cambrian radiation, the end-Permian extinction, and the end-Cretaceous extinction. However, important questions remain regarding the tempo and causes of evolutionary radiation and extinction. For example, what are the durations of mass extinctions? How long does ecological recovery take following a major extinction? Do evolutionary radiations correlate with changes in chemistry and temperature of the ocean-atmosphere system and global climate? Are there relationships between evolution and the aggregation and dispersal of supercontinents? Are apparently abrupt isotopic excursions in seawater chemistry globally synchronous and of similar duration? Although the biostratigraphic record has been historically used to address these questions, we are now moving into an era where an essential test of correlation and tempo will and must be high-precision geochronology of volcanic rocks interlayered with fossil-bearing rocks. This means moving beyond calibration of the time scale to understanding the detailed distribution of time in the rock record.

Volcanic rocks in the form of thin air-fall tuffs, regional ash-flow tuffs, and lavas are the most useful temporal markers in the geologic record. Volcanic rocks have long been appreciated as important markers even prior to the advent of high-precision dating. In many cases the physical volcanology and mineral chemistry of ash-beds have been used for regional correlation (e.g., Haynes 1994). Volcanic debris is often injected into the stratosphere by explosive eruption and can be transported hundreds to thousands of kilometers before being deposited. Individual ash layers in the rock record often range in thickness from a few millimeters to as much as several meters. Geochronological data obtained from such units can be used to estimate rates of sediment accumulation and biological evolution, calibrate excursions recorded in chemostratigraphic proxies, cali-

1529-6466/03/0053-0011$05.00

brate molecular clocks, constrain the timing of tectonic events, and confirm or deny problematic lithostratigraphic correlations (e.g., Ordovician bentonites). In the past decade the recognition and significance of volcanic ash-beds in the rock record has gained wider appreciation, although it is our opinion that many are still unrecognized.

In a broad sense the time scale is well-enough resolved through biostratigraphy and a coarse framework of absolute dates to predict the age of a volcanic rock interlayered with fossil-bearing rocks to within 5-10 Myr of its true age. However it is now possible to determine the age of Phanerozoic volcanic rocks to a precision approaching 0.1% or better, allowing a much finer resolution of time and process in the rock record. At the same time, by pushing the current analytical limits it has become necessary to examine in detail all possible sources of analytical uncertainty as well as geological complexity that can affect high-precision U-Pb geochronology, before we can determine the ultimate resolving power of the method. This paper will review the current state of the application of U-Pb geochronology to the stratigraphic record, evaluate the current limitations, and discuss the future.

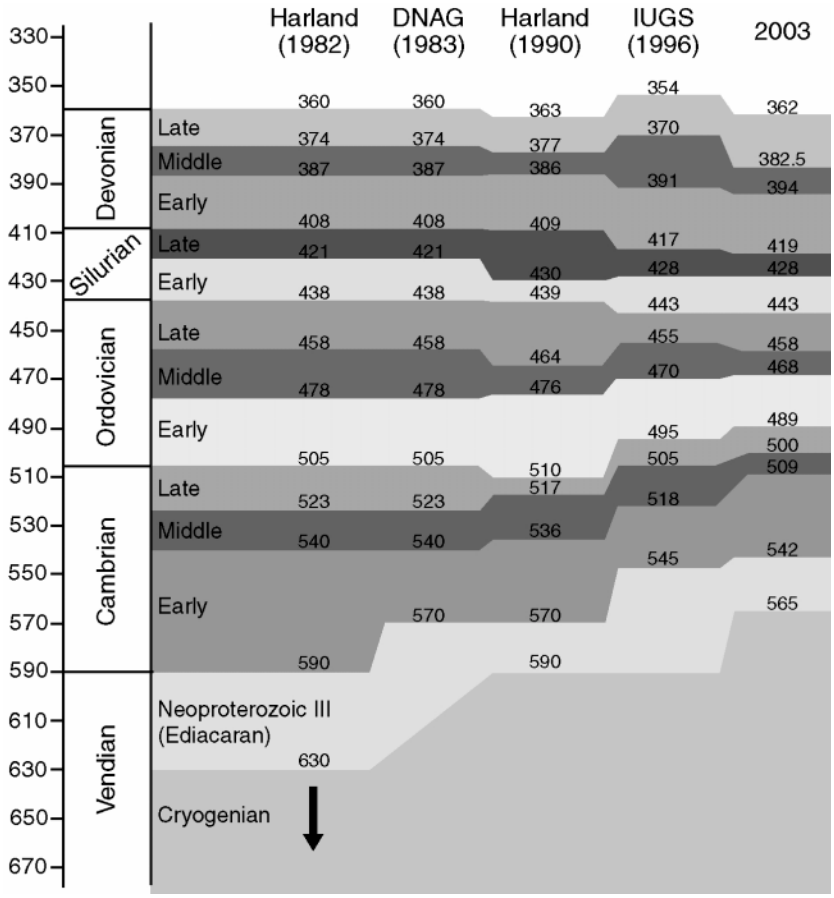


**Figure 1.** Evolution of Vendian-Early Paleozoic time scale since 1982. Modified after Bowring and Erwin (1998) with Silurian and Devonian constraints (2003 column) from Tucker et al (1990, 1998). IUGS from Gradstein and Ogg (1996).

## THE GEOLOGIC TIME SCALE

High-precision geochronology is revolutionizing our understanding of how time is distributed in the Vendian to Mesozoic rock record (Fig. 1). The unification of paleontological and geochronological records has allowed the development of a new field best described as quantitative biostratigraphy. For much of the Paleozoic rock record this field is in its infancy, and it is widely recognized that a comprehensive absolute time scale for much of the Paleozoic and Mesozoic, including some of the major extinctions, is far from complete. There have been a number of notable compilations of available geochronological constraints on the distribution of time in the rock record (e.g., Harland et al. 1990, Young and Laurie 1996). Unfortunately, in an attempt to include all available data, many of these time scales have typically averaged several dates obtained by different techniques and often of highly variable quality. The result, which is propagated into subsequent publications, is a time scale that is often poorly calibrated in absolute terms. However, the numbers of calibration studies and their geochronological resolution have increased in the past decade, which is in turn stimulating paleontological and paleoenvironmental research.

The geological time scale has two components: (1) a chronostratigraphic scale based on the lithostratigraphic record of geological and biological events established through the principles of superposition, which is calibrated in terms of (2) a geochronometric scale based on isotopic ages. The bounds of chronostratigraphic units, like the base of the Cambrian or the end-Permian and end-Cretaceous extinctions, are defined by the first appearance of diagnostic fossils in defined sections or GSSPs (Global Standard Stratotype-section and Point). Geochronometric calibration of a relative, chronostratigraphic time scale is conceptually straightforward. In the simplest case, a dateable volcanic rock occurs at or very close to a point in a stratigraphic section chosen as a global stratotype for the boundary between two geological intervals. Unfortunately, this situation is not common, and more often calibration requires the dating of rocks in sections other than the stratotype which are then correlated to the stratotype by means of biostratigraphy, chemostratigraphy, and magnetostratigraphy. In many cases the age of the boundary is estimated by interpolation.

It cannot be assumed that the first or last appearance of a fossil occurs at exactly the same time in different depositional settings. The terminal Neoproterozoic-Cambrian boundary is an excellent example. The boundary is formally defined as a point in rock in a stratigraphic section located in southeastern Newfoundland that coincides with the first appearance of a distinctive trace-fossil called *Phycodes pedum,* now known as *Treptictnus pedum* (Landing 1994). However, there are no volcanic rocks close to the boundary in Newfoundland. Consequently, the age of the boundary can only be calibrated through correlation with other sections that contain dateable rocks.

### Proxies for radiometric geochronology: chemostratigraphy

The use of chemostratigraphy as a tool for global correlation assumes that carbonate rocks precipitated from seawater record a global signal of the geochemistry of seawater at a given time. Thus, the variation in chemical signatures of carbonates such as carbon, oxygen, and strontium isotopes with stratigraphic position can be used to correlate between sections (e.g., Kaufman et al. 1997, Brasier et al. 1996, Pelechaty et al. 1996, Bartley 1998). This is especially useful for late Neoproterozoic and earliest Cambrian rocks that contain a paucity of biostratigraphically useful fossils. For example, the Newfoundland sections lack the small shelly fossils and the well-defined carbon-isotopic record that is found in rocks of similar age elsewhere. Other sections in northwestern Canada (Narbonne et al. 1994), northeastern Siberia (Knoll et al. 1995), and Namibia (Grotzinger et al. 1995) contain carbonates, fossils, and/or ash-beds which have been used to support the view that the base of the Cambrian Period is approximately coincident in time (Landing 1994) on a global scale. However, given interbasinal differences in accumulation rates, diagenesis, tectonic setting, unconformities, preservation potential, and first appearance of diagnostic fossils, detailed correlation of chemostratigraphic signals requires precise geochronology. In particular, evaluating the po-

tential of global diachroneity of a biostratigraphic boundary can only be done in the context of high-precision geochronology. A crucial issue in the evaluation of abrupt isotopic excursions such as are associated with the Neoproterozoic-Cambrian boundary and the Permo-Triassic boundary is their duration. Because accumulation rates can vary widely, the only way to test the global synchroneity and determine the duration of isotopic excursions is with high-precision geochronology.

The end-Permian extinction is characterized by an abrupt disappearance of Permian fossils followed by recovery to Triassic assemblages (Erwin 1993, 1994; Jin et al. 2000, Erwin et al. 2002). At the type section at Meishan, China, the boundary is marked by bentonites interlayered with fossil-bearing carbonate rocks. Chemostratigraphic studies from many different sections globally, both marine and terrestrial, indicate a shift in carbon isotopic values of at least -4‰ from the late Permian to the Early Triassic. However, whether the isotopic shift exactly coincides with the extinction and whether the extinction is globally synchronous are still open questions, resolvable only with the integration of high-precision geochronology, chemostratigraphy, and paleontology (Jin et al. 2000) from multiple stratigraphic sections.

## GEOCHRONOLOGICAL TECHNIQUES

Modern high-precision geochronological studies associated with calibration of the time scale rely on two principal geochronological methods: $^{40}Ar/^{39}Ar$ in the minerals biotite, hornblende, and sanidine, and U-Pb in zircons and less commonly baddeleyite, monazite and xenotime. Each system has strengths and limitations (above all the availability of appropriate minerals), but many silica-rich lavas and tuffs can be dated using either or both methods. The most profound differences between the two methods are that the U-Pb method exploits two independent chronometers ($^{238}U$-$^{206}Pb$, and $^{235}U$-$^{207}Pb$) that can be compared to evaluate open-system behavior, and when measured by isotope dilution can be gravimetrically calibrated to high precision and accuracy, whereas the Ar-Ar method, based on the singular decay of $^{40}K$-$^{40}Ar$, can partially evaluate open-system behavior through stepwise degassing, but relies on calibration with "standard" minerals. In the quest for ever more accurate and precise dates on volcanic rocks, it is becoming clear that both techniques can suffer from geological complexity such as post-depositional modification and pre- to syn-eruption inheritance of older minerals. Additionally, due to the low abundance of $^{235}U$ relative to $^{238}U$, studies of Mesozoic and younger zircons often rely on the more precise measurement of the $^{238}U$-$^{206}Pb$ system, compromising the evaluation of closed-system behavior.

Until now, these two techniques have been compared in only a few studies that were devoted to resolving the problem of the absolute calibration of $^{40}Ar/^{39}Ar$ mineral ages (e.g., Renne et al. 1998a, Villeneuve et al. 2000, Min et al. 2001, Schmitz and Bowring 2001). Although the dates of individual zircons are inherently more robust in absolute terms, the assumption that zircon crystallization can be equated with eruption age is not always warranted given evidence from some studies for resolvable magma residence times in upper crustal reservoirs (Christensen and DePaolo 1993, Davies et al. 1994, Reid et al. 1997, Reid and Coath 2000). Even in rocks where magma residence times are minimized, there is preliminary evidence that $^{40}Ar/^{39}Ar$ dates could be up to 1% younger than U-Pb zircon dates from the same rock (e.g., Min et al. 2001) but it is only recently that errors calculated for each date have been precise enough to make this potential bias noteworthy, or establish its cause. However, as the time scale becomes better calibrated it may be necessary to distinguish between $^{40}Ar/^{39}Ar$ and U-Pb years until systematic biases are reconciled.

There are two techniques for the measurement of U-Pb decay that have been applied to calibrating the time scale: Secondary Ion Mass Spectrometry (SIMS)— specifically the Sensitive High Resolution Ion MicroProbe (SHRIMP)—and conventional Isotope Dilution analysis using Thermal Ionization Mass Spectrometry (IDTIMS). The two techniques are fundamentally different and each has advantages and disadvantages that help to elucidate many of the issues associated with time scale geochronology (see Ireland and Williams, this volume, for review of SIMS; Parrish et al., this

volume, for a review of IDTIMS). Among their major differences is that the SIMS typically analyzes small, nanogram-sized domains within individual zircons, whereas state-of-the-art IDTIMS analyses are made on single grains, from less than one hundred to several thousands of nanograms in weight. While analyses performed with an ion-probe generally have very small amounts of common Pb, counting statistic limitations arise from the small quantity of zircon and radiogenic Pb being analyzed. Analyses of unknown zircons must also be referenced to a standard zircon of known age in order to calculate U-Pb ages and account for instrumental bias and drift. This calibration contributes a substantial amount of uncertainty to the calculated U-Pb dates. The appropriate selection and use of well characterized, concordant standards has been a recurring issue in SHRIMP U-Pb analysis (Compston 1999, 2000a, b; 2001)

With high spatial resolution comes a trade-off with precision, and the analytical errors for SHRIMP analyses are typically an order of magnitude greater than IDTIMS (Fig. 2, Compston 1999). This imprecision makes the detection of subtle amounts of Pb-loss or inheritance difficult or impossible. For time scale work, often 10-50 spots from a variety of zircons are analyzed and a weighted mean date is calculated using the individual $^{238}U$-$^{206}Pb$ dates (e.g., Claoue-Long et al. 1991, 1995; Compston 1999). This approach can yield reduced statistical uncertainties for samplings of Paleozoic zircons that are on the order of ±2-3 million years, assuming a single-aged population. It has become commonplace in zircon studies using the SHRIMP to assess large data sets with gross measured dispersion using the mixture modeling approach of Sambridge and Compston (1994). This approach attempts to statistically deconvolve discrete age components from variably complex probability distributions. In some cases, components older and younger than the interpreted age may be resolved from multi-modal distributions, and are usually attributed to inheritance and Pb-loss respectively. While a very powerful technique for recognizing multiple components in complex data sets, it cannot overcome the basic limitations of the large uncertainties associated with individual ion probe analyses, nor systematic errors associated with standardization.

Recent application of high-precision IDTIMS U-Pb zircon geochronology to Phanerozoic volcanic ash beds has pushed the limits of current analytical capability, and emphasized the rigorous assessment of analytical and geological uncertainty in U-Pb zircon age determinations (Tucker

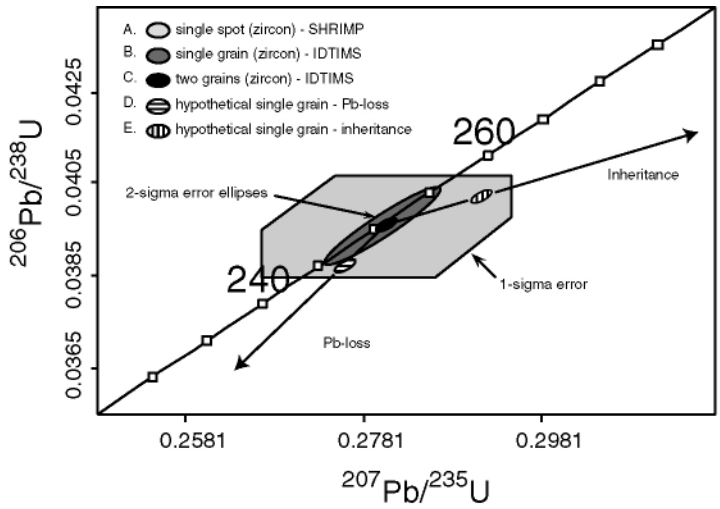


**Figure 2.** Concordia diagram comparing errors associated with SHRIMP (1s) and IDTIMS (2s) analysis for Late Permian zircons. SHRIMP analysis (A) is from Claoue-Long et al. (1991), and IDTIMS analyses (B and C) are from Bowring et al. (1998). IDTIMS errors are calculated after the algorithms of Ludwig (1980).

and McKerrow 1995, Brack et al. 1996, Mundil et al. 1996, Bowring et al. 1998, Tucker et al. 1998, Ludwig et al. 1999, Davidek et al. 1998, Mundil et al. 2001). Recently, Schmitz and Bowring (2001) investigated the precision, accuracy, and suitability of modern isotope dilution U-Pb zircon geochronology for the Cenozoic, by collecting a large data set of single- and multi-grain zircon and titanite analyses from the well-studied Oligocene Fish Canyon Tuff (FCT) (Lipman et al. 1970, Steven and Lipman 1976, Bachmann et al. 2000). With these data, it was possible to quantify the various sources of uncertainty in U-Pb zircon analysis, including geological factors like Pb-loss, inheritance, accurate initial common Pb corrections, and intermediate daughter product disequilibria, as well as analytical factors including instrumental fractionation, tracer calibration, and blank estimation. The results serve as an example of the resolving power and limitations of a reasonably straightforward U-Pb zircon data set.

The major sources of uncertainty in IDTIMS U-Pb analyses are: (1) measurement error, including uncertainty in mass fractionation and the linearity of the ion detection system; (2) common Pb correction, including both analytical blank and initial common Pb present in the zircon; (3) U/Pb tracer calibration; (4) U decay constant uncertainties and (5) U-series disequilibrium effects.

**Measurement uncertainty**

With modern ion-counting systems and stable, high-yield (>1%) ionization, Pb isotope ratios can be measured precisely (e.g., $^{207}Pb/^{206}Pb$, $\sigma_\mu \leq 0.05\%$) for samples containing as little as 5 picograms of radiogenic Pb. Mass dependent fractionation of both U and Pb ions during analysis is a potentially important source of error. U fractionation is best monitored by using a double spike ($^{233}U$, $^{235}U$, or $^{236}U$) and can be determined to 0.01%/amu or better. Lacking two constant abundance isotopes, Pb fractionation is most commonly estimated by repeated analysis and long-term reproducibility of the NIST SRM 981 Pb wire standard. Based on literature reports and our own experience, the magnitude of Pb isotope mass fractionation is typically in the range of 0.10-0.15%/amu on Faraday cups and 0.15-0.20%/amu for ion-counting Daly detection systems on VG-Micromass instruments. Our database of hundreds of NBS 981 runs illustrates the typical long-term reproducibility (±0.03-0.05%/amu) in fractionation with only a slight correlation with temperature. As many labs move to analyzing very small samples (<20 picograms of Pb), the question of whether fractionation changes with sample size must be evaluated (e.g., Roddick et al. 1987). At MIT we routinely analyze small (<100-200 picogram) NBS 981 standards for 6-8 hours and can show that fractionation tends to be somewhat higher at the lowest temperatures of a run (<1300°C), but is nearly constant until the load is taken to near exhaustion at very high temperatures (>1550°C) when it decreases. We view it essential that analysis protocols of samples resemble those of standards as closely as possible. In this regard, we note the intermittent trend in U-Pb geochronology to load a dissolved sample directly onto a Re filament without ion-exchange chromatography. While this clearly saves time and can reduce analytical blanks, the effect of additional matrix in the sample on Pb fractionation must be rigorously evaluated.

When analyzing small samples and standards with small ion-beams it is common to observe transient isobaric interferences across the Pb mass range, particularly at filament temperatures below approximately 1400°C (Parrish and Krogh 1987). In our experience these effects are minimized by the preparation of silica gel-phosphoric acid emitter solutions (cf. Gerstenberger and Haase 1997) that yield a stable ionization at relatively higher temperatures (1450-1500°C). Early transient interferences can be monitored and affected ratios discarded by examining the time series of ratio measurements, as well as the off-peak baselines. Another possible source of uncertainty that can arise is non-linearity of the ion-counting system. Typically, linearity is monitored by analysis of standard isotope ratios with a range of ion-beam intensities (Hayes et al. 1978) and Daly-type photomultiplier detectors can be shown to be linear to within ≤0.1% at count rates ≤1,500,000 cps.

**Common Pb correction**

All zircon analyses have a component of common Pb. Historically, there has been some controversy about how much common Pb is incorporated into the zircon crystal structure and how much occurs along fractures, in solid and fluid inclusions, and in the analytical blanks. Tom Krogh pioneered low blanks in zircon analyses in the 1970s and 1980s and first showed that most zircons contained little to no indigenous common Pb at the picogram level (Davis et al., this volume). Experimental work also determined the limited solubility of Pb in the crystalline zircon structure (Watson et al. 1997), and *in situ* SHRIMP analysis has further demonstrated the vanishingly small amounts of common Pb in the majority of zircons. Although there are documented exceptions including poorly understood incorporation into radiation damaged zircon (Mattinson 1994), most common Pb in IDTIMS analyses is apparently hosted by inclusions, present as surface contamination, or introduced during chemical processing.

As a result, minimization of laboratory blanks remains the single most important requirement for high-precision U-Pb zircon analysis, and in the last decade, most U-Pb laboratories have been able to reduce analytical blanks to below 5 picograms, and some to less than 1 picogram. With the growing appreciation that diamagnetic, clear, crack- and inclusion-free zircons separated from volcanic rocks have little to no indigenous common Pb, the assumption that all measured common Pb arises from laboratory blank is warranted for many samples with picogram levels of total common Pb. Most laboratories conservatively incorporate a substantial uncertainty in the magnitude of the laboratory blank (e.g., 50%) into error propagation, which is usually the dominant source of error in each analysis unless the blank is well constrained by numerous and consistent total procedural blank determinations (Ludwig 1980).

The isotopic composition of laboratory blank Pb is also of concern. Given that there are multiple sources of laboratory common Pb from airborne particulate, labware, and reagents, and that the contribution and isotopic composition of these sources change with time, it is challenging to determine an accurate isotopic composition of common Pb in a blank. This difficulty is only exacerbated when the measured ion beams constituting those blanks are small in magnitude. Nonetheless, most laboratories have characterized and adopted a reported isotopic composition with a realistically large uncertainty for the blank that includes temporal variability.

Even in the best geochronology labs the total amount of common Pb in an analysis can exceed estimated laboratory blanks, and the assignment of an isotopic composition to this supposed indigenous, or initial common Pb can have a discernable effect on the calculated date and error associated with an analysis, depending upon the contrast between the assumed blank and initial Pb isotopic compositions. Most geochronology labs use two approaches for estimating the composition of initial common Pb. The simplest is to use a model for Pb isotopic evolution such as that of Stacey and Kramers (1975), and assign a model composition corresponding to the nominal age of the zircon. It is ironic that while this model was proposed to describe the average evolution of Pb in a mantle reservoir, many silicic, zircon-bearing rocks are derived from melting older crust rather than mantle, thus calling into question the applicability of this model approach. Another approach is to use the isotopic composition of Pb in a comagmatic low U/Pb mineral such as alkali feldspar (Ludwig and Silver 1977, Housh and Bowring 1991). In general, the older the rocks the less likely it is that one can recover fresh feldspar and that its original isotopic composition can be determined. This problem is particularly acute in altered bentonitic ash layers without preserved feldspar.

Uncertainty in the composition of the initial common Pb is not usually propagated into the age error for many zircon geochronological applications, generally because of its minimal contribution for radiogenic samples. However, for high-precision geochronology and time scale calibration, where a complete description of uncertainties is vital to some interpretations, this systematic error is best propagated by calculating individual analysis dates and errors using reasonable bounds on initial common Pb compositions, deriving weighted means and errors for the resulting data sets, and ap-

propriately supplementing the weighted mean error calculated from the assumed average initial common Pb composition according to the resultant dispersion introduced by varying the common Pb composition.

We must emphasize, however, that in any U-Pb zircon analysis the most crucial parameter is the ratio of radiogenic to common Pb, often indirectly expressed by the measured $^{206}Pb/^{204}Pb$ ratio. The higher this ratio the less sensitive the analysis is to the content and composition(s) of both blank and initial common Pb. Ultimately, analyses with low radiogenic to common Pb ratios are best rejected or given less weight in age calculation, as incorrect assignment of common Pb and uncertainty can have a discernable effect on the calculated age. This is especially true for the analysis of young, low-U zircons where the radiogenic to common Pb ratio can approach unity (Bowring et al. 1998, Mundil et al. 2001). One can see this effect qualitatively in Figure 2, which shows representative errors for analyses of zircons from near the Permo-Triassic boundary at Meishan, South China. The error ellipse for a single SHRIMP analysis [A] is at one standard deviation (67% confidence interval) while those for two IDTIMS analyses [B and C] are two standard deviations (95% confidence interval). The IDTIMS analysis [B] represents a single grain with 26 picograms of total Pb with a blank of 2.6 picograms while [C] is two grains with a total of 12 picograms Pb and a blank of 2.1 picograms. The less favorable radiogenic Pb/common Pb ratio for [C] results in a proportionately larger error ellipse than for [B]. Also shown are error ellipses for hypothetical analyses that show a small amount of inheritance [D] and Pb-loss [E].

**Tracer calibration and interlaboratory comparison**

The uncertainty in U-Pb tracer calibration must be considered when comparing data between laboratories and can be among the larger sources of uncertainty (along with decay constant errors) in the absolute age of a population of zircons. The majority of laboratories have calibrated tracers against gravimetric standard solutions to arrive at an estimated uncertainty of approximately 0.1% ($2\sigma$). When this is propagated through error calculations, it introduces a proportionate uncertainty in the absolute age that is applicable to the intercomparison of U-Pb ages (but generally not Pb-Pb ages for clean $^{205}Pb$ spikes) between laboratories. In the next decade as more and more laboratories become involved in very high-precision geochronology of the time scale, subtle interlaboratory biases should be rigorously evaluated by analysis of a suite of concordant zircon secondary "standards" (e.g., Wiedenbeck et al. 1995, Schmitz et al. 2003).

**U decay constants**

Renne et al. (1998b) referred to the U-Pb zircon method as the "gold standard" of geochronology because of its unique attributes of having two completely independent decay schemes, well-calibrated decay constants, and extreme resistance to resetting. The $^{235}U$ and $^{238}U$ decay constants were precisely determined more than 30 years ago with $2\sigma$ errors of 0.136 and 0.108%, respectively (Jaffey et al. 1971), thus Begemann et al. (2001) suggest using the $^{206}Pb/^{238}U$ system as the absolute standard for age normalization because dates derived from this system are least affected by decay constant uncertainties. However, there has been discussion of the possibility of systematic errors in the U decay constants based on comparing the degree of concordance in zircon analyses (Mattinson 1987, 2000) and the suggestion that the counting errors associated with the constants of Jaffey et al. (1971) underestimate the true error. Schmitz and Bowring (2001) suggested on the basis of a large number of concordant analyses (corrected for disequilibrium effects) of the Fish Canyon tuff zircons that the published decay constants and their uncertainties appear robust. Furthermore, analysis of the commonly used 1.1 Ga ion microprobe zircon standard (AS-3) also yields a cluster of concordant and equivalent analyses (Schmitz et al. 2003). Further work using large data sets of different aged zircons is still necessary, but at present there is no compelling reason to not accept the published experimentally determined decay constants and uncertainties. Mattinson (1987) and Ludwig (2000) have suggested propagating the decay constant uncertainties into calculated zircon dates,

which can lead to very large errors in the $^{207}Pb/^{206}Pb$ date. While this is essential for intercomparison between U-Pb and $^{40}Ar/^{39}Ar$, a time scale built entirely on the U-Pb method need not include it in error calculation if the dates that are being compared all use the same decay constants.

## INTERMEDIATE DAUGHTER PRODUCT DISEQUILIBRIA

The U-Th-Pb systematics of young accessory minerals may be affected by disequilibrium partitioning of intermediate daughter nuclides within the decay chains during crystallization of the mineral-isotopic system under scrutiny. Sufficiently long-lived intermediate daughter products that may significantly perturb equilibrium U-Pb isotopic systematics are $^{230}Th$ and $^{234}U$ in the $^{238}U$-$^{206}Pb$ decay chain, and $^{231}Pa$ in the $^{235}U$-$^{207}Pb$ decay chain (Mattinson 1973, Schärer 1984). In the former decay chain, $^{234}U$ is not substantively fractionated from $^{238}U$ during high-temperature magmatic processes, such that only $^{230}Th$ disequilibrium need be considered. Because of the slightly greater ionic radius of Th relative to U and the octahedral site in zircon, intermediate daughter $^{230}Th$ is normally preferentially excluded from zircon, resulting in $^{230}Th$ deficiency and anomalously young $^{206}Pb/^{238}U$ dates for young zircon. An extremely rare exception to this deficiency has been noted in carbonatitic zircon (Amelin and Zaitsev 2002).

Disequilibrium between minerals and magma may be quantified and $^{230}Th$ deficiencies corrected with a standard methodology utilizing $^{232}Th/^{238}U$ ratios (cf. Schärer 1984). Evaluation of the disequilibrium partitioning is mainly limited by our knowledge of the Th/U of the magma coexisting with the crystal during growth. Assessing this ratio at the time of eruption can be relatively simple for unaltered volcanic rocks, through analysis of pumice or glassy lava compositions.

The large zircon data set for the Fish Canyon Tuff presented by Schmitz and Bowring (2001) serves to illustrate the general problems of initial intermediate daughter disequilibria, and their mitigation. Their analysis suggests that $^{230}Th$ disequilibrium corrected $^{206}Pb/^{238}U$ dates are generally shifted by only +0.08 Myr relative to measured $^{206}Pb/^{238}U$ dates, and that the magnitude of this correction is robust to within 0.02 Myr for large variations in magmatic Th/U. Thus uncertainties associated with $^{230}Th$ disequilibrium do not appear to hamper our ability to resolve time at the ±0.1 Ma level using zircon $^{206}Pb/^{238}U$ ages in Oligocene and certainly older volcanic rocks.

In the $^{235}U$-$^{207}Pb$ decay chain, $^{231}Pa$-disequilibrium effects should be of lesser magnitude than those described above for $^{230}Th$-disequilibrium, because of the shorter half-life of $^{231}Pa$ relative to $^{230}Th$—unless mineral-magma fractionation is significantly greater for Pa than for Th. While a quantitative knowledge of the partitioning of $^{231}Pa$ between accessory minerals and melts is lacking, qualitative assessments of Pa partitioning relative to U and Th, based on relative ionic radii, suggest that $Pa^{4+}$ depletion in zircon would be less than that of $Th^{4+}$ (Shannon 1976, Mattinson 1973, Barth et al. 1989). However, Barth et al. (1989) emphasized the likelihood that in relatively oxidizing magmatic conditions, protactinium is present as $Pa^{5+}$, in which case its minor enrichment relative to $U^{4+}$ may occur in zircon, due to its closer similarity in ionic radius to $Zr^{4+}$. Regardless of the details of $^{231}Pa$ partitioning, it does not appear that its associated disequilibrium effects in zircon commonly exceed those of $^{230}Th$; more dramatic postulated $^{231}Pa$ disequilibrium effects in zircon are extremely rare and are restricted to rocks with unusual alkaline, pegmatitic compositions (Mortensen et al. 1992, Anczkiewicz et al. 2001).

## GEOLOGICAL COMPLEXITY AND OPEN SYSTEM BEHAVIOR

### Crystal inheritance and Pb-loss

It is a common occurrence in airfall ash deposits to recognize zircon grains, often identical in appearance to the indigenous magmatic population, that are necessarily <1 to >>10 Myr older than the true age of the ash (e.g., Landing et al. 1998, Bowring et al. 1998, Mundil et al. 2001, Palfy et al. 2000). Since the lifespan of single strato-volcanoes to large magmatic arcs can be on the order of one to tens of millions of years respectively, the mechanisms and potential for this style of inherit-

ance is clear. The two major mechanisms include magmatic inheritance (overgrowth of an older core by new zircon) and/or physical addition of older grains into the eruption column or during dispersal and deposition of the ash. In our experience, older zircons can make up as much as 50% of the zircons recovered from certain ashes. Restricting analyses to single grains or grain fragments is the best way to detect and overcome this problem. On the other hand large error ellipses related to either measurement uncertainty or unfavorable radiogenic to common Pb values in some single-grain analyses can mask subtle inheritance.

Zircon analyses that are too young and/or exhibit discordance attributable to Pb-loss are also common in the study of volcanic ash beds. Pb-loss has been inferred from large data sets obtained by both conventional and ion-probe analysis (e.g., Compston 2001a,b), indicating the various spatial scales of the phenomenon. Experimental measurements of Pb diffusivity in zircon indicate that Pb-loss is not likely dominated by volume diffusion through crystalline zircon (Lee et al. 1997, Cherniak and Watson 2000) but rather related to loss from radiation-damaged domains through crystal defects and fractures. While selection of the best quality, diamagnetic zircons for analysis and the aggressive abrasion of their outer portions can minimize the effects of Pb-loss, it is a problem that can be difficult to recognize without a large number of analyses. Discordance of analyses is obviously the best indicator of Pb-loss, but unfortunately, for Late Paleozoic and younger zircons, the limited curvature of concordia combined with imprecision in the measured $^{207}Pb/^{235}U$ date can limit the discernment of discordance as an obvious signal of Pb-loss.

**Resolving a geological "age" from a large population of zircon dates**

For Paleozoic zircons a typical propagated error in individual zircon dates is about 0.3-1.5%, or several hundred thousand years to several million years. If it can be shown that the range of single zircon ages exceeds analytical uncertainty it raises the problem of distinguishing between the competing phenomena of zircon inheritance and Pb-loss in order to deconvolve the true eruption and depositional age of a volcanic unit. On the other hand, in tightly clustered data sets where Pb loss and inheritance are apparently minimal, then the small standard error statistics of the inverse variance weighted mean age of a population of zircons can place tight constraints on the eruption age of a tuff. Either scenario requires a closer examination of both the distribution of single zircon ages, as well as the applicability of the applied sample statistics.

Ideally one should obtain a relatively large number of zircon analyses in order to evaluate these issues through probability density functions (e.g., Sambridge and Compston 1994, Schmitz and Bowring 2001, Schmitz et al. 2003). If all analyses fall within two standard deviations of a single inverse-variance weighted mean, one may confidently conclude that it is consistent with a single episode of zircon growth. A fair question is how many analyses are enough? The answer in part lies in how the data are being interpreted—the higher the resolution and confidence desired the more data per rock that is required. For time scale work, our experience suggests that 10 to 20 or even more high quality zircon analyses, including a large cluster of concordant and equivalent data, are often necessary to arrive at a single ash bed age, depending upon the complexity of the zircon population.

A given U-Pb zircon data set provides a multiplicity of dates that can be used to calculate an age of crystallization, including the weighted mean $^{206}Pb/^{238}U$, $^{207}Pb/^{235}U$, or $^{207}Pb/^{206}Pb$ dates, the Concordia age algorithm of Ludwig (1999) which combines all three chronometers, or the upper intercept date of an array of variably discordant data. With optimal data sets of concordant and equivalent zircons, these dates converge and the Concordia age algorithm provides the best age estimator, including the appropriately minimized decay constant errors.

In early Paleozoic and older rocks, zircon analyses often yield discordia arrays for which an upper intercept date can be calculated; this date is generally more robust when anchored by one or more concordant analyses. When the lower intercept is within error of present day, the upper intercept age approaches the weighted mean $^{207}Pb/^{206}Pb$ date, and both can be robust and precise esti-

mates of the age of the rock (Davidek et al. 1998, Landing et al. 2000), although Ludwig (2000) has pointed out the magnification of decay constant errors associated with these ages.

In Late Paleozoic and younger rocks that have low U zircons, the lower abundances of $^{235}U$ and radiogenic $^{207}Pb$ result in a larger uncertainty in the $^{207}Pb/^{235}U$ date due to measurement errors and increased sensitivity to common Pb corrections. Small biases in $^{207}Pb/^{235}U$ are correspondingly magnified in the $^{207}Pb/^{206}Pb$ date because of the relatively reduced ingrowth of $^{207}Pb$ over the past several hundred million years (reflected in the limited curvature of concordia). Because of these factors the $^{207}Pb/^{206}Pb$ date is generally not the preferred age for Late Paleozoic and younger rocks. Instead, the U/Pb dates are more robust, and the weighted mean $^{206}Pb/^{238}U$ date is most often used to calculate the age of a rock because of its better precision and insensitivity to systematic error relative to the $^{207}Pb/^{235}U$ date (Kamo et al. 1996, Bowring et al. 1998, Mundil et al. 2001).

It should be remembered that the power of the U-Pb system derives in part from the fact that two independent decay paths can be used to evaluate concordance and closed system behavior. IDTIMS analyses of very small (low radiogenic Pb) samples or ones with a relatively high proportion of common Pb do not allow this power to be fully appreciated. However, with low blanks and reasonably high radiogenic to common Pb ratios it is possible to evaluate concordance of the two decay systems even in Cenozoic zircons (e.g., Schmitz and Bowring 2001).

More complex data sets with significant dispersion must be rigorously examined in terms of distinguishing the eruption age from the effects of Pb-loss and inheritance. It should be stressed that this level of attention is essential for establishing a very high-precision record. In complex zircon data sets, it is clear that at some point the rejection of outliers can devolve into a subjective process, and statistically valid means of identifying and rejecting outliers and incorporating excess scatter into age errors remain areas of active research (Ludwig and Mundil 2002). Looking to the future, establishing other geochemical fingerprints for inheritance and Pb-loss could partially resolve problematic data distributions. Nonetheless, in some cases neither careful statistical treatment nor analysis of additional zircons may adequately resolve problematic distributions. In these cases it may be more productive to attempt recollection of the ash layer in nearby sections, or to date another volcanic layer from the same general stratigraphic interval.

**Sample selection and analytical strategies**

The best way to approach high-precision calibration of the time scale by dating individual ash beds is to accumulate a large amount of data for each bed so that one can evaluate the potential effects of inheritance and Pb-loss. This involves processing enough rock so that a substantial number of the best quality, preferably large zircons can be isolated for analysis. In our experience, successful heavy mineral separation from clay-rich bentonitic ashes incorporates high-energy ultrasonication during settling of increasingly diluted slurries to minimize loss of zircons through flocculation. Resulting crystalline concentrates are processed by standard heavy liquid and magnetic methods to isolate the highest quality, nonmagnetic to diamagnetic zircons.

Ideally single grains of zircon should be analyzed, although as previous discussions make obvious, a smaller amount of radiogenic Pb analyzed in a single zircon translates into larger errors, so that at some point there are trade-offs between the requirements of analyzing single grains and obtaining adequate precision. Mundil et al. (2001) have discussed the potential for averaging bias in ages calculated from multi-grain zircon fractions picked from complex zircon populations. However, while many zircon populations from volcanic rocks can be quite complex, others are not, and as was documented in the case of the Fish Canyon Tuff, analysis of multiple grains of zircon can allow for more precise analyses with no observable bias in calculated dates (Schmitz and Bowring, 2001).

Most U-Pb workers favor aggressive air abrasion of zircons recovered from volcanic ashbeds. Two positive effects are generally noted with air-abrasion: reduced common Pb and enhanced concordance. Following the technique of Krogh (1982), abrasion appears to remove the outer and/

or damaged parts of the zircon crystals and only the best quality grain domains survive the process. The fine polishing of zircons resulting from abrasion with pyrite also minimizes the surface area of the grains, and corresponding sites for retention of surficial common Pb. Aggressive washing and ultrasonication with warm dilute $HNO_3$ is a necessary and effective means of removing surface correlated common Pb from abraded and unabraded zircons without discernable U/Pb fractionation. Mundil et al. (2001), following Mattinson (1994), has also suggested hot HF leaching as an alternative to mechanical abrasion as a means of improving concordance, although the increased potential for laboratory fractionation of U and Pb during leaching makes the process somewhat unattractive.

In an ideal situation, one has a sequence of volcanic rocks interlayered with fossil-bearing rocks so that the stratigraphic succession is known. A first order test of the geochronology is that the ash-beds yield ages that either all overlap within analytical uncertainties or correspond to the correct stratigraphic order. If neither of these situations result, then it is difficult to know which dates to accept as depositional ages. As discussed, it is quite possible to remobilized precursor volcaniclastic material with the magmatic products of an eruption, and to have resulting volcanic deposits with few to no indigenous zircons but many incorporated during eruption and deposition.

The best way to illustrate both the power and more problematic aspects of U-Pb zircon geochronology as applied to the calibration of the time scale is to discuss case studies such as the Neoproterozoic-Cambrian radiation, the Triassic-Jurassic boundary and the Permo-Triassic extinction, where high-precision geochronology is a crucial tool.

## THE NEOPROTEROZOIC-CAMBRIAN TRANSITION

It has long been recognized that all of the classes and orders of multicellular animals present today appear relatively suddenly in the fossil record in the lower Cambrian during the so-called "Cambrian explosion." The age and nature of the Neoproterozoic-Cambrian boundary has thus been of considerable interest for many years. Estimates for the absolute age of the boundary and the definition of the boundary itself have varied widely (Fig. 1), although 542 Ma is currently the best estimate (Grotzinger et al. 1995, Amthor et al. 2003). The possibility that a mass extinction coincides with the boundary (e.g., Knoll and Carroll 1999, Amthor et al. 2003) raises the important question whether it reflects a fundamental geological and/or biological event or whether the boundary is part of a protracted evolutionary history that culminates in a final pulse of increased fossil preservation. The past decade has seen dramatic new discoveries regarding the paleontology and chronostratigraphy of the transition between the late Neoproterozoic and the Cambrian (e.g., Grotzinger et al. 1995, Jensen et al. 1998, Gehling et al. 2001, Martin et al. 2000, Knoll and Carroll 1999, Erwin and Davidson 2001). This transition corresponds to a time of major tectonic and climatic change including the assembly and dispersal of a supercontinent, glaciation, and large fluctuations in the chemistry of the oceans and atmosphere (Hoffman et al. 1998, Kaufman et al. 1997, Knoll and Walter 1992). Chemostratigraphic and biostratigraphic studies are now focusing on evaluating the connections between tectonics, climate change and the evolution of life and the age, duration, and global synchroneity of dramatic isotopic excursions such as the one that coincides with the Neoproterozoic-Cambrian boundary (e.g., Bartley et al. 1998, Kaufman et al. 1997, Amthor et al. 2003). Further resolution of this question will depend on abundant high-precision geochronology of ash-beds integrated with the paleontological and chemostratigraphic records.

The dating of the Neoproterozoic-Cambrian boundary (see Fig. 1) is a good example of pushing the limits of geochronology to solve a problem. A surprisingly young estimate of ca. 543 Ma was published in 1993 (Bowring et al. 1993). This estimate was based on the age of a pumice-rich volcanic breccia erupted immediately above the base of the Cambrian as defined by lithological and chemostratigraphic correlation. The breccia is overlain by siltstones and sandstones that contain both Cambrian small shelly fossils and *Phycodes pedum* (Bowring et al. 1993). This volcanic breccia contains abundant xenoliths of country rock and many of the separated zircons were distinctly

older than the emplacement age. However, a population of grains yielded an upper intercept date of 543.8+5.1/-1.3 Ma that at the time was the first robust minimum age estimate for the boundary. Subsequent work in Namibia (Grotzinger et al. 1995) showed that an ash bed, overlain by Ediacaran fossils, had an age of 543.3±1 Ma and based on variations in carbon isotopes was assumed to be just below the Neoproterozoic-Cambrian boundary. The less precise age from the Siberian breccia is nominally older than the Namibian ash although they overlap within uncertainties. Most recently, Amthor et al. (2003) report the occurrence of the Neoproterozoic-Cambrian boundary from the subsurface of Oman with ash-beds on either side of the boundary. Chemostratigraphic and paleontological data are interpreted to indicate the simultaneous occurrence of an extinction of Precambrian shelly fossils (the lightly calcified *Namacalathus and Cloudina*) and a negative excursion in carbon isotopes at the boundary. The ash-beds on either side of the excursion have ages of 543 and 542 Ma consistent with the data from Namibia and provide the best estimate of the age of the boundary and a very short duration of the isotope excursion.

The questions that can now be asked are whether the Neoproterozoic-Cambrian boundary and associated carbon isotope excursion are globally synchronous, and whether there is a global -scale extinction across the boundary? The data that bear on the first question was obtained over a period of about ten years in the MIT geochronology lab where techniques and protocols have been and continue to be refined. Nonetheless there is a remarkable agreement for the age of the boundary around 542-543 Ma. The first determined and least precise date (Siberia) should now be revisited in an attempt to reduce errors and to evaluate any difference in age with Oman and Namibia. Clearly the data from Oman is now the most precise estimate of the age of the boundary and of the duration of the negative excursion in carbon isotopes. Future work could attempt to resolve small differences in time between the three sections. Ultimately this should be possible at the ±300-500 kyr level. An answer to the second question is more difficult but will involve study of the sections where Cambrian and Neoproterozoic fossils appear to coexist and establishment of a precise chronostratigraphy.

Figure 3 shows existing timing constraints and important fossil occurrences for late Neoproterozoic and Cambrian time as well as generalized variations in carbon isotopic composition of carbonates. Of particular importance are the coexistence of distinctive small shelly (*Cloudina-Namacalathus)* and Ediacaran fauna below the boundary, the negative spike in $\delta^{13}C$ close to the boundary, and the first appearance of *Treptichnus pedum* in the basal Cambrian. At present, the data suggest that late Neoproterozic time is best viewed as a period of biological diversification and preservation characterized by distinctive faunal assemblages and chemostratigraphic signals. Ediacaran fossils are present globally from >565 Ma to at least 543 Ma with the appearance of a mollusc-like animal (*Kimberella)* ca. 555 Ma (Martin et al. 2000). Ediacaran fossils disappear from the rock record ca. 542 Ma due either to closing of a taphonomic window (Gehling 1999) or because they suffered a mass extinction. As no known stratigraphic section across the transition has a combination of diagnostic fossils, chemostratigraphic constraints, and dated ash-beds, the nature and significance of the boundary is not fully understood. However, a number of studies indicate the occurrence of *T. pedum* or similar trace fossils below the putative boundary in the western US (Hagadorn and Waggoner 2000), Australia (Jenson et al. 1998), Namibia (Jenson et al. 2000) and even the type section in Newfoundland (Gehling et al. 2001) and Ediacaran fossils above the boundary (Hagadorn et al. 2000). Droser et al (1999) concluded that despite the uncertainties, *T. pedum* is still a reliable indicator for the approximate location of the boundary and represents an important evolutionary milestone. Thus, *T. Pedum* and other complex trace fossils became common at a time roughly coincident with the last occurrence of many Ediacaran soft-bodied taxa, the last occurrence of lightly calcified *Cloudina* and *Namacalathus*, and a major C-isotopic excursion (Grotzinger et al. 1995, Bartley et al. 1998, Amthor 2003). This raises the questions of whether or not the isotopic record of environmental change and the possible extinction are related (Bartley et al. 1998) and whether extinction may have been in part responsible for the Cambrian explosion?

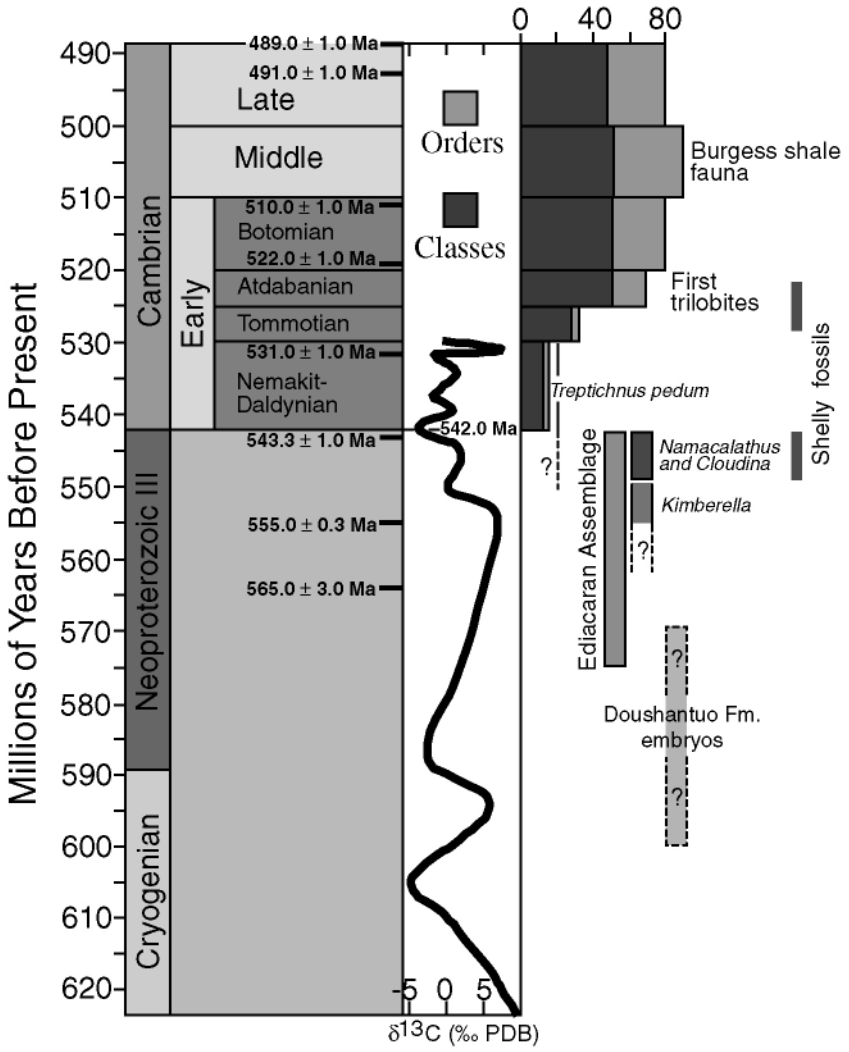


**Figure 3.** Time-scale for Vendian-Cambrian Periods showing distribution of various fauna and glacial events with $\delta^{13}C$ isotopic variation. Modified after Bowring et al. (1993), Bowring and Erwin (1998) and Knoll (1996).

What triggered the Cambrian radiation is still an open question. The relative roles of extrinsic (environment) and intrinsic (developmental) controls on this radiation are still not understood well. However, the idea that a major change occurred in the chemistry of the oceans and atmospheres, in particular a rise in oxygen concentrations, played a role in the dramatic increase in animal size and complexity is intriguing (Knoll 1996, Knoll and Carroll 1999). We believe that a well calibrated global chemostratigraphy and biostratigraphy will ultimately allow us to better understand this crucial transition in the history of life.

**Triassic-Jurassic boundary**

The Triassic-Jurassic (Tr-J) boundary is another excellent example of how U-Pb geochronology has been used to resolve the age and significance of a major extinction. The Tr-J boundary

marks one of the five largest mass extinctions in Earth history. There are both well-studied terrestrial (Olsen et al. 1996) and marine (Palfy et al. 1999) sections. For many years the age of the boundary was poorly constrained with estimates as low as 190 Ma (Seidemann 1988). Harland et al. (1990) proposed an age of 208.0±7.5 Ma whereas more recently Gradstein et al. (1994) have proposed a refined age of 205.7±4 Ma.

The cause of the extinction is not known, although both bolide impact (Olsen et al. 2002) and flood basalt magmatism (Marzoli et al. 1999) have been implicated. Olsen et al. (2002) reported that a rapid rise in dinosaur diversity, preserved in terrestrial rift-basin rocks of eastern North America, immediately followed the Tr-J boundary and that the boundary is associated with an iridium spike and a fern spore spike consistent with the extinction being caused by a bolide impact. Reports of shocked quartz from the Tr-J boundary in Italy support this idea (Bice et al. 1992).

Another potential cause of the Tr-J extinction is the eruption of a massive amount (ca. $2 \times 10^6$ $km^3$) of basaltic magma at ca. 200 Ma, remnants of which are now exposed in once-contiguous parts of North America, Europe, Africa, and South America (Marzoli et al. 1999). These magmatic rocks are referred to as the Central Atlantic Magmatic Province or CAMP (Marzoli et al. 1999). The basaltic and gabbroic rocks that occur on either side of the Tr-J boundary in the rift basins of the eastern U.S., as described below, are thought to be part of this event. A large number of Ar-Ar dates from a variety of intrusive and extrusive rocks from both the eastern U.S. and Brazil are consistent with emplacement of this magmatic province between 199 and 201 Ma and a possible link with the Tr-J extinction (Marzoli et al. 1999, Hames et al. 2000) that could involve high levels of atmospheric $CO_2$ and destabilization of methane hydrates (Beerling and Berner 2002, Palfy et al. 2001).

For terrestrial sections, Dunning and Hodych (1990) reported U-Pb zircon and baddeleyite dates of 201±1 Ma for two intrusive sills thought to be correlative with basalt flows in the lowermost Jurassic, and concluded that the boundary was slightly older than 201 Ma. Subsequently Hodych and Dunning (1992) reported a U-Pb zircon date of 202±1 Ma for the North Mountain basalt of Nova Scotia, which is interpreted by Olsen et al. (1987) to be less than 0.2 Ma younger than the T-J.

A U-Pb age of 199.6±0.3 Ma for has been reported (Palfy et al. 2000) for a tuff just below the base of the Jurassic from a marine section on Kunga Island in western Canada. This age coupled with additional data from other marine sections (Palfy et al. 1999, 2000) suggests an age of approximately 200 Ma for the marine Tr-J boundary. Palfy et al. (2000) compared the terrestrial and marine records and concluded that the marine extinction did not occur before 199.9 Ma and the terrestrial extinction no later than 200.6 Ma (youngest possible age of the intrusive sills considering uncertainties) and therefore the terrestrial extinction preceded that in the marine realm by 0.7 Myr. This discrepancy argues against a catastrophic bolide impact but could be consistent with a more complex chain of events that led to both extinctions (Palfy et al. 2000).

The age and significance of the Tr-J boundary highlights many of the issues discussed in this paper and is an excellent example of a problem that could benefit from additional high-precision geochronology. While intriguing, the apparent 0.7 Myr difference between the terrestrial and marine extinctions needs additional scrutiny. While both estimates rely on U-Pb zircon geochronology, they were obtained by two different laboratories with differing analytical parameters. The question of interlaboratory bias can only be evaluated by routine analysis of concordant zircon standards by both labs. While the marine and terrestrial ages appear to be distinct, confirmation with further analysis by both labs is desirable. Also, the apparent coincidence of the CAMP magmatism and the extinction based on Ar-Ar geochronology is noteworthy but must be tempered by the observation that Ar-Ar dates may be approximately 1% too young when compared to U-Pb dates (Min et al. 2001). If true, the 199-201 dates would be shifted by about 2 Myr. Clearly more high-precision U-Pb dates on the basaltic rocks would help with this evaluation as would Ar-Ar dates on the same rocks. Ultimately, dates on the Tr-J boundary from other localities would serve as additional tests and serve as a model for evaluating the detailed timing and causes of other mass extinctions.

## THE END-PERMIAN EXTINCTION

In south China, several marine stratigraphic sections preserve the Permo-Triassic boundary, including the type section at Meishan. Interlayered with the fossil-bearing rocks is a series of thin volcanic ash beds, which have been precisely dated using the U-Pb zircon technique (Bowring et al. 1998, Mundil et al. 2001). In these studies, ages of individual ash-beds were determined with uncertainties of less than 0.5 Myr. However despite analysis of more than 100 zircons in both studies there is a lack of consensus on the age of the boundary and the duration of the extinction.

The age, duration, and cause of extinction at the Permo-Triassic boundary have been the subject of considerable debate (Erwin 1993). Claoue-Long et al. (1991) obtained a SHRIMP U-Pb age on bed 25 at Meishan of 251.1±3.4 Ma. Subsequently, Campbell et al. (1992) dated a gabbro that cuts the Siberian traps and drew attention to the fact that within errors, the two overlapped in age and that the extinction could be due in part to the eruption. Renne et al. (1995) presented high-precision $^{40}Ar/^{39}Ar$ data for sanidine and plagioclase feldspar separated from Bed 25 at Meishan and calculated a weighted mean age of 250±1.5 Ma. In addition, they showed that this age was synchronous with the intrusion of a gabbro that cuts the lower third of the Siberian traps and suggested a casual link between the two events.

Bowring et al. (1998) published a series of ages for ash-beds interlayered with carbonate rocks from Meishan and two other localities in south China. The age of the boundary was estimated to be ca. 251.4±0.3 at Meishan and just younger than 251.7±0.2 at Heshan. This boundary age compares with a U-Pb zircon and baddeleyite age from the N'orlisk intrusion and lavas of 251.2±0.3 obtained by Kamo et al. (1996), again suggesting synchrony of the extinction and the eruption of the Siberian Traps.

The geochronological results from south China were used by Bowring et al. (1998) to draw two further conclusions. The first is that the age of the boundary is the same within errors for two sections 1500 km apart (Meishan and Heshan). The second is that the extinction occurs in less than 1 Myr. Three possible scenarios were suggested to explain the events at the P-T boundary. In the first, eruption of the Siberian flood basalts in the latest Changhsingian released large amounts of $CO_2$ (and possibly sulfates, producing acid rain) and initiated a period of global warming. Warming of shallow seas lowered the lysocline sufficiently to release some 1200 Gt of oceanic methane hydrates (Bowring et al. 1998). Following the arguments of Renne et al. (1995), a short volcanic winter may have been triggered by volcanic aerosols and was followed by greenhouse conditions and warming. This cooling-warming cycle could have triggered convective overturn of the oceans, dumping deep $CO_2$-rich bottom water onto the shelf regions (Knoll et al. 1996), leading to hypocapnia and a rise of atmospheric $CO_2$ levels.

In the second scenario, volcanism caused collapse of primary productivity and cessation of export of light carbon to the deep ocean, producing a transient isotopic shift after which the oceans returned to more normal $\delta^{13}C$ values of around 0 during recovery. It is possible that the export of sequestered light carbon and $CO_2$ charged water by upwelling, combined with volcanic-induced extinction could explain the observations. The third possibility is that the latest Permian biota was declining as a result of the above scenarios and that the collision of Earth with an icy object pushed the planet to the brink of total extinction (Bowring et al. 1998). All of the mechanisms discussed above have been operative at other times in Earth history and may have even caused other extinctions. However, none before or since has been as dramatic as the Permo-Triassic extinction. No single mechanism is apparently sufficient to explain all the geologic and paleontological data, but the massive eruption of the Siberian traps may well have been the proximal cause for a cascade of events leading to the apparent synchroneity of marine and terrestrial extinctions.

Mundil et al. (2001) challenged the conclusions of Bowring et al. (1998) with the publication of additional data for five ash beds from the Meishan section (Fig. 4). The data for each ash-bed were used to either calculate a weighted mean date or to estimate a minimum age of the bed based on interpreting the data in terms of inheritance and Pb-loss. In general, the calculated dates violate

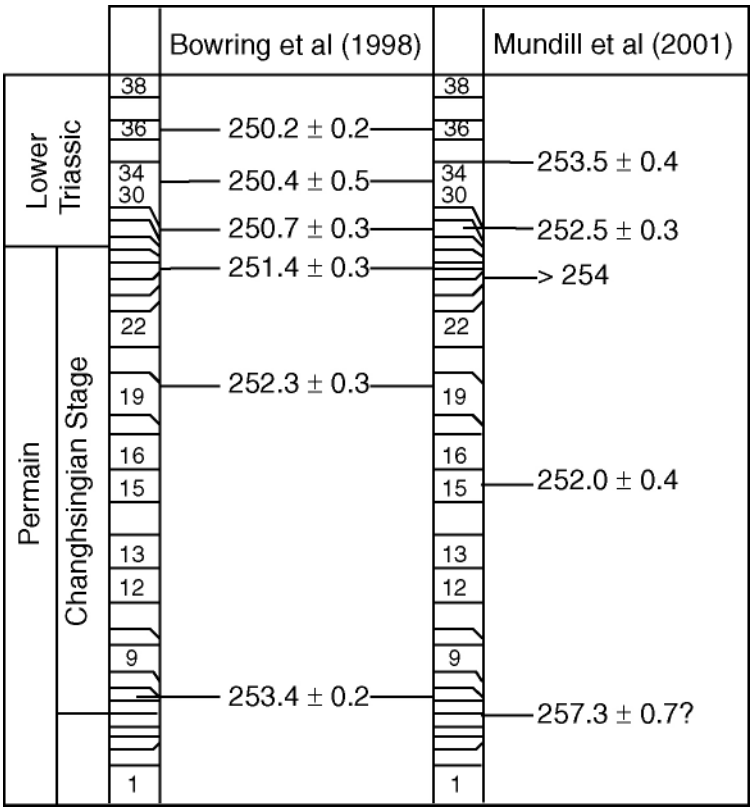


**Figure 4.** A simplified stratigraphic column from the Permo-Triassic section at Meishan China showing bed-by-bed comparison of dated ash-beds as reported by Bowring et al. (1998) and Mundil et al. (2001).

stratigraphic order; for example, one of the most precise dates of 252.0±0.4 Ma is reported for Bed 15 which is 17.3 m below the boundary, yet Bed 28, 0.08 m above the boundary has a reported date of 252.5±0.3 Ma (Fig. 4). Mundil et al. (2001) appear to hang their interpretation of the entire section on the latter date, yet it is difficult to understand how a similarly tight array of data indicating an age of 252.0 Ma for Bed 15 can be ignored.

One of the strongest criticisms of the Bowring et al. (1998) data set was that it included both single grain and multiple grain data. Mundil et al. argue that multiple grain analyses run the risk of averaging small differences in age and result in precise but inaccurate results. While this may be true, in single grains with small amounts of radiogenic Pb, analyses are much more susceptible to small differences in the isotopic composition and relative proportion of the blank, as well as measurement uncertainty. Thus it is not always clear whether small differences in dates of single grains are real or in part related to the problems of analyzing very small amounts of Pb. Thus, much as when comparing ion-microprobe analyses to conventional IDTIMS analyses, it is a question of whether taking the weighted mean of several large error ellipses associated with analyzing small amounts of zircon is better than combining enough grains together to yield a high sample/blank ratio and precise analysis.

If Siberian Traps volcanism was a driver for the Permo-Triassic extinction, precise geochronology should reveal a very close association. Kamo et al. (1996) obtained high precision, single-grain U-Pb geochronological data on both zircon and baddeleyite from the ore-bearing Noril'sk-1

intrusion that yielded an age of 251.2±0.3 Ma. In addition, Kamo et al. (2000) and Fedorenko et al. (2000) report and discuss respectively, U-Pb geochronological results from the Maymecha-Kotuy area that confirms the suggestion that the entire sequence was erupted in less than 1 Myr. From near the base of the sequence in the Maymecha-Kotuy area, perovskite from a mela-nephelinite has a date of 252.1±0.4 Ma and two lavas near the top yield U-Pb zircon dates of 251.1±0.5 Ma. At face value, the age and duration of the Siberian Traps overlaps the extinction based on the U-Pb dates obtained at Meishan (Bowring et. al. 1998), with the oldest dates at 252.1 Ma and the youngest at 251.1 Ma. In contrast, if the age of the extinction is as old or older than 253 Ma, as proposed by Mundil et al. (2001), then volcanism is distinctly younger. This is a matter that must be resolved with additional constraints on the age of the boundary both in China and in other localities. It is clear that we need to know the age and duration of both the Siberian Traps and the Permo-Triassic boundary to better than 200,000 years. This is surely a challenge for U-Pb geochronology.

The age of the Permo-Triassic boundary at Meishan is a good example of the issues associated with high-precision geochronology of critical intervals in earth history. It demonstrates the potential complexity of zircon populations in volcanic ash-beds and illustrates the need for dating multiple ash-beds in stratigraphic order. It also illustrates the unresolved analytical difficulties inherent in the analysis of picogram quantities of radiogenic Pb, and the current impasse between analysis of single zircon grains to isolate Pb-loss and inheritance issues and multiple grains to minimize measurement uncertainties. Hopefully, the zircon systematics of the Meishan ashes constitutes a worst-case scenario and other Phanerozoic sections will continue to yield more easily interpretable results. In fact the data that are emerging from the Triassic (Mundil et al. 1996, Brack et al. 1996, Palfy et al. 2003) are providing a consistent and highly resolved record for the post-extinction recovery and lending insight into the duration and periodicity of cycles preserved in carbonate platform rocks. We conclude by emphasizing the demonstrated ability of U-Pb zircon geochronology to resolve absolute Neoproterozoic to Phanerozoic time at the sub-million year level, and the important insights its application may reveal in the near future.

## SUMMARY

Until recently, the distribution of time in the geologic record has been viewed mostly in terms of biostratigraphy. However it has been shown that by integrating high-precision geochronology with paleontology one can begin to address fundamental issues such as rates of evolution, diachrony in the fossil record, and the affect of environmental change on the tempo of evolution. Only when the rock record is highly calibrated in an absolute sense will we fully appreciate the detailed history contained within. A highly calibrated rock record will lead to closer scrutiny of evolutionary change in index fossils such as conodonts and trilobites and could lead to major new insight into the causes of adaptations.

Modern U-Pb geochronological techniques can yield uncertainties approaching 0.1% for the ages of volcanic ash-beds interlayered with fossiliferous rocks. However there is a need for community-wide participation in the analysis of well-constrained ash-beds as well as "standard" zircons so that small interlaboratory biases can be included in propagated errors. The geochronological and paleontological communities can look forward to a highly resolved rock record that will permit a much more detailed understanding of earth history.

In the future, geochronology, paleontology, and molecular biology must be better integrated to determine rates of evolution, extinction, and recovery. Distinguishing between extrinsic and intrinsic controls on evolution will require a full understanding of the tempo of assembly and dispersal of continents and the related climatic changes. There is no doubt that a more comprehensive understanding of the distribution of time in the rock record will open vast new areas of study in the Earth Sciences.

## ACKNOWLEDGMENTS

MIT's work on high-precision U-Pb geochronology is and has been supported by NASA's Exobiology (NAG5-8814), The NASA Astrobiology Institute (NCC2-1053), and NSF (EAR 9725727 and EAR 9804988). We thank Dan Condon for discussion, review and a great deal of help with manuscript preparation. Randy Parrish provided a particularly thoughtful and thorough review, which greatly improved the manuscript. Chris Fedo and John Hanchar also reviewed the manuscript and their insightful comments are appreciated.

## REFERENCES

Amelin Y, Zaitsev AN (2002) Precise geochronology of phoscorites and carbonatites: The critical role of U-series disequilibrium in age interpretations. Geochim Cosmochim Acta 66:2399-2419

Amthor JE, Grotzinger JP, Schroder S, Bowring SA, Ramezani J, Martin MW Matter A (2003) Extinction of Cloudina and Namacalathus at the Precambrian boundary in Oman. Geology (in press)

Anczkeiwicz R, Oberli F, Burg JP, Villa IM, Guenther D, Meier M (2001) Timing of normal faulting along the Indus Suture in Pakistan Himalaya and a case of major $^{231}Pa/^{235}U$ initial disequilibrium in zircon. Earth Planet Sci Lett 191:101-114

Bachmann O, Dungan MA, Lipman PW (2000) Voluminous lava-like precursor to a major ash-flow tuff: low-column pyroclastic eruption of the Pagosa Peak Dacite, San Juan Volcanic Field, Colorado. J Volcanol Geotherm Res 98:153-171

Barth S, Oberli F, Meier M (1989) U-Th-Pb Systematics of morphologically characterized zircon and allanite—a high-resolution isotopic study of the alpine Rensen Pluton (Northern Italy). Earth Planet Sci Lett 95:235-254

Bartley JK, Pope M, Knoll AH, Semikhatov MA, Petrov PY (1998) A Vendian-Cambrian Boundary succession from the northwestern margin of the Siberian Platform: stratigraphy, paleontology, and correlation. Geol Mag 135:473-494

Beerling DJ, Berner RA (2002) Biogeochemical constraints on the Triassic-Jurassic boundary carbon cycle event. Global Biogeochemical Cycles 16:doi 10.1029/2001GB001637

Begemann F, Ludwig KR, Lugmair GW, Min K, Nyquist LE, Patchett PJ, Renne PR, Shih C-Y, Villa IM, Walker RJ (2001) Call for an improved set of decay constants for geochronological use. Geochim Cosmochim Acta 65:111-121

Bice DM, Newton CR, McCauley S, Reiners PW, McRoberts CA (1992) Shocked quartz at the Triassic/Jurassic boundary in Italy. Science 259:443-446

Bowring SA, Erwin DH (1998) A new look at evolutionary rates in deep time: uniting paleontology and high-precision geochronology. G S A Today 8:1-8

Bowring SA, Erwin DH, Jin YG, Martin MW, Davidek K, Wang W (1998) U/Pb zircon geochronology and tempo of the end-Permian mass extinction. Science 280:1039-1045

Bowring SA, Grotzinger JP, Isachsen CE, Knoll AH, Pelechaty SM, Kolosov P (1993) Calibrating rates of Early Cambrian evolution. Science 261:1293-1298

Brack P, Mundil R, Oberli F, Meier M, Rieber H (1996) Biostratigraphic and radiometric age data question the Milankovitch characteristics of the Latemar cycles (southern Alps, Italy). Geology 24:371-375

Brasier MD, Shields G, Kuleshov VN, Zhegallos, EA (1996) Integrated chemo-and biostratigraphic calibration of early animal evolution: Neoproterozoic-early Cambrian of southwest Mongolia. Geol Mag 133:445-85

Campbell IH, Czamanske GK, Fedorenko VA, Hill RI, Stepanov V (1992) Synchronism of the Siberian Traps and the Permian-Triassic boundary. Science 258:1760-1763

Cherniak DJ, Watson EB (2000) Pb diffusion in zircon. Chem Geol 172:5-24.

Christensen JN, DePaolo DJ (1993) Time-scales of large volume silicic magma systems: Sr isotopic systematics of phenocrysts and glass from the Bishop Tuff, Long Valley, California. Contrib Mineral Petrol 113:100-114

Claoue-Long JC, Zhang ZC, Ma GG, Du SH (1991) The age of the Permian-Triassic boundary. Earth Planet Sci Lett 105:182-190

Claoue-Long JC, Compston W, Roberts J, Fanning CM (1995) Two Carboniferous ages: A comparison of SHRIMP zircon dating with the conventional zircon ages and $^{40}Ar/^{39}Ar$ analysis. *In* Geochronology, Time Scales and Global Stratigraphic Correlation. SEPM Spec Publ 54:3-21

Compston W (2001) Effect of Pb loss on the ages of reference zircons QGNG and SL13, and of volcanic zircons from the early Devonian Merrions and Turondale Formations, New South Wales. Austral J Earth Sci 48:797-803

Compston W (2000a) Interpretation of SHRIMP and isotope dilution zircon ages for the Paleozoic time-scale: II. Silurian to Devonian. Mineral Mag 64:1127-1146

Compston W (2000b) Interpretations of SHRIMP and isotope dilution zircon ages for the geological time-scale: I. The early Ordovician and late Cambrian. Mineral Mag 64:43-57

Compston W (1999) Geological age by instrumental analysis: the 29th Hallimond Lecture. Mineral Mag 63:297-311

Davidek K, Landing E, Bowring SA, Westrop SR, Ruston AWA, Fortey RA, Adrian JM (1998) New uppermost

Cambrian U-Pb date from Avalonian Wales and age of the Cambrian-Ordovician boundary. Geol Mag 135:305-309
Davies GR, Halliday AN, Mahood GA, Hall CM (1994) Isotopic constraints on the production rates, crystallization histories and residence times of pre-caldera silicic magmas, Long Valley, California. Earth Planet Sci Lett 125:17-37
Droser ML, Gehling JG, Jensen S (1999) When the worm turned: Concordance of Early Cambrian ichnofabric and trace-fossil record in siliciclastic rocks of South Australia. Geology 27:625-628
Dunning GR, Hodych, JP (1990) U/Pb zircon and baddeleyite ages for the Palisades and Gettysburg sills of the northeastern United States: Implications for the age of the Triassic/Jurassic boundary. Geology 18:795-798
Erwin DH (1993) The Great Paleozoic Crisis. Columbia University Press, New York
Erwin DH (1994) The Permo-Triassic extinction. Nature 367:231-236
Erwin DH, Bowring SA, Jin YG (2002) End-Permian mass extinctions: a review. *In* Catastrophic Events and Mass Extinctions: Impacts and Beyond. Koeberl C, MacLeod KG (eds) Geol Soc Am Spec Paper 356:363-383
Erwin DH, Davidson EH (2002) The last common bilaterian ancestor. Development 129:3021-3032
Fedorenko V, Czamnske G, Zen'ko T, Budahn J, Siems D (2000) Field and geochemical studies of the melilite-bearing Arydzhangsky Suite, and an overall perspective on the Siberian alkaline-ultramafic flood basalt volcanic rocks. Intl Geol Rev 42:769-804
Gehling JG, Jensen S, Droser ML, Myrow PM, Narbonne GM (2001) Burrowing below the basal cambrian GSSP, Fortune Head, Newfoundland. Geol Mag 138:213-218
Gehling JG (1999) Microbial mats in terminal Proterozoic siliciclastics: Ediacaran death masks. Palaios 14:40-57.
Gerstenberger H, Haase G (1997) A highly effective emitter substance for mass spectrometric Pb isotope ratio determinations. Chem Geol 136:309-312
Gradstein FM, Ogg J (1996) A Phanerozoic time scale. Episodes 19:3-5
Gradstein FM, Agterberg FP, Ogg JG, Hardenbol J, van Veen P, Thierry J, Huang Z (1994) A Mesozoic time scale. J Geophys Res B 99:24051-24074
Grotzinger JP, Bowring SA, Saylor BZ, Kaufman AJ (1995) Biostratigraphic and geochronologic constraints on early animal evolution. Science 270:598-604
Hagadorn JW, Fedo CM, Waggoner BM (2000) Early Cambrian Ediacaran-type fossils from California. J Paleontol 74:731-740
Hagadorn JW, Waggoner B (2000) Ediacaran fossils from the southwestern Great Basin, United States. J Paleontol 74:349-359
Hames WE, Renne PR, Ruppel C (2000) New evidence for geologically instantaneous emplacement of earliest Jurassic Central Atlantic magmatic province basalts on the North American margin. Geology 28:859-862
Harland WB, Armstrong RL, Cox AV, Craig LE, Smith AG, Smith DG (1990) A Geologic Time Scale. Cambridge University Press, Cambridge, UK
Hayes JM, Matthews DE, Schoeller DA (1978) Effective dead-time of pulse-counting detector systems. Analyt Chem 50:25-32
Haynes JT (1994) The Ordovician Deicke and Millbrig K-bentonite beds of the Cincinnati Arch and the southern Valley and Ridge Province. Geol Soc Am Spec Paper 290
Hoffman PF, Kaufman AJ, Halverson GP, Schrag DP (1998) A Neoproterozoic snowball Earth. Science 281:342-346
Housh T, Bowring SA (1991) Lead isotopic heterogeneities within alkali feldspars: implications for the determination of initial lead isotopic compositions. Geochim Cosmochim Acta 55:2309-2316
Hodych JP, Dunning GR (1992) Did the Manicouagan impact trigger end-of-Triassic mass extinction? Geology 20:51-54
Jaffey AH, Flynn KF, Glendenin LE, Bentley WC, Essling AM (1971) Precision measurement of half-lives and specific activities of $^{235}U$ and $^{238}U$. Phys Rev C 4:1889-1906
Jensen S, Gehling JG, Droser ML (1998) Ediacara-type fossils in Cambrian sediments. Nature 393:567-569
Jensen S, Saylor BZ, Gehling JG, Germs GJB (2000) Complex trace fossils from the terminal Proterozoic of Namibia. Geology 28:143-146
Jin YG, Wang Y, Wang W, Shang QH, Cao CQ, Erwin DH (2000) Pattern of marine mass extinction near the Permian-Triassic boundary in South China. Science 289:432-436
Kamo SL, Czamanske GK, Krough TE (1996) A minimum U-Pb age for Siberian flood basalt volcanism. Geochem Cosmochim Acta 60:3505-3511
Kamo SL, Czamnske GK, Amelin Y, Fedorenko VA, Trofimov VR (2000) U-Pb zircon and baddeleyite and U-Th-Pb perovskite ages from Siberian flood volcanism, Maymecha-Kotuy area, Siberia.. Tenth Ann V.M. Goldschmidt Conf, J Conf Abstr 5:569
Kaufman AJ, Knoll AH, Narbonne GM (1997) Isotopes, ice ages, and terminal Proterozoic earth history. Proc Natl Acad Sci, USA 94:6600-6605
Knoll AH (1996) Daughter of time. Paleobiology 22:1-7
Knoll AH, Walter MR (1992) Latest Proterozoic stratigraphy and Earth history. Nature 356:673-678

Knoll AH, Carroll SB (1999) Early animal evolution: Emerging views from comparative biology and geology. Science 284:2129-2137
Knoll AH, Grotzinger JP, Kaufman AJ, Kolosov P (1995) Integrated approaches to terminal Proterozoic stratigraphy:An example from the Olenek Uplift, northeastern Siberia. Precambrian Res 73:251-270
Knoll AH, Bambach RK, Canfield DE, Grotzinger JP (1996) Comparative earth history and late Permian mass extinction. Science 273:452-457
Krogh TE (1982) Improved accuracy of U-Pb zircon ages by creation of more concordant systems using an air-abrasion technique. Geochim Cosmochim Acta 145:637-649
Landing E (1994) Precambrian-Cambrian boundary global stratotype ratified and a new perspective of Cambrian time. Geology 22:179-182
Landing E, Bowring SA, Davidek, KL, Westrop SR, Geyer G, Heldmaier W (1998) Duration of the early Cambrian: U-Pb ages of volcanic ashes from Avalon and Gondwana. Can J Earth Sci 35:329-338
Landing E, Bowring SA, Davidek KL, Rushton AWA, Fortey RA, Wimbledon WAP (2000) Cambrian-Ordovician boundary age and duration of the lowest Ordovician Tremadoc Series based on U-Pb zircon dates from Avalonian Wales. Geol Mag 137:485-494
Lee JKW, Williams IS, Ellis DJ (1997) Pb, U and Th diffusion in natural zircon. Nature 390:159-162
Lipman PW, Steven TA, Mehnert HH (1970) Volcanic history of the San Juan Mountains, Colorado, as indicated by potassium-argon dating. Geol Soc Am Bull 81:2329-2352
Ludwig KR (1980) Calculation of uncertainties of U-Pb isotope data. Earth Planet Sci Lett 46:212-220
Ludwig KR (1998) On the treatment of concordant uranium-lead ages. Geochim Cosmochim Acta 62:665-676
Ludwig KR (2000) Decay constant errors in U-Pb concordia-intercept ages. Chem. Geol. 166:315-318
Ludwig KR, Mundil R (2002) Extracting reliable U-Pb ages and errors from complex populations of zircons from Phanerozoic tuffs. Twelfth V.M. Goldschmidt Conf Abstr, Geochim Cosmochim Acta 66:A463
Ludwig KR, Silver LT (1977) Lead-isotope inhomogeneity in Precambrian igneous K-feldspars. Geochim Cosmochim Acta 41:1457-1471
Ludwig KR, Mundil R, Renne PR (1999) How well can we really do timescale geochronology with zircon uranium-lead? Ninth Ann V.M. Goldschmidt Conf, Lunar Planet Inst Contrib 971:178
Martin MW, Grazhdankin DV, Bowring SA, Evans DAD, Fedonkin MA, Kirschvink JL (2000) Age of Neoproterozoic bilatarian body and trace fossils, White Sea, Russia: Implications for metazoan evolution. Science 288:841-845
Marzoli A, Renne PR, Piccirillo EM, Ernesto M, Bellieni G, DeMin A (1999) Extensive 200-million-year-old continental flood basalts of the Central Atlantic Magmatic Province. Science 284:616-618
Mattinson JM (1973) Anomalous isotopic composition of lead in young zircons. Carnegie Inst Wash Yrbk 72:613-616
Mattinson JM (1987) U-Pb ages of zircons: a basic examination of error propagation. Chem Geol 66:151-162
Mattinson JM (1994) A study of complex discordance in zircons using step-wise dissolution techniques. Contrib Mineral Petrol 116:117-129
Mattinson JM (2000) Revising the "gold standard," the uranium decay constants of Jaffey et al. 1971. EOS Trans, Am Geophys Union 81:S444
Mortensen JK, Roddick JC, Parrish RR (1992) Evidence for high levels of unsupported 207-Pb in zircon from a granitic pegmatite: implications for interpretation of discordant U-Pb data. EOS Trans, Am Geophys Union 73:370
Min KW, Renne PR, Huff WD (2001) Ar-40/Ar-39 dating of Ordovician K-bentonites in Laurentia and Baltoscandia. Earth Planet Sci Lett 185:121-134
Mundil R, Brack P, Meier M, Rieber H, Oberli F (1996) High-resolution U-Pb dating of Middle Triassic volcaniclastics: time-scale calibration and verification of tuning parameters for carbonate sedimentation. Earth Planet Sci Lett 141:137-151
Mundil R, Metcalfe I, Ludwig KR, et al. (2001) Timing of the Permian-Triassic biotic crisis: implications from new zircon U/Pb age data (and their limitations) Earth Planet Sci Lett 187:131-145
Narbonne GM, Kaufman AJ, Knoll AH (1994) Integrated chemostratigraphy and biostratigraphy of the upper Windermere Supergroup (Neoproterozoic), northwestern Canada: Implications for correlation and the early evolution of animals. Geol Soc Am Bull 106:1281-1292
Olsen PE, Shubin NH, Anders MH (1987) New Early Jurassic tetrapod assemblages constrain Triassic-Jurassic tetrapod extinction event. Science 237:1025-1029.
Olsen PE, Kent DV, Cornet B, Witte WK, Schlische RW (1996a) High-resolution stratigraphy of the Newark rift basin (early Mesozoic, eastern North America). Geol Soc Am Bull 108:40-77
Olsen PE, Kent DV, Sues HD, Koeberl C, Huber H, Montanari A, Rainforth EC, Fowell SJ, Szajna MJ, Hartline BW (2002) Ascent of dinosaurs linked to an iridium anomaly at the Triassic-Jurassic boundary. Science 296:1305-1307
Pálfy J, Smith PL, Mortensen JK, Friedman, RM (1999) Integrated ammonite biochronology and U-Pb geochronometry from a basal Jurassic section in Alaska. Geol Soc Am Bull 111:1537-1549.
Pálfy J, Mortensen JK, Carter ES, Smith PL, Friedman RM, Tipper HW (2000) Timing the end-Triassic mass extinction: First on land, then in the sea? Geology 28:39-42
Pálfy J, Demeny A, Haas J, Hetenyi M, Orchard MJ, Veto I (2001) Carbon isotope anomaly and other geochemical

changes at the Triassic-Jurassic boundary from a marine section in Hungary. Geology 29:1047-1050
Pálfy J, Parrish RR, David K, Voros, A (2003) Middle Triassic integrated U-Pb geochronology and ammonoid biochronology from the Balaton Highland (Hungary). J Geol Soc London 160:271:284
Parrish RR, Krogh TE (1987) Synthesis and purification of $^{205}$Pb for U-Pb geochronology. Chem Geol 66:103-110
Pelechaty SM, Grotzinger JP, Kashirtsev VA, Zhernovsky VP (1996) Chemostratigraphic and sequence stratigraphic constraints on Vendian-Cambrian basin dynamics, northeast Siberian craton. J Geol 104:543-563
Reid MR, Coath CD (2000) *In situ* U-Pb ages of zircons from the Bishop Tuff: no evidence for long crystal residence times. Geology 28:443-446
Reid MR, Coath CD, Harrison TM, McKeegan KD (1997) Prolonged residence times for the youngest rhyolites associated with Long Valley Caldera: $^{230}$Th-$^{238}$U ion microprobe dating of young zircons. Earth Planet Sci Lett 150:27-39
Renne PR, Swisher CC, Deino AL, Karner DB, Owens TL, DePaolo DJ (1998a) Intercalibration of standards, absolute ages and uncertainties in Ar-40/Ar-39 dating. Chem Geol 145:117-152
Renne PR, Karner DB, Ludwig KR (1998b) Absolute ages aren't exactly. Science 282:1840-1841
Renne PR, Zhang Z, Richards MA, Black MT, Basu AR (1995) Synchrony and causal relations between Permian-Triassic boundary crises and Siberian flood volcanism. Science 269:1413-1416
Roddick JC, Loveridge WD, Parrish RR (1987) Precise U/Pb dating of zircon at the sub-nanogram Pb level. Chem Geol 66:111-121
Sambridge MS, Compston W (1994) Mixture modeling of multi-component data sets with application to ion-probe zircon ages. Earth Planet Sci Lett 128:373-90
Schärer U (1984) The effect of initial $^{230}$Th equilibrium on young U-Pb ages: the Makalu case, Himalaya. Earth Planet Sci Lett 67:191-204
Schmitz MD, Bowring SA (2001) U-Pb zircon and titanite systematics of the Fish Canyon Tuff: an assessment of high-precision U-Pb geochronology and its application to young volcanic rocks. Geochim Cosmochim Acta 65:2571-2587
Schmitz MD, Bowring SA, Ireland TR (2003) Evaluation of Duluth Complex Anorthositic Series (AS3) zircon as a U-Pb geochronological standard: new high-precision ID-TIMS results. Geochim Cosmochim Acta (in press)
Shannon RD (1976) Revised effective ionic radii and systematic studies of interatomic distances in halides and chalcogenides. Acta Crystallogr A32:751-767
Stacey JS, Kramers JD (1975) Approximation of terrestrial lead isotope evolution by a two-stage model. Earth Planet Sci Lett 26:207-221
Seidemann DE (1988) The hydrothermal addition excess $^{40}$Ar to the lava flows of the Early Jurassic in the Hartford basin, Connecticut and the Newark basin, New Jersey. Geol Soc Am Bull 95:594-598
Steven TA, Lipman PW (1976) Calderas of the San Juan volcanic field, southwestern Colorado. U. S. Geological Survey Professional Paper 958, United States Government Printing Office, Washington
Tucker RD, Krogh TE, Ross RJ, Williams SH (1990) Time-scale calibration by high-precision U-Pb zircon dating of interstratified volcanic ashes in the Ordovician and Lower Silurian stratotypes of Britain. Earth Planet Sci Lett 100:51-58
Tucker RD, McKerrow S (1995) Early Paleozoic geochronology: a review in light of new U-Pb zircon ages from Newfoundland and Britain. Can J Earth Sci 32:368-379
Tucker RD, Bradley DC, Ver Straeten CA, Harris AG, Ebert JR, McCutcheon SR (1998) New U-Pb zircon ages and the duration and division of Devonian time. Earth Planet Sci Lett 158:175-186
Villeneuve M, Sandeman HA, Davis WJ (2000) A method for intercalibration of U-Th-Pb and $^{40}$Ar-$^{39}$Ar ages in the Phanerozoic. Geochim Cosmochim Acta 23:4017-4030
Watson EB, Cherniak DJ, Hanchar JM, Harrison TM, Wark DA (1997) The incorporation of Pb into zircon. Chem Geol 141:19-31
Wiedenbeck M, Alle P, Corfu F, Griffin WL, Meier M, Oberli F, von Quadt A, Roddick JC, Spiegel W (1995) Three natural zircon standards for U-Th-Pb, Lu-Hf, trace element, and REE analyses. Geostandards Newslett 19:1-23
Young GC, Laurie JR (eds) (1996) An Australian Phanerozoic Timescale. Oxford University Press, New York

# 12 Lu–Hf and Sm–Nd isotope systems in zircon

**Peter D. Kinny**

*Tectonics Special Research Centre*
*Department of Applied Geology, Curtin University of Technology*
*Perth, 6845, Western Australia*

**Roland Maas**

*School of Earth Sciences, University of Melbourne*
*Parkville, 3010, Victoria, Australia*

## INTRODUCTION

As a significant carrier of uranium, thorium and the rare earth elements (REEs) at ppm level, and hafnium at the percent level, zircon hosts a remarkable number of long-lived radioactive isotopes and their stable decay products. These include $^{238}U$, $^{235}U$ and $^{232}Th$ which decay via intermediate steps to $^{206}Pb$, $^{207}Pb$ and $^{208}Pb$, respectively, $^{176}Lu$ which decays to $^{176}Hf$, $^{147}Sm$ which decays to $^{143}Nd$, and $^{138}La$ which undergoes branched decay to $^{138}Ce$ and $^{138}Ba$. This combination makes zircon one of the most versatile minerals available to the geochronologist. Whilst the majority of rock-dating studies involving zircon have utilized the U–Pb and Th–Pb decay schemes, as discussed in previous chapters, an increasing number of investigations are targeting the complementary age information available in the lesser known decay schemes. This chapter reviews the history of application of the Lu–Hf and Sm–Nd isotope systems in zircon and, in its conclusions, speculates on potential future use of the La–Ce system.

## THE Lu–Hf ISOTOPE SYSTEM IN NATURE

$^{176}Lu$ is an unstable radionuclide that undergoes spontaneous $\beta^-$ decay to stable $^{176}Hf$, with a half-life of approximately 35 billion years. Variations in the abundance of $^{176}Hf$ are conventionally expressed with respect to $^{177}Hf$ whose natural abundance is constant. Thus, the basic age equation for the Lu–Hf dating method, as applied to any closed system, is as follows:

$$(^{176}Hf/^{177}Hf)_t = (^{176}Hf/^{177}Hf)_{initial} + (^{176}Lu/^{177}Hf)_t \cdot (e^{\lambda t} - 1)$$

where t is the elapsed time, and $\lambda$ is the $^{176}Lu$ $\beta^-$ decay constant. The exact value of the decay constant $\lambda$ is currently under review. Most geological studies have either used the value $1.94 \times 10^{-11}\,y^{-1}$, originally calculated from the slope of a Lu–Hf isochron for the 4.56 Ga eucrite achondrite meteorites (Patchett and Tatsumoto 1980a, Tatsumoto et al. 1981), or alternatively $1.93 \times 10^{-11}\,y^{-1}$, as determined by a direct measurement of $\gamma$-ray activity (Sguigna et al. 1982). However, recent estimates both by direct scintillation counting (Nir-El and Lavi 1998) and by calibration of Lu–Hf isochron slopes against U–Pb ages of Lu-rich minerals (Scherer et al. 2001) indicate that a revised value of $1.86 \times 10^{-11}\,y^{-1}$ would be more appropriate. If this revised value is adopted, the immediate implication for all previous work is that Lu–Hf ages calculated using 1.93 or $1.94 \times 10^{-11}\,y^{-1}$ will be 4% too young, and the position of the bulk unfractionated Earth Hf isotope evolution curve, which is the principal reference for petrogenetic studies, will also shift, such that the magnitude of measured deviations from the curve will also change.

$^{176}Lu$ constitutes 2.6% of natural lutetium, the heaviest of the REEs. In terms of total rock budget, Lu tends to reside principally in heavy REE-rich minerals such as garnet, zircon and xenotime. Hafnium is a high field strength element (HFSE) whose geochemistry is virtually identical to zirco-

1529-6466/03/0053-0012$05.00

nium. Hence the principal site for Hf in rocks is as a minor element substitute for Zr in zircon and in other, rarer Zr-bearing minerals. Most zircon crystals contain 0.5-2.0 wt % $HfO_2$ (Hoskin and Schaltegger, this volume), but extremely Hf-rich zircons are reported, for example from rare-metal mineralized pegmatites (Correia Neves et al. 1974).

## Hafnium as a geochemical tracer

The Lu–Hf isotope system can be utilized to track the history of chemical differentiation of the silicate Earth (crust and mantle) by virtue of the fact that fractionation of Lu from Hf occurs during magma generation (Fig. 1). The once uniform, approximately chondritic initial Lu/Hf ratio for Earth has been progressively modified over time by episodes of partial melting in the upper mantle which, in generating basaltic magmas, have depleted the residual mantle in Hf (the more incompatible of the two elements) and correspondingly enriched the basaltic crust so generated. Over time, the Hf isotopic composition of the depleted mantle (Lu/Hf > chondrites) and of the enriched crust (Lu/Hf < chondrites) diverge from that of any remaining unfractionated material (Lu/Hf = chondritic), as shown in Figure 1.

As in many other isotope systems, deviations of Hf isotopic composition from chondritic at any time, t, are expressed in epsilon units (parts per ten thousand) as given by the following formula:

$$\varepsilon_{Hf} = [\ (^{176}Hf/^{177}Hf)_t / (^{176}Hf/^{177}Hf)_{chondrites} - 1\ ] \times 10^4$$

Thus, samples with higher than chondritic $^{176}Hf/^{177}Hf$ at time t have positive $\varepsilon_{Hf}$ values, whilst those with lower than chondritic $^{176}Hf/^{177}Hf$ have negative $\varepsilon_{Hf}$. Chondrites themselves have $\varepsilon_{Hf} = 0$.

The adopted reference parameters for the Solar System initial $^{176}Hf/^{177}Hf$ and present-day chon-

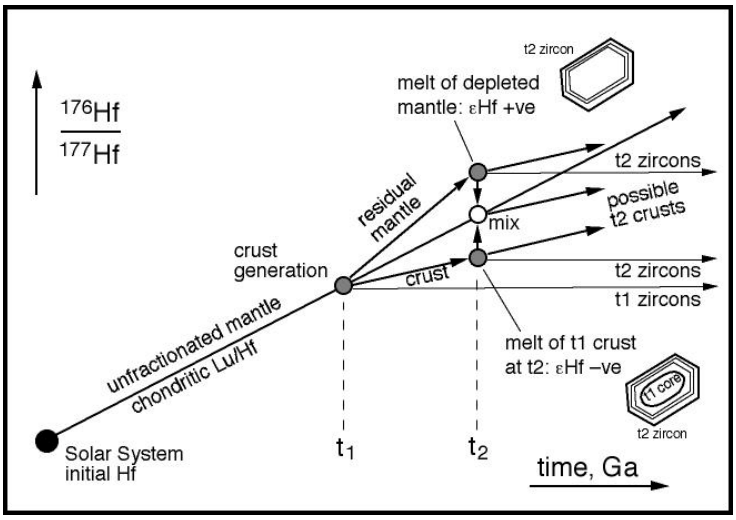


**Figure 1.** Schematic Hf isotope evolution diagram, modified after Patchett et al. (1981), showing how an episode of partial melting in Earth's mantle at time $t_1$ results in divergent Hf isotope evolution paths for the newly generated crust (low Lu/Hf) and the residual mantle (high Lu/Hf). Having extremely low Lu/Hf, any zircons formed within that crust will preserve its initial $^{176}Hf/^{177}Hf$ ratio, and hence over time diverge in composition from the remainder of the host rock. At time $t_2$ a variety of possible sources may contribute to newly formed crust. If wholly derived from depleted mantle, the initial $\varepsilon_{Hf}$ will be positive, however mixing with an undepleted or enriched source, for example by crustal contamination, may result in low positive, zero, or negative $\varepsilon_{Hf}$ at the time of crystallization depending on the balance of components. Any inherited zircon cores at $t_2$ would be expected to have lower $\varepsilon_{Hf}$ than the newly crystallized host rock.

**Table 1.** Bulk unfractionated silicate Earth reference parameters.

| $(^{176}Hf/^{177}Hf)_{today}$ | $(^{176}Lu/^{177}Hf)_{today}$ | $(^{176}Hf/^{177}Hf)_{init}$ | Parameters for initial Hf | Reference |
|---|---|---|---|---|
| 0.28286 ± 9 | 0.0334 | 0.27978 ± 9 | $t_0$ 4.55 Ga; $\lambda_{Lu}$ 1.94 × $10^{-11}$ | 1 |
| 0.282772 ± 29 | 0.0332 ± 2 | 0.279742 ± 29 | $t_0$ 4.56 Ga; $\lambda_{Lu}$ 1.93 × $10^{-11}$ | 2 |

1. Tatsumoto et al. 1981. 2. Blichert-Toft & Albarède 1997.

dritic $^{176}Lu/^{177}Hf$ are shown in Table 1. Uncertainties in these ratios have hindered the interpretation of Hf isotope data in situations where deviations from chondritic composition are small. Until recently, the uncertainty on the initial $^{176}Hf/^{177}Hf$ ratio, as determined from the eucrite meteorite isochron (Patchett and Tatsumoto 1980a, Tatsumoto et al. 1981), translated to a ±3 ε-unit uncertainty on the position of the evolution curve for the bulk unfractionated Earth.

## Hf ISOTOPES IN ZIRCON

Although zircon has a REE chondrite-normalized abundance pattern that typically rises steeply from La to Lu, the even greater affinity for Hf means that the Lu/Hf ratio in zircon is invariably very low, typically ~0.002. Thus the crystallization of zircon in any geological environment results in extreme fractionation of Lu/Hf between zircon and any other co-precipitating phases.

The $^{176}Lu/^{177}Hf$ ratio of zircon is usually < 0.0005, which means that time-integrated changes to the $^{176}Hf/^{177}Hf$ ratio as a result of *in situ* decay of $^{176}Lu$ proceed at virtually negligible rates. Hence, zircon effectively preserves the initial $^{176}Hf/^{177}Hf$ ratio, providing an enduring record of the Hf isotopic composition of their source environment at the time of crystallization. This ratio can then be used either to determine a Hf model age (with respect to undepleted or depleted mantle), contribute to a Lu–Hf isochron, or if the crystallization age of the zircon is known independently from U–Pb dating, to determine an initial $\varepsilon_{Hf}$ value with respect to the Hf isotope evolution reference curve for the bulk unfractionated Earth (Fig. 1). Thus, the Hf isotopic composition of zircon can be utilized as a geochemical tracer of a host rock's origin in exactly the same way whole-rock Nd isotopes are used. Hf is in fact a more sensitive tracer than Nd, as Lu/Hf in the depleted mantle has increased at approximately double the rate of Sm/Nd with respect to unfractionated material (Patchett and Tatsumoto 1980b). Furthermore, the well-known resilience of zircon to surficial weathering, transportation, and sedimentation processes means that the same isotopic tracing techniques can be applied to elucidate the origins of detrital zircon grains in sedimentary and meta-sedimentary rocks.

Verification that zircon effectively preserves the initial $^{176}Hf/^{177}Hf$ ratio of an igneous host rock was provided by a Lu–Hf isochron study of the early Archean Amîtsoq gneisses of West Greenland by Pettingill and Patchett (1981). Analyses of whole rocks and of zircon separates were regressed together to yield a combined Lu–Hf isochron age (Fig. 2). Although the sample set was neither strictly cogenetic nor contemporaneous, and the isochron poorly fit (MSWD ~ 12, with three rejected data points), the two analyzed zircon fractions plotted within error of each other, close to the *y*-axis intercept of the regression line defined by the whole-rock samples (which yielded a plausible age of 3.59±0.22 Ga ($\lambda_{Lu}$ = 1.94)) despite these rocks having experienced high-grade metamorphism in the late Archean (e.g., Nutman et al. 1996).

Early workers were understandably cautious in the use of zircon in Lu–Hf isotope studies, given the widespread phenomenon of zircon U–Pb isotopic discordance and the possibility that post-crystallization thermal disturbances might have an effect on zircon Hf compositions (Patchett et al. 1981, Patchett 1983, Smith et al. 1987). The principal concern was that addition of radiogenic Hf might occur during metamorphism, sourced from REE-rich accessory minerals such as monazite, allanite, xenotime or apatite that would have high Lu/Hf ratios. Part of the uncertainty was due to the fact that it was not always clear whether the observed U–Pb age discordance was due to the presence of younger zircon rims or to Pb loss from pre-existing zircon or due to other mechanisms. The problem was largely avoided through the selection of concordant populations as far as possible, and mechanical abrasion of grains to remove rims prior to sample digestion.

The possibility for open-system behavior of Hf isotopes in zircon was explored by a Hf study

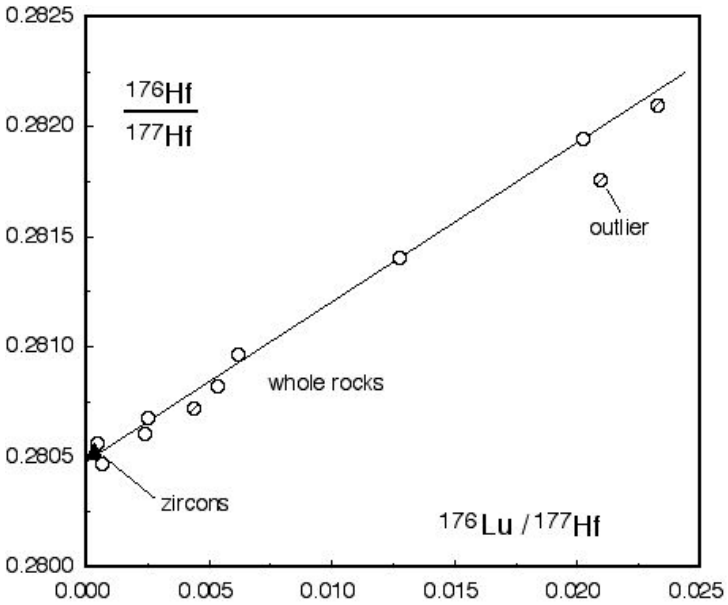


**Figure 2.** Lu/Hf isochron for the Amîtsoq gneisses, modified after Pettingill and Patchett (1981), showing how zircons may preserve the initial $^{176}Hf/^{177}Hf$ ratio of their igneous host rocks despite later metamorphism (providing that no older cores are present and that no new rims are added to the zircon during later events).

of variably discordant zircon populations separated from two Archean tonalitic gneisses from separate localities in the USA (Patchett 1983). Whereas on the one hand, a 3.18 Ga gneiss from the Granite Mountains, Wyoming, yielded identical $^{176}Hf/^{177}Hf$ ratios from both near-concordant and highly discordant zircon fractions, zircon from a gneiss from Watersmeet, Michigan, showed a systematic increase in $^{176}Hf/^{177}Hf$ with increasing U–Pb discordance. Patchett (op. cit.) surmized that the difference might be due to the presence among the Watersmeet zircon crystals of previously undetected metamorphic rims containing radiogenic Hf. This was later confirmed by the ion-probe Hf study of Kinny et al. (1991) which showed moreover that, aside from the newly-added rims, the remaining parts of the zircon crystals showed no detectable variation in $^{176}Hf/^{177}Hf$ irrespective of the amount of U–Pb age discordance.

This result raised confidence that it would be highly unlikely for the Hf composition of zircon to be modified significantly by exchange of Hf with the surrounding (Hf-poor) rock matrix during episodes of disturbance to the U–Pb system, other than through addition of Hf in rims of newly crystallized zircon. This was independently confirmed by Hoskin and Black (2000) who demonstrated that zircon may lose U, Th and radiogenic Pb differentially during metamorphism yet retain primary abundances of both Lu and Hf. Therefore, whilst the U–Pb isotopes are susceptible to resetting, Lu–Hf isotopes are not. This in-built resistance of zircon to Hf isotopic disturbance presents an important advantage over geochemical tracing based on whole-rock Nd isotope compositions since it is now clear that under certain circumstances Sm/Nd ratios may be disturbed during episodes of metamorphism (e.g., Gruau et al. 1996). This has led to the recent interest in applying the Lu–Hf system of zircon to study early Earth differentiation (Vervoort et al. 1996, Amelin et al. 1999, 2000). Hf analyses of zircon grains from the early Archean gneiss complex of West Greenland have confirmed that sources for the 3.82 to 3.65 Ga gneisses are not chondritic, implying early mantle depletion ($\varepsilon_{Hf}$ +0.5 to +5.0), but also suggest that previously reported highly positive $\varepsilon_{Nd}$ values may be artifacts of Sm/Nd disturbance during metamorphism (Vervoort et al. 1996).

## Measurement techniques

***Thermal Ionization Mass Spectrometry (TIMS).*** The earliest Hf isotopic studies of zircon were undertaken by conventional thermal ionization mass spectrometry of microgram quantities of purified Lu and Hf extracted from acid-digested samples via a series of cation-exchange columns (Patchett and Tatsumoto 1980c, Patchett et al. 1981, Corfu and Noble 1992, Barovich et al. 1995). Despite hafnium's relatively poor ionization efficiency, the high Hf content of zircon makes TIMS analysis of multigrain zircon separates easy in comparison to most whole-rock samples. Precision of < 0.005% on the measured $^{176}Hf/^{177}Hf$ ratio was readily obtained from combined samples of tens to hundreds of grains. Fractionation was monitored by assessment of the invariant $^{179}Hf/^{177}Hf$ ratio measured on prepared standard solutions.

***Secondary Ion Mass Spectrometry (SIMS).*** The first *in situ* microanalytical technique developed for Hf isotope measurements of zircon was the SIMS method of Kinny et al. (1991), undertaken using the original SHRIMP (sensitive high-resolution ion microprobe) at the Australian National University. Hf isotopic abundances were measured sequentially on an electron multiplier as $HfO^+$ species excavated from a 25-μm diameter area on individual sectioned zircon grains by a focused 10 kV oxygen ion beam. Counts taken on $^{176}Hf$ were corrected for the unresolvable spectral interferences $^{176}Yb$ and $^{176}Lu$, and correction of Hf isotope ratios for instrumental mass fractionation was based on the measured $^{178}Hf/^{180}Hf$ ratio. As a result of the small analytical volume, the low ionization efficiency for Hf and the limitations of single-collector ion counting, the precision of the measured $^{176}Hf/^{177}Hf$ ratios was an order of magnitude poorer than TIMS bulk zircon analyses, typically 0.05 % (or ±5 ε-units), and consequently the method was not widely adopted. However, SIMS technology (VG ISOLAB) was utilized subsequently as a means of enhancing ion yields of bulk samples prepared in the usual manner for TIMS analysis, by bombarding samples loaded onto a heated Re filament with a 15 kV Ar ion beam (Salters 1994).

***Inductively Coupled Plasma Mass Spectrometry (ICPMS).*** Currently the most popular method for Hf isotope analyses of zircon is plasma source mass spectrometry (e.g., Halliday et al. 1995) in which the sample is presented to the ionizing plasma either as an aspirated solution of chemically purified Lu and Hf (bulk method) or as material directly ejected from a zircon crystal by laser ablation (*in situ* method). In both methods, the sample aliquot is transferred to the mass analyzer (a double-focusing sector magnet) by a transporting gas, usually Ar. The combined isotope fractionation effects of the ablation/aspiration process and of the mass analyzer are monitored via internal and external standards. The use of multiple Faraday Cup detector arrays in modern instruments compensates for plasma instability to the extent that internal precision now approaches that of routine TIMS analysis, with the added appeal of rapid analysis time. The popularity of ICPMS has also led to development of improved chemical separation methods for Lu and Hf, optimized for the plasma source (Blichert-Toft et al. 1997) to the extent that single zircon grains containing as little as 25 ng of Hf can now be analyzed.

In the *in situ* method, material is ablated from a minimum 40- to 50-μm diameter area of an exposed zircon grain by a pulsed UV laser (see Kosler and Sylvester this volume). Excavating at a rate of 0.5-1.0 μm $s^{-1}$, the resultant analytical volume is up to 100 times that of an equivalent SIMS analysis, involving 10 to 50 ng of Hf (Thirlwall and Walder 1995, Griffin et al. 2000). The high temperature of the plasma results in fewer molecular interferences than are present in SIMS spectra, however, substantial corrections to the $^{176}Hf$ measurements are still required due to the presence of $^{176}Yb$ and $^{176}Lu$ isobars. Easy sample preparation, depth-profiling, and rapid analysis capability are the main advantages of laser ablation over conventional ICPMS.

## Studies of magmatic zircons

The pioneering survey of zircon Hf compositions in igneous rocks of Earth's crust by Patchett et al. (1981) demonstrated that zircon from mantle-derived igneous rocks provide an excellent record of the evolution of unfractionated and fractionated mantle reservoirs through time and hence pro-

vide a means of tracking the development of mantle heterogeneity. Depleted (high Lu/Hf) mantle was a detectable source for magmatic rocks as old as ca. 2.7 Ga, such that rocks of that age analyzed from the Archean block of southern Finland yielded $\varepsilon_{Hf}$ values of up to +14 (present-day oceanic basalts have $\varepsilon_{Hf}$ up to +23). Not all of the rocks from southern Finland analyzed by Patchett et al. (1981) showed such highly depleted Hf signatures; others yielded $\varepsilon_{Hf}$ values that were close to zero. The latter were interpreted as representing relatively undepleted mantle sources that coexisted spatially and temporally with the more highly depleted sources, although an alternative possibility is contamination of magma from a depleted mantle source with old crust carrying an enriched Hf signature (Fig. 1). The presence of such enriched (low Lu/Hf) reservoirs in the lower crust was demonstrated by the highly negative $\varepsilon_{Hf}$ values of -12 and -10 determined for the ca. 1.8 Ga Natannen and Vainospää granites which intrude Archean rocks of northern Finland and which are interpreted as largely crustally-derived melts. Another potential source for enriched Hf is oceanic crust returned to the mantle by subduction.

Among the studies of broadly contemporaneous suites of intrusions that have followed the work of Patchett et al. (1981), those with zircons having comparatively low positive $\varepsilon_{Hf}$ values, have generally been interpreted as indicating crustal contamination and/or the presence of zircon xenocrysts, whilst those with higher values have been interpreted as uncontaminated, mantle-derived magmas (e.g., Smith et al. 1987, Corfu and Noble 1992, Corfu and Stott 1993). Smith et al. (1987) showed that within a single volcanic sequence, a wide variation in $\varepsilon_{Hf}$ could occur, implying heterogeneity within and/or among magma sources, possibly related to variable depths of melting. Proceeding stratigraphically up the 2.75 Ga Michipicoten greenstone belt of the southern Superior Province, Canada, one passed from tholeiitic pillow basalts ($\varepsilon_{Hf}$ +8.7), through dacitic tuffs ($\varepsilon_{Hf}$ +2.0) to rhyolite ($\varepsilon_{Hf}$ -1.3). Smith et al. (1987) considered this trend as reflecting a gradual change in magma sources from depleted mantle initially, to increasingly enriched (crustal) sources. They also noted longer-term trends in $\varepsilon_{Hf}$ over the period of greenstone activity in the region.

**Studies of detrital zircon**

The well-documented resilience of zircon to rock weathering, transportation, and sedimentation processes results in major accumulations of detrital zircons in the thick clastic sedimentary sequences that accumulate on continental margins. Non-metamict zircons are able to survive the rigors of sedimentary sorting with only minor attrition and therefore provide an important record of sedimentary provenance as they preserve in their U–Pb and Hf isotopic compositions both chronological and geochemical information which can be used to identify likely sources for the zircons (see Fedo et al., this volume). Moreover, this resilient behavior of zircon leads to fractionation of Lu from Hf, because much of the eroded source rock's Hf is carried by zircons into sandy continental shelf deposits, whilst finer-grained, deeper water sediments acquire a higher proportion of the REE. This phenomenon was verified by Patchett et al. (1984) who demonstrated that compared to continental shelf sands and turbidite deposits, marine shales and clays have higher Lu/Hf ratios on average, whilst deep-sea red clays and Mn nodules show extreme Lu/Hf fractionation (with values up to 2.5 times the chondritic ratio). These results were in marked contrast to the lack of variation in Sm/Nd ratios among the same samples.

Hf isotope studies of detrital zircon have evolved with improving technology from studies based on the combined analysis of multiple grains (e.g., Stevenson and Patchett 1990) through to single-grain (e.g., Amelin et al. 1999, Bodet and Schärer 2000) and sub-grain scale studies (e.g., Knudsen et al. 2001). Early workers noted the potential problems caused by inheritance and metamorphic rims but merely hoped to minimize their contribution to bulk analyses by careful sample and grain selection. In more recent work involving single grains, mechanical abrasion (Krogh 1982) and cathodoluminescence (CL) and back-scattered electron (BSE) imaging have been employed, and grains recording highly discordant U–Pb ages avoided.

In the expectation that if large volumes of continental crust had existed in the early Archean

there should be significant fractions of early Archean zircon preserved in younger sedimentary sequences, Stevenson and Patchett (1990) studied zircon extracted from predominantly low-grade, quartz-rich metasediments from the Canadian Shield, North Atlantic, Wyoming, and Kaapvaal cratons as a means of assessing continental growth rates in the Archean. Zircon Hf $T_{CHUR}$ model ages (CHUR = chondritic undepleted reservoir) were compared with the stratigraphic ages of the host sequences (as best as they were known). Such model ages are calculated by extrapolating back from the present-day measured Hf isotope ratio to the point in time T at which the isotopic evolution curve for the sample (given its Lu/Hf ratio) intersects the CHUR evolution curve. Whilst the Neoarchean (3.0 to 2.5 Ga) sequences consistently showed close coincidence of the zircon Hf $T_{CHUR}$ model age and the deposition age, zircons from the Paleoproterozoic (2.5 to 2.0 Ga) sequences generally yielded older Hf $T_{CHUR}$ model ages (2.84 to 2.39 Ga). An alternative way of describing these results is to say that $\varepsilon_{Hf}$ values calculated at the time of deposition were close to zero for the Neoarchean samples and negative for the Paleoproterozoic ones. From the lack of older age signatures in the Neoarchean sequences, Stevenson and Patchett (op. cit.) concluded that prior to 3.0 Ga only small volumes of continental crust had existed, that these small nuclei grew rapidly during the Neoarchean, and that erosion of larger Neoarchean landmasses resulted in extensive inheritance of Neoarchean zircons in the Paleoproterozoic sequences.

The advantage of using Hf model ages over U–Pb ages for such a study is that whereas U–Pb dating can identify the igneous crystallization age of a segment of crust, Hf isotopes can distinguish juvenile, essentially mantle-derived crust of a given age ($\varepsilon_{Hf}$ positive, Hf model age close to crystallization age) from contemporary crust derived by remelting of older crust ($\varepsilon_{Hf}$ negative, Hf model age >> crystallization age). Thus the former existence of old crust may be detected both directly if old detrital zircons are present and indirectly if younger detrital zircons with old Hf isotope signatures are present.

The oldest known terrestrial zircon crystals are detrital grains ≥4.0 Ga old from the Mount Narryer and Jack Hills metasedimentary belts of Western Australia. Their Hf composition has been studied by Amelin et al. (1999) using LA-ICPMS, following reconnaissance SIMS analyses by Kinny et al. (1991). Out of 37 single grains from the Jack Hills studied by Amelin et al. (1999), five grains with $^{207}Pb/^{206}Pb$ ages > 4.0 Ga were found to have close to chondritic Hf compositions ($\varepsilon_{Hf}$ +1 to -1) at the indicated $^{207}Pb/^{206}Pb$ age. Another five grains with $^{207}Pb/^{206}Pb$ ages of 3.7 to 4.0 Ga ranged in $\varepsilon_{Hf}$ from 0 to -5 suggesting a trend to lower $\varepsilon_{Hf}$ as the early crust evolved. However, these highly negative values must be viewed with some caution, as the analyzed zircon crystals were discordant and could represent ≥4.0 Ga zircons that suffered early Pb loss, lowering their $^{207}Pb/^{206}Pb$ age while still plotting close to concordia. Certainly, the youngest detrital grains analyzed from the sample, with $^{207}Pb/^{206}Pb$ ages of ca. 3.4 Ga including some concordant grains, and $\varepsilon_{Hf}$ values of -4 to -9, can confidently be regarded as having been derived at least in part from remelting of an early sialic crust.

At the other end of the age spectrum, Bodet and Schärer (2000) studied detrital zircon and baddeleyite grains from four major rivers draining present-day Indochina—the Red, Mekong, Salween and Irrawaddy rivers—in order to examine the crustal architecture (past and present) of the predominantly sediment-covered southeast Asian continent. A high proportion of zircon and baddeleyite from the river sands recorded Proterozoic U–Pb ages. These were interpreted as having been derived from the exposed Phanerozoic cover sequences, rather than directly from basement rocks, implying that the older detrital grains had been through a number of sedimentary cycles. The Proterozoic age groups showed a progression from exclusively positive (i.e., primitive) initial $\varepsilon_{Hf}$ values for the >2.0 Ga grains, through to more variable sources for the 0.8 to 2.0 Ga grains, the latter ranging in $\varepsilon_{Hf}$ from -8 to +8. Zircons recording younger ages (≤0.5 Ga) were more readily matched to known orogenic events affecting SE Asia and adjacent areas, such as the Mesozoic Indosinian and Cenozoic Himalayan events, and were considered more likely to have been eroded directly from exposed plutons generated during these events. With few exceptions, the Indosinian

age group is dominated by grains derived from magmas of largely crustal origin ($\varepsilon_{Hf}$ -6 to -17), whilst the younger age groups encompassed both highly depleted and enriched source compositions ($\varepsilon_{Hf}$ -14 to +13).

**Studies of metamorphic zircon**

The presence of metamorphic zircon rims has generally been viewed as a nuisance by those wishing to study the Hf composition of original magmatic or detrital zircons in ancient metamorphosed rocks. As a result, there is comparatively little information on the Hf composition of zircon grown during metamorphism. Trace element studies (e.g., Hoskin and Black 2000, Rubatto 2002) have shown that metamorphic zircons in high-grade rocks (amphibolite, granulite and eclogite facies) have similar Hf abundances to igneous zircon, and either similar or lower HREE contents, although Hanchar and Rudnick (1995) showed that granulite facies metamorphic overgrowths from McBride, Australia, lower crustal xenoliths were depleted in Hf and the HREE relative to the igneous cores preserved in the zircon crystals. Thus in many cases Lu/Hf ratios should be comparable to or lower than those of typical igneous zircon, and metamorphic zircons should be as reliable at preserving their initial $^{176}Hf/^{177}Hf$ ratio. That ratio is likely to be highly variable depending on the source(s) of the Hf and the compositions of pre-existing and co-precipitating phases, though always at least as radiogenic as the Hf present in any original magmatic or detrital zircons.

**Studies of mantle zircons**

Zircons of likely mantle origin include those found in metasomatized peridotite, eclogite, as diamond inclusions, and in particular as members of megacryst suites associated with alkali basalt, kimberlite, carbonatite and other mafic-ultramafic magma types. Among these, only megacrystic zircons have been investigated for their Hf isotopic compositions so far (Kinny et al. 1989, Thirlwall and Walder 1995, Schärer et al. 1997, Griffin et al. 2000, Nowell et al. 2003). The results provide direct insights into the composition and evolution of the Earth's mantle, without fear of crustal contamination effects.

The most comprehensive study so far is that by Griffin et al. (2000) involving zircon from nineteen kimberlite localities in southern Africa, Siberia and Australia. The kimberlites studied by Griffin et al. span the age range 810 to 90 Ma and the majority of zircon megacrysts give U–Pb ages corresponding to the time of kimberlite emplacement, except for two localities where an additional older suite of megacrysts was identified: Timber Creek in northern Australia (ca. 1.46 Ga) and Jwaneng in Botswana (U–Pb ages up to 2.8 Ga, as previously identified by Kinny et al. 1989). The Hf compositions of the analyzed megacrysts are variable. For some localities the measured range in $\varepsilon_{Hf}$ is quite narrow: -2 to +1 for thirty megacrysts from the 90 Ma Monastery kimberlite, South Africa; +3 to +5 for the 170 Ma Orroroo kimberlite in South Australia; +6 to +10 for the young, 240 Ma megacryst suite from Jwaneng, Botswana. Others were more variable, most notably the 90 Ma Leicester kimberlite, South Africa, which had $\varepsilon_{Hf}$ ranging from -1 to -9 (six megacrysts); and the 92 Ma Orapa kimberlite, Botswana, with $\varepsilon_{Hf}$ ranging from 0 to -16 (nine megacrysts) and one at +13.

On face value, the fact that U–Pb ages for these megacrysts mostly correspond to the time of eruption of the host diatreme suggests a genetic link between the two, despite the common observation that zircon megacrysts show late-stage resorption textures and reaction rims of $ZrO_2$, implying that they were not in equilibrium with the mafic-ultramafic host magma. The origin of the megacryst suite-forming magma itself remains controversial. Whereas most of the megacryst zircon have Hf compositions consistent with a variably depleted mantle (OIB-type) source, the highly negative $\varepsilon_{Hf}$ values (down to -16) require an additional component of nonradiogenic Hf to be present. Griffin et al. (2000) argue that this extra component is likely to be ancient lithospheric mantle as represented by various suites of peridotite xenoliths entrained in the kimberlites and by the presence of older mantle zircons at some localities, but Nowell et al. (in press) argue for a sub-lithospheric source such as an isolated, ancient reservoir of subducted oceanic crust. The highly variable Hf composi-

tions of some individual suites, such as that at Orapa, imply considerable variability in the degree of interaction of the megacryst-forming magma(s) with this additional low Lu/Hf component.

It has often been argued that the U–Pb systems in these megacrysts would be continuously reset by the high temperatures of their mantle source regions such that any record of pre-eruption history would be lost. The occurrence of two distinct age groups of zircon megacrysts in the Jwaneng and Timber Creek kimberlites, each with distinct Hf isotope signatures (Kinny et al. 1989, Griffin et al. 2000) shows that this is not necessarily the case. The Hf isotope data show clearly that the older, Precambrian megacrysts from both localities are genetically distinct from the younger megacrysts, and hence that the latter are not merely old megacrysts whose U–Pb systems have been reset to the age of kimberlite pipe emplacement.

In the study by Schärer et al. (1997) of zircon and baddeleyite megacrysts from the Mbuji-Mayi kimberlite in Zaire, Hf isotopes again provided the critical information to discriminate between different possible scenarios to explain the U–Pb isotope systematics of the megacrysts. The combined U–Pb analyses of fragments of both zircon and baddeleyite megacrysts defined a discordance line projecting from the ~70 Ma eruption age of the host kimberlite back to ca. 2.5 Ga. The key question raised is whether the megacrysts are ca. 2.5 Ga grains that have suffered almost complete Pb loss at 70 Ma or whether they crystallized at 70 Ma, just prior to the eruption, and had incorporated trace amounts (<0.1 ppm in the zircon) of excess unsupported radiogenic Pb. Three zircon fractions from two megacrysts measured for Hf yield consistent isotopic compositions which translate to $\varepsilon_{Hf}$ values of +8 for t = 70 Ma and +66 for t = 2.5 Ga. Whereas the former value of $\varepsilon_{Hf}$ falls into the expected range for material sourced from depleted mantle at 70 Ma, the latter is unfeasibly high for any known reservoir at 2.5 Ga. Thus the Hf data strongly support, over alternative models, the interpretation that the megacrysts crystallized at ca. 70 Ma from depleted mantle, incorporating some ancient Pb. In addition, some variability in the measured $\varepsilon_{Hf}$ of the baddeleyite megacrysts (+5 to +10 for t = 70 Ma) again suggests small-scale heterogeneity in the mantle source (Schärer et al. 1997).

### Concluding remarks: Lu–Hf isotopes and zircon

The importance of the Lu–Hf isotope system in zircon clearly lies in its use as a geochemical tracer rather than as a geochronometer. There is little value in dating zircons by Lu–Hf (model ages or as part of mineral isochrons) when much higher age precision is normally obtainable using U–Pb isotopes. Studies combining both the Lu–Hf and U–Pb isotope systems are undoubtedly the most powerful, as the age of the zircon must be determined accurately if the petrogenetic information contained within the Hf initial ratio is to be divulged. The problem of dealing with complex zircon populations involving multiple age components and periods of isotopic disturbance can be dealt with by a variety of strategies, such as the use of *in situ* analytical techniques, CL and BSE imaging and single-grain abrasion methods, all of which can assist in identifying and targeting individual age components and in improving U–Pb age concordance. The full advantage of using Hf isotopes in zircon to trace rock origins and the evolution of Earth's crust and mantle over time, as opposed to using whole-rock Nd isotopes, can then be realized.

## Sm–Nd ISOTOPE STUDIES OF ZIRCON

Since its development during the 1970s, the Sm–Nd isotope technique has become a standard geochemical tool used widely for geochronology and isotopic tracing (see reviews by DePaolo 1988, Dickin 1995). Applications of the Sm–Nd technique involving zircon take advantage of the fact that zircon, like garnet, is among the few common minerals which favor the heavy rare earth elements (HREE) over the lighter rare earths (e.g., Gromet and Silver 1983, Fujimaki 1986, Hoskin and Schaltegger, this volume) and therefore has rather high Sm/Nd ratios amenable to high-precision dating. Furthermore, REE diffusion in zircon has been shown to be slow, allowing for the preservation of original REE patterns and, presumably, Sm–Nd isotopic signatures, through high-temperature events (Cherniak et al. 1997, Cherniak and Watson, this volume). Despite these poten-

tial advantages, only few case studies of Sm–Nd zircon dating have been published.

**REE patterns of zircon**

*In situ* microbeam studies of pure zircon have shown that a typical REE pattern for zircon is one characterized by strong LREE/HREE fractionation, with a relatively smooth increase in chondrite-normalized abundances from La to Lu, punctuated by both Ce excess and Eu depletion (e.g., Hinton and Upton 1991, Thomas et al. 2002, Rubatto 2002, Thomas et al., this volume; Hoskin and Schaltegger, this volume). Sm/Nd ratios of zircon are therefore high by comparison with other common minerals, and with crustal rocks in general. While this appears to be the normal REE signature for zircon, there is considerable variability (e.g., Heaman et al. 1990, Maas et al. 1992, Hoskin 2000). In bulk zircon fractions (≥1000 grains, or at least 10 mg are required for conventional Sm–Nd isotope work), such variability is amplified by the common presence of REE-rich impurities (minerals and melt inclusions). REE-rich inclusions are probably the reason for the relatively high Nd abundances (10-700 ppm) and low Sm/Nd ratios (≤0.65) reported in bulk zircon Sm–Nd isotope studies (cf. Nd abundances of often <1 ppm and Sm/Nd ratios up to 3 from ion microprobe data).

**Sm–Nd mineral dating of zircon**

The primary aim of nearly all Sm–Nd isotope studies of zircon published thus far has been the construction of mineral isochrons for granitic rocks and orthogneisses. Although successful in some cases, the isochrons were rarely accurate or precise enough to provide serious competition for U–Pb geochronology. More importantly, most studies have reported instances of zircon fractions plotting below the isochrons defined by other minerals (apatite, feldspars, titanite, etc.). These have been ascribed either to hydrothermal alteration or to the presence of inherited zircon contributing unequilibrated Nd to the analysis.

The first attempt to use zircon for Sm–Nd mineral dating targeted a tonalitic phase of the mid-Archean Watersmeet Gneiss in Michigan, USA (Futa 1986). Earlier isotopic work had established ages as old as ca. 3.6 Ga for these gneisses, but also produced Rb–Sr isotope evidence for a younger thermal overprint near 1.75 Ga. Sm–Nd isotopic data for whole rocks and various mineral fractions failed to provide clear age information: two whole-rock fractions, allanite, biotite and an impure plagioclase fraction clustered at low Sm/Nd, whilst apatite and titanite (with higher Sm/Nd) defined two subparallel lines (apatite-plagioclase, titanite-biotite/whole-rock) with apparent ages near 1.8 Ga. Clearly, the Sm–Nd isotope systems of apatite and titanite had been variably reset, presumably during the event recorded in the Rb–Sr data. Two zircon fractions with Sm/Nd ratios of 0.41 and 0.58 plotted well below any of the reference lines defined by the other minerals and yielded zircon-whole rock apparent ages near 1.0 Ga, considered to be geologically meaningless. The author speculated that the zircons could have been contaminated with nonradiogenic Nd derived from LREE-rich allanite (or monazite) during a hydrothermal alteration event. In retrospect it would have been more prudent to choose a simpler geological scenario to test the validity of such an isochron method involving zircon. As discussed above, a U–Pb and Lu–Hf study of zircons from the Watersmeet Gneiss (Kinny et al. 1991) later demonstrated the presence of at least two generations of zircon in these rocks, revealing a more complicated history than previously recognized.

More coherent mineral Sm–Nd isotope systematics were reported from a geologically simpler system, the Tertiary Bergell Intrusion in the Swiss Alps (von Blanckenburg 1992). Allanite, apatite, titanite, zircon and whole-rock fractions from a tonalite all yielded initial $\varepsilon_{Nd}$ values near -5, equivalent to an isochron age of 25±22 Ma (recalculated from the original data). This was consistent with the U–Pb zircon age of ca. 32 Ma, but imprecise due to the limited Sm/Nd dispersion of the minerals. Similar results were obtained from a granodiorite from the same complex, however the zircon fraction from that sample had an $\varepsilon_{Nd}$ value near -8 (for t = 32 Ma), somewhat lower than the allanite, apatite, titanite and whole-rock fractions which had $\varepsilon_{Nd}$ near -6. The difference was interpreted as

evidence for inherited Nd in the zircons, consistent with the evidence from U–Pb dating for ~10% of inherited zircon in this fraction.

Similar results were described from a Scottish pluton (Paterson et al. 1992). Zircon fractions from two phases within the zoned ca. 425 Ma Strontian Intrusion showed contrasting Sm–Nd isotopic characteristics. $\varepsilon_{Nd}$ values for apatite, titanite, zircon and whole-rock for the outer Loch Sunart hornblende-biotite granodiorite were similar near -0.5 (for t = 425 Ma), corresponding to an isochron age of 387±76 Ma, within error of the U–Pb zircon age. The Sm/Nd ratio of the zircon fraction was again quite low, which accounts for the poor precision of the isochron. By contrast, two zircon fractions from the inner phase, the Glen Sanda biotite granodiorite, had lower $\varepsilon_{Nd}$ for t = 425 Ma (-7.9) than coexisting apatite, monazite and whole-rock fractions (-4.6) and were therefore clearly out of equilibrium with their matrix. As in the Swiss example, this was explained as due to Nd inheritance within inherited zircon, consistent with evidence from U–Pb isotope data.

Li (1994) reported a similar isotopic contrast between zircon ($\varepsilon_{Nd}$ -8.2) and other minerals ($\varepsilon_{Nd}$ near -6) in the ca. 425 Ma Guidang hornblende-biotite granodiorite in south China. Once again, the zircon fraction had a relatively low Sm/Nd ratio (0.54) and plotted clearly below other data points (plagioclase, biotite, hornblende, apatite, titanite and whole-rock). The latter yielded a Sm–Nd isochron age of 428±12 Ma, identical to a Rb–Sr mineral isochron age and several concordant U–Pb zircon analyses. The U–Pb work also indicated a significant amount of inheritance that was interpreted as the reason for the Nd isotopic disequilibrium between zircon and its matrix.

Poitrasson et al. (1998) obtained a 291±13 Ma Sm–Nd isochron age for whole-rock, allanite, amphibole and inclusion-free zircon fractions from the ca. 283 Ma Manteluccia Granite, Corsica. A second fraction of inclusion-bearing zircon plotted slightly (~0.5 $\varepsilon_{Nd}$ units) below the isochron. This was thought to reflect the presence of inherited older zircon and apatite picked up during magma ascent. In both zircon fractions, Nd abundances are high (150, 420 ppm) and Sm/Nd ratios are low (<0.3). Metamict zircon from the nearby ca. 259 Ma Evisa Granite plotted well below an isochron formed by other minerals, and defined a second, younger, ca. 209 Ma isochron with the whole-rock and alkali feldspar. The zircon and alkali feldspar (and at least one further, LREE-rich mineral, presumably allanite which was not analyzed) were thought to have been affected by hydrothermal alteration at the time indicated by the younger isochron, which correlates with a widespread alteration event affecting Western Europe during the Lower Jurassic.

Sm–Nd dating of zircons in mafic metamorphic rocks has returned some of the most promising results to date. von Quadt (1992) obtained consistent U–Pb and Sm–Nd isochron ages for two mafic metamorphic rocks from the Tauern Window (Eastern Alps). These isochrons, in both cases controlled by high-Sm/Nd zircon, document events at ca. 490 and ca. 657 Ma, among the oldest recorded ages from the Alps.

Empirical evidence for a high closure temperature of the zircon Sm–Nd system was provided by Wernicke and Getty (1997) in a study of gneissic quartz diorite from the Skagit Gneiss Complex in the northwestern USA. Plagioclase, apatite and hornblende (low Sm/Nd) and two zircon fractions (~1 ppm Nd; Sm/Nd ~ 1.6) define a 68.3±2.1 Ma isochron age, very similar to a concordant U–Pb zircon age of 68±2 Ma. Two garnet fractions from the same meta-diorite sample combine with the plagioclase, apatite and hornblende to yield a 60.0±1.2 Ma Sm–Nd age. Based on the apparent absence of inherited zircon cores, the calcic chemistry and high temperature of the diorite magma (which would tend to dissolve of any inherited zircon Watson 1996), and the concordance of the U–Pb and Sm–Nd ages, it was argued that the quartz diorite was emplaced at 68 Ma, while the garnet Sm–Nd system closed after a further 8 Ma of slow cooling under amphibolite facies conditions. Thus, diffusion rates in the zircon Sm–Nd system appear to be no faster than in the U–Pb system (at least in the temperature range up to 700°C), and are clearly slower than in the garnet Sm–Nd system under the same conditions.

## Inherited Nd

Several of the reports discussed above describe zircon fractions that are out of isotopic equilibrium with their matrix. In each case, the zircon analyses plot below reference isochrons defined by the other minerals in the rock and they have lower initial $\varepsilon_{Nd}$. This has been ascribed to the presence of exotic Nd associated with inherited zircon (von Blanckenburg 1992, Paterson et al. 1992, Li 1994, Poitrasson et al. 1998). As discussed by Paterson et al. (1992), the observation that (presumably) inherited Nd has lower $\varepsilon_{Nd}$ than the magmatic minerals of the rock is opposite to the expected observation. As most zircon has higher Sm/Nd than average crust, inherited old zircon crystals should have relatively high $\varepsilon_{Nd}$ compared to crustal material of similar age. After appropriate aging, mixing of this inherited Nd (e.g., as inherited cores) with magmatic Nd hosted in melt-precipitated zircon in the same rock, should produce zircon fractions with an $\varepsilon_{Nd}$ that is higher than that of the pure melt-related Nd component of the system. In an attempt to explain this unexpected behavior of zircon Sm–Nd systems, Paterson et al. (1992) discussed mechanisms such as post-crystallization disturbance, recoil or diffusive loss of $^{143}$Nd, and mixing of zircon crystals from distinct magmas. However, the model that is most consistent with both the Sm–Nd and U–Pb isotopic evidence involves incorporation of zircon from an ancient crustal source (with very low $\varepsilon_{Nd}$) into a felsic magma that is itself predominantly derived from more juvenile (high $\varepsilon_{Nd}$) material (Fig. 3).

## Concluding remarks: Sm–Nd isotopes and zircon

With few exceptions, Sm–Nd mineral dating of igneous rocks using zircon is hampered by the common presence of (i) inherited Nd, presumably in discrete cores, resulting in poor isochron fits

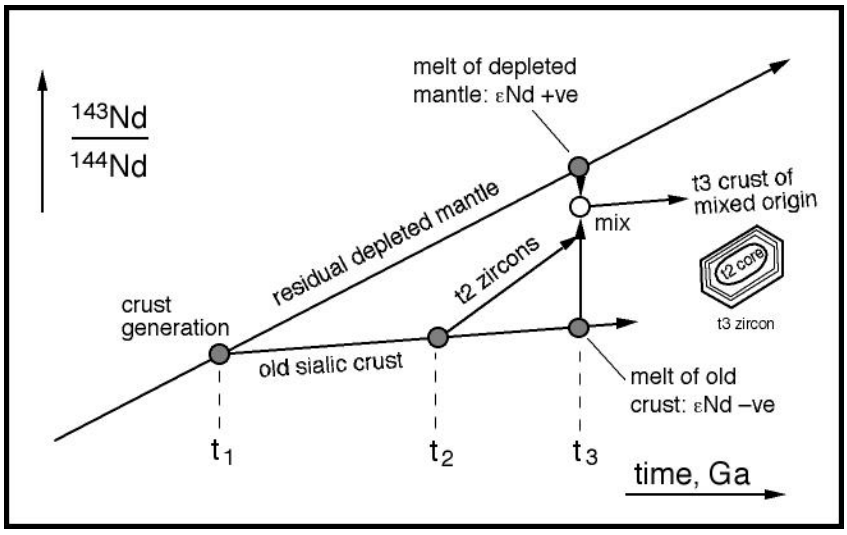


**Figure 3.** Schematic Nd isotope evolution diagram, modified after Paterson et al. (1992), showing how inherited zircon in a granite can have a lower initial $^{143}$Nd/$^{144}$Nd than the host rock, despite evolving with a long-term elevated Sm/Nd ratio. At time $t_1$, sialic crust forms with low Sm/Nd. At time $t_2$, zircon forms within this old crust (e.g., during a partial melting event). Typical for zircon, it has a higher Sm/Nd ratio than most other minerals in the rock. With time, zircon and its parent sialic crust will develop drastically different $^{143}$Nd/$^{144}$Nd ratios. At time $t_3$, renewed magmatic activity produces hybrid granitic magmas involving both old sialic crust and much younger, juvenile source rocks (e.g., by crustal assimilation into basaltic magma, or remelting of mixed crustal source rocks). Some old zircon survives as an inheritance fraction. If the initial $^{143}$Nd/$^{144}$Nd of the mixed magma is dominated by the more primitive component, its composition may be more radiogenic than the inherited zircon.

and/or age bias, and of (ii) REE-rich impurities, which typically lower the measured Sm/Nd ratio with respect to pure zircon, resulting in reduced isochron lengths and precision. Zircon Sm–Nd dating therefore is not competitive with other methods in terms of accuracy, precision and analytical effort. *In situ* microbeam techniques, although capable of avoiding such problems of inherited zircon and inclusions, are presently too imprecise to be a viable alternative and not sensitive enough to measure sub-ppm to ppm-level Nd and Sm in zircon. As it stands, therefore, Sm–Nd dating of zircon will likely remain on the fringes of geochronological interest, certainly in comparison to U–Pb and Lu–Hf studies.

## OUTLOOK

The resurgence of interest in Hf isotope studies involving zircon made possible by improved analytical methods is likely to continue into the near future, especially once the current uncertainty as to the value of the $^{176}$Lu decay constant and of the composition of the unfractionated silicate Earth over time is resolved. In addition to its value as a geochemical tracer, the resistance of zircon to exchange Hf with the external rock environment permits Hf isotope studies to make a fundamental contribution to understanding the mechanisms leading to U–Pb age discordance in zircon, because the Hf composition provides a means to discriminate between discordance generated by recrystallization (Hf unchanged) as opposed to by addition of a younger rim (exotic Hf added). For the same reason, Hf isotopes can indicate if and when complete resetting of U–Pb isotopes in zircon may have occurred, and thereby greatly assist in the interpretation of zircon ages from high-grade rocks derived from the lower crust and mantle. Advances in the understanding of the behavior of zircon in natural systems will likely come from U–Pb and Hf isotope studies integrated with trace element, microstructural and other spectroscopic data.

The use of zircon Sm–Nd systematics as a dating tool appears most promising for rocks containing low levels of inheritance, e.g., mafic rocks and their felsic differentiates. Acid leaching, used successfully in garnet geochronology, could be employed to purify powdered zircon separates and to increase their Sm/Nd ratios. Surprisingly, we have not found any examples of Sm–Nd isotopic tracing of mantle-derived zircons, even though this could yield insights into the evolution of the subcontinental mantle similar to those provided by *in situ* Hf isotopic studies. Apart from initial $\varepsilon_{Nd}$ values (calculated at the zircon's U–Pb age), mantle-derived zircon could also provide Nd model ages which would reflect the formation of partial melts and/or metasomatic fluids in the mantle. Because the Nd in old mantle zircons is likely to be highly radiogenic, such model ages may in fact be 'inverse,' i.e., their growth trajectories approaching the depleted mantle curve from the high-$\varepsilon_{Nd}$ side, the opposite of the traditional 'Nd crustal residence' age.

Finally, La–Ce isotope studies (e.g., Tanaka et al. 1987, Makishima and Nakamura 1991) of zircon potentially would provide initial $\varepsilon_{Ce}$ values without the need for significant age corrections because, like Lu/Hf, La/Ce in zircons is usually very low. Zircon Ce isotope studies could thus be used to track the Ce isotope evolution and therefore long-term La/Ce of the continental crust and mantle.

## ACKNOWLEDGMENTS

We thank John Hanchar and Paul Hoskin for the opportunity to undertake this review and for their most helpful reviews of the manuscript.

## REFERENCES

Amelin Y, Lee D-C, Halliday AN, Pidgeon RT (1999) Nature of the Earth's earliest crust from hafnium isotopes in single detrital zircons. Nature 399:252-255

Amelin Y, Lee D-C, Halliday AN (2000) Early-middle Archaean crustal evolution deduced from Lu-Hf and U-Pb isotopic studies of single zircon grains. Geochim Cosmochim Acta 64:4205-4225

Barovich KM, Beard BL, Cappel JB, Johnson CM, Kyser TK, Morgan BE (1995) A chemical method for hafnium separation from high-Ti whole-rock and zircon samples. Chem Geol 121:303-308

Blichert-Toft J, Albarède F (1997) The Lu-Hf isotope geochemistry of chondrites and the evolution of the mantle-

crust system. Earth Planet Sci Lett 148:243-258
Blichert-Toft J, Chauvel C, Albarède F (1997) Separation of Hf and Lu for high-precision isotope analysis of rock samples by magnetic sector-multiple collector ICP-MS. Contrib Mineral Petrol 127:248-260
Bodet F, Schärer U (2000) Evolution of the SE-Asian continent from U-Pb and Hf isotopes in single grains of zircon and baddeleyite from large rivers. Geochim Cosmochim Acta 64:2067-2091
Cherniak DJ, Hanchar, JM, Watson, EB (1997) Rare-earth diffusion in zircon. Chem Geol 134:289-301
Corfu F, Noble SR (1992) Genesis of the southern Abitibi greenstone belt, Superior Province, Canada: evidence from zircon Hf isotope analyses using a single filament technique. Geochim Cosmochim Acta 56:2081-2097
Corfu F, Stott GM (1993) Age and petrogenesis of two late Archean magmatic suites, northwestern Superior Province, Canada: Zircon U-Pb and Lu-Hf isotopic relations. J Petrol 34:817-838
Correia Neves JM, Lopes Nunes JE, Sahama ThG (1974) High hafnium members of the zircon-hafnon series from the granite pegmatites of Zambézia, Mozambique. Contrib Mineral Petrol 48:73-80
DePaolo DJ (1988) Neodymium Isotope Geochemistry: An Introduction. Springer-Verlag, New York
Dickin AP (1995) Radiogenic Isotope Geology. Cambridge University Press, Cambridge, UK
Fujimaki H (1986) Partition coefficients of Hf, Zr and REE between zircon, apatite and liquid. Contrib Mineral Petrol 94:42-45
Futa K (1986) Sm-Nd systematics of a tonalitic augen gneiss and its constituent minerals from northern Michigan. Geochim Cosmochim Acta 45:1245-1249
Griffin WL, Pearson NJ, Belousova E, Jackson SE, van Achterbergh E, O'Reilly SY, Shee SR (2000) The Hf isotope composition of cratonic mantle: LAM-MC-ICPMS analysis of zircon megacrysts in kimberlites. Geochim Cosmochim Acta 64:133-147
Gromet LP, Silver LT (1983) Rare earth element distributions among minerals in a granodiorite and their petrogenetic implications. Geochim Cosmochim Acta 47:925-939
Gruau G, Rosing M, Bridgwater D, Gill RCO (1996) Resetting of Sm-Nd systematics during metamorphism of >3.7-Ga rocks: implications for isotopic models of early Earth differentiation. Chem Geol 133:225-240
Halliday AN, Lee D-C, Christensen JN, Walder AJ, Freedman PA, Jones CE, Hall CM, Yi W, Teagle D (1995) Recent developments in inductively coupled plasma magnetic sector multiple collector mass spectrometry. Intl J Mass Spec Ion Proc 146/147:21-33
Hanchar JM, Rudnick RL (1995) Revealing hidden structures: the application of cathodoluminescence and backscattered electron imaging to dating zircons from lower crustal xenoliths. Lithos 36:289-303
Heaman LM, Bowins R, Crocket J (1990) The chemical composition of igneous zircon suites: implications for geochemical tracer studies. Geochim Cosmochim Acta 54:1597-1607
Hinton RW, Upton BGJ (1991) The chemistry of zircon: variations within and between large crystals from syenite and alkali basalt xenoliths. Geochim Cosmochim Acta 55:3287-3307
Hoskin PWO (2000) Patterns of chaos: fractal statistics and the oscillatory chemistry of zircon. Geochim Cosmochim Acta 64:1905-1923
Hoskin PWO, Black LP (2000) Metamorphic zircon formation by solid-state recrystallization of protolith igneous zircon. J Metamor Geol 18:423-439
Hoskin PWO, Ireland TR (2000) Rare earth element chemistry of zircon and its use as a provenance indicator. Geology 28:627-630
Kinny PD, Compston W, Bristow JW, Williams IS (1989) Archaean mantle xenocrysts in a Permian kimberlite: two generations of kimberlitic zircon in Jwaneng DK2, southern Botswana. *In* Kimberlites and Related Rocks. Vol 2. J Ross (ed) Geol Soc Austral Spec Publ 14:833-842
Kinny PD, Compston W, Williams IS (1991) A reconnaissance ion-probe study of hafnium isotopes in zircons. Geochim Cosmochim Acta 55:849-859
Knudsen T-L, Griffin WL, Hartz EH, Andresen A, Jackson SE (2001) In-situ hafnium and lead isotope analyses of detrital zircons from the Devonian sedimentary basin of NE Greenland: a record of repeated crustal reworking. Contrib Mineral Petrol 141:83-94
Krogh TE (1982) Improved accuracy of U-Pb zircon ages using an air abrasion technique. Geochim Cosmochim Acta 46:637-649
Li X (1994) A comprehensive U-Pb, Sm-Nd, Rb-Sr and $^{40}$Ar-$^{39}$Ar geochronological study on Guidong Granodiorite, southeast China: records of multiple tectonothermal events in a single pluton. Chem Geol 115:283-295
Maas R, Kinny PD, Williams IS, Froude DO, Compston W (1992) The Earth's oldest known crust: a geochronological and geochemical study of 3900-4200 Ma old detrital zircons from Mt. Narryer and Jack Hills, Western Australia. Geochim Cosmochim Acta 56:1281-1300
Makishima A, Nakamura E (1991) Precise measurement of cerium isotope composition in rock samples. Chem Geol 94:1-11
Nir-El Y, Lavi N (1998) Measurement of the half-life of $^{176}$Lu. Appl Rad Iso 49:1653-1655
Nowell GM, Pearson DG, Bell DR, Carlson RW, Smith CB, Kempton PD, Noble SR (2003) Hf isotope systematics of kimberlites and their megacrysts: new constraints on their source regions. J Petrol (in press)

Nutman AP, McGregor VR, Friend CRL, Bennett VC, Kinny PD (1996) The Itsaq Gneiss Complex of southern West Greenland: the world's most extensive record of early crustal evolution (3900-3600 Ma). Precambrian Res 78:1-39

Patchett PJ (1983) Importance of the Lu-Hf isotopic system in studies of planetary chronology and chemical evolution. Geochim Cosmochim Acta 47:81-91

Patchett PJ, Tatsumoto M (1980a) Lu-Hf total-rock isochron for the eucrite meteorites. Nature 288:571-574

Patchett PJ, Tatsumoto M (1980b) Hafnium isotope variations in oceanic basalts. Geophys Res Lett 7:1077-1080

Patchett PJ, Tatsumoto M (1980c) A routine high-precision method for Lu-Hf isotope geochemistry and chronology. Contrib Mineral Petrol 75:263-267

Patchett PJ, Kouvo O, Hedge CE, Tatsumoto M (1981) Evolution of continental crust and mantle heterogeneity: evidence from Hf isotopes. Contrib Mineral Petrol 78:279-297

Patchett PJ, White WM, Feldmann H, Kielinczuk S, Hofmann AW (1984) Hafnium/rare earth element fractionation in the sedimentary system and crustal recycling into the Earth's mantle. Earth Planet Sci Lett 69:365-378

Paterson BA, Rogers G, Stephens WE (1992) Evidence for inherited Sm-Nd isotopes in granitoid zircons. Contrib Mineral Petrol 111:378-390

Pettingill HS, Patchett PJ (1981) Lu-Hf total-rock age for the Amîtsoq gneisses, West Greenland. Earth Planet Sci Lett 55:150-156

Poitrasson F, Paquette J-L, Montel J-M, Pin C, Duthou J-L (1998) Importance of late-magmatic and hydrothermal fluids on the Sm-Nd isotope mineral systematics of hyper-solvus granite. Chem Geol 146:187-203

Rubatto D (2002) Zircon trace element geochemistry: partitioning with garnet and the link between U-Pb ages and metamorphism. Chem Geol 184:123-138

Salters VJM (1994) $^{176}Hf/^{177}Hf$ determination in small samples by a high-temperature SIMS technique. Analyt Chem 66:4186-4189

Schärer U, Corfu C, Demaiffe D (1997) U-Pb and Lu-Hf isotopes in baddeleyite and zircon megacrysts from the Mbuji-Mayi kimberlite: constraints on the subcontinental mantle. Chem Geol 143:1-16

Scherer E, Münker C, Mezger K (2001) Calibration of the lutetium-hafnium clock. Science 293:683-687

Sguigna AP, Larabee AJ, Waddington JC (1982) The half-life of $^{176}Lu$ by a $\gamma$–$\gamma$ coincidence measurement. Can J Phys 60:361-364

Smith PE, Tatsumoto M, Farquhar RM (1987) Zircon Lu-Hf systematics and the evolution of the Archean crust in the southern Superior Province, Canada. Contrib Mineral Petrol 97:93-104

Stevenson RK, Patchett PJ (1990) Implications for the evolution of continental crust from Hf isotope systematics of Archean detrital zircons. Geochim Cosmochim Acta 54:1683-1697

Tanaka T, Shimizu H, Kawata Y, Masuda A (1987) Combined La-Ce and Sm-Nd isotope systematics in petrogenetic studies. Nature 327:113-117

Tatsumoto M, Unruh DM, Patchett PJ (1981) U-Pb and Lu-Hf systematics of Antarctic meteorites. Proc 6th Symp Antarctic Meteor, Natl Inst Polar Res, Tokyo, p 237-249

Thirlwall MF, Walder AJ (1995) In situ hafnium isotope ratio analysis of zircon by inductively coupled plasma multiple collector mass spectrometry. Chem Geol 122:241-247

Thomas JB, Bodnar RJ, Shimizu N, Sinha AK (2002) Determination of zircon/melt trace element partition coefficients from SIMS analysis of melt inclusions in zircon. Geochim Cosmochim Acta 66:2887-2901

Vervoort JD, Patchett PJ, Gehrels GE, Nutman AP (1996) Constraints on early Earth differentiation from hafnium and neodymium isotopes. Nature 379:624-627

von Blanckenburg F (1992) Combined high-precision chronometry and geochemical tracing using accessory minerals: applied to the Central-Alpine Bergell intrusion (central Europe). Chem Geol 100:19-40

von Quadt A (1992) U-Pb zircon and Sm-Nd geochronology of mafic and ultramafic rocks from the central part of the Tauern Window (eastern Alps). Contrib Mineral Petrol 110:57-67

Watson EB (1996) Dissolution, growth and survival of zircons during crustal fusion: Kinetic principles, geological models and implications for isotopic inheritance. Trans Roy Soc Edinburgh: Earth Sci 87:43-56. Also: Geol Soc Am Spec Paper 315:43-56

Wernicke B, Getty SR (1997) Intracrustal subduction and gravity currents in the deep crust: Sm-Nd, Ar-Ar, and thermobarometric constraints from the Skagit Gneiss Complex, Washington. Geol Soc Am Bull 109:1149-1166

# Oxygen Isotopes in Zircon

**John W. Valley**

*Department of Geology & Geophysics*
*University of Wisconsin*
*Madison, Wisconsin 53706*

valley@geology.wisc.edu

## INTRODUCTION

Isotopic and trace element analysis of zircons can provide reliable and robust estimates of age, compositions of coexisting minerals and melts, and constraints on the genesis and protoliths of host rocks. Recent technological developments facilitate analysis of oxygen isotope ratios in zircon with high accuracy and precision by laser heating/ gas-source mass-spectrometry and *in situ* from thin sections or grain mounts by ion microprobe/ secondary ion mass-spectrometer. A large number of studies have shown that non-metamict zircons preserve their $\delta^{18}O$ value from the time of crystallization; hence oxygen isotope ratio can be correlated with age (U-Pb) or trace element composition. The zircon $\delta^{18}O$ record is generally preserved despite other minerals that have been reset by high-grade metamorphism or intense hydrothermal alteration. Thus the refractory nature and robust inheritance of zircon offers a potential means to sort out magmatic equilibration and reequilibration, and post-magmatic alteration, an eternal problem for igneous rocks. New processes and interpretations for igneous events have been proposed when the effects of post-magmatic exchange are fully recognized. Crustal recycling can be recognized from magmatic values of $\delta^{18}O$(zircon), and if source rocks are igneous and young at the time of melting, $\delta^{18}O$ will often be the best geochemical signature.

## ANALYSIS OF $\delta^{18}O$ IN ZIRCON

Microanalytical techniques are increasingly useful for stable isotope analysis of silicates. Both the laser fluorination/ mass-spectrometer and the ion microprobe/ secondary ion mass-spectrometer offer significant advantages over conventional techniques for analysis of zircon.

### Laser fluorination

Accurate analysis of $\delta^{18}O$ in refractory minerals such as zircon is optimized by use of a $CO_2$ laser ($\lambda$ = 10.6 μm). The best precision has been obtained when zircons are powdered before analysis. Accuracy and precision of ±0.05 to ±0.1‰ (1 standard deviation = 1sd) are reported for homogeneous samples of ~2 mg (~0.5 $mm^3$) (Valley et al. 1994, 1995). For the range of normal igneous zircon grain sizes, 2 mg represents a population of ten to several hundred crystals. The separation and selection of zircons is discussed below and can affect the quality of data. For large zircons, core to rim analytical transects are possible at ~500 μm spatial resolution using a thin diamond saw blade (Valley et al. 1998b). For large single crystals of zircon, in situ analysis by excimer laser (KrF at $\lambda$ = 248 nm and ArF at 193 nm) has yielded precision as good as ±0.12‰ from ~300 μm spots (Wiechert et al. 2002).

### Ion microprobe

Significantly enhanced spatial resolution for oxygen isotope analysis is obtained *in situ* from single zircon crystals in grain mounts or thin sections by use of an ion microprobe (Eiler et al. 1997, Valley et al. 1998a, Peck et al. 2001). Analytical precision for $\delta^{18}O$ of 0.5‰ can be obtained from ~3 ng samples (10 to 20 μm diameter spot, ~600 $\mu m^3$) by single collecting, small radius ion microprobe at high-energy offset. New multi-collecting, large radius instruments offer enhanced counting

1529-6466/03/0053-0013$05.00

efficiency and precision a factor of 2 or more better for similar spot sizes (McKeegan and Leshin 2001).

Figure 1 shows a large mm-size zircon megacryst J1-1 from Zwaneng kimberlite that has been micro sampled for laser fluorination and analyzed *in situ* at high mass-resolution with dual Faraday collectors on a Cameca 1270 ion microprobe (Valley and McKeegan, unpublished 2000). The two laser analyses consumed the top half of the crystal and yielded $\delta^{18}O = 4.69‰$. The 31 analyses by ion probe made shallow pits (1-3 mm) represented by the dots and average $\delta^{18}O = 4.49‰$. The agreement of the two techniques demonstrates accuracy approximately equal to precision on the homogeneous KIM-5 zircon standard (Table 1). In J1-1, intracrystalline zonation at the 0.1‰ level correlates with trace element zonation seen by electron microprobe analysis and imaged by cathodoluminescence (Fig. 1a). This is a dramatic improvement over the mg-size samples required by laser fluorination. This high spatial resolution for $\delta^{18}O$ is competitive with that of elemental analysis by electron microprobe, and brings the length scales of oxygen diffusion for igneous and metamorphic processes within the reach of stable isotope analysis. It also opens the door for investigation of zircon overgrowths and other intramineral variation within a sample.

## Standards

Table 1 summarizes data for zircon standards that have been analyzed for $\delta^{18}O$ by laser fluorination at the University of Wisconsin Stable Isotope Lab. Many of these zircons have been used as an ion microprobe standard for age or oxygen isotope ratio. Ion microprobe analysis indicates that Aber, J1-1, KIM-2, KIM-5, Mog, and 91500 are homogeneous at the 1‰ level; however more recent high precision analysis shows zonation in J1-1 at the 0.1‰ level (Fig. 1). Zircon 91500 has been the subject of inter-lab comparisons for oxygen isotope ratio by laser fluorination and ion microprobe, as well as age (U-Th-Pb, Lu-Hf), and major, minor, and trace

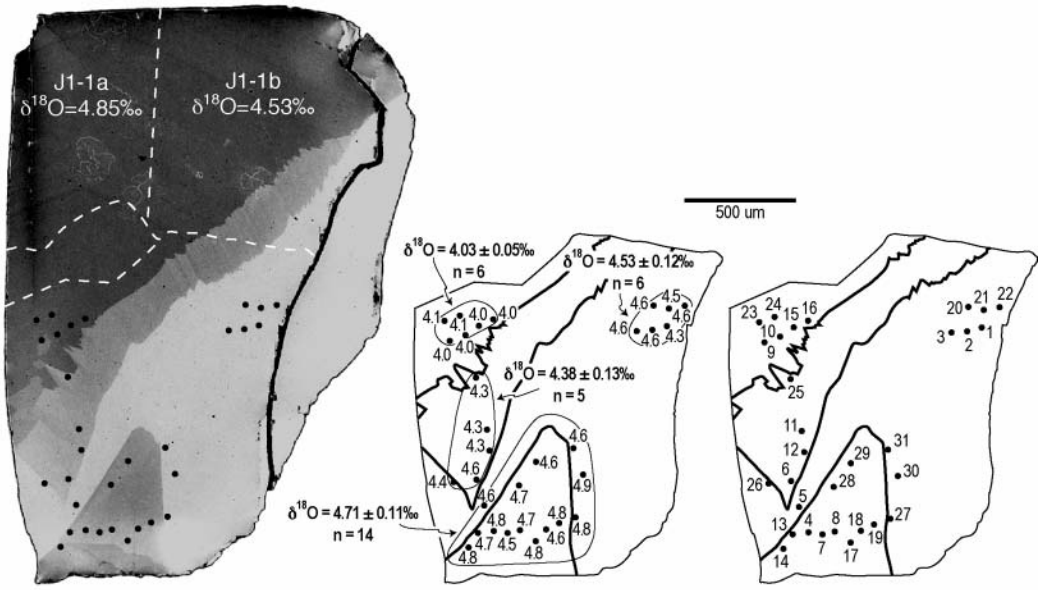


**Figure 1.** Ion microprobe analyses (dots) of $\delta^{18}O$ in a polished zircon. The top two pieces of the crystal (left) were separated for laser/fluorination; $\delta^{18}O = 4.7‰$ (Valley et al. 1998b). All three images show the remaining bottom piece of the crystal. The spot to spot precision is 0.1‰ (1sd) for 31 consecutive *in situ* analyses of $\delta^{18}O$ requiring about four hours by double-collecting Cameca 1270 (center). The order of analysis (right) was randomized to prevent systematic error. Note that the crystal is zoned in cathodoluminescence (left) due to variable trace element content and that $\delta^{18}O$ correlates with CL zoning (Valley and McKeegan, unpublished 2000).

element content (Wiedenbeck et al. 1995, Wiedenbeck et al. in prep.).

Accurate ion microprobe analysis depends on alternating analysis of samples and homogeneous standards. The instrumental mass fractionation (IMF) varies from about 0 to 40‰ / AMU depending on instrument type, operating conditions and mineral matrix. Routine attainment of the highest accuracy and precision will require optimization of these factors. The matrix correction is relatively small if zircon samples are compared to zircon standards. Nevertheless, Peck et al. (2001) report five zircon standards with variable $HfO_2$ suggesting that IMF varies about 1‰ / 1 wt % $HfO_2$, in good agreement with data from Eiler et al. (1997) for orthosilicates (Fig. 2). Over the relatively narrow range of hafnium content in normal igneous zircons (0.5-2.5 wt % $HfO_2$), this correction will be minor if an appropriate standard of the same composition is used, but chemical composition should be verified by electron microprobe as up to 26 wt % $HfO_2$ occurs in zircons from pegmatites (Fontan et al. 1980, Speer 1982).

For analysis of $\delta^{18}O$ in zircon by laser fluorination / mass-spectrometry, there is no mineral specific fractionation and it is not necessary to standardize with another zircon. The UWG-2 standard, Gore Mountain garnet, has been used to monitor all analyses of zircon at the Wisconsin Laboratory (Valley et al. 1995). This originally ~2 kg crystal is homogeneous in $\delta^{18}O$, easy to react by laser, yet completely resistant to pre-fluorination at room temperature (Table 1).

## ZIRCON SAMPLE PREPARATION

Zircon overgrowths, inheritance of multiple generations of zircon in a single sample, and radiation damage all present possible challenges to oxygen isotope studies. A variety of approaches are available to overcome potential problems through separation, preparation, imaging, and selection of zircons for analysis. The choice of correct procedure depends on the nature of the sample and the analytical technique. These procedures may be necessary for correct interpretation of laser fluorination data where multiple zircons are analyzed in bulk, but sample selection and imaging offer significant advantages for *in situ* analysis as well.

**Table 1.** Oxygen isotope ratio of zircon, baddeleyite, and garnet standards analyzed by laser fluorination at the University of Wisconsin.

| Standard | $\delta^{18}O$ ‰ SMOW | ± 1SD | N | age Ma | U ppm | $HfO_2$ wt.% | Refs. | Comments |
|---|---|---|---|---|---|---|---|---|
| | | | | | | **ZIRCON** | | |
| Aber | 5.05 | 0.05 | 3 | | | 0.75 | 3 | USNM #83829, Abercrombie R., NSW, Australia |
| BR231 | 9.81 | 0.04 | 3 | 571 | 772 | 1.30 | 4, 9 | 1.8g xt |
| G168 | 10.93 | 0.12 | 2 | 547 | 1499 | 1.21 | 4, 9 | 1.1g xt |
| J1-1, Jwan | 4.69 | 0.11 | 2 | 2643 | 14 | 0.93 | 1, 2 | 3mm xenocryst, kimberlite, Jwaneng, Botswana |
| KIM-1 | 5.20 | 0.02 | 2 | | | | 1 | 10mm xenocryst, kimberlite, Kimberley, S.A. |
| KIM-2 | 5.62 | 0.09 | 2 | | | 1.04 | 1,2 | 10mm xenocryst, kimberlite, Kimberley, S.A. |
| KIM-3 | 5.26 | 0.05 | 2 | | | | 1 | 10mm xenocryst, kimberlite, Kimberley, S.A. |
| KIM-4 | 5.33 | 0.08 | 2 | | | | 1 | 10mm xenocryst, kimberlite, Kimberley, S.A. |
| KIM-5 | 5.09 | 0.06 | 16 | | | 1.23 | 1, 3 | 10mm xenocryst, kimberlite, Kimberley, S.A. |
| Mog | 22.94 | 0.21 | 5 | | | 1.03 | 3 | USNM #R18113, placer, Mogok, Burma |
| UW-MT | 5.03 | 0.10 | 2 | | | | 4 | Mud Tank carbonatite, Australia |
| R33 | 5.55 | 0.04 | 3 | 419 | | | 4, 8 | monzodiorite, Braintree complex, Vermont, USA |
| Temora-1 | 7.93 | 0.04 | 3 | 417 | | | 4, 8 | gabbroic diorite, Temora, NSW, Australia |
| Temora-2 | 8.20 | 0.01 | 3 | 417 | | | 4, 8 | gabbroic diorite, Temora, NSW, Australia |
| 91500 | 10.07 | 0.03 | 7 | 1065 | 81 | 0.66 | 4, 5 | syenite gneiss, Renfrew, Ont., 238 g xt |
| | | | | | | **BADDELEYITE** | | |
| Phalabora | 3.2 | 1.5 | 6 | 2060 | 310 | | 4, 10 | 6cm xt w/apatite, Phalaborwa carbonatite, S.A. Heterogeneous in $\delta^{18}O$ |
| | | | | | | **GARNET** | | |
| UWG-1 | 6.3 | 0.13 | ~500 | | | | 6 | garnet amphibolite, Gore Mtn, NY, discontinued use after 1994, also called UWGMG |
| UWG-2 | 5.80 | 0.15 | 1081 | | | | 7 | ~2000g xt, Gore Mtn, NY, 1SE=±0.005‰ |

References: (1) Valley et al. 1998b, (2) Eiler et al. 1997, (3) Peck et al. 2001, (4) University of Wisconsin, Stable Isotope Lab., unpublished data (5) Wiedenbeck et al. 1995, (6) Valley et al. 1994, (7) Valley et al. 1995, (8) L. Black, pers. comm. 2001, (9) Kennedy 2000, (10) Reischmann 1995.
1 SD: standard deviation. When N=2, 1/2 of the difference is cited.

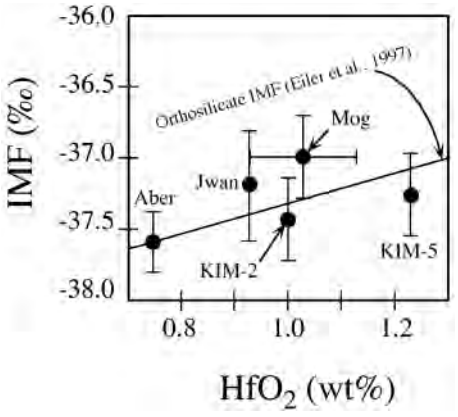


**Figure 2.** Instrumental mass fractionation (IMF) for ion microprobe analysis of $\delta^{18}O$ in zircon with known $HfO_2$ content. The orthosilicate IMF (line) was independently determined by Eiler et al. (1997). These data show that Hf substitution measurably affects data correction (from Peck et al. 2001).

**Mechanical separation of zircons**

Many procedures for separation of zircons from host rock are well known from geochronology studies, including grinding, acid dissolution of other minerals, hydrodynamic separation by Wilfley or gold table, heavy liquids, Frantz magnetic separator, and hand picking under a binocular microscope. Air abrasion is commonly applied to remove high uranium outer regions in igneous zircons and metamorphic overgrowths in order to improve concordance in geochronology (Krogh 1982a). Recently, the removal of rims by air abrasion of a population of small volcanic zircons permitted analysis by laser of the residual cores and the discovery, later confirmed by ion microprobe, that zircons were zoned core to rim by up to 5‰ in $\delta^{18}O$ (Bindeman and Valley (2000a, 2001, 2003).

A relatively new and very promising approach to zircon separation is the Electric Pulse Disintegration (EPD), which uses spark discharges of >100 kV to disaggregate a rock, largely along grain boundaries (Rudashevsky et al. 1995, Saint-Eidukat and Weiblen 1996). This technique can preserve delicate features in igneous, metamorphic, or sedimentary rocks. Cavosie et al. (2002) used EPD to disaggregate a sample of the Jack Hills metaconglomerate and they found a 4.33 Ga zircon core with an intact 3.7 Ga overgrowth. This is the earliest example of crustal recycling known. It is possible that similar overgrowths once existed on a 4.404 Ga zircon from this same outcrop (Wilde et al. 2001), but were broken off during mechanical crushing and grinding.

**Selection of zircons**

Once zircons are separated and concentrated, they can be sorted and specific populations selected for analysis. Full strength cold HF vigorously dissolves metamict zircon, but crystals with a low degree of radiation damage are not dissolved. This approach is avoided for geochronology because of potential lead loss, but it has been shown to be effective in removing contaminants, inclusions, and radiation damaged portions of zircon with no effect on the $\delta^{18}O$ of good crystalline material (King 1997, King et al. 1998b). Dissolution of crack-healing material can cause zircons to fall apart into shards of relatively fresher zircon.

Use of the Frantz magnetic separator was pioneered by Silver (1963) to concentrate zircons for geochronology (Krogh 1982b). Zircons with the lowest magnetic susceptibility tend to have the lowest concentration of uranium and to be most concordant on a Wetherill concordia diagram (Fig. 3). The uranium-rich zircons have suffered more radiation damage. This can cause the crystal to be crazed with microfractures due to hydration and swelling of damaged uranium-rich domains. Radiation damage also enhances diffusion and exchange of oxygen by creation of fast pathways of exchange, which can short-circuit slower volume diffusion. Analysis of different magnetic fractions of zircon from metamorphosed igneous rocks of the Adirondack Mountains shows that alteration of $\delta^{18}O$ can occur in less concordant samples, that presumably are radiation damaged, though many are not measurably affected (Fig. 4). In extreme cases of radiation damage, metamictization and microfracturing are common, facilitating late exchange of oxygen through short path-length diffusion in damaged material and precipitation of new phases in cracks. Bibikova et al. (1982) also found that metamict zircons are altered and have low $\delta^{18}O$ values. Magnetic separation of zircons

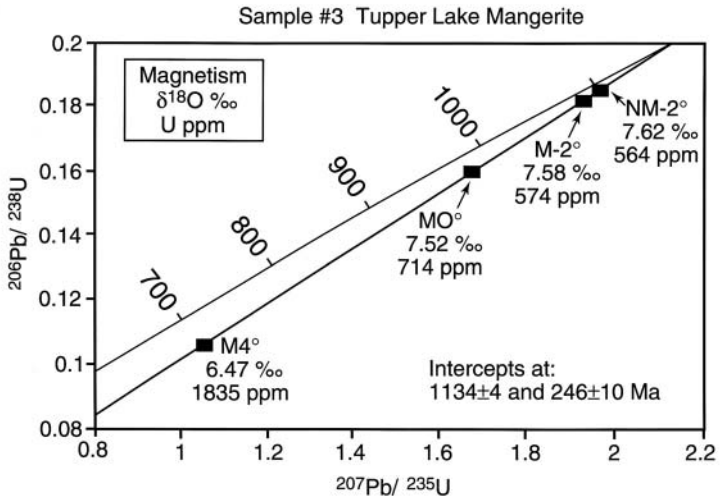


**Figure 3.** Concordia diagram for magmatic zircons from granulite facies, orthopyroxene-bearing monzonite (mangerite) from the Adirondack Highlands. Zircons were divided by Frantz magnetic separator from lowest to highest magnetic susceptibility (NM-2 < M-2 < M0 < M4). Lower magnetism correlates perfectly with more concordant ages, lower U content, and higher $\delta^{18}O$(Zc). The $\delta^{18}O$ of the least magnetic zircons (7.6‰) is consistent with magmatic $\delta^{18}O$ for the entire AMCG suite in the Adirondack Highlands, while the most magnetic and U-rich zircons are erratic and shifted in $\delta^{18}O$. In thin section, these isotopically shifted zircons are seen to be crazed by microfracture, presumably due to radiation damage resulting from high U and Th content. Such damaged zircons do not withstand HF treatment and should be removed from studies of magmatic $\delta^{18}O$ (data from Valley et al. 1994).

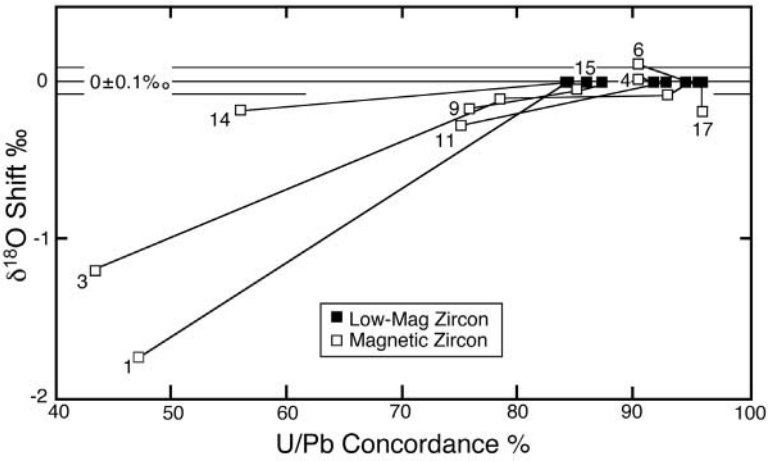


**Figure 4.** Percent concordance of U-Pb ages vs. shift in $\delta^{18}O$ for magmatic zircons from the Adirondack Mountains. Shift in $\delta^{18}O$ is normalized to $\delta^{18}O$ of the lowest magnetic fraction from a single sample, which is inferred by independent tests to be the primary magmatic $\delta^{18}O$ value. Some magnetic zircons have exchanged $\delta^{18}O$ during retrogression while others are not affected. Post magmatic exchange also correlates with higher U and Th content, and more radiation damage and microfractures (from Valley et al. 1994).

can remove metamict grains and is also an effective means to avoid crystals that contain inclusions of other more magnetic minerals (e.g., magnetite, monazite).

Size and shape are useful properties for selecting zircons. Analysis of sieved zircons from granites on the Isle of Skye, Scotland showed that large and small zircons have the same $\delta^{18}O$ values suggesting that intense hydrothermal alteration had no measurable effect on zircons (Monani and Valley 2001). In contrast, Bindeman and Valley (2000a, 2001) measured crystal size distributions

(CSD) of zircon separates from rhyolites at Yellowstone and analyzed $\delta^{18}O$ in large and small crystals (see Bindeman 2003). They found up to several per mil variation due to growth zoning and exchange in an evolving low $\delta^{18}O$ magma. They also compared CSDs for zircons separated by conventional crushing and Wilfley table separation to zircons obtained by wholesale dissolution of kilogram-size samples of tuff in HF. The CSDs are similar indicating that smaller zircons were not preferentially lost in the conventional procedure. Peck et al. (2003a) separated zircons by size (40 to 180 μm diameter) from granulite facies quartzite and granitic gneiss in order to empirically calibrate the rate of oxygen diffusion in zircon (discussed below).

### Imaging zircons

Zircon grains can be viewed and imaged by many techniques. Surprising new information about color, inclusions, zoning, or alteration can result from differences in optical illumination: binocular vs. petrographic microscope, light vs. dark field illumination, plain vs. crossed polarization, immersion in R.I. liquids vs. air, or differential (Normarski) interference contrast. Polished grain mounts or thin sections can also be imaged by cathodoluminescence (CL), backscattered electrons (BSE), and secondary electrons by electron microprobe or SEM, and minor to trace element compositions can be mapped be electron probe (Hanchar and Miller 1993, Hanchar and Rudnick 1995, Fournelle et al. 2000). For larger zircons, a cold cathode luminoscope mounted on a petrographic microscope is useful.

Radiation damage can be imaged in polished surfaces of zircon by fuming with HF vapor (Krogh and Davis 1975). Laser Raman spectroscopy provides a quantitative measure of radiation damage from spots of 1 μm or larger (Wopenka et al. 1996, Nasdala et al. 2001, Balan et al. 2001, Geisler et al. 2001, Geisler and Pidgeon 2001).

## OXYGEN ISOTOPE FRACTIONATION IN ZIRCON

The fractionation of oxygen isotopes among zircon and other phases has been estimated from: experiments (Sessions et al. 1996, 2003; Krylov et al. 2002); theoretical calculations based on spectroscopy (Kieffer 1982) or electrostatic potential (Smyth 1989); the increment method (Hoffbauer et al. 1994, Richter and Hoernes 1988, Zheng 1993); and by empirical measurements of natural samples (Valley et al. 1994, 2003; King et al. 2001). These varied calibrations are critically

**Table 2.** Oxygen isotope fractionations between zircon and selected minerals. Values are the $A_{A\text{-}B}$ coefficient from Eqn (1), below, where A and B are minerals from the Y- and X-axes, respectively.

| | Cc | Ab | Mu | F-Ph | An | Ph | Ap | Zc | Alm | Di | Gr | Gh | Ttn | Fo | Ru | Mt | Pv |
|---|---|---|---|---|---|---|---|---|---|---|---|---|---|---|---|---|---|
| Qt | 0.38 | 0.94 | 1.37 | 1.64 | 1.99 | 2.16 | 2.51 | 2.64 | 2.71 | 2.75 | 3.03 | 3.50 | 3.66 | 3.67 | 4.69 | 6.29 | 6.80 |
| Cc | | 0.56 | 0.99 | 1.26 | 1.61 | 1.78 | 2.13 | 2.26 | 2.33 | 2.37 | 2.65 | 3.12 | 3.28 | 3.29 | 4.31 | 5.91 | 6.42 |
| Ab | | | 0.43 | 0.70 | 1.05 | 1.22 | 1.57 | 1.70 | 1.77 | 1.81 | 2.09 | 2.56 | 2.72 | 2.73 | 3.75 | 5.35 | 5.86 |
| Mu | | | | 0.27 | 0.62 | 0.79 | 1.14 | 1.27 | 1.34 | 1.38 | 1.66 | 2.13 | 2.29 | 2.30 | 3.32 | 4.92 | 5.43 |
| F-Ph | | | | | 0.35 | 0.52 | 0.87 | 1.00 | 1.07 | 1.11 | 1.39 | 1.86 | 2.02 | 2.03 | 3.05 | 4.65 | 5.16 |
| An | | | | | | 0.17 | 0.52 | 0.65 | 0.72 | 0.76 | 1.04 | 1.51 | 1.67 | 1.68 | 2.70 | 4.30 | 4.81 |
| Ph | | | | | | | 0.35 | 0.48 | 0.55 | 0.59 | 0.87 | 1.34 | 1.50 | 1.51 | 2.53 | 4.13 | 4.64 |
| Ap | | | | | | | | 0.13 | 0.20 | 0.24 | 0.52 | 0.99 | 1.15 | 1.16 | 2.18 | 3.78 | 4.29 |
| Zc | | | | | | | | | 0.07 | 0.11 | 0.39 | 0.86 | 1.02 | 1.03 | 2.05 | 3.65 | 4.16 |
| Alm | | | | | | | | | | 0.04 | 0.32 | 0.79 | 0.95 | 0.96 | 1.98 | 3.58 | 4.09 |
| Di | | | | | | | | | | | 0.28 | 0.75 | 0.91 | 0.92 | 1.94 | 3.54 | 4.05 |
| Gr | | | | | | | | | | | | 0.47 | 0.63 | 0.64 | 1.66 | 3.26 | 3.77 |
| Gh | | | | | | | | | | | | | 0.16 | 0.17 | 1.19 | 2.79 | 3.30 |
| Ttn | | | | | | | | | | | | | | 0.01 | 1.03 | 2.63 | 3.14 |
| Fo | | | | | | | | | | | | | | | 1.02 | 2.62 | 3.13 |
| Ru | | | | | | | | | | | | | | | | 1.60 | 2.11 |
| Mt | | | | | | | | | | | | | | | | | 0.51 |

Eqn 1: $1000\ ln(\alpha_{A\text{-}B}) = A_{A\text{-}B}\ (10^6/T^2)$, (T in K). Values should not be extrapolated below ~600°C.
Abbreviations: Ab = albite, Al = almandine, An = anorthite, Ap = apatite, Cc = calcite, Di = diopside, F-Ph = fluorphlogopite, Fo = forsterite, Gh = gehlenite, Gr = grossular, Mu = muscovite, Mt = magnetite, Ph = phlogopite, Pv = perovskite, Qt = quartz, Ru = rutile, Ttn = titanite, Zc = zircon.
Data for Ab, An, Ap, Cc, Di, F-Ph, Fo, Gh, Mu, Mt, Ph, Pv, Qt, and Ru are from solid media exchange experiments with calcite summarized by Chacko et al. (2001). Data for Alm, Gr, Qt, Ttn, and Zc are from empirical calibrations summarized by Valley et al. (2003).

reviewed by Valley et al. (2003).

Self-consistent values for the fractionation of oxygen isotopes between zircon and other minerals come from the empirical calibrations for zircon and experimental studies for other minerals. Table 2 summarizes the empirically derived A coefficients for Equation (1):

$$\delta^{18}O_A - \delta^{18}O_B = \Delta_{A\text{-}B} \approx 1000\ ln\ (\alpha_{A\text{-}B}) = A_{A\text{-}B}\ 10^6 / T^2 \quad (T \text{ in K}) \qquad (1)$$

The largely empirical data sets of King et al. (2001) and Valley et al. (2003) can be combined with results from high-pressure experiments for calcite-mineral exchange summarized by Chacko et al. (2001) to create a matrix of A coefficients for 17 minerals (Table 2). It should be noted that the A coefficient assumes linearity of 1000 ln$\alpha$ vs. $1/T^2$, which is not always observed at low temperatures. These coefficients can be applied above ~600°C, but the specific data source should be evaluated for application at lower temperatures as discussed by Clayton and Kieffer (1991) and Chacko et al. (2001).

## OXYGEN DIFFUSION RATE IN ZIRCON

Volume diffusion through the crystal structure is potentially an important mechanism of oxygen exchange in zircon and other minerals (Eiler et al. 1992, 1993; Watson and Cherniak 1997, Kohn 1999, Peck et al. 2003a). Most commonly, this is modeled as exchange involving the entire volume of the entire crystal with flux normal to grain boundary (i.e., rim to core). Other mechanisms including recrystallization, overgrowths, precipitation of material along microfractures, and fast pathways of exchange (inclusions, crystal defects, $\alpha$- and fission-tracks) can also alter the $\delta^{18}O$ of zircon and cause isotope heterogeneity. However, these mechanisms depend on the details of local geologic environment that are inherently difficult to predict. The presence or absence of such features can generally be evaluated by U-Pb geochronology, imaging, or other tests described above. In contrast, rim to core volume diffusion is more predictable and is always operative, but its rate, which increases with temperature, may be so slow that the effect is neither measurable nor significant.

The rate of oxygen diffusion in zircon has been determined by: laboratory experiments, theoretical calculations, and empirical measurements in metamorphic rocks. These different techniques have yielded widely varying estimates of diffusion coefficient for both high $P_{H2O}$ (wet) and anhydrous (dry) conditions (Fig. 5a).

Watson and Cherniak (1997) measured the rate of oxygen diffusion in zircon under dry ($P_{H2O}$ < 1bar) and wet ($P_{H2O}$ = 70 bar to 10 kbar) experimental conditions using synthetic and natural zircon samples. No anisotropy of diffusion rate was observed in measurements made parallel and perpendicular to the crystallographic *c*-axis. The dry data confirm earlier experiments of Muehlenbachs and Kushiro (1974). Fortier and Giletti (1989) and Zheng and Fu (1998) estimated diffusion rate based on anion porosity, calibrated against experiments for other minerals. Kohn (1999) estimated the effect of water buffering reactions during retrogression.

Both Watson and Cherniak (1997) and Zheng and Fu (1998) found that diffusion is significantly faster at higher $P_{H2O}$, i.e., "wet" vs. "dry," an effect observed in many minerals (see Cole and Chakraborty 2001). The values of the diffusion coefficient (D) for oxygen, however, vary greatly and with the exception of the dry experiments, there is little agreement among studies (Fig. 5a).

Empirical measurements in high-grade metamorphic rocks provide an independent means to evaluate the rates of oxygen isotope exchange by diffusion (Valley et al. 1994, Peck et al. 2003a). These tests include laser fluorination and ion microprobe analyses of detrital zircons from quartzite and of magmatic zircons from granitic gneisses with known thermal histories. Figure 5b shows values of $\delta^{18}O$ of detrital zircons and metamorphic garnets plotted against $\delta^{18}O$ of the host quartzite. Vertical tie-lines connect analyses for different size fractions of zircon from a single rock. The values of $\delta^{18}O(Zc)$ are similar to those of protolith magmatic zircons throughout the Grenville Province (Peck et al. 2000), while $\delta^{18}O(Qt)$ is similar to the protolith sandstones. None of the twelve

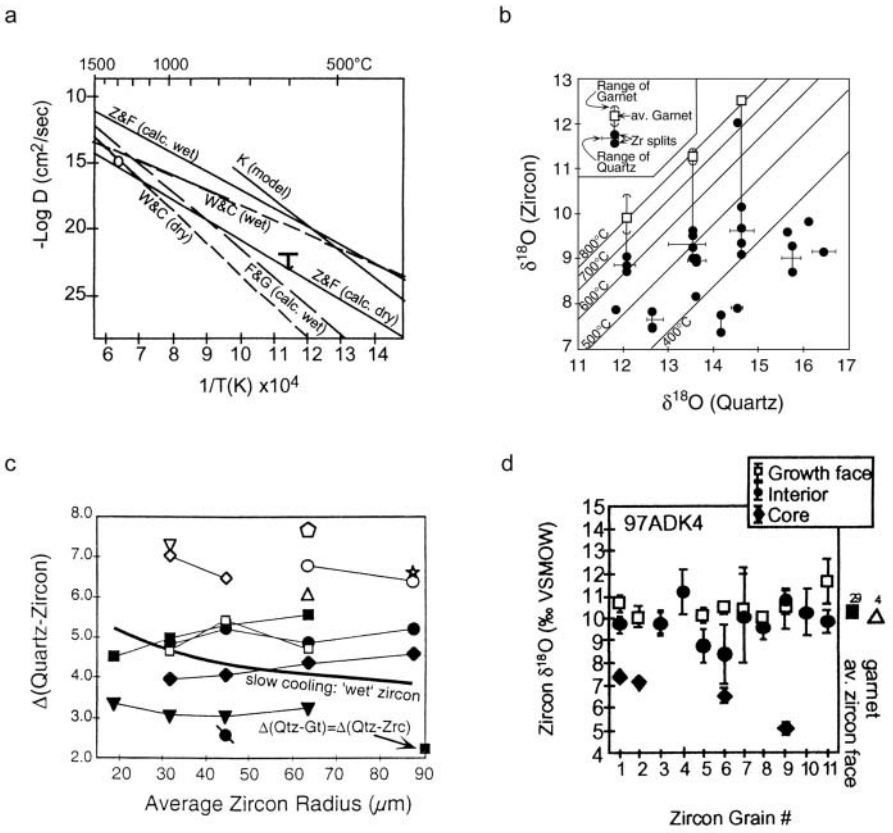


**Figure 5.** (a) Arrhenius plot of experimentally determined and calculated oxygen diffusion rate in zircon. W&C are experiments by Watson and Cherniak (1997). F&G and Z&F are calculated by Fortier and Giletti (1989) and Zheng and Fu (1998). "K model" is estimated for a cooling metabasite (Kohn 1999). The circle is a dry experiment by Muehlenbachs and Kushiro (1974). The bar with an arrow is an empirical calibration by Peck et al. (2003). (b) Values of $\delta^{18}O$(quartz) vs. $\delta^{18}O$(detrital Zc) from granulite facies Grenville quartzites. Zircons of different size from the same sample are connected with vertical tie-line. Zircons did not equilibrate with host quartz during metamorphism at 675-775°C. In contrast metamorphic garnets are equilibrated. (c) Values of $\Delta^{18}O$(Qt-Zc) vs. zircon crystal size for samples shown in 5b. Predicted relations for slow cooling and "wet" diffusion are shown. The lack of systematic relations with grain size show that zircons neither equilibrated at the peak of metamorphism nor were significantly altered after metamorphism. (d) Ion microprobe analyses of $\delta^{18}O$ from cores and rims of individual detrital zircons from Grenville quartzite 97ADK4. Analyses of grain interiors (filled circles and diamonds) and crystal growth faces (open squares) are shown. The variability of cores demonstrates preservation of premetamorphic magmatic compositions in zircon. The uniformity of data for the outer 3 μm on crystal faces shows exchange and equilibration is restricted to a micron-scale during metamorphism (from Peck et al. 2003a).

rocks containing quartz-zircon pairs have equilibrated at the peak metamorphic temperatures, 675-775°C. In contrast, all three of the quartz-garnet pairs record peak metamorphic temperatures (Peck et al. 2003a). Likewise, Bolz (2001) reports ion microprobe analyses of unexchanged detrital zircons that experienced 700-800°C contact metamorphism of Appin quartzite at Ballachulish, Scotland. Both studies show that zircons preserve premetamorphic values and that little exchange has occurred by diffusion or any other mechanism.

An examination of $\Delta^{18}O$(Qt-Zc) vs. zircon radius for twelve Grenville quartzites (Fig. 5c) reinforces the conclusion that zircons were not significantly affected by oxygen diffusion either

during prograde or retrograde metamorphism. Diffusion modeling allows prediction of the nature and magnitude of exchange, *if* diffusion was an important process for specified conditions. If the input includes D from experiments at $P_{H2O} > 70$ bar (Watson and Cherniak 1997), these calculations predict that zircons will completely equilibrate with quartz at metamorphic temperatures of 675-775°C and that further exchange during slow cooling will affect small zircons more than large zircons because of differences in surface area/ volume. The smooth curve in Figure 5c shows the predicted values of $\Delta^{18}O$(Qt-Zc). None of the twelve rocks follow this trend, predicted for $P_{H2O} > 70$ bar, and many have a different slope. Thus, Peck et al. (2003a) conclude that the lack of equilibrium values in zircon cannot be attributed to retrogression and must indicate preservation of premetamorphic $\delta^{18}O$. Similar calculations are made for values of $\delta^{18}O$(Zrc) measured in granitic gneisses, which are the rock type from which zircons are most commonly studied. The conclusions are similar; zircons do not show correlations predicted if diffusion was significant and the best interpretation is that zircons in granitic gneisses have also preserved approximately the original $\delta^{18}O$ from the time of magmatic crystallization. Clearly, the wet experimental data cannot be used to accurately model the natural processes of exchange in these rocks. However, the data agree with predictions of very much slower diffusion that are made using the data for anhydrous experiments (Watson and Cherniak 1997).

Two quartzites from Figure 5c were chosen for detailed study by ion microprobe (Peck et al. 2003a). Individual zircons were mounted first in acetone-soluble cement for analysis into polished surfaces in the center of the grain. Then crystals were freed, turned over, and remounted by pressing into indium such that the ion microprobe could depth profile into the outer 3 μm of crystal growth faces. These data are shown in Figure 5d. In spite of the larger analytical uncertainty of ion microprobe data, it is clear that the cores and interiors of zircons (diamonds and dots) are significantly lower in $\delta^{18}O$ than the outermost rims (growth faces = squares). The cores show considerable variability, presumably representing the mix of rocks in the sediment source region, while the faces are all the same within analytical uncertainty. The average $\delta^{18}O$(Zc face) is in equilibrium with the metamorphic garnet (triangle) and the host quartz. Thus, thin high $\delta^{18}O$ rims have formed by diffusion at ca. 675°C, but cores were not affected.

Zircon #9 from Figure 5d is shown as a CL image in Figure 6. The location of ion microprobe pits and $\delta^{18}O$ are shown for a polished surface through the crystal core. The inherited core of this crystal (bright CL) has low $\delta^{18}O$ (5.1‰), while the magmatic overgrowth (dark CL) is higher in $\delta^{18}O$ (10.6‰). At the time of magmatic overgrowth this internal boundary was a natural diffusion couple, i.e., a step discontinuity in $\delta^{18}O$, and the gradient is still 5.5‰ across a distance of less than 50 μm. Ion microprobe analysis, described above, suggests that this crystal also has a thin rim that exchanged during metamorphism with surrounding quartz, however, the steepness and the depth within the crystal of the gradient shown in Figure 6 show that it was not caused by metamorphic exchange at 700-800°C with quartz. Instead, the core rep-

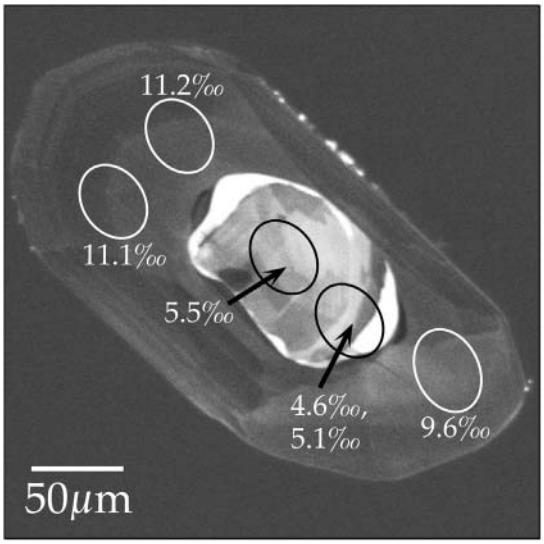


**Figure 6.** Cathodoluminescence image of detrital igneous zircon #9 from Figure 5d. The $\delta^{18}O$ of the inherited core is distinct from the magmatic overgrowth suggesting that $\delta^{18}O$ was preserved in the zircon core during a period of magmatic resorption and overgrowth that preceded granulite facies metamorphism (from Peck et al. 2003a).

resents a normal $\delta^{18}O$ zircon xenocryst that was inherited by a higher $\delta^{18}O$ igneous magma. The lower $\delta^{18}O$ core was preserved through the magmatic event and subsequent metamorphism due to slow diffusion of oxygen through the zircon.

Diffusion modeling based on the different values of D shown in Figure 5a lead to surprisingly different conclusions. The predicted closure temperature for oxygen diffusion in average-size igneous zircons under conditions of slow cooling is over 900°C using the dry data of Watson and Cherniak (1997), but the temperature is only 500-550°C using their wet data at $P_{H2O} \geq 70$ bar. Peck et al. (2003a) conclude that all available empirical data from quartzites and granitic gneisses support diffusion rates similar or possibly slower than the dry data. It is clear that magmatic zircons can preserve the igneous value of $\delta^{18}O$ through subsequent high grade metamorphism, hydrothermal alteration, and possibly magmatic assimilation or anatexis. This conclusion has been verified by many studies of magmatic zircons that are summarized below.

## ASSIMILATION VS. FRACTIONAL CRYSTALLIZATION

Analysis of zircon can provide a test of closed system magmatic crystallization vs. open system assimilation, contamination, or post magmatic alteration. In a simplified hypothetical case; if a suite of mafic to felsic magmas differentiate in a closed system from a common parent by fractional crystallization at constant temperature, then the $\delta^{18}O$ values of zircon crystallizing from each magma will be the same even though the whole rock $\delta^{18}O$ of the felsic magma can be 1-2‰ higher than its mafic sibling. This arises because all phases are assumed to be in equilibrium throughout the process and differentiation progresses by early removal of mafic minerals, which are lower in $\delta^{18}O$ than quartz and feldspar. The whole rock values increase as the percentage of higher $\delta^{18}O$ quartz and feldspar increases, but the $\Delta$(WR-Zc) increases at the same rate for the same reason, and $\delta^{18}O$ is unchanged for each mineral including zircon. Thus, the $\delta^{18}O$(WR) value increases as the percentage of high $\delta^{18}O$ minerals increases. Of course, temperature must decrease for crystallization to progress and the zircon saturation temperature is dependent on composition as well (Watson and Harrison 1983), but the effect of $\Delta T$ is not generally significant due to small differences in fractionation at magmatic temperatures.

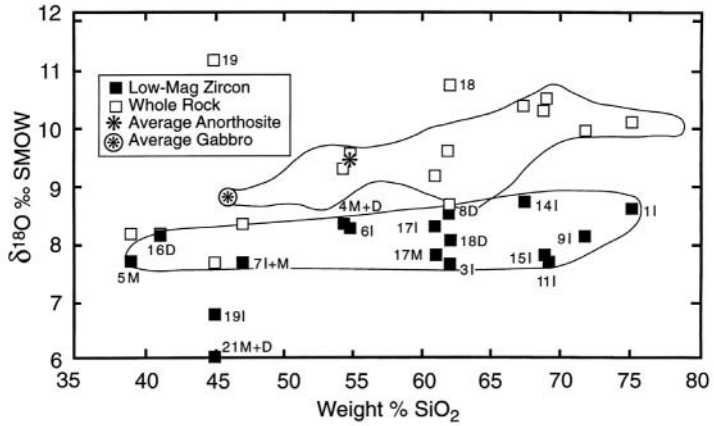


**Figure 7.** Plot of $\delta^{18}O$(low magnetism zircon) vs. wt % $SiO_2$ for metamorphosed igneous rocks of the AMCG suite, Adirondack Mountains. All AMCG zircons ($SiO_2$ = 39-75 %), except in two metagabbros, have constant $\delta^{18}O = 8.1 \pm 0.4$‰. This is over 2‰ higher than in a primitive mantle-derived mafic magma. Whole rock $\delta^{18}O$ increases with $SiO_2$ due to increasing abundance of high $\delta^{18}O$ minerals, feldspar and quartz. The generally high $\delta^{18}O$ of AMCG zircons results from magmatic processes before the crystallization of zircon (melting of the deep crust and/or contamination). In contrast to zircons, some whole rock compositions have been raised by post magmatic exchange (from Valley et al. 1994).

The assumption of equilibrium must also be evaluated, but appears correct for most simple plutonic systems. In contrast to the simplified model above, if material is added (or subtracted) from the magma, which is not in isotopic equilibrium, then $\delta^{18}O$ of the magma changes, as does $\delta^{18}O$ of subsequently crystallizing minerals including zircon. Changes in magma chemistry are often recorded by growth zoning in zircon. Such core to rim zonation of $\delta^{18}O$ in zircon provides important evidence for the genesis of low $\delta^{18}O$ rhyolites (see below).

Valley et al. (1994) analyzed $\delta^{18}O$ in zircon and whole rock powder from the Proterozoic anorthosite-mangerite-charnockite-granite (AMCG) suite in the Adirondack Mountains, NY (Fig. 7). Values of $\delta^{18}O(Zc)$ are constant at 8.1±0.4‰ (1sd, N = 13) for all but two metagabbro samples. While this uniformity is consistent with differentiation from a common parent, controversy over the relation of anorthosite massifs to their granitic envelope has generally been resolved in favor of a cogenetic, but not comagmatic model (Ashwal 1993). Thus, the two metagabbro samples provide critical evidence (#19, 21; Fig. 7). These rocks are thought to be samples of the anorthosite parent magma and the lower $\delta^{18}O$ (6-7‰) indicates that two differentiation trends exist, a steep one for anorthosite, which included significant contamination by high $\delta^{18}O$ crust, and a flat one for granitic rocks. Except for a few samples affected by post-magmatic exchange, the whole rock values of $\delta^{18}O$ increase regularly with $SiO_2$ wt % as predicted for the granitic trend. There is no evidence to support the once common misconception that metasom-atism was active during granulite facies metamorphism in these rocks (see Valley et al. 1990, Eiler and Valley 1994).

In rocks that contain more than one refractory magmatic mineral that crystallize at different times, it is possible to track open system contamination. Likewise, if zircon crystallizes over a period of time when magmatic composition changes, then core to rim growth zoning records this change. The contrast of magmatic garnet and zircon from the Idaho batholith is an example of the former test. Values of $\delta^{18}O(Zc)$ throughout the batholith average 6.9±0.9‰ and the fractionation $\Delta$(Gt-Zc) increases regularly with $\delta^{18}O(Zc)$ (Fig. 8). King and Valley (2001) suggest that progressive contamination has caused the increase in $\delta^{18}O$ of both minerals, but that zircon, which crystallized first, is less affected. If the contaminant was a high $\delta^{18}O$ sediment (average Belt series metasediment = 17‰) then the samples where $\Delta$(Gt-Zc) = 0.2‰ represent about 2% contamination, while the higher $\delta^{18}O$ samples with $\Delta$(Gt-Zc)~0.8‰ represent 10% contamination. In a similar study of the Dinkey Dome granite, central Sierra Nevada batholith, Lackey et al. (2002) found that $\delta^{18}O(Zc) = \delta^{18}O$(garnet) representing equilibration in five samples from the western half of the pluton. In contrast, $\delta^{18}O$(garnet) is ~0.5‰ less than $\delta^{18}O(Zc)$ in five samples from the eastern half of the pluton. Since the magmatic garnets crystallized later than zircons, these results indicate contamination of the Dinkey dome granite by low $\delta^{18}O$ material after zircon crystallized. This contamination is not apparent from analysis of $\delta^{18}O(Qt)$ or $\delta^{18}O(WR)$ due to the scatter of these values by post-magmatic alteration. The significance of such trends would be strengthened by garnet thermobarometry in rocks with appropriate mineral assemblages such as

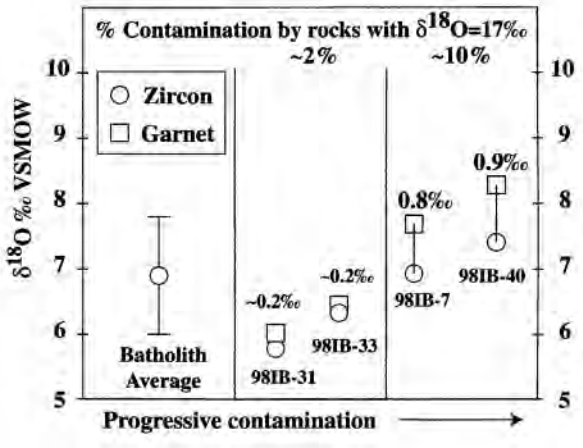


**Figure 8.** Plot of $\delta^{18}O$ zircon and garnet vs. contamination of granitic magmas in the Idaho batholith. Zircon crystallized earlier than magmatic garnet and thus records the composition of less contaminated magma than garnet. Contamination of magmas by ~10% of high $\delta^{18}O$ rocks such as the Belt Supergroup sediments would raise $\delta^{18}O$(magma) by ~0.9‰ (from King and Valley 2001).

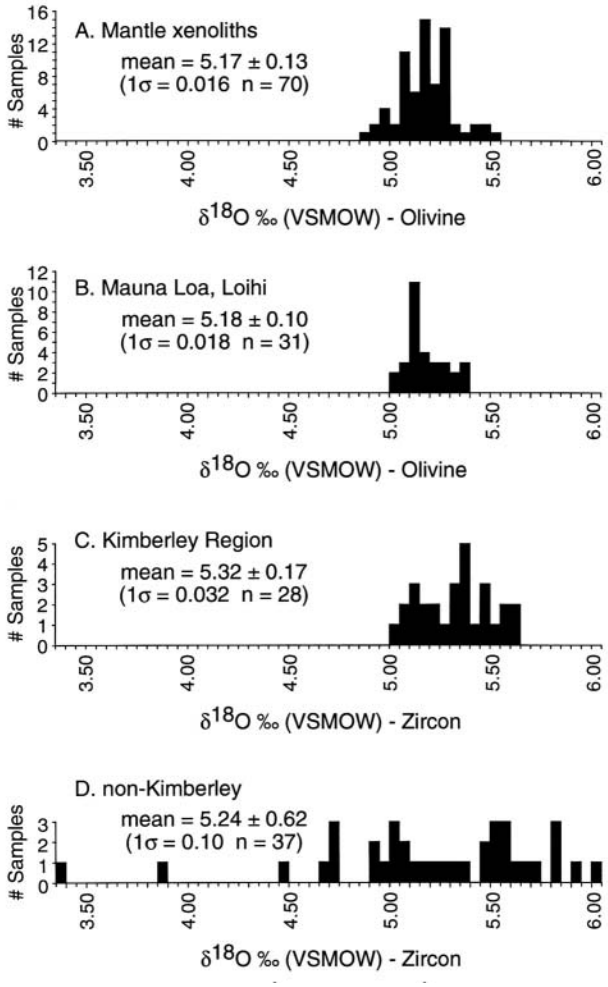


**Figure 9.** Values of $\delta^{18}O$ for olivine and zircon from mafic and ultramafic rocks. Zircon megacrysts from kimberlite (C) are in high temperature equilibrium with olivine from peridotite xenoliths (A) and oceanic basalts (B). The $\delta^{18}O$ of zircon in equilibrium with the mantle is thus 5.3±0.3‰ (from Valley et al. 1998b).

garnet + biotite or garnet + clinopyroxene, which fixes temperature, or garnet + aluminosilicate + plagioclase + quartz or garnet + quartz + pyroxene + plagioclase, which fixes pressure.

## MANTLE ZIRCONS

A distinctive suite of zircon megacrysts occurs in kimberlite at trace amounts (ppm) and are separated during diamond mining (Kresten et al. 1975, Valley et al. 1998b). Typically, these crystals are large (mm to cm), U-poor (<50 ppm), fractured, and coated with $ZrO_2$ (baddeleyite or tetragonal zirconia, Kresten et al. 1975). In most cases, the U-Pb age matches kimberlite magmatism. These characteristics identify megacrysts as mantle-derived and similar to zircons found associated with diamond, coesite, and other mantle material.

The mantle zircon megacrysts from kimberlite pipes near Kimberley, South Africa are remarkably constant in $\delta^{18}O$ (Fig. 9C) indicating a mantle value of 5.3±0.3‰ (2 sd, Valley et al. 1998b). The mantle zircon value is 0.15‰ higher than $\delta^{18}O$ measured for olivine from mantle xenoliths (Fig. 9A; Mattey et al. 1994) or from most ocean island basalts (Fig. 9B; Eiler et al. 1996), consistent with equilibration at mantle temperatures.

Zircons from kimberlites on the Siberian platform are slightly more variable than in S. Africa, with averages varying from 4.73±0.01‰ at Chomurdakh to 5.53±0.06‰ at Mir. While the analyzed sample set is small, the homogeneity at each pipe is striking, suggesting small, but significant regional differences in the $\delta^{18}O$ of mantle melts (Valley et al. 1998b).

Two suites of zircon megacrysts are found at Zwaneng, Botswana. One has Permian U-Pb ages (the eruption age of the pipe) and the other has Precambrian ages (Kinny et al. 1989). Eight Permian zircons are homogeneous at $\delta^{18}O$ = 5.74±0.13‰; however the Precambrian zircons are the only suite that has been found thus far to show significant variability, $\delta^{18}O$ = 3.37-4.72 (Valley et al. 1998b). One Precambrian zircon has been analyzed in detail by ion microprobe revealing that variability of 0.7‰ exists within the 3 mm crystal and correlates with zoning seen by cathodoluminescence (Fig. 1) suggesting growth zonation. While the Precambrian Zwaneng zircons are interpreted as mantle megacrysts (Kinny et al. 1989), it can be questioned if they have had an extended history in the crust as oxygen isotope zonation would be expected to homogenize by diffusion over 2 billion years at mantle temperatures. Values of $\delta^{18}O$ = 4.78±0.16 are also lower than normal for mantle zircon megacrysts from alkali basalts at Elie Ness, Scotland (Upton et al. 1999). These lower values suggest the burial of hydrothermally altered sea floor basalts into the mantle source regions for alkalic magmas.

## PRE-CAMBRIAN ZIRCONS

### Archean granitoids

The Superior Province is the largest Archean craton in the world. Like other Archean terranes, it is dominated by greenstone belts and granitic plutons. Understanding the magmatic source of these rocks provides insight into crustal growth in the Archean. While the granitoids are frequently metamorphosed, they preserve certain chemical distinctions that are difficult to distinguish in the field. Some of the syn- to post-tectonic plutons are chemically enriched and termed sanukitoids (Mg# > 0.60, Ni and Cr > 100 ppm, Sr and Ba > 1000 ppm, LREE > 100X chondrites, Shirey and Hanson 1984). The genesis of sanukitoid magmas is thought to be distinct from the more common TTG suite (tonalite, trondhjemite, granodiorite) and to result from melting of the mantle wedge, metasomatized by fluids from subducted upper oceanic crust (Fig. 10; Shirey and Hanson 1984, Stern et al. 1989, Stern and Hanson 1991).

The $\delta^{18}O$ of magmatic zircons from 59 granitoids across the Superior Province (Fig. 11) shows clear bimodality of $\delta^{18}O$, in spite of restricted total range in values (Fig. 12A, King et al. 1998b). Coexisting quartz was analyzed for some samples and the same bimodality is not seen (Fig. 12B), showing that zircons are the most faithful record of magmatic $\delta^{18}O$ and that quartz can be reset by post-magmatic events (see Valley and Graham 1996). Sanukitoid zircons average $\delta^{18}O$ = 6.4±0.2‰, while the

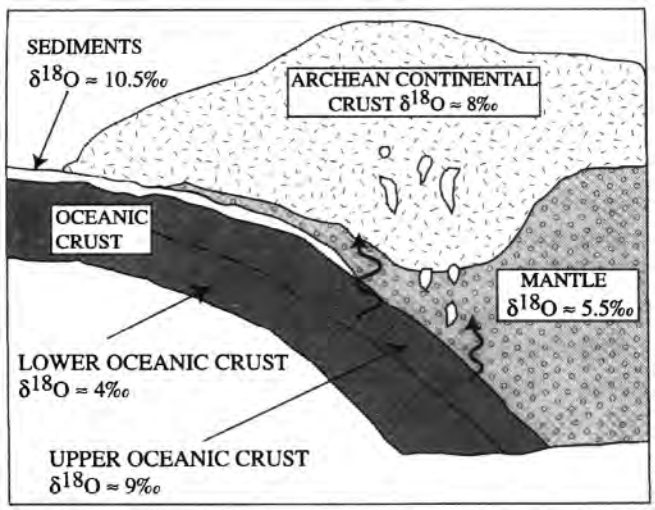


**Figure 10.** Schematic model for genesis of sanukitoid magmas after Stern et al. (1989). The relatively high $\delta^{18}O$ of sanukitoid magmas is inherited from high $\delta^{18}O$ fluids from the upper portions of subducted ocean crust (from King et al. 1998b).

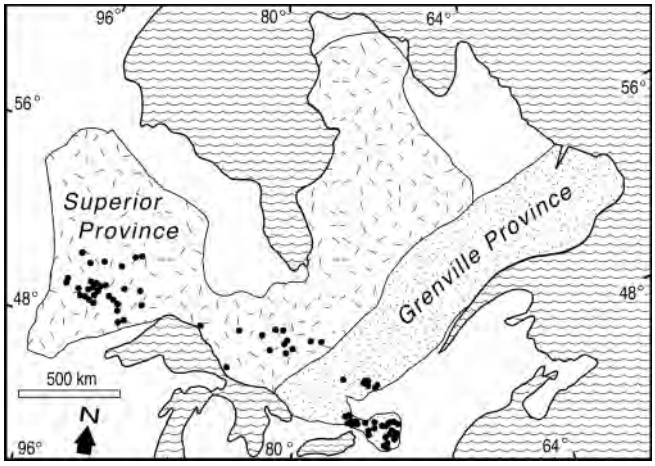


**Figure 11.** The Grenville and Superior Provinces of North America. Dots show zircon sample localities summarized by Peck et al. (2000). The Adirondack Mountains are a southeastern outlier of the Grenville (from Peck et al. 2000).

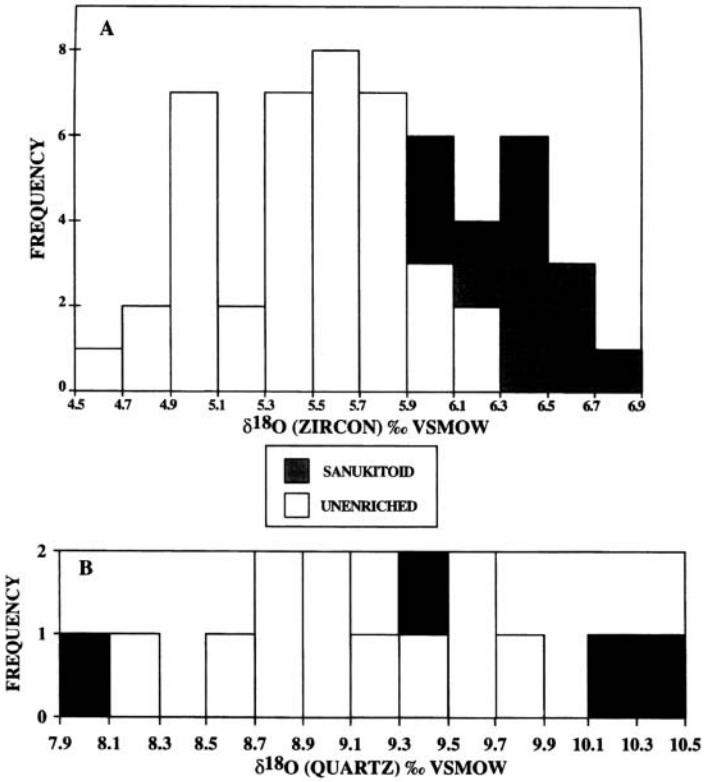


**Figure 12.** Histograms of $\delta^{18}O$(Zc) (A) and $\delta^{18}O$(Qt) (B) for granitoids from the Superior Province. Sanukitoid magmas are shown to be systematically higher in $\delta^{18}O$ by analysis of zircons, but this difference is not seen in analyses of quartz, which suffer variable amounts of post-magmatic exchange (from King et al. 1998b).

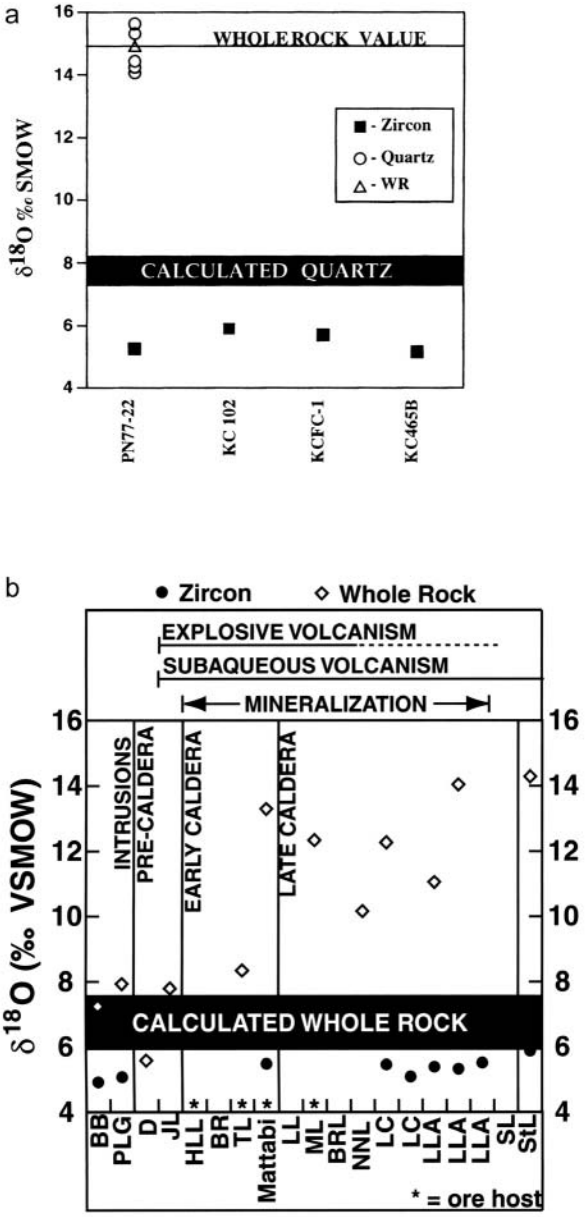


**Figure 13.** (a) Values of $\delta^{18}O$ for zircon, quartz and whole rock from rhyolites at the Kidd Creek Mine. "Calculated Quartz" is the $\delta^{18}O$ value in equilibrium with magmatic zircons at 900°C. Measured $\delta^{18}O(Qt)$ is ~7‰ higher than calculated, and individual quartz phenocrysts vary by up to 2‰ as the result of extreme hydrothermal alteration of quartz phenocrysts during silicification of rhyolite. Values of $\delta^{18}O(Zc)$ are identical to those in felsic volcanic rocks throughout the Superior province showing that zircons were not affected by post magmatic alteration (from King et al. 1997). (b) Values of $\delta^{18}O$ for zircons and whole rock from the Sturgeon Lake caldera complex. "Calculated whole rock" represents equilibrium at 800°C. Samples are arranged oldest to youngest (left to right). Stars indicate ore deposits. Measured whole rock $\delta^{18}O$ is elevated relative to zircons by post magmatic hydrothermal alteration (from King et al. 2000).

unenriched TTGs average 5.5±0.4‰. These values correspond to whole rock magma values of ~7 and 8‰, respectively, supporting the subduction-related model (Fig. 10).

**Volcanogenic massive sulfide deposits**

Kidd Creek (Ontario, 2.7 Ga) is one of the largest volcanogenic massive sulfide (VMS) Cu-Zn-Ag deposits in the world. The syngenetic origin of these ores is no longer in question, but the source and timing of high $\delta^{18}O$ values in associated rhyolites are disputed. Huston et al. (1996) and Taylor and Huston (1998) showed a correlation of $\delta^{18}O$ for quartz phenocrysts from rhyolite hosts to VMS deposits worldwide to the tonnage of zinc. These data included the footwall rhyolite at Kidd Creek. Huston et al. concluded that $\delta^{18}O(Qt)$ values are magmatic and they proposed a genetic model

correlating larger ore deposits to high-$\delta^{18}O$ S-type magmas, which formed from melting and assimilation of altered crust. More recently, Taylor and Huston (1999, p373) concluded: "In summary, the quartz phenocryst data suggest a minimum $\delta^{18}O$ value for most of the rhyolitic magmas in the Kidd Creek Volcanic Complex of 8.5 per mil."

King et al. (1997, 1998a) applied three tests to determine if the high $\delta^{18}O$ values of quartz in Kidd Creek rhyolites are magmatic or post magmatic in origin. If the phenocryst values are magmatic then: (1) quartz and zircon should preserve consistent high temperature fractionations; (2) quartz phenocrysts should have constant $\delta^{18}O$ at hand sample scale; and (3) individual quartz phenocrysts should be homogeneous in $\delta^{18}O$ or show minor magmatic growth zoning. These tests were guided by careful examination of textures in thin section by optical and cathodoluminescent microscopy (CL). Figure 13a shows $\delta^{18}O$ of zircons that had previously been dated by U-Pb. Eleven different magnetic splits from four rocks all have the same $\delta^{18}O(Zc) = 5.4\pm0.3‰$, which is indistinguishable from other TTG zircons in the same province (5.5±0.4‰, Fig. 12A) and is the mantle value that would be expected in a primitive I-type felsic magma. Such constant mantle-like values are found in zircons from all plutonic and volcanic rocks in the Superior Province with the exception of the sanukitoids (Fig. 14) and these values provide a boundary condition for evaluating post magmatic processes. Magmatic quartz in equilibrium with these zircons would have $\delta^{18}O \approx 7.5\text{-}8.0‰$ and whole rock values for the magma of 6.5 to 7.0‰ (Fig. 13a; $\Delta^{18}O(Qt\text{-}Zc) = 1.92$ at 900°C, Valley et al. 2003). All 27 of the measured quartz and all but a few of the 377 whole rock $\delta^{18}O$ values at Kidd Creek (Taylor and Huston 1999) are higher than these magmatic values indicating that quartz and rock matrix have been elevated in $\delta^{18}O$ by processes after the crystallization of zircon. Figure 13a shows the values of five individual quartz phenocrysts from one sample with a range of $\delta^{18}O = 14.2$ to 16.1. Ion microprobe analysis of single quartz crystals from this sample further shows intracrystalline variability of up to 4‰, which correlates to high $\delta^{18}O$ veins and crack-healing at the μm-scale, documenting the post-magmatic process whereby quartz values are elevated. Thus, none of the tests support the preservation of magmatic $\delta^{18}O$ values in quartz from these rhyolites. Recognition that magmatic values are 1 to 4‰ lower than previously thought has profound implications for the thermal and fluid history of the deposit. Oxygen isotope thermometry and calculation of fluid composition should not employ isotopically heterogeneous quartz unless an appropriate microanalytical technique is available. King et al. (1997, 1998a) conclude that zircons are the best record of magmatic $\delta^{18}O$ at Kidd Creek, that quartz and whole rock were elevated in $\delta^{18}O$ by post magmatic hydrothermal alteration as originally proposed by Beatty et al. (1988), and that the correlation seen by Huston et al. (1996) could arise if the specific characteristics of hydrothermal systems (size, source, duration, fracturing, temperature) create larger ore deposits and more intensely altered quartz.

The Sturgeon Lake caldera complex (Ontario, 2.7 Ga) is host to several VMS deposits. As at Kidd Creek, igneous zircons average $\delta^{18}O = 5.4\pm0.3‰$ (n = 12), but quartz and whole rock compositions have been elevated throughout the 18 Myr sequence by post magmatic hydrothermal alteration (Fig. 13b; King et al. 2000). The magnitude of $^{18}O/^{16}O$ enrichment is moderate, 1-2‰, in the pre- and early caldera units, but becomes greater, 4-7‰, in late and post-caldera rocks above the Mattabi unit, supporting the model that impermeable volcanic layers control the size and location of hydrothermal systems.

**Hadean detrital zircons**

Events of the first 500 Myr of Earth history are inherently uncertain because no known rocks have been preserved. The only solid evidence before 4.0 Ga comes from rare detrital and xenocrystic zircons, the oldest of which is 4.4 Ga (Wilde et al. 2001). Values of $\delta^{18}O$, measured in single zircons by ion microprobe (4.4-3.3 Ga; Fig. 15), show the same range in values, 5-8‰, as seen by conventional analysis, throughout the Archean (3.5-2.6 Ga; Fig. 16). Values of $\delta^{18}O(Zc)$ that are higher than 6.5‰ are above the mantle-derived value and suggest a history with surface alteration of protolith by liquid water at low temperatures to elevate $\delta^{18}O$, burial, melting to form high $\delta^{18}O$ felsic

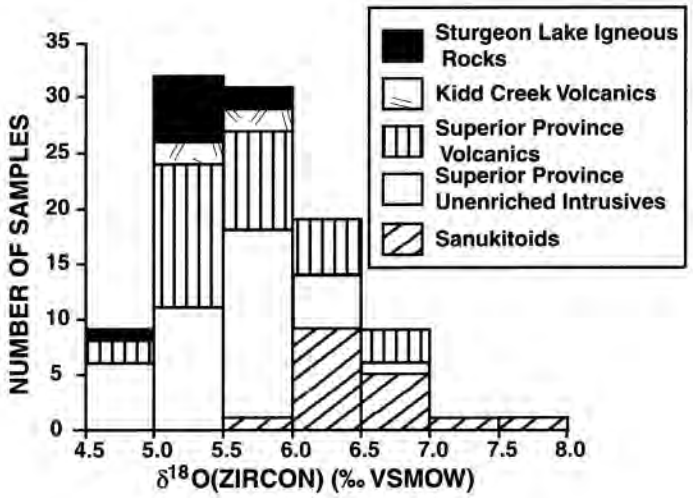


**Figure 14.** Histogram of $\delta^{18}O$ for magmatic zircons from volcanic and plutonic rocks of the Superior Province (from King et al. 2000).

magma, and then crystallization of high $\delta^{18}O$ zircon (Peck et al. 2001, Mojzsis et al. 2001, Valley et al. 2002). Other on-going measurements on these tiny (100-200 μm) time capsules include CL and BSE imaging, REE analysis, identification of μm-scale inclusions, nano-XANES (i.e., X-ray photo-electron emission spectro-microscopy; Gilbert et al. 2003), and radiogenic isotope geochemistry (Cavosie et al. 2002). There is no primitive reservoir in the mantle or in meteorites that can explain the geochemistry of the higher $\delta^{18}O$ zircons. The best interpretation of existing data is that the Earth cooled quickly after accretion, and formation of the core and the Moon, that liquid water was stable on the surface as early as 4.4 Ga, and that differentiated continental-type crust was starting to form. If the Earth's hydrosphere was in place by this time, surface temperatures are suggested below 200°C, low enough to precipitate oceans with possible biologic implications. The rapid cooling required by this hypothesis provides a boundary condition for models of insulation by the earliest atmosphere and for the energy input from Earth bombardment by meteorites (Fig. 17; Valley et al. 2002). Further samples are being sought to test these hypotheses.

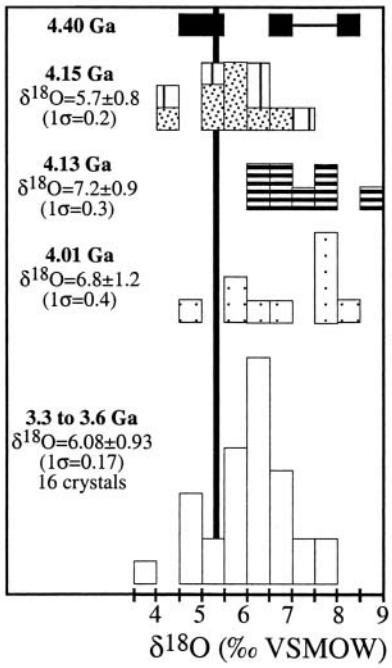


**Figure 15.** Compilation of $\delta^{18}O$ analyses by ion microprobe for detrital zircons from Jack Hills, Western Australia. All age groups except 4.15 Ga are elevated in $\delta^{18}O$ with respect to mantle values (solid line) or ion microprobe analyses of a homogeneous zircon standard (from Peck et al. 2002).

## Mid-Proterozoic

***Anorthosite suite.*** Magmatic zircons from the Grenville Province have been studied from:

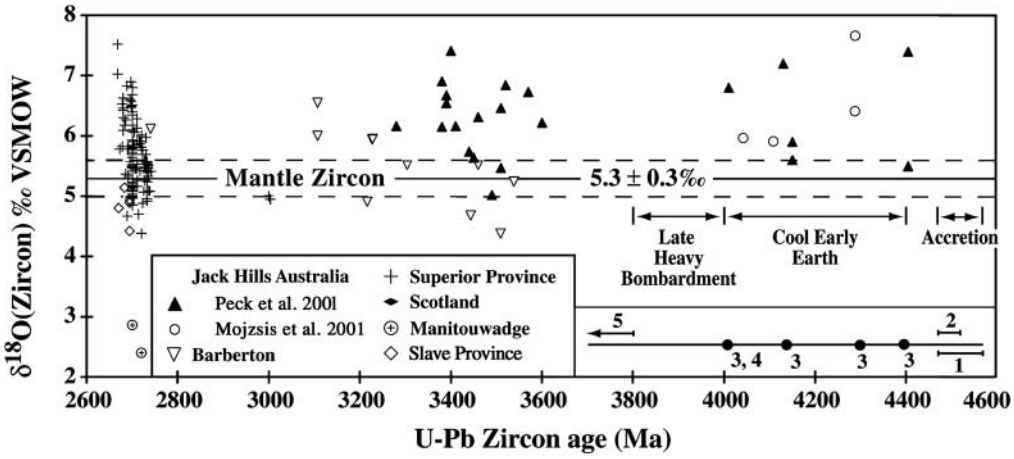


**Figure 16.** Crystallization age (U-Pb) and $\delta^{18}O$ for Archean magmatic zircons. A majority of magmas were primitive in $\delta^{18}O$ similar to the mantle today ("mantle zircon"), but some zircons are elevated as high as 7.5‰ due to melting of protoliths that were altered at low temperature by liquid water near the surface of the Earth. The timeline, lower right, shows: 1. accretion of Earth; 2. formation of Moon and Earth's core; 3. evidence for liquid water; 4. Acasta gneiss; 5. Isua metasediments (from Valley et al. 2002).

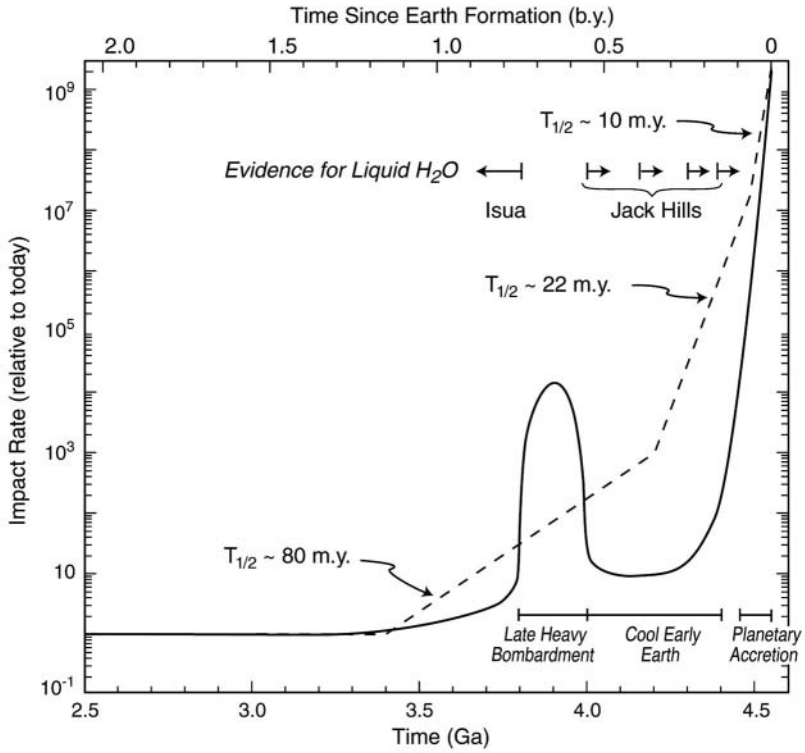


**Figure 17.** Estimates of meteorite flux for the first 2 Gyr of Earth history based on two hypotheses: exponential decay of impact rate (dashes) and cool early Earth / late heavy bombardment (solid curve). The hypothesis of a cool early Earth suggests that impact rate dropped precipitously by 4.4 Ga, consistent with relatively cool conditions and liquid water oceans (from Valley et al. 2002).

massif-type anorthosites and associated granitic rocks (AMCG suite), from granitic rocks of other age (non-AMCG), and from quartzites (detrital zircons) (Chiarenzelli and McLelland 1993, Valley et al. 1994, Peck 2000, Peck et al. 2003a,b; Clechenko et al. 2002). The intrusion of AMCG plutons as high $\delta^{18}O$ magmas is discussed above (Assimilation vs. Fractional Crystallization) and demonstrates a major crustal component in both the anorthosite and enclosing contemporaneous granitic rocks. (Fig. 18; open circles).

Zircons from monzosyenite associated with the Laramie anorthosite (Wyoming) have a uniform $\delta^{18}O = 7.4\pm0.2‰$ (O'Connor and Morrison 1999). In contrast to the Grenville anorthosites, this value is too high for magmatic equilibration with the associated anorthosite, suggesting a major crustal component to the granitic magmas and ruling out closed system fractionation from the same parent magma as anorthosite. One zircon from pegmatite associated with the San Gabriel anorthosite (Pacoima Canyon, California) has a mantle-like value of 5.69‰ warranting further study (Valley, unpublished).

***Grenville terrane boundaries.*** The Carthage-Colton Mylonite Zone and the Maberly Shear Zone are major terrane boundaries in the Grenville Province, separating the Adirondack Highlands, the Frontenac terrane, and the Sharbot Lake domain (Fig. 19). The Carthage-Colton and its continuation in Quebec, the Labelle Shear zone, extend over 400 km separating terranes with distinct lithology, and timing and intensity of metamorphism. Competing views interpret this boundary as the site of terrane docking during the Elzevirian Orogeny (ca. 1.35-1.18 Ga) or as a post metamorphic normal fault down-dropping amphibolite facies rocks of the NW Adirondacks to become adjacent to granulites in the Adirondack Highlands. Metamorphosed plutonic rocks of the ~1.15 Ga AMCG suite occur on both sides of this boundary suggesting that the terranes were juxtaposed by ~1.18 Ga (McLelland et al. 1996).

The high $\delta^{18}O$ of Adirondack and Frontenac orthogneisses has long been recognized (Taylor 1969, Shieh 1985, Morrison and Valley 1988). While metamorphic fluid-hosted origins for this anomaly have been proposed, the high $\delta^{18}O$ values in magmatic zircons from all phases of the AMCG suite (Valley et al. 1994, Clechenko et al. 2002, Peck et al. 2003a,b), preclude a post-metamorphic origin and demonstrates that these were high $\delta^{18}O$ magmas, as originally proposed by Valley and O'Neil (1984).

Figure 19 shows values of $\delta^{18}O$(Zc) from AMCG ortho-gneisses across the Adiron-dacks and Frontenac terrane (Peck et al. 2003b). Values of $\delta^{18}O$ are projected onto a NW-SE traverse. Remarkably homogeneous, yet elevated values of 8.2±0.6‰ are seen throughout the Adirondack Highlands. These high magmatic $\delta^{18}O$ values include granitic rocks that are 2-3‰ enriched in $^{18}O/^{16}O$ relative to primitive mantle-derived magmas. In con-

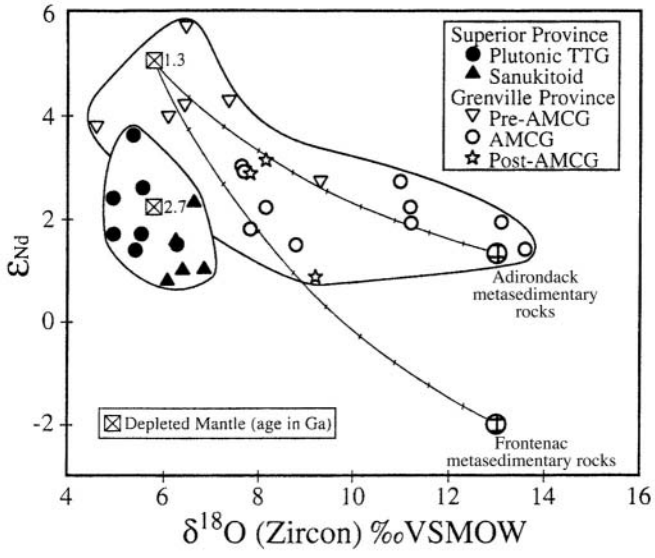


**Figure 18.** Values of whole rock $\varepsilon_{Nd}$ vs. $\delta^{18}O$(Zc). Superior Province samples show little variability and cluster around the value for depleted mantle at 2.7 Ga. Samples from AMCG and post-AMCG plutons in the Grenville fall along mixing trends with metasediment. Pre-AMCG magmas were more mantle-like (from Peck et al. 2000).

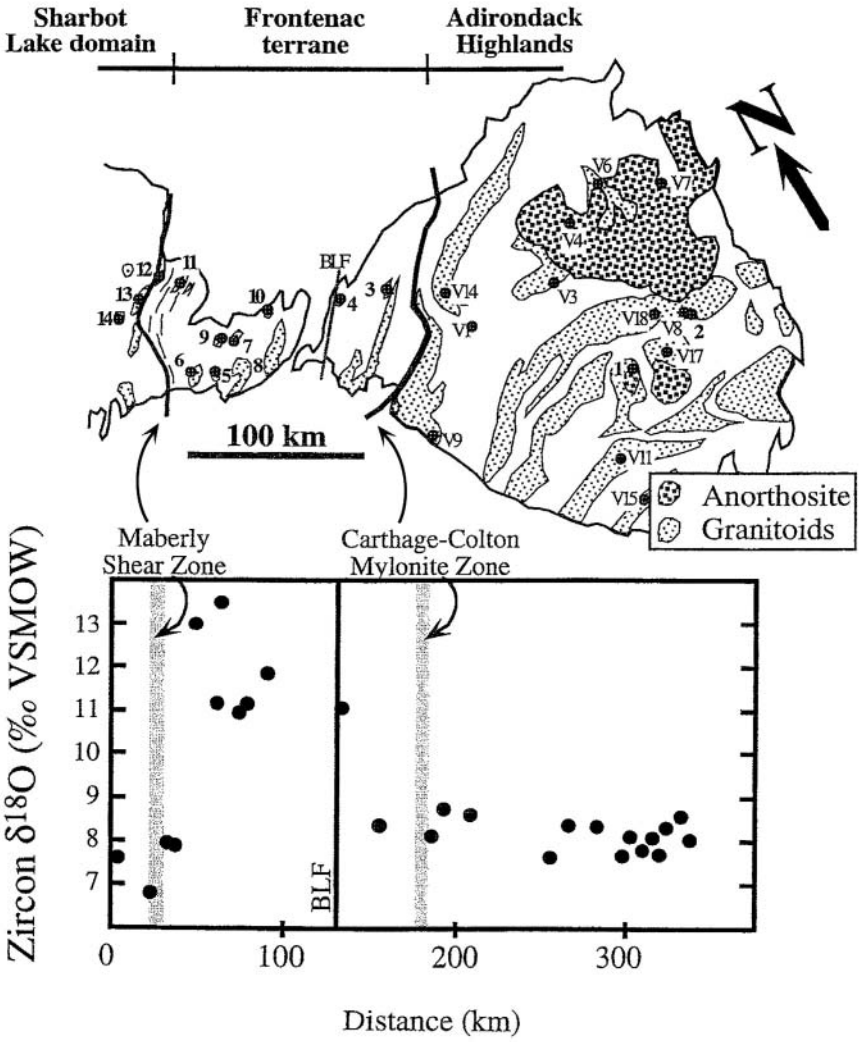


**Figure 19.** Values of $\delta^{18}O$(Zc) and sample locations from AMCG (anorthosite-suite) plutons (1180-1130 Ma) of the Adirondack Highlands and Frontenac terrane of the Grenville Province. The Carthage-Colton mylonite zone is a major shear zone separating the two terranes and extending over 400 km north into Quebec. Values of $\delta^{18}O$ are 2-3‰ higher than primitive mantle magmas in the Adirondacks, but jump to over 10‰ in the Frontenac revealing that high $\delta^{18}O$ sediments occur at depth. Subduction of supra-crustal rocks is proposed during the Elzevirian Orogeny followed by melting during AMCG plutonism (from Peck et al. 2003b).

trast, the zircons of the Frontenac terrane are higher still and more variable at 11.8±1.0‰. These values include the highest $\delta^{18}O$ yet measured in magmatic zircon (13.5‰) and represent granitic plutons with magmatic whole rock values up to 15‰. Farther to the NW, across the Maberly Shear Zone, this high $\delta^{18}O$ anomaly is not seen. While elevated $\delta^{18}O$ values extend from the Adirondack Highlands north to the Morin anorthosite (Peck and Valley 2000), the unusually high Frontenac values have not been found farther north along strike of the Frontenac Terrane. The $\delta^{18}O$ of Frontenac AMCG magmas cannot be caused by exchange with country rocks at the present levels of exposure (Peck et al. 2003b) and thus the zircon data document the otherwise undetected existence of unusually high $\delta^{18}O$ source rocks at depth. Consistent with the tectonic model of McLelland et al. (1996) and Wasteneys et al. (1999), Peck et al. (2003b) hypothesize subduction of high $\delta^{18}O$ sediments

and altered ocean crust during the Elzevirian Orogeny at ~1.2 Ga followed by melting and AMCG plutonism at 1.18-1.13 Ga. The surprising bimodality of $\delta^{18}O(Zc)$ across the Carthage-Colton mylonite for rocks of the same suite indicates that the deep crust under the Frontenac terrane is unique and suggests either that the Frontenac was the continental margin to Elzevirian subduction or that the two terranes were separated at that time.

***Finnish Svecofennian granitoids.*** Values of $\delta^{18}O(Zc)$ from 1.88-1.87 Ga post-kinematic, and 1.65-1.54 Ga anorogenic rapikivi, magmatism in Finland provide information on crustal evolution during the Svecofennian Orogeny (Elliott et al. 2001). Undeformed 1.88-1.87 Ga granitoids are relatively constant at $\delta^{18}O(Zc) = 6.22\pm0.48‰$, while three plutons adjacent to supracrustal lithologies are higher, 7.70±0.09‰. Values in 1.65-1.54 Ga plutons vary south to north across a probable terrane boundary and correlate with Nd isotopes; in the south $\delta^{18}O(Zc) = 6.14\pm0.07‰$ and $\varepsilon_{Nd} = -0.9$ to +0.7, while in the north $\delta^{18}O(Zc) = 7.95\pm0.68‰$ and $\varepsilon_{Nd} = 1.5$ to 3.0. Interestingly, the more evolved, higher $\delta^{18}O$ correlates to $\varepsilon_{Nd}$ that is slightly more primitive.

## CRUSTAL GROWTH AND MATURATION

The oxygen isotope geochemistry of crust-derived magmas reflects the long term mixing of mantle derived melts and the crust. Recycled sediments and other supra-crustal materials most commonly have $\delta^{18}O$ higher than the mantle due to low temperature processes, but a lower $\delta^{18}O$ is also possible. Through time, the crust has matured as granitoids with mildly elevated $\delta^{18}O$ are also recycled creating larger $^{18}O/^{16}O$ enrichment. Analyses of $\delta^{18}O$ in zircons that have been dated provide a record of the growth and maturation of the crust.

### Superior vs. Grenville province

Peck et al. (2000) compared Archean zircons (3.0-2.7 Ga) from the Superior Province (King et al. 1997, 1998b; King 1997) to Proterozoic zircons (1.3-1.0 Ga) from the Grenville Province (Valley et al. 1994, Peck 2000). Samples are from a 2000 km traverse across the Grenville Front (Fig. 11). A pronounced bimodality in $\delta^{18}O$ exists. Magmatic zircons from the Superior Province are relatively constant and mantle-like with average $\delta^{18}O = 5.7\pm0.6‰$ (1sd). In contrast, magmatic zircons from the Grenville are on average 2.5‰ higher and much more variable in $\delta^{18}O = 8.2\pm1.7‰$ (Fig. 20). Peck et al. (2000) conclude that the primitive values in the Superior Province result from relatively low amounts of crustal burial, subduction and recycling in the Archean, and from the relatively low and mantle-like $\delta^{18}O$ of Archean sediments that were available for recycling. In contrast, maturation of the crust by mid-Proterozoic time provided large amounts of higher $\delta^{18}O$ supracrustal material and active subduction promoted more vigorous recycling.

The rapid recycling of the

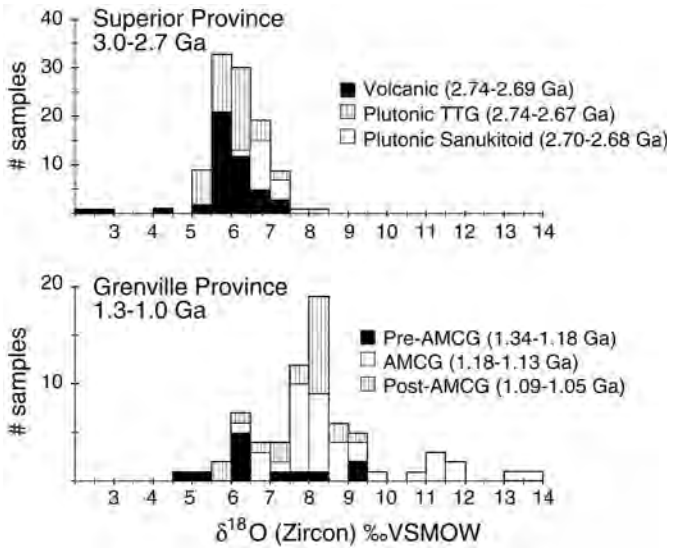


**Figure 20.** Values of $\delta^{18}O$ for magmatic zircons from the Grenville (1.3-1.0 Ga) and Superior Provinces (3.0-2.7 Ga). The Archean Superior Province samples have consistently low and primitive $\delta^{18}O(Zc) = 5.7\pm0.6‰$. The Proterozoic Grenville samples are more evolved with variable and high $\delta^{18}O(Zc) = 8.2\pm1.7‰$. (from Peck et al. 2000).

Grenville crust is dramatically demonstrated by the oxygen isotope ratios (Fig. 20), but is not well documented by radiogenic isotope studies. Peck et al. (2000) review published radiogenic isotope data and point out that the anorthosite-suite (AMCG) rocks, which comprise 30% of the Grenville, appear to be "juvenile Middle Proterozoic additions to only slightly older (<1.4 Ga) crust, suggesting a relatively short history, and likely derivation from the mantle." Figure 18 shows whole rock $\varepsilon_{Nd}$ vs. $\delta^{18}O(Zc)$. The $\varepsilon_{Nd}$ values for the Grenville at 1.3 Ga are positive with a restricted range of <5 $\varepsilon_{Nd}$ units showing that the recycled high $\delta^{18}O$ material was relatively juvenile, but radiogenic isotopes do not distinguish among Middle Proterozoic sources that are magmatic vs. sedimentary. In contrast to the Archean, where no recycling is evident, the Grenville data show a negative correlation of $\delta^{18}O(Zc)$ and $\varepsilon_{Nd}$ (Fig. 18). Thus, the high $\delta^{18}O$ values show that material recycled into the source regions of AMCG magmas had a relatively short history of low temperature alteration rapidly followed by subduction or burial, and melting.

**Evolution of magmatic $\delta^{18}O$ through time**

Magmatic zircons of known age (4.4 Ga to 0.2 Ma) have been analyzed by laser fluorination at the University of Wisconsin from over 600 rocks worldwide to test the generality of $\delta^{18}O$ differences between the Grenville and Superior Provinces (Fig. 21). U-Pb ages were determined previously for most samples by thermal ionization mass-spectrometry. The Jack Hills detrital zircons were analyzed *in situ* by ion microprobe.

The range and variability of $\delta^{18}O$ in the Archean is subdued. Values at ~2.7 Ga are largely from the Superior Province with most zircons in high temperature equilibrium with the mantle and a tail to higher values (Figs. 14, 16, 20a). No magmatic zircons have been analyzed in the Archean with $\delta^{18}O > 8‰$. Similar values come from the Lewisian (2.7 Ga), Slave Province (2.7 Ga), and Barberton (2.7-3.5 Ga, Kamo and Davis 1994). The Jack Hills zircons (4.4-3.1 Ga) are indistinguishable within uncertainty.

Values of $\delta^{18}O(Zc)$ are significantly more variable in the Proterozoic and Phanerozoic. Many values are above 8‰, suggesting that magmas with whole rock $\delta^{18}O > 9$-10‰ became common after 2.5 Ga and were derived from high $\delta^{18}O$ crustal rocks. However, values of $\delta^{18}O(Zc) > 10‰$ are not common. In the Grenville, they come from a relatively small group of plutons that were intensely studied (Shieh 1985, Peck et al. 2003b). Likewise samples with $\delta^{18}O < 5‰$ are over represented due to studies of low

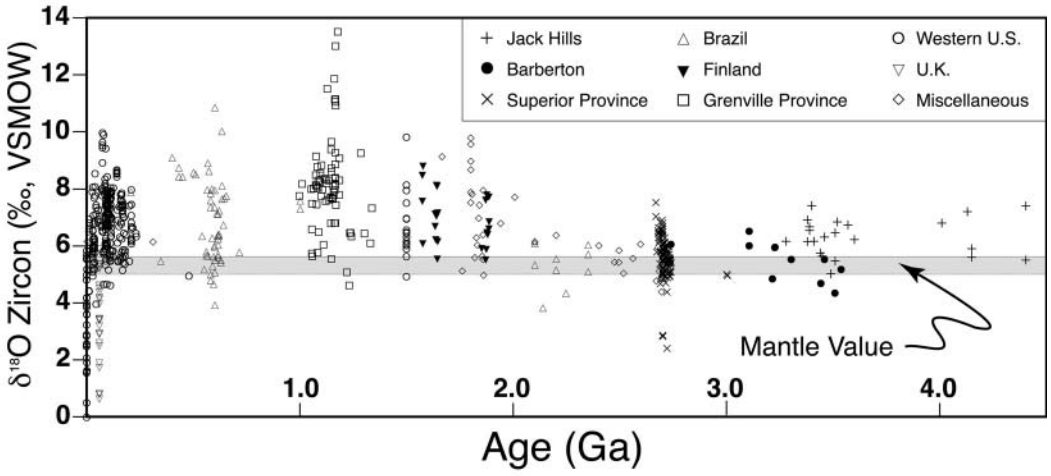


**Figure 21.** Compilation of $\delta^{18}O(Zc)$ vs. age for over 600 samples analyzed at the University of Wisconsin. Samples range in age from 4.4 Ga to 0.2 Ma and come from many terranes on seven continents. A remarkable uniformity is seen in the Archean, values cluster near the mantle ($\delta^{18}O(Zc) = 5.3\pm0.3‰$) with some values as high as 7.5‰ due to recycling of supracrustal material. High $\delta^{18}O$, above 8‰ does not become common until after 2 Ga, reflecting recycling of high $\delta^{18}O$ sediment. This change may be due to the onset of subduction, the evolution of mature sediments, or changes in the Earth's atmosphere near the end of the Archean.

$\delta^{18}O$ granites from the British Tertiary Igneous Province and low $\delta^{18}O$ rhyolites from Yellowstone.

The nature of the Archean-Proterozoic $\delta^{18}O(Zc)$ transition is not yet known due to the relatively small data set between 2.5 and 2.0 Ga. Perhaps this is a sharp transition at the end of the Archean or at some date within the next 500 m.y., or perhaps it was a gradual change. Either way, it is expected that many samples would be mantle-like and more analysis will be necessary to determine if higher $\delta^{18}O$ magmas existed at this time interval. Possible causes for this change include: changes in the composition and abundance of sediments available for recycling due to increased sedimentary environments at the end of the Archean; the onset or acceleration of subduction at the end of the Archean (if one rejects Archean subduction); or differences in weathering as the atmosphere became more oxygen rich at ~2.2 Ga.

## ULTRA-HIGH PRESSURE ECLOGITES, DABIE AND SULU

The Dabie-Sulu orogenic belt separates rocks of the Sino-Korean Plate from the Yangtze Plate in China. Movement along the Tan-Lu fault has separated Dabie Shan and Sulu by 500 km, but they are linked by unique petrologic and geochemical characteristics. Eclogite facies metamorphism produced rare ultra high pressure (UHP) mineral assemblages including coesite and diamond in the Triassic (245-210 Ma) and many UHP rocks are depleted in $^{18}O/^{16}O$ demarking an original area extending over 100 km, one of the major hydrothermally altered terranes on Earth. Values of $\delta^{18}O$(garnet) and $\delta^{18}O$(Qt) as low as –10‰ document exchange with heated meteoric waters, but the age of alteration has been uncertain.

Rumble et al. (2002) found values of $\delta^{18}O(Zc)$ = –0.2 to –7.4‰ from granites near Qinglongshan in Sulu and used *in situ* ion microprobe analysis to date zircon cores to 754-684 Ma. Air abrasion and laser fluorination of zircons revealed no zoning in $\delta^{18}O$ (cores vs. whole grains), showing that cores are low in $\delta^{18}O$ and thus that the low $\delta^{18}O$ anomaly was acquired almost 500 m.y. before UHP metamorphism. The coincidence of magmatism, extremely low $\delta^{18}O$ meteoric water, and Neoproterozoic continental glaciation (Nantuo tillite, ~800-700 Ma) has led to the proposal that granites intruded in proximity to glacial ice. Presumably, the granites were melted from, and contaminated by, low $\delta^{18}O$ hydrothermally altered country rocks as has been documented at Yellowstone (see, Bindeman and Valley 2001). Paleolatitudes of 29 to 43° are estimated for Dabie supporting the hypothesis that these conditions were part of a worldwide "Snowball Earth" event (Hoffman et al. 1998, Rumble et al. 2002). These conclusions are strengthened by Zheng et al. (2003) who analyzed 112 zircon samples from eclogites and granitic orthogneisses throughout Dabie and Sulu with values as low as –10‰, which are the lowest $\delta^{18}O$ zircons known. Values range from –4.6 to +8.9‰ in Dabie and –10.3 to +5.6‰ in Sulu.

In contrast to the metamorphosed granites, Wei and Valley (unpublished) analyzed zircons from 45 samples from 15 younger unmetamorphosed granitic plutons and associated country rocks at Dabie. Values for granite range from –1.63 to 6.08‰ with an average of 5.01±0.95‰ (n = 38). These values for unmetamorphosed granites are similar to other Mesozoic and Tertiary granites in eastern China and show that the ultra-low $\delta^{18}O$ anomaly at Dabie and Sulu is restricted to rocks that predated the ultra high-pressure metamorphism.

## FELSIC VOLCANISM, WESTERN UNITED STATES

Three volcanic centers from the western U.S. have produced large volume rhyolitic eruptions (≥650 $km^3$) and calderas, and have been studied in detail: Yellowstone, Timber Mountain/ Oasis Valley, and Long Valley. The analysis of $\delta^{18}O$ in magmatic zircons has provided information not previously available regarding the remelting of wall rocks, and the duration of magmas and magma chambers.

### Low $\delta^{18}O$-rhyolites, Yellowstone

The Yellowstone Plateau is the present terminus of an NE-migrating hotspot that has caused one of the largest centers of rhyolitic magmatism on Earth. Three massive (100-2500 $km^3$), caldera-

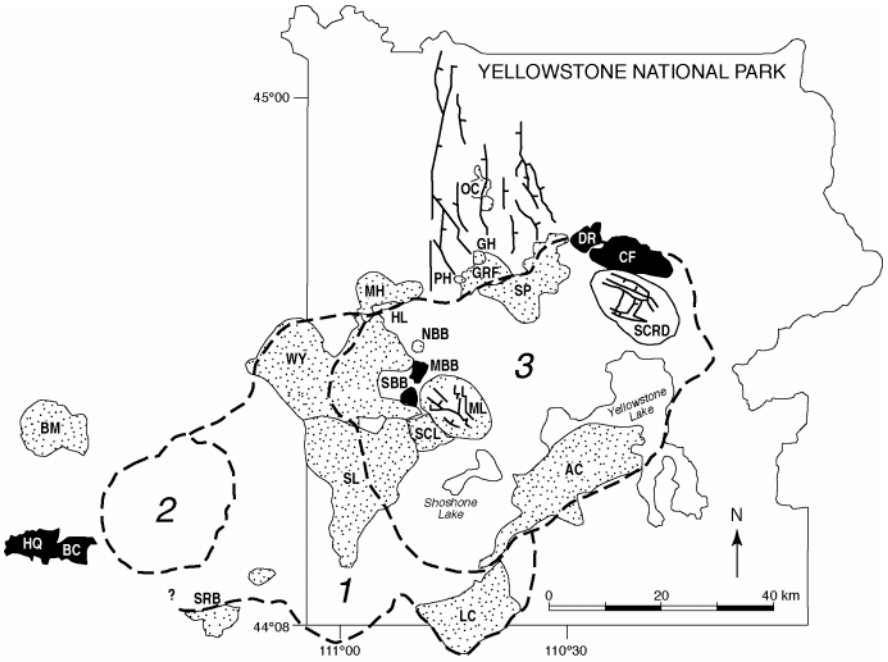


**Figure 22.** Yellowstone Plateau, showing the positions of major calderas: 1. Big Bend caldera, Huckleberry Ridge Tuff, 2.0 Ma, 2500 km$^3$; 2. Henry Forks caldera, Mesa Falls Tuff, 1.3 Ma, 300 km$^3$; 3. Yellowstone caldera, Lava Creek Tuff, 0.6 Ma, 1000 km$^3$. For sources of mapping, see Christiansen (2000). Flows in black are low $\delta^{18}O$ rhyolites. The Mallard Lake (ML) and Sour Creek (SCRD) resurgent domes are within Yellowstone caldera (from Bindeman and Valley 2001).

forming, and numerous smaller, lavas and tuffs (Fig. 22) have erupted over the past 2 million years, covering most of the western United States (Christiansen 2000). Early oxygen isotope analyses of quartz found that low $\delta^{18}O$ rhyolites follow each of the climactic eruptions (Fig. 23a; Lipman and Friedman 1975, Hildreth et al. 1984). The low $\delta^{18}O$ post-caldera rhyolites are relatively small (<50 km$^3$) and are themselves followed by a return to normal magmatic values.

The genesis of low $\delta^{18}O$ rhyolites at Yellowstone and the implications for explosive volcanism have been vigorously debated. Lipman and Friedman (1975) and Hildreth et al. (1984) proposed that low $\delta^{18}O$ meteoric waters coursed down the caldera-forming fracture system and interacted directly with underlying bodies of magma. Taylor and Sheppard (1986) argued that significant interaction of liquid water with a magma chamber was impossible on physical grounds. Instead, they proposed the assimilation of hydrothermally altered, low $\delta^{18}O$ wall rock. Likewise, Bacon et al. (1989) proposed that partial melting of wall rock caused low $\delta^{18}O$ magmas at Crater Lake.

Bindeman and Valley (2000a, 2001) separated and analyzed zircons and coexisting minerals from 25 lavas and tuffs at Yellowstone (Fig. 23b). The fractionation between quartz and zircon is equilibrated and normal (~2.1‰) for most magmas. In contrast, extreme disequilibrium was found among zircon and other minerals in low $\delta^{18}O$ rhyolites erupted after the two largest caldera-forming eruptions (Fig. 23b; Huckleberry Ridge at 2 Ma and Lava Creek at 0.6 Ma). This is evident from values of $\Delta$(Qt-Zc) that are too small for any magmatic temperature (Fig. 23d), or reversed, and from oxygen isotope zonation within zircons (Figs. 23c, 24). Zoning within single zircons shows rims up to 5‰ lower than cores based on: analysis of early-formed large zircons vs. late-formed smaller zircons; air abrasion of large zircons and comparison of cores to whole crystals; and ion microprobe analysis of cores and the outer 3 μm of rims (Fig. 24).

The discovery of isotopically zoned zircons at Yellowstone supports a revised model for the genesis of post-caldera magmas and low $\delta^{18}O$ rhyolites (Bindeman and Valley 2000a, 2001). Hy-

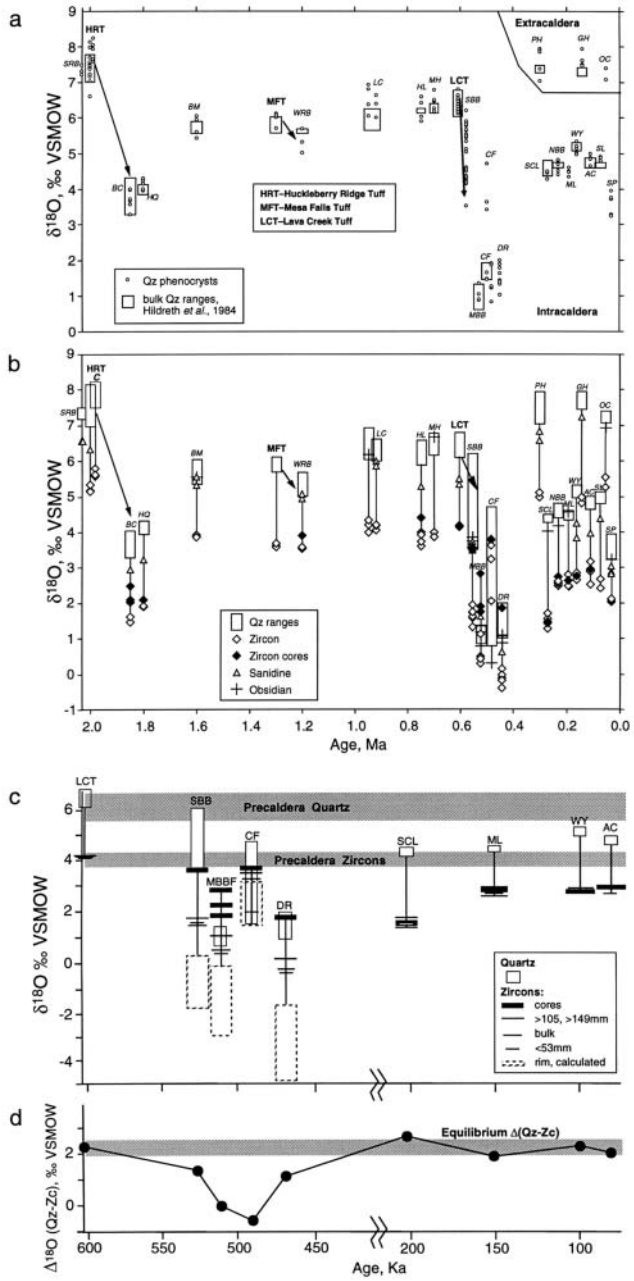


**Figure 23.** Evolution of $\delta^{18}O$ in Yellowstone magmas. Caldera-forming eruptions are Huckleberry Ridge Tuff (HRT), Mesa Falls Tuff (MFT), and Lava Creek Tuff (LCT). (a) Individual quartz phenocrysts and bulk quartz. (b) Zircon, sanidine, and obsidian. Air-abraded zircon cores are filled diamonds. (c) Post LCT intra-caldera lava flows. The range of individual quartz phenocrysts are shown in boxes. Zircons are plotted by crystal size. (d) $\Delta^{18}O$(Qt-Zc) for LCT and post-LCT lavas. The equilibrium value of $\Delta$(Qt-Zc) is 1.9-2.3‰ at 800-900°C. Note that only low $\delta^{18}O$ rhyolites have quartz and zircon that are not equilibrated (from Bindeman and Valley 2000a, 2001).

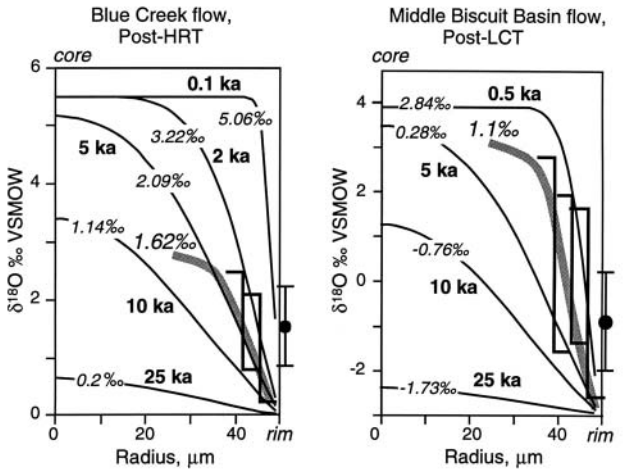


**Figure 24.** Zoning profiles for $\delta^{18}O$ in 50 μm radius zircons from Blue Creek and Middle Biscuit Basin flows, Yellowstone, based on: successive air abrasions and ion microprobe analysis of crystal growth faces (filled dots). The top of each bracket is the $\delta^{18}O$ of zircon cores after abrasion and the bottom of each bracket is the calculated $\delta^{18}O$ of removed rims. The radius at each step is calculated by weight. Thin curves are labeled with the bulk $\delta^{18}O$ of the grain (**bold** = measured; *italic* = estimated) and calculated using the "wet" diffusion rate (Watson and Cherniak 1997). The residence time (kyr) necessary to create each profile by diffusion between a higher $\delta^{18}O$ zircon xenocryst and a low $\delta^{18}O$ melt is shown (from Bindeman and Valley 2001).

drothermal alteration by heated meteoric waters lowers $\delta^{18}O$(WR) of rocks overlying the magma chamber, but refractory zircons and some quartz phenocrysts retain magmatic $\delta^{18}O$ (~4‰; Fig. 25,I). After climactic eruption, the roof drops to contact hot magmas remaining in the magma chamber (Fig. 25,II). Melting of the down-dropped roof zone forms magma, which is low in $\delta^{18}O$(WR), but has unaffected higher $\delta^{18}O$ zircons as xenocrysts. The eruption of these localized, small volume melts produces intra-caldera low $\delta^{18}O$ rhyolites (Fig. 25,III).

One of the implications of this model is that zoned zircons are xenocrysts from earlier rhyolites. This prediction has been verified by ion microprobe dating of post Lava Creek Tuff zircons (<0.65 Ma), which show that many zircon cores are inherited from earlier magmas (2.4 to 0.7 Ma; Bindeman et al. 2001a).

The failure of the magmatic system to achieve oxygen isotope equilibration with zircon cores provides information on the longevity of the post caldera magmas. The measured zonation profiles and low $\delta^{18}O$ rims have formed by either overgrowth of new magmatic zircon or by diffusion (Watson 1996, Watson and Cherniak 1997, Peck et al. 2003a). Bindeman and Valley (2001) estimate that if the profiles shown in Figure 24 formed by diffusion, it would take 500-10,000 years (time varies with choice of diffusion coefficient and crystal size).

**Timber Mountain / Oasis Valley Caldera Complex**

The SW Nevada Volcanic field includes four major caldera forming ash-flow sheets of the Timber Mountain / Oasis Valley caldera complex: Topopah Springs Tuff, >1200 $km^3$, 12.8 Ma; Tiva Canyon Tuff, 1000 $km^3$, 12.7 Ma; Rainier Mesa Tuff, 900 $km^3$, 11.6 Ma; and Ammonia Tanks Tuff, 1200 $km^3$, 11.45 Ma. Each tuff erupted an early, more voluminous rhyolite and later latite. Latites are characterized by higher values of: magmatic temperature, crystal content, and Zr, Sr, and REE content. Latites are lower in magmatic $\delta^{18}O$(WR) as calculated from $\delta^{18}O$ of phenocrysts and equilibrium fractionations. Figure 26 shows that the tuffs erupted in pairs separated by ~0.1 Myr and that the second tuff in each pair is depleted in $^{18}O/^{16}O$ by 1-2.5‰ (Bindeman and Valley 2000b, 2003). The low $\delta^{18}O$ tuffs and lavas contain zircons that are zoned by approximately 2‰ with higher $\delta^{18}O$ cores being recycled xenocrysts from melting of earlier tuffs.

These trends are similar to those observed at Yellowstone with the major difference that the volume of low $\delta^{18}O$ rhyolites is much larger and the depletions are smaller. It is likely that the four climactic eruptions expelled most of the magma from each magma chamber and that each new felsic magma formed by melting of shallow crust, heated by intrusion of mafic magma. Thus the oxygen

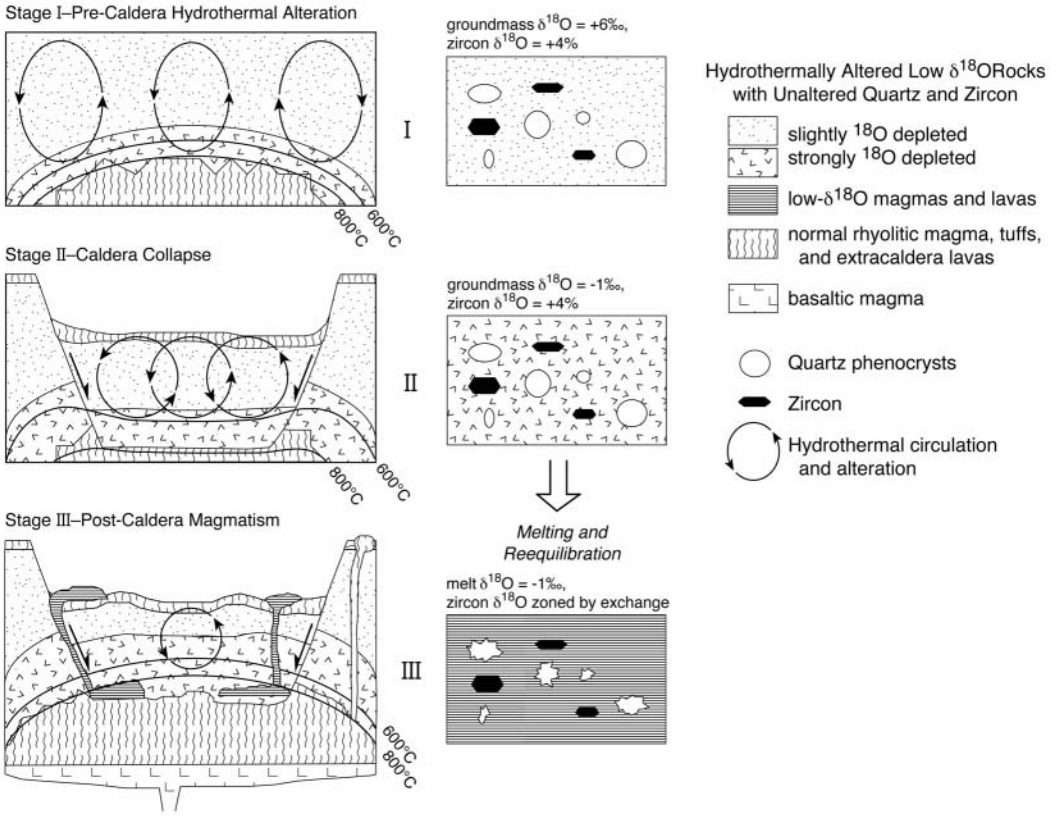


**Figure 25.** The bulk melting-caldera collapse model for generation of low $\delta^{18}O$ rhyolite. Stage I: hydrothermal alteration creates low $\delta^{18}O$ halo around earlier magma chamber. Quartz and zircon are not affected and retain normal $\delta^{18}O$. Stage II: Down drop of roof during caldera collapse brings altered, low $\delta^{18}O$ lavas from earlier eruptions into contact with high temperature melt remaining in magma chamber. Melting of the altered lavas creates a low $\delta^{18}O$ rhyolitic magma with normal $\delta^{18}O$ xenocrysts of zircon and quartz. Stage III: Some low $\delta^{18}O$ melts are isolated from the magma chamber and erupt as individual, small, post-caldera lavas (from Bindeman and Valley 2001).

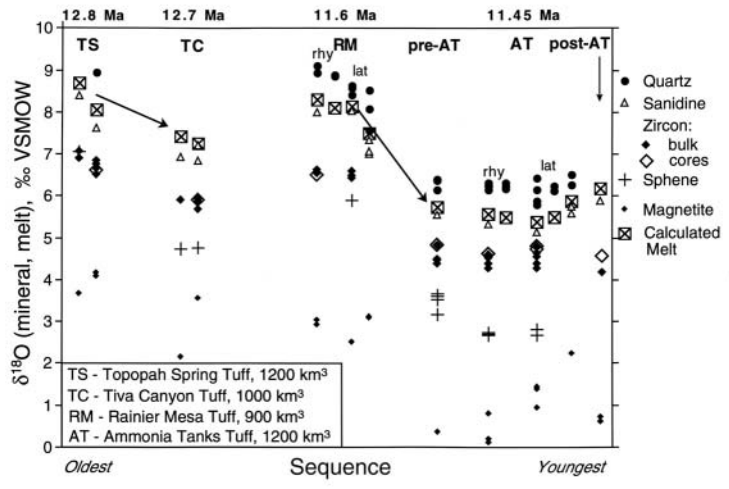


**Figure 26.** Evolution of $\delta^{18}O$ in minerals and melt for the four major caldera forming tuffs of the Timber Mountain/ Oasis Valley caldera complex. Data within each tuff are separated to show the early rhyolites and late higher temperature latites. Eruptions were paired, a normal $\delta^{18}O$ magma followed 0.1 Myr later by a significantly lower $\delta^{18}O$ magma. The Ammonia Tanks Tuff (AT) at 11.45 Ma is a low $\delta^{18}O$ rhyolite. Air-abraded cores of zircons are higher in $\delta^{18}O$ than bulk zircon concentrates or small zircons from AT, pre-AT or post AT lavas (from Bindeman and Valley 2003).

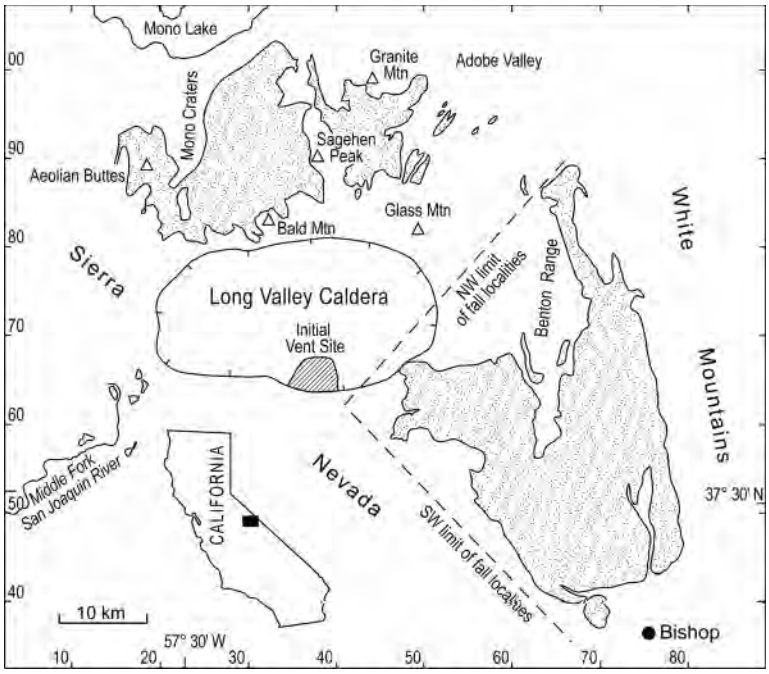


**Figure 27.** The Long Valley caldera and vicinity, California. Outcrop of the Bishop Tuff ash flow is stippled. The early phases of the Bishop Tuff erupted from the "initial vent site." The total erupted volume was 650 km$^3$ at 760 ka (from Wilson and Hildreth 1997).

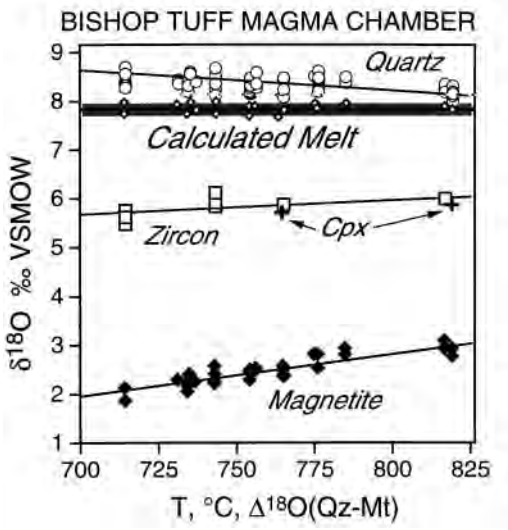


**Figure 28.** Values of $\delta^{18}O$ for quartz, magnetite, clinopyroxene, and zircon vs. temperature estimated from $\Delta^{18}O$(Qt-Mt) for the Bishop Tuff. The values of $\delta^{18}O$(melt) are remarkably constant (7.80±0.05‰) as calculated from $\delta^{18}O$(Zc) at the Qt-Mt temperature. The range of $\delta^{18}O$(Qt) and (Mt) values reflects exchange with a magma of constant $\delta^{18}O$(WR) and variable temperature (from Bindeman and Valley 2002).

isotope shifts are smaller, but the quantities of low $\delta^{18}O$ melt are larger.

The zoning of $\delta^{18}O$ seen in zircons from the Timber Mountain complex would be consistent with a residence time of approximately 10-15 ky for the normal $\delta^{18}O$ zircon xenocrysts in low $\delta^{18}O$ magmas. This is longer than the residence times inferred from zoning for zircons at Yellowstone, but shorter than the time intervals between successive caldera-forming eruptions i.e., Ammonia Tanks after Rainier Mesa Tuffs. This study demonstrates that large volume, high and low $\delta^{18}O$ magmas can be generated remarkable quickly without oxygen isotopic equilibration of xenocrystic material.

### Bishop Tuff, Long Valley caldera

The Bishop Tuff erupted (~650 km$^3$) in about one week from the Long Valley caldera at 0.76 Ma (Fig. 27). In spite of the climactic nature of the eruption, a clear volcanic stratigraphy exists for units subdividing the tuff (Wilson and Hildreth 1997). Temperature estimates for the magma based on $\Delta^{18}O$(Qt-Mt) (Fig. 28) increase from 715°C for the earliest tuffs (top of the magma chamber) to 815°C for late Bishop Tuff (deepest in the cham-

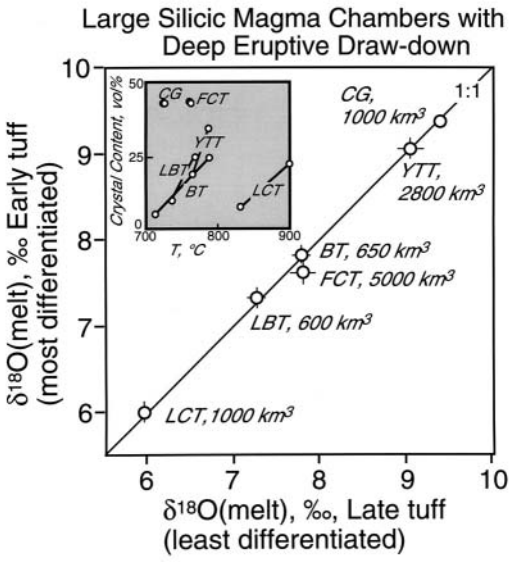


**Figure 29.** Oxygen isotope values calculated from $\delta^{18}O(Zc)$ for the early, most differentiated and late, least differentiated portions of major Quaternary ash flow tuffs. The good 1:1 correlation demonstrates vertical homogeneity of $\delta^{18}O$ within the magma chambers. BT = Bishop Tuff; CG = Cerro Galan; FCT = Fish Canyon Tuff; LBT = Lower Bandelier Tuff; LCT = Lava Creek Tuff; YTT = youngest Toba Tuff (from Bindeman and Valley 2003).

ber, Bindeman and Valley 2002). The oxygen isotope fractionations decrease smoothly for quartz, zircon and magnetite in response to this temperature increase, however the $\delta^{18}O$ of the magma remained constant, indicating that the Bishop Tuff magma chamber was homogeneous in $\delta^{18}O$ (Fig. 28). Such vertical homogeneity is estimated for at least five other Tertiary caldera-forming tuffs suggesting long-lived magmas and convective stirring processes that homogenized magma chambers (Fig. 29). It is further suggested that granitic batholiths worldwide could initially be homogeneous in $\delta^{18}O$ due to convection.

## PHANEROZOIC GRANITES

### British Tertiary Igneous Province

The felsic to mafic plutons and lavas of the British Tertiary Igneous Province relate to the opening of the N. Atlantic, outcrop along the coasts of Scotland and Ireland, and stitch across Archean, Proterozoic, and Paleozoic basement (Fig. 30). A classic bulls-eye pattern of low $\delta^{18}O$ surrounds many of the intrusive complexes due to post-magmatic hydrothermal alteration involving large fluxes of heated meteoric water in a shallow sub-volcanic environment (Fig. 31, Forester and Taylor 1977). However, the possibility of low $\delta^{18}O$ magmas and the genesis of the bimodal magmatism have been uncertain.

Magmatic zircons were separated and analyzed along with quartz from granites on Arran, Mull, and the four intrusive centers on Skye (Fig. 32; Gilliam and Valley 1997, Monani and Valley 2001). A majority of the zircon and quartz has $\delta^{18}O$ lower than the mantle value. The low $\delta^{18}O(Zc)$ values were evaluated for exchange with low $\delta^{18}O$ meteoric water by several tests. Imaging by CL and BSE shows typical magmatic growth patterns within euhedral grains. Analysis of zircons of different size or magnetism show no variability as predicted for subsolidus exchange. The fractionation $\Delta(Qt\text{-}Zc)$ does not correlate to $\delta^{18}O(Zc)$ as would be predicted for hydrothermal exchange and disequilibrium. Zircons separated from widely spaced localities within individual granite bodies of the Eastern Red Hills are identical in $\delta^{18}O$ even though the different bodies vary in $\delta^{18}O(Zc)$ from >5 to <0‰ (Fig. 32; #15, 16). Individual zircons analyzed by ion microprobe from single hand samples show no variability in $\delta^{18}O$. Thus, much of the $^{18}O/^{16}O$ depletion of granites from the Isle of Skye is magmatic in origin due to input from the crust. The subsequent low $\delta^{18}O$ hydrothermal overprint on feldspars and quartz is much less intense than has been thought previously.

The amount of crustal input required to generate the low $\delta^{18}O(Zc)$ values of 0 to 1‰ ($\delta^{18}O(WR)$ ~ 2‰, Glas Beinn Mohr granite, #15; Fig. 32) is greater than 40%, exceeding the energy budget of assimilation and suggesting that wholesale melting of granitic material was caused by mafic intrusions at depth. The $\delta^{18}O$ estimate differs from estimates based on trace elements and radiogenic isotopes. These other estimates support the hypothesis that granites were formed by differentiation of mantle melts with ≤10% crustal input and that there was an increasing percentage from the upper

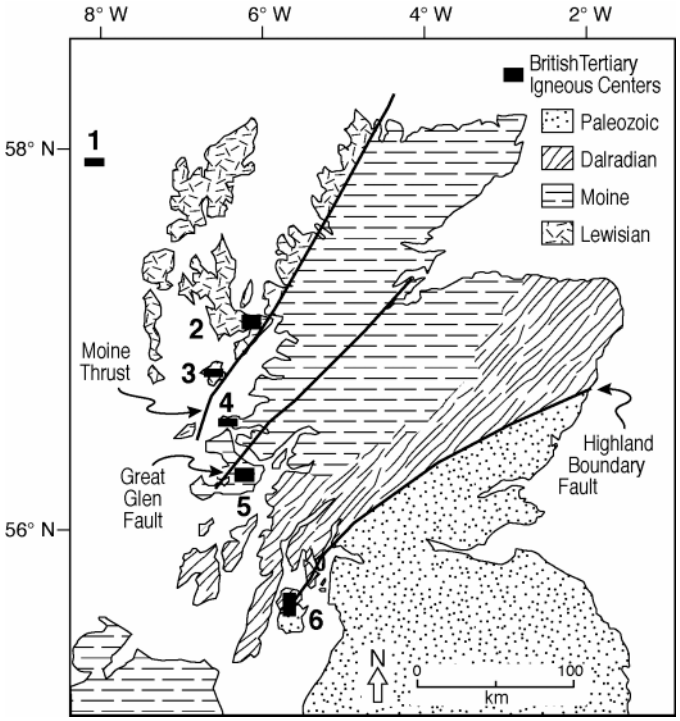


**Figure 30.** The British Tertiary Igneous Province intrudes Archean to Paleozoic terranes of western Scotland: 1. St. Kilda, 2. Skye, 3. Rhum, 4. Ardnamurchan, 5. Mull, 6. Arran (from Monani and Valley 2001).

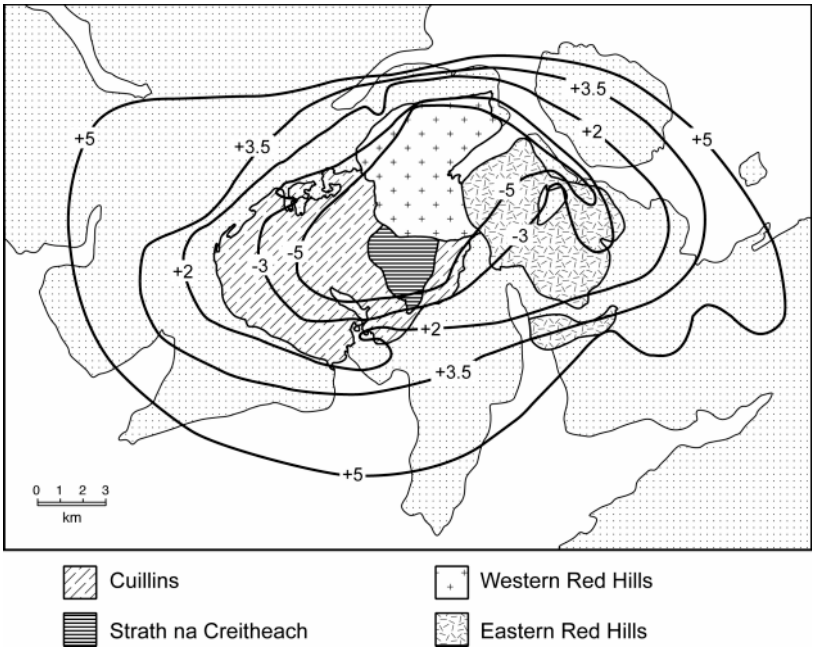


**Figure 31.** Contours of $\delta^{18}O$ from whole rock samples of basalt and mafic dikes, Isle of Skye. The bulls-eye pattern reflects the intensity of hydrothermal exchange with heated meteoric waters. Circulation of hydrothermal fluids was driven by heat from the four magmatic centers on Skye: the Cuillins, Strath na Creitheach, and the Western and Eastern Red Hills (from Forester and Taylor 1977).

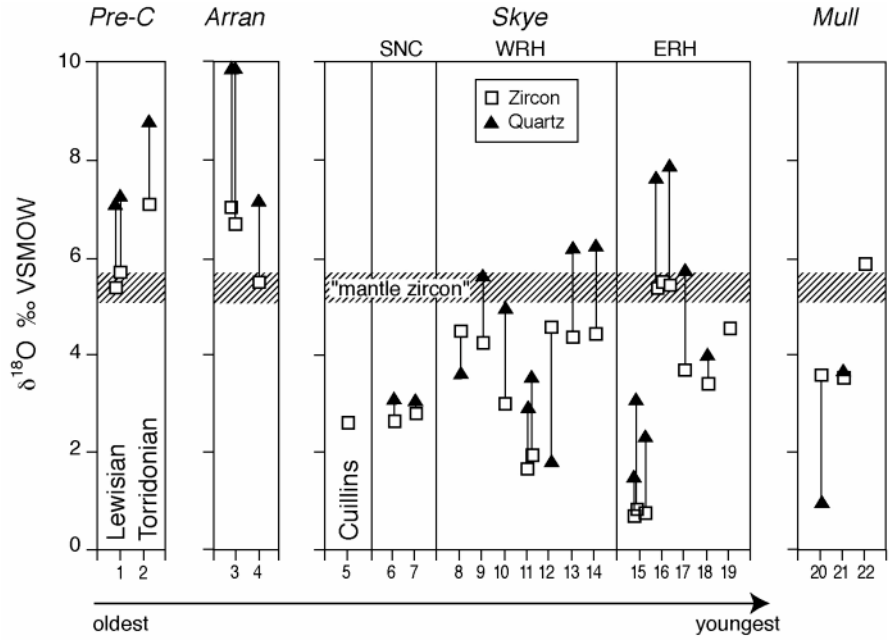


**Figure 32.** Values of $\delta^{18}O$ for zircon and quartz from granitic rocks of the British Tertiary Igneous Province. Granitic centers on the Isle of Skye are: SNC Strath na Creitheach, WRH Western Red Hills and ERH Eastern Red Hills. Values of $\delta^{18}O(Zc)$ are low indicating intrusion as low $\delta^{18}O$ magmas. Values of $\delta^{18}O(Qt)$ are not generally in equilibrium with zircon due to high temperature hydrothermal alteration of quartz (from Monani and Valley 2001).

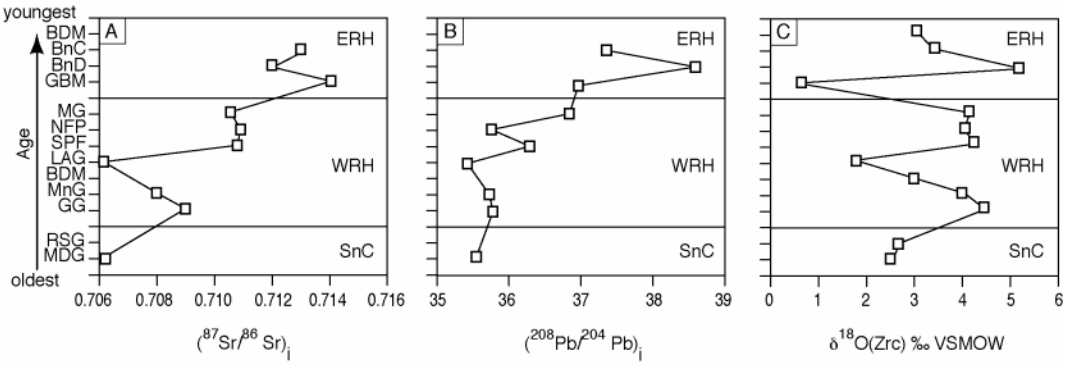


**Figure 33.** Initial Pb and Sr isotope ratios for whole rock samples of Skye granites (Dickin 1981, Dickin et al. 1984) and $\delta^{18}O(Zc)$ (Monani and Valley 2001) vs. relative age of intrusion. The three granitic centers on Skye are SNC, WRH, and ERH (defined in Fig. 32) (from Monani and Valley 2001).

crust (Fig. 33A,B; Dickin 1981, Dickin et al. 1984). This trend is not evident in the magmatic $\delta^{18}O$ values (Fig. 33C; Monani and Valley 2001) suggesting that $\delta^{18}O$ is decoupled from Sr and Pb because remelting of hydrothermally altered granites within a single suite can significantly impact $\delta^{18}O$ without affecting other geochemical systems.

The low $\delta^{18}O$ Red Hills granites on Skye provide an eroded view of the plutonic roots of a caldera environment like Yellowstone. Repeated magmatism within a shallow stationary center creates the perfect environment for hydrothermal alteration of early units, which are then available for remelting. The resultant recycled component may be indistinguishable with most geochemical

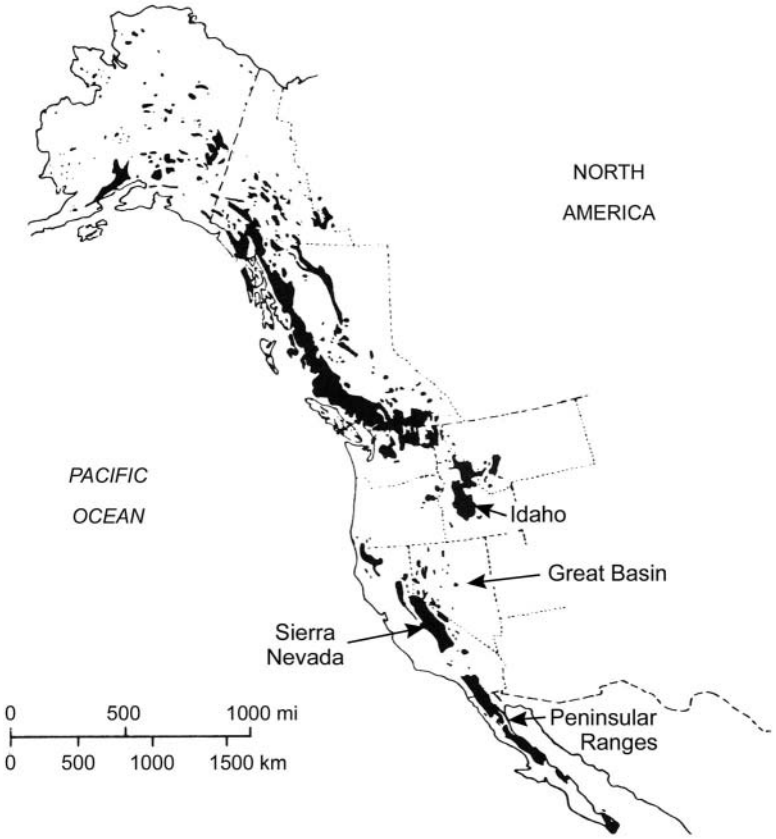


**Figure 34.** Major Cenozoic and Mesozoic batholiths of North America (black) (from Taylor 1986).

systems and is best resolved with stable isotopes ($\delta^{18}O$ and $\delta D$). Such magmatic "cannibalization" may be far more common than is generally recognized with important implications for the thermal budget of the crust.

**Mesozoic and Cenozoic granites of the western United States**

***Idaho batholith.*** The late Cretaceous and Tertiary granitic rocks of the Idaho batholith (Fig. 34) are intruded into the Precambrian margin of North America. Most rocks intrude Precambrian basement, but west of the Salmon River suture zone, granites intrude Triassic/Jurassic accreted terranes. The edge of the craton is marked by a sharp eastward increase in $^{87}Sr/^{86}Sr_i$ from 0.704 to 0.708 (the "0.706 line," Fig. 35), a decrease in $\varepsilon_{Nd}$ from ca. +6 to –16, and an increase in $\delta^{18}O$(WR) from 7 to 10‰ (Fig. 36) (Fleck and Criss 1985, Fleck 1990, King et al. 2003a).

The igneous values of $\delta^{18}O$ and $\delta D$ are overprinted in some minerals from most samples of the Idaho batholith by post magmatic exchange with heated meteoric water, especially near shallow Eocene plutons (Criss and Taylor 1983, Criss and Fleck 1990, Larson and Geist 1995, King and Valley 2001). Analysis of $\delta^{18}O$ in zircons records preserved magmatic values. The contrast with other minerals shows that details of the magmatic history have been obscured by the later alteration (King and Valley 2001). Values of $\delta^{18}O$(Zc) are relatively constant throughout the batholith in spite of a prolonged history of multiple intrusive pulses, and variable mineralogy, chemistry, and age. The northern lobe (Bitterroot) has an average $\delta^{18}O$(Zc) = 7.1±0.3‰, the southern lobe (Atlanta) is 7.0±1.0‰, and Eocene plutons are 7.2±0.2‰ with the exception of the Casto pluton, which is a low

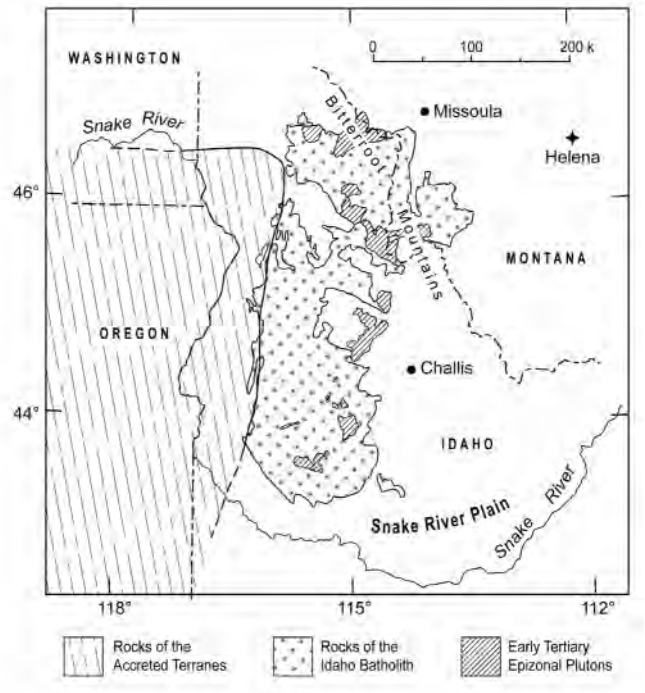


**Figure 35.** The Idaho batholith (stipple) and surrounding area. The solid curve along the west side of the batholith is the $Sr_i = 0.706$ line. Precambrian continental crust forms basement to the east. Accreted terranes to the west are late Paleozoic and early Mesozoic (from Fleck and Criss 1985).

$\delta^{18}O$ granite ($\delta^{18}O(Zc) = 4.0‰$; $\delta^{18}O(WR) \sim 5.5‰$). Thus, the initial magmatic $\delta^{18}O(WR)$ for most of the batholith was normal at ~8.5‰ and less variable than previously thought. However, small amounts of metasedimentary assimilation are "caught in the act" of elevating $\delta^{18}O$ by analysis of igneous garnets crystallized later and coexisting with zircons (Fig. 8). Presumably, this approach for studying contamination will also reveal differences in trace elements and other geochemical systems.

***Great Basin.*** The Great Basin of Nevada and Utah (Fig. 34) has undergone pulses of compressional and extensional tectonics, and extensive granitic plutonism. Numerous studies of this area have employed radiogenic and stable isotopes to document major crustal boundaries including the edge of the Precambrian craton (Fig. 37). Figure 37A shows Pb isotope zones (Zartman 1974), and isopleths for $^{87}Sr/^{86}Sr_i = 0.706$, $^{87}Sr/^{86}Sr_i = 0.708$ (Kistler and Peterman 1973), and $\varepsilon_{Nd} = -7$ (Farmer and DePaolo 1983). Figure 37B shows the three sub-divisions of Solomon and Taylor (1989) based on analysis of $\delta^{18}O$ in whole rock powders. The radiogenic data mark the cratonic margin at the 0.708 line with continental sediments grading into volcanic arc and ocean floor lithologies farther west. However, no oxygen isotope discontinuities have been found that coincide with the major radiogenic isotope boundaries.

King et al. (2003b) analyzed $\delta^{18}O$ in zircon, titanite, and/or quartz in 275 plutonic rocks from the Great Basin. The faithfulness with which each mineral has preserved magmatic $\delta^{18}O$ decreases: zircon > titanite > quartz. The data from these minerals gives sharper and more accurate trends in magmatic $\delta^{18}O$ than whole rock compositions, which are easily overprinted by alteration of feldspar. Granites of all ages show a difference in $\delta^{18}O(Zc)$ across the 0.706 line, but this is most pronounced in Cretaceous granites for which there is little overlap in data (Fig. 38). Thus oxygen isotope discontinuities do correlate with radiogenic isotope boundaries if the effects of postmagmatic exchange are properly recognized.

***Sierra Nevada.*** The oxygen isotope geochemistry of magmas of the Sierra Nevada batholith has long been a puzzle. Dramatic trends are seen in the Peninsular Ranges batholith farther south (Fig. 34) with $\delta^{18}O(WR)$ increasing west to east (Taylor 1986), and correlations of $\delta^{18}O$ to tectonic setting are described in the Idaho batholith and among plutons of the Great Basin. However, the variability of $\delta^{18}O$ within the Sierra Nevada has seemed erratic and uncorrelated with geologic features (Masi et al. 1981, Ross 1983). Complex relations in the Sierras could result from a number of factors including: post magmatic alteration, different contributions of continental vs. oceanic basement, the presence of granites from an earlier Jurassic arc, and variable amounts of uplift of a

vertically variable $\delta^{18}O$ profile in the Sierran Arc.

Lackey et al. (2001) report $\delta^{18}O$ of zircons from samples that were previously analyzed for U-Pb age, initial Pb isotope ratios, and $^{87}Sr/^{86}Sr_i$ (Chen and Moore 1982, Chen and Tilton 1991). At the latitude of Sequoia National Park (36.5° N), $\delta^{18}O(Zc)$ increases from 5.8 to 8.0, west to east in the western 40 km of the batholith and correlates with Sr and Pb isotopes. The positive correlation of $^{87}Sr/^{86}Sr_i$ and $\delta^{18}O$ is similar to the Peninsular Ranges batholith. The 0.706 line runs approximately N-S and crosses this 40-km traverse midway. West of 0.706, granites are in the Weakly Contaminated zone and to the east they are in the Strongly Contaminated-Reduced zone of Ague and Brimhall (1988). These zones are distinct in $^{206}Pb/^{204}Pb$ as well as $\delta^{18}O$: 18.658-18.741 and 5.9-7.0‰ in the west vs. 18.929-19.254 and 6.8-7.4‰ in the east. These differences are consistent with contamination by high $\delta^{18}O$ Kings sequence metasediments to the east. Contamination of some magmas by high $\delta^{18}O$ material west of the 0.706 line is observed in the zircon data, but was previously unrecognized by radiogenic isotope studies.

The depths of crystallization for Sierran granites are inferred from Al-in-hornblende barometry to increase from generally 3-6 km in the central and northern parts of the batholith to 30 km in the Tehachapi Mountains in the south. Lackey et al. (2003) show that $\delta^{18}O(Zc)$ in the Tehachapi/Lake Isabella regions is significantly higher than in the rest of the batholith, 7.8±0.8‰ vs. 6.1±0.8‰ (Fig. 39) suggesting that magmas of the southern Sierras were contaminated by significant amounts of high $\delta^{18}O$ material not seen in exposed portions of the batholith elsewhere. Comparison of $^{87}Sr/^{86}Sr_i$ and $\varepsilon_{Nd}$ to $\delta^{18}O$ suggests that the high $\delta^{18}O$ material was hydrothermally altered ocean crust or volcanic arc sediments.

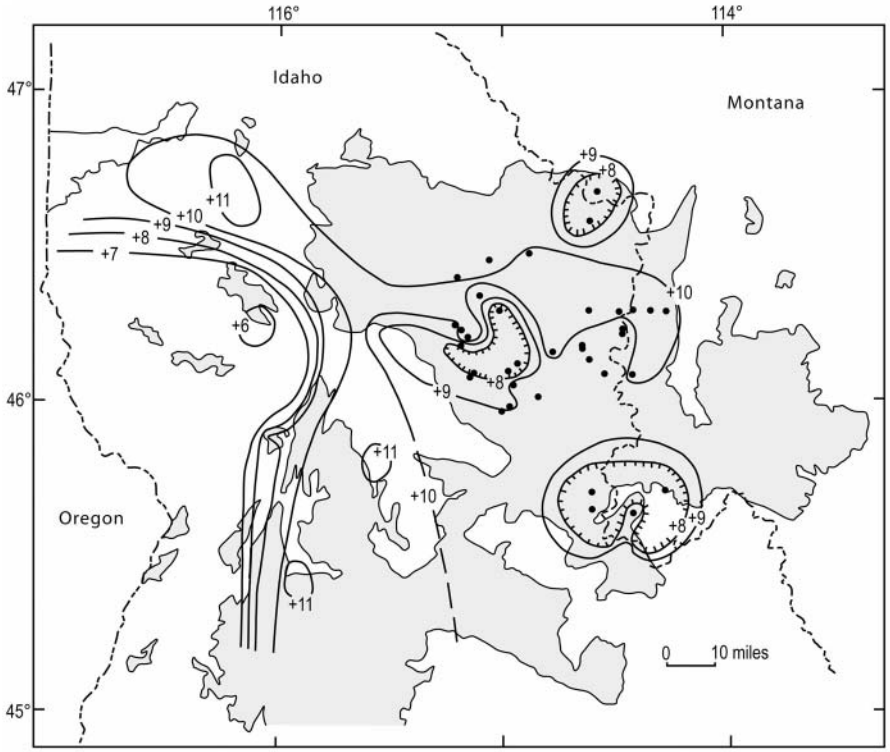


**Figure 36.** Contours of plutonic $\delta^{18}O(WR)$ in the Idaho Batholith and vicinity. Isopleths of $\delta^{18}O$ = 8-9‰ coincide with the $Sr_i$ = 0.706 line (Fig. 35). The hachured regions within the batholith mark areas of post-magmatic alteration of whole rock compositions by interaction with heated meteoric water (from Fleck and Criss 1985).

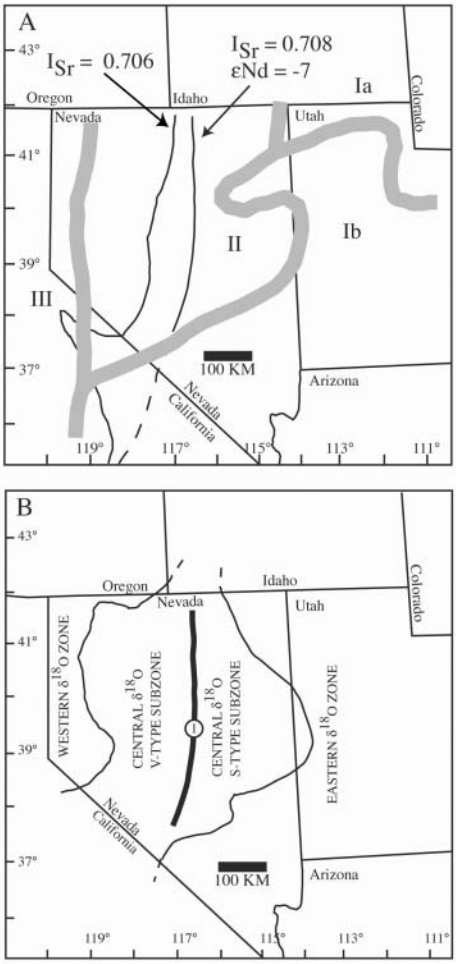


**Figure 37.** Isotopic discontinuities in plutonic rocks of the western United States. (A) $Sr_i$ = 0.706 and 0.708, and $\varepsilon_{Nd}$ = –7 lines, and Pb isotope zones Ia, Ib, II, and III. The region between the 0.706 and 0.708 lines is the transition between Precambrian continental crust to the east, and arc rocks to the west. (B) the western, central and eastern $\delta^{18}O$ zones of Solomon and Taylor (1989) based on analysis of whole rock powders. The heavy line marked 1 is $\varepsilon_{Nd}$ = –7. (from King et al. 2003b).

**A-type granites, northeastern China**

Phanerozoic granites represent 50-80% of mountainous areas in the Central Asian Orogenic Belt of northeastern China (Fig. 40). These rocks represent major pulses of I- and A-type plutonism in the Late Paleozoic to Late Mesozoic that are proposed to represent juvenile additions to crustal growth (Wu et al. 2000, 2002). Many granites have relatively low $^{87}Sr/^{86}Sr_i$ of 0.705, positive $\varepsilon_{Nd}$ of 0 to +4, model $T_{DM}$ ages of 1.3 to 0.5 Ga suggesting a dominantly primitive source; some granites that intrude Precambrian country rocks have negative $\varepsilon_{Nd}$ and older $T_{DM}$ suggesting involvement of Precambrian basement. These plutons are proposed to have formed in a post- or anorogenic tectonic setting. The primitive source rocks have been proposed to be either: (1) underplated basaltic melts near the base of the crust or (2) subducted ocean crust within the mantle (Wu et al. 2000, 2002; Wei et al. 2002). This distinction is important for models of crustal growth.

The Nianzishan granite is located in northeastern China (Fig. 40) and is representative of late Cretaceous A-type granites that most likely related to extension and rifting along the continental margin of eastern China in the southeastern part of the Central Asian Orogenic Belt (Wang et al. 1995, Wu et al. 2002, Wei et al. 2002, 2003). Minerals include quartz, K-feldspar, Na-amphibole, pyroxene, magnetite and zircon. Positive values of $\varepsilon_{Nd}$ (+4.27 to +0.86) and relatively young Nd model ages of 846-569 Ma suggest a significant mantle component to magmas. Miarolitic cavities and low $\delta^{18}O$(WR) (4.3 to –1.5‰) suggest intrusion at shallow levels in the crust and hydrothermal alteration by heated meteoric waters (see, Sheppard 1986). More recently, analysis of $\delta^{18}O$(Zc) reveals values of 4.2 to 3.1, showing that magmas were low in $\delta^{18}O$ before crystallization and documenting previously unrecognized remelting of hydrothermally altered oceanic or continental crust (Wei et al. 2002, 2003).

**Cenozoic granitoids of the Antarctic Peninsula**

Bolz (2001) reports ion microprobe analyses of zircons from two granites and a diorite (120-80 Ma) of the Rymill Coast and Eternity Range on the Antarctic Peninsula. Values of $\delta^{18}O$ for plagioclase, hornblende and biotite range from –4.6 to 0.7‰ due to high temperature exchange with meteoric water. Analyses of quartz range from 3.9 to 5.3‰ also due to alteration. In contrast to these variable and low values, the values of $\delta^{18}O$(Zc) for the three plutons are constant and mantle-like at 5.1-5.5‰. Individual spot analyses show no variability from zircon to zircon within the ±1‰ (1sd) precision of the SIMS data.

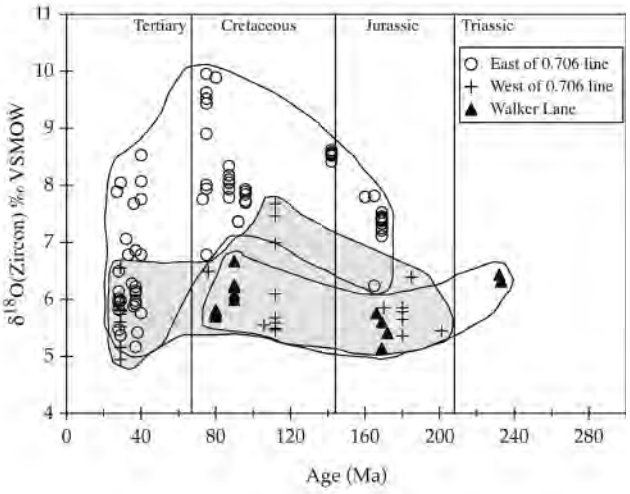


**Figure 38.** Values of $\delta^{18}O$(Zc) vs. age of pluton for granitic rocks of the Great Basin, western United States. Values east of the 0.706 line (open circles) are higher than to the west (crosses and triangles). East of the 0.706 line, $\delta^{18}O$ increases from Jurassic through Cretaceous. After 70 Ma and a break in plutonism, $\delta^{18}O$ returns to lower values. These trends are not seen in whole rock data (from King et al. 2003b).

### Fe-oxide melt in syenitic xenoliths

Globules of Fe-Ti-oxide melt in mafic to felsic xenoliths within Tertiary alkali basalts of the Carpathians are proposed to form by liquid immiscibility (Hurai et al. 1998). High iron oxide melt globules are found encased in glass pockets and within rock forming plagioclase and zircon. The $\delta^{18}O$(Zc) values of 5.1-5.6‰ are the same as mafic minerals and calcic plagioclase (4.9-5.9‰) from gabbroic xenoliths supporting a common mantle source for the Fe-oxide melt containing xenoliths.

### Magmatic epidote-bearing granitoids

Epidote in granitic rocks has been studied in detail to distinguish magmatic epidote, which has importance for estimation of pressure, water activity and uplift rates, from hydrothermal epidote, which records later, post-magmatic history.

Keane and Morrison (1997) studied four textural varieties of epidote in quartz monzonite of the Triassic Mt. Lowe intrusion, San Gabriel Mts., California. Three of these varieties show textural evidence of being magmatic: coarse euhedral and anhedral grains, and intergrowths showing crystal faces against hornblende or biotite. Only epidote in cross-cutting veins is clearly post-magmatic. However, microanalysis of $\delta^{18}O$(epidote) shows that both euhedral and anhedral epidote can be partially altered or exchanged. The

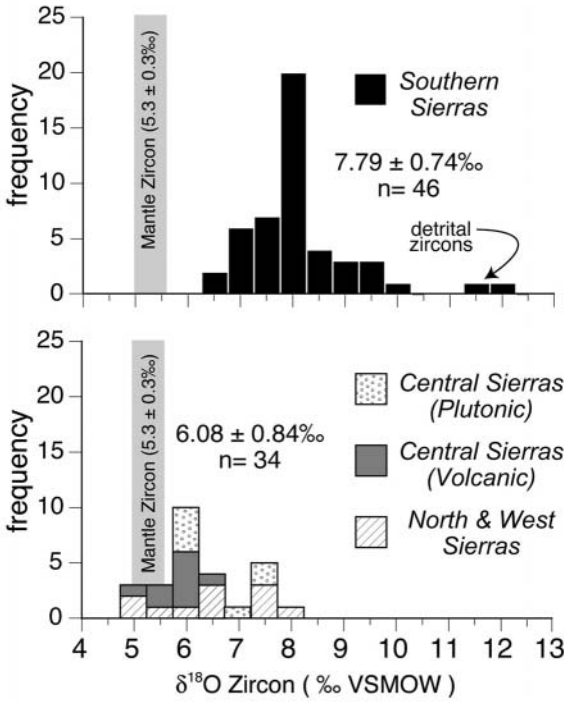


**Figure 39.** Oxygen isotope compositions of zircon from the Sierra Nevada batholith. Samples from the deeply exhumed (up to 30 km) southern portion of the batholith average over 1.5‰ higher $\delta^{18}O$ than the shallower 3-7 km rocks farther north. Granulite facies country rocks in the south are migmatitic suggesting that the deep portions of the batholith were contaminated by high $\delta^{18}O$ crust (from Lackey et al. 2003).

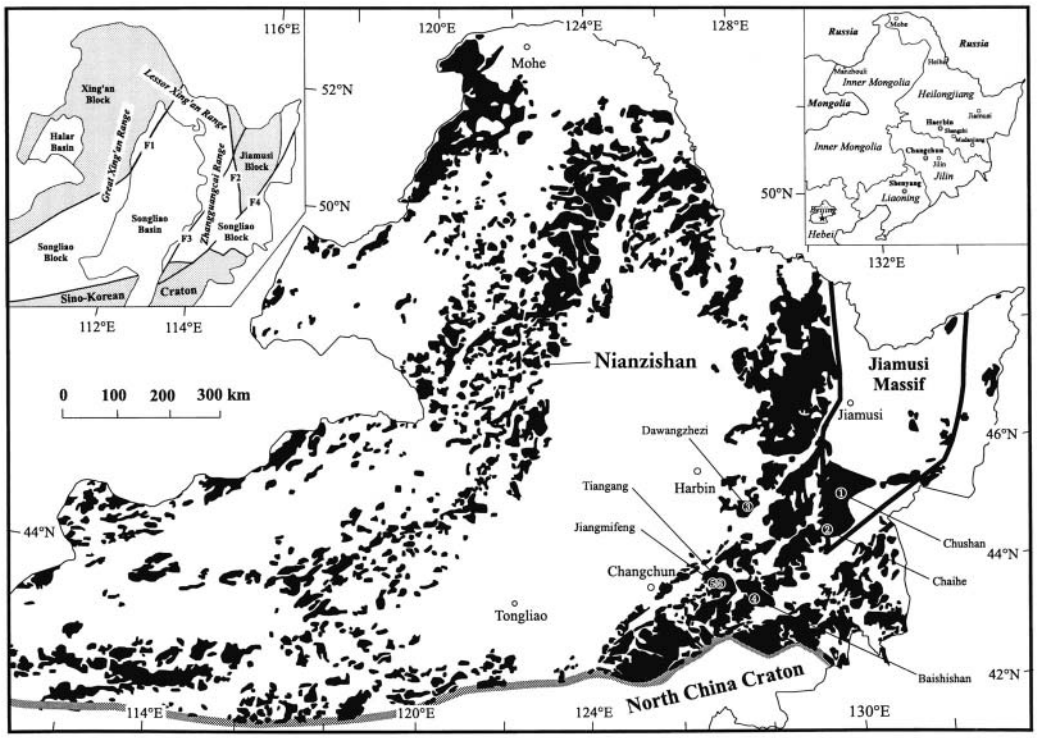


**Figure 40.** Phanerozoic granites of northeastern China occupy 50-80% of the exposed areas of mountains. F1, F2, F3, and F4 (inset) are the Nenjiang, Mudanjiang, Jiayi, and Dunmi Faults, respectively (from Wu et al. 2000).

euhedral grains are bimodal, $\delta^{18}O$ = 5.36±0.13‰ and 4.66±0.23‰. Analysis of magmatic zircons yields 5.70±0.15‰ suggesting that the values above 5‰ are magmatic and that lower values reflect subsolidus exchange. Thus, use of textural criteria alone can be misleading.

The Neoproterozoic Borborema province, northeastern Brazil contains a large volume of diverse granitic rocks recording two orogenic cycles: Cariris Velhos (1.1-0.95 Ga) and Brasiliano (0.73-0.52 Ga) (Fig. 41). Magmatic epidote is found in calc-alkalic, shoshonitic, and trondhjemitic granitoids in five tectonostratigraphic terranes of the province (Ferreira et al. 1998, Sial et al. 1999).

Ferreira et al. (2003) compared magmatic epidote, titanite, and zircon from two contrasting metaluminous granitoids that crystallized at different depths, Emas and Sao Rafael. Values of $\Delta^{18}O$(zircon-titanite) yield magmatic temperatures, but $\Delta^{18}O$ (quartz-magmatic epidote) and $\Delta^{18}O$(zircon-epidote) are self-consistent, and larger than predicted for magmatic temperatures. These fractionations suggest continuous, closed-system, sub-solidus exchange among all minerals except zircon and titanite. Values of $\delta^{18}O$(WR) were determined by analysis of $\delta^{18}O$(Zc) and calculation of $\delta^{18}O$(WR) based on the mineral mode.

Paradoxically, the Emas pluton has many I-type characteristics, but high $\delta^{18}O$(WR) = 11.6‰, while the Sao Rafael has Sr and Nd characteristics of S-type and low $\delta^{18}O$ = 7.9‰. Typically, the higher $\delta^{18}O$ values would be thought of as sediment derived. The reversal of values of $\delta^{18}O$(WR) thus indicates that systematics of oxygen isotopes are not coupled to radiogenic isotopes in these rocks. This can be explained if fluid-hosted processes such as hydrothermal exchange have altered the $\delta^{18}O$ of source rocks. If source rocks are magmatic and young at the time of melting, there may not be a radiogenic isotope contrast and the only signature of crustal recycling will be from stable isotopes. Several of the studies reviewed above support this conclusion and suggest that crustal recycling is more important than has generally been recognized.

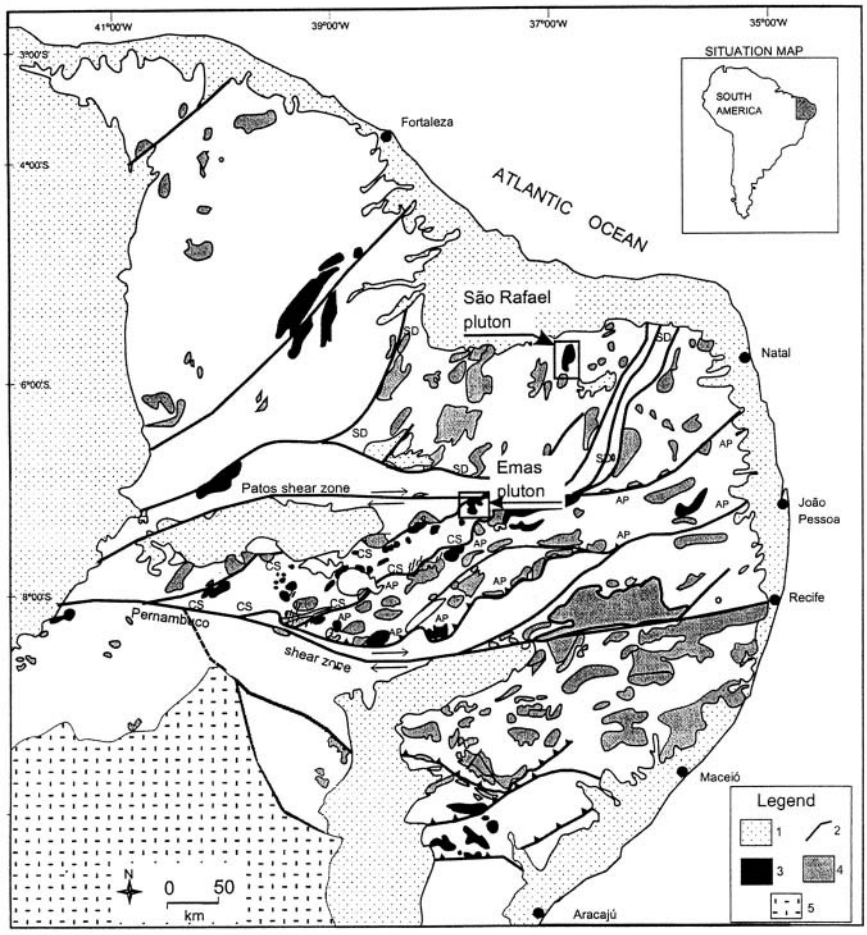


**Figure 41.** Granitoids of the Neoproterozoic Borborema province, Brazil. The Brasiliano-age Emas and Sao Rafael plutons are shown. 1 = Phanerozoic cover; 2 = major shear zones and terrane boundaries; 3 = magmatic epidote-bearing granitoids; 4 = other granitoids; 5 = Sao Francisco craton; SD = Serido terrane; CS = Cachoeirinha-Salgueiro terrane; AP = Alto Pajeu terrane (from Ferreira et al. 2003).

## ACKNOWLEDGMENTS

Pat Bickford, Ilya Bindeman, Aaron Cavosie, Cory Clechenko, Val Ferreira, John Hanchar, Liz King, Jade Star Lackey, William Peck, and Doug Rumble made perceptive comments on this paper. Mary Diman helped with drafting. NSF and DOE are thanked for supporting this research.

## REFERENCES

Ague JJ, Brimhall GH (1988) Regional variations in bulk chemistry, mineralogy, and compositions of mafic and accessory minerals in the batholiths of California. Geol Soc Am Bull 100:891-911

Ague JJ, Brimhall GH (1988) Magmatic arc asymmetry and distribution of anomalous plutonic belts in the batholiths of California: Effects of assimilation, crustal thickness, and depth of crystallization. Geol Soc Am Bull 100:912-927

Ashwal LD (1993) Anorthosites. Springer, Berlin, 422 p

Bacon CR, Adami LH, Lanphere MA (1989) Direct evidence for the origin of low-$^{18}O$ silicic magmas: quenched samples of a magma chamber's partially-fused granitoid walls, Crater Lake, Oregon. Earth Planet Sci Lett 96:199-208

Balan E, Neuville DR, Trocellier P, Fritsch E, Muller JP, Calas G (2001) Metamictization and chemical durability of

detrital zircon. Am Mineral 86:1025-1033
Beatty DW, Taylor HP Jr, Coad PR (1988) An oxygen isotope study of the Kidd Creek, Ontario, volcanogenic massive sulfide deposits:evidence for a high $^{18}O$ ore fluid. Econ Geol 83:1-17
Bibikova YV, Ustinov VI, Gracheva TV, Kiselevskiy MA, Shukolyukov YA (1982) Variations of isotope distribution in oxygen of accessory zircons. Doklady Akad. Nauk SSSR 264:698-700
Bindeman IN (2003) Crystal sizes in evolving silicic magma chambers. Geology 31 (in press)
Bindeman IN, Valley JW (2000a) Formation of low-$\delta^{18}O$ rhyolites after caldera collapse at Yellowstone, Wyoming, USA. Geology 28:719-722
Bindeman IN, Valley JW (2000b) Oxygen isotope study of accessory zircon, sphene and other minerals in carbonate cement of Trench 14, Yucca Mountain: No evidence for hydrothermal origin. Geol Soc Am Abstr Prog A-261
Bindeman IN, Valley JW (2001) Low $\delta^{18}O$ rhyolites from Yellowstone: Magmatic evolution based on analysis of zircons and individual phenocrysts. J Petrol 42:1491-1517
Bindeman IN, Valley JW (2002) Oxygen isotope study of the Long Valley magma system, California: Isotope thermometry and convection in large silicic magma bodies. Contrib Mineral Petrol 144:185-205
Bindeman IN, Valley JW (2003) Rapid generation of both high and low-$\delta^{18}O$, large volume silicic magmas at Timber Mountain/Oasis Valley caldera complex, Nevada. Geol Soc Am Bull 115 (in press)
Bindeman IN, Valley JW, Wooden JL, Persing HM (2001a) Post-caldera volcanism: *In situ* measurement of U-Pb age and oxygen isotope ratio in Pleistocene zircons from Yellowstone caldera. Earth Planet Sci Lett 189:197-206
Bolz V (2001) The oxygen isotope geochemistry of zircon as a petrographic tracer in high temperature contact metamorphic and granitic rocks. MS thesis, University of Edinburgh, 208 p
Cavosie AJ, Valley JW, Fournelle J, Wilde SA (2002) Implications for sources of Jack Hills metasediments: Detrital chromite. Geochim Cosmochim Acta 66:A125
Chacko T, Cole DR, Horita J (2001) Equilibrium oxygen, hydrogen and carbon isotope fractionation factors applicable to geologic systems. *In* Valley JW, Cole DR (eds) Stable Isotope Geochemistry. Rev Mineral Geochem 43:1-81
Chen JH, Moore JG (1982) Uranium-lead isotopic ages from the Sierra Nevada batholith, California. J Geophys Res B 87:4761-4784
Chen JH, Tilton GR (1991) Applications of lead and strontium isotopic relationships to the petrogenesis of granitoid rocks, central Sierra Nevada batholith, California. Geol Soc Am Bull 103:437-447
Chiarenzelli JR, McLelland JM (1993) Granulite facies metamorphism, palaeo-isotherms and disturbance of the U-Pb systematics of zircon in anorogenic plutonic rocks from the Adirondack Highlands. J Metamorph Geol 11:59-70
Christiansen RL (2000) The Quaternary and Pliocene Yellowstone Plateau volcanic field of Wyoming, Idaho, and Montana. U S Geol Surv Prof Paper 729-G, 145 p
Clayton RN, Kieffer SW (1991) Oxygen isotopic thermometer calibrations. *In* Taylor HP, O'Neil JR, Kaplan IR (eds) Stable Isotope Geochemistry. Geochem Soc Spec Pub 3:3-10
Clechenko CC, Valley JW, Hamilton MA, McLelland J, Bickford ME (2002) Direct U-Pb dating of the Marcy Anorthosite, Adirondacks, NY, USA. Goldschmidt Conf, Extended Abstr, Geochim Cosmochim Acta 66, Supplement 1:144
Cole DR, Chakraborty S (2001) Rates and mechanisms of isotopic exchange. *In* Valley JW, Cole DR (eds) Stable Isotope Geochemistry. Rev Mineral Geochem 43:83-223
Criss RE, Fleck RJ (1990) Oxygen isotope map of the giant metamorphic-hydrothermal system around the northern part of the Idaho batholith, U.S.A. Appl Geochem 5:641-655
Criss RE, Taylor HP (1983) An $^{18}O/^{16}O$ and D/H study of Tertiary hydrothermal systems in the southern half of the Idaho batholith. Geol Soc Am Bull 94:640-663
Dickin AP (1981) Isotope geochemistry of Tertiary igneous rocks from the Isle of Skye, N.W. Scotland. J Petrol 22:155-189
Dickin AP, Brown LR, Thompson RN, Halliday AN, Morrison MA (1984) Crustal contamination and the granite problem in the British Tertiary volcanic province. *In* Moorbath S, Thompson N, Oxburgh R (eds) The Relative Contributions of Mantle, Oceanic Crust and Continental Crust to Magma Genesis. Royal Soc London 310:755-780
Eiler JM, Valley JW (1994) Preservation of Pre-metamorphic Oxygen Isotope Ratios in Granitic Orthogneiss from the Adirondack Mts., N.Y. Geochim Cosmochim Acta 58:5525 5535
Eiler JM, Baumgartner LP, Valley JW (1992) Intercrystalline stable isotope diffusion: A fast grain boundary model. Contrib Mineral Petrol 112:543-557
Eiler JM, Valley JW, Baumgartner LP (1993) A new look at stable isotope thermometry. Geochim Cosmochim Acta 57:2571-2583
Eiler JM, Graham CM, Valley JW (1997) SIMS analysis of oxygen isotopes: Matrix effects in complex minerals and glasses. Chem Geol 13:221-244
Eiler JM, Farley KA, Valley JW, Hofmann AW, Stolper EM (1996) Oxygen isotope constraints on the sources of Hawaiian volcanism. Earth Planet Sci Lett 144:453-468
Eiler JM, Farley KA, Valley JW, Hauri E, Craig H, Hart SR, Stolper EM (1997) Oxygen isotope variations in Ocean Island Basalts. Geochim Cosmochim Acta 61:2281-2293

Elliot BA, Peck WH, Ramo O, Vaasjoki M, Valley JW (2001) Reconstruction of terrane boundaries in the Finnish Svecofennian: Oxygen isotopes from zircon. Geol Soc Am Abstr Progr 33:264

Farmer GL, DePaolo DJ (1983) Origin of Mesozoic and Tertiary granite in the western United States and implications for Pre-Mesozoic crustal structure: 1. Nd and Sr isotopic studies in the geocline of the northern Great Basin. J Geophys Res 88:3379-3401

Ferreira VP, Sial AN, Jardim de Sa EF (1998) Geochemical and isotopic signatures of Proterozoic granitoids in terranes of the Borborema structural province, northeastern Brazil. J South Am Earth Sci 11:439-455

Ferreira VP, Valley JW, Sial AN, Spicuzza MJ (2003) Oxygen isotope compositions and magmatic epidote from two contrasting metaluminous granitoids, NE Brazil. Contrib Mineral Petrol (in review)

Fleck RJ (1990) Neodymium, strontium, and trace-element evidence of crustal anatexis and magma mixing in the Idaho Batholith. *In* Anderson JL (ed) The Nature and Origin of Cordilleran Magmatism. Geol Soc Am Memoir 174:359-373

Fleck RJ, Criss RE (1985) Strontium and oxygen isotopic variations in Mesozoic and Tertiary plutons of central Idaho. Contrib Mineral Petrol 90:291-308

Fontan F, Monchous P, Autefage F (1980) Presence de zircons hafniferes dans des pegmatites granitiques des Pyrenees Ariegoises. Bull Soc franc Minéral Cristallogr 103:88-91

Forester RW, Taylor HP Jr (1977) $^{18}O/^{16}O$, D/ H, and $^{13}C/^{12}C$ studies of the Tertiary igneous complex of Skye, Scotland. Am J Sci 277:136-177

Fortier SM, Giletti BJ (1989) An empirical model for predicting diffusion coefficients in silicate minerals. Science 245:1481-1484

Fournelle JH, Bindeman I, Donovan JJ, Valley JW (2000) Quantitative EPMA Mapping of Minor and Trace Elements in Zircons from Yellowstone Tuffs and Lavas. EOS Trans Am Geoph Union S26-27

Geisler T, Pidgeon RT (2001) Significance of radiation damage on the integral SEM cathodoluminescence intensity of zircon: An experimental annealing study. N Jb Mineral Mh 10:433-445

Geisler T, Pidgeon RT, van Bronswijk W, Pleysier R (2001) Kinetics of thermal recovery and recrystallization of partially metamict zircon, a Raman spectroscopic study. Eur J Mineral 13:1163-1176

Gilbert B, Frazer BF, Naab F, Fournelle J, Valley JW, De Stasio G (2003) X-ray absorption spectroscopy of silicates for in situ, sub-micrometer mineral identification. Am Mineral (in press)

Gilliam CE, Valley J W (1997) Low $\delta^{18}O$ magma, Isle of Skye, Scotland: Evidence from zircons. Geochim Cosmochim Acta 61:4975-4981

Graham CM, Valley JW, Winter B L (1996) Ion microprobe analysis of $^{18}O/^{16}O$ in authigenic and detrital quartz in St. Peter sandstone, Michigan Basin and Wisconsin Arch, USA: Contrasting diagenetic histories. Geochim Cosmochim Acta 24:5101-5116

Hanchar JM, Miller CF (1993) Zircon zonation patterns as revealed by cathodoluminescence and backscattered electron images: Implications for interpretation of complex crustal histories. Chem Geol 110:1-13

Hanchar JM, Rudnick RL (1995) Revealing hidden structures: The application of cathodoluminescence and backscattered electron imaging to dating zircons from lower crustal xenoliths. Lithos 36:289-303

Hildreth W, Christiansen RL, O'Neil JR (1984) Catastrophic isotopic modification of rhyolitic magma at times of caldera subsidence, Yellowstone Plateau volcanic field. *In* Calderas and Associate Igneous Rocks. Am Geophys Union 89:8339-8369

Hoffbauer R, Hoernes S, Fiorentini E (1994) Oxygen isotope thermometry based on a refined increment method and its applications to granulite-grade rocks from Sri Lanka. Precambrian Res 66:199-220

Hoffman PF, Kaufman AJ, Halverson GP, Schrag DP (1998) A Neoproterozoic snowball Earth. Science 281:1342-1346

Hurai V, Simon K, Wiechert U, Hoefs J, Konecny P, Huraiova M, Pironon J, Lipka J (1998) Immiscible separation of metalliferous Fe/ Ti-oxide melts from fractionating alkali basalt: P-T-$f_{O2}$ conditions and two-liquid elemental partitioning. Contrib Mineral Petrol 133:12-29

Huston DL, Taylor BE, Bleeker W, Watanabe DH (1996) Productivity of volcanic-hosted massive sulfide districts: new constraints from the $\delta^{18}O$ of quartz phenocrysts in cogenetic felsic rocks. Geology 24:459-462

Kamo SL, Davis DW (1994) Reassessment of Archean crustal development in the Barberton Mountainland, South Africa, based on U-Pb dating. Tectonics 13:167-192

Keane SD, Morrison J (1997) Distinguishing magmatic from subsolidus epidote: laser probe oxygen isotope compositions. Contrib Mineral Petrol 126:265-274

Kennedy AK (2000) The search for new zircon standards for SIMS. *In* Woodhead JD, Hergt JM, Nobel WP (eds) Beyond 2000: New Frontiers in Isotope Geoscience. Lorne, 2000, Abstr Proc, p 109-111

Kieffer SW (1982) Thermodynamics and lattice vibrations of minerals: 5, Applications to phase equilibria, isotopic fractionation, and high-pressure thermodynamic properties. Rev Geophys Space Phys 20:827-849

King EM (1997) Oxygen isotope study of igneous rocks from the Superior Province, Canada. MS thesis, University of Wisconsin, Madison, 84 p

King EM (2001) Oxygen isotope study of magmatic source and alteration of granitic rocks in the Western United States and the Superior Province, Canada. PhD dissertation, University of Wisconsin, Madison, 224 p

King EM, Valley JW (2001) Source, magmatic contamination, and alteration of the Idaho batholith. Contrib Mineral

Petrol 142:72-88
King EM, Barrie CT, Valley JW (1997) Hydrothermal alteration of oxygen isotope ratios in quartz phenocrysts, Kidd Creek mine, Ontario: Magmatic values are preserved in zircon. Geology 25:1079-1082
King EM, Barrie CT, Valley JW (1998a) Hydrothermal alteration of oxygen isotope ratios in quartz phenocrysts, Kidd Creek Mine, Ontario: Magmatic values preserved in zircons: Reply. Geology 26:764
King EM, Valley JW, Davis DW, Edwards GR (1998b) Oxygen isotope ratios of Archean plutonic zircons from granite-greenstone belts of the Superior Province: Indicator of magmatic source. Precambrian Res 92:47-67
King EM, Valley JW, Davis DW (2000) Oxygen isotope evolution of volcanic rocks at the Sturgeon Lake volcanic complex, Ontario. Can J Earth Sci 37:39-50
King EM, Valley JW, Davis DW, Kowalis BJ (2001) Empirical determination of oxygen isotope fractionation factors for titanite with respect to zircon and quartz. Geochim Cosmochim Acta 65:3165-3175
King EM, Beard BL, Johnson CM, Valley JW (2003a) Oxygen and strontium isotopic evidence for assimilation and fractional crystallization in the Idaho batholith. Geol Soc Am Bull (in review)
King EM, Valley JW, Stockli DF, Wright JE (2003b) Oxygen isotope trends of granitic magmatism in the Great Basin. (in review)
Kinny PD, Compston W, Bristow JW, Williams IS (1989) Archaean mantle xenocrysts in a Permian kimberlite: Two generations of kimberlitic zircon in Jwaneng DK2, southern Botswana. Geol Soc Australia 14:833-842
Kistler RW, Peterman ZE (1973) Variations in Sr, Rb, K, Na, and initial $^{87}Sr/^{86}Sr$ in Mesozoic granitic rocks and intruded wall rocks in central California. Geol Soc Am Bull 84:3489-3512
Kohn MJ (1999) Why most "dry" rocks should cool "wet." Am Mineral 84:570-580
Kohn MJ, Valley JW (1998) Effects of cation substitutions in garnet and pyroxene on equilibrium oxygen isotope fractionations. J Metamorph Geol 16:625-639
Kresten P, Fels P, Berggren G (1975) Kimberlitic zircons: A possible aid on prospecting for kimberlites. Mineralium Deposita 10:47-56
Krogh TE, Davis GL (1975) Alteration in zircons and differential dissolution of altered and metamict zircon. Ann Rept Geophys Lab Carneg Inst Wash 74:619-622
Krogh TE (1982a) Improved accuracy of U-Pb zircon ages by the creation of more concordant systems using an air abrasion technique. Geochim Cosmochim Acta 46:637-649
Krogh TE (1982b) Improved accuracy of U-Pb zircon dating by selection of more concordant fractions using a high gradient magnetic separation technique. Geochim Cosmochim Acta 46:631-635
Krylov DP, Zagnitko VN, Hoernes S, Lugovaja IP, Hoffbauer R (2002) Oxygen isotope fractionation between zircon and water: Experimental determination and comparison with quartz-zircon calibrations. Eur J Mineral 14:849-853
Lackey JS, Valley JW, Saleeby JB (2003) Evidence from zircon for high $\delta^{18}O$ contamination of magmas in the deep Sierra Nevada Batholith, California. Geology (in review)
Lackey JS, Hinke HJ, Valley JW (2002) Tracking contamination in felsic magma chambers with $\delta^{18}O$ of magmatic garnet and zircon. Goldschmidt Conf, Extended Abstr, Geochim Cosmochim Acta 66, Supplement 1:428
Lackey JS, Valley JW, Chen JH (2001) Correlated O-Sr-Pb isotope ratios in the West-Central Sierra Nevada Batholith, California. Geol Soc Am Abstr Progr 33:295
Larson PB, Geist DJ (1995) On the origin of low-$^{18}O$ magmas: Evidence from the Casto pluton, Idaho. Geology 23:909-912
Lipman PW, Friedman I (1975) Interaction of meteoric water with magma: an oxygen-isotope study of ash-flow sheets from southern Nevada. Geol Soc Am Bull 86:695-702
Masi U, O'Neil JR, Kistler RW (1981) Stable isotope systematics in Mesozoic granites of central and northern California and southwestern Oregon. Contrib Mineral Petrol 76:116-126
Mattey D, Lowry D, Macpherson C (1994) Oxygen Isotope Composition of Mantle Peridotite. Earth Planet Sci Lett 128:231-241
McKeegan KD, Leshin LA (2001) Stable isotope variations in extraterrestrial materials. *In* Valley JW, Cole DR (eds) Stable Isotope Geochemistry. Rev Mineral Geochem 43:279-318
McLelland J, Daly JS, McLelland JM (1996) The Grenville orogenic cycle (ca. 1350-1000 Ma): An Adirondack perspective. Tectonophysics 265:1-28
Mojzsis SJ, Harrison TM, Pidgeon RT (2001) Oxygen-isotope evidence from ancient zircons for liquid water at the Earth's surface 4,300 Myr ago. Nature 409:178-181
Monani S, Valley JW (2001) Oxygen isotope ratio of zircon: magma genesis of low $\delta^{18}O$ granites from the British Tertiary Igneous Province, western Scotland. Earth Planet Sci Lett 184:377-392
Morrison J, Valley JW (1988) Contamination of the Marcy anorthosite massif, Adirondack Mountains, NY: Petrologic and isotopic evidence. Contrib Mineral Petrol 98:97-108
Muehlenbachs K, Kushiro I (1974) Measurements of oxygen diffusion in silicates. EOS Trans Am Geophys Union 56:459
Nasdala L, Wenzel M, Vavra G, Irmer G, Wenzel T, Kober B (2001) Metamictization of natural zircon: accumulation versus thermal annealing of radioactivity-induced damage. Contrib Mineral Petrol 141:125-144

O'Connor YL, Morrison J (1999) Oxygen isotope constraints on the petrogenesis of the Sybille Intrusion of the Proterozoic Laramie anorthosite complex. Contrib Mineral Petrol 136:81-91

Peck WH (2000) Oxygen Isotope Studies of Grenville Metamorphism and Magmatism. PhD dissertation, University of Wisconsin-Madison, 320 p

Peck WH, Valley JW (2000) Large crustal input to high $\delta^{18}O$ anorthosite massifs of the southern Grenville Province: new evidence from the Morin Complex, Quebec. Contrib Mineral Petrol 139:402-417

Peck WH, King EM, Valley JW (2000) Oxygen isotope perspective on Precambrian crustal growth and maturation. Geology 28:363-366

Peck WH, Valley JW, Graham CM (2003a) Slow oxygen diffusion rates in igneous zircons from metamorphic rocks. Am Mineral (in press)

Peck WH, Valley JW, Corriveau L, Davidson A, McLelland J, Farber D (2003b) Mapping terrane boundaries in the deep crust of the Grenville Province using oxygen isotope ratios of zircon from anorthosite-suite granitoids. *In* Proterozoic Evolution of the Grenville Orogen in North America. Geol Soc Am Memoir (in press)

Peck WH, Valley JW, Wilde SA, Graham CM (2001) Oxygen isotope ratios and rare earth elements in 3.3 to 4.4 Ga zircons: Ion microprobe evidence for high $\delta^{18}O$ continental crust and oceans in the Early Archean. Geochim Cosmochim Acta 65:4215-4229

Reischmann T (1995) Precise U/ Pb age determination with baddeleyite ($ZrO_2$), a case study from the Phalaborwa igneous complex, South Africa. S African J Geol 98:1-4

Richter R, Hoernes S (1988) The application of the increment method in comparison with experimentally derived and calculated O-isotope fractionations. Chemie Erde 48:1-18

Ross DC (1983) Generalized geologic map of the southern Sierra Nevada, California, showing the location of basement samples for which whole rock $\delta^{18}O$ has been determined. U S Geol Survey Open-File Report 83-0904, 1 sheet, 1:250,000

Rudashevsky NS, Burakov BE, Lupal SD, Thalhammer OAR, Saini-Eidukat B (1995) Liberation of accessory minerals from various rock types by electric-pulse disintegration-method and application. Trans Min Metall 104:C25-C28

Rumble D, Giorgis D, Ireland T, Zhang Z, Xu H, Yui TF, Yang J, Xu Z, Liou JG (2002) Low $\delta^{18}O$ zircons, U-Pb dating, and the age of the Qinglongshan oxygen and hydrogen isotope anomaly near Donghai in Jiangsu Province, China. Geochim Cosmochim Acta 66:2299-2306

Saint-Eidukat B, Weiblen PW (1996) A new method of fossil preparation, using high-voltage electric pulses. Curator 39:139-144

Sessions AL, Brady JB, Chamberlain CP (1996) Experimental calibration of an oxygen isotope fractionation factor for zircon. Geol Soc Am Abstr Progr 28:213

Sessions AL, Brady JB, Chamberlain CP, Rumble D (2003) Experimental measurement of oxygen isotope fractionation between calcite and zircon. Am Mineral (in review)

Sheppard SMF (1986) Igneous rocks: III Isotopic case studies of magmatism in Africa, Eurasia and oceanic islands. Rev Mineral 16:319-371

Shieh YN (1985) High-$^{18}O$ granitic plutons from the Frontenac Axis, Grenville Province of Ontario, Canada. Geochim Cosmochim Acta 49:117-123

Shirey SB, Hanson GN (1984) Mantle-derived Archaean monzodiorites and trachyandesites. Nature 310:222-224

Sial AN, Toselli AJ, Saavedra A, Parada MA, Ferreira VP (1999) Emplacement, petrological and magnetic susceptibility characteristics of diverse magmatic epidote-bearing granitoid rocks in Brazil, Argentina and Chile. Lithos 46:367-392

Silver LT (1963) The use of co-genetic uranium-lead isotope systems in zircons in geochronology. *In* Radioactive Dating. Intl Atomic Energy Agency, Symp Proc, Athens, p 279-287

Smyth JR (1989) Electrostatic characterization of oxygen sites in minerals. Geochim Cosmochim Acta 53:1101-1110

Solomon GC, Taylor HP (1989) Isotopic evidence for the origin of Mesozoic and Cenozoic granitic plutons in the northern Great Basin. Geology 17:591-594

Speer JA (1982) Zircon. Rev Mineral 5:67-112

Stern RA, Hanson GN (1991) Archean high-Mg granodiorite: A derivative of light rare earth element-enriched monzodiorite of mantle origin. J Petrol 32:201-238

Stern RA, Hanson GN, Shirey SB (1989) Petrogenesis of mantle-derived, LILE-enriched Archean monzodiorites and trachyandesites (sanukitoids) in southwestern Superior Province. Can J Earth Sci 26:1688-1712

Taylor BE, Huston DL (1998) Hydrothermal alteration of oxygen isotope ratios in quartz phenocrysts, Kidd Creek Mine, Ontario: Magmatic values preserved in zircons: comment. Geology 26:763-764

Taylor BE, Huston DL (1999) Regional $\delta^{18}O$ zoning and hydrogen isotope studies in the Kidd Creek volcanic complex, Timmins, Ontario. *In* Harrington MD, Barrie CT (eds) The giant Kidd Creek volcanogenic massive sulfide deposit, western Abitibi Subprovince, Canada. Econ Geol 10:351-378

Taylor HP (1969) Oxygen isotope studies of anorthosites, with particular reference to the origin of bodies in the Adirondack mountains, New York. *In* Isachsen Y (ed) Origin of Anorthosite and Related Rocks. New York State

Museum 18:111-134
Taylor HP (1986) Igneous rocks: II. Isotopic case studies of circumpacific magmatism. Rev Mineral 16:273-317
Taylor HP, Sheppard SMF (1986) Igneous rocks I. Processes of isotopic fractionation and isotope systematics. Rev Mineral 16:227-271
Upton BGJ, Hinton RW, Aspen P, Finch A, Valley JW (1999) Megacrysts and Associated Xenoliths: Evidence for Migration of Geochemically Enriched Melts in the Upper Mantle beneath Scotland. J Petrol 40:935-956
Valley JW, O'Neil JR (1984) Fluid Heterogeneity during Granulite Facies Metamorphism in the Adirondacks: Stable Isotope Evidence. Contrib Mineral Petrol 85:158-173
Valley JW, Graham CM (1991) Ion microprobe analysis of oxygen isotope ratios in metamorphic magnetite-diffusion reequilibration and implications for thermal history. Contrib Mineral Petrol 109:38-52
Valley JW, Graham CM (1993) Cryptic grain-scale heterogeneity of oxygen isotope ratios in metamorphic magnetite. Science 259:1729-1733
Valley JW, Graham CM (1996) Ion microprobe analysis of oxygen isotope ratios in quartz from Skye granite: healed micro-cracks, fluid flow, and hydro-thermal exchange. Contrib Mineral Petrol 124: 225-234
Valley JW, Taylor HP, O'Neil JR (eds) (1986) Stable Isotopes in High Temperature Geological Processes. Reviews in Mineralogy, Vol. 16, 570 p
Valley JW, Chiarenzelli J, McLelland JM (1994) Oxygen Isotope Geochemistry of Zircon. Earth Planet Sci Lett 126:187-206
Valley JW, Bindeman IN, Peck WH (2003) Empirical calibration of oxygen isotope fractionation in zircon. Geochim Cosmochim Acta (in press)
Valley JW, Kinny PD, Schulze DJ, Spicuzza MJ (1998b) Zircon Megacrysts from Kimberlite: Oxygen isotope heterogeneity among mantle melts. Contrib Mineral Petrol 133: 1-11
Valley JW, Peck WH, King EM, Wilde SA (2002) A cool early Earth. Geology 30:351-354
Valley JW, Graham CM, Harte B, Kinny P, Eiler J M (1998a) Ion microprobe analysis of oxygen, carbon, and hydrogen isotope ratios. Rev Econ Geol 7:73-98
Valley JW, Kitchen NE, Kohn MJ, Niendorf CR, Spicuzza MJ (1995) UWG-2, A garnet standard for oxygen isotope ratio: strategies for high precision and accuracy with laser heating. Geochim Cosmochim Acta 59:5223-5231
Wang DZ, Zhao GT, Qiu JS (1995) The tectonic constraint on the late Mesozoic A-type granitoids in eastern China. Geological J China Univ 1:13-21
Wasteneys H, McLelland J, Lumbers S (1999) Precise zircon geochronology in the Adirondack lowlands and implications for revising plate-tectonic models of the Central Metasedimentary belt and Adirondack Mountains, Grenville Province. Can J Earth Sci 36:967-984
Watson EB (1996) Dissolution, growth and survival of zircons during crustal fusion: kinetic principles, geological models and implications for isotopic inheritance. Trans R Soc Edinburgh 87:43-56
Watson EB, Cherniak DJ (1997) Oxygen diffusion in zircon. Earth Planet Sci Lett 148:527-544
Wei CS, Zheng YF, Zhao ZF, Valley JW (2002) Oxygen and neodymium isotope evidence for recycling of juvenile crust in northeast China. Geology 30:375-378
Wei CS, Valley JW, Zheng YF, Zhao ZF, Spicuzza MJ (2003) origin of low $\delta^{18}O$ magma: Zircon evidence of A-type granites in eastern China. (in review)
Wiechert U, Fiebig J, Przybilla R, Xiao Y, Hoefs J (2002) Excimer laser isotope-ratio-monitoring mass spectrometry for *in situ* oxygen isotope analysis. Chem Geol 182:179-194
Wiedenbeck M, Allé P, Corfu F, Griffin WL, Meier M, Oberli F, Von Quadt A, Roddick JC, Spiegel W (1995) Three natural zircon standards for U-Th-Pb, Lu-Hf, trace element and REE analyses. Geostandards Newslett 19:1-23
Wilde SA, Valley JW, Peck WH, Graham CM (2001) Evidence from detrital zircons for the Existence of continental crust and oceans on the Earth 4.4 Gyr ago. Nature 409:175-178
Wilson CJN, Hildreth W (1997) The Bishop Tuff: New insights from eruptive stratigraphy. J Geol 105:407-439
Wopenka B, Jolliff BL, Zinner E, Kremser DT (1996) Trace element zoning and incipient metamictization in a lunar zircon: application of three microprobe techniques. Am Mineral 81:902-912
Wu FY, Jahn BM, Wilde SA, Sun DY (2000) Phanerozoic continental growth: Sr-Nd isotopic evidence from the granites of northeastern China. Tectonophysics 328:89-113
Wu FY, Sun DY, Li H, Jahn BM, Wilde S (2002) A-type granites in northeastern China: Age and geochemical constraints on their petrogenesis. Chem Geol 187:143-173
Zartman RE (1974) Lead isotopic provinces in the Cordillera of western United States and their geologic significance. Econ Geol 69:792-805
Zheng YF (1993) Calculation of oxygen isotope fractionation in anhydrous silicate minerals. Earth Planet Sci Lett 120:247-263
Zheng YF, Fu B (1998) Estimation of oxygen diffusivity from anion porosity in minerals. Geochem J 32:71-89
Zheng YF, Gong B, Chen F-K (2003) Evidence from magmatic zircons for Neoproterozoic meteoric-hydrothermal alteration and snowball Earth event. (unpublished manuscript)

# Radiation Effects in Zircon

**Rodney C. Ewing**

*Department of Nuclear Engineering & Radiological Sciences*
*Department of Materials Science & Engineering*
*Department of Geological Sciences*
*University of Michigan*
*Ann Arbor, Michigan 48109*

**Alkiviathes Meldrum**

*Department of Physics*
*The University of Alberta*
*Edmonton, Alberta*
*Canada T6G 2J1*

**LuMin Wang**

*Department of Nuclear Engineering & Radiological Sciences*
*University of Michigan*
*Ann Arbor, Michigan 48109*

**William J. Weber and L. René Corrales**

*Pacific Northwest National Laboratory*
*P.O. Box 999*
*Richland, Washington 99352*

## INTRODUCTION

The widespread distribution of zircon in the continental crust, its tendency to concentrate trace elements, particularly lanthanides and actinides, its use in age-dating, and its resistance to chemical and physical degradation have made zircon the most important accessory mineral in geologic studies. Because zircon is highly refractory, it also has important industrial applications, including its use as a lining material in high-temperature furnaces. However, during the past decade, zircon has also been proposed for advanced technology applications, such as a durable material for the immobilization of plutonium (Ewing et al. 1995) or, when modified by ion-beam irradiation, as an optic waveguide material (Babsail et al. 1991). In all of these applications, the change in properties as a function of increasing radiation dose is crucial (see for example, Lumpkin 2001). In this chapter, we summarize the state-of-knowledge on the radiation damage accumulation process in zircon.

Although the concentrations of uranium and thorium are generally low (typically less than 5,000 ppm) in natural zircon, some zircon crystals are of great age (the oldest dated zircon grains are >4 Ga) and, thus, have calculated doses of $>10^{19}$ α-decay events/g, well beyond the dose required for the radiation-induced transformation to the aperiodic, metamict state. In an α-decay event, the α-particle dissipates most of its energy (4.0 to 6.0 MeV for actinides) by ionization processes over a range of 10 to 20 μm, but undergoes enough elastic collisions along its path to produce approximately one hundred isolated atomic displacements. The largest number of displacements occurs near the end of the α-particle trajectory. The more massive, but lower energy, α-recoil (70 keV $^{234}$Th-recoil from decay of $^{238}$U) dissipates nearly all of its energy in elastic collisions over only 30 to 40 nm, transferring enough kinetic energy to cause ~1,000 atomic displacements

1529-6466/03/0053-0014$05.00

according to calculations (Weber 1993). This creates a "cascade" of atomic collisions in which the total energy can be as much as 1 eV/atom, and whose structure and evolution can only be modeled by computer simulations. The cascade duration is extremely short ($<10^{-12}$ s), after which displacements by elastic interactions cease and the cascade gradually loses energy as it cools to ambient temperature, typically "quenching" in nanoseconds. During this cooling phase, relaxation and diffusion reduce the number of displaced atoms in the cascade, and the final damage state consists of a small low-density core surrounded by a halo of interstitials (Slater 1951, Brinkman 1954, Trachenko et al. 2002, 2003). A single α-decay event generates approximately 700 to 2,000 "permanently" displaced atoms, significantly more than the 0.1 displacements generated per β-decay event (Weber 1993, Weber et al. 1998). In the decay chain of $^{238}$U, there are eight α-decay events; $^{232}$Th has six. Because of the large number of atomic displacements during an α-decay event, the accumulation and overlap of the individual cascades, as well as the presence of still crystalline but highly-strained domains, has a profound effect on the structure and properties of the damaged solid. In the case of zircon, there is a dramatic decrease in density (17%), a decrease in birefringence until isotropic, a decrease in the elastic moduli (69%), a decrease in hardness (40%), an increase in fracture toughness (Chakoumakos et al. 1987, Chakoumakos et al. 1991) and an increase in dissolution rate of one to two orders of magnitude (Ewing et al. 1982). Over extended time, the final damage microstructure is both time and temperature dependent because of annealing and recrystallization of damaged and strained domains (Weber et al. 1997).

Zircon figured prominently in the earliest studies of the metamict state and radiation damage (see Ewing 1994 for a summary of this early history). Stackelberg and Rottenbach (1940) had noted changes in density, refractive indices and birefringence with increasing α-decay dose and even tried to test this hypothesis by irradiating a thin slab of zircon with α-particles, perhaps the first ion-beam modification experiment. Still, metamict minerals remained a mineralogical oddity for several decades, until the systematic review of radiation-induced property changes by Pabst (1952) in his Presidential Address to the Mineralogical Society of America. Early studies of the helium method for age determination (Hurley and Fairbairn 1952) led to the idea that radiation-damage accumulation could be used for age-dating minerals. Hurley and Fairbairn (1953) completed the first systematic study of a suite of increasingly damaged zircon crystals and quantified the amount of damage based on X-ray diffraction data. This paper is remarkable, as it relates their results for zircon to the new field of radiation damage in reactor materials and draws heavily on what was known at that time about the physics of the radiation damage process. Although their interpretation was limited by a lack of experimental data (e.g., they estimated that 5,000 atoms were permanently displaced by each α-decay event), their approach was sound and laid the foundations of the work that continues today. Holland and Gottfried (1955) completed a classic study of the effects of α-decay events on density, optical properties and unit cell parameters as determined by X-ray diffraction. Their paper remained a standard reference for the effects of radiation on silicates, but further advances in knowledge had to await the development of more controlled irradiation experiments. Accelerated damage techniques, including doping with extremely short-lived actinides that transmuted by α-decay, such as $^{238}$Pu with a half-life of 87.7 years (Exarhos 1984, Weber 1991, Weber et al. 1994, Burakov et al. 2002, Burakov et al. in press), neutron irradiation (Crawford and Wittels 1956, Hayahshi et al. 1990) and ion beam irradiation (Cartz and Fournelle 1979, Wang and Ewing 1992a,b; Ewing et al. 2000) were used to great advantage in simulating the α-decay event damage in natural zircon. We now have experimental data from irradiation experiments with dose rates that vary by more than fifteen orders of magnitude (displaced atoms/s) over a range of temperature from –260 to 800°C (Meldrum et al. 1999a). Based on the studies summarized in this chapter, one can safely state that there is no other mineral or complex ceramic for which there is so much information on the process and effects of radiation damage.

During the 1990s, there has been a small "explosion" of work on radiation damage effects in ceramics in general, and specifically on zircon (Ewing et al. 2000). The experimental work is of

three types:

1. Natural zircon crystals. In these studies, there is generally no lack of material and a wide variety of analytical techniques may be used; however, the conclusions of these studies are always limited by a lack of knowledge of the thermal history of the samples.
2. $^{238}$Pu-doped synthetic zircon. These studies are generally conducted under ambient conditions, followed by thermal annealing studies. These are long-term studies, lasting several decades, and the results for only a few samples of longer-term experiments are just now available. Because of restrictions on handling Pu-bearing samples, analytical studies have been limited to simple density determinations, structural analysis using X-ray diffraction, electron microprobe analysis and some spectroscopic studies.
3. Ion-beam irradiated zircon. In these studies, both heavy- and light-ion irradiations have been completed at precisely controlled temperatures. Although the physics of the damage process allows one to correlate the results to α-decay damage, the experimental configuration has limitations. *In situ* irradiations combined with high resolution electron microscopy allow one to observe changes in the atomic-scale structure in real time and determine the dose at which the material becomes amorphous as a function of temperature; however, the high surface area to volume ratio of the thin wedge of the electron transparent region may affect the damage accumulation process as defects migrate to the surface. Most recently, bulk irradiations, followed by examination of samples cut perpendicular to the surface (parallel to the trajectory of the ion), allow one to follow damage effects because the amount of damage varies along the trajectory of the implanted ion. These samples are generally examined by high-resolution transmission electron microscopy (HRTEM) (Lian et al. 2001; Lian et al. in press) or utilize surface techniques, such as X-ray photoelectron spectroscopy (XPS) (Chen et al. 2002). Such studies are time consuming, but can provide critical information on oxidation states, defect formation and migration mechanisms.

Finally, during the past five years, there has been an increased effort to simulation cascade formation and the evolution of the damage microstructure. Computational limitations currently restrict such dynamic calculations to cells that contain less than 400,000 atoms and time periods for cascade evolution of up to 20 picoseconds. The future challenge is in designing experiments and simulations that can be used to test the various models of damage accumulation.

In this chapter, we first review the experimental results for radiation-damaged zircon. We explicitly focus on displacement damage that results from α-decay event cascade formation. The experimental results are then discussed in terms of the different models that have been used to describe the damage accumulation process. The next section summarizes the recent results of computer simulations of atomic-scale processes during the damage process. Despite the substantial progress of the last decade, many questions remain, and these are discussed in the last section.

## EXPERIMENTAL RESULTS

We have organized the discussion of experimental results according to the length-scale sampled by each technique. We begin with a discussion of changes in bulk properties, then long-range effects (10 to 100 nm) that capture the changes in the connectivity of the coordination polyhedra, as well as the presence of domains of different structures (e.g., periodic, strained periodic, and aperiodic). Finally, we discuss short-range effects (<1 nm) that reflect changes in the nearest-neighbor coordination geometries. Although this is a convenient and revealing means of following the damage accumulation process, the changes in structure of the damaged material occur at all length-scales simultaneously. No single technique can provide a clear picture of this heterogeneous transition as it occurs over the entire range of dose (Salje et al. 1999). Even a single technique, such as X-ray diffraction, will provide different types of data, e.g., Bragg diffraction maxima from the periodic domains and a diffuse scattering component from interstitial defects and amorphous domains.

Several different units are used to measure the radiation dose, depending on the type of ex-

periment. In studies of naturally damaged or Pu-doped zircon, the age and actinide concentration are used to calculate the dose; whereas, in ion beam experiments, the radiation fluence (ions/cm$^2$) is measured. In order to compare the amount of damage in natural, Pu-doped, and ion-irradiated zircons, these measurements are converted to a radiation dose, in units of displacements-per-atom (dpa). To convert the fluence to units of dose, a simple formula is used:

$$D_{dpa} = JF/n \quad (1)$$

where $D_{dpa}$ is dose in dpa, J is the number of atomic displacements caused by each ion per unit depth, F is the fluence, and n is the atomic density. J depends on a variety of parameters, including incident ion mass and energy and the displacement energy ($E_d$) of the target atoms. Monte Carlo computer simulations are used to estimate J. The number of displacements per ion varies inversely with $E_d$ (i.e., the higher the displacement energy, the fewer displacements are caused by each incident ion).

Atomic displacement energies are known for only a relatively few ceramic materials, most of which are simple oxides such as $Al_2O_3$, MgO, ZnO, CaO, and $UO_2$ (Zinkle and Kinoshita 1997). Displacement energies generally range from 10 to 70 eV. For example, in $Al_2O_3$, the typically used displacement energies are 20 eV for Al and 50 eV for oxygen. More recently, molecular dynamics simulations have extended the range of materials for which $E_d$ can be estimated to more complex materials. For zircon, $E_d$ is 89 eV (Zr), 48 eV (Si), and 28 eV (O) (Park et al. 2001).

In order to make quantitative comparisons of the amount of radiation damage in natural and ion-beam-irradiated specimens, the measured concentration of U and Th is also converted to a displacement dose. This can be done in two steps:

$$D_\alpha = 8\,N_{238}[\exp(t/\tau_{(238)}) - 1] + 7\,N_{235}[\exp(t/\tau_{(235)}) - 1] + 6\,N_{232}[\exp(t/\tau_{(232)}) - 1] \quad (2)$$

where $D_\alpha$ is the dose in units of α-decays/g, $N_{238}$, $N_{235}$, and $N_{232}$ are the measured number of atoms/g of $^{238}$U, $^{235}$U, and $^{232}$Th, $\tau_{(238)}$, $\tau_{(235)}$, and $\tau_{(232)}$ are their respective half-lives, and t is the geologic age. Studies of radiation damage in minerals usually report $D_\alpha$. To convert to a dose in dpa:

$$D_{dpa} = \frac{D_\alpha WN}{aA} \quad (3)$$

where A is Avogadro's number, W is the molecular weight of the mineral, n is the average number of displacements per α–decay, and a is the number of atoms per formula unit. The n term is analogous to J in Equation (1) and can be obtained by using the computer simulation (which requires a value for $E_d$). An advantage to using dpa as the unit of dose is that variations in the displacement energy, $E_d$, affects Equations (1) and (3) in exactly the same way, so that quantitative comparisons between ion-irradiated and α-decay-damaged materials may be made. The observed amount of disorder may also depend on the flux; however, the calculated number of displacements per atom is independent of this parameter.

## Bulk properties

***Density.*** The variation in density as a function of α-decay event dose is important because this relationship is used to distinguish among the different models of damage accumulation mechanism. The effects of increasing damage on the density of natural zircon crystals from Sri Lanka (~570 Ma) have been carefully measured in several papers (e.g., Holland and Gottfried 1955, Murakami et al. 1991). The density decreased by 17% from ~4.7 to 3.90 g/cm$^3$ at a dose of $10^{19}$ α-decays/g. The rate of change in density is sigmoidal: i.e., the change is slow at low doses, followed by a more rapid

decrease between 2 to $8 \times 10^{18}$ α-decays/g, and finally approaching a saturation value of 3.9 g/cm$^3$ at doses greater than $8 \times 10^{18}$ α-decays/g.

Weber (1990) reported density measurements for synthetic zircon doped with 8 mol % $^{238}$Pu ($Pu_{0.08}Zr_{0.92}SiO_4$). This zircon showed a more rapid density decrease at doses below ~$6 \times 10^{18}$ α-decays/g than natural zircon. The density of the Pu-substituted zircon saturated at approximately 4.0 g/cm$^3$. The shallower initial density decrease in natural zircon was attributed to the effects of thermal recovery over geologic time of damaged, but not yet amorphous material (Weber 1990, Murakami et al. 1991). The overall density of Pu-doped zircon decreased by 14.1% before reaching saturation, as compared to a decrease of 15.6% for natural zircon (Weber 1990).

Weber (1990) and Murakami (1991) described dose-dependent density decrease by:

$$\Delta\rho/\rho = A[1 - \exp(-(BD)^n)] \quad (4)$$

where $\Delta\rho/\rho$ is the density change normalized to the density of the initially crystalline zircon, A is the relative density change at saturation, B is the mass of material damaged per α-decay event, D is the α-decay dose, and n is an "order parameter" that gives the sigmoidal shape to the curve. B was found to be approximately 2-3 $\times 10^{-19}$g, corresponding to a total of 4,000-6,000 atoms of "damaged material" per α-decay event (this number is greater than the calculated number of displaced atoms, because the "damaged" volume is the affected volume per α-decay event that contains all the damage, defects and amorphous domains). The order parameter has values between 1.7-2.3 (Weber 1990, Murakami et al. 1991), but the order parameter has no specific physical meaning. Weber et al. (1994) expressed the normalized macroscopic volume swelling $\Delta V_m/V_0$ as:

$$\Delta V_m/V_0 = f_c\Delta V_{uc}/V_0 + f_a\Delta V_a/V_0 \quad (5)$$

in which $\Delta V_{uc}/V_0$ is the normalized unit-cell volume of the crystalline phase, $\Delta V_a/V_0$ is the normalized volume of amorphous zircon, $f_c$ is the mass fraction of crystalline zircon, $f_a$ is the mass fraction of amorphous zircon, and $V_0$ is the normalization parameter (i.e., macroscopic or unit-cell volume of undamaged zircon). In order to apply this equation to obtain the dose dependence of the amorphous fraction ($f_a$), the unit-cell swelling is measured by X-ray diffraction (Weber et al. 1994). Recently, Trachenko et al. (2003) have modeled the volume expansion as a percolation phenomena with a discontinuity in the swelling curve at the percolation threshold.

***Optical.*** Crystalline zircon is uniaxial (refractive indices $n_\varepsilon = 1.984$ and $n_\omega = 1.924$), whereas, amorphous zircon is optically isotropic (Holland and Gottfried 1955). Both indices are independent of dose up to ~$2 \times 10^{18}$ α-decays/g, after which the refractive indices decrease with dose until they saturate at $n_\varepsilon = n_\omega = 1.81$. The very regular decrease in birefringence can be used to estimate the α-decay event dose (Chakoumakos et al. 1987) and the related change in density (Sahama 1981). A careful correlation of electron microprobe analyses of U- and Th-content to calculated dose shows a linear relationship to birefringence (Palenik et al. in press).

***Mechanical.*** Özkan (1976) measured a 69% decrease in the elastic modulus and a 7% decrease in Poisson's ratio for a heavily damaged zircon crystal ($\rho = 3.994$ g/cm$^2$). The longitudinal and shear elastic moduli decreased with increasing radiation dose reaching saturation values of 1.5 $\times 10^{12}$ and $0.49 \times 10^{12}$ dyne/cm$^2$, respectively. Chakoumakos et al. (1991) measured a 40% decrease in hardness and 29% decrease in the elastic modulus (using a nano-indenter for a 275 nm indentation depth) in a zoned zircon where the maximum dose was $10^{19}$ α-decays/g. The radiation "softening" was accompanied by an unmeasured increase in fracture toughness. This was spectacularly evident in the distribution of fractures in a highly zoned zircon in which fractures in the low dose zones did not propagate across the high-dose zones (Chakoumakos et al. 1987, Chakoumakos et al. 1991). The decreases in hardness (70%) and elastic modulus (42%) were confirmed by nano-indenter measurements of Pb-implanted (540 keV) zircon at doses of $10^{13}$ to $10^{14}$ Pb/cm$^2$ (Oliver et al.

1994). Prior to the radiation "softening"; however, there was a slight increase in hardness (11%) up to a dose of $10^{13}$ Pb/cm$^2$. Lee and Tromp (1995) modeled the distribution of fractures in zoned zircon accounting for the changes in mechanical properties and the stresses that result from the volume expansion of the highly damaged zones.

***Thermal.*** The thermal conductivity of zircon decreases by ~25% with increasing dose, due to phonon scattering at α-decay-induced defects (Crawford 1965). In a very preliminary study Raychaudhuri et al. (1980) has shown that metamictization leads to thermal conductivity values comparable to those of other disordered solids.

***Chemical durability.*** Crystalline zircon is stable to such an extent that the equilibrium concentrations of dissolved Zr and Si are on the order of $10^{-9}$ moles/L (0.1 ppb) at 25°C (Tole 1985). Dissolution of highly damaged zircon follows a first-order reaction, based on Si concentrations. Concentrations of Zr remain below 0.05 ppm (the instrument detection limit) due to precipitation of $ZrO_2$ and $ZrSiO_4$ (Tole 1985). The leach rate of zircon increases with α-decay damage by one to two orders of magnitude (Ewing et al. 1982). Recently, a high-temperature Soxhlet extractor was designed to measure the forward rate of dissolution of zircon in the range of 120 to 250°C (Helean et al. 1999). The measured rates are as follows: $4.1 \times 10^{-4}$ (g)(m$^{-2}$)(day$^{-1}$) at 250°C, $1.7 \times 10^{-4}$ g·m$^{-2}$day$^{-1}$ at 200°C and $7.1 \times 10^{-5}$ g·m$^{-2}$day$^{-1}$ at 120°C. Using the same experimental technique, Gong et al. (in preparation) completed leaching experiments on highly damaged zircon over the temperature range of 150 to 250°C and measured a three order of magnitude increase in normalized mass loss based on silicon concentrations in solution. The effect of radiation damage on the chemical durability of zircon has also been demonstrated in a field study on the weathering of zircon in detrital sediments of the Amazon Basin (Balan et al. 2001). Their results demonstrate a dramatic decrease in chemical durability at doses greater than $3.5 \times 10^{18}$ α-decays/g. This is higher than the dose at the first percolation point ($2 \times 10^{18}$ α-decays/g, Ríos et al. 2000a), the point at which the aperiodic domains become fully connected to one another (approximately 30-40% of the total volume is amorphous). When the amorphous domains become interconnected the transport properties of zircon change and both loss of elements by diffusion and bulk dissolution proceed rapidly (Jonckheere and Gögen 2001).

## Long range order

***X-ray diffraction.*** The sharp Bragg X-ray diffraction maxima associated with long-range periodicity show a pronounced decrease in intensity and shift to lower values of 2θ with increasing α-decay event dose (Holland and Gottfried 1955, Murakami et al. 1991). The intensity decrease is rapid at low doses, followed by a more gradual dose-dependent decrease until the Bragg diffraction maxima are no longer evident (e.g., Pabst 1952, Holland and Gottfried 1955, Pellas 1965, Vance and Anderson 1972, Weber 1990, Weber et al. 1994; see Fig. 1). A similar effect is observed in ion-irradiated (3 MeV $Ar^+$) synthetic zircon (Karioris et al. 1982). Holland and Gottfried (1955) observed a complete loss of Bragg diffraction intensity at a dose of $10 \times 10^{18}$ α-decays/g, for the Sri Lanka zircon.

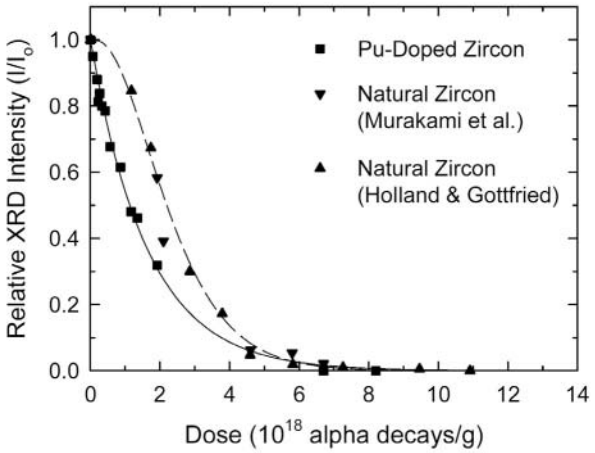


**Figure 1.** Relative XRD intensities in Pu-doped and natural zircons. [Used by permission of the Materials Research Society, from Weber (1990) *Journal of Material Research*, Vol. 5, Fig. 1, p. 2689.]

Weber (1990) found that after reaching a dose of $6.7 \times 10^{18}$ α-decays/g, the Pu-substituted zircon was X-ray diffraction amorphous. For both natural and Pu-doped zircon, the decrease in diffraction intensity followed an exponential of the form:

$$I/I_0 = \exp(-BD) \quad (6)$$

where B is, again, the mass of material damaged per α-decay event and D is the α-decay dose. The best fit was obtained for $B = 6.12 \times 10^{-19}$ g for Pu-doped zircon and $B = 6.71 \times 10^{-19}$ g for natural zircon (Weber 1990). The earlier data of Holland and Gottfried (1955) and Murakami et al. (1986) are offset at low dose with respect to Pu-doped zircon (Fig. 1), suggesting a so-called "incubation" dose for natural zircon (Weber 1990, Weber et al. 1994). This offset could be due to thermal recovery of lightly damaged regions or point defects over geologic time.

Murakami et al. (1986, 1991) reported detailed X-ray powder diffraction measurements from a suite of Sri Lanka zircon specimens. Three distinct damage stages were identified. At doses below $3 \times 10^{18}$ α-decays/g, the initially narrow and intense Bragg maxima decreased by a factor of ~2 and were shifted to slightly lower 2θ, but they remained sharp. This was attributed to the combined effects of unit-cell expansion and strain fields surrounding the expanding damaged regions. In the second stage, which occurs at higher damage levels, the intensity of the Bragg maxima decreased by several orders of magnitude, and the intensity of the diffuse scattering component on the high-2θ side of the Bragg maxima increased substantially. The Bragg maxima at this stage were weak, skewed, and broadened. In the third stage ($>8 \times 10^{18}$ α-decays/g) there was no trace of Bragg diffraction maxima. The dose for the complete disappearance of the Bragg maxima depends on the sensitivity of the experiment for detecting crystalline remnants, but the value of $8 \times 10^{18}$ α-decays/g obtained by Murakami et al. (1991) has since been confirmed by Ríos et al. (2000a).

The unit-cell parameters were determined by refinement of the X-ray diffraction data. This is more reliably accomplished for low α-decay doses, when the Bragg peaks are still sharp; at higher doses the error in the unit cell parameters is large (Murakami et al. 1991). Several authors have observed that in natural zircon, the net expansion is greater along the *c*-axis than along the *a*-axis, and that there is a significant suppression of unit-cell expansion along the *a*-axis at low doses (Holland and Gottfried 1955, Weber 1990, Murakami et al. 1991, Biagini et al. 1997, Ríos et al. 2000b). The $ZrO_8$ polyhedra are particularly susceptible to volume expansion with increasing α-decay dose, and since they are isolated from one another along the *c*-axis, the structure can expand more freely along this direction (Ríos et al. 2000b). Furthermore, recrystallization is more efficient parallel to the *a*-axis due to tilting of coordination polyhedra around corner-sharing links (Ríos et al. 2000b). In contrast, the rate of lattice expansion was similar along the *a*- and *c*-directions for both Pu-doped (Weber 1990) and neutron-irradiated (Crawford and Whittles 1952) zircon, and in both cases, there was no suppression of the expansion along the *a*-axis, suggesting preferential recovery parallel to the *a*- axis over geologic time for natural zircon.

The increase in amorphous fraction ($f_a$) as a function of dose is an important relationship that distinguishes the different models of damage accumulation. Weber (1990) and Weber et al. (1994) combined the X-ray diffraction data with the macroscopic swelling data to estimate the relationship between $f_a$ and dose, using Equation (5). They assumed that (i): $V_a/V_0 = 16.6\%$ (the observed macroscopic swelling of Pu-substituted zircon at saturation), (ii) $f_a + f_c = 1$, and (iii): $\Delta V_m/V_0$ is simply the measured dose-dependent volumetric swelling. The unit-cell expansion ($\Delta V_{uc}/V_0$) was then obtained from the measured shift in the Bragg diffraction maxima. The amorphous fraction obtained with this method varied sigmoidally as a function of α-decay dose (Fig. 2). By plotting the unit-cell and macroscopic swelling independently, Weber (1990) also demonstrated that the volume expansion at low doses is due mostly to unit-cell expansion, but at higher doses the contribution from amorphous zircon dominates. A similar analysis for the Sri Lanka zircon was performed on the data of Holland and Gottfried (1955), with similarly sigmoidal results (Weber 1990, Weber et al. 1994).

However, the curves were offset by ~$10^{18}$ α-decays/g with respect to the Pu-doped zircon (Fig. 2), a fact that was attributed to long-term thermal recovery of lightly damaged zircon under geologic conditions.

Murakami et al. (1991) proposed that there is not a single structure for amorphous zircon, but instead, they observed that the density of aperiodic zircon continued to decrease with increasing α-decay dose even after the sample was X-ray diffraction amorphous. This may result from the fact that the X-ray diffraction of amorphous zircon still contained a substantial crystalline fraction. This observation has since been confirmed by Ríos et al. (2000a) who showed that even the highly damaged zircon still had a crystalline component. Thus, the density of the sample depends on the structure of the crystalline and amorphous domains and the proportion of amorphous to crystalline material, all of which change with dose. At doses below 2 × $10^{18}$ α-decays/g, the diffuse scattering is shifted to larger diffraction angles and originates from the "compressed" crystalline domains due to the expansion of the damaged domains (Ríos and Salje 1999, Ríos et al. 2000a). At these low doses, macroscopic swelling is dominated by the unit-cell expansion, which also compresses the still-isolated amorphous zones. At this stage, radiation damage produces mainly shear waves in the crystal lattice whose signature is a non-isotropic diffuse scattering around the main Bragg peaks (Ríos and Salje 1999). At higher doses, the amorphous domains become interconnected, the amount of residual crystalline material diminishes, and the amorphous structure is free to swell to its maximum value of ~18%.

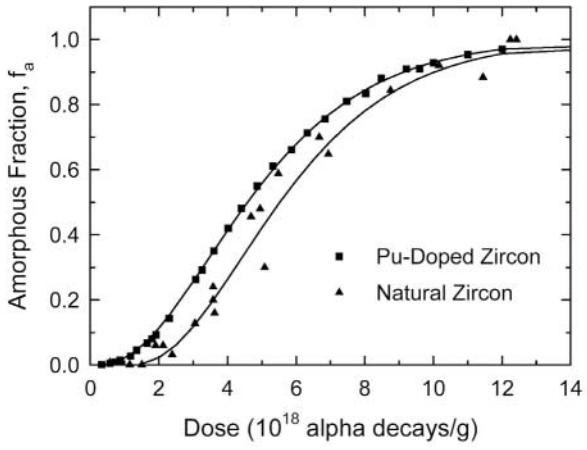


**Figure 2.** Amorphous fraction, $f_a$, as a function of dose in Pu-doped and natural zircons. [Used by permission of the Materials Research Society, from Weber (1990) *Journal of Material Research*, Vol. 5, Fig. 12, p. 2695.]

The X-ray diffraction and macroscopic swelling data have been interpreted in terms of a structure consisting of percolating crystalline or amorphous domains (Salje et al. 1999, Ríos et al. 2000a). At low α-decay doses, isolated amorphous regions accumulate and, as the dose increases, they gradually become interconnected.

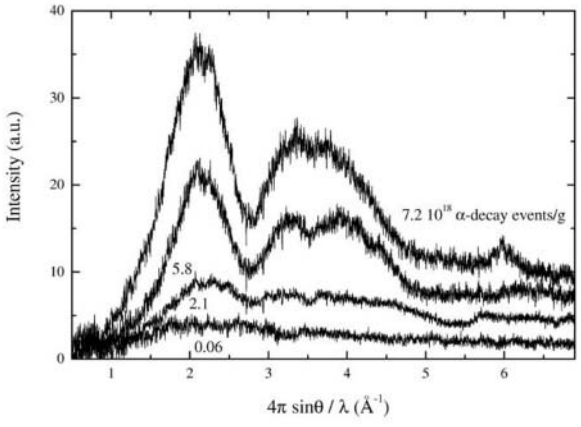


**Figure 3.** Diffractograms of zircon samples (from the bottom to the top) 4403, 4303, 4304 and 3107. The numbers in the figure indicate the corresponding doses in units of $10^{18}$ α events/g. For the first three samples any contribution from crystalline areas has been removed. For the last sample (3017), which has a high degree of radiation damage, crystalline area could still be seen, as the peak at 6 Å$^{-1}$ demonstrates. Notice the background increase with the increasing dose. [Used by permission of the Institute of Physics Publishing, Inc., from Ríos et al. (2000a) *Journal of Physics: Condensed Matter*, Vol. 12, Fig. 5, p. 2408.]

Below this first "percolation point" ($2 \times 10^{18}$ α-decays/g for the Sri Lanka zircon) the swelling of amorphous domains is negative due to the expansion of the crystalline structure. The second percolation point is reached below $8 \times 10^{18}$ α-decays/g, at which point the crystalline regions no longer percolate, and the swelling begins to approach the maximum of 18%. Between the percolation points, amorphous domains can be densified or expanded, depending on the local environment.

Ríos et al. (2000a) used a highly sensitive 7-circle, single-crystal X-ray diffractometer to obtain precise data to estimate the amorphous fraction as a function of α-decay dose (Fig. 3). The amorphous fraction was obtained directly from the X-ray diffraction results by comparing scattering intensities to those from crystalline and amorphous reference specimens:

$$f_a = (I - I_{cryst})/I_{am} \quad (7)$$

where I is the diffuse scattering intensity from the specimen in question, and $I_{cryst}$, and $I_{am}$ are the intensities obtained from undamaged and X-ray diffraction amorphous zircon, respectively. The background and the Bragg reflections were subtracted and the intensity was integrated at values of $4\pi\sin\theta/\lambda > 5$ Å$^{-1}$. The resulting amorphous fraction for a suite of Sri Lanka zircon crystals is plotted in Figure 4. The important observations are: (1) there is no offset at low does (i.e., no "incubation" dose); and (2) the curve is not sigmoidal. The line fit is the solution to Equation (6) with $B = 2.7 \times 10^{-19}$ g. The direct increase of $f_a$ with dose is different than the more sigmoidal curve obtained using macroscopic swelling data (Weber 1990, Murakami et al. 1991, Weber et al. 1994). In fact, Ríos et al. showed that that $V_a/V_0$ in Equation (5) is not constant but depends on the degree of damage, so that previous assumptions used to generate the dose dependence of the amorphous fraction may not have been strictly valid.

***Neutron diffraction.*** There is one neutron diffraction study of a $^{238}$Pu-doped zircon that has reached a dose of $2.8 \times 19^{19}$ α-decays/g, nearly three times the dose required to fully amorphize zircon (Fortner et al. 1999). No evidence of residual microcrystallinity was found. The pair-distribution function indicated that the fully amorphous zircon had the structure of an oxide glass with the structural units of zircon largely preserved and little phase separation.

***Transmission electron microscopy (TEM).*** The first systematic TEM study of radiation effects in zircon as a function of increasing α-decay dose was completed by Bursill and McLaren (1966). They confirmed the three stage model of damage accumulation (Holland and Gottfried 1955) that was based on x-ray diffraction data; however, they showed that zircon at Stage III of the

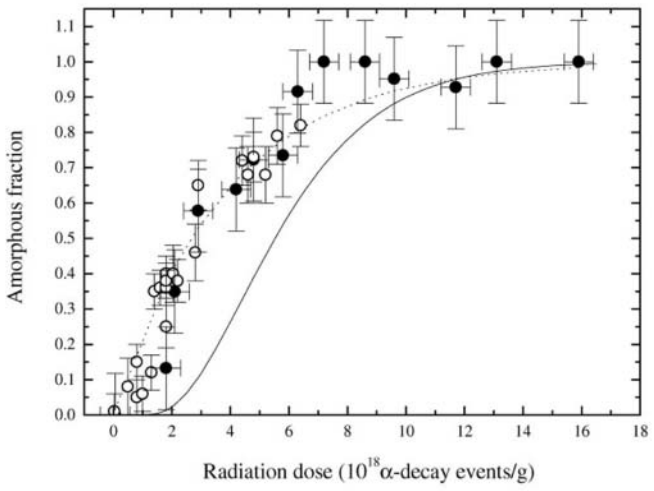


**Figure 4.** Amorphous fraction, $f_a^{exp}$, in various zircon samples versus radiation dose. Full circles represent the experimental data as determined following the expression given in Ríos et al. (2000a); the dotted line show the best fit obtained using the direct amorphization model. Open circles indicate data from infrared spectroscopy. The continuous line is the $f_a$ obtained from an equation by Weber (1993). The error bars for the dose are estimated to be about $\pm 0.5 \times 10^{18}$ α-decay events/g. [Used by permission of the Institute of Physics Publishing, Inc., from Ríos et al. (2000a) *Journal of Physics: Condensed Matter*, Vol. 12, Fig. 6, p. 2409.]

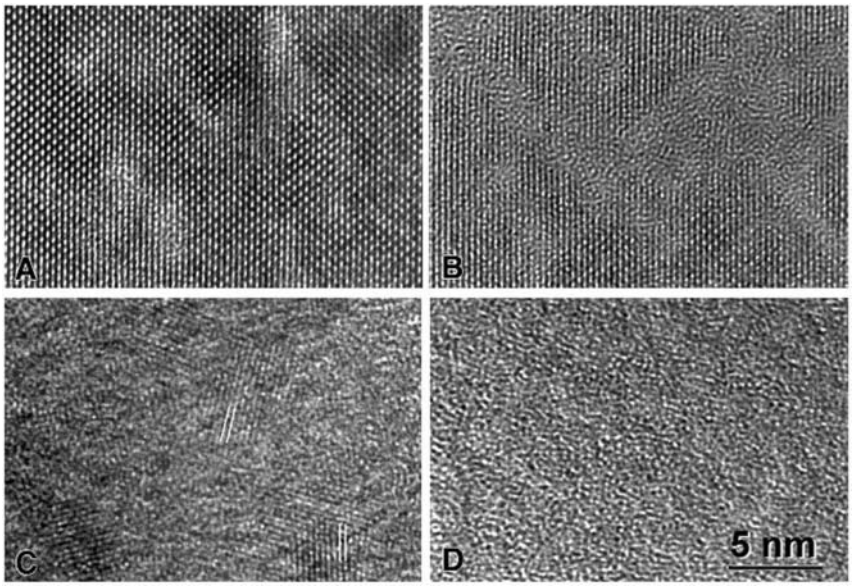


**Figure 5.** HRTEM micrographs of self-radiation damage in natural zircons showing increased degree of amorphization with increasing dose: (a) 0.0025 dpa; (b) 0.091 dpa; (c) 0.32 dpa; (d) 0.50 dpa. The spacing marked in (c) is 0.33 nm (the (200) d-spacing). The slight rotation of the remaining crystallites in the amorphous matrix in (c) is caused by local strain fields induced by amorphization. [Used by permission of the Materials Research Society, from Weber et al. (1994) *Journal of Material Research*, Vol. 9, Fig. 2, p. 690.]

damage state (apparently amorphous as determined by X-ray diffraction) actually consisted of slightly misoriented crystallites of "normal" zircon approximately 10 nm in size. They also identified small amounts of $ZrO_2$ in highly damaged zircon. On annealing, voids or bubbles formed (probably of He) in one sample, as well as dislocation loops on {101}, due to the condensation of point defects. Subsequent TEM studies (Headley et al. 1981, 1982b; Yada et al. 1981, 1987; Murakami et al. 1991, Weber et al. 1994, Palenik et al. in press) confirmed the evolution of the microstructure with increasing α-decay event damage. A typical sequence is shown in Figure 5. At very low doses (>0.01 dpa), zircon shows no evidence of damage and has a well-defined atomic-scale periodicity. At a low α-decay dose (0.01 to 0.3 dpa), regions (2-5 nm) of mottled diffraction contrast occur. With increasing α-decay dose, lattice fringe-free areas of mottled diffraction contrast become more numerous and interconnected, and at a still higher dose (> 0.3 dpa), the microstructure consists of crystalline islands in an aperiodic matrix. These crystallites are rotated by up to 15° with respect to the original lattice orientation. Above 0.5 dpa ($10^{19}$ α-decays/g), the zircon appears to be fully aperiodic, as evidenced from electron diffraction and HRTEM imaging.

Although there is a long history of the use of ion beam irradiations to simulate the α-decay and fission track damage effects in zircon (Cartz and Fournelle 1979, Karioris et al. 1981, Headley et al. 1982a, Petit et al. 1987, Bursill and Braunshausen 1990), Wang et al. (1991, 1993) and Wang and Ewing (1992a) were the first to complete *in situ* TEM studies of amorphization of zircon during an ion beam irradiation, using the HVEM-Tandem Facility at Argonne National Laboratory (Wang 1998). This facility consists of a modified 1 MeV electron microscope interfaced with a 2 MeV tandem ion accelerator that allowed *in situ* observation of the sample over a wide range of temperatures (Ewing et al. 2000). The initial irradiations were with 700 and 1500 keV $Kr^+$, 1500 keV $Xe^+$ and 400 keV $He^+$ (Wang and Ewing 1992a). The evolution of electron-diffraction patterns with increasing dose is comparable in many respects with the X-ray diffraction and TEM results for natural zircon (Murakami et al. 1991, Weber et al. 1994). At low to intermediate doses (< 0.2 dpa), the higher-order maxima become fainter and a diffuse diffraction "halo" develops around the trans-

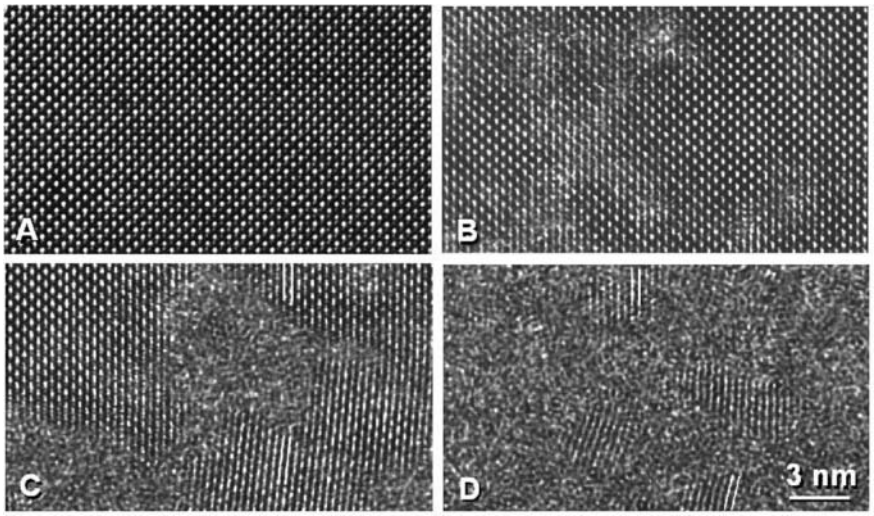


**Figure 6.** HRTEM images of crystalline to amorphous transformation in synthetic zircon irradiated with 1.5 MeV $Kr^+$ ions at 300 K: (a) unirradiated; (b) 0.057 dpa; (c) 0.17 dpa; (d) 0.34 dpa. Complete amorphization was achieved at 0.55 dpa. The spacing marked in (c) and (d) is 0.33 nm (the (200) d-spacing). Note the similarity of the images in (b), (c), and (d) with those for self-radiation damage of natural zircon in Figs. 5(a), (b), and (c). [Used by permission of the Materials Research Society, from Weber et al. (1994) *Journal of Material Research*, Vol. 9, Fig. 8, p. 694.]

mitted beam. At higher doses (0.2 to 0.5 dpa), the diffuse scattering becomes stronger, the higher-order maxima disappear entirely, and the remaining electron-diffraction maxima show an arc-like appearance characteristic of crystallites that are slightly rotated (e.g., Headley et al. 1981, Wang and Ewing 1992a, Weber et al. 1994, Meldrum et al. 1999a). At still higher doses (> 0.5 dpa), all of the diffraction maxima disappear, leaving the transmitted beam and the diffuse diffraction halo as the only remaining features in the electron-diffraction patterns. High-resolution TEM images of the fully-damaged zircon confirm the complete loss of lattice fringes. A sequence of high-resolution images of zircon irradiated with 1.5 MeV $Kr^+$ is shown in Figure 6 (Weber et al. 1994). The overall microstructural evolution with increasing ion dose closely parallels that of $\alpha$-decay damage in natural zircon. Weber et al. (1994) found that the amorphization dose of the ion-irradiated zircon (0.55 dpa) was similar to that $\alpha$-decay-amorphized zircon (0.50 dpa). In a later study (Weber et al. 1999), an even lower amorphization dose (0.30 dpa) was determined for ion-irradiated zircon.

Numerous *in situ* ion beam irradiations studies have now been completed on zircon (see summary by Ewing et al. 2000). Although ion beam irradiation reproduces the microstructure of $\alpha$-decay damaged zircon under controlled temperature conditions, there are a number of experimental limitations. The high surface area to irradiated volume ratio in the electron-transparent region of the sample may affect the damage accumulation process, that is isolated defects migrate and are annihilated at the surface. The electron beam may cause radiation-enhanced migration of defects; thus, increasing the dose required for amorphization. Finally, the dose rates for the ion beam irradiations are many orders of magnitude greater than that for natural or Pu-doped zircon. The first two limitations can be overcome by bulk irradiations of zircon followed by cross-sectional HRTEM analysis. These studies are now in progress. There are also important limitations related to the HRTEM technique. In a systematic study of simulated images of mixed crystalline and aperiodic domains, Miller and Ewing (1992) demonstrated that there can be a substantial fraction (up to 20%) of aperiodic material (e.g., isolated cascades in a crystalline matrix) present, but not evident in the high-resolution TEM image. Depending on the thickness of the examined region, the crystalline fraction dominates the HRTEM image. Based on the simulated images, a single $\alpha$-recoil cascade should

have an apparent diameter of less than 4.0 nm. These calculations confirm that TEM studies cannot provide a quantitative estimate of the amorphous fraction. Zircon that appears completely amorphous by HRTEM/selected area electron diffraction (SAED) still retains evidence of residual atomic-scale order. Murakami et al. (1991) observed textured or braided regions in electron-diffraction amorphous zircon. Nasdala et al. (2002a,b) used image processing techniques to highlight the presence of discontinuous, "warped," and uneven lattice fringes within the structure of amorphous zircon.

Several observations can be drawn from TEM studies that support and clarify the X-ray diffraction results. First, the amorphization process is clearly heterogeneous. Even at low doses there are isolated regions that appear to be amorphous in high-resolution images. The rotated crystalline islands observed by TEM in highly damaged zircon also suggests the presence of considerable strain or shearing due to the volume expansion of the amorphous material. Diffuse X-ray scattering also suggested the presence of shear waves in the crystalline lattice (Ríos and Salje 1999).

## Short-range order

A variety of spectroscopic techniques have been used to study radiation damage accumulation in zircon. Depending on the technique, one may obtain information on changes in the nearest neighbor coordination geometries, the connectivity between coordination polyhedra over several coordination spheres, or the oxidation state of actinide elements (e.g., U and Pu). There is no single technique that provides all three types of information. In this section we review the spectroscopic studies of damage accumulation in zircon using X-ray absorption spectroscopy and nuclear magnetic resonance. However, the most detailed studies have used infrared and Raman spectroscopies to great advantage, and these results are summarized in the chapter by Nasdala et al. (this volume).

***X-ray absorption spectroscopy.*** Extend X-ray absorption fine structure (EXAFS) spectroscopy is a sensitive probe of the local coordination and bonding geometry at the nearest-neighbor level; thus, EXAFS is very useful for characterizing the fully-damaged state of zircon (Barinsky and Kulikova 1977, Nakai et al. 1987, Greegor et al. 1990). Farges and Calas (1991) and Farges (1994) completed the first detailed EXAFS study of radiation damaged natural zircon. With increasing α-decay events dose, the mean <Zr-O> distance decreased by 0.06 Å with respect to crystalline zircon. The next-nearest-neighbor <Zr-Zr> distances are shorter in metamict zircon than in crystalline zircon (3.34 vs. 3.64 Å). For metamict zircon, Zr was in 7-fold coordination, as compared to the 8-fold coordination in crystalline zircon. Based on bond-valence theory (Brown and Shannon 1973), the relatively smaller $Zr^{4+}$ cation is expected to be in 7-fold coordination, suggesting that as a result of metamictization, there is a "relaxation" of the $ZrO_8$ polyhedra to a more stable local configuration (Farges and Calas 1991). There was no evidence for radiation-induced decomposition into constituent oxides. In a later study, Farges (1994) suggested that at temperatures below 900 K the structure of naturally amorphized

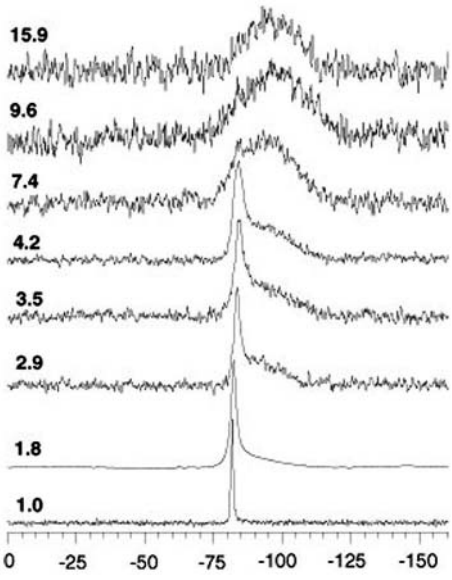


**Figure 7.** Series of $^{29}Si$ MASNMR spectra of zircon with increasing accumulated α dose (upwards). Increasing numbers indicate the dose × $10^{18}$ α events/g and refer to: Moroto, UG9A, Cam26, Cam25, Z5, Sand9, Ti8, and Sand4, respectively. The horizontal scale indicates chemical shift in ppm. [Used by permission of the American Institute of Physics, from Farnan and Salje (2001) *Journal of Applied Physics*, Vol. 89, Fig. 2, p. 2085.]

zircon consists of Zr- and Si-rich "nanodomains" with separate oxygen networks.

Pu-doped zircon ($Zr_{0.92}Pu_{0.08}SiO_4$) powders were synthesized with different ratios of $^{238}Pu$ and $^{239}Pu$ (Exharos 1984, Weber 1990) and studied using XAS by Begg et al. (2000). Because of the differences in half-life for the Pu isotopes (87.7 and 24,100 years, respectively) different α-decay doses were obtained for each sample. In experiments that lasted over 18 years, the $^{239}Pu$-doped zircon remained highly crystalline after a dose of $1.2 \times 10^{17}$ α-decays/g, while the $^{238}Pu$-doped zircon was fully-metamict at a dose of $2.8 \times 10^{19}$ α-decays/g. Based on X-ray diffraction analysis there was no evidence of long-range periodicity in the highly-damaged $^{238}Pu$-zircon; however, the amorphous state retained the distorted, nearest-neighbor zircon structure, consisting of rotated $ZrO_8$ and $SiO_4$ tetrahedra (Begg et al. 2000), consistent with the interpretation of XAS results by Barinsky and Kulikova (1977) for fully-metamict natural zircon. Begg et al. (2000) found no evidence to Zr and Si-rich domains of different coordination numbers.

***Nuclear magnetic resonance.*** The XAS data provide conflicting interpretations of the coordination of Zr (7 vs. 8) in the fully-damaged state. It may be reasonable to expect both types of coordination polyhedra in the aperiodic structure of the fully-damaged zircon. The retention of 8-fold coordination of Zr in the highly distorted structure suggests the possibility of some polymerization of the [$SiO_4$] units. Farnan (1999) used magic-angle spinning NMR to compare a natural zircon crystal that had experienced only $0.5\text{-}0.8 \times 10^{18}$ α-decays/g with one that had experienced a more significant α-decay dose ($1.8 \times 10^{18}$ /g). MAS-NMR is particularly sensitive to polymerization of $SiO_4$ tetrahedra. In the lower-dose zircon, a sharp peak was observed at a chemical shift of -81.6 ppm. This peak is characteristic of $^{29}Si$ in isolated $SiO_4$ tetrahedra. In the higher-dose sample, the $^{29}Si$ peak was slightly wider and an additional broad component centered at -90 ppm was identified. This slightly larger chemical shift corresponds to silicon tetrahedra sharing two bridging oxygens. In fact, the broad nature of this peak suggests that the number of shared oxygens per $SiO_4$ tetrahedron ranges from 0 to 4 in the higher-dose sample.

Farnan and Salje (2001) obtained a more complete picture by characterizing a suite of samples ranging in dose from $1.0 \times 10^{18}$ to $15.9 \times 10^{18}$ α-decays/g (Fig. 7). The NMR peak corresponding to $^{29}Si$ in isolated tetrahedra first broadens and shifts from -81.5 to -83.7 ppm. Farnan (1999) also observed the broadening of the $^{29}Si$ peak, and tentatively attributed it to contributions to the NMR signal from strain or defects in the still-crystalline regions. The peak shift may be due to increased polymerization, even in the crystalline areas. Farnan and Salje (2001) confirmed the development of a broad peak at a slightly higher chemical shift, characteristic of damaged or amorphous zircon. This amorphous peak also gradually shifted from -86 to -96 ppm with increasing dose, signifying increased polymerization. These combined changes suggest that the structures of both the crystalline and the amorphous regions are not constant but evolve continuously with increasing α-decay dose. This observation was interpreted in terms of the percolation model of Salje et al. (1999) and Trachencko et al. (2000) who noted that the structure of crystalline and amorphous zircon is different in the three percolation regimes.

Polymerization of the $SiO_4$ tetrahedra, as implied by the NMR data, is consistent with the earlier EXAFS results (Farges and Calas 1991) that indicated a decreased coordination of the Zr in metamict zircon. However, Farnan and Salje (2001) showed that in highly damaged or amorphous zircon there is an average of 2-3 bridging oxygens per silicon tetrahedron. These are too many bridging oxygen atoms to make up for the one removed from the Zr coordination polyhedron. In order to maintain charge balance, Farnan and Salje therefore suggested the presence of oxygen interstitials in metamict zircon.

Farnan (1999) observed that the integrated intensities of the sharp and broad peaks can be used to give a measure of the amount of Si in "amorphous" regions, assuming that the concentrations of paramagnetic defects and $U^{4+}$ are negligible (both cause nearby silicon atoms to be undetectable). Farnan and Salje (2001) used the integrated peak intensities to determine the amorphous fraction as a function of α-decay dose. The results did not show a sigmoidal increase in the amor-

phous fraction, $f_a$, with dose, which agrees with the X-ray diffraction results of Ríos (2000a) and the infrared spectroscopy results of Zhang et al. (2001). At low doses, the amorphous fraction detected by NMR was higher than that expected from macroscopic volume swelling, which implies negligible swelling of amorphous domains. This is consistent with X-ray diffraction results that suggest a densification of amorphous regions below the first percolation point.

**Recovery of radiation damage**

The final damaged microstructure of metamict zircon depends on the kinetics of damage accumulation and the kinetics of defect recovery and/or recrystallization. These processes are highly dependent on the ambient temperature and on the irradiation conditions (e.g., dose rate, ion mass and energy, presence of impurities, etc.). In some instances, the recovery processes dominate, and crystallinity is preserved, even at relatively low temperatures. In one of the more striking mineralogical examples, monazite ($CePO_4$) remains crystalline despite extremely high $\alpha$-decay doses (Meldrum et al. 1996, 1998a, 2000). In contrast, natural zircon is frequently found in a moderately- to highly-damaged state, suggesting that the kinetics of the recovery mechanisms are slower in zircon than in monazite. Recrystallization of zircon is a complex process in which several intermediate phase assemblages may form, depending on annealing conditions and the initial microstructure. Studies of the microstructural evolution on annealing of radiation-damaged zircon have been complemented by recent thermodynamic results (Ellsworth et al. 1994). This combination of microstructural and thermodynamic data can provide a more complete picture of the recrystallization mechanisms in zircon.

***Recrystallization mechanisms.*** In general, there are two broad types of recrystallization mechanisms. Type I recrystallization is purely thermal: it occurs on time scales longer than cascade quench times and is due to defect diffusion processes. In general, Type I recovery processes dominate at longer times or at higher temperatures and become particularly important in natural specimens stored at ambient conditions for geologic periods. Type II recrystallization occurs during irradiation—it is a nearly instantaneous process that either decreases the amount of residual damage produced by each displacement event or leads to the annihilation of pre-existing irradiation-induced defects or other types of damage. Type II annealing can be divided into at least two distinct processes. Type IIa recrystallization is due to the increased mobility of interstitials and other point defects during irradiation. This "irradiation-enhanced diffusion" leads to a greater degree of point defect recombination and annihilation. Point defect annihilation is most effective at structural boundaries between amorphous and damaged, but still-crystalline, regions. Type IIb recrystallization occurs within individual displacement cascades. Disordered and highly energetic material can recrystallize epitaxially at the cascade peripheries as the displacement cascade cools to ambient temperature. As the temperature is increased, the cascade cooling time increases from picoseconds to nanoseconds or longer, increasing the effectiveness of Type IIb recrystallization. Type IIb recrystallization has not been directly observed due to the very short timescales involved, but its effects on damage accumulation have been well analyzed and modeled since its elaboration in the classic papers by Morehead and Crowder (1970a,b), and recent experimental evidence supports the importance of this process (Newcomer et al. 1996).

During irradiation, both Types I and II recrystallization processes contribute to dynamic recovery of zircon, but some mechanisms may be more dominant than others in certain temperature regimes. Type I recrystallization can be particularly important in natural samples. Its effects can be straightforwardly investigated and characterized in controlled experiments in which radiation-damaged zircon is thermally annealed in the laboratory. In contrast, Type II recrystallization processes cannot be directly investigated because of the short timescales. However, techniques in which the competing effects of damage accumulation and recrystallization can be simultaneously measured *in situ* can illuminate the effects of Type II recrystallization. With the help of computer simulations, the complex and dynamic damage and recovery processes that occur during picosecond to nanosec-

ond timescales are now better understood than ever before.

***Type I recrystallization.*** In moderately damaged zircon that still retains a significant fraction of crystalline material, Farges (1994), Geisler et al. (2001a), and Zhang et al. (2000c) described a two-stage damage recovery process. In the first stage, X-ray diffraction measurements of air-annealed zircon showed a progressive decrease of the *a* cell parameter with increasing temperature. This effect saturated at ~600°C (Farges 1994). Geisler et al. (2001a) found that the first stage occurs below ~727°C (1000 K) and is characterized by the recovery of short-range order and point defect recombination, as measured by the shift of Raman bands to higher phonon frequencies. Zhang et al. (2000c) observed lattice recovery of partially damaged zircon at temperatures as low as 727°C. When the first stage is complete, the zircon consisted of well-crystallized regions interspersed with still-amorphous domains. The onset of the second stage occurs at higher temperatures. Above 727°C (Zhang et al. 2000c) or 893°C (Geisler et al. 2001a), the $\nu_3$ Raman line-widths decrease and the scattering intensity increases, suggesting a decrease in the amorphous fraction caused by epitaxial recrystallization at the internal crystalline-amorphous boundaries. An initially broad and poorly defined infrared reflectivity peak at 900-1000 $cm^{-1}$ recovered at ~727°C when annealed in an $N_2$ atmosphere (Zhang et al. 2000a). Above 600°C, Farges (1994) reported an increase in the intensity of the Bragg peaks and a gradual increase in the coordination of the Zr cations from seven-fold to eight-fold. This structural reorganization was completed at 900°C. Each of these observations is consistent with high-temperature epitaxial recrystallization of amorphous zircon.

Capitani et al. (2000) performed *in-situ* heating experiments in a transmission electron microscope in order to directly observe the damage recovery process. In a moderately damaged sample ($7\text{-}8 \times 10^{18}$ $\alpha$-decays/g), the initial microstructure consisted of nanoscale grains of crystallographically oriented zircon embedded in an amorphous matrix. These crystalline domains increased in size at a temperature of 827°C (1100 K). This recrystallization occurred epitaxially at the boundaries of the particles. At 927°C, the pre-existing crystalline domains continued to grow but nanoscale grains of tetragonal $ZrO_2$ nucleated in the still-amorphous regions. At 1127°C, there were no amorphous domains or $ZrO_2$ remaining, and the sample consisted of a single crystal of zircon.

The somewhat different temperatures reported in these studies for the onset of epitaxial thermal recrystallization of moderately damaged zircon may be due to the different annealing environments. As noted by Pidgeon et al. (1966) and Geisler et al. (2001b), annealing under hydrothermal conditions is much faster than in an ambient, dry atmosphere. Meldrum et al. (2002a, and references therein) reported faster annealing of perovskites when annealed in air, as compared to the high-vacuum environment in the TEM. These observations are consistent with the slightly higher temperatures reported by Capitani et al. (2001) for TEM-annealed zircon as compared to the studies of Zhang et al. (2000a) and Geisler et al. (2001a). Furthermore, as reported by Biagini et al. (1997), X-ray diffraction is less sensitive to residual damage in annealed specimens than infrared spectroscopy. Therefore, the different techniques may also account for the temperature differences summarized above.

In contrast to the case of moderately damaged specimens, heavily damaged or amorphous zircon segregates into its constituent oxides at high temperatures. For example, Ellsworth et al. (1994) reported the formation of $ZrO_2$ only in the most damaged annealed zircon. Zhang et al. (2000a) heated a highly damaged sample ($15.9 \times 10^{18}$ $\alpha$-decays/g) in an $N_2$ ambient. Above 827°C, the sample decomposed into a mixed assemblage of tetragonal $ZrO_2$ and amorphous $SiO_2$. Capitani et al. (2000) observed the formation of randomly-oriented <10 nm grains of tetragonal $ZrO_2$ at 927°C. Continued heating to 1127°C increased the size of the $ZrO_2$ nanocrystals to 30 nm. Zhang et al. (2000c) reported the formation of tetragonal $ZrO_2$ at 850°C. Weber (1990) observed a peak in density recovery at 1050°C in the Pu-substituted samples, which was attributed to the formation of some $ZrO_2$, as observed by XRD (in a nitrogen atmosphere glove-box). Begg et al. (2000) annealed Pu-substituted zircon that was fully amorphous, as determined by powder XRD. The Pu-substituted zircon decomposed into its constituent oxides at 1000°C. McLaren et al. (1994) observed the for-

mation of $ZrO_2$ at 900°C, in strongly zoned, chemically variable zircon annealed in dry air. In their specimens, heavily damaged optically isotropic zones alternated with less damaged anisotropic zones. Zirconia crystallites approximately 10 nm in diameter were observed to form in both the optically isotropic and anisotropic zones.

At higher temperatures, several authors have reported that the tetragonal $ZrO_2$ crystallites convert to the monoclinic polymorph, baddelyite. McLaren et al. (1994) observed that at 1250°C, the $ZrO_2$ in optically isotropic (i.e., amorphous) zones transformed to baddeleyite with a grain size of ~100 nm, but the initially anisotropic zones reverted to single-crystal zircon containing isolated baddeleyite crystallites. Zhang et al. (2000c) reported the formation of baddeleyite at 1327°C, in their heavily damaged samples. The formation of monoclinic zirconia is not reported in all investigations, so its presence may also be related to the annealing conditions and the microstructure of the specimens.

As the temperature increases, the phase-segregated oxides recrystallize to randomly-oriented polycrystalline zircon with a grain size of up to several hundred nanometers. This process is completed between 1127 and 1227°C (Zhang et al. 2000a, 2002), 1300°C (Nasdala et al. 2002a), and 1327°C (Capitani et al. 2000). Weber (1990) could not unambiguously determine the onset temperature for recrystallization of Pu-doped zircon, but found that the process was completed at 1465°C. Begg et al. (2000) reported that the Pu-substituted zircon decomposed into the component oxides at 1000°C and reverted to crystalline zircon at 1200°C. Zhang et al. (2000c) found that full recovery of the zircon structure requires temperatures in excess of 1227°C. In contrast, Pu-doped specimens that were heated rapidly to 1200°C recrystallized directly to polycrystalline zircon, without first decomposing into the constituent oxides (Begg et al. 2000).

These studies show that for slow or stepwise heating, recrystallization of heavily damaged zircon takes place in three stages:

1. Decomposition of amorphous zircon into tetragonal $ZrO_2$ crystallites and amorphous $SiO_2$. The $SiO_2$ is structurally distinct from conventional $SiO_2$ glass (e.g., Zhang et al. 2000c). This stage occurs at temperatures up to 1127°C.
2. Tetragonal-to-monoclinic phase transformation in the $ZrO_2$ crystallites. When reported, this stage occurs at temperatures up to 1327°C. This transition appears to depend on the time and temperature during stepwise heating experiments and is not reported in all experiments.
3. Formation of coarse-grained (several hundred nanometers), randomly oriented, polycrystalline zircon. This stage has been observed at temperatures between 1127 and 1465°C.

The energetics of radiation damage recovery reported by Ellsworth et al. (1994) can be compared with the microstructure evolution discussed above. Metamict zircon was found to have the highest enthalpy relative to crystalline zircon, followed by tetragonal zirconia + silica glass, and then baddeleyite + quartz. This is exactly the same sequence as reported in Stages 1, 2, and 3. However, the formation of monoclinic zirconia at higher temperatures than the tetragonal phase may be somewhat surprising based on the known stability fields for zirconia (monoclinic $ZrO_2$ transforms to the tetragonal polymorph on heating above ~1200°C). In small particles, surface energy effects can play an important role in stabilizing the various phases. Due to its lower surface energy, tetragonal zirconia is, in fact, the stable room-temperature structure for particle radii below ~5 nm, when the matrix is silica glass (Meldrum et al., in press). The thermodynamics of the phase transitions in annealed zircon are, therefore, strongly affected by the $ZrO_2$-matrix interface.

Finally, Zhang et al. (2000c) reported the formation of an intermediate phase during recrystallization of heavily damaged zircon at temperatures between 527 and 1127°C. This phase gave characteristic Raman peaks at 670, 798, and 1175 $cm^{-1}$, which cannot be attributed to $SiO_2$ glass, $ZrO_2$, or zircon. The authors speculated on the presence of a new type of Si-O-Si linkage.

***Type II recrystallization.*** By measuring the amorphization dose as a function of temperature, *in situ* irradiation experiments permit the effects of Type II recovery to be measured directly. A frequently used technique for investigating Type II recrystallization processes in zircon has involved measuring the amorphization dose as a function of temperature *in situ* during ion beam

irradiation in a transmission electron microscope. The temperatures employed must be lower than those at which Type I recrystallization can be important on the timescale of the experiment. Such measurements have been obtained for natural or synthetic zircon irradiated with $Ne^+$ (Devanathan et al. 1998), $Kr^+$ (Weber et al. 1994, Meldrum et al. 1999b), $Xe^+$ (Meldrum et al. 1999b), $Pb^+$ (Weber et al. 1999), and $Bi^+$ (Weber et al. 1999; see Fig. 9 below). At low temperatures, the amorphization dose is relatively constant for all ion masses. As the temperature increases, a point is reached at which the measured amorphization dose begins to increase. At this temperature, recrystallization processes compete with damage accumulation on the timescale of the experiment. For the $Kr^+$ and $Xe^+$ irradiations, the amorphization curve appears to follow a two-step dependence on temperature. The low-temperature recovery stage was attributed to recombination and annihilation of isolated defects (Type IIa annealing); whereas, the high-temperature stage was attributed to enhanced, epitaxial recrystallization at cascade peripheries (Type IIb annealing). This behavior is not duplicated in the Pb (Meldrum, unpublished data) and Bi (Weber et al. 1999) irradiation results.

At higher temperatures, the amorphization doses increase rapidly and, at the so-called critical temperature ($T_c$), Type II (and/or Type I) recrystallization is so efficient that the zircon does not become electron-diffraction amorphous. The critical temperature can be estimated from the data in Figure 8 as the temperature at which the amorphization curve goes to infinity. Depending on the mass of the incident ions, the critical temperature for zircon is between 527 and 750°C and with the exception of the 600 keV Bi irradiation, $T_c$ increases somewhat with increasing ion mass. The mass-dependent increase in $T_c$ has been observed for many materials and is due to the structure of the damaged material (e.g., Koike et al. 1989). More massive ions produce more concentrated damaged regions; whereas, light ions produce isolated defects and smaller displacement cascades that anneal more rapidly at lower temperatures.

The critical temperature for zircon is unusually high, compared to most other minerals and ceramics (see Ewing et al. 2000). Type II recrystallization is, therefore, slower or less effective in zircon than for many related phases. Particularly striking is the difference between zircon-structure orthosilicates and orthophosphates. The critical temperatures for the orthosilicate phases are higher by several hundred degrees (Meldrum et al. 2000), with only a modest dependence on structure type. This has been attributed to the lower connectivity of the $PO_4$ tetrahedra, which would permit easier rotation and reorganization of these structural units. In contrast, the possible high connectivity of the $SiO_4$ tetrahedra in zircon imposes more severe structural constraints on the recrystallization process (Hobbs 1994).

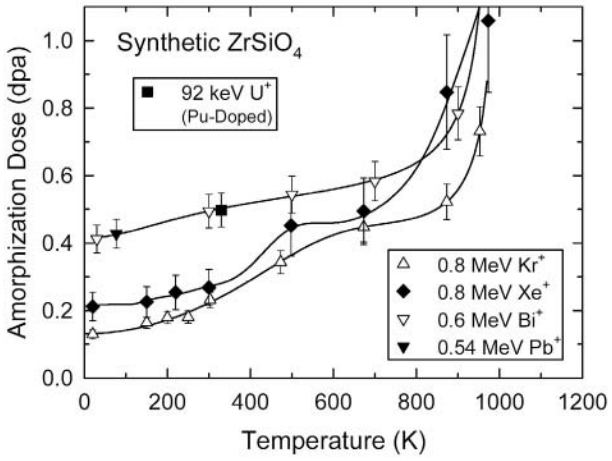


**Figure 8.** Temperature dependence of amorphization dose in synthetic zircons under irradiation with different ions and including the results from alpha decay in Pu-doped zircon. [Used by permission of the Materials Research Society, from Weber et al. (1999) in *Microstructural Processes in Irradiated Materials* (edited by S.J. Zinkle et al.), *Materials Research Society Symposium Proceedings*, Vol. 540, Fig. 1, p. 368.]

Meldrum et al. (1998b, 1999b) showed that nanocrystalline zirconia can precipitate during $Kr^+$ or $Xe^+$ irradiation of crystalline zircon at temperatures above ~775°C. The tetragonal zirconia occurred as

randomly oriented grains approximately 3 nm in diameter surrounded by an amorphous $SiO_2$ matrix. This phase decomposition occurred at lower temperatures (<675°C) in zircon that was pre-amorphized by ion irradiation. The precipitation of tetragonal zirconia was attributed to the formation of a liquid-like state in the collision cascades, followed by nucleation of $ZrO_2$ during the cascade-cooling phase. The $ZrO_2$ nucleates at higher temperatures in crystalline zircon than in pre-amorphized zircon because of competition with Type IIb recrystallization at the cascade peripheries. Another possible interpretation of the results of Meldrum et al. (1998b) is that the zirconia forms purely as a result of irradiation-enhanced cation diffusion at elevated temperatures; therefore, the formation of zirconia has less to do with the evolution of the displacement cascade. Interestingly, the zirconia nanoparticles are themselves susceptible to irradiation-induced amorphization at temperatures below 450°C (Meldrum et al. 2002b), in contrast to bulk $ZrO_2$, which cannot be amorphized by ion irradiation.

***Recrystallization in geologic environments.*** Recrystallization and defect recovery are kinetic processes that are strongly dependent on time and temperature. Processes that are only apparent at high temperatures in the laboratory may be important at considerably lower temperature over geologic time. The early results were somewhat contradictory concerning the recrystallization of zircon at low temperatures over long timescales. Lumpkin and Ewing (1988) found that the calculated dose for the amorphization of natural zircon increased with the geologic age due to annealing. Using a model based on the fission-track fading, they calculated a "half life" of 400 Ma for the $\alpha$-recoil damage cascades in zircon. The calculated half-life should depend on the damage rate and the recovery kinetics (specifically, temperature). While Weber et al. (1994) initially reported similar amorphization doses for ion-beam-irradiated and Sri Lanka zircon, more recent analysis (Weber et al. 1999) showed that the amorphization dose for ion-beam-amorphized natural zircon is less than that for $\alpha$-decay-amorphized Sri Lanka zircon, suggesting some recovery on geologic time scales. Likewise, a comparison of unit-cell parameters (as discussed above) for lightly damaged zircon (Weber 1990) shows strong evidence of lattice relaxation along the *a*-axis in Sri Lanka zircon as compared to neutron-irradiated and Pu-doped zircon, supporting defect recovery in lightly-damaged zircon over geologic time.

Nasdala et al. (1998) found that the U-Pb isotope discordance in zircon does not always correlate with the degree of damage as estimated by the width of the $\nu_3$ Raman peak—possibly as a result of annealing at temperatures above 227°C (Geisler et al. 2001b). Nasdala et al. (2001b) reported that zircon stored in geologically "cold" environments shows no appreciable recrystallization. However, such specimens were rare and most of the zircon specimens, including those from Sri Lanka, provided evidence in favor of recrystallization over geologic time, as determined by the narrower-than-expected $\nu_3$ peak. Complete retention of damage was only observed at the lowest $\alpha$–decay doses; whereas, at higher doses the $\nu_3$ Raman peak-broadening increasingly deviates from the expected linear relationship (Nasdala et al. 2001, Balan et al. 2001). However, Geisler et al. (2001b) suggested that "geologic" recrystallization is only significant at high temperatures (they calculated that it would take 370 Ma to recrystallize "metamict" zircon at a temperature of 700°C). Some disagreement remains as to the interpretation of the Raman spectroscopic data and how the long-term Type I annealing affects the measured Raman bandwidth and frequency (e.g., see Geisler and Pidgeon 2002, Nasdala et al. 2002a).

Meldrum et al. (1998a, 1999a) found that the amorphization dose for natural zircon can be higher than that measured by the *in-situ* laboratory experiments. They observed that since thermal recrystallization is a diffusion-driven process, it occurs at all temperatures, but at different rates. A model was derived that accounted separately for Type I and Type II recrystallization, which allowed the ion beam irradiation data to be compared to data on natural zircon over a wide range of geologic ages (Fig. 9). The curves in Figure 9 are extrapolated from the irradiation data and represent the onset of observable damage (lower curve) and "complete" amorphization (upper curve), as measured by electron diffraction. The data points represent literature data on "crystalline" and "metamict"

zircon from a wide range of sources. The important point here is that the data sets are broadly consistent with the ion beam results (i.e., the structural state of zircon generally plots in the expected field) despite the different experimental techniques used to measure the degree of damage and the different thermal histories of the various specimens.

There are two implications inherent in Figure 9. First, the results suggest that it is possible to extract information from the ion irradiation experiments that is directly applicable to α-decay-damaged zircon, despite the enormous difference in dose rate. This was accomplished by including Type I (thermal recrystallization) in the model of damage accumulation and recovery. Second, the generally consistent results in Figure 9 imply that given enough time, zircon can recrystallize at geologically "cool" temperatures. Temperatures as low as 100-200°C seem to be sufficient to produce measurable recovery effects over extremely long time scales. This result is consistent with the observation of recovery in various suites of zircon (Nasdala et al. 2001) and with the long-term annealing of damage cascades as modeled by Lumpkin and Ewing (1988).

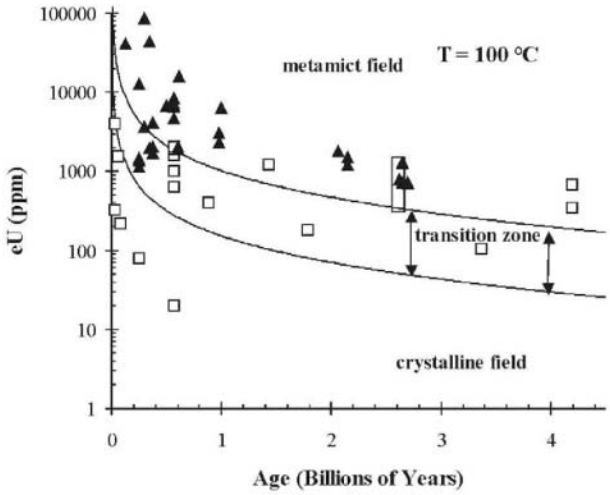


**Figure 9.** Crystalline-to-amorphous transition plotted as functions of equivalent uranium content and age. The lower curve represents the onset of observable damage as measured by electron diffraction, and the upper curve is for "complete" amorphization, at a temperature of 100°C. The open squares represent natural "crystalline" zircon from a variety of locations whose age and equivalent uranium content were measured or calculated. The filled triangles are for "amorphous" natural zircon from different localities. The curves delineate the crystalline-amorphous boundary fairly well, despite the different thermal histories and geologic environments of the different specimens. At higher ambient temperatures, the transitions would be shifted to higher uranium content. [Modified after Meldrum et al. (1999a).]

Recrystallization of radiation-damaged zircon is a complex, multifaceted process that involves different physical mechanisms. Purely thermal, diffusion-driven recrystallization is probably the dominant mechanism in natural zircon, even at relatively low geologic temperatures. The ultimate microstructure depends sensitively on the damage and recovery rates and on the annealing temperature. In contrast, recrystallization that occurs during ion bombardment is largely responsible for the structure of the damaged state. If this recrystallization mechanism is effective, the total atomic disorder produced per damage event will be relatively low. Physically realistic modeling of the various simultaneous damage and recovery processes in zircon present a unique and difficult challenge that will be described in more detail in the following section.

## MODELS OF DAMAGE ACCUMULATION

During the past decade, there has been a major effort to model the damage accumulation process in natural, Pu-doped and ion-irradiated zircon. As previously discussed, each of these experiments provides different amounts of damaged material, from the single crystals of natural zircon to the thin damaged layers of irradiated zircon, and the irradiation experiments are completed at very different dose rates. A critical aspect of the modeling effort has been the determination of the amorphous fraction, for which the measured value is different depending on the type of analytical

technique used, as the analytical method implicitly defines the damaged volume that is considered to be amorphous. One of the most sensitive methods of measuring the amorphous fraction has been the recent use of a 7-circle diffractometer to measure the diffuse diffraction signals from single crystals of zircon (Ríos et al. 2000a). Their results provide strong evidence in support of the direct impact model of damage accumulation; however, with natural samples there is always the issue of annealing over geologic periods. Thus, in this section, we focus the review on data obtained by ion beam irradiations of zircon.

Because of the close, although not perfect, correspondence between the results from actinide-doping experiments (U, Th and Pu) and ion beam experiments (Weber et al. 1994, Weber and Ewing 2000, 2002) substantial effort has been devoted to systematic ion beam experiments combined with *in situ* TEM examination because the irradiation conditions and temperature (-260 to 1000°C) can be carefully controlled. The ion beam studies investigate the effects of temperature, ion mass and energy on the amorphization dose. These studies provide important information on the formation of collision cascades and defect annealing mechanisms (Weber et al. 1994, SX Wang et al. 1998, Weber et al. 1999 and SX Wang et al. 2001). A good summary of the different models can be found in Weber (2000). The experimental data for ion beam-irradiated zircon are designed to test and refine these models.

**Temperature**

The dose required for complete amorphization of zircon irradiated by 1.5 MeV $Kr^+$ increases with temperature in two distinct stages (Fig. 10) (Weber et al. 1994), a behavior similar to that observed in $Ni_xTi_{1-x}$ alloys (Delage et al. 1989). The increase in amorphization dose with temperature (Fig. 10) may be due either to a decrease in the average cascade size caused by thermal relaxation or a reduction in the surviving amorphous volume as a result of thermal annealing of irradiation-induced defects. The first stage (Stage I), which occurs below 300 K, may, as an example, be associated with the intra-cascade recombination of closely-spaced defects, such as the close-pair recombination process suggested by Delage et al. (1989). As the temperature increases above 300 K, the Stage I annealing process ends (Stage I defects have recombined), and the dose for complete amorphization is constant, independent of temperature, between 300 to 473 K. Above 473 K, the amorphization dose again increases with temperature (Stage II), perhaps due to additional intra-cascade recombination of point defects or as a result of irradiation-enhanced epitaxial recrystallization (point defect annihilation at the crystalline-amorphous interface). The second stage (Fig. 10) is a common feature in irradiated

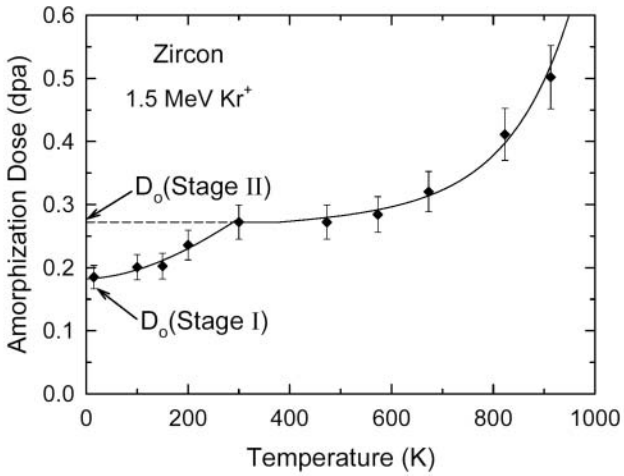


**Figure 10.** Temperature dependence of amorphization dose in natural zircon under irradiation with 1.5 MeV $Kr^+$ ions. [Based on Weber et al. (1994, 1999).]

materials, as well as zircon, and is generally ascribed to irradiation-enhanced recovery processes in amorphization models. Thermal recovery processes alone would exhibit a much sharper increase in amorphization dose with temperature (Weber 2000), and this type of behavior was illustrated in the model used to describe recent set of systematic data for orthosilicates (Meldrum et al. 1999c). Minerals can show a wide variety of behaviors, depending on their structures and compositions, and the two-stage process is not commonly observed (Ewing et al. 2000).

Regardless of the mechanism of damage recovery, the temperature dependence of amorphization dose has be described by the following expression (Weber and Wang 1993, 1994):

$$\ln(1 - D_o/D) = \ln(1/\varphi\sigma\tau) - E_a/kT, \quad (8)$$

where D is the amorphization dose at temperature, T, $D_o$ is the extrapolated amorphization dose at 0 K associated with the damage accumulation stage, $\varphi$ is the ion flux, $\sigma$ is the cascade damage cross section, $\tau$ is a time constant, and $E_a$ is the activation energy for the irradiation-assisted recovery process. A more general form of Equation (8) that has been used for a wide range of materials has been given by Weber (2000):

$$\ln[1 - (D_o/D)^{1/m}] = C - E_a/nkT, \quad (9)$$

where C is a constant dependent on damage rate and both m and n are model dependent order parameters.

Using the model described by Equation (8), an activation energy, $E_a$, associated with each dynamic recovery stage was determined from the data in Figure 10. The amorphization dose, $D_o$, associated with each dynamic recovery stage is also shown in Figure 10. For Stage I, $D_o$ is estimated to be 0.18 dpa, and for Stage II, $D_o$ is estimated to be 0.27 dpa. An Arrhenius plot of $\ln(1 - D_o/D)$ versus 1/kT (Weber et al. 1994) yields $E_a$ as the slope. The activation energy determined by linear regression analysis for Stage I is 0.02±0.01 eV, and the activation energy determined for Stage II is 0.31±0.03 eV. Incorporating these parameters into Equation (8) provides an excellent fit to the data in Figure 10, as shown by the curve. Using a more complex model that assumes only thermal annealing and experimental data obtained under slightly different irradiation conditions, Meldrum et al. (1999a) obtained activation energies of 1.0 to 1.8 eV for Stage I and 3.1 to 3.6 eV for Stage II. As noted by Weber (2000), the dynamic recovery processes within each stage are probably more complex than the single activation energy process suggested by either the irradiation-assisted recovery model represented by Equation (8) or the thermal recovery model of Meldrum et al. (1999a). The actual behavior probably involves both irradiated-assisted and thermal recovery processes, but the number of parameters involved makes fitting to limited data sets challenging.

The low value of the activation energy for Stage I determined by Weber et al. (1994) suggests an irradiation-enhanced close-pair recombination process, while the higher activation energy of Meldrum et al. (1999a) suggests a thermal diffusion process. In either case, or combination thereof, these processes occur nearly instantaneously above 300 K. While these recovery processes are insufficient to prevent complete amorphization, they reduce the amount of damage that survives each cascade at temperatures above 300 K. Weber et al. (1994) noted that the activation energy determined for Stage II annealing in zircon is similar to activation energies reported in other materials for an irradiation-enhanced epitaxial recrystallization, which is a process stimulated by the irradiation-induced defects. The thermal activation energies of 3.1 to 3.6 eV determined for Stage II by Meldrum et al. (1999a) are in reasonable agreement with the activation energy, 3.6 eV, for thermal track annealing (epitaxial thermal recrystallization) in zircon (Virk 1995). As noted above, the actual behavior in zircon may be due to a more complex combination of all of these recovery processes. Nevertheless, as the temperature approaches the temperature for amorphization, $T_c$, the dynamic recovery rates become increasingly large, competing with the damage production rate. Above $T_c$, the damage recovery rates dominate and inhibit amorphization.

A general relationship for the dependence of amorphization temperature on activation energy can be derived from all these models (Weber et al. 1994, Meldrum et al. 1999a, Weber 2000) and expressed as:

$$T_c = E_a/[k \ln \Omega], \quad (10)$$

where $\Omega$ is a constant that is independent of damage rate for irradiation-assisted processes and dependent on damage rate for thermal recovery processes (Weber 2000). In Equation (8), $\Omega$ is given by $1/\varphi\sigma\tau$, which has been determined from the fit of the equation to the data in Figure 10. Using these parameters and Equation (10), the critical temperature, $T_c$, for zircon under these irradiation conditions is estimated to be 1101 K. In general, this is not an accurate way to determine $T_c$. However, Weber and Ewing (2002) have reported that $T_c$ for synthetic zircon is 975 K for a range of ions at a given dose rate and, thus, $T_c$ appears to be controlled mainly by thermal recovery processes. Using these results and Equation (10), Weber and Ewing (2002) predicted the dose rate dependence of $T_c$ for plutonium-containing zircon. By extending this analysis to the lower damage rates of natural minerals, the value for $T_c$ for zircon should have an upper limit of 460 K.

The models represented by Equations (8) and (9), as well as similar models on the temperature dependence of amorphization dose, are limited and can only be applied to data of the type shown in Figure 8. As such they do not describe the evolution of damage, but only the temperature dependence of attaining the final amorphous state. Thus, data of the type shown in Figure 10 cannot be used to confirm the mechanism of amorphization. Determining the mechanism of amorphization requires data on the evolution of the amorphous state, expressed as an amorphous fraction as a function of dose. While such models have been derived for various amorphization mechanisms (Weber et al. 1994, Meldrum et al. 1999a, Weber 2000), the mechanism of amorphization remains problematic due to a lack of data and limitations in directly measuring the amorphous fraction. Depending on the analytical technique, the "amorphous" fraction may include defect-rich crystalline domains or even isolated defects.

Based on a model of direct impact and cascade overlap, SX Wang et al. (1998, 2001) developed a different approach to describe irradiation-induced amorphization. In their model, each incident ion was assumed to create a small amorphous volume due to the rapid "quenching" of the "molten"-like displacement cascade. By analogy, the amorphization process was considered to be the result of "cascade quenching." The general features of a "quenched" cascade are similar, that is a less dense amorphous core, surrounded by halo of high defect density that grades into the crystalline matrix. Because of the presence of the crystalline matrix around the amorphous cascade core, the dominant recrystallization process is epitaxial annealing at the amorphous domain boundaries. Thus, epitaxial-recrystallization was assumed to be the recovery process during cascade "quenching."

The equation that describes the damage accumulation process is based on the damage volume of a single cascade. The formation of the individual displacement cascade with a volume, $V_0$, was initially assumed to remove all of the crystallinity within its boundary. The "crystallization efficiency," A, represents the volume fraction of the recrystallized shell within a single cascade, for a crystalline matrix. If there are amorphous "cores" left in the displacement cascades, the amorphous fraction will accumulate with the increasing ion dose. Because epitaxial growth relies on a crystalline interface, an increasing amorphous fraction in the material reduces the extent of recrystallization of a cascade. This process is described by the following differential equation:

, (11)

where N is the number of ions; m is the number of individual sub-cascades created by one incident ion; $V_T$ is the total volume of the thin sample (or the damaged layer); $V_c$ is the crystalline volume within $V_T$; $V_0$ is the volume of a sub-cascade. The recrystallized volume may develop in any direction from that surface. In this model, Wang et al. (2001) have adopted a simple description of the recrystallization process: with the last term at the right hand side of Equation (11). Integrating the equation from zero to N ions (the initial condition is that $V_c/V_T = 1$ when N = 0) and using D for ion dose, the amorphous fraction, $f_a$, is:

$$f_a = 1 - \frac{1}{\sqrt{A + (1-A)\cdot \exp\left(\frac{mV_0}{h}\cdot 2(1-A)\cdot D\right)}} \tag{12}$$

where h is the sample thickness (assuming h < ion range).

The amorphous fraction as a function of ion dose has been plotted for different crystallization efficiency values using Equation (12). For small A, $f_a$ behaves as a simple exponential function. For large A, especially for A close to 1, the $f_a \sim D$ curve is sigmoidal, and the sigmoidal character of the curve becomes more obvious with increasing A. When A = 1, $f_a$ is zero regardless of dose. Thus the different $f_a \sim D$ curve shapes previously assumed to represent different amorphization mechanisms (Gibbons 1972), i.e., from defect accumulation to multiple cascade overlap to direct impact cascade amorphization, may all be explained by the cascade "quenching" model by only varying the crystallization efficiency parameter, A. Because A represents the recrystallization efficiency, it must vary with the temperature and the properties of the target material. The recrystallization efficiency may be given by:

$$A = A_0 \cdot \exp[-E_a/(k\ T)], \tag{13}$$

where $A_0$ is a pre-exponential constant; $E_a$ is the activation energy for the dynamic annealing of a cascade; k is the Boltzmann's constant; T is the sample temperature.

The pre-exponential constant, $A_0$, can be determined by specifying a boundary condition. According to Equation (13), A increases with increasing temperature. When the temperature reaches a certain value, A equals 1 (A approaches 1 with increasing temperature because this causes a decrease in the cascade volume due to recrystallization). At a critical temperature, $T_c$, the entire damaged volume is recrystallized (no further amorphization occurs when $T \bullet T_c$). Using $T_c$ as a boundary condition, Equation (13) becomes:

$$A = \begin{cases} \exp\left[\dfrac{E_a}{k}\left(\dfrac{1}{T_c} - \dfrac{1}{T}\right)\right], & for \quad T < T_c \\ A = 1, \quad for \quad T \geq T_c \end{cases} \tag{14}$$

or

$$A \mid \begin{cases} \left[1 - \dfrac{T_c - 4\,T}{T_m - 4\,T}\right]^b, & for \quad T \{ T_c \\ A \mid 1, \quad for \quad T \varnothing T_c \end{cases} \tag{15}$$

where b is a sub-cascade shape-parameter that has a value between 2 to 3, depending on cascade shape (b = 2 for a cylinder, b = 3 for a sphere, 2 < b < 3 for an ellipsoid); $T_m$ is the melting temperature of the target material; $T_c$ is the critical temperature of the sample above which full recrystalli-

dose have been derived and simplified as:

$$D_c = \frac{D_0}{1 + \exp\left[\frac{E_a}{k}\left(\frac{1}{T_c} - \frac{1}{T}\right)\right]} \tag{16}$$

or

$$D_c = \frac{D_0}{\left[\frac{T_c}{T_m}\right)^3}^{\beta}, \tag{17}$$

where $D_0$ is the amorphization dose extrapolated to T = 0 K. $D_0$ incorporates all the temperature independent terms (h, m, $V_0$ and $\Delta_c$). This model also provides an excellent fit to the temperature dependence of amorphization dose in zircon under 1.5 MeV $Kr^+$ irradiation (SX Wang et al. 2001).

**Ion mass and energy**

Irradiations of single crystals of zircon have been completed at room temperature with 1.5 MeV $Xe^+$, 0.7 MeV $Kr^+$, 1.5 MeV $Kr^+$, 1.5 MeV $Ar^+$, 0.8 MeV $Ne^+$, 0.54 MeV $Pb^+$ 0.6 MeV $Bi^+$ ions to investigate the effects of damage energy density (eV/nm/ion) on the amorphization dose (Weber et al. 1994, 1999). Complete amorphization occurred for all ions and energies. The effect of the damage energy density on the amorphization dose is shown in Figure 11. Also shown is the amorphization dose (2.3 dpa) for a 2 MeV $He^+$ implant in zircon, as well as the amorphization dose (0.59 dpa) corresponding to $f_a$ = 95% in polycrystalline Pu-doped zircon (this dose calculation includes only the 92 keV $U^+$ recoil-nucleus contribution). These results show that the amorphization dose under the high dose rates (~$10^{-4}$ to $10^{-3}$ dpa/s) for heavy-ion irradiations is nearly identical to that of Pu-doped zircon ($3 \times 10^{-9}$ dpa/s), which suggests that the amorphization process is independent of the damage source and dose rate. The minimum in amorphization dose for the 1.5 MeV $Ar^+$ irradiation, as compared to the heavier ions, may reflect the greater survivability of point defects from intra-cascade recombination due to the smaller cascade size created by the lower average recoil energy. In the case of $Ne^+$ and $He^+$ irradiation, the damage consists of a larger fraction of isolated displacements (point defects) and small well-separated displacement sub-cascades. Consequently, significant recovery of the isolated point defects (e.g., close pairs) will occur during irradiation, and substantial cascade overlap, particularly for the $He^+$ irradiations, is required to achieve the critical defect density for amorphization. These results have shown that the kinetics of amorphization are qualitatively different for light and heavy ions.

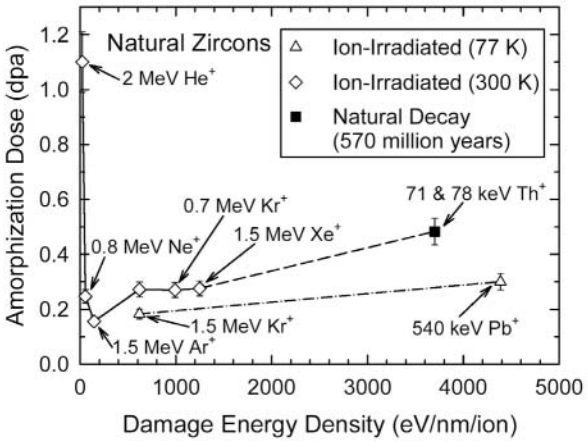


**Figure 11.** Dependence of amorphization dose on damage energy density in natural zircons under different irradiation conditions. [Modified from Weber et al. (1999).]

Recently, Weber et al. (1999) have summarized all of the ion beam irradiation results for zircon. The general fea-

tures of the damage process are clear: The amorphization dose for zircon exhibits two distinct stages with increasing temperature (Fig. 10). The transition temperature between stages for natural zircon occurs at a much lower temperature (300 K) than for synthetic zircon (500 K), perhaps due to the presence of impurities in the natural zircon. The amorphization dose also increases with damage energy density, as determined by varying the mass and energy of the ions. This is behavior may seem to be inconsistent with the direct impact model, but also may reflect the effect of changes in the cascade size and geometry on relaxation and recrystallization processes. At present, no single model captures the behavior of zircon from the three types of radiation experiments, and different analytical techniques sample different volumes of "damaged" material. The three models that we have presented (Weber et al. 1994, Meldrum et al. 1999a, SX Wang et al. 2001) are certainly over simplifications of the damage accumulation process; however, they do give the reader a good sense of the types of processes that occur during the damage process. There are at present a variety of models, some representing combinations of processes (Weber 2000), but no single analytical technique provides the required resolution over all dose ranges to distinguish among these models. The critically missing information has been the description of cascade formation and relaxation processes and the interactions between the cascades as they overlap. This has led to the recent spate of simulation studies described in the next section.

## COMPUTER SIMULATION OF DEFECT FORMATION AND RADIATION DAMAGE

Atomistic computer simulations have been used to understand atomic-level processes related to the radiation damage process during cascade formation. Theoretical methods, such as *ab initi*o calculations and molecular dynamics (MD) simulations, are used to study the behavior of intrinsic, or native, defects (e.g., interstitials and vacancies) and extrinsic defects associated with impurities, and to determine the minimum energies required to permanently displace atoms due to the transfer of kinetic energy. With the advent of large-scale computing, MD simulations are also used to determine the distribution and nature of intrinsic defects, extended defect structures, and solid-state transformations resulting from the collision cascade produced by energetic ions, such as the $\alpha$-particle and recoil nucleus produced in an $\alpha$-decay event. At present, three computer simulation methods have been used to study intrinsic defects and radiation damage processes. One is based on well-established static-lattice energy minimization methods (Catlow and Mackrodt 1982, Agullo-Lopez et al. 1988), and another is based on MD methods (Agullo-Lopez et al. 1988, Eckstein 1991). Both employ empirical interatomic potentials to describe the interactions between all atoms (e.g., Zr-O, Zr-Zr, Si-O; Si-Si, and Zr-Si). The third method, which is applicable only to defect production from ion-solid interactions, is the binary collision approximation, BCA, (Eckstein 1991, Robinson 1994) that employs a universal scattering potential to describe the scattering physics between atoms. The BCA is a higher energy approximation, in which the trajectories of energetic particles are simulated by a series of two-body collisions. Static-lattice methods are essentially "zero Kelvin" calculations, with no representation of thermal effects. In contrast, MD simulations include the kinetic energy explicitly by solving, in an iterative numerical procedure, Newton's equations of motion for an ensemble of particles. The main limitation of the MD technique is the narrow range of time-scales (picoseconds to nanoseconds) that can be simulated.

Computer simulation of radiation damage processes in metals and semiconductors is a mature area of research (Guinan and Kinney 1981, Robinson 1994, Gao and Bacon 1995, Gao and Weber 2002, Nord et al. 2002), where the results provide important atomic-level insights into the radiation damage process and interpretation of experimental data. In contrast, computational studies of defects and radiation damage processes in zircon are a rather new effort (Crocombette and Ghaleb 1998b, Meis and Gale 1998, Williford et al. 1998). The essential concern in the application of these techniques is that the interatomic potentials must not only accurately describe the crystal structure, but also the elastic constants, defect formation and migration energies, and the hard-sphere scatter-

ing physics of energetic particles at short interaction distances.

**Intrinsic and extrinsic defect energies**

The formation energies of native defects and impurities in zircon are important to: (1) identifying the lowest energy configurations for interstitial and vacancy defects, (2) determining the probability for stable anti-site defects, and (3) identifying the stable configurations for incorporation of impurities, such as U, Th and Pu, and the decay-products, such as helium. In addition, the migration energies of the intrinsic defects determine the nature of the damage recovery processes and self-diffusion mechanisms that occur as a function of time and temperature.

Static, energy minimization methods, using classical potentials based on either rigid ion or shell models, have been used to determine the formation energies of vacancy and Frenkel defects in zircon (Meis and Gale 1998, Williford et al. 1999, Akhtar and Waseem 2001, Park et al. 2001). The standard method for determining the formation energy of a vacancy is to calculate the difference in bulk potential energy, with and without the defect, correcting appropriately for the chemical potential of the affected species. Despite their differences, it is useful that classical interatomic potentials yield formation energies for vacancies on the order of 80, 105, and 24 eV for Zr, Si, and O, respectively. These are rather high, but do not consider the defect reactions necessary to form a vacancy by actual Schottky or Frenkel mechanisms, which maintain charge neutrality and stoichiometry. Based on different interatomic potentials, the formation energies for intrinsic Frenkel defects (interstitial-vacancy pairs) on the Zr and O sublattices have been calculated to be 9.4 and 8.2 eV by Meis and Gale (1998), 15.6 and 6.3 eV by Akhtar and Waseem (2001), and 31.7 and 9.0 eV by Park et al. (2001), respectively. A more accurate determination of the defect formation energies may be obtained by *ab initio* methods. These methods have been applied to determine the structural properties of the low-pressure and high-pressure phases of zircon with high accuracy (Crocombette and Ghaleb 1998a), and similar methods have been applied to determine the defect formation energies (Crocombette 1999). The *ab initio* calculations yield formation energies for Zr, Si, and O vacancies of 5.9, 5.8 and 5.6 eV, respectively, and for Zr, Si, and O interstitials of 18.0, 17.0, and 1.7 eV, respectively (Crocombette 1999). The formation energies for intrinsic Frenkel defects, determined by *ab initio* calculations, are 24.0, 22.9, and 7.3 eV for Zr, Si, and O, respectively. Using classical potentials, the formation energy for the Si intrinsic Frenkel defect is estimated to be 13.9 eV (Akhtar and Waseem 2001) or 24.3 eV (Park et al. 2001). There are considerable differences between the *ab initio* and classical potential results, particularly for the cations, that are not sufficiently understood. However, all the results indicate high formation energies, which suggests that it should be difficult to form intrinsic defects in zircon.

Based on rigid ion classical potentials, the migration energies for Zr and O vacancies along different paths have been calculated (Williford et al. 1999). Both Zr and O vacancies migrate three-dimensionally with activation energies of 1.27±0.11 and 1.08±0.09 eV, respectively. These low vacancy migration energies, suggest radiation-induced vacancies should migrate and anneal in the crystalline structure at intermediate temperatures at laboratory time scales and at ambient temperatures over geologic time scales. Migration energies have not been calculated for interstitial defects. The activation energy for thermal diffusion is the sum of the formation and migration energies for the defect responsible for diffusion. The activation energy (8.4 eV) for Hf diffusion has been experimentally determined by Cherniak et al. (1997), which should be similar to that of Zr because of their similar size and charge. Likewise, the activation energy for O diffusion (4.7 eV) has been experimentally determined by Watson and Cherniak (1997). If thermal self-diffusion occurs by intrinsic vacancy migration, as is usually assumed, and if the calculated vacancy migration energies are reasonably accurate, then the formation energies for intrinsic vacancies are much lower than the calculated Frenkel defect energies. Either the calculations have large errors or another intrinsic vacancy formation process, such as the Schottky defect, may occur. However, both *ab initio* (Crocombette 1999) and classical potential (Akhtar and Waseem 2001) calculations indicate higher

formation energies of 34.1 and 8.52 eV, respectively, for intrinsic Schottky defects.

The formation energy (9.4 eV) for the extrinsic defect formed by the substitution of $U^{4+}$ for $Zr^{4+}$ has been determined using classical potentials (Meis and Gale 1998). Because of the interest in using zircon to immobilize plutonium, the formation energy of $Pu^{4+}$ substitution for $Zr^{4+}$ was determined to be 8.3±0.2 eV using classical potentials (Meis and Gale 1998, Williford et al. 2000), while that of $Pu^{3+}$ substitution for $Zr^{4+}$ is 37.75 eV (Williford et al. 2000). The lower energy for substitution of $Pu^{4+}$ relative to $U^{4+}$ may be due to the slightly smaller ionic radius of Pu as compared to U. By taking into account the defect and lattice formation energies, the actual energy required for the substitution of $U^{4+}$ for $Zr^{4+}$ is 0.28 eV per U atom (Akhtar and Waseem 2001), while that for the substitution of $Pu^{4+}$ for $Zr^{4+}$ is 0.26 eV per Pu atom (Williford et al. 2000). In the case of $Pu^{3+}$ substitution on the $Zr^{4+}$ site, as might be the case for preparation under reducing conditions, the lowest energy defect configuration (1.02 eV per Pu atom) is for a defect cluster consisting of two $Pu^{3+}$ substitutions on near-neighbor $Zr^{4+}$ sites and a neighboring charge-compensating oxygen vacancy (Williford et al. 2000, Muller and Weber 2001).

Using transition state theory (Henderson 1972), the activation energies for self-diffusion in zircon of $U^{4+}$ and $Pu^{4+}$ in the presence of intrinsic vacancies are 5.9 and 5.6 eV along the [021] direction, respectively; and 9.3 eV for both $U^{4+}$ and $Pu^{4+}$ along the [111] direction (Meis and Gale 1998). The calculated activation energy for U diffusion is slightly lower than the average experimental value (7.5 eV) determined for U self-diffusion (Cherniak et al. 1997). This suggests formation energies for intrinsic vacancies of 1.5 to 2.0 eV, much lower than those calculated.

## Threshold displacement energies

One of the fundamental parameters affecting radiation damage in a material is the threshold displacement energy, $E_d$, which is the minimum kinetic energy necessary to displace an atom from its normal site. The parameter $E_d$ is essential for quantifying an irradiation dose in terms of the number of displaced atoms in the irradiated material, which allows quantitative comparisons of α-decay event damage with neutron or ion-beam irradiation damage. Static energy minimization methods using classical potentials were first employed to determine the threshold displacement energies in zircon (Williford et al. 1998). Similar calculations have been performed more recently (Meis, personal communication). The results are summarized in Table 1. While the Zr and O displacement energies are similar, there is a significant difference in the Si displacement energies that result from differences in interatomic potentials. The threshold displacement energies of Williford et al. (1998) have been used in comparisons of radiation damage in zircon due to α-decay and ion irradiations (Weber et al. 1999).

Two studies (Park et al. 2001, Crocombette and Ghaleb 2001) have used classical potential based MD simulations to determine threshold displacement energies (Table 1). The results of the MD study by Park et al. (2001) showed that threshold displacement events occur at energies ranging from 23 to 200 eV. In nearly all cases, the threshold displacement events produce multiple displacements (multiple Frenkel pairs, antisite defects and replacements). The production of a single Frenkel pair is rare. The threshold displacement energies determined by Park et al. (2001) are significantly less than those calculated by Crocombette and Ghaleb (2001).

With the exception of the early results by Williford et al. (1998), the more recent static and MD results in Table 1 are consistent in that oxygen has a much lower displacement energy than Zr or Si, which exhibit comparable displacement energies (within 10 eV). While there are few experi-

**Table 1.** Calculated threshold displacement energies in zircon.

| *Method* | *Zr (eV)* | *Si (eV)* | *O (eV)* | *Reference* |
|---|---|---|---|---|
| energy minimization | 80 | 20 | 45 | Williford et al. 1998 |
| energy minimization | 76 | 85 | 38 | Meis, personal communication |
| molecular dynamics | 90 | 98 | 32 | Crocombette & Ghaleb 2001 |
| molecular dynamics | 60 | 48 | 23 | Park et al. 2001 |

mental results, the displacement energies for Zr in Table 1 are in reasonable agreement with the values (41 to 97 eV) estimated for Zr in zircon from experiment (Devanathan et al. 1998).

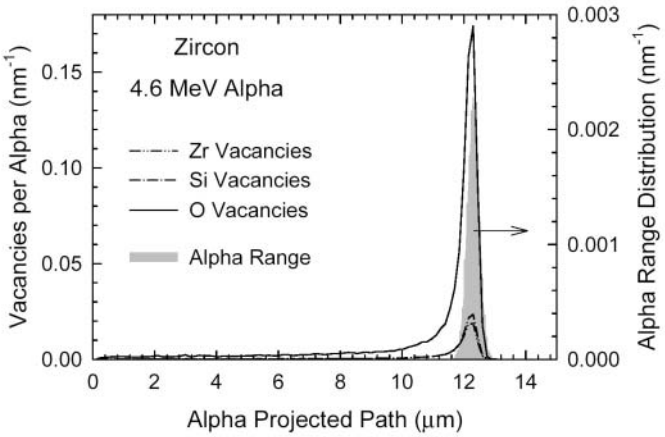


**Figure 12.** Calculated number of vacancies produced along the path of 4.6 MeV alpha particles in zircon, along with the distribution of alpha particle ranges, using the BCA code SRIM.

## Collision cascades

Energetic α-particles in an α-decay event dissipate most of their energy by ionization processes over a range of 16 to 22 μm, but undergo enough elastic collisions along their path to produce several hundred isolated atomic displacements. The largest number of displacements occurs near the end of the alpha-particle range. The partitioning of the energy loss by alpha-particles between ionization and elastic collisions, the range of the alpha particles, and the distribution of displaced atoms, if the threshold displacement energies are known, can be determined by computational approaches based on the binary collision approximation (BCA). The more massive but lower energy alpha-recoil particle accounts for most of the total number of displacements produced by alpha decay in zircon. The alpha-recoil loses nearly all of its energy in elastic collisions over a very short range (30 to 40 nm), producing a highly localized collision cascade of 1000 to 2000 displacements. The density of energy deposited into the crystal structure by an alpha-recoil cascade is high (up to 1 eV/atom) and occurs over a very short time ($<10^{-12}$ s). The spatial extent of the alpha-recoil cascade can be calculated reasonably well by BCA codes, but the binary collision approximation is generally not as quantitative for determining the number of displacements or nature of the damage on such a localized cascade. The binary collision approximation also does not account for any simultaneous recombination events that may occur. Molecular dynamic simulations provide the only means of calculating the primary damage state in such cascades. While such simulations can be performed, the results are sensitive to interatomic potentials, and current methodologies limit the range of energies that can be simulated.

Given the threshold displacement energies, the production of displacements in these polyatomic materials by ballistic processes can be determined by computational approaches based on the binary collision approximation (BCA). These computational approaches generally involve using codes, such as TRIM (Ziegler et al. 1985, Ziegler 2002) and MARLOWE (Robinson 1994, Oak Ridge National Laboratory 2002), in which the elastic atomic scattering is described by a universal screened scattering potential. The universal screened scattering potential developed by Ziegler, Biersack and Littmark (1985), the ZBL potential, is most commonly used because it provides a reasonably accurate description of the nuclear stopping power and energy dissipated by elastic atomic scattering collisions, which has been demonstrated by consistent agreement with experimental measurements of scattering cross sections and energetic particle ranges in solids. The TRIM (Transport and Range of Ions in Matter) code assumes an aperiodic solid and uses a Monte Carlo method to determine the scattering angle and energy transfer that results from each binary elastic collision. TRIM is now part of a package of programs in SRIM (Stopping and Range of Ions in Matter) (Ziegler 2002). MARLOWE is a BCA code that does take into account atomic-scale periodicity. The binary collision approximation, however, is a high-energy approximation that is most appropriate for high-energy collisions and for light ions, e.g., α-particles. Using the threshold displacement energies

from Park et al. (2001), calculations with TRIM of the atomic displacements produced by the 4.6 MeV α-particle from the decay of $^{235}$U are shown in Figure 12 as a function of projected range. The average range of the α-particle is 12.1±0.3 μm, and a total of about 178 displaced atoms, mostly oxygen, are produced by each α-particle, primarily near the end of the range.

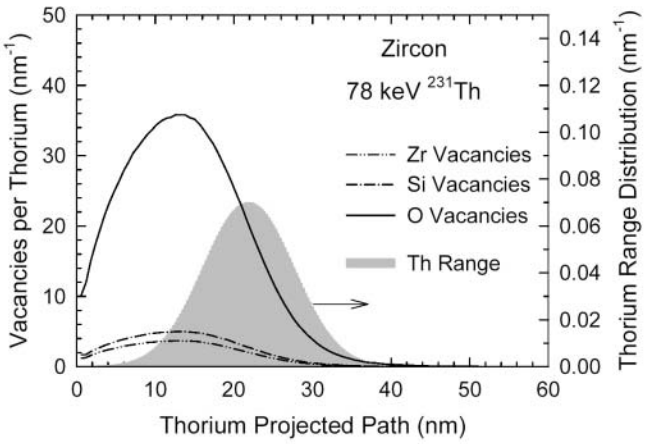


**Figure 13.** Calculated number of vacancies produced along the path of 78 keV $^{231}$Th recoils in zircon, along with the distribution of Th ranges, using the BCA code SRIM.

At low energies the trajectories of recoils are not easily described by discrete collisions, such as in an α-recoil cascade, and the BCA is less useful because it fails to account for the simultaneous recombination of Frenkel pairs, as well as amorphization processes that may be associated with high-energy deposition. However, the spatial extent of the cascade and range of the α-recoil are well described by the BCA. Using the same threshold displacement energies as above, TRIM calculations for 78 keV $^{231}$Th recoils released in α-decay of $^{235}$U in zircon are shown in Figure 13, as a function of projected range. The average range for 78 keV $^{231}$Th α-recoils is 21.7±5.7 nm, and a total of 932 atoms are displaced by elastic collisions, mostly oxygens. Similar results are obtained using MARLOWE, which incorporates the structure of zircon, and a typical α-recoil cascade is illustrated in Figure 14. The $^{231}$Th recoil shown in Figure 14 has a range of 24 nm, and the cascade exhibits the branching typical of sub-cascade development. Because MARLOWE, and other BCA codes, do not account for defect recombination or collective displacements associated with direct impact amorphization, the region of high defect density along part of the U recoil track may occur as an amorphous domain in an actual material.

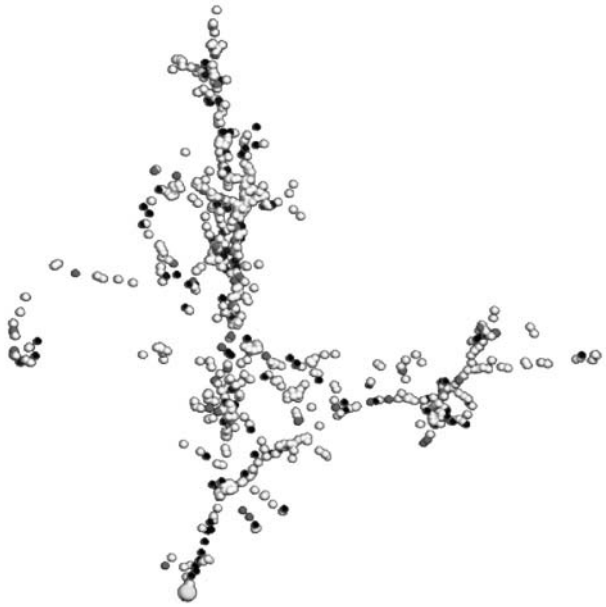

**Figure 14.** Calculated spatial distribution of vacancies produced by a typical 78 keV $^{231}$Th recoil in zircon using the BCA code MARLOWE.

While MD simulations provide the only means of eventually calculating the nature of the primary damage state from energetic cascades in zircon, the total volume necessary to contain the α-recoil cascade in Figure 14 is $1.56 \times 10^4$ nm$^3$, containing 1.44 million atoms. Such large arrays of atoms with their complex interactions cannot be handled by current MD calculations. Thus, MD simulations of realistic α-recoil cascades are not presently feasible, and MD simu-

lations of α-particle cascades may remain beyond the computational capability of MD methods for some time to come. As a result, the BCA calculations provide the most realistic simulation of α-particle damage, and those on α-recoils provide a good representation of the spatial extent of the cascade and the branching that is expected due to sub-cascade formation. The BCA codes provide a means of semi-quantitatively comparing the results from ion-beam irradiation of zircon by different masses and energies and with the results of self-radiation due to α-decay. In many materials, the essential physics of damage production can be obtained from less energetic cascades, and the standard approach is to investigate cascade damage production as a function of recoil energy. The recoils can be incorporated U or self-ions, such as Zr, Si, or O.

Because of the small time (picoseconds) and distance scales (tens of nanometers) associated with damage production, MD simulations are ideally suited for the study of primary damage processes and understanding the atomic-level dynamics of the structural response to a recoil event. Studies of cascades in oxides, such as zircon, by MD simulation have been limited by the computational cost associated with the long range of the Coulomb interaction and the lack of reliable interatomic potentials. For MD simulations of displacement cascades, the interatomic potentials need to describe the structure, elastic constants, and defect energies, as well as correctly describe the physics of classical atomic scattering, within the repulsive component of the potential, that is associated with the energetic elastic collision processes. Classical atomic scattering and nuclear stopping are well described by the ZBL universal scattering potential developed by Ziegler et al. (1985). As a result, experienced researchers have long employed the ZBL potential to describe the short-range interactions in MD simulations of collision cascades in metals, semiconductors, and oxides. Under such conditions, the ZBL potential is smoothly fitted to the potential for medium-range and long-range interactions. Alternatively, some researchers have used *ab initio* quantum mechanical calculations to determine the repulsive nature of the interatomic potential, but even under these conditions, the ZBL potential is often used as a benchmark for validating the potential. It is important to note that while the BCA codes take into consideration both electronic and nuclear interactions, the MD approach generally only considers the nuclear (i.e., elastic scattering) interactions.

Due to computational constraints, most MD simulations of zircon have been of low-energy displacement cascades (Crocombette and Ghaleb 1998b, 1999, 2001; Devanathan et al. 2002, Trachenko et al. 2001, 2002). Crocombette and Ghaleb (1998b, 1999, 2001) used a Born-Mayer-Huggins potential fit to the ZBL potential for atomic distances less than 0.1 nm. Similarly, Devanathan et al. (2002) used the rigid ion potential of Park et al. (2001) with energy partitioned into long-range (Coulombic) interactions, short-range (Buckingham-type potential) interactions, and close-pair (ZBL potential) interactions. Trachenko et al. (2001) used a Coulombic model with Buckingham-type and three-body potentials, but no modification was made to account for the hard-sphere collisions at short interaction distances. Trachenko et al. (2002) did use a short-range repulsive potential correction to the Buckingham-type potential; however, the repulsive potential differs significantly from the ZBL potential and predicts significantly larger scattering cross sections for some atom pairs. This affects the interactions and ranges of the primary and secondary recoils, thus affecting the distribution in energy deposition and spatial extent of the cascade. The differences in the potentials, and perhaps, in the simulation methodologies, have led to significant differences in the results reported by Trachenko et al. (2001, 2002) and others (Crocombette and Ghaleb 1998b, 1999, 2001; Devanathan et al. 2002).

Crocombette and Ghaleb (1998b) investigated low energy displacement cascades initiated by self-ions with energies from 0.5 to 2.0 keV. They also investigated the cascade produced by 4 and 5 keV U recoils in pure zircon (containing only the one U substituted for Zr) and in which 4 and 12% of the Zr atoms are replaced by U (Crocombette and Ghaleb 1999, 2001). As expected, they found a linear increase in crystal volume with increasing U. Both self-ions (Zr, Si, and O) and the U recoils produced displaced atoms, with over half recovering to their original sites within less than a picosecond. They did not observe the collective movement of the silicon tetrahedra, as has been

observed in glasses (Delaye and Ghaleb 1997), and they reported that no displaced Si atom had the same oxygen neighbors before and after the collision. The low-energy U-cascades result in the creation of a cylindrical amorphous region along the path of the U-recoil, which has a range of about 4 to 5 nm. The amount of disorder decreased from the core to the outer shell of the track. The structure of the amorphous core is similar to that of the bulk amorphous volume created by a MD simulation of a melt-quenched zircon. The number of oxygen displacements is a factor of 5 to 20 higher than either the Zr or Si displacements, which is generally consistent with the more recent calculations of threshold displacement energies (Table 1). Surprisingly, no isolated point defects are observed. Many Zr atoms exhibited a decrease in coordination number from eight to seven or six in the cascade core, which is consistent with some experimental observations (Farges and Calas 1991, Farges 1994, Hess et al. 1998). At the same time, they observed some Si atoms are coordinated by five O atoms, which they attribute to a possible non-physical aberration of the empirical potential due to the lack of three-body terms. While the $SiO_4$ tetrahedra in crystalline zircon are isolated, they exhibit some polymerization in the core of the cascade. However, some connectivity between $SiO_4$ tetrahedra is expected due to the random displacement and relaxation of individual atoms. There are experimental NMR (Farnan and Salje 2001) and infrared absorption (Zhang and Salje 2001) evidence for some $SiO_4$ polymerization in natural zircons, but synthetic zircons irradiated at room temperature do not exhibit significant polymerization (Begg et al. 2000). The polymerization observed in these MD studies (Crocombette and Ghaleb 1999, 2001) and other similar studies (Devanathan et al. 2002, Trachenko et al. 2002) might be an artifact of using empirical potentials for Si-Si and Si-O interactions derived for quartz.

Low-energy displacement cascades that are caused by 0.25 to 1.0 keV Zr recoils were investigated by Devanathan et al. (2002). The displacement cascade is linear (cylindrical) along the ion track, similar to previous observations (Crocombette and Ghaleb 2001), due to inefficient energy transfer between the sublattices associated with the differences in threshold displacement energies (Table 1) and atomic masses. Figure 15 illustrates the evolution of displaced atoms (only vacancies) produced by a 1 keV Zr cascade. An atom is considered displaced if it moved out of its Wigner-Seitz cell (i.e., a space-filling polyhedral cell centered at each atom in the original crystal structure). Devanathan et al. (2002) preferred this criterion to the criteria employed by others (Crocombette and Ghaleb 2001, Trachenko et al. 2001) that are based on the distance moved by an atom, because in the latter case the number of displacements varies with the displacement cutoff distance chosen and the choice of this distance is arbitrary. The total number of atoms displaced by a 1 keV Zr-recoil is large (110 atoms after 10 ps), and as in the case of Crocombette and Ghaleb (2001), the number of O displacements is significantly larger than the number of either Zr or Si displacements. The primary damage state produced by low-energy

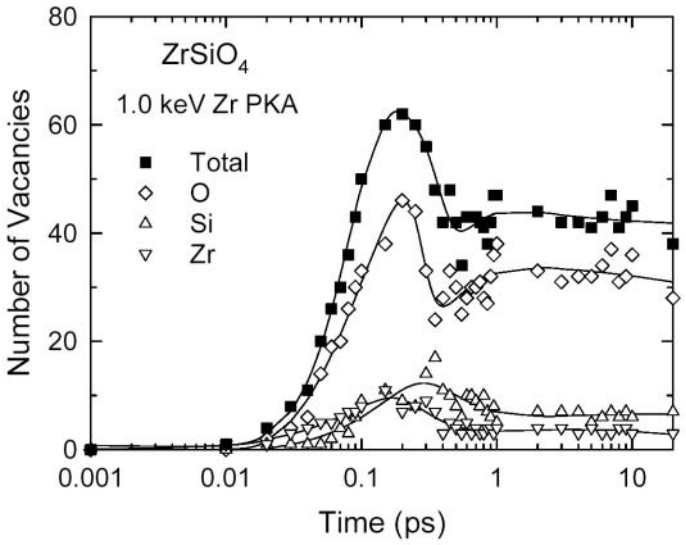


**Figure 15.** The total number of vacancies and number of vacancies produced on each sublattice by a 1 keV Zr recoil cascade in zircon as a function of time from the generation of the Zr recoil.

cascades consisted of O replacements produced primarily by a ring-like sequence of replacement events on the O sublattice, similar to that observed for O threshold displacement processes (Park et al. 2001), Si interstitials interconnected by O interstitials, vacancy clusters, and anti-site defects. The fraction of Si atoms with one or more bridging O neighbors increased with increasing Zr-recoil energy. While the melt-quenched state in this study exhibited a degree of $SiO_4$ polymerization, similar to the melt-quenched state of Crocombette and Ghaleb (2001), the number of bridging O atoms connected to other Si atoms showed a distribution from zero to four that peak at one, which is different than the distribution of Crocombette and Ghaleb (2001) that ranged from zero to five and was a maximum at two and three bridging oxygen atoms per silicon. Similarly, in the study of Devanathan et al. (2002), the melt quench state did not exhibit 5-fold coordinated Si atoms. This supports the conclusion of Crocombette and Ghaleb (2001) that this configuration may be an artifact of their potential.

The evolution of damage from 1 keV Zr-cascades were studied by Trachenko et al. (2001) using MD simulations. Similar to the results of Crocombette and Ghaleb (1998b, 1999, 2001) and Devanathan et al. (2002), they found that 1 keV Zr cascades produce more O displacements than Zr or Si displacements at 300 K, with the number of O displacements being 4 and 10 times greater than the number Si and Zr displacements, respectively. Because there are four times as many O atoms as Si atoms in zircon, this implies that the O and Si threshold displacement energies must be similar and that the Zr displacement energy is somewhat larger. This is consistent with the threshold displacement energies in Table 1. They also investigated the effects of overlapping cascades on damage production and found that the number of displacements produced by each cascade increases with each subsequent cascade. After several cascades overlapped, the number of Si and O displacements become comparable; however, the number of Zr-displacements remains about a factor of three less than either the number of Si or O displacements. They also reported polymerization of $SiO_4$ tetrahedra and the formation of both 5-fold and 6-fold coordinated Si in the cascades.

Trachenko et al. (2002) also studied 30 and 70 keV Zr-recoils in zircon using simulation cells containing 192,000 and 375,000 atoms, respectively. They did not observe any subcascades or branching that might be expected in such energetic cascades; instead, they found a highly polymerized sphere of $SiO_n$ surrounding the core of the cascade. This is not too surprising for the empirical potential used, since it produces a very dense collision cascade (relative to BCA estimates) in which the O and Si displacements outnumber the Zr displacements by nearly factors of two and three, respectively. Thus, in the core of the cascade, there should be a slight excess of vacancies that is surrounded by a halo of damage containing an excess of Si and O interstitials.

## UNRESOLVED RESEARCH ISSUES

Because of the importance of radiation effects on zircon in geological and materials science applications, there has been a recent, substantial effort to understand the processes and effects of α-decay event damage in zircon and related phases. Indeed, over 100 of the papers cited in this summary have been published since 1990. Even with this impressive effort, a number of important issues remain unresolved.

**1. What is the "amorphous" fraction?** As has been shown in the summary of the simulations of the effects of a single α-decay event, an α-recoil cascade consists of a series of different damage domains—a less-dense core surrounded by a high density of interstitial defects that grades into highly strained crystalline domains. The α-particle leaves a string of isolated defects along its trajectory with most of the ballistic interactions occurring at the end of its path. A fundamental issue is the definition of the nature of a "damaged" domain. While an isolated point defect is not usually considered to form an amorphous domain, at what point is a cluster of defects considered an "amorphous" domain? Depending on the analytical technique used to measure the "amorphous" fraction, the proportion of crystalline to amorphous volume varies, as each technique probes, with varying efficiencies, different "amorphous" volumes. The ability to distinguish among the different

amorphization mechanisms is directly dependent on our ability to determine the relationship between the amorphous fraction, $f_a$, and dose. However, we have made progress. We can say that the damage accumulation process is heterogeneous, that is it occurs with the formation of individual cascades and that the amorphous volume increases as the number of cascades increases. Our present analytical techniques, however, do not provide much experimental insight into what happens in individual cascades or when cascades overlap, and the present level of simulations of cascade interactions do not reach the relevant spatial and temporal scales.

**2. What is the structure of amorphous zircon?** Although a variety of analytical techniques have been used to study the structure of highly-damaged, "amorphous" zircon, contradictions remain. Some studies have cited evidence for Zr-rich and Si-rich nano-domains in highly damaged zircon, but for most samples this is not evident. There are differences in the estimates of the degree of increased polymerization of the [$SiO_4$] tetrahedral monomers. There are differences in the estimates of the coordination number of Zr (7 vs. 8) and Si (3 to 5) in damaged zircon. Indeed, there is, at present, no unique description of the fully-damaged state of zircon. Perhaps, it is unreasonable to expect a completely consistent picture to evolve from the present sample set. Clearly, natural zircon experiences different degrees of annealing with different thermal histories. The microstructure that evolves during annealing depends on the initial damage-state. For the ion beam irradiation experiments, the type of irradiation, e.g., mass and energy, and the dose rate also affect the structure. There might be more progress made if research focused on studies of carefully prepared bulk samples of amorphous material, for example by sol-gel or rapid quenching techniques, and comparison to amorphous structures produced in simulations by "quenching." The experience gained from studying these aperiodic samples could then be applied to partially- or highly-damaged zircon. Similarly, using advanced analytical techniques currently being applied to characterize the structure of nanoscale films, the structure of the thick amorphous layers (0.5 to 1.0 μm) formed during ion-beam irradiation could be characterized on single crystals of synthetic zircon.

**3. What are the effects of variations in ion mass, ion energy and temperature on cascade formation?** Although we will always struggle with the definition and determination of the amorphous fraction, systematic irradiations of synthetic zircon crystals with different ion energies and masses over a wide temperature range can provide data that will allow us to distinguish between different damage mechanisms and damage accumulation models. These systematic studies will necessarily resolve the wide variations in even simple calculations of the number of atomic displacements per α-decay event, which presently vary from 800 to 4,000. The experimental studies would benefit greatly by similarly systematic simulations of cascade formation over relevant energy, length and time scales.

**4. To what extent does zircon anneal at low temperatures over geologic time?** There is compelling evidence that the radiation damage in natural zircon can and does anneal at essentially ambient conditions. However, we have very limited data on the activation energies of the different annealing mechanisms, e.g., point defects vs. cascade recrystallization. At present, we cannot use the extent of damage annealing to reconstruct the thermal history of a natural zircon. However, given the variety of damage effects, point defects, recoil cascades and fission tracks, it may be possible to constrain the thermal history of a well-characterized zircon based on its damage microstructure.

**5. What are the damage recovery processes?** For moderately damaged zircon, the two stages (defect recovery in the crystalline structure, followed by epitaxial recrystallization at higher temperatures) are well described. However, the process that dominates depends on the initial damage state. The presence of isolated defects will affect the energetics of the recrystallization process. There continue to be disagreements on the relative efficiencies of point defect recovery versus recrystallization of the cascade as a function of temperature. The activation energies for the different recrystallization mechanisms are similarly problematic. Again, the contradictions in experimental results are most likely the result of using natural zircon samples that have different levels of damage and different initial microstructures. Experimental studies of damage recovery processes in

ion-beam irradiated single crystals, for which the thermal history is well controlled, and computer simulations of defect migration and recrystallization processes can provide a fundamental understanding of damage recovery processes in zircon that can be used to model recovery processes from different damage states over geologic time.

## ACKNOWLEDGMENTS

All of the authors of this chapter have benefited from sustained funding by the Office of Basic Energy Sciences of the U.S. Department of Energy. This funding has enabled two decades of collaboration between university investigators, first at the University of New Mexico and now at the University of Michigan, and the colleagues at Pacific Northwest National Laboratory. During this period we have had numerous collaborators who appear as co-authors on the cited publications. These collaborations are too numerous to enumerate, but we want to emphasize that it was only through these collaborative efforts that we were able to contribute to the fundamental understanding of radiation damage effects in zircon that are summarized in this chapter. Parts of this chapter were presented by RCE in 2002 in his Presidential Address to the Mineralogical Society of America. RCE notes with gratitude the encouragement and guidance of Professor Adolf Pabst during the earliest stages of this research nearly 30 years ago. We thank John Hanchar, Lutz Nasdala, Chris Palenik, and Susana Ríos for their careful and thoughtful reviews of this chapter.

## REFERENCES

Agullo-Lopez F, Catlow CRA, Townsend PD (1988) Point defects in materials. Chapter 11 In Computer Modelling Techniques. Academic Press, London, p 341-372

Akhtar MJ, Waseem S (2001) Atomistic simulation studies of zircon. Chem Phys 274:109-120

Babsail L, Hamelin N, Townsend PD (1991) Helium-ion implanted wave-guides in zircon. Nucl Instr Meth Phys Res B59/60:1219-1222

Balan E, Neuville DR, Trocellier P, Fritsch E, Muller JP, Calas G (2001) Metamictization and chemical durability of detrital zircon. Am Mineral 86:1025-1033

Barinsky RL, Kulikova IM (1977) Metamict transformation in some niobates and zircons according to X-ray absorption spectra. Phys Chem Mineral 1:325-333

Begg BD, Hess NJ, Weber WJ, Conradson SD, Scheiger MJ, Ewing RC (2000) XAS and XRD study of annealed $^{238}$Pu- and $^{239}$Pu-substituted zircons ($Zr_{0.92}Pu_{0.08}SiO_4$). J Nucl Mater 278:121-224

Biagini R, Memmi I, Olmi F (1997) Radiation damage in zircons. N Jahrb Mineral Monat 6:257-270

Brinkman JA (1954) On the nature of radiation damage in metals. J Appl Phys 25:961-970

Brown ID, Shannon RD (1973) Empirical bond strength-bond length curves for oxides. Acta Crystallogr A29:266-282

Burakov BE, Hanchar JM, Zamoryanskaya MV, Garbuzov VM, Zirlin VA (2002) Synthesis and investigation of Pu-doped single crystal zircon, $(Zr,Pu)SiO_4$. Radiochim Acta 90:95-97

Burakov BE, Hanchar JM, Zamoryanskaya MV, Anderson EB, Garbuzov VM, Kitsay AA, Krivovichev SV (in press) Investigation of single crystal zircon, $(Zr,Pu)SiO_4$, doped with $^{238}$Pu. Radiochim Acta

Bursill LA, McLaren AC (1966) Transmission electron microscope study of natural radiation damage in zircon ($ZrSiO_4$). Phys Stat Solidi 13:331-343

Bursill LA, Braunshausen G (1990) Heavy-ion irradiation tracks in zircon. Phil Mag A62:395-420

Capitani GC, Leroux H, Doukhan JC, Ríos S, Zhang M, Salje EKH (2000) A TEM investigation of natural metamict zircons: structure and recovery of amorphous domains. Phys Chem Mineral 27:545-556

Cartz L, Fournelle R (1979) Metamict zircon formed by heavy ion bombardment. Radiation Effects 41:211-217

Catlow CRA, Mackrodt WC (eds) (1982) Computer Simulation of Solids. Lecture Notes in Physics, Vol. 166. Springer, Berlin

Chakoumakos BC, Murakami T, Lumpkin GR, Ewing RC (1987) Alpha-decay induced fracturing in zircon: The transition from the crystalline to the metamict state. Science 236:1556-1559

Chakoumakos BC, Oliver WC, Lumpkin GR, Ewing RC (1991) Hardness and elastic modulus of zircon as a function of heavy-particle irradiation dose: I. *In situ* α-decay event damage. Rad Effects Defects Solids 118: 393-403

Chen J, Lian J, Wang, LM, Ewing RC, Wang RG, Pan W (2002) X-ray photoelectron spectroscopy study of disordering in $Gd_2(Ti_{1-x}Zr_x)_2O_7$ pyrochlores. Phys Rev Lett 88:105901-1 – 105901-4

Cherniak DJ, Hanchar JM, Watson EB (1997) Diffusion of tetravalent cations in zircon. Contrib Mineral Petrol 127: 383-390.

Crawford JH (1965) Radiation damage in solids: A survey. Ceram Bull 44:963-970
Crawford JH, Wittels MC (1956) A review of investigations of radiation effects in covalent and ionic crystals. *In* Proceedings of International Conference on Peaceful Uses of Atomic Energy, vol 7, United Nations, New York, p 654-665
Crocombette J-P (1999) Theoretical study of point defects in crystalline zircon. Phys Chem Mineral 27:138-143
Crocombette J-P, Ghaleb D (1998a) Modeling the structure of zircon ($ZrSiO_4$): empirical potentials, *ab initi*o electron structure. J Nucl Mater 257: 282-286
Crocombette J-P, Ghaleb D (1998b) Molecular dynamics simulation of displacement cascades in zircon ($ZrSiO_4$). *In* Scientific Basis for Nuclear Waste Management XXI. McKinley IG, McCombie C (eds) Mater Res Soc Symp Proc, vol 506, Warrendale, Pennsylvania, p 101-108
Crocombette J-P, Ghaleb D (1999) Molecular dynamics simulation of recoil nucleus displacement cascade in zircon. *In* Microstructural Processes in Irradiated Materials. Zinkle SJ, Lucas GE, Ewing RC, Williams JS (eds) Mater Res Soc Symp Proc, vol 540, Warrendale, Pennsylvania, p 343-348
Crocombette J-P, Ghaleb D (2001) Molecular dynamics modeling of irradiation damage in pure and uranium-doped zircon. J Nucl Mater 295:167-178
Delage J, Popoola O, Villain JP, Moine P (1989) Temperature-dependence of amorphization and precipitation processes in $Ni^+$ implanted and $N^+$ implanted $Ni_xTi_{1-x}$ alloys. Mater Sci Engr A115:133-138
Delaye J-M, Ghaleb D (1997) Molecular dynamics simulations of low-energy atomic displacement cascades in a simplified nuclear glass. J Nucl Mater 244:22-28
Devanathan R, Weber WJ, Boatner LA (1998) Response of zircon to electron and $Ne^+$ irradiation. *In* Phase Transformations and Systems Driven Far from Equilibrium. Atzmon M, Bellon P, Trivedi R (eds) Mater Res Soc Symp Proc, vol 481, Warrendale, Pennsylvania, p 419-424
Devanathan R, Weber WJ, Corrales LR (2002) Atomistic simulation of displacement cascades in zircon. *In* Scientific Basis for Nuclear Waste Management XXV. McGrail BP, Cragnolino GA (eds) Mater Res Soc Symp Proc, vol 713, Warrendale, Pennsylvania, JJ11.36.
Eckstein W (1991) Computer Simulation of Ion-Solid Interactions. Springer-Verlag, Berlin
Ellsworth S, Navrotsky A, Ewing RC (1994) Energetics of radiation damage in natural zircon ($ZrSiO_4$). Phys Chem Mineral 21:140-149
Ewing RC (1994) The metamict state: 1993 – The centennial. Nucl Instru Method Phys Res B91:22-29
Ewing RC, Haaker RF, Lutze W (1982) Leachability of zircon as a function of alpha dose. *In* Scientific Basis for Radioactive Waste Management V. Lutze W (ed) Elsevier, Amsterdam, p 389-397
Ewing RC, Lutze W, Weber WJ (1995) Zircon: A host-phase for the disposal of weapons plutonium. J Mater Res 10: 243-246
Ewing RC, Meldrum A, Wang LM, Wang SX (2000) Radiation-induced amorphization. *In* Transformation Processes in Minerals. Redfern SAT and Carpenter MA (eds) Rev Mineral Geochem 39:319-361
Exarhos GJ (1984) Induced swelling in radiation damaged $ZrSiO_4$. Nucl Instr Method Phys Res B1: 538-541
Farnan I (1999) Si-29 NMR characterization of the crystalline-amorphous transition in $ZrSiO_4$. Phase Transitions 69:47-60
Farnan I, Salje EKH (2001) The degree and nature of radiation damage in zircon observed by $^{29}Si$ nuclear magnetic resonance. J Appl Phys 89:2084-2090
Farges F (1994) The structure of metamict zircon: A temperature-dependent EXAFS study. Phys Chem Minerals 20:504-514
Farges F, Calas G (1991) Structural analysis of radiation damage in zircon and thorite: An X-ray absorption spectroscopic study. Am Mineral 76:60-73
Fortner JA, Badyal Y, Price DCL, Hanchar JM, Weber WJ (1999) Structural analysis of a completely amorphous $^{238}Pu$-doped zircon by neutron diffraction. *In:* Mater Res Soc Symp Proc, vol. 540, Zinkle SJ, Lucas GE, Ewing RC, Williams JS (eds) Warrendale, Pennsylvania, p 349-353
Gao F, Bacon DJ (1995) Molecular dynamics study of displacement cascades in $Ni_3Al$: I. General features and defect production efficiency. Phil Mag A71: 43-64
Gao F, Weber WJ (2002) Cascade overlap and amorphization in 3C-SiC: Defect accumulation, topological features, and disordering. Phys Rev B66:024106-11
Geisler T, Pidgeon RT (2002) Raman scattering from metamict zircon: comments on "Metamictisation of natural zircon: accumulation versus thermal annealing of radioactivity-induced damage. Contrib Mineral Petrol 143:750-755
Geisler T, Pidgeon RT, van Broswijk W, Pleysier R (2001a) Kinetics of thermal recovery and recrystallization of partially metamict zircon: a Raman spectroscopic study. Eur J Mineral 13:1163-1176.
Geisler T, Ulonska M, Schleicher H, Pidgeon RT, van Bronswijk W (2001b) Leaching and differential recrystallization of metamict zircon under experimental hydrothermal conditions. Contrib Mineral Petrol 141:53-65
Gibbons JF (1972) Ion implantation in semiconductors—Part II: Damage production and annealing. Proc IEEE

60:1062-1096
Greegor RB, Lytle FW, Ewing RC (1990) X-ray absorption spectroscopic investigation of Zr in metamict and annealed zircon. Ann Meeting Mater Res Soc, abstr, pA24
Guinan MW, Kinney JH (1981) Molecular dynamic calculations of energetic displacement cascades. J Nucl Mater 103 & 104:1319-1323
Hayashi M, Shinno I, Taguchi S, Sugihara S (1990) ESR signals of zircon irradiated with thermal neutrons and γ-rays. J Mineral Petrol Econ Geol 85:27-33
Headley TJ, Ewing RC, Haaker RF (1981) The structure of the metamict state. Nature 293:449-450
Headley TJ, Arnold GW, Northrup CJM (1982a) Dose-dependence of Pb-ion implantation damage in zirconolite, hollandite and zircon. *In* Scientific Basis for Radioactive Waste Management V, Lutze W (ed) Elsevier Science Publishing, New York, p 379-388
Headley TJ, Ewing RC, Haaker RF (1982b) High-resolution study of the metamict state in zircon. *In* 39th Ann Proc Electron Micros Soc Am, Bailey GW (ed) San Francisco Press, San Francisco, p 112-113
Helean KB, Lutze W, Ewing RC (1999) Dissolution studies of inert materials. *In:* Environmental Issues and Waste Management Technologies in the Ceramic and Nuclear Industries IV. Marra JC and Chandler GT (eds) Am Ceram Soc Ceram Trans 93:297-304
Henderson B (1972) Defects in Crystalline Solids. Edward Arnold, London
Hess NJ, Weber WJ, Conradson SD (1998) X-ray absorption fine structure of aged, Pu-doped glass and ceramic waste forms. J Nucl Mater 254:175-184
Hobbs LW (1994) Topology and geometry in the irradiation-induced amorphization of insulators. Nucl Instru Meth Phys Res B91:30-42
Holland HD, Gottfried D. (1955) The effect of nuclear radiation on the structure of zircon. Acta Crystallogr 8:291-300
Hurley PM, Fairbairn HW (1952) Alpha-radiation damage in zircon. J Appl Phys 23:1408
Hurley PM, Fairbairn HW (1953) Radiation damage in zircon: A possible age method. Geol Soc Am Bull 64:659-674
Jonckheere R, Gögen K (2001) A Monte-Carlo calculation of the size distribution of latent alpha-recoil tracks. Nucl Instru Method Phys Res B183:347-357
Karioris FG, Gowda KA, Cartz L (1981) Heavy ion bombardment of monoclinic $ThSiO_4$, $ThO_2$ and monazite. Rad Effects Lett 58:1-3
Karioris, FG, Appaji Gowda K, Cartz L, Labbe JC (1982) Damage cross-sections of heavy ions in crystal structures. J Nucl Mater 108/109:748-750
Koike J, Okamoto PR, Rehn LE (1989) The dose, temperature, and projectile-mass dependence for irradiation-induced amorphization of CuTi. J Mater Res 4:1143-1150
Lee JKW, Tromp J (1995) Self-induced fracture generation in zircon. J Geophys Res 100:71,753-17,770
Lian J, Wang LM, Wang SX, Chen J, Boatner LA, Ewing RC (2001) Nanoscale manipulation of pyrochlore: new nanocomposite ionic conductors. Phys Rev Lett 87:145901-1 – 145901-4
Lian J, Ríos S, Boatner LA, Wang LM, Ewing RC (in press) Microstructural evolution and nanocrystal formation of $Pb^+$-implanted ZrSiO4 single crystals. J. Appl. Phys.
Lumpkin GR (2001) Alpha-decay damage and aqueous durability of actinide host phases in natural systems. J Nucl Mater 289:136-166
Lumpkin GR, Ewing RC (1988) Alpha-decay damage in minerals of the pyrochlore group. Phys Chem Minerals 16:2-20
McLaren AC, FitzGerald JD, Williams JS (1994) The microstructure of zircon and its influence on the age determination from Pb/U isotopic ratios measured by ion microprobe. Geochim Cosmochim Acta 58:993-1005
Meis C, Gale JD (1998) Computational study of tetravalent uranium and plutonium lattice diffusion in zircon. Mater Sci Engin B 57:52-61
Meldrum A, Wang LM, Ewing RC (1996) Ion beam-induced amorphization of monazite. Nucl Instru Method Phys Res B116:220-224
Meldrum A, Boatner LA, Weber WJ, Ewing RC (1998a) Radiation damage in zircon and monazite. Geochim Cosmochim Acta 62:2509-2520
Meldrum A, Zinkle SJ, Boatner LA, Ewing RC (1998b) A transient liquid-like state in the displacement cascades of zircon, hafnon, and thorite. Nature 395:56-58
Meldrum A, Zinkle SJ, Boatner LA, Wang SX, Wang LM, Ewing RC (1999a) Effects of dose rate and temperature on the crystalline-to-metamict transformation in the $ABO_4$ orthosilicates. Can Mineral 37:207-221
Meldrum A, Zinkle SJ, Boatner LA, Ewing RC (1999b) Heavy-ion irradiation effects in the $ABO_4$ orthosilicates: decomposition, amorphization, and recrystallization. Phys Rev B59:3981-3992
Meldrum A, Boatner LA, Ewing RC (2000) A comparison of radiation effects in crystalline $ABO_4$-type phosphates and silicates. Mineral Mag 64:183-192
Meldrum A, Boatner LA, Weber WJ, Ewing RC (2002a) Amorphization and recrystallization of the $ABO_3$ oxides.

J Nucl Mater 300:242-254
Meldrum A, Boatner LA, Ewing RC (2002b) Nanocrystalline zirconia can be amorphized by ion irradiation. Phys Rev Lett 88:025503-1 – 025503-4
Meldrum A, Boatner LA, Ewing RC (in press) Size effects in the irradiation-induced crystalline-to-amorphous transformation. Nucl Instru Method Phys Res
Miller ML, Ewing RC (1992) Image simulation of partially amorphous materials. Ultramicroscopy 48: 203-237
Morehead FF Jr, Crowder BL (1970a) A model for the formation of amorphous silicon by ion bombardment. Radiation Effects 6:27-32
Morehead FF, Crowder BL, Title RS (1970b) Formation of amorphous silicon by ion-bombardment as a function of ion, temperature, and dose. J Appl Phys 43:1112-1972
Muller I, Weber WJ (2001) Plutonium in crystalline ceramics and glasses. MRS Bulletin 26:698-706
Murakami T, Chakoumakos BC, Ewing RC (1986) X-ray powder diffraction analysis of alpha-event radiation damage in zircon ($ZrSiO_4$). *In* Advances in Ceramics: Nuclear Waste Management II. Clark DE, White WB, Machiels J (eds) Am Ceram Soc, Columbus, Ohio, p 745-753
Murakami T, Chakoumakos BC, Ewing RC, Lumpkin GR, Weber WJ (1991) Alpha-decay event damage in zircon. Am Mineral 76:1510-1532
Nakai I, Akimoto J, Imafuku M, Miyawaki R, Sugitani Y, Koto K (1987) Characterization of the amorphous state in metamict silicates and niobates by EXAFS and XANES analyses. Phys Chem Minerals 15:113-124
Nasdala L, Pidgeon RT, Wolf D, Irmer G (1998) Metamictization and U-Pb isotopic discordance in single zircons: a combined Raman microprobe and SHRIMP ion probe study. Mineral Petrol 62:1-27
Nasdala L, Wenzel M, Vavra G, Irmer G, Wenzel T, Kober B (2001) Metamictization of natural zircon: accumulation versus thermal annealing of radioactivity-induced damage. Contrib Mineral Petrol 141:125-144
Nasdala L, Imer G, Jonckheere R (2002a) Radiation damage ages: Practical concept or impractical vision? Reply to two comments on "Metamictisation of natural zircon: Accumulation versus thermal annealing of radioactivity-induced damage", erratum, and further discussion. Contrib Mineral Petrol 143:758-765
Nasdala L, Lengauer CL, Hanchar JM, Kronz A, Wirth R, Blanc P, Kennedy AK, Seydoux-Guillaume A-M (2002b) Annealing radiation damage and the recovery of cathodoluminescence. Chemical Geology 191:121-140
Newcomer PP, Barbour JC, Wang LM, Venturini EL, Kwak JF, Ewing RC, Miller ML, Morosin B (1996) Temperature dependent microstructural modification in ion irradiated Tl-type high temperature superconductors. Physica C: Supeconductivity 267:243-253
Nord J, Nordlund K, Keinonen J (2002) Amorphization mechanism and defect structures in ion-beam amorphized Si, Ge, and GaAs. Phys Rev B65:165329-1 – 165329-6
Oak Ridge National Laboratory (2002) http://www.ssd.ornl.gov/Programs/MARLOWE/Marlowe.htm
Oliver WC, McCallum JC, Chakoumakos BC, Boatner LA (1994) Hardness and elastic modulus of zircon as a function of heavy-particle irradiation dose: II. Pb-ion implantation damage. Rad Effects Defects Solids 132:131-141
Özkan H (1976) Effect of nuclear radiation on the elastic moduli of zircon. J Appl Phys 47:4772-4779
Pabst A (1952) The metamict state. Am Mineral 37:137-157
Palenik CS, Ewing RC, Nasdala L (in press) Radiation damage in a zoned zircon crystal. Am Mineral
Park B, Weber WJ, Corrales LR (2001) Molecular dynamics simulation study of threshold displacements and defect formation in zircon. Phys Rev B64:174108-1 – 174108-16
Pellas P (1965) Étude sur la recristallisation thermique des zircons métamictes. Mémoires du Muséum National D'Histoire Naturelle Serie C, Sciences de la Terre XII:227-253
Petit JC, Dran JC, Gianantonio DM (1987) Effects of ion implantation on the dissolution of minerals Part II: selective dissolution. Bull Minéral 110:25-42
Pidgeon RT, O'Neil JR, Silver LT (1966) Uranium and lead isotopic stability in metamict zircon under experimental hydrothermal conditions. Science 154:1538-1540
Raychaudhuri AK, Peech JM, Pohl RO (1980) Phonon scattering in glasses and highly disordered crystals. *In* Proc Third Intl Conf Phonon Scattering in Solids. Maris H (ed) Plenum Press, New York, p 1-3
Ríos S, Salje EKH (1999) Diffuse X-ray scattering from weakly metamict zircon. J Phys: Condensed Matter 11:8947-8956
Ríos S, Salje EKH, Zhang M, Ewing RC (2000a) Amorphization in zircon: evidence for direct impact damage. J Phys: Condensed Matter 12:2401-2412
Ríos S, Malcherek T, Salje EKH, Domenaghetti C (2000b) Localized defects in radiation-damaged zircon. Acta Crystallogr B56:947-952
Robinson MT (1994) Basic physics of radiation damage production. J Nucl Mater 216:1-28
Sahama TG (1981) Growth structure in Ceylon zircon. Bull Minéral 104:89-94
Salje EKH, Chrosch J, Ewing RC (1999) Is "metamictization" of zircon a phase transition? Am Mineral 84:1107-

1116
Slater JC (1951) The effects of radiation on materials. J Appl Phys 22:237-256
Speer JA (1982) Zircon. Rev Mineral 5:67-112
v Stackelberg M, Rottenbach E (1940) Dichte und struktur des zircons, III & IV. Z Kristallogr 97:173-182; 207-208
Tole MP (1985) The kinetics of dissolution of zircon ($ZrSiO_4$). Geochim Cosmochim Acta 49:453-458
Trachenko KO, Dove MT, Salje EKH (2000) Modelling the percolation-type transition in radiation damage. J Appl Phys 87:7702-7707
Trachenko KO, Dove MT, Salje EKH (2001) Atomistic modeling of radiation damage in zircon. J Phys: Condensed Matter 13:1947-1959
Trachenko KO, Dove MT, Salje EKH (2002) Structural changes in zircon under α-decay irradiation. Phys Rev B 65:180102
Trachenko KO, Dove MT, Salje EKH (2003) Large swelling and percolation in irradiated zircon. J Phys: Condens Matter 15:L1-L7
Vance ER (1975) α-Recoil damage in zircon. Rad Effects 24:1-6
Vance ER, Anderson BW (1972) Study of metamict Ceylon zircons. Mineral Mag 38:605-613
Virk HS (1995) Single activation-energy model of radiation-damage in solid-state nuclear track detectors. Rad Effects Defects Solids 133:87-95
Wang LM (1998) Application of advanced electron microscopy techniques to the studies of radiation effects in ceramic materials. Nucl Instr Meth Phys Res B141:312-325
Wang LM, Ewing RC (1992a) Ion beam induced amorphization of complex ceramic materials-minerals. Mater Res Soc Bull 17(5):38-44
Wang LM, Ewing RC (1992b) Detailed *in situ* study of ion beam-induced amorphization of zircon. Nucl Instru Method Phys Res B65:324-329
Wang LM, Eby RK, Janeczek J, Ewing RC (1991) *In situ* TEM study of ion-beam-induced amorphization of crystalline natural silicates. Nucl Instr Method Phys Res B59:395-400
Wang LM, Ewing RC, Weber WJ, Eby RK (1993) Temperature dependence of amorphization dose for ion beam irradiated zircon and olivine. *In* Mater Res Soc Symp Proc. vol 279, Nastasi M, Harriott LR, Herbots N, Averback RS (eds) Warrendale, Pennsylvania, p 451-456
Wang SX, Wang LM, Ewing RC (1998) A model for irradiation-induced amorphization. *In* Mater Res Soc Symp Proc vol 504, Barbour JC, Roorda S, Ila D, Tsujioka M (eds) Warrendale, Pennsylvania, p 165-170
Wang SX, Wang LM, Ewing RC (2001) Irradiation induced-amorphization: the effects of temperature, ion species, dose rate, and materials. Phys Rev B63:41051-41058
Watson EB, Cherniak DJ (1997) Oxygen diffusion in zircon. Earth Planet Sci Lett 148:527-544
Weber WJ (1990) Radiation-induced defects and amorphization in zircon. J Mater Res 5:2687-2697
Weber WJ (1991) Self-radiation damage and recovery in Pu-doped zircon. Rad Effects Defects Solids 115:341-349
Weber WJ (1993) Alpha-decay-induced amorphization in complex silicate structures. J Am Ceram Soc 76:1729-1738
Weber WJ (2000) Models and mechanisms of irradiation-induced amorphization in ceramics. Nucl Instr Method Phys Res B 166-167:98-106
Weber WJ, Ewing RC (2000) Plutonium immobilization and radiation effects. Science 289:2051-2052
Weber WJ, Ewing RC (2002) Radiation effects in crystalline oxide host phases for the immobilization of actinides. *In* Scientific Basis for Nuclear Waste Management XXV. McGrail BP, Cragnolino GA (eds) Mater Res Soc Symp Proc vol 713, Warrendale, Pennsylvania, p 443-454
Weber WJ, Wang LM (1993) Irradiation induced amorphization of $Ca_2La_8(SiO_4)_6O_2$ single crystals. *In* Mater Res Soc Symp Proc vol. 279, Nastasi M, Harriott LR, Herbots N, Averback RS (eds) Warrendale, Pennsylvania, p 523-528
Weber WJ, Wang LM (1994) Effect of temperature and recoil-energy spectra on irradiation-induced amorphization in $Ca_2La_8(SiO_4)_6O_2$. Nucl Instr Method Phys Res B 91:63-66
Weber WJ, Ewing RC, Wang LM (1994) The radiation-induced crystalline-to-amorphous transition in zircon. J Mater Res 9:688-698
Weber WJ, Ewing RC, Meldrum A (1997) The kinetics of alpha-decay-induced amorphization in zircon and apatite containing weapons-grade plutonium or other actinides. J Nucl Mater 250:147-155
Weber WJ, Ewing RC, Catlow CRA, de la Rubia TD, Hobbs LW, Kinoshita C, Matzke Hj, Motta AT, Nastasi M, Salje EKH, Vance ER, Zinkle SJ (1998) Radiation effects in crystalline ceramics for the immobilization of high-level nuclear waste and plutonium. J Mater Res 13:1434-1484
Weber WJ, Devanathan R, Meldrum A, Boatner LA, Ewing RC, Wang LM (1999) The effect of temperature and recoil spectra on amorphization in zircon. *In* Microstructural Processes in Irradiated Materials. Zinkle SJ, Lucas GE, Ewing RC, Williams JS (eds) Mater Res Soc Symp Proc, vol 540, Warrendale, Pennsylvania, p 367-372
Williford RE, Devanathan R, Weber WJ (1998) Computer simulation of displacement threshold energies for several

ceramic materials. Nucl Instr Method Phys Res B141: 98-103
Williford RE, Weber WJ, Devanathan R, Cormack AN (1999) Native vacancy migrations in zircon. J Nucl Mater 273:164-170
Williford RE, Begg BD, Weber WJ, Hess NJ (2000) Computer simulation of $Pu^{3+}$ and $Pu^{4+}$ substitutions in zircon. J Nucl Mater 278:207-211
Yada K, Takayoshi T, Sunagawa I (1981) Application of lattice imagery to radiation damage investigation in natural zircon. Phys Chem Minerals 7:47-52
Yada K, Takayoshi T, Sunagawa I (1987) Radiation induced lattice defects in natural zircon ($ZrSiO_4$) observed at atomic resolution. Phys Chem Minerals 14:197-204
Zhang M, Salje EKH, Ewing RC, Farnan I, Ríos S, Schlüter, Leggo P (2000a) α-decay damage and recrystallization in zircon: Evidence for an intermediate state from infrared spectroscopy. J Phys: Condensed Matter 12:5189-5199
Zhang M, Salje EKH, Farnan I, Graeme-Barber A, Daniel P, Ewing RC, Clark AM, Leroux H (2000b) Metamictization of zircon: Raman spectroscopic study. J Phys: Condensed Matter 12:1915-1925
Zhang M, Salje EKH, Capitani GC, Leroux H, Clark AM, Schlüter J, Ewing RC (2000c) Annealing of α-decay damage in zircon: a Raman spectroscopic study. J Phys: Condensed Matter 12:3131-3148
Zhang M, Salje EKH (2001) Infrared spectroscopic analysis of zircon: Radiation damage and the metamict state. J Phys: Condensed Matter 13:3057-3071
Zhang M, Salje EKH, Ewing RC (2002) Infrared spectra of Si-O overtones, hydrous species, and U ions in metamict zircon: radiation damage and recrystallization. J Phys: Condensed Matter 14:3333-3352
Ziegler JF, Biersack JP, Littmark U (1985) The Stopping and Range of Ions in Solids. Pergamon, New York.
Ziegler JF (2002) http://www.SRIM.org/
Zinkle SJ, Kinoshita C (1997) Defect production in ceramics. J Nucl Mater 251:200-217F

# 15 Spectroscopic methods applied to zircon

**Lutz Nasdala**

*Institut für Geowissenschaften – Mineralogie*
*Johannes Gutenberg-Universität Mainz*
*D-55099 Mainz, Germany*

**Ming Zhang**

*Department of Earth Sciences, University of Cambridge*
*Downing Street, Cambridge CB2 3EQ, United Kingdom*

**Ulf Kempe**

*Institut für Mineralogie*
*Technische Universität Bergakademie Freiberg*
*Brennhausgasse 14, D-09596 Freiberg, Germany*

**Gérard Panczer**

*Laboratoire de Physico-Chimie des matériaux Luminescents, UMR 5620 CNRS*
*Université Claude Bernard – Lyon 1*
*69622 Villeurbanne, France*

**Michael Gaft**

*International Technologies Laser*
*Rishon-Lezion 75140, Israel*

**Michael Andrut**

*Institut für Mineralogie und Kristallographie*
*Universität Wien – Geozentrum*
*A-1090 Wien, Austria*

**Michael Plötze**

*Institut für Geotechnik*
*Eidgenössische Technische Hochschule Zürich*
*CH-8093 Zürich, Switzerland*

## INTRODUCTION

Natural and synthetic (pure and doped) zircon ($ZrSiO_4$) have been studied with a variety of spectroscopic techniques. These techniques are based on different physical phenomena, for instance transitions between spin states of nuclei and electrons, energetic transitions of valence electrons, intra-molecular vibrations, or vibrations of atoms and molecular units in the lattice. All of the diverse spectroscopic techniques, however, have in common that they probe energy differences between a ground and excited states, mostly upon interaction of the mineral with incident radiation. Such interactions are not only determined by the excited elementary particles or molecules themselves but depend greatly on their local environments (i.e. number, type, valence and geometrical arrangement of neighboring atoms). Spectroscopic techniques are thus sensitive to the local structure and provide information on the short-range order.

Most research on zircon crystals using spectroscopic techniques was done to study their "real structures," that is the characterization of deviations from "perfect" zircon. Such features include

1529-6466/03/0053-0015$05.00

the incorporation of non-formula elements, structural defects and the presence of inclusions and other impurities. Correspondingly, most of the spectroscopic investigations can be assigned to two major groups. The first group represents studies done to characterize the structural position and local environment of non-formula elements when incorporated in the zircon lattice, and accompanying effects on physical properties. The second group comprises studies subjected to the real structures of "metamict" zircon samples, i.e., changes of the zircon structure caused by the impact of self-irradiation and upon recovery from radiation damage (Ewing et al., this volume).

It is most obvious that a spectroscopic bulk or point analysis will first of all yield a spectrum (i.e. a plot of the intensity of the respective physical parameter versus wavelength, frequency or wavenumber), and this is what is used in most studies. In addition, image generation based on spectroscopic data has become an increasingly applied discipline. Natural zircon crystals are normally not homogeneous in terms of chemical and structural composition, but rather show a heterogeneous pattern, which is referred to as "internal structure." Examples include oscillatory growth zoning (e.g., Connelly 2000, Hoskin 2000), sector zoning (e.g., Vavra et al. 1999) and recrystallization patterns (e.g., Pidgeon 1992). Such internal structures of natural and synthetic zircon crystals are most easily studied in electron microprobes by backscattered electron (BSE) imaging. Among the spectroscopic techniques, cathodoluminescence (CL) imaging is most commonly used. Because there is a separate chapter on internal structures and their BSE and CL imaging (Corfu et al., this volume), we will not discuss CL imaging in great detail here. Even though other spectroscopic techniques such as confocal Raman microprobe and laser-induced luminescence analysis have only been used sparsely thus far for image formation and the study of internal structures, they have a great potential in the future.

This chapter gives an overview of the diverse applications of spectroscopic analytical techniques to the investigation and characterization of zircon. This summarizing overview makes no claim to be exhaustive. It is rather focused on the more commonly used techniques such as luminescence and vibrational spectroscopy whereas other spectroscopic methods (e.g., spin resonance, thermoluminescence, photo-electron and X-ray spectroscopy) are discussed only briefly or not at all. The goal of this chapter is to demonstrate the versatile use of spectroscopic analyses and the wealth of obtained information, underlining that modern spectroscopic methods are by far more than just complementary techniques to X-ray diffraction and chemical analysis.

## LUMINESCENCE SPECTROSCOPY OF ZIRCON

### Cathodoluminescence of zircon

***Introductory remarks.*** Over the last decades, CL imaging of polished grains has become a routinely used technique for the study of internal structures of zircon crystals (e.g., Sommerauer 1976, Hoffman and Long 1984, Marshall 1988, Vavra 1990, Halden and Hawthorne 1993, Koschek 1993, Hanchar and Miller 1993, Vavra 1994, Hanchar and Rudnick 1995, Hoskin 2000). Introduction of CL technique as a standard method in zircon studies was especially stimulated by the use of the U-Pb isotope system of this mineral in geochronological research (e.g., Gebauer 1990, Roger et al. 1995, Vavra et al. 1996, 1999; Whitehouse et al. 1999, Connelly 2000, Poller 2000, Rubatto and Gebauer 2000, Hermann et al. 2001). Currently, most common CL technique is panchromatic (integral) imaging using a CL detector attached to a scanning electron microscope (SEM-CL). Cathodoluminescence imaging by the aid of an optical CL microscope (OM-CL) or a combination of both methods are applied more sparsely, but until the event of modern SEM-based systems, OM-CL was the standard way of doing CL microscopy. The one primary advantage of using an OM-CL based system is that color variations in minerals can be easily seen with the unaided eye, and any photographs taken (using film or digitally) can be corrected for color accuracy (Hanchar and Rudnik 1995, Götze 1998, Götze et al. 1999, Kempe et al. 1999). Even though quite a number of studies were addressed to the study of causes of the CL emission (Sommerauer 1976, Hoffman

and Long 1984, Lork and Koschek 1991, Ohnenstetter et al. 1991, Yang et al. 1992, Remond et al. 1992, Hanchar and Rudnick 1995, Phillips et al. 1996, Kempe et al. 2000, Rubatto and Gebauer 2000, Remond et al. 2000, Poller et al. 2001), there is still controversy about the nature of the CL signal and factors influencing the CL intensity in panchromatic SEM-CL images of natural zircon crystals. However, sound understanding of the CL mechanisms is fundamental for correct interpretation of the CL intensity. In the following, we give a critical overview of the current state of knowledge of CL research.

***Generation of cathodoluminescence in natural zircon.*** Cathodoluminescence emission results from the interaction of a primary electron beam with solids characterized by a band gap (semiconductors and insulators). The energies of the primary electron beam (up to >20 keV) and of backscattered electrons are well above the excitation energies of the CL, which are on the order of several eV. However, primary and backscattered electrons may transfer most of their energy to the lattice in the form of heat (temperatures as high as 600-700°C may be reached), characteristic and continuum X-rays, Auger electrons etc. (cf. Goldstein et al. 1981), and generate secondary electrons. These secondary electrons are characterized by a continuous energy spectrum just in the range of the excitation levels of the CL emission. The secondary electrons thus cause CL activation, provided the emission is not suppressed by quenching mechanisms (see below). In the simplest case, bonding electrons from the valence band may be excited to the conduction band and released to the ground state under emission of photons (see intrinsic luminescence in Fig. 1). The width of the band gap (i.e. the energy difference between valence and conduction bands; cf. Fig. 1) is characteristic of the investigated material and the related emission for zircon lies in the ultraviolet (UV) range around 230-280 nm (Votyakov et al. 1986, Krasnobayev et al. 1988, Cesbron et al. 1993). However, energy relaxation (the return of the excited electron to its ground level) is also possible via other radiative or non-radiative transitions involving local defects. Moreover, some centers may be directly excited (i.e. not involving band transitions or other defects) and with relaxation mecha-

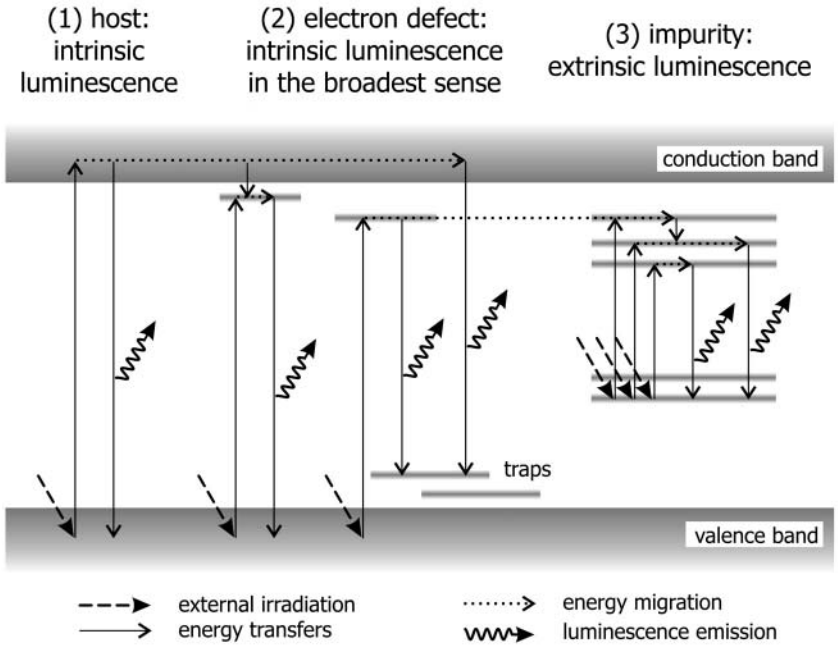


**Figure 1.** Simplified energy diagram showing the three principal types of luminescence generation upon electron beam irradiation. Cathodoluminescence emission may be caused by (1) band-band transitions, (2) band, trap, and electron-defect assisted transitions and (3) impurity state transitions within forbidden band gaps.

nisms that are hardly influenced by the local crystal field, as may often be found for trivalent rare earth element (REE) centers. For further details on the basic physics of CL see Marshall (1988), Remond et al. (1992, 2000), Blanc et al. (2000), and Townsend and Rowlands (2000).

Information from spectral CL studies (emission wavelength, peak width, and lifetime of the excited state) can be used to identify the emission centers. However, CL activation by the electron beam is not selective. Combination of CL studies with other techniques such as photoluminescence (PL), X-ray absorption fine structure (XAFS), or electron paramagnetic resonance (EPR) is mandatory for sound interpretation but systematic investigations on natural zircon are still scarce.

Cathodoluminescence spectra of natural zircon are complex, as they consist of different types of simultaneously emitted bands. A glance at the published data suggests that in many cases, CL is dominated by broad-band emissions (e.g., Marshall 1988, Ohnenstetter et al. 1991, Lork and Koschek 1991, Yang et al. 1992, Remond et al. 1992, Cesbron et al. 1993, Hanchar and Rudnick 1995, Götze et al. 1999, Kempe et al. 1999, 2000, Remond et al. 2000, Poller et al. 2001). For example, intrinsic luminescence and CL emission via electron defect centers localized on oxygen-bearing anion groups ($[SiO_4]^{n-}$ in zircon) appear as broad bands in CL spectra. However, CL spectra of natural zircon samples may also show a predominance or important role of narrow emission bands (Hanchar and Rudnick 1995, Götze et al. 1999, Kempe et al. 1999, Remond et al. 2000; see Figs. 2 and 3). Narrow line groups often centered at 480 and 575 nm and weaker emissions centered at 666 and 755 nm are assigned to $Dy^{3+}$ impurities (e.g., Marshall 1988, Ohnenstetter et al.

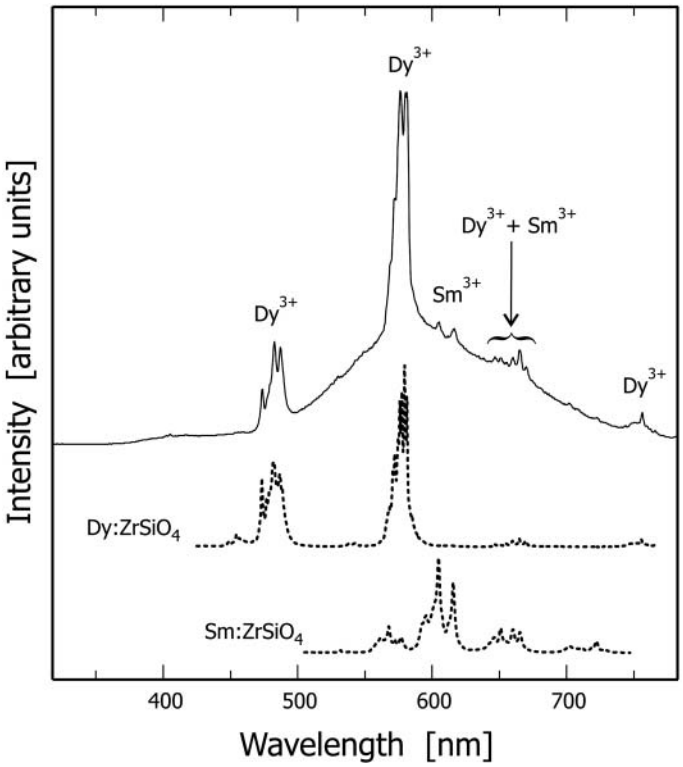


**Figure 2.** Cathodoluminescence spectrum (solid) of a zircon from the Cretaceous quartz sand deposit of Weferlingen, Germany (after Götze et al. 1999, redrawn and modified). The spectrum shows groups of narrow emission bands of rare earth elements, superimposed on a "yellow" broad-band emission in the range 500-700 nm. The assignment of the $Dy^{3+}$ and $Sm^{3+}$ band groups is underlined by comparison of this spectrum with two CL spectra (dotted) of synthetic, REE+P-doped zircon crystals (JM Hanchar, unpublished).

1991, Yang et al. 1992, Remond et al. 1992, Hanchar and Rudnick 1995, Götze et al. 1999, Kempe et al. 2000, Remond et al. 2000). This interpretation is supported by the investigation of synthetic zircon doped with $Dy^{3+}$ (Fig. 2; cf. Cesbron et al. 1993, Blanc et al. 2000). More rarely, emission lines of other REE centers such as $Er^{3+}$ (at 475 and 530 nm, Remond et al. 1992, 2000), $Sm^{3+}$ (at 605 and 702 nm, Götze et al. 1999, see Fig. 2), $Tb^{3+}$ (at 548 nm, Yang et al. 1992, Hanchar and Rudnick 1995, Nasdala et al. 2002a), $Gd^{3+}$ (at 313 nm, Nasdala et al. 2002a) and $Nd^{3+}$ (emission at 885 nm, Götze et al. 1999) were reported. Analogous to $Dy^{3+}$, the interpretation for the $Er^{3+}$, $Sm^{3+}$, $Tb^{3+}$, $Gd^{3+}$, and $Nd^{3+}$ centers is verified by the comparison with spectra of synthetic samples (Blanc et al. 2000, see examples in Fig. 2).

Our understanding of the broad-band emissions of zircon is still poor. In accordance with the prevailing type of broad-band emission in the blue or yellow region of the spectra, Ohnenstetter et al. (1991) and Remond et al. (1992) distinguished blue and yellow luminescent zircon. There are contradictory results of spectroscopic investigations on the "blue" band emission discussed in more detail elsewhere (Kempe et al. 2000). It must, however, be mentioned that the intensity maximum of the "blue" emission lies in the UV range between 200-400 nm where most CL systems show a dramatic decrease in sensitivity, also known as quantum efficiency, or spectral response, and the spectral response of the detector used should be taken into account when quantifying CL spectra. Several spectra published in the literature suggest that "blue" zircon CL is caused by a broad band centered near 365 nm (Iacconi et al. 1980, Krasnobayev et al. 1988, Remond et al. 1992, Yang et al. 1992, Cesbron et al. 1993, Poller et al. 2001, Nasdala et al. 2002a). Iacconi et al. (1980) suggested that the "blue" luminescence of zircon is analogous to the "blue" luminescence of other silicates and can be explained by emission from electron defects localized at $SiO_4$ groups (cf. also Yang et al. 1992, Kempe et al. 2000). Electron defects are formed under irradiation and released electrons are trapped, for example, on a Si site ($Si^{4+} + e^- \rightarrow Si^{3+}$). Electron defects may also be stabilized by impurities such as $Dy^{3+}$ (Krasnobayev et al. 1988, Gaft 1992, Claridge et al. 2000a). For instance, the emission band at 385 nm, observed in CL (Yang et al. 1992) as well as in thermoluminescence (TL) spectra (Kirsh and Townsend 1987, Laruhin et al. 2002) of natural zircon seems to involve both [$SiO_4$]-related centers and REE ions.

The "yellow" broad-band emission is often centered at 560 nm (Fig. 3D). The nature of this emission is also explained by contradictory models (e.g., Gaft 1992, Kempe et al. 2000). Possible models suggest additional electron defects on the $SiO_4$ tetrahedron, for example stabilized by Zr vacancies (Claridge et al. 2000), or emission from $Yb^{2+}$ impurities (Kempe et al. 2000). However, all authors agree that the "yellow" emission center is of radiogenic origin, i.e. it is only generated in solids that were affected by radioactive irradiation (Gaft 1992, Remond et al. 1992, 2000; Kempe et al. 2000).

***Factors leading to variations in the cathodoluminescence intensity.*** Potential causes of intensity variations of the observed CL signal include CL quenching and various effects of the crystallinity. The emission of CL may be quenched by optical absorption processes. Furthermore, there is a drastic decrease of the defect-related CL efficiency at elevated temperatures. However, even at constant temperature, the intensity of a certain $REE^{3+}$ emission is not simply a linear function of the total content of the respective REE. The concentration of a luminescent center may deviate from the respective total element content if there are variations in the valence state. Further, interaction between neighboring emission centers of the same type may lead to energy migration and CL quenching (self-quenching or concentration-quenching) at higher concentration levels. Moreover, interaction between centers belonging to different types is also possible. In these cases, the energy may be transferred to other CL active emission centers or to centers with non-radiative relaxation (quenching centers). In both cases, however, the CL of the $REE^{3+}$ center under consideration is quenched. By contrast, the CL emission from a $REE^{3+}$ center may also be enhanced by energy transfer from other centers (sensitizing). To give an example, self-quenching of $Dy^{3+}$ starts at around 1 atm % Dy according to Iacconi and Caruba (1980). The same authors found that $Dy^{3+}$

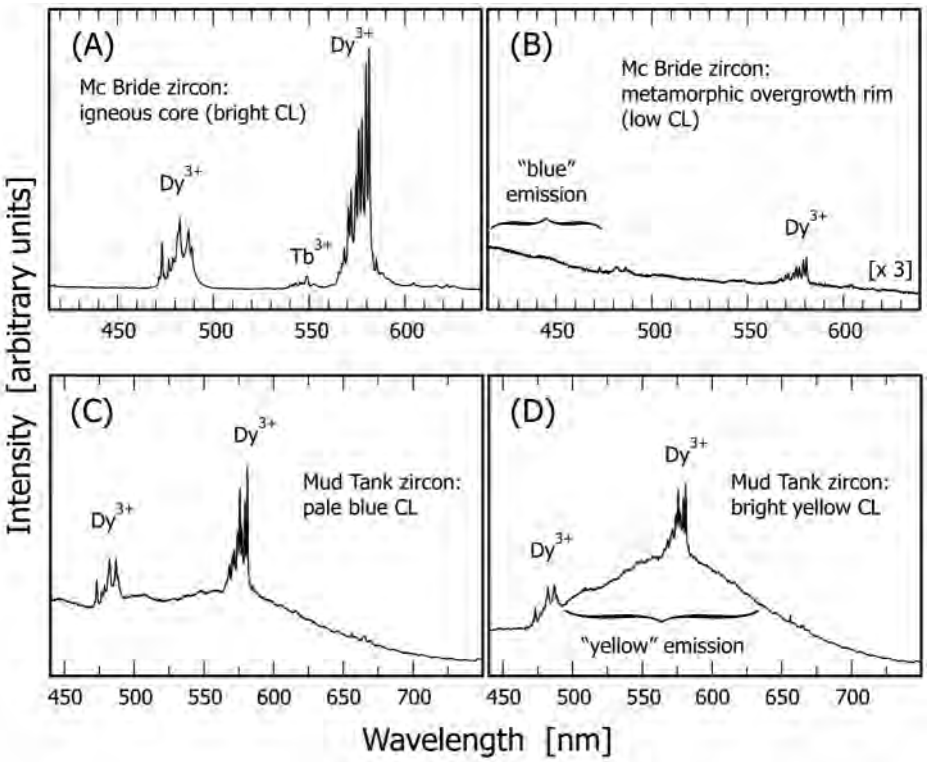


**Figure 3.** Complex contribution of broad-band and narrow-band emissions on the total CL signal. (A) Cathodoluminescence spectrum of an igneous core in a zircon from a xenolith, McBride province, Queensland, Australia. (B) Corresponding spectrum (intensity 3× expanded) of a metamorphic overgrowth rim in the same crystal as in A, showing very low CL intensity. Spectra modified after Hanchar and Rudnick (1995). Bright CL observed from the igneous core is due to strong REE emission bands. (C) Cathodoluminescence spectrum from a micro-area that appeared bluish in the CL microscope. Zoned zircon crystal from the Mud Tank carbonatite, Northern Territory, Australia. (D) Corresponding spectrum (same intensity scale) obtained from a yellow CL area in the same crystal as in C. Spectra from JM Hanchar and PWO Hoskin (unpublished); for sample description see Hanchar et al. (1997). The total CL emission of the blue zone appeared clearly less intense with the unaided eye, even though the $Dy^{3+}$ emission bands are more intense. The brighter appearance of the yellow zone is due to the more intense yellow broad-band emission. All spectra were taken from areas 10 × 10 mm in size and are corrected for the instrument response (resolution 0.15 nm).

quenches the "blue" zircon CL starting from about 0.01 atm % Dy.

Intrinsic CL is closely related to the structural perfection of the host lattice. If the degree of crystallinity of zircon decreases, the emission of intrinsic CL decreases, too. This interrelation (Hoffman and Long 1984) was recently supported by combined SEM-CL and Raman microprobe studies (Kempe et al. 2000, Nasdala et al. 2002a). For zircon crystals that have not experienced self-irradiation and external irradiation, secondary recrystallization or hydrothermal alteration, the degree of crystallinity and related intrinsic CL intensity depend on the concentration of primary lattice defects (cf. Figs. 4E and F). Primary defects in natural zircon are often related to the incorporation of trace elements (Sommerauer 1976, Gracheva et al. 1981, Kempe et al. 2000). Note that the contents of typical trace elements in zircon, excluding Hf, are usually found to be correlated (Romans et al. 1975, Speer 1980, Hoffman and Long 1984, Bibikova et al. 1991, Benisek and Finger 1993, Hanchar and Miller 1993, Hanchar and Rudnick 1995, Rubatto and Gebauer 2000, Kempe et al. 2000). Thermal recrystallization, as for instance under high temperature metamorphic condi-

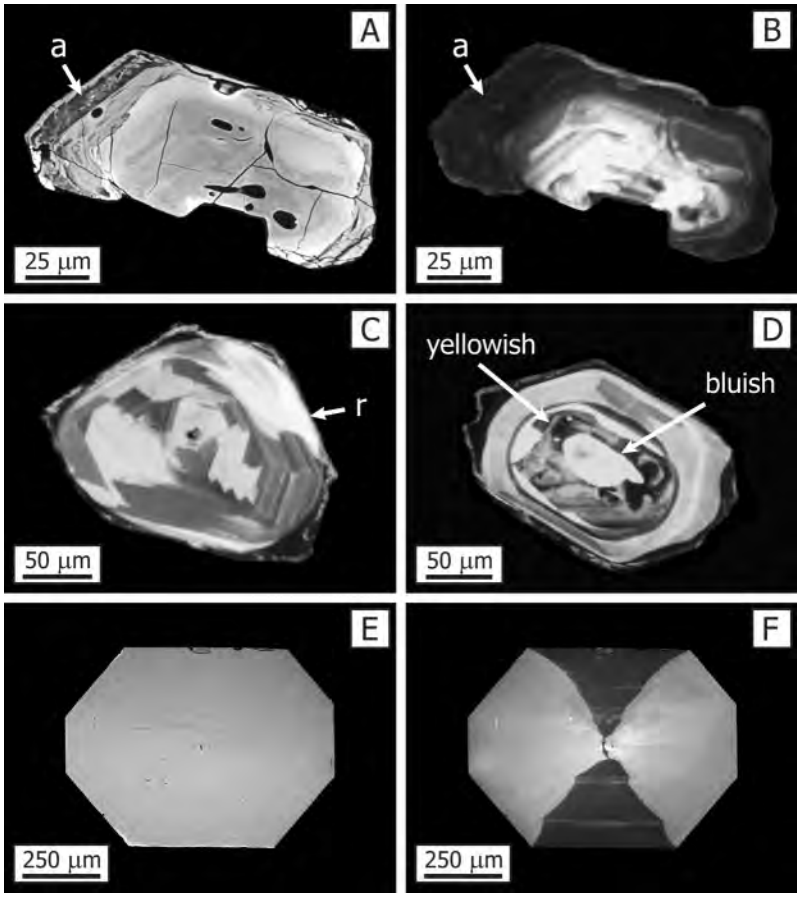


**Figure 4.** Images of zircon crystals obtained in a SEM (A-D, U Kempe, unpublished; E-F, A Kronz, unpublished). (A) Zircon grain with a hydrothermally altered rim (marked a) from the Eibenstock granite, Blauenthal, German Erzgebirge (BSE image). (B) Panchromatic CL image of the same grain as in A, showing CL quenching in the alteration zone (a) which is enriched in U, Th, Ca, Fe and Y. (C) Panchromatic CL image of a patchily recrystallized zircon from the Saxonian Granulite Complex, Germany. The recrystallized, yellowish luminescent area (r) emits particularly intense CL. (D) Zircon from the Saxonian Granulite Complex, Germany. The panchromatic CL image was obtained with a PMT (Oxford R4) that is more sensitive the blue than in the yellow region of the electromagnetic spectrum. As an analytical artifact, the CL intensity of a bluish luminescent core in a yellowish luminescent zircon is apparently overestimated. (E) Pure, synthetic $ZrSiO_4$ crystal, grown using the Li-Mo flux technique (Hanchar et al. 2001), BSE image. (F) Cathodoluminescence image of the crystal shown in E, revealing clear sector zoning that cannot be seen in the BSE mode. The CL emission is probably related to defects, pointing to local differences in the primary crystallinity.

tions, may improve the crystallinity of zircon through recovery from radiation damage and loss of trace elements. Correspondingly, thermally recrystallized zircon grains often show relatively high CL intensity (Fig. 4C, cf. Gebauer 1990, Vavra et al. 1999, Kempe et al. 2000, Rubatto and Gebauer 2000, Geisler et al. 2001a). By contrast, hydrothermal alteration processes may often decrease the degree of crystallinity and CL intensity. Altered areas with quenched CL are often enriched in Fe, Y, P, Ca, and U (Fig. 4A-B, Kempe et al. 2000). No correlation has been found between CL intensity and Hf content in zircon, and based on the electronic configuration of the Hf atom, it seems unlikely that Hf would contribute to the CL emission of natural zircon.

Uranium and thorium impurities have rather indirect effects on the zircon CL. Poller (2000)

and Poller et al. (2000, 2001) proposed that "U (and Hf) plays an important role in quenching the CL". This hypothesis was disproved by results of heating experiments (Geisler et al. 2001a, Nasdala et al. 2002a). After being annealed, zircon crystals were found to show strongly enhanced CL intensity even though the U (and Hf) content remained the same. Therefore, it was concluded in these studies that the mere presence of U does not quench the CL but rather the CL emission is greatly suppressed by radiation effects. The radioactive decay of trace actinides (U and Th) and their unstable daughter nuclei damages the zircon structure (Ewing et al., this volume). This radiation damage, in turn, leads to a drastic decrease of the CL intensity, particularly of the broad-band emissions. Note that even though most of the structural damage of natural zircon crystals is due to their self-irradiation, other factors such as primary lattice defects and distortions need also be considered when discussing the correlation between CL intensity and structural damage (cf. Figs. 4E and 4F). Also, the influence of Th on the structural damage and, with that, on the CL was considered insignificant in some of the earlier CL studies. However, this is only true for zircon with low Th/U ratio. In rare cases, high Th/U ratios well above one, then often accompanied by Th concentrations in the $10^3$ ppm range, were found. Examples are zircon crystals from Tsakhir, Mongolian Altai, showing no SEM-CL (Kempe et al., unpublished) and primarily zoned (i.e. not recrystallized) patches in zircon grains from the Jack Hills, Western Australia (Nasdala et al. 1996), which also show extremely low CL emission (Kempe et al. 2000).

Another important effect which may be caused by self-irradiation as well as external irradiation is charge transfer (exchange of electrons and holes between neighboring centers) modifying the defect structure of the crystal. This process is well documented for natural fluorite (Chatagnon et al. 1982, Kempe et al. 2002). Similar processes are also of relevance for natural zircon (Solntsev and Shcherbakova 1973, Iacconi and Caruba 1980, Iacconi et al. 1980, Krasnobayev et al. 1988, Claridge et al. 2000). Radiation-induced charge conversion (changes in the valence state of impurity ions) produces additional electron defects that enhance broad-band CL. Charge transfer processes induced by irradiation in more or less well-crystallized zircon grains may be inverted at relatively low temperatures. "Blue" zircon CL anneals at lower temperatures than "yellow" CL because the "yellow" trap lies deeper in the band gap. However, detailed investigations on this subject are still needed.

***Instrumental factors.*** The CL intensity in panchromatic images may be modified by the detection system used. As an analytical artifact, systems with high sensitivity in the blue region yield enhanced intensities for bluish luminescent zircon whereas the "blue" broad-band luminescence is suppressed in images obtained with detectors having low sensitivity in this wavelength range (Fig. 4D; cf. Kempe et al. 2000). Note that intensity relations between different bands and lines observed in a given CL spectrum depend also on the detection mode, i.e., parallel measurement with a multichannel detector [e.g., charge-coupled device (CCD) detector, or diode array detector] or serial data collection with a photomultiplier (PMT). In a similar manner, the presence of narrow $Dy^{3+}$ lines is visible in CL color images as a greenish tint even when broad-band emission prevails (e.g., Götze et al. 1999, Kempe et al. 1999). By contrast, $Dy^{3+}$ lines have only in rare cases (cf. Figs. 3A and B) a notable influence on the intensity patterns in panchromatic SEM-CL images, which is due to their low impact on the integral CL intensity (Kempe et al. 2000). Monochromatic CL imaging, however, makes it possible to trace the distribution of individual emission centers throughout a crystal. Using this technique, it has been shown that the spatial distribution of luminescent $REE^{3+}$ impurities and electron-defect related emission centers may be quite different in one and the same crystal (Remond et al. 2000, Kempe et al. 2000).

It is essential for the correct interpretation of zircon CL images and spectra to estimate the escape depth of the CL signal. Several experiments have shown that escape depths of zircon CL are significantly larger than that of secondary and backscattered electrons. A possible explanation refers to a high efficiency of carrier diffusion with an escape of the electrons and holes away from the excitation site and following recombination for the band-related CL (Kempe et al. 2000, Norman 2002). Possible three-dimensional effects should, therefore, be considered in interpreting zircon CL

images and spectra (Kempe et al. 2000).

Although CL imaging of natural zircon is widely used in geosciences and has been the subject of quite a number of studies, some of the observed phenomena still cannot be explained in a fully convincing way by the existing theories on the CL intensity. This situation means that a simple relationship between the content of one or two trace elements in natural zircon and the panchromatic CL intensity (e.g., Vavra 1990, Poller et al. 2001) cannot be expected. Natural zircon crystals are virtually multi-doped systems and CL emission may be affected by the degree of crystallinity, the electronic structure, self- and external irradiation and the thermal history of the sample.

**Laser-induced time-resolved photoluminescence of zircon**

***Introduction: Steady-state and time-resolved luminescenc***e. Conventionally used steady-state or continuous-wave (CW) luminescence is a process where the excitation sources pump the sample at constant intensity over time necessary to perform the measurement. The final result is, analogous to the CL discussed above, an emission spectrum. The specificity of the technique can be improved by employing a tunable laser as the active component of the system. In an ideal system the exciting wavelength would be tunable through the large fraction of the ultraviolet and visible region of the electromagnetic spectrum. Such a system would enable one to study both the excitation and emission behavior of luminescence centers.

In spite of the great progress that has been achieved in the study of steady-state luminescence of minerals, a great number of the observed luminescence phenomena in minerals are not yet well understood. The reason is that minerals are co-doped, multi-ion compounds and the steady-state spectroscopy may be inadequate as the discriminatory power of the normal emission spectra is somewhat limited. Therefore, we need to assume that the majority of luminescence spectra published thus far is likely to consist of overlaps of several types of emissions. There is, however, another physical parameter that may be extremely useful, namely, the fluorescence lifetime or decay time. This is the exponential decay time for the fluorescence emission assuming pulse excitation. The decay time is a measure of the transition probability from the emitting level. Luminescence can be observed over time range of femto- to milliseconds. Decay time is a characteristic and unique property and no two luminescence emissions will have exactly the same decay time. The enormous dynamic temporal time range combined with intrinsic sensitivity makes time-resolved luminescence a uniquely powerful spectroscopic tool.

Both the spectral and temporal nature of the luminescence emission bands can be determined by means of time-resolved spectroscopy. By using such techniques, it is possible to separate overlapping emissions that have different origins and, therefore, different luminescence lifetimes. For this, the intensity in a specific time "window" at a given delay after the excitation pulse is recorded, where both delay and gate width have to be carefully chosen. The added value of the method is the energetic selectivity of a laser beam, which enables one to combine time-resolved spectroscopy with monochromatic excitation. Time-resolved luminescence thus provides numerous ways to detect the presence of luminescence centers (transition elements, lanthanides and actinides) in natural zircon, which would have been obscured by strong broad-band emissions under continuous excitation (steady state laser or electronic excitations).

***Intrinsic broad-band photoluminescence.*** The PL spectrum of zircon (i.e. light emission excited by light) is similarly complex in nature as the CL discussed above. Apart from impurity-related emissions, which will be discussed below, the PL spectrum of natural zircon is often characterized by a broad intrinsic band (Taraschan 1978, Shinno 1986, Krasnobayev et al.1988, Votyakov et al. 1993, Gorobets and Rogozin 2001) in the yellow range of the electromagnetic spectrum (Fig. 5). The excitation of this emission band peaks at 310 nm (i.e., this yellow PL is most intense with 310 nm excitation). The broad yellow band at 575 nm has a decay time of 25-35 μs. It was also observed as a result of n-irradiation and α-irradiation of synthetic, initially non-luminescent $ZrSiO_4$, with the

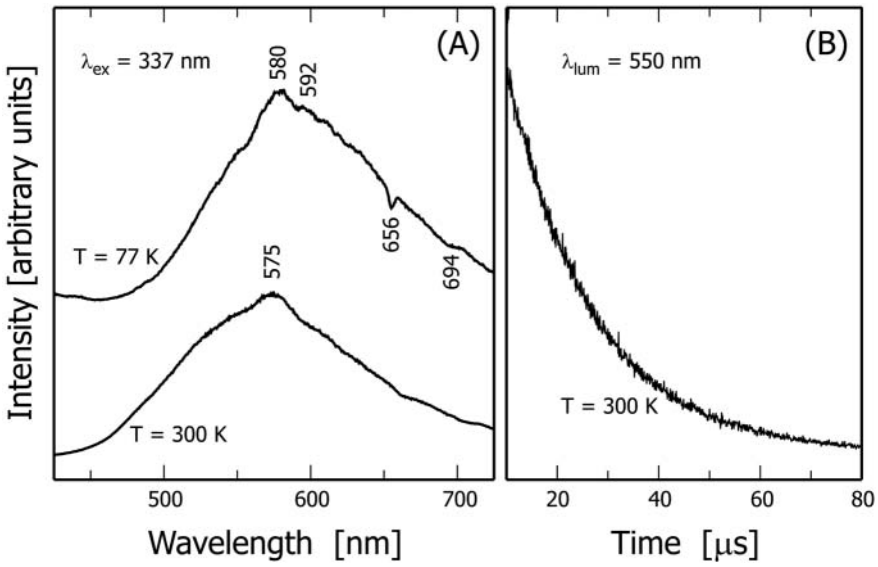


**Figure 5**. Intrinsic broad-band PL, which was observed from all investigated natural zircon samples thus far. (A) Spectra obtained at 300 and 77 K (spectral resolution ~1 nm). The two "negative" lines are caused by impurity $U^{4+}$, through reabsorption of light. (B) Decay of the yellow broad-band PL. Note that the decay of the emission intensity was not measured at the band maximum but at the high frequency slope of the band (550 nm). This was done to avoid any biased results that could potentially be caused by effects of the $Dy^{3+}$ emission peaking at 575 nm. Redrawn (modified) from Gaft et al. (2002).

band intensity increasing proportionally with the irradiation time (Gaft et al. 2002). Analyses at 300 and 77 K with different laser excitations, delays and gates showed that, in spite of the very broad half-width and the apparently asymmetric shape, this luminescence consists of only one band. Gaft et al. (2002) found that for both alpha and neutron irradiation, such induced luminescence is stable for at least several years after irradiation. The spectral shape of this radiation-induced luminescence is very close to those of natural zircon samples. Its decay time is of approximately 30-35 μs and the intensity remains stable after heat-treatment up to 700°C, which is also characteristic for natural zircon. Gaft et al. (2002) therefore concluded that the "classical" yellow luminescence band of natural zircon ($\lambda_{max}$ = 575 nm; half-width $\Delta$ = 160 nm; decay time $\tau$ = 25-35 μs), is connected with radiation-induced centers. In minerals, the source of irradiation may be connected with radioactive decay of U and Th impurities. The exact type of the yellow luminescence center needs clarification.

***Impurity-related photoluminescence***. Impurity-related centers in zircon may give rise to broad-band and narrow-band PL emissions. Only a brief overview is given in the following. For more details on impurity-related PL see, for instance, Taraschan (1978), Shinno (1987), Krasnobayev et al.(1988), Votyakov et al.(1993), Gaft et al.(2000b) and Gorobets and Rogozin (2001). Zircon crystals containing uranium show often intense, green luminescence that is assigned to $(UO_2)^{2+}$ centers (Fig. 6). This luminescence was also observed in synthetic zircon doped with U and P. By contrast, in synthetic zircon crystals doped either with Th and P or U only, such luminescence was not obtained. The causal connection of this emission with uranium is underlined by the fact that its intensity correlates with the U content determined by ICP-MS. Another typical luminescence feature of many natural zircon samples is a broad, deep red luminescence band (Fig. 6). This red emission is connected with forbidden d-d transitions in $Fe^{3+}$. It is thermally stable and dominates in zircon samples that were heat-treated at 800°C. The decay time of 1-2 ms is very long and, correspondingly, the red $Fe^{3+}$ emission appears especially intense in spectra with long delay times in which the stronger yellow luminescence is already quenched. Strong luminescence of $Cr^{3+}$and

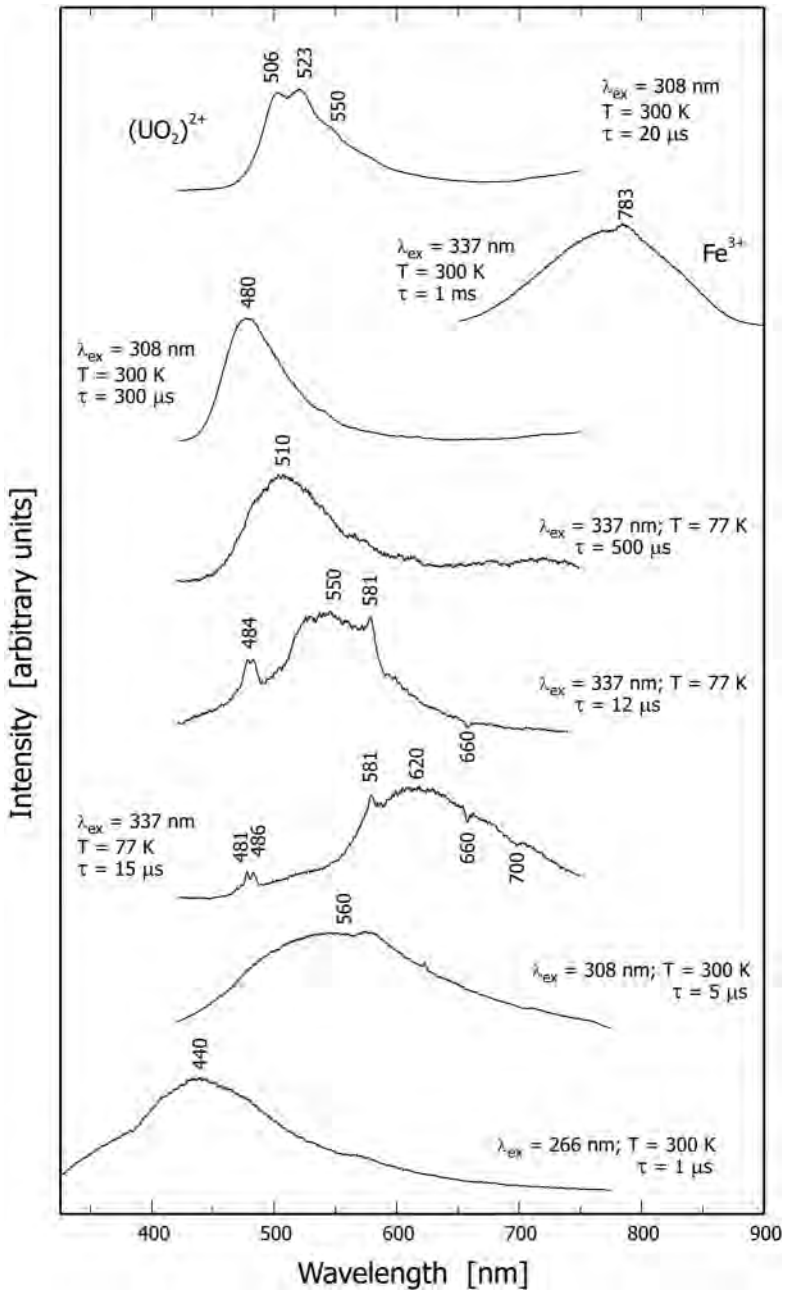


**Figure 6.** Impurity broad-band PL in natural zircon samples (delay time 10 ns, gate 19 ms, spectral resolution ~1 nm). Excitation wavelength, temperature and decay time (τ) are individually reported for each spectrum. The two upper spectra are assigned to $(UO_2)^{2+}$ and $Fe^{3+}$, respectively. The other six spectra show emissions of unidentified centers. As in Figure 5, "negative" reabsorption lines in the range 650-700 nm are due to traces of $U^{4+}$. Spectra: G Panczer and M Gaft (unpublished).

$Cr^{5+}$ in the red and IR parts of the electromagnetic spectrum has been observed from synthetic, doped $ZrSiO_4$ but not for natural zircon thus far. Finally, $REE^{3+}$ centers, which give rise to mostly narrow-band emissions, are particularly typical of zircon. There are several REE impurities that are not detectable or difficult to detect under UV excitation but easily revealed by laser-induced

**Table 1.** Examples for characteristic emission lines and decay times of chromium and rare-earth elements in natural zircon. Data after Gaft et al. (2000a,b,c; 2001).

| Center | $\lambda_{lum}$ [nm] | $\lambda_{ex}$ [nm] | t [µs] | Transition |
|---|---|---|---|---|
| $Cr^{3+}$ | 694 | 532 | 3-5 | $^2E \rightarrow {}^4A_2$ (R-lines), |
| | 775 | | 3-5 | $^4T_2 \rightarrow {}^4A_2$ (broad) |
| $Cr^{5+}$ (300 K) | 1213 | 532 | $2 \times 10^{-1}$ | $^2E \rightarrow {}^2T_2$ |
| $Cr^{5+}$ (12 K) | 1132 | 532, 1060 | $2 \times 10^{-2}$ | $^2E \rightarrow {}^2T_2$, $^2B_1 \rightarrow {}^2A_1$ |
| | 1154 | | | |
| | 1191 | | | |
| | 1215 | | | |
| | 1258 | | | |
| $Ce^{3+}$ | 355 | 266 | $2 \times 10^{-2}$ | $^2D \rightarrow {}^2F$ |
| $Pr^{3+}$ | 489 | 337 | 1 | $^3P_0 \rightarrow {}^3H_4$ |
| | 596 | | 10 | $^1D_2 \rightarrow {}^3H_4$ |
| | 621 | | 10 | $^1D_2 \rightarrow {}^3H_4$ |
| $Sm^{3+}$ | 565 | 337 | 550 | $^4G_{5/2} \rightarrow {}^6H_{5/2}$ |
| | 601, 612 | | 550 | $^4G_{5/2} \rightarrow {}^6H_{7/2}$ |
| | 647 | | 550 | $^4G_{5/2} \rightarrow {}^6H_{9/2}$ |
| $Eu^{3+}$ | 596 | 337 | 1500 | $^5D_0 \rightarrow {}^7F_1$ |
| | 616 | | 50 | $^5D_0 \rightarrow {}^7F_2$ |
| | 654 | | 1500 | $^5D_0 \rightarrow {}^7F_3$ |
| | 702 | | 1500 | $^5D_0 \rightarrow {}^7F_4$ |
| | 707 | | 1500 | $^5D_0 \rightarrow {}^7F_4$ |
| $Gd^{3+}$ | 312 | 266 | 2500 | $^6P \rightarrow {}^8S_{7/2}$ |
| $Tb^{3+}$ | 383 | 266 | 325 | $^5D_3 \rightarrow {}^7F_6$ |
| | 415 | | 325 | $^5D_3 \rightarrow {}^7F_5$ |
| | 437 | | 325 | $^5D_3 \rightarrow {}^7F_4$ |
| | 489 | | 2400 | $^5D_4 \rightarrow {}^7F_6$ |
| | 548 | | 2400 | $^5D_4 \rightarrow {}^7F_5$ |
| $Dy^{3+}$ | 478 | 337 | 120 | $^4F_{9/2} \rightarrow {}^6H_{15/2}$ |
| | 575 | | 120 | $^4F_{9/2} \rightarrow {}^6H_{13/2}$ |
| $Ho^{3+}$ | 549 | 337 | 1 | $^5S_2 \rightarrow {}^5I_8$ |
| | 665 | | 1 | $^5F_3 \rightarrow {}^5I_7$ |
| $Er^{3+}$ | 549 | 337 | 10 | $^4S_{3/2} \rightarrow {}^4I_{15/2}$ |
| | 559 | | 10 | $^4S_{3/2} \rightarrow {}^4I_{15/2}$ |
| $Tm^{3+}$ | 289 | 266 | 15 | $^1I_6 \rightarrow {}^3H_4$ |
| | 347 | | 15 | $^1I_6 \rightarrow {}^3H_6$ |
| | 458 | | 5 | $^1D_2 \rightarrow {}^3H_4$ |
| | 483 | | 120 | $^1G_4 \rightarrow {}^3H_6$ |

or/and time-resolved luminescence spectroscopy. The characteristics of $REE^{3+}$ emission lines identified for zircon are given in Table 1 and selected spectra are presented in Figure 7.

In addition, a number of unidentified luminescence bands (Fig. 6) were observed from natural zircon samples. These are usually obscured by stronger emissions and may be detected only by time-resolved spectroscopy. These bands are most probably related to impurities. To identify the exact nature of these impurities, synthetic $ZrSiO_4$ doped with potential activators such as Mn, Cr, Ti, Co, Ni, Pb and Sb have been studied (Gaft et al. 2002). Bands similar to those detected in natural zircon, however, were not observed from the synthetic samples. The nature of the corresponding luminescence centers needs further investigation.

The emission of PL does not only depend on the luminescent center itself but is also affected by crystal field effects (cf. Marfunin 1979a,b), particularly in radiation-damaged zircon. Because it is known that the yellow PL of natural zircon is partially radiation-induced, nominally pure zircon irradiated by different doses of X-ray, γ-ray, neutron and α-irradiation have been studied (Gaft et al. 2002). Table 2 presents the comparison of the half width of the $Dy^{3+}$ main emission line obtained from different natural and synthetic samples. Note that its FWHM (full width at half band-maximum) shows clear correlation with the degree of crystallinity. Another example is presented in Figure 8, which shows the broadening of several $REE^{3+}$ emissions (see in particular the two $^4G_{5/2} \rightarrow {}^6H_{7/2}$ transitions of $Sm^{3+}$ at 604 and 615 nm). Photoluminescence and especially time-resolved PL thus allows one to estimate the concentration of irradiation-induced defects via the intensity of the broad defect emission or via the width of the rare earth emission lines.

## VIBRATIONAL SPECTROSCOPY OF ZIRCON

### Infrared absorption spectroscopy of zircon

***Assignment of infrared absorption bands.*** For the tetragonal $ZrSiO_4$ ($I4_1/amd$), seven infrared-active modes (internal = $2A_{2u} + 2E_u$, external = $A_{2u} + 2E_u$) are predicted by group theory (Dawson et al. 1971). According to the selection rules, modes of $E_u$ symmetry are observed when the electric vector of the incident infrared radiation, ***E***, is perpendicular to the c-axis while those of $A_{2u}$ symmetry are observed when ***E*** is parallel to the *c*-axis. Polarized infrared (IR) measurements were carried out to identify the $E_u$ and $A_{2u}$ modes and to obtain the transverse optical (TO) and longitudinal optical (LO) modes (Dawson et al. 1971, Gervais et al. 1973, Zhang and Salje 2001). Frequencies of the main infrared-active TO and LO modes, their damping and band assignments are compiled in Table 3. Among the four internal $SiO_4$ vibrations, two are assigned to

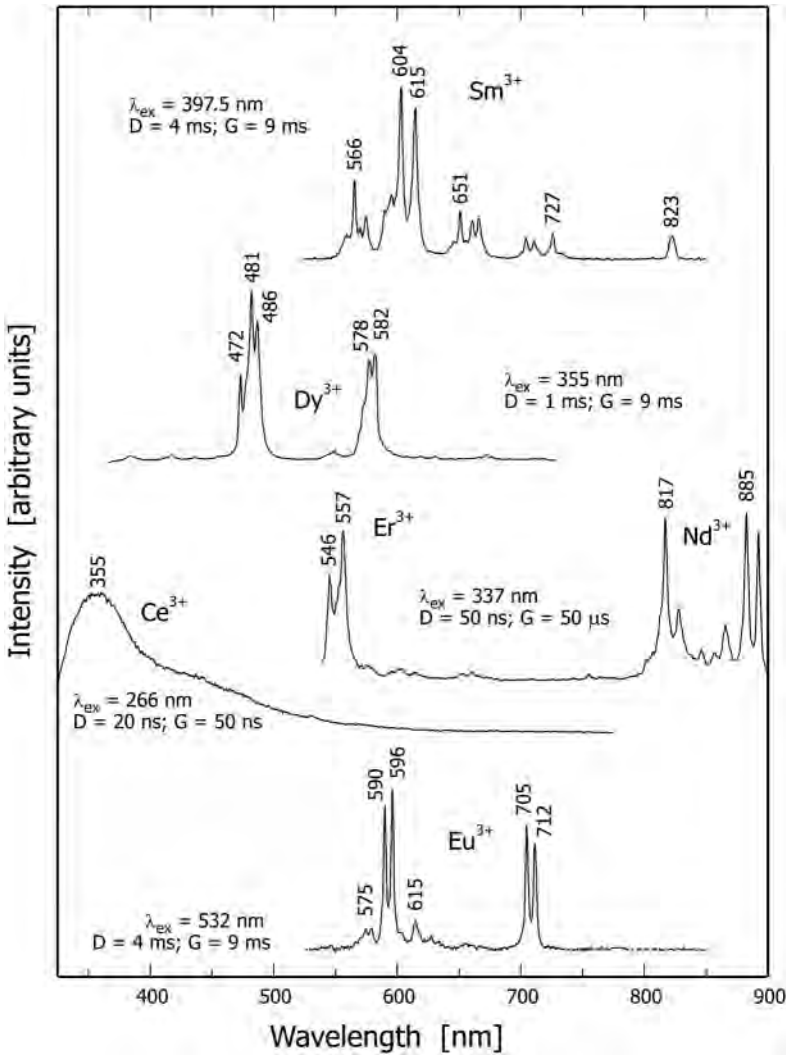


**Figure 7.** Examples for time-resolved spectra of emission lines of rare-earth elements in zircon (spectral resolution ~1 nm). Excitation wavelength, delay (D) and gate (G) are given for each individual spectrum. Spectra: G Panczer and M Gaft (unpublished).

**Table 2.** Effects of the crystallinity of zircon on the half-width of the 581 nm $Dy^{3+}$ emission line ($^4F_{9/2} \rightarrow {}^6H_{13/2}$). Data after Panczer (2001).

| Sample | Band half-width [nm] |
|---|---|
| Synthetic, $Dy^{3+}$-doped zircon | 0.57 |
| Natural zircon, non-metamict | 0.76 |
| Natural zircon, metamict (untreated) | 2.10 |
| Natural zircon, metamict (heat-treated at 800°C) | 0.72 |

**Table 3.** Infrared-active TO and LO modes of crystalline zircon. Data after Zhang and Salje (2001).

| $E_u$ ($\boldsymbol{E} \perp$ c) | | | | | $A_{2u}$ ($\boldsymbol{E} \parallel$ c) | | | | |
|---|---|---|---|---|---|---|---|---|---|
| $w_{TO}$ | $G_{TO}$ | $w_{LO}$ | $G_{LO}$ | assignment | $w_{TO}$ | $G_{TO}$ | $w_{LO}$ | $G_{LO}$ | assignment |
| 282 | 7 | 351 | 7 | external (R) | 338 | 10 | 475 | 12 | external (T) |
| 385 | 9 | 416 | 7 | external (T) | 606 | 9 | 644 | 17 | $\nu_4(SiO_4)$ |
| 431 | 5 | 470 | 3 | $\nu_4(SiO_4)$ | 980 | 13 | 1101 | 15 | $\nu_3(SiO_4)$ |
| 880 | 11 | 1030 | 12 | $\nu_3(SiO_4)$ | | | | | |

All values (frequency $w$ and damping $G$) are given in $cm^{-1}$.
R = rotary vibration, T = translatory vibration.

$\nu_3(SiO_4)$ (anti-symmetric stretching, $A_{2u}$ at 980 $cm^{-1}$ and $E_u$ at 880 $cm^{-1}$) and the other two are assigned to $\nu_4(SiO_4)$ (anti-symmetric bending, $A_{2u}$ at 606 $cm^{-1}$ and $E_u$ at 431 $cm^{-1}$), whereas the $\nu_1(SiO_4)$ and $\nu_2(SiO_4)$ modes (symmetric stretching and bending vibrations of the tetrahedrons, respectively) are not infrared active due to symmetry reason. By contrast, Kolesov et al. (2001) listed the $A_{2u}$ mode near 980 $cm^{-1}$ as $\nu_1(SiO_4)$. The assignment of the three external modes (two translatory and one rotary) in the far-infrared, which are mainly related to $SiO_4$ group motions against Zr atoms and motions of Zr atoms (Farmer 1974), is still controversial. Dawson et al. (1971) and Kolesov et al. (2001) assigned the $E_u$ mode near 385 $cm^{-1}$ mainly as a rotary vibration of the $SiO_4$ tetrahedrons and the $E_u$ mode near 282 $cm^{-1}$ as a translatory mode, whereas Farmer (1974) and Zhang et al. (2001) attributed the former as translatory mode and the latter as rotary vibration.

An advantage of the infrared spectroscopy is that the absorption of infrared light is mainly dependent on atomic masses and the length and strength of interatomic bonds. Therefore, infrared spectra can give valuable information on the crystal structure, composition and surface of the studied material. Due to its short length scale it probes, infrared spectroscopy may reveal local structural configuration of crystalline and amorphous phases. In addition, using polarized incident radiation, one can obtain information of anisotropy and anharmonicity, and determine dielectric constants as well as TO and LO phonon bands from infrared reflection spectroscopy.

The effect of cation substitutions and chemical impurities on IR band frequencies of zircon

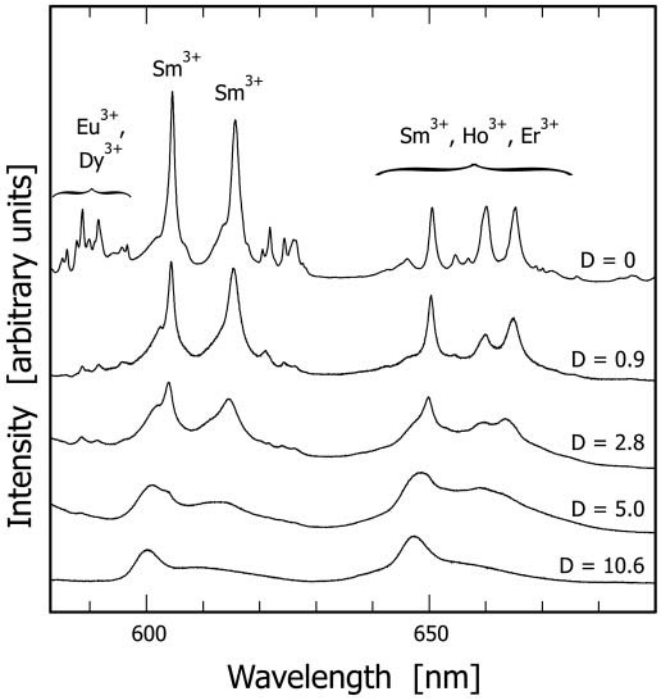


**Figure 8.** Effects of radiation damage in zircon crystals from Sri Lanka on their laser-induced PL spectra, here shown for the red region of the electromagnetic spectrum. Spectra (488 nm excitation, resolution 0.1 nm) were modified from Nasdala et al. (submitted) and are stacked for more clarity. With increasing radiation damage, $REE^{3+}$ emission lines are broadened. To provide a measure for the increasing metamictization, radiation doses (D) are given in $10^{18}$ α-events per gram. These values represent the total time-integrated self-irradiation lasting for a ~550-570 Myr period (the U-Pb zircon age). Note that the Sri Lankan zircon crystals have experienced partial structural reconstitution (e.g., Nasdala et al. 2001d). The presently observed radiation damage is, therefore, significantly lowered and does not correspond with the calculated α-doses anymore. To provide comparability with the literature, however, total α-doses are given in this and the following figures.

and structural analogues has been the subject of several spectroscopic investigations. Hubin and Tarte (1971) studied the relationship between the frequencies of the stretching and bending bands of the $SiO_4$ and $GeO_4$ groups and ionic radius of tetravalent Zr, U, Th, Hf, and Ce ions. These authors found that among the cations studied, the substitution of $Hf^{4+}$ for $Zr^{4+}$ results in a small frequency shift due to the close values of the radius, whereas substitutions of other ions with relatively large radius (e.g., $U^{4+}$ and $Th^{4+}$) causes a more pronounced impact on the bands frequencies. More detailed investigations of the vibrational spectra of zircon, thorite, hafnon, coffinite and their structural analogues, as well as calculations of the constants and frequencies of the vibrations, active in IR- and Raman spectroscopy, were reported, for instance, by Caruba et al. (1975), Povarennych et al. (1977), Lazarev et al. (1980), and Heyns et al. (1990). Infrared data of synthetic hydroxylated zircon crystals (Caruba et al. 1985) showed that the incorporation of $(OH)^-$ groups in the zircon lattice results in changes of unit-cell parameters as well as frequency shifts of the main $\nu_3$ ($SiO_4$) and $\nu_4$($SiO_4$) IR modes.

***Effects of radiation damage on the phonon spectrum of zircon.*** In addition to the assignment of the infrared spectrum of crystalline zircon and the identification of this mineral using IR spectroscopy as a fingerprint technique, many of the early IR studies on zircon were subjected to radiation damage phenomena (e.g., Launer 1952, Saksena 1961, Akhmanova and Leonova 1961, 1963;

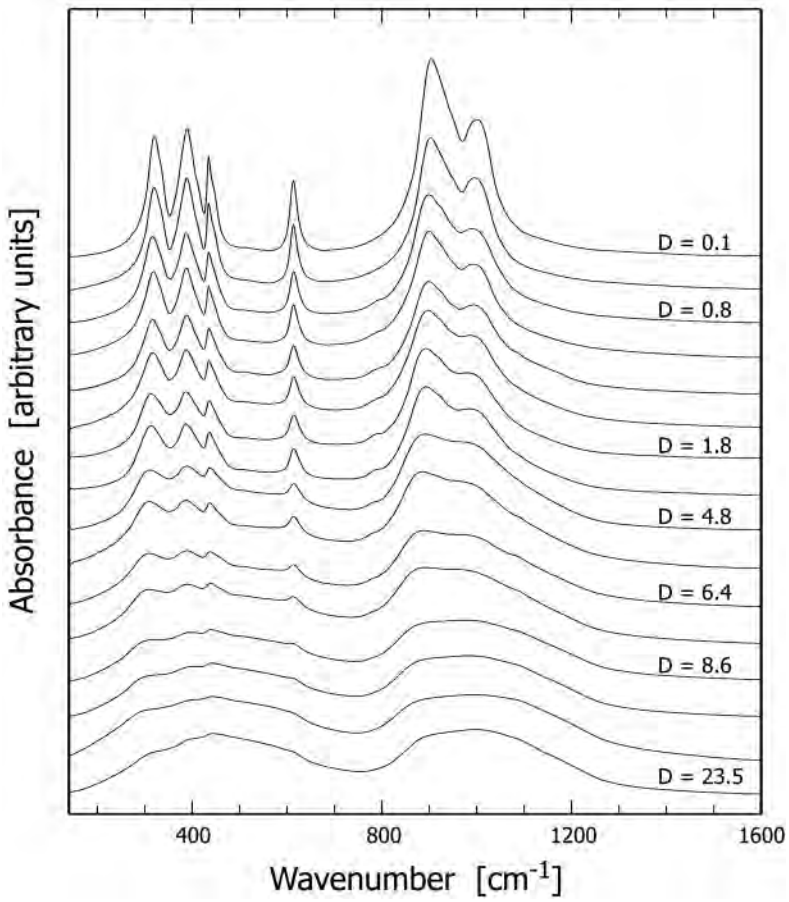


**Figure 9.** Radiation damage effects in zircon crystals from Sri Lanka on their infrared spectra in the range 150-1600 $cm^{-1}$ (redrawn after Zhang and Salje 2001, modified). Absorption spectra are stacked for more clarity. Doses are given as in Figure 8.

Kristanovic 1964, Alexanian et al. 1966). Figure 9 shows the effect of α-event damage on the infrared spectrum of zircon. Different spectral parameters have been used to estimate the degree of damage or radiation dose, as for instance the width of the 616 $cm^{-1}$ band (Deliens et al. 1977), the position and shape of the $\nu_3(SiO_4)$ band near 980 $cm^{-1}$ (Rakovich and Gevorkyan 1988, Yang et al. 1990), the infrared reflectivity of intratetrahedral bands (Zhang and Salje 2001) and multi-phonon interactions (Wasilewski et al. 1973, Woodhead et al. 1991a, Zhang et al. 2002). Zhang and Salje (2001) demonstrated how to use the effective medium theory, an approach used to study effective dielectric and optical properties of materials with multi-phases (Granqvist and Hunderi 1978), to quantitatively analyze the fraction of the amorphous phase in metamict zircon.

Extensive IR spectroscopic investigations were stimulated by the aim to understand the real structure of metamict zircon and structural changes at the atomic level caused by the impact of radioactivity. Based on previous investigations, Pellas (1965) proposed that zircon decomposes into $ZrO_2$ and $SiO_2$ as a result of metamictization. Wasilewski et al. (1973) reported infrared data supporting the decomposition model, and these authors suggested a two-stage damage process involving the deformation of $SiO_4$ tetrahedrons and the sequent breakdown of the zircon lattice into the oxides. However, the model was contradictory to the results of Akhmanova and Leonova (1961) and Vance (1975) who did not detect characteristic signals of $ZrO_2$ and $SiO_2$ in untreated zircon samples. Wasilewski et al. (1973) argued that the absence of the oxides in the study of Akhmanova and Leonova (1961) could be due to incurred insufficient radiation damage. Recent spectral studies, however, did not favor $ZrO_2$ and $SiO_2$ as the final state of metamictization of zircon. Based on their mid-infrared data, Woodhead et al. (1991a) reported that the structure of metamict zircon consisted of distorted and disoriented isolated $SiO_4$ tetrahedrons with few if any undisplaced Zr cations. Polarized reflectance measurements (Zhang et al. 2000c) revealed that in the $SiO_4$ stretching region, the spectra of metamict zircon show features very different from that of glassy $SiO_2$. Zhang and Salje (2001) observed the change of local configurations in zircon crystals and the formation of new Si–O–Si linkages and possible partial polymerization, i.e., $SiO_4$ tetrahedrons may not remain fully isolated in metamict zircon. Partial polymerization in metamict zircon was also revealed by $^{29}Si$ nuclear magnetic resonance (NMR) measurements (Farnan and Salje 2001).

Infrared spectroscopic characterization of thermally or hydrothermally annealed zircon has resulted in new insights into the recrystallization and structural recovery of metamict zircon. The effect of high-temperature annealing on infrared spectra of metamict zircon was an increase in intensity and band sharpening. (e.g., Biagini et al. 1997). Vance (1975) showed that the decomposition of metamict zircon into $ZrO_2$ and $SiO_2$ could take place during high-temperature annealing. The recent study of Colombo et al. (1999) reported a two-stage recovery, a relaxation of the $SiO_4$ tetrahedrons and the possible formation of new phases. Zhang et al. (2000c) concluded from the oriented dependence of mid-infrared spectra obtained from metamict zircon that the recrystallization process in zircon involves epitaxial growth of the residual crystalline phase and reaction of $ZrO_2$ and $SiO_2$ produced by decomposition. Infrared data also showed that recrystallization of zircon is a multi-stage process and that it strongly depends on the initial degree of damage of the metamict zircon (Zhang and Salje 2002). The recrystallization process was also characterized using multi-phonon bands (Woodhead 1991a, Zhang et al. 2002). Geisler et al (2002) used the powder absorption technique to monitor the structural recovery and recrystallization in a highly metamict zircon upon hydrothermal annealing. Their data revealed spectral variations taking place at temperature as low as 200°C and the presence of monoclinic $ZrO_2$ at higher temperatures.

***Hydrous species in zircon.*** Hydrous species (OH and $H_2O$) in zircon have been the subject of extensive infrared studies. Natural zircon containing as much as 16.6 wt % water (which is more than 50 mol %) was described by Coleman and Erd (1961). Such high water content was always related to a significantly radiation-damaged structure. By contrast, only traces of $(OH)^-$ groups are primarily incorporated in (crystalline) zircon (Woodhead et al. 1999a,b, Ilchenko and Korzhinskaya 1993, Ilchenko 1994, Nasdala et al. 2001b).

Infrared spectroscopy has been widely used to investigate hydrous species in zircon because of its high sensitivity to hydrogen-bearing substances and advantages in determination of the directions of O–H dipoles. Most infrared studies on hydrous species in zircon have been focused on the following issues: (1) the nature of hydrous species and their incorporation into the crystal lattice of zircon, (2) their possible role in metamictization, and (3) their thermal stabilities and their role in the recrystallization process.

Frondel (1953) proposed the substitution $(OH)_4 \leftrightarrow SiO_4$ in zircon. By contrast, Mumpton and Roy (1961) found that data from chemical analysis of natural zircon lie along $ZrSiO_4$-$H_2O$ join and this was taken as evidence for the presence of molecular $H_2O$ rather than $(OH)^-$ groups by these authors. Studies of Rudnitskaya and Lipova (1972) suggested the simultaneous occurrence of molecular water and hydroxyl groups. An infrared study of Woodhead et al. (1991b) indicated that the principal hydrous component in metamict zircon is $(OH)^-$ rather than $H_2O$ because of the lack of the H-O-H bending mode near 1630 $cm^{-1}$ and the combination (bending + stretching) mode at around 5200 $cm^{-1}$. The results from most recent spectral investigations of hydrous species in zircon are still controversial. The work of Nasdala et al. (2001b) indicated the simultaneous presence of both hydroxyl groups and molecular water in metamict zircon whereas the results of Zhang et al. (2002) essentially supported the observations of $(OH)^-$ by Woodhead et al. (1991b). Few studies to determine hydrogen locations in natural zircon have been done thus far. Woodhead et al. (1991b) suggested that the 3420 $cm^{-1}$ ($\boldsymbol{E} \parallel c$) and 3385 $cm^{-1}$ ($\boldsymbol{E} \perp c$) are associated with Si-occupied tetrahedrons, and weak absorption near 3510 $cm^{-1}$ ($\boldsymbol{E} \parallel c > \boldsymbol{E} \perp c$) is attributed to OH sites at vacant tetrahedrons. Ilchenko and Korzhinskaya (1993) and Ilchenko (1994) found wide set of hydroxyl groups of different thermal stability in zircon crystals from kimberlites. Nasdala et al. (2001b) proposed three crystallographic models for probable locations of $(OH)^-$ groups in crystalline zircon. As the local structure of the metamict state of zircon is still under debate, it is currently impossible to obtain a clear picture on the hydrous sites in metamict state. The hydrous ions in amorphized materials are expected to have complex sites which produce a broad absorption between 2500 and 3600 $cm^{-1}$.

The possible role of hydrous components in metamictization and recrystallization in metamict minerals has drawn the attention of researchers. Figure 10 shows the effect of radiation damage on the O–H stretching bands in zircon. Studies of Frondel and Collette (1957) and Geisler et al. (2002) indicated that the presence of $H_2O$ appears to lower the recrystallization temperature and increases the recrystallization rate of metamict zircon. By contrast, results obtained from hydrothermal experiments (Pidgeon et al. 1966, 1973) suggested that $H_2O$ has little effect on the recrystallization rate of metamict zircon. Based on the similarities of spectral features between synthesized hydroxylated zircon and metamict zircon, Caruba et al. (1985) proposed that natural metamict zircon is formed at low temperature in a hydrous and fluorinated environment and OH is essential in metamictization process. A hypothesis that hydrous species stabilize the metamict state of zircon was proposed by Aines and Rossman (1985, 1986). By contrast, recent investigations suggested that hydrous species in metamict zircon are predominantly secondary in nature, i.e. the majority of hydrogen incorporation into metamict zircon must have occurred during or after sustaining radiation damage (Woodhead et al. 1991b, Nasdala et al. 2001b, Zhang et al. 2002). In these same studies it has also turned out that hydrogen incorporation is not necessary to stabilize the metamict state, even though hydrous species may help to compensate for local charge imbalance.

## Raman spectroscopy of zircon

***Introductory remarks.*** Infrared absorption and Stokes-type Raman scattering are similar insofar as energy of an incident beam of light is used to excite vibrations of molecular units and lattice vibrations in the analyzed sample. Quantum energies of these vibrations (phonons) correspond typically with the photon quantum energies of mid-infrared light, which is why infrared light can be absorbed upon the excitation of vibrations. Raman spectroscopy uses ultraviolet, visible or near

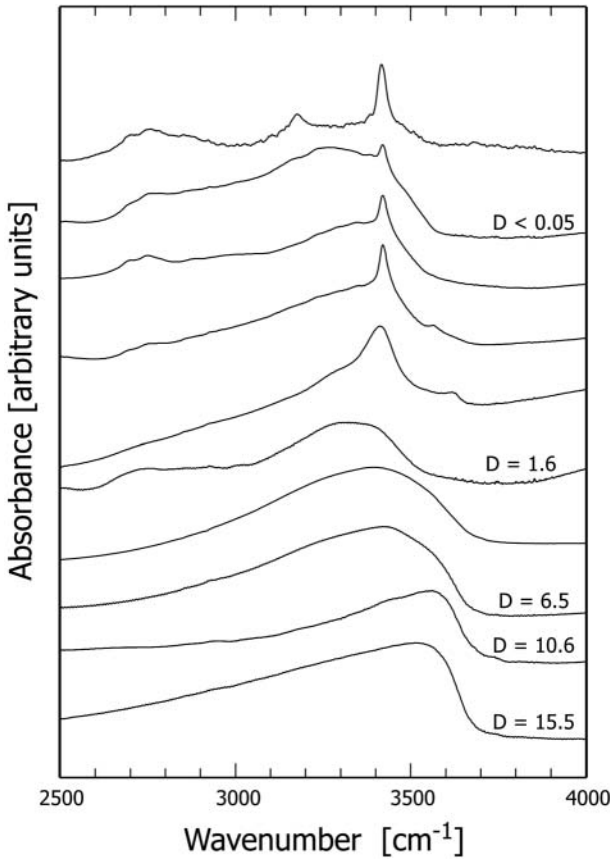


**Figure 10.** Polarized infrared absorption spectra (***E*** ‖ *c*) in the O–H stretching region obtained from natural zircon crystals of different origin (redrawn after Nasdala et al. 2001b, modified). Spectra are shown stacked, with increasing metamictization from top to bottom. Since samples had different thicknesses, intensities of absorption bands cannot be directly compared. Doses for five zircon samples from Sri Lanka are given as in Figure 8.

infrared light. Due to their much higher energies, such photons cannot be absorbed though the excitation of vibrations only. By contrast, if light and sample interact in a way that inelastic collisions of photons with the molecule or lattice result in the excitation of vibrations in the sample (Raman scattering), only a small portion of the photon energy is used. Correspondingly, the resulting Stokes-type Raman scattered light has lost this energy portion and is shifted towards lower wavenumbers (redshift). Analogous to the infrared absorption, the Raman effect is sensitive to the nearest environment of the vibrating bond(s). Raman spectra provide information about the local symmetry such as geometrical factors, bond force ratios and bond distances, and the short-range order of the analyzed material. For the physical background see, for example, Long (1977) and McMillan (1985).

***Raman spectrum of crystalline, pure $ZrSiO_4$.*** The number and symmetry of Raman- and infrared active vibrations are derived through group theory and symmetry analysis (e.g., Dawson et al. 1971). From this, twelve Raman-active ($2A_{1g} + 4B_{1g} + B_{2g} + 5E_g$) in addition to seven infrared-active modes are predicted. The Raman spectrum of zircon is shown in Figure 11. It is dominated by internal vibrations of $SiO_4$ tetrahedrons, with the most intense band at 1008 $cm^{-1}$ ($B_{1g}$ mode, only observed with ***E*** _|_ c) assigned to the antisymmetric $SiO_4$ stretching mode. To avoid confusion of terms, it should be noted that the nomenclature for internal vibrations is inconsistently used in the literature. For example, the antisymmetric $SiO_4$ stretching ($\nu_3$ internal mode) is sometimes referred

to as $\nu_3$(Si–O) and sometimes as $\nu_3(SiO_4)$. We prefer to use the latter expression in this paper. Internal stretching and bending modes involve vibrations of all bonds of a molecular unit. The four Si–O bonds of a tetrahedron cannot vibrate independently from one another. Also, it is obvious that at least two bonds must stretch to get an antisymmetric vibration. Expressions such as $\nu_3$(Si–O) seem, therefore, somewhat imprecise.

Even though the Raman spectra of zircon-type orthosilicate minerals are well known since the 1970s (Griffith 1970, Dawson et al. 1971, Nicola and Rutt 1974, Syme et al. 1977, Mazhenov et al. 1979), there is still some disagreement about the assignment of observed Raman bands to vibrations. The interpretation of the three main bands at 439, 974 and 1008 $cm^{-1}$ (Fig. 11) as internal $SiO_4$ modes is apparently unambiguous. It is also generally agreed that the three bands at 202, 214 and 225 $cm^{-1}$ are lattice modes (i.e. vibrations involving movements of $SiO_4$ tetrahedrons and Zr ions). There is, however, disagreement about the 202 $cm^{-1}$ band which was interpreted as rotary (Nicola and Rutt 1974) and translatory vibration (Dawson et al. 1971, Syme te al. 1977, Mazhenov et al. 1979, Kolesov et al. 2001). The relatively strong band at 356 $cm^{-1}$ band was described as external lattice mode by Syme et al. (1977) and Mazhenov et al. (1979) and as internal mode [$\nu_4(SiO_4)$, antisymmetric bending] by Dawson et al. (1971) and Ilchenko et al. (1988). The latter assignment seems problematic because the antisymmetric bending of $SiO_4$ tetrahedrons ($\nu_4$), involving movements of $Si^{4+}$ ions, is to be expected at higher frequency than their symmetric bending $\nu_2$ at 439 $cm^{-1}$ (analogous to the higher frequency of $\nu_3$ when compared with $\nu_1$, cf. Fig. 11). Correspondingly, Kolesov et al. (2001) have assigned two low-intensity bands at 641 $cm^{-1}$ ($B_{1g}$) and 546 $cm^{-1}$ ($E_g$) to internal $\nu_4(SiO_4)$ vibrations whereas they described the strong 356 $cm^{-1}$ band as external mode. The assignment of the 641 $cm^{-1}$ band to $\nu_4(SiO_4)$, however, was critically discussed by Hoskin and Rodgers (1996) who suspected this $\nu_4$ mode might either be incorrectly assigned or mixed with an external mode. Similar disagreement exists for the band at 393 $cm^{-1}$ band (internal, Dawson et al.

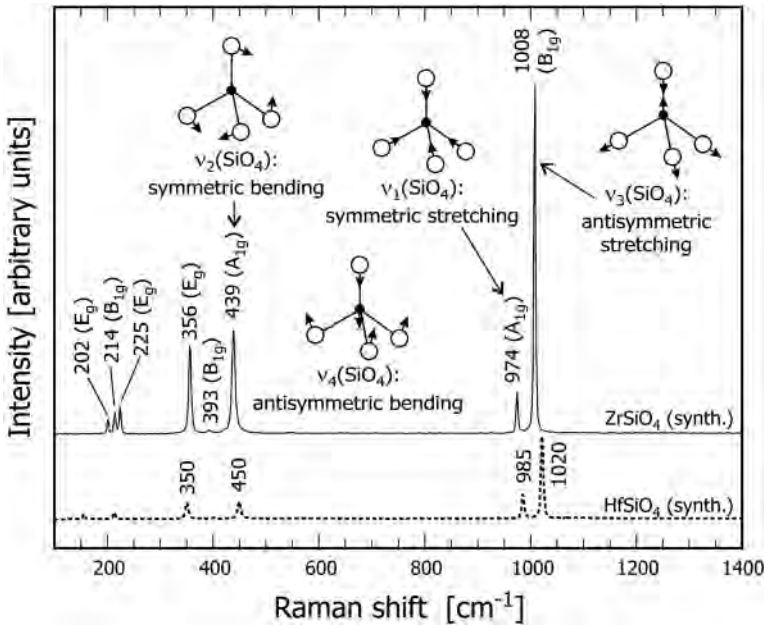


**Figure 11.** Raman spectrum of zircon with general band assignment for the most intense bands. For the internal $SiO_4$ vibrations, small sketches depict movements of oxygen (white balls) and silicon atoms (small black balls). The internal $\nu_4(SiO_4)$ vibration, the assignment of which is still controversial, is not related to a certain band in the picture. The Raman spectrum of hafnon (dotted) is shown for comparison. Note that the spectra of the two orthosilicate minerals are dominated by a greatly similar "fingerprint" pattern of $SiO_4$ vibrations.

1971, external, Syme et al. 1977).

In spite of these minor uncertainties about the band assignment, the Raman spectrum of zircon is highly typical of this mineral and facilitates its unambiguous identification by Raman "fingerprinting." Raman spectroscopy is also routinely applied for the identification and characterization of solid, fluid and gas inclusions in zircon. Apart from the general petrologic and mineralogical interest in inclusions, the host mineral zircon has gained particular attention for such studies. To give an example, due to its extraordinary chemical and physical stability, zircon is able to "trap" high-temperature and high-pressure phases such as microdiamonds (Nasdala and Massonne 2000) and facilitates their transportation to the Earth's surface without transformation or decomposition.

***Effects of the chemical composition on the Raman spectrum.*** The incorporation of non-formula elements in crystalline solids causes general changes of Raman spectral parameters for both internal and external modes, which include frequency shifts, band width increase and also changes of the band shapes such as asymmetries. Depending on nature, extent and effects of the incorporation (e.g., substitution of ions in the lattice with or without major symmetry decrease, incorporation of other molecular units, formation of clusters), Raman bands of the host mineral may also split and lose intensity and additional bands may appear.

In general, effects of non-formula elements in zircon on the Raman spectrum are widely similar to changes in the infrared absorption spectrum (see above). Only a limited number of systematic investigations have been done so far to study and quantify how variations in the chemical composition affect the Raman spectrum of zircon. The substitution of $Th^{4+}$, $U^{4+}$ or $Hf^{4+}$ for $^{[8]}Zr^{4+}$ does not cause major structural changes except unit cell expansion or contraction, respectively. The pattern of Raman bands remains therefore essentially the same but vibrational frequencies shift due to slightly changed bond forces and bond angles and different cation masses. This was first observed by simply comparing the spectra of zircon with $ThSiO_4$ (Syme et al. 1977) and $HfSiO_4$ (Nicola and Rutt 1974). Raman spectral changes in the zircon-hafnon solid solution were studied in more detail by Hoskin and Rodgers (1996). A study on zircon crystals doped with Y and rare earth elements is currently in progress (Hanchar et al. in preparation). As an example, we present Raman spectra of $ZrSiO_4$ doped with $Yb^{3+}$+$P^{5+}$ (Yb in the range 4-12 wt %) in Figure 12. De Waal et al. (1996) studied $ZrSiO_4$ doped with vanadium and they reported additional, low-intensity Raman bands assigned to vibrations of $(VO_4)^{4-}$ groups. These authors concluded that $V^{4+}$ most probably occupies the $^{[4]}Si^{4+}$ site, which is in contrast to earlier results [e.g., Demiray et al. (1970) concluded from electronic absorption measurements that $V^{4+}$ occupies the $^{[8]}Zr^{4+}$ site].

Even though a large number of non-formula elements can be incorporated by natural zircon, their concentration is mostly clearly below the 1 wt % level except for hafnium. Correspondingly, Raman spectra of most natural zircon samples show only minor effects due to their actual chemical composition. Based on the Raman data of Hoskin and Rodgers (1996) it may be concluded that even if as much as 25 % of all $^{[8]}Zr^{4+}$ ions were replaced by $Hf^{4+}$, frequency upshifts of the four main Raman bands (cf. Fig. 11) would not exceed 3 $cm^{-1}$. Spectral changes caused by the mere presence of uranium are almost negligible because of the low $U^{4+}$ concentration in natural zircon. Nasdala et al. (2002a) found that Raman shifts and band widths obtained for a crystalline zircon containing ~ 6000 ppm U and ~16300 ppm Hf (produced through heating of a natural, metamict gemstone) deviated less than 1 $cm^{-1}$ from data of pure $ZrSiO_4$. Also, Nasdala et al. (2001b) found that obtaining O–H stretching and particularly O–H–O bending bands from natural zircon containing hydrous species below 0.5 wt % $H_2O$ is close to the analytical limits of current Raman systems. More pronounced Raman spectral changes are, therefore, only expected for (rare) natural zircon samples which are exceptionally rich in non-formula elements, such as in hydrothermal alteration zones (cf. Frondel 1953, Pointer et al. 1988, Rubin et al. 1989).

***Effects of radiation damage on the Raman spectrum.*** More than 40 years ago (Launer 1952, Akhmanova and Leonova 1961, Saksena 1961) infrared studies showed that there are dramatic changes in the vibrational behavior of natural zircon in dependence on the degree of

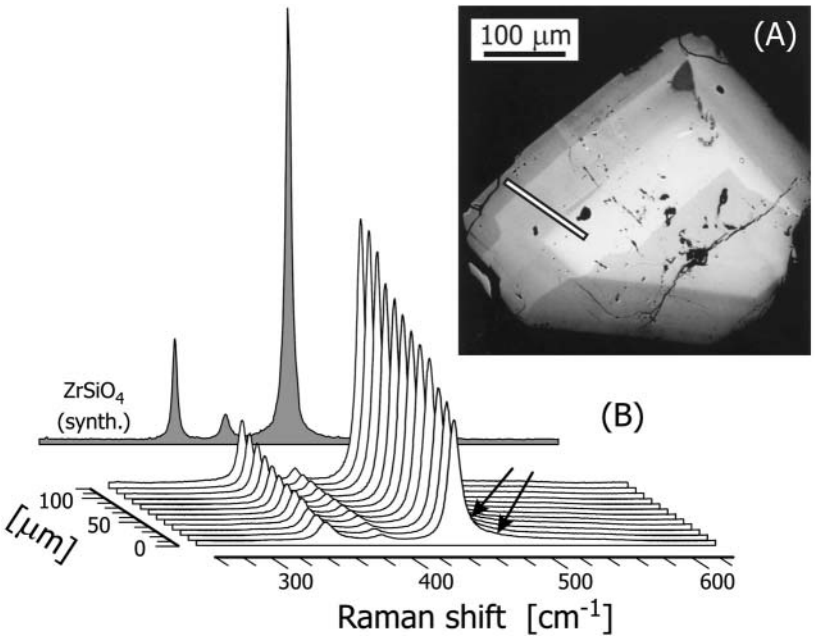


**Figure 12.** Example for Raman spectral changes caused by non-formula elements. (A) Backscattered electron (BSE) image of a zircon crystal doped with $Yb^{3+}$ (4-12 wt %) and $P^{5+}$ (for details see Hanchar et al. 2001). Bright BSE zones correspond to high dopant levels and vice versa. (B) Raman line scan, i.e., point measurements placed 11 µm apart from one another, obtained along the trace shown in A (JM Hanchar and L Nasdala, unpublished). Only a part of each Raman spectrum is shown in the plot for more clarity. The spectrum of pure $ZrSiO_4$ obtained under similar orientation (gray) is also shown for comparison (cf. also Fig. 11). With increasing Yb concentration, heights of Raman bands decrease and their widths increase. Note the clear asymmetry of the $\nu_2(SiO_4)$ band at the high-frequency side, marked with two arrows.

metamictization. In view of this, it seems surprising that no attempts were made to apply Raman spectroscopy to the study of radiation-damaged zircon until the early 1990s (Nasdala 1993, Nasdala et al. 1995). Since then, Raman spectroscopy has gained increasing attention as an undemanding but powerful technique that facilitates quantitative estimation of the degree of metamictization in zircon single crystals or micro-areas. This technique has the analytical advantages that analyses can be made without destruction of the sample, sample preparation is virtually unnecessary, and analyses can be done on a micron-scale (modern confocal Raman systems have a lateral resolution of about 1 µm and a volume resolution better than 5 $\mu m^3$, respectively). Applications were presented, for instance, by Nasdala et al. (1996), Wopenka et al. (1996), Pidgeon et al. (1998), Nasdala et al. (1998a,b; 1999), Zhang et al. (2000a,b), Balan et al. (2001), Geisler et al. (2001a,b), Högdahl et al. (2001) and Nasdala et al. (2001a,b,d; 2002a). These studies made use of the Raman spectroscopic determination of the degree of radiation damage in zircon micro-areas to constrain U-Th-Pb dating results, to estimate the ratio between α-damage retention and recovery, and to relate observed changes of chemical and physical parameters to the structural damage.

Raman spectral changes caused by radiation damage are presented in Figure 13. Causes for these spectral changes can be adequately explained only for little to moderately metamict zircon, i.e., below the first percolation point [cf. the percolation model for metamictization (Salje et al. 1999); see also Ewing et al. (this volume)]. Any interpretation needs to be cautiously done for higher degrees of radiation damage, particularly in view of the still insufficient knowledge about the real structures of strongly metamict zircon.

Raman spectra of little to moderately metamict zircon samples show the same band pattern

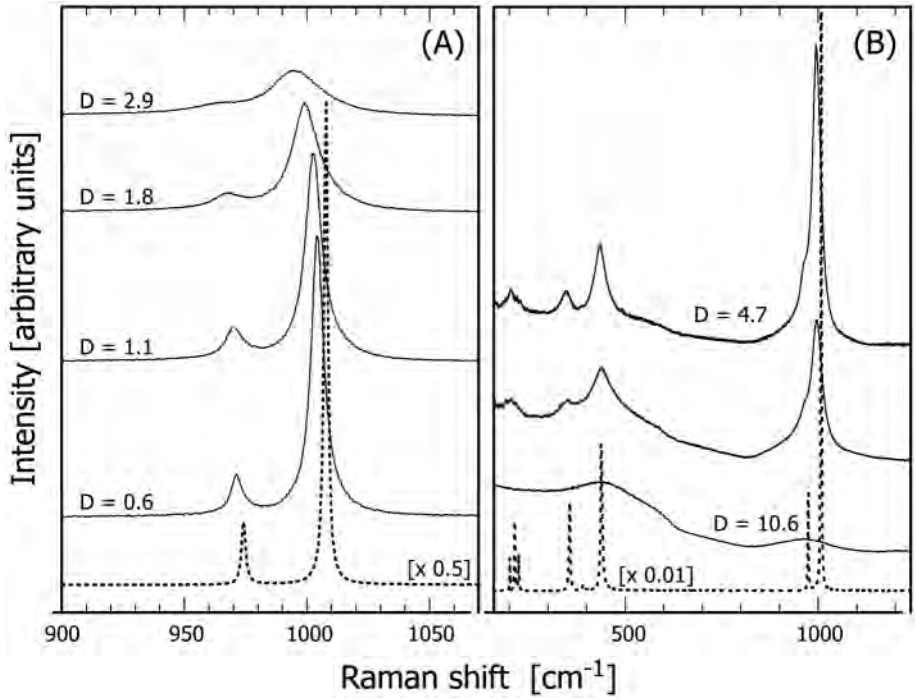


**Figure 13.** Effects of metamictization on the Raman spectra of zircon. (A) Four spectra in the $SiO_4$ stretching range obtained from little to moderately metamict, gemstone-quality zircon crystals from Sri Lanka (Nasdala et al. submitted), in comparison with non-metamict, synthetic $ZrSiO_4$ (dotted). With increasing radiation damage, Raman bands are lowered in intensity, become significantly broader and shift towards lower wavenumbers. (B) Spectra of strongly metamict zircon samples (solid, after Nasdala et al. 2002b, modified) in comparison with synthetic $ZrSiO_4$ (dotted). Note that at high damage levels, the broadened and weakened Raman signal of the remnant crystalline zircon does not have a flat background anymore but it rather overlaps with the Raman pattern of amorphous $ZrSiO_4$. The spectrum marked "D = 10.6" shows only the Raman signal of amorphous zircon. Self-irradiation doses (D) for six zircon samples from Sri Lanka age given as in Figure 8.

as crystalline zircon, however, bands are clearly broadened (decreasing short-range order) and shifted towards lower wavenumbers (structural widening). The bands are still well shaped (symmetric Gaussian-Lorentzian peaks) at this stage (see Fig. 13A). Nasdala et al. (1998a) found that the FWHM of the intense $\nu_3(SiO_4)$ mode at ~1000 $cm^{-1}$ increases most sensitively with increasing radiation damage. This parameter was then used in most of the recent studies to estimate the degree of metamictization. The $\nu_3(SiO_4)$ broadening reflects the decreasing short range order or the increasing irregularity of $SiO_4$ tetrahedrons, respectively, caused by their distortion and tilting in the lattice. At advanced radiation damage [FWHM of the $\nu_3(SiO_4)$ band above 20 $cm^{-1}$], Raman bands of crystalline zircon continue to broaden and loose intensity and become increasingly asymmetric. The reason for the latter is still unclear. Band asymmetries (also observed in solid solutions) could, for example, point to greatly different site symmetries, partial polymerization of $SiO_4$ tetrahedrons (cf. Zhang and Salje 2001) but also to confinement effects [i.e. band broadening of lattice modes due to phonon lifetime decrease in very small (below 3 nm) particles]. The latter was proposed by Geisler et al. (2001b), though for zircon samples showing symmetric bands, which is most unlikely. Critical aspects of the phonon confinement hypothesis in the case of zircon will not be discussed here; the reader is referred to Nasdala et al. (2002b).

With progressive metamictization, the Raman signal of the amorphous volume fraction increases (Fig. 13B). Since crystalline zircon is a much better Raman scatterer than amorphous zircon (note the tremendous intensity loss of Raman bands upon metamictization), Raman spectra

are dominated by Raman bands of crystalline zircon even at high levels of radiation damage. To elucidate this with an example, see the upper Raman spectrum shown in Figure 13B. The amorphous fraction of this particular zircon has not been determined, however, for the Sri Lankan zircon, a total self-irradiation dose of $4.7 \times 10^{18}$ $\alpha$-events per gram would correspond to an amorphous volume fraction of 40 % (Holland and Gottfried 1955, X-ray diffraction) or 65-70 % [Ríos et al. 2000 (X-ray diffraction), Farnan and Salje 2001 (NMR), Zhang and Salje 2001 (infrared absorption)], respectively. In spite of the high fraction of amorphous zircon, the discussed Raman spectrum is dominated by strongly broadened bands of the remnant crystalline fraction. Note that even at elevated radiation damage, only Raman bands of (crystalline) zircon or amorphous $ZrSiO_4$ are observed, which reconfirms that self-irradiation does not cause major decomposition of zircon into oxides.

More recently, Raman spectroscopy is also applied to study the recovery of zircon from radiation damage upon annealing in the laboratory (Zhang et al. 2000b, Geisler 2001b, Nasdala 2002a,b) and natural alteration processes (Nasdala 2002b, A Willner, in preparation). All of these studies reconfirmed that structural reconstitution is not the direct inverse of progressive metamictization. For example, band broadening and frequency decrease correlate in the progressive metamictization process (Fig. 13), but this is not necessarily true anymore after the annealing treatment. Heat treatment of a moderately metamict zircon may cause marked frequency increase and only moderate FWHM decrease whereas electron beam irradiation would cause preferential FWHM decrease without major frequency change (Fig. 14B). Precise interpretation of these observations cannot be given at present. It is clear, however, that (1) the recovery strongly depends on the treatment, (2) causes of the spectral changes in radiation-damaged zircon may be heterogeneously removed during the reconstitution process, and (3) additional effects such as micro-strain and temperature-induced nucleation need to be considered. For example, as mentioned above, crystalline $ZrO_2$ is not formed due to self-irradiation only but is typically observed upon heat-treatment of highly metamict zircon. Therefore, even though being a most powerful tool for the study of radiation-damaged zircon and its changed chemical and physical properties, laboratory experiments are unable to retrace metamictization step by step back to undamaged zircon.

***Image generation from Raman scattered light.*** There are two general ways to generate images from Raman data. The direct imaging technique uses the CCD detector of a Raman system like a photocamera. Such images show the intensity distribution of light of a certain (pre-set) wavelength range in the pictured area. The Raman mapping technique is greatly different. Here, a full Raman spectrum is obtained for each pixel of the map. Images age generated through processing the whole data set and may show the x-y-distribution of virtually any Raman parameter (such as band intensities, intensity ratios, background slopes, FWHMs, degrees of band asymmetry). Raman maps are typically generated from data sets containing about 10000 spectra. Advantages and disadvantages of the two techniques were compared by Lehnert (2000) and Nasdala (2002). In Figures 14 and 15, we present examples for Raman mapping. We have elucidated above that Raman spectra of natural zircon samples are closely controlled by radiation damage whereas the chemical composition has mostly only minor effects. Images generated from Raman data of natural zircon crystals thus show mainly the distribution of radiation damage. This technique opens up great opportunities for the study of internal structures. For instance, Raman images and maps combined with element maps from electron microprobe and SEM analysis may prove useful to distinguish between chemical and structural causes of intensity variations in CL images of natural zircon grains.

## OTHER SPECTROSCOPIC TECHNIQUES

### Electronic absorption spectroscopy

***General remarks.*** Colors of minerals are caused by wavenumber-dependent processes in the visible part of the electromagnetic spectrum, which are studied by means of optical spectroscopy [also electronic or ultraviolet-visible-near infrared (UV-VIS-NIR) spectroscopy]. Electronic spectra

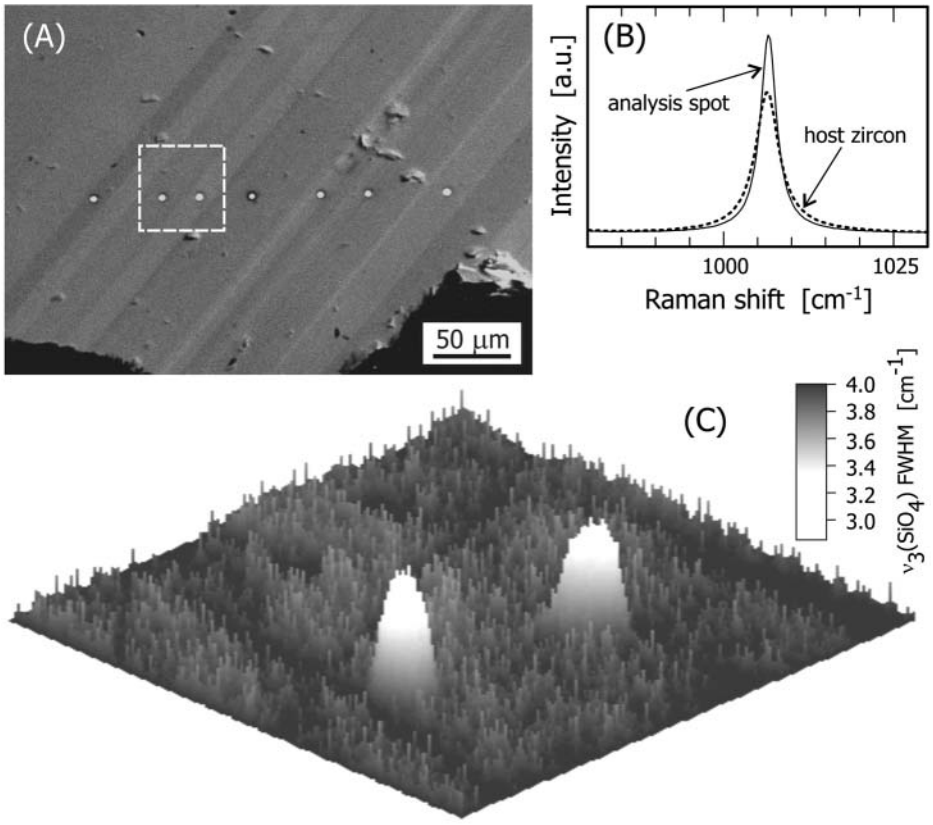


**Figure 14.** Local structural reconstitution of zircon caused by the impact of the electron beam during electron microprobe analysis. (A) Cathodoluminescence image of a zircon from a syenite gneiss, Renfrew County, Ontario (sample 91500, for description see Wiedenbeck et al. 1995). The locations of seven electron microprobe analyses are indicated by small bright spots. (B) Raman point analyses done in and outside the left spot in A. Structural recovery in the analysis spot areas is recognized from the FWHM decrease, which is not accompanied by notable band frequency increase in this case. (C) Raman map (area marked in A) in perspective representation, showing the lateral extension of structural effects.

are concerned with qualitative and quantitative measurements of the absorption, reflection and emission of light on powdered samples or single crystals in the spectral range 40000 to 4000 $cm^{-1}$ (250 to 2500 nm). Absorption spectra of minerals in this energy range are affected by a number of different phenomena which are given in the following. Approximate energy ranges and the theory describing the respective process are given in squared brackets. (1) Ligand-metal charge transfer (LM-CT) [>30000 $cm^{-1}$, molecular orbital (MO) theory, self-consistent field X-alpha (SCF-X) procedure] describes transitions between energy states predominantly centered at the oxygen ligands of coordination polyhedra and those predominantly centered at the central ion. (2) Metal-metal charge transfer (MM-CT), [24000-9000 $cm^{-1}$, exchange theory] is related to electron hopping between transition metal cations in edge- or face-sharing coordination polyhedra. (3) Crystal field transitions [30000-4000 $cm^{-1}$, crystal field theory, superposition model (SM), angular overlap model (AOM)] include electronic transitions between crystal field split d- or f-states, localized at cations. (4) Absorption due to color centers is caused by excitations of electrons allocated at lattice defects. (5) In addition, fundamental, overtones and combination modes of groups or molecules can be found up to ~8000 $cm^{-1}$ [vibrational theory of isolated groups].

Zircon may show a large variety of colors, depending on the content of transition metals and

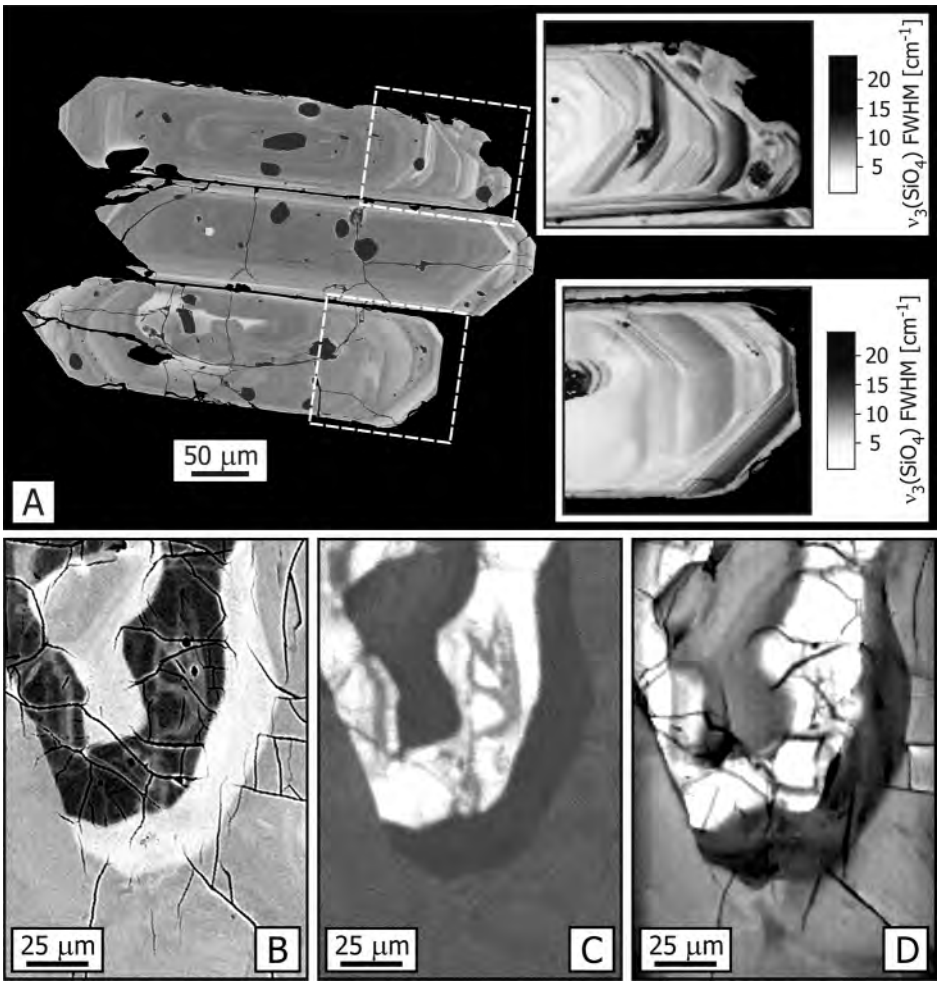


**Figure 15.** Two examples for the application of Raman microprobe analysis for revealing internal structures of zircon crystals. (A) Backscattered electrons image and two Raman maps obtained from of a group of zircon crystals from the Gold Butte block, Nevada (for sample description see Reiners et al. 2002). (B) Backscattered electrons image a heterogeneous area in a zircon from the Adirondack Mountains, New York State (cf. Figs. 4A and 4B in Nasdala et al. 2002a). (C) Cathodoluminescence image of the same area as in B. (D) Raman map of the same area as in B, generated from ~22,000 spectra (bright = narrow-band widths, well ordered, dark = broad-band widths, disordered). The three Raman-based images (in A and D) show the lateral distribution of the broadening of the $\nu_3(SiO_4)$ Raman band and are thus virtually maps of the crystallinity.

radiation induced color centers (Burns 1993, Anderson and Payne 1998). Colors of crystalline to moderately radiation-damaged zircon samples range from colorless to pale brown, brown, olive, yellow, orange, green and blue. Highly metamict zircon samples are often dark brownish to almost black (in early papers described as "cyrtolith" or "malacon"), but may also have gemstone quality, then typically showing bottle-green color. Early optical absorption studies on natural zircon were pioneered by gemologists for identification purposes. Anderson (1971) and Anderson and Payne (1998) gave overviews of the respective literature.

***Cations affecting the color of zircon.*** It is well known that a large variety of ions can be incorporated into the zircon lattice. Among them, cations with partly filled valence electron shells (transition metals, lanthanides, actinides and REE) give rise to coloration. A number of these

species has been the subject for detailed optical investigations in the past, and these studies are summarized in the following. Accordingly, this subchapter deals with crystal field transitions. For the theoretical principles and a comprehensive overview, the reader is referred to the basic literature (e.g., Ballhausen 1962, Figgis 1966, Lever 1968, Newman 1971, Schläfer and Gliemann 1980, Lever 1984, Newman and Ng 1989). Applications of the crystal-field theory in geosciences are, for instance, given in the reviews by Burns (1970, 1993) and Langer (1988, 1990). Books and articles reviewing mineral spectroscopy along with an extensive list of optical mineral data were compiled by Rossman (1988). Lever (1968, 1984) compiled extensive data about inorganic and organic substances.

Anderson and Payne (1940) attributed the visible absorption spectrum of natural zircon to uranium impurities. The polarization behavior of synthetic $U^{4+}$-doped zircon at low temperatures was first studied by Richman et al. (1967) who found that tetravalent uranium was substituting for $Zr^{4+}$ (Fig. 16) Absorption bands were observed in the spectral range 23700 to 4850 $cm^{-1}$ and were assigned to their respective transitions. Mackey et al. (1975) proposed an alternative band assignment, and Vance and Mackey (1978) undertook a study to reproduce the absorption spectrum of $U^{4+}$ in the isomorphous lattices of hafnon and thorite. However, no significant information was obtained on the validity of the previous interpretation, which is still under debate. Phenomenologically, the spectrum of synthetic $U^{4+}$-doped zircon is widely similar to those of natural zircon, though the latter show often broadened bands due to radiation damage (e.g., Anderson 1963). Vance and Anderson (1972a,b) performed detailed studies on natural radiation damaged zircon and found, beside the $U^{4+}$ spectrum, additional absorption bands that were associated with $U^{4+}$ in cubic or tetragonal $ZrO_2$. This interpretation was supported by the observation that after heat-treatment, $ZrO_2$ had formed and the additional lines were also intensified. Later, Vance (1974) extended these investigations into the IR spectral range and described further bands of $U^{4+}$-bearing $ZrO_2$. Vance and Mackey (1974) found two additional bands in some absorption spectra of natural U-bearing zircon in the infrared region at 9030 and 6700 $cm^{-1}$, which were attributed to the presence of $U^{5+}$ (cf. Fig. 17). These same authors have also studied synthetic, U-doped zircon (Vance and Mackey 1975, 1978). Previous results for natural zircon were confirmed and it was shown that the $U^{5+}$ is only remotely

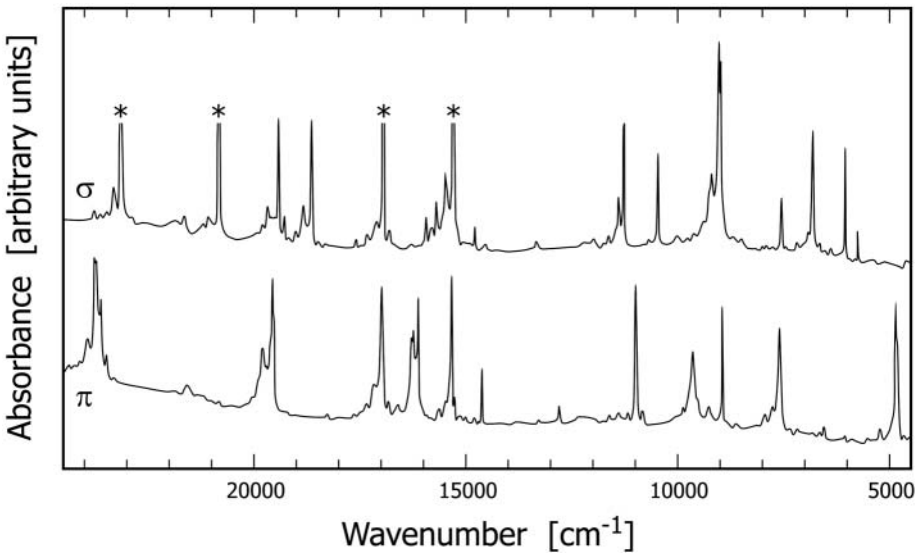


**Figure 16.** Absorption spectra of $U^{4+}$ in zircon at 4.2 K for the two polarizations σ (***E*** ∥ *c* and ***H*** ⊥ *c*) and π (***E*** ⊥ *c* and ***H*** ∥ *c*), obtained from a synthetic zircon crystal doped with uranium (after Richman et al. 1967, redrawn). Bands marked with an asterisk were too intense. The absorption edge is not shown in the spectra but was reported at ~33000 $cm^{-1}$ in the original paper.

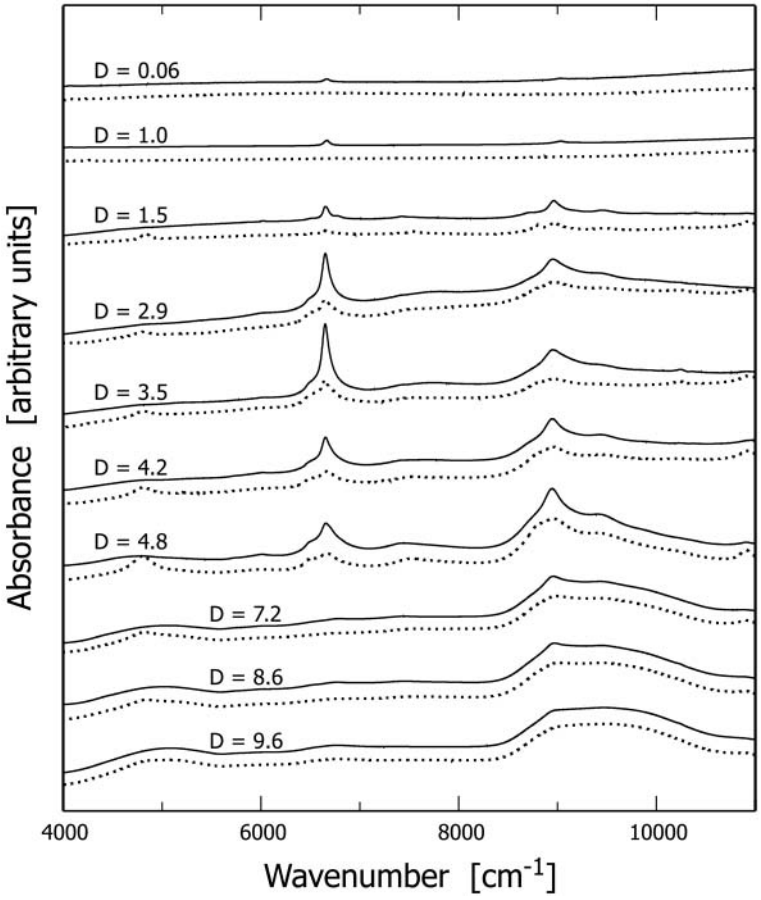


**Figure 17.** Absorption spectra in the near infrared range obtained from zircon crystals from Sri Lanka having different degrees of radiation damage (redrawn after Zhang et al. 2002). Solid graphs, $\boldsymbol{E} \perp c$, dotted graphs, $\boldsymbol{E} \parallel c$. Spectra are stacked for more clarity of the presentation. Doses are given as in Figure 8. The bands at 6668 and 9030 $cm^{-1}$ are assigned to $U^{5+}$ absorption centers.

charge-compensated by trivalent ions. Zhang et al. (2002) investigated effects of radiation damage and thermal annealing on uranium ions in crystalline and metamict zircon. They found that $U^{4+}$ and $U^{5+}$ signals have different responses to radiation damage. Tetravalent uranium becomes the dominate component in the amorphous phase. Zhang et al. (2002) concluded that due to ionization, the valence of uranium ions may change during the metamictization process.

Fielding (1970) investigated natural zircon that exhibited red colored zones. He reported unpolarized spectra and attributed a broad absorption band around 20000 $cm^{-1}$ to $Nb^{4+}$ substituting for $Zr^{4+}$. The low energy wing of this band extends into the visible spectral region causing the red color. Other observed spectral features around 15000 to 6000 $cm^{-1}$ were ascribed to uranium, rare earths and iron, but no further details were given. Vance and Mackey (1975) argued that two features of the spectrum at 9000 and 6700 $cm^{-1}$ arise due to $U^{5+}$ (see above).

Belletti et al. (1995) synthesized Cr-doped zircon. The crystals exhibited bluish to greenish color. Polarized absorption spectra, recorded in the spectral region 25000 to 6000 $cm^{-1}$ at various temperatures between 10 K and 300 K, were interpreted on the basis of local $D_{2d}$ symmetry for $Cr^{4+}$ hosting on the $Si^{4+}$ site. The intense absorption bands around 9600-12500 $cm^{-1}$, 15000-19500 $cm^{-1}$,

and 20500-24000 $cm^{-1}$, were assigned to spin allowed d-d transitions. However, Gaft et al. (2000c) investigated synthetic Cr-doped zircon using luminescence spectroscopy and found no evidence of $Cr^{4+}$, rather they found $Cr^{3+}$ and $Cr^{5+}$. Gaft et al. (2000c) concluded that one possible mechanism of charge compensation is a double substitution $Cr^{3+}$–$Cr^{5+}$ within two $Zr^{4+}$–$Si^{4+}$ neighbors of the zircon lattice.

Synthetic zircon doped with vanadium exhibits a blue color, which was attributed to $V^{4+}$ substituting for $Zr^{4+}$ (Booth and Peel 1962). Note that this assignment is contradictory with the Raman results of De Waal et al. (1996) discussed above. Booth and Peel (1962) argued that tri- and pentavalent vanadium may also contribute to the blue coloration. To clarify this, Demiray et al. (1970) measured reflectance spectra of powdered, synthetic V-doped zircon. They reported three broad absorption bands at 37500, 16000 and 6750 $cm^{-1}$, which they assigned to spin-allowed d-d transitions based on their crystal field analysis for a local $D_{2d}$ symmetry. A shoulder near 13000 $cm^{-1}$ was interpreted as spin-forbidden transition. The absorption edge was observed at around 48000 $cm^{-1}$. The results of Demiray et al. (1970) seem somewhat questionable. The absorption edge of pure zircon lies around 33000 $cm^{-1}$ (e.g., Richman et al. 1967) and it is well known that it shifts to lower energies due to cation substitutions. For instance, Vance (1974) reported the absorption edge at 23800 $cm^{-1}$. Silicates without any significant content of transition metal ions generally show an absorption edge around 35000 $cm^{-1}$. At higher energies the metal-oxygen charge transfer already causes total absorption. Therefore, the reported spin-allowed transition at 37500 $cm^{-1}$ reported by Demiray et al. (1979) is most probably an artifact.

Although $Np^{4+}$ and $Pu^{4+}$ were not found in natural samples, they will be briefly mentioned here. Polarized optical absorption spectra in conjunction with EPR investigations were conducted at low temperature (4.2 K) on $Np^{4+}$ and $Pu^{4+}$ in single zircon crystals by Poirot et al. (1988, 1989). The energy levels were assigned on a basis of local $D_{2d}$ symmetry site for both ions, thus substituting for $Zr^{4+}$ analogous to $U^{4+}$.

***Future needs.*** The available data on absorption spectroscopic studies are scarce, especially quantitative ones. This might perhaps be due to circumstances that limit the quality of absorption spectra, as for example cases in which the respective cation of interest has only trace concentration, superposition of absorption lines or problems in the identification of electronic transitions. The assignment of the absorption bands to the respective transitions in f-elements is a tedious task. In contrast to most $3d^N$-elements, spin-orbit interaction in f-elements cannot be neglected (e.g., Lever 1968, Marfunin 1979). The $U^{4+}$ ion in zircon is an excellent example for this. Seventy electronic transitions are to be expected for $U^{4+}$ (Richman et al. 1967) but Richman et al. (1967) and Mackey et al. (1975) assigned only 30 $U^{4+}$ bands. Actually, more bands were found in the spectra, but weak bands were supposed to be partly of vibrational origin and were not taken into account. Also, the various parameter sets employed to describe the spectra are the result of different approximations by the respective authors. Accordingly, an improvement of the crystal field model is necessary, and/or comparison with *ab-initio* calculations in the near future will help to clarify the existing uncertainties.

The influence of the radiation damage upon the absorption bands has been recognized (Taran et al. 1990a,b), but has not been investigated in detail. Heat-treatment experiments of radiation damaged zircon addressed to study annealing effects on the behavior of absorption bands are needed. Principally, band narrowing due to "healing" of the structure was already mentioned, but quantitative data are missing. First results in the course of systematic studies on the oxidation state of uranium in metamict and annealed zircon were recently obtained by Zhang et al. (submitted).

The color of natural zircon is in first instance caused by the absorption edge whereas transition metals causing an absorption in the visible spectral region seem to have minor importance in most cases. Especially f-f transitions (actinides and lanthanides) are weak and faint in most natural zircon samples. It is also to be expected that radiation damage in zircon causes the absorption edge to shift into the visible spectral region (for fluorite shown by Trinkler et al. 1993, for biotite shown by Nasdala et al. 2001c). It is clear that more detailed data on the various radiation-induced color centers are needed. Absorption spectroscopy will prove useful for this purpose, especially

when employed in combination with other spectroscopic techniques.

**Mössbauer spectroscopy**

Only a few attempts have been made thus far to employ $^{57}$Fe Mössbauer spectroscopy to the investigation of the valence and structural position of iron ions when incorporated in the zircon lattice. It is well known that natural zircon commonly contains iron as a trace element in the range up to a few hundred ppm. Zircon analyses with significantly higher Fe content have occasionally been reported (e.g., Nechaev et al. 1986, Pointer et al. 1988) but it is generally agreed that exceptionally high iron concentrations are most probably due to finely dispersed inclusions of Fe-phases rather than extensive Fe substitution into the zircon structure.

Berry et al. (1996) observed the simultaneous presence of two iron species in Mössbauer spectra of synthetic $ZrSiO_4$ doped with 0.2-1.8 wt % Fe: a $Fe^{3+}$ doublet interpreted as representing iron substitution in the zircon structure and a $Fe^{3+}$ sextet due to the presence of hematite inclusions. To avoid the Mössbauer signal of incorporated Fe-bearing minerals, Blaum and Nasdala (1999) studied nine natural zircon samples with low Fe concentrations <200 ppm. They found that $^{57}$Fe Mössbauer spectra of well crystallized and metamict zircon showed wide similarity, with ferric iron always being the dominant Fe species. Hawthorne et al. (1991) concluded from the Mössbauer spectra of one crystalline and one metamict titanite that the accumulation of radiation damage might be accompanied by partial $Fe^{3+} \rightarrow Fe^{2+}$ reduction. In contrast, Blaum and Nasdala (1999) found no correlation between the degree of radiation damage and the $Fe^{2+}/Fe^{3+}$ ratio in zircon.

The assignment of the various iron species to certain lattice sites is still under debate. Mössbauer spectra of natural low-Fe zircon samples are dominated by a $Fe^{3+}$ doublet with relatively low quadrupole splitting of $\Delta$ = 0.30-0.32 mm/s [$Fe^{3+}$(I) in Fig. 18], which corresponds to a highly symmetric site. Its chemical shift of $\delta$ = 0.2 mm/s (relative to $\alpha$-Fe) suggests tetrahedrally coordinated Fe. The best candidate for this $^{[4]}Fe^{3+}$ seems the nearly symmetric, empty [4]-coordinated site in the zircon lattice (cf. Finch et al. 2001) with a cation–oxygen distance of 1.84 Å (Fig. 18). Incorporation of $Fe^{3+}$ at the comparably "narrow" Si sites (Si–O bond distance 1.62 Å) seems more difficult and, if possible at all, it must be accompanied by significant widening and distortion of tetrahedra. Blaum and Nasdala (1999) have also speculated that both ferrous and ferric iron could occupy the empty [6]-coordinated site in the zircon lattice (Robinson et al. 1971; Fig. 19). Hypothetical Fe substitution at the $^{[8]}$Zr site is only possible for the (larger) $Fe^{2+}$. It seems, however, unlikely that the occasionally found, low $Fe^{2+}$ portion in natural zircon is [8]-coordinated. Such $^{[8]}Fe^{2+}$ species is expected to show large quadrupole splittings ($\Delta$ ~ 3.5 mm/s, Burns 1994), which was, however, not observed by Blaum and Nasdala (1999; cf. Fig. 18).

All of the above assignments, however, are somewhat questioned by widely similar parameters for the main $Fe^{3+}$ doublet in Mössbauer spectra obtained from little and highly metamict zircon. This observation would imply that the short-range order around the Fe sites remains unaffected by the radiation damage whereas the short-range order of other sites decreases. It must therefore be cautiously considered that even in low-Fe zircon, iron might be present as a sub-micrometer phase or cluster, rather than being incorporated in the zircon structure.

**Electron paramagnetic resonance**

***General remarks.*** Electron paramagnetic resonance (also electron spin resonance, ESR) is a spectroscopic method that detects chemical species with unpaired electrons. The technique is based on the interaction between the magnetic moment of these unpaired electrons and microwaves in an external magnetic field. Resonant microwave absorption occurs between the energy levels of the ground state of the unpaired electrons which are split in the EPR spectrometer's uniform magnetic field (usually 0-1 T). Electron paramagnetic resonance spectroscopy is a very powerful method for investigating the detailed physical properties, structural position and local

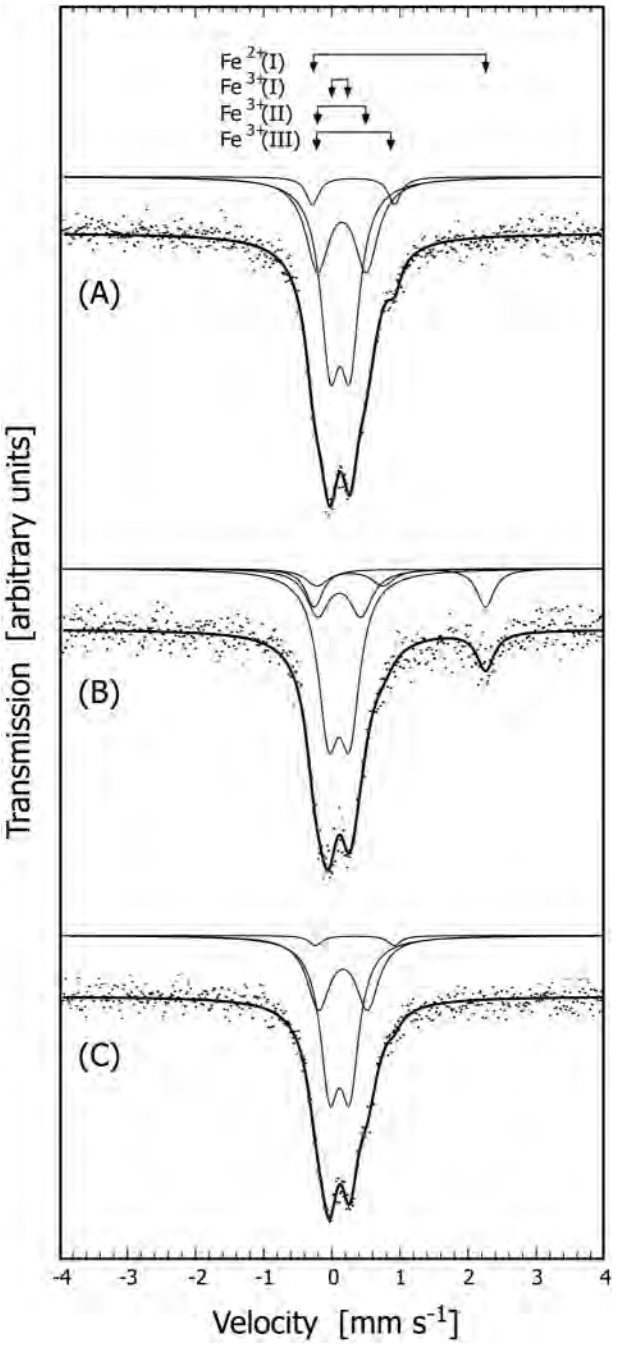


**Figure 18.** Comparison of three $^{57}Fe$ Mössbauer spectra (stacked) of natural zircon samples (Blaum and Nasdala 1999, P Blaum, unpublished). (A) Crystalline zircon from Miask, Ural Mountains, without detectable ferrous iron. (B) Crystalline zircon from Miask, Ural Mountains, showing doublets of ferric and ferrous iron. (C) Highly metamict zircon from Sri Lanka ($UO_2$ ~ 0.86 wt %). Note the wide similarity (quadrupole splitting, chemical shift, relative intensity) of fitted $Fe^{3+}$ and $Fe^{2+}$ doublets (assignment on the top), which are apparently unaffected by the different degrees of radiation damage.

environment of paramagnetic defects in ionic materials. There are two types of paramagnetic centers in such materials, namely, impurities of paramagnetic ions and radiation-induced electron- and hole-centers. Paramagnetic ions are transition ions in the relevant valence state with unpaired *d*- and *f*-electrons. In some cases, these ions reach the paramagnetic valence state after electron or hole capture due to irradiation processes. Especially radiation-induced intrinsic electron-hole centers can be investigated effectively by means of EPR as an excellent method for the identification of point defects, their local environment, and kinetics of the processes involving these defects. For the fundamentals of EPR, the reader is referred to the numerous works published on this subject, e.g., Abragam and Bleaney (1969), Wertz and Bolton (1972), Marfunin (1979) and Calas (1988).

***Impurities of paramagnetic ions.*** In the unit cell there are four $ZrO_8$ and four $SiO_4^{4-}$ groups each set of which are both crystallographically ($D_{2d}$) and magnetically equivalent. Due to the fact that the neighboring [$SiO_4$] tetrahedra are equally divided into two non-equivalent sets with different Zr-O bond lengths (2.13 Å and 2.27 Å, respectively) there are two types of O-sites. From EPR data, most of the non-formula paramagnetic ions were assigned to the "dodecahedral" Zr site. Various rare-earth ions (4*f*-ions), which play a crucial role in the CL and TL spectra of zircon, were found substituting for $Zr^{4+}$ and forming paramagnetic centers.

One of the first described paramagnetic centers in zircon is $Gd^{3+}$ (Hutton and Troup 1964,

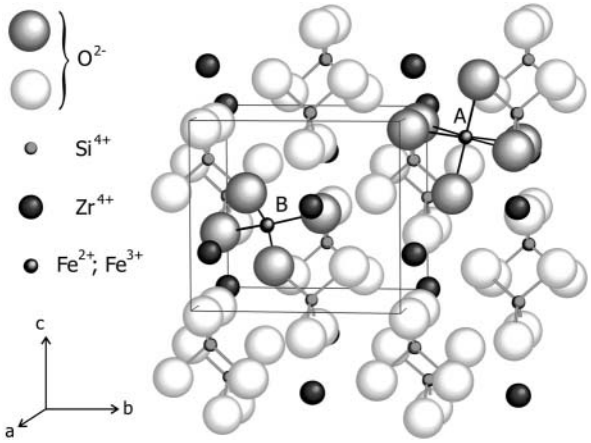


**Figure 19.** The crystal structure of zircon. Hypothetical iron incorporation at normally empty sites in the structure is shown. (A) Six-coordinated site, slightly elongated parallel to the *c*-axis (see Robinson et al. 1971). (B) Highly symmetric, four-coordinated site (see Finch et al. 2001). These two sites could also be acceptors for the incorporation of other medium-sized cations.

Abraham et al. 1969; Fig. 20). Further REE centers, not observable with EPR at room temperature, are $Er^{3+}$ (Valishev et al. 1965), $Dy^{3+}$ (Ball 1971), $Tm^{2+}$ (Bershov 1971) and $Tb^{4+}$ (Hutton and Milne 1969). Diamagnetic incorporated *d*- and *f*-ions can be transformed to the paramagnetic state by trapping of an electron due to self-irradiation as well as external irradiation. These charge transfer processes modify the defect structure forming electron- or hole-centers with anomalous valence state of the incorporated ion. E.g., the $Tb^{4+}$ forms by electron-hole capture on $Tb^{3+}$. The electron-hole is not only occupying the terbium position but also the nearest oxygen site. The presence of two different oxygen sites in the zircon lattice causes the appearance of two physically different EPR spectra (Bershov 1971). The paramagnetic $Nb^{4+}$ center was found in natural (Vinokurov et al. 1963) and synthetic Nb-doped zircon (Di Gregorio et al. 1980). It results from electron capture by $Nb^{5+}$ occupying a $Zr^{4+}$ site. The same type is the $Ti^{3+}$ center (Samoilovich et al. 1968, Solntsev and Shcherbakova 1972, Claridge et al. 1995). For both centers hyperfine interaction with a $Y^{3+}$ or a P-ion which isomorphously replaces a next-nearest-neighboring $Zr^{4+}$ ion were reported for synthetic crystals irradiated at 77 K (Solntsev and Shcherbakova 1974, Claridge et al. 1997, Tennant and Claridge 1999). A $Mo^{5+}$ center on $Zr^{4+}$ site was described for synthetic zircon crystals (Krasnobayev et al. 1988). Further paramagnetic d-ions incorporated at the $Zr^{4+}$ site in zircon are $Fe^{3+}$ (Vinokurov et al. 1972), $V^{4+}$ (Ball and Wanklyn 1976) and in synthetic doped crystals $Np^{4+}$ (Poirot et al. 1988). Interestingly so far neither in natural nor in synthetic zircon paramagnetic uranium centers were described with the EPR.

Besides the paramagnetic ions which were in natural crystals mostly assigned to the "dodecahedral" $Zr^{4+}$ site especially in 3*d*- and 4*d*-ion doped synthetic crystals the "tetrahedral" $Si^{4+}$ site or a possible incorporation on both sites was suggested for $Ti^{3+}$ (Claridge et al. 1999a), $Mo^{5+}$ (Krasnobayev et al. 1988, Eftaxias et al. 1989), $V^{4+}$ (Di Gregorio et al. 1982), $Cr^{3+}$ (Claridge et al. 1999b) and $Fe^{3+}$ (Ball and van Wyk 2000). Berry et al. (1996) reported that iron in doped zircon is accommodated as $\alpha$-$Fe_2O_3$ inclusions and as $Fe^{3+}$ centers in low symmetric rhombic sites, at higher iron concentration also in axial sites. Such normally empty, axial sites in the zircon structure having [6]- and [4]-coordination were described by Robinson et al. (1971) and Finch et al. (2001), respectively (Fig. 19 and Mössbauer spectroscopy above). Both spectra of $Fe^{3+}$ on the $Zr^{4+}$ site and on the $Si^{4+}$ site were found by Vinokurov et al. (1972) only in natural zircon crystals from kimberlites. The incorporation of paramagnetic *d*-ions at these structural sites must be accompanied by signifi-

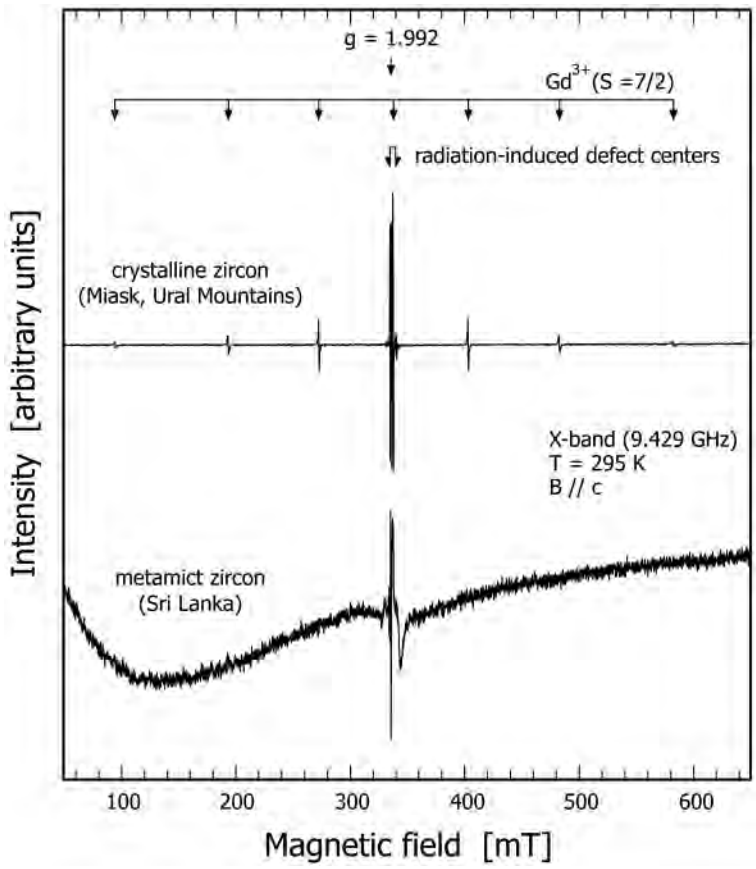


**Figure 20.** Typical EPR spectra of little and highly radiation-damaged, natural zircon (M Plötze and L Nasdala, unpublished). Both of the spectra are dominated by signals of radiation-induced electron-hole centers. In addition, the upper spectrum (crystalline zircon) shows the signal of $Gd^{3+}$. The latter is not resolved in the EPR spectrum of metamict zircon, which is probably due to broadening of the crystal-field parameters and accompanying broadening of the spin-Hamiltonian terms.

cant distortions of both the octahedron and tetrahedron but appears probable especially under extreme crystallization conditions e.g. in kimberlites or high doping synthesis. However, their unequivocal assignment to certain structural sites is presently impossible from EPR data and need further experiments, e.g. measurements of the interactions with O-ligands in $^{17}O$ enriched samples or EXAFS measurements.

***Intrinsic radiation-induced paramagnetic centers.*** Besides the paramagnetic centers related to paramagnetic ions, a large number of intrinsic paramagnetic species in zircon was observed and characterized by EPR. These centers are formed by trapping of electrons or electron-holes in the zircon lattice as a result of natural self-irradiation or artificial ionizing radiation. The number and nature of the paramagnetic defects depend on the impurity content, the previous heat treatment of the crystal, the type of the radiation, the temperatures during irradiation and potential subsequent heating and, finally, the temperature at which the EPR measurements are performed. Most of the known radiation-induced paramagnetic electron-hole centers are thermally unstable and anneal at room temperature.

Irradiation causes the formation of the $d^1$ $Zr^{3+}$ electron center on the $Zr^{4+}$ site, which is therefore a prominent center in irradiated crystals. Recent studies showed that the $Zr^{3+}$ center results from trapping of an electron at a $Zr^{4+}$ site stabilized by a $P^{5+}$ ion at a closely neighbored $Si^{4+}$ site

(Claridge et al. 2000b).

As the only anion in the ideal zircon crystal lattice, $O^{2-}$ serves as the only host for electron holes to be formed during ionizing irradiation. There are two non-equivalent oxygen sites and, correspondingly two possible types of O-sites for trapping of paramagnetic electron-holes in the zircon lattice. Oxygenic hole-centers result from trapping of an electron-hole in a ligand oxygen *p* orbital, which is stabilized by a closely neighbored impurity cation. For example, the negative charge created by a trivalent ion substituted at a neighboring $Si^{4+}$ or $Zr^{4+}$ site assists trapping of the oxygenic hole after ionizing irradiation (Claridge et al. 2000a, and references therein). The $[AlO_4]^0$ center is a hole-center, with the hole on a short bond ligand O position, interacting with a $^{27}Al^{3+}$ nucleus located in an adjacent $Si^{4+}$ lattice position (Solntsev and Shcherbakova 1973, Claridge et al. 1994b). The precursor state for this center is the diamagnetic $[AlO_4]^-$ associated with an adjacent charge compensating cation $M^+$ ($H^+$, $Li^+$, $Na^+$). In contrast to alpha-quartz, where the same center was observed (Nuttall and Weil 1981a,b), in zircon a $M^+$ compensator was not detected inferring either the compensation is remote or the compensator is able to diffuse away even by irradiation at 77 K. A further center of this type is $[BO_4]^0$ (Walsby et al. 2000). The center $[SiO_4]^{3-}$-$Y^{3+}$, found in natural zircon numbers also among this group, however, here a stabilizing yttrium is incorporated at the zirconium site (Bershov 1971, Vinokurov et al. 1971, Barker and Hutton 1973, Danby and Hutton 1980, Claridge et al. 2000a).

The group of radiation-induced electron- or hole-centers which are related to zirconium and oxygen vacancies are described by the formula $[SiO_m]^{n-}$ (e.g., Samoylovich et al. 1968, Solntsev et al. 1974, Krasnobayev et al. 1988, Kalinichenko et al. 1990, Claridge et al. 2000a, Laruhin et al. 2002). The hole-centers were produced by trapping of an electron-hole on the ligand oxygen *p* orbital. Two distinct hole-centers $[SiO_2]^{3-}$ according to the two types of O-sites for trapping of paramagnetic holes were described by Claridge et al. (1994). The center with the hole located in a 2p orbital of an oxygen of the $[SiO_4]$-group directed towards the neighboring $Zr^{4+}$ vacancy is reasonably stable even at room temperature (Claridge et al. 1999). The electron-centers $[SiO_4]^{5-}$, $[SiO_3]^{3-}$ and $[SiO_2]^-$ were produced by trapping of an electron at the silicon oxide group. The most important electron-center is represented by $[SiO_4]^{5-}$ (Solntsev et al. 1974). It is moderately stable at room temperature (Laruhin et al. 2002).

As was already mentioned in the previous paragraphs, the radiation-induced paramagnetic centers affect the broadband luminescence emission. They are also influencing the optical absorption behavior. With various techniques of EPR and fission track imaging Kasuya et al. (1990) found a positive correlation between the density of $O^-$ hole-centers, the fission-track density and the red coloring of zircon. A relationship between radiation-induced paramagnetic centers and the red color was described also by Taran et al. (1990b) in combined optical absorption and EPR investigations of zircon from kimberlites.

**Other spectroscopic methods**

Solid state NMR spectroscopy has been employed to characterize and determine the chemical and physical properties of zircon. Its applications have focused on several research areas. Firstly, $^{29}Si$ NMR and $^{29}Si$ magic angle sample spinning (MAS-NMR) techniques were commonly used to investigate and characterize the crystallization or formation of $ZrSiO_4$ from $ZrO_2$-$SiO_2$ gel and aqueous sols (Hartman et al. 1990, Tartaj et al. 1994, Bhattacharya et al. 1996, Valéro et al. 1999, Veytizou et al 2000). Secondly, $^{29}Si$ NMR was employed to study the metamictization process of zircon (Rudnitskaya and Lipova 1972, Kalinichenko et al. 1990, Farana and Salje 2001). Data from $^{29}Si$ NMR (Kalinichenko et al. 1990, Farana and Salje 2001) showed that $\alpha$-decay damage causes new signals indicative of partial polymerization. In addition, Kalinichenko et al. (1990) and Valéro et al. (1999) characterized hydrous components in zircon using $^1H$ NMR. Applications of $^{91}Zr$ and $^{17}O$ NMR in zircon are scarce (Bastow 1990, Carlisle et al. 1991), which is probably due to experimental difficulties. Dajda et al. (2003) recently studied the local structure and site occupancies of pure

and vanadium-doped zircon as well as sol-gels with solid-state NMR or MAS NMR spectra of $^{29}Si$, $^{17}O$, $^{91}Zr$ and $^{51}V$. Their results suggested that vanadium substitution occurs on both the tetrahedral and dodecahedral sites within the zircon lattice with a small preference for the tetrahedral site. These authors also observed a third peak at relatively high vanadium concentration (0.92 mol % $V^{4+}$) and this was interpreted as a third substitution within the zircon lattice.

There are also a number of papers in which X-ray absorption spectroscopy (i.e. extended X-ray absorption fine structure, EXAFS, X-ray absorption near edge structure, XANES) was employed to study the real structure of radiation-damaged zircon. These studies, as well as the NMR work related to radiation damage phenomena in zircon, are discussed by Ewing et al. (this volume).

## ACKNOWLEDGMENTS

We are indebted to Peter Blaum, Jens Götze, John M. Hanchar, Wolfgang Hofmeister, Paul W.O. Hoskin, Andreas Kronz, Peter W. Reiners and Michael Wiedenbeck for providing samples, data, spectra and images. Special thanks are due to Dieter Wolf for many stimulating discussions. Constructive reviews of the manuscript by Michail N. Taran, Glenn Waychunas and Brigitte Wopenka are gratefully acknowledged. Thanks are also due to Wolfgang Zirbs, John M. Hanchar and Christopher M. Fedo for editorial help.

## REFERENCES

Abragam A, Bleaney B (1970) Electron Paramagnetic Resonance of Transition Ions. Clarendon Press, Oxford

Abraham MM, Clark GW, Finch CB, Reynolds RW, Zeldes H (1969) Ground-state splitting of trivalent Gd and Cm in $ZrSiO_4$, $HfSiO_4$, and $ThSiO_4$, determined by ESR. J Chem Phys 50:2057-2062

Aines RD, Rossman GR (1985) The high temperature behavior of trace hydrous components in silicate minerals. Am Mineral 70:1169-1179

Aines RD, Rossman GR (1986) Relationship between radiation damage and trace water in zircon, quartz, and topaz. Am Mineral 71:1186-1193

Akhmanova MV, Leonova LL (1961) Investigation of the metamict decay of zircon with the aid of infrared absorption spectra. Geokhimiya 1961:401-414 (in Russian)

Akhmanova MV, Leonova LL (1963) Investigation of the metamict decay of silicates with the aid of infrared spectroscopy. Trudy Mineral Muzeya AN SSSR im A.E. Fersmana 14:3-31 (in Russian)

Alexanian C, Morel P, Le Bouffant L (1966) Infrared absorption spectra of natural minerals. Bull Soc Fr Ceram 71:3-38

Anderson BW (1963) Absorption spectra and properties of metamict zircons. J Gemmol 9:1-6

Anderson BW (1971) Gem Testing. Butterworths, London

Anderson BW, Payne CJ (1940) Recent investigations of zircon. IV. The absorption spectrum. Gemmologist 9:1-5

Anderson BW, Payne J (1998) Absorption spectra of zircon. *In* The Spectroscope and Gemmology. Mitchell RJ (ed) Gemstone Press, Woodstock, Vermont

Balan E, Neuville DR, Trocellier P, Fritsch E, Muller J-P, Calas G (2001) Metamictization and chemical durability of detrital zircon. Am Mineral 86:1025-1033

Ball D (1971) Paramagnetic resonance of $Er^{3+}$ and $Dy^{3+}$ in natural single crystals of zircon. Phys status solidi (b) 46:635-641

Ball D, van Wyk JA (2000) The electron paramagnetic resonance of $Fe^{3+}$ observed in two axial sites in synthetic single crystals of zircon ($ZrSiO_4$). Phys status solidi (b) 218:545-551

Ball D, Wanklyn BM (1976) Coloured synthetic zircon crystals. Phys status solidi (a) 36:307-316

Ballhausen CJ (1962) Introduction to Crystal Field Theory. McGraw Hill, New York

Bastow TJ (1990) $^{91}Zr$ nuclear qundrupole coupling in zircon ($ZrSiO_4$). J Phys: Condens Matter 2:6327-6330

Belletti A, Borromei R, Oleari L (1995) Absorption spectra of zircon crystals doped with Cr(IV): $ZrSiO_4$:$Cr^{4+}$. Inorg Chim Acta 235:349-355

Barker PR, Hutton DR (1973) A colour centre in natural zircon. Phys status solidi (b) 60:k109-k111

Benisek A, Finger F (1993) Factors controlling the development of prism faces in granite zircons: a microprobe study. Contrib Mineral Petrol 114:441-451

Berry FJ, Eadon D, Holloway J, Smart LE (1996) Iron-doped zirconium silicate. Part 1: The location of iron. J Mater Chem 6:221-225

Bershov LV (1971) Isomorphism of $Tb^{4+}$, $Tu^{2+}$ and $Y^{3+}$ in zircon. Geokhimiya 1971:48-53 (in Russian)

Bhattacharya AK, Hartridge A and Mallick KK 1996 An X-ray diffraction and NMR study into the mechanism of zircon formation from aqueous sols. J Mater Sci 31:5873-5876

Biagini R, Memmi I, Olmi F (1997) Radiation damage in zircons. N Jb Mineral Mh 1997:257-270
Bibikova EV, Senin VG, Legkova GA (1991) Geochemical and age heterogeneity of accessory zircon from the Novopavlovskij Complex (Ukrainain shield). Geokhimiya 1991:1426-1436
Blanc P, Baumer A, Cesbron F, Ohnenstetter D, Panczer G, Remond G (2000) Systematic cathodoluminescence spectral analysis of synthetic doped minerals: anhydrite, apatite, calcite, fluorite, scheelite and zircon. *In* Cathodoluminescence in Geosciences. Pagel M, Barbin V, Blanc P, Ohnenstetter D (eds) Springer, Berlin–Heidelberg, p 126-160
Blaum P, Nasdala L (1999): The incorporation of iron in zircon, $ZrSiO_4$: a $^{57}Fe$ Mössbauer study. Eur J Mineral 11:35
Booth CA, Peel GN (1962) Preparation and properties of some zircon stains. Trans Brit Ceram Soc 61:359-400
Burns RG (1970) Mineralogical Applications of Crystal Field Theory: 1st Edn. Cambridge University Press, Cambridge
Burns RG (1993) Mineralogical Applications of Crystal Field Theory: 2nd Edn. Cambridge University Press, Cambridge
Burns RG (1994) Mineral Mössbauer spectroscopy: correlations between chemical shift and quadrupole splitting parameters. Hyperfine Interactions 91:739-745
Calas G (1988) Electron paramagnetic resonance. Rev Mineral 18:513-571
Carlisle BB, Brown RJC, Bastow TJ (1991) Zirconium-91 NQR in zircon. J Phys: Condens Matter 3:3675-3676
Caruba R, Baumer A, Turco G (1975) Nouvelles syntheses hydrothermales du zircon: substitutions isomorphiques, relation morphologie-milieu de croissance. Geochim Cosmochim Acta 39:11-26
Caruba R, Baumer A, Ganteaume M, Iacconi P (1985) An experimental study of hydroxyl groups and water in synthetic and natural zircons: A model of the metamict state. Am Mineral 70:1224-1231
Cesbron F, Ohnenstetter D, Blanc Ph, Rouer O, Sichere MC (1993) Incorporation de terres rares dans des zircons de synthese: etude par cathodoluminescence. C R Acad Sci Paris 316(II):1231-1238
Chatagnon B, Galland D, Gloux P, Meary A (1982) L'ion paramagnetique $Tm^{2+}$ dans la fluorit. Mineral Deposita 17:411-422
Claridge RFC, Mackle KM, Sutton GLA, Tennant WC (1994a) Zircon EPR revisited: 10 K EPR of three low-symmetry centres in irradiated zircon (zircon silicate). J Phys: Condens Matter 6:3429-3436
Claridge RFC, Mackle KM, Sutton GLA, Tennant WC (1994b) 10 K EPR of an oxygen-hole aluminium centre, $[AlO_4]^0$, in x-irradiated zircon, $ZrSiO_4$. J Phys: Condens Matter 6:10415-10422
Claridge RFC, McGavin DG, Tennant WC (1995) 10 K electron paramagnetic resonance of a $d^1$ $Ti^{3+}$ centre in X-irradiated zircon (zirconium silicate). J Phys: Condens Matter 7:9049-9060
Claridge RFC, Taylor KC, Tennant WC, Walsby CJ (1997) X-band electron paramagnetic resonance of a new $Ti^{3+}$ centre in x-irradiated zircon. J Phys: Condens Matter 9:3075-3080
Claridge RFC, Lees NS, Tennant WC, Walsby CJ (1999a) Two $Ti^{3+}$ centres studied by X-band electron paramagnetic resonance at 10 K in zircon. J Phys: Condens Matter 11:3571-3580
Claridge RFC, Tennant WC, Schweizer S, Spaeth J-M (1999b) Structural models for room temperature stable radiation-induced centers in zircon. J Phys: Condens Matter 11:8579-8589
Claridge RFC, Lees NS, Tennant WC, Walsby CJ (2000a) Oxygenic-hole centres in X-irradiated zircon: 10 K EPR studies. J Phys: Condens Matter 12:1431-1440
Claridge RFC, Tennant WC, Walsby CJ, Schweizer S, Spaeth J-M (2000b) An EPR/ENDOR investigation of a $[ZrPO_4]$ centre in x-irradiated zircon: the Zr(α) centre. J Phys: Condens Matter 12:1421-1430
Coleman RC, Erd RC (1961) Hydrozircon from the Wind River formation, Wyoming. U S Geol Surv Bull 424C:297-300
Colombo M, Chrosch J, Biagini R, Memmi I (1999) An IR analysis of the role of $SiO_4$ tetrahedra in thermally annealed $ZrSiO_4$. N Jb Mineral Mh 1999:113-122
Connelly JN (2000) Degree of preservation of igneous zonation in zircon as a signpost for concordancy in U/Pb geochronology. Chem Geol 172:25-39
Dajda N, Dixon JM, Smith ME (2003) Atomic site preferences and structural evolution in vanadium-doped $ZrSiO_4$ from multinuclear solid-state NMR. Phys Rev B (in press)
Danby RJ, Hutton DR (1980) A new radiation defect center in natural zircon. Phys status solidi (b) 98:k125-k128
Dawson P, Hargreave MM, Wilkinson GF (1971) The vibrational spectrum of zircon ($ZrSiO_4$). J Phys C: Solid State Phys 4:240-256
Deliens M, Delhal J, Tarte P (1977) Metamictization and U-Pb systematics—A study by infrared absorption spectrometry of Precambrian zircons. Earth Planet Sci Lett 33:331-344
Demiray T, Nath DK, Hummel F (1970) Zircon-vanadium blue pigment. J Am Ceram Soc 53:1-4
De Waal D, Heynd AM, Pretorius G, Clark RJH (1996) Raman spectroscopic investigations of ZrSiO4:V4+, the blue vanadium pigment. J Raman Spectros 27:657-662
Di Gregorio S, Greenblatt M, Pifer JH (1980) ESR of $Nb^{4+}$ in zircon. Phys status solidi (b) 101:k147-k150
Di Gregorio S, Greenblatt M, Pifer JH, Sturge MD (1982) An ESR and optical study of $V^{4+}$ in zircon-type crystals. J Chem Phys 76:2931-2937
Eftaxias K, Fielding PE, Lehmann G (1989) $Mo^{5+}$ in synthetic zircon crystals. Chem Phys Lett 160:36-38
Farmer VC, editor (1975) The Infrared Spectra of Minerals. Mineralogical Society, London
Farnan I, Salje EKH (2001) The degree and nature of radiation damage in zircon observed by $^{29}Si$ nuclear magnetic

resonance. J Appl Phys 89:2084-2090
Fielding PE (1970) The distribution of uranium, rare earths, and color centers in a crystal of natural zircon. Am Mineral 55:428-440
Figgis BN (1966) Introduction to Ligand Fields. Interscience, New York
Finch RJ, Hanchar JM, Hoskin PWO, Burns PC (2001) Rare earth elements in synthetic zircon: Part 2. A single-crystal X-ray study of xenotime substitution. Am Mineral 86:681-689
Frondel C (1953) Hydroxyl substitution in thorite and zircon. Am Mineral 38:1007-1018
Frondel C, Collette R (1957) Hydrothermal synthesis of zircon. Am Mineral 42:759-765
Gaft M (1992) Application of thermal treatment of zircon for the interpretation of luminescence centres. J Thermal Anal 38:2281-2290
Gaft M, Panczer G, Reisfeld R, Shinno I (2000a) Laser-induced luminescence of rare-earth elements in natural zircon. J Alloys Com 300-301:267-274
Gaft M, Panczer G, Reisfeld R, Shinno I, Champagnon B, Boulon G (2000b) Laser-induced $Eu^{3+}$ luminescence in zircon ZrSiO4. J Luminesc 87-89:1032-1035
Gaft M, Boulon G, Panczer G, Guyot Y, Reisfeld R, Votyakov, Bulka G (2000c) Unexpected luminescence of $Cr^{5+}$ and $Cr^{3+}$ ions in $ZrSiO_4$ zircon crystals. J Luminesc 87-89:1118-1121
Gaft M, Panczer G, Reisfeld R, Uspensky E (2001) Laser-induced time-resolved luminescence as a tool for rare-earth element identification in minerals. Phys Chem Minerals 28:347-363
Gaft M, Shinno I, Panczer G, Reisfeld R (2002) Laser-induced time-resolved spectroscopy of visible broad luminescence bands in zircon. Mineral Petrol (in press)
Gebauer D (1990) Isotopic systems - geochronology of eclogites. *In* Eclogite Facies Rocks. Carswell DA (ed) Blackie, Glasgow–London, p 141-159
Geisler T, Ulonska M, Schleicher H, Pidgeon RT, van Bronswijk W (2001a) Leaching and differential recrystallization of metamict zircon under experimental hydrothermal conditions. Contrib Mineral Petrol 141:53-65
Geisler T, Pidgeon RT, von Bronswijk W, Pleysier R (2001b) Kinetics of thermal recovery and recrystallization of partially metamict zircon: a Raman spectroscopic study. Eur J Mineral 13:1163-1176
Geisler T, Zhang M, Farna I, Salje EKH (2002) Recrystallzation of heavily metamict zircon under different hydrothermal P-T-t-X conditions. Eur J Mineral 14:51
Gervais F, Piriou B, Cabannes F (1973) Anharmonicity in silicate crystals: Temperature dependence of $A_u$ type vibrational modes in $ZrSiO_4$ and $LiAlSi_2O_6$. J Phys Chem Solids 34:1785-1796
Goldstein JI, Newbury P, Echlin P, Joy DC, Fiori C, Lifshin E (1981) Scanning Electron Microscopy and X-ray Microanalysis. Plenum Press, New York
Gorobets B, Rogozin A (2001) Luminescence Spectra of Minerals (reference book). VIMS, Moscow (in Russian)
Götze J (1998) Principle and advantages of cathodoluminescence microscopy. Microsc Analysis, Eur Ed 55:17-19
Götze J, Kempe U, Habermann D, Nasdala L, Neuser RD, Richter DK (1999) High-resolution cathodo-luminescence combined with SHRIMP ion probe measurements of detrital zircons. Mineral Mag 63:179-187
Gracheva TV, Bibikova EV, Akhmanova MV (1981) Ascertaining of geochronologic role of metamictization degree of zircon using IR spectroscopy. Geokhimiya 1981:274-291 (in Russian)
Granqvist CG, Hunderi O (1978) Optical properties of Ag-$SiO_2$ cermet films: A comparison of effective-medium theories. Phys Rev B 18:2897-2906
Griffith WP (1970) Raman studies on rock-forming minerals. Part I. Orthosilicates and cyclosilicates. J Chem Soc (A) 1969:1372-1377
Halden NM, Hawthorne FC (1993) The fractal geometry of oscillatory zoning in crystals: Application to zircon. Am Mineral 78:1113-1116
Hanchar JM, Miller CF (1993) Zircon zonation patterns as revealed by cathodoluminescence and backscattered electron images: Implications for interpretation of complex crustal histories. Chem Geol 110:1-13
Hanchar JM, Rudnick RL (1995) Revealing hidden structures: The application of cathodoluminescence and back-scattered electron imaging to dating zircons from lower crustal xenoliths. Lithos 36:289-303
Hanchar JM, Hoskin PWO, Jackson SG, Hinton RW, Thibault Y, Finch RJ, Wolf S, Watson EB, Hemming S, Hanson B, Lindstrom DJ (1997) Rare earth elements and the Ce anomaly in terrestrial zircons. EOS Trans, Am Geophys Union 78:F783
Hanchar JM, Finch RJ, Hoskin PWO, Watson EB, Cherniak DJ, Mariano AN (2001) Rare earth elements in synthetic zircon: Part 1. Synthesis, and rare earth element and phosphorus doping. Am Mineral 86:667-680
Hartman JS, Millard RL and Vance ER 1990 A $Si^{29}$ magic angle spinning NMR and DTA study of thermal crystallization of sphene and zircon gels. J Mater Sci 25:2785-2790
Hawthorne FC, Groat LA, Raudsepp M, Ball NA, Kimata M, Spike FD, Gaba R, Halden NM, Lumpkin GR, Ewing RC, Greegor RB, Lytle FW, Ercit TC, Rossman GR, Wicks FJ, Ramik RA, Sherriff BL, Fleet ME, McCammon C (1991) Alpha-decay damage in titanite. Am Mineral 76:370-396
Hermann J, Rubatto D, Korsakov A, Shatsky VS (2001) Multiple zircon growth during fast exhumation of diamondiferous, deeply subducted continental crust (Kokchetav Massif, Kazakhstan). Contrib Mineral Petrol 141:66-82

Heyns AM, Range KJ, Wildenauer M (1990) The vibrational spectra of $NbBO_4$, $TaBO_4$, $NaNb_3O_8$, and $NaTa_3O_8$. Spectrochim Acta 46A:1621-1628
Hoffman JF, Long JVP (1984) Unusual sector zoning in Lewisian zircons. Mineral Mag 48:513-517
Högdahl K, Gromet L-P, Broman C (2001) Low P-T Caledonian resetting of U-rich Paleoproterozoic zircons, central Sweden. Am Mineral 86:534-546
Hoskin PWO (2000) Patterns of chaos: fractal statistics and the oscillatory chemistry of zircon. Geochim Cosmochim Acta 64:1905-1923
Hoskin PWO, Rodgers KA (1996) Raman spectral shift in the isomorphous series $(Zr_{1-x}Hf_x)SiO_4$. Eur J Solid State Inorg Chem 33:1111-1121
Hubin R and Tarte P (1971) Etude infrarouge des orthosilicates et des orthogermanates—IV. Structures scheelite et zircon. Spectrochim Acta 27A:683-690
Hutton D, Milne B (1969) Paramagnetic resonance of $Tb^{4+}$ in zircon. J Phys C 2:2297-2300
Hutton DR, Troup GJ (1964) Paramagnetic resonance of $Gd^{3+}$ in zircon. Brit J Appl Phys 15:405-406
Iacconi P, Caruba R (1980) Trapping and emission centres in X-irradiated zircon (III. Influence of trivalent rare-earth impurities). Phys stat solidi (a) 62:589-596
Iacconi P, Deville A, Gaillard B (1980) Trapping and emission centres in X-irradiated zircon (II. Contribution of the $SiO_4^{4-}$ groups). Phys stat solidi (a) 59:639-646
Ilchenko EA (1994) On hydroxyl-bearing zircons from kimberlites and kimberlite-like rocks. Mineral Zh 16:46-61 (in Russian)
Ilchenko EA, Korzhinskaya VS (1993) On hydroxyls in synthetic and natural zircons. Mineral Zh 15:26-39 (in Russian)
Ilchenko EA, Gevorkjan SV, Mitskevich BF (1988) Constitution features of zircons from the rocks of the Ukrainian shield derived from IR-spectroscopic data. Mineral Zh 10:78-83 (in Russian)
Ilchenko EA, Gevorkyjan SV, Mizkevich NYu (1989) Infrared spectroscopic characterization of zircons from rocks from the Ukrainian Shield. Mineral Zh 10:78-83 (in Russian)
Judd BR, Runciman WA (1976) Transverse Zeeman effect for ions in uniaxial crystals. Proc R Soc London 352A:91-108
Kalinichenko AM, Proshko VYa, Derskij LS, Matyash IV, Shcherbak DN, Gamarnik MYa, Ponomarenko AN (1990) On the metamictness of zircon with the aid of radiospectroscopy. Mineral Zh 12:38-43 (in Russian)
Kasuya M, Furusawa M, Ikeya M (1990) Distributions of paramagnetic centers and alpha-emitters in a zircon single crystal. Nucl Tracks Rad Meas 17:563-568
Kempe U, Götze J, Dandar S, Habermann D (1999) Magmatic and metasomatic processes during formation of the Nb-Zr-REE deposits Khaldzan Buregte and Tsakhir (Mongolian Altai): Indications from a combined CL-SEM study. Mineral Mag 63:165-177
Kempe U, Gruner T, Nasdala L, Wolf D (2000) Relevance of cathodoluminescence for the interpretation of U-Pb zircon ages, with an example of an application to a study of zircons from the Saxonian Granulite Complex, Germany. *In* Cathodoluminescence in Geosciences. Pagel M, Barbin V, Blanc P, Ohnenstetter D (eds) Springer-Verlag, Berlin–Heidelberg, p 415-455
Kempe U, Plötze M, Brachmann, A, Böttcher R (2002) Stabilisation of divalent rare earth elements in natural fluorite. Mineral Petrol 76:213-214
Kirsh Y, Townsend PD (1987) Electron and hole centers produced in zircon by X-irradiation at room temperature. J Phys C: Solid State Phys 20:967-980
Kolesov BA, Geiger CA, Armbruster T (2001) The dynamic properties of zircon studied by single-crystal X-ray diffraction and Raman spectroscopy. Eur J Mineral 13:939-948
Koschek G (1993) Origin and significance of the SEM cathodoluminescence from zircon. J Microscopy 171:223-232
Krasnobayev A, Votyakov S, Krohalev V (1988) Spectroscopy of zircons (properties and geological application). Nauka, Moscow (in Russian)
Kristanovic I (1964) X-ray investigation of zircon crystals containing OH groups. Am Mineral 49:1146-1148
Langer K (1988) UV to NIR spectra of silicate minerals obtained by microscope spectrometry and their use in mineral thermodynamics and kinetics. *In* Physical properties and thermodynamic behaviour of minerals. Salje EHK (ed) D Reidel Publishing, p 639-685
Langer K (1990) High pressure spectroscopy. *In* Absorption Spectroscopy in Mineralogy. Mottana A, Burragato F (eds) Elsevier, Amsterdam, p 228-276
Laruhin MA, van Es HJ, Bulka GR, Turkin, AA, Vainshtein, DI, den Hartog HW (2002) EPR study of radiation-induced defects in the thermoluminescence dating medium zircon ($ZrSiO_4$). J Phys: Condens Matter 14:3813-3831
Launer PJ (1952) Regularities in the infrared absorption spectra of silicate minerals. Am Mineral 37:764-784
Lazarev AN, Mirgorodskiy AP, Mazhenov NA (1980) Resonance interactions of the localized vibrators in crystals of $ABO_4$-type: vibration spectra of crystals with zircon and xenotime structures. *In* The Vibration of Oxide Lattices. Nauka, Leningrad, p 72-99 (in Russian)
Lehnert R., 2000. Beyond imagination—image formation based on Raman spectroscopy. GIT Imaging and Microscopy 2/2000:6-9.

Lever ABP (1968) Inorganic Electronic Spectroscopy. 1st Edn. Elsevier, Amsterdam
Lever ABP (1984) Inorganic Electronic Spectroscopy. 2nd Edn. Elsevier, Amsterdam
Long DA (1977) Raman Spectroscopy. McGraw Hill, New York, 276 p
Lork A, Koschek G (1991) Einsatz der KL-Technik bei der Beurteilung isotopengeochemisch bestimmter Alter von Zirkonen. Beitr Elektronenmikroskop Direktabb Oberfl 24:147-166
Mackey DJ, Runciman WA, Vance ER (1975) Crystal-field calculations for energy levels of $U^{4+}$ in zirconium silicate. Phys Rev B 11:211-218
Marfunin AS (1979a) Physics of minerals and inorganic materials. Springer-Verlag, New York
Marfunin AS (1979b) Spectroscopy, luminescence and radiation centers in minerals. Springer-Verlag, Berlin
Marshall DJ (1988) Cathodoluminescence of Geological Materials. Unwin Hyman, Boston
Mazhenov NA, Murgorodskij AP, Lazarev AN (1979) Resonance-splitting of inner vibrational frequencies of heavy anions in zircon ($ZrSiO_4$) crystals. Inorg Mater 15:495-503 (in Russian)
McLaren AC, Fitz Gerald JD, Williams IS (1994) The microstructure of zircon and its influence on the age determination from Pb/U isotopic ratios measured by ion microprobe. Geochim Cosmochim Acta 58:993-1005
McMillan P (1985) Vibrational spectroscopy in the mineral science. Rev Mineral 14:9-63
Mumpton FA, Roy R (1961) Hydrothermal stability studies of the zircon-thorite group. Geochim Cosmochim Acta 21:217-238
Nasdala L (1993) Ramanspektroskopische Untersuchungen an ausgewählten Mineralen. PhD dissertation, Bergakademie, Freiberg
Nasdala L (2002) Raman mapping – a tool for revealing internal structures of minerals. Acta Universitatis Carolinae, Geologica 46:61-62.
Nasdala L, Massonne H-J (2000) Microdiamonds from the Saxonian Erzgebirge, Germany: *in situ* micro-Raman characterization. Eur J Mineral 12:495-498
Nasdala L, Irmer G, Wolf D (1995) The degree of metamictization in zircon: a Raman spectroscopic study. Eur J Mineral 7:471-478
Nasdala L, Pidgeon RT, Wolf D (1996) Heterogeneous metamictization of zircon on a microscale. Geochim Cosmochim Acta 60:1091-1097
Nasdala L, Pidgeon RT, Wolf D, Irmer G (1998a) Metamictization and U-Pb isotopic discordance in single zircons: a combined Raman microprobe and SHRIMP ion probe study. Mineral Petrol 62:1-27
Nasdala L, Götze J, Pidgeon RT, Kempe U, Seifert T (1998b) Constraining a U-Pb age: micro-scale characterization of zircons from Saxonian Rotliegend rhyolites. Contrib Mineral Petrol 132:300-306
Nasdala L, Wenzel T, Pidgeon RT, Kronz A (1999) Internal structures and dating of complex zircons from Meissen Massif monzonites, Saxony. Chem Geol 156:331-341
Nasdala L, Banerjee A, Häger T, Hofmeister W (2001a) Laser-Raman micro-spectroscopy in mineralogical research. Microsc Analysis, Eur Ed 70:7-9
Nasdala L, Beran A, Libowitzky E, Wolf D (2001b) The incorporation of hydroxyl groups and molecular water in natural zircon ($ZrSiO_4$). Am J Sci 301:831-857
Nasdala L, Wenzel M, Andrut M, Wirth R, Blaum P (2001c) The nature of radiohaloes in biotite: Experimental studies and modeling. Am Mineral 86:498-512
Nasdala L, Wenzel M, Vavra G, Irmer G, Wenzel T, Kober B (2001d): Metamictisation of natural zircon: Accumulation versus thermal annealing of radioactivity-induced damage. Contrib Mineral Petrol 141:125-144
Nasdala L, Lengauer CL, Hanchar JM, Kronz A, Wirth R, Blanc P, Kennedy AK, Seydoux-Guillaume A-M (2002a) Annealing radiation damage and the recovery of cathodoluminescence. Chem Geol 191:121-140
Nasdala L, Irmer G, Jonckheere R (2002b) Radiation damage ages: Practical concept or impractical vision? – Reply to two comments on "Metamictization of natural zircon: Accumulation versus thermal annealing of radioactivity-induced damage", and further discussion. Contrib Mineral Petrol 143:758-765
Nasdala L, Garver JI, Reiners PW, Kennedy AK, Stern RA, Balan E, Wirth R (submitted) Incomplete retention of radiation damage in zircon from Sri Lanka. Am Mineral
Nechaev SV, Krivdik SG, Krochuk VM, Mizkevich NYu, Tkachuk VI (1986) Zircons form syenites from the Yastrebezkij Massif (Ukrainian Shield)—indicators for conditions of their crystallization. Mineral Zh 8:45-56 (in Russian)
Newman DJ (1971) Theory of lanthanide crystal fields. Adv Phys 20:197-256
Newman DJ, Ng B (1989) The superposition model of crystal fields. Rep Prog Phys 52:699-763
Nicola JH, Rutt HN (1974) A comparative study of zircon ($ZrSiO_4$) and hafnon ($HfSiO_4$) Raman spectra. J Phys C: Solid State Phys 7:1381-1386
Norman CE (2002) Reaching the spatial resolution limits of SEM-based CL and EBIC. Eur Microsc Anal 76:9-12
Nuttall RHD, Weil JA (1981a) The magnetic properties of the oxygen-hole aluminium centers in crystalline $SiO_2$. I. $[AlO_4]^0$. Can J Phys 59:1696-1708
Nuttall RHD, Weil JA (1981b) The magnetic properties of the oxygen-hole aluminium centers in crystalline $SiO_2$. II. $[AlO_4/H^+]^+$ and $[AlO_4/Li^+]^+$. Can J Phys 59:1709-1718

Ohnenstetter D, Cesbron F, Remond G, Caruba R, Claude JM (1991) Emissions de cathodoluminescence de deux populations de zircons naturels: tentative d'interpretation. C R Acad Sci Paris 313:641-647

Panczer G (2001) La photoluminescence résolue en temps, nouvel outil pour la minéralogie. Habilitation thesis, Université Claude Bernard, Lyon

Pellas P (1965) Étude sur la recristallisation thermique des zircons métamictes. Mémoires du Museum National d'Histoire Naturelle, Sér C, Sciences de la Terre, 12:227-253

Phillips MR, Kalceff MAS, Moon AR (1996) Cathodoluminescence spectroscopy of natural zircon (abstr). *In* Intl Conf on Cathodoluminescence and Related Techniques in Geosciences and Geomaterials. Pagel M (ed) Nancy, p 115-116

Pidgeon RT (1992) Recrystallization of oscillatory zoned zircon: some geochronological and petrological implications. Contrib Mineral Petrol 110:463-472

Pidgeon RT, O'Neill J, Silver LT (1966) Uranium and lead isotopic stability in a metamict zircon under experimental hydrothermal conditions. Science 154:1538-1540

Pidgeon RT, O'Neill J, Silver LT (1973) Observations on the crystallinity and the U-Pb isotopic system of a metamict Ceylon zircon under experimental hydrothermal conditions. Fortschr Mineral 50:118

Pidgeon RT, Nasdala L, Todt W (1998) Determination of radiation damage ages on parts of zircon grains by Raman microprobe: implications for annealing history and U-Pb stability. Mineral Mag 62A:1174-1175

Pointer CM, Ashworth JR, Ixer RA (1988) The zircon-thorite mineral group in metasomatized granite, Ririwai, Nigeria. 2. Zoning, alteration and exsolution in zircon. Mineral Petrol 39:21-37

Poirot I, Kot W, Shalimoff G, Edelstein N, Abraham MM, Finch CB, Boatner LA (1988) Optical and EPR investigations of $Np^{4+}$ in single crystals of $ZrSiO_4$. Phys Rev B: Condens Matter 37:3255-3264

Poirot IS, Kot WK, Edelstein NM, Abraham MM, Finch CB, Boatner LA (1989) Optical study and analysis of $Pu^{4+}$ in single crystals of $ZrSiO_4$. Phys Rev B: Condens Matter 39:6388-94

Poller U (2000) A combination of single zircon dating by TIMS and cathodoluminescence investigations on the same grain: the CLC method—U-Pb geochronology for metamorphic rocks. *In* Cathodoluminescence in Geosciences. Pagel M, Barbin V, Blanc P, Ohnenstetter D (eds) Springer, Berlin–Heidelberg, p 401-414

Poller U, Huth J, Hoppe P (2000) SEE und U-Th-Pb Ionensondenmikroanalysen an Zirkonen zum Verständnis von Kathodolumineszenzsignalen. Eur J Mineral 12:155

Poller U, Huth J, Hoppe P, Williams IS (2001) REE, U, Th, and Hf distribution in zircon from Western Carpathian Variscan granitoids: a combined cathodoluminescence and ion microprobe study. Am J Sci 301:858-876

Povarennych AS, Melnik YuP, Shabalin BG (1977) On synthesis and IR-spectra of zircon and hafnon. Geol Zh 37:131-135 (in Russian)

Rakovich FI, Gevorkyan SV (1988) Zircons, associated with uranium minerals. Mineral sbornik 42:65-68 (in Russian)

Reiners PW, Farley KA, Hickes HJ (2002) He diffusion and (U-Th)/He thermochronometry of zircon: Initial results from Fish Canyon Tuff and Gold Butte, Nevada. Tectonophysics 349:297-308

Remond G, Cesbron F, Chapoulie R, Ohnenstetter D, Roques-Carmes C, Schvoerer M (1992) Cathodoluminescence applied to the microcharacterization of mineral materials: a present status in experimentation and interpretation. Scanning Microsc Intl 6:23-68

Remond G, Phillips MR, Roques-Carmes C (2000) Importance of instrumental and experimental factors on the interpretation of cathodoluminescence data from wide band gap materials. *In* Cathodoluminescence in Geosciences. Pagel M, Barbin V, Blanc P, Ohnenstetter D (eds) Springer, Berlin–Heidelberg, p 59-126

Richman I, Kisliuk P, Wong EY (1967) Absorption spectrum of $U^{4+}$ in zircon ($ZrSiO_4$). Phys Rev 155:262-267

Ríos S, Salje EKH, Zhang M, Ewing RC (2000) Amorphization in zircon: evidence for direct impact damage. J Phys: Condens Matter 12:2401-2412

Robinson K, Gibbs GV, Ribbe PH (1971) The structure of zircon: a comparison with garnet. Am Mineral 56:782-790

Roger F, Calassou S, Lancelot J, Malavieille J, Mattauer M, Zhiqin Xu, Ziwen H, Liwei H (1995) Miocene emplacement and deformation of the Koga Shan granite (Xianshui He fault zone, west Sichuan, China): geodynamic implications. Earth Planet Sci Lett 130:201-216

Romans PA, Brown LL, White JC (1975) An electron microprobe study of yttrium, rare earth, and phosphorus distribution in zoned and ordinary zircon. Am Mineral 60:475-480

Rossman GR (1988) Optical spectroscopy. Rev Mineral 18:207-254

Rubatto D, Gebauer D (2000) Use of cathodoluminescence for U-Pb zircon dating by ion microprobe: some examples from the Western Alps. *In* Cathodoluminescence in Geosciences. Pagel M, Barbin V, Blanc P, Ohnenstetter D (eds) Springer, Berlin–Heidelberg, p 373-400

Rubin JN, Henry CD, Price JG (1989) Hydrothermal zircons and zircon overgrowths, Sierra Blance Peaks, Texas. Am Mineral 74:865-869

Rudnitskaya ES, Lipova E (1972) Infrared spectroscopic and nuclear magnetic resonance study of metamict zircon. Geologiya i Razvedka 4:43-50 (in Russian)

Saksena VD (1961) Infrared absorption studies of some silicate structures. Trans Faraday Soc 57:242

Salje EKH, Chrosch, J, Ewing RC (1999) Is "metamictization" of zircon a phase transition? Am Mineral 84:1107-1116

Samoylovich MI, Novozhilov AI, Barsanov GP (1968) Electron paramagnetic resonance in irradiated zircons containing vicarious elements. Geokhimiya 1968:494-495 (in Russian)
Schläfer HL, Gliemann G (1980) Einführung in die Ligandenfeldtheorie. Akademische Verlagsgesellschaft, Frankfurt/Main
Shinno I (1986) Three types of photo-luminescence in natural zircon. J Japan Assoc Mineral Petrol Econ Geol 81:433-445
Shinno I (1987) Color and photo-luminescence of rare-earth element doped zircon. Mineral J 13/5:239-253
Solntsev VP, Shcherbakova MYa (1972) Electron paramagnetic resonance of $Ti^{3+}$ in alpha-quartz and zircon. Zh Strukt Khim 13:924-927 (in Russian)
Solntsev VI, Shcherbakova MYa (1973) A study of lattice defects in irradiated zircon by the EPR method. Doklady Akademii Nauk SSSR 212:156-158 (in Russian)
Solntsev VP, Shcherbakova MYa (1974) Charge compensation mechanisms and the form in which Nb and Y are incorporated into the structure of zircon. Inorg Mater 10:1574-1577
Solntsev VP, Shcherbakova Mya, Dvornikov EV (1974) $SiO_2^-$, $SiO_3^{3-}$, and $SiO_4^{5-}$ radicals in the $ZrSiO_4$ structure from electron paramagnetic resonance data. Zh strukt khim 15:217-221 (in Russian; English abstr: J Struct Chem 15:201-204)
Sommerauer J (1976) Die chemisch-physikalische Stabilität natürlicher Zirkone und ihr U-(Th)-Pb System. PhD dissertation, Eidgenössische Technische Hochschule, Zürich
Speer JA (1980) Zircon. Rev Mineral 5:67-103
Syme RWG, Lockwood DJ, Kerr J (1977) Raman spectrum of synthetic zircon ($ZrSiO_4$) and thorite ($ThSiO_4$). J Phys C: Solid State Phys 10:1335-1348
Taran MN, Bagmut NN, Kislyakova TY, Kvasnitsa VN (1990a) Spectral characteristics of zircon from mantle-derived rocks and its prospecting significance. Mineral Sbornik 44:60-64 (in Russian)
Taran MN, Bagmut NN, Kvasnytsya VN, Kharkiv AD (1990b) Optical and ESR spectra of natural zircons of kimberlitic type. Mineral Zh 12:44-51 (in Russian)
Tarashchan A (1978) Luminescence of Minerals. Naukova Dumka, Kiev, 296 p (in Russian)
Tartaj P, Sanz J, Serna CJ and Ocana M 1994 Zircon formation from amorphous spherical $ZrSiO_4$ particles obtained by hydrolyses of aerosols. J Mater Sci 29:6533-6538
Tennant WC, Claridge RFC (1999) Large-magnitude high-spin nuclear parameters in a $Ti^{3+}$ center from X-band EPR measurements at 10 K. J Magn Reson 137:122-131
Townsend PD, Rowlands AP (2000) Information encoded in cathodoluminescece emission spectra. *In* Cathodoluminescence in Geosciences. Pagel M, Barbin V, Blanc P, Ohnenstetter D (eds), Springer, Berlin–Heidelberg, p 41-57
Trinkler M, Kempe U, Plötze M, Rieser U (1993) Über rosa und braunen Fluorit aus Sn-W-Lagerstätten. Chem Erde 53:165-181
Valéro R, Delmotte L, Louis J, Durand B, Guth JL and Chopin T (1999) A new hydrothermal fluoro-zircon. J Mater Chem 9:117-123
Vance ER (1974) The anomalous optical absorption spectrum of low zircon. Mineral Mag 39:709-714
Vance ER (1975) α-recoil damage in zircon. Radiat Eff 24:1-6
Vance ER, Anderson BW (1972a) Study of metamict Ceylon zircon. Mineral Mag 38:605-613
Vance ER, Anderson BW (1972b) Differences among low Ceylon zircons. Mineral Mag 38:721-724
Vance ER, Mackey DJ (1974) Optical study of $U^{5+}$ in zircon. J Phys C: Solid State Phys 7:1898-1909
Vance ER, Mackey DJ (1975) Further studies of the optical absorption spectrum of $U^{5+}$ in zircon. J Phys C: Solid State Phys 8:3439-3447
Vance ER, Mackey DJ (1978) Optical spectra of $U^{4+}$ and $U^{5+}$ in zircon, hafnon, and thorite. Phys Rev B 18:185-189
Valishev RM, Vinokurov VM, Zaripov MM, Stepanov VG (1965) Electron paramagnetic resonance of the $Er^{3+}$ ions in zircon $ZrSiO_4$ crystals. Geokhimiya 1965:1265 (in Russian)
Vavra G (1990) On the kinematics of zircon growth and its petrogenetic significance: a cathodo-luminescence study. Contrib Mineral Petrol 106:90-99
Vavra G (1994) Systematics of internal zircon morphology in major Variscan granitoid types. Contrib Mineral Petrol 117:331-344
Vavra G, Gebauer D, Schmid R, Compston W (1996) Multiple zircon growth and recrystallization during polyphase Late Carboniferous to Triassic metamorphism in granulites of the Ivrea Zone (Southern Alps): an ion microprobe (SHRIMP) study. Contrib Mineral Petrol 122:337-358
Vavra G, Schmid R, Gebauer D (1999) Internal morphology, habit and U-Th-Pb microanalysis of amphibolite-to-granulite facies zircons: geochronology of the Ivrea Zone (Southern Alps). Contrib Mineral Petrol 134:380-404
Veytizou C, Quinson JF and Douy A (2000) Sol-gel synthesis via aqueous semi-alkoxide route and characterization of zircon powder. J Mater Chem 10:365-370
Vinokurov VM, Gainullina NM, Evgrafova LA, Nizamutdinov NM, Suslina AN (1971) $Zr^{4+} \rightarrow Y^{3+}$ isomorphism in zircon and the associated charge compensation. Kristallografiya 16:318-323 (in Russian; English abstr: Sov Phys

Crystallogr 16:262-265)
Vinokurov VM, Gainullina NM, Nizamutdinov NM, Krasnobayev AA (1972) Distribution of admixed $Fe^{3+}$ ions in the single zircon crystals from the kimberlite pipe "Mir." Geokhimiya 1972:1402-1405 (in Russian; English translation: Geochim Intl 9:952-954)
Vinokurov VM, Zaripov MM, Polskiy YuE, Stepanov VG, Chirkin GK, Shekun LYa (1963) Radiospectroscopic detection of small amounts of $Eu^{2+}$, $Gd^{3+}$ and $Nb^{4+}$ and their isomorphism in fluorite and zircon. Geokhimiya 1963:1002-1007 (in Russian)
Votyakov SL, Ivanov IP, Krasnobayev AA, Krokhalev VY, Korzhinskaya VS (1986) Spectroscopic-luminescent properties of zircon orthosilicate grown by the hydrothermal method. Neorganicheskie materialy 22:281-286 (in Russian)
Votyakov SL, Krasnobayev AA, Krokhalev VY (1993) The Problems of Applied Spectroscopy of Minerals. Nauka, Ekaterinburg, 233 p (in Russian)
Walsby CJ, Lees NS, Tennant WC, Claridge RFC (2000) 15 K EPR of an oxygen-hole boron center, $[BO_4]^0$, in x-irradiated zircon. J Phys: Condens Matter 12:1441-1450
Wasilewski PJ, Senftle FE, Vaz JE, Thorpe AN, Alexander CC (1973) A study of the natural a-recoil damage in zircon by infrared spectra. Radiat Eff 17:191-199
Wertz JE, Bolton JR (1972) Electron spin resonance elementary theory and practical applications. McGraw-Hill, New York
Whitehouse MJ, Kamber BS, Moorbath S (1999) Age significance of U-Th-Pb zircon data from early Archean rocks of west Greenland - a reassessment based on combined ion-microprobe and imaging studies. Chem Geol 160:201-224
Wiedenbeck M, Allé P, Corfu F, Griffin WL, Meier M, Oberli F, von Quadt A, Roddick JC, Spiegel W (1995) Three natural zircon standards for U-Th-Pb, Lu-Hf, trace element and REE analysis. Geostandards Newsletter 19(1):1-23
Woodhead JA, Rossman GR, Silver LT (1991a) The metamictization of zircon: radiation dose-dependent structural characteristics. Am Mineral 76:74-82
Woodhead JA, Rossman GR, Thomas AP (1991b) Hydrous species in zircon. Am Mineral 76:1533-1546
Wopenka B, Jolliff BL, Zinner E, Kremser DT (1996) Trace element zoning and incipient metamictization in a lunar zircon: application of three microprobe techniques. Am Mineral 81:902-912
Yang B, Luff BJ, Townsend PD (1992) Cathodoluminescence of natural zircons. J Phys: Condens Matter 4:5617-5624
Yang XM, Zhang PS, Zhan WL (1990) Infrared-spectra effect of alpha-decay damage in zircon structure. Chinese Sci Bull 35:1988-1991
Zhang M, Salje EKH (2001) Infrared spectroscopic analysis of zircon: Radiation damage and the metamict state. J Phys: Condens Matter 13: 3057-3071
Zhang M, Salje EKH (2003) Spectroscopic characterization of metamictization and recrystallization in zircon and titanite. Phase Transitions 76:117-136
Zhang M, Salje EKH, Farnan I, Graeme-Barber A, Daniel P, Ewing RC, Clark AM, Lennox H (2000a) Metamictization of zircon: Raman spectroscopic study. J Phys: Condens Matter 12:1915-1925
Zhang M, Salje EKH, Capitani GC, Leroux H, Clark AM, Schlüter J, Ewing RC (2000b) Annealing of a-decay damage in zircon: a Raman spectroscopic study. J Phys: Condens Matter 12:3131-3148
Zhang M, Salje EKH, Ewing RC, Farnan I, Ríos S, Schlüter J, Leggo P (2000c) $\alpha$-decay damage and recrystallization in zircon: Evidence for an intermediate state from infrared spectroscopy. J Phys: Condens Matter 12:5189-5199
Zhang M, Salje EKH, Ewing RC (2002) IR Spectra of Si-O overtones, hydrous species and U ions in metamict zircon: Radiation damage and recrystallization. J Phys: Condens Matter 14:3333-3352
Zhang M, Salje EKH, Ewing RC (submitted) Oxidation state of uranium in metamict and annealed zircon: Near infrared spectroscopic quantitative analysis. EUG, Nice

# 16 Atlas of Zircon Textures

**Fernando Corfu**

*Institute of Geology, University of Oslo*
*P B 1047 Blindern*
*N-0316 Oslo, Norway*

**John M. Hanchar**

*Department of Earth and Environmental Sciences*
*The George Washington University*
*Washington, D.C. 20006*

**Paul W.O. Hoskin**

*Institut für Mineralogie, Petrologie und Geochemie*
*Albert-Ludwigs-Universität Freiburg*
*D-79104 Freiburg, Germany*

**Peter Kinny**

*Department of Applied Geology*
*Curtin University of Technology*
*Perth WA 6845, Australia*

## INTRODUCTION

The mineral zircon is extremely variable both in terms of external morphology and internal textures. These features reflect the geologic history of the mineral, especially the relevant episode(s) of magmatic or metamorphic crystallization (and recrystallization), strain imposed both by external forces and by internal volume expansion caused by metamictization, and chemical alteration. The paper presents a selection of both the most typical, but also of the less common, features seen in zircon, categorized according to the different geological processes responsible for their formation. The atlas is intended as a general guide for the interpretation of zircon characteristics, and of related isotopic data.

Zircon has become one of the most widely used minerals for the extraction of information on the prehistory and genesis of magmatic, metamorphic and sedimentary rocks. Much of the geological usefulness of zircon stems from its suitability as a geochronometer based on the decay of U (and Th) to Pb, but in addition it is also the major host of the radiogenic isotopic tracer Hf, and it is used to determine oxygen isotopic compositions and REE and other trace element abundances, all of which yield useful clues concerning the history of the host rock, and in some case, the parent rock in which the precursor zircon crystallized.

One of the major advantages of zircon is its ability to survive magmatic, metamorphic and erosional processes that destroy most other common minerals. Zircon-forming events tend to be preserved as distinct structural entities on a pre-existing zircon grain. Because of this ability, quite commonly zircon consists of distinct segments, each preserving a particular period of zircon-formation (or consumption). A long experience and modern instrumentation and techniques have provided the "zircon community" the means to image and interpret preserved textures, and hence to decipher the history and evolution of a rock. One of the most critical tasks is the proper assignment of particular zircon domains or grains to a specific stage in the history of a rock. This is relatively simple and straightforward in many cases where a proper understanding of the geological setting, simple logical deduction, and common sense lead to unambiguous and straightforward interpreta-

1529-6466/03/0053-0016$05.00

tions, but it can be an extremely difficult task in other cases where the interpretation may be affected more strongly by the bias of the investigator than by purely objective criteria. This is sometimes the case in complex gneiss terranes, as exemplified by the recent debate on the history of the Early Archean gneisses in Greenland (e.g., Nutman et al. 1993, 2002; Whitehouse et al. 1999, Myers and Crowley 2000). The interpretation of age and isotopic relations is affected, on the one hand, by the particular megascopic and petrologic relationships of a rock unit and, on the other hand, by the characteristics of the minerals analyzed, most commonly the external and internal characteristics of the accessory mineral zircon.

The intent of this chapter is to provide an overview of the variety of textural relations observed in zircon and their links to particular rock forming and modifying processes. The selection includes both the most common as well as rare textures observed in nature. The zircon pictures and figures are categorized according to their inferred genetic context. The examples chosen, from our own collections, from colleagues, and from the literature, are based mainly on well-understood geological situations where the geological context provides a measure of assurance that the interpretation is valid.

## ZIRCON IMAGING

In common rocks zircon ranges in size from about 20 to 200 μm (Silver and Deutsch 1963). Larger zircon grains, up to several cm wide (or even up to 30 cm long as for exceptional examples from carbonatite in the Northern Territories, Australia), can be found in granitic pegmatites, syenites, kimberlites and carbonatites, whereas very small zircons may be present in aphanitic volcanic rocks, and in late stage crystallization in plutonic rocks. Observations of the external and internal properties of zircon are, therefore, made by means of microscopic observation or X-ray or electron scattering techniques.

A binocular microscope (BM; Table 1) allows us to observe macroscopic properties, such as color, degree of transparency or opacity, external morphology and form development, and the presence of inclusions, fractures and alteration. For this task it is generally useful to hold the zircon grains in a dish in ethanol in order to improve the optical quality over that obtained by observing in air. Alcohol also makes it simpler to move, turn or hand-pick the grains and to distinguish zircon from other minerals such as apatite, quartz, feldspar and titanite. Still better optical observation is facilitated by setting the zircons in dense fluids such as immersion oils, glycerine or methylene iodide, although these are usually too cumbersome for routine observation (use of methylene iodide and some immersion oils requires a special ventilation set-up because of health risks). Grain-mounts can be prepared with Canada Balsam, piperine, or various epoxy resins, but it becomes more difficult to subsequently remove the grains for isotope dilution analysis if certain epoxy resins are used.

Insights into the internal texture of zircon can be obtained with a petrographic microscope using either transmitted or reflected light. Transmitted light (TL) is useful for viewing zircon in thin section or grain mount and can reveal features such as growth zoning and metamict zones, which display different interference colors when viewed in crossed-polarized light (Chakoumakos et al. 1987, Murakami et al. 1991, Ewing et al., this volume). Observation in thin section is also useful for establishing the relations of zircon to the main rock-forming minerals. The drawback of the method is usually the small size of zircon that challenges the power of resolution of microscopes, and the difficulty of distinguishing zircon from monazite or other high-relief–high-birefringence minerals. Reflected light microscopy (RL) of polished grain-mounts, briefly etched with dilute HF vapor, is very effective in revealing growth zoning, alteration, and other features in old, relatively metamict zircons (e.g., Krogh and Davis 1974, 1975; Fig. 1.1). These techniques, BM, TL and RL (with HF etching), are

**Table 1.** List of abbreviations used in the paper.

| Imaging technique | Abbreviation |
|---|---|
| Binocular microscope | BM |
| Transmitted light microscopy | TL |
| Reflected light microscopy | RL |
| U-mapping | UM |
| Cathodoluminescence | CL |
| Back-scattered electron microscopy | BSE |
| Secondary electron microscopy | SEM |

generally not capable to properly reveal the internal textural complexity of non-metamict, crystalline zircon crystals providing zircon images that appear unzoned and internally featureless (Rudnick and Williams 1987, Hanchar and Rudnick 1995).

Uranium (and Th) maps (UM) can be obtained by inducing fission tracks in a special detector laid upon polished zircon grains by exposing them to a neutron flux in a reactor (Fig. 1.8) (e.g., Duchesne et al. 1987). Alternatively, autoradiography using a nuclear emulsion technique has been used to map α-particle tracks in zircon (e.g., Silver and Deutsch 1963).

The best resolution of internal textures is provided by cathodoluminescence (CL) or backscattered electron (BSE) imaging (Fig. 1.2–1.7). It has long been known that certain minerals, including zircon, exhibit CL when bombarded with electrons (Crookes 1879). Cathodoluminescence has been widely applied as a petrologic tool in the Earth sciences since the mid-1960s (e.g., Long and Agrell 1965, Smith and Stenstrom 1965) and this technique has been used over the past thirty-years to investigate a wide spectrum of problems in sedimentary petrology (Owen and Carozzi 1986, Owen 1987), igneous and metamorphic petrology and geochronology (e.g., Sippel 1968, 1971; Görz et al. 1970, Malcuit and Heimlich 1972, Sommerauer 1974, Ono 1976, Vocke and Hanson 1981, Vavra 1990, 1993; Hanchar and Miller 1993, and numerous other studies since the mid-1990s).

The elemental, or structural, controls of the CL emission is generally well understood for most minerals (Marshall 1988) and is usually attributed to the electronic transitions of 5d-electron transition elements, of 4f-electron electronic transitions of the trivalent rare earth elements (REEs), vibrational luminescence of the uranyl ion, or defect-related phenomena (Marshall 1988). In zircon, there is usually a broad band emission in either the blue or yellow regions, or both, of the electromagnetic spectrum upon which are superimposed sharp peaks of the trivalent REEs. $Dy^{3+}$ is considered to be the principal elemental factor (e.g., Mariano 1978, 1989; Remond et al. 1992, Hanchar and Rudnick 1995), although other constituents such as $Sm^{3+}$, $Eu^{2+}$ and $Tb^{3+}$ may also be CL emitters in zircon (e.g., Ohnenstetter et al. 1991, Yang et al. 1992). The presence of $U^{4+}$ and the resulting radiation damage from its decay may also suppress the CL emission (see Nasdala et al. in this volume for a more thorough discussion of the CL of zircon). Ohnenstetter et al. (1991) have

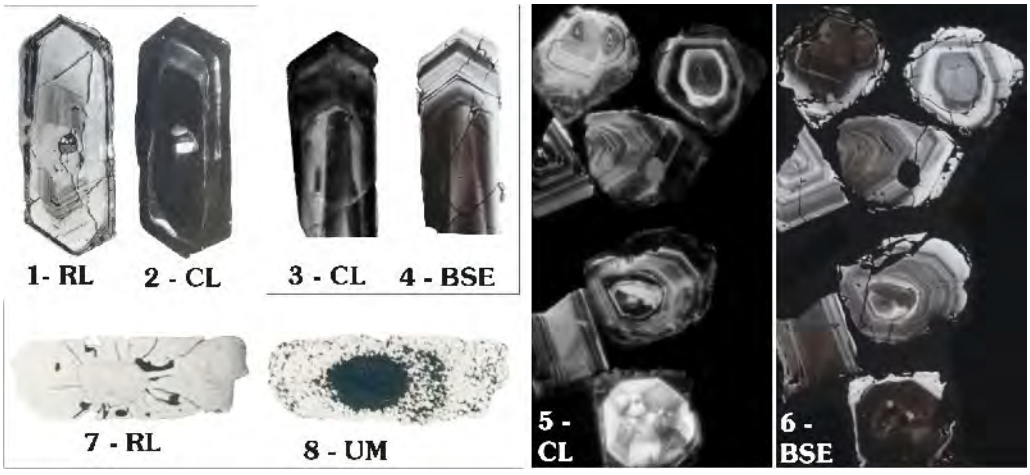


**Figure 1.** Imaging techniques.**(1-2)** Same zircon imaged with RL, after polishing and etching the surface with HF vapor, and CL; modified from Nemchin and Pidgeon (1997). **(3-4** and **5-6)** Comparison of CL and BSE imaging (from J.M. Hanchar, unpublished results); **(7-8)** RL image of polished zircon crystal reveals inner core and radially fractured outer shell; UM image highlights the zonation indicating very high concentrations of U in the centre, more moderate values in an intermediate shell and lower concentrations in the rim; modified from Duchesne et al. (1987).

suggested that the broad-band blue CL emission may be defect-related due to the presence of $Y^{3+}$ and that the broad band yellow CL emission may also be defect-related due to the presence of $Ti^{4+}$ or $U^{4+}$.

Back-scattered electron imaging reveals contrasts in average atomic number of regions of a phase; the higher the number, the more electrons an area will "reflect" and the brighter it will appear in the resulting image. Back-scattered electron imaging is now widely used in a variety of geologic studies and is recognized as a powerful tool for studying zonation in minerals and especially accessory minerals (e.g., Wayne and Sinha 1988, 1992; Krinsley and Manley 1989, Paterson et al. 1989, 1992a,b; Paterson and Stephens 1992, Miller et al. 1992, and numerous studies since the mid-1990s). The element primarily responsible for these BSE intensity variations in crustal zircon is Hf, with U having a secondary effect (Hanchar and Miller 1993).

In investigating zircons with these imaging techniques we have found that in many cases both techniques reveal similar features, however, usually the bright areas in CL are dark in BSE and vice versa—an observation noted by Hanchar and Miller (1993), Koschek (1993) and many other workers (Fig. 1.3-1.6). We have found that CL is generally more useful than BSE in identifying different growth regions in zircon due to the greater range in intensity of the CL emission and the additional variations in color (if done using a petrographic microscope based CL system and using color negative or slide film, or a digital camera). In addition, different growth events often have characteristic CL emission colors and this attribute of using CL can help locate *in situ* analysis locations of different isotopic age. Using a scanning electron microscope based CL system obviously reveals similar features in zircons, but unless false-color processing is done, images are in grey-scale only and the different colored CL regions remain unnoticed.

## MORPHOLOGY OF ZIRCON

Zircon is tetragonal and most commonly grows as doubly-terminated prismatic crystals with elongation (length-to-width) ratios ranging from 1 to 5. This ratio is commonly believed to reflect crystallization velocity. Indeed, needle-shaped acicular zircon crystals are common in rapidly crystallized, porphyritic, sub-volcanic intrusions, high-level granites, and gabbros (e.g., Fig. 2.15–2.18),

**Figure 2.** External morphology variations.All grains are between 70 and 250 μm in size. **(1-21)** Variable morphology characteristics in terms of length to width ratios and typology. The latter is shown in the general context of the diagram of Pupin (1980) which is based on the relative development of the prismatic (vertical axis) and pyramidal crystal faces (horizontal axis). Note also the local presence of xenocrystic cores, inclusions of other minerals and degree of fracturing. 1 – modified from Pupin (1980), TL; 2 – only one pyramid is developed on a large subrounded core, from F. Corfu (unpublished data), BM; 3 – modified from Machado et al. (1989), BM; 4 – from F. Corfu (unpublished data), BM; 5 – ghost xenocrystic core evidenced only by bubble structure, modified from Oberli et al. (1994), TL; 6 – modified from Kröner et al. (1998), SEM; 7 – complex twinning, modified from Jocelyn and Pidgeon (1974), BM; 8 – zircon crystal totally lacking prismatic faces, from U. Schaltegger (unpublished data), SEM; 9, 10 – flat shaped, twinned crystals, from F. Corfu (unpublished data), BM; 11, 12 – modified from Pupin (1980), TL; 13,14,15 – from F. Corfu (unpublished data), BM; 16 – modified from Moser (1997), SEM; 17, 18 – highly fractured prisms in gabbro, modified from Corfu and Stott (1998), BM; 19, 20 – prominent cores overgrown by clean prisms, modified from Palmer and Davis (1987), BM; 21 – modified from Corfu and Ayres (1984), BM. **(22)** Zircon aggregate in A-type pluton, modified from Charoy and Raimbault (1994), SEM. **(23)** Thin-walled hollow zircon crystal, modified from Huneke and Rossman (1978), SEM. **(24)** Zircon fragment, typical of populations extracted from many mafic rocks, modified from Abati et al (1999), SEM. **(25-27)** Composite, resorbed grains (cauliflower zircon); 25, 27 – in meta-trondhjemite, modified from Pin and Lancelot (1982), SEM; 26 – in mafic gneiss, modified from Peucat et al. (1990), BM. **(28-30)** Magmatically resorbed grains without overgrowths. 28 – free xenocryst in granitoid rock, modified from Corfu and Ayres (1994), BM; 29-30 – highly resorbed xenocrysts in pyroclastic volcanic rock (from F. Corfu, unpublished data), BM. **(31-34)** Sub-rounded to multifaceted zircon in metamorphic rocks. 31 – in metagabbro, modified from van Breemen et al. (1986), SEM; 32 – in leucogranulite, modified from Kröner et al. (1998), SEM; 33,34 – in lower crustal xenolith, modified from Chen et al. (1998), SEM. **(35-36)** Meteorite impact related zircons. 35 – resorbed shocked zircon with traces of planar deformation features; 36 – post impact growth of polycrystalline zircon; both modified from Moser (1997), SEM.

whereas stubby and equant forms are more common in deep-seated, slowly cooled intrusions (Fig. 2.13–2.14).

Other factors affecting the shape of the zircon crystals are the composition and possibly the temperature of the crystallization medium. Systematic examination of zircon typology has led to the establishment of the widely used "Pupin diagram" (Fig. 2 inset), in which zircon crystals are classified according to the relative development of the {100} vs. {110} prismatic forms and the {211} vs. {101} pyramidal crystal forms (Pupin 1980). In general, zircon grains from relatively dry alkalic and tholeiitic igneous rocks tend to be dominated by {100} and {101} forms, where those

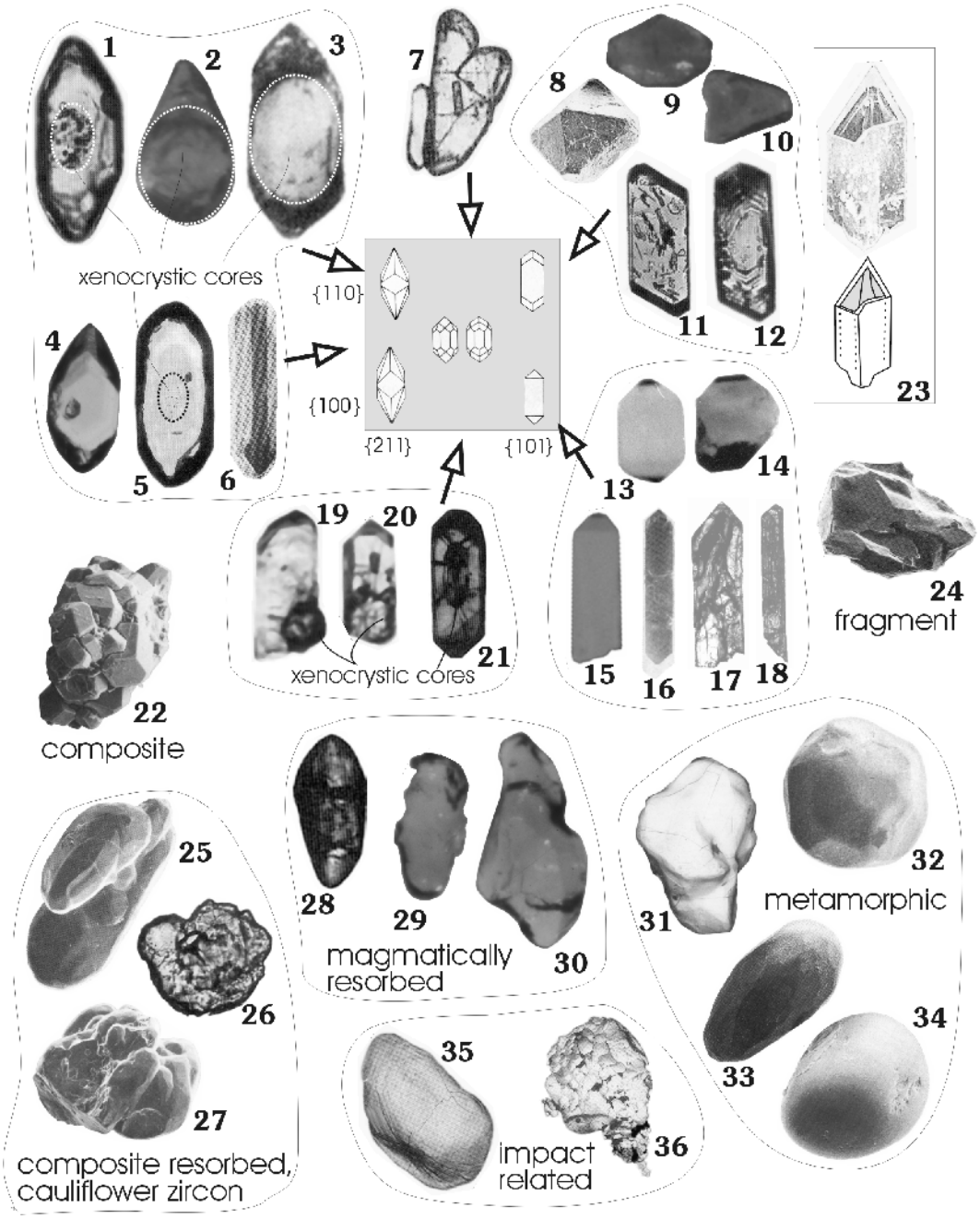

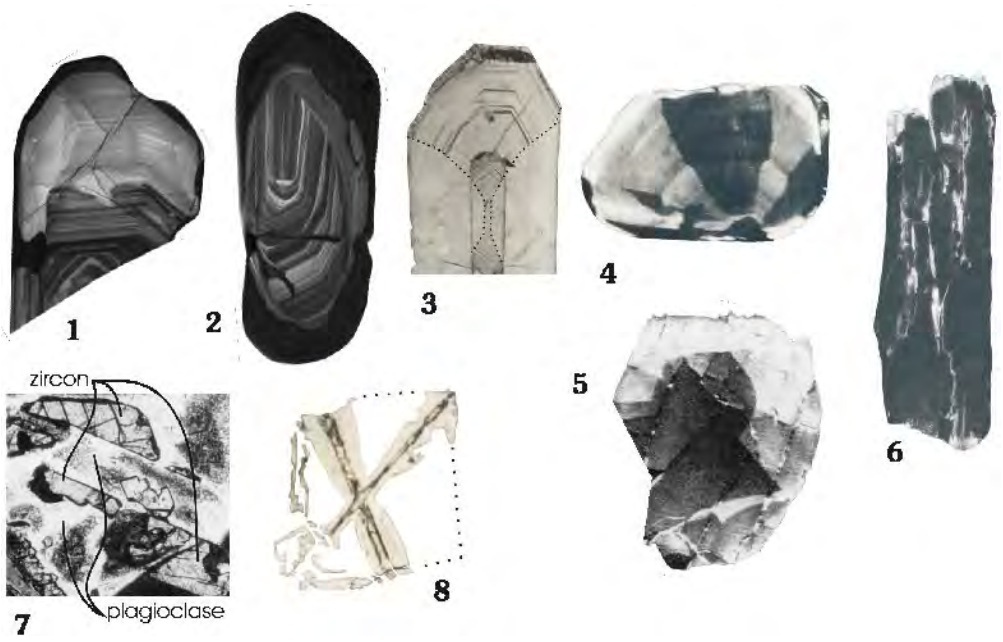


**Figure 3.** Complex and other types of zoning in magmatic rocks. All grains are between 70 and 250 μm. **(1-2)** Complex growth zoning with local intermediate resorption in zircon from anatectic granite, from P. Kinny (unpublished data), CL. **(3-4)** Sector zoning; 3 – section parallel to the c-axis (dotted line highlights the boundary between sectors), modified from Krogh (1982), RL of vapor etched grain; 4 – section normal to the c-axis, modified from Hoffman and Long (1984), CL. **(5-6)** Patchy zoning; 5 – zircon in norite with broad zoning superimposed by irregular domainal texture, modified from Paquette et al. (1995), CL; 6 – bright seams indicate altered fractures disrupting original zoning; modified from Vavra and Hansen (1991), CL. **(7-8)** Skeletal growth; 7 – incomplete zircon fragments growing on opposite sides of plagioclase, modified from Paquette et al. (1995), TL; 8 – incomplete zircon due to rapid growth, section perpendicular to the c-axis, modified from Krogh et al. (1982), TL.

from aluminous to calc-alkaline rocks exhibit various combinations of forms with a prominent presence of {211}, and those from water-rich granites and pegmatites tend to have {110} and {101} as their dominant forms. Pupin (1980) related the relative development of the prismatic faces mainly to the temperature of crystallization whereas the pyramidal faces were linked to chemical factors, and suggested that the typological parameters of a zircon population can be used to describe the evolution of a magma system. The somewhat simplistic nature of this interpretation has been challenged by Vavra (1993), who introduced a more sophisticated method to determine the relative growth-rates of zircon forms in order to characterize the kinetics of a crystallizing environment. Benisek and Finger (1993) also showed that compositional factors have a significant effect on the development of prism faces in zircon.

As mentioned above, the velocity of crystallization appears to be the major controlling factor of the elongation ratio for zircon. Skeletal zircon crystals are the most extreme form of rapid growth. Such zircons, observed locally in mafic and undersaturated alkaline rocks (Figs. 3.7 and 3.8) are characterized by the development of crystal-beams and walls surrounding empty space (Bossart et al. 1986). A comparable zircon type, exhibiting hollow prisms or other incompletely grown crystals, has been reported from cavities in basaltic andesite and interpreted to indicate rapid growth from a vapor phase (Fig. 2.23; Huneke and Rossman 1978). Many magmas tend to reach zircon saturation relatively early in their evolution and thus precipitation of zircon can accompany that of most other minerals. In some magmas, however, saturation is only reached late in the crystallization history, either because of very low Zr contents, or high Zr solubility or both (see Hanchar and Watson, this

volume). In these cases zircon forms late in pools of highly fractionated magma, either in isolated magma pools or interstitially to other minerals. Such zircons commonly exhibit only partially developed crystal faces (e.g., Poldervaart 1956, Scoates and Chamberlain 1995; Fig. 3.7), and they are recovered from mineral separation as an assortment of broken fragments (Fig. 2.24). This is a common feature for gabbroic rocks.

The opposite case occurs when a magma is oversaturated with respect to zircon for part or most of its crystallization. Such magmas are unable to completely dissolve restitic or assimilated zircon, which quite commonly become the seed of newly grown magmatic zircon. The appearance of xenocrystic zircon can thus range from highly "polished" grains free of any overgrowth (Figs. 2.28–2.30) to subrounded grains totally enclosed in new zircon mantles (Figs. 2.1–2.3; 2.19–2.21). In some rocks one can observe a whole range of occurrences from overgrowth-free xenocrystic zircon, xenocrystic cores and volumetrically-large mantles, to entirely new igneous zircon. In addition, newly-grown zircon crystals can themselves exhibit evidence for multiple stages of growth and corrosion. All these features can be linked to complex magma evolution from initial formation by source melting, through various stages of movement through the crust, contamination and perhaps mixing with different magma batches, fractional crystallization and differentiation, with loss of cumulates and vapor, and final emplacement or extrusion. The solubility of zircon itself is largely a function of the composition of the system, described by the parameter $M = (2Ca + Na + K)/(Si \times Al)$ as well as $H_2O$ content and temperature (Watson 1979, 1996; Harrison and Watson 1983, Watson and Harrison 1983, Hanchar et al., this volume).

Besides resorption that may occur when zircon is immersed in magma, resorption and modification, including recrystallization and Ostwald coarsening (Watson et al. 1989) can result from metamorphism. The slow diffusivity of most cations in non-metamict zircon suggests that no substantial water-free recrystallization will occur over geologically significant time periods by volume diffusion alone at the temperature conditions in normal continental crust (Cherniak et al. 1997a,b; Cherniak and Watson 2001, Cherniak and Watson, this volume). It is thus likely that any subsolidus modification of zircon will reflect active corrosion and precipitation mechanisms related to a fluid phase. Hence, it is also likely that any such reaction will occur coevally with metamorphic reaction of other mineral phases present in a rock.

As far as the external morphology is concerned, metamorphically grown, or metamorphically modified zircon crystals are generally characterized by subrounded and highly resorbed shapes (Figs. 2.25–2.27, 2.31–2.34), but euhedral shapes are also possible, especially in very fluid-rich systems such as in amphibolite facies mica schists or migmatites. Where in the former case, the development of crystal faces was probably facilitated mainly by the presence of aqueous or carbonic fluids, in the case of migmatites, zircon is likely to have grown in contact with a melt phase, and hence, strictly speaking is no longer metamorphic but magmatic. As for the subrounded metamorphic zircon type, it is possible to recognize various degrees of modification. Zircon crystals in some gneisses may only exhibit moderate rounding of the crystal edges whereas in others the original crystal shape has been destroyed, and the final product being smoothly subrounded grains (Fig. 2.31). This is commonly the case in granulite facies rocks, where zircon grains sometimes display multifaceted exteriors (Figs. 2.32–2.33). The grains may consist largely of reworked original zircon, or at the other extreme, comprise entirely new-grown metamorphic zircon. Metamorphosed mafic rocks locally contain irregular zircon grains such as the cauliflower type of Peucat et al. (1990) (Figs. 2.25–2.27). In some instances the shape of these grains may reflect resorption of originally irregular and fragmented zircons such as those recovered from some mafic rocks (Fig. 2.24), or of the composite crystals found in some granites (Fig. 2.22), but in other cases they likely represent metamorphically grown polycrystalline zircon. These are discussed in more detail later in this chapter. A special case shown in Figures 2.35 and 2.36 is that of shocked zircons from meteorite impact craters that reveal both traces of impact-related fracturing and rapid new growth of polycrystalline zircon in the immediate aftermath of impact.

## ZONING TEXTURES IN IGNEOUS ZIRCON

One of the more typical features of magmatic zircon is the presence of well developed growth zoning. This feature is best seen in CL and BSE images, but in zircon affected by metamictization of U-rich areas, zoning can be revealed very well by microscopic examination (BM, RL, TL).

The zoning reflects compositional variation of Zr and Si and more importantly, variations in Hf, P, Y, the REE, U and Th—up to an order of magnitude for some of these elements (e.g., Köppel and Sommerauer 1974, Benisek and Finger 1993, Hanchar and Rudnick 1995, Fowler et al. 2002, and many other studies). The composition of the zones tends to vary between two end-members, one of which is very low in trace-elements, approaching the composition of pure zircon, and the other a zircon component highly enriched in trace elements with up to several wt % of the impurity element (Speer 1982). The mode of development of the zoning also varies widely. In some cases one observes an almost bimodal succession of trace-element rich and trace-element poor bands with almost no intermediate compositions (Figs. 4.1 and 4.2) where in other cases the zones span a much wider compositional range (Figs. 4.3–4.12), or the compositional difference becomes very small yielding only faintly visible zoning patterns (Figs. 4.13–4.15), and in some cases there is no visible zoning at all (Fig. 4.16). The thickness of the bands also varies widely. For example the bands in Figure 4.1 are on the order of 20-100 μm wide, while those in Figure 4.2 are barely 5-10 μm wide. Fowler et al. (2002) show that periodicity can be observed at different scales in their zircon megacryst, ranging from 0.5 mm down to a few μm. Moreover, within individual crystals one can observe strong variations in the relative development of zoned domains, such as in Figures 4.11 and 4.12 where one large uniform central zone is succeeded by much finer oscillatory-zoned bands. Halden and Hawthorne (1993) have shown that the zoning pattern of zircon from a carbonatite can be quantified by spectral analysis.

The origin of growth zoning is discussed in some detail by Mattinson et al. (1996) who conclude that episodic growth results from the interplay between the stage of crystal growth, the nature of the crystal-liquid interface, the degree of supersaturation of the melt, the rates of diffusion, and the state of oxidation.

In the only study yet published that investigates zircon zonation patterns in zircon populations from a range of related rocks, Hoskin (2000) analyzed the variation of oscillatory zoning in zircon (Fig. 4.17) from compositional sectors of a zoned I-type pluton ($SiO_2$ from 50-75 wt %; diorite to aplite zones) using CL images and fractal statistical characterization. It was found that trace-element incorporation into zircon was affected by "external forcing" (processes occurring within the magma system and not at the crystal/melt interface). The result of external forcing is to impose increasing order (as measured by the mean Lyapounov exponent, $\lambda_m$, a statistical parameter) on the oscillatory zoning pattern as magmatic differentiation proceeds. The correlation between magmatic differentiation and increasing zonation order is related to ordering in the melt by polymerization. Hoskin (2000) presented a model for zonation pattern generation that accounts for dynamics at the zircon/melt interface, cation substitution, diffusion, and melt polymerization and structure generation. This model remains untested, although new generation ion probes (e.g., nanoSIMS) may provide a means to test the model.

It is quite commonly observed that regular growth zoning is interrupted by textural discontinuities along which the original zoning is resorbed and succeeded by the deposition of new-growth-zoned zircon (Figs. 4.1, 3.1 and 3.2). These resorption intervals probably reflect intermediate periods of Zr undersaturation in the magma, owing to large-scale mixing phenomena, or to local kinetic phenomena. For example, the zircon shown in Figure 4.15 derives from the charnockitic phase of a zoned pluton and is characterized by an irregular subrounded external appearance, an almost uniform internal texture, and evidence of marginal resorption and reprecipitation. These textures suggest that it may have formed by very slow and complex crystallization of a magma body with prolonged residence time in the lower crust. In contrast, the coeval zircon in a mangeritic part of the same pluton displays simple growth zoning and no evidence of resorption (zircon not shown).

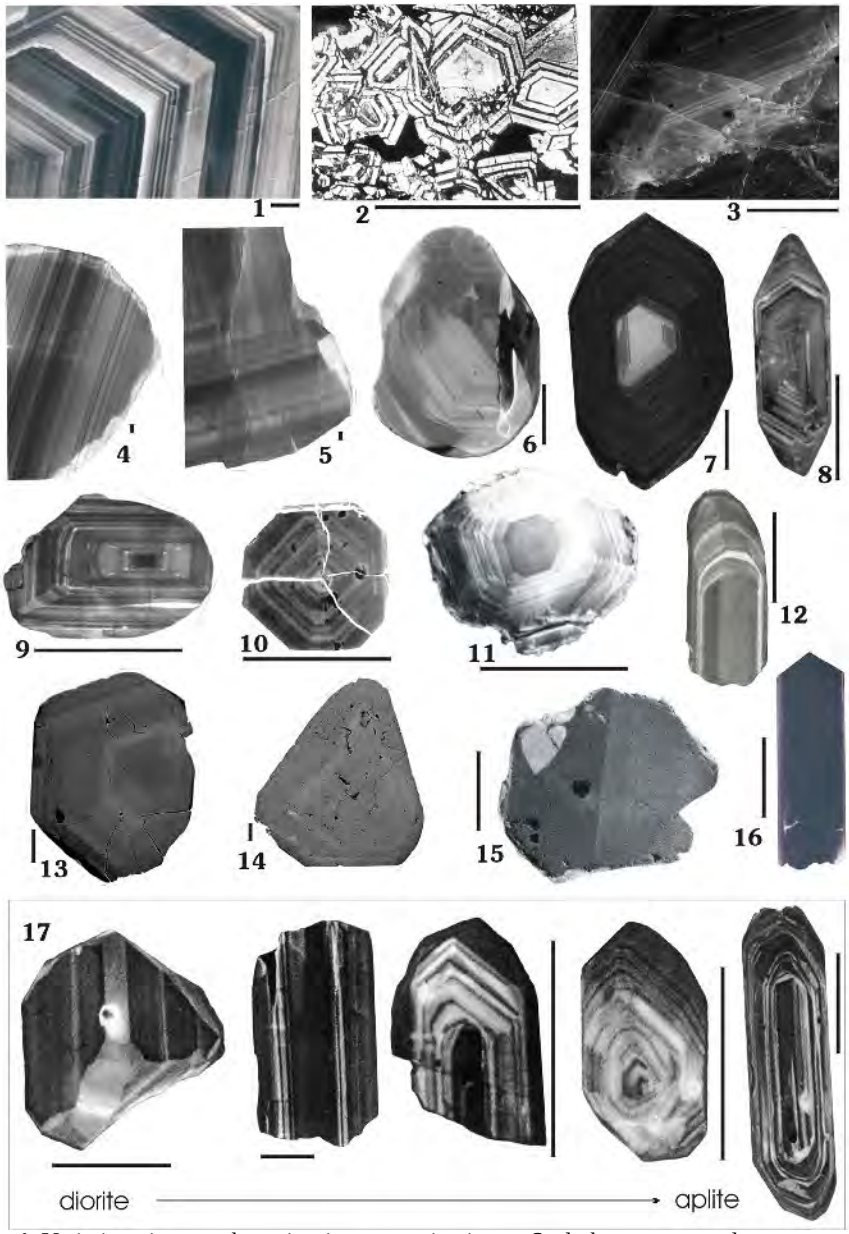


**Figure 4.** Variations in growth zoning in magmatic zircon. Scale bar corresponds to approximately 100 μm. **(1)** Zoned crystal from larvikite, from S. Dahlgren, unpublished data), CL. **(2)** Bimodal zoning, peralkaline complex, modified from Smith et al. (1991), BSE. **(3)** finely zoned crystal from carbonatite, from J. Hanchar (unpublished data), CL. **(4, 5**) zoned megacrystic zircon from kimberlite, from P. Kinny (unpublished data), CL. **(6-12)** growth zoning in typical crustal rocks: 6- from J. Hanchar (unpublished data), CL; 7 – from P. Kinny (unpublished data), CL; 8 – Poller (1997), CL; 9 – from P. Kinny (unpublished data), Cl; 10 – modified from Benisek and Finger (1993), BSE; 11 – from F. Corfu (unpublished data), CL, 12 – modified from Christoffel et al. (1999), CL. **(13-15)** Faint and broad zoning: 13 – carbonatite, from J. Hanchar (unpublished data), CL; 14 – pegmatite, from J. Hanchar (unpublished data), CL; 15 – mangerite (from F. Corfu (unpublished data), CL. **(16)** Homogeneous unzoned zircon in dacite, modified from Zeck and Williams (2002), CL. **(17)** Transition in style of zoning with differentiation of a pluton from diorite, through granodiorite, different adamellite phases, and finally aplite. Broad zones in zircon of diorite tend to become progressively narrower, but more frequent as the magma evolves; modified from Hoskin (2000), CL.

A special case of zoning is sector zoning. In the crystal shown in Figure 3.3, a section parallel to the c-axis, the pyramidal sectors are enriched in U (and presumably other trace-elements) whereas the prismatic sectors contain less U (Krogh 1982). In the example shown in Figure 3.4, the sectors are defined by variations between the two prismatic faces. Microprobe analyses of the different sectors reveal variations of 20-100% in Hf and Y, in part correlating with smaller changes in Zr and Si, (U is below detection limit; Hoffman and Long 1984). The development of sector zoning in zircon has been attributed to kinetic factors and rapid changes in the growth environment during crystal development (e.g., Paterson and Stephens 1992). Watson and Liang (1995) propose, however, that the occurrence of sector zoning is mainly dependent on the relation between growth rates and lattice diffusivity. In their model, particular growth surfaces are initially enriched in some elements with respect to others and these disparities are then preserved in the growing crystal if lattice diffusion is sufficiently slow. Vavra et al. (1996) attribute sector zoning to rapidly fluctuating and unequal growth rates related to the roughness of the growth surface and degree of saturation of the growth medium.

The skeletal zircon in Figure 3.8 represents an extreme case of preferential growth along specific crystallographic directions. Here, one of the prismatic faces has grown along four "ridges" that extend from the centre of the crystal (which presumably runs parallel to the c-axis). The second prismatic face only started to develop in exterior parts of the crystal late in the crystallization sequence. The central regions of the ridges remained hollow and locally may have been filled with high-U zircon, now highly metamict. Such cavities occur commonly in rapidly grown, elongated prismatic zircons.

A particular type of zoning is the irregular and patchy texture shown in Figure 3.5 (Paquette et al. 1995). This type of texture is reminiscent of undulatory extinction in strained quartz, and may reflect strain experienced by zircon during final magmatic emplacement. A distinct bending of very thin zircon crystals was observed by the first author in crystals 0.5-2 cm long from pegmatitic phases of two massive gabbroic intrusions, although the zircon was not examined by CL. The texture shown in Figure 3.5 suggests that the microfractures between the various domains were subsequently healed by new zircon growth during cooling. A somewhat similar patchy texture in elongated crystals with faint zoning and irregular longitudinal streaks (Fig. 3.6) has been interpreted by Vavra and Hansen (1991) to indicate local recrystallization along longitudinal microfractures.

Perfectly euhedral prisms without any evidence of zoning are locally observed in some rocks (Fig. 4.16). It is not clear whether the lack of zoning is due to the insufficient resolution of the imaging techniques used, or whether the particular growth environment and kinetics have contributed to form compositionally homogeneous crystals, or whether original zonation patterns have been destroyed.

## XENOCRYSTIC CORES

The occurrence of xenocrystic zircon is a common feature of many igneous rocks. Zircon xenocrysts occur as cores mantled by newly grown magmatic zircon, or simply as unmantled subrounded or rarely euhedral crystals (such as when zircon is assimilated into a magma during late-stage crystallization, with too little time for corrosion or overgrowth). The recognition of xenocrystic cores is easy in some rocks but more difficult in others. Where there are distinct differences in U-content between a core and rim, differential metamictization expands the high-U part and transforms the original colorless domains into pink to brown, or even opaque, zircon. If the core is richer in U than the rim, core expansion will eventually cause fracturing of the more rigid rim (Figs. 2.19–2.21; 5.1–5.4). In the opposite case, with a low-U core surrounded by a high-U rim, there is generally no fracturing (Figs. 2.1 and 2.3, but see Figs. 13.1 and 13.2 below) but the rim will become much darker than the core. The presence of such fracture patterns and the differential coloration allow us to identify core-rim textures by simple microscopic (BM) examination. For solution-based isotope analysis it is usually relatively simple to break-off cores and rims and analyze

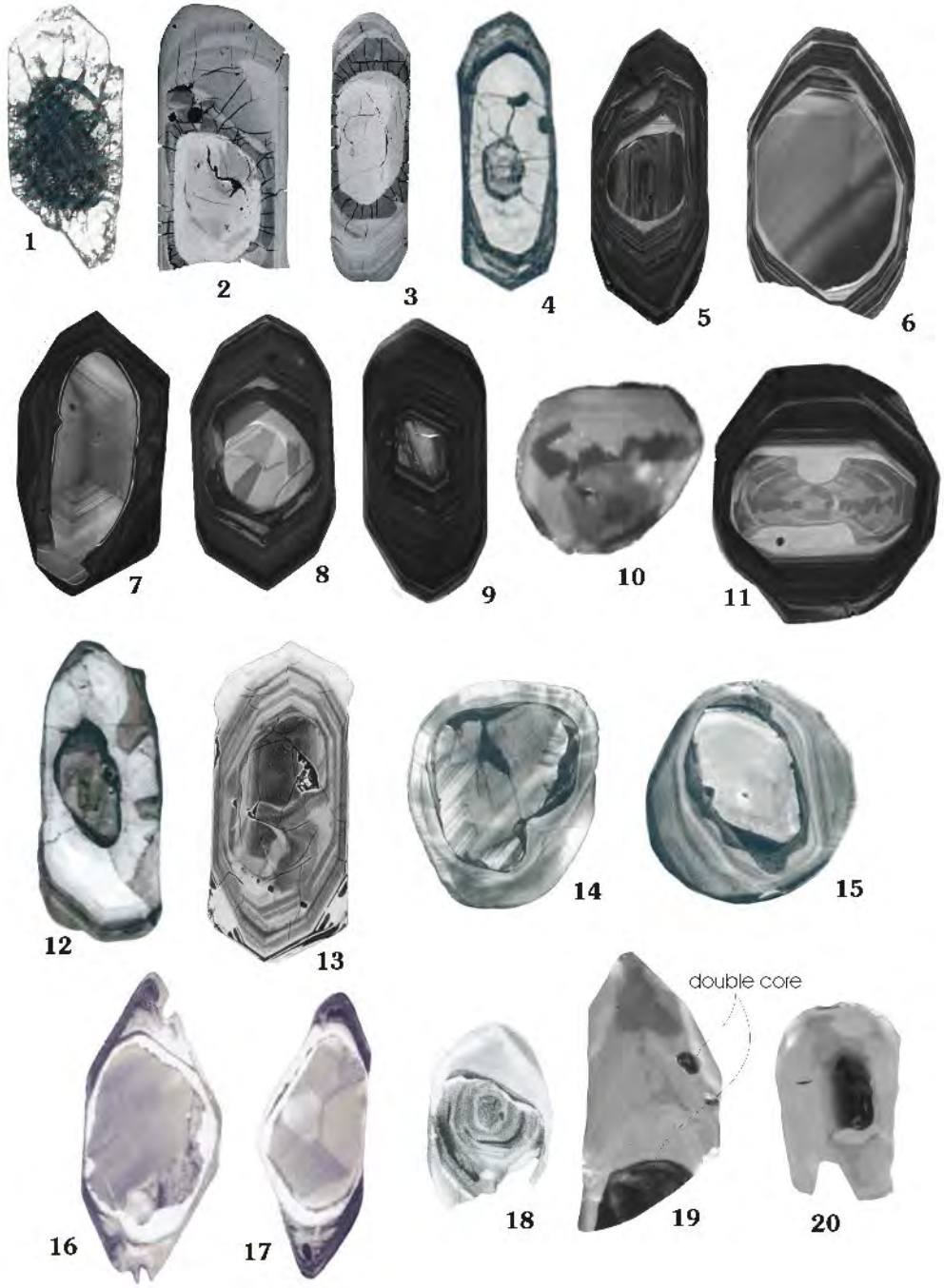


**Figure 5.** Variable appearance of xenocrystic cores in magmatic and high-grade meta-morphic rocks. **(1-20)** Variable appearance of xenocrystic cores in magmatic (1-13, 16-20) and high-grade metamorphic rocks (14-15), (all grains were between 70 and 250 μm in size); 1- Large metamict core has expanded and cracked the rim, modified from Welin et al. (1982), TL; 2, 3 – from J. Hanchar (unpublished data), BSE; 4 – modified from Corfu and Ayres (1984), RL; 5, 6, 7, 8, 9 – from P. Kinny (unpublished data), CL; 10 – from J. Hanchar (unpublished data), CL; 11 – from P. Kinny (unpublished data), CL; 12 – modified from Andersson and Williams (2001), CL; 13 – modified from Paterson et al. (1992b), BSE; 14-15 detrital cores, modified from Vavra et al. (1996), CL; 16,17 – modified from Zeck and Williams (2002), CL; 18 – modified from Whitehouse et al. (1999), CL; 19, 20 – from D. Moser (unpublished data), CL.

them separately for age determination. In some cases the only visible sign of a xenocrystic core is a trail of small bubbles at the core-rim boundary (Fig. 2.5).

Detection of core-rim textures becomes much more difficult in cases were both core and rim are low in U, and can thus remain colorless and unfractured even after 2 or 3 billion years. In such cases a simple visual examination under a binocular microscope will in general not be able to reveal the presence of a xenocrystic core, and even techniques like HF-etching may not help. By contrast, the application of CL or BSE imaging is successful in the majority of cases (e.g., Figs. 3.2, 5.5, 5.6, and 7.8 and 9.14 below) and, as noted above, it is often the case that different growth events preserved in zircon emit different color CL emission.

Xenocrystic cores are commonly differentiated from their rims by geometrically irregular surfaces, which truncate internal zoning (Figs. 5.5–5.8, 5.11 and 5.18) or separate subrounded, unzoned, or chaotically zoned cores from growth zoned rims (Fig. 5.2–5.3, 5.9, 5.12–5.16 and 5.19–5.20). Such discontinuities can indicate deep resorption of the early zircon phase (Figs. 5.7, 5.11–5.13), and locally they reveal that new zircon growth has occurred in a different crystallographic orientation than the substrate zircon (Fig. 5.11). In specific situations, however, it can be difficult to distinguish a xenocrystic core from other features such as zones of local recrystallization or specific magmatic growth bands, or to exactly locate the actual boundary between a core and a magmatic rim (Figs. 5.4, 5.12, 5.16 and 5.17). It is common to have more than one discontinuity within an individual zircon, and, in principle, they could indicate the presence of multiple core generations, a combination of core (early) and mantle (later) resorption events, or multiple stages of magmatic resorption within a single magmatic event. Interpretations can commonly be made with confidence, or the possibilities reduced, when the textural observations are combined with isotopic analysis of specific zones.

In some instances zoned xenocrystic cores can retain a euhedral outline that progresses—without apparent discontinuity—into zoned rims. In such cases, only isotopic analysis of specific areas (crystal middle and crystal edge) can delineate the presence of a xenocrystic core (Paterson et al. 1992b).

Some difficulties are met when one attempts to evaluate the origin of xenocrystic cores. In specific cases, key evidence can be provided by direct field observation. For example, xenocrystic cores found in zircon grown in a migmatite within a clastic sedimentary sequence, or in a classical S-type granitic body, can readily be interpreted as being of detrital origin. The frequency of isotopic ages and age omissions obtained for xenocrystic zircon populations can be linked to potential sedimentary sources. In the case of xenocrystic zircon cores found in granitic bodies of less obvious crustal origin it is not possible in general to unambiguously verify a detrital origin. If the source-region of a granitoid body is a mixed gneissic terrane, then the xenocrystic zircons could be both supracrustal and magmatic in origin; in other cases one could easily expect that multistage magmatic zircon will become incorporated into newly grown igneous zircon. Hence, in most cases a clear and straightforward interpretation of the origin of xenocrystic cores is not possible.

Xenocrystic cores themselves do not yield many clues as to their origin. Occasionally they preserve the abrasions and fracturing caused by erosion and sedimentation process (Figs. 5.14 and 5.15) that support independent evidence for a detrital origin, but otherwise such clues are too ambiguous to be trusted.

## SUBSOLIDUS MODIFICATIONS AND GROWTH OF ZIRCON

### Late-magmatic phenomena

Zircon can be affected by various processes at various times: the final stages of magmatic crystallization, during slow cooling of large intrusive bodies, and by later metamorphic events. Distinction between the effects of the processes is not always straightforward, and there is not always consensus on the interpretation of secondary textures.

Modifications of magmatic zircon during late and post-magmatic cooling tends to result in a disruption of concentric oscillatory zoning. One of the most commonly observed textures is the development of irregular domains of homogenous, low-U zircon cutting discordantly across growth zoned domains (Figs. 6.1–6.7). These domains are thought to develop by recrystallization, a process promoted by the relative instability of trace-element-rich domains with respect to trace-element-poor zircon. Recrystallization is probably promoted by the presence of magmatically derived aqueous fluids in deep-seated settings (Pidgeon 1992, Nemchin and Pidgeon 1997, Schaltegger et al. 1999). The recrystallization process expels trace elements, shifting the composition closer to that of pure zircon, and apparently concentrates the impurities in trace element-rich convolute zones (Figs. 6.5, 6.10–6.12 and 6.17; Pidgeon et al. 1998).

Another process appears to involve metasomatic replacement of zircon creating trace-element-rich domains. For example, the zircon prism displayed in Figure 6.16 is characterized by a mosaic texture which appears to have developed by modification of an originally low-U zircon, either during a late magmatic stage or subsequent metamorphism (Corfu and Ayres 1984). The occurrence of "bent" prisms in this population suggests that development of the mosaic texture may have been preceded by the formation of a patchy (strained) texture similar to that observed in Figure 3.5.

**Medium to high temperature metamorphism**

The three zircons shown in Figures 6.13–6.15 display the progressive development of a veined and brecciated texture starting from relatively homogeneous zircon (Ashwal et al. 1999). U-Pb dating indicates that the amount of veining affecting these zircon grains correlates with the degree of younging, indicating that loss of Pb was caused by metamorphic recrystallization, in which case grain boundary diffusion most likely overrode volume diffusion. Similarly, the bulbous replacement or recrystallization texture displayed by the zircon crystal in Figure 6.6 has been shown to have occurred during a metamorphic event (Schaltegger et al. 2002). Connelly (2001) has documented very subtle metamorphic recrystallization, which has led to a gradual but homogeneous fading of original growth zoning and is correlated with extensive amounts of Pb loss.

Zircon in high-grade metamorphic rocks display a wide diversity and complexity of textures that reflect variations in the physico-chemical conditions and the duration of each metamorphic event, and are caused by modifications of pre-existing structures and/or by growth of new zircon (Fig. 7). The least severely affected zircon grains can partially preserve vestiges of an original growth zoning, only locally modified by metamorphism, thus displaying textures closely resembling those for late-magmatic recrystallization as discussed above (Figs. 7.1–7.5; cf. Fig. 6) (Hoskin and Black 2000). Igneous protolith zircon from the Proterozoic Georgetown Region, Australia, experienced variable recrystallization during an upper-amphibolite-grade event. The zircon largely preserves igneous oscillatory zoning, although this becomes progressively convoluted, blurred and thickened in response to metamorphism. The dominant texture, however, is transgressive (across all pre-existing textures) zircon patches and lobes. Areas of recrystallization occur dominantly at crystal terminations, but also anywhere else within the interior of a crystal and sometimes apparently not connected to the crystal surface. Of significance is the preservation of relics of primary textures (growth zoning) within areas of recrystallisation. These relics are termed the "ghost texture" and are responsible for "mixed" isotopic ages and trace-element abundances between growth-zoned and fully recrystallized areas. Hoskin and Black (2000) interpreted these textures to represent recrystallization in the solid-state because ghost textures and the isolation of some recrystallized areas from the crystal surface are inconsistent with a local dissolution/reprecipitation (fluid) process.

In general, zircon in granulite facies rocks tends to be characterized by very chaotic textures. Concentric zoning, when present (Figs. 7.6–7.12), is rather irregular and resembles only weakly the parallel or regular geometry of zoned magmatic zircon (cf. Fig. 4). Some variants of sector and fir-tree zoning are very common (Figs. 7.13–7.19), the latter reflecting strong fluctuations of growth rates (Vavra et al. 1996). The most extreme textural types have abstract and chaotic designs that

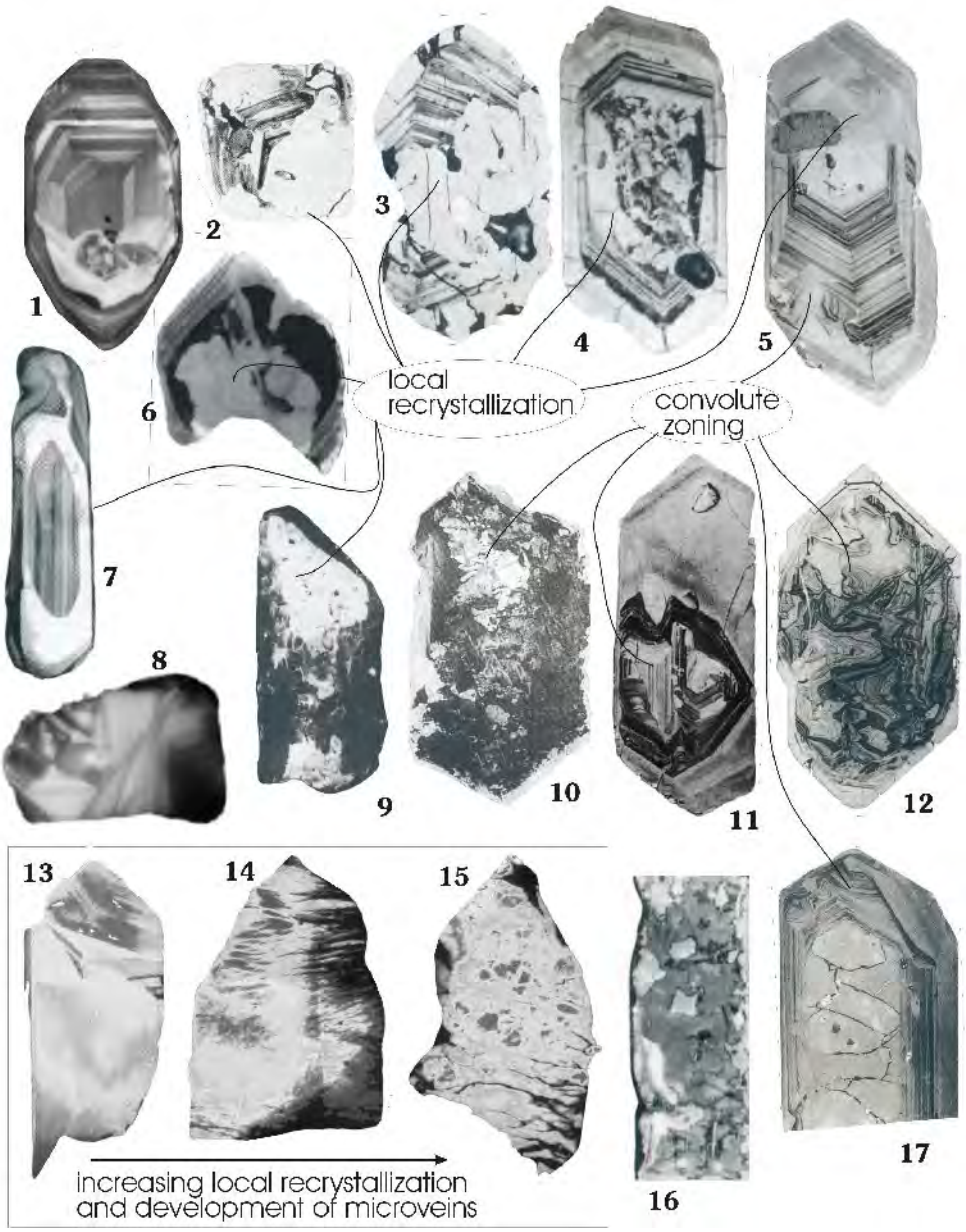


**Figure 6.** Late to post-magmatic recrystallization of zircon. The grains shown are between 70 and 250 μm in size. **(1)** Oscillatory zoning cut off by area of re-homogenized zircon, modified from Poller (1997), CL. **(2-7)** Partially preserved growth zoned zircon penetrated by trangressive zones of recrystallization and with local development of convolute zoning; 2,3 – modified from Pidgeon (1992); RL; 4, 5 - modified from Nemchin and Pidgeon (1997), RL; 6 – modified from Schaltegger et al. (2002), CL; 7 - modified from Andersson and Williams (2001), CL. **(8)** "cross-bedding type" texture (from J. Hanchar, unpublished data) **(9-12, 17)** Heterogeneous patchy pattern and convolute zoning attributed to post-crystallization purification of crystal structure with progressive migration of trace element rich bands; 9 - modified from Vavra and Hansen (1991), CL; 10 – modified from Mulch et al. (2002), CL; 11, 12, 17 – modified from Pidgeon et al. (1998), RL. **(13-15)** Zircon in leuconorite exhibiting increasing amount of local recrystallization and microveining (with addition of U), which correlates with resetting of U-Pb age, modified from Ashwal et al. (1999), CL. **(16)** Patchy, mosaic texture, indicating metasomatic replacement of low-U domain by zircon richer in U (and presumably other trace elements), modified from Corfu and Ayres (1984), RL.

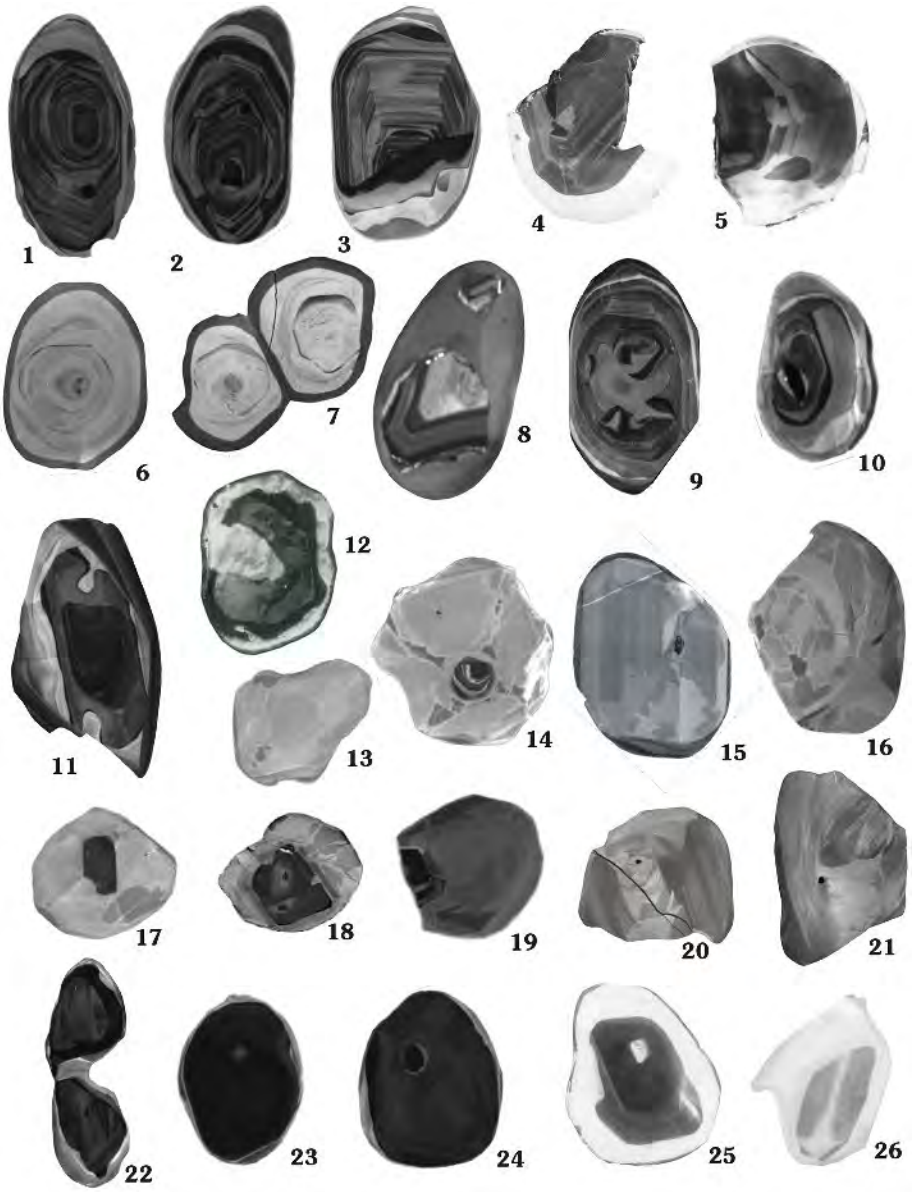


**Figure 7.** Recrystallization and new growth of zircon in high-grade metamorphic rocks. All grains between 70 and 350 μm in size. **(1-5)** Original euhedral zircon is cut by recrystallized or newly grown domains of more homogeneous composition; 1, 2 – Akilia gneisses, from P. Kinny (unpublished data), CL; 3– Akilia gneisses, modified from Nutman et al. (2002); 4, 5 – lower crustal xenoliths, modified from Moser and Heaman (1997), CL. **(6-12)** Zircon displaying very irregular concentric zoning locally overprinted by zones of recrystallization or new growth; 6, 7, 8 – lower crustal xenolith, from M. Schmitz (unpublished data), CL; 9, 10, 11 – in various metamorphic rocks, from P. Kinny (unpublished data), CL; 12 – in mafic granulite, modified from Peucat et al. (1990), CL. **(13-19)** Sector and fir-tree zoning, locally surrounding older zircon components; 14,16 – in lower crustal xenolith, modified from Schmitz and Bowring (2002b), CL; 15 – in granulite facies rock, modified from Pidgeon et al. (2000), CL; 13,17,18 – in high-grade gneisses, from P. Kinny (unpublished data), CL. **(20-22)** Chaotic textures with local appearance of 'flow' domains; 20,21 – lower crustal xenoliths, modified from Schmitz and Bowring (2001), CL; 22 – in migmatitic gneiss, from P. Kinny (unpublished data), CL. **(23-25)** Bands or other large segment of homogeneously textured zircon; 23, 24 – Akilia gneiss, from P. Kinny (unpublished data), CL; 25 – lower crustal xenolith, modified from Moser and Heaman (1997), CL, 26 – in granulite, modified from Bingen et al. (2001a), CL.

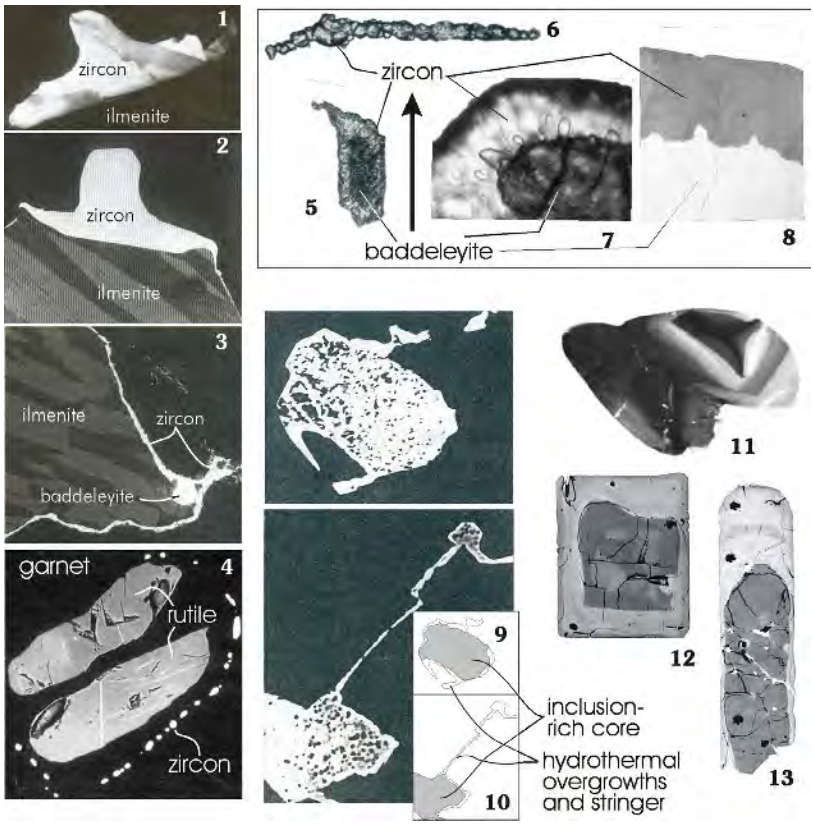


**Figure 8.** Modes of metamorphic-hydrothermal zircon growth. **(1-3)** Development of zircon in granulites; 1,2 – hat-shaped zircon wrapping around ilmenite, 3 – Thin layer of zircon coating ilmenite, in contact with a baddeleyite grain; modified from Bingen et al. (2001a), 1 = CL, 300µm wide; 2, 3 = BSE, 100 µm wide. **(4)** Zircon forms string of beads around rutile, both surrounded by garnet, modified from Bingen et al. (2001a), BSE, 100 µm wide. **(5-8)** Formation of zircon from baddeleyite; 5 – zircon corona around baddeleyite, TL (thin section), 100 µm long; 6 – chain of zircon crystals in plagioclase (complete reaction from baddeleyite); TL (thin section), 250 µm long; 7, 8 – detail of zircon-baddeleyite relationship, TL (7) and BSE (8), image ca. 80 µm wide; all modified from Davidson and van Breemen (1988). **(9-10)** Late-magmatic zircon, inclusion (thorite) – rich, overgrowth by hydrothermal, inclusion-free zircon, modified from Rubin et al. (1989), BSE, grains are 5 to 10 µm wide. **(11)** Metasomatic zircon in ultramafic rock, modified from Grieco et al. (2001), CL. **(12-13)** U-rich hydrothermal replacement rims around low-U zircon, from J. Hanchar (unpublished data) BSE, both crystals are ca. 100 µm wide.

combine stepwise growth patterns with flow structures (Figs. 7.20–7.22). Besides these geometrically complex patterns, it is not uncommon to find zircons, or at least large domains of zircons, that are completely homogeneous (or nearly so) when examined by common imaging techniques (Figs. 7.23–7.26; also parts of other grains in Fig. 7). In the case of domains that are homogeneously dark in CL (or light in BSE), they can be suspected to be free of zoning because the luminescence may be poisoned by high trace-element contents or by metamictization. However, the domains that provide very bright CL images are likely to be genuinely homogeneous as they have very low trace-element contents. Figures 7.8, 7.11 and 7.12, in particular, indicate how such domains evolve as marginal bands and as lobes that locally penetrate the interior of grains, but locally they also form amoebic zones entirely enclosed in the centre of the grains (Fig. 7.9).

Bingen et al. (2001a) describe how metamorphic zircon in a granulite developed hat-shaped overgrowths on older zircon and ilmenite (Fig. 7.26), or very long, thin coatings following the

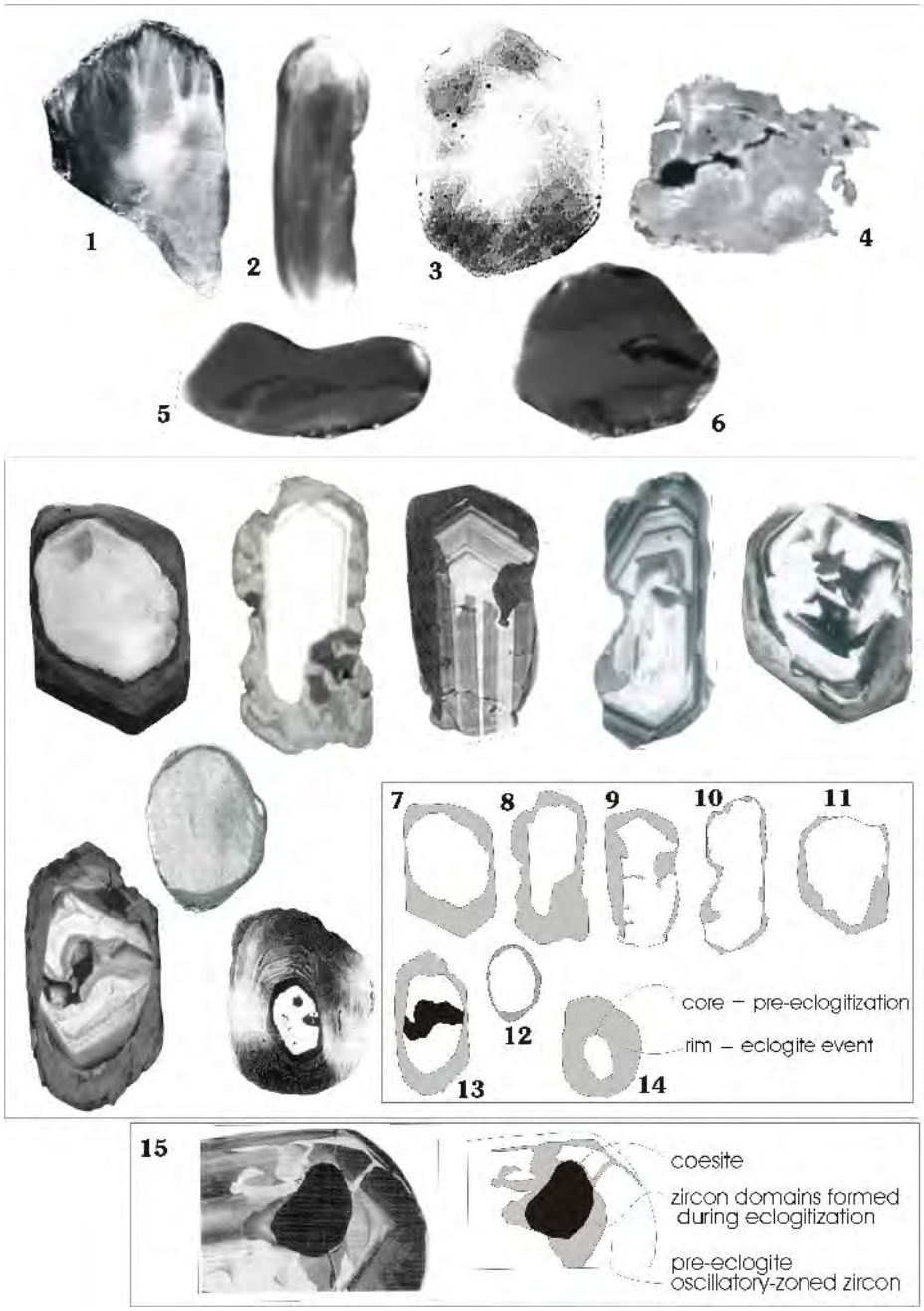


**Figure 9.** Zircon in high-pressure rocks. The grains shown are all between 70 and 300 μm in size. **(1-3)** Irregular, diffuse (auroral-light) zoning; 1 – Corfu et al. (2002), CL; 2 – modified from Schmitz and Bowring (2002a), CL; 3 – modified from Rowley et al. (1997), CL. **(4-6)** Largely homogeneous texture; 4 – modified from Lopez Sanchez-Vizcaino et al. (2001), CL; 5,6 – modified from Schmitz and Bowring (2002a), CL. **(7-14)** Eclogitic zircon replacing and rimming pre-metamorphic phase; 7- modified from Rubatto et al. (1998), CL; 8 – modified from Hacker et al. (1998), CL; 9 – modified from Gebauer et al. (1997), CL; 10,11 – modified from Rubatto and Gebauer (1999), CL; 12 - modified from Oberli et al. (1994), CL; 13 – modified from Liermann et al. (2002), CL; 14 - modified from Rowley et al. (1997), CL. **(15)** Relationship between old-zoned zircon and zircon domains formed metamorphically together with the coesite pseudo-inclusion, modified from Gebauer et al. (1997), CL.

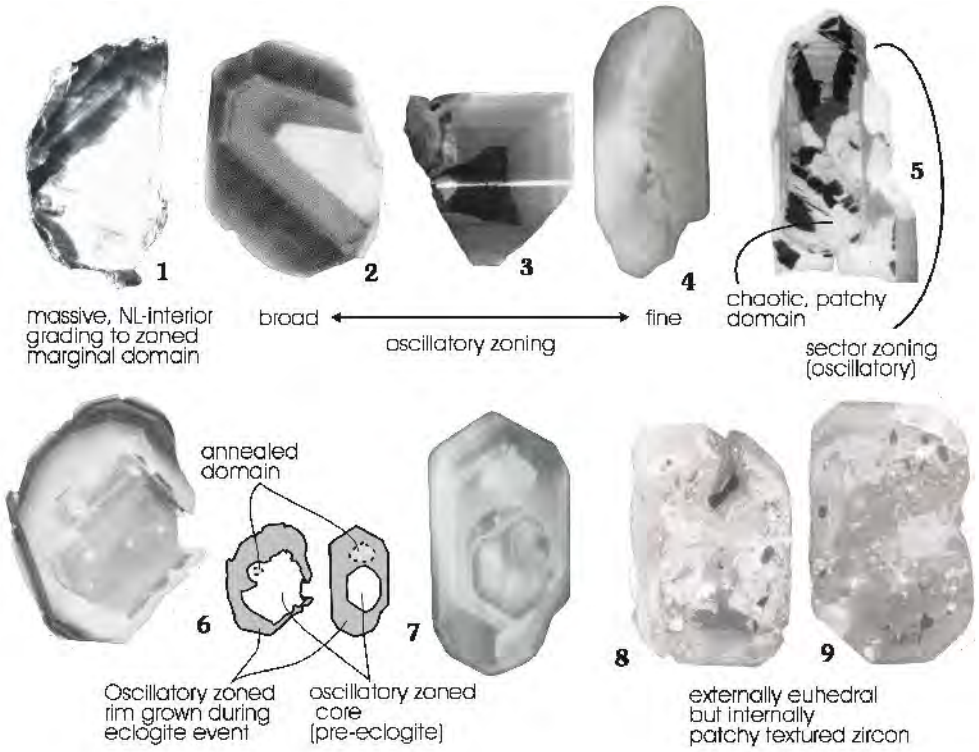


**Figure 10.** Zoning of zircon in high-pressure rocks. The grains shown are all between 70 and 300 μm in size. **(1)** Internal diffuse zoning rimmed by growth zoned marginal domain; Corfu et al. (2002), CL. **(2-4)** Variation in growth zoning, 2 – modified from Gebauer et al. (1997), CL; 3 – modified from Rubatto et al.(1998), CL; 4 – modified from Bingen et al. (2001b), CL. **(5)** complex zoning, modified from Rubatto et al. (1998), CL. **(6-7)** cored eclogitic zircon with zoned texture; 6 – modified from Gebauer et al. (1997), CL; 7 - modified from Bingen et al. (2001b), CL. **(8-9)** Patchy textured zircon in eclogite, modified from Bröcker and Enders (1999), CL.

grain-boundary of or fractures in ilmenite (Figs. 8.1–8.3), and deduce that the required Zr was provided by the breakdown of ilmenite and baddeleyite.

**High-pressure metamorphism**

Understanding the nature of zircon in eclogites is an intriguing and difficult task, especially given that the dating of high-pressure events is significant for the reconstruction of the history of ancient collisional belts. In the simplest cases, eclogite zircons are subrounded and somewhat irregular, but display relatively homogeneous internal textures. The example in Figure 9.1 exhibits a wavy “auroral light” texture. This texture is typical for a zircon population yielding an isotopic age that dates a high-pressure event (Corfu et al. 2002). A similar texture is also shown by the grains in Figures 9.2 and 9.3, whereas those in Figures 9.4–9.6 are more uniform but locally contain darker zones.

In general, eclogites contain complex zircon types. One common type contains two distinct phases, older relicts pre-dating eclogitization of the rock surrounded and/or penetrated by new metamorphic zircon (Figs. 9.7–9.15). Cores can be homogeneous or growth zoned, locally with traces of earlier resorption and recrystallization (Figs. 9.9 and 9.13). Metamorphic rims are generally homogeneous to somewhat heterogeneous, and are separated from cores by irregular interfaces indicative of corrosion. The latter feature is especially evident in Figure 9.15, which shows new metamorphic

zircon developed, together with coesite, in a cavern in the interior of the original crystal. The new material likely penetrated from outside the crystal along a network of thin fractures.

The homogeneity of metamorphic zircon and intra-crystalline domains discussed above contrasts with the oscillatory zoning shown by zircon in Figure 10. The metamorphic nature of the latter is supported, in each case, by the consistency of their U-Pb ages within geological context. In general, the zoning is regular, defining either very fine or very coarse bands, and is quite similar to that of magmatic zircon (Figs. 10.1–10.4; 10.6 and 10.7). A complex pattern more typical of granulite facies zircon crystals is shown by the grain in Figure 10.5. The grain shown in Figure 10.1 is the only grain within a zircon population (examined by CL; see also Fig. 9.1) that shows such marginal fine-scale zoning. More prominent development at the margin of the grain is also evident in Figure 10.6. The presence of such zoning in metamorphic zircon runs against "common wisdom" and has caused some consternation in the literature. Gebauer et al. (1997) suggest that the zoning seen in such grains (Figs. 10.2 and 10.6) probably reflects crystallization in local melt or supercritical fluids that may have developed at peak metamorphic conditions. They also draw attention to the occurrence within these grains of homogeneous domains around small inclusions, suggesting that they represent zones of annealing that caused exchange of chemical elements with the inclusion (Figs. 10.6 and 10.7).

A more unusual texture is the highly irregular patchy pattern (Figs. 10.8 and 10.9) observed in euhedral zircon from a low-temperature eclogite from Greece (Bröcker and Enders 1999). The authors interpret the zircons as having formed by metasomatic processes during a high-pressure event, although it could be argued that the eclogite event may only have caused textural disruption rather than new zircon formation. Some clues concerning the mechanisms that form zircon in eclogite have been provided by Bingen et al. (2001b) who suggest that zircon coronas around ilmenite are cannibalized during breakdown of ilmenite (to rutile and garnet; Fig. 8.4) to form larger zircon grains.

## HYDROTHERMAL ZIRCON

This is a somewhat artificial subdivision since it could be that all metamorphic zircon growth (and resorption) occurs only in the presence of a fluid phase (silicate melt or aqueous fluid). The reaction producing zircon during baddeleyite breakdown (Figs. 8.5–8.8; Davidson and van Breemen 1988) involves the addition of silica and probably also other cations, since such zircons have, for example, quite different Th/U ratios than the parent baddeleyite. The transport of silica and other cations is probably via aqueous fluid. Other examples of zircon growth that may have been assisted by fluid are the growth of zircon on ilmenite (Figs. 8.1–8.3) in granulites and the coronas of microzircons observed around rutile in eclogites (Fig. 8.4).

Hydrothermal zircon growth has been described in a peralkaline environment (Figs. 8.9 and 8.10; Rubin et al. 1989), where metasomatism appears to have occurred during late-stage magmatic crystallization. The metasomatic zircon shown in Figure 8.11 developed during metasomatism of ultramafic rocks in the mantle (Grieco et al. 2001). In a similar setting, zircon has been observed in association with baddeleyite/zirconolite rims in metasomatic veins cutting mantle peridotite (Kinny and Dawson 1992). The examples in Figures 8.12 and 8.13 indicate the formation of high-U zircon margins, which in some cases are simple overgrowths, but more commonly are embayments into low-U regions in the zircon crystals. These high U regions may have formed by metasomatism, or by recrystallization, or dissolution and reprecipitation during an event, which probably was accompanied by regional hydrothermal activity (McLelland et al. 2001, Hanchar et al. in preparation). The well preserved outer boundary of the crystal would tend to support some simple replacement mechanism although the nature of this process remains elusive. The pattern observed for the grains in Figures 3.6 and 6.13–6.15 may well fit a similar process. Most likely, these high-U regions in the zircon crystals are not the result of simple volume diffusion of U diffusing in and Zr diffusing out based on the sluggish kinetics of U-diffusion in zircon under crustal conditions (Cherniak et al. 1997b).

Although on occasions workers suggest that their zircons are of hydrothermal origin, ambiguity still exists. Unequivocal occurrences of aqueous-fluid precipitated zircon reveal it to have a

"spongy" texture (Wayne and Sinha 1992, Hacker et al. 1998—Fig. 3 therein; Hoskin et al. 1998) and to be extremely enriched in high-field strength elements, the REE (Hoskin et al. 1998), non-radiogenic lead (Watson et al. 1997) and F (Hoskin 1999). We consider these characteristics to be useful criteria for identifying zircon crystallization from aqueous fluids at low pressure (<2 kbar), low temperature (<500°C) and high water/rock ratios.

## KIMBERLITIC AND MANTLE-RELATED ZIRCON

The term "kimberlitic zircon" is used here to refer to megacrystic zircons commonly found in kimberlite, carbonatite, alkali basalt and other magmas of deep-seated origin, and more rarely found as a component of syenitic xenoliths carried by such magmas. The dominant characteristic of kimberlitic zircon is their common large size (up to cm size) and anhedral morphology (Kresten et al. 1975; Belousova et al. 1998). The internal textures display a broad range of variation. The megacrysts shown in Figures 11.1–11.4 are largely homogeneous, except for some faint outlines of large angular domains, possibly related to fracturing. The grain in Figure 11.5 preserves a very faint

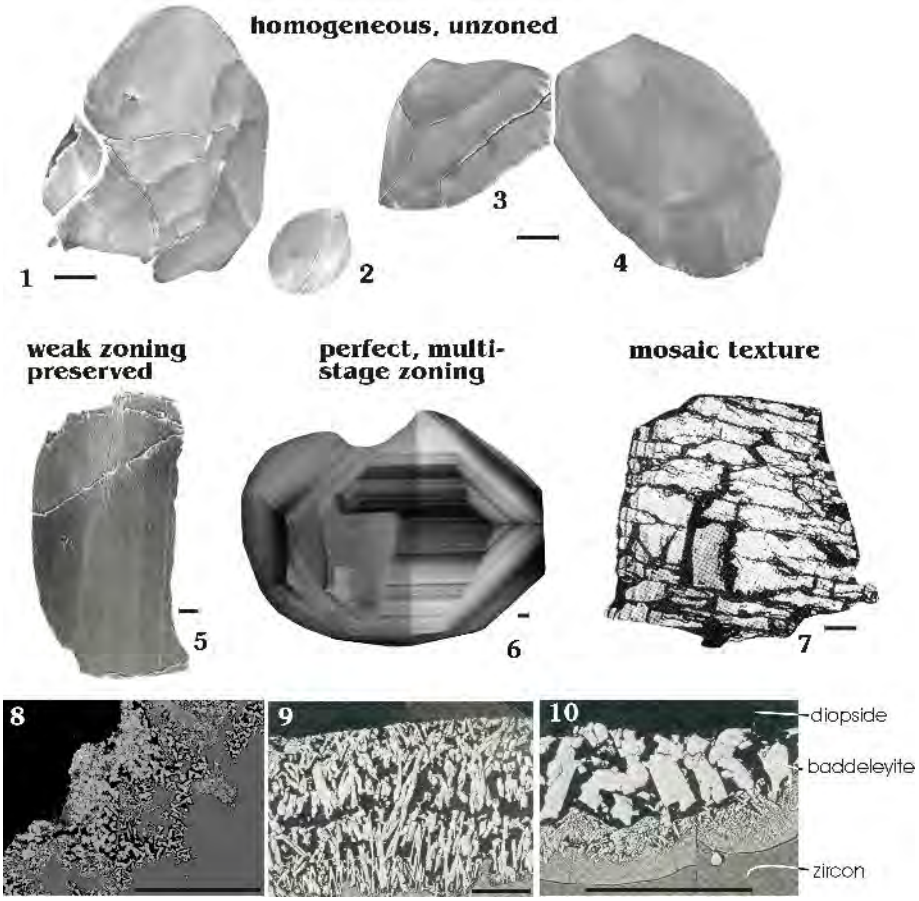


**Figure 11.** Kimberlitic zircon. Scale bar is ca. 100 μm. **(1-4)** Homogeneously textured zircon in metasomatized mantle xenolith in kimberlite, from P. Kinny (unpublished data), CL. **(5)** Faintly zone kimberlitic zircon, modified from Schärer et al. (1997), CL. **(6)** Well zoned kimberlitic zircon, from P. Kinny (unpublished data), CL. **(7)** Mosaic texture under polarized light, modified from Schärer et al. (1997), TL. **(8-10)** Breakdown of kimberlitic zircon to baddeleyite, 8 – from P. Kinny (unpublished data), BSE; 9,10 – modified from Heaman and LeCheminant (1993); BSE.

and broad zoning texture. By contrast, the grain shown in Figure 11.6 reveals a splendid, though complex, growth zoning. Two similar grains are shown in Figures 4.4 and 4.5. The reason for these variations is not clear. Perhaps the poor development of zoning in some grains may be related to prolonged residence of the megacrysts at very high temperatures in the mantle, which may have led to partial or complete homogenization of any original zoning, in which case those megacrysts with well preserved zoning would not have remained in the source region for a long time. Certainly, the commonly observed age relation of megacrysts to the erupting magma is one of short pre-eruptive residence time for the megacrysts, but there are exceptions. Another common observation is that, where present, the oscillatory zonation in kimberlitic zircons is often truncated by the anhedral grain margin (e.g., Figs. 4.4 and 4.5) indicating that despite their large size they have been substantially resorbed from originally larger grain-sizes.

Figure 11.7 illustrates a polarized light view of the same grain seen in Figure 11.5. The distinct mosaic structure has been interpreted as a possible brittle stress-related feature affecting the zircon at great depths (Schärer et al. 1997) although this is more likely due to rapid pressure reduction prior to eruption.

Figures 11.8–11.10 show a commonly observed reaction rim between zircon and other silicates leading to the formation of intervening baddeleyite and occasionally also zirconolite (Heaman and LeCheminant 1993). These desilification reactions have been linked to episodes of metasomatism in the mantle, but may also develop during late-stage contact of zircon megacrysts with a silica-undersaturated, ascending magma.

## IMPACT-RELATED TEXTURES

A rare class of zircon comprises those grains related to large meteorite impacts. Their most diagnostic characteristic is the presence of multiple sets of planar deformation features (Figs. 12.1–12.6 and Fig. 2.35), which are revealed particularly well by scanning electron microscopy (SEM) on etched surfaces (Bohor et al. 1993). These features, however, can often also be seen with normal transmitted or reflected light microscopy (Figs. 12.2 and 12.4) in grain-mounts, or in thin section. Under a binocular microscope, shocked grains appear whitish and highly turbid to completely opaque, but occasionally it is possible to detect the characteristic planar features (Krogh et al. 1984, 1993).

At increasing degrees of shock the zircons develop granular textures and turn into polycrystalline grains (Figs. 12.7 and 2.36). Under the most extreme conditions they start to melt, a process that results in textures such as those shown in Figures 12.8 and 12.9. Shocked zircon grains that get trapped in an impact melt layer may grow new rims, which are distinguished mainly by their lack of impact-related deformation, indicating that they formed after the immediate impact event (Figs. 12.5, 12.6 and 2.16). Such zircons are invaluable for dating the time of the impact (Kamo et al. 1996, Moser 1997, Gibson et al. 1997).

## FRACTURING

Differential metamictization of zircon causes volume expansion of the U-rich domains (Holland and Gottfried 1955) with consequent fracturing of the more resistant and brittle low-U domains (e.g., Chakoumakos et al. 1987; Figs. 13.1–13.4). Typically the fractures start at the interface with the more metamict domains or with high-U inclusions and develop radially outward across the low-U bands (Figs. 2-19–2.21; 5.1–5.4; 13.1 and 13.2). There is also a second type of fracture which develops concentrically along the boundary between high and low U domains (Figs. 13.2 and 13.3). Lee and Tromp (1995) discuss the parameters involved in the development of such fracture systems concluding that they are controlled principally by the degree of metamictization, the relative "shell" thickness and the confining (external) pressure. They also suggest that the latter factor may provide a tool to estimate the depth of residence of a rock. This may not be achievable, however, because the elevated temperatures of the lower crust increase the rates of self annealing to the point where zircon fractures are rarely developed. This is demonstrated by the generally very

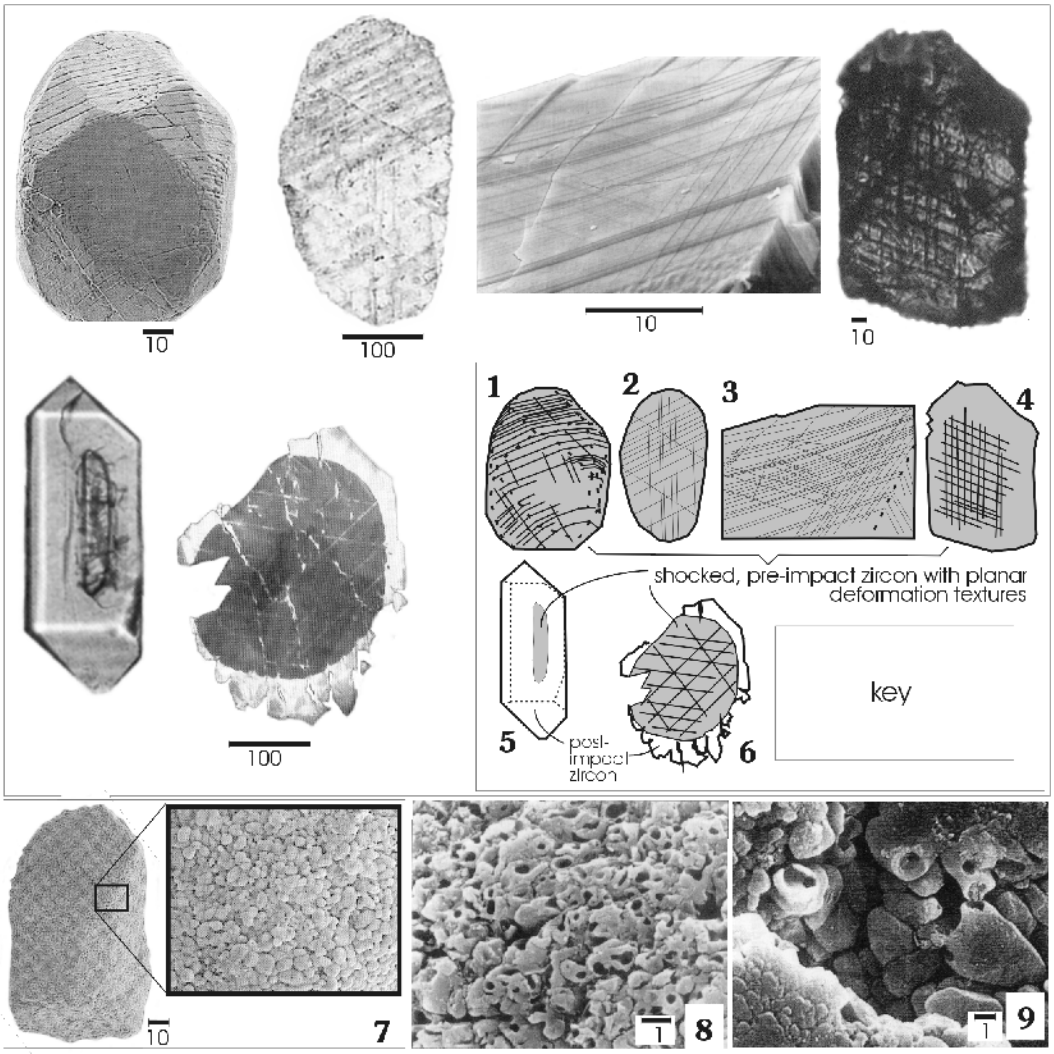


**Figure 12.** Appearance and texture of zircon in meteorite impact structures. **(1, 2)** Shocked zircon crystals from charnockite in Vredefort structure, modified from Kamo et al. (1996), 1 = SEM, 2 = TL, crossed nicols. **(3**) Euhedral zircon with three sets of planar deformation features; Manicouagan impact crater, modified from Bohor et al. (1993); SEM. **(4)** Multiple sets of planar deformation features in shocked zircon in Copper Cliff rhyolite, Sudbury structure, from F. Corfu (unpublished data), TL. **(5, 6)** Zircons from post-impact granite from Vredefort structure, modified from Gibson et al. (1997); 5 – euhedral crystal without shock-related features enclosing a fractured core (RL); 6 – zircon core with three sets of planar deformation features surrounded by post-impact unfractured zircon rim (CL). **(7)** granular zircon grain from granophyric part of melt-breccia dyke, Vredefort structure, modified from Kamo et al. (1996), SEM. **(8, 9)** polycrystalline grains with degassing and melting textures; 8 – K/T distal impact ejecta, Berwind Canyon, Colorado, modified from Bohor et al. (1993); SEM; 9 – Onaping Formation (impact melt), Sudbury structure, modified from Krogh et al. (1996), SEM.

good preservation of zircon in exhumed lower crustal rocks (e.g., Rudnick and Williams 1987, Hanchar and Rudnick 1995).

The parallel breaking shown by the zircon from a lower crustal xenolith in Figure 13.5 is a more rare occurrence. It has been interpreted to represent rapid decompression during eruption of the carrier volcanic rock (Rudnick and Williams 1987). It might be analogous to the deformation

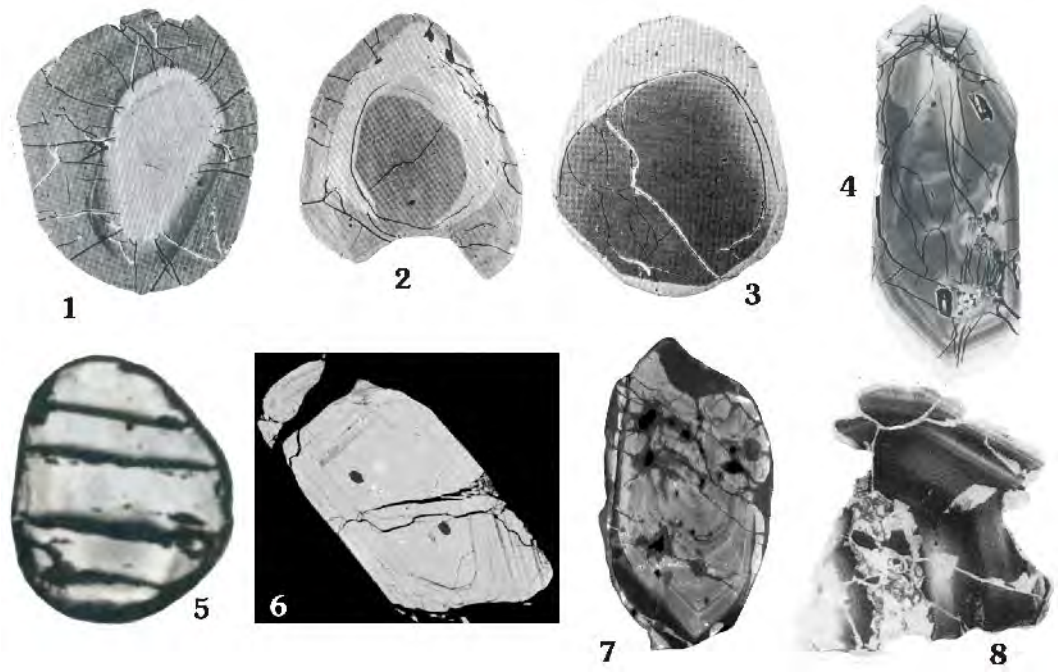


**Figure 13.** Fracture patterns in zircon. **(1-3)** Radial and concentric fractures in zircon from the Musgrave Ranges (modified from Lee and Tromp 1995; BSE); 1- radial fractures starting at the margin of the high-U+Th central part and propagating into the external, low-U+Th shell; 2 – expansion of the middle, U-Th-rich shell causes concentric fractures along the central part and radial fractures in the rim; 3 – metamictization of the high-Th+U rim causes concentric fracturing of the interface to the less metamict inner part. **(4)** Fractured zircon from Strontian pluton (modified from Paterson et al. 1992b, BSE); most of the cracks propagate from two spots that contain U+Th-rich inclusions but the fractures become concentric along the margin to the outermost high-U+Th rim. **(5)** Zircon from lower crustal xenolith (eastern Australia) showing pronounced parallel parting, apparently reflecting deformation during rapid decompression (modified from Rudnick and Williams 1987, TL). **(6)** Zoned zircon from a Witwatersrand conglomerate fractured during compaction between quartz and pyrite pebbles; the fractures are now healed with quartz; modified from Medenbach (1976), RL on polished section. **(7)** Ancient fractures, propagating from inclusions, were healed by the low-luminescence material grown metamorphically in external domains of zircon from upper crustal xenolith; modified from Schmitz and Bowring (2001), CL. **(8)** Fractures healed by luminescent material; modified from Rubatto et al. (1998), CL.

mechanism producing mosaic textures observed in some kimberlitic zircons (Fig. 11.7). Other factors that cause zircon fracturing are external stresses during mylonitization (Wayne and Sinha 1988) or diagenesis (Fig. 13.6; Medenbach 1976). When subjected to progressive diagenesis, or other metamorphic overprints, such fracture systems may heal and only be visible in specific circumstances (Fig. 13.7–13.8; also Figs. 3.5, 3.6 and 9.15).

## ALTERATION

Chemical alteration is generally seen in zircon grains that are extensively metamictized and where pathways are available (e.g., grain boundary diffusion) for fluids to penetrate the structure. These pathways are most commonly the fracture systems discussed above, but occasionally also textural discontinuities (e.g., zoning, Fig. 14.5) and interfaces between zircon and inclusions of other minerals (Fig. 14.7). Alteration typically forms bulbous, botryoidal fronts, but locally also feathery textures (Fig. 14.2), that propagate along the cracks and within the crystal. The grain shown in Figure 14.1 consists of a low-U central part, surrounded by a high-U mantle, itself locally rimmed

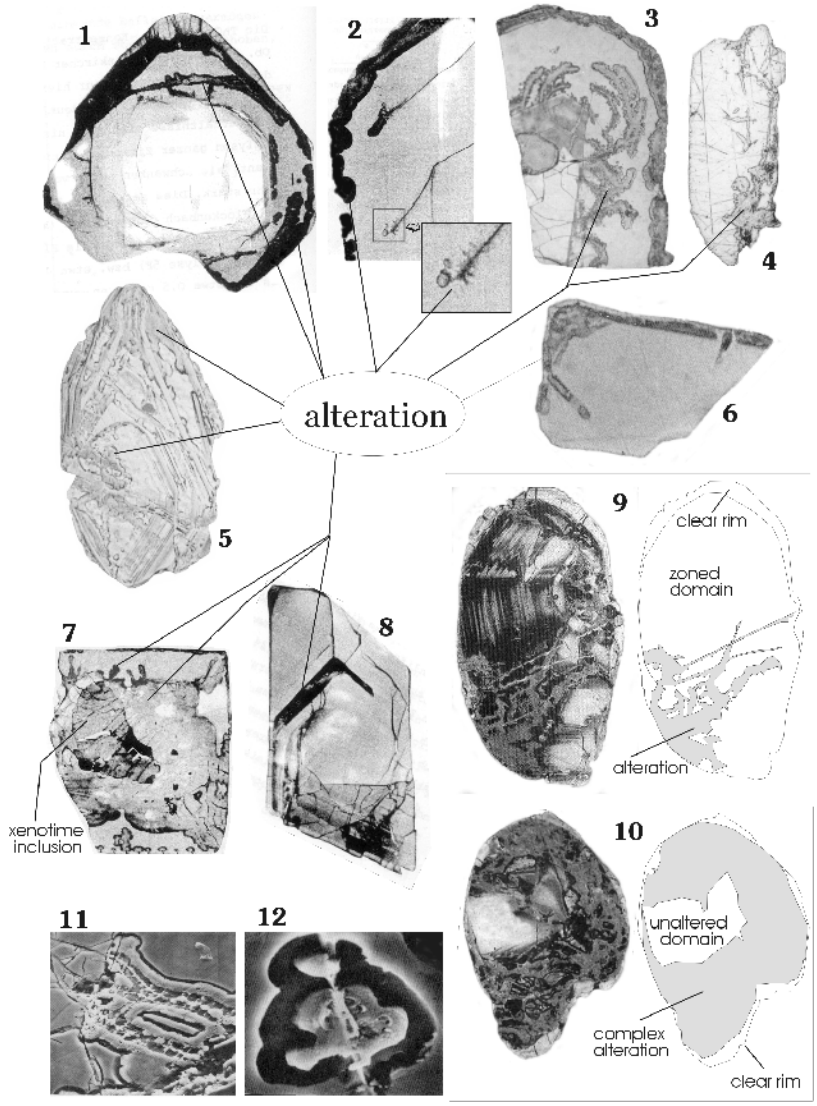


**Figure 14.** Patterns of alteration in zircon. **(1)** Alteration developed along concentric fractures parallel to the boundary between the low-U interior part of the zircon and the high-U outer shell; an outermost low-U rim has radial cracks, which have allowed the access of the fluids; modified from Medenbach (1976), RL. **(2)** Detail of a high-U zircon showing an outermost alteration ring and two internal alteration fronts with botryoidal and feathery propagation patterns; modified from Medenbach 1976), RL. **(3)** Zircon grain with low-U, fractured interior part surrounded by a high-U external band; alteration has developed both along an external rim and along curvilinear paths originating at the fractures in the euhedral, low-U inner zone; modified from Krogh and Davis (1974), RL. **(4)** Local alteration around fractures parallel and orthogonal to the c-axis; from F. Corfu (unpublished data), RL. **(5)** Zoned zircon with alteration controlled mainly by crystallographic discontinuities; modified from van Breemen et al. (1987), BSE. **(6)** High-U, homogeneous zircon with alteration restricted to its margin; modified from Krogh (1982), RL.**(7)** Zircon grain with a large inclusion of xenotime surrounded by an extensive zone of hydration propagating outwards, and with minor appendices moving inwards from the margin; modified from Medenbach (1976), RL. **(8)** Extensively altered, narrow high-U zones inside largely low-U zircon; modified from Medenbach (1976), RL. **(9,10)** Complexly zoned and altered zircon from the 4.0 Ga Acasta gneiss; modified from Bowring and Williams (1999), RL. **(11,12)** Brief exposure to HF vapor has dissolved the altered and hydrated part leaving behind ridges and plateaus of unaltered zircon; modified from Krogh and Davis (1975), SEM.

by a thin low-U zone. The latter is radially cracked allowing fluids to penetrate into the high-U material, which became altered—the alteration front propagating along concentric fractures. In Figure 14.3, a low-U central zone has become fractured allowing access (presumably from areas along the c-axis) to fluids, which then attack the surrounding metamict zone. The latter is also affected by alteration along an outer ring, the two alteration zones gradually approaching each other. Figures 14.4–14.6 and 14.7 illustrate other combinations of the same phenomenon, whereas Figure 14.8 displays the case of a predominantly low-U zircon with just a few high-U zones that have been reached by fluids along cracks in the low-U material and have become almost totally altered. The two grains in Figures 14.9 and 14.10 are ancient zircon crystals from the Acasta gneiss (Bowring and Williams 1999) that exhibit extremely complex alteration patterns penetrating zoned zircon domains and totally enclosing local islands of homogeneous unaltered zircon.

The alteration process has been shown to hydrate zircon, leaching some elements such as Pb and depositing others such as Fe and Ca (and possibly common Pb), hence making the mineral unsuitable for isotopic analysis (Krogh and Davis 1974, 1975; Medenbach 1976, Krogh 1982). The altered zones are much more soluble than crystalline zircon, and can be easily dissolved by brief exposures to dilute Hf vapor, providing a 3-dimensional image of the alteration process (Figs. 14.11 and 14.12).

## INCLUSIONS, INTERGROWTHS AND OVERGROWTHS OF ZIRCON AND OTHER MINERALS

The relations between zircon and the minerals it includes, or which it is included in or overgrown, can provide important clues concerning crystallization conditions and paragenetic associations. This information can be critical when it comes to the interpretation of U-Pb zircon ages. Zircon crystals commonly carry inclusions of other minerals (Figs. 2.4, 2.7, 2.11, 13.4; 15.1–15.12; 15.18–5.19), especially of the main rock-forming minerals such as biotite, quartz and feldspar, but their relative abundance varies significantly between different populations. The study of mineral inclusions in metamorphic zircon helps to constrain the relative paragenesis of zircon with respect to the main rock-forming minerals. Zircons also often contain inclusions of melt that was present when the zircon crystallized (see Thomas et al., this volume, for a discussion of melt inclusions in zircon crystals). As an example, the zircon grains shown in Figures 15.1–15.3 include, or are included in, high pressure minerals such as diamond, garnet and coesite. Inclusions of melt and fluids (Figs. 15.5–15.9) can provide information on the composition of magma and gases at particular stages in the evolution of a magmatic or metamorphic system. Figure 15.9 illustrates the particular example of a kimberlitic zircon including both solid mineral inclusions as well as numerous fluid inclusions, which display very distinct crystallographically controlled arrangements.

Figures 15.10 and 15.11 show examples of zircon containing numerous inclusions of common minerals such as quartz and apatite, together with U and Th-rich components and many cavities. In general, the interpretation of such inclusions in highly metamict and altered grains is difficult because the inclusions could be either real xenocrysts or exsolved phases, or phases introduced after the formation of zircon. This is the case with the zircon grain shown in Figure 15.13 that contains secondary monazite crystallized along a crack in the crystal, or the zircon in Figure 15.12 that contains abundant galena introduced into the zircon long after its original crystallization. Figure 9.15 is an example of where omphacite was included in the zircon grain but it is surrounded by healed cracks, hence it was formed during the secondary eclogite event that affected the zircon (Gebauer et al. 1997). The crystallographically controlled baddeleyite inclusions in zircon (Fig. 15.14) presumably reflect the breakdown of zircon to baddeleyite and silica (cf. also McLaren et al. 1994).

The structural affinity (i.e., isostructural) of zircon and xenotime means that the two minerals are locally found in association with each other in the form of xenotime overgrown by zircon (Figs. 14.7; 15.17), or the other way around (Figs. 15.16 and 15.17), or as complex intergrowths (Figs. 15.18 and 15.19). The two xenotime crystals attached to zircon in Figure 15.15 were formed during diagenesis and can thus be used to constrain the age of sedimentation (e.g., Fletcher et al. 2000).

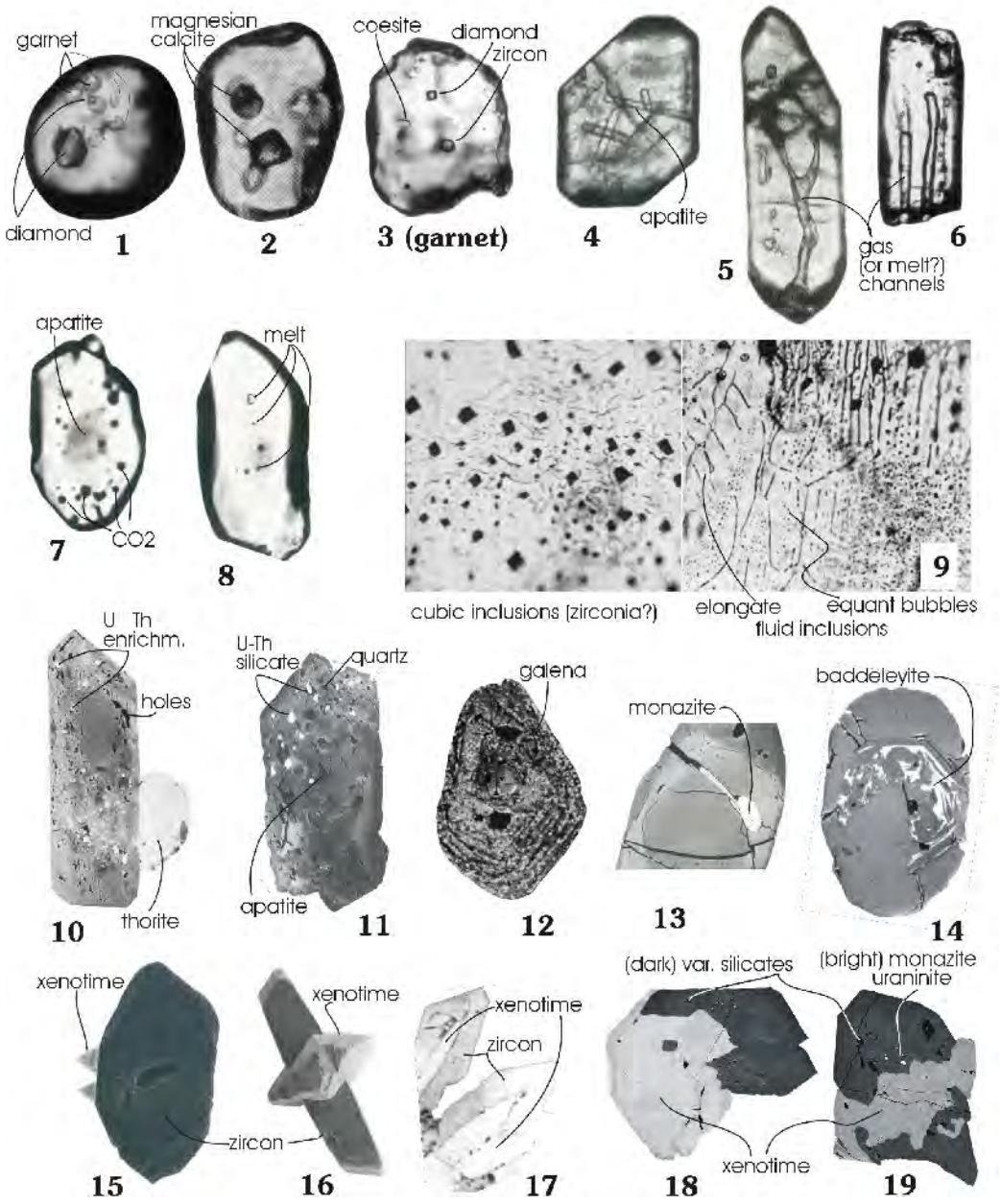


## CONCLUDING REMARKS

The above presentation emphasizes the variety of internal and external features that characterise zircon, and shows how such features can be used to extract valuable information concerning the geological history and petrogenetic context of zircon. The diagnostic value of such studies is naturally much increased once the zircon features are considered in conjunction with elemental or isotopic constraints from the same mineral and in the context of well characterised rock units. It is also important to keep in mind that the interpretation of some features such as growth zoning or resorption phenomena can be somewhat ambiguous and controversial. Thus some caution is required when textural interpretations are carried out.

**Figure 15.** Inclusions, intergrowths, and overgrowths in zircon. All grains shown here are about 100 to 200 μm in size. **(1-3)** Zircon from an ultra-high pressure gneiss contains inclusions of garnet and diamond (1), and magnesian calcite (2) but is itself included in garnet together with diamonds and coesite (3); (modified from Korsakov et al. 2002, TL). **(4-5)** Zircon in granitic rock with needle like apatite inclusions (4) and an elongated, bifurcating cavity (with melt?) (5); (modified from Bussy and Cadoppi 1996, TL). **(6)** Tubular cavities in zircon from charnockite (modified from Chiarenzelli and McLelland 1993; TL). **(7-8)** Melt inclusions (8) and $CO_2$ plus an apatite inclusion (7) in zircon from a lower crustal xenolith (modified from Rudnick and Williams 1987, TL). **(9)** Inclusions in zircon of kimberlite. **Left:** cubic minerals (zirconia?; 10-20 μm wide); **right:** oriented trails of fluid inclusions (droplets or elongated channels, <10 μm wide)(modified from Kresten et al. 1975, TL). **(10)** Porous zircon from peralkaline granite with numerous U and Th rich inclusions and a lateral overgrowth of thorite (modified from Poitrasson et al. 1998, BSE). **(11)** Inclusions of quartz, apatite and a U-Th silicate phase in zircon from diorite (modified from Mulch et al. 2002, BSE). **(12)** zircon from a sedimentary rock in the Oklo fossil reactor; the crystal is sprinkled with galena inclusions (white spots) introduced during late hydrothermal events (modified from Mathieu et al. 2001, BSE). **(13)** Monazite growing in a fracture in zircon (modified from Barbey et al. 1989, BSE)**. (14)** Baddeleyite replacement inside zoned zircon from tonalitic gneiss (modified from Barth et al. 2002, BSE). **(15)** Detrital zircon with lateral outgrowths of two diagenetic xenotime crystals (modified from Fletcher et al. 2000, BSE). **(16)** Euhedral xenotime overgrowing zircon (modified from Schärer et al. 1994, SEM). **(17)** Zircon overgrowths on xenotime crystals in peralkaline magmatic complex (modified from Smith et al. 1991, BSE). **(18-19)** Intergrowth of zircon and xenotime in leucogranite sill. Convolutely zoned cores of both phases are rimmed by oscillatory zoned material and then by a broad homogeneous mantle (modified from Viskupic 2003, CL).

## ACKNOWLEDGMENTS

Thanks to Sven Dahlgren, Desmond Moser, Urs Schaltegger, Mark Schmitz and Karen Viskupic for providing unpublished images and Mark Schmitz for his attentive review.

## REFERENCES

Abati J, Dunning GR, Arenas R, Diaz Garcia F, Gonzalez Cuadra P, Martinez Catalan JR, Andonaegui P (1999) Early Ordovician orogenic event in Galicia (NW Spain): Evidence from U-Pb ages in the uppermost unit of the Ordenes Complex. Earth Planet Sci Lett 165:213-228

Andersson J, Williams IS (2001) Late-magmatic modification of zircon in the 1.38 Ga Tjärnesjö granite, eastern Sveconorwegian orogen, SW Sweden. *In* Andersson J (2001) Sveconorwegian orogenesis in the southwestern Baltic Shield—Zircon geochronology and tectonothermal setting of orthogneisses in SW Sweden. Doctoral thesis, Lund University, Sweden

Ashwal LD, Tucker RD, Zinner EK (1999) Slow cooling of deep crustal granulites and Pb-loss in zircon. Geochim Cosmochim Acta 63:2839-2851

Barbey P, Bertrand J-M, Angoua S, Dautel D (1989) Petrology and U/Pb geochronology of the Telohat migmatites, Aleksod, Central Hoggar, Algeria. Contrib Mineral Petrol 101:207-219

Barth MG, Rudnick RL, Carlson RW, Horn I, McDonough WF (2002) Re-Os and U-Pb geochronological constraints on the eclogite-tonalite connection in the Archean Man Shield, West Africa. Precambrian Res 118:267-283

Belousova EA, Griffin WL, Pearson NJ (1998) Trace element composition and cathodoluminescence properties of southern African kimberlitic zircons. Mineral Mag 62:355-366

Benisek A, Finger F (1993) Factors controlling the development of prism faces in granite zircons: A microprobe study. Contrib Mineral Petrol 114:441-451

Bingen B, Austrheim H, Whitehouse M (2001a) Ilmenite as a source for zirconium during high-grade metamorphism? Textural evidence from the Caledonides of western Norway and implications for zircon geochronology. J Petrol 42:355-375

Bingen B, Davis WJ, Austrheim H (2001b). Zircon U-Pb geochronology in the Bergen arc eclogites and their Proterozoic protoliths, and implications for the pre-Scandian evolution of the Caledonides in western Norway. Geol Soc Am Bull 113:640-649

Bohor BF, Betterton WJ, Krogh TE (1993) Impact-shocked zircons: discovery of shock-induced textures reflecting increasing degrees of shock metamorphism. Earth Planet Sci Lett 119:419-424

Bossart PJ, Meier M, Oberli F, Steiger RH (1986) Morphology versus U-Pb systematics in zircon: A high-resolution isotopic study of a zircon population from a Variscan dyke in the Central Alps. Earth Planet Sci Let 78:339-354

Bowring SA, Williams IS (1999) Priscoan (4.00-4.03 Ga) orthogneisses from northwestern Canada. Contrib Min-

eral Petrol 134:3-16
Bröcker M, Enders M (1999) U-Pb zircon geochronology of unusual eclogite-facies rocks from Syros and Tinos (Cyclades, Greece). Geol Mag 136:111-118
Bussy F, Cadoppi P (1996) U-Pb zircon dating of granitoids from the Dora-Maira massif (western Italian Alps). Swiss Bull Mineral Petrol 76:217-233
Chiarenzelli JR, McLelland JM (1993) Granulite facies metamorphism, palaeo-isotherms and disturbance of the U-Pb systematics of zircon in anorogenic plutonic rocks from the Adirondack Highlands. J Metamor Geol 11:59-70
Chakoumakos BC, Murakami T, Lumpkin GR, Ewing RC (1987) Alpha-decay-induced fracturing in zircon: the transition from the crystalline to the metamict state. Science 236:1556-1559
Charoy B, Raimbault L (1994) Zr, Th, and REE-rich biotite differentiates in the A-type granite pluton of Suzhou (Eastern China): the key role of fluorine. J Petrol 35:919-962
Chen YD, O'Reilly SY, Griffin WL, Krogh TE (1998) Combined U-Pb dating and Sm-Nd studies of lower crustal and mantle xenoliths from the Delegate basaltic pipes, southeastern Australia. Contrib Mineral Petrol 130:154-161
Cherniak DJ, Hanchar JM, Watson EB (1997a) Rare-earth diffusion in zircon. Chem Geol 134:289-301
Cherniak DJ, Hanchar JM, Watson EB (1997b) Diffusion of tetravalent cations in zircon. Contrib Mineral Petrol 127:383-390
Cherniak DJ, Watson EB (2001) Pb diffusion in zircon. Chem Geol 172:5-24
Christoffel CA, Connelly JN, Åhäll K-I (1999) Timing and characterization of recurrent pre-Sveconorwegian metamorphism and deformation in the Varberg-Halmstad region of SW Sweden. Precambrian Res 98:173-195
Connelly JN (2001) Degree of preservation of igneous zonation in zircon as a signpost for concordancy in U/Pb geochronology. Chem Geol 172:25-39
Corfu F, Ayres LD (1984) U-Pb ages and genetic significance of heterogeneous zircon populations in rocks from the Favourable Lake area, northwestern Ontario. Contrib Mineral Petrol 88:86-101
Corfu F, Stott GM (1998) The Shebandowan greenstone belt, western Superior Province: U-Pb ages, tectonic implications and correlations. Geol Soc Am Bull 110:1467-1484
Corfu F, Krogh Ravna E, Kullerud K (2002) A Late Ordovician U-Pb age for HP metamorphism of the Tromsdalstind eclogite in the Uppermost Allochthon of the Scandinavian Caledonides. 12th Annual Goldschmidt Conference, Geochim Cosmochim Acta 77:A153
Crookes W (1879) Contributions to molecular physics in high vacua. Phil Trans Roy Soc 170:641-642
Davidson A, van Breemen O (1988) Baddeleyite-zircon relationships in coronitic metagabbro, Grenville Province, Ontario: Implications for geochronology. Contrib Mineral Petrol 100:291-299
Duchesne JC, Caruba R, Iacconi P (1987) Zircon in charnockitic rocks from Rogaland (southwest Norway): Petrogenetic implications. Lithos 20:357-368
Fletcher IR, Rasmussen B, McNaughton NJ (2000) SHRIMP U-Pb geochronology of authigenic xenotime and its potential for dating sedimentary basins. Austral J Earth Sci 47:845-859
Fowler A, Prokoph A, Stern R, Dupuis C (2002) Organization of oscillatory zoning in zircon: Analysis, scaling, geochemistry, and model of a zircon from Kipawa, Quebec, Canada. Geochim Cosmochim Acta 66:311-328
Gebauer D, Schertl H-P, Brix M, Schreyer W (1997) 35 Ma old ultrahigh-pressure metamorphism and evidence for very rapid exhumation in the Dora Maira Massif, Western Alps. Lithos 41:5-24
Gibson RL, Armstrong RA, Reimold WU (1997) The age and thermal evolution of the Vredefort impact structure: A single-grain zircon study. Geochim Cosmochim Acta 61:1531-1540
Görz H, Bhalla RJRSB, White EW (1970) Detailed cathodoluminescence characterization of common silicates. Space Sci Applic Solid State Luminesc Phen, MRL Publ 70-101:62-70
Grieco G, Ferrario A, von Quadt, A, Koeppel V, Mathez EA (2001) The zircon-bearing chromitites of the phlogopite peridotite of Finero (Ivrea Zone, Southern Alps): Evidence and geochronology of a metasomatized mantle slab. J Petrol 42:89-101
Hacker BR, Ratschbacher L, Webb L, Ireland T, Walker D, Shuwen D (1998) U/Pb zircon ages constrain the architecture of ultrahigh-pressure Qinling-Dabie Orogen, China. Earth Planet Sci Lett 161:215-230
Halden NM, Hawthorne FC (1993) The fractal geometry of oscillatory zoning in crystals: Application to zircon. Am Mineral 78:1113-1116
Hanchar JM, Miller CF (1993) Zircon zonation patterns as revealed by cathodoluminescence and backscattered electron images: Implications for interpretation of complex crustal histories. Chem Geol 110:1-13
Hanchar JM, Rudnick RL (1995) Revealing hidden structures: the application of cathodoluminescence and backscattered electron imaging to dating zircons from lower crustal xenoliths. Lithos 36:289-303
Harrison TM, Watson EB (1983) Kinetics of zircon dissolution and zirconium diffusion in granitic melts of variable water content. Contrib Mineral Petrol 84:67-72
Heaman LM, LeCheminant AN (1993) Paragenesis and U-Pb systematics of baddeleyite ($ZrO_2$). Chem Geol 110:95-126

Hoffman JF, Long JVP (1984) Unusual sector zoning in Lewisian zircons. Mineral Mag 48:513-517
Holland HD and Gottfried D (1955) The effect of nuclear radiation on the structure of zircon. Acta Crystallogr 8:291-300
Hoskin PWO (1999) SIMS determination of μg $g^{-1}$-level fluorine in geological samples and its concentration in NIST SRM 610. Geostand Newslett: J Geostand Geoanal 23:69-76
Hoskin PWO (2000) Patterns of chaos: Fractal statistics and the oscillatory chemistry of zircon. Geochim Cosmochim Acta 64:1905-1923
Hoskin PWO, Black LP (2000) Metamorphic zircon formation by solid-state recrystallization of protolith igneous zircon. J Metamor Geol 18:423-439
Hoskin PWO, Kinny PD, Wyborn D (1998) Chemistry of hydrothermal zircon: Investigating timing and nature of water-rock interaction. *In* Water-rock Interaction. Arehart GB, Hulston JR (eds) Balkema, Rotterdam, The Netherlands, p 545-548
Huneke JC, Rossman GR (1978) Zircons of Summit Rock, Oregon. Mineral Record 392-393
Jocelyn J, Pidgeon RT (1974) Examples of twinning and parallel growth in zircons from some Precambrain granites and gneisses. Mineral Mag 39:587-594
Kamo SL, Reimold WU, Krogh TE, Colliston WP (1996) A 2.023 Ga age for the Vredefort impact event and a first report of shock metamorphosed zircons in pseudotachylitic breccias and Granophyre. Earth Planet Sci Lett 144:369-387
Kinny PD and Dawson JB (1992) A mantle metasomatic injection event linked to Late Cretaceous kimberlite magmatism. Nature 360:723-726
Köppel V, Sommerauer J (1974) Trace elements and the behaviour of the U-Pb system in inherited and newly formed zircons. Contrib Mineral Petrol 43:71-82
Korsakov AV, Shatsky VS, Sobolev NV, Zayachokovsky AA (2002) Garnet-biotite-clinozoisite gneiss: A new type of diamondiferous metamorphic rock from the Kokchetav Massif. Eur J Mineral 14:915-928
Koschek G (1993) Origin and significance of the SEM cathodoluminescence from zircon. J Micros 171:223-232
Kresten P, Fels P, Berggren G (1975) Kimberlitic zircons—a possible aid in prospecting for kimberlites. Mineral Dep 10:47-56
Krinsley DH, Manley CR (1989) Backscattered electron microscopy as an advanced technique in petrography. J Geol Educ 37:202-209
Krogh TE (1982) Improved accuracy of U-Pb zircon ages by the creation of more concordant systems using an air abrasion technique. Geochim Cosmochim Acta 46:637-649
Krogh TE, Davis GL (1974) Alteration in zircons with discordant U-Pb ages. Carnegie Inst Washington Yrbk 73:560-567
Krogh TE, Davis GL (1975) Alteration in zircons and differential dissolution of altered and metamict zircon. Carnegie Inst Washington Yrbk 74:619-623
Krogh TE, McNutt RH, Davis GL (1982) Two high precision U-Pb zircon ages for the Sudbury Nickel Irruptive. Can J Earth Sci 19:723-728
Krogh TE, Davis DW, Corfu F (1984) Precise U-Pb zircon and baddeleyite ages for the Sudbury area. Ontario Geol Surv Spec Vol 1:431-446
Krogh TE, Kamo SL, Bohor BF (1993) Fingerprinting the K/T impact site and determining the time of impact by U-Pb dating of single shocked zircons from distal ejecta. Earth Planet Sci Lett 119:425-429
Krogh TE, Kamo SL, Bohor B (1996) Shock metamorphosed zircons with correlated U-Pb discordance and melt rocks with concordant protolith ages indicate an impact origin for the Sudbury Structure. *In* Earth Processes: Reading the Isotopic Code. Basu A, Hart S (eds) Am Geophys Union, Geophys Monogr 95:343-353
Kröner A, Jaeckel P, Reischman T, Kroner U (1998) Further evidence for an early Carboniferous (~340 Ma) age of high-grade metamorphism in the Saxonian granulite complex. Geol Rundsch 86:751-766
Lee JKW, Tromp J (1995) Self-induced fracture generation in zircon. J Geophys Res 100:17753-17770
Liermann H-P, Isachsen C, Altenberger U, Oberhänsli R (2002) Behaviour of zircon during high-pressure, low-temperature metamorphism: Case study from the Internal Unit of the Sesia Zone (Western Italian Alps). Eur J Mineral 14:61-71
Long JVP, Agrell SO (1965) The cathodoluminescence of minerals in thin section. Mineral Mag 34:318-326
Lopez Sanchez-Vizcaino V, Rubatto D, Gomez-Pugnaire MT, Trommsdorff V, Münterer O. (2001) Middle Miocene high-pressure metamorphism and fast exhumation of the Nevado-Filabride Complex, SE Spain. Terra Nova 13:327-332
Machado N, Goulet N, Gariépy C (1989) U-Pb geochronology of reactivated Archean basement and of Hudsonian metamorphism in the northern Labrador Trough. Can J Earth Sci 26:1-15
Malcuit RJ, Heimlich RA (1972) Zircons from Precambrian Gneiss, southern Bighorn Mountains, Wyoming. Am Mineral 57:1190-1209
Mariano AN (1978) The application of cathodoluminescence for carbonatite exploration and characterization. Proc Intl Symp Carbonatites. Brasil Depart Nac Prod Mineral, Brasilia, 39-57

Mariano AN (1989) Cathodoluminescence emission spectra of rare earth element activators in minerals. Rev Mineral 21:339-348

Marshall DJ (1988) Cathodoluminescence of geological materials. Unwin Hyman, London

Mathieu R, Zetterström L, Cuney M, Gauthier-Lafaye F, Hidaka H (2001) Alteration of monazite and zircon and lead migration as geochemical tracers of fluid paleocirculations around the Oklo-Okélobondo and Bangombé natural nuclear reaction zones (Francesville basin, Gabon). Chem Geol 171:147-171

Mattinson JM, Graubard CM, Parkinson DL, McLelland WC (1996) U-Pb reverse discordance in zircons: the role of fine-scale oscillatory zoning and sub-microscopic transport of Pb. Am Geophys Union, Geophys Monogr 95:355-370

McLaren AC, FitzGerald JD, Williams IS (1994). The microstructure of zircon and its influence on the age determination from U-Pb isotopic ratios measured by ion microprobe. Geochim Cosmochim Acta 58:993-1005

McLelland J, Hamilton M, Selleck B, McLelland J, Walker D, Orrell S (2001) Zircon U-Pb geochronology of the Ottawan Orogeny, Adirondack Highlands, New York: Regional and tectonic implications. Precambrian Res 109:39-72

Medenbach O (1976) Geochemie der Elemente in Zirkon und ihre räumliche Verteilung—eine Untersuchung mit der Elektronenstrahlmikrosonde. Doctoral thesis, Ruprecht-Karl-Universität, Heidelberg, Germany

Miller CF, Hanchar JM, Wooden JL, Bennett VC, Harrison TM, Wark DA, Foster DA (1992) Source region of a granite batholith: Evidence from lower crustal xenoliths and inherited accessory minerals. Trans Roy Soc Edinburgh 83:49-62

Moser DE (1997) Dating the shock wave and thermal imprint of the giant Vredefort impact, South Africa. Geology 25:7-10

Moser DE, Heaman LM (1997) Proterozoic zircon growth in Archean lower crustal xenoliths, southern Superior craton—a consequence of Matachewan ocean opening. Contrib Mineral Petrol 128:164-175

Mulch A, Rosenau M, Dörr W, Handy MR (2002) The age and structure of dikes along the tectonic contact of the Ivrea-Verbano and Strona-Ceneri Zones (southern Alps, Northern Italy, Switzerland). Swiss Bull Mineral Petrol 82:55-76

Murakami T, Chakoumakos BC, Ewing RC, Lumpkin GR, Weber WJ (1991) Alpha-decay event damage in zircon. Am Mineral 76:1510-1532

Myers JS, Crowley JL (2000) Vestiges of life in the oldest Greenland rocks? A review of early Archean geology in the Godthåbsfjord region, and reappraisal of field evidence for >3850 Ma life on Akilia. Precambrian Res 103:101-124

Nemchin AA, Pidgeon RT (1997) Evolution of the Darling Range Batholith, Yilgarn Craton, Western Australia: A SHRIMP zircon study. J Petrol 38:625-649

Nutman AP, Friend CRL, Kinny PD, McGregor VR, (1993) Anatomy of an Early Archaean gneiss complex: 3900 to 3600 Ma crustal evolution in southern West Greenland. Geology 21:415-418

Nutman AP, McGregor VR, Shiraishi K, Friend CRL, Bennett VC, Kinny PD (2002) •3850 Ma BIF and mafic inclusions in the Early Archaean Itsaq Gneiss Complex around Akilia, southern West Greenland? The difficulties of precise dating of zircon-free protoliths in migmatites. Precambrian Res 117:185-224

Oberli F, Meier M, Biino GG (1994) Time constraints on the pre-Variscan magmatic/metamorphic evolution of the Gotthard and Tavetsch units derived from single zircon U-Pb results. Swiss Bull Mineral Petrol 74:483-488

Ohnenstetter D, Cesbron F, Remond G, Caruba R, Claude J-M (1991) Émissions de cathodoluminescence de deux populations de zircons naturels: téntative d'interpretation. C R Acad Sci Paris 313:641-647

Ono A (1976) Chemistry and zoning of zircon from some Japanese granitic rocks. J Japan Assoc Mineral Petrol Econ Geol 71:6-17

Owen MR (1987) Hafnium content of detrital zircons: A new tool for provenance study. J Sed Petrol 57:824-830

Owen MR, Carozzi AV (1986) Southern provenance of upper Jackfork Sandstone, southern Ouachita Mountains: Cathodoluminescence petrology. Geol Soc Am Bull 97:110-115

Palmer HC, Davis DW (1987) Paleomagnetism and U-Pb geochronology of volcanic rocks from Michipicoten Island, Lake Superior, Canada: Precise calibration of the Keweenawan polar wander track. Precambrian Res 37:157-171

Paquette JL, Monchoux P, Couturier M (1995) Geochemical and isotopic study of a norite-eclogite transition in the European Variscan belt: Implications for U-Pb zircon systematics in metabasic rocks. Geochim Cosmochim Acta 59:1611-1622

Paterson BA, Stephens WE (1992) Kinetically induced compositional zoning in titanite: Implications for accessory-phase/ melt partitioning of trace elements. Contrib Mineral Petrol 109:373-385

Paterson BE, Stephens WE, Herd DA (1989) Zoning in granitoid accessory minerals as revealed by backscattered electron imagery. Mineral Mag 53:55-62

Paterson BA, Rogers G, Stephens WE (1992a) Evidence for inherited Sm-Nd isotopes in granitoid zircons. Contrib Mineral Petrol 111:378-390

Paterson BA, Stephens WE, Rogers G, Williams IS, Hinton RW, Herd DA (1992b) The nature of zircon inheritance in two granite plutons. Trans Roy Soc Edinburgh: Earth Sci 83:459-471

Peucat JJ, Bernard-Griffiths J, Gil Ibarguchi JI, Dallmeyer RD, Menot RP, Cornichet J, Iglesias Ponce de León M (1990) Geochemical and geochronological cross-section of the deep Variscan crust: The Cabo Ortegal high-pressure nappe (northwestern Spain). Tectonophysics 177:263-292

Pidgeon RT (1992) Recrystallization of oscillatory zoned zircon: some geochronological and petrological implications. Contrib Mineral Petrol 110:463-472

Pidgeon RT, Nemchin AA, Hitchen GJ (1998) Internal structures of zircons from Archean granites from the Darling Range batholith: Implications for zircon stability and the interpretation of zircon U-Pb ages. Contrib Mineral Petrol 132:288-299

Pidgeon RT, Nemchin AA, Kinny PD (2000) Fir-tree and nebulously zoned zircons from granulite facies rocks: Evidence for zircon growth and interaction with metamorphic fluids. Goldschmidt 2000, J Conf Abstr 5:798

Pin C, Lancelot J (1982) U-Pb dating of an Early Paleozoic bimodal magmatism in the French Massif Central and its further metamorphic evolution. Contrib Mineral Petrol 79:1-12

Poitrasson F, Paquette J-L, Montel J-M, Pin C, Duthou J-L (1998) Importance of late-magmatic and hydrothermal fluids on the Sm-Nd isotope mineral systematics of hypersolvus granite. Chem Geol 146:187-203

Poldervaart A (1956) Zircon in rocks. 2. Igneous rocks. A, J Sci 254:521-554

Poller U (1997) U-Pb single zircon study of gabbroic and granitic rocks of Val Barlas-ch (Silvretta nappe, Switzerland). Swiss Bull Mineral Petrol 77:351-359

Pupin JP (1980) Zircon and granite petrology. Contrib Mineral Petrol 73:207-220

Remond G, Cesbron F, Chapoulie R, Ohnenstetter D, Roques-Carmes C, Schoverer M (1992) Cathodoluminescence applied to the microcharacterization of mineral materials: A present status in experimentation and interpretation. Scan Microsc 6:23-68

Rowley DB, Xue F, Tucker RD, Peng ZX, Baker J, Davis A (1997) Ages of ultrahigh pressure metamorphism and protolith orthogneisses from the eastern Dabie Shan: U/Pb zircon geochronology. Earth Planet Sci Lett 151:191-203

Rubatto D, Gebauer D (1999) Eo/Oligocene (35 Ma) high-pressure metamorphism in the Gornergrat Zone (Monte Rosa, Western Alps): Implications for paleogeography. Swiss Bull Mineral Petrol 79:353-362

Rubatto D, Gebauer D, Fanning M (1998) Jurassic formation and Eocene subduction of the Zermatt-Saas-Fee ophiolites: Implications for the geodynamic evolution of the Central and Western Alps. Contrib Mineral Petrol 132:269-287

Rubin JN, Henri CD, Price JG (1989) Hydrothermal zircons and zircon overgrowths, Sierra Blanca Peaks, Texas. Am Mineral 74:865-869

Rudnick RL, Williams IS (1987) Dating the lower crust by ion microprobe. Earth Planet Sci Lett 85:145-161

Schaltegger U, Gebauer D, von Quadt A (2002) The mafic-ultramafic rock association of Loderio-Biasca (lower Pennine nappes, Ticino, Switzerland): Cambrian oceanic magmatism and its bearing on early Paleozoic paleogeography. Chem Geol 186:265-279

Schaltegger U, Fanning CM, Gunther D, Maurin JC, Schulmann K, Gebauer D (1999) Growth, annealing and recrystallization of zircon and preservation of monazite in high-grade metamorphism: Conventional and *in situ* U-Pb isotope, cathodoluminescence and microchemical evidence. Contrib Mineral Petrol 134:186-201

Schärer U, Zhang L-S, Tapponnier P (1994) Duration of strike slip movement in large shear zones: The Red River belt, China. Earth Planet Sci Lett 126:379-397

Schärer U, Corfu F, Demaiffe D (1997) U-Pb and Lu-Hf isotopes in baddeleyite and zircon megacrysts from the Mbuji-Mayi kimberlite: Constraints on the subcontinental mantle. Chem Geol 143:1-16

Schmitz MD, Bowring SA (2001) The significance of U-Pb zircon dates in lower crustal xenoliths from the southwestern margin of the Kaapvaal Craton, southern Africa. Chem Geol 172:59-76

Schmitz MD, Bowring SA (2002a) High precision U-Pb zircon geochronology of southern African cratonic mantle eclogites and implications for subcontinental lithospheric mantle evolution and metasomatism. EOS Trans, Am Geophys Union 83:S376

Schmitz, MD, Bowring SA (2002b) Ultrahigh-temperature metamorphism in the lower crust during Neoarchean Ventersdorp rifting and magmatism, Kaapvaal Craton, southern Africa. Geol Soc Am Bull (in press)

Scoates JS, Chamberlain KR (1995) Baddeleyite ($ZrO_2$) and zircon ($ZrSiO_4$) from anorthositic rocks of the Laramie anorthosite complex, Wyoming: Petrologic consequences and U-Pb ages. Am Mineral 80:1317-1327

Silver LT, Deutsch S (1963) Uranium-lead isotopic variations in zircons: A case study. J Geol 71:721-758

Sippel RF (1968) Sandstone petrology, evidence from luminescence petrography. J Sed Petrol 38:530-554

Sippel RF (1971) Luminescence petrography of the Apollo 12 rocks and comparative features in terrestrial rocks and meteorites. Proc Second Lunar Conf 1. MIT, Cambridge, Massachusetts, p 247-263

Smith DGW, de St. Jorre L, Reed SJB, Long JVP (1991). Zonally metamictized and other zircons from Thor Lake, Northwest Territories. Can Mineral 29:301-309

Smith JV, Stenstrom RC (1965) Electron-excited luminescence as a petrologic tool. J Geol 73:627-635

Sommerauer J (1974) Trace element distribution patterns and the mineralogical stability of zircon—an application for combined electron microprobe techniques. Electron Micros Soc S Afr Proc 4:71-72

Speer JA (1982) Zircon. Rev Mineral 5(2nd edn):67-112

van Breemen O, Davidson A, Loveridge WD, Sullivan RW (1986) U-Pb zircon geochronology of Grenville tectonites, granulite and igneous precursors, Parry Sound, Ontario. *In* The Grenville Province, Moore JM, Davidson A, Baer AJ (eds) Geol Assoc Can Spec Paper 3, p 191-207

van Breemen O, Henderson JB, Loveridge WD, Thompson PH (1987) U-Pb zircon and monazite geochronology and zircon morphology of granulites and granite from the Thelon Tectonic Zone, Healey Lake and Artillery Lake map areas, N.W.T. Geol Surv Can Paper 87-1A:783-801

Vavra G (1990) On the kinematics of zircon growth and its petrogenetic significance: A cathodoluminescence study. Contrib Mineral Petrol 106:90-99

Vavra G (1993) A guide to quantitative morphology of accessory zircon. Chem Geol 110:15-28

Vavra G, Hansen BT (1991) Cathodoluminescence studies and U-Pb dating of zircons in pre-Mesozoic gneisses of the Tauern Window: Implications for the Pennine basement evolution. Geol Rundsch 80:703-715

Vavra G, Gebauer D, Schmid R, Compston W (1996) Multiple zircon growth and recrystallization during polyphase Late Carboniferous to Triassic metamorphism in granulites of the Ivrea zone (Southern Alps): An ion microprobe (SHRIMP) study. Contrib Mineral Petrol 122:337-358

Viskupic K (2003) Crustal melting in the Himalayan orogen: field, geochemical and geochronological studies in the Everest region, Nepal. PhD thesis, Massachusetts Institute of Technology, 190 p

Vocke RD Jr, Hanson GN (1981) U-Pb zircon ages and petrogenetic implications for two basement units from Victoria valley, Antarctica. *In* Antarctica Research Series, Dry Valley Drilling Project. McGinnis L (ed) Am Geophys Union, Washington, DC, 33:247-255

Watson EB (1979) Zircon saturation in felsic liquids: Experimental results and applications to trace element geochemistry. Contrib Mineral Petrol 70:407-419

Watson EB (1996) Dissolution, growth and survival of zircons during crustal fusion: kinetic principles, geological models and implications for isotopic inheritance. Trans Roy Soc Edinburgh: Earth Sci 87:43-56

Watson EB, Harrison TM (1983) Zircon saturation revisited: temperature and composition effects in a variety of crustal magma types. Earth Planet Sci Lett 64:295-304

Watson EB, Liang Y (1995) A simple model for sector zoning in slowly grown crystals: Implications for growth rate and lattice diffusion, with emphasis on accessory minerals in crustal rocks. Am Mineral 80:1179-1187

Watson EB, Vicenzi EP, Rapp RP (1989) Inclusion/host relations involving accessory minerals in high-grade metamorphic and anatectic rocks. Contrib Mineral Petrol 101:220-231

Watson EB, Cherniak DJ, Hanchar JM, Harrison, TM, Wark DA (1997) The incorporation of Pb into zircon. Chem Geol 141:19-31

Wayne DM, Sinha AK (1988) Physical and chemical response of zircons to deformation. Contrib Mineral Petrol 98:109-121

Wayne DM, Sinha AK (1992) Stability of zircon U-Pb systematics in a greenschist-grade mylonite: an example from the Rockfish Valley fault zone, central Virginia, USA. J Geol 100:593-603

Welin E, Gorbatschev R, Kähr A-M (1982) Zircon dating of polymetamorphic rocks in southwestern Sweden. Sver Geol Unders C797:1-34

Whitehouse MJ, Kamber BS, Moorbath S (1999) Age significance of U-Th-Pb zircon data from early Archaean rocks of West Greenland-a reassessment based on combined ion-microprobe and imaging studies. Chem Geol 160:201-224

Yang B, Luff, BJ, Townsend, PD (1992) Cathodoluminescence of natural zircons. J Phys: Condens Matter 4:5617-5624

Zeck HP, Williams IS (2002) Inherited and magmatic zircon from Neogene Hoyazo cordierite dacite, SE Spain—anatectic source rock provenance and magmatic evolution. J Petrol 43:1089-1104

# 16 Atlas of Zircon Textures

**Fernando Corfu**

*Institute of Geology, University of Oslo*
*P B 1047 Blindern*
*N-0316 Oslo, Norway*

**John M. Hanchar**

*Department of Earth and Environmental Sciences*
*The George Washington University*
*Washington, D.C. 20006*

**Paul W.O. Hoskin**

*Institut für Mineralogie, Petrologie und Geochemie*
*Albert-Ludwigs-Universität Freiburg*
*D-79104 Freiburg, Germany*

**Peter Kinny**

*Department of Applied Geology*
*Curtin University of Technology*
*Perth WA 6845, Australia*

## INTRODUCTION

The mineral zircon is extremely variable both in terms of external morphology and internal textures. These features reflect the geologic history of the mineral, especially the relevant episode(s) of magmatic or metamorphic crystallization (and recrystallization), strain imposed both by external forces and by internal volume expansion caused by metamictization, and chemical alteration. The paper presents a selection of both the most typical, but also of the less common, features seen in zircon, categorized according to the different geological processes responsible for their formation. The atlas is intended as a general guide for the interpretation of zircon characteristics, and of related isotopic data.

Zircon has become one of the most widely used minerals for the extraction of information on the prehistory and genesis of magmatic, metamorphic and sedimentary rocks. Much of the geological usefulness of zircon stems from its suitability as a geochronometer based on the decay of U (and Th) to Pb, but in addition it is also the major host of the radiogenic isotopic tracer Hf, and it is used to determine oxygen isotopic compositions and REE and other trace element abundances, all of which yield useful clues concerning the history of the host rock, and in some case, the parent rock in which the precursor zircon crystallized.

One of the major advantages of zircon is its ability to survive magmatic, metamorphic and erosional processes that destroy most other common minerals. Zircon-forming events tend to be preserved as distinct structural entities on a pre-existing zircon grain. Because of this ability, quite commonly zircon consists of distinct segments, each preserving a particular period of zircon-formation (or consumption). A long experience and modern instrumentation and techniques have provided the "zircon community" the means to image and interpret preserved textures, and hence to decipher the history and evolution of a rock. One of the most critical tasks is the proper assignment of particular zircon domains or grains to a specific stage in the history of a rock. This is relatively simple and straightforward in many cases where a proper understanding of the geological setting, simple logical deduction, and common sense lead to unambiguous and straightforward interpreta-

1529-6466/03/0053-0016$05.00

tions, but it can be an extremely difficult task in other cases where the interpretation may be affected more strongly by the bias of the investigator than by purely objective criteria. This is sometimes the case in complex gneiss terranes, as exemplified by the recent debate on the history of the Early Archean gneisses in Greenland (e.g., Nutman et al. 1993, 2002; Whitehouse et al. 1999, Myers and Crowley 2000). The interpretation of age and isotopic relations is affected, on the one hand, by the particular megascopic and petrologic relationships of a rock unit and, on the other hand, by the characteristics of the minerals analyzed, most commonly the external and internal characteristics of the accessory mineral zircon.

The intent of this chapter is to provide an overview of the variety of textural relations observed in zircon and their links to particular rock forming and modifying processes. The selection includes both the most common as well as rare textures observed in nature. The zircon pictures and figures are categorized according to their inferred genetic context. The examples chosen, from our own collections, from colleagues, and from the literature, are based mainly on well-understood geological situations where the geological context provides a measure of assurance that the interpretation is valid.

## ZIRCON IMAGING

In common rocks zircon ranges in size from about 20 to 200 μm (Silver and Deutsch 1963). Larger zircon grains, up to several cm wide (or even up to 30 cm long as for exceptional examples from carbonatite in the Northern Territories, Australia), can be found in granitic pegmatites, syenites, kimberlites and carbonatites, whereas very small zircons may be present in aphanitic volcanic rocks, and in late stage crystallization in plutonic rocks. Observations of the external and internal properties of zircon are, therefore, made by means of microscopic observation or X-ray or electron scattering techniques.

A binocular microscope (BM; Table 1) allows us to observe macroscopic properties, such as color, degree of transparency or opacity, external morphology and form development, and the presence of inclusions, fractures and alteration. For this task it is generally useful to hold the zircon grains in a dish in ethanol in order to improve the optical quality over that obtained by observing in air. Alcohol also makes it simpler to move, turn or hand-pick the grains and to distinguish zircon from other minerals such as apatite, quartz, feldspar and titanite. Still better optical observation is facilitated by setting the zircons in dense fluids such as immersion oils, glycerine or methylene iodide, although these are usually too cumbersome for routine observation (use of methylene iodide and some immersion oils requires a special ventilation set-up because of health risks). Grain-mounts can be prepared with Canada Balsam, piperine, or various epoxy resins, but it becomes more difficult to subsequently remove the grains for isotope dilution analysis if certain epoxy resins are used.

Insights into the internal texture of zircon can be obtained with a petrographic microscope using either transmitted or reflected light. Transmitted light (TL) is useful for viewing zircon in thin section or grain mount and can reveal features such as growth zoning and metamict zones, which display different interference colors when viewed in crossed-polarized light (Chakoumakos et al. 1987, Murakami et al. 1991, Ewing et al., this volume). Observation in thin section is also useful for establishing the relations of zircon to the main rock-forming minerals. The drawback of the method is usually the small size of zircon that challenges the power of resolution of microscopes, and the difficulty of distinguishing zircon from monazite or other high-relief–high-birefringence minerals. Reflected light microscopy (RL) of polished grain-mounts, briefly etched with dilute HF vapor, is very effective in revealing growth zoning, alteration, and other features in old, relatively metamict zircons (e.g., Krogh and Davis 1974, 1975; Fig. 1.1). These techniques, BM, TL and RL (with HF etching), are

**Table 1.** List of abbreviations used in the paper.

| Imaging technique | Abbreviation |
|---|---|
| Binocular microscope | BM |
| Transmitted light microscopy | TL |
| Reflected light microscopy | RL |
| U-mapping | UM |
| Cathodoluminescence | CL |
| Back-scattered electron microscopy | BSE |
| Secondary electron microscopy | SEM |

generally not capable to properly reveal the internal textural complexity of non-metamict, crystalline zircon crystals providing zircon images that appear unzoned and internally featureless (Rudnick and Williams 1987, Hanchar and Rudnick 1995).

Uranium (and Th) maps (UM) can be obtained by inducing fission tracks in a special detector laid upon polished zircon grains by exposing them to a neutron flux in a reactor (Fig. 1.8) (e.g., Duchesne et al. 1987). Alternatively, autoradiography using a nuclear emulsion technique has been used to map α-particle tracks in zircon (e.g., Silver and Deutsch 1963).

The best resolution of internal textures is provided by cathodoluminescence (CL) or backscattered electron (BSE) imaging (Fig. 1.2–1.7). It has long been known that certain minerals, including zircon, exhibit CL when bombarded with electrons (Crookes 1879). Cathodoluminescence has been widely applied as a petrologic tool in the Earth sciences since the mid-1960s (e.g., Long and Agrell 1965, Smith and Stenstrom 1965) and this technique has been used over the past thirty-years to investigate a wide spectrum of problems in sedimentary petrology (Owen and Carozzi 1986, Owen 1987), igneous and metamorphic petrology and geochronology (e.g., Sippel 1968, 1971; Görz et al. 1970, Malcuit and Heimlich 1972, Sommerauer 1974, Ono 1976, Vocke and Hanson 1981, Vavra 1990, 1993; Hanchar and Miller 1993, and numerous other studies since the mid-1990s).

The elemental, or structural, controls of the CL emission is generally well understood for most minerals (Marshall 1988) and is usually attributed to the electronic transitions of 5d-electron transition elements, of 4f-electron electronic transitions of the trivalent rare earth elements (REEs), vibrational luminescence of the uranyl ion, or defect-related phenomena (Marshall 1988). In zircon, there is usually a broad band emission in either the blue or yellow regions, or both, of the electromagnetic spectrum upon which are superimposed sharp peaks of the trivalent REEs. $Dy^{3+}$ is considered to be the principal elemental factor (e.g., Mariano 1978, 1989; Remond et al. 1992, Hanchar and Rudnick 1995), although other constituents such as $Sm^{3+}$, $Eu^{2+}$ and $Tb^{3+}$ may also be CL emitters in zircon (e.g., Ohnenstetter et al. 1991, Yang et al. 1992). The presence of $U^{4+}$ and the resulting radiation damage from its decay may also suppress the CL emission (see Nasdala et al. in this volume for a more thorough discussion of the CL of zircon). Ohnenstetter et al. (1991) have

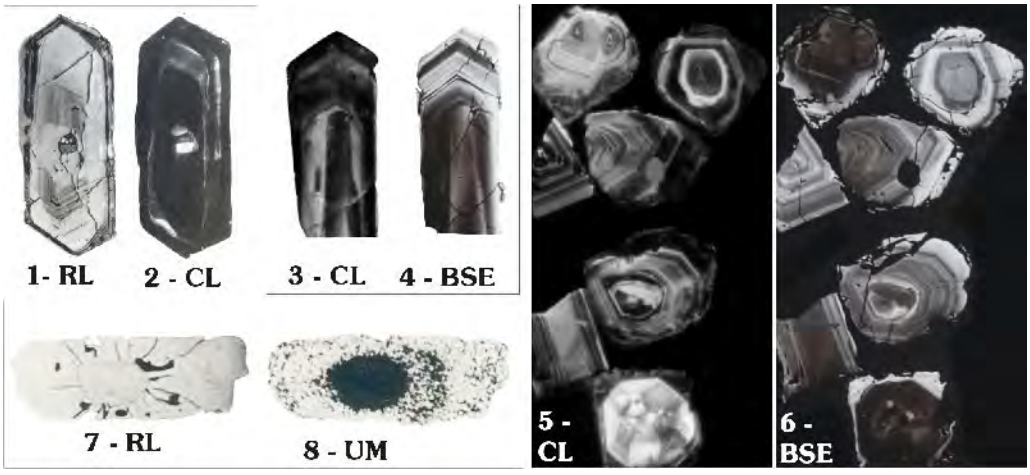


**Figure 1.** Imaging techniques.**(1-2)** Same zircon imaged with RL, after polishing and etching the surface with HF vapor, and CL; modified from Nemchin and Pidgeon (1997). **(3-4** and **5-6)** Comparison of CL and BSE imaging (from J.M. Hanchar, unpublished results); **(7-8)** RL image of polished zircon crystal reveals inner core and radially fractured outer shell; UM image highlights the zonation indicating very high concentrations of U in the centre, more moderate values in an intermediate shell and lower concentrations in the rim; modified from Duchesne et al. (1987).

suggested that the broad-band blue CL emission may be defect-related due to the presence of $Y^{3+}$ and that the broad band yellow CL emission may also be defect-related due to the presence of $Ti^{4+}$ or $U^{4+}$.

Back-scattered electron imaging reveals contrasts in average atomic number of regions of a phase; the higher the number, the more electrons an area will "reflect" and the brighter it will appear in the resulting image. Back-scattered electron imaging is now widely used in a variety of geologic studies and is recognized as a powerful tool for studying zonation in minerals and especially accessory minerals (e.g., Wayne and Sinha 1988, 1992; Krinsley and Manley 1989, Paterson et al. 1989, 1992a,b; Paterson and Stephens 1992, Miller et al. 1992, and numerous studies since the mid-1990s). The element primarily responsible for these BSE intensity variations in crustal zircon is Hf, with U having a secondary effect (Hanchar and Miller 1993).

In investigating zircons with these imaging techniques we have found that in many cases both techniques reveal similar features, however, usually the bright areas in CL are dark in BSE and vice versa—an observation noted by Hanchar and Miller (1993), Koschek (1993) and many other workers (Fig. 1.3-1.6). We have found that CL is generally more useful than BSE in identifying different growth regions in zircon due to the greater range in intensity of the CL emission and the additional variations in color (if done using a petrographic microscope based CL system and using color negative or slide film, or a digital camera). In addition, different growth events often have characteristic CL emission colors and this attribute of using CL can help locate *in situ* analysis locations of different isotopic age. Using a scanning electron microscope based CL system obviously reveals similar features in zircons, but unless false-color processing is done, images are in grey-scale only and the different colored CL regions remain unnoticed.

## MORPHOLOGY OF ZIRCON

Zircon is tetragonal and most commonly grows as doubly-terminated prismatic crystals with elongation (length-to-width) ratios ranging from 1 to 5. This ratio is commonly believed to reflect crystallization velocity. Indeed, needle-shaped acicular zircon crystals are common in rapidly crystallized, porphyritic, sub-volcanic intrusions, high-level granites, and gabbros (e.g., Fig. 2.15–2.18),

**Figure 2.** External morphology variations.All grains are between 70 and 250 μm in size. **(1-21)** Variable morphology characteristics in terms of length to width ratios and typology. The latter is shown in the general context of the diagram of Pupin (1980) which is based on the relative development of the prismatic (vertical axis) and pyramidal crystal faces (horizontal axis). Note also the local presence of xenocrystic cores, inclusions of other minerals and degree of fracturing. 1 – modified from Pupin (1980), TL; 2 – only one pyramid is developed on a large subrounded core, from F. Corfu (unpublished data), BM; 3 – modified from Machado et al. (1989), BM; 4 – from F. Corfu (unpublished data), BM; 5 – ghost xenocrystic core evidenced only by bubble structure, modified from Oberli et al. (1994), TL; 6 – modified from Kröner et al. (1998), SEM; 7 – complex twinning, modified from Jocelyn and Pidgeon (1974), BM; 8 – zircon crystal totally lacking prismatic faces, from U. Schaltegger (unpublished data), SEM; 9, 10 – flat shaped, twinned crystals, from F. Corfu (unpublished data), BM; 11, 12 – modified from Pupin (1980), TL; 13,14,15 – from F. Corfu (unpublished data), BM; 16 – modified from Moser (1997), SEM; 17, 18 – highly fractured prisms in gabbro, modified from Corfu and Stott (1998), BM; 19, 20 – prominent cores overgrown by clean prisms, modified from Palmer and Davis (1987), BM; 21 – modified from Corfu and Ayres (1984), BM. **(22)** Zircon aggregate in A-type pluton, modified from Charoy and Raimbault (1994), SEM. **(23)** Thin-walled hollow zircon crystal, modified from Huneke and Rossman (1978), SEM. **(24)** Zircon fragment, typical of populations extracted from many mafic rocks, modified from Abati et al (1999), SEM. **(25-27)** Composite, resorbed grains (cauliflower zircon); 25, 27 – in meta-trondhjemite, modified from Pin and Lancelot (1982), SEM; 26 – in mafic gneiss, modified from Peucat et al. (1990), BM. **(28-30)** Magmatically resorbed grains without overgrowths. 28 – free xenocryst in granitoid rock, modified from Corfu and Ayres (1994), BM; 29-30 – highly resorbed xenocrysts in pyroclastic volcanic rock (from F. Corfu, unpublished data), BM. **(31-34)** Sub-rounded to multifaceted zircon in metamorphic rocks. 31 – in metagabbro, modified from van Breemen et al. (1986), SEM; 32 – in leucogranulite, modified from Kröner et al. (1998), SEM; 33,34 – in lower crustal xenolith, modified from Chen et al. (1998), SEM. **(35-36)** Meteorite impact related zircons. 35 – resorbed shocked zircon with traces of planar deformation features; 36 – post impact growth of polycrystalline zircon; both modified from Moser (1997), SEM.

whereas stubby and equant forms are more common in deep-seated, slowly cooled intrusions (Fig. 2.13–2.14).

Other factors affecting the shape of the zircon crystals are the composition and possibly the temperature of the crystallization medium. Systematic examination of zircon typology has led to the establishment of the widely used "Pupin diagram" (Fig. 2 inset), in which zircon crystals are classified according to the relative development of the {100} vs. {110} prismatic forms and the {211} vs. {101} pyramidal crystal forms (Pupin 1980). In general, zircon grains from relatively dry alkalic and tholeiitic igneous rocks tend to be dominated by {100} and {101} forms, where those

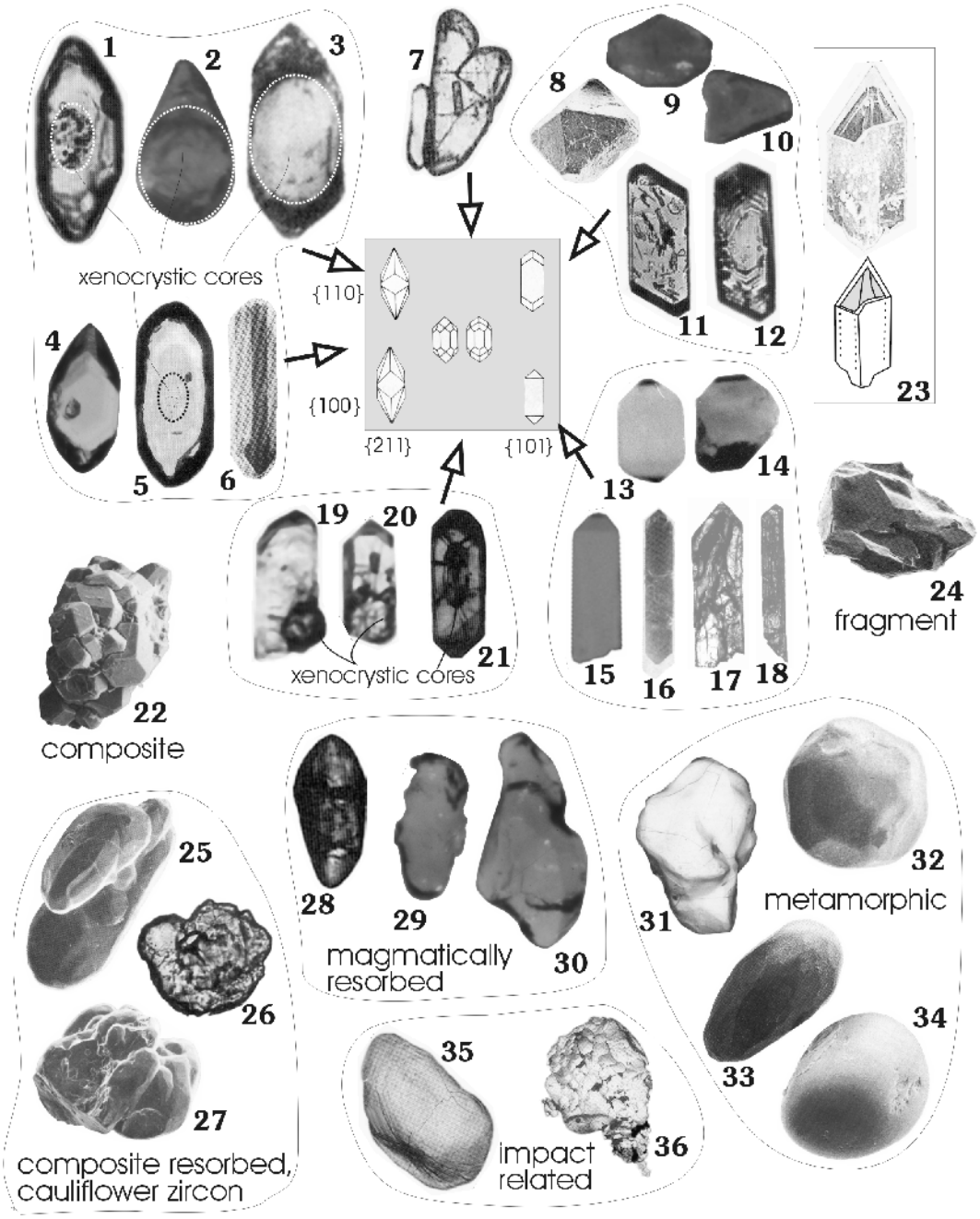

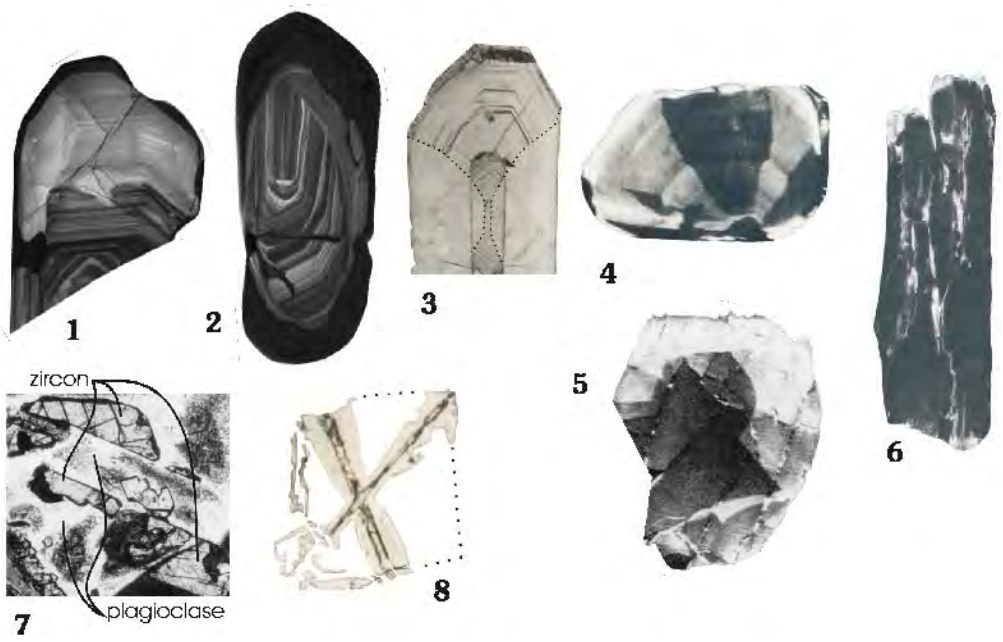


**Figure 3.** Complex and other types of zoning in magmatic rocks. All grains are between 70 and 250 μm. **(1-2)** Complex growth zoning with local intermediate resorption in zircon from anatectic granite, from P. Kinny (unpublished data), CL. **(3-4)** Sector zoning; 3 – section parallel to the c-axis (dotted line highlights the boundary between sectors), modified from Krogh (1982), RL of vapor etched grain; 4 – section normal to the c-axis, modified from Hoffman and Long (1984), CL. **(5-6)** Patchy zoning; 5 – zircon in norite with broad zoning superimposed by irregular domainal texture, modified from Paquette et al. (1995), CL; 6 – bright seams indicate altered fractures disrupting original zoning; modified from Vavra and Hansen (1991), CL. **(7-8)** Skeletal growth; 7 – incomplete zircon fragments growing on opposite sides of plagioclase, modified from Paquette et al. (1995), TL; 8 – incomplete zircon due to rapid growth, section perpendicular to the c-axis, modified from Krogh et al. (1982), TL.

from aluminous to calc-alkaline rocks exhibit various combinations of forms with a prominent presence of {211}, and those from water-rich granites and pegmatites tend to have {110} and {101} as their dominant forms. Pupin (1980) related the relative development of the prismatic faces mainly to the temperature of crystallization whereas the pyramidal faces were linked to chemical factors, and suggested that the typological parameters of a zircon population can be used to describe the evolution of a magma system. The somewhat simplistic nature of this interpretation has been challenged by Vavra (1993), who introduced a more sophisticated method to determine the relative growth-rates of zircon forms in order to characterize the kinetics of a crystallizing environment. Benisek and Finger (1993) also showed that compositional factors have a significant effect on the development of prism faces in zircon.

As mentioned above, the velocity of crystallization appears to be the major controlling factor of the elongation ratio for zircon. Skeletal zircon crystals are the most extreme form of rapid growth. Such zircons, observed locally in mafic and undersaturated alkaline rocks (Figs. 3.7 and 3.8) are characterized by the development of crystal-beams and walls surrounding empty space (Bossart et al. 1986). A comparable zircon type, exhibiting hollow prisms or other incompletely grown crystals, has been reported from cavities in basaltic andesite and interpreted to indicate rapid growth from a vapor phase (Fig. 2.23; Huneke and Rossman 1978). Many magmas tend to reach zircon saturation relatively early in their evolution and thus precipitation of zircon can accompany that of most other minerals. In some magmas, however, saturation is only reached late in the crystallization history, either because of very low Zr contents, or high Zr solubility or both (see Hanchar and Watson, this

volume). In these cases zircon forms late in pools of highly fractionated magma, either in isolated magma pools or interstitially to other minerals. Such zircons commonly exhibit only partially developed crystal faces (e.g., Poldervaart 1956, Scoates and Chamberlain 1995; Fig. 3.7), and they are recovered from mineral separation as an assortment of broken fragments (Fig. 2.24). This is a common feature for gabbroic rocks.

The opposite case occurs when a magma is oversaturated with respect to zircon for part or most of its crystallization. Such magmas are unable to completely dissolve restitic or assimilated zircon, which quite commonly become the seed of newly grown magmatic zircon. The appearance of xenocrystic zircon can thus range from highly "polished" grains free of any overgrowth (Figs. 2.28–2.30) to subrounded grains totally enclosed in new zircon mantles (Figs. 2.1–2.3; 2.19–2.21). In some rocks one can observe a whole range of occurrences from overgrowth-free xenocrystic zircon, xenocrystic cores and volumetrically-large mantles, to entirely new igneous zircon. In addition, newly-grown zircon crystals can themselves exhibit evidence for multiple stages of growth and corrosion. All these features can be linked to complex magma evolution from initial formation by source melting, through various stages of movement through the crust, contamination and perhaps mixing with different magma batches, fractional crystallization and differentiation, with loss of cumulates and vapor, and final emplacement or extrusion. The solubility of zircon itself is largely a function of the composition of the system, described by the parameter $M = (2Ca + Na + K)/(Si \times Al)$ as well as $H_2O$ content and temperature (Watson 1979, 1996; Harrison and Watson 1983, Watson and Harrison 1983, Hanchar et al., this volume).

Besides resorption that may occur when zircon is immersed in magma, resorption and modification, including recrystallization and Ostwald coarsening (Watson et al. 1989) can result from metamorphism. The slow diffusivity of most cations in non-metamict zircon suggests that no substantial water-free recrystallization will occur over geologically significant time periods by volume diffusion alone at the temperature conditions in normal continental crust (Cherniak et al. 1997a,b; Cherniak and Watson 2001, Cherniak and Watson, this volume). It is thus likely that any subsolidus modification of zircon will reflect active corrosion and precipitation mechanisms related to a fluid phase. Hence, it is also likely that any such reaction will occur coevally with metamorphic reaction of other mineral phases present in a rock.

As far as the external morphology is concerned, metamorphically grown, or metamorphically modified zircon crystals are generally characterized by subrounded and highly resorbed shapes (Figs. 2.25–2.27, 2.31–2.34), but euhedral shapes are also possible, especially in very fluid-rich systems such as in amphibolite facies mica schists or migmatites. Where in the former case, the development of crystal faces was probably facilitated mainly by the presence of aqueous or carbonic fluids, in the case of migmatites, zircon is likely to have grown in contact with a melt phase, and hence, strictly speaking is no longer metamorphic but magmatic. As for the subrounded metamorphic zircon type, it is possible to recognize various degrees of modification. Zircon crystals in some gneisses may only exhibit moderate rounding of the crystal edges whereas in others the original crystal shape has been destroyed, and the final product being smoothly subrounded grains (Fig. 2.31). This is commonly the case in granulite facies rocks, where zircon grains sometimes display multifaceted exteriors (Figs. 2.32–2.33). The grains may consist largely of reworked original zircon, or at the other extreme, comprise entirely new-grown metamorphic zircon. Metamorphosed mafic rocks locally contain irregular zircon grains such as the cauliflower type of Peucat et al. (1990) (Figs. 2.25–2.27). In some instances the shape of these grains may reflect resorption of originally irregular and fragmented zircons such as those recovered from some mafic rocks (Fig. 2.24), or of the composite crystals found in some granites (Fig. 2.22), but in other cases they likely represent metamorphically grown polycrystalline zircon. These are discussed in more detail later in this chapter. A special case shown in Figures 2.35 and 2.36 is that of shocked zircons from meteorite impact craters that reveal both traces of impact-related fracturing and rapid new growth of polycrystalline zircon in the immediate aftermath of impact.

## ZONING TEXTURES IN IGNEOUS ZIRCON

One of the more typical features of magmatic zircon is the presence of well developed growth zoning. This feature is best seen in CL and BSE images, but in zircon affected by metamictization of U-rich areas, zoning can be revealed very well by microscopic examination (BM, RL, TL).

The zoning reflects compositional variation of Zr and Si and more importantly, variations in Hf, P, Y, the REE, U and Th—up to an order of magnitude for some of these elements (e.g., Köppel and Sommerauer 1974, Benisek and Finger 1993, Hanchar and Rudnick 1995, Fowler et al. 2002, and many other studies). The composition of the zones tends to vary between two end-members, one of which is very low in trace-elements, approaching the composition of pure zircon, and the other a zircon component highly enriched in trace elements with up to several wt % of the impurity element (Speer 1982). The mode of development of the zoning also varies widely. In some cases one observes an almost bimodal succession of trace-element rich and trace-element poor bands with almost no intermediate compositions (Figs. 4.1 and 4.2) where in other cases the zones span a much wider compositional range (Figs. 4.3–4.12), or the compositional difference becomes very small yielding only faintly visible zoning patterns (Figs. 4.13–4.15), and in some cases there is no visible zoning at all (Fig. 4.16). The thickness of the bands also varies widely. For example the bands in Figure 4.1 are on the order of 20-100 μm wide, while those in Figure 4.2 are barely 5-10 μm wide. Fowler et al. (2002) show that periodicity can be observed at different scales in their zircon megacryst, ranging from 0.5 mm down to a few μm. Moreover, within individual crystals one can observe strong variations in the relative development of zoned domains, such as in Figures 4.11 and 4.12 where one large uniform central zone is succeeded by much finer oscillatory-zoned bands. Halden and Hawthorne (1993) have shown that the zoning pattern of zircon from a carbonatite can be quantified by spectral analysis.

The origin of growth zoning is discussed in some detail by Mattinson et al. (1996) who conclude that episodic growth results from the interplay between the stage of crystal growth, the nature of the crystal-liquid interface, the degree of supersaturation of the melt, the rates of diffusion, and the state of oxidation.

In the only study yet published that investigates zircon zonation patterns in zircon populations from a range of related rocks, Hoskin (2000) analyzed the variation of oscillatory zoning in zircon (Fig. 4.17) from compositional sectors of a zoned I-type pluton ($SiO_2$ from 50-75 wt %; diorite to aplite zones) using CL images and fractal statistical characterization. It was found that trace-element incorporation into zircon was affected by "external forcing" (processes occurring within the magma system and not at the crystal/melt interface). The result of external forcing is to impose increasing order (as measured by the mean Lyapounov exponent, $\lambda_m$, a statistical parameter) on the oscillatory zoning pattern as magmatic differentiation proceeds. The correlation between magmatic differentiation and increasing zonation order is related to ordering in the melt by polymerization. Hoskin (2000) presented a model for zonation pattern generation that accounts for dynamics at the zircon/melt interface, cation substitution, diffusion, and melt polymerization and structure generation. This model remains untested, although new generation ion probes (e.g., nanoSIMS) may provide a means to test the model.

It is quite commonly observed that regular growth zoning is interrupted by textural discontinuities along which the original zoning is resorbed and succeeded by the deposition of new-growth-zoned zircon (Figs. 4.1, 3.1 and 3.2). These resorption intervals probably reflect intermediate periods of Zr undersaturation in the magma, owing to large-scale mixing phenomena, or to local kinetic phenomena. For example, the zircon shown in Figure 4.15 derives from the charnockitic phase of a zoned pluton and is characterized by an irregular subrounded external appearance, an almost uniform internal texture, and evidence of marginal resorption and reprecipitation. These textures suggest that it may have formed by very slow and complex crystallization of a magma body with prolonged residence time in the lower crust. In contrast, the coeval zircon in a mangeritic part of the same pluton displays simple growth zoning and no evidence of resorption (zircon not shown).

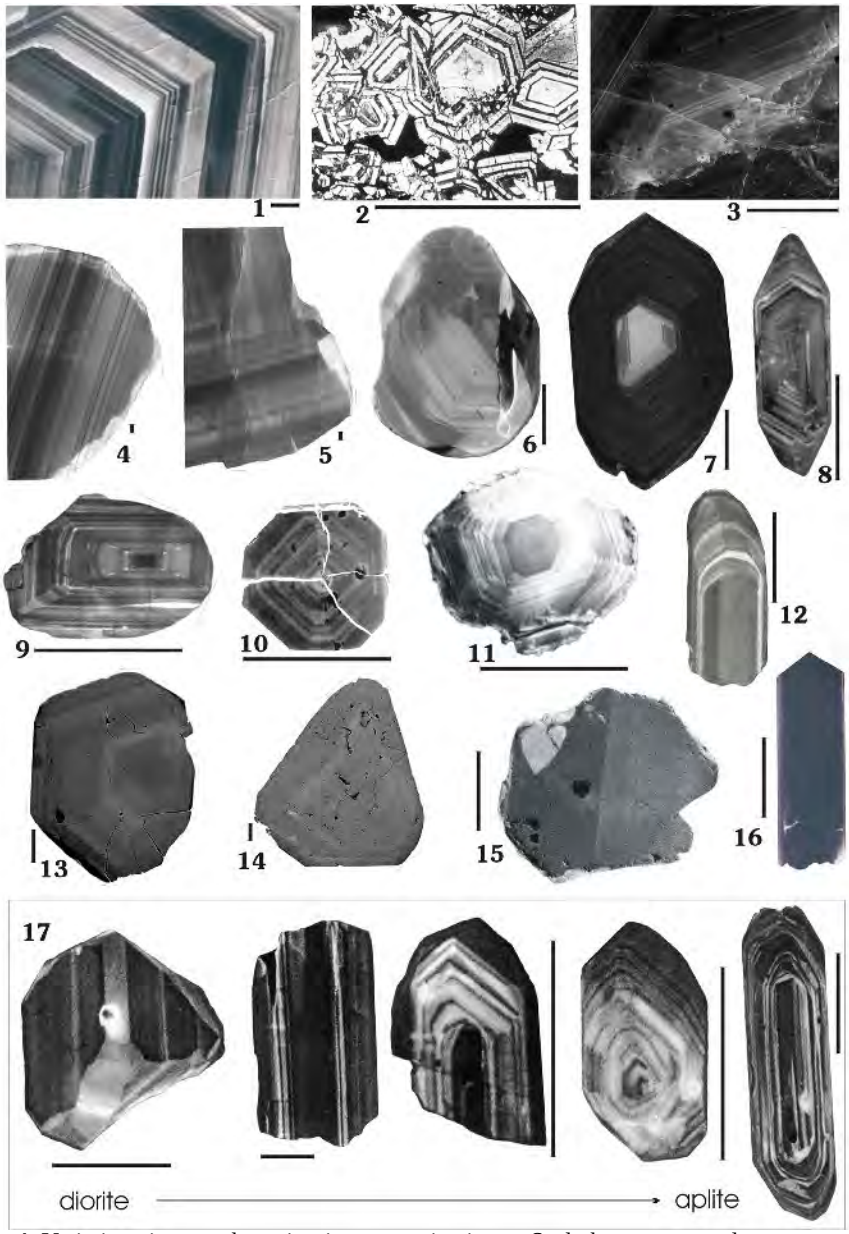


**Figure 4.** Variations in growth zoning in magmatic zircon. Scale bar corresponds to approximately 100 μm. **(1)** Zoned crystal from larvikite, from S. Dahlgren, unpublished data), CL. **(2)** Bimodal zoning, peralkaline complex, modified from Smith et al. (1991), BSE. **(3)** finely zoned crystal from carbonatite, from J. Hanchar (unpublished data), CL. **(4, 5**) zoned megacrystic zircon from kimberlite, from P. Kinny (unpublished data), CL. **(6-12)** growth zoning in typical crustal rocks: 6- from J. Hanchar (unpublished data), CL; 7 – from P. Kinny (unpublished data), CL; 8 – Poller (1997), CL; 9 – from P. Kinny (unpublished data), Cl; 10 – modified from Benisek and Finger (1993), BSE; 11 – from F. Corfu (unpublished data), CL, 12 – modified from Christoffel et al. (1999), CL. **(13-15)** Faint and broad zoning: 13 – carbonatite, from J. Hanchar (unpublished data), CL; 14 – pegmatite, from J. Hanchar (unpublished data), CL; 15 – mangerite (from F. Corfu (unpublished data), CL. **(16)** Homogeneous unzoned zircon in dacite, modified from Zeck and Williams (2002), CL. **(17)** Transition in style of zoning with differentiation of a pluton from diorite, through granodiorite, different adamellite phases, and finally aplite. Broad zones in zircon of diorite tend to become progressively narrower, but more frequent as the magma evolves; modified from Hoskin (2000), CL.

A special case of zoning is sector zoning. In the crystal shown in Figure 3.3, a section parallel to the c-axis, the pyramidal sectors are enriched in U (and presumably other trace-elements) whereas the prismatic sectors contain less U (Krogh 1982). In the example shown in Figure 3.4, the sectors are defined by variations between the two prismatic faces. Microprobe analyses of the different sectors reveal variations of 20-100% in Hf and Y, in part correlating with smaller changes in Zr and Si, (U is below detection limit; Hoffman and Long 1984). The development of sector zoning in zircon has been attributed to kinetic factors and rapid changes in the growth environment during crystal development (e.g., Paterson and Stephens 1992). Watson and Liang (1995) propose, however, that the occurrence of sector zoning is mainly dependent on the relation between growth rates and lattice diffusivity. In their model, particular growth surfaces are initially enriched in some elements with respect to others and these disparities are then preserved in the growing crystal if lattice diffusion is sufficiently slow. Vavra et al. (1996) attribute sector zoning to rapidly fluctuating and unequal growth rates related to the roughness of the growth surface and degree of saturation of the growth medium.

The skeletal zircon in Figure 3.8 represents an extreme case of preferential growth along specific crystallographic directions. Here, one of the prismatic faces has grown along four "ridges" that extend from the centre of the crystal (which presumably runs parallel to the c-axis). The second prismatic face only started to develop in exterior parts of the crystal late in the crystallization sequence. The central regions of the ridges remained hollow and locally may have been filled with high-U zircon, now highly metamict. Such cavities occur commonly in rapidly grown, elongated prismatic zircons.

A particular type of zoning is the irregular and patchy texture shown in Figure 3.5 (Paquette et al. 1995). This type of texture is reminiscent of undulatory extinction in strained quartz, and may reflect strain experienced by zircon during final magmatic emplacement. A distinct bending of very thin zircon crystals was observed by the first author in crystals 0.5-2 cm long from pegmatitic phases of two massive gabbroic intrusions, although the zircon was not examined by CL. The texture shown in Figure 3.5 suggests that the microfractures between the various domains were subsequently healed by new zircon growth during cooling. A somewhat similar patchy texture in elongated crystals with faint zoning and irregular longitudinal streaks (Fig. 3.6) has been interpreted by Vavra and Hansen (1991) to indicate local recrystallization along longitudinal microfractures.

Perfectly euhedral prisms without any evidence of zoning are locally observed in some rocks (Fig. 4.16). It is not clear whether the lack of zoning is due to the insufficient resolution of the imaging techniques used, or whether the particular growth environment and kinetics have contributed to form compositionally homogeneous crystals, or whether original zonation patterns have been destroyed.

## XENOCRYSTIC CORES

The occurrence of xenocrystic zircon is a common feature of many igneous rocks. Zircon xenocrysts occur as cores mantled by newly grown magmatic zircon, or simply as unmantled subrounded or rarely euhedral crystals (such as when zircon is assimilated into a magma during late-stage crystallization, with too little time for corrosion or overgrowth). The recognition of xenocrystic cores is easy in some rocks but more difficult in others. Where there are distinct differences in U-content between a core and rim, differential metamictization expands the high-U part and transforms the original colorless domains into pink to brown, or even opaque, zircon. If the core is richer in U than the rim, core expansion will eventually cause fracturing of the more rigid rim (Figs. 2.19–2.21; 5.1–5.4). In the opposite case, with a low-U core surrounded by a high-U rim, there is generally no fracturing (Figs. 2.1 and 2.3, but see Figs. 13.1 and 13.2 below) but the rim will become much darker than the core. The presence of such fracture patterns and the differential coloration allow us to identify core-rim textures by simple microscopic (BM) examination. For solution-based isotope analysis it is usually relatively simple to break-off cores and rims and analyze

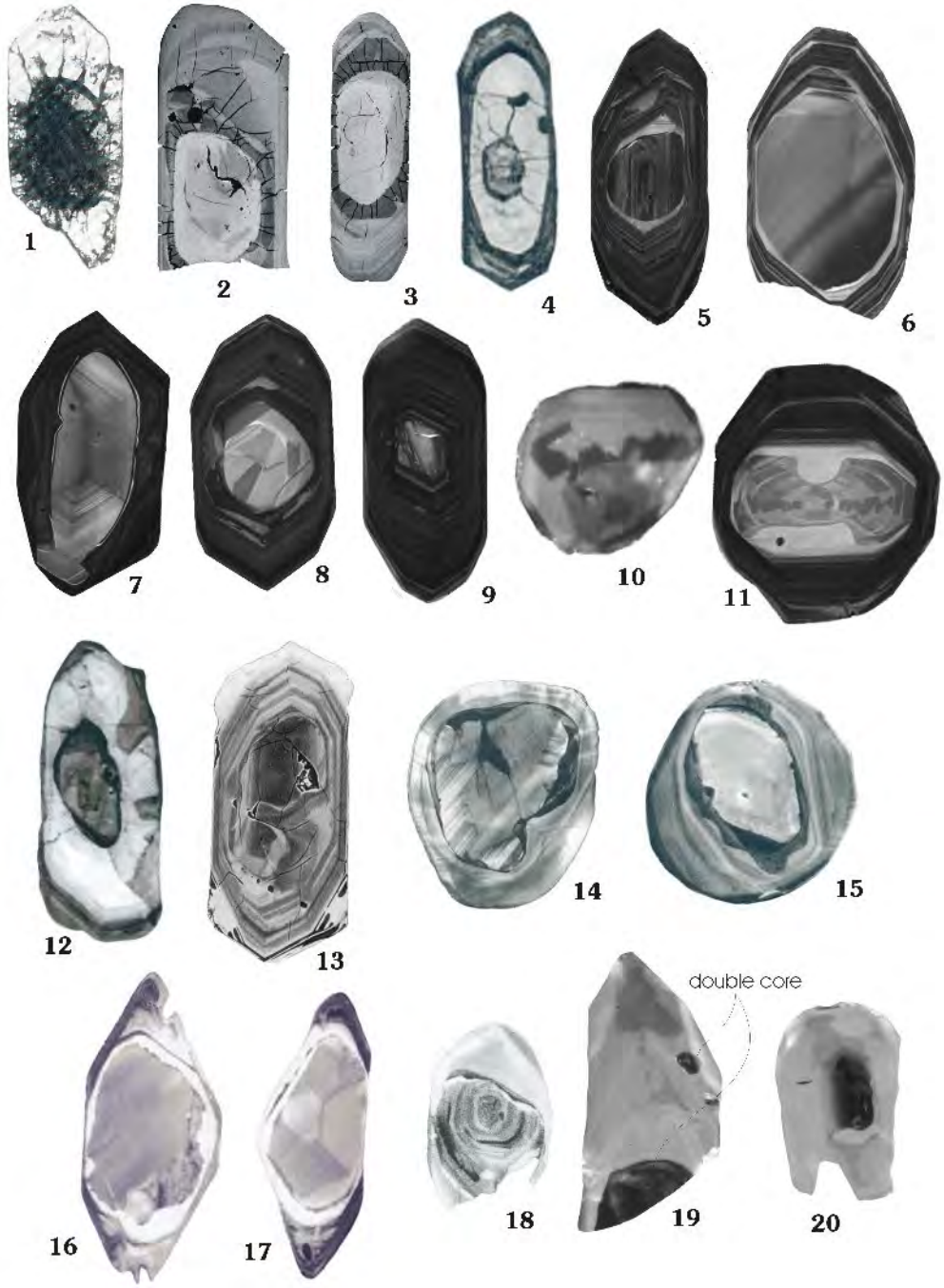


**Figure 5.** Variable appearance of xenocrystic cores in magmatic and high-grade meta-morphic rocks. **(1-20)** Variable appearance of xenocrystic cores in magmatic (1-13, 16-20) and high-grade metamorphic rocks (14-15), (all grains were between 70 and 250 μm in size); 1- Large metamict core has expanded and cracked the rim, modified from Welin et al. (1982), TL; 2, 3 – from J. Hanchar (unpublished data), BSE; 4 – modified from Corfu and Ayres (1984), RL; 5, 6, 7, 8, 9 – from P. Kinny (unpublished data), CL; 10 – from J. Hanchar (unpublished data), CL; 11 – from P. Kinny (unpublished data), CL; 12 – modified from Andersson and Williams (2001), CL; 13 – modified from Paterson et al. (1992b), BSE; 14-15 detrital cores, modified from Vavra et al. (1996), CL; 16,17 – modified from Zeck and Williams (2002), CL; 18 – modified from Whitehouse et al. (1999), CL; 19, 20 – from D. Moser (unpublished data), CL.

them separately for age determination. In some cases the only visible sign of a xenocrystic core is a trail of small bubbles at the core-rim boundary (Fig. 2.5).

Detection of core-rim textures becomes much more difficult in cases were both core and rim are low in U, and can thus remain colorless and unfractured even after 2 or 3 billion years. In such cases a simple visual examination under a binocular microscope will in general not be able to reveal the presence of a xenocrystic core, and even techniques like HF-etching may not help. By contrast, the application of CL or BSE imaging is successful in the majority of cases (e.g., Figs. 3.2, 5.5, 5.6, and 7.8 and 9.14 below) and, as noted above, it is often the case that different growth events preserved in zircon emit different color CL emission.

Xenocrystic cores are commonly differentiated from their rims by geometrically irregular surfaces, which truncate internal zoning (Figs. 5.5–5.8, 5.11 and 5.18) or separate subrounded, unzoned, or chaotically zoned cores from growth zoned rims (Fig. 5.2–5.3, 5.9, 5.12–5.16 and 5.19–5.20). Such discontinuities can indicate deep resorption of the early zircon phase (Figs. 5.7, 5.11–5.13), and locally they reveal that new zircon growth has occurred in a different crystallographic orientation than the substrate zircon (Fig. 5.11). In specific situations, however, it can be difficult to distinguish a xenocrystic core from other features such as zones of local recrystallization or specific magmatic growth bands, or to exactly locate the actual boundary between a core and a magmatic rim (Figs. 5.4, 5.12, 5.16 and 5.17). It is common to have more than one discontinuity within an individual zircon, and, in principle, they could indicate the presence of multiple core generations, a combination of core (early) and mantle (later) resorption events, or multiple stages of magmatic resorption within a single magmatic event. Interpretations can commonly be made with confidence, or the possibilities reduced, when the textural observations are combined with isotopic analysis of specific zones.

In some instances zoned xenocrystic cores can retain a euhedral outline that progresses—without apparent discontinuity—into zoned rims. In such cases, only isotopic analysis of specific areas (crystal middle and crystal edge) can delineate the presence of a xenocrystic core (Paterson et al. 1992b).

Some difficulties are met when one attempts to evaluate the origin of xenocrystic cores. In specific cases, key evidence can be provided by direct field observation. For example, xenocrystic cores found in zircon grown in a migmatite within a clastic sedimentary sequence, or in a classical S-type granitic body, can readily be interpreted as being of detrital origin. The frequency of isotopic ages and age omissions obtained for xenocrystic zircon populations can be linked to potential sedimentary sources. In the case of xenocrystic zircon cores found in granitic bodies of less obvious crustal origin it is not possible in general to unambiguously verify a detrital origin. If the source-region of a granitoid body is a mixed gneissic terrane, then the xenocrystic zircons could be both supracrustal and magmatic in origin; in other cases one could easily expect that multistage magmatic zircon will become incorporated into newly grown igneous zircon. Hence, in most cases a clear and straightforward interpretation of the origin of xenocrystic cores is not possible.

Xenocrystic cores themselves do not yield many clues as to their origin. Occasionally they preserve the abrasions and fracturing caused by erosion and sedimentation process (Figs. 5.14 and 5.15) that support independent evidence for a detrital origin, but otherwise such clues are too ambiguous to be trusted.

## SUBSOLIDUS MODIFICATIONS AND GROWTH OF ZIRCON

### Late-magmatic phenomena

Zircon can be affected by various processes at various times: the final stages of magmatic crystallization, during slow cooling of large intrusive bodies, and by later metamorphic events. Distinction between the effects of the processes is not always straightforward, and there is not always consensus on the interpretation of secondary textures.

Modifications of magmatic zircon during late and post-magmatic cooling tends to result in a disruption of concentric oscillatory zoning. One of the most commonly observed textures is the development of irregular domains of homogenous, low-U zircon cutting discordantly across growth zoned domains (Figs. 6.1–6.7). These domains are thought to develop by recrystallization, a process promoted by the relative instability of trace-element-rich domains with respect to trace-element-poor zircon. Recrystallization is probably promoted by the presence of magmatically derived aqueous fluids in deep-seated settings (Pidgeon 1992, Nemchin and Pidgeon 1997, Schaltegger et al. 1999). The recrystallization process expels trace elements, shifting the composition closer to that of pure zircon, and apparently concentrates the impurities in trace element-rich convolute zones (Figs. 6.5, 6.10–6.12 and 6.17; Pidgeon et al. 1998).

Another process appears to involve metasomatic replacement of zircon creating trace-element-rich domains. For example, the zircon prism displayed in Figure 6.16 is characterized by a mosaic texture which appears to have developed by modification of an originally low-U zircon, either during a late magmatic stage or subsequent metamorphism (Corfu and Ayres 1984). The occurrence of "bent" prisms in this population suggests that development of the mosaic texture may have been preceded by the formation of a patchy (strained) texture similar to that observed in Figure 3.5.

**Medium to high temperature metamorphism**

The three zircons shown in Figures 6.13–6.15 display the progressive development of a veined and brecciated texture starting from relatively homogeneous zircon (Ashwal et al. 1999). U-Pb dating indicates that the amount of veining affecting these zircon grains correlates with the degree of younging, indicating that loss of Pb was caused by metamorphic recrystallization, in which case grain boundary diffusion most likely overrode volume diffusion. Similarly, the bulbous replacement or recrystallization texture displayed by the zircon crystal in Figure 6.6 has been shown to have occurred during a metamorphic event (Schaltegger et al. 2002). Connelly (2001) has documented very subtle metamorphic recrystallization, which has led to a gradual but homogeneous fading of original growth zoning and is correlated with extensive amounts of Pb loss.

Zircon in high-grade metamorphic rocks display a wide diversity and complexity of textures that reflect variations in the physico-chemical conditions and the duration of each metamorphic event, and are caused by modifications of pre-existing structures and/or by growth of new zircon (Fig. 7). The least severely affected zircon grains can partially preserve vestiges of an original growth zoning, only locally modified by metamorphism, thus displaying textures closely resembling those for late-magmatic recrystallization as discussed above (Figs. 7.1–7.5; cf. Fig. 6) (Hoskin and Black 2000). Igneous protolith zircon from the Proterozoic Georgetown Region, Australia, experienced variable recrystallization during an upper-amphibolite-grade event. The zircon largely preserves igneous oscillatory zoning, although this becomes progressively convoluted, blurred and thickened in response to metamorphism. The dominant texture, however, is transgressive (across all pre-existing textures) zircon patches and lobes. Areas of recrystallization occur dominantly at crystal terminations, but also anywhere else within the interior of a crystal and sometimes apparently not connected to the crystal surface. Of significance is the preservation of relics of primary textures (growth zoning) within areas of recrystallisation. These relics are termed the "ghost texture" and are responsible for "mixed" isotopic ages and trace-element abundances between growth-zoned and fully recrystallized areas. Hoskin and Black (2000) interpreted these textures to represent recrystallization in the solid-state because ghost textures and the isolation of some recrystallized areas from the crystal surface are inconsistent with a local dissolution/reprecipitation (fluid) process.

In general, zircon in granulite facies rocks tends to be characterized by very chaotic textures. Concentric zoning, when present (Figs. 7.6–7.12), is rather irregular and resembles only weakly the parallel or regular geometry of zoned magmatic zircon (cf. Fig. 4). Some variants of sector and fir-tree zoning are very common (Figs. 7.13–7.19), the latter reflecting strong fluctuations of growth rates (Vavra et al. 1996). The most extreme textural types have abstract and chaotic designs that

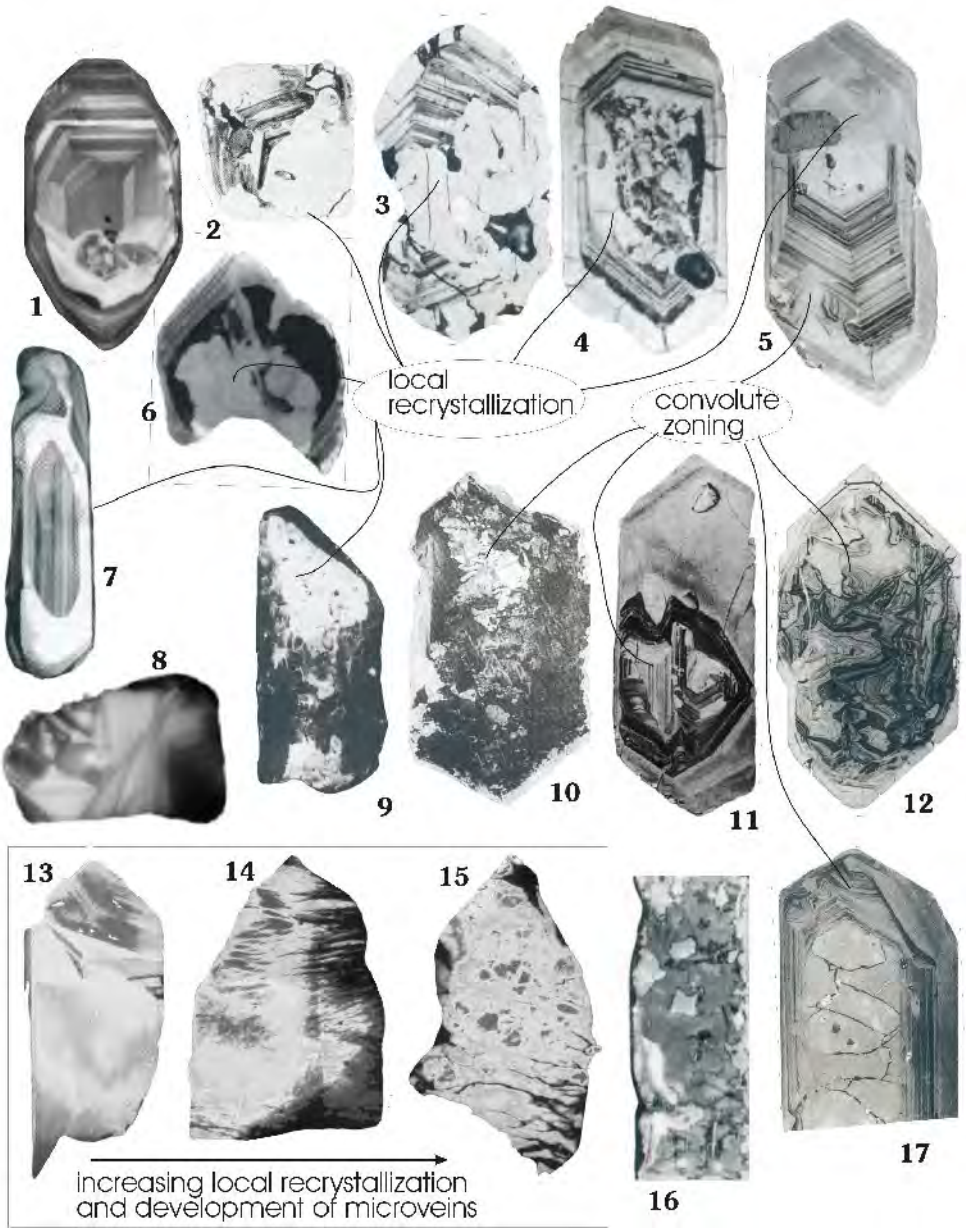


**Figure 6.** Late to post-magmatic recrystallization of zircon. The grains shown are between 70 and 250 μm in size. **(1)** Oscillatory zoning cut off by area of re-homogenized zircon, modified from Poller (1997), CL. **(2-7)** Partially preserved growth zoned zircon penetrated by trangressive zones of recrystallization and with local development of convolute zoning; 2,3 – modified from Pidgeon (1992); RL; 4, 5 - modified from Nemchin and Pidgeon (1997), RL; 6 – modified from Schaltegger et al. (2002), CL; 7 - modified from Andersson and Williams (2001), CL. **(8)** "cross-bedding type" texture (from J. Hanchar, unpublished data) **(9-12, 17)** Heterogeneous patchy pattern and convolute zoning attributed to post-crystallization purification of crystal structure with progressive migration of trace element rich bands; 9 - modified from Vavra and Hansen (1991), CL; 10 – modified from Mulch et al. (2002), CL; 11, 12, 17 – modified from Pidgeon et al. (1998), RL. **(13-15)** Zircon in leuconorite exhibiting increasing amount of local recrystallization and microveining (with addition of U), which correlates with resetting of U-Pb age, modified from Ashwal et al. (1999), CL. **(16)** Patchy, mosaic texture, indicating metasomatic replacement of low-U domain by zircon richer in U (and presumably other trace elements), modified from Corfu and Ayres (1984), RL.

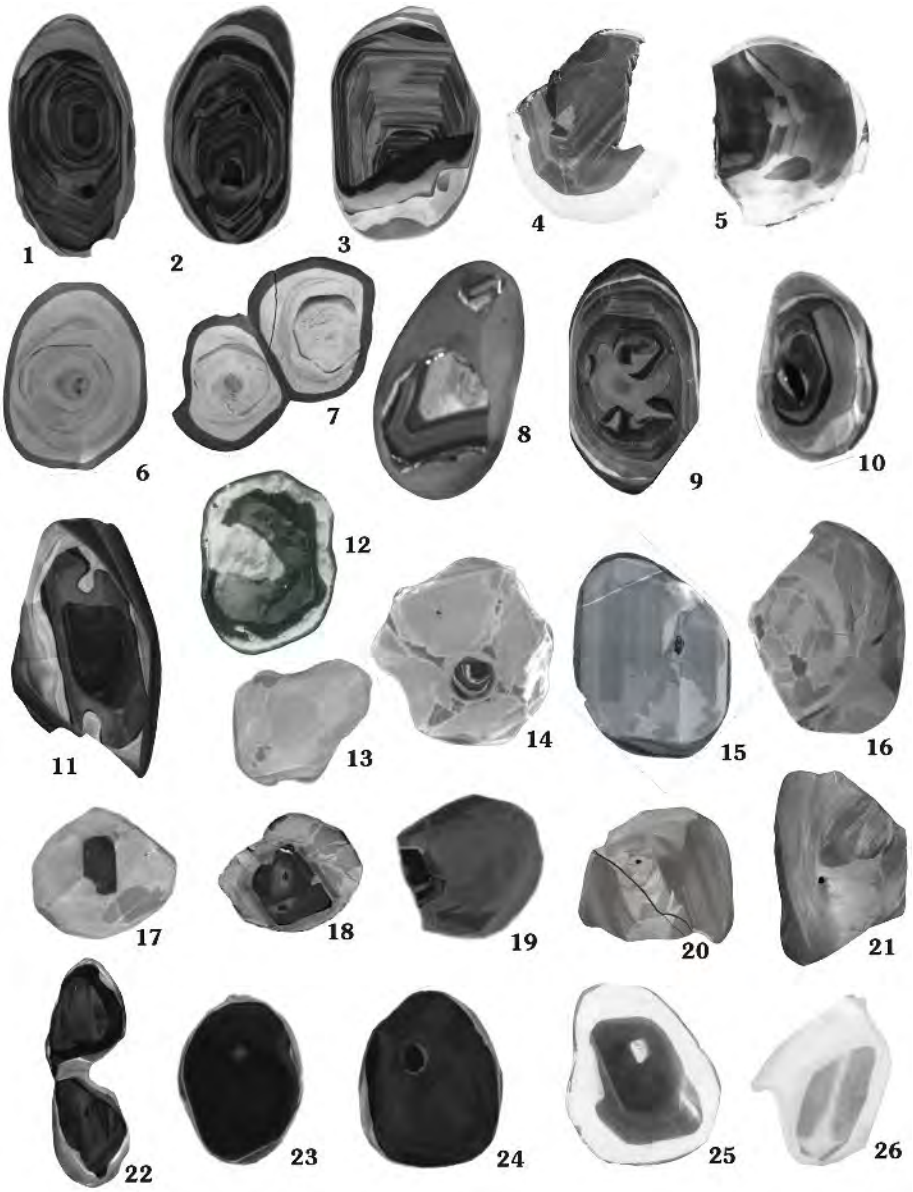


**Figure 7.** Recrystallization and new growth of zircon in high-grade metamorphic rocks. All grains between 70 and 350 μm in size. **(1-5)** Original euhedral zircon is cut by recrystallized or newly grown domains of more homogeneous composition; 1, 2 – Akilia gneisses, from P. Kinny (unpublished data), CL; 3– Akilia gneisses, modified from Nutman et al. (2002); 4, 5 – lower crustal xenoliths, modified from Moser and Heaman (1997), CL. **(6-12)** Zircon displaying very irregular concentric zoning locally overprinted by zones of recrystallization or new growth; 6, 7, 8 – lower crustal xenolith, from M. Schmitz (unpublished data), CL; 9, 10, 11 – in various metamorphic rocks, from P. Kinny (unpublished data), CL; 12 – in mafic granulite, modified from Peucat et al. (1990), CL. **(13-19)** Sector and fir-tree zoning, locally surrounding older zircon components; 14,16 – in lower crustal xenolith, modified from Schmitz and Bowring (2002b), CL; 15 – in granulite facies rock, modified from Pidgeon et al. (2000), CL; 13,17,18 – in high-grade gneisses, from P. Kinny (unpublished data), CL. **(20-22)** Chaotic textures with local appearance of 'flow' domains; 20,21 – lower crustal xenoliths, modified from Schmitz and Bowring (2001), CL; 22 – in migmatitic gneiss, from P. Kinny (unpublished data), CL. **(23-25)** Bands or other large segment of homogeneously textured zircon; 23, 24 – Akilia gneiss, from P. Kinny (unpublished data), CL; 25 – lower crustal xenolith, modified from Moser and Heaman (1997), CL, 26 – in granulite, modified from Bingen et al. (2001a), CL.

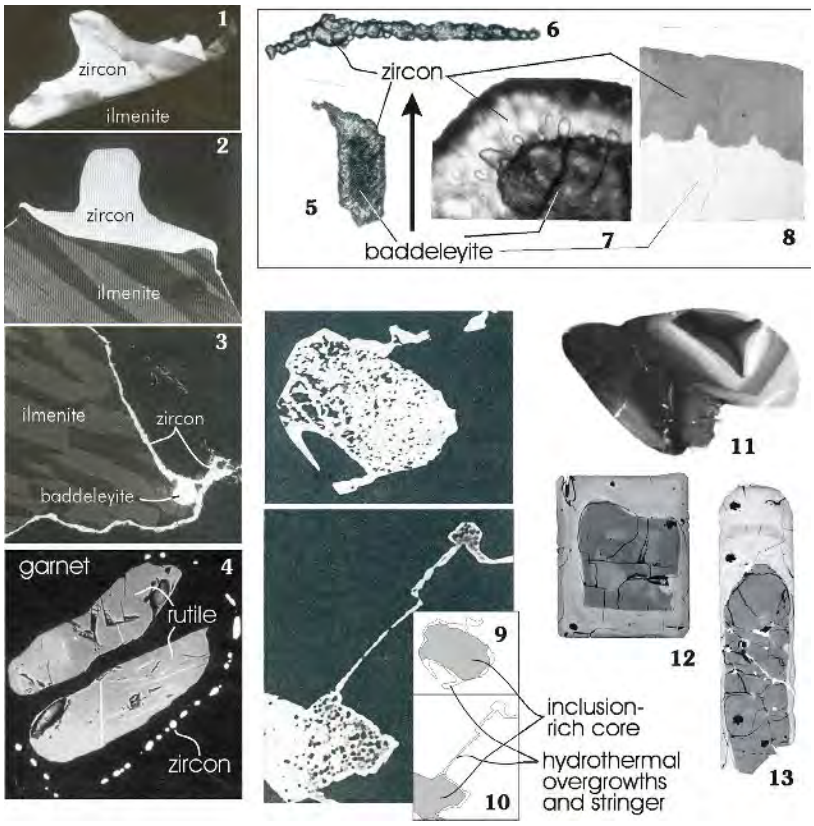


**Figure 8.** Modes of metamorphic-hydrothermal zircon growth. **(1-3)** Development of zircon in granulites; 1,2 – hat-shaped zircon wrapping around ilmenite, 3 – Thin layer of zircon coating ilmenite, in contact with a baddeleyite grain; modified from Bingen et al. (2001a), 1 = CL, 300µm wide; 2, 3 = BSE, 100 µm wide. **(4)** Zircon forms string of beads around rutile, both surrounded by garnet, modified from Bingen et al. (2001a), BSE, 100 µm wide. **(5-8)** Formation of zircon from baddeleyite; 5 – zircon corona around baddeleyite, TL (thin section), 100 µm long; 6 – chain of zircon crystals in plagioclase (complete reaction from baddeleyite); TL (thin section), 250 µm long; 7, 8 – detail of zircon-baddeleyite relationship, TL (7) and BSE (8), image ca. 80 µm wide; all modified from Davidson and van Breemen (1988). **(9-10)** Late-magmatic zircon, inclusion (thorite) – rich, overgrowth by hydrothermal, inclusion-free zircon, modified from Rubin et al. (1989), BSE, grains are 5 to 10 µm wide. **(11)** Metasomatic zircon in ultramafic rock, modified from Grieco et al. (2001), CL. **(12-13)** U-rich hydrothermal replacement rims around low-U zircon, from J. Hanchar (unpublished data) BSE, both crystals are ca. 100 µm wide.

combine stepwise growth patterns with flow structures (Figs. 7.20–7.22). Besides these geometrically complex patterns, it is not uncommon to find zircons, or at least large domains of zircons, that are completely homogeneous (or nearly so) when examined by common imaging techniques (Figs. 7.23–7.26; also parts of other grains in Fig. 7). In the case of domains that are homogeneously dark in CL (or light in BSE), they can be suspected to be free of zoning because the luminescence may be poisoned by high trace-element contents or by metamictization. However, the domains that provide very bright CL images are likely to be genuinely homogeneous as they have very low trace-element contents. Figures 7.8, 7.11 and 7.12, in particular, indicate how such domains evolve as marginal bands and as lobes that locally penetrate the interior of grains, but locally they also form amoebic zones entirely enclosed in the centre of the grains (Fig. 7.9).

Bingen et al. (2001a) describe how metamorphic zircon in a granulite developed hat-shaped overgrowths on older zircon and ilmenite (Fig. 7.26), or very long, thin coatings following the

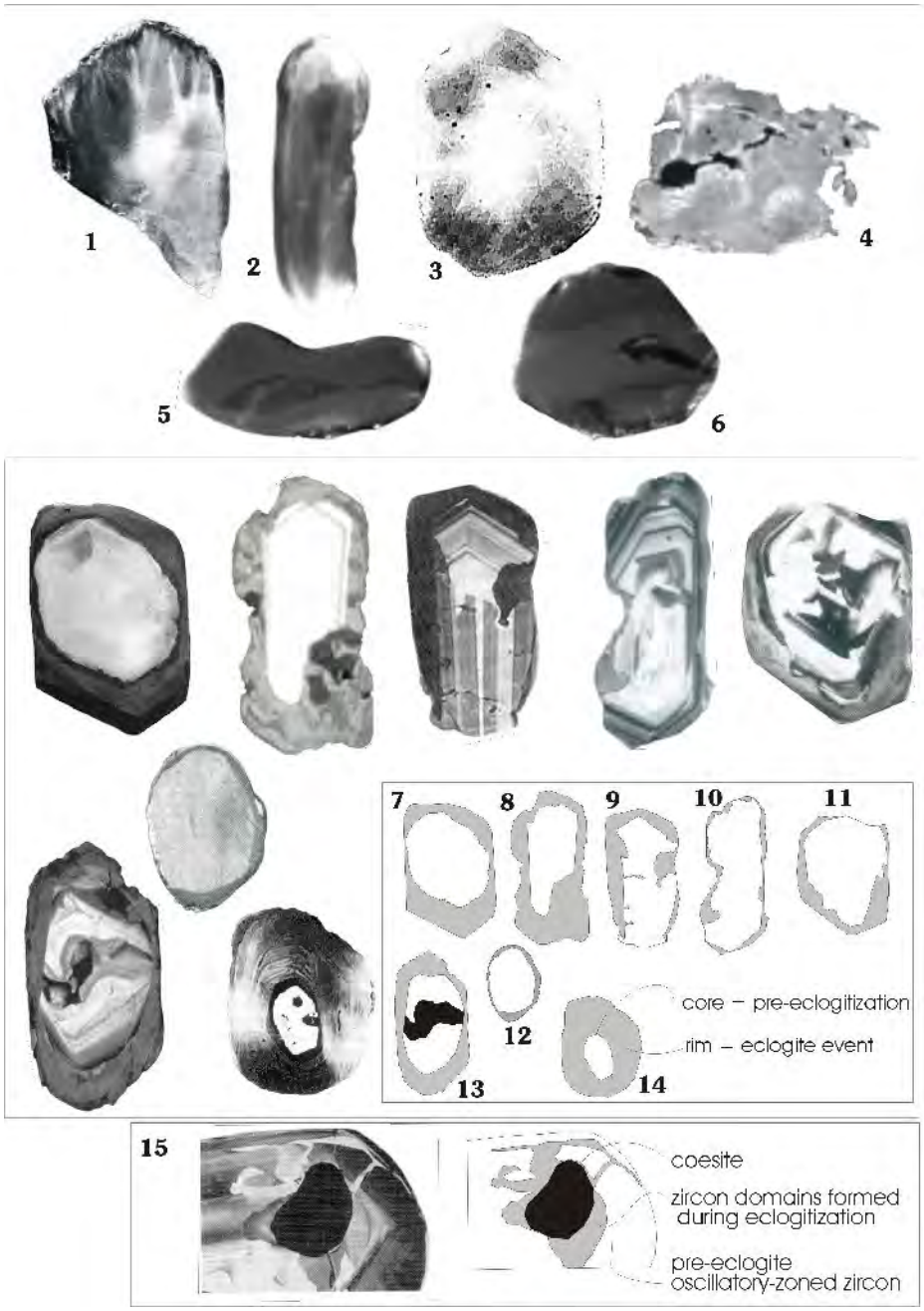


**Figure 9.** Zircon in high-pressure rocks. The grains shown are all between 70 and 300 μm in size. **(1-3)** Irregular, diffuse (auroral-light) zoning; 1 – Corfu et al. (2002), CL; 2 – modified from Schmitz and Bowring (2002a), CL; 3 – modified from Rowley et al. (1997), CL. **(4-6)** Largely homogeneous texture; 4 – modified from Lopez Sanchez-Vizcaino et al. (2001), CL; 5,6 – modified from Schmitz and Bowring (2002a), CL. **(7-14)** Eclogitic zircon replacing and rimming pre-metamorphic phase; 7- modified from Rubatto et al. (1998), CL; 8 – modified from Hacker et al. (1998), CL; 9 – modified from Gebauer et al. (1997), CL; 10,11 – modified from Rubatto and Gebauer (1999), CL; 12 - modified from Oberli et al. (1994), CL; 13 – modified from Liermann et al. (2002), CL; 14 - modified from Rowley et al. (1997), CL. **(15)** Relationship between old-zoned zircon and zircon domains formed metamorphically together with the coesite pseudo-inclusion, modified from Gebauer et al. (1997), CL.

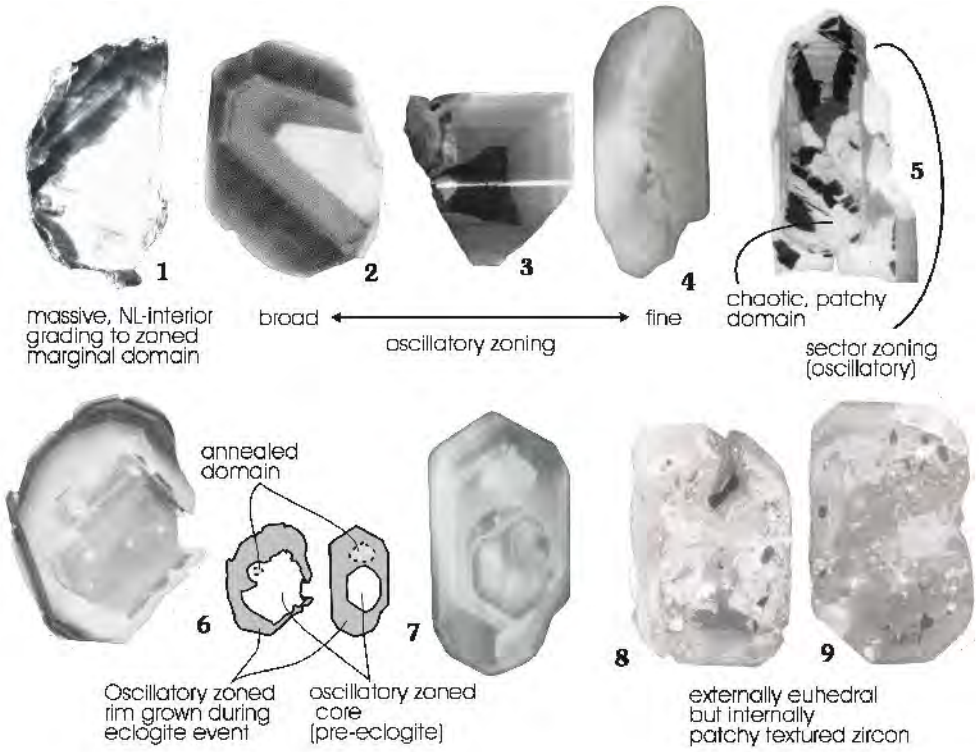


**Figure 10.** Zoning of zircon in high-pressure rocks. The grains shown are all between 70 and 300 μm in size. **(1)** Internal diffuse zoning rimmed by growth zoned marginal domain; Corfu et al. (2002), CL. **(2-4)** Variation in growth zoning, 2 – modified from Gebauer et al. (1997), CL; 3 – modified from Rubatto et al.(1998), CL; 4 – modified from Bingen et al. (2001b), CL. **(5)** complex zoning, modified from Rubatto et al. (1998), CL. **(6-7)** cored eclogitic zircon with zoned texture; 6 – modified from Gebauer et al. (1997), CL; 7 - modified from Bingen et al. (2001b), CL. **(8-9)** Patchy textured zircon in eclogite, modified from Bröcker and Enders (1999), CL.

grain-boundary of or fractures in ilmenite (Figs. 8.1–8.3), and deduce that the required Zr was provided by the breakdown of ilmenite and baddeleyite.

**High-pressure metamorphism**

Understanding the nature of zircon in eclogites is an intriguing and difficult task, especially given that the dating of high-pressure events is significant for the reconstruction of the history of ancient collisional belts. In the simplest cases, eclogite zircons are subrounded and somewhat irregular, but display relatively homogeneous internal textures. The example in Figure 9.1 exhibits a wavy “auroral light” texture. This texture is typical for a zircon population yielding an isotopic age that dates a high-pressure event (Corfu et al. 2002). A similar texture is also shown by the grains in Figures 9.2 and 9.3, whereas those in Figures 9.4–9.6 are more uniform but locally contain darker zones.

In general, eclogites contain complex zircon types. One common type contains two distinct phases, older relicts pre-dating eclogitization of the rock surrounded and/or penetrated by new metamorphic zircon (Figs. 9.7–9.15). Cores can be homogeneous or growth zoned, locally with traces of earlier resorption and recrystallization (Figs. 9.9 and 9.13). Metamorphic rims are generally homogeneous to somewhat heterogeneous, and are separated from cores by irregular interfaces indicative of corrosion. The latter feature is especially evident in Figure 9.15, which shows new metamorphic

zircon developed, together with coesite, in a cavern in the interior of the original crystal. The new material likely penetrated from outside the crystal along a network of thin fractures.

The homogeneity of metamorphic zircon and intra-crystalline domains discussed above contrasts with the oscillatory zoning shown by zircon in Figure 10. The metamorphic nature of the latter is supported, in each case, by the consistency of their U-Pb ages within geological context. In general, the zoning is regular, defining either very fine or very coarse bands, and is quite similar to that of magmatic zircon (Figs. 10.1–10.4; 10.6 and 10.7). A complex pattern more typical of granulite facies zircon crystals is shown by the grain in Figure 10.5. The grain shown in Figure 10.1 is the only grain within a zircon population (examined by CL; see also Fig. 9.1) that shows such marginal fine-scale zoning. More prominent development at the margin of the grain is also evident in Figure 10.6. The presence of such zoning in metamorphic zircon runs against "common wisdom" and has caused some consternation in the literature. Gebauer et al. (1997) suggest that the zoning seen in such grains (Figs. 10.2 and 10.6) probably reflects crystallization in local melt or supercritical fluids that may have developed at peak metamorphic conditions. They also draw attention to the occurrence within these grains of homogeneous domains around small inclusions, suggesting that they represent zones of annealing that caused exchange of chemical elements with the inclusion (Figs. 10.6 and 10.7).

A more unusual texture is the highly irregular patchy pattern (Figs. 10.8 and 10.9) observed in euhedral zircon from a low-temperature eclogite from Greece (Bröcker and Enders 1999). The authors interpret the zircons as having formed by metasomatic processes during a high-pressure event, although it could be argued that the eclogite event may only have caused textural disruption rather than new zircon formation. Some clues concerning the mechanisms that form zircon in eclogite have been provided by Bingen et al. (2001b) who suggest that zircon coronas around ilmenite are cannibalized during breakdown of ilmenite (to rutile and garnet; Fig. 8.4) to form larger zircon grains.

## HYDROTHERMAL ZIRCON

This is a somewhat artificial subdivision since it could be that all metamorphic zircon growth (and resorption) occurs only in the presence of a fluid phase (silicate melt or aqueous fluid). The reaction producing zircon during baddeleyite breakdown (Figs. 8.5–8.8; Davidson and van Breemen 1988) involves the addition of silica and probably also other cations, since such zircons have, for example, quite different Th/U ratios than the parent baddeleyite. The transport of silica and other cations is probably via aqueous fluid. Other examples of zircon growth that may have been assisted by fluid are the growth of zircon on ilmenite (Figs. 8.1–8.3) in granulites and the coronas of microzircons observed around rutile in eclogites (Fig. 8.4).

Hydrothermal zircon growth has been described in a peralkaline environment (Figs. 8.9 and 8.10; Rubin et al. 1989), where metasomatism appears to have occurred during late-stage magmatic crystallization. The metasomatic zircon shown in Figure 8.11 developed during metasomatism of ultramafic rocks in the mantle (Grieco et al. 2001). In a similar setting, zircon has been observed in association with baddeleyite/zirconolite rims in metasomatic veins cutting mantle peridotite (Kinny and Dawson 1992). The examples in Figures 8.12 and 8.13 indicate the formation of high-U zircon margins, which in some cases are simple overgrowths, but more commonly are embayments into low-U regions in the zircon crystals. These high U regions may have formed by metasomatism, or by recrystallization, or dissolution and reprecipitation during an event, which probably was accompanied by regional hydrothermal activity (McLelland et al. 2001, Hanchar et al. in preparation). The well preserved outer boundary of the crystal would tend to support some simple replacement mechanism although the nature of this process remains elusive. The pattern observed for the grains in Figures 3.6 and 6.13–6.15 may well fit a similar process. Most likely, these high-U regions in the zircon crystals are not the result of simple volume diffusion of U diffusing in and Zr diffusing out based on the sluggish kinetics of U-diffusion in zircon under crustal conditions (Cherniak et al. 1997b).

Although on occasions workers suggest that their zircons are of hydrothermal origin, ambiguity still exists. Unequivocal occurrences of aqueous-fluid precipitated zircon reveal it to have a

"spongy" texture (Wayne and Sinha 1992, Hacker et al. 1998—Fig. 3 therein; Hoskin et al. 1998) and to be extremely enriched in high-field strength elements, the REE (Hoskin et al. 1998), non-radiogenic lead (Watson et al. 1997) and F (Hoskin 1999). We consider these characteristics to be useful criteria for identifying zircon crystallization from aqueous fluids at low pressure (<2 kbar), low temperature (<500°C) and high water/rock ratios.

## KIMBERLITIC AND MANTLE-RELATED ZIRCON

The term "kimberlitic zircon" is used here to refer to megacrystic zircons commonly found in kimberlite, carbonatite, alkali basalt and other magmas of deep-seated origin, and more rarely found as a component of syenitic xenoliths carried by such magmas. The dominant characteristic of kimberlitic zircon is their common large size (up to cm size) and anhedral morphology (Kresten et al. 1975; Belousova et al. 1998). The internal textures display a broad range of variation. The megacrysts shown in Figures 11.1–11.4 are largely homogeneous, except for some faint outlines of large angular domains, possibly related to fracturing. The grain in Figure 11.5 preserves a very faint

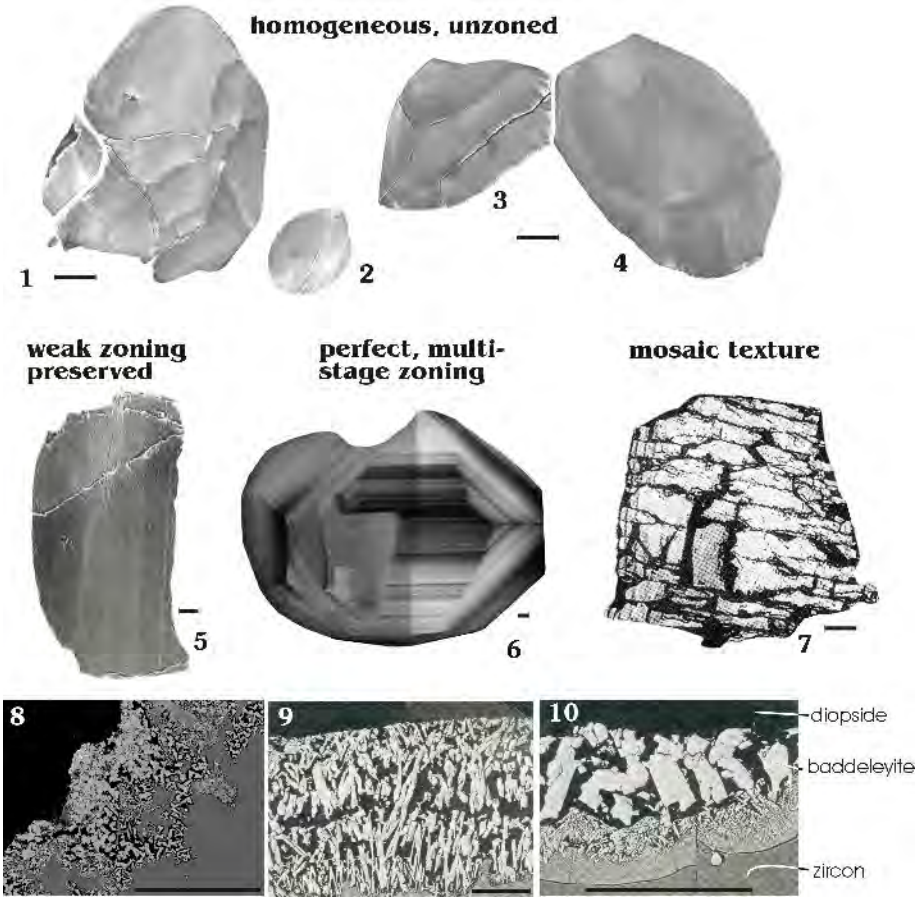


**Figure 11.** Kimberlitic zircon. Scale bar is ca. 100 μm. **(1-4)** Homogeneously textured zircon in metasomatized mantle xenolith in kimberlite, from P. Kinny (unpublished data), CL. **(5)** Faintly zone kimberlitic zircon, modified from Schärer et al. (1997), CL. **(6)** Well zoned kimberlitic zircon, from P. Kinny (unpublished data), CL. **(7)** Mosaic texture under polarized light, modified from Schärer et al. (1997), TL. **(8-10)** Breakdown of kimberlitic zircon to baddeleyite, 8 – from P. Kinny (unpublished data), BSE; 9,10 – modified from Heaman and LeCheminant (1993); BSE.

and broad zoning texture. By contrast, the grain shown in Figure 11.6 reveals a splendid, though complex, growth zoning. Two similar grains are shown in Figures 4.4 and 4.5. The reason for these variations is not clear. Perhaps the poor development of zoning in some grains may be related to prolonged residence of the megacrysts at very high temperatures in the mantle, which may have led to partial or complete homogenization of any original zoning, in which case those megacrysts with well preserved zoning would not have remained in the source region for a long time. Certainly, the commonly observed age relation of megacrysts to the erupting magma is one of short pre-eruptive residence time for the megacrysts, but there are exceptions. Another common observation is that, where present, the oscillatory zonation in kimberlitic zircons is often truncated by the anhedral grain margin (e.g., Figs. 4.4 and 4.5) indicating that despite their large size they have been substantially resorbed from originally larger grain-sizes.

Figure 11.7 illustrates a polarized light view of the same grain seen in Figure 11.5. The distinct mosaic structure has been interpreted as a possible brittle stress-related feature affecting the zircon at great depths (Schärer et al. 1997) although this is more likely due to rapid pressure reduction prior to eruption.

Figures 11.8–11.10 show a commonly observed reaction rim between zircon and other silicates leading to the formation of intervening baddeleyite and occasionally also zirconolite (Heaman and LeCheminant 1993). These desilification reactions have been linked to episodes of metasomatism in the mantle, but may also develop during late-stage contact of zircon megacrysts with a silica-undersaturated, ascending magma.

## IMPACT-RELATED TEXTURES

A rare class of zircon comprises those grains related to large meteorite impacts. Their most diagnostic characteristic is the presence of multiple sets of planar deformation features (Figs. 12.1–12.6 and Fig. 2.35), which are revealed particularly well by scanning electron microscopy (SEM) on etched surfaces (Bohor et al. 1993). These features, however, can often also be seen with normal transmitted or reflected light microscopy (Figs. 12.2 and 12.4) in grain-mounts, or in thin section. Under a binocular microscope, shocked grains appear whitish and highly turbid to completely opaque, but occasionally it is possible to detect the characteristic planar features (Krogh et al. 1984, 1993).

At increasing degrees of shock the zircons develop granular textures and turn into polycrystalline grains (Figs. 12.7 and 2.36). Under the most extreme conditions they start to melt, a process that results in textures such as those shown in Figures 12.8 and 12.9. Shocked zircon grains that get trapped in an impact melt layer may grow new rims, which are distinguished mainly by their lack of impact-related deformation, indicating that they formed after the immediate impact event (Figs. 12.5, 12.6 and 2.16). Such zircons are invaluable for dating the time of the impact (Kamo et al. 1996, Moser 1997, Gibson et al. 1997).

## FRACTURING

Differential metamictization of zircon causes volume expansion of the U-rich domains (Holland and Gottfried 1955) with consequent fracturing of the more resistant and brittle low-U domains (e.g., Chakoumakos et al. 1987; Figs. 13.1–13.4). Typically the fractures start at the interface with the more metamict domains or with high-U inclusions and develop radially outward across the low-U bands (Figs. 2-19–2.21; 5.1–5.4; 13.1 and 13.2). There is also a second type of fracture which develops concentrically along the boundary between high and low U domains (Figs. 13.2 and 13.3). Lee and Tromp (1995) discuss the parameters involved in the development of such fracture systems concluding that they are controlled principally by the degree of metamictization, the relative "shell" thickness and the confining (external) pressure. They also suggest that the latter factor may provide a tool to estimate the depth of residence of a rock. This may not be achievable, however, because the elevated temperatures of the lower crust increase the rates of self annealing to the point where zircon fractures are rarely developed. This is demonstrated by the generally very

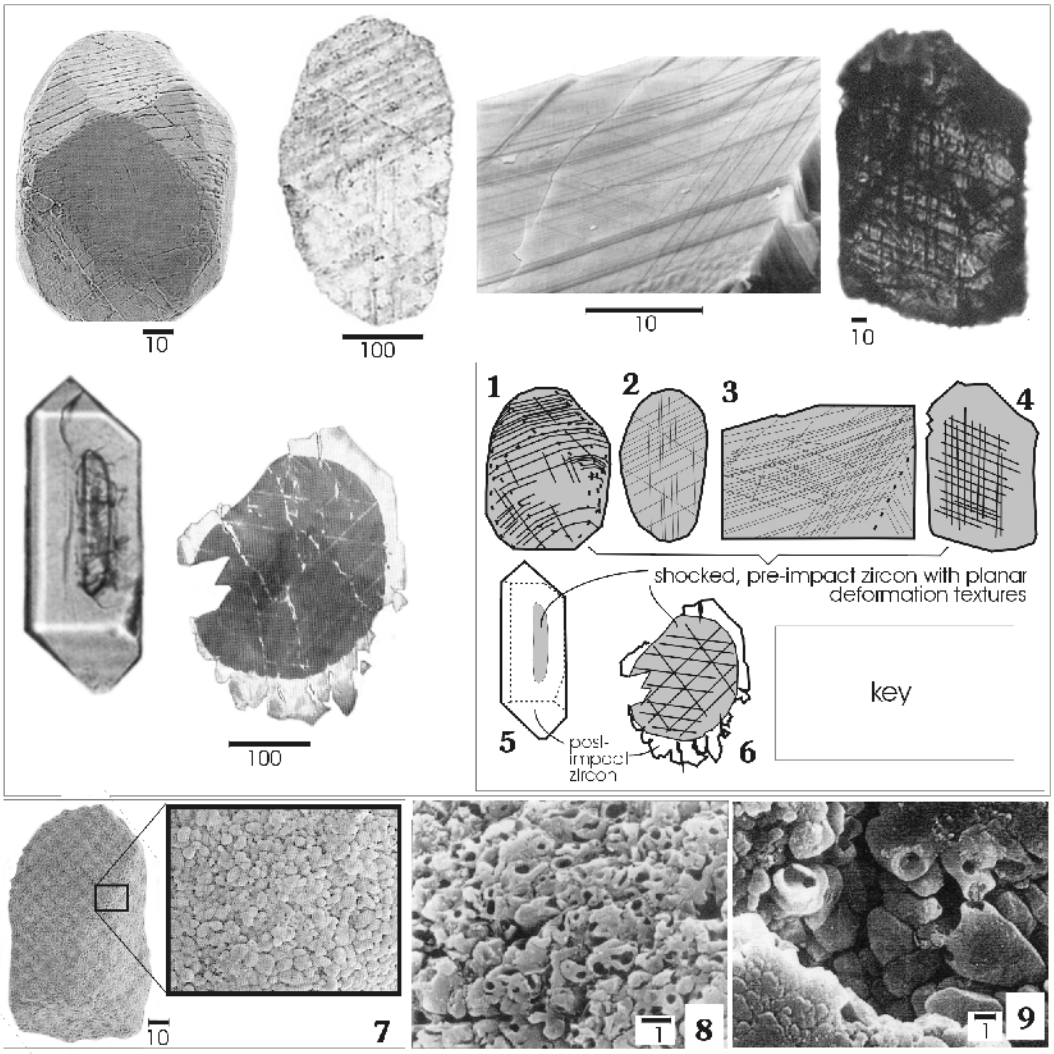


**Figure 12.** Appearance and texture of zircon in meteorite impact structures. **(1, 2)** Shocked zircon crystals from charnockite in Vredefort structure, modified from Kamo et al. (1996), 1 = SEM, 2 = TL, crossed nicols. **(3**) Euhedral zircon with three sets of planar deformation features; Manicouagan impact crater, modified from Bohor et al. (1993); SEM. **(4)** Multiple sets of planar deformation features in shocked zircon in Copper Cliff rhyolite, Sudbury structure, from F. Corfu (unpublished data), TL. **(5, 6)** Zircons from post-impact granite from Vredefort structure, modified from Gibson et al. (1997); 5 – euhedral crystal without shock-related features enclosing a fractured core (RL); 6 – zircon core with three sets of planar deformation features surrounded by post-impact unfractured zircon rim (CL). **(7)** granular zircon grain from granophyric part of melt-breccia dyke, Vredefort structure, modified from Kamo et al. (1996), SEM. **(8, 9)** polycrystalline grains with degassing and melting textures; 8 – K/T distal impact ejecta, Berwind Canyon, Colorado, modified from Bohor et al. (1993); SEM; 9 – Onaping Formation (impact melt), Sudbury structure, modified from Krogh et al. (1996), SEM.

good preservation of zircon in exhumed lower crustal rocks (e.g., Rudnick and Williams 1987, Hanchar and Rudnick 1995).

The parallel breaking shown by the zircon from a lower crustal xenolith in Figure 13.5 is a more rare occurrence. It has been interpreted to represent rapid decompression during eruption of the carrier volcanic rock (Rudnick and Williams 1987). It might be analogous to the deformation

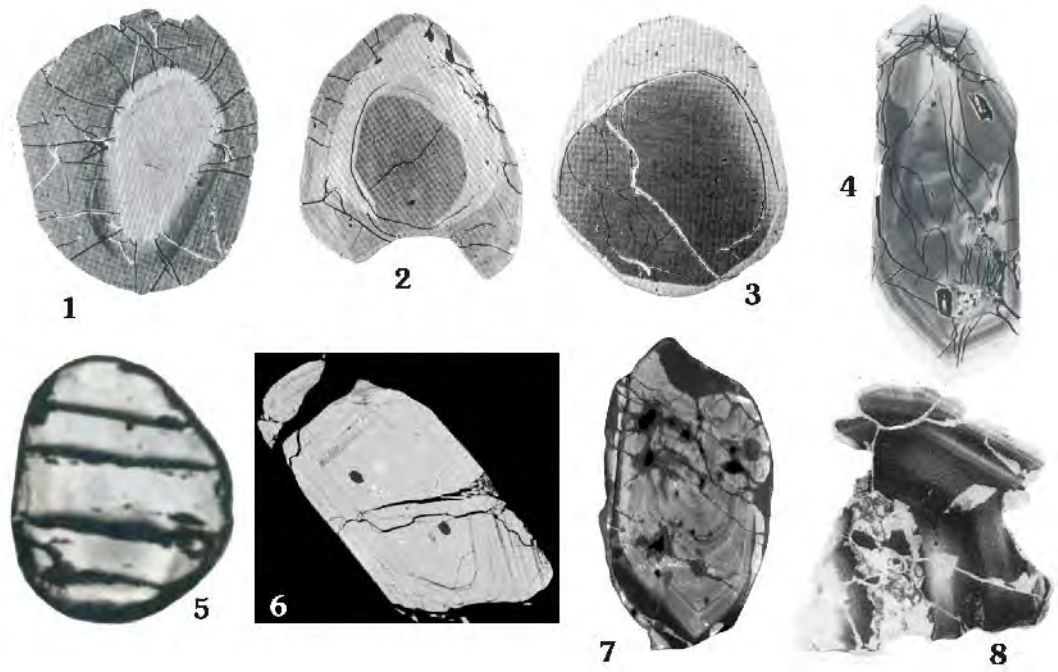


**Figure 13.** Fracture patterns in zircon. **(1-3)** Radial and concentric fractures in zircon from the Musgrave Ranges (modified from Lee and Tromp 1995; BSE); 1- radial fractures starting at the margin of the high-U+Th central part and propagating into the external, low-U+Th shell; 2 – expansion of the middle, U-Th-rich shell causes concentric fractures along the central part and radial fractures in the rim; 3 – metamictization of the high-Th+U rim causes concentric fracturing of the interface to the less metamict inner part. **(4)** Fractured zircon from Strontian pluton (modified from Paterson et al. 1992b, BSE); most of the cracks propagate from two spots that contain U+Th-rich inclusions but the fractures become concentric along the margin to the outermost high-U+Th rim. **(5)** Zircon from lower crustal xenolith (eastern Australia) showing pronounced parallel parting, apparently reflecting deformation during rapid decompression (modified from Rudnick and Williams 1987, TL). **(6)** Zoned zircon from a Witwatersrand conglomerate fractured during compaction between quartz and pyrite pebbles; the fractures are now healed with quartz; modified from Medenbach (1976), RL on polished section. **(7)** Ancient fractures, propagating from inclusions, were healed by the low-luminescence material grown metamorphically in external domains of zircon from upper crustal xenolith; modified from Schmitz and Bowring (2001), CL. **(8)** Fractures healed by luminescent material; modified from Rubatto et al. (1998), CL.

mechanism producing mosaic textures observed in some kimberlitic zircons (Fig. 11.7). Other factors that cause zircon fracturing are external stresses during mylonitization (Wayne and Sinha 1988) or diagenesis (Fig. 13.6; Medenbach 1976). When subjected to progressive diagenesis, or other metamorphic overprints, such fracture systems may heal and only be visible in specific circumstances (Fig. 13.7–13.8; also Figs. 3.5, 3.6 and 9.15).

## ALTERATION

Chemical alteration is generally seen in zircon grains that are extensively metamictized and where pathways are available (e.g., grain boundary diffusion) for fluids to penetrate the structure. These pathways are most commonly the fracture systems discussed above, but occasionally also textural discontinuities (e.g., zoning, Fig. 14.5) and interfaces between zircon and inclusions of other minerals (Fig. 14.7). Alteration typically forms bulbous, botryoidal fronts, but locally also feathery textures (Fig. 14.2), that propagate along the cracks and within the crystal. The grain shown in Figure 14.1 consists of a low-U central part, surrounded by a high-U mantle, itself locally rimmed

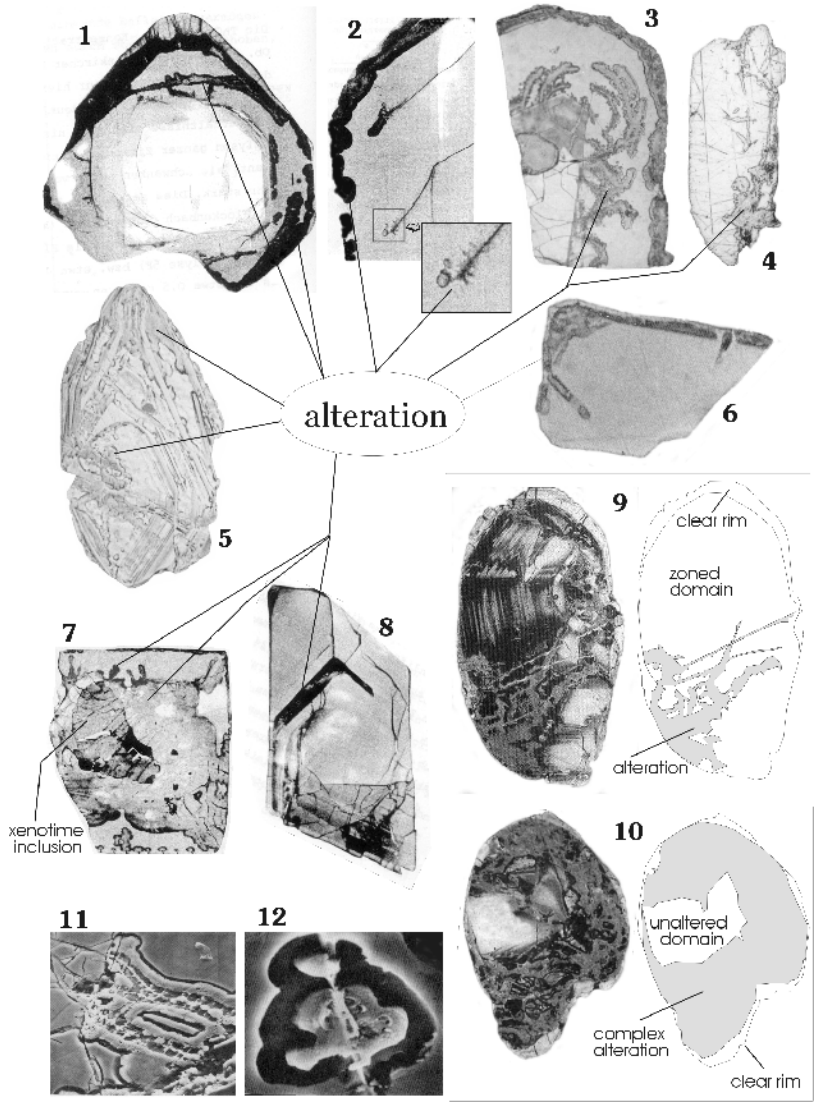


**Figure 14.** Patterns of alteration in zircon. **(1)** Alteration developed along concentric fractures parallel to the boundary between the low-U interior part of the zircon and the high-U outer shell; an outermost low-U rim has radial cracks, which have allowed the access of the fluids; modified from Medenbach (1976), RL. **(2)** Detail of a high-U zircon showing an outermost alteration ring and two internal alteration fronts with botryoidal and feathery propagation patterns; modified from Medenbach 1976), RL. **(3)** Zircon grain with low-U, fractured interior part surrounded by a high-U external band; alteration has developed both along an external rim and along curvilinear paths originating at the fractures in the euhedral, low-U inner zone; modified from Krogh and Davis (1974), RL. **(4)** Local alteration around fractures parallel and orthogonal to the c-axis; from F. Corfu (unpublished data), RL. **(5)** Zoned zircon with alteration controlled mainly by crystallographic discontinuities; modified from van Breemen et al. (1987), BSE. **(6)** High-U, homogeneous zircon with alteration restricted to its margin; modified from Krogh (1982), RL.**(7)** Zircon grain with a large inclusion of xenotime surrounded by an extensive zone of hydration propagating outwards, and with minor appendices moving inwards from the margin; modified from Medenbach (1976), RL. **(8)** Extensively altered, narrow high-U zones inside largely low-U zircon; modified from Medenbach (1976), RL. **(9,10)** Complexly zoned and altered zircon from the 4.0 Ga Acasta gneiss; modified from Bowring and Williams (1999), RL. **(11,12)** Brief exposure to HF vapor has dissolved the altered and hydrated part leaving behind ridges and plateaus of unaltered zircon; modified from Krogh and Davis (1975), SEM.

by a thin low-U zone. The latter is radially cracked allowing fluids to penetrate into the high-U material, which became altered—the alteration front propagating along concentric fractures. In Figure 14.3, a low-U central zone has become fractured allowing access (presumably from areas along the c-axis) to fluids, which then attack the surrounding metamict zone. The latter is also affected by alteration along an outer ring, the two alteration zones gradually approaching each other. Figures 14.4–14.6 and 14.7 illustrate other combinations of the same phenomenon, whereas Figure 14.8 displays the case of a predominantly low-U zircon with just a few high-U zones that have been reached by fluids along cracks in the low-U material and have become almost totally altered. The two grains in Figures 14.9 and 14.10 are ancient zircon crystals from the Acasta gneiss (Bowring and Williams 1999) that exhibit extremely complex alteration patterns penetrating zoned zircon domains and totally enclosing local islands of homogeneous unaltered zircon.

The alteration process has been shown to hydrate zircon, leaching some elements such as Pb and depositing others such as Fe and Ca (and possibly common Pb), hence making the mineral unsuitable for isotopic analysis (Krogh and Davis 1974, 1975; Medenbach 1976, Krogh 1982). The altered zones are much more soluble than crystalline zircon, and can be easily dissolved by brief exposures to dilute Hf vapor, providing a 3-dimensional image of the alteration process (Figs. 14.11 and 14.12).

## INCLUSIONS, INTERGROWTHS AND OVERGROWTHS OF ZIRCON AND OTHER MINERALS

The relations between zircon and the minerals it includes, or which it is included in or overgrown, can provide important clues concerning crystallization conditions and paragenetic associations. This information can be critical when it comes to the interpretation of U-Pb zircon ages. Zircon crystals commonly carry inclusions of other minerals (Figs. 2.4, 2.7, 2.11, 13.4; 15.1–15.12; 15.18–5.19), especially of the main rock-forming minerals such as biotite, quartz and feldspar, but their relative abundance varies significantly between different populations. The study of mineral inclusions in metamorphic zircon helps to constrain the relative paragenesis of zircon with respect to the main rock-forming minerals. Zircons also often contain inclusions of melt that was present when the zircon crystallized (see Thomas et al., this volume, for a discussion of melt inclusions in zircon crystals). As an example, the zircon grains shown in Figures 15.1–15.3 include, or are included in, high pressure minerals such as diamond, garnet and coesite. Inclusions of melt and fluids (Figs. 15.5–15.9) can provide information on the composition of magma and gases at particular stages in the evolution of a magmatic or metamorphic system. Figure 15.9 illustrates the particular example of a kimberlitic zircon including both solid mineral inclusions as well as numerous fluid inclusions, which display very distinct crystallographically controlled arrangements.

Figures 15.10 and 15.11 show examples of zircon containing numerous inclusions of common minerals such as quartz and apatite, together with U and Th-rich components and many cavities. In general, the interpretation of such inclusions in highly metamict and altered grains is difficult because the inclusions could be either real xenocrysts or exsolved phases, or phases introduced after the formation of zircon. This is the case with the zircon grain shown in Figure 15.13 that contains secondary monazite crystallized along a crack in the crystal, or the zircon in Figure 15.12 that contains abundant galena introduced into the zircon long after its original crystallization. Figure 9.15 is an example of where omphacite was included in the zircon grain but it is surrounded by healed cracks, hence it was formed during the secondary eclogite event that affected the zircon (Gebauer et al. 1997). The crystallographically controlled baddeleyite inclusions in zircon (Fig. 15.14) presumably reflect the breakdown of zircon to baddeleyite and silica (cf. also McLaren et al. 1994).

The structural affinity (i.e., isostructural) of zircon and xenotime means that the two minerals are locally found in association with each other in the form of xenotime overgrown by zircon (Figs. 14.7; 15.17), or the other way around (Figs. 15.16 and 15.17), or as complex intergrowths (Figs. 15.18 and 15.19). The two xenotime crystals attached to zircon in Figure 15.15 were formed during diagenesis and can thus be used to constrain the age of sedimentation (e.g., Fletcher et al. 2000).

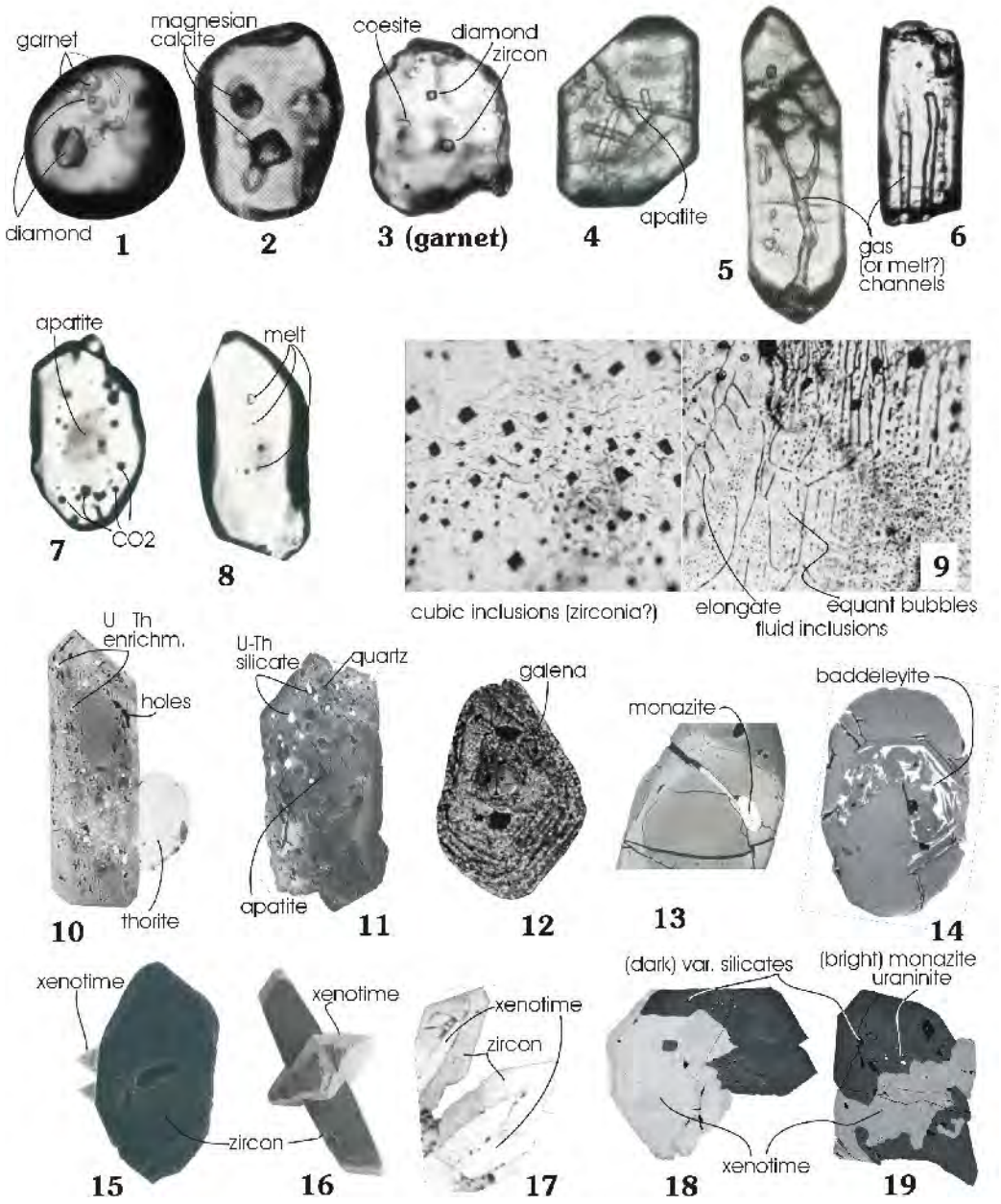


## CONCLUDING REMARKS

The above presentation emphasizes the variety of internal and external features that characterise zircon, and shows how such features can be used to extract valuable information concerning the geological history and petrogenetic context of zircon. The diagnostic value of such studies is naturally much increased once the zircon features are considered in conjunction with elemental or isotopic constraints from the same mineral and in the context of well characterised rock units. It is also important to keep in mind that the interpretation of some features such as growth zoning or resorption phenomena can be somewhat ambiguous and controversial. Thus some caution is required when textural interpretations are carried out.

**Figure 15.** Inclusions, intergrowths, and overgrowths in zircon. All grains shown here are about 100 to 200 μm in size. **(1-3)** Zircon from an ultra-high pressure gneiss contains inclusions of garnet and diamond (1), and magnesian calcite (2) but is itself included in garnet together with diamonds and coesite (3); (modified from Korsakov et al. 2002, TL). **(4-5)** Zircon in granitic rock with needle like apatite inclusions (4) and an elongated, bifurcating cavity (with melt?) (5); (modified from Bussy and Cadoppi 1996, TL). **(6)** Tubular cavities in zircon from charnockite (modified from Chiarenzelli and McLelland 1993; TL). **(7-8)** Melt inclusions (8) and $CO_2$ plus an apatite inclusion (7) in zircon from a lower crustal xenolith (modified from Rudnick and Williams 1987, TL). **(9)** Inclusions in zircon of kimberlite. **Left:** cubic minerals (zirconia?; 10-20 μm wide); **right:** oriented trails of fluid inclusions (droplets or elongated channels, <10 μm wide)(modified from Kresten et al. 1975, TL). **(10)** Porous zircon from peralkaline granite with numerous U and Th rich inclusions and a lateral overgrowth of thorite (modified from Poitrasson et al. 1998, BSE). **(11)** Inclusions of quartz, apatite and a U-Th silicate phase in zircon from diorite (modified from Mulch et al. 2002, BSE). **(12)** zircon from a sedimentary rock in the Oklo fossil reactor; the crystal is sprinkled with galena inclusions (white spots) introduced during late hydrothermal events (modified from Mathieu et al. 2001, BSE). **(13)** Monazite growing in a fracture in zircon (modified from Barbey et al. 1989, BSE)**. (14)** Baddeleyite replacement inside zoned zircon from tonalitic gneiss (modified from Barth et al. 2002, BSE). **(15)** Detrital zircon with lateral outgrowths of two diagenetic xenotime crystals (modified from Fletcher et al. 2000, BSE). **(16)** Euhedral xenotime overgrowing zircon (modified from Schärer et al. 1994, SEM). **(17)** Zircon overgrowths on xenotime crystals in peralkaline magmatic complex (modified from Smith et al. 1991, BSE). **(18-19)** Intergrowth of zircon and xenotime in leucogranite sill. Convolutely zoned cores of both phases are rimmed by oscillatory zoned material and then by a broad homogeneous mantle (modified from Viskupic 2003, CL).

## ACKNOWLEDGMENTS

Thanks to Sven Dahlgren, Desmond Moser, Urs Schaltegger, Mark Schmitz and Karen Viskupic for providing unpublished images and Mark Schmitz for his attentive review.

## REFERENCES

Abati J, Dunning GR, Arenas R, Diaz Garcia F, Gonzalez Cuadra P, Martinez Catalan JR, Andonaegui P (1999) Early Ordovician orogenic event in Galicia (NW Spain): Evidence from U-Pb ages in the uppermost unit of the Ordenes Complex. Earth Planet Sci Lett 165:213-228

Andersson J, Williams IS (2001) Late-magmatic modification of zircon in the 1.38 Ga Tjärnesjö granite, eastern Sveconorwegian orogen, SW Sweden. *In* Andersson J (2001) Sveconorwegian orogenesis in the southwestern Baltic Shield—Zircon geochronology and tectonothermal setting of orthogneisses in SW Sweden. Doctoral thesis, Lund University, Sweden

Ashwal LD, Tucker RD, Zinner EK (1999) Slow cooling of deep crustal granulites and Pb-loss in zircon. Geochim Cosmochim Acta 63:2839-2851

Barbey P, Bertrand J-M, Angoua S, Dautel D (1989) Petrology and U/Pb geochronology of the Telohat migmatites, Aleksod, Central Hoggar, Algeria. Contrib Mineral Petrol 101:207-219

Barth MG, Rudnick RL, Carlson RW, Horn I, McDonough WF (2002) Re-Os and U-Pb geochronological constraints on the eclogite-tonalite connection in the Archean Man Shield, West Africa. Precambrian Res 118:267-283

Belousova EA, Griffin WL, Pearson NJ (1998) Trace element composition and cathodoluminescence properties of southern African kimberlitic zircons. Mineral Mag 62:355-366

Benisek A, Finger F (1993) Factors controlling the development of prism faces in granite zircons: A microprobe study. Contrib Mineral Petrol 114:441-451

Bingen B, Austrheim H, Whitehouse M (2001a) Ilmenite as a source for zirconium during high-grade metamorphism? Textural evidence from the Caledonides of western Norway and implications for zircon geochronology. J Petrol 42:355-375

Bingen B, Davis WJ, Austrheim H (2001b). Zircon U-Pb geochronology in the Bergen arc eclogites and their Proterozoic protoliths, and implications for the pre-Scandian evolution of the Caledonides in western Norway. Geol Soc Am Bull 113:640-649

Bohor BF, Betterton WJ, Krogh TE (1993) Impact-shocked zircons: discovery of shock-induced textures reflecting increasing degrees of shock metamorphism. Earth Planet Sci Lett 119:419-424

Bossart PJ, Meier M, Oberli F, Steiger RH (1986) Morphology versus U-Pb systematics in zircon: A high-resolution isotopic study of a zircon population from a Variscan dyke in the Central Alps. Earth Planet Sci Let 78:339-354

Bowring SA, Williams IS (1999) Priscoan (4.00-4.03 Ga) orthogneisses from northwestern Canada. Contrib Min-

eral Petrol 134:3-16
Bröcker M, Enders M (1999) U-Pb zircon geochronology of unusual eclogite-facies rocks from Syros and Tinos (Cyclades, Greece). Geol Mag 136:111-118
Bussy F, Cadoppi P (1996) U-Pb zircon dating of granitoids from the Dora-Maira massif (western Italian Alps). Swiss Bull Mineral Petrol 76:217-233
Chiarenzelli JR, McLelland JM (1993) Granulite facies metamorphism, palaeo-isotherms and disturbance of the U-Pb systematics of zircon in anorogenic plutonic rocks from the Adirondack Highlands. J Metamor Geol 11:59-70
Chakoumakos BC, Murakami T, Lumpkin GR, Ewing RC (1987) Alpha-decay-induced fracturing in zircon: the transition from the crystalline to the metamict state. Science 236:1556-1559
Charoy B, Raimbault L (1994) Zr, Th, and REE-rich biotite differentiates in the A-type granite pluton of Suzhou (Eastern China): the key role of fluorine. J Petrol 35:919-962
Chen YD, O'Reilly SY, Griffin WL, Krogh TE (1998) Combined U-Pb dating and Sm-Nd studies of lower crustal and mantle xenoliths from the Delegate basaltic pipes, southeastern Australia. Contrib Mineral Petrol 130:154-161
Cherniak DJ, Hanchar JM, Watson EB (1997a) Rare-earth diffusion in zircon. Chem Geol 134:289-301
Cherniak DJ, Hanchar JM, Watson EB (1997b) Diffusion of tetravalent cations in zircon. Contrib Mineral Petrol 127:383-390
Cherniak DJ, Watson EB (2001) Pb diffusion in zircon. Chem Geol 172:5-24
Christoffel CA, Connelly JN, Åhäll K-I (1999) Timing and characterization of recurrent pre-Sveconorwegian metamorphism and deformation in the Varberg-Halmstad region of SW Sweden. Precambrian Res 98:173-195
Connelly JN (2001) Degree of preservation of igneous zonation in zircon as a signpost for concordancy in U/Pb geochronology. Chem Geol 172:25-39
Corfu F, Ayres LD (1984) U-Pb ages and genetic significance of heterogeneous zircon populations in rocks from the Favourable Lake area, northwestern Ontario. Contrib Mineral Petrol 88:86-101
Corfu F, Stott GM (1998) The Shebandowan greenstone belt, western Superior Province: U-Pb ages, tectonic implications and correlations. Geol Soc Am Bull 110:1467-1484
Corfu F, Krogh Ravna E, Kullerud K (2002) A Late Ordovician U-Pb age for HP metamorphism of the Tromsdalstind eclogite in the Uppermost Allochthon of the Scandinavian Caledonides. 12th Annual Goldschmidt Conference, Geochim Cosmochim Acta 77:A153
Crookes W (1879) Contributions to molecular physics in high vacua. Phil Trans Roy Soc 170:641-642
Davidson A, van Breemen O (1988) Baddeleyite-zircon relationships in coronitic metagabbro, Grenville Province, Ontario: Implications for geochronology. Contrib Mineral Petrol 100:291-299
Duchesne JC, Caruba R, Iacconi P (1987) Zircon in charnockitic rocks from Rogaland (southwest Norway): Petrogenetic implications. Lithos 20:357-368
Fletcher IR, Rasmussen B, McNaughton NJ (2000) SHRIMP U-Pb geochronology of authigenic xenotime and its potential for dating sedimentary basins. Austral J Earth Sci 47:845-859
Fowler A, Prokoph A, Stern R, Dupuis C (2002) Organization of oscillatory zoning in zircon: Analysis, scaling, geochemistry, and model of a zircon from Kipawa, Quebec, Canada. Geochim Cosmochim Acta 66:311-328
Gebauer D, Schertl H-P, Brix M, Schreyer W (1997) 35 Ma old ultrahigh-pressure metamorphism and evidence for very rapid exhumation in the Dora Maira Massif, Western Alps. Lithos 41:5-24
Gibson RL, Armstrong RA, Reimold WU (1997) The age and thermal evolution of the Vredefort impact structure: A single-grain zircon study. Geochim Cosmochim Acta 61:1531-1540
Görz H, Bhalla RJRSB, White EW (1970) Detailed cathodoluminescence characterization of common silicates. Space Sci Applic Solid State Luminesc Phen, MRL Publ 70-101:62-70
Grieco G, Ferrario A, von Quadt, A, Koeppel V, Mathez EA (2001) The zircon-bearing chromitites of the phlogopite peridotite of Finero (Ivrea Zone, Southern Alps): Evidence and geochronology of a metasomatized mantle slab. J Petrol 42:89-101
Hacker BR, Ratschbacher L, Webb L, Ireland T, Walker D, Shuwen D (1998) U/Pb zircon ages constrain the architecture of ultrahigh-pressure Qinling-Dabie Orogen, China. Earth Planet Sci Lett 161:215-230
Halden NM, Hawthorne FC (1993) The fractal geometry of oscillatory zoning in crystals: Application to zircon. Am Mineral 78:1113-1116
Hanchar JM, Miller CF (1993) Zircon zonation patterns as revealed by cathodoluminescence and backscattered electron images: Implications for interpretation of complex crustal histories. Chem Geol 110:1-13
Hanchar JM, Rudnick RL (1995) Revealing hidden structures: the application of cathodoluminescence and backscattered electron imaging to dating zircons from lower crustal xenoliths. Lithos 36:289-303
Harrison TM, Watson EB (1983) Kinetics of zircon dissolution and zirconium diffusion in granitic melts of variable water content. Contrib Mineral Petrol 84:67-72
Heaman LM, LeCheminant AN (1993) Paragenesis and U-Pb systematics of baddeleyite ($ZrO_2$). Chem Geol 110:95-126

Hoffman JF, Long JVP (1984) Unusual sector zoning in Lewisian zircons. Mineral Mag 48:513-517
Holland HD and Gottfried D (1955) The effect of nuclear radiation on the structure of zircon. Acta Crystallogr 8:291-300
Hoskin PWO (1999) SIMS determination of μg $g^{-1}$-level fluorine in geological samples and its concentration in NIST SRM 610. Geostand Newslett: J Geostand Geoanal 23:69-76
Hoskin PWO (2000) Patterns of chaos: Fractal statistics and the oscillatory chemistry of zircon. Geochim Cosmochim Acta 64:1905-1923
Hoskin PWO, Black LP (2000) Metamorphic zircon formation by solid-state recrystallization of protolith igneous zircon. J Metamor Geol 18:423-439
Hoskin PWO, Kinny PD, Wyborn D (1998) Chemistry of hydrothermal zircon: Investigating timing and nature of water-rock interaction. *In* Water-rock Interaction. Arehart GB, Hulston JR (eds) Balkema, Rotterdam, The Netherlands, p 545-548
Huneke JC, Rossman GR (1978) Zircons of Summit Rock, Oregon. Mineral Record 392-393
Jocelyn J, Pidgeon RT (1974) Examples of twinning and parallel growth in zircons from some Precambrain granites and gneisses. Mineral Mag 39:587-594
Kamo SL, Reimold WU, Krogh TE, Colliston WP (1996) A 2.023 Ga age for the Vredefort impact event and a first report of shock metamorphosed zircons in pseudotachylitic breccias and Granophyre. Earth Planet Sci Lett 144:369-387
Kinny PD and Dawson JB (1992) A mantle metasomatic injection event linked to Late Cretaceous kimberlite magmatism. Nature 360:723-726
Köppel V, Sommerauer J (1974) Trace elements and the behaviour of the U-Pb system in inherited and newly formed zircons. Contrib Mineral Petrol 43:71-82
Korsakov AV, Shatsky VS, Sobolev NV, Zayachokovsky AA (2002) Garnet-biotite-clinozoisite gneiss: A new type of diamondiferous metamorphic rock from the Kokchetav Massif. Eur J Mineral 14:915-928
Koschek G (1993) Origin and significance of the SEM cathodoluminescence from zircon. J Micros 171:223-232
Kresten P, Fels P, Berggren G (1975) Kimberlitic zircons—a possible aid in prospecting for kimberlites. Mineral Dep 10:47-56
Krinsley DH, Manley CR (1989) Backscattered electron microscopy as an advanced technique in petrography. J Geol Educ 37:202-209
Krogh TE (1982) Improved accuracy of U-Pb zircon ages by the creation of more concordant systems using an air abrasion technique. Geochim Cosmochim Acta 46:637-649
Krogh TE, Davis GL (1974) Alteration in zircons with discordant U-Pb ages. Carnegie Inst Washington Yrbk 73:560-567
Krogh TE, Davis GL (1975) Alteration in zircons and differential dissolution of altered and metamict zircon. Carnegie Inst Washington Yrbk 74:619-623
Krogh TE, McNutt RH, Davis GL (1982) Two high precision U-Pb zircon ages for the Sudbury Nickel Irruptive. Can J Earth Sci 19:723-728
Krogh TE, Davis DW, Corfu F (1984) Precise U-Pb zircon and baddeleyite ages for the Sudbury area. Ontario Geol Surv Spec Vol 1:431-446
Krogh TE, Kamo SL, Bohor BF (1993) Fingerprinting the K/T impact site and determining the time of impact by U-Pb dating of single shocked zircons from distal ejecta. Earth Planet Sci Lett 119:425-429
Krogh TE, Kamo SL, Bohor B (1996) Shock metamorphosed zircons with correlated U-Pb discordance and melt rocks with concordant protolith ages indicate an impact origin for the Sudbury Structure. *In* Earth Processes: Reading the Isotopic Code. Basu A, Hart S (eds) Am Geophys Union, Geophys Monogr 95:343-353
Kröner A, Jaeckel P, Reischman T, Kroner U (1998) Further evidence for an early Carboniferous (~340 Ma) age of high-grade metamorphism in the Saxonian granulite complex. Geol Rundsch 86:751-766
Lee JKW, Tromp J (1995) Self-induced fracture generation in zircon. J Geophys Res 100:17753-17770
Liermann H-P, Isachsen C, Altenberger U, Oberhänsli R (2002) Behaviour of zircon during high-pressure, low-temperature metamorphism: Case study from the Internal Unit of the Sesia Zone (Western Italian Alps). Eur J Mineral 14:61-71
Long JVP, Agrell SO (1965) The cathodoluminescence of minerals in thin section. Mineral Mag 34:318-326
Lopez Sanchez-Vizcaino V, Rubatto D, Gomez-Pugnaire MT, Trommsdorff V, Münterer O. (2001) Middle Miocene high-pressure metamorphism and fast exhumation of the Nevado-Filabride Complex, SE Spain. Terra Nova 13:327-332
Machado N, Goulet N, Gariépy C (1989) U-Pb geochronology of reactivated Archean basement and of Hudsonian metamorphism in the northern Labrador Trough. Can J Earth Sci 26:1-15
Malcuit RJ, Heimlich RA (1972) Zircons from Precambrian Gneiss, southern Bighorn Mountains, Wyoming. Am Mineral 57:1190-1209
Mariano AN (1978) The application of cathodoluminescence for carbonatite exploration and characterization. Proc Intl Symp Carbonatites. Brasil Depart Nac Prod Mineral, Brasilia, 39-57

Mariano AN (1989) Cathodoluminescence emission spectra of rare earth element activators in minerals. Rev Mineral 21:339-348

Marshall DJ (1988) Cathodoluminescence of geological materials. Unwin Hyman, London

Mathieu R, Zetterström L, Cuney M, Gauthier-Lafaye F, Hidaka H (2001) Alteration of monazite and zircon and lead migration as geochemical tracers of fluid paleocirculations around the Oklo-Okélobondo and Bangombé natural nuclear reaction zones (Francesville basin, Gabon). Chem Geol 171:147-171

Mattinson JM, Graubard CM, Parkinson DL, McLelland WC (1996) U-Pb reverse discordance in zircons: the role of fine-scale oscillatory zoning and sub-microscopic transport of Pb. Am Geophys Union, Geophys Monogr 95:355-370

McLaren AC, FitzGerald JD, Williams IS (1994). The microstructure of zircon and its influence on the age determination from U-Pb isotopic ratios measured by ion microprobe. Geochim Cosmochim Acta 58:993-1005

McLelland J, Hamilton M, Selleck B, McLelland J, Walker D, Orrell S (2001) Zircon U-Pb geochronology of the Ottawan Orogeny, Adirondack Highlands, New York: Regional and tectonic implications. Precambrian Res 109:39-72

Medenbach O (1976) Geochemie der Elemente in Zirkon und ihre räumliche Verteilung—eine Untersuchung mit der Elektronenstrahlmikrosonde. Doctoral thesis, Ruprecht-Karl-Universität, Heidelberg, Germany

Miller CF, Hanchar JM, Wooden JL, Bennett VC, Harrison TM, Wark DA, Foster DA (1992) Source region of a granite batholith: Evidence from lower crustal xenoliths and inherited accessory minerals. Trans Roy Soc Edinburgh 83:49-62

Moser DE (1997) Dating the shock wave and thermal imprint of the giant Vredefort impact, South Africa. Geology 25:7-10

Moser DE, Heaman LM (1997) Proterozoic zircon growth in Archean lower crustal xenoliths, southern Superior craton—a consequence of Matachewan ocean opening. Contrib Mineral Petrol 128:164-175

Mulch A, Rosenau M, Dörr W, Handy MR (2002) The age and structure of dikes along the tectonic contact of the Ivrea-Verbano and Strona-Ceneri Zones (southern Alps, Northern Italy, Switzerland). Swiss Bull Mineral Petrol 82:55-76

Murakami T, Chakoumakos BC, Ewing RC, Lumpkin GR, Weber WJ (1991) Alpha-decay event damage in zircon. Am Mineral 76:1510-1532

Myers JS, Crowley JL (2000) Vestiges of life in the oldest Greenland rocks? A review of early Archean geology in the Godthåbsfjord region, and reappraisal of field evidence for >3850 Ma life on Akilia. Precambrian Res 103:101-124

Nemchin AA, Pidgeon RT (1997) Evolution of the Darling Range Batholith, Yilgarn Craton, Western Australia: A SHRIMP zircon study. J Petrol 38:625-649

Nutman AP, Friend CRL, Kinny PD, McGregor VR, (1993) Anatomy of an Early Archaean gneiss complex: 3900 to 3600 Ma crustal evolution in southern West Greenland. Geology 21:415-418

Nutman AP, McGregor VR, Shiraishi K, Friend CRL, Bennett VC, Kinny PD (2002) •3850 Ma BIF and mafic inclusions in the Early Archaean Itsaq Gneiss Complex around Akilia, southern West Greenland? The difficulties of precise dating of zircon-free protoliths in migmatites. Precambrian Res 117:185-224

Oberli F, Meier M, Biino GG (1994) Time constraints on the pre-Variscan magmatic/metamorphic evolution of the Gotthard and Tavetsch units derived from single zircon U-Pb results. Swiss Bull Mineral Petrol 74:483-488

Ohnenstetter D, Cesbron F, Remond G, Caruba R, Claude J-M (1991) Émissions de cathodoluminescence de deux populations de zircons naturels: téntative d'interpretation. C R Acad Sci Paris 313:641-647

Ono A (1976) Chemistry and zoning of zircon from some Japanese granitic rocks. J Japan Assoc Mineral Petrol Econ Geol 71:6-17

Owen MR (1987) Hafnium content of detrital zircons: A new tool for provenance study. J Sed Petrol 57:824-830

Owen MR, Carozzi AV (1986) Southern provenance of upper Jackfork Sandstone, southern Ouachita Mountains: Cathodoluminescence petrology. Geol Soc Am Bull 97:110-115

Palmer HC, Davis DW (1987) Paleomagnetism and U-Pb geochronology of volcanic rocks from Michipicoten Island, Lake Superior, Canada: Precise calibration of the Keweenawan polar wander track. Precambrian Res 37:157-171

Paquette JL, Monchoux P, Couturier M (1995) Geochemical and isotopic study of a norite-eclogite transition in the European Variscan belt: Implications for U-Pb zircon systematics in metabasic rocks. Geochim Cosmochim Acta 59:1611-1622

Paterson BA, Stephens WE (1992) Kinetically induced compositional zoning in titanite: Implications for accessory-phase/ melt partitioning of trace elements. Contrib Mineral Petrol 109:373-385

Paterson BE, Stephens WE, Herd DA (1989) Zoning in granitoid accessory minerals as revealed by backscattered electron imagery. Mineral Mag 53:55-62

Paterson BA, Rogers G, Stephens WE (1992a) Evidence for inherited Sm-Nd isotopes in granitoid zircons. Contrib Mineral Petrol 111:378-390

Paterson BA, Stephens WE, Rogers G, Williams IS, Hinton RW, Herd DA (1992b) The nature of zircon inheritance in two granite plutons. Trans Roy Soc Edinburgh: Earth Sci 83:459-471

Peucat JJ, Bernard-Griffiths J, Gil Ibarguchi JI, Dallmeyer RD, Menot RP, Cornichet J, Iglesias Ponce de León M (1990) Geochemical and geochronological cross-section of the deep Variscan crust: The Cabo Ortegal high-pressure nappe (northwestern Spain). Tectonophysics 177:263-292

Pidgeon RT (1992) Recrystallization of oscillatory zoned zircon: some geochronological and petrological implications. Contrib Mineral Petrol 110:463-472

Pidgeon RT, Nemchin AA, Hitchen GJ (1998) Internal structures of zircons from Archean granites from the Darling Range batholith: Implications for zircon stability and the interpretation of zircon U-Pb ages. Contrib Mineral Petrol 132:288-299

Pidgeon RT, Nemchin AA, Kinny PD (2000) Fir-tree and nebulously zoned zircons from granulite facies rocks: Evidence for zircon growth and interaction with metamorphic fluids. Goldschmidt 2000, J Conf Abstr 5:798

Pin C, Lancelot J (1982) U-Pb dating of an Early Paleozoic bimodal magmatism in the French Massif Central and its further metamorphic evolution. Contrib Mineral Petrol 79:1-12

Poitrasson F, Paquette J-L, Montel J-M, Pin C, Duthou J-L (1998) Importance of late-magmatic and hydrothermal fluids on the Sm-Nd isotope mineral systematics of hypersolvus granite. Chem Geol 146:187-203

Poldervaart A (1956) Zircon in rocks. 2. Igneous rocks. A, J Sci 254:521-554

Poller U (1997) U-Pb single zircon study of gabbroic and granitic rocks of Val Barlas-ch (Silvretta nappe, Switzerland). Swiss Bull Mineral Petrol 77:351-359

Pupin JP (1980) Zircon and granite petrology. Contrib Mineral Petrol 73:207-220

Remond G, Cesbron F, Chapoulie R, Ohnenstetter D, Roques-Carmes C, Schoverer M (1992) Cathodoluminescence applied to the microcharacterization of mineral materials: A present status in experimentation and interpretation. Scan Microsc 6:23-68

Rowley DB, Xue F, Tucker RD, Peng ZX, Baker J, Davis A (1997) Ages of ultrahigh pressure metamorphism and protolith orthogneisses from the eastern Dabie Shan: U/Pb zircon geochronology. Earth Planet Sci Lett 151:191-203

Rubatto D, Gebauer D (1999) Eo/Oligocene (35 Ma) high-pressure metamorphism in the Gornergrat Zone (Monte Rosa, Western Alps): Implications for paleogeography. Swiss Bull Mineral Petrol 79:353-362

Rubatto D, Gebauer D, Fanning M (1998) Jurassic formation and Eocene subduction of the Zermatt-Saas-Fee ophiolites: Implications for the geodynamic evolution of the Central and Western Alps. Contrib Mineral Petrol 132:269-287

Rubin JN, Henri CD, Price JG (1989) Hydrothermal zircons and zircon overgrowths, Sierra Blanca Peaks, Texas. Am Mineral 74:865-869

Rudnick RL, Williams IS (1987) Dating the lower crust by ion microprobe. Earth Planet Sci Lett 85:145-161

Schaltegger U, Gebauer D, von Quadt A (2002) The mafic-ultramafic rock association of Loderio-Biasca (lower Pennine nappes, Ticino, Switzerland): Cambrian oceanic magmatism and its bearing on early Paleozoic paleogeography. Chem Geol 186:265-279

Schaltegger U, Fanning CM, Gunther D, Maurin JC, Schulmann K, Gebauer D (1999) Growth, annealing and recrystallization of zircon and preservation of monazite in high-grade metamorphism: Conventional and *in situ* U-Pb isotope, cathodoluminescence and microchemical evidence. Contrib Mineral Petrol 134:186-201

Schärer U, Zhang L-S, Tapponnier P (1994) Duration of strike slip movement in large shear zones: The Red River belt, China. Earth Planet Sci Lett 126:379-397

Schärer U, Corfu F, Demaiffe D (1997) U-Pb and Lu-Hf isotopes in baddeleyite and zircon megacrysts from the Mbuji-Mayi kimberlite: Constraints on the subcontinental mantle. Chem Geol 143:1-16

Schmitz MD, Bowring SA (2001) The significance of U-Pb zircon dates in lower crustal xenoliths from the southwestern margin of the Kaapvaal Craton, southern Africa. Chem Geol 172:59-76

Schmitz MD, Bowring SA (2002a) High precision U-Pb zircon geochronology of southern African cratonic mantle eclogites and implications for subcontinental lithospheric mantle evolution and metasomatism. EOS Trans, Am Geophys Union 83:S376

Schmitz, MD, Bowring SA (2002b) Ultrahigh-temperature metamorphism in the lower crust during Neoarchean Ventersdorp rifting and magmatism, Kaapvaal Craton, southern Africa. Geol Soc Am Bull (in press)

Scoates JS, Chamberlain KR (1995) Baddeleyite ($ZrO_2$) and zircon ($ZrSiO_4$) from anorthositic rocks of the Laramie anorthosite complex, Wyoming: Petrologic consequences and U-Pb ages. Am Mineral 80:1317-1327

Silver LT, Deutsch S (1963) Uranium-lead isotopic variations in zircons: A case study. J Geol 71:721-758

Sippel RF (1968) Sandstone petrology, evidence from luminescence petrography. J Sed Petrol 38:530-554

Sippel RF (1971) Luminescence petrography of the Apollo 12 rocks and comparative features in terrestrial rocks and meteorites. Proc Second Lunar Conf 1. MIT, Cambridge, Massachusetts, p 247-263

Smith DGW, de St. Jorre L, Reed SJB, Long JVP (1991). Zonally metamictized and other zircons from Thor Lake, Northwest Territories. Can Mineral 29:301-309

Smith JV, Stenstrom RC (1965) Electron-excited luminescence as a petrologic tool. J Geol 73:627-635

Sommerauer J (1974) Trace element distribution patterns and the mineralogical stability of zircon—an application for combined electron microprobe techniques. Electron Micros Soc S Afr Proc 4:71-72

Speer JA (1982) Zircon. Rev Mineral 5(2nd edn):67-112

van Breemen O, Davidson A, Loveridge WD, Sullivan RW (1986) U-Pb zircon geochronology of Grenville tectonites, granulite and igneous precursors, Parry Sound, Ontario. *In* The Grenville Province, Moore JM, Davidson A, Baer AJ (eds) Geol Assoc Can Spec Paper 3, p 191-207

van Breemen O, Henderson JB, Loveridge WD, Thompson PH (1987) U-Pb zircon and monazite geochronology and zircon morphology of granulites and granite from the Thelon Tectonic Zone, Healey Lake and Artillery Lake map areas, N.W.T. Geol Surv Can Paper 87-1A:783-801

Vavra G (1990) On the kinematics of zircon growth and its petrogenetic significance: A cathodoluminescence study. Contrib Mineral Petrol 106:90-99

Vavra G (1993) A guide to quantitative morphology of accessory zircon. Chem Geol 110:15-28

Vavra G, Hansen BT (1991) Cathodoluminescence studies and U-Pb dating of zircons in pre-Mesozoic gneisses of the Tauern Window: Implications for the Pennine basement evolution. Geol Rundsch 80:703-715

Vavra G, Gebauer D, Schmid R, Compston W (1996) Multiple zircon growth and recrystallization during polyphase Late Carboniferous to Triassic metamorphism in granulites of the Ivrea zone (Southern Alps): An ion microprobe (SHRIMP) study. Contrib Mineral Petrol 122:337-358

Viskupic K (2003) Crustal melting in the Himalayan orogen: field, geochemical and geochronological studies in the Everest region, Nepal. PhD thesis, Massachusetts Institute of Technology, 190 p

Vocke RD Jr, Hanson GN (1981) U-Pb zircon ages and petrogenetic implications for two basement units from Victoria valley, Antarctica. *In* Antarctica Research Series, Dry Valley Drilling Project. McGinnis L (ed) Am Geophys Union, Washington, DC, 33:247-255

Watson EB (1979) Zircon saturation in felsic liquids: Experimental results and applications to trace element geochemistry. Contrib Mineral Petrol 70:407-419

Watson EB (1996) Dissolution, growth and survival of zircons during crustal fusion: kinetic principles, geological models and implications for isotopic inheritance. Trans Roy Soc Edinburgh: Earth Sci 87:43-56

Watson EB, Harrison TM (1983) Zircon saturation revisited: temperature and composition effects in a variety of crustal magma types. Earth Planet Sci Lett 64:295-304

Watson EB, Liang Y (1995) A simple model for sector zoning in slowly grown crystals: Implications for growth rate and lattice diffusion, with emphasis on accessory minerals in crustal rocks. Am Mineral 80:1179-1187

Watson EB, Vicenzi EP, Rapp RP (1989) Inclusion/host relations involving accessory minerals in high-grade metamorphic and anatectic rocks. Contrib Mineral Petrol 101:220-231

Watson EB, Cherniak DJ, Hanchar JM, Harrison, TM, Wark DA (1997) The incorporation of Pb into zircon. Chem Geol 141:19-31

Wayne DM, Sinha AK (1988) Physical and chemical response of zircons to deformation. Contrib Mineral Petrol 98:109-121

Wayne DM, Sinha AK (1992) Stability of zircon U-Pb systematics in a greenschist-grade mylonite: an example from the Rockfish Valley fault zone, central Virginia, USA. J Geol 100:593-603

Welin E, Gorbatschev R, Kähr A-M (1982) Zircon dating of polymetamorphic rocks in southwestern Sweden. Sver Geol Unders C797:1-34

Whitehouse MJ, Kamber BS, Moorbath S (1999) Age significance of U-Th-Pb zircon data from early Archaean rocks of West Greenland-a reassessment based on combined ion-microprobe and imaging studies. Chem Geol 160:201-224

Yang B, Luff, BJ, Townsend, PD (1992) Cathodoluminescence of natural zircons. J Phys: Condens Matter 4:5617-5624

Zeck HP, Williams IS (2002) Inherited and magmatic zircon from Neogene Hoyazo cordierite dacite, SE Spain—anatectic source rock provenance and magmatic evolution. J Petrol 43:1089-1104